

DELIVERABLE

D10.1 - Technical report on SERA Transnational Access activities TA1-TA10 M36

Work package	WP8-WP17
Lead	EU CENTRE
Authors	<p>I. Lanese, A. Pavese, E. Rizzo Parisi, M. Furinghetti (EU CENTRE); M. Lamperti Tornaghi, G. Tsionis, P. Pegon, J. Molina, M. Peroni (JRC); V. Crozet, I. Politopoulos, T. Chaudat, S. Vasic, A. Le Maout, G. Rastello (CEA); A.A. Correia, P.X. Candeias, A. Campos Costa, F.L. Ribeiro (LNEC); S. Bousias, X. Palios, N. Stathas, E. Strepelias (University of Patras); C. Cengiz, F. De Luca, M. Dietz, L. Dihoru, D. Karamitros, G. Mylonakis, A. Sextos, A. Crew, R. De Risi, R. White, C. Taylor (University of Bristol); Z. Rakicevic, A. Bogdanovic, L. Krstevska, R. Apostolska, G. Jekic, I. Gjorgjiev, B. Petreski, A. Poposka, F. Manojlovski, A. Shoklarovski (IZIIS); A. Fusco, S.P.G. Madabhushi, G. Viggiani, S.K. Haigh, T. Garala (University of Cambridge); A. Vratsikidis, M. Manakou, A. Anastasiadis, C. Amendola, S. Argyroudis, D. Pitilakis (EUROSEISTEST and EUROPROTEAS); J. Schweitzer, A. Meslem (NORSAR); TA users: G. Abate, G. Abbiati, O. Adamidis, K. Agis, D. Aliperti, J. Almeida, I. Anastasopoulos, G. Angjeliu, G. Anoyatis, M. Antonelli, C. Antonopoulos, Z.A. Arama, B.B. Ayraçma, I.E. Bal, S. Baraccani, E. Bayram, A. Benavent-Climent, A. Benedetti, L. Berto, K. Beyer, S. Bhattacharya, S. Bianchi, N. Bianchini, E. Bilotta, S. Biondi, C. Boursianis, G. Brando, B. Briseghella, M. Broccardo, B. Broderick, O. Bursi, C. Butenweg, R. Cairo, C. Calderini, P. M. Calvi, G. Camata, G. Caputo, S. Carbonari, P. Casadei, M.G. Castellano, X. Chen, C. Chrysostomou, U. Çilingir, M. Ciucci, J. Ciurlanti, E. Conte, R. Conti, D. Coronelli, S. Corsico, P. Covi, M. Dall'Acqua, L. Danciu, M. D'Aniello, L. De Dancis, M. DeJong, J. De Novais Bastos, F. De Silva, F. Dezi, S. Diamantopoulos, R. Di Laora, F. Di Michele, R. Dinescu, L. Di Sarno, J. Distl, M.</p>

Dolšek, P. El Boueiz, A. Elghazouli, A. Elkady, FG. Esfahani, M. Ferreira, A. Filiatrault, G. Fiorentino, M. Fishinger, J. Fisker, J. Fontiela, F. Fossi, D. Foti, M. Fragiadakis, F. Freddi, A. Gajo, C. Galasso, M. Gams, F. Gara, F. Gatti, B. Ghiassi, B. Gilardi, A. Goev, J. Goggins, S. Grammatikou, G. Granello, D. Grant, S. Grasso, G. Guerrini, S. Gunay, L. Hagsten, E. Hernández-Montes, T.C. Hutchinson, A. Ilki, M. Infantino, M. Iovino, T. Isakovic, S. Ivorra, Y. Jiang, V. Kapetanidis, T. L. Karavasilis, M. Karpala, K. Kassas, A.M. Kaynia, A. Kazantzi, P. Kloukinas, K. Kolozvari, S. Kontoe, M. Koronides, M. Korzen, M. Kosič, P. Kotronis, P. Kowalczyk, M. Kramar, A. Kwiecień, O-S. Kwon, N. Kyriakides, R. Landolfo, D. Lavorato, D. Lignos, F. Lopes-Caballero, P. Lourenço, E. Lozinca, D. Malomo, G. Manolis, S. Mansour, M. Marinković, M. Mariotti, E. Marotti, L. Martinelli, A. Marzani, M.R. Massimino, N. Mendes, B. Mihaylov, E. Miranda, G. Miranda, S. Mitoulis, K. Mosalam, A. Muttoni, V. Nappa, C. Nardin, T. Netti, C. Nuti, U. Ozcamur, A.G. Ozcebe, S. Öztoprak, A. Pagliaroli, A. Palermo, M. Palmieri, S. Pampanin, F. Paolacci, R. Pascu, A. Penna, D. Perrone, E.-V. Picoulis, A. Pinho Ramos, A. Plötz, V. Popa, C. Prum, I. Psycharis, V. Quaglini, G. Quinci, L. Ragni, S. Riemer, I. Rocca, M. Rossi, T. Rousakis, E. Rovithis, A. Sadowski, A. Saetta, S. Salawdeh, I. Senaldi, F. Silvestri, S. Silvestri, A.L. Simonelli, C. Smerzini, E. Smyrou, T. Sonneman, E. Spacone, B. Stojadinovic, H. Sucuoğlu, I. Taflampas, T. Taniguchi, B. Teymür, D. Theodossopoulos, I. Tomić, N. Tondini, A. Topa Gomes, S. Touhami, A. Trandafir, E. Tubaldi, V. Vacca, D. Vamvatsikos, H. Varum, M. F. Vassiliou, A. Viskovic, C. Vrettos, J. Wallace, F. Weber, B. Zajac, L. Zdravkovic, F. Zeighami, K.-U. Ziener, F. Zotti

Reviewers S. Peloso, R. Nascimbene (EUCENTRE)

Approval Management Board

Status Final

Dissemination level Public

Delivery deadline 30.04.2020

Submission date 27.04.2020

Intranet path DOCUMENTS/DELIVERABLES/SERA_D10.1_Technical_report_on_SERA_Transnational_Access_activities_TA1-TA10_M36

Table of Contents

Summary	15
1 JRC ELSA	21
1.1 Project #1 – EQUFIRE - Multi-hazard performance assessment of structural and non-structural components subjected to seismic and fire following earthquake by means of geographically distributed testing	22
1.1.1 Introduction.....	22
1.1.2 Design of the test specimen	23
1.1.3 Experimental programme and setup at BAM	26
1.1.4 Experimental programme and setup at JRC	27
1.1.5 Simulation algorithm for the hybrid tests.....	28
1.1.6 Experimental results.....	30
1.1.7 Main outcomes and discussion	33
1.1.8 References.....	34
1.2 Project #2 – SlabSTRESS - SLAB STructural RESponse for Seismic European Design	35
1.2.1 Introduction.....	35
1.2.2 Test specimen.....	37
1.2.3 Experimental programme and setup.....	40
1.2.4 Pseudo-dynamic tests	41
1.2.5 Cyclic tests	42
1.2.6 Loading system.....	42
1.2.7 Transducers for local measurements	42
1.2.8 Observation during testing.....	43
1.2.9 Conclusions and outlook	44
1.2.10 References.....	44
2 EUCENTRE	47
2.1 Project #3 – Dynamic testing of variable friction seismic isolation devices and isolated systems	48
2.1.1 Introduction.....	48
2.1.2 Main research objectives and expected contribution to the seismology and earthquake engineering community	49
2.1.3 Numerical-Experimental Testing campaign	52
2.1.4 Development of a 3D VFS numerical model.....	58
2.1.5 OpenSees implementation	59
2.1.6 Partial processing of the experimental results and preliminary validation of VFS model..	60
2.1.7 Development of a Direct Displacement-Based Design procedure for structures isolated via VFS	60
2.1.8 Validation of the proposed design method via extensive parametric study	62

2.1.9	VFS performance evaluation via extensive parametric study.....	63
2.1.10	Investigation of using VFS as passive adaptive devices	65
2.1.11	Conclusions and outlook	70
2.2	Project #18 – SEismic Response of Actual steel SILOS (SERA-SILOS)	71
2.2.1	Introduction.....	71
2.2.2	Test specimen.....	72
2.2.3	Analytical predictions and numerical models.....	73
2.2.4	Test setup: instrumentation and setup	75
2.2.5	Observation during testing.....	78
2.2.6	Preliminary results.....	81
2.2.7	Conclusions and outlook	86
2.2.8	References.....	86
2.3	Project #34 – Seismic performance of multi-component systems in special risk industrial facilities	87
2.3.1	Introduction.....	87
2.3.2	Three storey steel moment resisting frame with installations	88
2.3.3	Numerical model, modal analysis, preliminary simulation results	91
2.3.4	Test set-up and measurements.....	95
2.3.5	Observation during testing.....	99
2.3.6	Preliminary results.....	101
2.3.7	Conclusions and outlook	107
2.3.8	Literature.....	108
3	CEA	110
3.1	Project #4 – SE.RE.ME. – Seismic Resilience of Museum contEnts.....	110
3.1.1	Introduction.....	110
3.1.2	Museum contents tested	113
3.1.3	Numerical simulations	119
3.1.4	Test setup	122
3.1.5	Observations and preliminary results.....	126
3.1.6	Conclusions	128
3.1.7	List of publications.....	129
3.1.8	References.....	129
3.2	Project #5 –Full-scale experimental validation of steel moment frame with EU qualified joints and energy efficient claddings under near fault seismic scenarios	130
3.2.1	Introduction.....	130
3.2.2	Specimen.....	131
3.2.3	Numerical simulations	133
3.2.4	Test setup	142

3.2.5	Conclusion	143
4	LNEC	144
4.1	Project #6 – (Towards the) Ultimate Earthquake proof Building System: development and testing of integrated low-damage technologies for structural and non-structural elements	145
4.1.1	Introduction.....	145
4.1.2	Test specimens	147
4.1.3	Numerical prediction	150
4.1.4	Test setup	151
4.1.5	Observation during testing.....	154
4.1.6	Preliminary results.....	155
4.1.7	Conclusions	158
4.1.8	References.....	158
4.2	Project #7 – Seismic Response of Masonry Cross Vaults: shaking table tests and numerical validations	159
4.2.1	Introduction.....	160
4.2.2	Test specimens	162
4.2.3	Numerical simulations	165
4.2.4	Test setup	166
4.2.5	Observation during testing.....	168
4.2.6	Preliminary results.....	170
4.2.7	Conclusions	170
4.2.8	References.....	171
4.3	Project #19 – Seismic Testing of Adjacent Interacting Masonry Structures (AIMS)	172
4.3.1	Introduction.....	172
4.3.2	Test unit.....	173
4.3.3	Numerical simulations	177
4.3.4	Test setup	178
4.3.5	Preliminary results.....	180
4.3.6	Conclusions	182
4.3.7	References.....	183
5	STRULAB - University of Patras.....	185
5.1	Project #8 – ARISTA – Seismic Assessment of ReInforced Concrete frames with SmooTh bArs – Proposals for EC8-Part 3	185
5.1.1	Introduction.....	185
5.1.2	Test structure	187
5.1.3	Test setup and testing program	189
5.1.4	Results	190
	Global Response	190

Flexural behaviour of columns	191
Beam/column joints	194
Bar strains.....	195
Concrete strains	197
Effects and behaviour of the FRP overlays at joints and around column ends.....	198
5.1.5 Conclusions and outlook	199
5.2 Project #9 – ARCO – Effect of Axial Restraint on the Seismic Behaviour of Shear-Dominated Coupling Beams.....	200
5.2.1 Introduction.....	200
5.2.2 Test specimens.....	201
Geometrical properties, reinforcement layout and material properties.....	201
5.2.3 Test setup	203
Loading procedure	206
5.2.4 Test Results	207
Specimen RB1.....	207
Specimen RB2.....	208
Specimen RB3.....	209
RB4 specimen	211
Effect of axial restraint	212
Effect of longitudinal reinforcement ratio and loading history	214
5.2.5 Conclusions	215
5.3 Project #20 – hybrid Testing of an Existing Steel FRaMe with Infills under Multiple EarthquakeS (HITFRAMES)	216
5.3.1 Introduction.....	216
5.3.2 Test specimen.....	217
5.3.3 Numerical prediction.....	219
5.3.4 Test setup.....	222
5.3.5 Observation during testing.....	226
5.3.6 Preliminary results.....	228
5.3.7 Conclusions and outlook	229
6 University of Bristol	231
6.1 Project #10 – SERENA – Seismic Response of Novel Integral Abutment-Bridges	232
6.1.1 Introduction.....	232
6.1.2 Identification of prototype	233
6.1.3 Scaling Prototype to Model.....	234
6.1.4 Test configuration and instrumentation layout.....	236
6.1.5 Observation during testing.....	241
6.1.6 Preliminary results.....	243

6.1.7	Conclusions and outlook	246
6.1.8	References.....	247
6.2	Project #11 – 3DRock - Statistical verification and validation of 3D seismic rocking motion models	248
6.2.1	Introduction.....	248
6.2.2	Specimens	250
	Free Rocking specimens (Figure 362)	250
	Wobbling Frame specimen (Figure 363 and Figure 364).....	251
6.2.3	Test setup	251
	Excitations	251
6.2.4	Scaling of the ground motion ensembles	254
	Instrumentation	254
6.2.5	Observations during testing	254
6.2.6	Preliminary results.....	255
	Free Rocking columns.....	255
	Wobbling Frame	256
6.2.7	Conclusions and outlook	258
6.2.8	References.....	259
6.3	Project #12 – REBOND – REsponse of as-Built and strengthened three-leaf masONry walls by Dynamic tests	262
6.3.1	Introduction.....	262
6.3.2	Wall design	263
6.3.3	Seismic input	264
	Dynamic tests	266
6.3.4	Test configuration and instrumentation layout.....	268
	Base	269
	Wall	270
	Support system.....	271
	Steel frame top and additional mass.....	272
	Reinforcement by KERAKOLL group	275
6.3.5	Preliminary results.....	276
6.3.6	Conclusions and outlook	277
6.3.7	References.....	278
6.4	Project #21 – NSFUSE - Ductile steel fuses for the protection of critical non-structural components	279
6.4.1	Introduction.....	279
6.4.2	Test specimen.....	281
6.4.3	Numerical model / prediction / simulation	283

6.4.4	Test setup	285
6.4.5	Test observations	286
6.4.6	Results / Preliminary results	287
6.4.7	Conclusions and outlook	292
6.4.8	References.....	292
6.5	Project #22 – SEBESMOVA3D - SEismic BEhavior of Scaled MOdels of groin VAults made by 3D printers (SEBESMOVA3D).....	293
6.5.1	Introduction.....	293
6.5.2	Design of the vault prototype.....	294
6.5.3	Test setup (construction phases)	296
6.5.4	Testing instrumentation	297
6.5.5	Testing program	298
6.5.6	Observation during testing: dynamic properties.....	300
6.5.7	Preliminary results: collapse behaviour and numerical modelling	302
6.5.8	Conclusions and outlook	306
6.5.9	References.....	307
6.6	Project #35 – SHATTENFEE - SHaking Table TEsting for Near Fault Effect Evaluation (SHATTENFEE)	307
6.6.1	Introduction.....	308
6.6.2	Identification of prototype and preliminary analysis.....	309
6.6.3	From the Prototype to the Model	312
	Scaling factors - geometry	312
	Scaling factors – Time	312
6.6.4	Test configuration	313
6.6.5	Test rig.....	313
6.6.6	Instrumentation layout.....	314
6.6.7	Test phases.....	315
6.6.8	Preliminary results.....	317
	Vertical dynamic identification.....	317
	Compression wave velocity V_p	318
	Response in terms of amplification	319
6.6.9	Conclusions and outlook	320
6.6.10	References.....	321
6.7	Project #36 – SSI-STEEL Soil-Structures Interaction effects for STEEL structures.....	322
6.7.1	Introduction.....	322
6.7.2	Identification of prototypes: Design of the frames to be tested	324
6.7.3	Scaling Prototype to Model	330
6.7.4	Test configuration and instrumentation layout.....	330

6.7.5	Preliminary results.....	335
6.7.6	Conclusions and outlook	335
6.7.7	References.....	337
7	IZIIS DYNLAB - University in Skopje.....	339
7.1	Project #13 - Influence of the floor to piers interaction on the seismic response of coupled wall systems	340
7.1.1	Introduction.....	340
7.1.2	Test unit_MODEL01.....	341
7.1.3	Test setup	342
7.1.4	Testing protocol	345
7.1.5	Observation during testing.....	347
7.1.6	Results	348
7.1.7	Test unit_MODEL02.....	351
7.1.8	Test setup	353
7.1.9	Testing protocol	356
7.1.10	Observation during testing.....	358
7.1.11	Results	358
7.1.12	Conclusions and outlook	362
7.2	Project #23 – Investigation of Seismic Deformation Demand, Capacity and Control in a Novel Self-Centring Steel Braced Frame (SC-CBF)	363
7.2.1	Introduction.....	363
7.2.2	Test specimen.....	365
7.2.3	Test setup	367
7.2.4	Observation during testing.....	376
7.2.5	Results	377
7.2.6	Conclusions and outlook	379
7.2.7	References.....	380
7.3	Project #37 – INFills and MASONry structures protected by deformable POLyurethanes in seismic areas (INMASPOL).....	381
7.3.1	Introduction.....	382
7.3.2	Test specimen.....	382
7.3.3	Test setup	383
7.3.4	Observation during testing.....	387
7.3.5	Results	388
	Setup with wall infills type B tested in-plane (Phase A and A').....	388
	Setup with wall infills type C tested in-plane (Phase B and B')	389
7.3.6	Conclusions and outlook	391
8	University of Cambridge	392

8.1	Project #14 – Seismic behaviour of anchored Steel Sheet-Piling (SSP) retaining walls: experimental investigation, theoretical interpretation and guidelines for design	393
8.1.1	Summary of the project.....	393
8.1.2	Main research objectives and expected contribution to the seismology and earthquake engineering community	394
8.1.3	Project status.....	394
8.1.4	Conclusions	398
8.2	Project #15 – STILUS – Structure-Tunnel Interaction in Liquefiable Sand	399
8.2.1	Summary of the project.....	399
8.2.2	Model Layouts	402
8.2.3	Experimental Results	404
8.2.4	Conclusions	408
8.3	Project #24 – Seismic Behaviour of Rigid Pile Inclusions	409
8.3.1	Introduction.....	409
8.3.2	Test specimen.....	409
8.3.3	Test setup	411
8.3.4	Results	412
8.3.5	Conclusions	415
8.4	Project #25 – COSMO: Change Of Seismic MOtion due to pile-soil kinematic interaction..	416
8.4.1	Introduction.....	416
	Objectives.....	416
8.4.2	Test specimens.....	418
	MODEL CONTAINER.....	418
	MODEL PILE FOUNDATION AND SUPERSTRUCTURE	418
	CLAY.....	421
	INSTRUMENTS	421
	T-BAR PENETROMETER	421
8.4.3	Test setup	422
8.4.4	Results	425
8.4.5	Conclusions	433
9	EUROSEISTEST and EUROPROTEAS	436
9.1	Project # 16 – IMPEC – On the broadband synthetic signals enhancement for 3D Physic based numerical analysis, the EUROSEISTEST Case study.....	437
9.1.1	Introduction.....	437
9.1.2	EUROSEISTEST Array.....	438
9.1.3	Numerical model	439
9.1.4	Test setup	440
9.1.5	Observation during testing.....	440

9.1.6	Results	440
9.1.7	Conclusions and outlook	443
9.1.8	References.....	443
9.2	Project # 26 – Dynamic Soil Structure Interaction: Three-dimensional Time-domain Analysis of Field Model Scale Experiments	445
9.2.1	Introduction.....	445
9.2.2	EUROPROTEAS.....	448
9.2.3	Numerical model	449
9.2.4	Test setup	451
9.2.5	Observation during testing.....	453
9.2.6	Results	454
9.2.7	Conclusions and outlook	457
9.2.8	References.....	459
9.3	Project # 27 – SISIFO – Seismic Impedance for Soil-structure Interaction From On-site tests ..	460
9.3.1	Introduction.....	460
9.3.2	EUROPROTEAS.....	461
9.3.3	Background.....	462
9.3.4	Test setup	464
9.3.5	Observations during testing.....	467
9.3.6	Results	468
9.3.8	References.....	475
9.4	Project # 28 – Ambient and forced vibration techniques for improving design and performance assessment of structures with consideration of soil-structure interaction	477
9.4.1	Introduction.....	477
9.4.2	EUROPROTEAS.....	478
9.4.3	Test setup	479
9.4.4	Observation during testing.....	481
9.4.5	Results	482
9.4.6	Conclusions and outlook	492
9.4.7	References.....	494
9.5	Project # 29 – Seismic SITE effects in sedimentary basins from 3D physics-based numerical modeling (SITE3D)	494
9.5.1	Introduction.....	494
9.5.2	EUROSEISTEST Array.....	495
9.5.3	Numerical model	496
9.5.4	Test setup	499
9.5.5	Observation during testing.....	499
9.5.6	Preliminary results.....	499

9.5.7	Conclusions and outlook	504
9.5.8	References.....	504
9.6	Project # 30 – Comparison of rocking on rigid and compliant base using the EUROPROTEAS real-scale facility.....	505
9.6.1	Introduction.....	505
9.6.2	EUROPROTEAS.....	507
9.6.3	Numerical model / prediction / simulation	508
9.6.4	Test setup	510
9.6.5	Observation during testing.....	513
9.6.6	Results	515
9.6.7	Conclusions and outlook	521
9.6.8	References.....	522
9.7	Project # 38 – Resonant metamaterial-based earthquake risk mitigation of large-scale structures and infrastructure systems: assessment of an innovative proof-of-concept via medium-size scale testing.....	523
9.7.1	Introduction.....	524
9.7.2	Test object.....	525
9.7.3	Numerical simulations	527
9.7.4	Test setup	528
9.7.5	Observation during tests	531
9.7.6	Preliminary Results.....	531
9.7.7	Conclusions and outlook	534
9.7.8	References.....	535
9.8	Project # 39 – “DYMOBRIS” Dynamic identification and Monitoring of scoured BRIdgeS under earthquake hazard	536
9.8.1	Introduction.....	536
9.8.2	EUROPROTEAS.....	538
9.8.3	Numerical model and predictions	539
9.8.4	Test setup	544
9.8.5	Observation during testing.....	546
9.8.6	Preliminary results.....	546
9.8.7	References.....	549
9.9	Project # 40 – SOil Frame-Interaction Analysis through large-scale tests and advanced numerical finite element modeling (Acronym: SOFIA)	551
9.9.1	Introduction.....	551
9.9.2	EUROPROTEAS.....	552
9.9.3	Numerical model	555
9.9.4	Test setup	556
9.9.5	Observation during testing.....	558

9.9.6	Results	561
9.9.7	Conclusions and outlook	564
9.9.8	References.....	564
10	NORSAR.....	568
10.1	Project # 17 – Blind beamforming in array processing.....	569
10.1.1	Project Summary	569
10.1.2	Main Research Objectives	569
10.1.3	Main Research Outcomes and Outlook.....	570
10.2	Project #31 – Seismic tremor detection in Greece using small aperture arrays.....	570
10.2.1	Project Summary	570
10.2.2	Main Research Objectives	571
10.2.3	Main Research Outcomes and Outlook.....	571
10.3	Project #32 – A new velocity model up to 300 km deep based on receiver function data from the NORES array (Baltic Shield)	572
10.3.1	Project Summary	572
10.3.2	Main Research Objectives	572
10.3.3	Main Research Outcomes and Outlook.....	573
10.4	Project #33 – Joint processing of seismo-acoustic array data as tool to discriminate between man-made explosions and earthquakes.....	573
10.4.1	Project Summary	573
10.4.2	Main Research Objectives	574
10.4.3	Main Research Outcomes and Outlook.....	574
10.5	Project #41 – Earthquake Spectral Provisions and Urban Fragility Evaluation - ESPUFE	575
10.5.1	Project Summary	575
10.5.2	Main Research Objectives	575
10.5.3	Main Research Outcomes and Outlook.....	576
10.6	Project #42 – Beamforming of aftershock strong-motion time-histories recorded on the ICEARRAY for earthquake source studies	577
10.6.1	Project Summary	577
10.6.2	Main Research Objectives	577
10.6.3	Main Research Outcomes and Outlook.....	577
10.7	Project #43 – Investigation of (micro-)seismicity of the Laptev Sea using a small-aperture array	578
10.7.1	Project Summary	578
10.7.2	Main Research Objectives	578
10.7.3	Main Research Outcomes and Outlook.....	579
10.8	Project 44 – Design, location and processing of a regional array in SW Portugal - Europe	579
10.8.1	Project Summary	579
10.8.2	Main Research Objectives	580

10.8.3	Main Research Outcomes and Outlook.....	580
10.9	References.....	580
Contact	582

Summary

The SERA project, funded by the European Union within the Horizon 2020 Research and Innovation programme under grant agreement No.730900, involved in the Transnational Access (TA) framework 44 User Groups composed by 261 EU and extra-EU talented researchers.

TA offers a combined and integrated access to the largest collection of high-class experimental facilities for earthquake engineering in Europe – and worldwide – including reaction walls, shake tables, bearing testing facilities and centrifuges, to two facilities for integrated studies on geotechnical site effects and engineering seismology, and to a unique infrastructure in Europe for array seismology.

TA provides to the selected researchers access to the infrastructures for the design and the implementation of the testing campaign under several points of view. The services provided to the users, starting from the collaboration with national and international experts in the field, include technical assistance in the definition of the specimen, the testing setup and protocol, assistance for the proper instrumentation choice and positioning, data-processing, results interpretations and advanced numerical modeling.

Proposals have been submitted by heterogeneous User Groups, composed by both universities and private companies often in joined applications, coming from 31 different countries. The selected proposals addressed a very wide spectrum of topics, ranging from the further improvement of the most advanced testing techniques, such as dynamic hybrid and geographically distributed testing, to the vulnerability of existing historical buildings, industrial facilities, bridges, to design code improvement and large database analysis. In Figure 1 and Figure 2, pictures of 2 of the 44 experimental testing campaigns are shown.



Figure 1: SLABSTRESS project @JRC Research Infrastructure



Figure 2: SERA-SILOS project @EUCENTRE Research Infrastructure

The best and most innovative proposals have been selected by a panel of international experts (TA-SEP – Selection and Evaluation Panel –) through a grading based on multiple criteria:

- Fundamental Scientific and Technical value and interest
- Originality and innovation
- Quality of proposing team
- Importance for public safety
- Importance for European standardisation
- Importance for European integration and cohesion
- Importance for sustainable growth
- Importance for European competitiveness
- Importance and relevance to TA facility's own scientific interest
- Synergies and complementarities with other TA tests
- Previous use of TA facility by any in the user team
- Cost and feasibility according to TA facility
- Availability of similar infrastructures in any of the users' countries

The 10 Research Infrastructures (RIs) offering TA within SERA are very experienced and very well trained in the implementation of experimental campaigns and collaboration with international researchers. In Table 1 the consortium RIs are listed.

SERA TA FACILITIES

• ELSA Reaction Wall, JRC, Ispra (IT)
• Shake Lab Bearing Tester and Shake Table, EUCENTRE, Pavia (IT)
• AZALEE Shake Table TAMARIS/CEA, Paris (FR)
• LNEC-3D Shake Table LNEC, Lisbon (PT)
• STRULAB Reaction Wall, University of Patras, Patras (GR)
• EQUALS Shake Table, University of Bristol, Bristol (UK)
• DYNLAB Shake Table IZIIS, Skopje (MK)
• Centrifuge University of Cambridge, Cambridge (UK)
• EUROSEISTEST and EUROPROTEAS, Aristotle University, Thessaloniki (GR)
• Array Seismology NORAR, Kjeller (NO)

Table 1: SERA TA Research Infrastructures

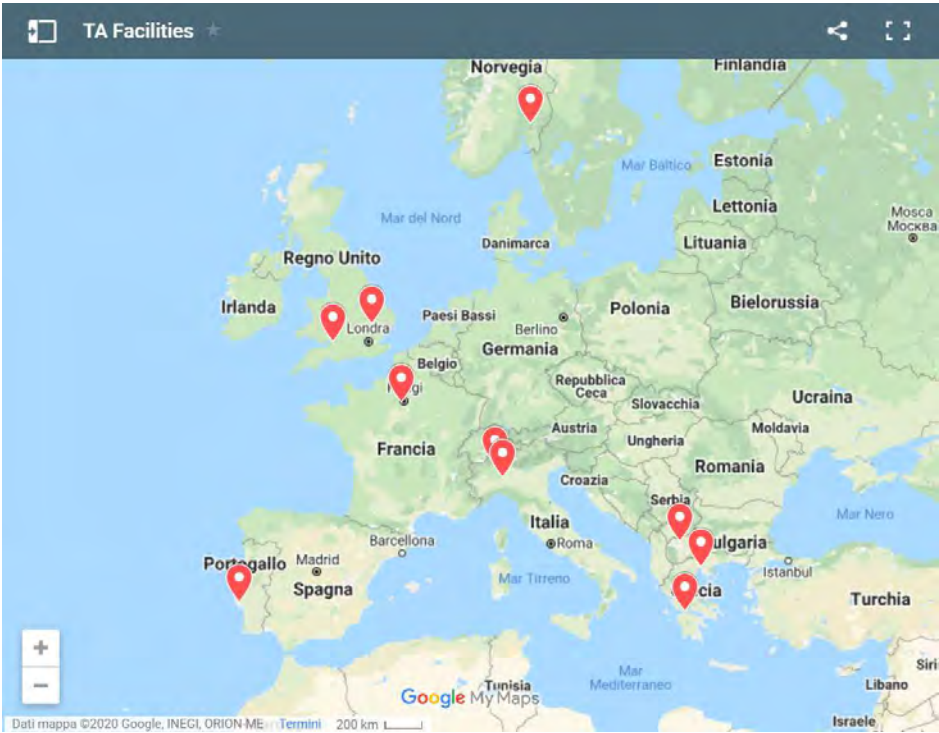


Figure 3: SERA TA Research Infrastructures location

In the following tables, the projects selected across the three calls for proposal and the hosting infrastructure are listed.

PROJECTS SELECTED IN THE 1st CALL FOR PROPOSALS

Number of Project	Title of Project	Hosting Research Infrastructure
1	EQUFIRE – Multi-hazard performance assessment of structural and non-structural components subjected to seismic and fire following earthquake by means of geographically distributed testing	JRC
2	SLAB STRESS – SLAB STructural RESponse for Seismic European Design	JRC
3	Dynamic testing of variable friction seismic isolation devices and isolated systems	EUCENTRE
4	SE.RE.M.E. – SEismic RESilience of Museum contEnts	CEA
5	FUTURE – Full-scale experimental validation of steel moment frame with EU qualified joints and energy efficient claddings under near fault seismic scenarios	CEA
6	(Towards the) Ultimate Earthquake proof Building System: development and testing of integrated low-damage technologies for structural and non-structural elements	LNEC
7	Seismic Response of Masonry Cross Vaults: Shaking table tests and numerical validations	LNEC
8	ARISTA – Seismic Assessment of ReInforced Concrete frames with SmooTh bArs – Proposals for EC8-Part 3	STRULAB
9	ARCO – Effect of Axial Restraint on the Seismic Behaviour of Shear-Dominated COupling Beams	STRULAB
10	Seismic Response of Novel Integral Abutment-Bridges	University of Bristol
11	Statistical verification and validation of 3D seismic rocking motion models	University of Bristol
12	RE-BOND – REsponse of as-Built and strengthened three-leaf masONry walls by Dynamic tests	University of Bristol
13	Influence of the floor-to-wall interaction on the seismic response of coupled wall systems	IZIIS
14	Seismic behaviour of anchored Steel Sheet-Piling (SSP) retaining walls: experimental investigation, theoretical interpretation and guidelines for design	University of Cambridge
15	STILUS – Structure-Tunnel Interaction in LiqUefiable Sand	University of Cambridge
16	IMPEC – On the broadband synthetic signals enhanceMent for 3D Physic based numerical analysis, the EUROSEISTEST Case study	EUROSEISTEST and EUROPROTEAS
17	Blind beamforming in array processing	NORSAR

Table 2: Projects selected within the 1st call for proposals

PROJECTS SELECTED IN THE 2nd CALL FOR PROPOSALS

Number of Project	Title of Project	Hosting Research Infrastructure
18	SEismic Response of Actual steel SILOS (SERA-SILOS)	EUCENTRE
19	Seismic Testing of Adjacent Interacting Masonry Structures (AIMS)	LNEC
20	Hybrid Testing of an Existing Steel FRAME with Infills under Multiple Earthquakes (HITFRAMES)	STRULAB
21	NSFuse: Ductile steel fuses for the protection of critical nonstructural components	University of Bristol
22	SEismic BEhavior of Scaled MOdels of groin VAults made by 3D printers (SEBESMOVA3D)	University of Bristol
23	Investigation of Seismic Deformation Demand, Capacity and Control in a Novel Self-Centring Steel Braced Frame (SC-CBF)	IZIIS
24	Seismic Behaviour of Rigid Pile Inclusions	University of Cambridge
25	COSMO: Change Of Seismic MOTion due to pile-soil kinematic interaction	University of Cambridge
26	Dynamic Soil Structure Interaction: Three-dimensional Time-domain Analysis of Field Model Scale Experiments	EUROSEISTEST and EUROPROTEAS
27	"SISIFO" Seismic Impedance for Soil-structure Interaction From On-site tests	EUROSEISTEST and EUROPROTEAS
28	Ambient and forced vibration techniques for improving design and performance assessment of structures with consideration of soil-structure interaction	EUROSEISTEST and EUROPROTEAS
29	Seismic SITE effects in sedimentary basins from 3D physics-based numerical modeling (SITE3D)	EUROSEISTEST and EUROPROTEAS
30	Comparison of rocking on rigid and compliant base using the EUROPROTEAS real-scale facility	EUROSEISTEST and EUROPROTEAS
31	Seismic tremor detection in Greece using small aperture arrays	NORSAR
32	The velocity model up to 300 km deep using NORSAR array data (Baltic Shield) based on P and S receiver functions	NORSAR
33	Joint processing of seismo-acoustic array data as tool to discriminate between man-made explosions and earthquakes	NORSAR

Table 3: Projects selected within the 2nd call for proposals

PROJECTS SELECTED IN THE 3rd CALL FOR PROPOSALS

Number of Project	Title of Project	Hosting Research Infrastructure
34	Seismic performance of multi-component systems in special risk industrial facilities	EU CENTRE
35	SHAKing Table testing for Near Fault Effect Evaluation (SHATTENFEE)	University of Bristol
36	SSI-STEEL: Soil-Structures Interaction effects for STEEL structures	University of Bristol
37	INfills and MASonry structures protected by deformable POLyurethanes in seismic areas (INMASPOL)	IZIIS
38	Resonant metamaterial-based earthquake risk mitigation of large-scale structures and infrastructure systems: assessment of an innovative proof-of-concept via medium-size scale testing	EUROSEISTEST and EUROPROTEAS
39	“DYMOBRIS” Dynamic identification and Monitoring of scoured BRIDGEs under earthquake hazard	EUROSEISTEST and EUROPROTEAS
40	SOIL Frame-Interaction Analysis through large-scale tests and advanced numerical finite element modeling (Acronym: SOFIA)	EUROSEISTEST and EUROPROTEAS
41	Earthquake Spectral Provisions and Urban Fragility Evaluation	NORSAR
42	Beamforming of aftershock strong-motion time-histories recorded on the ICEARRAY for earthquake source studies	NORSAR
43	Investigation of (micro)seismicity of the Laptev Sea using a small-aperture array	NORSAR
44	Design, location and processing of a regional array in SW Portugal - Europe	NORSAR

Table 4: Projects selected within the 3rd call for proposals

In the next chapters of this document, all TA projects technical reports organized by hosting Research Infrastructure are reported. Since the world sanitary emergency referred as COVID-19 affected also EU countries from the beginning of 2020, some of the experimental activities have been more complex to manage and sometimes slightly delayed. In order to make available an updated and detailed description of all the activities carried out within the SERA TA framework, possibly not compatible with the submission date of this document, an integrated and open-access publication will be produced in the next months. The publication will be the “Proceedings of the Seismology and Earthquake Engineering Research Infrastructure Alliance for Europe – SERA Project –”, published by EU CENTRE and advertised through the SERA (<http://www.sera-eu.org/en/home/>) and SERA TA (<https://sera-ta.eucentre.it/>) web portals.

1 JRC ELSA

The European Laboratory for Structural Assessment (ELSA) is a research infrastructure of the European Commission's Joint Research Centre. The kernel of ELSA is the Reaction Wall. It consists of a reinforced concrete vertical wall and a horizontal floor rigidly connected together to test the vulnerability of buildings to earthquakes and other hazards. By means of computer-controlled hydraulic actuators it is possible to expose full-scale structures to loads of dynamic strong forces and control the resulting movements with high precision. The wall and the floor are designed to resist the forces, typically several MN, which are necessary to deform and seriously damage the full-scale test models of structures. The ELSA Reaction Wall is the largest facility of its kind in Europe and one of the largest in the world – only exceeded in Japan.

Following the first call for proposals, two projects were assigned: EQUFIRE (Multi-hazard performance assessment of structural and non-structural components subjected to seismic and fire following earthquake by means of geographically distributed testing) and SlabSTRESS (Slab structural response for seismic European design). These projects cover the full availability for transnational access offered by the JRC ELSA Reaction Wall.

The EQUFIRE project aimed to study the post-earthquake fire performance of steel frame structures and comprised distributed tests at JRC and at the Federal Institute for Materials Research and Testing (BAM), Germany. The user team was made up of researchers from the Federal Institute for Materials Research and Testing (team leader), University of Trento, ETH Zürich and Aarhus University and of industrial partners from Etex and Xella. The tests at BAM were performed from 16 October 2019 to 14 November 2019. The experimental activity at JRC started in January 2020 and was interrupted following the spread of the corona virus and the Decree of the Italian government of 8 March 2020. At that time, it was planned to complete mounting the specimen and set-up until 13 March 2020, perform preliminary tests from 16 to 20 March 2020 and complete the experimental campaign by mid-April. The details of the project are given in 1.1.

The SlabSTRESS project aimed to verify the seismic performance of flat slab frames in a structure with earthquake resistant ductile walls and to study the performance of the system beyond the design displacements. The user team was made up of researchers from Politecnico di Milano (team leader), Ecole Polytechnique Fédérale de Lausanne, Nova University of Lisbon and Technical University of Bucharest. Five access days were delivered on 16 October 2019, 21 October 2019, 23 October 2019, 2 December 2019 and 4 December 2019. A blind prediction competition is ongoing until 31 August 2020 and for this reason not all results are presented in detail in 1.2. All data of the SlabSTRESS project are uploaded in the local node of the SERIES database and will be made available in September 2020.

The following meetings were organised within WP 8 at JRC Ispra:

- 20 February 2018, meeting with EQUFIRE users to plan the project
- 23 February 2018, meeting with SlabSTRESS users to plan the project
- 21 March 2018, SERA TA-SEP meeting
- 4 February 2019, meeting with EQUFIRE users to discuss the details of the project
- 9-19 December 2019, working visit of EQUFIRE user G. Abbiati (University of Aarhus) to develop a working version of the pseudo-dynamic algorithms with substructuring that will be used during the tests
- 26-27 February 2020, working visit of EQUFIRE users G. Abbiati (University of Aarhus) and Patrick Covi (University of Trento) to discuss, implement and check the simulations and real-time control system – the meeting was cancelled because of the situation with covid-19 in Italy.

1.1 Project #1 – EQUFIRE - Multi-hazard performance assessment of structural and non-structural components subjected to seismic and fire following earthquake by means of geographically distributed testing

Authors

M. Lamperti Tornaghi⁽¹⁾, G. Tsionis⁽¹⁾, P. Pegon⁽¹⁾, J. Molina⁽¹⁾, M. Peroni⁽¹⁾, M. Korzen⁽²⁾, S. Riemer⁽²⁾, K.-U. Ziener⁽²⁾, N. Tondini⁽³⁾, P. Covi⁽³⁾, G. Abbiati⁽⁴⁾, M. Antonelli⁽⁵⁾, B. Gilardi⁽⁶⁾, L. Danciu⁽⁷⁾

⁽¹⁾ *European Commission, Joint Research Centre, Ispra, Italy*

⁽²⁾ *Bundesanstalt für Materialforschung und –prüfung (BAM), Berlin, Germany*

⁽³⁾ *Department of Civil, Environmental and Mechanical Engineering, University of Trento, Trento, Italy*

⁽⁴⁾ *Aarhus University, Aarhus, Denmark*

⁽⁵⁾ *Etex Building Performance S.p.A., Belgium*

⁽⁶⁾ *Xella Italia S.r.l., Italy*

⁽⁷⁾ *ETH Zürich, Zurich, Switzerland*

1.1.1 Introduction

Many historical events (e.g. the 1096 San Francisco, 1923 Tokyo, 1995 Kobe, 1999 Turkey, 2011 Tohoku and 2011 Christchurch earthquakes) have shown that, after an earthquake, fire may be triggered by earthquake-induced rupture of gas piping, failure of electrical systems, etc. The structural fire performance can then deteriorate because the fire acts on a previously damaged structure. In addition, the earthquake may have damaged fire protection elements and the fire can spread more rapidly if compartmentation walls have failed. This is particularly relevant for steel structures as the high thermal conductivity of elements with small thickness entails quick temperature rise with consequent fast loss of strength and stiffness.

The effects of seismic and fire actions have been traditionally studied separately because: i) the inherent issues related to each action are quite complex per se; ii) researchers and practitioners are typically specialised in one particular field; iii) experimental facilities have been conceived to reproduce one of the two actions; iv) full-scale tests are very expensive and feasible in very few facilities; v) there is lack of numerical codes capable of performing fire following earthquake (FFE) analysis at low computational cost.

Most of the works in literature involve numerical simulations on steel moment resisting frames [1-4] and only a few of them are dedicated to buckling-restrained and conventional brace systems, e.g. [5, 6] that developed a framework for evaluating the post-earthquake performance of steel structures in a multi-hazard context that incorporates tools for probabilistic structural analysis under fire and seismic loads. Experimental studies have been performed on single elements [7], beam-column joints made of filled steel tubes [8], and full-scale reinforced concrete frames [9]. The study of literature reveals that several numerical studies on the post-earthquake fire behaviour of structural components have been

carried out without being supported by comprehensive experimental research. Moreover, works on non-structural components are also very limited.

Therefore, the EQUFIRE project aimed to provide experimental data to study the post-earthquake fire performance of steel frame structures. The project studied a steel frame building with concentric bracings by seismic pseudo-dynamic tests of a real-scale one-storey frame at the ELSA Reaction Wall and tests of single elements subjected to fire following earthquake at the furnace of the Federal Institute for Materials Research and Testing. The experimental results serve to study the response of structural and non-structural components, and their interaction with different fire protection systems, to scenarios of fire following earthquake, with a view to providing sound experimental evidence and knowledge for improving existing design guidelines and future standards.

1.1.2 Design of the test specimen

A four-storey three-bay steel frame with concentric bracings in the central bay was selected for the experimental campaign. This frame is part of an office building with a square plan (12.5 m x 12.5 m) and is located in Lisbon (Portugal) in an area of medium-high seismicity. The storey height is 3 m with the exception of the first floor, which is 3.6 m high. The lateral force resisting system consists of concentric braced frames (CBF) placed on the perimeter and at the centre of the building (see Figure 4). Figure 4 also shows the member sizes and the location of the test frame. Figure 5 (left) shows the gravity loads acting simultaneously with the seismic load, and the fire load considered at one column adjacent to the diagonals of the bracing.

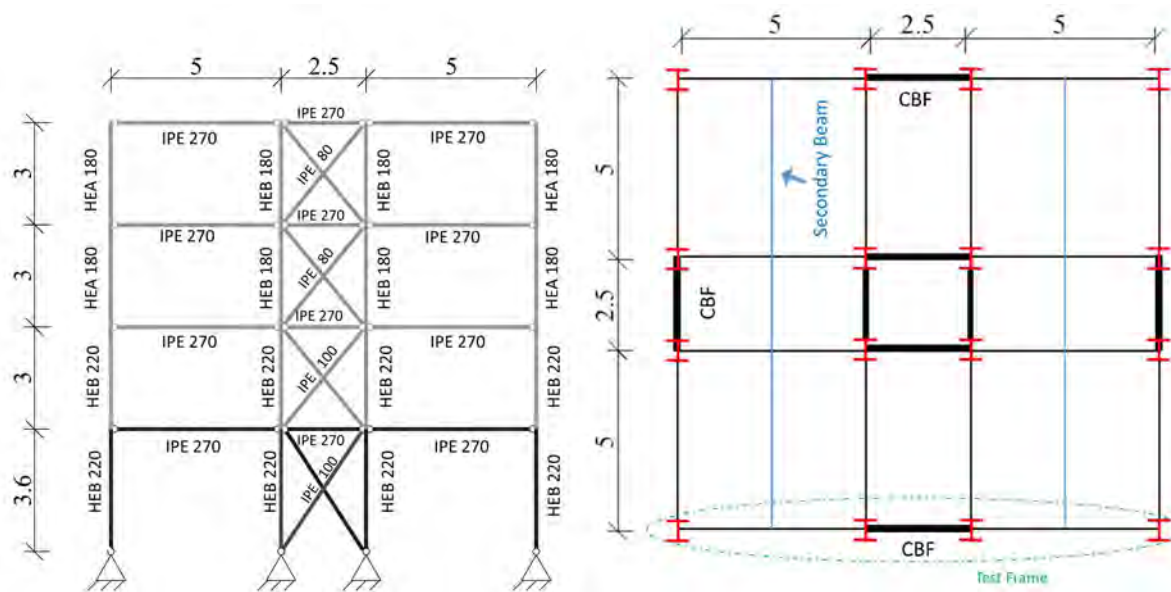


Figure 4: Elevation and plan of the building (dimensions in meters)

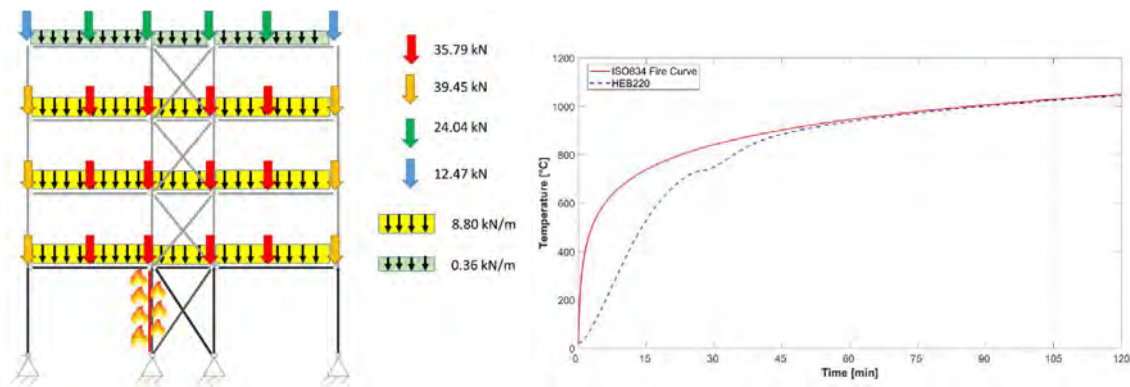


Figure 5: Live and fire loads (left); ISO 834 heating curves and temperature of the HEB220 column (right)

IPE sections with the weak axis in the plane of the frame were used for the bracing elements to force in-plane buckling. This choice was made for essentially two reasons: i) to avoid damage in the walls where the bracing is inserted in; ii) to keep a 2D modelling of the frame meaningful so that to maintain low computational demand for the hybrid tests.

According to Eurocode 8 [12], the frame was designed for seismic resistance following the capacity design criterion and a nonlinear dynamic 3D analysis was employed. In particular, the concept of High Ductility Class was exploited with dissipation in the bracing members. The general modelling assumptions were the following:

- Only the bracing diagonal in tension was modelled at the ultimate (life safety) limit state.
- The columns were considered continuous along the height of the structure.
- All connections of the beams and diagonals were assumed pinned.
- Masses were considered lumped at the floors, following the assumption of rigid diaphragms.
- The building was regular in plan and in elevation.
- The building was located in Lisbon.

Seismic hazard maps of Portugal were used to identify the peak ground acceleration (PGA). Therefore, a reference PGA of 0.186 g, type B soil and a type 1 elastic spectrum were assumed for the design of the structure and then all the structural verifications described by Eurocode 8 [12] were carried out.

For the fire load, a prescriptive approach was chosen and in particular, the standard ISO 834 [13] heating curve was employed. This choice was made because it is easily reproducible in a furnace. Figure 5 (right) illustrates the evolution in time of the temperature of the gas and of the temperature at the base of an unprotected HEB 220 steel column, calculated according to a lumped mass approach.

A set of fifteen accelerograms was selected considering the type of spectrum, earthquake scenario (magnitude range, distance range, style-of-faulting), local site conditions, period range, and ground motion components using the INGV/EPOS/ORFEUS European strong motion database [14]. The accelerograms were modified to match the target spectrum in the period range of 0.4 - 0.9 s that includes the fundamental period of the structure. The accelerograms were used to perform nonlinear time-history analyses and fire following earthquake analyses. A 2D and 3D model of the building were created using OpenSees [15], SAFIR [16] and ABAQUS [17] software to conduct seismic, fire and FFE numerical analyses.

Among the fifteen accelerograms, the one shown in Figure 6 was selected for the experimental hybrid tests and the numerical analyses, based on three main requirements:

- The selected accelerogram had to cause significant damage to the bracing elements.

- The horizontal displacement of the first floor had to be equal or lower than ± 30 mm to be compatible with the stroke of the horizontal actuator inside the BAM furnace.
- The axial force of the interior columns at the base of the second floor had to be below 1000 kN to be compatible with the actuators used to impose the vertical loads on the specimen at the ELSA Reaction Wall.

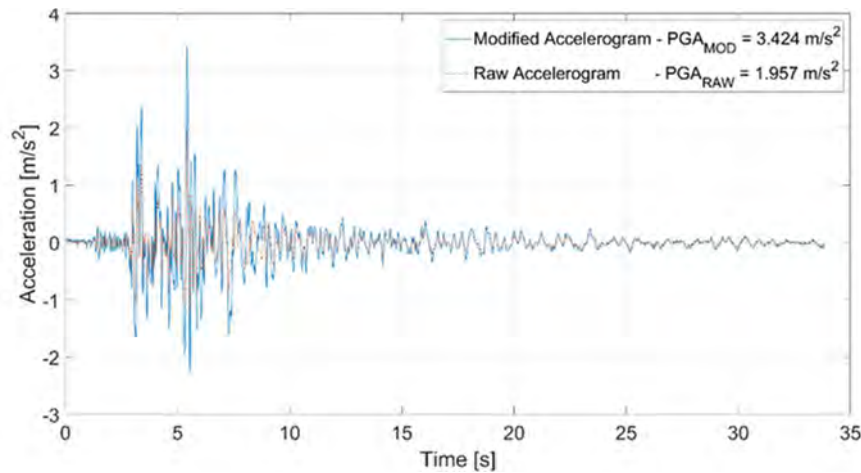


Figure 6: Earthquake acceleration time-history

A nonlinear finite element model in OpenSees was used to evaluate the FFE response of the structure, which is expected to experience large displacements and plastic deformations of the bracing elements during the seismic action and nonlinear behaviour of the column under fire condition. Fifteen nonlinear thermomechanical beam elements, endowed with material and geometric nonlinearities, were used for the column subjected to fire action. The elastic-plastic constitutive law provided by Eurocode 3 [18] was adopted to model the mechanical properties of steel at elevated temperatures. Temperature dependency of elastic modulus, yield strength and strain proportional limit was accounted for according to Eurocode 3 [19]. Seven nonlinear beam elements based on corotational formulation and the uniaxial Giuffre-Menegotto-Pinto steel material, with isotropic strain hardening (Steel02Material) [20] and geometric nonlinearities, was used for the bracing diagonals. Nonlinear beam elements were used for all elements to check that non-dissipative elements remain in the elastic field according to the design calculation.

Figure 7 illustrates the results of the numerical simulation of the FFE test on the bare structure (without fire protection) for the selected acceleration time-history followed by the ISO 834 [12] heating curve. The energy dissipation was concentrated in the braces and in particular at the ground floor. The interior columns and all the other elements remained in the elastic field during the seismic event. Collapse occurred 24 minutes after the start of the fire. Figure 7 also shows the final deformed configuration of the steel frame at the end of the simulation.

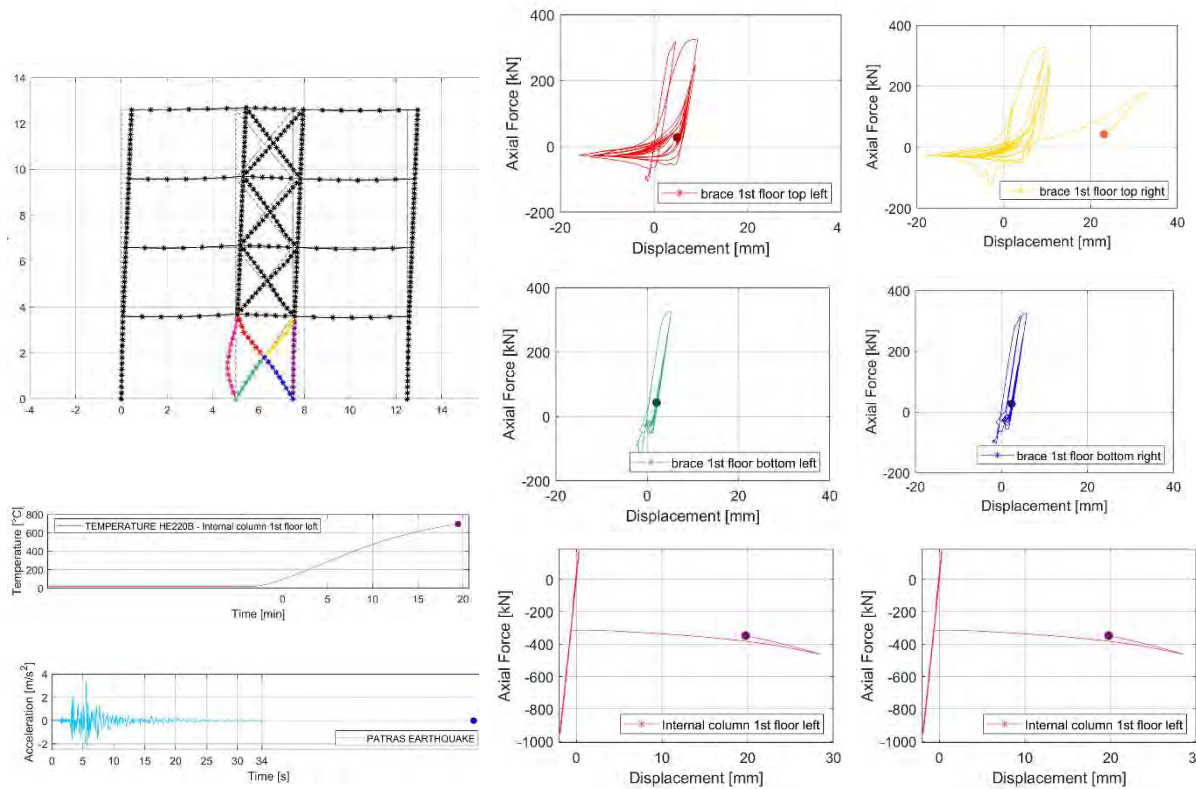


Figure 7: Numerical simulation of fire following earthquake with OpenSees

1.1.3 Experimental programme and setup at BAM

The experimental tests at BAM were performed using the sub-structuring technique shown in Figure 8, in which the physical column was heated by the standard ISO 834 curve and a constant numerical axial stiffness representative of the surrounding structure was applied as boundary condition at the top of the physical column. During the FFE tests, the axial force of the column was measured and then used to obtain the effect, in terms of displacement, of the rest of the structure. Those displacements were imposed on the column in order to keep the two substructures in mechanical equilibrium.

Five FFE tests were conducted at BAM:

- Test #0 Column E: without fire protection;
- Test #1 Column A: without fire protection;
- Test #2 Column B: PROMATECT-H fire protection boards designed for seismic regions;
- Test #3 Column C: conventional PROMATECT-H fire protection boards (not designed for seismic regions);
- Test #4 Column D: sprayed vermiculite coating, designed for applications in seismic regions, in which a mechanical reinforcing mesh is placed in the middle of the coating to retain it.

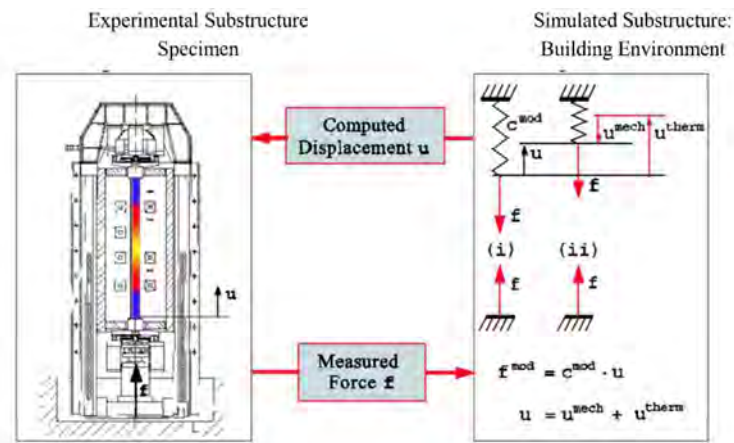


Figure 8: Sub-structuring method implemented for the tests at BAM [21]

The specimens were instrumented with thermocouples to measure the temperature at different positions of the cross-section and along the height. In detail, each specimen was equipped with 20 sheath thermocouples: six sensors in each section (two on the web and four on the flanges) at three different heights along the column and additionally one sensor at the top and the base of the column. Six plate thermometers according to EN 1363-1 [22] measured the temperature inside the furnace. Additionally, two thermocouples measured the ambient temperature of the laboratory.

Each test was conducted as follows: the column was first subjected to horizontal and vertical displacement histories resulting from seismic nonlinear time-history numerical analysis and then the furnace was switched on and the ISO 834 curve was followed with constant axial stiffness, representative of the surrounding structure, as boundary condition.

1.1.4 Experimental programme and setup at JRC

The experimental mock-up at ELSA Reaction Wall (Figure 9) represents the ground floor of the four-storey frame. It is a three-bay steel frame with concentric bracing in the central bay. The span of the outer bays is 5 m, while the interior one has a span of 2.5 m. The inter-storey height is 3.6 m. A secondary frame, parallel to the main one is used to prevent out-of-plane deformation during the test. The two frames are fastened to the strong floor and are connected together by steel rods, which do not alter the seismic response of the mock-up.



Figure 9: Side view (left) and bird's-eye view (right) of the specimen and set up at the ELSA Reaction Wall

The frame is made of S355 steel, for columns and beams, while the braces are made of S275 steel. The profiles used are HEB220 for columns, IPE270 for beams and IPE100 for braces.

Two 600 kN pistons apply the vertical load on each internal column, whereas lateral loads are applied through 500 kN actuators connected to the ELSA Reaction Wall, one for the main frame and another for the secondary frame.

Load cells measure the loads applied by the vertical and horizontal actuators. Since the frame is statically indeterminate, the two central columns and the three beams are equipped with strain gauges that measure their internal axial loads. In parallel, displacement transducers measure the vertical deformation of the central columns, the axial deformation of the braces, as well as the lateral displacement of the whole frame.

To further reduce any possible interference from the secondary frame and eliminate any relative displacement during testing, the actuator of the safety frame applied the same displacement as the actuator of the main one.

The procedure for the hybrid tests at the ELSA Reaction Wall is described in section Figure 6. Five tests are foreseen with the acceleration time history shown in Figure 6:

- Test 1, bare frame without fire protection;
- Test 2, frame with PROMATECT-H fire protection boards designed for seismic regions;
- Test 3, frame with conventional PROMATECT-H fire protection boards (not designed for seismic regions);
- Test 4, frame with sprayed vermiculite coating designed for applications in seismic regions;
- Test 5, frame with walls made of autoclaved aerated concrete blocks built in the two longest bays, to verify whether these can provide effective fire compartmentation without altering the seismic response of the frame.

The bracing and the column on which the fire protection has been applied will be replaced at the end of each of the tests 2, 3 and 4.

1.1.5 Simulation algorithm for the hybrid tests

In order to enable hybrid simulation with mixed force- and displacement-controlled degrees of freedom (DOFs), a specific simulation algorithm was developed. A pair of Lagrange multiplier vectors are introduced to enforce both horizontal and vertical displacement compatibility between the physical substructure (PS) and the numerical one (NS). The NS is characterised by a dynamic balance equation that is solved with the Newmark- α method:

$$\mathbf{M}^N \ddot{\mathbf{u}}_{k+1}^N + [(1 + \alpha)\mathbf{r}_{k+1}^N(\mathbf{u}_{k+1}^N) - \alpha\mathbf{r}_k^N(\mathbf{u}_k^N)] - [(1 + \alpha)\mathbf{f}_{k+1}^N - \alpha\mathbf{f}_k^N] - [(1 + \alpha)\mathbf{L}^{N,vT}\boldsymbol{\lambda}_{k+1}^v - \alpha\mathbf{L}^{N,vT}\boldsymbol{\lambda}_k^v] - [(1 + \alpha)\mathbf{L}^{N,hT}\boldsymbol{\lambda}_{k+1}^h - \alpha\mathbf{L}^{N,hT}\boldsymbol{\lambda}_k^h] = \mathbf{0} \quad (1)$$

In Equation (1) \mathbf{K}^N and \mathbf{M}^N are the stiffness and mass matrices of the NS, whereas \mathbf{u}^N , \mathbf{r}^N and \mathbf{f}^N are the displacement, restoring force and external load vectors. Boolean matrices $\mathbf{L}^{(N,v)}$ and $\mathbf{L}^{(N,h)}$ locate interface Lagrange multipliers corresponding to the vertical and horizontal interface DOFs respectively. Finally, parameter α modulates algorithmic damping. Accordingly, the PS is characterised by two static balance equations; one refers to the vertical force-controlled DOFs whereas the other refers to the horizontal displacement-controlled DOFs.

$$\begin{cases} \mathbf{r}_{k+1}^{P,h}(\mathbf{u}_{k+1}^{P,h}, \mathbf{r}_{k+1}^{P,v}) - \mathbf{L}^{P,h^T} \boldsymbol{\lambda}_{k+1}^h = \mathbf{0} \\ \mathbf{r}_{k+1}^{P,v} - \mathbf{L}^{P,v^T} \boldsymbol{\lambda}_{k+1}^v = \mathbf{0} \end{cases} \quad (2)$$

Superscripts ^h and ^v are used to distinguish between vertical and horizontal DOFs. $\mathbf{u}^{(p,v)}$ and $\mathbf{u}^{(p,h)}$ are vertical and horizontal displacement vectors of the PS, while $\mathbf{r}^{(p,v)}$ and $\mathbf{r}^{(p,h)}$ are the corresponding restoring force vectors. Boolean matrices $\mathbf{L}^{(p,v)}$ and $\mathbf{L}^{(p,h)}$ locate interface Lagrange multipliers corresponding to the vertical and horizontal DOFs, respectively. The two following equations define the compatibility between NS and PS.

$$\begin{cases} \mathbf{L}^{N,h} \mathbf{u}_{k+1}^N + \mathbf{L}^{P,h} \mathbf{u}_{k+1}^{P,h} = \mathbf{0} \\ \mathbf{L}^{N,v} \mathbf{u}_{k+1}^N + \mathbf{L}^{P,v} \mathbf{u}_{k+1}^{P,v}(\mathbf{u}_{k+1}^{P,h}, \mathbf{r}_{k+1}^{P,v}) = \mathbf{0} \end{cases} \quad (3)$$

The solution of the system of equations is computed via operator splitting, i.e. with a single Newton iteration and a constant Jacobian. The procedure was verified considering the linear partitioned finite-element model of the frame reported in [23].

As can be observed in Figure 10, only three DOFs are coupled between PS and NS. In fact, a master-slave relation is imposed on all horizontal DOFs of the first storey to follow DOF (10,1).

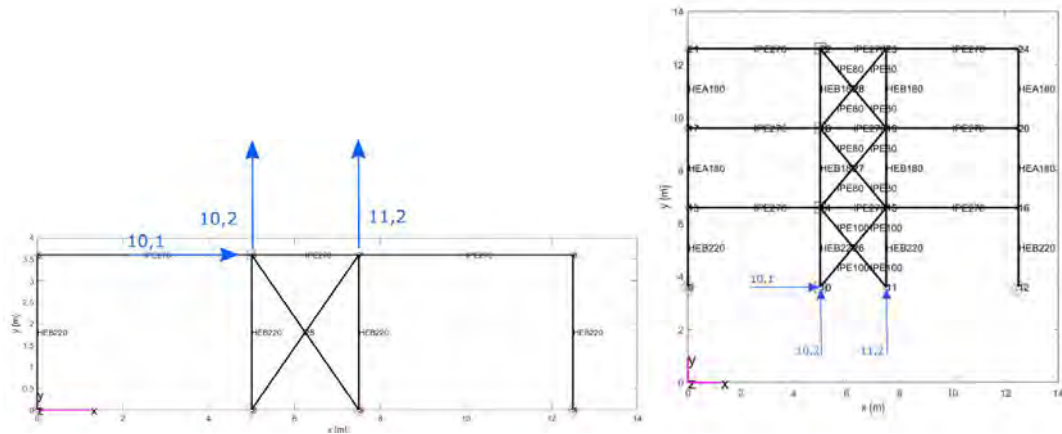


Figure 10: Partitioned model of the frame: PS (left) and NS (right)

Since external columns are connected to the braced frame by means of truss elements, the vertical displacement at their base is blocked on the NS. Figure 11 provides a comparison between a reference solution computed with a monolithic finite element model and the solution obtained with the proposed procedure. As can be appreciated, the dynamic response predicted by the proposed scheme reproduces the reference solution.

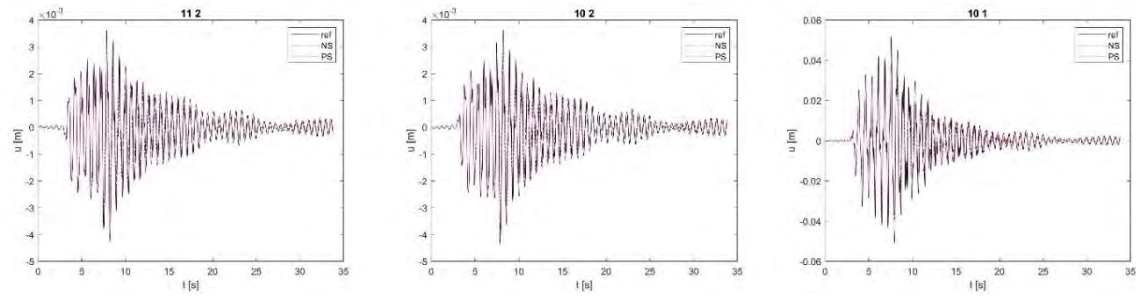


Figure 11: Comparison of displacement response histories of coupled DOFs: horizontal (left), vertical left (centre) and vertical right (right)

1.1.6 Experimental results

The results of the experimental tests at BAM are summarized in the following. The response history of the unprotected steel frame computed with OpenSees was verified against the results of the experimental tests at BAM. Figure 12 shows the input accelerogram, the deformed shape of the frame at the end of the simulation, and the comparison of the results of the seismic test and of the numerical simulations in terms of horizontal displacement, axial displacement and axial force for all tested columns. The comparison demonstrates good agreement. There is a little difference in negative vertical displacements, because the vertical actuator of the furnace is not designed to apply tension forces to the specimen.

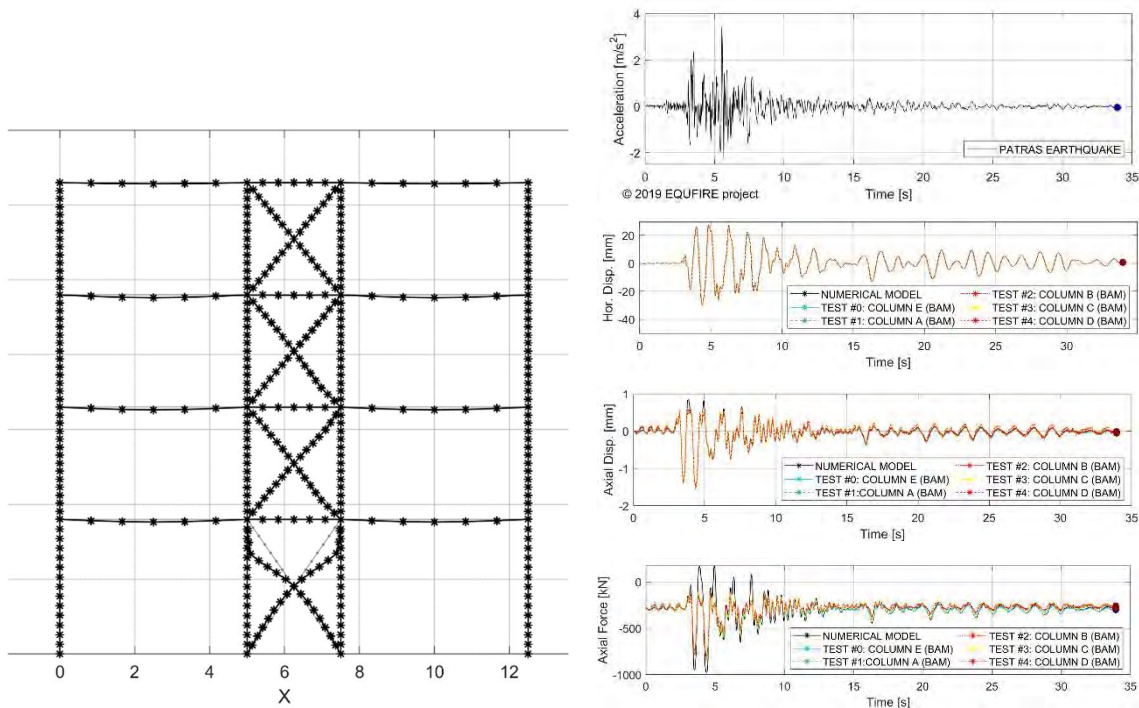


Figure 12: Comparison between the numerical model and the seismic tests at BAM

Figure 13 shows the comparison of the experimental and numerical (before and after the calibration) results for the FFE tests on the unprotected columns A and E, in terms of the evolution of the mean temperature, axial displacement and axial force. The calibration consisted in modelling the base of the columns with its actual initial stiffness and applying the recorded temperature evolution in the columns.

The comparison demonstrated the good repeatability of the FFE test procedures. Figure 13 shows also a snapshot of the test.

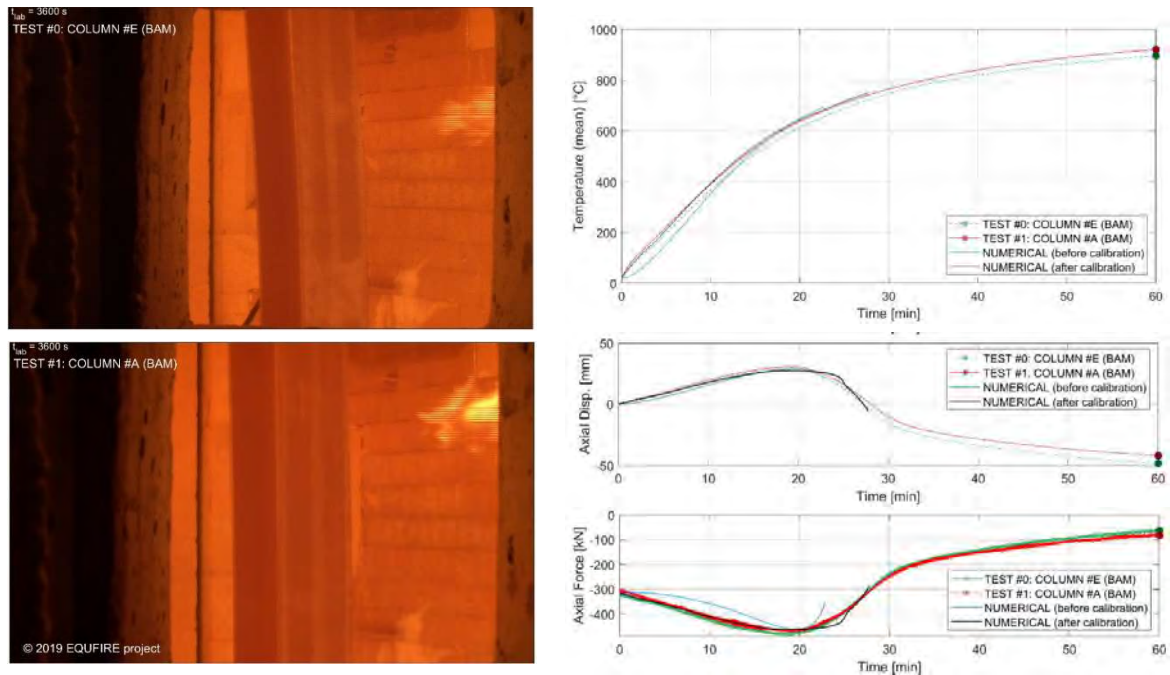


Figure 13: Comparison between the results of the numerical model and the FFE tests on the unprotected columns

Figure 14 shows the comparison of the evolution of the mean temperature, axial displacement and axial force of the FFE tests on the specimens with the three fire protection solutions (conventional boards, seismic-resistant boards and vermiculite sprayed coating). Test #2 was interrupted due to a malfunctioning of a component and then was restarted. The specimens with the two different types of fire protection boards (columns B and C) showed similar performance. The vermiculite sprayed fire protection delayed the development of the temperature in column D with respect to columns B and C. Figure 14 shows also a snapshot of the test.

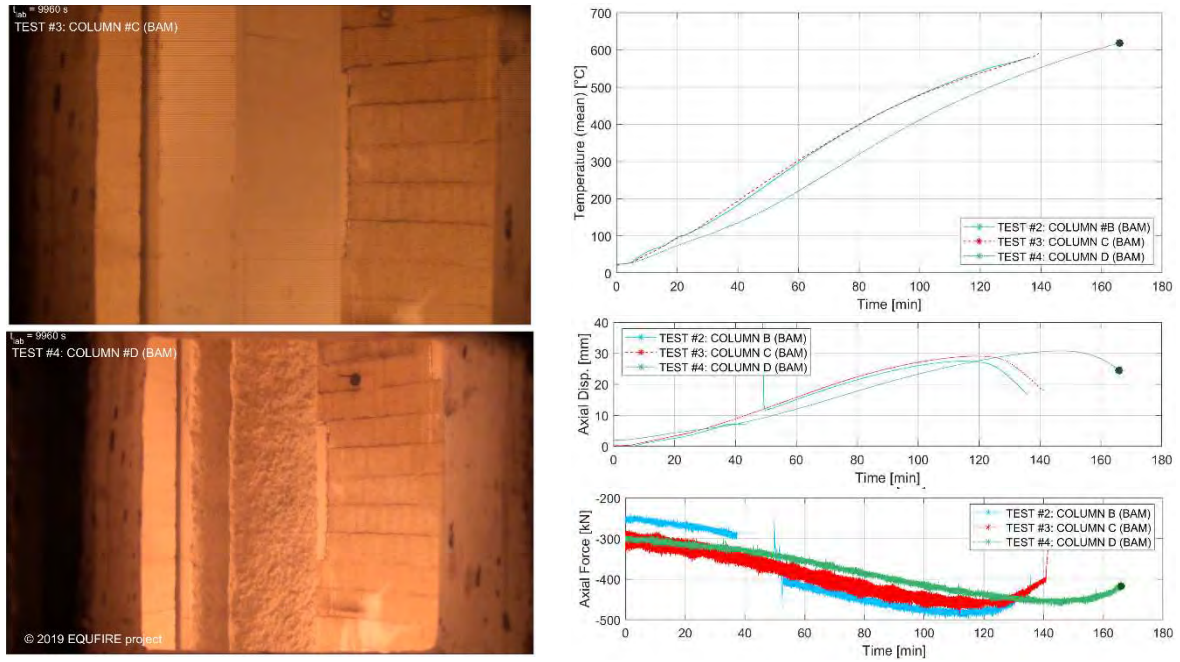


Figure 14: Comparison between the results of the numerical model and the FFE tests on the unprotected columns

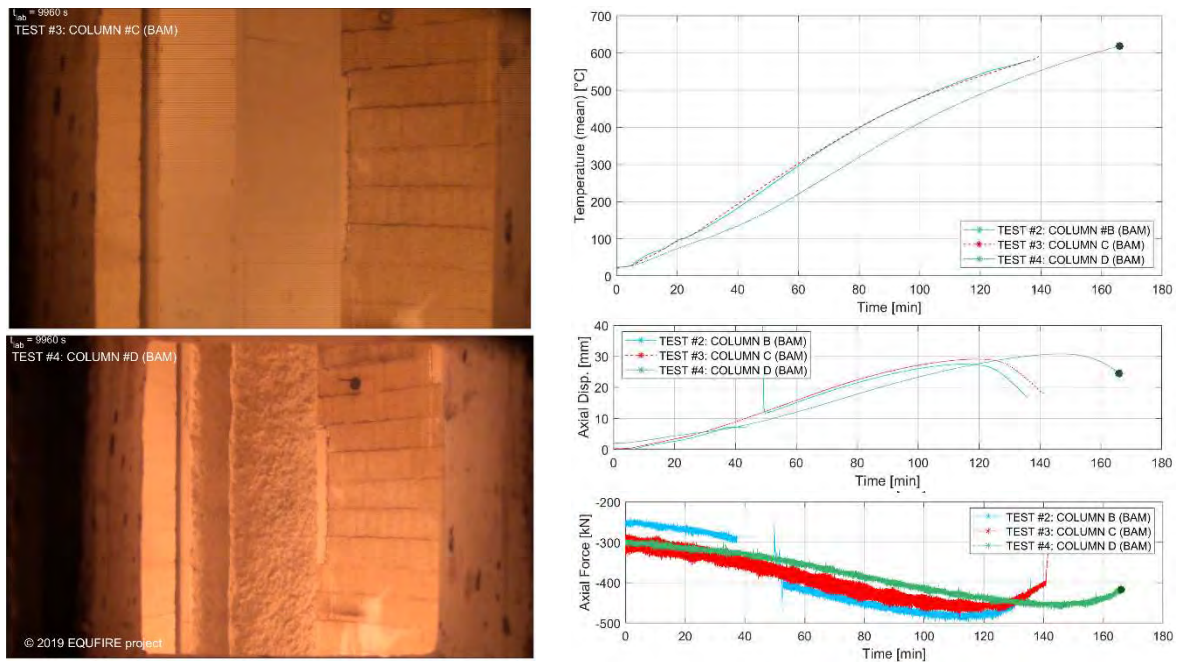


Figure 15: Mean specimen temperature, axial displacement and axial force of the protected for FFE tests of the protected columns

As shown in Figure 16 and Figure 17, cracks on the fire protection elements developed due to the combination of seismic and fire actions. However, those cracks were not large enough to compromise the fire resistance of the columns. This was mainly due to the fact that the column is not a dissipative element and to the laboratory limitations in applying horizontal displacements.



Figure 16: Damage of the fire protection elements due to the combination of seismic and fire actions: test#2 column B (left), test#3 column C (centre), test#4 column D (right)

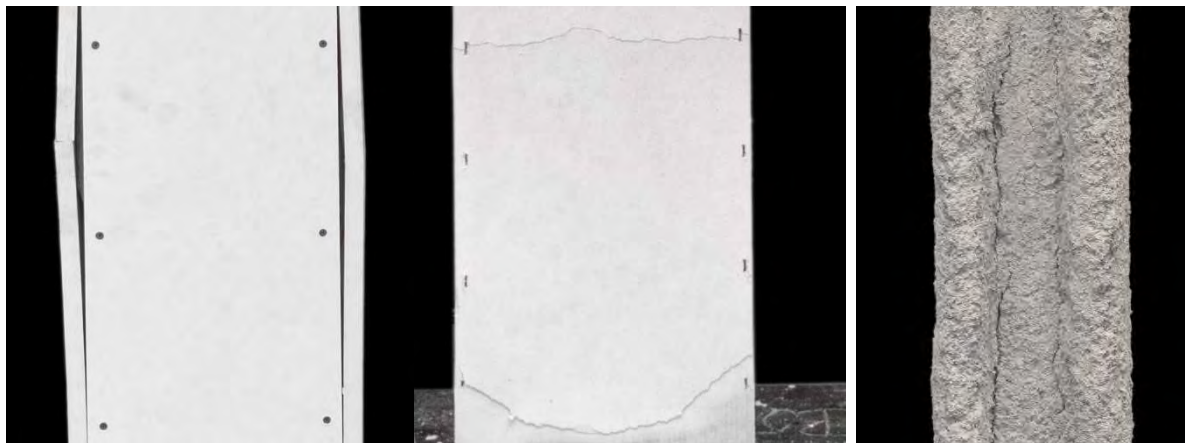


Figure 17: Damage on the fire protection elements due to the combination of seismic and fire actions: test#2 column B (left), test#3 column C (centre), test#4 column D (right)

1.1.7 Main outcomes and discussion

The EQUFIRE project focused on a three-bay, four-storey steel frame with concentric bracing in the central span, subjected to fire following an earthquake, with the aim to study the performance of structural and non-structural components. Five preliminary FFE substructure tests were carried out at the BAM laboratory.

The comparison between the numerical analyses and the experimental results for the unprotected columns demonstrate a good agreement for both seismic and fire actions. Furthermore, the proposed simulation algorithm provided results in good agreement with the reference solution calculated with a monolithic FE model. The following full-scale hybrid experiments will further confirm its reliability.

Tests for fire after earthquake were carried out on two unprotected steel columns and three columns with different fire protection solutions: conventional and earthquake-proof panels and vermiculite sprayed coating. In terms of fire protection, no serious damage was observed that would undermine the fire resistance of the columns. A more significant damage to the fire protection of the dissipative elements (bracing system) is expected during the FFE test series at the ELSA Reaction Wall. Indeed, testing a complete bracing system, including the dissipative braces, should reproduce the actual earthquake conditions, where the compressed brace is expected to cause more severe damage to the fire protection elements due to buckling under large horizontal displacement.

1.1.8 References

- [1] Della Corte G, Landolfo R, Mazzolani FM (2003): Post earthquake fire resistance of moment resisting steel frames. *Fire Safety Journal*, 38 (7), 593-612.
- [2] Memari M, Mahmoud M, Ellingwood B (2014): Post-earthquake fire performance of moment resisting frames with reduced beam section connections. *Journal of Constructional Steel Research*, 103, 215-229.
- [3] Behnam B, Ronagh HR (2015): Post-earthquake fire performance-based behavior of unprotected moment resisting 2D steel frames. *KSCE Journal of Civil Engineering* 19 (1), 274-284.
- [4] Keller WJ, Pessiki SP (2012): Effect of earthquake-induced damage to spray-applied fire-resistive insulation on the response of steel moment-frame beam-column connections during fire exposure. *Journal of Fire Protection Engineering* 22 (4), 271-299.
- [5] Talebi E, Tahir M, Zahmatkesh F, Kueh A, Said A (2016): Fire resistance of a damaged building employing buckling restrained braced system. *International Journal of Advanced Steel Construction*, 14 (1), 1-21.
- [6] Khorasani NE, Garlock MEM, Quiel SE (2015): Modeling steel structures in OpenSees: Enhancements for fire and multi-hazard probabilistic analyses. *Computers and Structures*, 157, 218-231.
- [7] Braxtan NL, Pessiki SP (2011): Postearthquake fire performance of sprayed fire-resistive material on steel moment frames. *Journal of Structural Engineering*, 137 (9), 946-953.
- [8] Pucinotti R, Bursi OS, Demonceau JF (2011): Post-earthquake fire and seismic performance of welded steel-concrete composite beam-to-column joints. *Journal of Constructional Steel Research*, 67, 1358-1375.
- [9] Kamath P, Sharma UK, Kumar V, Bhargava P, Usmani A, Singh B, Singh Y, Torero J, Gillie M, Pankaj P (2015): Full-scale fire test on an earthquake-damaged reinforced concrete frame. *Fire Safety Journal*, 73, 1-19.
- [10] Meacham BJ (2106): Post-earthquake fire performance of buildings: Summary of a large-scale experiment and conceptual framework for integrated performance-based seismic and fire design. *Fire Technology*, 52 (4), 1133-1157.
- [11] CEN (2019): EN 10025-2, Hot rolled products of structural steels. Technical delivery conditions for non-alloy structural steels. European Committee for Standardization.
- [12] CEN (2004): EN 1998-1 Eurocode 8: Design of structures for earthquake resistance - Part 1: General rules, seismic actions and rules for buildings. European Committee for Standardization.
- [13] ISO (1999): ISO 834-1:1999, Fire-resistance tests -Elements of building construction- Part 1: General requirements. International Organization for Standardization.
- [14] Luzi L, Puglia R, Russo E, ORFEUS WG5 (2016): Engineering Strong Motion Database, version 1.0. Istituto Nazionale di Geofisica e Vulcanologia, Observatories & Research Facilities for European Seismology.
- [15] McKenna F (2011): OpenSees: A framework for earthquake engineering simulation. *Computing in Science and Engineering*, 13.
- [16] Franssen, J-M, Gernay, T. (2017): Modeling structures in fire with safirR©: Theoretical background and capabilities. *Journal of Structural Fire Engineering*, 8 (3), 300-323.
- [17] ABAQUS (2011): ABAQUS Documentation, Dassault Systèmes.
- [18] CEN (2005): EN 1993-1-2 Eurocode 3: Design of steel structures - Part 1-1: General rules and rules for buildings. European Committee for Standardization.
- [19] CEN (2005): EN 1993-1-2 Eurocode 3: Design of steel structures - Part 1-2: General rules - Structural fire design. European Committee for Standardization.
- [20] Silva V, Crowley H, Varum H, Pinho R (2015): Seismic risk assessment for mainland Portugal. *Bulletin of Earthquake Engineering*, 13, 429-457.
- [21] Korzen M, Magonette G, Buchet P. (1999): Mechanical loading of columns in fire tests by means of the substructuring method, 8th INTERFLAM '99: Fire science and engineering conference.

- [22] CEN (2012): EN 1363-1:1999 Fire Resistance Tests-Part 1: General Requirements. European Committee for Standardization.
- [23] Filippou FC, Popov EP, Bertero VV (1983): Effects of Bond Deterioration on Hysteretic Behavior of Reinforced Concrete Joints, Report EERC 83-19. Earthquake Engineering Research Center, University of California, Berkeley.

1.2 Project #2 – SlabSTRESS - SLAB STructural RESponse for Seismic European Design

Authors

M. Lamperti Tornaghi⁽¹⁾, G. Tsionis⁽¹⁾, P. Pegon⁽¹⁾, J. Molina⁽¹⁾, M. Peroni⁽¹⁾, D. Coronelli⁽²⁾, L. Martinelli⁽²⁾, T. Netti⁽²⁾, G. Angjeliu⁽²⁾, C. Boursianis⁽²⁾, A. Pinho Ramos⁽³⁾, R. Marreiros⁽³⁾, R. Pascu⁽⁴⁾, E. Lozinca⁽⁴⁾, V. Popa⁽⁴⁾, A. Muttoni⁽⁵⁾

⁽¹⁾ *European Commission, Joint Research Centre, Ispra, Italy*

⁽²⁾ *Department of Civil and Environmental Engineering, Politecnico di Milano, Milan, Italy*

⁽³⁾ *Department of Civil Engineering, Universidade de NOVA de Lisboa, Lisbon, Portugal*

⁽⁴⁾ *Universitatea Tehnica de Constructii Bucuresti, Bucharest, Romania*

⁽⁵⁾ *Ecole Polytechnique Fédérale de Lausanne, Lausanne, Swiss Confederation*

1.2.1 Introduction

Flat slab concrete buildings for office, commercial and residential use are built in many countries, but their behaviour under seismic and gravitational action is not yet fully understood. Many studies have been undertaken in North America and Asia, but European research is lagging behind and the current version of Eurocode 8 [1] does not cover the design of buildings with flat slab frames used as primary seismic elements. The SlabSTRESS (www.slabstress.org) project was therefore launched at the ELSA Reaction Wall of the Joint Research Centre, within the Transnational Access activities of the SERA project.

Design of flat slab frames in Europe developed mainly in North-European non-seismic countries [2-4]. The specifications of Eurocode 2 ‘Design of concrete structures’ [5] consider the design of flat slabs and punching verifications for the effects of gravity loading. Eurocode 8 ‘Design of structures for Earthquake resistance’ [1] does not include specific rules for flat slabs. The scientific community has expressed the aspiration to advance the knowledge and develop adequate code provision [6, 7].

For the time being, design is carried out considering the provisions given by Eurocode 8 for secondary elements coupled with a primary dissipative earthquake resistant system; the former must bear gravity loads at the maximum design lateral deformations reached by the latter. These deformations are calculated for the design actions on the primary system, multiplied by the behaviour factor. In addition, the code specifies that the secondary elements must give a contribution lower than 15 % of the total stiffness of the structure.

Research in North America produced a wide database of tests and code specifications for flat slab design for gravity combined with seismic loads. A set of results is shown in Figure 18 for tests on interior slab-columns connections.

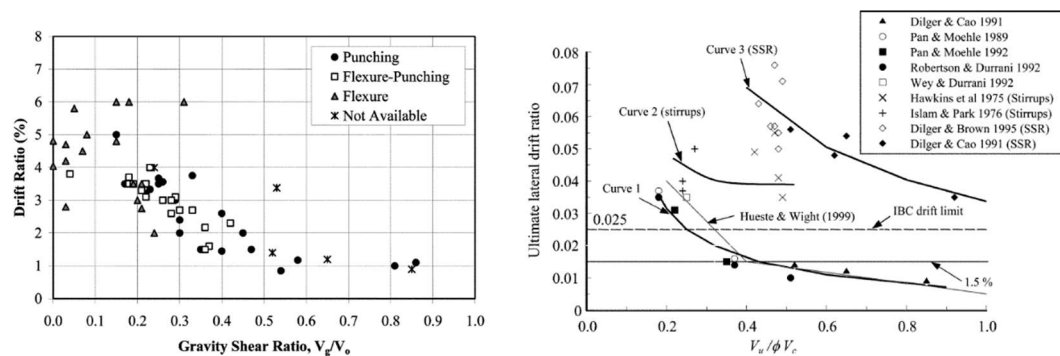


Figure 18: Ultimate drift capacity and gravity shear ratio. Test results for interior connections without transverse reinforcement (left) [8] and test results without and with transverse reinforcement [9] (right)

Experimental activity in Europe started on slab-column connections under cyclic loading. Research at EPFL [10] tested full-scale slab-column connections without transverse reinforcement to compare the effects of monotonic and cyclic loading, different gravity shear ratios and reinforcement ratios. For slabs subjected to low gravity loads, and for lower reinforcement ratios in particular, lateral drift cycles led to reduction of flexural strength and ultimate drift capacity when compared to monotonic tests.

Researchers at FCT/UNL in Portugal have developed a test setup [11] to test flat slab-column connections, with realistic conditions of slab continuity, under combined gravity loading and reversed horizontal cyclic drifts. Besides specimens without punching shear reinforcement, a series of specimens with punching shear reinforcement and solutions to enhance the deformation capacity, such as stirrups [12], headed studs [13, 14], post-installed bolts [15], fibre-reinforced concrete [16] and high-strength concrete [17] have been tested with promising results. Isufi et al. [18] studied the numerical models of flat slab frames calibrated on these experimental results. Although the test setup of FCT/UNL overcomes some of the limitations of past tests on specimens that represent only the hogging moment region of the slab, testing full-scale specimens is more realistic. Furthermore, the tests at FCT/UNL have been limited to interior slab-column connections.

Previous tests of real-scale multi-storey flat-slab buildings are very limited. Coelho et al. [19] carried out pseudo-dynamic tests at the ELSA laboratory on a three-storey building with only one bay in each direction (7.0 m and 4.0 m respectively). The connections had overhangs along two of the four sides (1.5 m and 1.25 m respectively) and the floors were 0.3 m thick waffle slabs with thick slab around the columns extending in plan four times the slab thickness. The columns were rectangular, 0.3 m \times 0.5 m reduced to 0.3 m \times 0.4 m at the last floor. For the 475 years return period earthquake (ultimate limit state) the structure reached a displacement of 162 mm at the second storey (1.64 % drift) with cracking around the columns. In a following test for the 2000 years return period earthquake, a failure in the test set-up caused the jacks to pull the structure to failure and a drift capacity of 4.3 % was reached. Heavy damage in the slab around the columns was accumulated at different floors and the top floor slab was nearly detached from the column at two connections.

Fick et al. [20] tested under cyclic lateral loading a flat-slab structure with two floor panels in plan and three storeys (plan dimensions: 9.1 m \times 15.2 m, height: 9 m, slab thickness: 0.18 m). The spans measured 6.1 m in each direction, with 1.5 m overhangs all around the perimeter. The columns were square (46 cm \times 46 cm). This resulted in a structure with only two types of connection, edge and corner,

with an important influence of the overhangs. The test was stopped after a connection punched at 3.3 % drift.

The North-American code ACI318 [9] and design philosophy [8] are based on a database of results mainly on individual connections, with or without shear reinforcement (Figure 18). A central aspect for slabs without transverse steel is that ultimate drift ratio reduces with increasing gravity shear ratios (GSR). The GSR is the ratio between the acting vertical shear force and the punching shear resistance according to ACI318 [8]. Transverse steel increases the ultimate drift ratio of connections, with some reduction of ultimate drift capacity with the gravity shear ratio. Hence, the results for the two tests above must be compared considering the gravity shear ratio ensuing from the specimen design and the gravity loading. Fick et al [20] report a GSR value of 0.21, while a nominal value close to 0.4 is calculated for [19]. For a gravity shear ratio of 0.21 in [20], ultimate drift values in the database [8] range from 2.7 to 3.6 %. For gravity shear ratio 0.4 in [19], the ultimate drift is between 1.5 and 2.6 %. It should be considered that the structure in [20] had a particular geometric configuration and a part of waffle slabs.

This experimental background shows the need for a comprehensive experimental study on a real scale structure. The SlabSTRESS programme was proposed with the aim of providing support for the European design codes by studying the response of a full-scale two-storey building for seismic and gravity actions, different types of connections (corner, edge and interior), the redistribution of load effects in floors with realistic boundary conditions, different longitudinal reinforcement layouts, with and without transverse steel reinforcement. The aim of the testing phases presented here is twofold: first to verify, for actions corresponding to the serviceability and ultimate limit states, the seismic performance of flat slab frames in a structure with earthquake resistant ductile walls (tests A); secondly to study the performance of the system beyond the design displacements (tests B). The first aim corresponds to verifying the requirement that the structure should bear gravity loads in correspondence of the maximum lateral displacement reached for the design action. The latter provides understanding of the deformation capacity of the system.

1.2.2 Test specimen

The structure is a reinforced concrete (RC) building with two 0.2 m thick flat slabs supported by columns, as shown in Figure 19. Preliminary design was carried out according to the Italian national design code NTC 2018 [21] and was finalised with code provisions compatible with Eurocode 2 [5] and Eurocode 8 [1].

The structure was conceived with primary seismic RC walls while the columns and the slabs were assumed as secondary seismic elements, not forming part of the seismic action resisting system of the building. The strength and stiffness of the secondary elements against seismic actions is neglected and their stiffness may not exceed 15 % of the stiffness of primary members [1]. The structure belongs to the ductile wall system structural type, with uncoupled walls. A basic value of the behaviour factor $q_0 = 4$ is assigned to this type both by Eurocode 8 and NTC 2018.

The building includes six panels with spans on column axes 4.5 m, 5 m and 4.5 m in the long direction and 4.5 m and 4.5 m in the short one. The slab of the second floor is provided with transverse reinforcement, although not requested from the design. Total dimensions of the floors are 14.5 m x 9.5 m. The slab thickness is 20 cm. Columns dimensions are 0.40 m x 0.40 m, 0.35 m x 0.35 m and 0.30 m x 0.30 m for the interior, edge and corner columns respectively. Column height is 3.0 m between each slab. A specific feature is that the columns are made of RC portions above and below the slab, and have a structural steel stub at mid-height to measure internal column forces. The walls are rectangular with cross-section dimensions 1.5 m x 0.32 m and are designed as ductile walls according

to NTC 2018 and Eurocode 8. Finally, the structure has a reinforced concrete foundation with a slab and a grid of stiffening beams in correspondence of the column lines.

The following loads, usual for residential buildings, were considered in the design of the slab and of the building: self-weight of the slab = 5 kN/m^2 , permanent non-structural load = 3 kN/m^2 , live loads = 2 kN/m^2 . The load combinations were according to EN 1990.

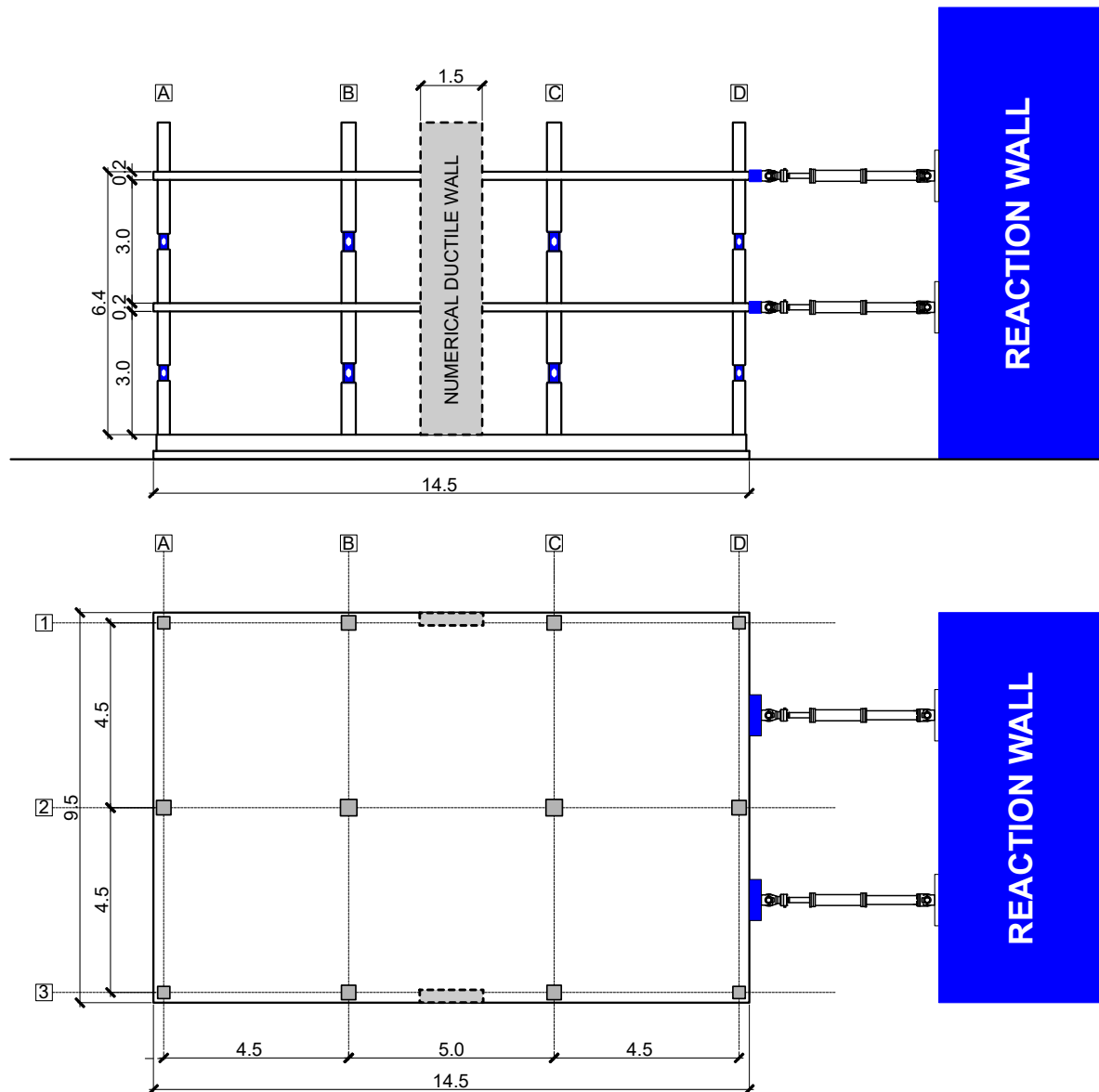


Figure 19: Mock-up for the experimental campaign

Concrete class C30/37 was selected for the slabs and the columns. The slab longitudinal reinforcement steel was class B450C (typically prescribed by the Italian code when ductile behaviour is required). Welded studs with yield stress $f_{yk} \geq 500 \text{ MPa}$ were used as transverse reinforcement in the slab of the second storey. The column longitudinal reinforcement was B500B with the exception of column bases where steel B450C (according to NTC 2018) was used, since plastic hinging was expected. The column transverse reinforcement was of class B450A according to NTC 2018.

The design seismic action was obtained adopting a behaviour factor $q = 4$ and considering the structure as located in the city of Gemona, region of Friuli-Venezia Giulia (Italy), that was struck by a $6.5 M_w$ earthquake in 1976. The design spectra of NTC 2018 at ultimate limit state (ULS) and serviceability limit

state (SLS) were used. From the modal analysis of the structure considering cracked sections, the first vibration period in the direction of the walls is $T_1 = 0.315$ s. This value falls on the constant acceleration part of the ULS spectrum (spectral ordinate of the design spectrum $S_d = 153.06$ cm/s², for $q = 4$). For the SLS spectrum, the spectral ordinate is $S_a = 182.3$ cm/s². It is worth recalling that NTC 2018 prescribes verification at SLS for an elastic response spectrum, differently from Eurocode 8 where the inter-storey drifts at SLS are directly derived from those computed using the design spectrum at the ULS.

The ductile structural walls, which make up the primary seismic structure, were not part of the constructed building, but were numerically simulated during the pseudo-dynamic tests. A linear model, equivalent of the nonlinear response, of these walls was developed to this end with the following procedure. A nonlinear model of the walls was developed in the research computer code NONDA [22] with two (one per storey) RCIZ [23] wall elements adopted to model each wall. These elements include shear-bending-axial force interaction. The nonlinear numerical model of the structure was used to compute the time-history response at the ULS and SLS to an earthquake compatible with the site spectrum and to obtain a pushover curve for a linear distribution of lateral forces that approximates the inertial forces when the structure vibrates in its first mode. The pushover curve was used, along with the displacement coming from the time-history analysis, to identify the stiffness and damping of the equivalent linear model used during the pseudo-dynamic tests.

The signal selected for the numerical analyses and the pseudo-dynamic tests is the Y-component of signal 007142ya from the M_w 6.3 Bingöl earthquake of 01/05/2003. The signal has been selected with the REXEL computer code [24] as one best matching the code spectrum for ULS and SLS at the site. Matching the site elastic response spectra requires the original peak ground acceleration (PGA) of 2.92 m/s² to be scaled at 87 % and 31 %, respectively. The pseudo-acceleration response spectra of the selected accelerogram and the design spectra at ULS and SLS are shown in Figure 20 together with the acceleration time history of the selected signal.

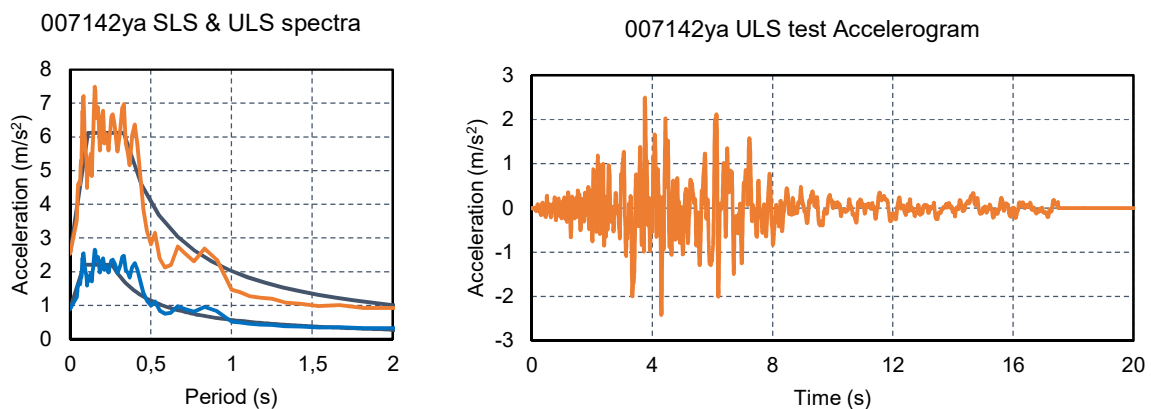


Figure 20: Pseudo-acceleration response spectrum of the selected signal and design spectra at SLS and ULS (left) and acceleration time history of the selected signal (right)

As previously mentioned, the slab-column connections of the first storey had no punching shear reinforcement, whereas the connections in the second storey were reinforced with headed studs. Headed studs were chosen for the second storey as one of the most efficient and practical methods of enhancing the deformation capacity of slab-column connections [13, 25, 26]. Since punching shear reinforcement was not required to carry the gravity loads at the ultimate limit state, the purpose of providing transverse reinforcement at the second storey was to enhance the deformation capacity of the slab-column connections under lateral loading by preventing punching shear failure at low drifts. Commercially available studs were used. The layout and the diameter of studs, as well as the extent of

the shear-reinforced zone, were determined to avoid punching failure for the gravity loads outside the reinforced zone. The layout presented in Figure 21 was chosen with five rows of 10 mm studs spaced at 90 mm. Detailing requirements of the respective European Technical Approval were followed.

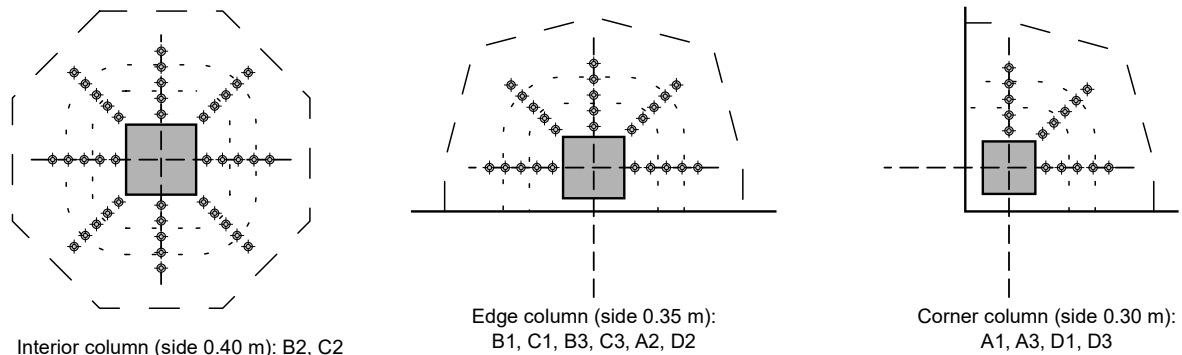


Figure 21: Layout of punching shear reinforcement

After test B1 and before test B2 (see Table 1), the slab of the first floor was strengthened for punching at connections B1, C2 and C3, using 10 mm post-installed shear bolts (Figure 21). In the past, this strengthening solution has been tested under seismic-type loading only on interior or edge slab-column connections [12, 27, 28]. The remaining connections were left as-built to offer valuable information on the performance of slab-column connections that have not undergone repair. Past studies dealing specifically with this topic are limited and they only cover single interior connections [14]. To facilitate the interpretation of the results, the layout of the post-installed bolts was kept the same as the layout of the studs used in the second floor. Figure 22 shows the studs and post-installed bolts used as punching shear reinforcement.



Figure 22: Shear reinforcement on edge columns: pre-installed at second floor (left) and post-installed at first floor (right)

To study the effect of flexural reinforcement distribution over the column, two different flexural reinforcement layouts were used in slab-column connections in symmetrical locations, with regard to the central axis along the shortest direction of the specimen.

1.2.3 Experimental programme and setup

According to the objectives described in the previous paragraphs, the test sequence has been planned to assess the seismic design employing a limited number of tests, in order to achieve a progressive and controlled damage of slab-column joints. The test programme is summarised in Table 5. Two hybrid

pseudo-dynamic tests were performed on the physical specimen coupled to virtual (numerically simulated) shear walls to assess the seismic performance at SLS and ULS (A1 and A2 respectively). A cyclic quasi-static test (B1) followed until punching was observed on the first floor. A number of slab-column connections at the first floor were repaired as described above and a cyclic test was performed until most of connections were damaged (B1-R). The aim of the final cyclic test was to examine the ultimate capacity of the structure (B2).

TEST ID	A1	A2	B1	B1-R	B2
TEST TYPE	Pseudo-dynamic	Pseudo-dynamic	Cyclic	Cyclic	Cyclic
ASSESSMENT	SLS design	ULS design	1 st floor punching	1 st floor after retrofitting	2 nd floor punching

Table 5: Test programme

The experimental programme included two different setups to verify the effect of transverse punching reinforcement: the first floor without transversal reinforcement and the second floor with cast-in-situ steel studs as in Figure 22 (left). In turn, each floor has two different longitudinal slab reinforcement layouts: the West side (alignments A and B) with rebars uniformly spread throughout the slab, while the East side (alignments C and D) with rebars concentrated close to columns, yet maintaining the same overall reinforcement ratio. Transverse reinforcement bars with the same specifications and in the same positions as those on the second floor were post-inserted the first floor slab, Figure 22 (right).

1.2.4 Pseudo-dynamic tests

The pseudo-dynamic method mates the properties of the structure as a physical quasi-static model tested in the laboratory with a numerical model representing the inertia [29]. The equation of motion of a model idealised in this form may be expressed as an ordinary differential second-order equation:

$$\mathbf{M} \mathbf{a}(t) + \mathbf{C} \mathbf{v}(t) + \mathbf{R}(t) = \mathbf{P}_{\text{eff}}(t) \quad (4)$$

This implies that the structure can be analysed as if it was supported on a fixed foundation and subjected to an effective force vector $\mathbf{P}_{\text{eff}}(t) = -\mathbf{M} \mathbf{I} a_g(t)$, where \mathbf{I} is a vector of zeros and ones and $a_g(t)$ is the ground acceleration time history. The mass matrix, \mathbf{M} , the viscous damping matrix, \mathbf{C} (typically null) [29], and the excitation force vector, $\mathbf{P}_{\text{eff}}(t)$, are all numerically specified. The restoring force vector, $\mathbf{R}(t)$, which is, in principle, nonlinear with respect to the displacement vector, $\mathbf{d}(t)$, is experimentally measured. At each time step t , the equation is numerically solved with the restoring forces, $\mathbf{R}(t)$, measured at time t by the actuator load cells, to obtain the acceleration, $\mathbf{a}(t)$, velocity, $\mathbf{v}(t)$ and displacement, $\mathbf{d}(t + \Delta t)$, at the next time step. The displacements calculated at step $t + \Delta t$ are then imposed on the structure by means of actuators and at the end of the step their load cells measure the restoring forces $\mathbf{R}(t + \Delta t)$ to be used for the calculation of the response to the next time step. An equation of motion with two degrees of freedom (displacement x , parallel to the East-West direction for the mock-up) was used. The actuators used two high-resolution optical encoders mounted on two reference frames as feedback for the proportional-integral-derivative controller (PID), to impose the calculated displacements of each floor without torsion. The mass for tests A1 and A2 was assumed to be 137 tonnes at the 1st floor and 139 tonnes at the 2nd floor. The reference input motion used in the pseudo-dynamic tests was a unidirectional 15 s-long time history, shown in Figure 20 (left). A zero-acceleration signal was added after the end of the record, to allow a free vibration of the test structure.

1.2.5 Cyclic tests

The cyclic displacement protocol was composed of increasing steps, in turn made of three cycles. The displacement history is presented in Figure 23. At the end of the test, in case a residual load occurred, the system was manually returned to a zero-load position through small cycles around the zero displacement.

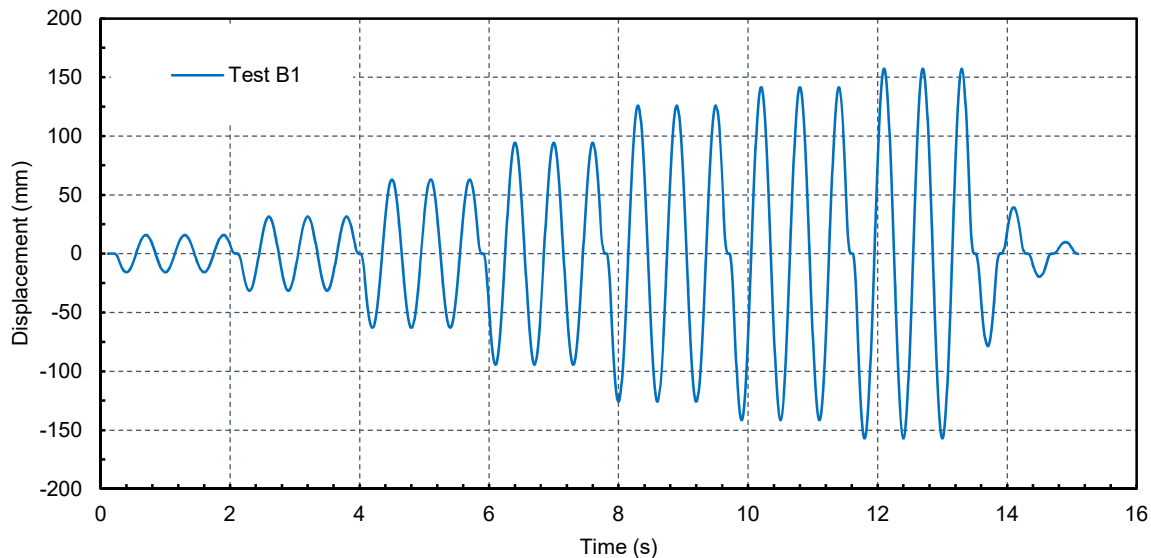


Figure 23: Displacement history for cyclic test B1

1.2.6 Loading system

A pair of hydraulic actuators, connected to the ELSA reaction wall, imposed the displacements to each floor. Each jack had 500 kN of working load and was equipped with a load cell for continuous measurement of the supplied load. The total load capacity was 2000 kN. The actuators were connected to steel beams that were in turn bolted to rebars cast into the slabs. Reinforcing bars, post-tensioned at over 500 kN for each actuator, were used to avoid the gap between the metal beams and the slabs and allow a two-sided coupling of the structure with the actuators. Two high-resolution (2 μ m) displacement transducers continuously measured the horizontal displacement at each floor level. These optical encoders were mounted on two reference frames and served as feedback for the PID controller for each actuator, as shown in Figure 19 and Figure 24.

1.2.7 Transducers for local measurements

Local measurements of displacement, rotation and strain were acquired using a network of electrical transducers. At each column, a control unit for the analog-to-digital conversion collected a cluster of signals (displacements, rotations and deformations) that were continuously streamed by electrical transducers placed from the foundation to the roof. The signals were digitally converted and routed through a local data network to a central unit, together with the signals (load and displacement) from the actuators.

In order to analyse each slab-column connection individually and to reconstruct the actions within the joints, it is necessary to know the column internal actions. Since it is not possible to do this directly, sensors have been specially designed and positioned in the mid-height of each column to measure the

shear and axial forces and the bending moment. These devices provided accurate shear and bending moment measurements in all columns during the experimental campaign.

A reduction of the measure points was allowed by the double symmetry of the mock-up. The sensors to measure the kinematics (displacement, rotation and local deformation) were installed in all columns of the central alignment (A2, B2, C2 and D2) and only on two columns of each external alignment (A1, B1, C3 and D3). Differently, the devices for measuring internal actions were placed on each column; otherwise, it would be impossible to reconstruct the internal equilibrium conditions of the structure.

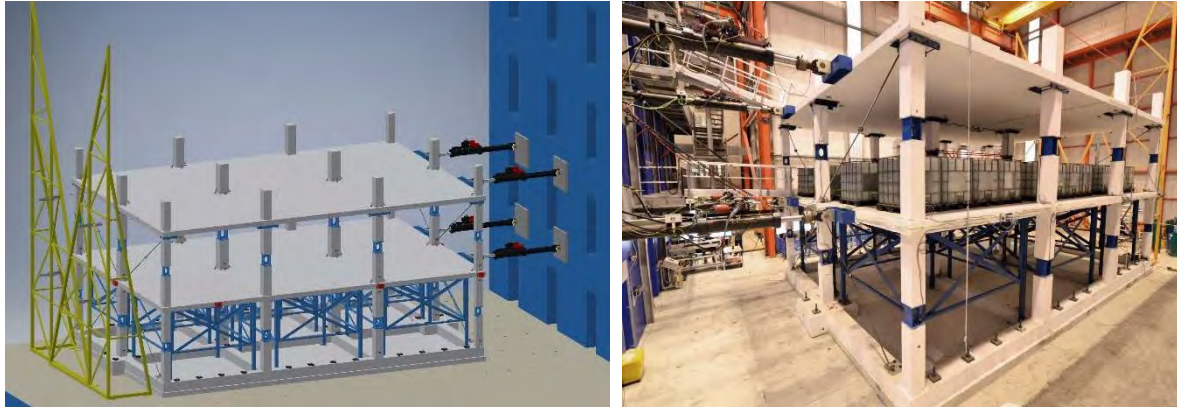


Figure 24: Test set-up: South-West rendering view (left) and North-East view (right)

1.2.8 Observation during testing

The global response in terms of base shear force versus the displacement recorded on the second floor is presented in the following. Figure 25 (left) shows the response of the flat-slab structure for test A2 using the ULS accelerogram. The base shear is the sum of the reaction forces of the actuators on the physical frame structure within the pseudo-dynamic response of a system with the shear resistant walls modelled with equivalent elastic stiffness and viscous damping. The maximum global relative drift reached approximately 22 mm, equal to a drift ratio of 0.35 % (top displacement divided by the height of the structure = 6400 mm).

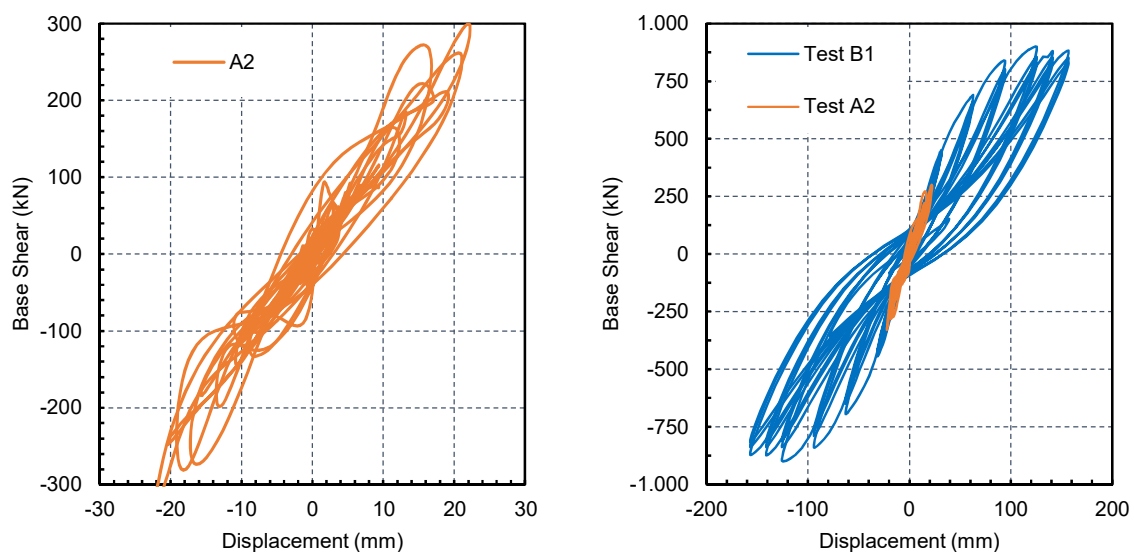


Figure 25: Base shear versus top displacement of the flat slab frame for test A2 (left) and for tests A2 and B1 (right)

Figure 25 (right) shows the results of test B1 compared with test A2, where the equal response for the cycles up to 0.4 % drift is evident. The structure reached a yield point between 1.5 % and 2 % drift. This can be related to yielding at the base of the ground floor columns. A progressive stiffness loss and pinching of the cycles with the increase of the displacement took place. The choice of the maximum relative inter-storey drift imposed in this test corresponds to the maximum value reached in slab-column connections in previous tests (Figure 18). The SlabSTRESS specimen reached 2.5 % drift (160 mm displacement) in Test B1. The base shear force remained nearly constant beyond drift of 1.5 %. In the repetition of cycles of equal amplitude starting from 1.5 % drift (95 mm displacement) a small loss of resistance occurred, indicating a sound global structural response up to 2.5 % drift.

1.2.9 Conclusions and outlook

The results of the seismic test at ULS indicate that flat slab frames combined with earthquake-resistant walls have nearly elastic response, with a maximum drift ratio of about 0.4 % for an accelerogram compatible with the ULS.

In the following cyclic tests, the response of the structure was explored up to the maximum drifts reached in the literature tests on individual connections (1.5 – 2.5 %) for gravity shear ratio of 0.4. The mock-up showed a good overall response up to 2.5 % drift ratio. The cyclic test has shown that the system can achieve high drift with limited or no strength deterioration and with satisfactory ductility and energy dissipation. No punching occurred in interior connections, while edge and corner joints were damaged. The results summarised above indicate that the combination of flat slab frames with different types of primary seismic systems can be explored. At the same time, these results confirm the need to perform large-scale tests on full-size buildings to understand the overall seismic behaviour of the building and to validate the experimental campaigns previously undertaken on sub-assemblies and small-scale tests.

The features of a seismic retrofitting system for flat-slab have been described. The tests showed that the system, previously used in individual connections, can be inserted in a building structure. The subsequent testing phases will examine the effectiveness of this solution.

Further research developments will analyse the damage accumulation, comparing the response of individual slab-to-column joints, to understand the role of different details of slab longitudinal and transverse reinforcement.

The outlooks of the SlabSTRESS programme are the development of the procedure for the seismic design of flat slab frames with better consideration of the role of primary and secondary seismic elements. The experimental results of the slab-column connections will be used also to verify and improve, where needed, the punching shear provisions and detailing rules of Model Code and Eurocodes 2 and 8.

1.2.10 References

- [1] CEN (2004): EN 1998-1 Eurocode 8: Design of structures for earthquake resistance – Part 1: General rules, seismic actions and rules for buildings.
- [2] Kinnunen S, Nylander H (1960): Punching of Concrete Slabs without Shear Reinforcement, Transactions of the Royal Institute of Technology, No. 158, Elander.
- [3] Nielsen MP (1998): Limit Analysis and Concrete Plasticity. CRC Press, 2nd edition.
- [4] Muttoni A (2008): Punching shear strength of reinforced concrete slabs without transverse reinforcement. ACI Structural Journal, 105 (6), 440-450.

- [5] CEN (2004): EN 1992-1-1 Eurocode 2: Design of concrete structures - Part 1-1: General rules and rules for buildings.
- [6] Pinto A, Taucer F, Dimova S (2007): Pre-normative research needs to achieve improved design guidelines for seismic protection in the EU. JRC Scientific and Technical Report, EUR 22858 ISSN 1018-5593, European Commission - Joint Research Centre, Ispra, Italy.
- [7] Fardis MN (2009): Seismic Design, Assessment and Retrofitting of Concrete Buildings based on EN-Eurocode 8, Springer Science & Business Media.
- [8] Hueste MB, Bai JW (2007): Seismic retrofit of a reinforced concrete flat-slab structure: Part I-seismic performance evaluation. *Engineering Structures*, 29 (6), 1165-1177.
- [9] ACI-ASCE Committee 421 (2015) ACI 421.3R-15 Guide to design of reinforced two-way slab systems. Reported by Joint ACI-ASCE Committee 421.
- [10] Drakatos IS, Muttoni A, Beyer K (2016): Internal slab-column connections under monotonic and cyclic imposed rotations. *Engineering Structures*, (123), 501-516.
- [11] Almeida AF, Inácio MM, Lúcio VJ, Ramos AP (2016): Punching behaviour of RC flat slabs under reversed horizontal cyclic loading. *Engineering structures*, (117), 204-219.
- [12] Almeida AF, Alcobia B, Ornelas M, Marreiros R, Ramos AP (2019): Behaviour of reinforced-concrete flat slabs with stirrups under reversed horizontal cyclic loading. *Magazine of Concrete Research*, 1-8.
- [13] Isufi B, Ramos AP, Lúcio V (2019): Reversed horizontal cyclic loading tests of flat slab specimens with studs as shear reinforcement. *Structural Concrete*, 20(1), 330-347.
- [14] Isufi B, Ramos AP, Lúcio V (2020): Post-earthquake Performance of a Slab-Column Connection with Punching Shear Reinforcement. *Journal of Earthquake Engineering*, (22) 1-23.
- [15] Almeida AF, Ramos AP, Lúcio V, Marreiros R (2019): Behavior of RC flat slabs with shear bolts under reversed horizontal cyclic loading. *Structural Concrete*, 22.
- [16] Gouveia ND, Faria DM, Ramos AP (2019): Assessment of SFRC flat slab punching behaviour—part II: reversed horizontal cyclic loading. *Magazine of Concrete Research*. 71 (1), 26-42.
- [17] Inácio MM, Lapi M, Ramos AP (2020): Punching of reinforced concrete flat slabs—Rational use of high strength concrete. *Engineering Structures*, (206).
- [18] Isufi B, Cismasiu I, Marreiros R, Ramos AP, Lúcio V (2020): Role of punching shear reinforcement in the seismic performance of flat slab frames. *Engineering Structures*, (207).
- [19] Coelho E, Candeias P, Anamateros G, Zaharia R, Taucer F, Pinto AV (2004): Assessment of the seismic behaviour of RC flat slab building structures. 13th World Conference on Earthquake Engineering WCEE13, Vancouver, Canada.
- [20] Fick DR, Sozen MA, Kreger ME (2017): Response of Full-Scale Three-Story Flat-Plate Test Structure to Cycles of Increasing Lateral Load. *ACI Structural Journal*. 114 (6).
- [21] Ministero delle Infrastrutture e dei Trasporti (2018): NTC 2018, DECRETO 17 gennaio 2018, Aggiornamento delle «Norme tecniche per le costruzioni».
- [22] Martinelli L, Mulas MG, Perotti F (1996): The seismic response of concentrically braced moment-resisting steel frames. *Earthquake engineering & structural dynamics*, 25 (11), 1275-1299.
- [23] Martinelli L (2008): Modeling shear-flexure interaction in reinforced concrete elements subjected to cyclic lateral loading. *ACI Structural Journal*, 105 (6), 675-684.
- [24] Iervolino I, Galasso C, Cosenza E (2010): REXEL: computer aided record selection for code-based seismic structural analysis. *Bulletin of Earthquake Engineering*. 8 (2):339-362.
- [25] Dilger WH, Cao H (1994): Behavior of Slab-Column Connections under Reversed Cyclic Loading, 5th International Colloquium on Concrete, Cairo, Egypt.
- [26] Robertson IN, Kawai T, Lee J, Enomoto B (2002): Cyclic testing of slab-column connections with shear reinforcement. *ACI Structural Journal*. 99 (5), 605-613.
- [27] Bu W, Polak MA (2009): Seismic retrofit of reinforced concrete slab-column connections using shear bolts. *ACI Structural Journal*. 106 (4), 514.
- [28] Polak MA (2005) Ductility of reinforced concrete flat slab-column connections. *Computer-Aided Civil and Infrastructure Engineering*. 20 (3), 184-193.

- [29] Pegon P, Molina FJ, Magonette G (2008): Continuous pseudo-dynamic testing at ELSA. Hybrid simulation; theory, implementation and applications. CRC Press, 1st edition.

2 EUCENTRE

Eucentre is a private non-profit foundation that pursues a mission of research, training and service provision in the field of earthquake engineering and, more generally, of risk engineering.

Founded in 2005 as an evolution of the European Centre for Training and Research in Earthquake Engineering already active in Pavia since 2003, it was established by four Founders, the University of Pavia, the University School for Advanced Studies IUSS of Pavia, the Italian Department of Civil Protection, the National Institute of Geophysics and Volcanology, to further develop the scientific, research and training expertise in the sector present in Pavia.

Eucentre currently operates within an international network with other research centres, earthquake engineering laboratories, institutions and companies. Eucentre is also Centre of Competence of the Italian Department of Civil Protection, to which it provides emergency support, elaboration of risk scenarios and research activities for the improvement of Civil Protection activities.

Together with the two Pavia universities, Eucentre also offers training courses for undergraduate and postgraduate students and for practitioners in the field of earthquake engineering and risk management.

Today Eucentre has an important asset of experimental labs consisting of:

- High performance uniaxial shaking table;
- Multi-axial shaking table (6 DoFs)
- Strong floor-reaction wall system;
- Dynamic testing system for bearings and isolators;
- Damper testing system;
- Contactless motion capture system;
- Mobile laboratory;
- Mobile unit for structural assessment.

The above – fully internally designed – testing facilities have been implemented throughout the years, together with the Foundation growth and the progressively gained expertise in almost two decades of wide spectrum experimental campaigns, design and implementation of often totally customized testing setup.

Today Eucentre is an international reference centre for institutions, for which it operates in the definition of emergency plans, in the elaboration of risk scenarios, in the vulnerability assessment of buildings and infrastructures, and for companies, to which it offers experimental and supporting services for the seismic design in various sectors such as civil engineering, transport networks, energy production and transport, hydrocarbon extraction, production of industrial devices, certification of anti-seismic devices.

Within SERA Transnational Access framework, three experimental campaigns have been successfully implemented and finalized.

The first project named “Dynamic testing of variable friction seismic isolation devices and isolated systems” aimed at the design and validation of innovative base isolation devices characterized by an optimized response against both minor and severe earthquakes. The dynamic hybrid testing technique, already implemented at Eucentre laboratories 8 years ago, widely increased the number of test runs

and the number of different devices that was possible to test compared to a typical shake table testing campaign.

The second project “Seismic Response of Actual Steel SILOS – SERA SILOS –” resulted in an excellent and synergic collaboration between Eucentre, the User Group and the external service suppliers involved in the testing campaign. After the numerical simulation and test design phases, more than 200 shaking table tests between random, earthquakes, sine and impulse signals have been performed both on fixed and base isolated Silo configurations.

The third and last foreseen project “Seismic Performance of multi-component systems in special risk Industrial Facilities – SPIF –” had as objective the holistic investigation of the seismic behavior of industrial plants equipped with complex process technology by means of shaking table tests. The structural or process-related interactions can lead to serious secondary damages, which, in addition to loss of production, also pose a danger to humans and the environment if hazardous substances are released due to leakages. The structure is a full-scale three-storey steel frame equipped with vertical and horizontal vessels, a more than 60 m long steel pipeline, an electrical cabinet and a typical conveyor system. The whole structural system (and non-structural components) has been tested both in fixed and seismic isolated configuration.

2.1 Project #3 – Dynamic testing of variable friction seismic isolation devices and isolated systems

Authors

H. Sucuoğlu⁽¹⁾, I. Lanese⁽²⁾, A. Pavese^(2, 6), P. M. Calvi⁽³⁾, C. Galasso⁽⁴⁾, U. Ozcamur⁽⁵⁾, V. Quaglini⁽⁷⁾

⁽¹⁾ *Middle East Technical University*

⁽²⁾ *EUCENTRE Foundation, Pavia, Italy*

⁽³⁾ *University of Washington*

⁽⁴⁾ *University College London*

⁽⁵⁾ *TIS Technological Isolation System*

⁽⁶⁾ *University of Pavia, Pavia, Italy*

⁽⁷⁾ *Politecnico di Milano, Italy*

2.1.1 Introduction

Seismic isolation is the prominent seismic protection technology for buildings, bridges and generally different kind of structures. It aims to significantly, or in many cases totally, reducing structural/non-structural seismic vulnerability under severe earthquake ground motions. Seismic isolation is implemented with isolation devices of two basic types: rubber bearings with lead core, and friction pendulum devices. Steel-based friction pendulum devices are gaining increasing popularity over rubber isolators and are being widely used in several applications worldwide. This is mainly due to the versatility in design and production, and their easier implementation in practice. The variability of the

seismic demand is much less in friction pendulum devices. Moreover, torsional eccentricity imposed by the distribution of friction pendulum devices along the isolation interface is less significant compared to the rubber devices, hence their re-centring capacity is higher.

The main focus of the proposed project is to improve friction pendulum isolation devices by imposing variable friction properties along the sliding surfaces. Although there are several theoretical studies in literature on the theory and analysis of variable friction devices, there is no developed technology yet. The variable friction devices that will be developed within the scope of the proposed project will be designed and produced by the industrial partner TIS. The validation of the proposed concept will be performed through characterization tests following an EN15129-like type testing protocol, then moving to seismic tests once satisfactory preliminary results are obtained. The dynamic response of the isolated system under uniaxial seismic excitation will be observed. An improved definition of ground motion intensity measures (IMs) will be developed, particularly in near-fault conditions, as well as the corresponding hazard-compatible record selection procedures for friction based isolation devices. Finally, non-linear numerical models will be implemented and calibrated through the experimental data for predicting the isolator and system response accurately, and then, based on a larger analytical study (i.e., simulation-based) propose design procedures for structures isolated with variable friction devices.

2.1.2 Main research objectives and expected contribution to the seismology and earthquake engineering community

The main objectives of the proposed research are:

- To develop variable friction seismic isolation devices;
- Conduct dynamic verification tests in a certified and qualified laboratory equipped with real-time seismic testing facilities;
- Develop analytical procedures for response prediction, and calibrate analytical models with the test results;
- Propose design procedures for buildings isolated with variable friction pendulum devices;
- Perform extensive parametric study on the performance of buildings isolated with variable friction pendulum devices.

The industrial partner TIS, which is producing friction pendulum devices in Ankara, Turkey, recently worked on the development of variable friction devices in its R&D department by applying several treatment techniques on the stainless steel friction surfaces of friction pendulum isolators through a grant from the Turkish Research Council (TUBITAK). This project was completed in 2017, where a certain progress was achieved. Two different friction coefficients have been obtained by applying two different polishing techniques on the stainless steel sliding surfaces of the friction pendulum isolators. The friction coefficients obtained between the treated surfaces and the PTFE based friction material used by TIS are 4.5-5% with advanced polishing, and 6.5-7% with ordinary polishing, under a common vertical pressure of 45 MPa. The third and the lowest friction will be obtained by applying circular perforations to the advanced polished steel surface for increasing pressure underneath the slider pad, further reducing the friction. There is an inverse relation between interface pressure and the coefficient of friction.

Milano Polytechnic and TIS worked on the development of a new material with lower friction properties. Possible application of this material to the variable friction device is meant to be investigated in the project to obtain another set of variable friction surfaces.

Variable friction surfaces will be implemented on the curved circular stainless steel sheets in concentric circular bands, from lowest friction at the centre to the highest at the periphery. The lowest friction

region at the centre is merely a circular hole with a calculated radius and the edges trimmed smoothly in order to prevent consumption of the friction material. Different friction materials for obtaining different sets of variable friction coefficients will be also developed. Such materials will be assessed by Milano Polytechnic University and material wear tests in combination with different steel surfaces will be conducted at their laboratories within the scope of the project. Pressure and velocity dependence relation for different friction materials and mating surfaces will be established at these tests and used for preliminary evaluation of the material combinations.

Once the variable friction pendulum devices are designed for a selected superstructure weight, vibration period and design displacement, they will be produced by TIS at their factory in Ankara, and four devices will be shipped to EUCENTRE for seismic verification testing. The first set of tests on the new devices will be conducted on the Bearing Tester System (test press) by applying the EN 15129 testing protocol for friction pendulum prototypes. These tests will reveal the cyclic force-displacement characteristics and their stability under axisymmetric displacement reversals. Then, the devices will be subjected to real seismic tests within a simple structural context; a 1-storey isolated building will be considered.

A typical prototype device that will be tested at the EUCENTRE Lab Bearing Tester is shown in Figure 26.

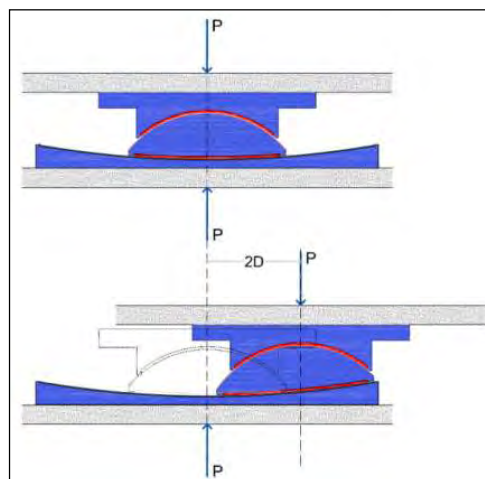


Figure 26: Prototype isolator

Upon completion of the experimental testing program, analytical models for the force-displacement behaviour of variable friction devices under imposed displacement reversals that mimic seismic excitation will be refined. Analytical studies will be conducted at the University of Washington, the Middle East Technical University, and, partly at UCL (for uncertainty characterization of the developed analytical models). These models will then be calibrated with the test results for improving their prediction capability. Major response parameters for analytical prediction are the maximum displacement demand, residual displacement of the isolators and maximum base shear transmitted to the superstructure.

Due to the strongly non-linear constitutive behaviour typical of many isolation devices (as those developed here), the seismic response of base-isolated buildings is usually evaluated through non-linear dynamic analysis. In this type of analysis, a suitable set of ground motions is needed for representing the earthquake loads and for exciting the structural model. Many methods can be found in the literature for defining the ground motions. When natural accelerograms are used, the methods mainly differ from each other based on the IMs used for scaling the records to the defined earthquake intensity level. Investigations have been carried out for evaluating the predictive capability of the

intensity measures used in these methods. While many studies focused on ordinary buildings, only a very few are focused on base-isolated ones. Hence, a further objective of the proposed research is to evaluate the most commonly used IM, which are currently available in the literature, with respect to their capability to predict the seismic response of base-isolated buildings implementing the newly developed variable friction seismic isolation devices. Selected for the investigation will be a set of frame structures characterized by a different number of storeys and base-isolated with systems having different properties (e.g. uniform and variable friction). Different sets of accelerograms, consisting of ordinary and pulse-like near-fault records, will be used in the analyses and in the evaluation of the IMs. Modified versions of existing IMs will be proposed, with the intent of improving the correlations between the considered IMs and response quantities of interest, in a performance-based earthquake engineering (PBEE) framework.

The final phase of analytical studies is concerned with developing a design procedure under design earthquake excitation. An equivalent linear analysis procedure which conforms to the existing code procedures for isolator design will be established where the basic design parameters are equivalent stiffness and damping at the design displacement and the base shear force transmitted to the superstructure.

In summary, the expected outcome of the proposed project is a new seismic isolation device with more favourable characteristics compared to the existing friction pendulum devices with uniform friction. Variable friction requires less curvature, hence larger radius of curvature for equivalent energy dissipation, and lower restoring force compared to the uniform friction device. This results in smaller devices for the same design displacement. Related savings in material leads to reduced cost of devices, which is essential for their wide spread public use in earthquake protection. Lower curvature also reduces the vertical accelerations resulting from pendulum motion. A low friction coefficient at the centre during activation of the isolation mode is a further advantage for reducing floor accelerations of the superstructure which is critical for protecting acceleration sensitive equipment. The only expected problem can be a reduced recentring capability due to higher friction and lower curvature of the sliding surface. An extensive analytical study will be carried out to investigate the effect of residual displacements at the end of the ground excitation.

The present research is expected to give a significant contribution to the seismology and earthquake engineering community. Modern earthquake engineering is a fairly young field of engineering science, not older than 80 years. The advances in engineering seismology and structural analysis methods had been remarkable during these decades which eventually lead to the development of modern earthquake resistant design procedures and the associated seismic design codes. Despite such significant progress, the ultimate performance objective of “no damage to structures under strong earthquakes” had never been achieved. This is indeed impossible with the conventional construction materials and techniques due to their limited capacities which are easily exceeded by the excessive demands produced by strong earthquakes. The only possibility for meeting this fundamental objective is introducing new technologies to earthquake resistant construction.

Seismic isolation is the only successful technology so far. Although it was developed almost 40 years ago, its implementation in practice had been very limited. One of the basic reasons for its limited use is the high cost of isolation devices. The basic motivation, originality and innovation of the proposed project comes from introducing variable friction to sliding surfaces of friction pendulum devices for developing smaller, hence cheaper devices for obtaining equivalent seismic performance. Variable friction is a simple idea, but not so easy to realize. It has not been developed and produced before, hence it is original. Analytical solution of isolator response with variable friction applied to a single pendulum device is available, but it is not yet available for double pendulum devices. It will be

investigated how variable friction with circular bands can be formulated in a double pendulum device. Once a stable, symmetrical response is obtained, then the concept will be extended to double pendulum devices for further testing. Whether implemented to single or double pendulum devices, the proposed research is both original and innovative because this technology has not been developed before and produced as a new product by anybody else.

Imposing variable friction along the sliding surfaces does not add to the cost of devices, but increases the effectiveness of isolators significantly. The User Group will conduct a comprehensive cost-benefit analysis for variable friction devices in comparison to the uniform friction pendulum devices for proving their economic feasibility in earthquake protection. Broader impact of a new technology or invention can be proved if it can be easily used in practice. This depends on the robustness of its response, and the market price. The aim of the proposed research is to show that it is possible to obtain the desired robustness of seismic response and a significantly cheaper product can be obtained when variable friction is implemented. Lower curvature will reduce the steel waste remarkably, and higher restoring force will reduce the device radius due to lower displacement demand. The result of the combined benefit is a smaller isolation device with a reduced cost.

In summary, the project can offer tremendous opportunities for broader impact on Society, Economy, Knowledge and People.

- Society: Findings from the project can contribute to increase society's seismic safety and resilience by:
 - o protecting critical structures/infrastructure, and allowing them to remain operational (e.g. hospitals, schools, etc.) or to “return to normal” as soon as possible;
 - o increasing the safety of the population, particularly in the case of critical structures/infrastructure.
- Economy: Apart from the social risks, extreme loads result in enormous economic losses related to repair costs, loss of building occupation, business interruption, or building demolition due to irreparable damage. The project can eliminate these economic losses by avoiding (or significantly reducing) damage. More in general, the proposed research on variable friction seismic isolation devices and isolated systems will significantly contribute to the competitiveness of several European industries (e.g., engineering consultants, construction companies, etc.) and stakeholders with a characterized technology to increase their markets worldwide through new technologies offering higher performance and lower prices. The ultimate goal is to create a vibrant core of activities in which research is driven by genuine user priorities, and industry in turn benefits from access to state-of-the-art techniques and innovation assembled by world-leading experts.
- Knowledge & People: The project addresses major intellectual challenges by going beyond the state-of-the-art in the field of seismic isolation, seismic design, earthquake response assessment, and design of resilient and sustainable structural systems. Therefore, the project will raise major international interest, providing several stakeholders with an innovative, advanced, performance-based framework (and related computational tools) for designing isolated structures and infrastructure. The project will also provide training to postgraduate students (at MSc and PhD level) collaborating with the investigators involved in the different tasks at the different institutions and contribute to the Continued Professional Development of industrial partners.

2.1.3 Numerical-Experimental Testing campaign

In a preliminary phase, small scale tests have been conducted to experimentally assess the effectiveness of the proposed concept. The research group has been investigating variable friction surfaces on a small scale model of a flat bearing, using a custom biaxial testing system.

The test piece consists of a flat pad of sliding material (diameter 50 mm) rubbing on a stainless steel sheet. The surface of the stainless steel sheet exhibits two areas with different roughness: a “smooth” area with $R_a = 0,02 - 0,04 \mu\text{m}$, and a “rough” area with $R_a = 6 - 10 \mu\text{m}$ (Figure 27).

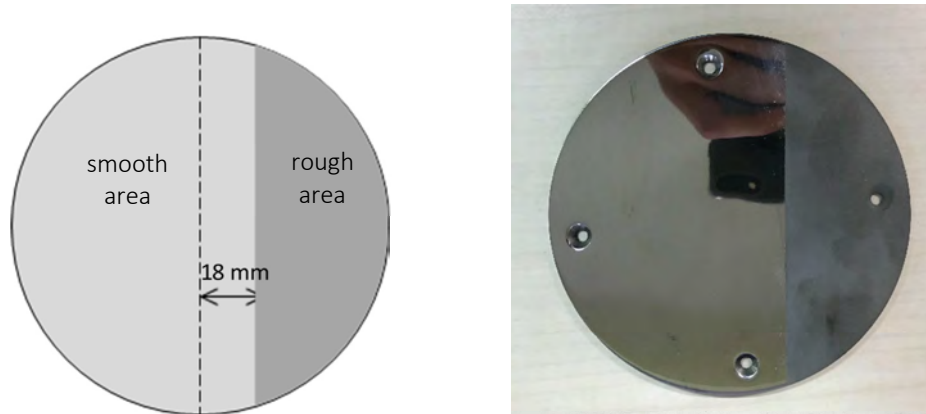


Figure 27: Dimensions of the test sample (left) and picture of the stainless steel plate (right)

Tests were performed at two levels of contact pressure on the pad surface, namely 22.5 MPa and 45 MPa. Each test consisted of 100 fully reversed cycles with total amplitude (peak-to-peak) of 30 mm at three different velocities: 1 mm/s, 50 mm/s and 100 mm/s.

Typical results are illustrated in Figure 28, in terms of ratio of horizontal to vertical force (i.e. the coefficient of friction versus displacement plots at two velocities. Only results at 22.5 MPa contact pressure are shown, but consistent results were obtained at either pressure level.

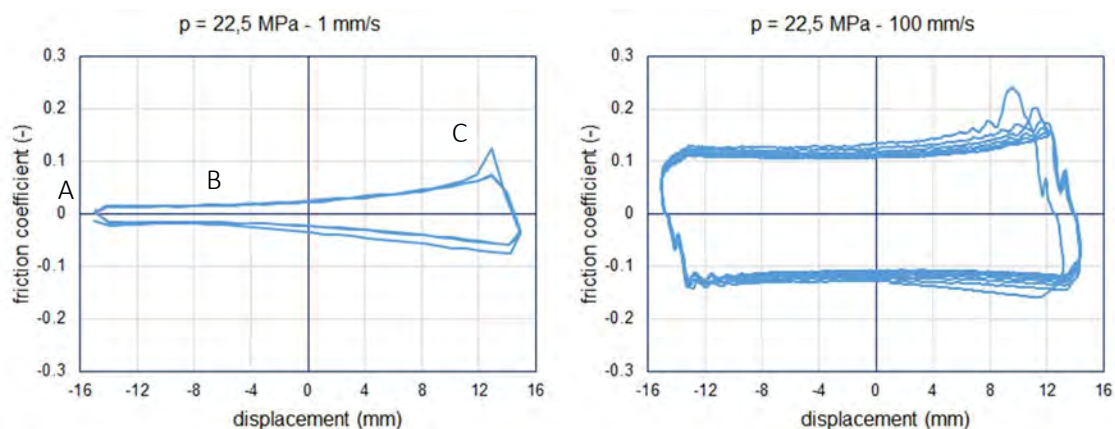


Figure 28: Friction – displacement plots at different velocities

The test at very low velocity (1 mm/s) shows the expected behaviour of the variable friction bearing, with a steady and low coefficient of friction as far as the pad slides on the smooth surface (branch OA), and a stiffening response as the pad crosses the rough surface (branch AB). Depending on the pad position, the coefficient of friction increases from a minimum value of 1.3% to a maximum value of 12.5% at the first cycle and 7.4% at the subsequent cycles (six-folds increase).

By increasing the velocity, the change of the coefficient of friction with surface roughness is less pronounced, though still important: at 100 mm/s the coefficient of friction ranges from 12% to 23.8% at the first cycle and 22% at the subsequent cycles (two-folds increase). This behaviour is ascribed to the effect of heating of the sliding pad, which produces a most important decrease in the coefficient of

friction over the rough area, where friction is higher, than over the smooth area. It is also worth noting that good stability of the friction plots over the duration of the test, corresponding to an accumulated slide path of 6000 mm.

In conclusion, the small scale tests have provided an independent confirmation of the feasibility of manufacturing variable friction sliding bearings with stable and consistent behaviour even during sustained motion; further they have addressed to need of sliding material with a good stability of the coefficient of friction with temperature.

Afterwards, full-scale experiments were conducted on a total of six Single Variable Friction System (VFS) and two Double Curvature VFS prototypes at the experimental facilities of using the Bearing Tester System (BTS) shown in Figure 29.

Each prototype bearing of the first category consisted of a conventional single friction pendulum system with rigid slider, but the concave stainless steel sliding surface was treated using different polishing techniques to achieve spatially varying frictional properties. Namely, three areas (in some specimens only two), with different roughness were obtained: starting from the centre of the device, a low friction “polished” surface, a medium friction “unpolished” one, and a high friction “sandblasted” region. A schematic drawing and a plan view of one of the full-scale prototype VFS bearing with polished and unpolished treatment are shown in Figure 30.

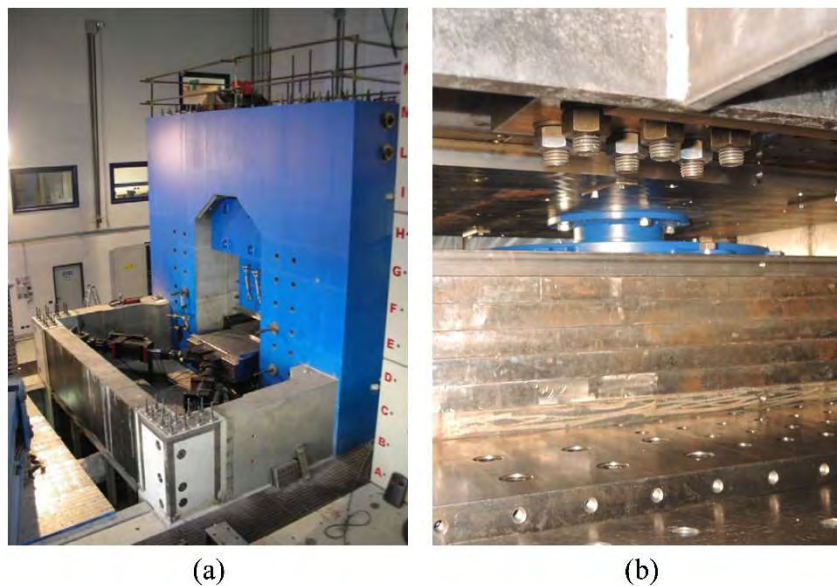


Figure 29: (a) The EUCENTRE BTS; (b) Elevation view of the bearing test setup

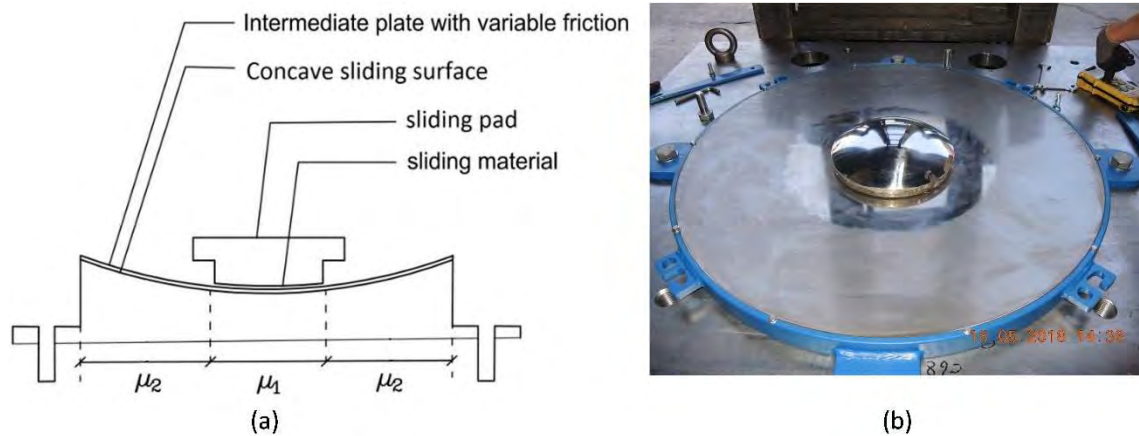


Figure 30: (a) Schematic drawing of a two-ring VFS bearing; (b) Plan view of the concave sliding surface and the slider of the prototype VFS bearing

The main properties of one of the tested VFS prototypes are summarized in Table 6. The parameters reported in the table represent the radius of the sliding pad (r_0), the radius of the low friction area (r_1), the external radius of the medium friction area (r_2), the coefficient of friction between the sliding pad and the low friction area (μ_1), the coefficient of friction between the sliding pad and the medium friction area (μ_2), and the radius of curvature of the sliding surface (R).

Prototype #	r_0 (m)	r_1 (m)	r_2 (m)	μ_1 (%)	μ_2 (%)	R
1	0.125	0.150	0.450	7.0	9.2	4.5

Table 6: Properties of the tested VFS prototypes

The dynamic coefficients of friction between the sliding pad and the sliding surface were equal to 7.0% and 9.2% for the smooth and the rough areas, respectively. These values have been obtained through friction characterization tests performed in the laboratory.

Following the friction characterization tests, the VFS prototypes were subjected to the testing program recommended by the European standard EN 15129. The program comprised a series of unidirectional harmonic displacement histories, with different displacement amplitudes and frequencies. A list of the tests conducted is summarized in Table 7. For brevity, only some of the main results are presented herein. For the presented tests, the displacement amplitude of the harmonic motion was 0.3 m, and the peak velocities were 500 mm/sec and 200 mm/sec.

Test name	Ampl. [m]	Max.vel. [m/s]	load shape	Vert.load [kN]	cycles
Frictional resistance	± 0.006	0.0001	triangle	2000	1
Service	± 0.060	0.005	sine	2000	20
Benchmark	± 0.300	0.050	sine	2000	3
Dynamic 1	± 0.075	0.500	sine	2000	3
Dynamic 2	± 0.150	0.500	sine	2000	3
Dynamic 3	± 0.300	0.500	sine	2000	3
Seismic	± 0.300	0.500	sine	1000	3
Seismic	± 0.300	0.500	sine	2500	3
Bidirectional	± 0.300	0.500	sine	2000	3
Property verification	± 0.300	0.500	sine	2000	3

Table 7: Testing program on Group 1 VFS prototypes

Both single and double VFS devices were then subjected to hybrid tests, simulating the response of a base isolated single-story structure. The stiffness of the superstructure (treated as a linear-elastic single-degree of freedom system) was selected to achieve different natural periods of vibration ranging from 0.4 to 1 second. The tests were performed under the application of recorded ground motions with different intensities. The peak velocity recorded during these tests reported was approximately 1 m/sec.

The horizontal force-displacement response characterizing the VFS prototypes is reported in Figure 31. The black lines represent the first-cycle response, while the grey lines refer to the second and third loading cycles. It can be seen that the first-cycle response differs quite significantly from that of the subsequent cycles. In particular, the effects of the variable friction are clearly visible in the first cycle, but they tend to disappear in later loops. This undesirable discrepancy was ascribed to the creation of a transfer film of the sliding material on the mating surface, which smoothed the surface and made the sliding behaviour more uniform over the two areas with different roughness. At the current stage, this still represents a major challenge and one of the main constraints limiting the possible frictional properties that can be selected for a VFS. Additionally, μ_1 and μ_2 are only marginally different in their initial values, thus the variability of the friction coefficient is low.

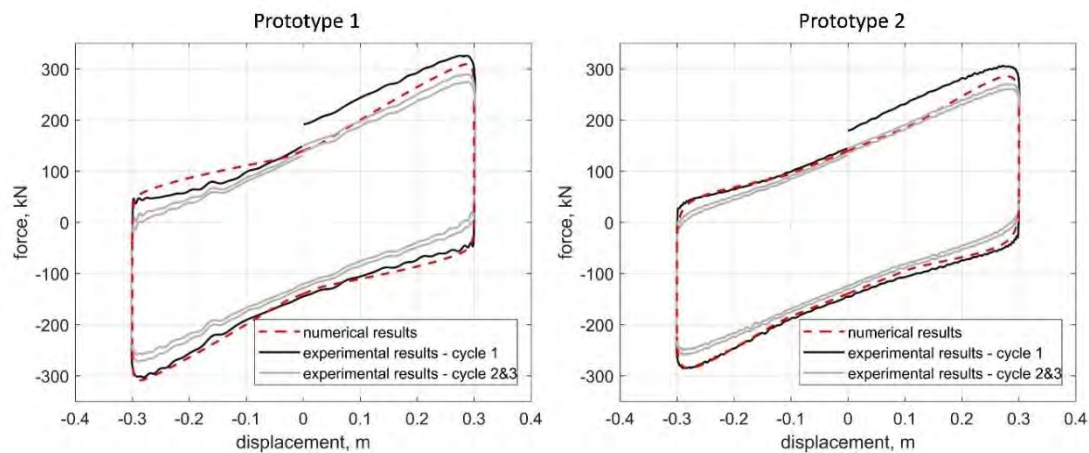


Figure 31: Comparison between the hysteretic curves from numerical model and experimental data for Group 1 VFS prototypes





Figure 32: Test of VSP and failure of the high friction sliding surface

Since in the first specimens the transition between the regions with different friction was not that evident and further reduced in the subsequent cycles, a sliding surface with the lowest and highest friction was considered as well. This abrupt response modification gave some interesting preliminary results, while resulted in the failure of the specimen due to the loss of bonding of the surface with the bottom steel plate (Figure 32).

The non-optimal response obtained from testing the bearings led the research team to opt reconsider the original plan, which involved shake table testing of a one-storey case-study structure, and opt for hybrid simulation (also referred as hybrid testing) to maximize the testing days and the different devices possible configurations (single and double CSS, different sliding materials, different sliding surface treatments). The hybrid testing technique consists in combining a numerical model of a portion of the structure to be tested, together with a physical portion, generally the one(s) difficult to model and/or under experimental investigation. These two systems interact with each other in real-time, in order to represent the experimental test of the whole structural system. In this case, the physical system was the isolation device prototype, while the numerical system was a 2-DOF structure, identical of the one initially foreseen (R.C. slab on the isolation system and a 1-storey frame structure on top of it). The whole system was subjected to real ground motions as the input of the hybrid testing. Since the physical devices have been tested on the Bearing Tester instead of the shake table, bigger and realistic slider dimensions have been considered (Figure 33).

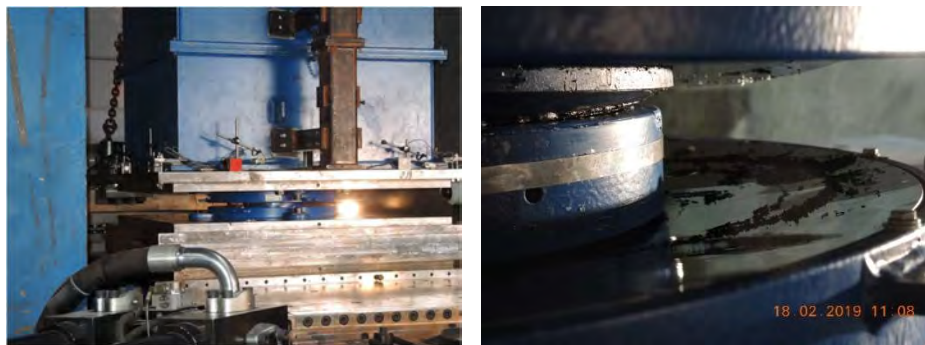


Figure 33: Test on the EUCENTRE Bearing Tester through hybrid testing technique

The horizontal force-displacement responses characterizing the VFS prototype undergoing a realistic ground motion in the context of hybrid testing is shown in Figure 34. The black dashed lines represent the experimental results, while the grey solid lines represent the numerical predictions, obtained using the newly developed model described later.

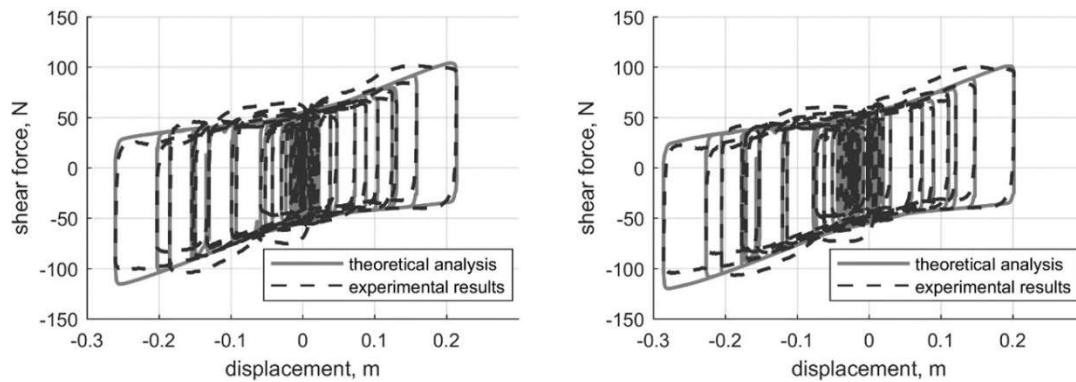


Figure 34: Comparison between the hysteretic curves from numerical model and experimental data for Group 2 VFS prototype

The research activities related on numerical aspects can be summarized as follows:

1. Development of a 3D numerical model to simulate the response of VFS in the context of non-linear static and dynamic analysis;
2. Implementation of the 3D VFS model into OpenSees;
3. Partial processing of the experimental results and preliminary validation of the developed numerical model, using the results of the available experiments;
4. Development of a Direct Displacement-Based Design procedure for structures isolated via VFS;
5. Validation of the proposed design method via extensive parametric study conducted on Single- and Multi-degree of freedom (SDOF and MDOF) (involving > 1,000,000 non-linear time history analysis);
6. VFS performance evaluation via extensive parametric study conducted on Single- and Multi-degree of freedom (involving > 1,000,000 non-linear time history analysis);
7. Investigation of using VFS as passive adaptive devices via parametric study conducted on Multi-degree of freedom systems.

The research activities listed above are described in more detail in the following of this section.

2.1.4 Development of a 3D VFS numerical model

The VFS numerical model was developed based on the bi-directional plasticity model traditionally used to represent the hysteretic behaviour of the single Friction Pendulum (FP) bearing. This plasticity model was adapted and used to implement the response of VFSs. To this end, the “yield force” term present in the FP model was modified in order to account for the fact that in a VFS the “yield force” is a function of the radial position of the sliding pad.

To deal with the bearing response in the horizontal directions, an iterative procedure was implemented for state determination (evaluating shear forces and tangent stiffness matrix given horizontal displacements of the sliding pad). Initial evaluation of the “yield” strength, for the circular interaction surface is needed based on the bearing absolute velocity, the force normal to the sliding surface (which depends on the selected friction model), and the position of the sliding pad. This was done using a numerical return-mapping algorithm for state determination of a rate independent plasticity model.

The VFS model developed accounts for complex aspects of the bearing response, such as simultaneous influence of velocity and axial force on the coefficient of friction, and vertical-horizontal coupling effect due to the geometric radius of curvature.

2.1.5 OpenSees implementation

The VFS model briefly described above was developed and implemented based on the framework of the original Single Friction Pendulum Bearing Element that is readily available in OpenSees.

Figure 35 and Figure 36 show a schematic view of the VFS element and the implementation algorithm, respectively. These systems are treated as two-node elements, in which one node represents the concave/at sliding surface and the other represents the sliding pad. The element can have zero length or it can be assigned the actual bearing height by depending the nodal coordinates to corresponding values.

Various modelling options are available but not reported here for the sake of brevity.

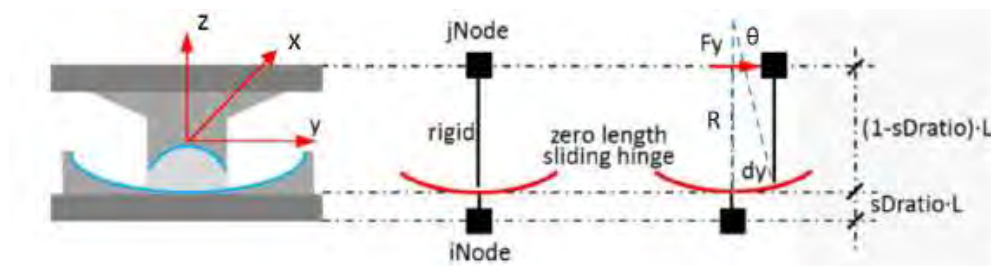


Figure 35: Schematic drawing of the Variable Friction Pendulum element in OpenSees.

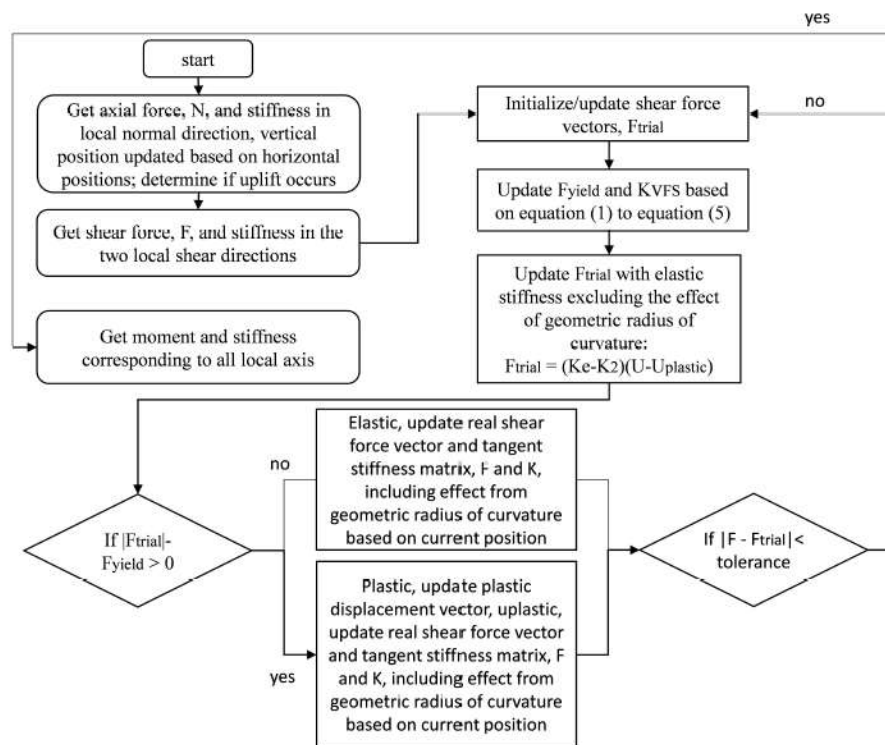


Figure 36: Algorithm for VFSs implementation into OpenSees

2.1.6 Partial processing of the experimental results and preliminary validation of VFS model

The results of the experimental program described above were processed and used to provide some initial validation of the VFS theoretical behaviour and of the numerical element described above.

Some of the comparisons between experimental responses and numerical predictions were shown earlier. Overall, the numerical predictions were in good agreement with the experimental results. The preliminary results obtained are very promising and suggest that the numerical element developed can adequately capture the mechanics of the VFSs tested, in the context of time history analyses. However, more experimental evidence is needed (including 3-D testing) before definitive conclusions can be drawn.

At this stage of the work, the VFSs were modelled using a velocity-dependent friction model while pressure-dependency was neglected because the axial force remained approximately constant throughout the tests. The relationship between the sliding velocity and the coefficient of friction used was:

$$\mu(v) = \mu_{max} \times (1 - (1 - \tilde{\mu}_v)e^{-av})$$

where $\mu(v)$ represents the coefficient of friction as a function of sliding velocity, μ_{max} is the coefficient of friction at high sliding velocity, $\tilde{\mu}_v$ is the ratio between the coefficient of friction at slow sliding velocity and μ_{max} , and a is a constant describing the transition rate from low to high sliding velocity regimes. Past studies suggest that the value of the coefficient a can range from 20 sec/m to over 100 sec/m depending on the sliding material utilized. In the present work, it was found that setting a equal to 20 sec/m provided the best match between the experimental results and the numerical predictions. The parameter $\tilde{\mu}_v$ was set equal to 0.5, which is consistent with past studies.

2.1.7 Development of a Direct Displacement-Based Design procedure for structures isolated via VFS

A direct displacement-based design method was implemented for VFSs. As an example, this design method is summarized in Figure 37 (alongside the design Equations, reported in Figure 38), for Adaptive VFSs isolating a flexible SDOF structure. Analogous approaches have been developed for VFSs isolating different types of MDOF structures.

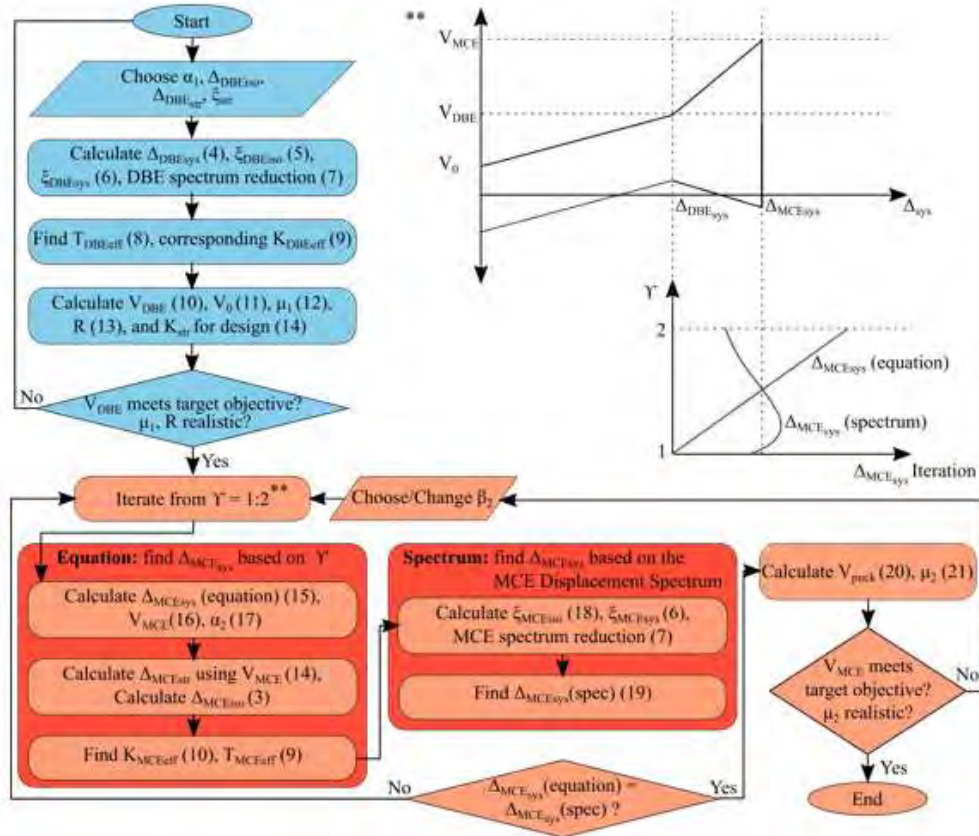


Figure 37: Adaptive VFS Design Flowchart

$$\Delta_{sys} = \Delta_{str} + \Delta_{iso} \quad (4)$$

$$\xi_{DBE_{iso}} = 2/(\pi\alpha_1) \quad (5)$$

$$\xi_{sys} = (\xi_{str}\Delta_{str} + \xi_{iso}\Delta_{iso})/\Delta_{sys} \quad (6)$$

$$\eta = \sqrt{0.07/(0.02 + \xi_{sys})} \quad (7)$$

$$T_{eff} = T_{spec}\Delta_{sys}/(\Delta_{spec}\eta) \quad (8)$$

$$K_{eff} = 4\pi^2 m/T_{eff}^2 \quad (9)$$

$$V = K_{eff}\Delta_{sys} \quad (10)$$

$$V_0 = V_{DBE}/\alpha_1 \quad (11)$$

$$\mu_1 = V_0/W \quad (12)$$

$$R = W\Delta_{DBE_{iso}}/(V_{DBE} - V_0) \quad (13)$$

$$K_{str} = V_{DBE}/\Delta_{DBE_{str}} \quad (14)$$

$$\Delta_{MCE_{sys}}(guess) = \gamma\Delta_{DBE_{sys}} \quad (15)$$

$$V_{MCE} = V_{DBE} + \frac{\Delta_{MCE_{sys}} - \Delta_{DBE_{sys}}}{1/K_{str} + \beta_2 W/R} \quad (16)$$

$$\alpha_2 = V_{MCE}/V_{DBE} \quad (17)$$

$$\xi_{MCE_{iso}} = \frac{2\gamma + (\alpha_2 - \alpha_1)(\gamma - 1) - (\alpha_1 - 1)(\gamma - 1)^2}{\pi\alpha_2\gamma} \quad (18)$$

$$\Delta_{MCE_{sys}}(spec) = \Delta_{spec}T_{eff}/T_{spec}\sqrt{0.07/(0.02 + \xi_{sys})} \quad (19)$$

$$V_{puck} = V_{DBE} + \beta_2(W/R)d_{puck} \quad (20)$$

$$\mu_2 = (V_{puck} - W/R(\Delta_{DBE_{iso}} + d_{puck}))/W \quad (21)$$

Figure 38: Adaptive VFS Design Equations

It should be noted that damping of VFSs is represented using Equivalent Viscous Damping (EVD), which is based on Jacobsen's equivalence between the energy dissipated in a cycle of the system and the energy dissipated by an equivalent viscous system. In order to validate the expression for use in design, a suite of over 600,000 NLTHAs was conducted and compared to equivalent EVD values. Reasonably

good agreement between the equation and analysis data was found (see Figure 39), thus Eq. (18) was used in the AVFS design process.

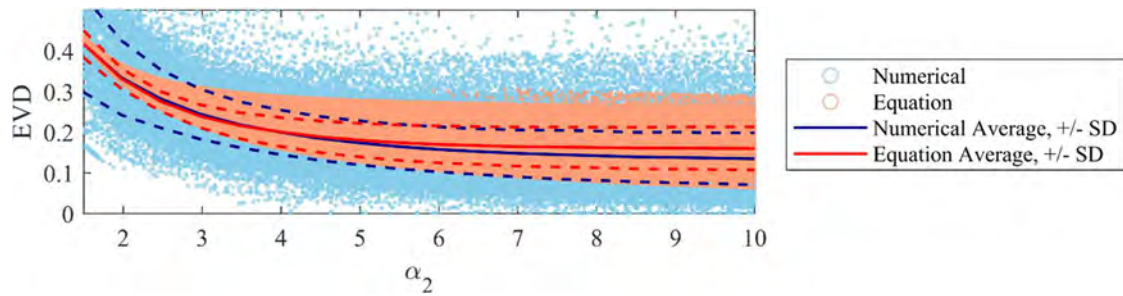


Figure 39: Equivalent Viscous Damping of AVFS

2.1.8 Validation of the proposed design method via extensive parametric study

In order to test the reliability of the design approach developed, several parametric studies were conducted that involved more than 1,000,000 non-linear time history analyses.

For instance, one of those studies involved two sets of VF devices that were designed for the demand of 5 different US cities: one set for rigid structures, and one set for flexible. Each city had 20 far-field ground motions (10 pairs). The VFS bearings were designed to achieve desired performance under the DBE and MCE design levels.

The results from all devices (pertaining to this particular study) normalized by their respective design values can be seen in Figure 40.

Each boxplot represents a device design, with the thick horizontal black line representing the mean of the 20 NLTHA for that device, the error bars showing maximum and minimum values, and the dots representing outliers. It can be seen that, on average, both displacements and forces are overall well predicted (yet somewhat conservative).

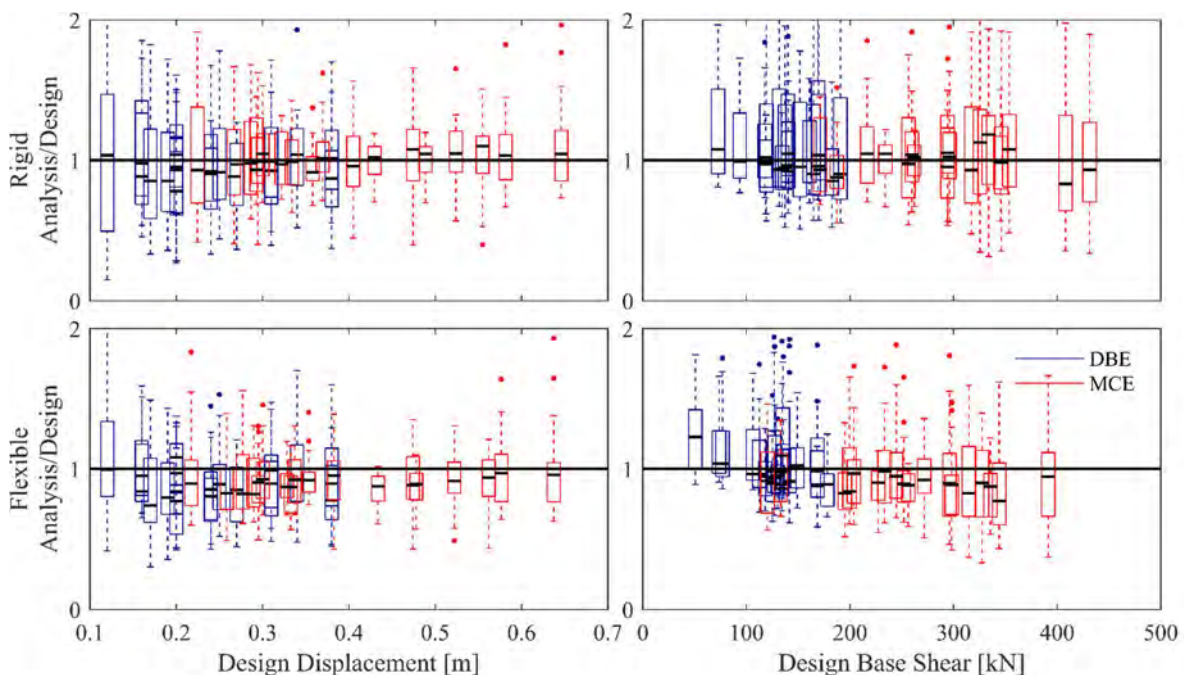


Figure 40: Design vs. NLTHA for Rigid and Flexible SDOF Systems

2.1.9 VFS performance evaluation via extensive parametric study

Several case-study structures were analysed to evaluate the performance of VFSs in the context of protecting structures against the effects of earthquakes. Overall, the results collected showed that, VFSs can be used to reduce the maximum base shear and the maximum displacement at the bearing level, while maintaining the residual displacement within reasonable ranges.

One of the many case-study structures considered is outlined in Figure 41 as an example. The case study structure reported here consists of a 2D, base-isolated, steel moment resisting frame with a constant bay width of 30 feet and a constant story height of 13 feet.

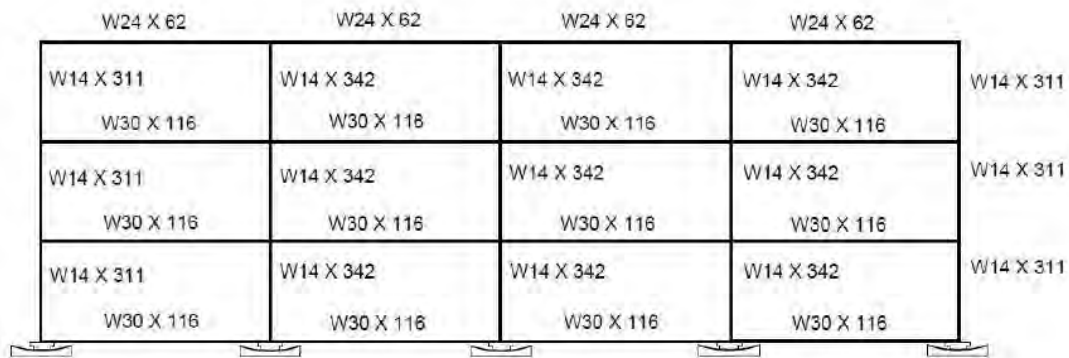


Figure 41: Three-story steel moment resisting frame

A set of VFSs with different characteristics were designed following the approach briefly described earlier, to enhance the seismic performance of the case-study structure. Their hysteretic responses are outlined in Figure 42.

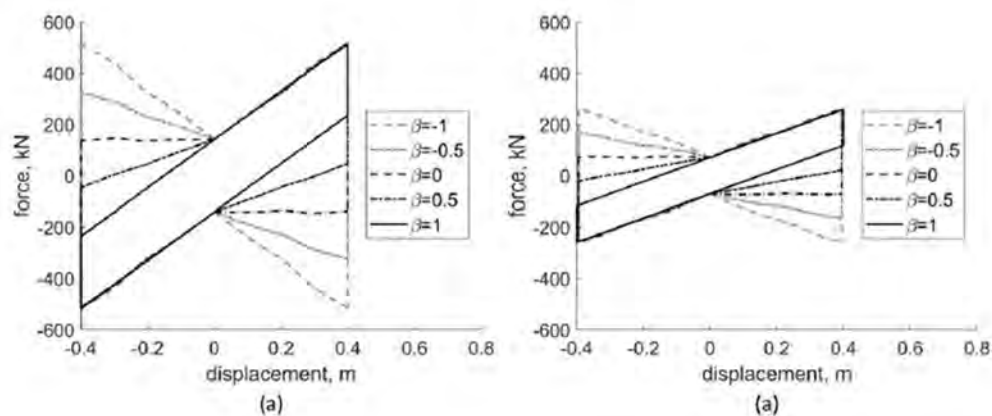


Figure 42: Theoretical true hysteretic behaviour of VFSs under (a) interior, (b) exterior columns

Some of the key results of the analyses are illustrated in Figure 43. Performance comparisons between VFSs with different β values are provided in terms of maximum base shear, maximum displacement, and normalized residual displacement (with respect to the maximum displacement).

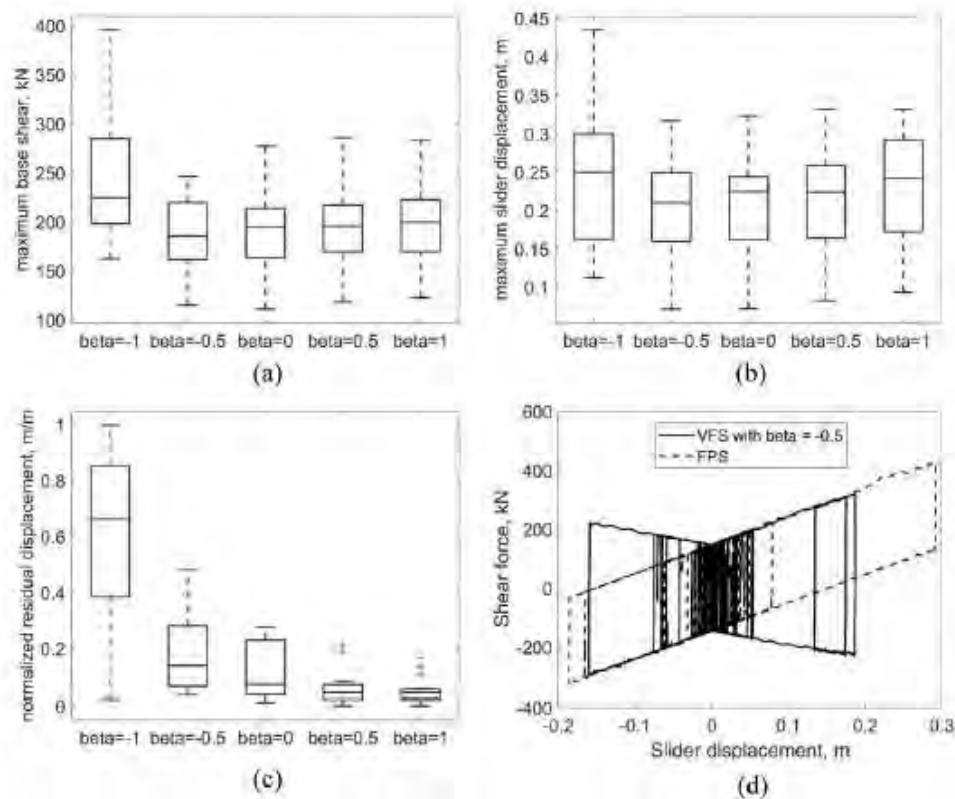


Figure 43: (a) Maximum base shear comparison; (b) maximum displacement comparison; (c) normalized residual displacement comparison; (d) example hysteresis

A 3-D case study structure, as shown in Figure 44, is also presented in this report. The case study structure is a 3D steel moment resisting frame with a constant bay width of 12 feet and a constant story height of 12 feet, selected from OpenSees (2016) library.

Four VFS sets characterized by β values ranging from -1.0 to 0.5 (increment of 0.5) were designed to match the backbone force-displacement response of the “baseline” isolators (i.e. Friction Pendulum Systems). Their theoretical hysteresses are shown in Figure 44 (b).

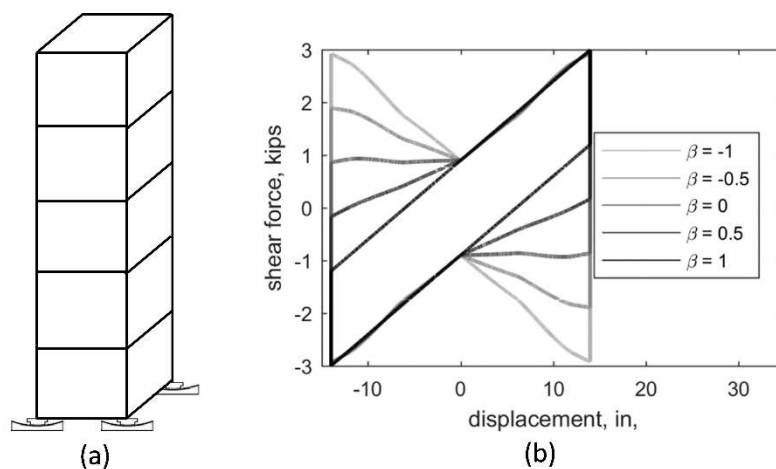


Figure 44: (a) 3D view of the five-story-one-bay structure in OpenSees Single Friction Pendulum Bearing Element example; (b) theoretical hysteretic behaviour of VFSs

Some of the key results of the analyses are summarized in Figure 45. Performance comparisons between VFSs with different β values are provided in terms of maximum base shear, maximum displacement, and normalized residual displacement (with respect to the maximum displacement). An example set of displacement trajectory comparison among different VFSs (with the same ground motion) are shown in

Figure 46. The stars and circles in

Figure 46 indicate where the residual displacements and maximum displacements occur, respectively. In

Figure 46, the colour of the curve changes from light grey to black as an indication of time.

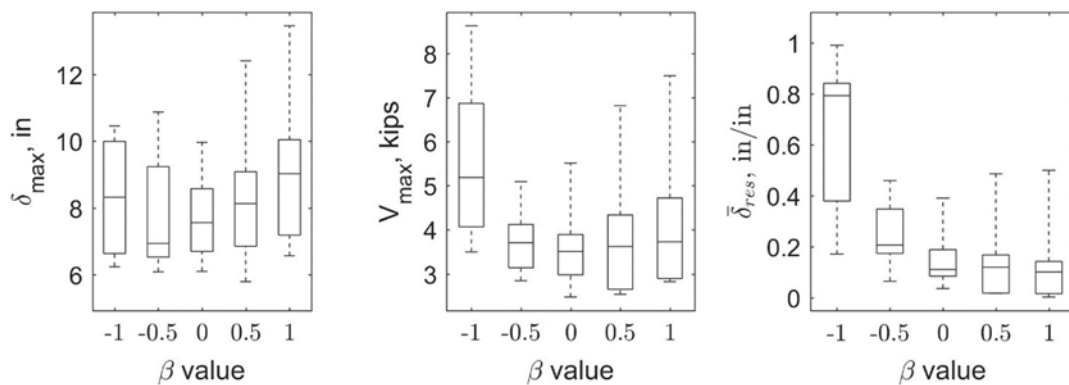


Figure 45: Comparison of maximum displacement, maximum base shear, and normalized residual displacement for 3D analyses

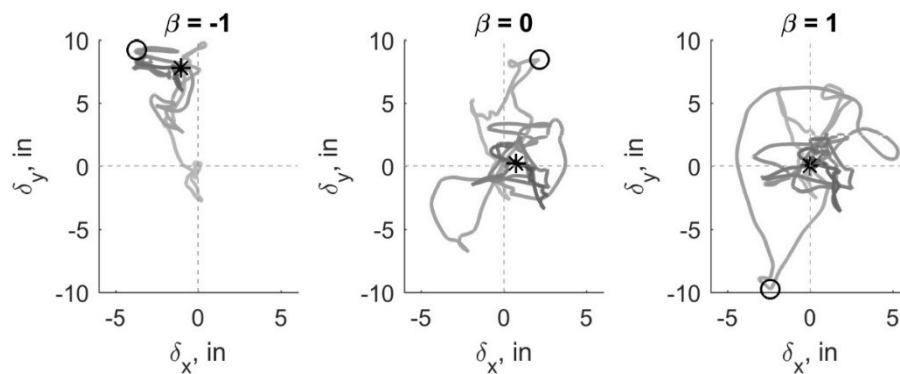


Figure 46: Example bearing trajectory comparison from 3D non-linear time history analyses

2.1.10 Investigation of using VFS as passive adaptive devices

Variable Friction Pendulum Systems can also achieve adaptive behaviour under multiple seismic hazard levels. The results in this study show that, when designed to achieve the same maximum slider displacement under MCE level hazard, VFS isolated structure can achieve lower peak inter-story drift and peak floor accelerations under SLE and DBE level events.

Case study structures include 3- and 9-story steel braced frames isolated with VFS and FPS characterized by various equivalent natural period values and damping levels. For brevity, the case for the 3-story structure equivalent natural period equals to 3 second and equivalent damping ratio equals to 25% is shown here.

As shown in Figure 47 the median demand hazard curves, when designed to have the same maximum slider displacement at MCE level hazard, AVFS achieves approximately 15% reduction in both peak inter-story drift and peak floor acceleration at both SLE and DBE levels.

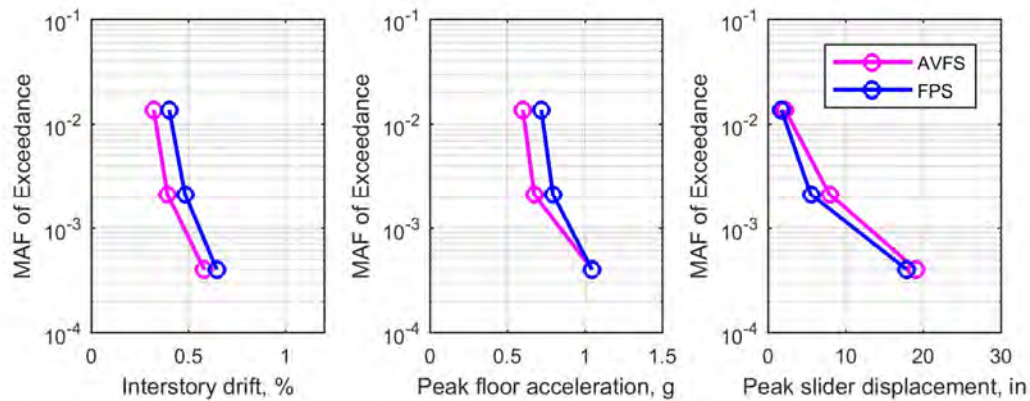


Figure 47: Median demand hazard curves for peak inter-story drift, peak floor acceleration, and peak slider displacement for three-story isolated buildings on adaptive variable friction pendulum systems and friction pendulum systems

Variable Behaviour Double Curved Surface Sliders (VF-DCSS):

This part of the report contains information regarding the testing campaign and evaluation of the results of variable behaviour double curved surface sliders (VF-DCSS). While the concept is similar to the VFP, the achievement is done differently and the stability of the response turned out to be significantly higher for VF-DCSS according to the hybrid tests. For these reasons, notwithstanding the higher complexity of the system, the last part of the experimental campaign was focused on the latter technology.

Two prototypes with different frictional properties have been designed, manufactured and tested. The geometrical properties of both prototypes are the same and shown in the section view provided in Figure 48. In the first prototype device, lubricated and dry friction materials are used, resulting a large gap between friction coefficients and non-simultaneous motion throughout the complete cyclic motion. In the second prototype device, two different dry friction materials which have less friction coefficient difference is used. Simultaneous motion is expected on the second prototype device.

The parametric hysteretic behaviour of the articulated double-surface variable base isolation devices is shown in Figure 49.

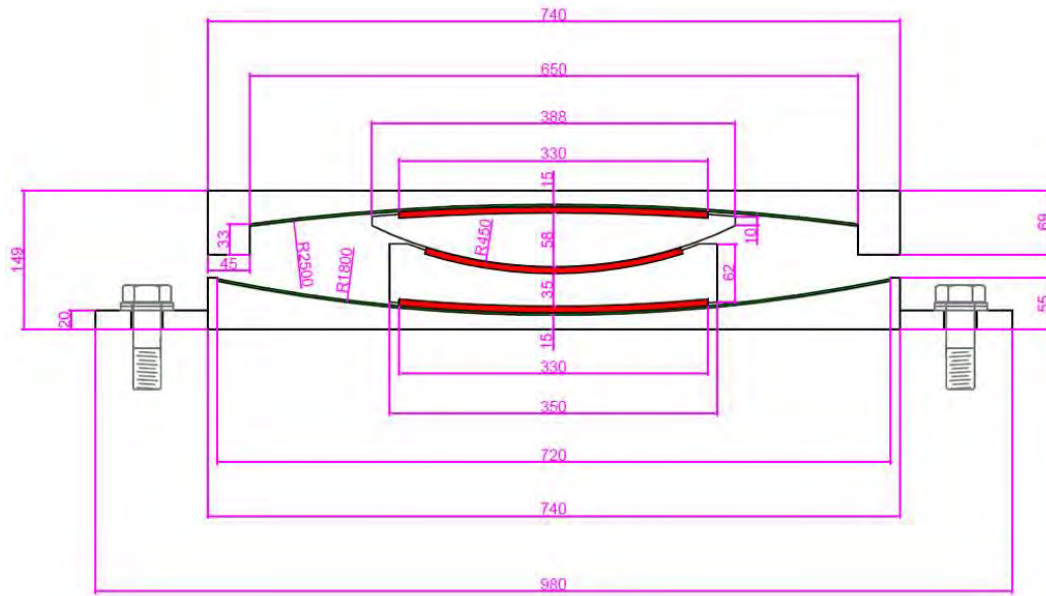


Figure 48: Section view of the prototype VF-DCSS devices

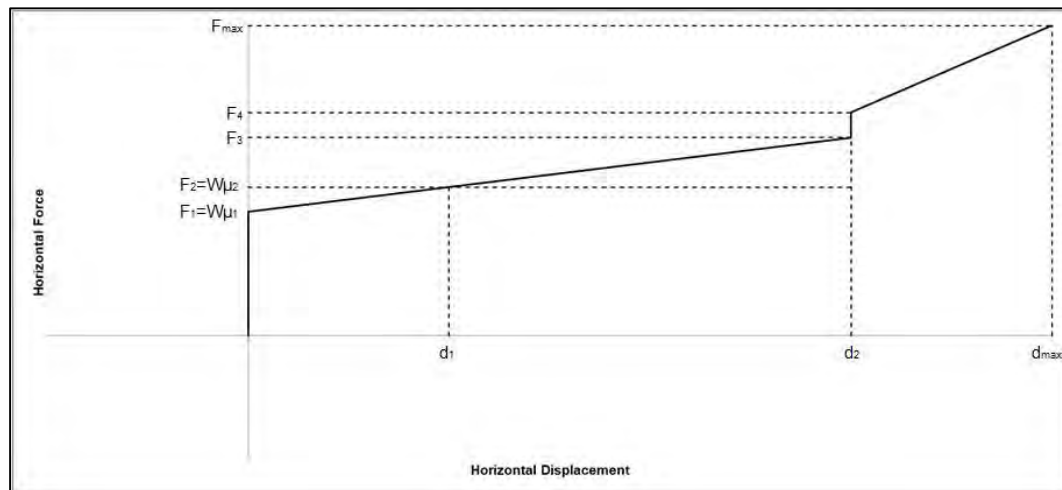


Figure 49: Parameters used to obtain the 1-D modelling equations of VF-DCSS

In Figure 49,

d_1 : The displacement of the primary surface only. This is based on the fact that the motion occurs only on the primary surface until the breakaway force of the secondary surface is reached.

d_2 : The displacement that is reached when the intermediate element hits the wall of the backing plate.

d_{max} : Displacement capacity of the device.

 $F_1 = W\mu_1$: Breakaway force of the primary sliding surface $F_2 = W\mu_2$: Breakaway force of the secondary sliding surface

F_3 : The horizontal force reached when the intermediate element hits the wall of the backing plate, just before hitting the wall.

F_4 : The horizontal force after the jump caused by the hit.

F_{max} : The maximum horizontal force expected on the device.

Firstly, calculation of d_1 is given in Equation 1.

$$d_1 = R_1(\mu_2 - \mu_1) \quad (1)$$

Using Equation 2, the displacements on the sliding surfaces until the intermediate element hits the wall of the backing plate are calculated as provided in Equation 3.

$$\Delta F_i = \Delta d_i \frac{W}{R_1} \text{ and } \Delta F_j = \Delta d_j \frac{W}{R_2} \quad (2)$$

where,

ΔF_i and ΔF_j : Unit change of horizontal force on the primary and secondary sliding surfaces

Δd_i and Δd_j : Unit displacement change on the primary and secondary sliding surfaces

$$\Delta d_2 = \Delta d_1 \frac{R_2}{R_1} \quad (3)$$

For the relative displacement on the primary surface, Δd_1 , the relative displacement on the secondary surface, Δd_2 , is calculated. As a result, the total displacement until the intermediate element hits the wall of the backing plate, d_2 , is obtained.

The horizontal forces are calculated by considering the post-yield stiffness (i.e. W/R) for each motion phase. The force increase in the jumping point is calculated as given in Equation 4.

$$F_4 - F_3 = W(\mu_2 - \mu_1) \quad (4)$$

In Figure 50, the VF-DCSS force and displacement response in hybrid test # HT8_116 (PGA = 2g) is shown. The increase of friction and simultaneous curved surface radius reduction can be clearly appreciated for relative displacements higher than 190 mm.

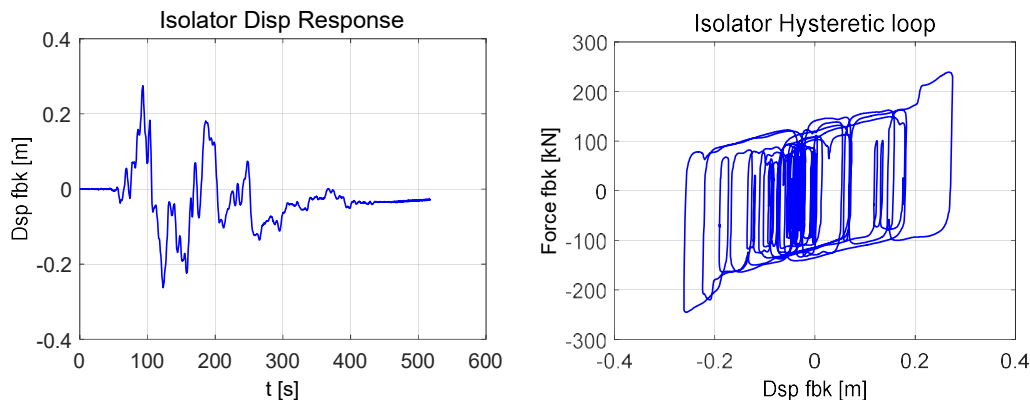


Figure 50: Variable-friction DCSS response in test HT8_116, PGA = 2g

21 dynamic and 117 hybrid tests have been performed on the prototypes. Several of those test results have been chosen, presented and discussed in this part of this report.

The test results of the first and second prototype devices are presented in Figure 51 and Figure 52, respectively, with their corresponding expected theoretical behaviour.

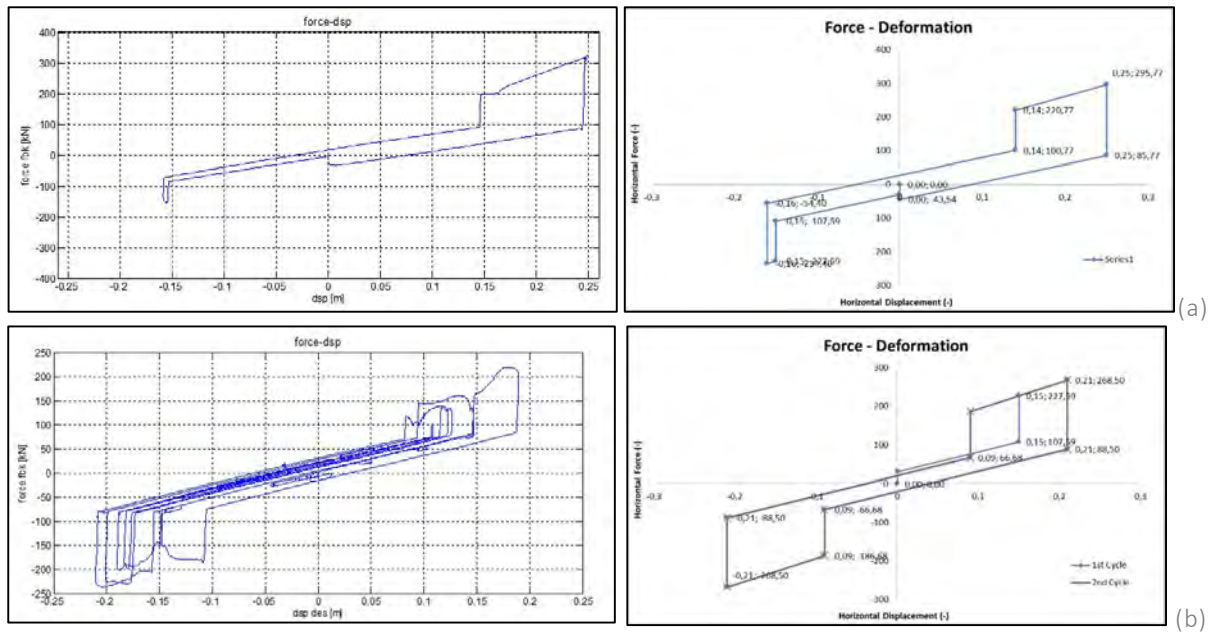


Figure 51: Experimental and theoretical hysteretic behaviour during dynamic (a) and hybrid (b) testing of the first articulated double-surface variable base isolation device prototype

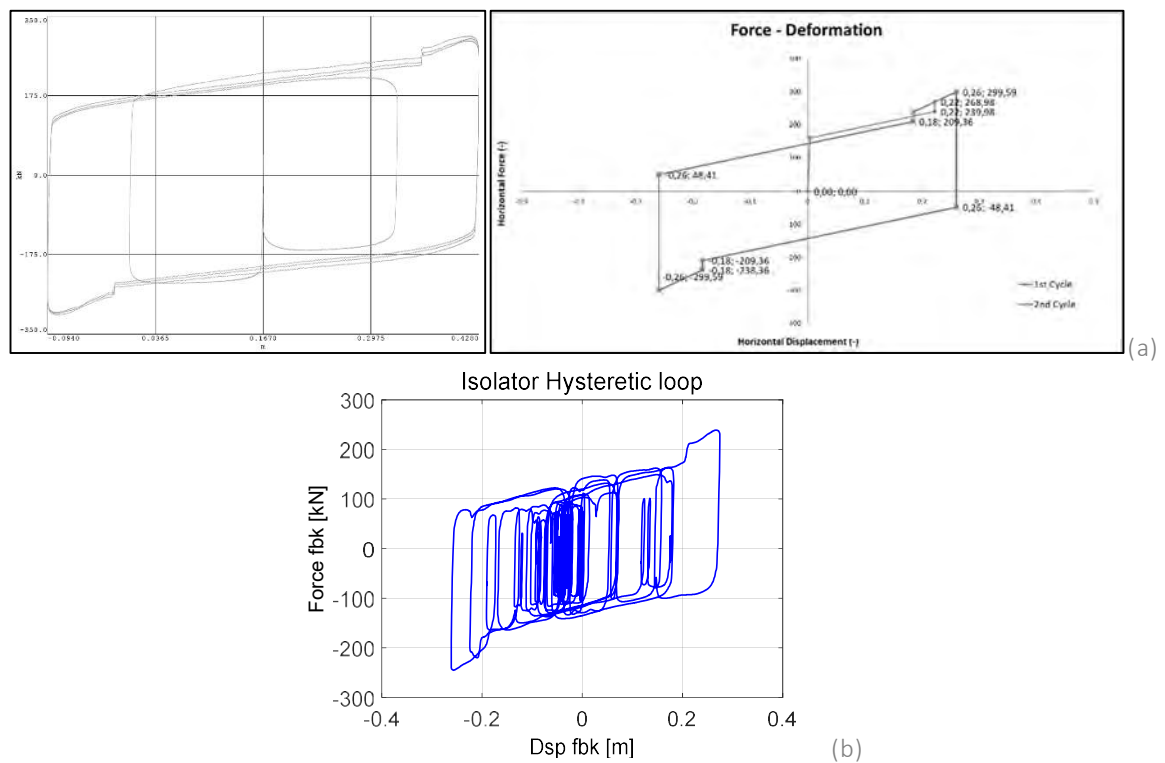


Figure 52: Experimental and theoretical hysteretic behaviour during dynamic (a) testing and experimental behaviour during hybrid (b) testing of the second articulated double-surface variable base isolation device prototype

2.1.11 Conclusions and outlook

Evaluation of the results and the possible future studies according to the test results are summarized in this part of the report.

Considering the results presented in Figure 33 and Figure 34, it can be stated that the actual test data is almost a perfect match with the theoretical behaviour. The behaviours of the prototype devices are consistent in all of the tests. The maximum horizontal force, the displacement values at which the activation of movements in the first and the second sliding surfaces occur and post-yield stiffness values are almost the same for the entire testing campaign, in both quasi-static benchmark tests and the hybrid tests. It can also be concluded that the sliding velocity does not change the behaviour and the characteristics of this device.

During the hybrid tests of the first prototype, it is observed that the motion phases are well-separated. It is expected since the friction coefficient difference is very high in the first prototype. In the second prototype, the behaviour is more complex since the motion phases are not separated completely and simultaneous movement occurs on the sliding surfaces. This was also predicted before the tests and the modelling was performed accordingly. It can be concluded that the characteristic properties of the articulated double-surface variable base isolation devices (or VF-DCSS) can be designed for different performance levels for each project. This would allow a more sophisticated design and performance for the base isolation systems. However, in order to make this estimation correctly, it is essential to develop in advance modeling equations.

Although the 1-D theoretical model seems to be matching with the actual test results well, it is not possible to estimate the exact behaviour of the device at each time step during the time history analysis. Therefore, it is required to develop a more detailed and sophisticated theoretical model that allows behaviour prediction at each time interval during time histories and valid for any movement in 2-D motion plane of the device.

If the final location of the articulated intermediate element is investigated, it is seen that the intermediate element is not at the centre at the end of most tests. It is also observed that location of the intermediate element is highly correlated with the ground motion property. This indicates a possible problem of re-centering for articulated double-surface variable base isolation devices.

When the friction coefficient difference is too much between dry and lubricated friction materials, the jumps on the horizontal force is observed to be high, which may have a negative impact on the superstructure due to sudden increase of the horizontal force and accelerations during the ground motion. In order to reduce this effect, it is possible to reduce the difference between friction coefficients and/or change the geometrical properties of the sliding surfaces. In any case, effect of impact force on the superstructure could not be captured in the hybrid testing campaign and needed to be evaluated within a more advanced analysis.

These results shall be considered preliminary and it shall be noted that more tests need to be performed in the future within the scope of this study so that the real behaviour of articulated variable friction devices would be captured accurately and the proper seismic design of the devices can be done.

2.2 Project #18 – SEismic Response of Actual steel SILOS (SERA-SILOS)

Authors

S. Silvestri⁽¹⁾, I. Lanese⁽²⁾, M. Furinghetti^(2, 5), A. Pavese^(2, 5), E. Rizzo Parisi⁽²⁾, S. Mansour^{(1), (3)}, J. Distl⁽⁴⁾, E. Hernández-Montes⁽⁶⁾, A. Sadowski⁽⁷⁾, T. Taniguchi⁽⁸⁾, F. Weber⁽⁹⁾

⁽¹⁾ *Department DICAM, University of Bologna, Bologna, Italy*

⁽²⁾ *EUCENTRE, Pavia, Italy*

⁽³⁾ *AGI EMEA Ltd, Ozzano dell'Emilia (Bologna), Italy*

⁽⁴⁾ *Maurer Engineering GmbH, Munich, Germany*

⁽⁵⁾ *University of Pavia, Pavia, Italy*

⁽⁶⁾ *University of Granada, Granada, Spain*

⁽⁷⁾ *Imperial College London, London, United Kingdom*

⁽⁸⁾ *Tottori University, Tottori, Japan*

⁽⁹⁾ *Maurer Switzerland GmbH, Pfaffhausen, Switzerland*

2.2.1 Introduction

The structural design of steel silos containing granular material represents a challenging issue. They differ from many other civil structures since the weight of the silo structure is sensibly lower than the one of the ensiled particulate material and, in case of earthquake ground motion, the particle-structure interaction plays a fundamental role on the global dynamic response. The complex mechanism through which the ensiled material interacts with the silo wall has been studied since the XIX century. Nonetheless, several issues are still to be addressed and structural failures still occur in the filling and, especially, the discharge phases as well as during strong ground motions. Both metal and concrete silos are known for their relatively high failure rate, a state of affairs due partly to the complexity of the structural response but also to the significant uncertainty inherent in the loading assessment. In particular, silos are known to frequently fail or be seriously damaged during large earthquakes, such as during the 1974 Lima (Peru), the 1987 Edgecumbe (New Zealand), the 1999 Chi-Chi (Taiwan) and the 2003 Zemmouri (Algeria) earthquakes [1].

The seismic assessment of such silos focuses on the estimation of the quasi-static horizontal forces generated on the silo wall by the ensiled mass. In this respect, the seismic design of silos is usually performed on the basis of the identification of an "effective mass", which interacts with the silo wall under seismic excitation, that is, the fraction of the total ensiled mass supported horizontally by the silo wall.

For flat-bottom circular silos, the EN 1998-4 [2] considers an effective mass equalling roughly 80% of the total ensiled mass, according to the research works by Rotter and Hull [3] and the analytical studies by Younan and Veletsos [4,5], balanced by the horizontal actions provided by the silo wall. However, there is strong evidence that this formulation is too conservative [6,7]. By means of extensive numerical simulations, Holler and Meskouris [8] showed that, while for slender silos the Eurocode 8 provisions

provide a reasonable performance indicator, for squat silos a more appropriate (with respect to that of EC8) effective mass should be considered.

Starting from the widely adopted classical approach of Janssen [9,10], Silvestri et al. [11,12] studied analytically the load imparted by an incompressible ensiled content under constant horizontal acceleration confined in a flat-bottom cylindrical container. The theory was developed by simulating the earthquake ground motion with time-constant vertical and horizontal accelerations and was carried out by means of simple dynamic equilibrium equations that take into consideration the specific mutual actions developing in the ensiled granular solid (in particular, horizontal and vertical shear forces). The findings indicated that in case of squat silos characterized by low but typical height to diameter aspect ratios, the portion of the granular solid mass that interacts with the silo walls turns out to be noticeably smaller than the total mass of the granular solid in the silo and the effective mass adopted by Eurocode 8.

The theory has so far been validated only on shaking-table tests [13] performed in the Bristol EQUALS lab on a small-scale Plexiglass cylindrical specimen with different heights of the ensiled material (about 0.5 mm diameter Ballotini glass) and different values of the particle-wall friction. The results indicate that for squat flat-bottom silos, the effective mass is indeed lower than the Eurocode specification, suggesting that the specification is overly conservative and that the particle-wall friction coefficient strongly affects the overturning moment at the silo base [13]. These findings are also consistent with the numerical results obtained by Holler and Meskouris [8] with reference to FEM models of real silos under earthquake excitation. Experimental verification on a full-scale actual silo specimen is thus desirable.

In this respect, a wide shaking-table experimental campaign was carried out at the EUCENTRE lab in Pavia (Italy) between February and March 2019 on a full-scale flat-bottom manufactured steel silo filled with soft wheat, considering both fixed-based and seismically isolated-base conditions.

2.2.2 Test specimen

A flat-bottom cylindrical silo placed on a r.c. plate has been tested in both fixed-base and isolated-base configurations. It is the smallest actual silo manufactured by the Italian company AGI-EMEA (ex AGI-FRAME) (Figure 53).

The total height including the inclined roof is $H = 5.5$ m and the radius is $R = 1.82$ m. The silo wall is realized by 5 stripes of horizontal corrugated sheets (ferrules) with thickness equal to 1 mm. Each strip is high 881 mm. The silo wall is supported by 8 vertical stiffeners characterised by a hat-shaped thin open cross-section which changes in thickness along the height (from the top to the bottom: 1.5, 2, and 3 mm). Ferrules and stiffeners are made of S350GD steel with Z450 galvanization. The stiffeners are connected to the silo wall by M10 (class 8.8, hot galvanized) 70mm-spaced bolts. The silo roof is made by 16 inclined metal sheets.

The silo is filled with soft wheat up to a 3.3 m height, in order to reproduce an aspect ratio $H/2R$ roughly equal to 1 (squat silo). Specific weight of the used wheat is 8.04 kN/m³; grain-grain friction coefficient and pressure ratio are tentatively estimated to be around 0.55 and 0.60, respectively, but specific tests are currently under development.

The weight of the steel silo itself is around 12 kN, the amount of granular solid is around 285 kN, the weight of the 4.8 m × 4.8 m × 0.4 m r.c. plate is 230 kN; leading to a total weight of 527 kN.

The isolators put between the table and the r.c. plate are Curved Surface Sliders friction pendulum devices manufactured by the MAURER company (Germany) in order to obtain a 3 s period of vibration (radius = 2.2364 m, max allowable displacement = 0.2 m).



Figure 53: Tested silo

2.2.3 Analytical predictions and numerical models

In the test design phase, analytical formulations have been applied and numerical models have been developed to provide estimations of the static pressures and dynamic overpressures produced by the granular material onto the wall of the silo and of the fundamental frequency of the "filled-silo system".

Regarding the analytical formulations available in the scientific literature, (i) the Eurocode provisions [2], (ii) the Silvestri et al. (2012) [11] theory and (iii) the Pieraccini et al. (2015) [12] theory (that provides a refinement version of the previous one) have been considered. For the static pressures, the first and the third formulations make use of the Janssen exponential model that fully exploits the grain-wall friction coefficient, while the second one considers a more conservative linear ("geostatic") model corresponding to the Taylor's 1st order expansion of the Janssen model

function. For the dynamic overpressures, the EC formulation considers an effective mass equalling roughly 80% of the total ensiled mass, whilst the second and the third formulations, accounting for the mutual actions in the ensiled granular solid (specifically: horizontal and vertical shear forces), lead to a smaller effective mass for squat silos.

Regarding the numerical models, three Finite Element models have been developed using SAP2000 software: (i) a coarse isotropic model, (ii) a geometrically refined model, and (iii) an orthotropic ferrule model. In all cases, the cylinder was created starting from 48 equally-distributed radial points (every one spanning an angle equal to 7.5°). The first coarse model (Figure 54a) has been built with plain shell elements for the wall, beam elements for the stiffeners placed in contact with the sheets with respect to their centroids and a simplified roof shape. On the other hand, the refined model (Figure 54b) is characterised by shell elements carefully detailed to represent the actual corrugated geometry of the wall (wavelength equal to 70 mm), carefully detailed, beam elements for the stiffeners that are placed in their real position accounting for the eccentricity between their centroids and the wall (stiffeners are bolted to the wall in their web), a roof shaped in accordance with its geometrical section. Finally, the orthotropic ferrule model (Figure 54c) makes use of the coarse model geometry but shell elements are characterised by equivalent orthotropic stiffness parameters, as defined in EN1993-4-1:2002. For each model, the granular solid effects have been considered in two different ways: (i) using brick elements considering the ensiled content as elastic material (Young modulus tentatively assumed equal to $E = 2.3 \text{ MPa}$), and (ii) using joint loads determined according to the three above-mentioned pressures formulations.

As illustrative example, Figure 55 reports the predicted profiles of the total (static + dynamic) horizontal pressure exerted by the granular solid onto the silo wall, in case of base input acceleration equal to $0.52g$, as obtained using both the analytical formulations and the FE orthotropic ferrule model with elastic granular material as subjected to an artificial earthquake ground motion.

The fundamental frequency of the system has been estimated from the different FE models, as well as by means of three prediction methods proposed by Pieraccini et al. (2017) [14], that are all based on the modelling of the silo as an equivalent shear-flexural cantilever beam with an applied mass equal to the mass of the silo structure plus the seismic effective mass of the ensiled content: a fully analytical formula, an approximate code-like formula for steel silos containing common grain-like materials, and a FE modelling technique. Figure 54c presents the shape of the first mode of vibration as taken from the FE orthotropic model, while Table 8 summarizes the predictions of the fundamental frequency. Inspection of Table 8 shows that the FE models with elastic granular material provide the smaller values of the frequency, since they consider the whole mass in motion. The Pieraccini et al. (2017) analytical formulations show the largest values. The numerical model built according to the Pieraccini et al. (2017) suggestions and considering the Eurocode 8 effective mass gives a value smaller than the same model considering the effective mass of the Pieraccini et al. (2015) theory, since the effective mass in motion of the latter is near the half of the former.

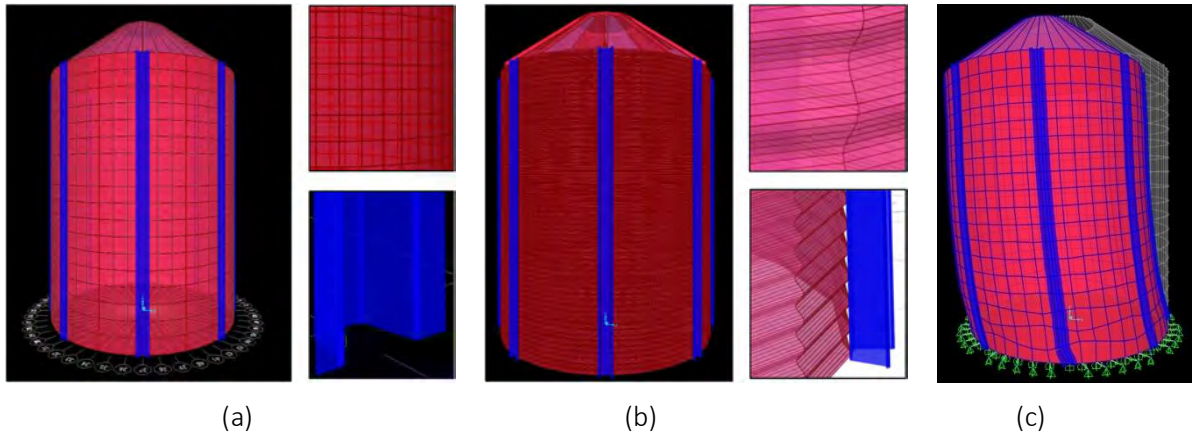


Figure 54: Numerical FE models: (a) course model: global view and details, (b) refined model: global view and details, (c) shape of the first mode of vibration of the orthotropic model

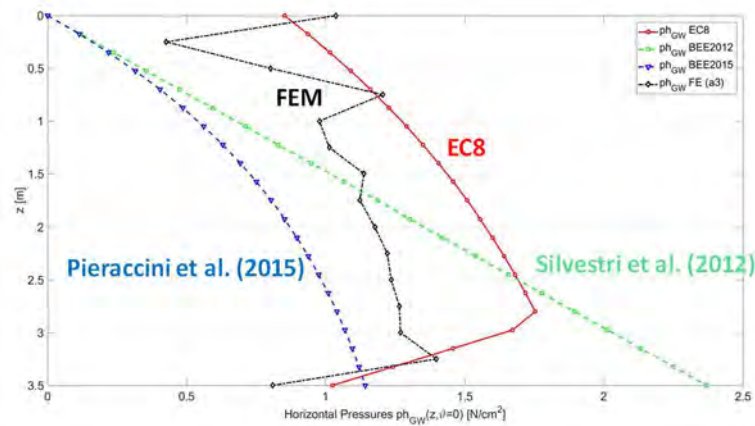


Figure 55: Predicted profiles of the total horizontal pressure exerted by the granular solid onto the silo wall

Type of model	Model	f1 [Hz]
Numerical	Coarse isotropic FE model + elastic granular material (E=2.3 MPa)	7.10
Numerical	Refined FE model + elastic granular material (E=2.3 MPa)	7.09
Numerical	Orthotropic FE model + elastic granular material (E=2.3 MPa)	7.08
Analytical	Pieraccini et al. (2017) approximated code-like formula	30.21
Analytical	Pieraccini et al. (2017) rigorous formula	22.57
Numerical	Pieraccini et al. (2017) FE model with EC8 effective mass	9.66
Numerical	Pieraccini et al. (2017) FE model with BEE2015 effective mass	15.27

Table 8: Prediction of the fundamental periods of vibration and frequency for the "grain-silo" system

2.2.4 Test setup: instrumentation and setup

Several sensors have been used to monitor the static and dynamic response of the filled-silo system, including:

- 15 uniaxial accelerometers, placed at different heights of the silo, to reproduce the acceleration profile and to gain information regarding the dynamic amplification of the dynamic system (Figure 56a);

- 6 triaxial accelerometers inside the granular solid: 4 placed at different heights in the middle of the stored wheat and 2 close to the internal wall of the silo in correspondence of stiffener #8 (Figure 56a);
- 24 strain gauges on the external surfaces of the stiffeners and sheets;
- 14 gauges at level 0.42m from the r.c. plate, placed vertically on the stiffeners #4, #5, #6, #7 and #8 (Figure 56d);
- 4 gauges at level 0.49 m, which is higher than the first level by the height of the corrugation wave, placed vertically on both stiffeners #7 and #8;
- 4 gauges at level 1.50 m from the r.c. plate on both stiffeners #4 and #8 in vertical direction;
- 1 strain gauge at level 2.50 m from the r.c. plate on the stiffener #8 in vertical direction too;
- 1 gauge placed horizontally on the sheet wall at level 0.42 m from the r.c. plate;
- 4 load cells (Figure 56b) installed on the internal side of the wall at two heights of the silo near the stiffeners #4 and #8 (the ones aligned to the input motion) in order to measure the horizontal pressures between the wheat particles and the wall. Cells 1 and 2 are placed at the base level at 0.42 m from the r.c. plate, while cells 3 and 4 are placed at the product mid-height level at 1.50 m from the r.c. plate;
- 4 vertical graduated bars on the top internal side of the silo to measure the height of granular material (Figure 56e);
- 8 LVDT displacement transducers to get the relative motion between the r.c. plate and shaking table (2 horizontals along the input direction and 2 horizontals along the orthogonal direction, and 4 vertical) for the isolated-base case.

In addition, an optical system (10 High Definition video-cameras + 70 markers) to monitor the displacements of stiffeners #4, #5, #6, #7 and #8, wall, roof, r.c. plate and shaking-table (Figure 56c).

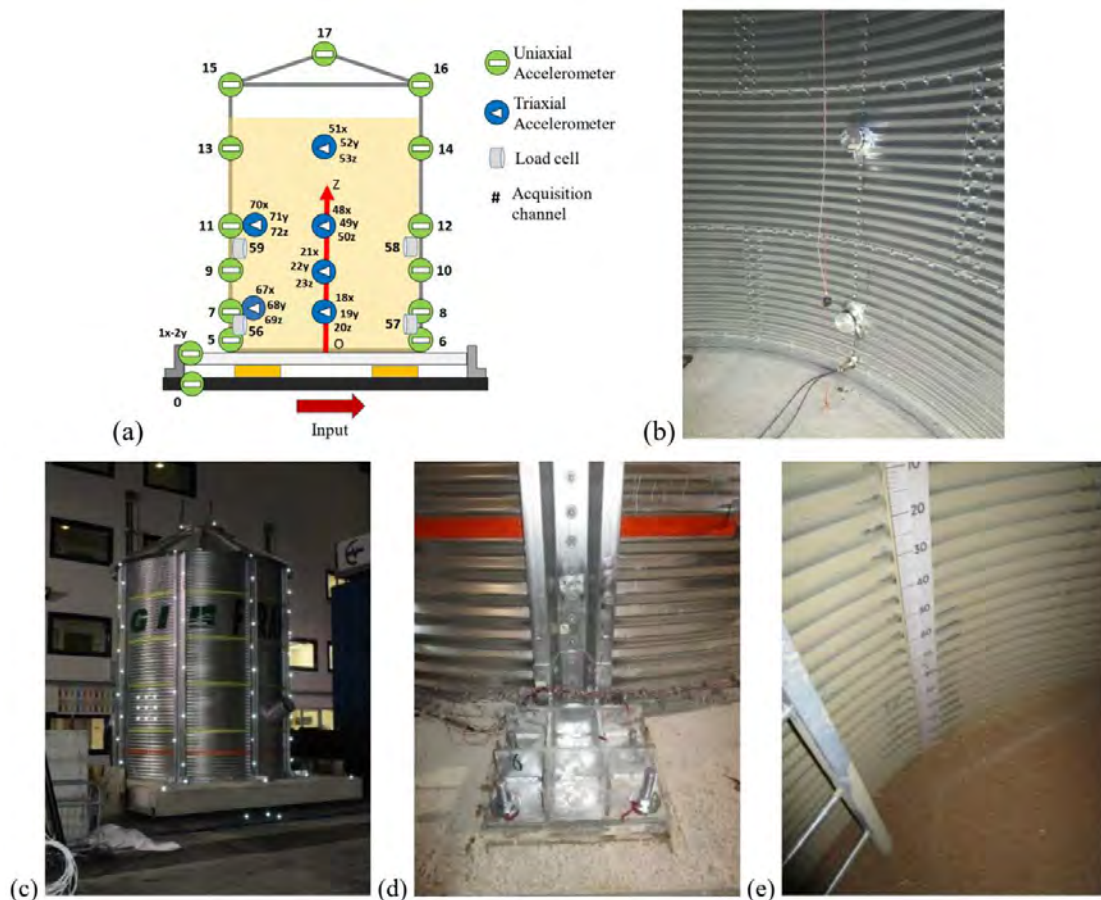


Figure 56: (a) Accelerometers (b) Load cells (c) Markers (d) Strain gauges (e) Graduated bars

More than 250 dynamic tests have been carried out considering different types of input at the shaking table level. White-noise random signals have been applied to obtain the basic dynamic properties of the filled-silo system. Low-frequency (namely, 1 and 2 Hz) sinusoidal inputs have been then used. Using low-frequency input allows to achieve a large duration for which the acceleration can be reasonably considered constant in time (around the peak of the sinusoid). Furthermore, three earthquake records were considered as input for the table, the first one is an artificial earthquake record (a1), while the second (rs1) was a real record of Campano Lucano earthquake (Irpina, Italy, 23/11/1980) which was identified as a “far-from-resonance frequency content” input for the tested silo. In the contrary, other real record (rs3) of Kalamata earthquake (Greece, 13/09/1986) was identified as a “close-to-resonance frequency content” input. Finally, sinusoidal tests at constant amplitude and increasing frequency have been carried out. Table 9 lists all the performed tests.

FIXED-BASE			ISOLATED-BASE		
Peak Table Acceleration	Test Number	Type of signal	Peak Table Acceleration	Test Number	Type of signal
0.07 g	1	random	0.05 g	148-165	random
0.10 g	2-9	sin 0.5 Hz	0.10 g	166-168	a1 eqke
	10-13	rs1 eqke	0.30 g	169-170	random
	14-16	a1 eqke	0.10 g	171-174	a1 eqke
	17-19	rs3 eqke	0.20 g	175-179	a1 eqke
0.15 g	20-21	random	0.15 g	180-182	random
0.20 g	22-26	sin 1 Hz	0.30 g	183-187	a1 eqke
	29-31	rs1 eqke	0.20 g	188	random
	32-34	a1 eqke	0.40 g	189-193	a1 eqke
	35-38	rs3 eqke	0.45 g	194	a1 eqke
	39-40	random	0.50 g	195	a1 eqke
0.30 g	41-45	sin 1 Hz	0.55 g	196	a1 eqke
	46-48	rs1 eqke	0.20 g	198-200	random
	49-51	a1 eqke	0.10 g	201-205	rs3 eqke
	53-55	rs3 eqke	0.20 g	206-210	rs3 eqke
0.40 g	56-59	sin 1 Hz	0.30 g	211-215	rs3 eqke
	60-62	rs1 eqke	0.40 g	216-220	rs3 eqke
	63-66	a1 eqke	0.45 g	221	rs3 eqke
	67-69	rs3 eqke	0.50 g	222	rs3 eqke
0.50 g	71-76	sin 1 Hz	0.55 g	223	rs3 eqke
	77-80	rs1 eqke	0.10 g	224-227	rs1 eqke
	81-83	a1 eqke	0.20 g	228-232	rs1 eqke
	84-86	rs3 eqke	0.25 g	233	rs1 eqke
0.07 g	88-89	random	0.30 g	234-235	rs1 eqke
0.15 g	90-91	random	0.35 g	236	rs1 eqke
0.20 g	92-93	random	0.10 g	238-242	pulse
0.25 g	94-96	random	0.20 g	243-247	pulse
0.10 g	97-101	sin 0.5 Hz	0.30 g	248	pulse
0.20 g	102-106	sin 1 Hz	0.10 g	249-253	sin 0.7 Hz
0.30 g	107-111	sin 1 Hz		254-256	sin 0.6 Hz
0.40 g	112-116	sin 1 Hz			
0.50 g	117-121	sin 1 Hz			
0.60 g	122	rs3 eqke			
	123	rs1 eqke			
	124	rs3 eqke			
	125	a1 eqke			
0.10 g	126-129	sin 5 Hz			

	130-134	sin 6 Hz
	135-139	sin 7 Hz
	140-145	sin 8 Hz

Table 9: List of the performed shaking-table tests

2.2.5 Observation during testing

During the filling of grain into the silo, attention has been paid to horizontal pressures and strains. As illustrative examples, Figure 57 shows the pressure values captured by the four load cells and Figure 58a shows the strain values measured in three different points of the cross section (Figure 58b) at the base (42 cm from the r.c. plate level) of the stiffener #8. The eccentricity (even if classified “small” with respect to EN1991-4 19) caused by the filling procedure determined a non-synchronous activation of the load cells. At the base level ($z = 42$ cm) cell 2 loaded earlier than cell 1 on the other side. The same occurred at the grain mid-height level ($z = 150$ cm): cell 3 loaded earlier than cell 4. Since the wheat was introduced using three trucks with unknown flow rates, it is not possible to fit the filling phase record with any pressure profile. However, if a uniform flow rate is assumed (so that time uniformly corresponds to height), from a qualitative point of view, the plot is consistent with the Janssen (1895) static pressure model [9].

Moreover, the strain plots of the gauges on the stiffener #8 clearly indicate that the two monitored points on the web (channels 35 and 36) present the same strain value, whilst the point on the flange (channel 37) presents a different one, as it could be expected considering a combined axial-flexural response of the stiffener. Local stresses, as simply obtained using the Hooke’s law, in the stiffeners at the end of the filling process are around 30-50 MPa. Also, the strain plots highlight an oscillatory behaviour (with a period of about 8 min) of the stresses in the stiffeners, probably due to some periodic grain slip related to the corrugation waves of the silo wall.

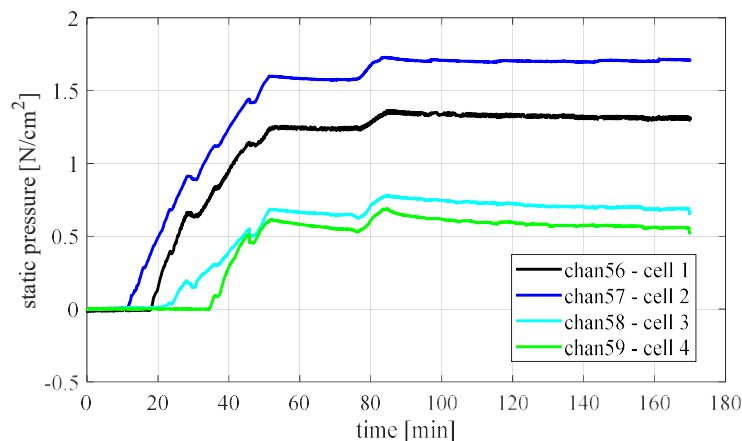


Figure 57: Static pressure values as recorded by the four load cells during filling phase

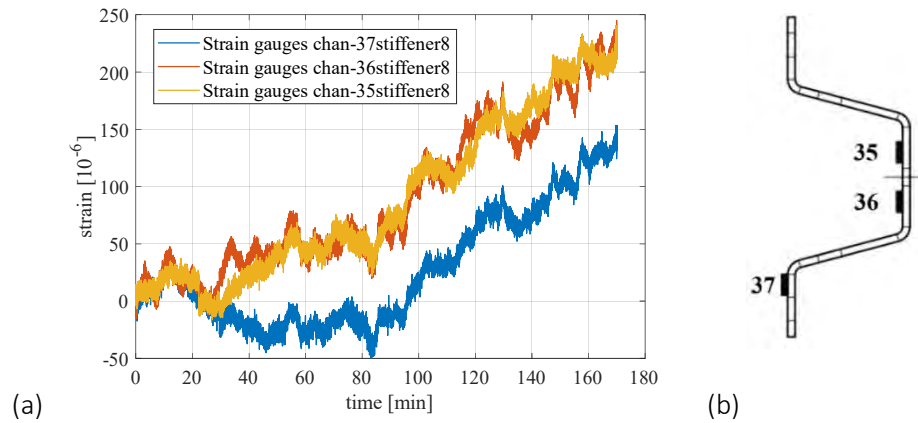


Figure 58: (a) Strain values registration at the base of stiffener #8 during filling phase. (b) Stiffener cross-section with the strain gauges positions

During the whole experimental campaign (from the filling day, 20-Feb-2019, up to the final day of the tests, 5-Mar-2019), it was possible to record the static pressures produced by the grain on the silo wall in four points. Figure 59 displays the static pressure values as captured by the four load cells before each single test. Many interesting issues have been noticed and are still under study. The initial pressures at the end of the filling day are not symmetrical (cell 2 provides a larger value than cell 1, and the same for cell 3 with respect to cell 4) as expected, due to non-concentric filling. The dynamic tests started after five days, during which cell 2 recorded an increase in the pressure, cell 3 a decrease, whilst cell 1 and 4 (on the other side) showed no significant changes. During the first dynamic tests, cells 1 and 2 at the lower level tended to reach similar values, close to the linear (geostatic) pressure model prediction: $p_{h,1-2} = K \cdot \gamma \cdot z_{1-2} = 0.55 \times 8040 \text{ N/m}^3 \times 2.88 \text{ m} = 1.27 \text{ N/cm}^2$. The same occurred for cells 3 and 4 at the higher level: $p_{h,3-4} = K \cdot \gamma \cdot z_{3-4} = 0.55 \times 8040 \text{ N/m}^3 \times 1.80 \text{ m} = 0.79 \text{ N/cm}^2$. Generally speaking, dramatic changes in the static pressure values have been observed (e.g. high-intensity random vibration may switch the maximum pressure from one side to the other side of the silo). Moreover, a considerable drop in the pressure values occurred during the rest day (28-Feb-2019) necessary to switch from the fixed-based (FIX) to the isolated-based (ISO) configuration.

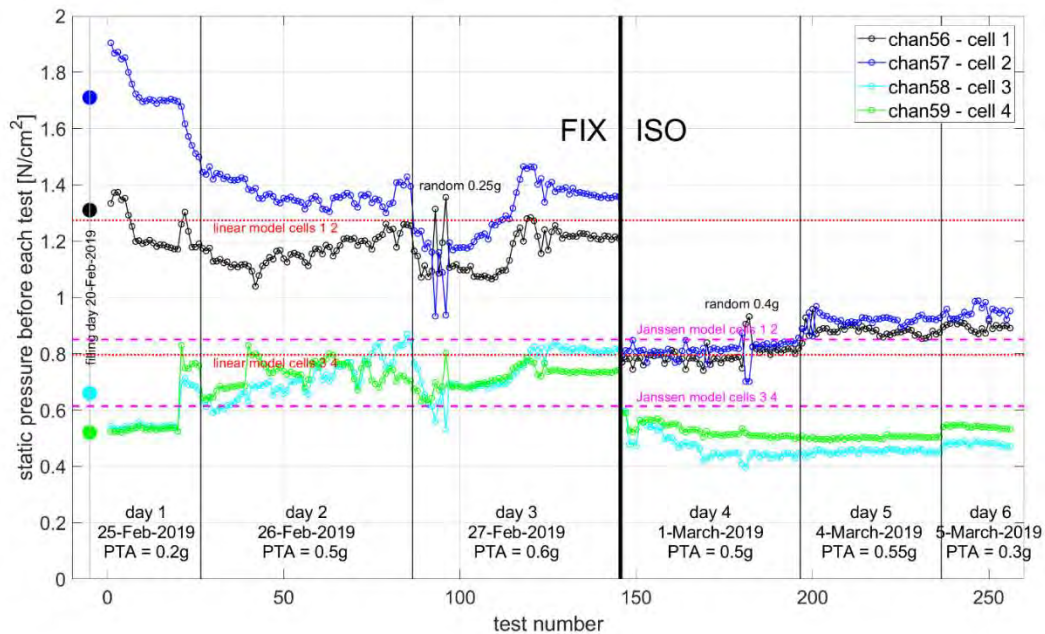


Figure 59: Static pressure values as recorded by the four load cells before each single test

During the dynamic testing phase, the experimental frequencies have been obtained from the response of the silo as subjected to white-noise random signals for various peak table acceleration levels. The system transfer function has been obtained as the square root of the ratio of the periodogram (which is an estimate of the Power Spectral Density, using Welch method with Hamming windows) of the acceleration signal registered at a given level divided by the periodogram of the table acceleration signal. Table 9 collects the frequencies as evaluated both before and after grain compaction. Compaction appeared for table accelerations larger than 0.5 g (tests n. 71-83), almost consistent with the value of the internal friction coefficient of the granular solid (around 0.55): the solid free-surface has been kept monitored during the tests by visual method and four vertical graduated bars. It can be noticed that the fundamental frequency of the filled-silo system depends on both the acceleration and the compaction level: it decreases with increasing acceleration (more “effective mass”) and it increases with increasing compaction (higher stiffness provided by grain material). Note that, in order to obtain a fundamental frequency of about 11 Hz with the orthotropic FE model in which the ensiled content is modelled as an elastic material, an equivalent Young modulus of about $E=6.5$ MPa should be used for the ensiled content.

Peak Table Acceleration	First set of tests before grain compaction		Second set of tests after grain compaction	
RND	Test N.	f (Hz)	Test N.	f (Hz)
0.07 g	1	10.8	88; 89	12.3
0.15 g	20; 21	10.0	90; 91	11.3
0.20 g	39; 40	10.3	92; 93	10.7
0.25 g	-	-	94; 95; 96	10.7

Table 10: Experimental frequencies

Illustrative plots of the estimate of the Power Spectrum Density of the input signal (accelerometer n. 1 on the r.c. plate) and of the output signal (accelerometer n. 13 on the stiffener at height 2.85 m) are reported in Figure 60a, as obtained for the 0.15g random input test (tests n. 90-91). Figure 60b compares the square root of their ratio, i.e. the module of the transfer function of the filled-silo system (red colour), with a first rough approximation of the module of the transfer function, as obtained by simply dividing the FFTs of the two signals (black colour).

Similarly, it is possible to obtain the transfer functions of the system considering the recorded signals at different heights. Figure 61a and b show that the dynamic amplification increases along the height of the silo and decreases with the input acceleration level, due to a simultaneous increase in the damping ratio. From the transfer function amplitude of the filled-silo system, a rough indication on the damping ratio can be inferred: if a maximum amplification around 4 is considered for the resonance frequency, then a damping ratio around 12% is obtained.

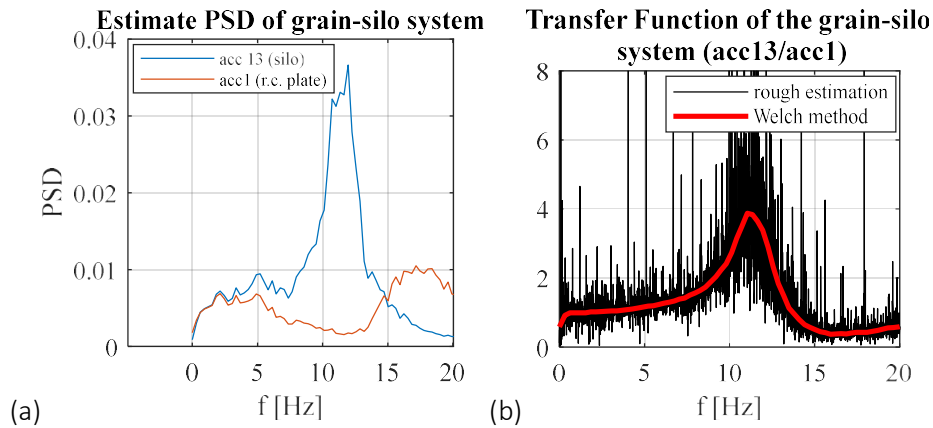


Figure 60: (a) PSD estimate. (b) Transfer function of the filled-silo system

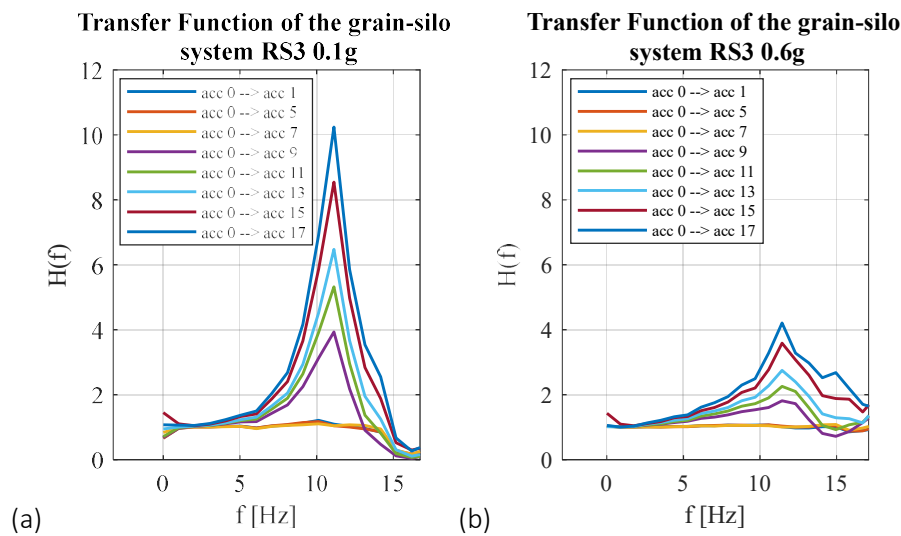


Figure 61: Transfer functions of the system, as obtained for two earthquake tests: (a) rs3 0.1g, (b) rs3 0.6g

2.2.6 Preliminary results

Interpretation of the huge number of data recorded during the experimental shaking-table tests is still under development. Hereafter, selected preliminary results are presented.

As far as the dynamic amplification of the filled-silo system is concerned, Figure 62 displays the so-called Peak Acceleration Profiles, as they collect the maximum accelerations measured at different heights of the silo wall, for two types of signal: 1 Hz sinusoidal and rs3 earthquake for several tests with different Peak Table Accelerations (PTA). It can be noticed that the response of the filled-silo system is substantially not affected by dynamic amplification for the sinusoidal input (Figure 62a), whilst a slight amplification (1.3-1.5 at the top-surface level of the ensiled material, and 1.4-1.8 at the base roof level) is observed for the rs3 earthquake (Figure 62b) which is a “close-to-resonance frequency content” real record. Again, the dynamic amplification seems to decrease for increasing PTA from 0.1g to 0.4g. This may be ascribed to a higher damping ratio provided by the granular solid.

As far as the pressures exerted by the grain on the silo wall are concerned, the following Figure 63a and b report the total (static + dynamic) pressure values measured by the four load cells placed at two heights of the silo wall, for the 0.3g 1 Hz sinusoidal and for the 0.3g rs3 earthquake input, respectively. Figure 64a and b compare the dynamic overpressures measured at different acceleration levels for the

1 Hz sinusoidal and the rs3 earthquake inputs. It can be noticed that the measured dynamic pressure values increase from the top to the bottom of the silo, somehow following a linear profile.

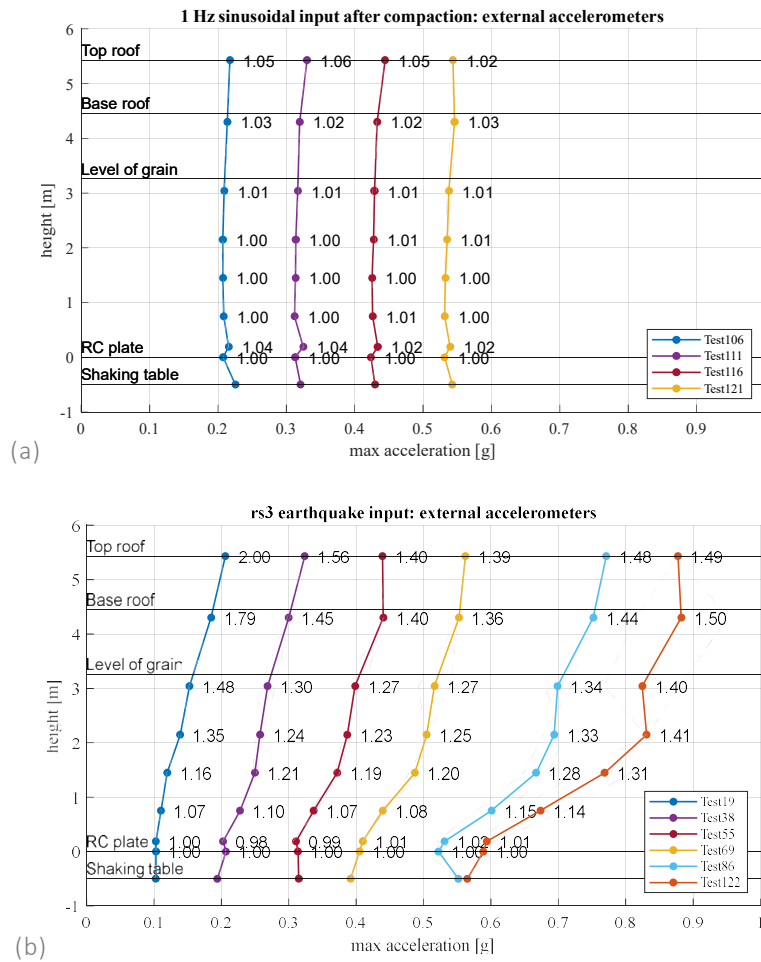


Figure 62: Peak Acceleration Profiles and dynamic amplification factors for (a) 1 Hz sinusoidal input and (b) rs3 earthquake input

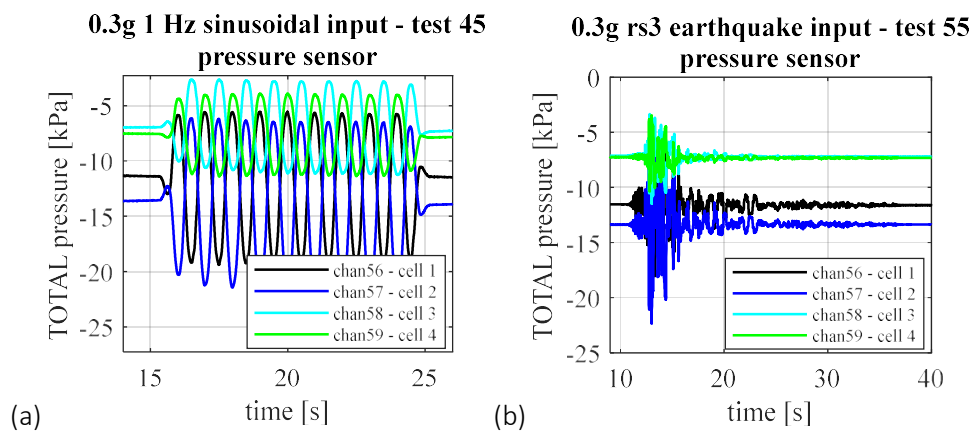


Figure 63: Horizontal total (static + dynamic) pressures measured by the four load cells during two tests

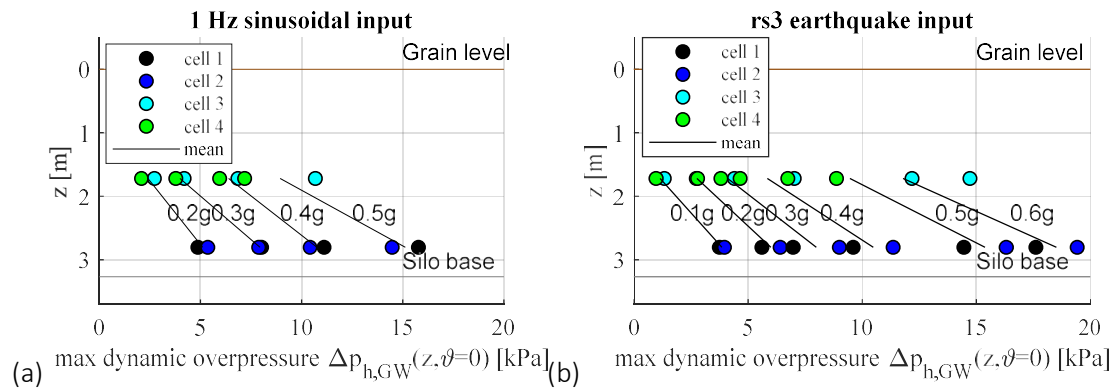


Figure 64: Maximum horizontal dynamic overpressures measured by the four load cells for various (a) sinusoidal and (b) earthquake tests

Figure 65a shows the dependence of the dynamic overpressure profile on the nominal PTA for the a1 artificial earthquake input. It can be noticed that the dynamic pressure increases almost linearly with the acceleration level, with a change of slope for acceleration values around 0.5g, corresponding to the internal friction coefficient of the granular solid.

Figure 66 displays the displacement profile, measured with HD video-cameras, at the time instant for which the displacement of the marker positioned at the grain level on the silo stiffener (the red one in Figure 66) is maximised during the 0.5g rs3 earthquake input. The maximum displacement value at the roof level is around 2 mm, whilst the maximum one at the free-surface level is around 1.5 mm.

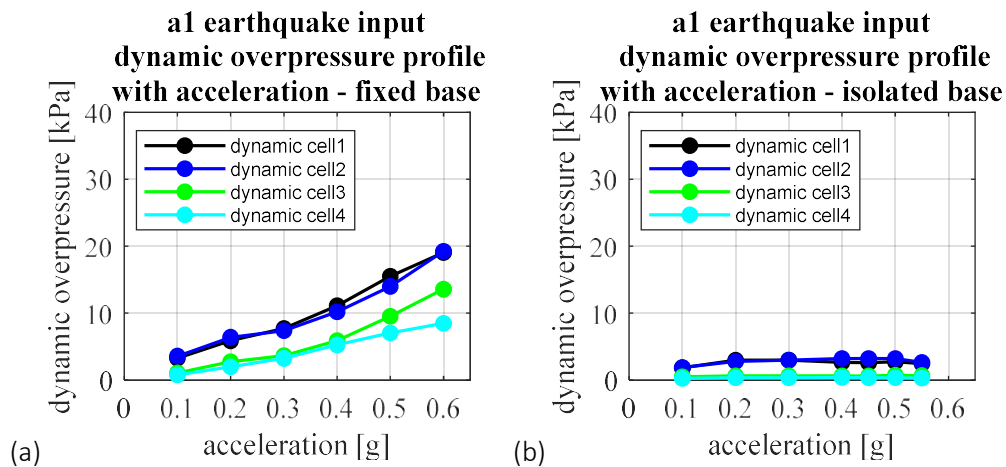


Figure 65: Dynamic overpressure profile with nominal Peak Table Acceleration for a1 earthquake input for (a) fixed-base and (b) isolated-base

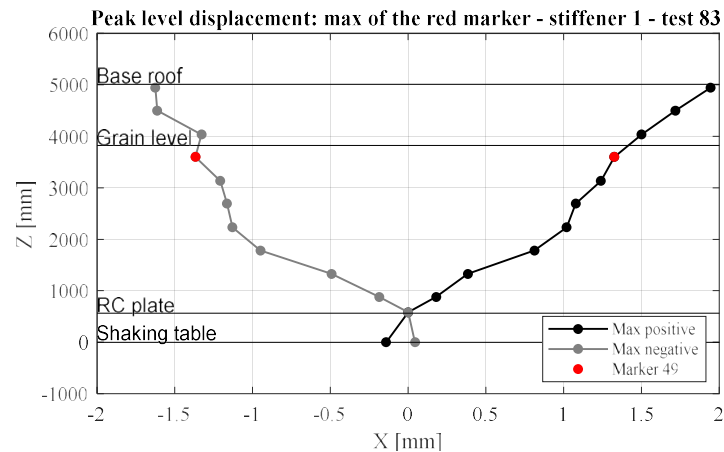


Figure 66: Maximum positive and negative displacement profiles at the time instant of maximum displacements at the grain free-surface level

The silo has also been tested in seismically isolated conditions, by removing the steel anchorages used to fix the r.c. plate to the table in the first fixed-base configuration.

In this project, the dynamic properties of the overall isolation system have been evaluated, through actual sinusoidal shaking-table tests of the isolated silo. The actuation force directly corresponds to the isolation force response, thus directly related to the whole set of four installed devices. The results obtained (not reported here for sake of conciseness) highlight the commonly known cyclic effect of Curved Surface Slider devices: as the number of applied cycles increases, the frictional force response decreases, with consequent reduction of the hysteretic energy. Initial friction coefficient is around 9%, whilst long-lasting one around 6%.

The target mechanical frequency (0.3 Hz) of the isolated-base silo has been experimentally found from the spectrogram built with reference to the relative horizontal displacement (along the input direction) between the r.c. plate and the shaking-table during Test N. 196 (0.55g a1 earthquake), which is shown in Figure 67.

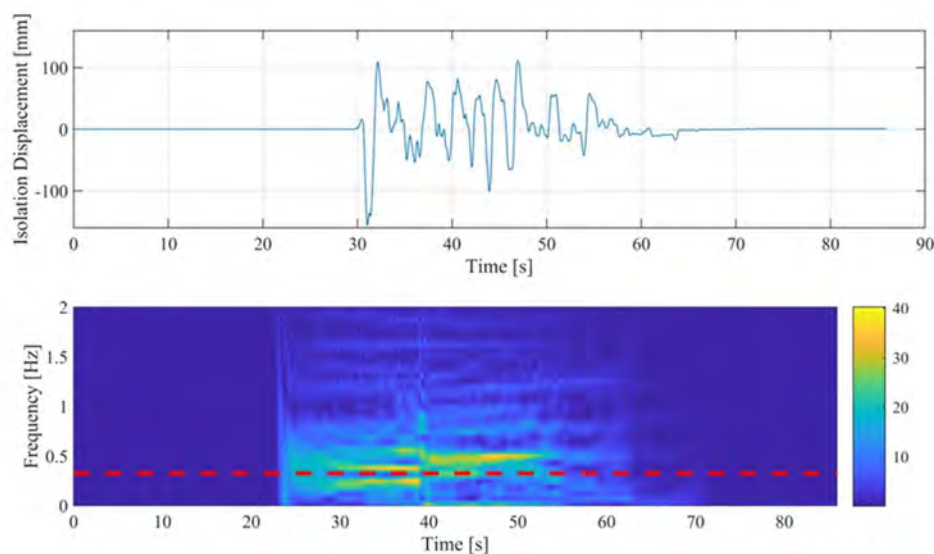


Figure 67: (a) Relative displacement response between the r.c. plate and the shaking-table during Test N. 196 (b) Corresponding spectrogram

Figure 65b shows the dependence of the dynamic overpressure profile on the nominal PTA for the a1 artificial earthquake input. It can be noticed that the pressure, for inertia forces larger than the friction forces of the Curved Surface Sliders pendulum devices (namely, for accelerations larger than 0.05 g - 0.10 g), is constant and independent of the Peak Table Acceleration. The comparison between Figure 65a and b highlights the effectiveness of base isolation in breaking down the dynamic overpressure on the silo wall.

Figure 68a and b display the relative displacement between the table and the superstructure (silo on the r.c. plate), i.e. the displacement developed by the isolators, for the rs1 and rs3 earthquake inputs, both scaled at 0.3 g. Two simple 2-dofs models have been prepared to predict this maximum relative displacement: one linear equivalent model with friction coefficient equal to 5%, and another non-linear model with friction coefficient equal to 8%. It can be noticed that the non-linear model is capable of well capturing the measured displacement.

Finally, Figure 69 displays the Peak Acceleration Profiles for the a1 earthquake input: the acceleration that reaches the base of the silo is, in all cases, around 0.1 g, comparable with the friction coefficient of the Curved Surface Sliders pendulum devices.

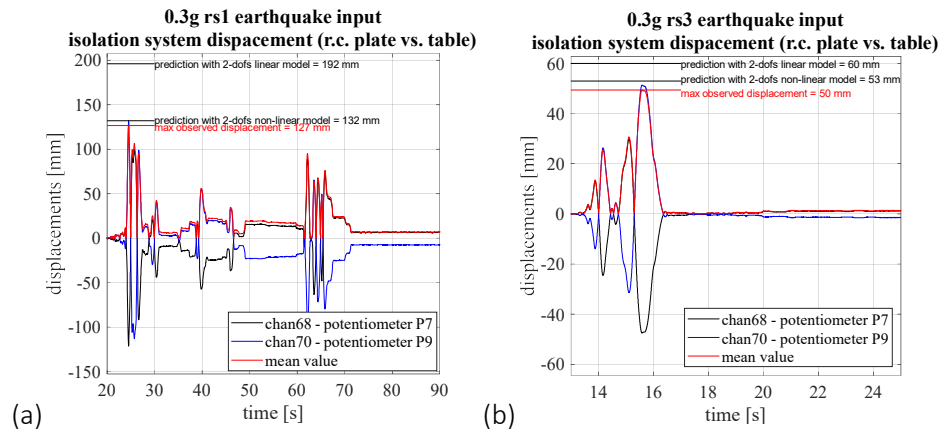


Figure 68: Relative displacements developed by the isolators placed between the table and the superstructure (silo on the r.c. plate) for the rs1 (a) and rs3 (b) earthquake inputs, both scaled at 0.3g

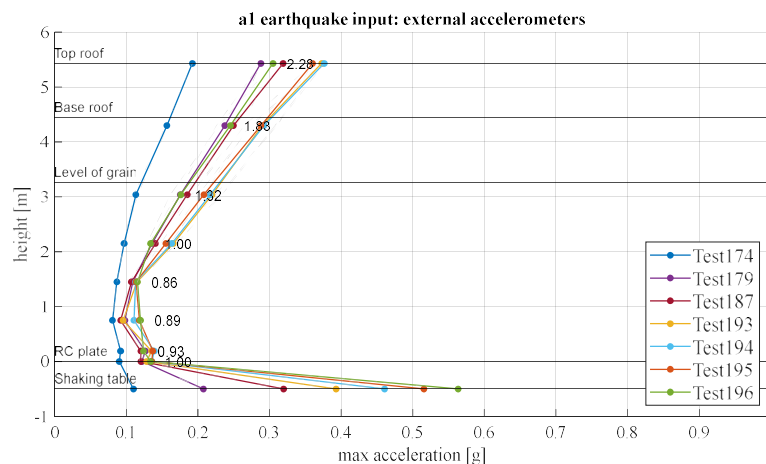


Figure 69: Peak Acceleration Profiles and dynamic amplification factors for a1 earthquake input

2.2.7 Conclusions and outlook

This document reports on the filling phase recording and several shaking-table tests on a 5.5m-high 3.64m-diameter flat-bottom cylindrical steel silo in fixed-base and isolated-base conditions. The silo is filled in quasi-concentric way up to 3.3m height with soft wheat, in order to achieve an aspect ratio $H/2R$ roughly equal to 1.

Interpretation of the huge number of data recorded during the experimental shaking-table tests is still under development. Selected preliminary results have been presented.

The horizontal static pressure distribution during the filling phase is qualitatively consistent with the Janssen static pressure model, but quantitatively closer to the linear geostatic one (around 1.3 N/cm² at 42 cm from the r.c. plate). As far as the dynamic results are concerned, the resonance frequency is around 11 Hz and slightly changes according to type of signal. In particular, it decreases with increasing acceleration (larger “effective mass”) and it increases with increasing grain compaction (higher stiffness provided by grain material). No significant dynamic amplification has been observed for low-frequency sinusoidal inputs. For the most demanding earthquake input (in terms of close-to-resonance frequency content), the dynamic amplification increases along the silo height up to values around 1.5. However, it slightly decreases with increasing acceleration, consistent with an increase in the damping ratio. The measured dynamic over-pressures seem to linearly increase with grain depth (from the top to the bottom) and a bilinear trend with the acceleration, with a slope-changing point for accelerations corresponding to the range of values of the grain internal friction coefficient (0.40-0.60). Concerning the base-isolated configuration, the analysis of the base shear response under sinusoidal acceleration input highlights the common behaviour of friction-based isolation devices under multi-cyclic excitations: namely, the friction coefficient continuously decreases (from 9% to 6%) due to heating phenomena, which occur at all sliding interfaces. Overall, the isolation system significantly mitigates both dynamic over-pressures and accelerations on the silo superstructure.

Detailed interpretation of tests results is still in progress and will be the object of future works.

2.2.8 References

- [1] Dogangun A, Karaca Z, Durmus A, Sezen H. Cause of damage and failures in silo structures. *Journal of Performance of Constructed Facilities ASCE* 2009; Vol. March-April, 65–71.
- [2] EN 1998-4, Eurocode 8. Design of structures for earthquake resistance, Part 4 -Silos, tanks and pipelines, CEN, Brussels 2006.
- [3] Rotter JM, Hull TS. Wall loads in squat steel silos during earthquakes. *Engineering Structures* 1989; 11(3):139–147.
- [4] Younan AH, Veletsos AS. Dynamics of solid-containing tanks. I: rigid tanks. *Journal of Structural Engineering* 1998; 124(1):52–61.
- [5] Veletsos A, Younan AH. Dynamics of solid-containing tanks. II: flexible tanks. *Journal of Structural Engineering* 1998; 124(1):62–70.
- [6] Dvornik J, Lazarevic D. Loading of granular material on silo walls. *Processing of the 1st Conference on Applied Mathematics and Computation*, Rogina M, Hari V, Limić N, Tutek Z (eds). Dubrovnik, Croatia, 1999; 215–222.
- [7] Wagner R, Noh S-Y, Butenweg C, Meskouris K. Seismic excited granular material silo. In *Proceedings of Eurodyn 2002*, Grundmann H, Schueller GI (eds). 2002; 253–258. 90 5809510X:307-333.

- [8] Holler S, Meskouris K. Granular material silos under dynamic excitation: numerical simulation and experimental validation. *Journal of Structural Engineering*, ASCE 2006; 132(10):1573–1579.
- [9] Janssen HA. Versuche über Getreidedruck in Silozellen. *Zeitschrift des vereinesdeutscherIngenieure* 1895; 1045.
- [10] Sperl M. Experiments on corn pressure in silo cells—translation and comment of Janssen’s paper from 1895. *Granular Matter* 2006; 8(2):59–65.
- [11] Silvestri S, Gasparini G, Trombetti T, Foti D. On the evaluation of the horizontal forces produced by grain-like material inside silos during earthquakes. *Bulletin of Earthquake Engineering* 2012; 10:1535–1560.
- [12] Pieraccini L, Silvestri S and Trombetti T, Refinements to the Silvestri’s theory for the evaluation of the seismic actions in flat-bottom silos containing grain-like material, *Bulletin of Earthquake Engineering*, 2015; 13(11), pp. 3493-3525.
- [13] Silvestri S, Ivorra S, Di Chiacchio L, Trombetti T, Foti D, Gasparini G, Pieraccini L, Dietz M, Taylor C. Shaking-table tests of flat-bottom circular silos containing grain-like material. *Earthquake Engineering & Structural Dynamics*, 2016; 45:69–89.
- [14] Pieraccini L, Palermo M, Silvestri S, Trombetti T. On the Fundamental Periods of Vibration of Flat-Bottom Ground-Supported Circular Silos containing Grain-like Material. *Proceedings of the 16th World Conference on Earthquake Engineering (16WCEE)*, Santiago, Chile, 9-13 January 2017, Paper N° 2041.

2.3 Project #34 – Seismic performance of multi-component systems in special risk industrial facilities

Authors

C. Butenweg⁽¹⁾, I. Lanese⁽²⁾, E. Rizzo Parisi⁽²⁾, A. Pavese^{(2),(3)}, F. Paolacci⁽⁴⁾, O. Bursi⁽⁵⁾, M. Marinković⁽⁶⁾, M. Ciucci⁽⁷⁾, G. Quinci⁽⁴⁾, C. Nardin⁽⁵⁾

⁽¹⁾ RWTH Aachen University, Center for Wind and Earthquake Engineering, Aachen, Germany

⁽²⁾ EUCENTRE, European Centre for Training and Research in Earthquake Engineering, Pavia, Italy

⁽³⁾ University of Pavia, Pavia, Italy

⁽⁴⁾ ROMA Tre University, Rome, Italy

⁽⁵⁾ University of Trento, Trento, Italy

⁽⁶⁾ University of Belgrade, Belgrade, Serbia

⁽⁷⁾ DIT, INAIL, Italy

2.3.1 Introduction

Past earthquakes demonstrated the high vulnerability of industrial facilities equipped with complex process technologies leading to serious damage of the process equipment and multiple and simultaneous release of hazardous substances in industrial facilities. The Tang-Shan earthquake

(Beijing, China) in 1976 seriously damaged the highly industrialized zones and coal mines in its vicinity. The 1989 Loma Prieta and the 1994 Northridge earthquakes damaged factories and energy supply facilities. The Kocaeli (Turkey) and Chi-Chi (Taiwan) earthquakes in 1999 damaged petroleum complexes and thermal power stations. The 2011 Daiichi earthquake led to the Fukushima nuclear disaster, and more recently Emilia-Romagna (2012) damaging approximately 500 small scale factories.

The seismic behaviour of industrial facilities was intensively studied [1] with numerical models and several component-based fragility curves were developed. In general, floor response spectra of the primary structure are used to determine the response of installed components [2, 3]. However, this approach does not consider dynamic interaction between the structure and the installations and thus the effect of seismic response of the installations on the response of the structure and vice versa. Most experimental studies described in the literature deal with specific components tests [7, 8], for instance tests of pipe joints [4, 5], fire sprinkler piping systems [10, 11] or investigation of floor response spectra [6]. Only a limited number of full-scale tests [9] have been conducted so far.

A variety of construction measures and techniques have been developed in order to improve the behaviour of industrial structures and their installed components. One option is to install seismic isolation measures [10, 12] to the overall structure or specific components. Furthermore, the isolation of single components is an effective and well-accepted solution to decouple substructure and components [13]. Increased effort to develop powerful monitoring systems that quickly recognize dangerous patterns and consequences in case of seismic events are developed and coupled with automatic shutdown devices [14, 15]. Their use, mainly focused on NPP so far, will continue to increase with the introduction of digital building models.

The current code-based approach for the seismic design of industrial facilities is considered not enough for ensure proper safety conditions against exceptional event entailing loss of content and related consequences. Accordingly, SPIF project (Seismic Performance of Multi-Component Systems in Special Risk Industrial Facilities) was proposed within the framework of the European H2020 - SERA funding scheme (Seismology and Earthquake Engineering Research Infrastructure Alliance for Europe).

The proposed project aims to investigate the seismic behaviour of multi-component systems in nuclear and special risk industrial facilities by means of shaking table tests paying special attention on the interactions between the primary structure and components as well as between the components themselves. Due to high cost of the process engineering components and due to the risk of operational interruptions and the release of harmful substances into air, water and ground in case of damage occur, the planned investigations are of utmost importance.

The test structure is a three-storey moment resisting steel frame with vertical and horizontal vessels and cabinets, arranged on the three levels and connected by pipes. The dynamic behaviour of the test structure and installations is investigated with and without base isolation.

The achieved results on the seismic behaviour of the multi-component test structure with mutual interactions can be used for probabilistic safety analyses in power plants as well as in industrial plants. In addition, important findings can be derived for the definition of performance limits, the isolation of structural systems in plants and the use of sensor systems for rapid damage assessment.

2.3.2 Three storey steel moment resisting frame with installations

The primary steel structure of the prototype is a three-storey moment resisting frame with flexible diaphragm, dimensions of 3.7 x 3.7 m in the horizontal plane and an interstorey height of 3.1 m. Figure 70 shows the CAD-model and a photo of the test structure on the shaking table at EUCENTRE

laboratory. The structural system is a moment resisting frame in the direction of seismic actions and fully clamped to the reinforced concrete slab. In perpendicular direction strong diagonals are installed to limit translational movements and torsional effects. The supporting beams of the installations are hinged connected to the crossbeams, which are fastened to the frame beams by standardised hinged connections with web stiffeners.

In total four tanks are installed: two vertical tanks on the first level and two horizontal tanks on the second level. Furthermore, one electrical cabinet is placed on the first level. The piping layout is composed by DN 100 pipes, except the one suspended at the third level, which is composed by pipes with diameter of DN 80. In addition, single degree of freedom (SDOF) oscillators are installed on each of the three levels to investigate the component response for different periods in the linear and non-linear range. Finally, a conveyor is installed on the reinforced concrete slab.

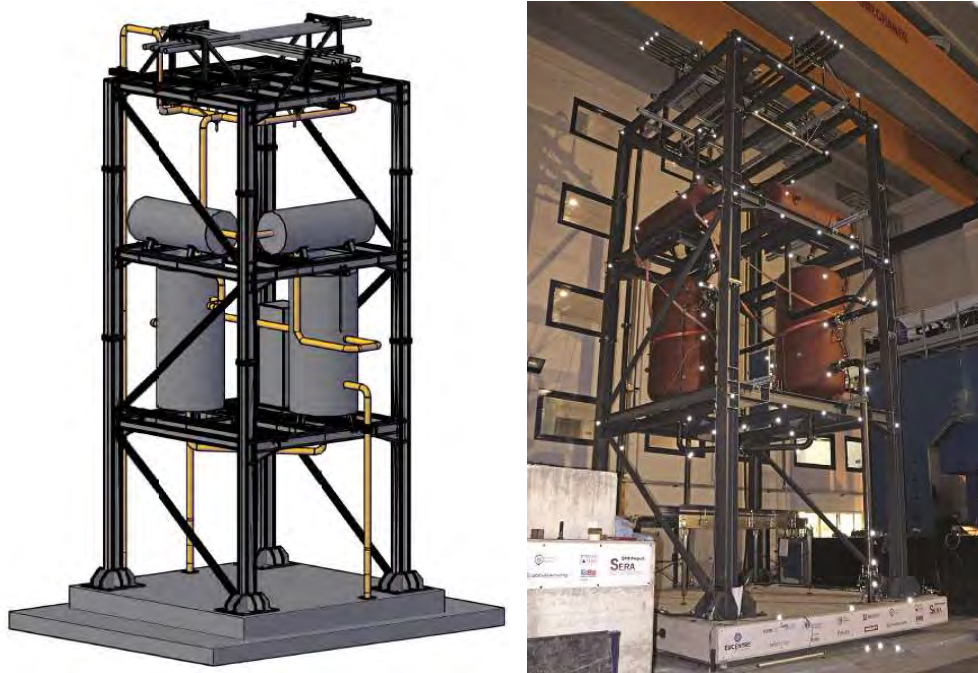


Figure 70: Test structure with installations: CAD-model (left) and structure on the shaking table (right)

The steel columns are welded on steel base plates, which are anchored to the reinforced concrete slab using a combination of special chemical anchors and continuous anchors through the slab with a thickness of 40 cm. The reinforced concrete slab is placed on isolators with bottom and top plates rigidly connected to the shaking table and the slab. The isolators can be deactivated by the installation of additional steel reaction structures on each side. This set-up allows to investigate both isolated and non-isolated configuration. The side view of the reinforced concrete base plate, isolators and mountable steel supports is shown in Figure 71.

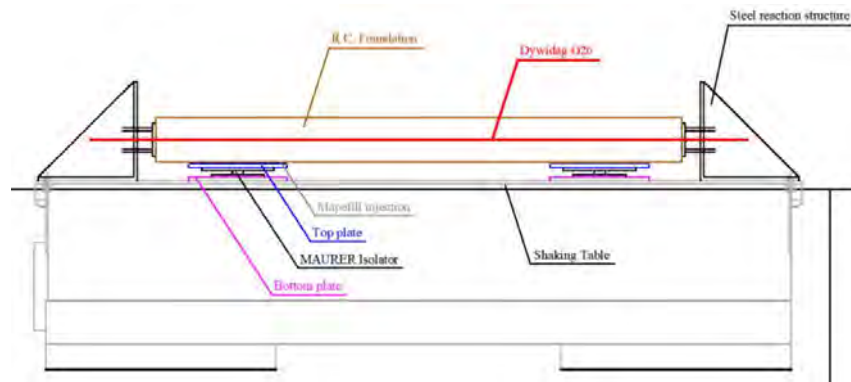


Figure 71: Reinforced concrete plate, isolators and mountable steel supports

Figure 72 shows the horizontal and vertical tanks with dimensions and supports. Figure 73 shows the cabinet on the first floor, the conveyor placed on the reinforced concrete slab and the single SDOF oscillators installed on each storey.

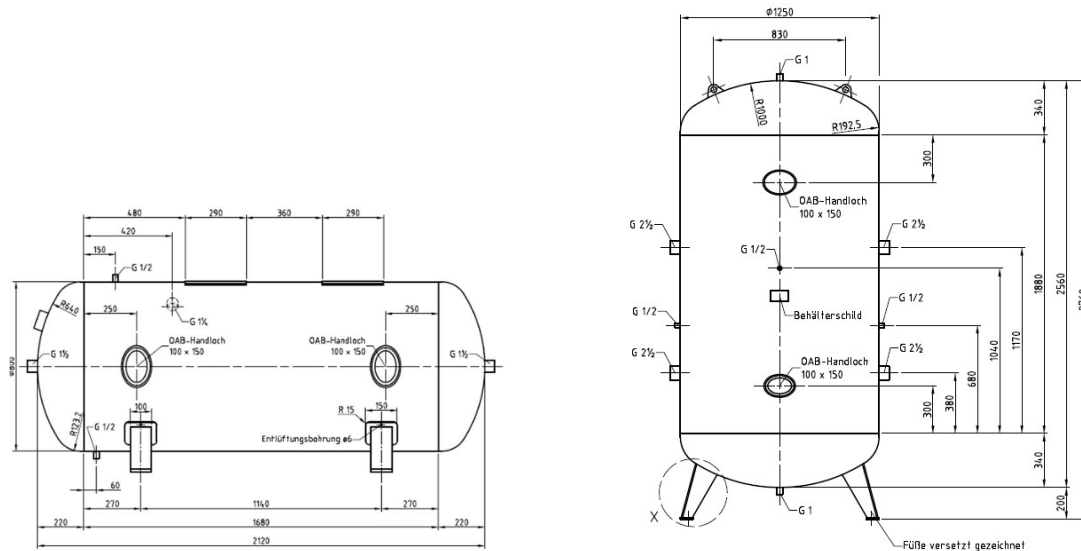
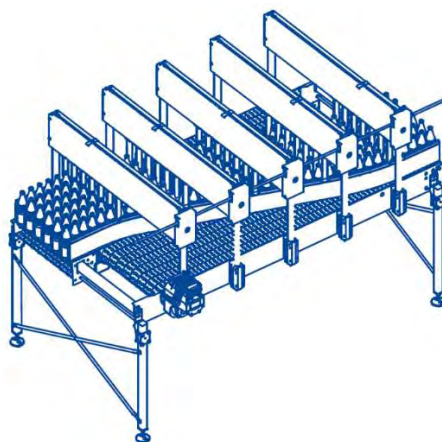


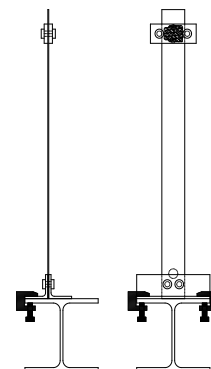
Figure 72: Installed horizontal (left) and vertical (right) pressure vessels (Producer: Behälter KG, Breme)



a)



b)



c)

Figure 73: a) Cabinet on the first floor, b) Conveyor, c) SDOF oscillator

2.3.3 Numerical model, modal analysis, preliminary simulation results

For the prediction of the tests results detailed numerical models were developed by the project partners in Aachen (CWE) with ANSYS, in Rome (ROMATRE) with MIDAS and in Trento (UNITR) with SAP 2000. In the following the simulation models and selected results obtained by CWE and ROMATRE are presented. The primary steel structure is idealized with beam elements and the tanks are modelled with shell elements. The pipes and flanges are modelled completely by shell elements in ANSYS and in MIDAS by means of linear beam elements for the straight pipes and with shell elements for the critical pipe sections like elbows and tee joints. Figure 74 and Figure 75 depict the numerical models.

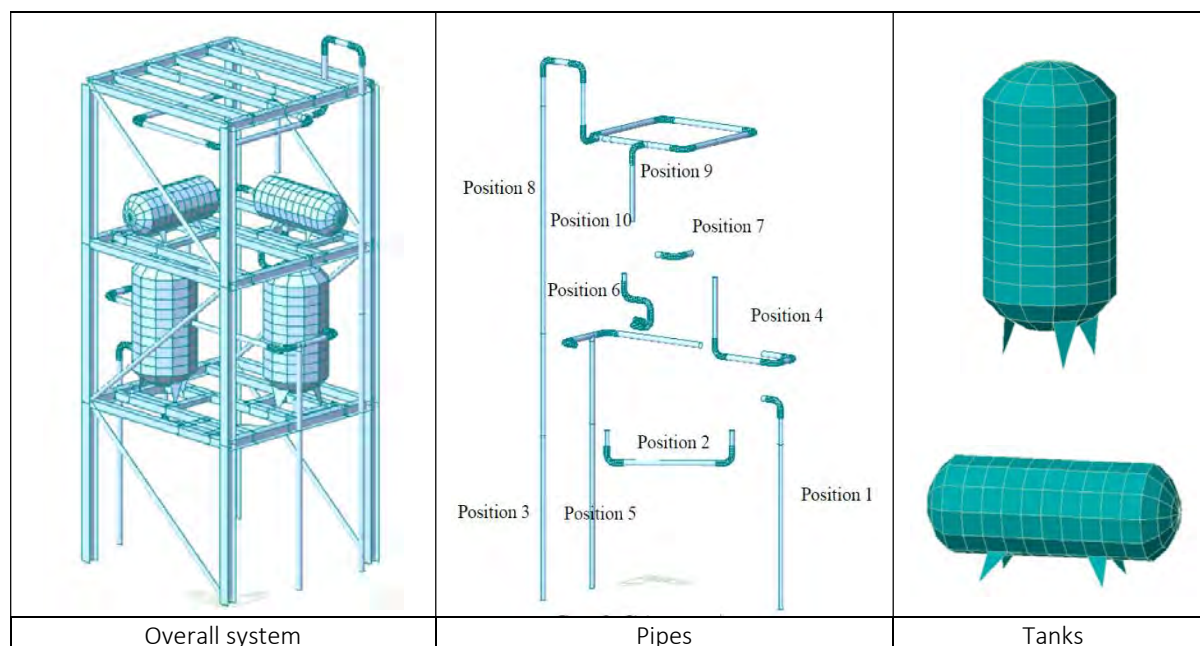


Figure 74: Simulation model in MIDAS (ROMATRE)

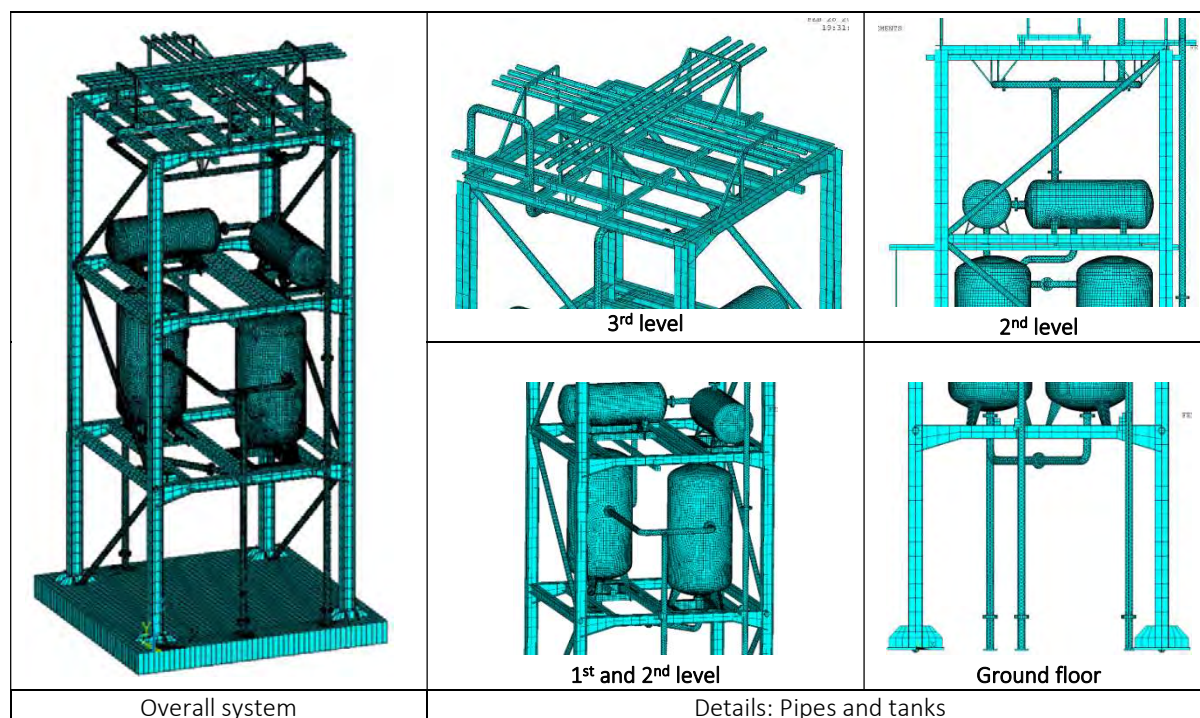


Figure 75: Simulation model in ANSYS (CWE)

The results of the modal analysis for both models are shown in Figure 76. The first eigenmode obtained with the ANSYS model is a local mode, since only the pipes on the third floor vibrate and only a low percentage of mass is activated. The local mode is not represented by the model in MIDAS as the pipes on the third floor are not part of the model. However, the global eigenmode with a high percentage of activated mass is estimated by both numerical models at 2.9 Hz. The higher eigenmodes with local vibrations of the installations on each floor level are calculated for frequencies higher than 4.5 Hz.

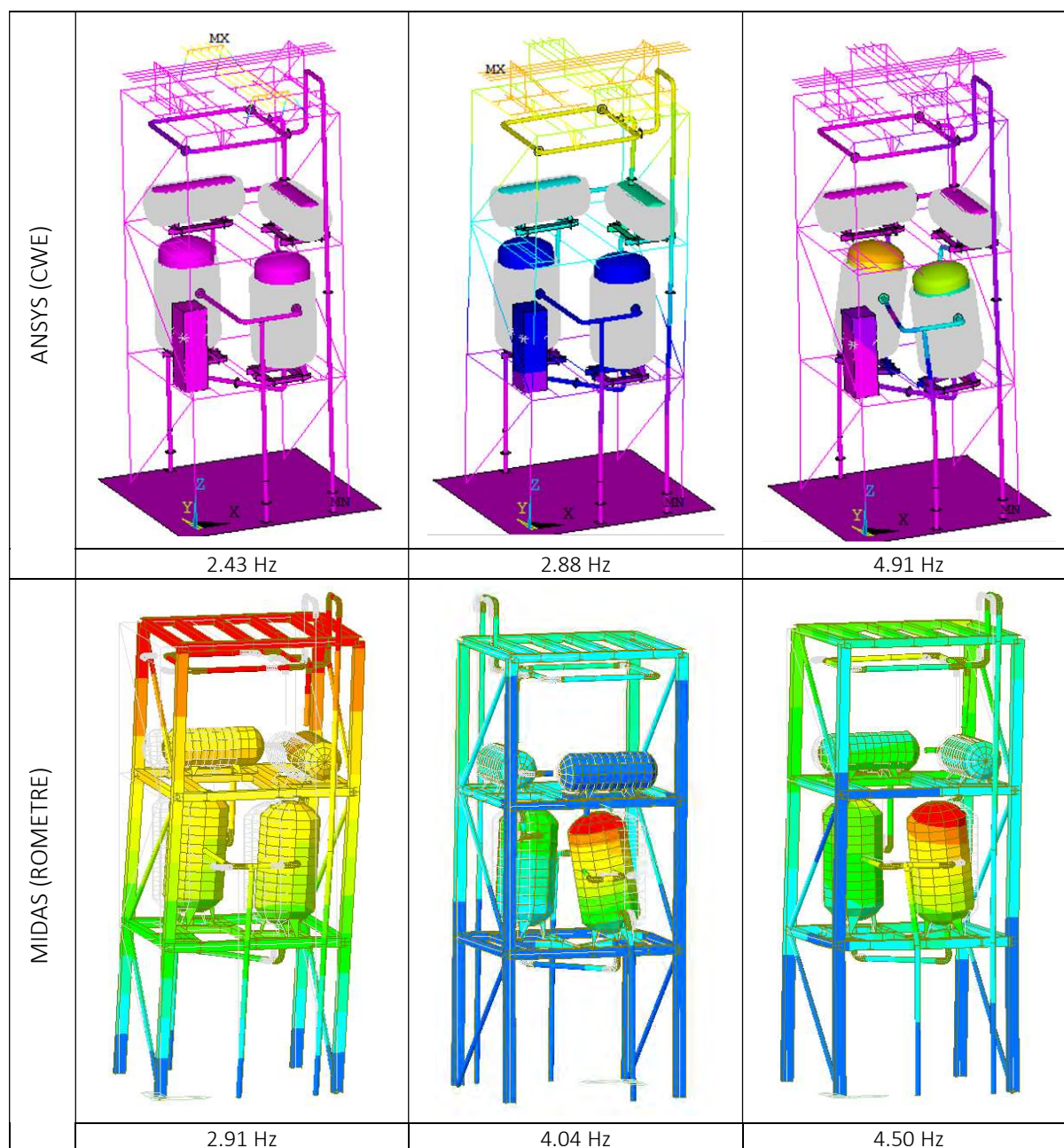


Figure 76: Vibration modes of the structure

The applied seismic action is defined as a linear elastic response spectrum of Type 1 with soil condition C according to Eurocode 8. A set of 10 stochastically independent accelerograms was generated. The control spectra of the generated accelerograms are shown in Figure 77. Based on simulations with all generated accelerograms, the accelerogram TH8 was selected for the shaking table tests. Figure 78 shows the accelerogram TH8 for a reference PGA of $0.635g$ m/s^2 . The accelerogram was applied with a sampling rate of 256 Hz, a total duration of 25s and baseline correction. The corresponding control

spectrum in comparison to the target spectrum according to Eurocode 8 is shown in Figure 79. During the test campaign the accelerogram TH8 was scaled up to a maximum of 111%.

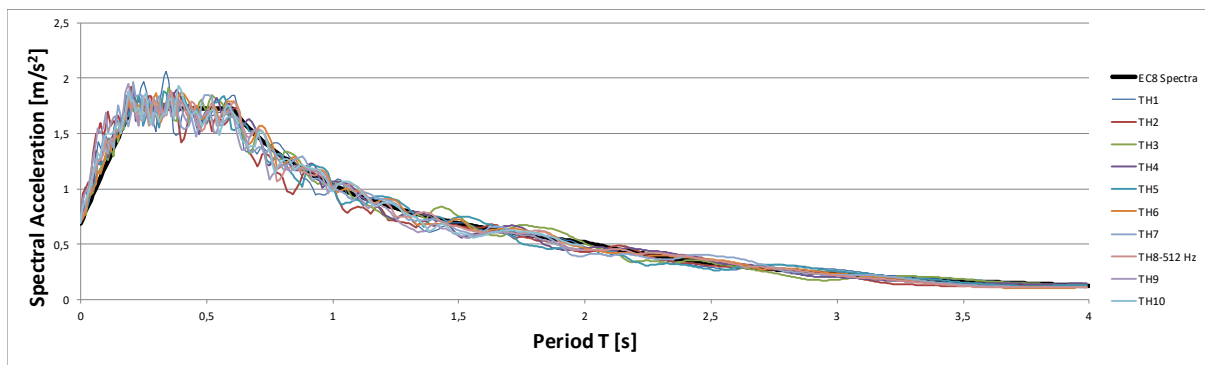


Figure 77: Elastic response spectra according to Eurocode 8 and control spectra for TH1-TH10

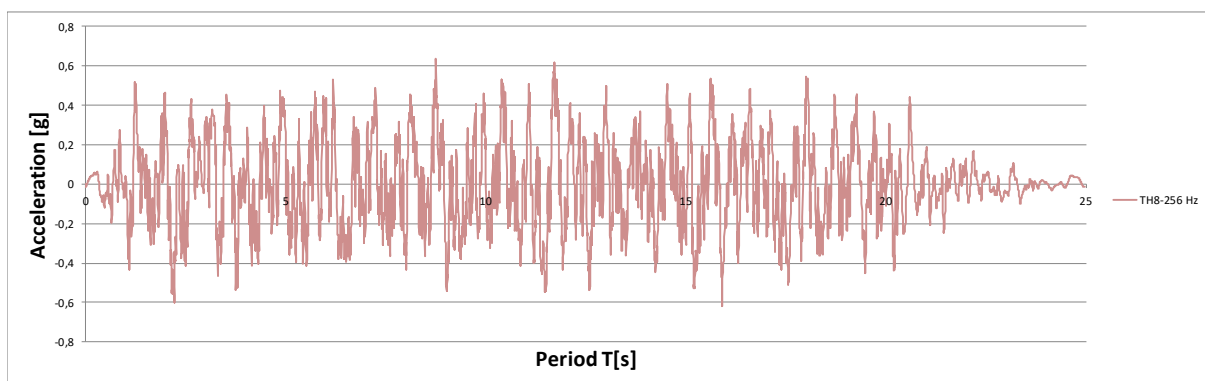


Figure 78: Accelerogram TH8

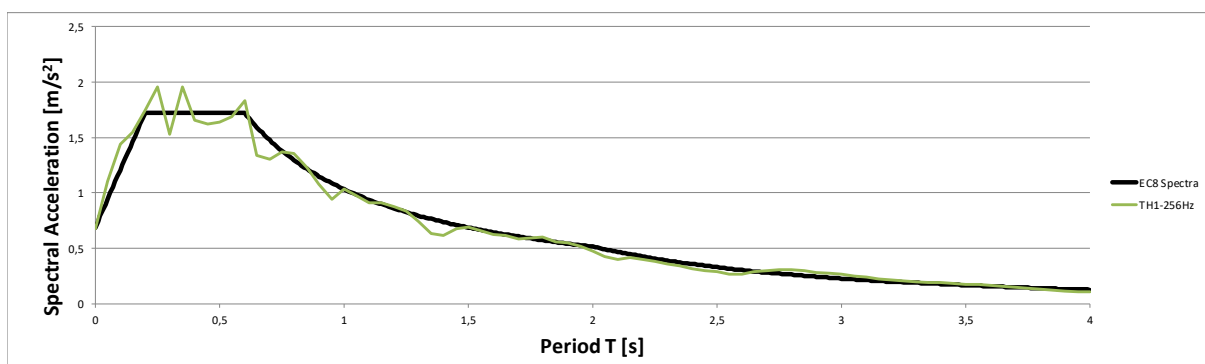


Figure 79: Target spectrum according to Eurocode 8 and control spectrum for TH8

Figure 80 shows the stresses as result of a response spectrum analysis with the ANSYS-model for selected pipe positions. The stress levels show, that a yielding can take part in critical cross section. However, pipes are quite flexible and it can be expected that the maximum allowable strains in tension and compression are not exceeded.

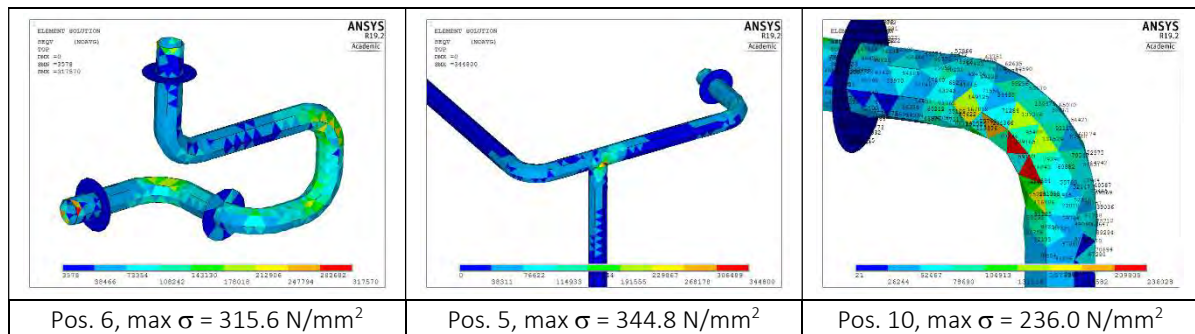


Figure 80: Stress distributions in pipes for Pos. 5, 6 and 10

Figure 81 shows the stress distribution for a vertical tank with special attention on the stressed footings of the tank. The stresses are highly localized and the yield strength is exceeded. However, due to overstrength and stress redistribution a total failure with overturning of the tank is not expected.

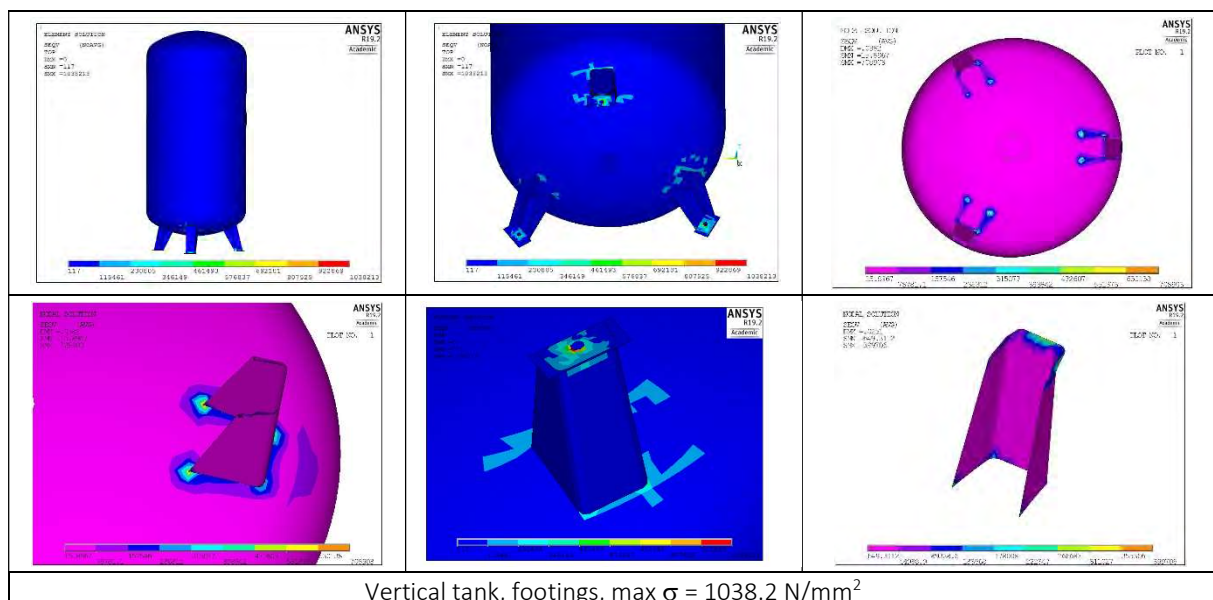


Figure 81: Vertical tank: Stress distribution in tank wall and footings

The results of time-history analyses carried out with MIDAS (ROMATRE) are shown in Figure 82. For each storey the acceleration time histories and corresponding transfer functions are shown for the evaluation points. Again, the fundamental frequency is clearly identified at about 2.9 Hz as already predicted by response spectrum analyses. Furthermore, the evaluation of the resulting stresses show clearly that the primary steel structure remains in the elastic field in accordance with the design conditions.

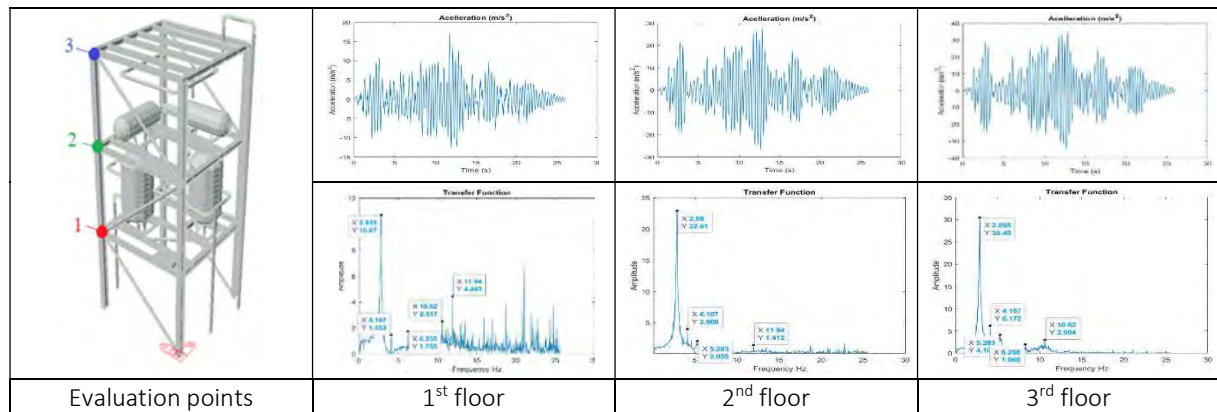


Figure 82: Acceleration time histories and corresponding transfer functions at 1st, 2nd and 3rd floor

Table 11 summarizes the global behaviour of the primary steel structure in terms of the total base shear, overturning moment and maximum horizontal displacement at the 3rd level for the maximum applied PGA of 7,05 m/s². Furthermore, the maximum normal force and moment is given for the columns, decisive to control the anchorage of the structure. These global values are continuously checked during the test execution to control the safe condition of the overall system.

Total base shear [kN]	Overturning moment [kNm]	max. N [kN] columns	max. M [kNm] columns	max d [cm] 3 rd level
290 kN	1610 kNm	163 kN	119 kNm	7.5

Table 11: Characterisation of the global structural behaviour

2.3.4 Test set-up and measurements

The test structure is erected on a reinforced concrete slab and each column of the three-story steel frame is mounted by strong base plates with stiffeners to the slab with dimensions of 4.8 m x 4.8 m and a thickness of 0.4 m. For the first testing phase the slab is placed on isolators, which bottom and top plates are rigidly connected to the shaking table and the bottom of the RC slab. The isolators and their installation is shown in Figure 83 and Figure 84.

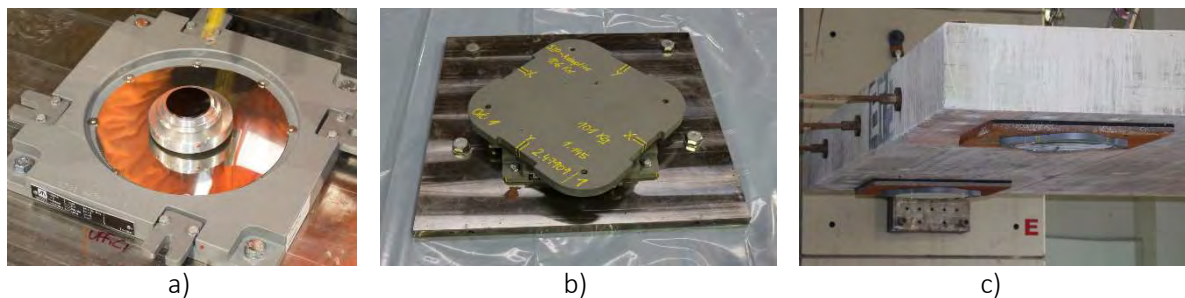


Figure 83: a) Base isolator on shaking table, b) Base Isolator with top plate, c) RC-slab with top plate

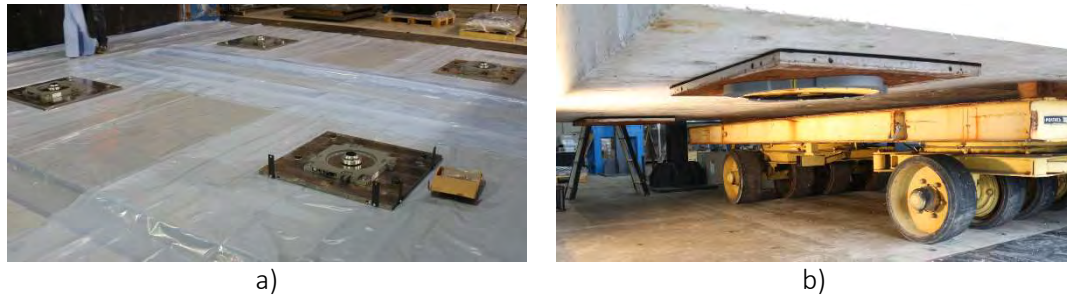


Figure 84: a) Isolators on the shaking table, b) Installation of the RC slab with base isolation

By installing additional horizontal steel supports, the isolators can be deactivated and the horizontal movement of the table is then transferred directly to the test structure. Additionally, the RC-slab is fixed by through anchors to the shaking table. The test set-up was already successfully developed and applied in the SERA-SILOS project (<https://sera-ta.eucentre.it/sera-ta-project-18/>). Figure 85 shows the fixation of the slab by steel supports and the anchorage of the RC-slab to the shaking table.

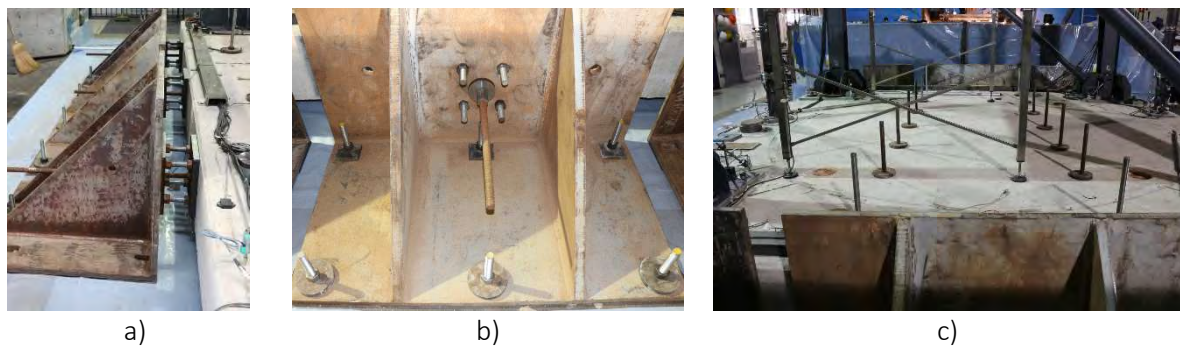


Figure 85: a) Steel support, b) Anchorage of the steel support, c) Through anchors to the shaking table

The primary steel structure is designed in the lowest ductility class according to Eurocode 8 for a PGA of 6 m/s^2 . The structural system in the direction of the seismic action is a moment resisting frame and fully clamped to the reinforced concrete slab. The frame corners are executed as bolted connections with welded stiffeners and haunches. Figure 86 shows the strong frame corner on the first level, Figure 87 shows the test structure and installations on each floor level.

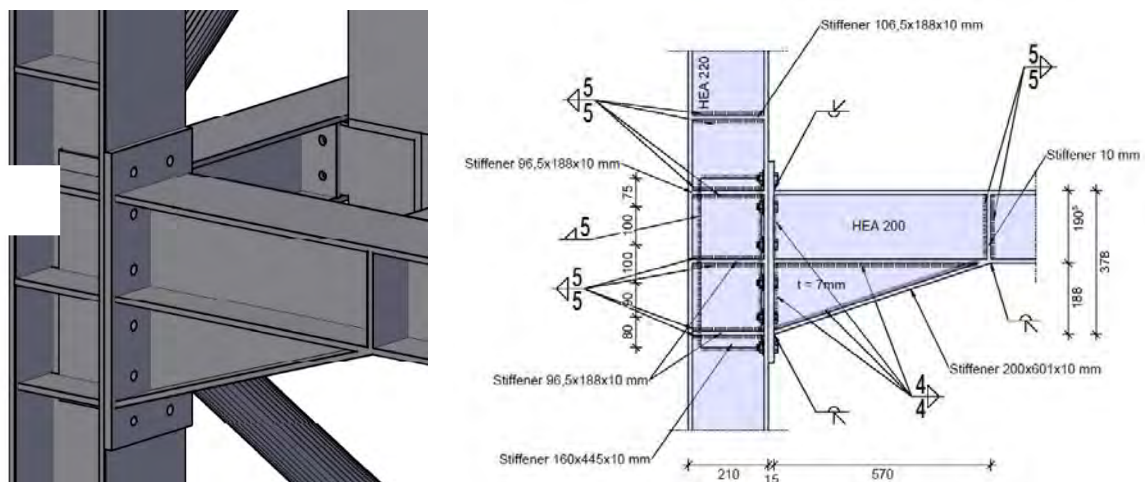


Figure 86: Bolted frame connection with stiffeners and haunch

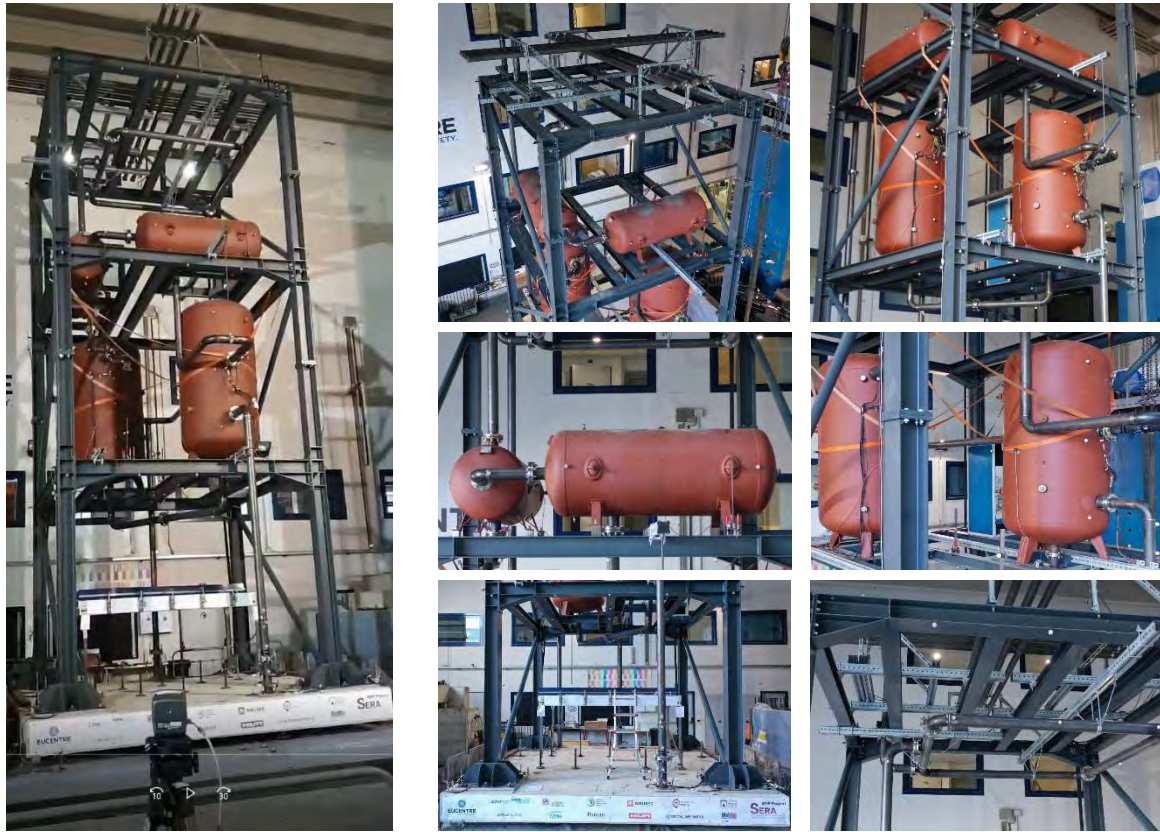


Figure 87: Test structure and installations on each floor level

The pipe branches with the most critical bolted flange joints are filled with water and pressurized at 20 bars. Storage tanks are instead filled with aggregates to avoid the release of water. The filling level of all tanks is 80% and the specific weight of the aggregates corresponds to the specific weight of water.

The structure has been instrumented by a variety of common and innovative sensors (Figure 88 to Figure 91) such as:

- accelerometers, placed at the frame floors, on the tanks, pipes on the third floor and other components;
- strain gauges, to monitor the stresses at the base of the columns, of the uplift retaining bars and next to the four most critical flange joints (water filled pipes);
- displacement transducers, to monitor the relative motion between the RC slab and the shaking table, the possible uplift of the frame anchorage plates, and on some flanges, monitored with strain gauges and optic fibers as well;
- optic fibers sensors, to detected leakage of the two most critical flange joints;
- contactless machine vision system, based on infrared cameras and reflective markers, to monitor the 3D absolute displacement of 78 points between structure and components.

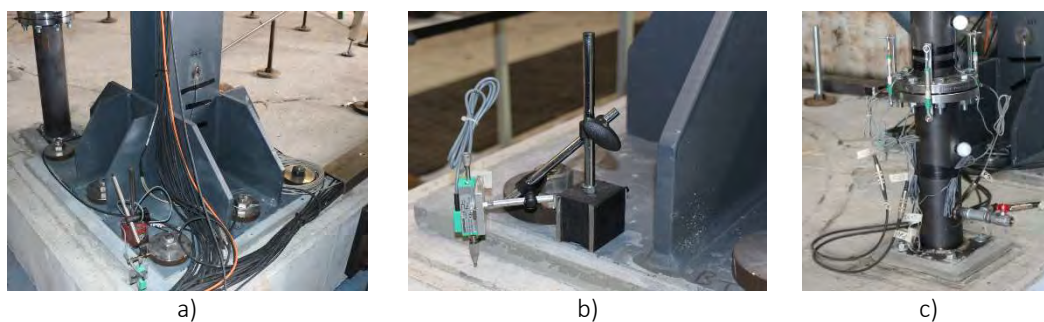


Figure 88: a) and b) Strain gauges, displacement transducers at the anchorage, b) Strain gauges, markers and displacement transducers at Pos. 1 of the pipe system

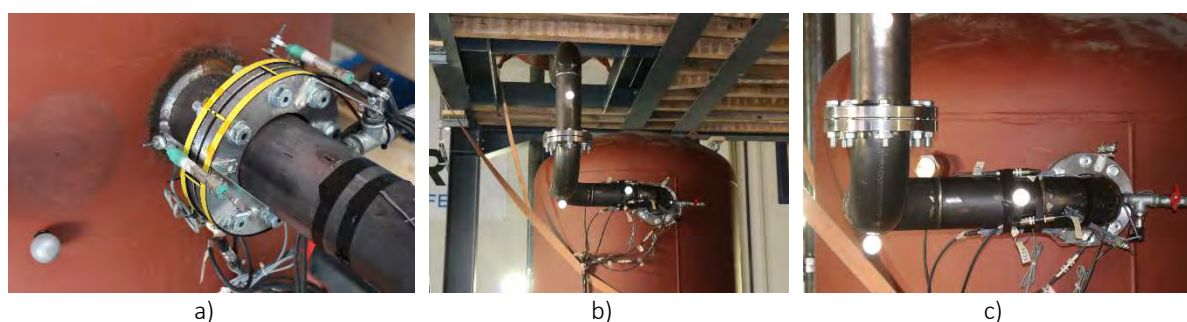


Figure 89: Instrumentation of tanks and pipes on the 1st floor: a) Strain gauges, displacement transducers and optical fibre system, b) and c) Markers and strain gauges



Figure 90: Instrumentation of tanks and pipes on the 2nd floor: a) Accelerometer on top of the horizontal tank, b) Markers on horizontal tanks and pipes

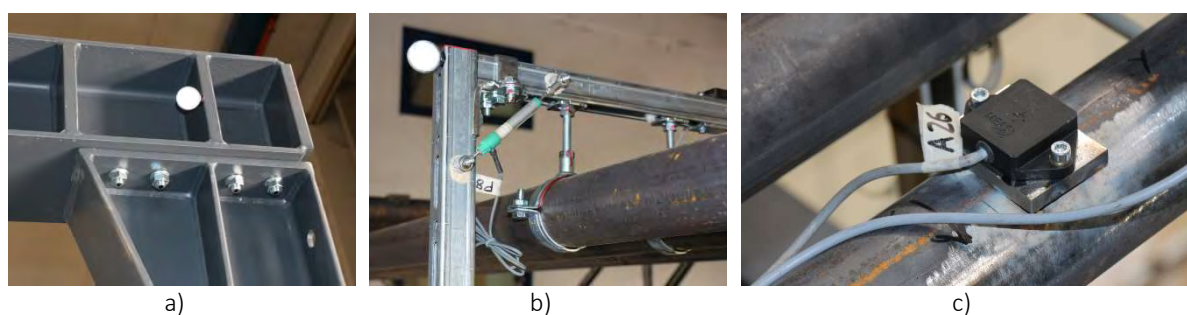


Figure 91: Instrumentation of tanks and pipes on the 3rd floor and roof top: a) Marker, b) Displacement transducer, c) Accelerometer on pipe DN 80

2.3.5 Observation during testing

During the experimental tests, different levels of PGA have been imposed to the test structure. The applied levels of PGA with respect to the reference PGA of 0,635g (Figure 78) range from 25% to 111%. During the test program, a series of tests with lower PGA-levels have been performed for the tuning of the shaking table, but not reported herein. Hereinafter, main observations in terms of damage for each run of the shaking table tests are reported. In particular, up to a PGA-level of 50% no visible damage has been detected both in the moment resisting steel frame and installations. The component with considerable and visible displacements was Tank 2 in all runs.

During the tuning phase of TH8_70%, TH8_37% was considered and performed twice; this second tuning run caused damage to one suspended pipe system at the third floor (Figure 92). One bolt of the angle connector between the horizontal and the vertical channel of one transversally braced pipe suspension frame loosened and slipped out of the vertical profile slot. When inserting this bolt connection, the wing-nut must be 90° rotated into its final clamping position, before being prestressed to the prescribed level according to the manufacturer's instruction guide. It is currently under investigation whether the failure occurred due to a not compliant installation, or because of the series of test and tuning runs that caused high accelerations and long sessions of repeated vibrations. For safety reasons, the pipe rack was removed before any subsequent test run.

During the test with a PGA-level of 70%, large displacements of Tank 2 at the first floor were measured caused by rocking of the tank on the cross-beams. The interaction caused damage to the connection between the cross and frame beam. The connection shows a warping (Figure 93a) of the web and crack initiation in the transition zone from the beam to the connection area with the continued web (Figure 93b, c). In order to proceed the tests with higher PGA-levels, the connection was strengthened by an additional profile bolted on top of the cross and frame beam (Figure 94).

The effect was more evident during subsequent runs with some other cross beams experiencing the same type of damage, in particular at a scaling factor of 100% (Figure 95). The last test carried out with a scaling factor of 111% (Figure 96, induced further damage of the cross-beams underneath the vertical tanks. Furthermore, the conveyor on the RC slab collapsed due to the failure of the supporting system in the final test. The damage of the conveyor is shown in Figure 97.

RUN	PGA Level	OBSERVATION	Figure
TH8_25%	0.159g	- Overall elastic behaviour	-
TH8_37%	0.235g	- Overall elastic behaviour	-
TH8_50%	0.318g	- Overall elastic behaviour - Some drops in pressure of pipes recovered before the next test	-
TH8_37%	0.235g	- 3 rd floor: Collapse of pipe rack in the transversal direction	Figure 92
TH8_70%	0.445g	- Large displacements (+/- 30 mm) of vertical Tank 2 at 1 st floor - Relevant rotation of the cross beam under the vertical Tank 2 and warping of the web - Strengthening of the cross-beam underneath Tank 2	Figure 93 Figure 94
TH8_100%	0.635g	- Other cross beams experienced cracking	Figure 95
TH8_111%	0.705g	- Cracking on cross beams significantly increased - Failure of bracing supporting the conveyor	Figure 96 Figure 97

Table 12: Schematic observations versus PGA-levels



Figure 92: Damage of suspended pipes at 3rd floor

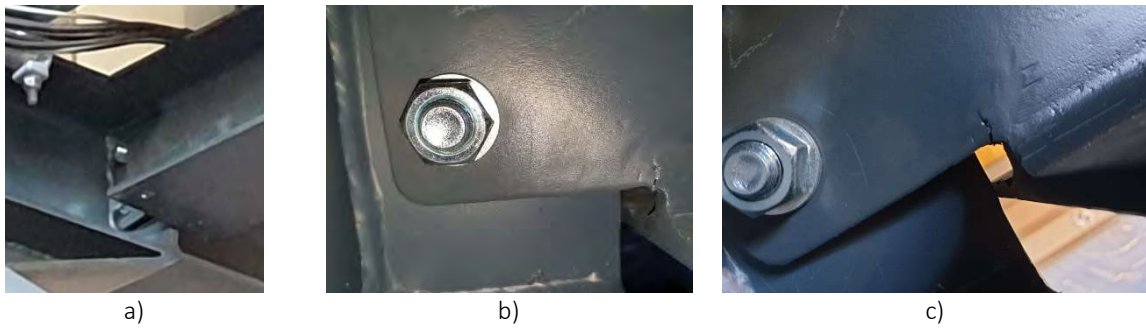


Figure 93: a) Warping of the web, b), c) Crack propagation in the web of the cross beam - Tank 2 (70%)



Figure 94: Strengthening: Additional profile connected to the cross and frame beam by bolts - Tank 2



Figure 95: Cracks in the web of the cross-beam (100%)

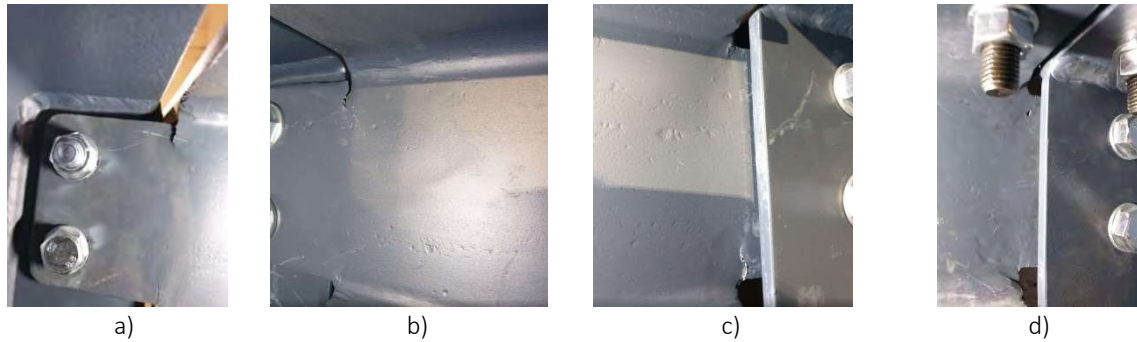


Figure 96: a) – d) Cracks in the web of the cross-beam - Tank 2 and other cross beams (111%)



Figure 97: Collapse of the supporting system of the conveyor

2.3.6 Preliminary results

The first step includes the processing and analysis of the signals recorded during the experimental campaign in order to perform a system identification of the SPIF structure. Hereinafter, first results of identification are reported, carried out for random noise applied as input to the SPIF structure.

As preliminary control, a fast Fourier transform (FFT) of all acquired data of accelerometer sensors installed on the primary steel structure has been carried out. In order to investigate amplitude vs frequency of some recorded signals, the power spectral density by the Welch's method has also been computed.

In particular, measured data along the seismic input direction were processed at the levels of the shaking table, RC slab and on the first, second and third floor. As an example, the results obtained by processing data acquired in accelerometers installed on column NE on the 3rd floor are illustrated in Figure 98.

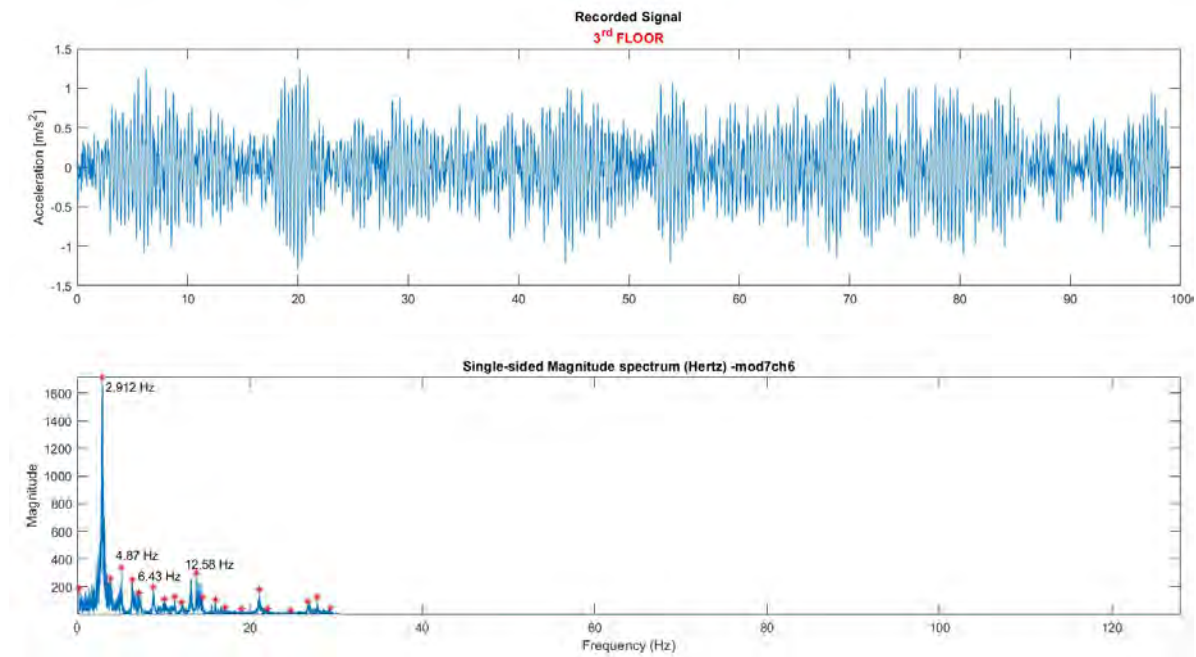


Figure 98: Recorded acceleration signal at 3rd floor and FFT for random input RND13 excitation

More precisely, for each run of the experimental campaign, it has been estimated a matrix of frequency response functions (FRF) from the excitation signal of the shaking table and the response signals of the overall structure, processed with a sampling rate 256 Hz. Along this line, frequency histories data corresponding to Fourier transform of the time domain signals. A good matching in terms of frequency content with the predicted simulated response can be noticed (Figure 76). In particular, the first natural frequency is very close to the numerical one, as well as the frequency of higher modes. Similar results were obtained in terms of Frequency Response Function of the signals. An example of processed data and frequency content is illustrated in Figure 99.

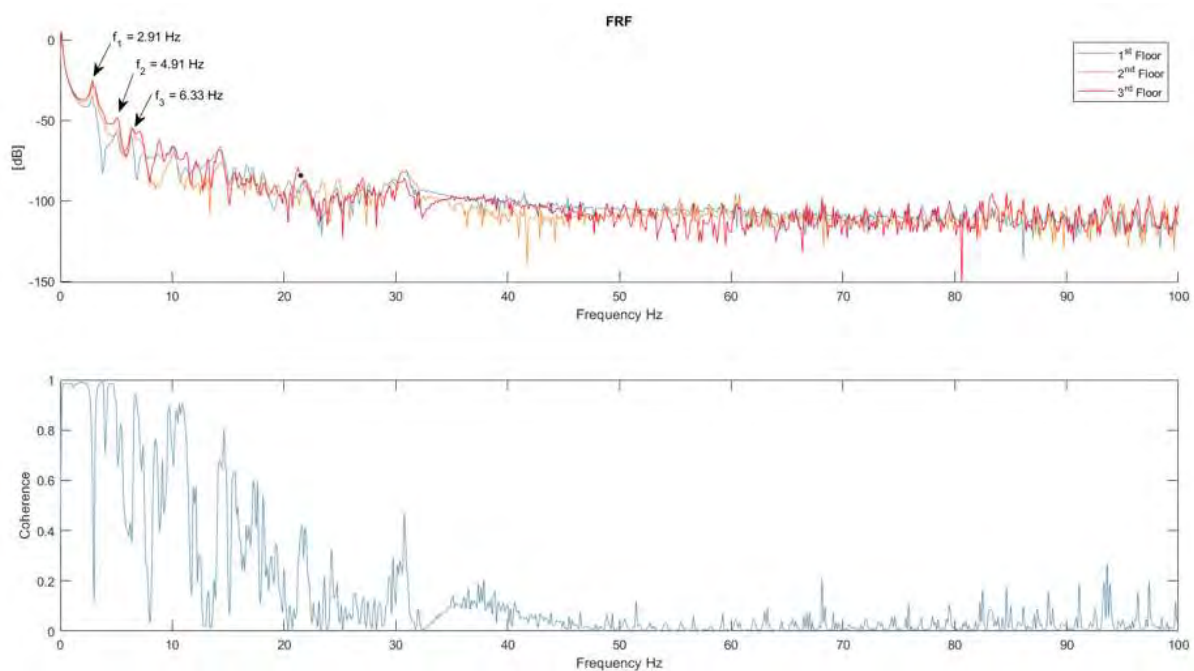


Figure 99: FRF for a random signal RND13 in input and magnitude-squared coherence

Representative results of the moment resisting frame in terms of acceleration and displacement time histories at each floor level are presented in the following. The results are shown for the PGA-levels of 37%, 70% and 111%. Figure 100 to Figure 102 depict the acceleration time histories on each floor level and the acceleration profile along the structural height. The overall behaviour observed is clearly linear for all PGA-levels, including the maximum one. The acceleration profile indicates the absence of nonlinear effects in the primary steel structure.

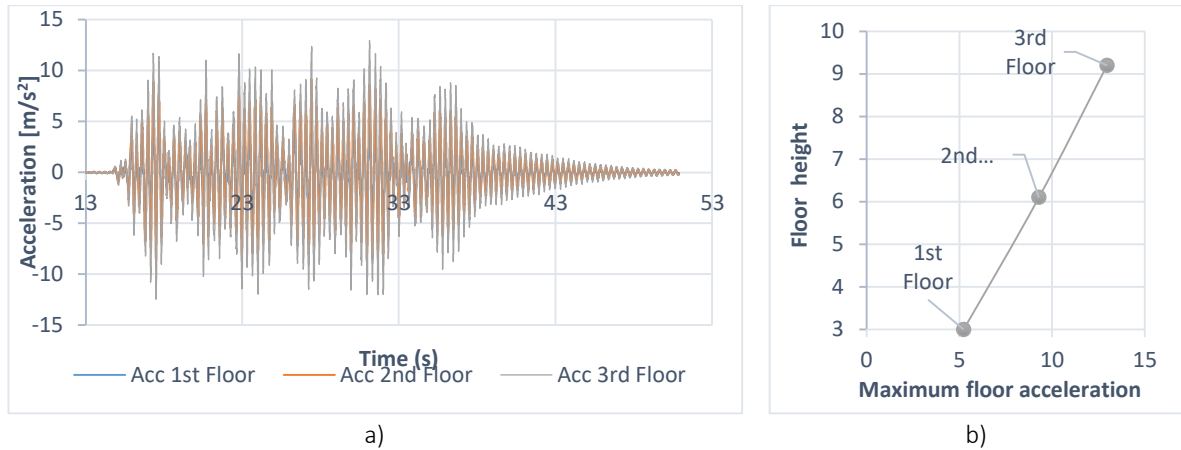


Figure 100: a) TH of the floor accelerations, b) Acceleration profile (PGA-level: 37%)

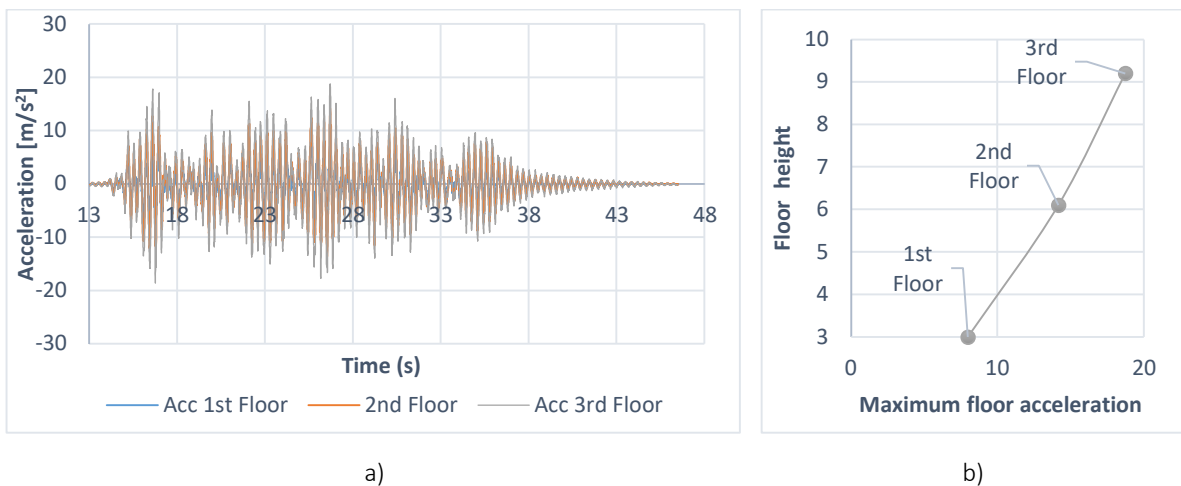


Figure 101: a) TH of the floor accelerations, b) Acceleration profile (PGA-level: 70%)

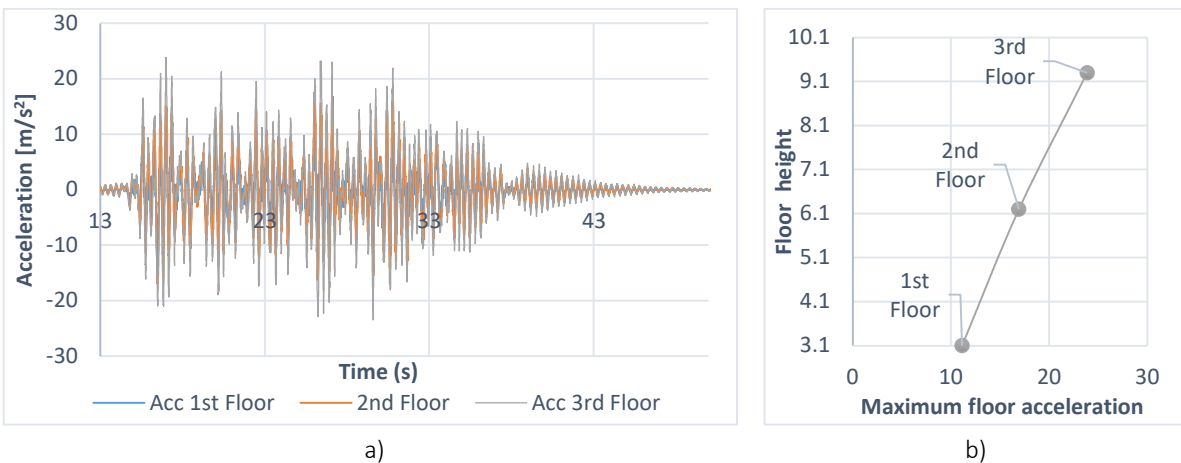


Figure 102: a) TH of the floor accelerations, b) Acceleration profile along the height (PGA-level: 111%)

Figure 103 to Figure 105 show the time histories and the profile along height. Again, the results clarify the almost linear elastic behaviour of the primary steel structure. Furthermore, the results show clearly the dominant 1st frequency with an almost linear distribution of the displacements along the height for all levels of PGA, as numerically predicted (Figure 76).

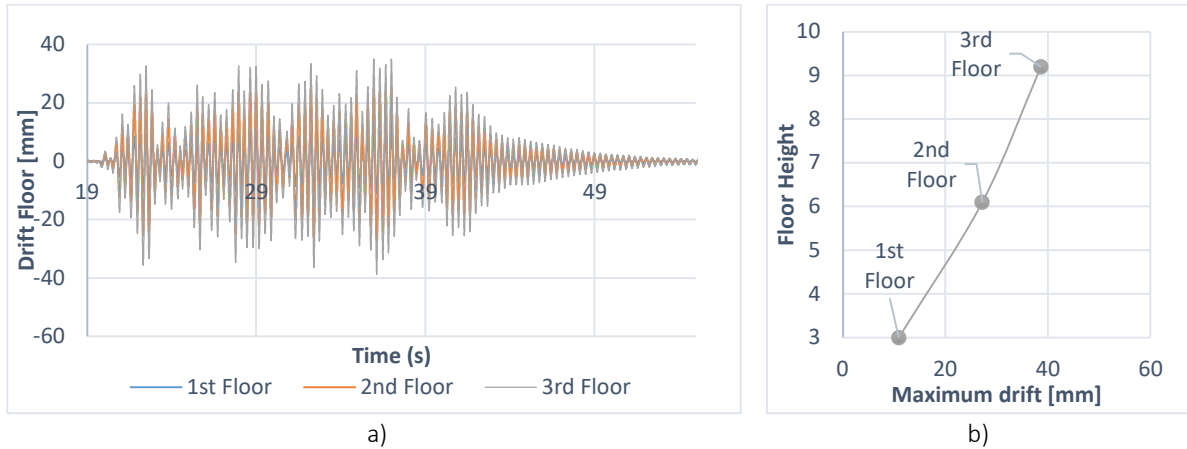


Figure 103: a) TH of drift floor displacements b) Drift floor profile along the height (PGA-level: 37%)

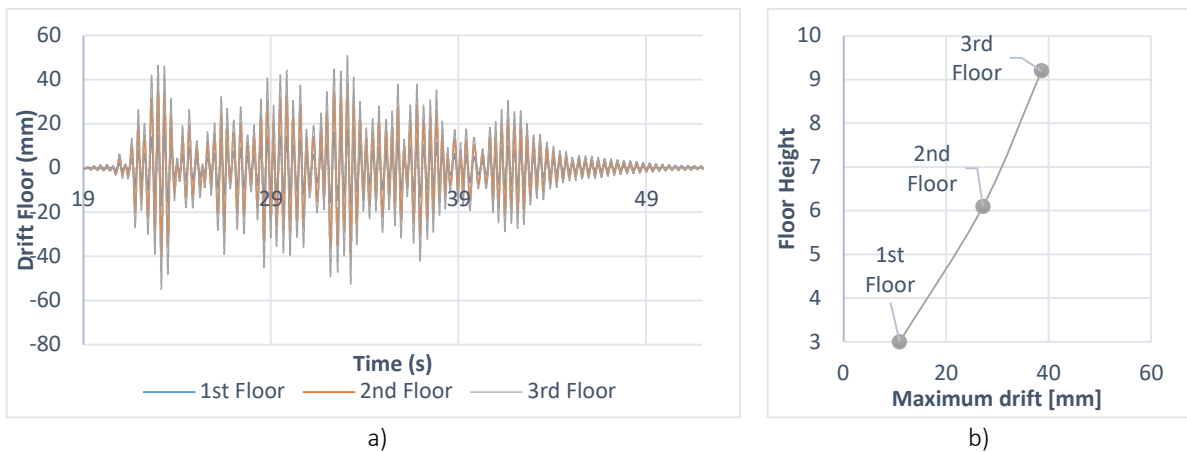


Figure 104: a) TH of the drift floor displacements b) Drift floor profile along the height (PGA-level: 70%)

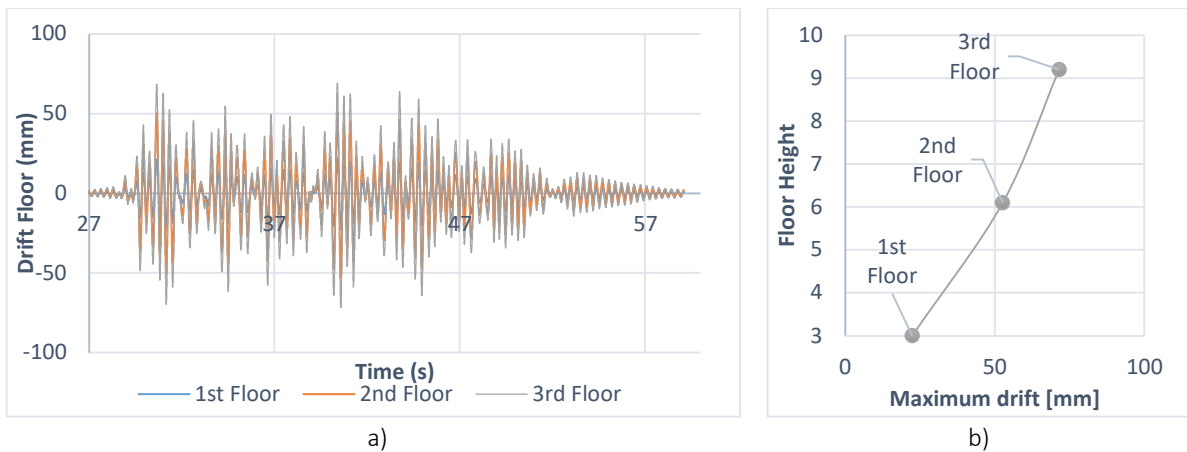


Figure 105: a) TH of the drift floor displacements b) Drift floor profile along the height (PGA-level: 111%)

The elastic behaviour of the moment resisting steel frame is also confirmed by the measurements of strain gauges, located at the base of the columns, whose strains are clearly under the yielding level, as shown in Figure 106.

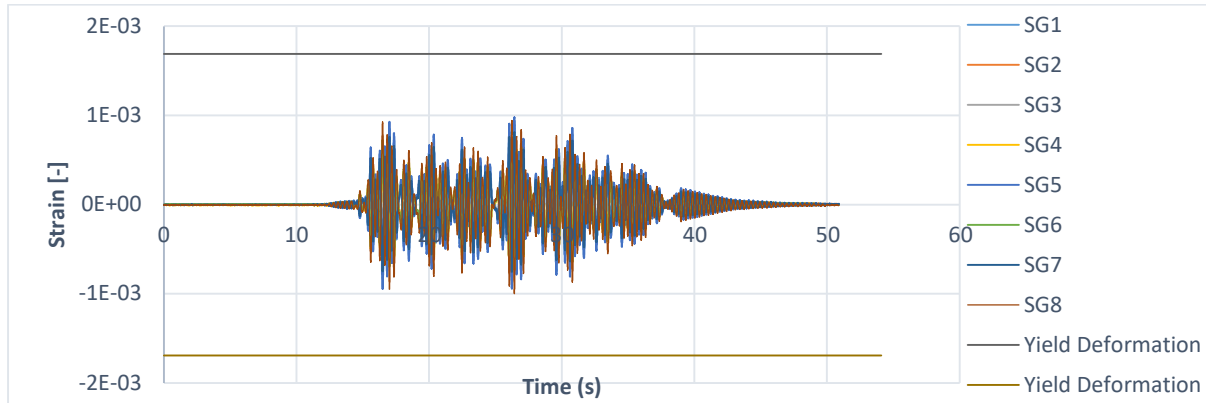


Figure 106: TH of column frame deformations at the base section for (PGA-level: 111%)

The dynamic behaviour of the pipes, tanks, flanged connections have been preliminary investigated in terms of accelerations and displacements for the tanks and deformations and displacements for the flanged joints of pipes.

The vertical tanks at the first level, especially Tank 2, experienced large displacements until substantial damage of the cross-beam at a PGA-level of 70% occurred. Figure 107 to Figure 109 show the time histories of the floor and tank acceleration and the time histories for the relative displacements between the floor level and the tank.

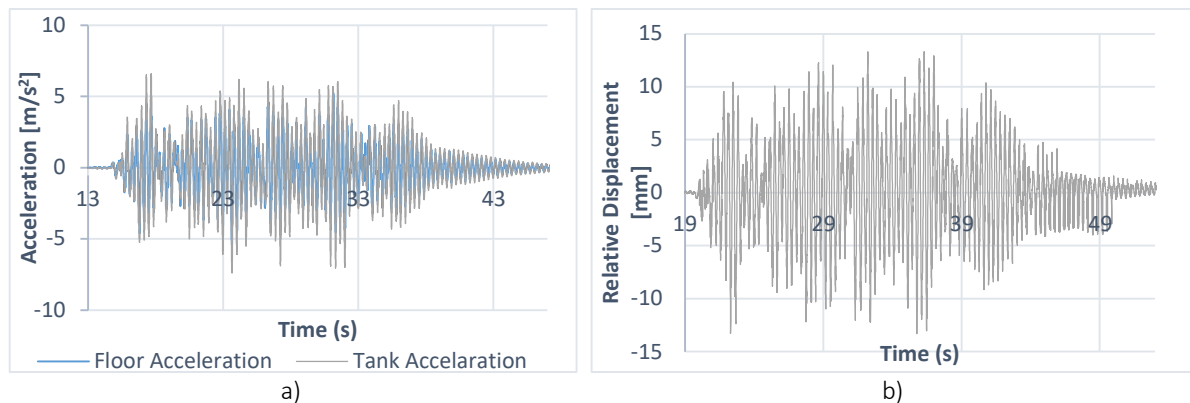


Figure 107: a) TH of floor acceleration b) TH of relative displacement of Tank 2 (PGA-level: 37%)

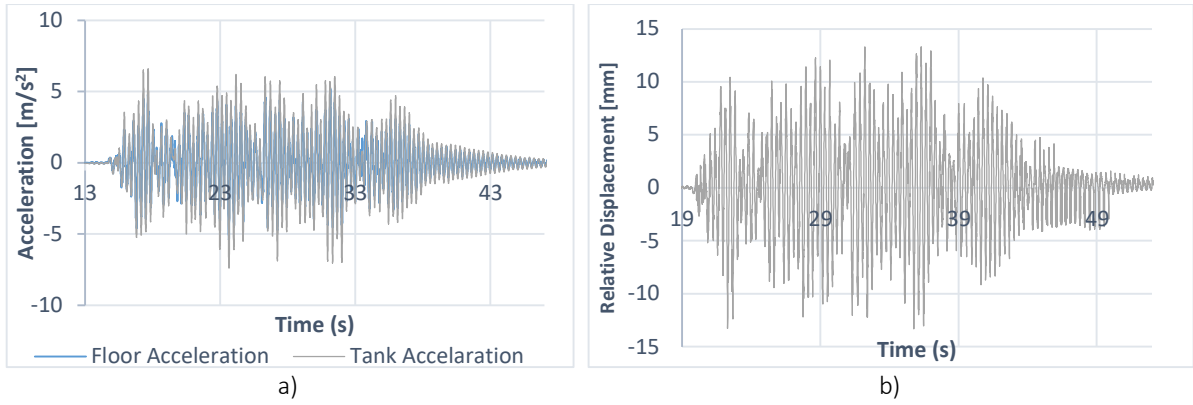


Figure 108: a) TH of floor acceleration b) TH of relative displacement of Tank 2 (PGA-level: 70%)

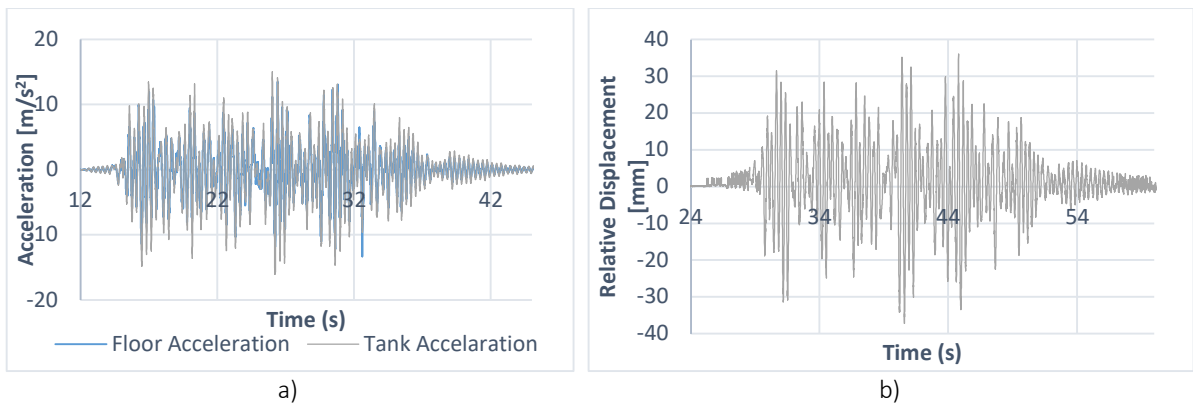


Figure 109: a) TH of floor acceleration b) TH of relative displacement of Tank 2 (PGA-level: 111%)

Figure 110 to Figure 112 show the time histories of the flange deformation and flange opening at the joint at the base of Pos. 5 (Figure 74) for three different PGA-levels. No leakage was noticed in the flange joints during all the test because of limited values of deformations and displacements.

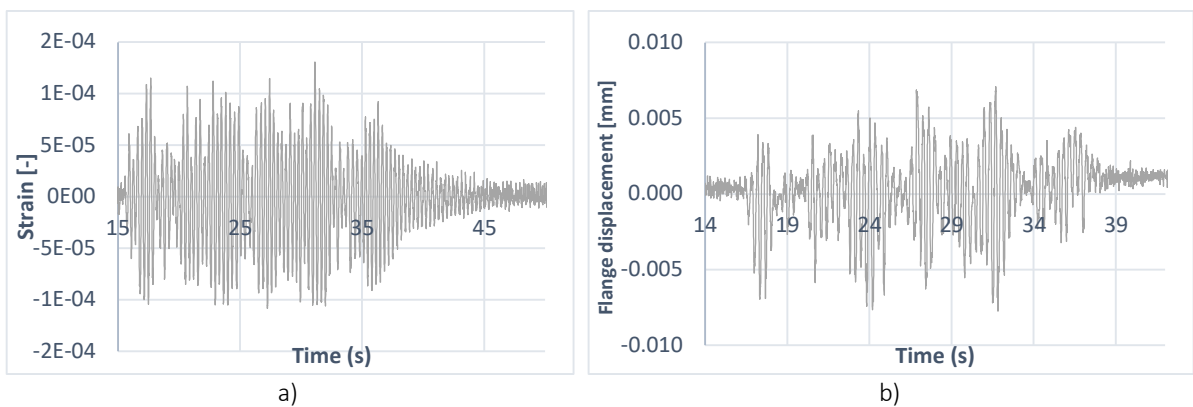


Figure 110: a) TH of flange deformation, b) TH of flange opening (PGA-level: 37%)

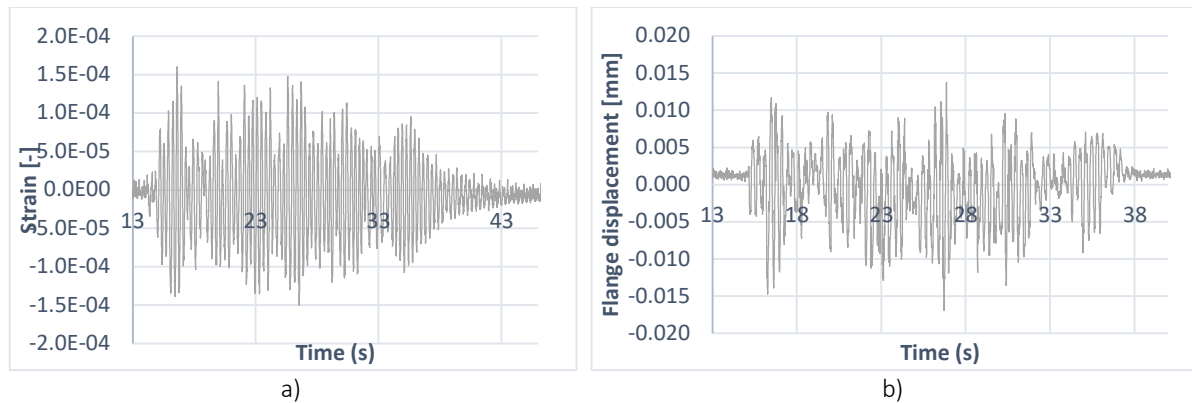


Figure 111: a) TH of flange deformation, b) TH of flange opening (PGA-level: 70%)

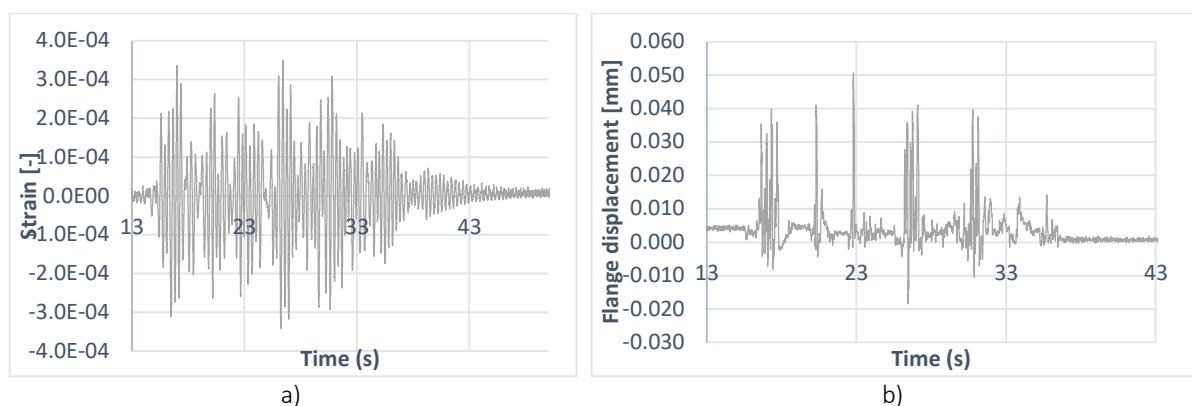


Figure 112: a) TH of flange deformation, b) TH of flange opening (PGA-level: 111%)

2.3.7 Conclusions and outlook

The SERA SPIF project was successfully carried out; the tests were carried out 1 month before the SERA project end, therefore data-processing, damage assessment and results interpretation are still ongoing, and only preliminary results are presented in this document. The world sanitary emergency of SARS-COVID-19 arose right before the experimental phases, preventing the User Group to come to the RI, and preventing the access to the Research Infrastructure right after the end of the testing campaign.

The results of the isolated tests were not presented here, as the base isolators failed at a very low level of PGA, likely due to their small size needed to make them compliant with the actual payload, typical of shake table systems, but quite smaller than usual real installations. There are ongoing discussions to substitute the isolators and to repeat the isolated tests. On the other hand, the tests on the non-isolated configuration have been properly executed, achieving a nominal PGA-level of 0,705g (the real PGA was about 0.8g).

The preliminary results showed a dominant 1st frequency of 2.9 Hz and an almost linear elastic behaviour of the primary steel structure for all PGA-levels. The maximum accelerations on the 3rd level reached accelerations up to almost 25 m/s^2 . The acceleration profile along the height was linear for all PGA-levels. The first damage occurred to one suspended pipe system on the 3rd floor during the tuning phase for PGA-level 70%. The vertical tanks on the 1st level interacted very strongly with the steel structure and caused substantial damage to the cross-beam at a PGA-level of 70%. The damaged cross-beam was strengthened in order to proceed the tests with higher PGA-levels. During subsequent runs with PGA-levels of 100% and 111% further cross beams experienced the same type of damage. No

leakages were noticed in the flange joints of the pressurized pipe branches up to the maximum PGA-level of 111% because of limited values of flange deformations and flange openings. Finally, the conveyor on the RC slab collapsed due to the failure of the supporting system in the final test. Overall, the test results will provide a better understanding of dynamic interaction effects between the primary structure and the installations and thus the effect of seismic response of the installations on the response of the structure and vice versa. The dissemination of the project results is supported by a blind prediction contest, which was announced and will be finalized and evaluated till the end of June 2020.

2.3.8 Literature

- [1] Klinkel, S., Butenweg, C., Lin, G., & Holtschoppen, B. (2016). *Seismic Design of Industrial Facilities*. Springer Vieweg.
- [2] Hoffmeister, B., Gündel, M., & Feldmann, M. (2011). Floor response spectra for dissipative steel supports of industrial equipment. In *COMPDYN 2011, III ECCOMAS Thematic conference on computational methods in structural dynamics and earthquake engineering*, Corfu, Greece, 26e28 May 2011.
- [3] Medina, R. A., Sankaranarayanan, R., & Kingston, K. M. (2006). Floor response spectra for light components mounted on regular moment-resisting frame structures. *Engineering structures*, 28(14), 1927-1940.
- [4] Ju, B. S., & Gupta, A. (2015). Seismic fragility of threaded Tee-joint connections in piping systems. *International Journal of Pressure Vessels and Piping*, 132, 106-118.
- [5] Goodwin, E., Maragakis, E., & Itani, A. (2004, August). Seismic evaluation of hospital piping systems. In *Proceedings of the 13th world conference on earthquake engineering*, Vancouver, BC, Canada, Paper (No. 1081).
- [6] Nims, D. K., & Kelly, J. M. (1990, October). Experimental study of alternate support systems for the seismic restraint of piping. In *Applied Technology Council (ATC) Proceedings of Seminar and Workshop on Seismic Design and Performance of Equipment and Nonstructural Elements in Buildings and Industrial Structures (ATC-29)*, Irvine, CA.
- [7] Retamales, R., Mosqueda, G., Filiatrault, A., & Reinhorn, A. M. (2006). Experimental study on the seismic behavior of nonstructural components subjected to full-scale floor motions. In *8th US National Conference on Earthquake Engineering*.
- [8] Astroza, R., Pantoli, E., Selva, F., Restrepo, J. I., Hutchinson, T. C., & Conte, J. P. (2015). Experimental Evaluation of the Seismic Response of a Rooftop-Mounted Cooling Tower. *Earthquake Spectra*, 31(3), 1567-1589.
- [9] Mosqueda, G., Retamales, R., Keller, D., Filiatrault, A., & Reinhorn, A. (2006). Experimental evaluation of nonstructural components under full-scale floor motions. In *Proceedings of the 4th International conference on earthquake engineering*, Taipei, Taiwan, Paper (No. 301).
- [10] Guzman, J., & Ryan, K. L. (2015). Data from the Network for Earthquake Engineering Simulation/E-Defense collaborative test program on innovative isolation systems and nonstructural components. *Earthquake Spectra*, 31(2), 1195-1209.
- [11] Rahmanishamsi, E., Soroushian, S., & Maragakis, E. M. (2014). Seismic response of ceiling/piping/partition systems in NEESR-GC system-level experiments. In *Structures Congress 2014* (pp. 1824-1835).

- [12] Cazadiou, S., Patisson, L., & Diaz, S. (2014). International Fusion Reactor-Tokamak Complex Seismic Isolation. In *Seismic Design of Industrial Facilities* (pp. 157-167). Springer Vieweg, Wiesbaden.
- [13] Nawrotzki, P., & Siepe, D. (2014). Strategies for the Seismic Protection of Power Plant Equipment. In *Seismic Design of Industrial Facilities* (pp. 169-176). Springer Vieweg, Wiesbaden.
- [14] Stiegler, A., Nitzpon, H. J., & Bolleter, W. (2014). MARMOT-A Certified Seismic Monitoring System for Vulnerable Industrial Facilities. In *Seismic Design of Industrial Facilities* (pp. 177-185). Springer Vieweg, Wiesbaden.
- [15] Hollender, F., Girard, J. P., Girard, D., & Sauvignet, S. (2014). Automatic or Manual Safe Shutdown of Industrial Facilities on Earthquake Signal, Guidelines to Meet the New French Regulation: Seismological and Instrumental Aspects. In *Seismic Design of Industrial Facilities* (pp. 187-195). Springer Vieweg, Wiesbaden.

3 CEA

The TAMARIS infrastructure and its main shaking table AZALEE, to which access is offered, belong to CEA's Seismic Mechanics Study Laboratory (EMSI), who is leading the French SEISM Institute, is part of the Paris Saclay University regrouping about 19 academic partners and research institutes, and has international RTD collaborations with other facilities (EU, Japan, China, USA). The AZALEE shaking table, with 100t allowable model mass, is one of the largest shaking tables in Europe. To date, tests with masses up to 92t have been successfully performed. The shaking table is 6mx6m and 6 Degrees-of-Freedom (DoF), allowing testing specimens under independent excitations of various types: sinusoidal, random, shock and time-history with 0 to 100 Hz frequency ranges. Maximum accelerations of 1 g and 2 g in the horizontal and vertical directions, respectively, can be applied to specimens with the maximum payload of the table. The peak velocity of the shaking table is 1m/s, peak displacements are 0.125 m and 0.1 m in the horizontal and vertical directions, respectively.

The areas of research supported by the infrastructure cover a variety of experimental and analytical RTD national and international projects, both in the nuclear and non-nuclear fields, for equipment, buildings and soil-structure interaction; both new and existing structures are addressed. Assessment and retrofitting of existing buildings and equipment are of special interest for the laboratory.

3.1 Project #4 – SE.RE.ME. – Seismic Resilience of Museum contEnts

Authors

M. Fragiadakis⁽¹⁾, L. DiSarno⁽²⁾, A. Saetta⁽³⁾, M.G. Castellano⁽⁴⁾, I. Rocca⁽³⁾, S. Diamantopoulos⁽¹⁾, V. Crozet⁽⁷⁾, I. Politopoulos⁽⁷⁾, T. Chaudat⁽⁷⁾, S. Vasic⁽⁷⁾, I.E. Bal⁽⁶⁾, E. Smyrou⁽⁶⁾, I. Psycharis⁽¹⁾, T.C. Hutchinson⁽⁵⁾, L. Berto⁽³⁾

⁽¹⁾ School of Civil Engineering, National Technical University of Athens, Iroon Polytechniou, 15780, Athens, Greece

⁽²⁾ University of Sannio, Benevento, Italy, University of Liverpool, UK

⁽³⁾ University IUAV of Venice, 30135 Venice, Italy

⁽⁴⁾ Research & Development Supervisor, Technical Department, Via Scapacchiò 41 - 35030 Selvazzano Dentro (PD) - Italy

⁽⁵⁾ Department of Structural Engineering, University of California, San Diego, 9500 Gilman Dr., MC 008, La Jolla, CA 92093-0085

⁽⁶⁾ Research Centre for Built Environment NoorderRuimte Hanze University of Applied Sciences Groningen, The Netherlands

⁽⁷⁾ DEN - Service d'Etudes Mécaniques et Thermiques (SEMT), CEA, Université Paris-Saclay, 91191, Gif-sur-Yvette, France

3.1.1 Introduction

Earthquake actions pose an immense threat to museums and their contents. For example, during the recent earthquakes on 21 July 2017 and 24 March 2020, in the island of Kos (Greece) and in Zagreb

(Croatia), respectively, severe and widespread damage were reported in the archaeological museums of the cities. The earthquakes extensively damaged the sculpture exhibition, where many artefacts were dislocated, leaned against the walls, or overturned. In the case of heavy and slender sculptures, the overturning mechanism, apart from damaging the sculptures themselves, poses a serious threat to other standing exhibits in the gallery and the visitors. It is, therefore, of paramount importance to rely on methods and tools for characterizing the seismic risk of museum artefacts and, where necessary, proposing cost-efficient protective measures.

The study of the seismic behaviour of museum assets and the investigation of novel and cost-effective risk mitigation schemes for improving the seismic resilience of European museums has received little attention in the past. The H2020-SERA project Seismic Resilience of Museum contEnts (SEREME) aims to fill this gap through extensive shake table tests on real-scale busts and statues. The aim of this large experimental campaign is to understand the seismic response of statues and busts and then develop novel and cost-effective risk mitigation schemes for improving the seismic resilience of museum valuable contents. The study focuses on the investigation of the seismic response of two real-scale marble roman statues and three busts of roman emperors standing on pedestals of different types and size. Both isolated and non-isolated artefacts are considered, while two new and highly efficient base isolation systems, tailored to art objects, are tested dynamically under seismic scenarios. The tested isolators include a pendulum-based system and devices with Shape Memory Alloy (SMA) wires. Furthermore, the importance of the hosting building is examined. Specifically tailored, numerical models of varying complexity, for single and two-block rocking systems, will be developed for the needs of this study and will be assessed with the aid of the experimental results of the SEREME campaign.

The study of the seismic vulnerability of museum artefacts, especially of slender, human-formed statues, is related to the research on the dynamic response of rocking rigid blocks. The dynamic characteristics of the hosting structures are also important. This is evident from the fact that, on many occasions, damage to the structure was reported leaving the exhibits intact and vice-versa. Although the problem is coupled, it can be studied looking separately at the structure and its contents, provided that the contents are not attached to the building. The seismic response of building contents is a topic of growing interest, since it is directly related to seismic loss assessment and earthquake community resilience. Building contents can be either attached to the structure, or may consist of objects that are simply standing. Museum exhibits belong generally to the latter category, while free-standing components are often studied as rocking objects. The response of the latter components is sensitive to acceleration and velocity-based quantities and also their geometry. Today, there is lack of standards, while the existing approaches in the literature are general in concept and do not sufficiently address the mechanisms of the variety of rocking objects. The reliability of such analytical approaches has also been scarcely validated with extensive testing, such as shake experiments.

Common structural analysis and design methods require the assessment of stress resultants and displacement-based quantities. Additionally, the three-dimensional rocking response has not received the interest it deserves. On the other hand, building contents, in most cases, consist of objects that are freestanding. There are recent works in which the seismic response of freestanding contents is investigated, e.g. Berto et al. (2013), Chiozzi et al. (2015) and Di Sarno et al. (2017), among others. Museum exhibits belong to the latter category and the free-standing components are often studied as rocking objects, hence their response is sensitive to acceleration and velocity-based quantities. Geometrical properties of the artefacts also have significant effects on the dynamics and earthquake response of the components. Additionally, when free-standing components are placed on a pedestal, made either from marble or steel, their dynamic response is more difficult to be predicted with simplified methods.

The seminal analytical work carried out on the seismic response of rocking objects in the 60's by Housner (1963) stimulated several quantitative studies that have focused primarily on numerical solutions, e.g. Zhang and Makris (2001), Voyagaki et al. (2013), Dimitrakopoulos and Fung (2016), Diamantopoulos and Fragiadakis (2019). Recently, however, Purvance et al. (2008) carried out extensive experimental and numerical studies in order to investigate the overturning response of symmetric and asymmetric blocks with both simple and complex basal contact conditions and also proposed block overturning fragilities. Similarly, ready-to-use fragility curves were proposed by Konstantinidis and Makris (2009) through a comprehensive experimental program on full-scale freestanding laboratory equipment located on several floor levels. The latter studies, however, focused primarily on the behaviour of single blocks. Dual block systems were first studied numerically by Psycharis (1990), while the recent experimental work of Wittich and Hutchinson (2017) studied asymmetric free-standing component configurations. It is worth noting that, for rocking rigid objects, such as artefacts, the response, at least in terms of overturning motion, is size-dependent, thus the scaling of the specimens is not possible and the experimental tests should be based on full-scale specimens.

Nowadays, considering the huge earthquake losses registered in the recent earthquakes, especially in the Mediterranean region, it is also deemed imperative to propose viable and cost-effective seismic protection measures for free-standing statues and busts. Podany (2015) discussed a range of retrofitting measures based on the best practice followed by the J. Paul Getty Museum in Los Angeles, in California, where a newly developed base isolation device has been employed. However, the effectiveness of the use of seismic isolators for light weight components should be further investigated to characterize thresholds for accelerations and horizontal displacements for an adequate seismic protection of the artefacts.

The H2020-SERA SEREME project aims to fill the experimental gaps highlighted above and to include comprehensive shake-table tests of several configuration of free-standing and base isolated statues and busts. The freestanding artefacts are installed either directly on the marble floor, or on a pedestal. The objective of the campaign was to give insight on the seismic behaviour of statues and busts as well as to evaluate the effectiveness of two different seismic risk mitigation systems. A total of 5 pairs of real scale marble artefacts were tested, 3 busts installed on marble pedestals and 2 statues. Seven different testing arrangements (also termed "Configurations") were considered during this experimental campaign and more than 400 seismic tests were performed. Two innovative base isolation devices were utilized as retrofitting remedies. The first system is a combination of friction pendulum isolators (Castellano et al. 2016), a system designed for light components. The second system is a newly developed device utilizing shape memory alloy wires in the horizontal plane. The isolation devices tested are patented systems, namely ISOLART® PENDULUM & ISOLART® SMA, which are manufactured by the Italian company FIP Mec, a member of the User Team. In order to obtain a direct evaluation of the isolator effectiveness, for each test configuration, pairs of two similar artefacts were tested together in an isolated and a non-isolated arrangement. The shake-table tests were carried out considering uniaxial, biaxial and triaxial earthquake loadings at increasing amplitudes. In order to evaluate the influence of the frequency content and the directionality of the seismic excitation, 13 different waveforms were applied to the shake table (8 uni-directional motions, 3 bi-directional motions and 2 tri-directional motions). Regarding the instrumentation, the artefacts motions were recorded using accelerometers, gyroscopic and displacement sensors.

3.1.2 Museum contents tested

The experimental campaign of SEREME focused on the investigation of the seismic behaviour of real-scale marble statues and busts standing on pedestals, as shown in Figure 114. The case study statues and busts were selected with different geometry and weights; they are replicas of ancient roman emperors. Five busts of roman emperors were utilized: two of emperor Traiano, two of Augusto and one of Tito. Furthermore, four statues were also purchased, two standing on a low height marble pedestal (quoted as “Figura Femminile”) and two simple female form statues (quoted as “Fanciulla”). Since all specimens are made from solid marble, the average weight of the busts is 250-300kg, while that of the statues was 500-600kg. The replicas of the same statue/bust have approximately the same geometry, but they are not perfectly identical (Figure 113). The seismic response of a display case was also examined.



Figure 113. Components used for the shake table tests: (a) Busts and display case, (b) female statues

The busts are placed on a pedestal which is used to bring the specimens to the eye-level of the visitor (Figure 114). Three different pedestal types were identified and then adopted for the experimental tests: (i) solid pedestal, with dimensions 45×45×100 cm, (ii) hollow pedestal, with dimensions 35×35×100 cm, and (iii) modern type metallic pedestals that were provided by the Italian manufacturer Fallani. The traditional, hollow and solid, pedestals were made of concrete which has a specific weight close to that of marble. To reproduce realistic conditions for in-situ friction, on the upper and the lower face of the pedestals, 3 cm thick marble plates were installed, as also shown in Figure 114. Solid pedestals have large weights (nearly 500kg) and they also employ large bases, thus these pedestals are not prone to uplift. On the other hand, hollow pedestals are slender with weight 226kg and have a base with smaller width equal to 35cm. Furthermore, its centre of gravity is much higher compared to the solid case. The metallic pedestal has a large square base with side equal to 85 cm and it weighs only 85 kg.

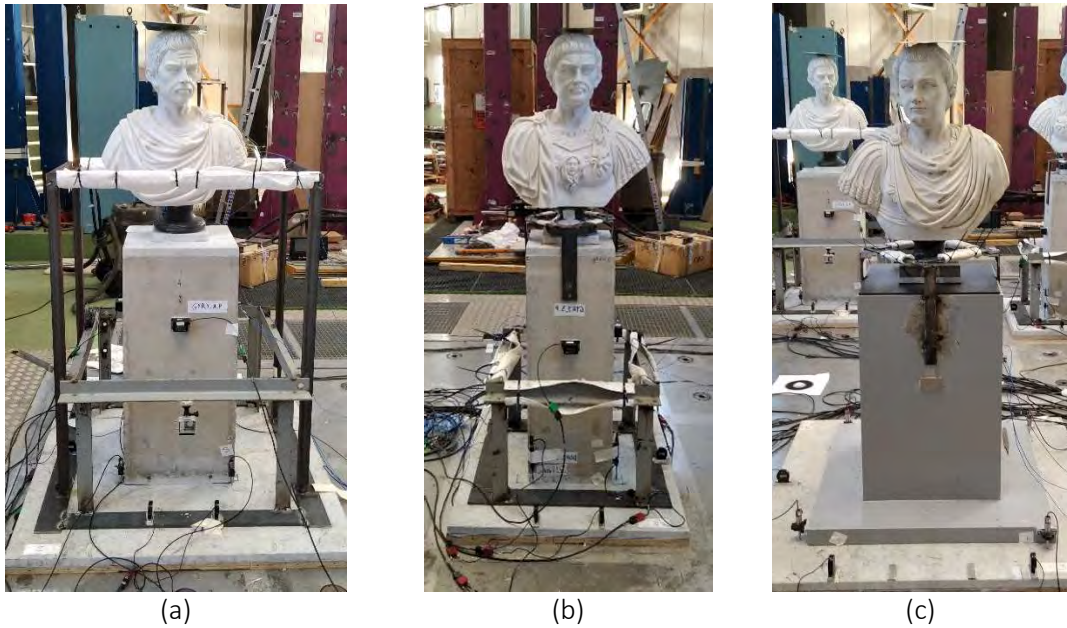


Figure 114. Busts on (a) a solid/large and hollow/small pedestal; (b) a hollow/small pedestal; (c) a metallic/modern pedestal.

In order to simulate the floor of museums, where typically busts and statues are hosted, the non-isolated specimens were placed on a marble floor surface. The marble has thickness equal to 3 cm and it is positioned on stiff wood also 3 cm thick. Both marble and wood were directly bolted on the shake table. All specimens are placed on top of the marble floor and pedestal without any connection material. In the case of isolated specimens, the isolator was bolted on the table with the aid of specific holders that adjusts the holes of the table to the holes of the device. For the SMA isolators, marble plates were glued on the upper surface of the isolator, while the specimens are simply standing.

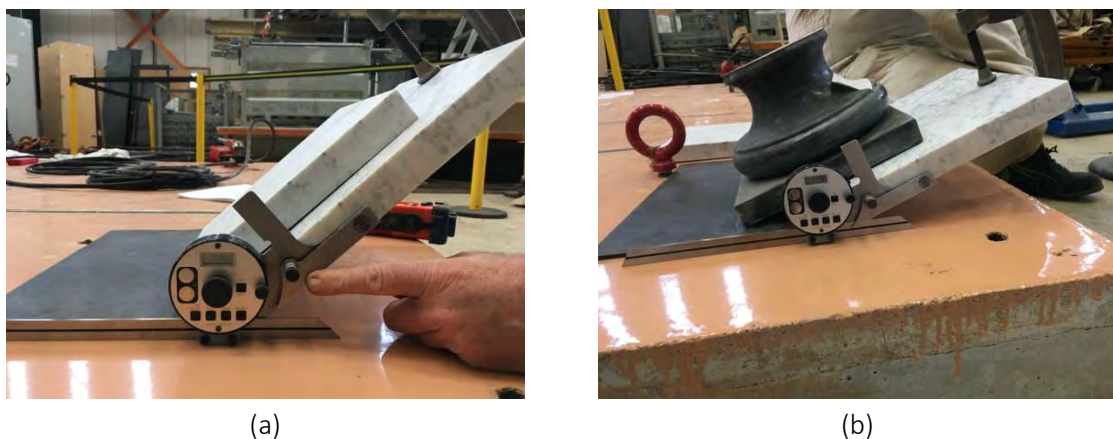


Figure 115. Tilt tests to determine the friction coefficient: (a) plate-plate interface, (b) bust-plate interface

The static friction coefficient was measured for the marble-marble interface with inclined as shown in Figure 115. The inclined tests were repeated 10 times in order to determine the mean friction angle. For the plate-plate marble interface the mean friction coefficient μ was found equal to 0.79, while for the bust-plate interface it was found equal to 0.39. The values of the friction coefficient for plate-plate interface that were derived experimentally comply with those provided in the literature. Conversely, the friction marble-plate interface was found unexpectedly low. However, both mean values were also

verified during the shake table tests where sliding was observed approximately at peak ground acceleration (PGA) values close to the ones measured (the condition to have friction is $PGA > \mu g$). To increase the friction coefficient, where necessary, a thin layer of a rubber material was glued at the bottom of the busts. The friction coefficient at the interface of the marble floor and the bottom of the statues was found sufficiently high and thus no measures were required.

Laser scanning was carried out by a joint research team before moving them the artefacts from the vendor to CEA. Digitalization with laser scanning provides the geometrical properties of the specimens. The purpose of laser scanning is two-fold: (i) it provides a finite element (FE) mesh of the geometry of the artefacts that can be used to perform numerical simulations, and (ii) it allows the calculation of fundamental properties of the components, such as the centre of mass (CM), the total mass, the rotational moments of inertia and the distance of the CM from the pivot points. Furthermore, the laser scanning verified that the specimens are made from solid marble through calculating the ratio of the scanned volume over the measured weight of each specimen. Example of laser scanning information obtained are shown in Figure 116 for the bust of Emperor Augustus.

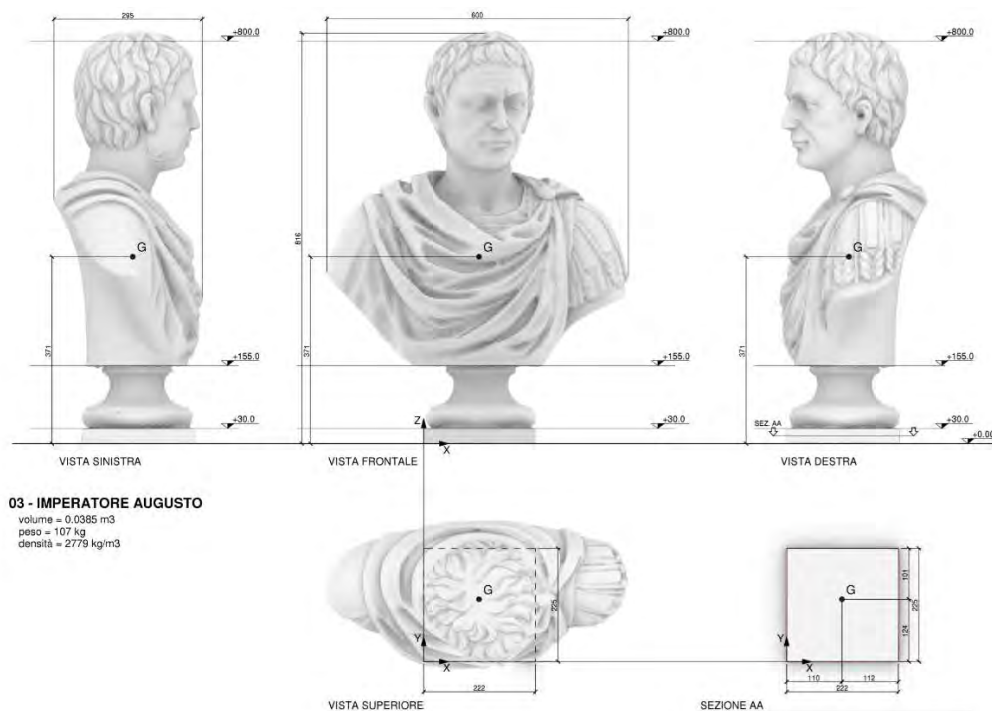


Figure 116. (a) Geometric properties of the Emperor August bust

Two different base isolator technologies were adopted (Figure 117): a friction pendulum isolator and an innovative device with shape memory alloy (SMA) wires. The tested seismic isolator systems were manufactured by the Italian company FIP Mec srl: the selected isolators are marketed as ISOLART® SMA and ISOLART® PENDULUM, respectively. ISOLART® PENDULUM, is similar to common pendulum isolators used for structures, but it consists of different materials and it has been designed specifically for low-mass structures such as objects of art. The main difference between the two isolation devices is the range of mass of the objects to seismically isolate. For ordinary friction pendulum bearings, the friction can be large because of low vertical pressure. To overcome the problem, an increase of the vertical force, or a decrease of the friction coefficient is required. For this purpose, the friction pendulum was used to isolate several artefacts together which are standing on a heavy steel plate, thus increasing the vertical force (Figure 117a). Therefore, three pendulum isolators were employed to

isolate a floor on which a group of artefacts (2 or 3 artefacts) was installed. The installation of the ISOLART® PENDULUM devices is shown in Figure 117a.

ISOLART® SMA, i.e. the SMA-based isolator, is a novel isolator based on SMA wires that are effective in limiting the horizontal displacements of the device. ISOLART® SMA is a patented isolation system which takes advantage of the super-elastic properties of SMA wires, i.e. their capacity to have a stress-induced non-linear behaviour similar to elasto-plastic behaviour up to high deformations (about 7%) and unload to zero displacement. As shown Figure 117b, the SMA isolator can be used to isolate a single specimen each time, which is a significant advantage. Although all SMA isolators adopted have the same dimensions, the properties of the SMA may differ. Three different types of SMA isolators were tested.

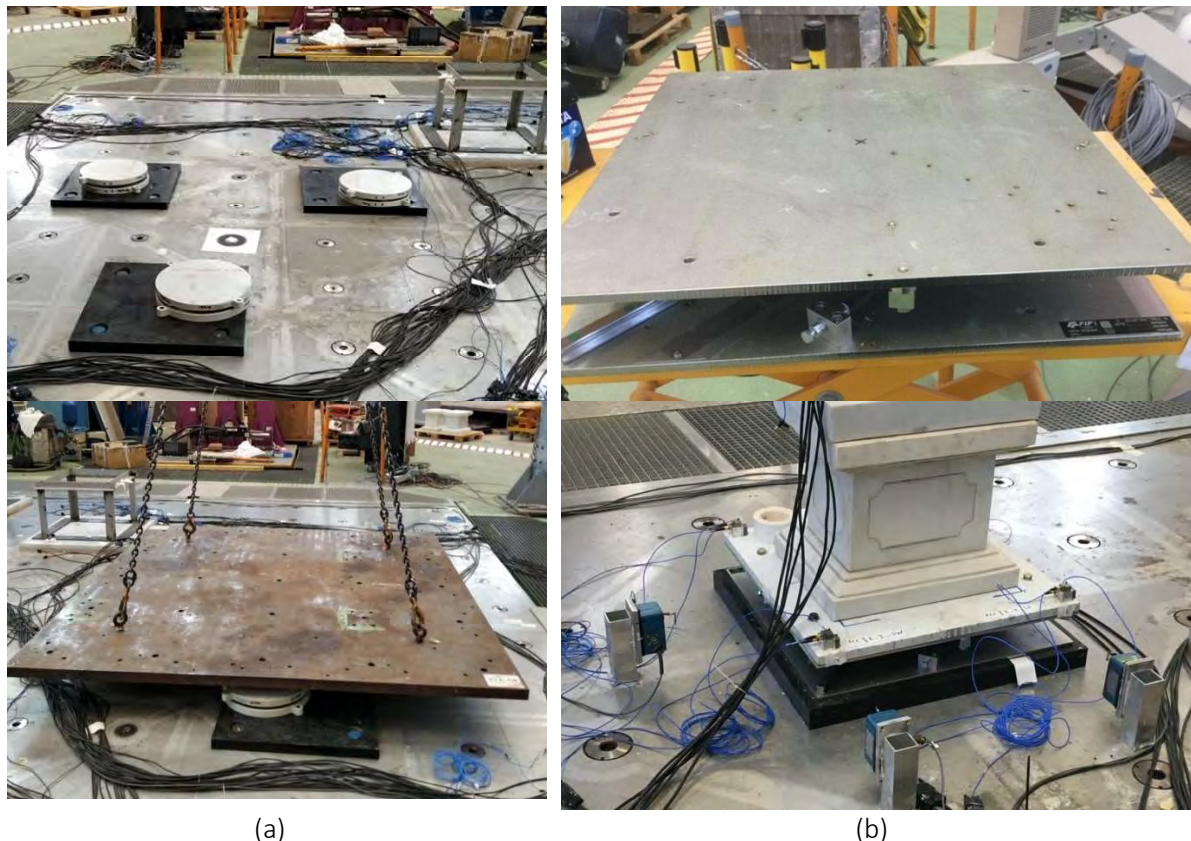


Figure 117 Tested isolation systems: (a) friction pendulum isolator, (b) SMA isolator

Due to the large variety of specimens, pedestals and isolators, seven different Configurations were analysed experimentally using the 6-DOFs shake table AZALEE. The seven testing configurations were designed taking into consideration the limited testing time available and also the needs of the project. The tests of each configuration lasted approximately 2, or 3 days. Configuration 1, was sub-divided into five sub-configurations, shown in Figure 118 up to Figure 122 and considers only the SMA isolators. The caption of each figure explains the properties of the tested configuration. In order to obtain a direct comparison between the isolated and the non-isolated case, the sub-configurations compare pairs of two similar artefacts tested side-by-side in an isolated and a non-isolated arrangement. Instead of testing simultaneously more than a pair of specimens, single pairs were considered every time. This practice offered speed during the tests, while it also allowed to focus on one tested pair every time. In configurations I.4 and I.5 a display case was tested, first isolated and then non-isolated.

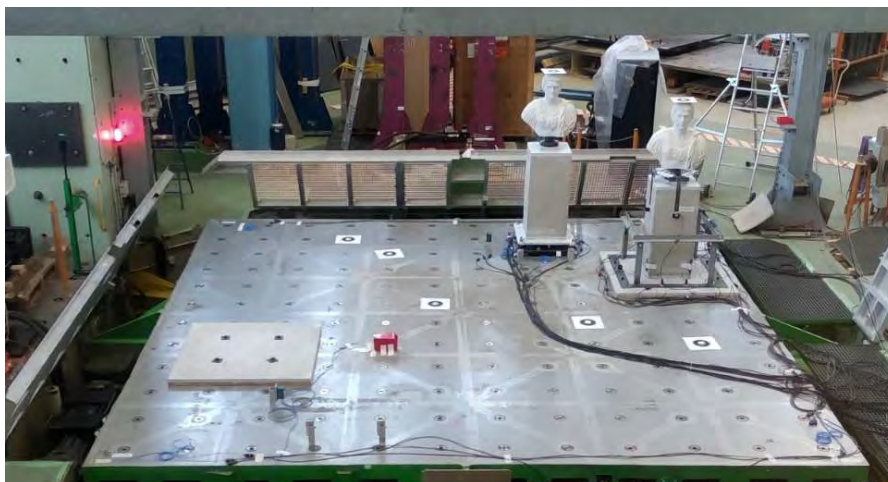


Figure 118. Configuration I-1: Traiano bust on solid pedestal; on marble and on SMA isolator

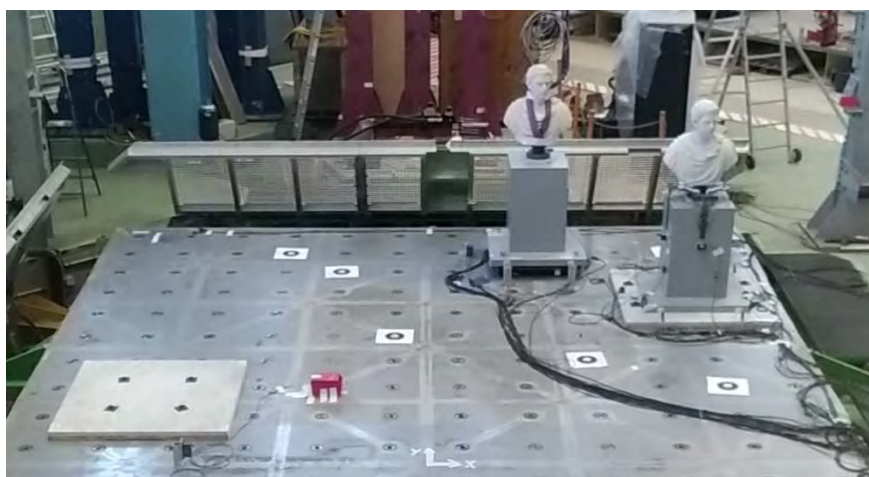


Figure 119: Configuration I-2: Traiano bust on steel metallic pedestal; on marble and on SMA isolator



Figure 120: Configuration I-3: Augusto bust on hollow pedestal; on marble and on SMA isolator



Figure 121: Configuration I-4: Female statue (Figura femminile) standing on the ground pedestal and non-isolated display case and isolated display case (SMA isolator)



Figure 122: Configuration I-5: Female statue (Fanciulla) standing on the ground pedestal and non-isolated display case and non-isolated display case



Figure 123: Configuration II: Non-isolated vs isolated statues (friction pendulum system). The pairs of specimens compared are: (i) Traiano bust on solid pedestal, (ii) Fanciulla and (iii) Figura femminile



Figure 124: Configuration III: Non-isolated vs isolated statues (friction pendulum system). The pairs of specimens compared are: (i) Tito bust on metallic pedestal, (ii) Augusto bust on solid pedestal, and (iii) Traiano bust on hollow pedestal

Configurations II and III are shown in Figure 123 and Figure 124, respectively. These two configurations test the friction pendulum as seismic isolator. In Figure 123, the two female statues and one bust were positioned on top of the friction pendulum isolators. The specimens were positioned on the steel plate in way that the centre of mass of the specimens approximately coincides with the centre of mass of the plate. Configuration III (Figure 124) compares simultaneously the three different types of pedestals. Since only five busts were available, for the metallic pedestals only the non-isolated case was considered. Furthermore, the upper face of the metallic pedestals was reinforced with an 8mm thick steel plate which considerable improved the performance of the system compared to Configuration I.2 (Figure 119).

3.1.3 Numerical simulations

Due to the complex geometry of museum exhibits and the uncertainties of the problem, the numerical simulation of artefacts and museum exhibit systems presents significant difficulties. Complex simulations should be repeated for each exhibit, or for groups of exhibits with similar geometrical characteristics. Moreover, despite the great value of museum exhibits, in practice all decisions about their safety are taken by museum curators, who have empirical knowledge, e.g. experience of past earthquakes, but no technical background to perform sophisticated computer simulations.

Specimen	Standing conditions	Rocking Acceleration (g)		Overturning (mm/s)	
		$a_{rock,B,x}$	$a_{rock,B,y}$	$V_{cr,X}$	$V_{cr,Y}$
Figura Femminile with pedestal		0.244	0.207	0.446	0.344
Fanciulla		0.296	0.226	0.382	0.289
Emperor Traiano	Bust only	0.240	0.236	0.297	0.308
	Bust on solid pedestal	0.330	0.331	0.423	0.424
	Bust on hollow pedestal	0.207	0.208	0.280	0.281
	Bust on steel pedestal	0.293	0.292		
Emperor Tito	Bust only	0.283	0.254	0.262	0.309
Emperor Augusto	Bust on solid pedestal	0.283	0.253	0.257	0.304
	Bust on hollow pedestal	0.220	0.216	0.294	0.29
	Bust on steel pedestal	0.318	0.310		

Table 13 Peak ground acceleration that initiate rocking and overturning velocity estimates

The possible methods of analysis are either simplified calculations based on first principles, or advanced methods of analysis, e.g. analyses using FE modelling, or the discrete element method (DEM). Simplifications are based on simplifying the geometry to one or two rectangular, rigid bodies. These are basic geometric calculations that do not require engineering knowledge, but give useful information such as the maximum ground acceleration for which the system will slide or will engage into a rocking motion. When laser scanning information is available, these calculations are more accurate and, despite their simplicity, they are very important and helpful. Table 13 shows the peak ground acceleration values that initiate rocking for each of the specimen considered. In the case of busts standing on a pedestal, the two bodies are, crudely, assumed to behave as a single body. Table 13 also shows the velocity that triggers overturning motion according the relationship proposed by Ishiyama (1982). This is a conservative lower bound estimation, as opposed to the rocking initiation acceleration which is exact.

Laser scanning was adopted for determining the geometric characteristics of the busts and of the statues that were tested. The scanning provides FE models that allow to perform simulations, but with increased CPU requirements. Furthermore, the accuracy of the scanning is very high and results to very fine and detailed finite element models which do not offer more accuracy but they require excessive memory and CPU resources. It is, therefore, necessary to also have simple models for the seismic response prediction.

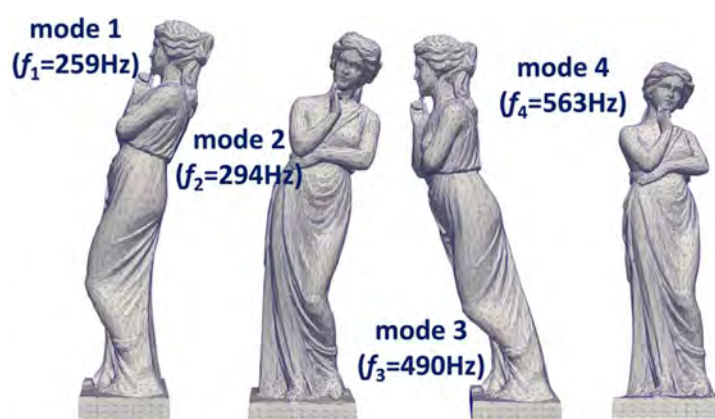


Figure 125 Eigenmodes of the Fanciulla statue obtained with CASTEM software

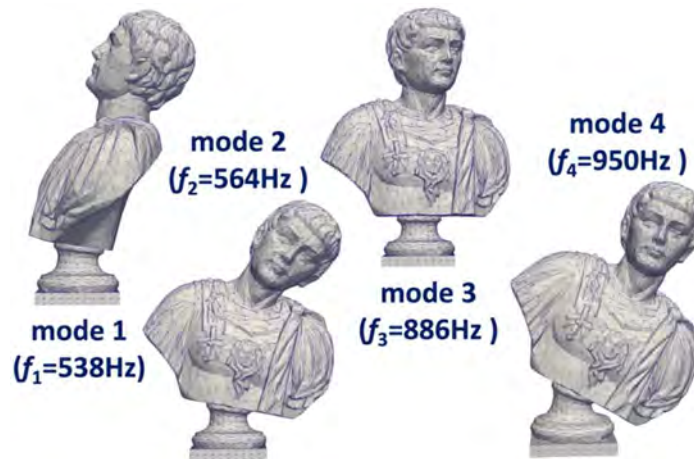


Figure 126 Eigenmodes of the Traiano bust obtained with CASTEM software

FE simulations were performed using both CASTEM and Abaqus software. Figure 125 and Figure 126 show the first four eigenmodes of the Fanciulla statue and of the bust of emperor Traiano, respectively. As expected, the statue has much lower frequencies compared to those of the bust which is practically rigid. The FE method offers several advantages concerning the accuracy, but there are also difficulties in utilizing the analytical simulation approach. The surface-to-surface interaction between the upper surface of the pedestal and the lower surface of the bust requires knowledge of the friction coefficient and the damping ratio, while damping of the motion due to rocking impacts cannot be introduced in a straightforward manner. Also, the FE method is more realistic if the bodies have some flexibility. Introducing the flexibility and the real modulus of elasticity of the artefacts will increase the CPU time, thus making prohibitive a large number of simulations. On the other hand, the Discrete Element Method (DEM) assumes that the objects are rigid and consequently can be adopted with reduced computational costs. For the interaction between the surfaces, appropriately calibrated springs should be introduced in the model. Psycharis et al. (2013) have described the numerical model for the simulation of a multi-drum ancient column which is subjected to natural ground motion records. The column consists of eight rigid bodies, the upper placed on the top of the lower. In this work the 3DEC software has been used for the simulation of a problem that has similarities to the problem at hand.

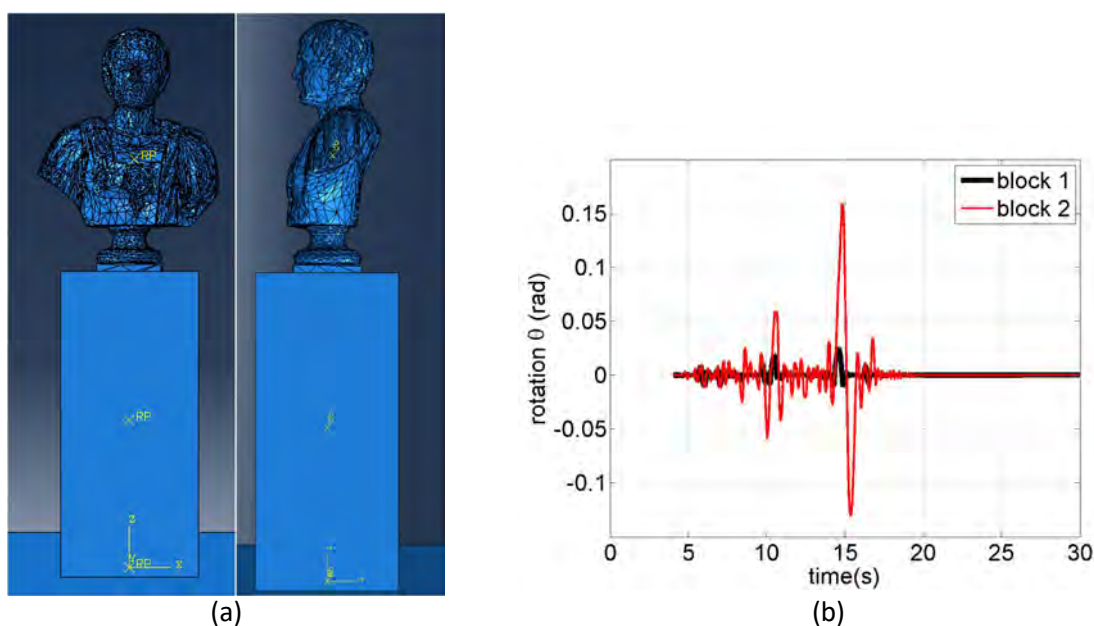


Figure 127. (a) Finite Element model (pedestal-bust), (b) response time history

Models that consider either two-block assemblies (pedestal-bust) or freestanding, symmetric or asymmetric, rocking blocks (a freestanding statue or a bust that rocks on a pedestal in rest) are a possible alternative to the costly FEM and DEM simulations. Such simple models are typically limited to one-direction simulations and hence the procedure should be repeated for both the longitudinal and the transverse direction due to the asymmetry of the specimens. A simplified approach is offered by using the equation of motion proposed by Housner (1963). A possible way to handle the equations of Housner (1963) has been proposed by Diamantopoulos and Fragiadakis (2019). For the two-block case and for simplicity reasons the work of Psycharis (1990) can be adopted. Vlachos *et al.* (2019) presented a first attempt to extend the two-block problem in case of asymmetric upper block when the pedestal is symmetric.

3.1.4 Test setup

To evaluate the influence of frequency content of the excitation, as well as the directionality of the seismic input, five different earthquake ground motions were adopted in this experimental study. The ground motion records and their properties are shown in Table 14, while Figure 128 shows the acceleration response spectra of the three components of the ground motions adopted (only Kalamata is not shown). The records were applied in different combinations every time, i.e. first the X-component was applied alone, the Y component afterwards and then the X and Y components were applied simultaneously.

Earthquake	Date	Mw	Station	Distance hypocentral	Soil category	PGA (g)
Emilia, Italy	29.05.2012	6.0	T0800	14.4	C* (EC8)	L: 0.33 T: 0.25 V: 0.33
Athens, Greece	07.09.1999	5.9	Syntagma Metro B	10.0	Stiff soil	L: 0.109, T: 0.086, V: 0.087
L'Aquila, Italy	06.04.2009	6.3	Aterno river-AQA	< 2km	Stiff soil	L: 0.45, T: 0.39, V: 0.37
Kalamata, Greece	09/13/1986	6.2	Nomarchia	5.0	Stiff soil	L: 0.22, T: 0.29
Kobe, Japan	1/16/1995	6.9	Takatori, Japan	22.2 (< 1.5 km)	C* (EC8)	L: 0.068
Emilia, Italy – first storey	29.05.2012	6.0	T0800	14.4	C* (EC8)	L: 0.37

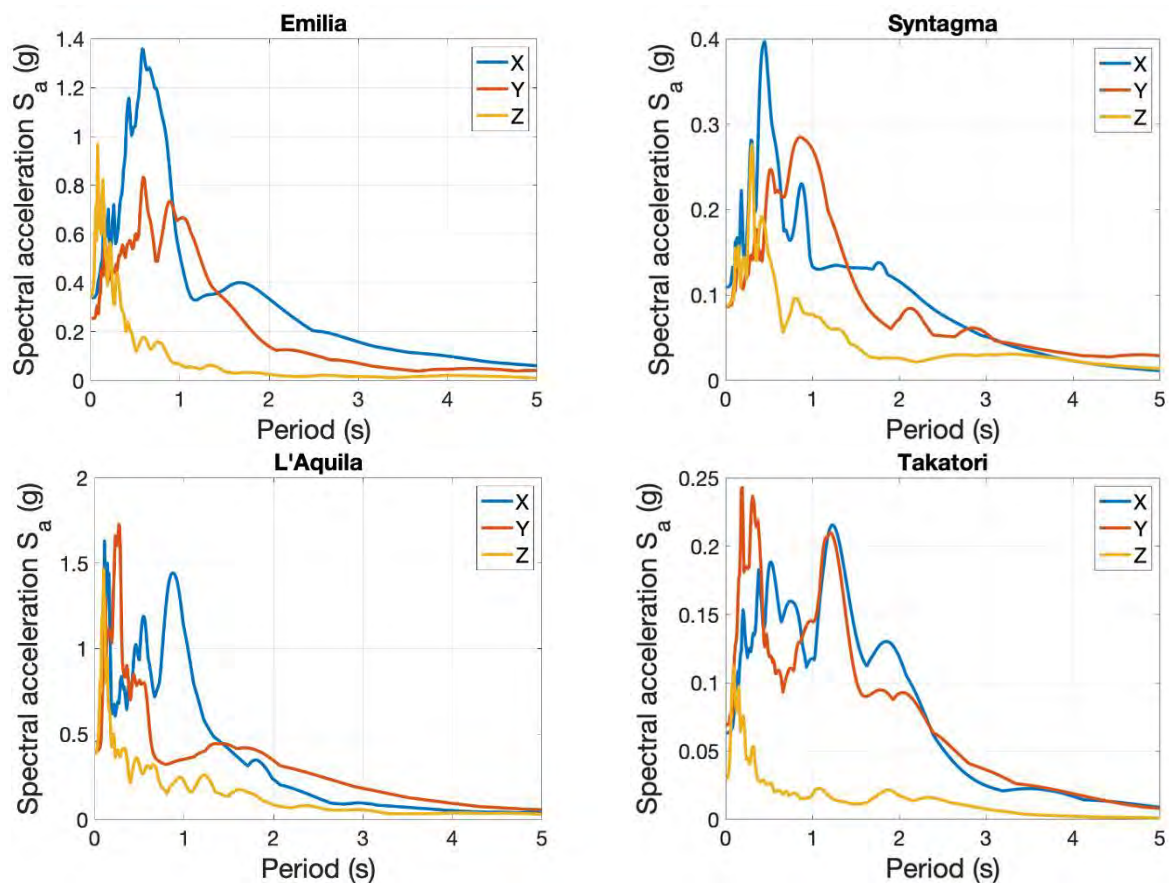
Table 14 Ground motion records used for the testing campaign

The record combinations adopted are listed in Table 15. For each record combination, the ground motion amplitude was gradually scaled up. In general, the target intensity levels considered were: 0.15g, 0.20g, 0.25g, 0.35g, 0.40g and 0.50g. For simulations where simultaneously two, or three, components were considered, a uniform scaling factor was adopted for all record components considered, while the target acceleration refers either to the X-, or the Y-component. When both X and Y are present, it refers to the X-component. For the Takatori and the Kalamata records, the maximum permissible scaling factor is controlled by the maximum allowable displacement of the shake table that cannot exceed 10cm. As expected, differences between target PGA and the PGA measured as input to the shake table were observed. On average 25-40 shake table runs were performed for each of the seven tested configurations.

ID	Record	Components	Target PGA
1	Emilia	X	0.15, 0.25, 0.35, 0.40, 0.50
2	Emilia	Y	0.15, 0.25, 0.35, 0.40, 0.50
3	Emilia	XYZ	0.15, 0.25, 0.35, 0.40, 0.50
4	Emilia	XY	0.15, 0.25, 0.35, 0.40, 0.50
5	Emilia	Y (first floor)	0.15, 0.25, 0.35, 0.40, 0.50
6	Emilia	YZ (first floor)	0.15, 0.25, 0.35, 0.40, 0.50
7	Syntagma	X	0.15, 0.25, 0.35, 0.40, 0.50
8	Takatori	Y applied on X	0.10, 0.15
9	Takatori	YZ applied on X	0.10, 0.13, 0.2, 0.24
10	Takatori	Y	0.10, 0.18, 0.2, 0.24
11	L'Aquila	X	0.15, 0.25, 0.35, 0.40, 0.50
12	L'Aquila	XYZ	0.15, 0.25, 0.35, 0.40, 0.50
13	Kalamata	X	0.15, 0.20, 0.25, 0.30

Table 15 Record combinations

Apart from five naturally recorded ground motions, the acceleration response history of the first floor of the museum was considered. The museum is the Archaeological museum of Pella in Greece. This is a new reinforced concrete building. The building was modelled with OpenSees software and it was subjected to the five ground motion records of Table 14. Since it is a two storey RC building with many shear walls, it is a quite stiff structure ($T_x = 0.17s$, $T_y = 0.14s$) and hence large amplifications were observed at the stories. Among the various floor acceleration histories, the first storey of the Emilia 2012 (Italy) response acceleration was adopted for the tests. The response spectrum of this record is also shown in Figure 128.



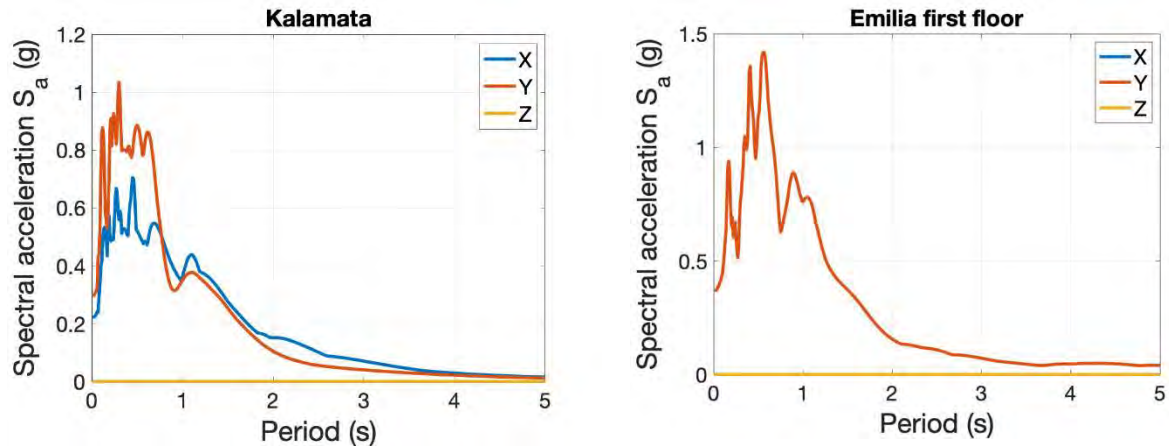


Figure 128. Acceleration spectra of the records used for the test campaign

A state-of-the-art and dense instrumentation scheme was adopted for monitoring the response of the table, the isolators, the pedestals, the busts and the statues. The instrumentation includes triaxial accelerometers, gyroscopic and displacement sensors. The instrumentation of Configuration I.1 is shown in Figure 129 and Figure 130. Triaxial accelerometers were installed at each corner of the shake table. At the middle of the table triaxial accelerometers and both displacement and velocity sensors were also installed. The instrumentation of the pedestals includes measurement of the accelerations (face 3) and the angular velocities (faces 1, 2, 4) in all axes X, Y, Z and for isolated and non-isolated cases. At the base of the pedestal and at all faces, displacement sensors were installed in order to record the longitudinal, the lateral and the vertical displacement.

The busts and the statues were instrumented with triaxial accelerometers and gyroscopic sensors. The labelling adopted and the channels installed for Configuration I.1 are shown in Figure 129 and Figure 130. For the isolators, displacement sensors and accelerometers were installed at the upper plate. For example, for the SMA case (Figure 130), on the upper plate and on the faces 1 and 2 longitudinal and lateral displacement measurements were installed. Furthermore, on the southwest (SW), southeast (SE) and northwest (NW) corners, triaxial accelerometers were also installed. For the friction pendulum case, the only difference is that the displacement record on face 1 was measured from the middle of the upper plate, while for the case with SMA case the horizontal displacement was measured from the south corner of face 1. Overall, for Configuration I.1-I.5 the number of the active channels ranges from 62 to 77, while for Configuration II and III, the number of channels was 97 and 106, respectively.

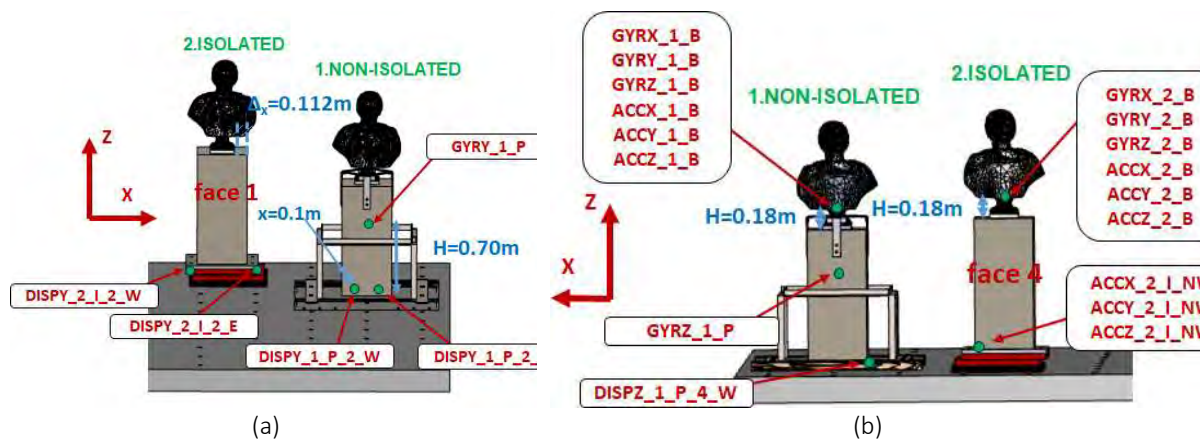


Figure 129. Monitoring for Configuration I-1: front view and rear view

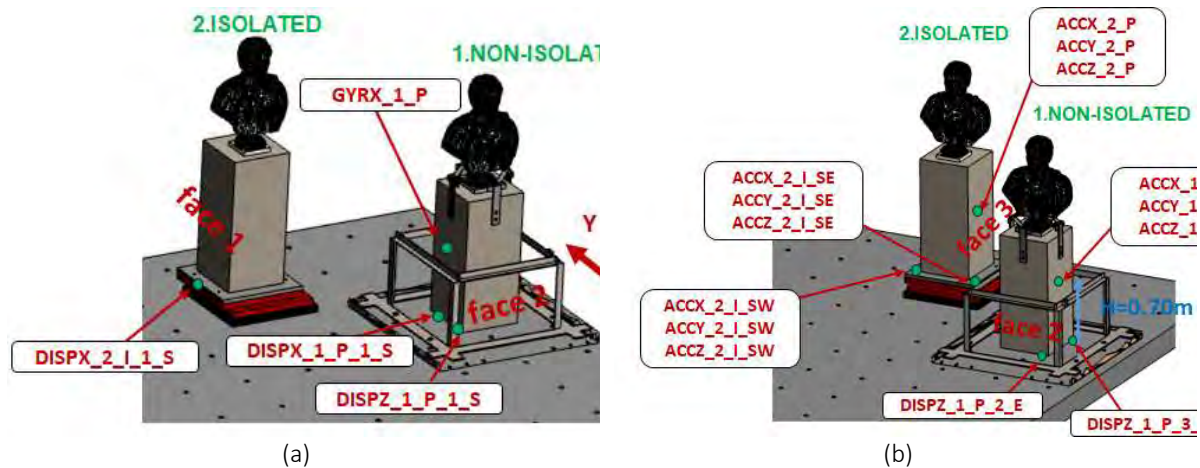


Figure 130. Monitoring for Configuration I-1: left view and right view

A novel videometric system was adopted in order to monitor the displacements of the specimens. A special camera has been installed at the roof of the lab, above the shake table (Figure 131a). The displacements were measured using special markers that were glued on the top of each statue/bust, e.g. see Figure 124. Ad-hoc software (Figure 131b) is utilized to monitor the movement of the targets at the top of the specimens and records the displacements of all specimens simultaneously.

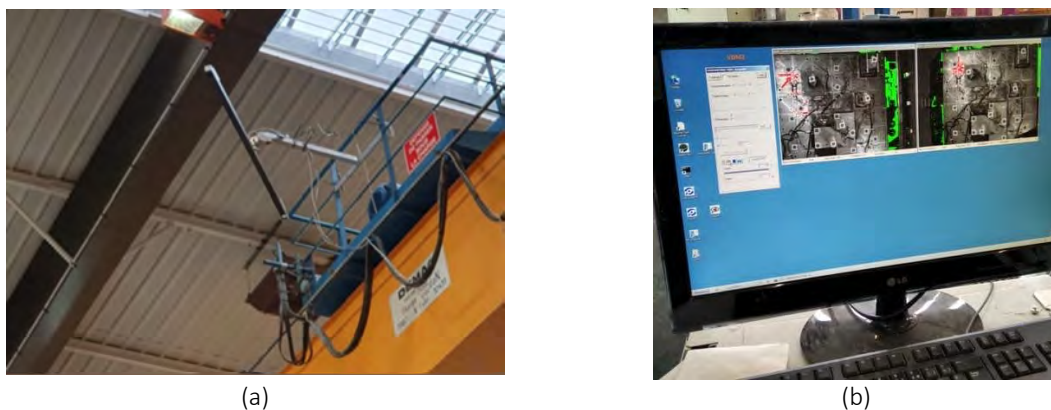


Figure 131. Measuring displacements using vide metric camera (a) the methodology, (b) videometric camera above the seismic simulator

Due to the characteristic properties of the tested specimens, special protection measures had to be taken. Specifically-tailored protection measures were developed for the needs of SEREME project. These measures were applied primarily on the non-isolated specimens, since, in principle, the isolated specimens are already protected. Solutions like hanging the specimens from ropes were not preferred, since the ropes were found in the past that they affect the response of the specimens and moreover because a special structure should have been built around the table in order to suspend the ropes. The system adopted for the bust-pedestal system is shown in Figure 132a and b. The protection consists of an upper and a lower basket. The upper basket successfully blocks the overrunning of the bust, while the lower basket protects the pedestal. The upper basket was found quite efficient during the tests. Furthermore, Figure 132c shows the basket adopted for the protection of the statues. These baskets are considerably higher compared to those of the busts and were also successful during the tests.

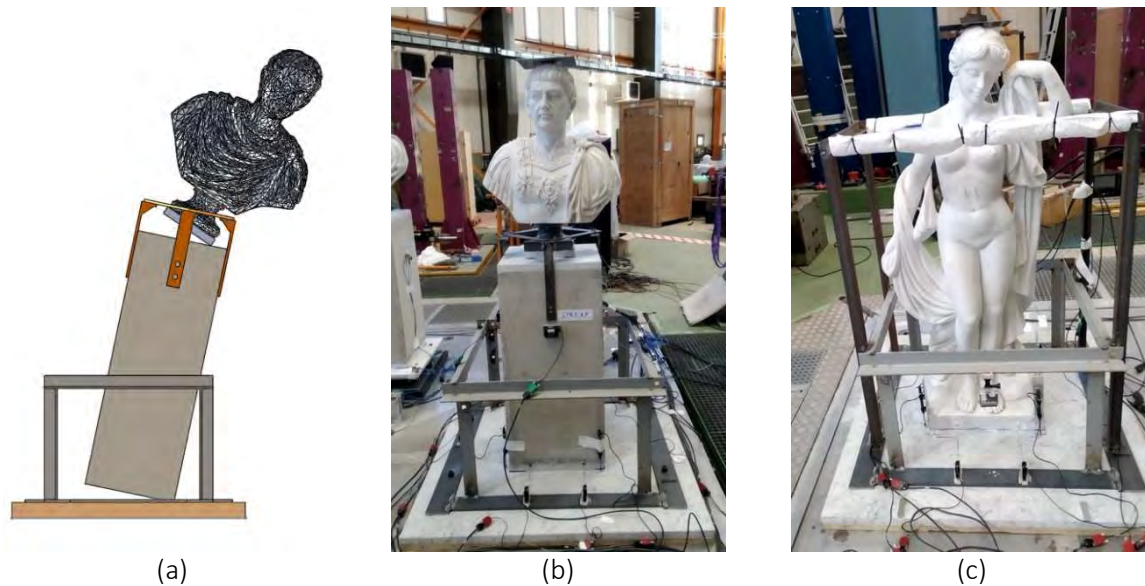


Figure 132. Protection measures adopted

3.1.5 Observations and preliminary results

A vast amount of data was obtained during the experimental campaign that lasted approximately two months. The User Team is currently working on post-processing the experimental data. However, very interesting observations were made during the campaign. Due to the protection measures no major damage on the specimens occurred, while the most typical damage type observed is the failure at the corners of the specimens. This damage is shown in Figure 132 for both the bust and the statues. This type of damage happened practically to all busts of Configuration I.1-I.5, while the damage of statue shown in Figure 132b happened once. Since a large number of tests had to be repeated, the marble bases of the busts were replaced, while for the statue the failed wedge shown in Figure 132b was repaired by gluing it back and retesting the statue isolated. No damage occurred at the pedestals. The metallic modern pedestals when tested in Configuration I.2, exhibited some mild bending of their upper face, where the bust was standing. The lateral bending due to the selfweight of the bust affected the dynamic response. In order to mitigate this effect, in Configuration III, an 8mm thick plate was used to reinforce the pedestal.



Figure 133. Typical damage at the base of the specimens: (a) bust, (b) base of the statue

Figure 134 summarizes the response of the non-isolated bust in Configuration I.1 where the bust of emperor Traiano was positioned on top of the solid pedestal. The solid pedestal, due to its massive geometry, never uplifted and hence only rocking of the bust was observed. As expected from the PGA values of Table 13, no uplift occurred for PGA values below 0.20g. Note that the accelerations of Figure 134 are the theoretical predictions; the latter differ, sometimes considerably, from the values recorded on the shake table. Comparing record combinations 1 and 2 to combinations 3 and 4, it is evident that the bidirectional ground shaking is more severe for the bust, since overturning was observed at much lower accelerations for the Emilia earthquake. This observation also holds for the L'Aquila record (combinations 11 and 12). The Takatori and Kalamata ground motions have a low recorded PGA and have a large frequency content. These records were scaled but they were not critical for the busts, as opposed to the Syntagma ground motion which was severe.

Different observations hold also for the SMA isolated specimen. As show in Figure 135, the specimen was safe for most ground motion levels, practically for most ground motions. The Emilia XYZ ground motion produced sliding and rocking that threatened the bust for a PGA of 0.40g. This is attributed to the large vertical acceleration component. This was also seen for the first-floor response when a vertical component is present. Interestingly, rocking was observed also for the Takatori and the Kalamata ground motions.

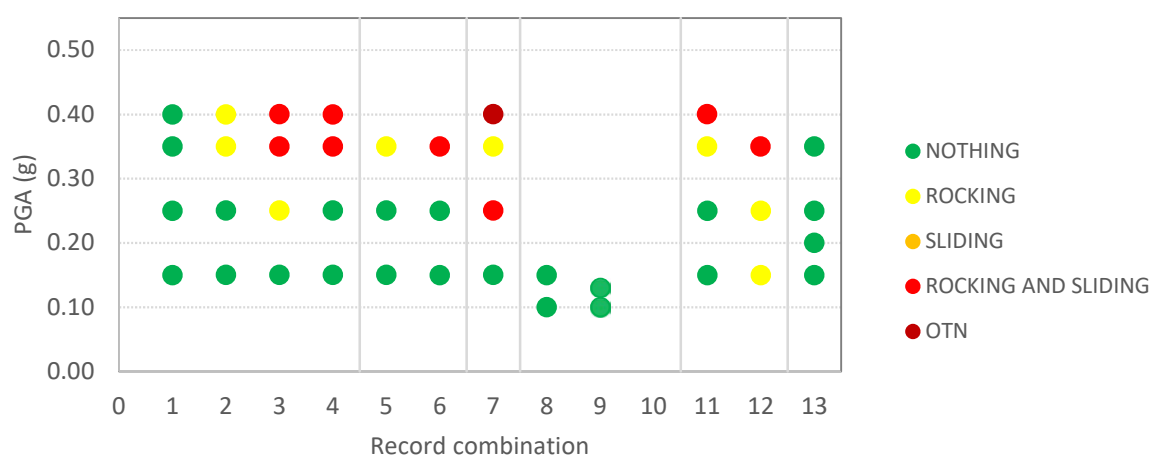


Figure 134. Response of the non-isolated bust of Configuration I.1

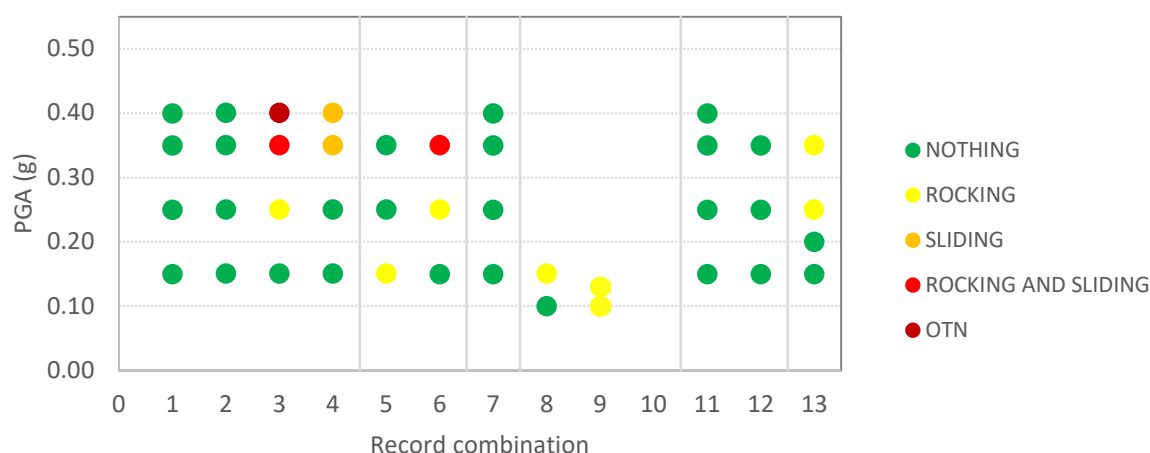


Figure 135. Response of the SMA-isolated bust of Configuration I.1

Important findings were obtained from the experimental campaign and are briefly summarized as follows:

- For high excitation intensity tests, the non-isolated artefacts are prone to show a complex rocking and sliding behaviour. The impact induced by the rocking motion can be a source of damage to the base of the busts, especially at the corner points of the base of the bust.
- The response of the busts on the solid and the on the hollow pedestal is substantially different. The uplift of the hollow pedestal was always small and difficult to identify visually. However, it is clear that it considerably affected the seismic response. Whether the bust is safer on the solid, or on the hollow pedestal is a topic that deserves further research; the tests have shown that the safety depends also on the ground motion frequency content.
- Tests where the friction coefficient between the bust and the pedestal was low, i.e. when friction coefficients vary between 0.20 and 0.30, revealed that sliding is a beneficial response mode for the bust. If the sliding motion of the rigid object is controlled, then some sliding is desirable.
- In most of the cases, the considered mitigation methods have been effective in the prevention of the rocking/sliding behaviour of the artefacts. As a result, these mitigation methods improved significantly the seismic behaviour of the artefacts. Especially the friction-pendulum system was very efficient in practically all tests. Some attention is required in the case of high vertical component. Although the vertical earthquakes considered were very strong, some attention is required in this respect.
- The metallic pedestals, due to their geometry, did not uplift and hence they were equally efficient as the solid ones, provided that they can fully support the weight of the artwork.
- The response of the statues was well predicted and with no surprises. When the input acceleration was below the rocking initiation threshold, the statues performed some high frequency oscillation.
- The base of some of the statues was not fully flat, due to structural imperfections. This lack of planarity affected the response and threatened the safety of the statues. This issue has been also reported in previous research in the literature.
- The simplified calculations, summarized in Table 13, are very important and useful. Such information should be always advised when taking seismic protection measures for artefacts.

3.1.6 Conclusions

The project presents an extensive experimental campaign on the seismic response of artefacts, with emphasis on statues and busts. The tests took place in the framework of SEREME project (Seismic Resilience of Museum Contents) at the AZALEE seismic simulator of CEA in Saclay, Paris under the auspices of the SERA project. The campaign aims to help us understand the seismic behaviour of the selected statues and busts and then to develop novel and cost-effective risk mitigation schemes for improving the seismic resilience of valuable objects hosted in European museums. Two real-scale marble (replicas are usually made from gypsum) roman statues and three busts of three roman emperors standing on three pedestals of different types and size are investigated concerning their response under seismic loading. The artefacts are considered either isolated or non-isolated. In the latter case, two new and highly efficient base isolation systems, tailored to art objects, are tested. The efficiency and the effectiveness of the isolators are of the main interest for the authors. The first isolator is a pendulum-based system, while the second utilizes Shape Memory Alloy wires. Different configurations were considered for examining all cases. The importance of the hosting building is also examined, i.e. building type, stiffness and story that hosts the artefacts. Specifically tailored, numerical

models of varying complexity and Finite Element models for single and two-block rocking systems were developed for the needs of this study and are also assessed against the experimental results.

3.1.7 List of publications

- Fragiadakis M., L. DiSarno, A. Saetta, M.G. Castellano, I. Rocca, S. Diamantopoulos, V. Crozet, I. Politopoulos, T. Chaudat, S. Vasic, I.E. Bal, E. Smyrou, I. Psycharis, T.C. Hutchinson, L. Berto Seismic response assessment and protection of statues and busts Art Collections 2020, Historical Research Session (ARCO 2020, HR), May 28th-30th 2020, Università degli Studi di Firenze, Italy.
- Fragiadakis M., L. DiSarno, A. Saetta, M.G. Castellano, I. Politopoulos, T. Chaudat, I. Psycharis, T.C. Hutchinson, I.E. Bal, E. Smyrou, L. Berto, I. Rocca, S. Vasic, S. Diamantopoulos., Experimental seismic assessment and protection of museum artefacts, EUROdyn 2020, XI International Conference on Structural Dynamics, 23–25 November 2020, Athens, Greece.

3.1.8 References

- Berto L., Favaretto T., Saetta A., 2013. Seismic risk mitigation technique for art objects: experimental evaluation and numerical modeling of double concave curved surface sliders. *Bulletin of Earthquake Engineering*, 11(5): 1817-1840.
- Chiozzi, A., Simoni, M. and Tralli, A., 2015. Base isolation of heavy non-structural monolithic objects at the top of a masonry monumental construction. *Materials and Structures*, 49(6): 2113-2130.
- Di Sarno, L., Magliulo, G., D'Angela, D. and Cosenza, E., 2017. Experimental assessment of the seismic performance of hospital cabinets using shake table testing. *Earthquake Eng. Struct. Dyn.*, 48(1), 103–123.
- Housner WG., 1963. The behaviour of inverted pendulum structures during earthquake. *Bulletin of the Seismological Society of America*, 53: 403-417.
- Voyagaki, E., Psycharis, I.N., Mylonakis, G., 2013. Rocking response and overturning criteria for free standing rigid blocks to single-lobe pulses. *Soil Dynamics and Earthquake Engineering*, 46:85-95.
- Zhang, J, Makris, N., 2001. Rocking response of free-standing blocks under cycloidal pulses. *Journal of Engineering Mechanics*, 127: 473-483.
- Dimitrakopoulos, E., Fung, E., 2016. Closed-form rocking overturning conditions for a family of pulse ground motions. *Proceedings of the Royal Society of London A: Mathematical, Physical and Engineering Sciences*, 472.
- Diamantopoulos, S., Fragiadakis, M., 2019. Seismic response assessment of rocking systems using single degree-of-freedom oscillators. *Earthquake Eng. Struct. Dyn.*, 48(7), 689–708.
- Purvance, M.D., Anooshehpour, A., Brune, J.N., 2008. Free-standing block overturning fragilities: numerical simulation and experimental validation. *Earthquake Eng. Struct. Dyn.*, 37(5):791–808.
- Konstantinidis, D., Makris, N., 2009. Experimental and analytical studies on the response of freestanding laboratory equipment to earthquake shaking. *Earthquake Eng. Struct. Dyn.*, 38(6):827–848.
- Psycharis, I.N., 1990. Dynamic behaviour of rocking two-block assemblies. *Earthquake Eng. Struct. Dyn.*, 19: 555–575.
- Wittich, C.E., Hutchinson, T.C., 2017. Shake table tests of unattached, asymmetric, dual-body systems. *Earthquake Eng. Struct. Dyn.*, 46(9): 1391–1410.
- Psycharis, I., Fragiadakis, M., Stefanou, I., 2013. Seismic reliability assessment of classical columns subjected to near source ground motions. *Earthquake Eng. Struct. Dyn.*, 42(14): 2061-2079.
- Calio, I., Marletta, M., 2003. Passive control of the seismic rocking response of art objects. *Engineering Structures*, 25(8): 1009-1018.

- Contento, A., Di Egidio, A., 2014. On the use of base isolation for the protection of rigid bodies placed on a multi-storey frame under seismic excitation. *Engineering Structures*, 62–63: 1–10,
- Podany, J., 2015. An overview of Seismic Damage Mitigation for Museums. *International Symposium on Advances of Protection Devices for Museum Exhibits*, Beijing & Shanghai, China, April 13-15 2015.
- Castellano, M.G., Pigouni, A.E., Marcolin, L., Infanti, S., Baggio, S., Berto, L., Faccio, P., Rocca, I., Saetta, A., 2016. Testing of the seismic isolation system for the bust of Francesco I d'Este in Modena, Italy. *Proceedings of 10th international conference on Structural Analysis of Historical Constructions (SAHC 2016)*, Leuven, Belgium, September 13-15, 2016.
- Ishiyama YY., 1982. Motions of rigid bodies and criteria for overturning by earthquake excitations. *Earthquake Eng. Struct. Dyn.*, 10(5):635–650.
- Vlachos, N., Diamantopoulos, S., Fragiadakis, M., 2019. Seismic response assessment of artefacts freestanding on a solid pedestal. *4th Hellenic National Conference on Earthquake Engineering and Technical Seismology*, Athens, 5-7 September 2019.

3.2 Project #5 –Full-scale experimental validation of steel moment frame with EU qualified joints and energy efficient claddings under near fault seismic scenarios

Authors

M. D’Aniello⁽¹⁾, L. Di Sarno⁽¹⁾, R. Landolfo⁽¹⁾,
A. Le Maout⁽²⁾, G. Rastiello⁽²⁾

⁽¹⁾ University of Naples "Federico II", Naples, Italy

⁽²⁾ DEN - Service d'Etudes Mécaniques et Thermiques (SEMT), CEA, Université Paris-Saclay, 91191, Gif-sur-Yvette, France

3.2.1 Introduction

There is a great wealth of numerical and experimental research dealing with the seismic response assessment of new steel moment resisting frames (MRFs). Such research has shown that: (i) the seismic behavior of MRFs is largely influenced by the behavior of the joints; (ii) the loading protocol adopted to qualify/test beam-to-column joints are representative of cumulative and maximum rotation demands imposed by far-field seismic ground motions and (iii) the design of new steel MRFs according to EC8 is mostly influenced by the serviceability checks (i.e. damage limitation requirements).

It is worth noting that most of the existing studies conducted focused mainly on the testing of sub-assembly, without accounting for the response of the building as a whole. Additionally, the loading protocols used for qualifying the joints do not mimic actual earthquake demands at near-collapse conditions. This is also the case of near-fault (NF) seismic input. Furthermore, there is a lack of knowledge of the behavior of steel joints when subjected to NF seismic demand. Additionally, earthquake reconnaissance studies have shown that the ratio of vertical-to-horizontal peak ground acceleration can be larger in NF than in far-fault seismic events. Near-fault strong motions tend to

increase the inelastic demand on structural steel members and joints. On the other hand, the use of special ductile energy efficient claddings can be beneficial to relax the drift limitations, thus allowing to optimize the structural design (i.e. reducing the design over-strength), reducing the use of material, constructional costs and encouraging the adoption of more sustainable solutions. The use of such ductile non-structural components will also lower the earthquake-induced losses arising from claddings.

The experimental project FUTURE aims to qualify the behavior of steel moment frames equipped with three different types of detachable beam-to-column Joints. The project investigates also the influence of energy efficient ductile non-structural claddings under NF seismic scenarios. Therefore, a two-story 50-ton scale 2/3 model was then designed and manufactured.

The main findings expected from the tests are as follows:

1. Provide design rules for steel frames under combined effects of horizontal and vertical components NF, which are yet not considered in the design standards for new and existing structures;
2. Validate the response of MRFs equipped with EU prequalified joints (i.e., extended stiffened, haunched and dog-bone) under NF earthquakes as well as to demonstrate the effectiveness of the new design rules for joints currently implemented in the draft of the amended EN1993:1-8;
3. Verify the efficiency of slab-to-beam and slab-to-joint details to avoid the composite action at joint level but to ensure effective torsional restraints to beams;
4. Demonstrate the efficiency of fully detachable dissipative beam-to-column joints, which allow easy replacement once the seismic damage is occurred;
5. Contribute with new background data for the assessment and the repairing/retrofitting of steel frames (e.g. the use of bolted dog-bone joints is representative of potential retrofitting solution) in order to update the next version of EN1998-3;
6. Verify the revised requirements about P-Delta effects currently proposed by WG2 CEN-TC 250/SC8 and ECCS-TC13 for the amended version of EN1998-1;
7. Validate the use of special energy efficient and extra-ductile claddings for MRFs, characterized by drift limits at DL/SLS larger than 1.5% of the interstory height.
8. Develop experimentally-based fragility relationships for such ductile non-structural components, which tend to minimize the earthquake losses due to claddings.

3.2.2 Specimen

The experimental mockup is a two-story one-bay steel frame (5 m x 5 m) that has been sub-structured from a reference steel building that is a typical example of archetype for multi—story office building of the typical EU practice. The reference structure was designed according to the updated provisions of the amended EN 1998-1-1 and EN1988-1-2 and EN 1993-1 and EN1993-1-8, since the members of the research units are actively involved in the revision of both EC8 and EC3. The experimental mock-up is shown in Figure 136.

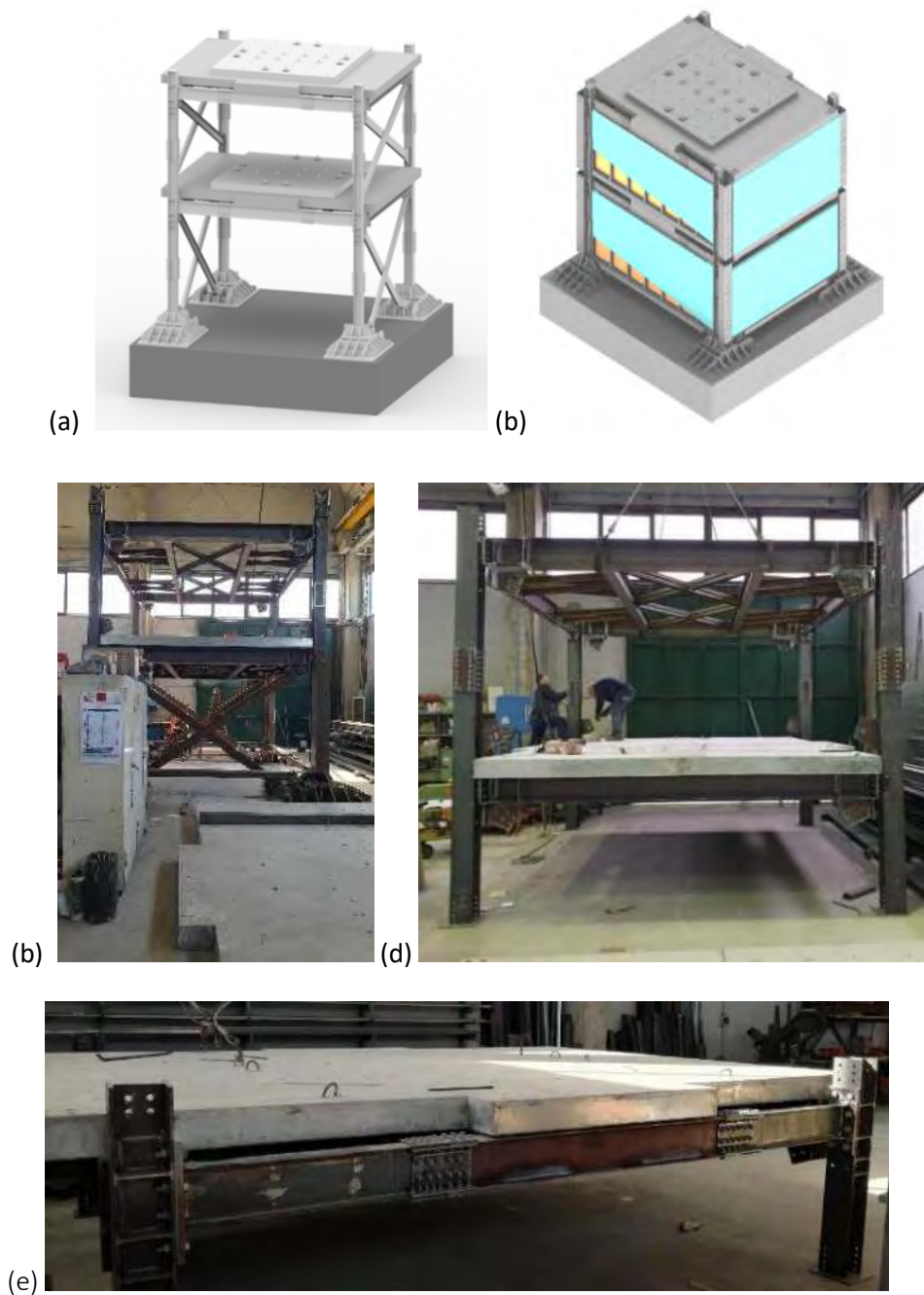


Figure 136: the FUTURE mockup: overall layout without (a) and with cladding (b); the mounted mockup (c) and some intermediate erection phases (d, e)

The mock-up has been designed to detach and replace easily all components that will experience plastic deformations, namely the column ends at the base level and the end portions of the beams with corresponding end-plate connections. Three types of beam-to-column joints are examined (Figure 137), namely reduced beam section (RBS), haunched (H) and extended stiffened (ES). The end-plate connections of haunched and RBS joints were designed as full-strength, namely to be stronger than the connected beam segment where plastic deformations are expected. ES joints were designed with equal strength connections, namely designed to guarantee the contemporary yielding of both connection and beam. In addition, for all joint configurations the column web panel was designed to be stronger than the connected beam and connections in order to remain elastic during the test loading. A further hierarchical criterion was adopted to avoid the failure of the bolts, so that the design tensile strength

of each bolt row should be larger than the strength of the connected plate accounting for both the random variability of its yield stress and the relevant strain hardening.

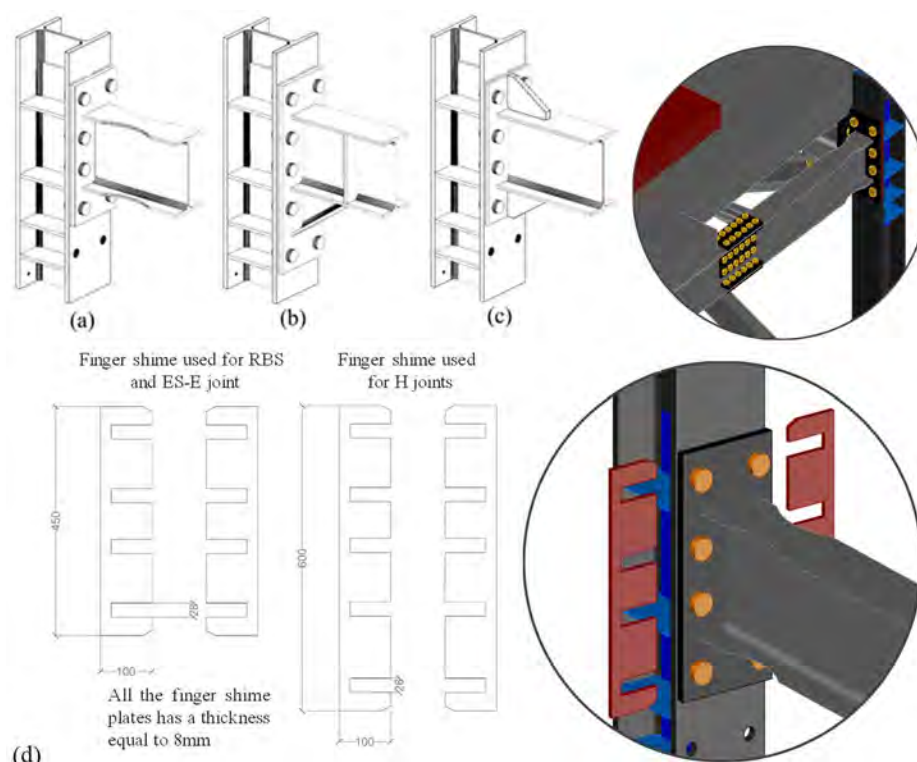


Figure 137: Investigated joints: a) Reduced beam section (RBS), b) Haunched (H) and c) Extended stiffened equal strength (ES)

To facilitate the replacement of the dissipative beam segments with the relevant connections, finger shims are designed and inserted between the end-plate of the connection and the column flange (Figure 137d).

To speed up the assembling of the mockup in the laboratory, the prefabricated solid slabs have been designed to be mounted on the mockup. In addition, to make easier this phase, each slab consists of two sub-parts to be connected together. Figure 136 shows some details of the slab, where it can be easily recognized how simple is their positioning and assembling on the steel frame.

A qualified steel company that is particularly specialized in high-quality welding techniques as well as specified for this type of manufacturing fabricated the steel mockup and the two prefabricated slabs in Italy near Naples.

3.2.3 Numerical simulations

The behavior of joints under both monotonic and cyclic loads was investigated by means of finite element (FE) simulations carried out in ABAQUS in order to verify the effectiveness of the design procedure. Parametric analyses were also carried out to investigate the influence of the finger shims on both non-linear behavior of the joints that are used for constructional reasons to simplify the demounting and mounting of the joints after each test. The results show that the design criteria are effective to guarantee the required performance of the joints and, despite the cumulative plastic deformation in the dissipative elements, the introduction of the finger shims are useful for the

dismantling phase. The main results relative to local response quantities of the joints are summarized hereinafter.

Figure 138 shows the results of both monotonic and cyclic analyses of RBS joints. The monotonic analyses were performed up to 10% of joint rotation while the AISC341 loading protocol was used for cyclic simulations. Most of the plastic deformations are concentrated in the RBS section with the activation of a perfect plastic hinge leaving the connection almost elastic. However, some plastic deformation can be observed around the weld between the beam flange and the end-plate at a high level of imposed rotation (10%). The joints show a very ductile behavior up to 6% of chord rotation with small decrease of resistance due to beam geometrical imperfections. Comparing the results in terms of backbone curve no appreciable differences can be observed between the joints with and without finger shims. These considerations are also confirmed by the PEEQ distribution on both the investigated joints.

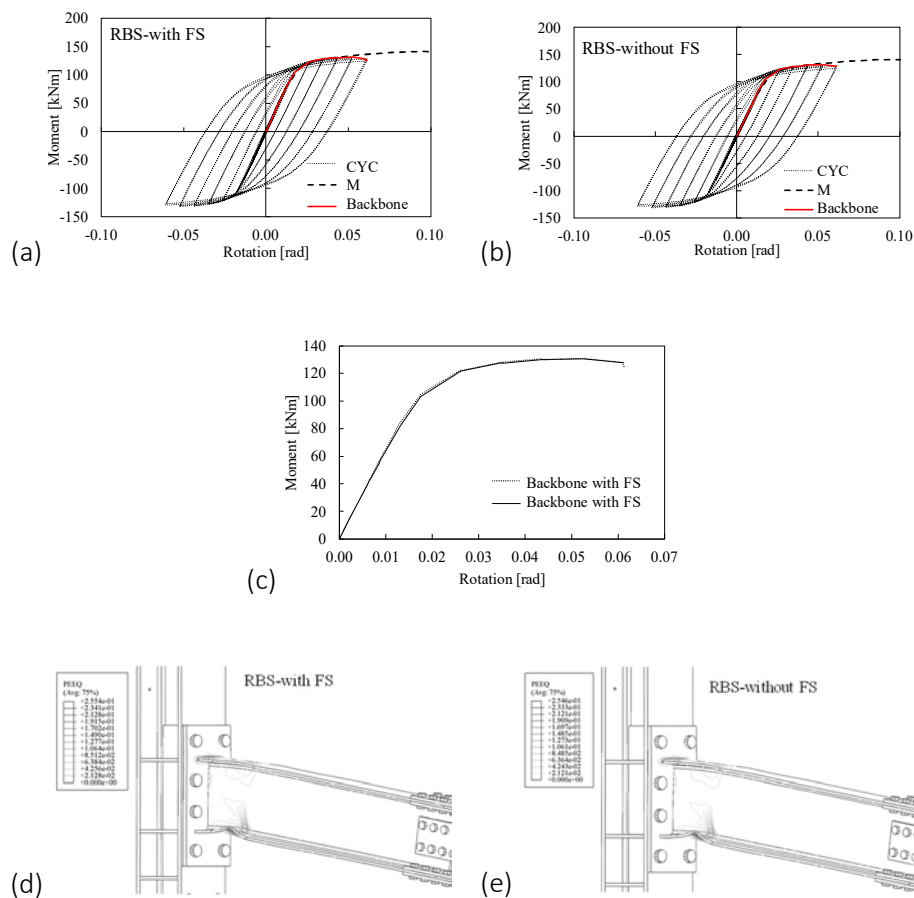


Figure 138: Monotonic and cyclic behavior of RBS joints with and without finger shims

The results in terms of moment rotation curves and distribution of PEEQ for haunched joints with and without finger shims are summarized in Figure 139. As for the previous configuration, also for haunched joints the plastic hinge forms at the extremity of the beam, leaving the connection and column web panel in elastic range. However, a larger reduction of resistance due to the beam flange local instability can be observed at 3.5% of rotation. The decrease of resistance is smaller than 20% at a 4% of rotation, hence these joints conform with both European and American requirements. As in the previous case also for this type of connection, no appreciable differences can be observed between the joints with and without the finger shims.

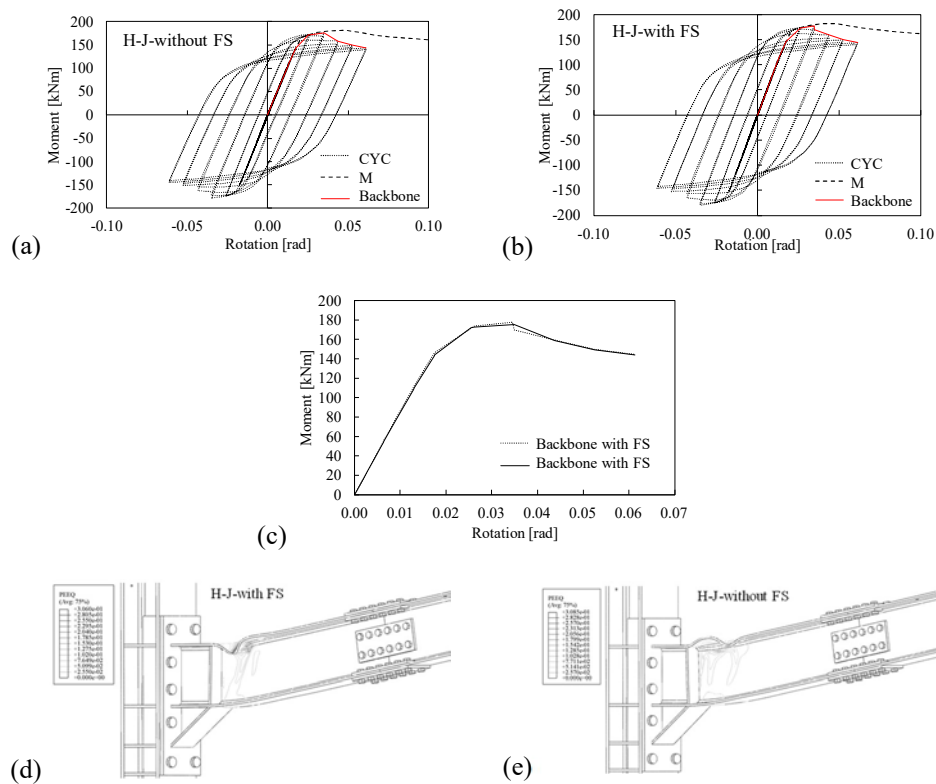
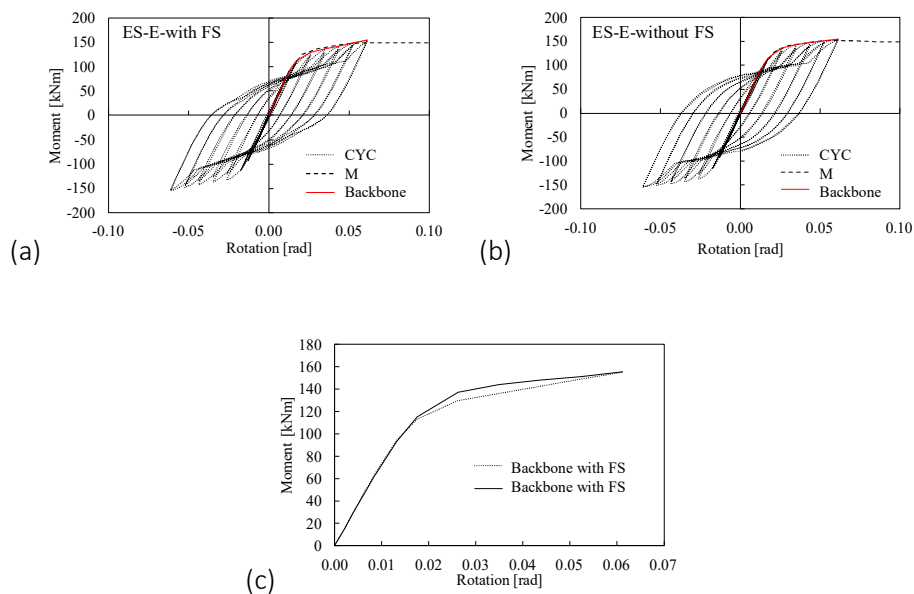


Figure 139: Monotonic and cyclic behavior of haunched joints with and without finger shims

In addition, the extended stiffened equal strength joints show a very ductile behavior with plastic deformation in both beam and connection (Figure 140). Differently from the previous cases, the presence of finger shims gives some slight difference in terms of moment-rotation response curves, but negligible differences in terms of distribution of plastic deformations. The reason of such differences is mainly due to the longer length of the bolt shanks in the joints with finger shims, which increases the deformability and the gap opening of the connection in its non-linear range.



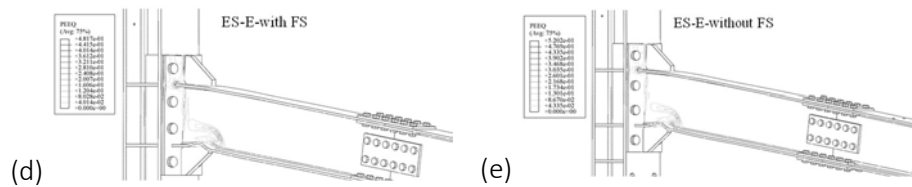


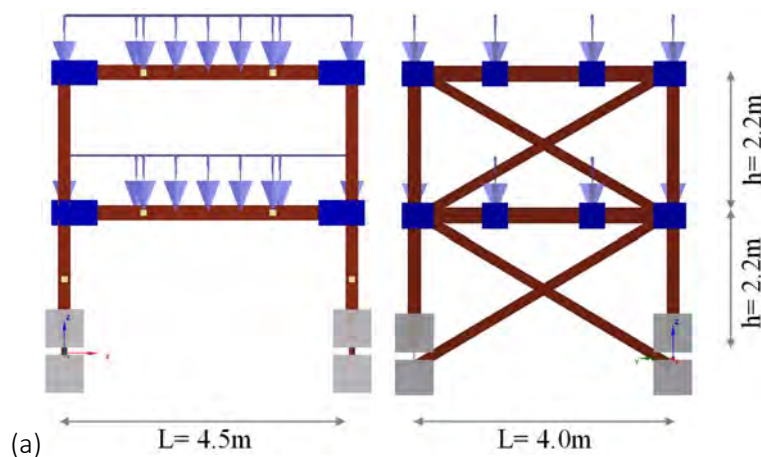
Figure 140: Monotonic and cyclic behavior of ES-E joints with and without finger shims

Based on these results, we can point out the following remarks:

- The bolted joint with reduced beam section ensures excellent ductile behavior up to rotation of 6% without showing any resistance decrease. Finger shims do not influence the performance of this type of joint.
- The haunched joint designed in accordance with the criteria developed within the Equaljoints research project allow to obtain a full rigid/full strength joint. The response is not affected by the introduction of the finger shim plates
- Differently from the previous cases, we can observe the influence of the finger shim plate for equal strength connection due to the larger deformability of the connection and some variation of the distribution of the contact forces when the connection opens. However, the presence of finger shims does not significantly modify the global performance of the joint.

Preliminary numerical global analyses have been also performed in order to predict the system response of the experimental mock-up that will be tested. Maximum interstory and residual drifts, the displacement at the base and the overall overturning moments have been evaluated considering a set of NF records.

The analyses have been performed using a very refined SEISMOSTRUCT model, which incorporates all geometrical and mechanical features of the structures. The non-linearities are modelled using lumped springs which were calibrated against the results of FE simulation carried out in ABAQUS software.



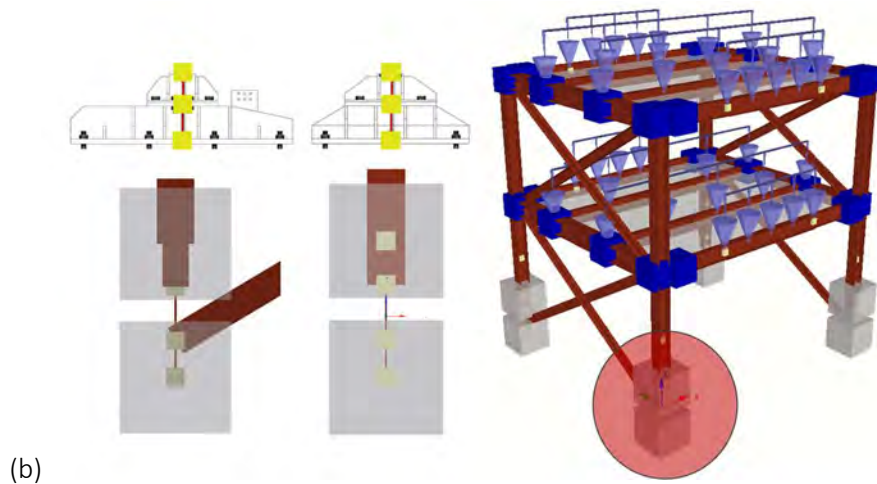


Figure 141: Numerical model of the 3D mockup: a) planar views, b) 3D view and details of the rigid offset used for to model the base-column connection

The numerical model of the mockup is shown in Figure 141. Figure 141a shows the planar views of the model in both longitudinal and transverse direction, while Figure 141b shows the 3D layout of the model. In addition, Figure 141b shows the details of the rigid offset that have been modelled to account for the presence of stiffeners and steel footings at the base of the mockup.

For the sake of brevity, the results are shown for the case of haunched and RBS joints which correspond to the upper and lower bound range of behavior that the structure may exhibit.

The non-linear behavior of beams and columns were modelled with lumped non-linear springs that were calibrated on the basis of the finite element simulations carried out in ABAQUS. In particular, Figure 142 shows the comparison of the FE simulation of the column segment at the base of the mockup and the corresponding numerical simulation in SEISMOSTRUCT software under cyclic loading history (i.e. AISC341-16 loading protocol). As it can be observed, the prediction of the numerical model is satisfactory.

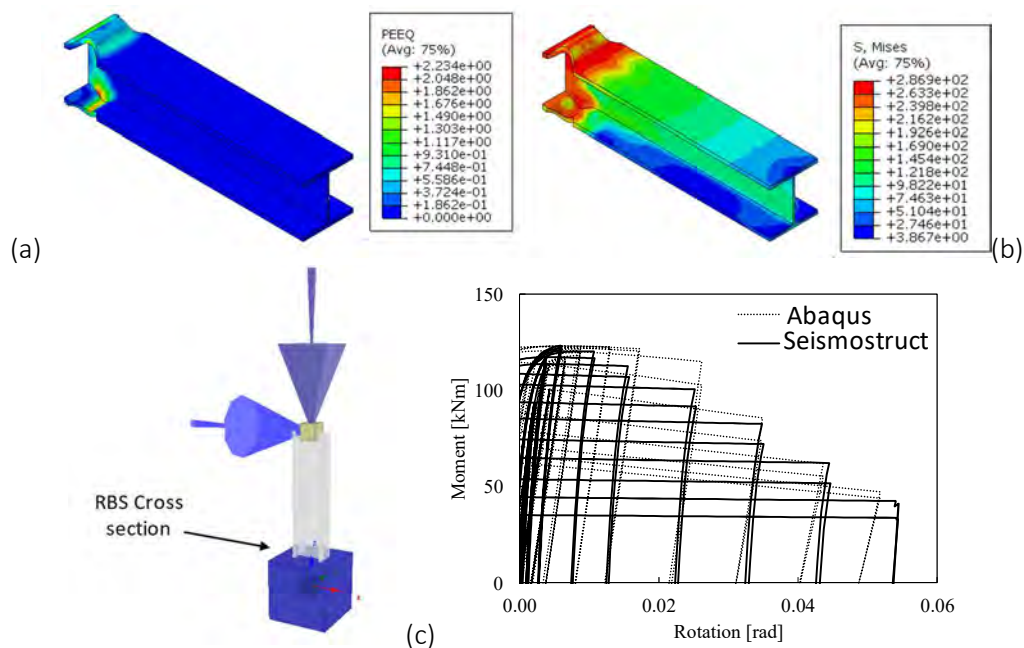


Figure 142: FE simulation of the column segment at the base (a); model in SEISMOSTRUCT (b); comparison between the FE simulation and the numerical analysis (c)

Figure 143 shows the comparison between FE simulation of the joints and the corresponding numerical simulation of the non-linear springs adopted for the beam-to-column joints. In addition, in this case there is a satisfactory correspondence.

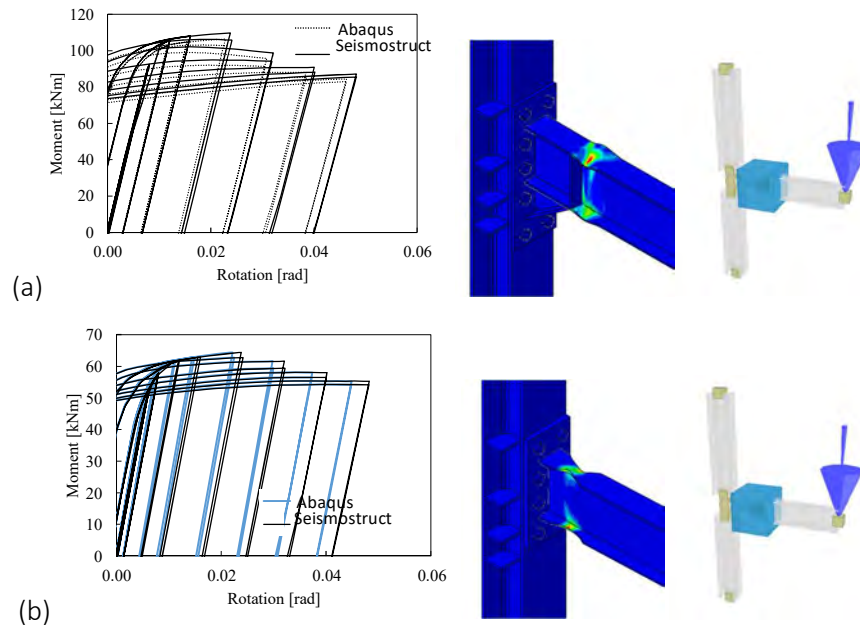


Figure 143: FE simulation vs numerical simulation of the joints: Haunched (a) and RBS (b)

The nonlinear analyses were performed considering the set of NF records reported in Table 16. The corresponding spectra are reported in Figure 144 and compared to the EC8 spectrum at ultimate limit state.

								PGA			PGV			PGD		
ID	Earthquake	Date	M _s	d _e	h	Station	Site	Long	Trasv	Vert	Long	Trasv	Vert	Long	Trasv	Vert
[-]	[-]	[-]	[-]	[km]	[km]	[-]	[-]	[g]	[g]	[g]	[cm/s]	[cm/s]	[cm/s]	[cm]	[cm]	[cm]
LP19-70	LOMA PRIETA, USA	18/10/1989	6.93	7.17	17	COR	S	0.47	0.64	0.43	47.03	55.55	23.33	12.05	9.61	9.20
LP40-70	LOMA PRIETA, USA	18/10/1989	6.93	27.23	17	SAR	S	0.32	0.50	0.35	42.58	41.25	25.72	26.32	15.80	14.14
NICS-70	MANAGUA, Nicaragua	23/12/1972	6.24	28	5	MAN	S	0.33	0.37	0.32	29.88	35.26	18.03	6.36	14.61	6.86
NO2-70	NORTHIDGE, USA	17/01/1994	6.7	20.27	18	NFS	S	0.59	0.58	0.55	94.72	74.84	30.74	30.47	17.60	12.79
SLV2-70	EL SALVADOR	10/10/1986	5.8	7.93	7	CIG	R	0.42	0.66	0.38	61.19	79.49	11.38	16.27	11.81	2.72
AQA	L'AQUILA, ITALIA	06/04/2009	6.3	4.62	8.8	AQA	B	0.44	0.40	0.47	22.17	25.98	8.03	4.08	4.07	5.46
AQG	L'AQUILA, ITALIA	06/04/2009	6.3	4.53	8.8	AQG	A	0.52	0.47	0.24	28.98	25.42	8.70	2.93	4.18	3.45
AQK	L'AQUILA, ITALIA	06/04/2009	6.3	1.75	8.8	AQK	B	0.35	0.33	0.37	29.60	26.50	17.58	8.89	5.45	24.03
AQV	L'AQUILA, ITALIA	06/04/2009	6.3	4.41	8.8	AQV	B	0.55	0.66	0.52	35.25	32.90	9.78	4.93	4.95	6.53
NO	NORTHIDGE, USA	17/01/1994	6.7	5.41	18	ST24436	C	1.78	0.99	1.05	112.84	77.55	73.53	33.00	30.49	20.68
KO	KOCAELI	17/08/1999	7.6	5.31	15	ST553_Izmit	C	0.31	0.36	0.21	41.36	53.94	15.58	14.97	13.56	6.87

Table 16: Near-fault records used for the preliminary non-linear dynamic analyses of the case study frame

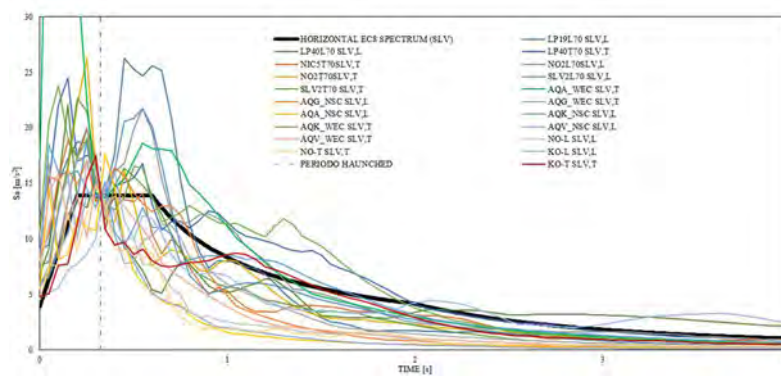


Figure 144: Spectra of the records in Table 16 vs. EC8 spectrum

The non-linear dynamic response of the mock-up shows a large plastic deformation at both significant damage (SD) and near collapse (NC) limit states. In all investigated cases a large difference in terms of interstory drift can be observed between the first and the second story. The latter response demonstrates that the plastic deformations are mainly concentrated within the beams and the columns at the first floor, as also confirmed by the result in terms of residual drifts at the end of the numerical test. Figure 145a summarizes the demand in terms of interstory drift ratios at SD limit state for the mockup equipped with RBS joints, while Figure 145b shows the demand at NC limit state. As it can be observed the analyses confirm an almost uniform demand at both storys, which is associated to a global mechanism.

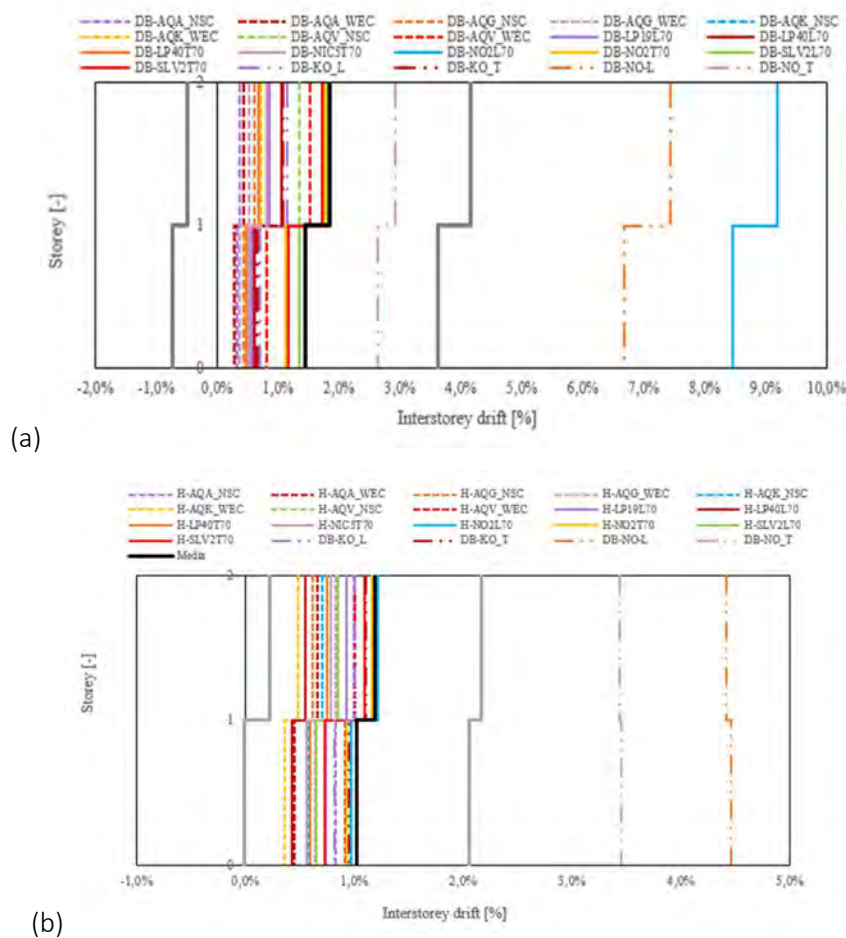


Figure 145: Interstory drift demand for Mockup with RBS joints: a) Significant damage limit state; b) Near Collapse limit state

Figure 146a summarizes the demand in terms of interstorey drift ratios at SD limit state for the mockup equipped with Haunched joints, while Figure 146b shows the demand at NC limit state. It can be observed a larger concentration of demand and damage in the upper story, even though a global mechanism occurs.

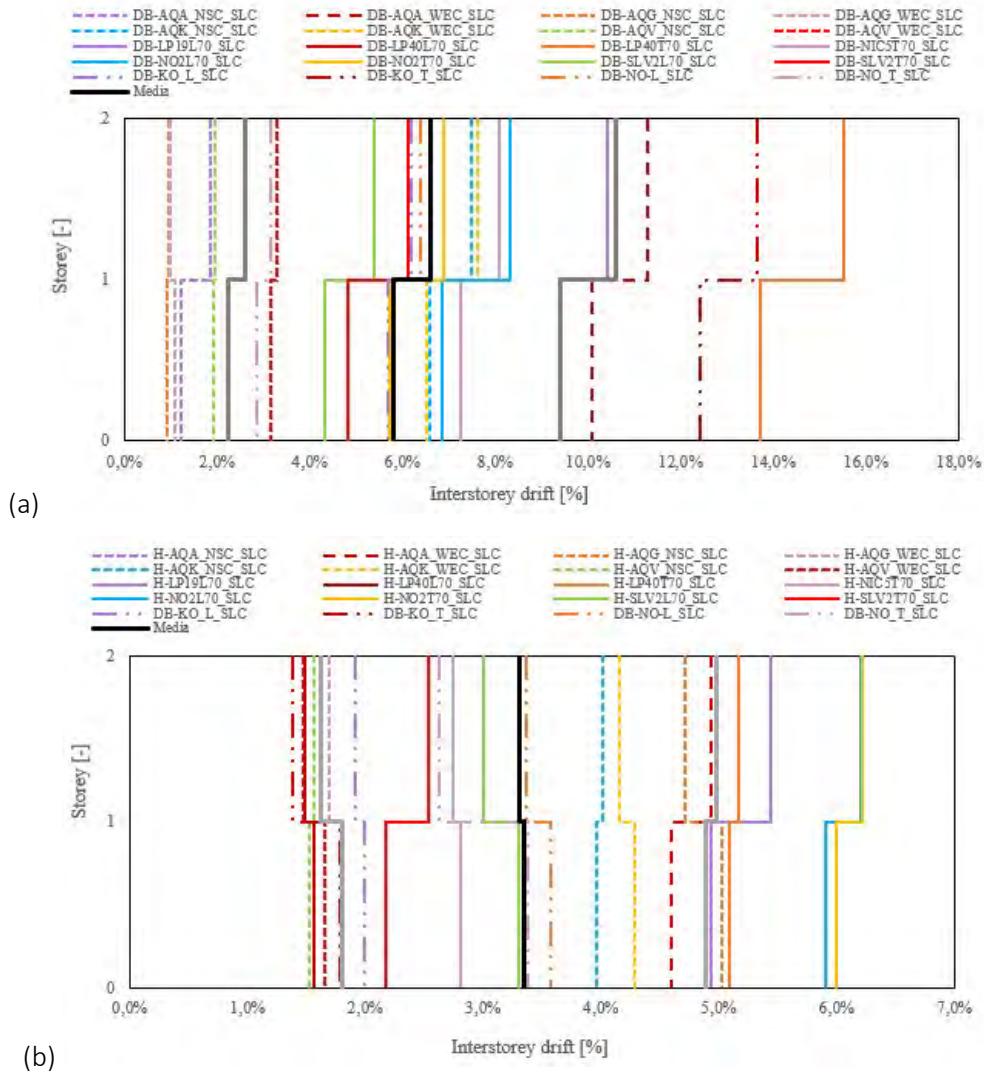


Figure 146: Interstorey drift demand for mockup with haunched joints: a) Significant damage limit state; b) Near Collapse limit state

The overturning moment relative to the investigated scenarios, show a very large action on the shaking table. Indeed, the overturning moments vary from an average 1300kNm (Figure 147a) to about 1800kNm (Figure 147a) for the range of examined records.

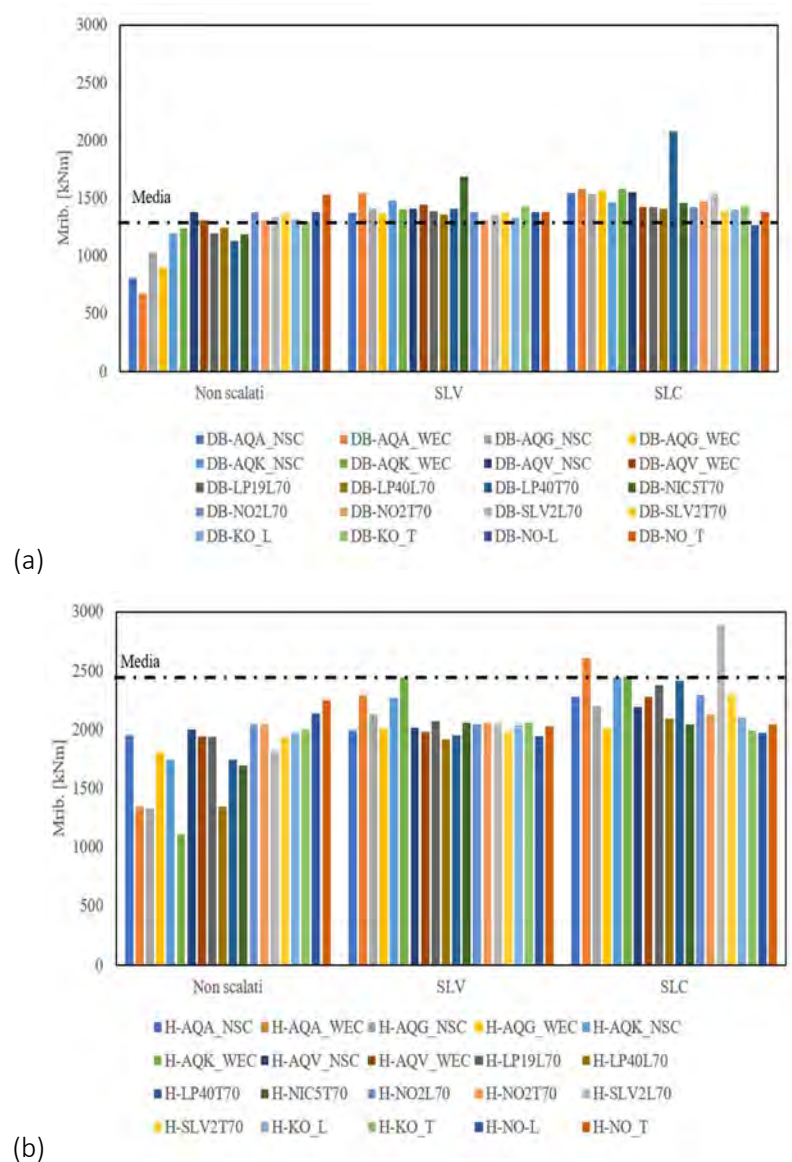


Figure 147: Overturning moments at the base of the mockup with RBS joints (a) and Haunched joints (b).

Displacements at the base of the mockup							
Record	Scaling level	RBS	Haunched	Record	Scaling level	RBS	Haunched
I-I	I-I	[cm]	[cm]	I-I	I-I	[cm]	[cm]
LP19-70	Unscaled	2,8	1,9	NIC5-70	Unscaled	1,89	1,61
	Significant Damage	4,8	3,7		Significant Damage	1,76	1,4
	Near Collapse	8,2	6,3		Near Collapse	2,99	2,38
LP40170	Unscaled	2	1,7	LP40170	Unscaled	1,71	1,47
	Significant Damage	3,5	3,2		Significant Damage	1,6	1,28
	Near Collapse	6	5,5		Near Collapse	2,71	2,17
NO2170	Unscaled	4,8	3,6	NO2170	Unscaled	3,71	3,4
	Significant Damage	8,3	7		Significant Damage	3,46	2,96
	Near Collapse	14,2	11,9		Near Collapse	5,89	5,03
SLV2170	Unscaled	3,4	2,5	SLV2170	Unscaled	3,77	3,12
	Significant Damage	6	4,8		Significant Damage	3,51	2,71
	Near Collapse	10,2	8,2		Near Collapse	5,97	4,62
NO_L	Unscaled	10,2	9,1	NO_T	Unscaled	8,13	7,85
	Significant Damage	17,7	17,5		Significant Damage	7,58	6,83
	Near Collapse	30,1	29,7		Near Collapse	12,89	11,62
KO_L	Unscaled	2,5	2,4	KO_T	Unscaled	2,58	2,67
	Significant Damage	4,4	4,6		Significant Damage	2,41	2,32
	Near Collapse	7,5	7,8		Near Collapse	4,09	3,95
AQA_NSC	Unscaled	4,4	3	AQA_WEC	Unscaled	1,11	0,85
	Significant Damage	7,7	5,8		Significant Damage	1,03	0,74
	Near Collapse	13,1	9,9		Near Collapse	1,76	1,25
AQG_NSC	Unscaled	2,4	1,7	AQG_WEC	Unscaled	2,17	1,99
	Significant Damage	4,2	3,3		Significant Damage	2,02	1,73
	Near Collapse	7,1	5,6		Near Collapse	3,44	2,94
AQK_NSC	Unscaled	1,9	1,6	AQK_WEC	Unscaled	1,35	1,12
	Significant Damage	3,3	3,1		Significant Damage	1,26	0,97
	Near Collapse	5,6	5,2		Near Collapse	2,14	1,65
AQV_NSC	Unscaled	4,2	3,4	AQV_WEC	Unscaled	3,66	2,95
	Significant Damage	7,3	6,6		Significant Damage	3,41	2,57
	Near Collapse	12,5	11,2		Near Collapse	5,81	4,37

Table 17: Maxima estimated displacements at the base of the mockup.

Finally, the maximum displacements at the base of the mockup were also evaluated and reported in Table 17, where it can be observed that in the most of cases the expected values are compatible with the capability of the shake table.

3.2.4 Test setup

The experimental program consists of two phases; each of them repeated three times (i.e. one per examined type of beam-to-column joint). In the first phase, the entire mockup (i.e. frame + claddings) is subjected to base ground motion incrementally increased to cover Full Operation (FO), Damage Limitation (DL/ SLS) and Significant Damage (SD/ULS) earthquake intensity levels as defined in the new draft version of Eurocode 8. In the second phase, after the removal of the cladding and the replacement of the base columns (if damaged), the damaged joints are replaced without mounting new cladding and the acceleration is incrementally increased up to Near collapse (NC) earthquake intensity. The experimental campaign is supported by comprehensive numerical analyses of the entire mockup and its components to simulate both the pre- and post-test conditions.

At this stage, the mockup is fully completed and ready to be tested, but the experimental campaign is not yet carried out owing to the unpredictable emergency of COVID virus that is currently affecting all European countries, especially Italy and France.

Nevertheless, all the preliminary issues that are relevant for the shake table tests have been carried out. Strong motion input signals, instrumentation, test sequence and preliminary analyses have been carefully assessed. As soon as governmental containment measures will be relaxed, the delivery, assembly, instrumentation and testing will be carried out by using the 6DoF AZALEE shake table.

For the sake of clarity, Figure 148 illustrates pictorially all instruments, measuring devices along with their location, that are going to be employed for the dynamic tests.

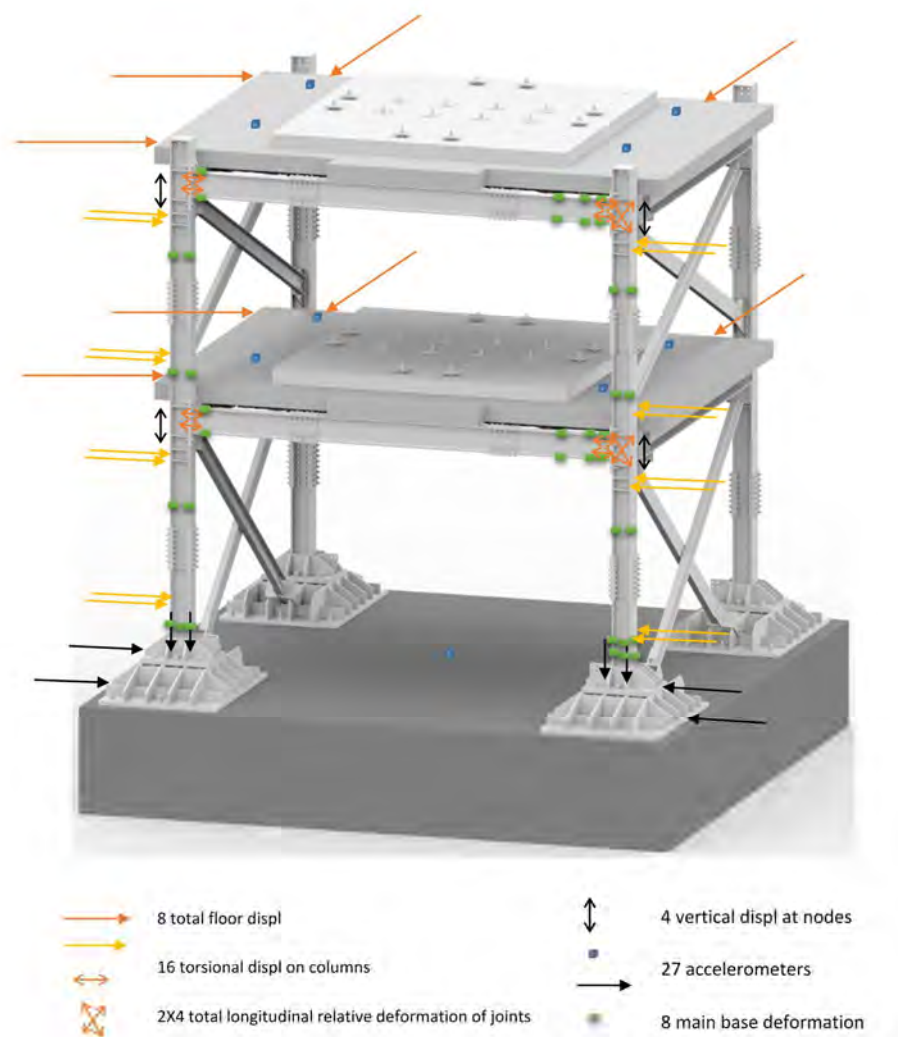


Figure 148: Plan layout of instrumentation and measurement devices.

3.2.5 Conclusion

At this stage, the mockup is ready, the preliminary analyses are carried out, but the experimental campaign is not yet carried out owing to the unpredictable emergency of COVID virus that is currently affecting all European countries, especially Italy and France.

Nevertheless, all the preparatory work that was necessary to perform the experimental campaign were completed, in particular the excitation signals, instrumentation, test sequence and preliminary numerical simulations. As soon as the containment measures will be relaxed, the delivery, assembly, instrumentation and testing will be carried out.

4 LNEC

The Earthquake Engineering and Structural Dynamics Unit of LNEC runs an infrastructure with a 5.6 m x 6.4 m 3D shaking table (LNEC-3D), to which access is offered, located in a large testing hall with 10 m height and an overhead crane with 400 kN capacity, resulting in a versatile test facility that can be used for a variety of earthquake and dynamic load tests.

The LNEC-3D shaking table (ST) has three independent translational degrees of freedom, with the rotational ones being passively restrained via a stiff torque tube system. The actuators allow for dynamic forces of 1000 kN in the vertical and 700 kN in the horizontal directions to be applied to the system, with peak velocities up to 0.7 m/s and peak displacements of ± 0.2 m in all directions.

The control of the ST is fully digital, allowing input displacements of any form in a frequency range of 0-40 Hz. The digital control hardware and software was upgraded in 2011 into a more advanced and open platform, whereby the introduction of new control strategies or the implementation of new test strategies (e.g. hybrid simulations) is facilitated. The acquisition system allows a large number of physical variables (such as pressures, forces, accelerations, displacements, strains, etc.) to be monitored, using the extensive instrumentation available or specially developed instrumentation.

The LNEC-3D ST was designed specifically for testing structures and components up to collapse or near-collapse conditions. It has a large capacity in terms of payload (max. weight of 40 tonnes), allowing tests on medium-sized structures or larger structures at reduced scale. A special feature of this installation is that the ST is surrounded by three stiff reaction walls, which can be used for different test setups.

During SERA, LNEC is hosting 3 User Groups (UGs) and Projects, for a total of 75 access days. In the 1st call for TA Projects, 5 UGs applied to LNEC as the 1st choice as TA host and 3 UGs applied to LNEC as the 2nd choice for hosting institution. Two projects were selected:

- Project # 6 – (Towards the) Ultimate Earthquake proof Building System: development and testing of integrated low-damage technologies for structural and non-structural elements;
- Project # 7 – Seismic Response of Masonry Cross Vaults: shaking table tests and numerical validations.

In the 2nd call for TA projects, the 3rd UG was selected, among additional 8 applications from which 3 had LNEC as the 1st choice as TA host. The selected project was:

- Project # 19 – Seismic Testing of Adjacent Interacting Masonry Structures.

The 3 projects compose a very complete set of tests, resulting on important developments for both new structures, with innovative materials and construction techniques, and for the assessment of existing structures, representative of heritage buildings or typical city centre buildings. Moreover, it is noteworthy to point out that *the 3 projects correspond to a total of 8 independent shaking table tests*, since they include the test of more than one specimen or the test of the original specimen which is later retrofitted and tested again.

The design of the models, the test setup and the instrumentation plan were developed by the UGs and LNEC's research team, taking into account the constraints of the facility and the objectives of the UGs. The construction of the specimens and the preparation for the tests followed.

After tuning the shake table motions to the target ones, the testing was performed and the post-treatment of results was made or is underway. Numerical modelling was involved at different stages of the activities, be it as preliminary simulations or *a posteriori* calibration and validation simulations. Finally, the data curation of the test results is ongoing for dissemination to the wider scientific

community in the experimental database of the SERA project and several scientific publications have been published or are being prepared.

4.1 Project #6 – (Towards the) Ultimate Earthquake proof Building System: development and testing of integrated low-damage technologies for structural and non-structural elements

Authors

S. Pampanin⁽¹⁾, J. Ciurlanti⁽¹⁾, S. Bianchi⁽¹⁾, D. Perrone⁽²⁾, M. Palmieri⁽³⁾, D. Grant⁽⁴⁾, G. Granello⁽⁵⁾, A. Palermo⁽⁵⁾, A. Filiatrault⁽²⁾, A.A. Correia⁽⁶⁾, P.X. Candeias⁽⁶⁾, A. Campos Costa⁽⁶⁾

⁽¹⁾ *Sapienza University of Rome, Rome, Italy*

⁽²⁾ *IUSS, University School for Advanced Studies, Pavia, Italy*

⁽³⁾ *ARUP, Amsterdam, Netherlands*

⁽⁴⁾ *ARUP, London, United Kingdom*

⁽⁵⁾ *University of Canterbury, Christchurch, New Zealand*

⁽⁶⁾ *LNEC, National Laboratory for Civil Engineering, Lisbon, Portugal*

4.1.1 Introduction

The seismic design of modern buildings follows a performance-based approach targeting Life-Safety criteria. Structures are conceived as ductile systems where inelasticity is concentrated within discrete plastic hinge regions as per capacity-design principles and this primary structure is designed for allowing buildings to sway and stand during earthquakes and people to evacuate. As continuously highlighted after past seismic events, notwithstanding these buildings performed as expected depending on the seismic intensity level they were subjected to, the Life-safety design philosophy is no longer acceptable due to the significant damage to both structural and non-structural components which can result (Figure 149, left). Repairing traditional structures may be uneconomical when compared with the cost of demolition and re-construction of the entire building system, in terms of money and time.

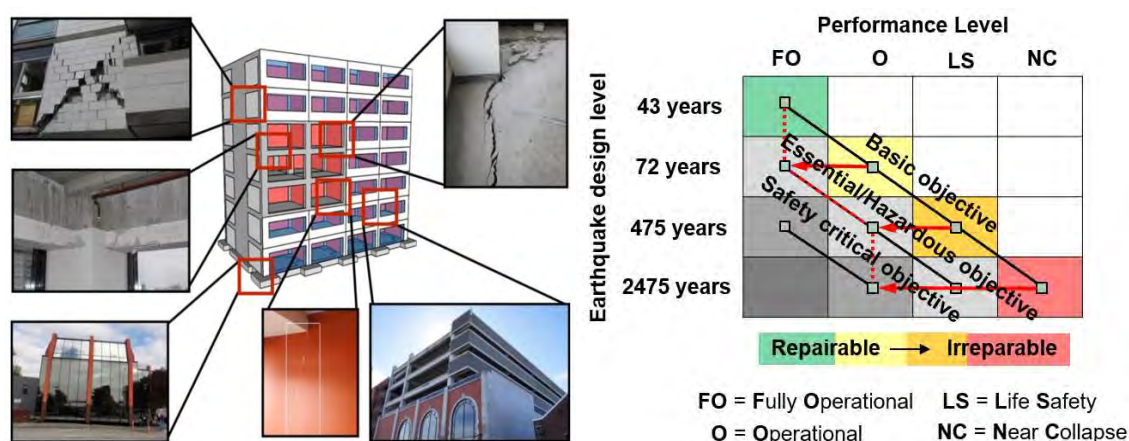


Figure 149: Left – typical damage occurring in modern RC buildings (Johnston et al., 2014); Right – seismic performance design objective matrix of SEAOC Vision 2000 (1995) modified to achieve a damage-control design philosophy (Pampanin, 2012, 2015)

The high socio-economic impact of moderate-to-strong earthquakes and the increased public awareness of seismic risk have facilitated the acceptance and implementation of damage-control technologies, whose development is nowadays demanded. Performance-based design criteria and objectives need a shift towards a low-damage design approach (Figure 149, right) and technical solutions for engineers and stakeholders to control the performance/damage of the entire building system, including superstructure, foundation systems and non-structural elements. Moreover, this new design philosophy should be considered to define an ultimate “earthquake-proof” building system (Pampanin, 2012, 2015).

Apart from well-known innovative techniques such as base isolation and supplemental dissipative braces, more recently developed “low-damage” systems are receiving attention by the engineering community. These solutions are based on a combination of self-centering and dissipative capabilities and are called as PRESSS (PREcast Seismic Structural System) technology for concrete (Priestley et al., 1999; Pampanin, 2005; Pampanin et al., 2010) and Pres-Lam (Prestressed Laminated) for timber (Palermo et al., 2005; Pampanin et al., 2006, 2013). Nevertheless, protecting the primary structure from extensive damage is not enough for the actual society expectation, whilst the structural skeleton should be “dressed” using low-damage non-structural components, i.e. exterior enclosures, partitions, ceilings, services and contents. Therefore, innovative technological solutions have been recently developed and studied with the aim of mitigating the damage to either vertical or horizontal elements (Baird et al., 2013; Tasligedik et al., 2014; Tasligedik and Pampanin, 2016; Pourali et al., 2017).

The integrated structural/non-structural system comprising all these low-damage solutions should represent the next generation of modern structures. However, notwithstanding initial studies on such type of integrated system (Johnston et al., 2014), more comprehensive investigations are required for demonstrating the high seismic capability of this building solution and refining the construction detailing. With this aim, as part of the H2020 SERA project, 3D shaking-table testing of a half-scale integrated low-damage system were carried out at the National Laboratory for Civil Engineering (LNEC) in Lisbon, Portugal. The project was proposed and developed with the aim of promoting a research effort within the European industry/community for the wider uptake of an integrated low damage building system, including skeleton and non-structural components for the next generation of buildings. An overview of the entire research programme is provided within this report, focusing on the description of the test specimen, on its construction/assembly phases as well as on the experimental setup and test and initial research outcomes.

4.1.2 Test specimens

Three different system configurations have been tested, corresponding to three testing Phases (Figure 150), namely:

- the *Skeleton Building*, made of post-tensioned timber beams, precast concrete columns and hybrid rocking-dissipative connections (beam-column joint, column base) in the longitudinal direction and post-tensioned rocking-dissipative low-damage timber walls in the opposite transverse direction. Both frame and wall systems comprised external “Plug&Play” dissipaters. Regarding the flooring systems, two different typologies were introduced: 1) a Timber-Concrete Composite (TCC) flooring system for the first level and 2) a Pre-stressed Timber-Concrete flooring system (3PT) on the second level of the Test Building.
- *Option 1 configuration*, comprising fiber-reinforced gypsum partition walls with low-damage detailing, built on the first floor of the specimen in both the structural directions.
- *Option 2 configuration*, representing an integrated structural/non-structural solution. The Skeleton Building was “dressed” using Glass Fiber Reinforced Concrete (GFRC) cladding systems in the frame direction and spider glazing curtain walls in the wall direction, while the internal gypsum wall was substituted by a masonry partition made of low-damage detailing.



Figure 150: Test specimen configurations – Skeleton Building (left), Option1 (centre), Option2 (right) (Pampanin et al., 2020)

The Test Building was designed considering a hypothetical full-scale Prototype Building with typical structural dimensions of an inner core of multi-storey commercial buildings, while ensuring the specimen could fit to the weight limitations of the shaking table as well as being compatible to the size of the steel foundation already available at LNEC. The Prototype Building is a two-storey structure with two seismic resistant post-tensioned timber-concrete frames in the longitudinal direction and two post-tensioned timber walls in the transverse direction. The structural system was designed for the Ultimate Limit State (475-years return period earthquake for an Importance Class 2) following the Direct-Displacement Based Design (DDBD) procedure by Priestley et al. (2007) and Pampanin et al. (2010), as well as considering the seismic demand associated to a seismicity representative of a high seismic zone in Italy, with PGA of 0.353 g at ULS. Then, the Cauchy-Froude similitude of constant stress and constant acceleration was applied to determine the geometrical configuration of the 1:2 ($\lambda=0.5$) scale Test Specimen configuration. The specimen components were designed considering the scaled forces from the Prototype Building as well as applying the same DDBD procedure, as further verification. Additional masses (driving masses) were required to be added to the Test Specimen when compared to the Prototype Building, representing the increased density required by scaling. The global geometry of the specimen and its components can be found in Figure 151.

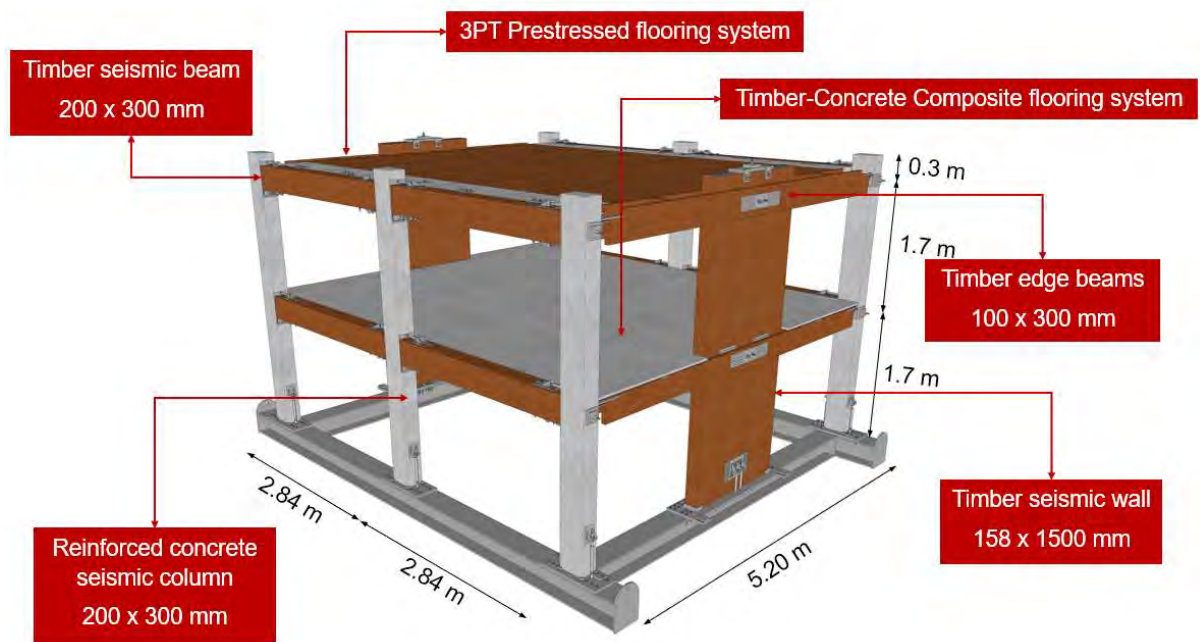


Figure 151: Global dimensions of the Skeleton Building (Pampanin et al., 2020)

Concerning the structural system, the hybrid connections (beam-column joint, column base and wall base) were designed considering the forces obtained from the DDBD procedure and following the procedure described in the NZCS PRESS Design Handbook (Pampanin et al., 2010) for the concrete elements and the STIC Design Guidelines (Pampanin et al., 2013) for the timber components. Apart from the design of the post-tensioned tendons/cables (1/2" or 3/8" wire strands for the beams and 18WR threaded bars for the walls) and of the external dissipaters (16 mm or 20 mm mild steel bars necked down to 6.8/8.8 mm for the beam dissipaters, from 20 mm to 14/15.6 mm for the column dissipaters, and from 16 mm to 11 mm for the wall dissipaters), all the steel assemblies (steel plates, bolts/screws/nails, welding) introduced for correctly realizing the hybrid connections were properly verified using formulations from international codes (European, Italian and New Zealand).

Concerning the flooring systems, the first level was a Timber-Concrete Composite (TCC) floor designed following the STIC (2012) and AS/NZS 1170 series (2002), consisting of 120 x 220 mm timber joists, 12.5 mm plywood and 27.5 mm concrete slab. On the other hand, the second floor was a 3PT prestressed timber-concrete floor (Palermo and Pampanin, 2017) composed of 1076 x 120 mm timber-concrete beams comprising 3 wire-strands of 5.2 mm diameter. Furthermore, many other structural details were introduced for providing the correct functionality to the entire system. A detailed description of the structural design and detailing can be found in Pampanin et al. (2020) and Ciurlanti et al. (2020).

The *Skeleton Building* was entirely built outside the shaking table, on a steel foundation. After the introduction of specific measurements to strongly fix the steel foundation plates of columns and walls to the existing foundation, the assembly of the Test Building involved different construction phases. Some photos of the construction phases as well as some specimen detailing are shown in Figure 152.

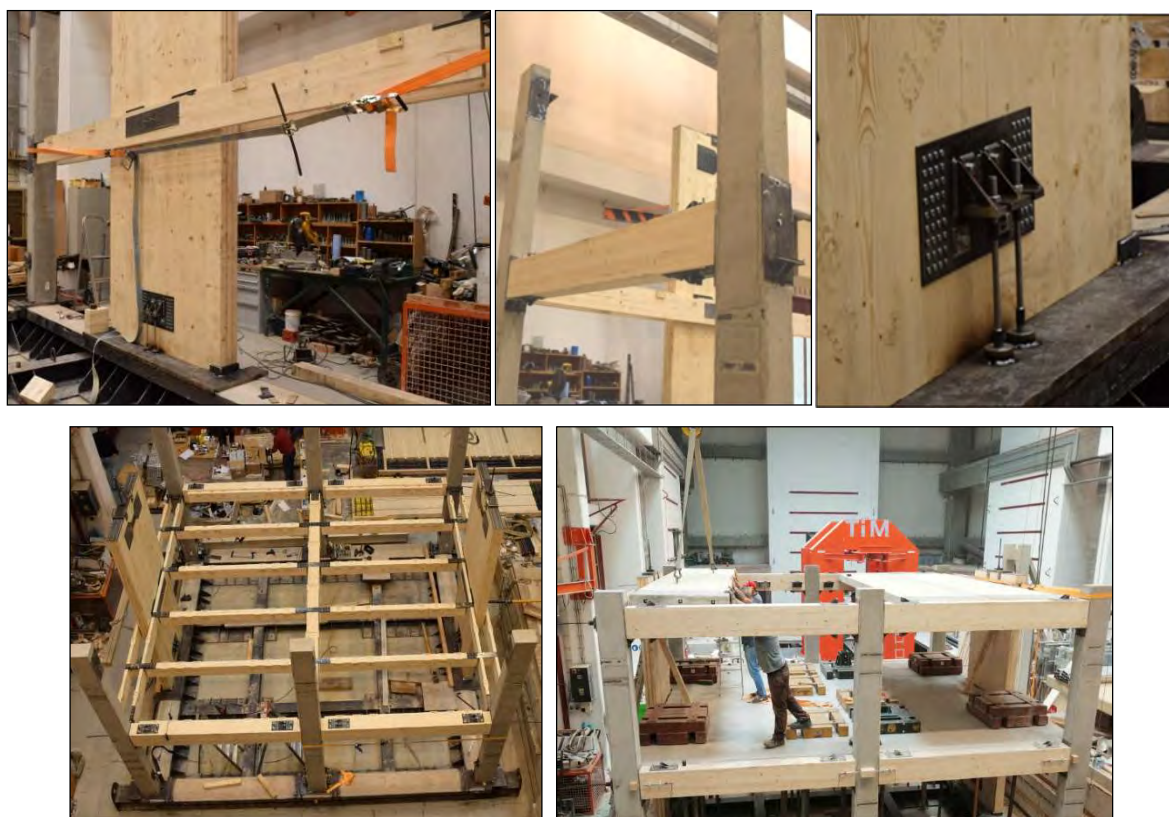


Figure 152: Construction of the Test specimen – assembly of the lateral beams to the wall (top, left), lifting and positioning of the seismic beams (top, centre), detail of the wall dissipaters (top, right), assembly of the timber joists on the first floor (bottom, left), assembly of the 3PT flooring system (top, right)

Regarding the non-structural elements, apart from the low-damage masonry partition of *Option 2* fully designed referring to Tasligedik and Pampanin (2016), the systems were proposed by the related industry suppliers and their details were discussed to be adapted to the existing structural skeleton.

Concerning the partitions tested during the second experimental phase (*Option 1*), the system consisted of two orthogonal walls: a 5 m-long wall with openings in the wall direction and a 2.5 m-long monolithic wall in the frame direction. These walls comprised steel sub-frames covered by fiber-reinforced ceramic gypsum panels. Specific measurements were included during the construction of the system, i.e. introduction of horizontal and vertical gaps, telescopic joints. During the third testing phase, this system was demolished to be substituted by a masonry partition with low-damage detailing, i.e. 90 mm thick rocking vertical panels built inside an internal steel frame. Specific detailing was introduced to define the low-damage solution, i.e. steel frames separated by lateral gaps. More details on the two partition systems can be found in Bianchi et al. (2020).

External enclosures were then introduced to cover the structural skeleton during the last testing phase (*Option 2*): GFRC cladding systems in the frame direction and spider glazing in the wall direction. The cladding system consisted of Glass Fiber Reinforced Concrete (GFRC) panels with a central opening connected through stirrups to a steel frame which, in turn, was attached to the structural members using two restraint anchorages at the bottom and two sliding connections on the top. Concurrently, spider glazing walls covered the structural skeleton in the opposite direction and were composed of 10+1.52Pvb+10 mm laminated glass panels fixed to the structural skeleton using steel assemblies specifically manufactured. The façade system was made of articulated screws (hinges) consisting of

spherical joints inserted within holes in the glass panels, whereas these joints were bolted to spider connectors coupled to the structural system (edge beams and steel foundation).

Some photos of the non-structural elements tested during Phases 2 and 3 of the experimental campaign are presented in Figure 153.

4.1.3 Numerical prediction

Numerical modelling was implemented to predict the building performance under seismic loading. Specifically, a model based on a lumped-plasticity approach was defined and non-linear static and time-history analyses were performed using Ruaumoko3D (Carr, 2003).

A three dimensional lumped-mass and lumped-plasticity model was implemented as shown in Figure 154. The structural members were modelled as elastic (Giberson) components and the inelastic behaviour was concentrated at the connection interfaces. The material stiffness was assumed as per design values. The non-linearity of the system was concentrated into two inelastic rotational springs in parallel, representing the moment contributions to the rocking connections. The springs were zero-length elements, fixed between the rigid link of the column and the elastic beam element. The parameters of the hysteresis rules describing the springs were determined to match the moment-rotation relationships evaluated during the building design. The post-tensioned tendons/bars were represented by multi-linear elastic moment rotation curves, while for the mild steel (dissipator) springs a kinematic hysteresis (multi-linear plastic) was assigned. Additional (rotational) springs were introduced for simulating the out-of-plane behaviour of the hybrid connections. Rigid restraints were inserted at the base of the vertical members and, finally, the total building mass was applied to both structural directions and distributed across the nodes at each storey level.



Figure 153: Non-structural elements – fiber-reinforced gypsum partition (top, left), low-damage masonry infill wall (top, right), GFRC façade system in the frame direction (bottom, left), detail of the hinge spider-plate assembly (bottom, centre), assembly of the spider glazing façade in the wall direction (bottom, right)

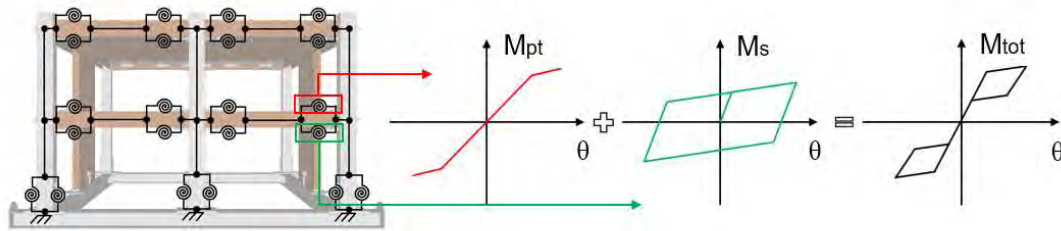


Figure 154: Numerical model of the Test Building implemented in Ruaumoko3D (Ciurlanti et al., 2020)

Non-linear static and push-pull analyses were initially performed to capture the quasi static monotonic and cyclic behaviour of the model. In Figure 155 the numerical push-over curves are compared to the analytical curves obtained from the DDBD procedure. Adopting a Capacity-Spectrum approach and converting the curves into acceleration/displacement values in the Acceleration-Displacement Response Spectrum (ADRS) domain, the performance points describing the expected seismic demand can be estimated for both building structural directions.

Ultimately, time-history analyses were performed to evaluate the maximum inter-storey drift and floor accelerations to be expected at each intensity level and earthquake motion to be simulated by the shaking table.

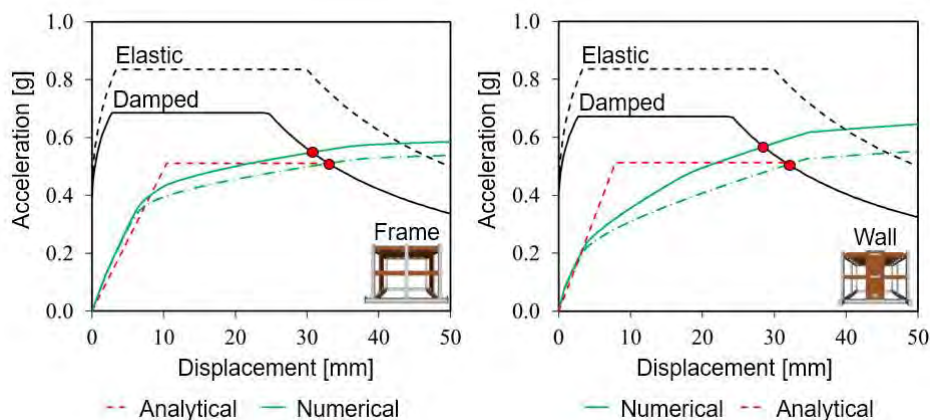


Figure 155: Push-over curves in the ADRS domain: Analytical (DDBD) vs. Numerical (w/o and with out-of-plane springs) (Ciurlanti et al. 2020)

4.1.4 Test setup

The monitoring system of the Test Building consisted of a combination of sensors: accelerometers, LVDT transducers, potentiometers, load cells, optical devices, strain gauges. The instrumentation was used to analyse the global behaviour of the building, to determine the local response of the structural connections and to study the seismic performance of the non-structural elements. Considering the instrumentation and channels available for the data acquisition, the monitoring system was designed trying to find the best solution during each testing phase.

During the first testing phase (*Skeleton Building*) all the sensors were used for monitoring the seismic response of the structural skeleton and its connections. At the foundation level, 4 accelerometers were used for measuring the acceleration of the shaking table in all the three directions and the impact effect at the base of a rocking column. LVDT transducers or potentiometers were introduced for monitoring the opening/closing of the gaps at the base of two opposite concrete columns and of the two timber walls (Figure 156, left). Concerning the two building levels, accelerometers were introduced for

monitoring the four lateral columns at the corners and the two timber walls in both longitudinal and transverse directions, as well as the vertical accelerations on the two timber-concrete floors. LVDT transducers monitored the opening/closing of the gaps at the beam-column interface for two opposite corners. Figure 156 (centre) shows one of the fully monitored beam-column joints.



Figure 156: Monitoring system – LVDTs/potentiometers at the base of a timber wall (left), load-cell, accelerometers and LVDTs monitoring a beam-column joint (centre), “Plug&Play” dissipaters (right)

2D optical devices were introduced to control the displacements of one structural frame, while load cells acquired the variation of post-tensioning force during the earthquake shakings for all the wire-strands and threaded bars. Finally, strain gauges were attached to selected external dissipaters for recording the force developing under seismic motions. The strain gauges were fixed to the internal fuse of the Plug&Play dissipaters using glue (Figure 156, right), and afterwards the dissipaters were completed introducing steel tubes filled using epoxy for anti-buckling action. Before bolting the Plug&Play into their anchorages, the monitored dissipaters were subjected to tensile testing, within the elastic range, with the aim of calibrating the strain gauges' measurements.

Due to the need for monitoring both the structural system and the internal partitions during the second testing phase (*Option 1*), some of the accelerograms and transducers were removed from the structural system and positioned on the internal gypsum partitions. The partition wall in the frame direction was fully monitored using LVDT transducers and accelerometers (Figure 157, top-left).





Figure 157: Monitoring system – sensors on the fiber-reinforced gypsum partition in the frame direction (top, left); LVDT transducers on a lateral low-damage masonry wall and accelerometer at the middle of the panel (top, centre and right); accelerometer at the middle of the GFRG panel (bottom, left) and LVDT monitoring the anchorage-column relative displacement (bottom, centre); transducers recording the glass/column and glass/glass displacements (bottom, right)

Concerning the last specimen configuration, due to the large number of components to be monitored some of the external façades and rocking walls were more thoroughly instrumented than others. Regarding the masonry rocking wall, two lateral walls were monitored using LVDTs for measuring the horizontal relative displacements between the column and the wall and between two adjacent walls as well as the vertical wall/floor relative displacements (Figure 157, top-centre), while an accelerometer was positioned at the centre of the wall for recording the out-of-plane accelerations (Figure 157, top-right). Regarding the cladding systems, accelerometers were installed for controlling both the in-plane (Figure 157, bottom-left) and the out-of-plane accelerations, while LVDTs were used for measuring the relative displacements between the cladding system and the column (Figure 157, bottom-centre), as well as between two panels. Finally, for the case of the spider glazing glass façade, the glass panel in the upper-left corner of a façade was fully monitored for the in-plane accelerations at the spider connectors and at the middle of the panel, and for the out-of-plane accelerations at the centre of the panel and along the diagonal direction. Furthermore, LVDTs were introduced for monitoring the relative displacements in the horizontal and vertical directions between the façade and the structural skeleton and between adjacent panels (Figure 157, bottom-right).

After the definition of the instrumentation plan, the test matrix was identified. Four levels of earthquake intensity were tested on the shaking table, namely: LS1, representing the Damage Control limit state (TR = 50 years); LS2, representing more than a Serviceability limit state (TR = 101 years); LS3, i.e. the Life-Safety limit state (TR = 475 years); and LS4, corresponding to the condition of TR = 1500 years, more than the Collapse-Prevention limit state. Then, 5 different ground motions were selected to be scaled at each of these seismic intensity levels: 3 Far-Field earthquakes (EQ1, EQ2, EQ3) and 2 Near-Fault records (EQ4, EQ5). An additional earthquake was introduced to represent a shaking motion with high vertical acceleration (EQ6). All the cited earthquakes are summarized in Table 18.

ID	Event	Station	Record ID	Year	M _w
EQ ₁	Cape Mendocino	Eureka – Myrtle & West	FF02	1992	7.0
EQ ₂	Landers	Morongo Valley	FF03	1992	7.3
EQ ₃	Darfield	REHS	FF15	2010	7.1
EQ ₄	Imperial Valley-06	El Centro Array #4	NF01	1979	6.5
EQ ₅	Christchurch	CCCC	NF13	2011	6.3
EQ ₆	L'Aquila	AQV	AQ	2009	6.3

Table 18: Selected earthquake motions

These ground motions were scaled using the methodology described within the NZS 1170.5 (2004). The scale factors k_1 were limited to the range of 0.33 - 3.0 and the first period T_1 of 0.4 s for the full-scale Prototype Building was used for implementing the procedure. Finally, the obtained records were further scaled in time for respecting the similitude requirements. The scaling factors k_1 of all the records were determined at the Life-Safety limit state (LS3), while the scaling SF at the different intensity levels was defined assuming that the average spectrum from the earthquakes at the Life-Safety limit state represented the reference condition with SF equal to 1.

The experimental campaign was carried out by incrementally increasing the seismic intensity in different directions and the test sequence was thus conceived as: 1) the building was subjected to 1D input motions in both the horizontal (X or Y) and vertical (Z) directions; 2) then, to 2D input motions in the horizontal direction (XY), and 3) finally to 3D input motions considering the combination of the XY input with the vertical excitation (XY+Z). In addition to the ground motion test sequence, a white noise motion was run before and after each intensity level for dynamic identification of the specimen.

4.1.5 Observation during testing

The shaking table tests confirmed the high potential of the integrated low-damage structural system. Regarding the structural skeleton, the system behaved as expected having a very high seismic performance, in this case proved through three-dimensional shakings and for the case of a timber-concrete frame-wall structure. However, due to the great number of earthquake motions (up to 400) and to the different system configurations analysed, the experimental testing led to expected damage conditions as well as to identify other damages to be taken into consideration when designing the structural detailing.

The yielding and consequent permanent deformations of the external dissipaters is one of the expected damage conditions for such type of structures. The inelastic demand is accommodated within these elements, representing the only component to be substituted after earthquake. During the seismic tests this damage state was achieved after many shakings and particularly during the Life-Safety test sequence (Figure 158, left). Other damage conditions for the structural system were related to: 1) the second building floor, due to the pounding effects on the lateral seismic beams which, in turn, after many tests brought to a rotation of these beams around their axis; 2) the central beam of the TCC floor which supported a large vertical loading due to the presence of 6 steel masses (around 3.6 tons) on its influence area, not only contributing to the horizontal seismic inertia but also imposing additional vertical inertial loads on the building floor.

Regarding the non-structural elements, they had an excellent seismic performance if compared to more traditional non-structural solutions, i.e. the damage conditions were achieved for higher values of seismic demand. However, some damage states were observed.

Damage to the fiber-reinforced gypsum partition was mainly related to diagonal cracking from the corners of the door openings (Figure 158, centre). These cracks formed during the LS1 sequence (less than 0.04 mm for an inter-storey drift of around 0.4%) and continued to open until the end of the tests (larger than 2 mm for inter-storey drift larger than 1%). Detachment of the silicone sealant and loss of adhesive in the corners of the partition wall was also observed from LS2, while initial crushing of the panels was noticed in some corners after the LS4 sequence.



Figure 158: Yielding of the external wall dissipaters (left), diagonal cracking of the gypsum partitions (centre), out-of-plane displacements of the glass panels (right)

Concerning the GFRC facades, these components had very high seismic performance during the earthquake shakings and no damage was observed after all the testing sequence. Regarding the spider glazing systems, no cracking of the glass panels was observed and they behaved very well in the in-plane direction. However, comparatively large displacements in the out-of-plane direction of the glass panels relative to each other (maximum of around 14 mm) were found (Figure 158, right). This was related to the yielding and elongation of the hinge bolt fittings subjected to high forces in this direction due to the inertia force provided by the glass panel.

Finally, for the low-damage infill wall, the seismic behaviour of this solution confirmed the high potential of applying low-damage detailing to such type of partition walls. Overall, the infill wall did not suffer any serious in-plane damage and did not lose its out-of-plane capacity, which was due to the in-plane integrity of the clay brick infill wall and the integrity of the sub-frame system. No damage was observed after the first two levels of seismic intensity, then initial detachment of silicone sealant in the corners as well as initial sliding of the masonry walls inside the frames was noticed. Only after the last seismic intensity sequence, cracking of the mortar surrounding one brick located in the upper-left corner of a rocking wall was observed.

4.1.6 Preliminary results

For the control of the shaking table, the compatible displacement and acceleration time series were sampled at 200 Hz through Fourier filters, both low and high pass, integration, differentiation and detrending. The digital signal processing, in both time and frequency domains, was carried out using the LNEC-SPA software. Shaking table data acquisition was collected via a high-rate acquisition system. All data was collected at a sample frequency of 4000 Hz to ensure high-quality sampling, which was then filtered and decimated to 200 Hz. Butterworth bandpass filtering was applied to all recorded acceleration data across the frequencies of 0.1-20 Hz to eliminate noise outside the range of interest.

Considering a specific earthquake, for each structural direction and building level, average values of the inter-storey drift/floor acceleration can be obtained from a preliminary data post-processing. Taking

into account all the sensors monitoring a direction/level and considering all the earthquake sequence of a determined intensity level (LS_i , $i=1,2,3,4$) the maximum values of these demand parameters can be calculated. The maximum values of the inter-storey drift ratios and the floor accelerations for each intensity level and building direction are summarized in Table 19 for *Option 1* and *Option 2* specimen configurations. In the same table, for the different tested non-structural components, the maximum accelerations and relative displacements between such element and the primary structure can be found.

Concerning the global performance, the specimen behaved as expected with demand parameters coherent with the ones calculated during the design process. Regarding the non-structural components, the in-plane behaviour confirmed the good response of these components due to the introduced non-structural detailing, while the out-of-plane accelerations allowed to define the relative amplification factors which were estimated to be in the range of 2-3 for all the non-structural systems when compared to the building levels, apart from the masonry infills where the amplification is found to be around 2.

Dynamic identification of the entire specimen and of the non-structural systems was carried out after each intensity level sequence, through white noise signals and using impact hammer inputs respectively. Elaborating the acceleration data through the transfer function method, the natural frequencies of the structure and of all the interior walls/envelopes can be identified and are listed in Table 20 for *Option 1* and *Option 2* specimen configurations.

Comparing the natural period for both building directions between *Option 2* and *Option 1* configurations it can be highlighted that the stiffness provided by the non-structural components reduced the natural periods, although the building mass increased.

Regarding the structural system, the decreasing value of frequency was mainly due to the yielding and consequent permanent deformations of the external dissipaters, nevertheless, this loss of capacity was mainly related to the high number of shakings to which they were subjected. Notwithstanding no failure of the dissipaters was observed, they were fully replaced between each testing phase of the experimental campaign, in order to re-establish the initial capacity for the structure.

The evolution of frequencies for the non-structural systems highlights their loss of capacity: 1) no reduction is observed for the glass panels, 2) very reduced reductions are noticed for the fiber-gypsum partition and the GFRG façade, while 3) for the infill partition wall a modification of the natural vibration is mainly identified when moving from LS_2 (more than Serviceability Limit State) to LS_3 limit state (Life-Safety).

Intensity Level		LS1		LS2		LS3		LS4	
Direction		Frame	Wall	Frame	Wall	Frame	Wall	Frame	Wall
<i>Option 1</i>									
Acceleration [g]	Table	0.17	0.20	0.29	0.25	0.35	0.38	0.35	0.43
	Floor 1	0.35	0.36	0.56	0.42	0.63	0.68	0.67	0.65
	Floor 2	0.55	0.67	0.86	0.82	0.90	1.49	1.16	1.48
	Partition	0.53	1.20	0.86	1.27	0.99	1.64	1.12	1.68
Inter-storey drift [%]	Level 0/1	0.46	0.49	0.92	0.69	0.96	1.54	1.14	1.11
	Level 1/2	0.40	0.39	0.79	0.56	0.86	1.61	0.95	1.07
Rel. displ. [mm]	Partition	5.49	1.23	12.82	1.67	14.01	9.72	12.75	6.48
<i>Option 2</i>									
Acceleration [g]	Table	0.14	0.17	0.22	0.17	0.34	0.32	0.41	0.47
	Floor 1	0.26	0.31	0.38	0.28	0.53	0.48	0.60	0.59
	Floor 2	0.44	0.54	0.46	0.50	0.91	0.97	1.08	1.24
	GFRC f.	-	0.79	-	0.79	-	1.12	-	1.52
	Glass f.	0.59	0.39	0.97	0.35	1.09	0.69	1.47	0.99
	Partition	0.40	-	0.55	-	0.82	-	0.96	-
Inter-storey drift [%]	Level 0/1	0.36	0.57	0.55	0.36	0.74	0.94	1.01	0.94
	Level 1/2	0.29	0.32	0.58	0.33	0.58	0.69	0.76	1.04
Rel. displ. [mm]	GFRC f.	3.97	-	5.52	-	9.21	-	12.15	-
	Glass f.	-	2.76	-	2.38	-	4.55	-	5.32
	Partition	-	3.02	-	1.93	-	6.53	-	9.91

Table 19: Summary of the maximum recorded quantities (Bianchi et al., 2020)

Configuration	Option 1			Option 2				
System	Frame	Wall	Gypsum wall	Frame	Wall	Masonry wall	GFRC panel	Glass panel
Initial	3.50	3.71	21.00	3.66	3.90	16.27	69.00	37.35
After LS1	3.37	3.12	20.00	3.53	3.87	16.02	69.00	37.05
After LS2	3.08	3.12	19.71	3.47	3.71	-	-	32.44
After LS3	3.03	2.59	19.06	3.35	3.32	15.43	68.75	26.17
After LS4	2.88	2.54	18.70	3.08	2.98	15.27	68.59	15.02

Table 20: Frequencies [Hz] of the first mode of vibration of the structure and the non-structural elements

4.1.7 Conclusions

This report described one of the H2020 SERA project transnational access experimental activities, involving 3D shaking table tests of a two-storey 1:2 scaled fully prefabricated dry-assembled building with two bay timber-concrete low-damage seismic frames and post-tensioned rocking dissipative timber seismic walls and comprising different low-damage or high-performance non-structural components (fiber-reinforced gypsum and masonry partitions/glass and GFRC façades). The aim of the project was to promote a research effort within the European environment for the development of an integrated low-damage building system.

An overview of the full experimental campaign was provided, which consisted of three different testing phases and specimen configurations, i.e. *Skeleton Building, Option 1* (*Skeleton Building* with internal gypsum partitions), *Option 2* (Integrated system made of an internal masonry wall and exterior envelopes). The overall research project was described, from the Test Building and its structural and non-structural detailing, to the test setup and to preliminary results. The dynamic shaking table tests confirmed the seismic performance of the low-damage skeleton for timber-concrete structures and proved the high potential for implementing an integrated low-damage or high-performance structural/non-structural building solution for the next generation of buildings. However, the observed damage conditions will suggest improvements to the system detailing to be applied and studied in future research.

4.1.8 References

- AS/NZS 1170 (2002). *Australian/New Zealand Standard 1170*, Standards Australia/Standards New Zealand.
- Baird A., Palermo A., Pampanin S. (2013). Controlling Seismic Response using Passive Energy Dissipating Cladding Connections, *2013 NZSEE Conference*, Wellington, New Zealand.
- Bianchi S., Ciurlanti J., Pampanin S., Perrone D., Filiatrault A. (2020). Seismic demand and performance evaluation of non-structural elements in a low-damage building system. *17th World Conference on Earthquake Engineering*, Sendai, Japan.
- Carr A.J. (2003). *Ruaumoko Program for Inelastic Dynamic Analysis – User Manual*. University of Canterbury, Christchurch, New Zealand.
- Ciurlanti J., Bianchi S., Pampanin S. (2020). Shake-table tests of a timber-concrete low-damage building: analytical/numerical vs. experimental results. *17th World Conference on Earthquake Engineering*, Sendai, Japan.
- Johnston H.C., Watson C.P., Pampanin S., Palermo A. (2014). Shake table testing of an integrated low-damage frame building, *2014 NZSEE Conference*, Auckland, New Zealand.
- NZS 1170.5 (2004). *Structural design actions – Part 5: Earthquake actions*. Standards New Zealand.
- Palermo A., Pampanin S., Buchanan A.H., Newcombe M.P. (2005). Seismic design of multi-storey buildings using Laminated Veneer Lumber (LVL), *NZ Society for Earthquake Eng. conference*, Wairakei, New Zealand.
- Palermo A., Pampanin S., Buchanan A. (2006). Experimental investigations on LVL seismic resistant wall and frame subassemblies, *1st ECEES*, Geneva, Italy.
- Palermo A., Pampanin S. (2017). *Pre-stressed beams or panels (3PT)*, United States Patent n. US9809979B2 (filed in 2014), Japan Patent n. JP6373975B2 (filed in 2014), Canada Patent n. CA2909402C.

- Pampanin, S. (2005). Emerging solutions for high seismic performance of precast -prestressed concrete buildings, *Journal of Advanced Concrete Technologies*, 3(2):202–222.
- Pampanin S. (2012). Reality-check and renewed challenges in earthquake engineering: implementing low-damage structural systems – from theory to practice. *Bulletin of NZ Society and Earthquake Engineering*, 45(4):137–160.
- Pampanin S. (2015). Towards the “Ultimate Earthquake-Proof” Building: Development of an Integrated Low-Damage System. Perspectives on European Earthquake Engineering and Seismology (A. Ansal, ed.), *Geotechnical, Geological and Earthquake Engineering 39*, Springer Nature, Switzerland.
- Pampanin S., Palermo A., Buchanan A., Fragiocomo M., Deam B. (2006). Code provisions for seismic design of multi-storey post-tensioned timber buildings, *CIB Workshop*, Florence, Italy.
- Pampanin S., Marriott D., Palermo A., and New Zealand Concrete Society (2010). *PRESSS Design Handbook*, Auckland, New Zealand.
- Pampanin S., Palermo A.G. and Buchanan A. (2013). *Structural Timber Innovation Company Inc., Post-Tensioned Timber Buildings – Design Guide*, Christchurch: Structural Timber Innovation Company.
- Pampanin S., Ciurlanti J., Bianchi S., Perrone D., Palmieri M., Grant D., Granello G., Palermo A., Filiatrault A., Campos Costa A., Candeias P.X., Correia A.A. (2020). Enhancing seismic safety and reducing seismic losses: overview and preliminary results of SERA Project – 3D shaking table tests on an integrated low-damage building system. *17th World Conference on Earthquake Engineering*, Sendai, Japan.
- Pourali A., Dhakal R.P., MacRae G.A., and Tasligedik A.S. (2017). Fully-floating suspended ceiling system: experimental evaluation of the effect of mass and elastic isolation, *16th World Conference on Earthquake Engineering*, Santiago, Chile.
- Priestley M.J.N., Sritharan S., Conley J.R., and Pampanin S. (1999). Preliminary Results and Conclusions from the PRESSS Five-Story Precast Concrete Test Building, *PCI Journal*, 44(6):42–67.
- Priestley M.J.N., Calvi G.M., Kowalsky M.J. (2007). *Direct Displacement-Based Seismic Design of Structures*. 1st edition, IUSS Press, Pavia, Italy.
- Structural Timber Innovation Company (2012). *Design Guide Australia and New Zealand – Timber Concrete Composite Floor Systems*, STIC, New Zealand.
- Tasligedik A.S., Pampanin S., Palermo A. (2014). Low damage seismic solutions for non-structural drywall partitions, *Bulletin of Earthquake Engineering*, 13(4):1029–1050.
- Tasligedik A.S., and Pampanin S. (2016). Rocking Cantilever Clay Brick Infill Wall Panels: A Novel Low Damage Infill Wall System, *Journal of Earthquake Engineering*, 21(7):1023-1049.

4.2 Project #7 – Seismic Response of Masonry Cross Vaults: shaking table tests and numerical validations

Authors

C. Calderini⁽¹⁾, N. Bianchini⁽²⁾, M. Rossi⁽¹⁾, N. Mendes⁽²⁾, P. Lourenço⁽²⁾, P. Candeias⁽³⁾, A.A. Correia⁽³⁾, A. Campos Costa⁽³⁾, P. Casadei⁽⁴⁾

⁽¹⁾ University of Genoa, Genoa, Italy

⁽²⁾ *University of Minho, Guimarães, Portugal*

⁽³⁾ *LNEC, National Laboratory for Civil Engineering, Lisbon, Portugal*

⁽⁴⁾ *Kerakoll Ibérica S.A., Spain*

4.2.1 Introduction

The observation of damage caused by past seismic events demonstrates the high vulnerability of historic masonry buildings. Several types of mechanisms can be activated during an earthquake. The mechanisms that involve the horizontal structural elements are dangerous and fundamental for the seismic performance of buildings. Thus, these types of mechanisms should be better investigated (Rossi, 2015).

Widely spread among monumental masonry buildings (mainly in churches and palaces), masonry cross vaults are some of the most vulnerable horizontal structural elements. Acting as both a ceiling and a structural horizontal diaphragm with significant mass, vaults' mechanical behaviour affects the overall seismic response of buildings, in terms of strength, stiffness, and ductility. Moreover, their local damage and collapse may produce significant losses in terms of cultural assets and casualties.

Because of these reasons, the seismic assessment and the seismic vulnerability reduction of masonry vaults are interesting topics, which deserve attention and care by the research community. The need of care is associated to several open issues that researchers and practitioners have to face when dealing with masonry cross vaults. In fact, many authors highlighted the difficulties on analysing the complex 3D behaviour of existing masonry cross vaults. These structures may be damaged due to the interaction with adjacent structural elements or with the counteraction system (such as flying buttresses or foundations). Moreover, in general, there is not the possibility of knowing their thickness and the different sizes of cross vaults may lead to difficult comparisons from the structural point of view (Bertolesi et al., 2019). In the last twenty years, giant steps were certainly made in the safety assessment of masonry structures and the design of interventions in heritage buildings. However, there is still a lot to be done.

Most of the studies, in the past, were oriented to the description of the structural response of vertical masonry structures, disregarding the role of horizontal diaphragms. These were neglected in the analyses (since considered very deformable, such as the case of timber floors), or considered infinitely stiff (since substituted by, or reinforced with, RC elements). Conservation and safety issues pushed towards a different approach: on the one hand, the substitution of timber floors with RC floors, as well as the reinforcement of masonry vault with concrete “jackets” is not acceptable anymore; on the other hand, recent earthquakes showed that the introduction of excessively rigid diaphragms may compromise the structural response of the masonry building. Today, improved structural analyses and assessment procedures requires improved models for diaphragms. This is one of the most crucial issues in structural masonry modelling and analysis.

Another large quantity of past studies was oriented to the description of the behaviour of masonry arched structures (arches and vaults). These studies were mainly focused on the analysis of special buildings, such as churches and monumental structures, and were mainly based on the study of the equilibrium of rigid blocks, disregarding the deformability of such structures in the elastic and inelastic field and the limited strength of the material in compression. Moreover, as already stated, they considered the 2D behaviour of the arch/vault only, disregarding their 3D behaviour involving shear/sliding mechanisms. Today, such approaches should be improved, in particular for complex 3D vaults such as the ones considered in this research project.

Two PhD studies which have been recently developed, namely the work carried out by Gaetani (2016, 2017) and Rossi (2015, 2017), represent the starting point of this investigation work.

Gaetani's work, performed at the University of Sapienza and University of Minho, corresponds to a phased study based on a wide literature review, numerical analyses and experimental activities with the aim of an expedite assessment of the seismic capacity and the failure mechanism for groin vaults. Moreover, a standard limit analysis code was implemented. Rossi's research, performed at the University of Genoa, presents the experimental investigation of groin vaults, subjected to static actions, with the use of a small-scale mock-up.

Previous investigations, from the state-of-art until the experimental campaigns and the theory of scaled tests design lead up to the definition of the shaking table tests, performed at the National Laboratory for Civil Engineering (LNEC) in Lisbon, Portugal, in the framework of the transnational activities of the H2020 SERA project. The preparation and operation of the shaking table follows standard protocols to achieve the target motions, as proposed by Candeias et al. (2017).

In particular, three sets of shaking table tests were planned:

1. Tests on a 1:5 scale cross vault made of 3D-printed blocks assembled with dry joints (Rossi, 2015): to validate the efficacy of static tests on reduced scale mock-ups, performed in earlier studies, and to describe the seismic dynamic response of masonry vaults;
2. Tests on a 1:1 scale model of a brick unreinforced masonry cross vault: investigating the behaviour of brick masonry cross vaults under different seismic inputs, in terms of damage, displacement capacity and peak acceleration;
3. Tests on a 1:1 scale model of a brick reinforced masonry cross vault: to evaluate the effectiveness of reinforcing techniques to repair the vaults tested in b).

The originality and innovation of the proposed research lies in several aspects:

- Despite both the structural and architectural relevance of masonry cross vaults, only a few experimental tests were carried out and can be found in the literature;
- The test setup was designed in order to reproduce the diaphragm shear response of cross vault (which is very difficult to model dynamically). Moreover, since the setup considers the vault only, it allows to disregard the "filter effect" produced by its supporting structures (piers or columns) on the dynamic action applied;
- The innovativeness of the proposed strengthening technique, since based on highly efficient and compatible materials. The efficiency of the technique was never tested on masonry cross vaults in the dynamic field.

The theoretical interpretation of the results, aims not only to calibrate advanced non-linear numerical models but also to validate/propose safety assessment procedures to be implemented in European codes.

The broader impacts of the research regard the safety and preservation of historical masonry buildings in the European earthquake prone areas. It is well known that policies for the preservation of cultural heritage, in the structural field, are based on two main lines of development: the improvement of safety assessment procedures and the improvement of strengthening techniques. The idea is that, for heritage buildings, the safety should be guaranteed with "minimum intervention", which is one of the pillars of conservation theory. In this framework, the more reliable the safety assessment procedures are, the less interventions are needed; the more efficient the strengthening interventions are, the less interventions are required.

In conclusion, by improving the knowledge and the modelling/analyses approaches of vaulted masonry structures, this research contributes to a better safety assessment of heritage buildings and to a better

design of strengthening interventions, thus contributing to an improvement of the safety and preservation policies of heritage buildings in the EU.

4.2.2 Test specimens

Reduced scale vault 1:5

The tests were performed on a 1:5 scale model made by 3D printed plastic blocks with dry joints (Figure 159). The same mock-up was already tested under static conditions by Rossi (2015; 2017). The blocks were 3D printed with the SLS (Selective Laser Sintering) technology: an efficient method to generate small-scale models with high geometrical accuracy (0.1 mm), low cost and short time of production. Moreover, it allows for the production of blocks with large stiffness (to guarantee the rigid block assumption and the repeatability of the tests by minimizing the damage due to impacts) and large friction (to inhibit the sliding between blocks).

The shape and the geometry of the scaled model derived from the intersection of two semi-circular barrel vaults, generating a squared base groin vault with a net span of 0.620 m and a rise of 0.225 m. The model is made up of 1132 blocks. The standard blocks were designed considering the typical dimensions of clay bricks, which are $0.06 \times 0.12 \times 0.24 \text{ m}^3$ in order to keep a classic bond stereotomy of medieval groin vaults.

Blocks of different dimensions are placed along the outer edges of the webs to guarantee the offset of the joints. Blocks' shape is slightly trapezoidal in order to compensate for the absence of mortar between them. Special care was taken to design the stereotomy of the elements located along the diagonals to guarantee the correct interlocking between adjacent webs. Each block was identified by a numerical code, in order to easily rebuild the model after each test.

Full scale vault

The physical full-scale groin vault mock-up and the testing setup designed for the shaking table tests is herein described. The mock-up's geometry and test setup were designed taking into account the dimensions and load capacity of the 3D LNEC shaking table. The brick vault model's size is about $3.5 \times 3.5 \text{ m}^2$ in plan and includes two semi-circular barrel vaults with a net span of 2.9 m, with a rise of 0.80 m and constant thickness of 0.12 m. A plan view and a lateral view of the mock-up are shown in Figure 160 and Figure 161, respectively. On the side, simulating the lateral continuous wall, the vault's supports are built on two masonry piers which are clamped on a RC slab placed on the shaking table. In order to increase the piers' stiffness and to avoid relative displacements between the two piers, a steel frame made with IPE and UPN profiles is also introduced.

On the opposite side that simulates the colonnade, the two supports are left free to move in all directions on a movable system of wheels. Moreover, steel masses are added to the supports (between the vault's abutments and the wheels) in order to simulate the weight of the roof and the roof's supporting wall. In addition, in order to avoid any rotational movement of the supports, the four abutments are linked to each other by couples of steel rods with rods ends characterized by plain spherical bearings. An overlying infill is built in correspondence of the four vault's corners in order to cover 50% of the total height of the vault. To avoid local failures at the supports, steel plates were added along the height of the supports and the infill. The steel profiles also aim to increase the stiffness of the supports and prevent their deformation. The total mass of the mock-up, excluding the steel rods, is equal to 5.15 tons.

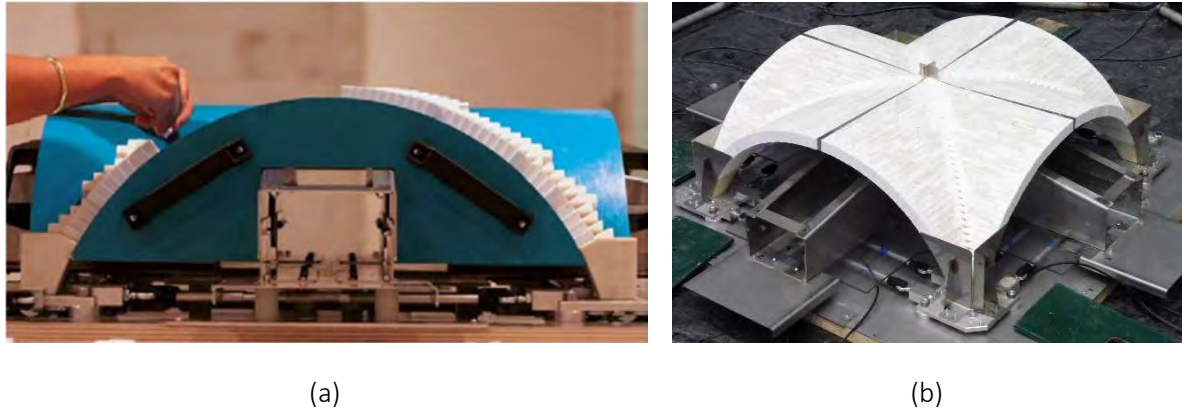


Figure 159: (a) Details of the construction on the plywood scaffolding and (b) the model fully assembled

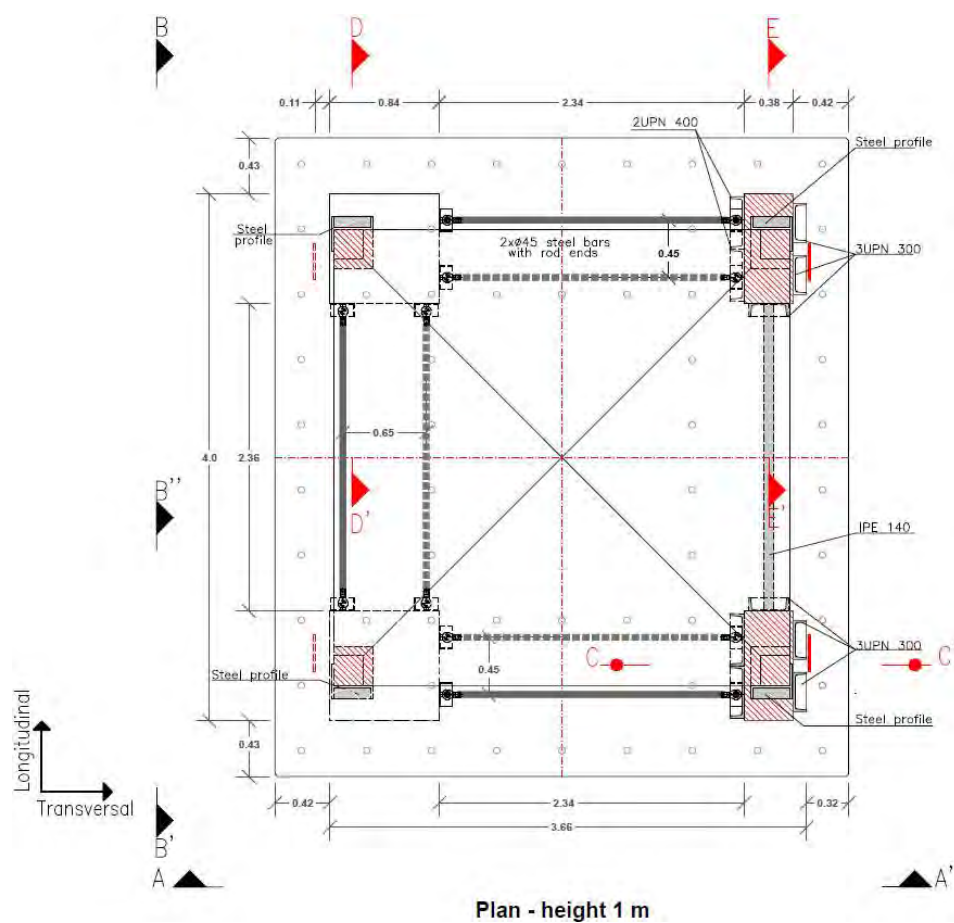


Figure 160: Plan view of the model (dimensions in meters). In red the elements made of masonry, in grey the elements made of steel

The strengthened configuration adopts the performance of Textile Reinforced Mortar (TRM) technique, used as retrofitting of the full-scale model using the mesh GeoSteel Grid 200 and the hydraulic lime mortar GeoCalce® G Antisismico, provided by Kerakoll. The shaking table tests are performed on the model, after establishing a level of admissible damage, without reaching the collapse, in stepwise increasing earthquake inputs, with intertwined dynamic identification tests. The TRM is applied to the extrados of the vault as introduced in Figure 162. This approach aims at evaluating the performance of the retrofitted vault to quantitatively estimate the effect of the strengthening technique.

This task is very important to partially overcome the lack of knowledge in the evaluation of the strengthening techniques in masonry cross vaults. The majority of retrofitting jobs, in fact, are implemented on arches or barrel vaults.

It is important to mention that dynamic identification tests are the tool for evaluating the dynamic properties of the structures and repeating them at the various stages of the shaking table testing allows to determine the evolution of dynamic properties of the mock-up.

Moreover, the material properties are obtained by performing the following complete set of material characterization tests:

- Determination of consistence of fresh mortar (by flow table) – EN 1015-3 (CEN, 2004);
- Bulk sampling of mortars and preparation of test mortars – EN 1015-2 (CEN, 1999);
- Flexural strength of hardened mortar – EN 1015-11 (CEN, 2006);
- Compressive strength of hardened mortar – EN 1015-11 (CEN, 2006);
- Testing of hardened concrete to depict the secant modulus of elasticity in compression – EN 12390-13 (BS EN 12390-3:2009, 2011);
- Axial compression tests on unconfined masonry – EN 772-1 ASTM D2938-95 (ASTM 2938-95);
- Diagonal compression tests to depict the tensile strength of masonry – ASTM E519-02 LUM B6 (RILEM TC – LUM B6, 1991);
- Determination of initial shear strength (triplets tests)– EN 1052-3 (CEN, 2004).

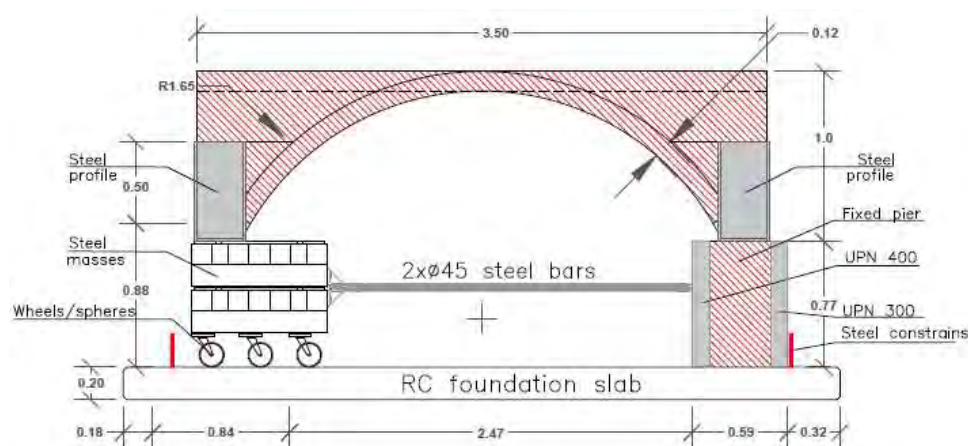


Figure 161: View A-A' of the model built on a RC slab fixed to the shaking table (dimensions in meters). In red the elements made of masonry, in grey the elements made of steel

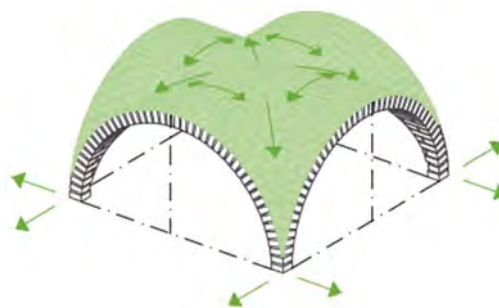


Figure 162: Extrados and intrados disposition of TRM on the masonry cross vault (Kerakoll Guidelines)

4.2.3 Numerical simulations

Several numerical models were built considering, namely, the finite element method, with macro and micro-modelling strategies, and discrete element methods, reproducing both the reduced scale and full-scale vaults. The experimental tests are reproduced in the Diana finite element environment (DIANA, 2019). After a detailed calibration of the models, the final aim is to compare the previous static investigation carried out by Rossi et al. (2017) with the dynamic tests from both experimental and numerical points of view.

The same type of analyses and configurations used in the FEM analysis are adopted for the DEM numerical modelling into the 3DEC software (Itasca, 2014). The comparison between the two approaches is the early result of this task; the comparison is suitable if the numerical model is properly calibrated considering the experimental results. The calibration phase follows the model updating criterion in order to keep the same dynamic properties of the mock-up: several eigenvalue analyses are performed on the FE and DE models to maintain the same natural frequencies and mode shapes, determined during the dynamic identification tests of the setup.

Nonlinear dynamic analyses are useful to compare the results obtained by the two different strategies and by the experimental campaign, using the same ground motion (Emilia's earthquake). The comparison takes place in terms of maximum capacity, failure mechanism, displacements, and hysteretic behaviour. The amplification factor along the height of the structure is not considered in the experimental campaign, while from the numerical point of view this aspect is investigated further.

What was done for the unreinforced model, is replicated for the strengthened configuration also from the numerical point of view. Table 21 summarises the numerical simulations performed.

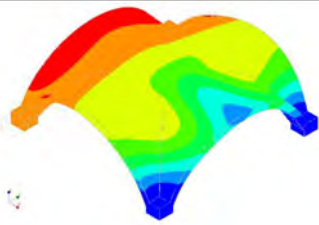
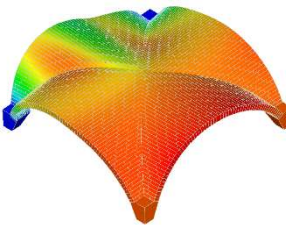
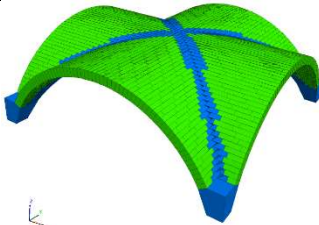
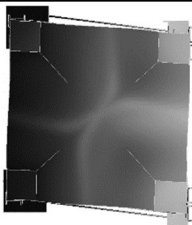
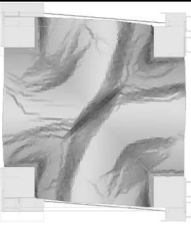
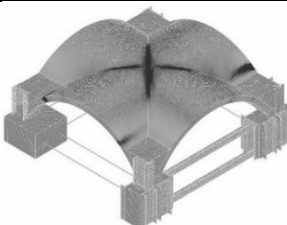
Reduced model 1:5			
	Macro-model – FEM	Micro-model – FEM	Discrete element method
Analyses			
	Modal analysis	Pushover & Time history analysis	Pushover & Time history analysis
Full scale model			
	Macro-model – FEM		
Analyses			
	Modal analysis	Pushover	Time history analysis

Table 21: Summary of the models and of the main analyses performed

Numerical simulations are performed to assess the efficacy of different modelling strategies and analysis techniques. The final aims are to improve the safety assessment procedures proposed for historic masonry buildings in Eurocode 8 – Part 3 and to provide better seismic assessment techniques

and strengthening measures. The main results of the comparison between both modelling approaches allows to define the contribution of the parameters on the local failures of masonry cross vaults, as a function of the type and quality of the masonry, masonry bond and knowledge level of the properties of the structure.

Finally, parametric numerical analyses are performed on the basis of calibrated models in order to define performance indicators for the TRM solutions.

4.2.4 Test setup

Reduced scale vault 1:5

The setup was carefully designed in order to get the shear failure on the mock-up, with similar conditions to the real prototypes and measuring the relevant effects, which are necessary for its performance assessment (Figure 163). The abutments $p1$ and $p2$ were anchored to the ground with bolts, while $p3$ and $p4$ were left free to move on the flat surface.

The instrumentation of the small-scale groin vault was defined according to the expected behaviour of this kind of mock-up under seismic actions. Therefore, the bases, the movable plates and the lateral arch (west side) are of interest. Due to the reduced geometrical dimensions of the model, specific equipment was implemented. One linear variable displacement transducer ($LDVT_1$), located at the NW corner, measuring the relative longitudinal displacement of the movable piers. Six piezoelectric accelerometers (named PCB_{1x} , PCB_{1y} , PCB_{1z} , PCB_{2x} , PCB_{2y} , PCB_{2z} in Figure 163) were placed at the bottom of the vault to evaluate the response of the fixed plate, while five variable capacitance unidirectional accelerometers (VCO_{1x} , VCO_{2y} , VCO_{3x} , VCO_{4y} , VCO_{5z}) were placed on the vault itself, mainly due to the fact that their dimensions and weight are compatible with the dimension of the blocks. Moreover, two optical cameras are used to record the response of the key of the western arch and of the movable piers respectively along the plane xy (H_{1xy}) and yz (H_{2yz}).

Figure 163 shows the location of the reduced scale model placed on the shaking table of LNEC and the instrumentation plan.

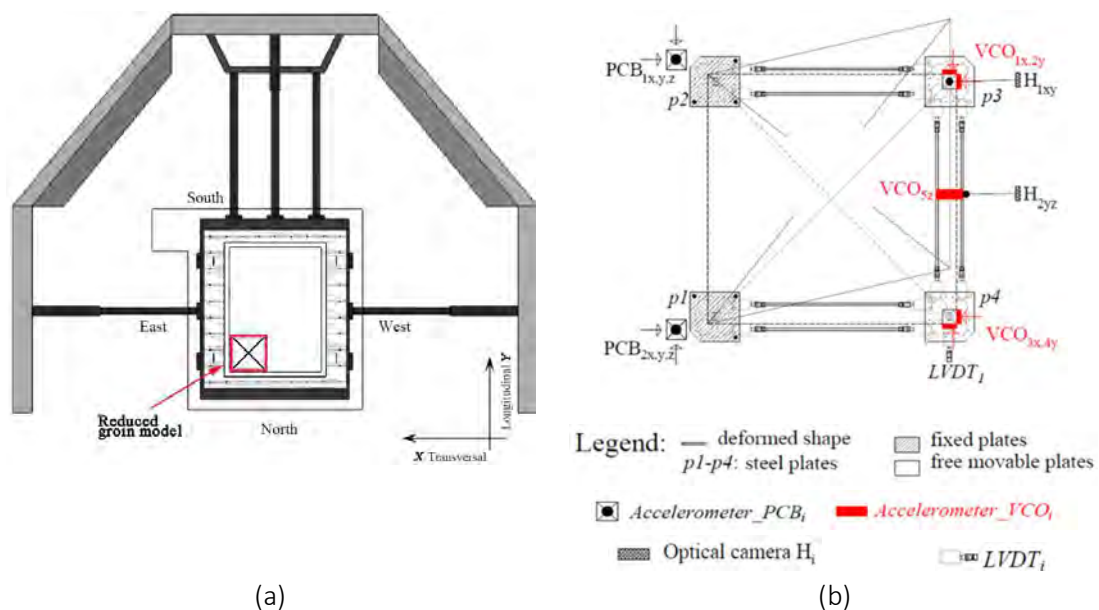


Figure 163: Shaking table: (a) plan with the location of the model; (b) Instrumentation setup: top view

Two video cameras are placed to record the tests, one exactly at the top of the model and one located in front of the East façade on a tripod outside of the shaking table. The video recordings are used to evaluate the collapse mechanism.

The first set of tests considers three seismic inputs respectively: base impulse signal (retracing the same input used by Gaetani (2016), the natural input referring to the Emilia Romagna earthquake (2012), and an artificial seismic motion, considering the seismicity of Emilia Romagna's territory.

The first type of test, the base impulse signal, is particularly suitable for rocking-type structures, such as dry-joint masonry vaults, due to the fact that they are particularly vulnerable to impulse loading (Dejong et al., 2008). It consists in a sine-shaped pulse, accurately processed to meet the features of the shaking table. The goal of this study is to define the capacity of the vault under base impulse excitation characterised by a very short-period motion and later on validate the FE numerical model based on rigid infinitely resistant voussoirs and friction interface elements, following an approach similar to the one carried out by Gaetani (2016).

The second kind of tests are useful mainly to compare the capacity and the mechanisms with the natural ground motion represented by Emilia's earthquake in 2012. The correct amplification factor needed for the similitude of the 1:5 scaled model is considered.

This mock-up is tested using Emilia Romagna earthquake (natural and artificial) along the longitudinal direction of the vault (Figure 164) to compare these two inputs. Afterwards, a sine-shaped pulse, shown in Figure 165, is applied to the reduced mock-up.

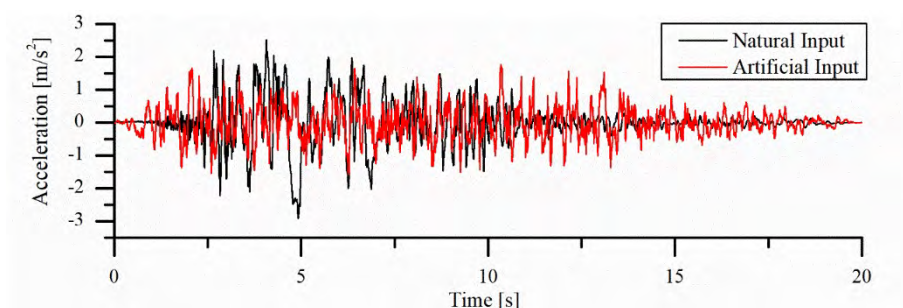


Figure 164: Acceleration time history recorded by Mirandola seismic station along the longitudinal (May 29th) and an artificial input created by the code spectrum for Mirandola's Municipality

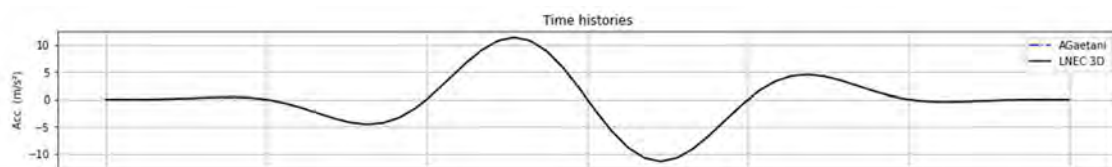


Figure 165: Base input shape impulse motion

Full scale vault

Figure 166 shows the full-scale model in a 3D AutoCad environment. As previously mentioned, the shake table tests on a 1:1 scale model of a brick masonry cross vault consider two configurations: unreinforced and strengthened, using only the Emilia Romagna earthquake (Figure 167). This seismic

input is applied in increasing intensity stages, in order to control the level of damage, until the moment when the structure needs a strengthening intervention.

In the full-scale model, and differently from the assumptions for the reduced-scale model, the weight of the roof over the vaults and the weight of the columns above the supports of the vault were also taken into account, considering four additional steel masses with dimensions 0.84 m x 0.84 m x 0.27 m and 1.2 tons each, provided by LNEC.

In order to replicate the expected shear failure of the specimen on the shake table, the supports of the vault have asymmetric boundary conditions. The fixed lateral piers have all the three translations constrained, while the steel masses have only the vertical direction fixed, allowing the movement in the longitudinal and transverse direction when the model is subjected to horizontal static and dynamic loads.

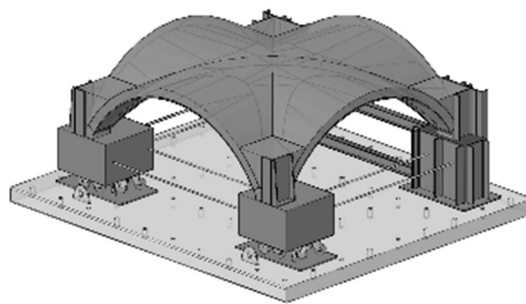


Figure 166: Full-scale model defined for this work

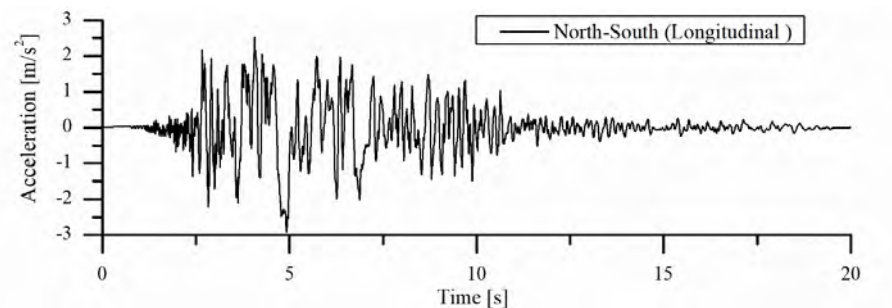


Figure 167: Acceleration time history recorded by Mirandola seismic station along the longitudinal (May 29th)

4.2.5 Observation during testing

The collapse mechanism obtained for 75% of the Mirandola earthquake applied in the longitudinal direction (from North to South) on the reduced mock-up is herein shown and evaluated. The collapse mechanism is discussed using a sequence of photos, where the number and locations of the hinges is also evaluated. Figure 168 presents the more intense phase before the collapse of the vault, shown at a rate of five frames per second, with the camera placed at the top of the central key of the model.

The key of the vault is the first to collapse, due to the low compressive stresses between blocks. The fall of these blocks do not interfere with the development of the shear failure, which is the first to occur at 2 s while the hinges are starting to appear. The external edges (North and West side) continue to

stand, even when the other sides already fell down. The location of the hinges was observed from the East façade, where it is possible to notice the similarities with the quasi-static tests (Figure 169).

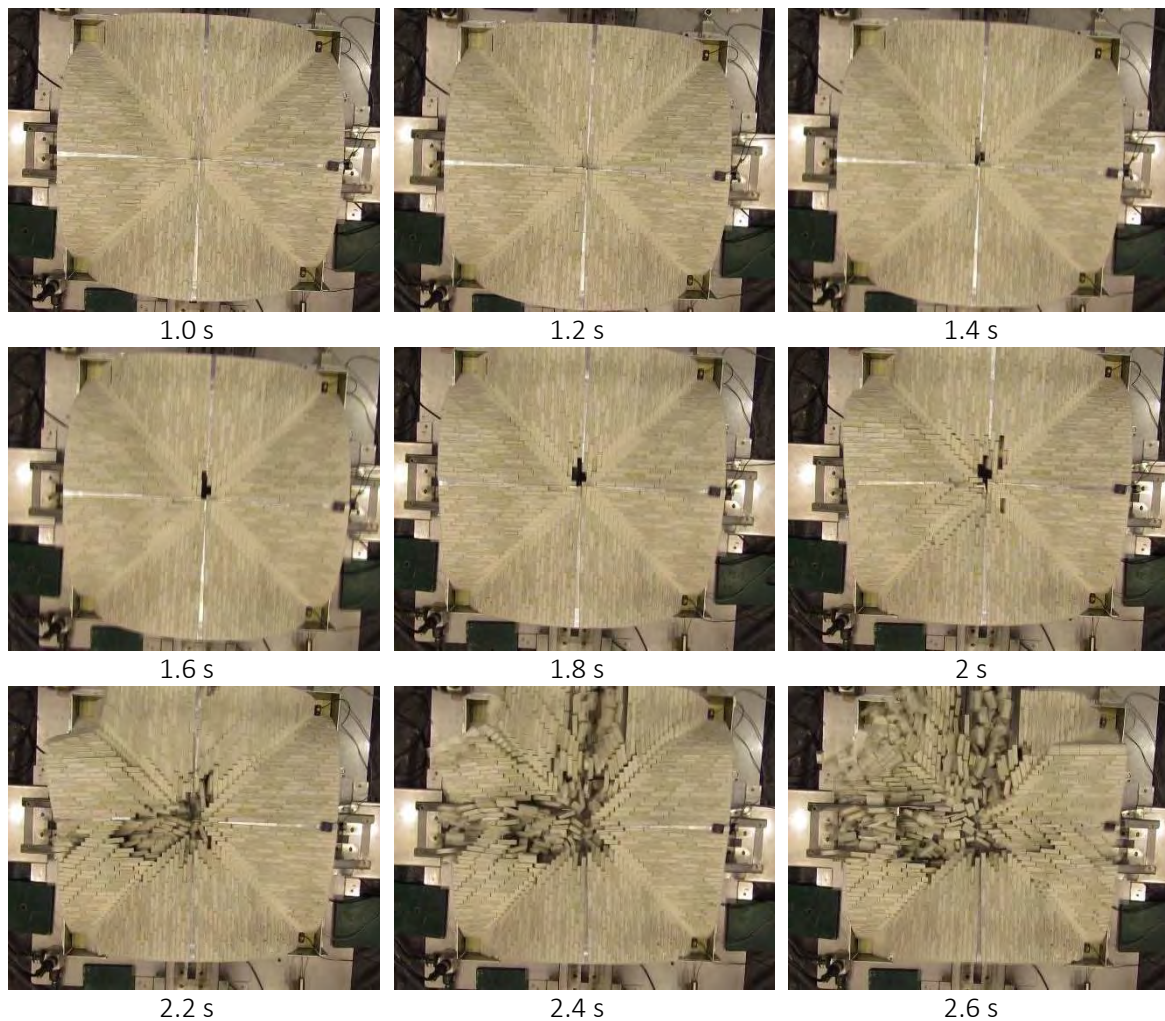


Figure 168: Damage progression of the mock-up during the intense phase of the seismic input 75% (5 frames/s). (Left side: fixed supports; right side: movable supports)

The steel plates at the corners make the boundaries of the shell of the vault stiffer and, therefore, two hinges take location where the effects of the steel plates do not act anymore. This is in agreement with the prediction of Oppenheim (1992) and De Lorenzis et al. (2007) based on the minimum energy formulations. The arch mechanism is clear (four-hinges mechanism) and it is mainly associated to the edge side where the supports are fixed and the response is more rigid (Figure 169).

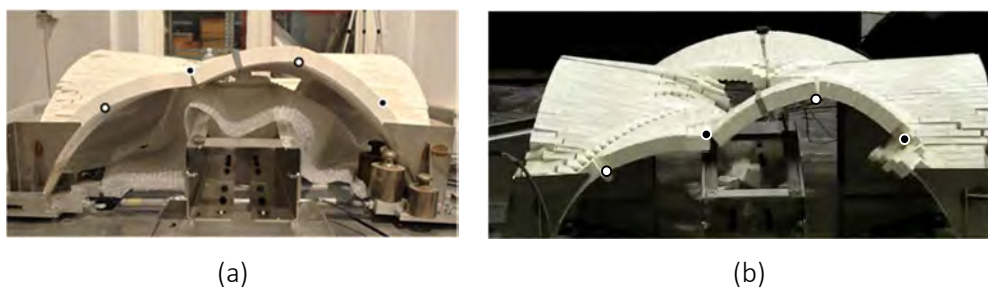


Figure 169: Comparison between the (a) quasi-static tests performed by Rossi (2015) and (b) the shaking table tests

4.2.6 Preliminary results

The dynamic identification tests on the reduced-scale vault allow to evaluate the variations on modal properties of the model as function of the construction process and amplitude of the seismic action. The results of the shaking table tests were evaluated and compared with the quasi-static tests, leading to the following conclusions: (a) the location of the hinges is similar and clearly evident from the side where the structure is more rigid (East side); (b) the shear failure was obtained showing, as expected, the main concentrations of damage along the rib of the vault; (c) the capacity of the structure is higher than the capacity obtained from the quasi-static tests, namely about 1.5 times, showing a spectral amplitude at collapse equal to 0.55 g, not taking into account the amplification in elevation on the structure. More comprehensive numerical works are ongoing.

The eigenvalue analysis performed on the full-scale vault, allowing to detect the first longitudinal mode, associated the shear failure of the vault with a first mode frequency equal to 7 Hz. Furthermore, the direct comparison between static and dynamic results lead to the following conclusions: (a) the static configuration was used to design the first setup of the model, but it was not indicative of the expected dynamic response that occurs on the shaking table; (b) the shear failure was obtained and the main concentrations of damage occurred along the rib of the vault; (c) the role of the infill brought a positive contribution to avoid a localized damage close to the supports, since it increased the effective thickness of the vault; making the model stiffer and more resistant.

4.2.7 Conclusions

This research project wanted to assess the seismic performance of masonry cross vaults through the use of a replicable scaled mock-up (1:5) made by 3D printed plastic blocks with dry joints and through the use of a full-scale brick masonry cross vault before and after the application of the strengthening with TRM technique. The main focus is the study of the shear failure along the shell of the vault itself which very often occurs during earthquakes in monumental buildings (e.g. churches and palaces).

Shaking table tests on both the models and numerical validations (with the finite element method and the discrete element method) are the tools considered to achieve the objectives of the project.

From the experimental and numerical studies related to the reduced scale vault, it was possible to observe a systematic location of the hinges in concordance with the Heyman's theory. The shear failure was obtained by designing specific boundary conditions, showing, as expected, the main concentrations of damage along the rib of the vault. The capacity of the structure under dynamic loading is higher than the capacity obtained from the quasi-static tests, previously performed by Rossi et al. (2017).

The expected outcomes cited in the previous deliverables have been satisfied, namely: evaluation of the maximum acceleration applicable to cross vaults, evaluation of the diaphragm stiffness and ultimate displacement capacity of cross vaults, identification of the damage mechanisms, evaluation of the role of the seismic input on the dynamic response of these vaults, comparison between static and dynamic tests and evaluation of the influence of the test type.

Additionally, in the full-scale vault, a thorough design was fundamental to assure the occurrence of shear behaviour along the shell of the vault. An iterative process was necessary to achieve the best design to match with LNEC's shaking table characteristics. Moreover, the importance of the application of a compatible strengthening technique allows to evaluate the efficiency of TRM technique, covering the lack of knowledge in this field.

In conclusion, by improving the knowledge and the modelling/analyses approaches of vaulted masonry structures, this research contributes to a better safety assessment of heritage buildings and to a better

design of strengthening interventions, thus contributing to an improvement of the safety and preservation policies of heritage buildings in the EU.

4.2.8 References

- ASTM 2938-95 (1995). *Standard test method for unconfined compressive strength*, ASTM.
- Bertolesi E., Adam J.M., Rinaudo P., Calderón P.A. (2019). Research and practice on masonry cross vaults – A review, *Engineering Structures*, 180:67–88. DOI: 10.1016/j.engstruct.2018.10.085.
- BS EN 12390-3:2009 (2011). *Testing hardened concrete*, British Standards.
- Candeias P.X., Campos Costa A., Mendes N., Costa A.A., Lourenço P.B. (2017). Experimental Assessment of the Out-of-Plane Performance of Masonry Buildings Through Shaking Table Tests, *International Journal of Architectural Heritage*, 11(1):31–58. DOI: 10.1080/15583058.2016.1238975.
- CEN (1999). *Methods of test for mortar for masonry – Part 2: Bulk sampling of mortars and preparation of test mortars*, European Committee for Standardization.
- CEN (2004). *Methods of test for mortar for masonry – Part 3: Determination of consistence of fresh mortar (by flow table)*, European Committee for Standardization.
- CEN (2006). *Methods of test for mortar for masonry – Part 11: Determination of flexural and compressive strength of hardened mortar*, European Committee for Standardization.
- DeJong M. J., De Lorenzis L., Adams S., Ochsendorf J. A. (2008). Rocking Stability of Masonry Arches in Seismic Regions. *Earthquake Spectra*, 24(4):847–865. DOI: 10.1193/1.2985763.
- De Lorenzis L., Dimitri R., La Tegola A. (2007). Reduction of the lateral thrust of masonry arches and vaults with FRP composites, *Construction and Building Materials*, 21:1415–1430. DOI: 10.1016/j.conbuildmat.2006.07.009.
- DIANA (2019). *DIANA finite element analysis; Documentation release 10.3*, Edited by F. Denise and M. Jonna, DIANA FEA BV, Delft, The Netherlands.
- Gaetani, A. (2016). *Seismic Performance of Masonry Cross Vaults: Learning from Historical Developments and Experimental Testing*, PhD Thesis, University of Minho.
- Gaetani A., Lourenço P.B., Monti G., Milani G. (2017). A parametric investigation on the seismic capacity of masonry cross vaults, *Engineering Structures*, 148:686–703. DOI: 10.1016/j.engstruct.2017.07.013.
- Itasca (2014). *UDEC – Universal Distinct Element Code Version 6.0*, Itasca Consulting Group Inc., Minneapolis, USA.
- Oppenheim I.J. (1992). The masonry arch as a four-link mechanism under base motion, *Earthquake Engineering and Structural Dynamics*, 21(11):1005–1017. DOI: 10.1002/eqe.4290211105.
- Rossi M. (2015). *Evaluation of the seismic response of masonry cross-vaults*, PhD Thesis, University of Genoa.
- Rossi M., Calvo Barentin C., Van Mele T., Block P. (2017). Experimental study on the behaviour of masonry pavilion vaults on spreading supports, *Structures*, 11:110–120. DOI: 10.1016/j.istruc.2017.04.008.
- RILEM TC – LUM B6 (1991). *Diagonal tensile strength tests of small wall specimens*, In: RILEM Recommendations for the Testing and Use of Constructions Materials, RILEM.

4.3 Project #19 – Seismic Testing of Adjacent Interacting Masonry Structures (AIMS)

Authors

I. Tomić⁽¹⁾, A. Penna⁽²⁾, M. DeJong⁽³⁾, C. Butenweg⁽⁴⁾, A.A. Correia⁽⁵⁾, P.X. Candeias⁽⁵⁾, F.L. Ribeiro⁽⁵⁾, I. Senaldi⁽²⁾, G. Guerrini⁽⁶⁾, D. Malomo⁽³⁾, K. Beyer⁽¹⁾

⁽¹⁾ EPFL, École Polytechnique Fédérale de Lausanne (EPFL), Lausanne, Switzerland

⁽²⁾ University of Pavia, Pavia, Italy

⁽³⁾ University of California, Berkeley, USA

⁽⁴⁾ RWTH Aachen University, Aachen, Germany

⁽⁵⁾ LNEC, National Laboratory for Civil Engineering, Lisbon, Portugal

⁽⁶⁾ EUCENTRE European Centre for Training and Research in Earthquake Engineering, Pavia, Italy

4.3.1 Introduction

Historical city centres throughout Europe have developed and densified during long periods. The densification caused the historical centres to be characterized by masonry building aggregates. In building aggregates, façades of adjacent buildings often share a structural wall. Connection between older and newer unit is often done through weakly interlocking stones or by a dry joint. Furthermore, since the densification was often a process spanning throughout long time periods, it is not uncommon for adjacent units to be constructed of different materials, to have different distributions of openings and different floor and roof heights. However, advances in the development of analysis methods for such aggregates have been impeded by the lack of experimental data.

One large scale campaign was performed at EUCENTRE in Pavia, Italy (Guerrini et al., 2017, 2019; Senaldi et al., 2019). The specimen was a half-scale stone masonry aggregate of a similar typology. A unidirectional shaking table test was performed with increasing PGA stages. After reaching the significant damage, the specimen was retrofitted and the test continued. No full separation of the units was detected, most likely because of the existing interlocking of the stones between the units at their interface.

Although modelling guidelines and experimental data to calibrate the models is missing, various authors have performed numerical analyses of masonry aggregates. The macro-element approach using the Tremuri software (Lagomarsino et al., 2013) and the macro-element developed by Penna et al. (2014) are used in Senaldi et al. (2010) to study the behaviour of single units within an aggregate. Numerical modelling and experimental results from the abovementioned EUCENTRE campaign are compared in Senaldi et al. (2019). A simplified non-linear methodology is proposed in Formisano et al. (2013), while a simplified large-scale assessment procedure for seismic vulnerability of masonry aggregates is proposed in Formisano et al. (2015), by adding five additional aggregate parameters to the well-known vulnerability form for masonry buildings. Theoretical and numerical approaches were used for case studies in Maio et al. (2015) and Formisano (2017), whereas non-linear boundary connections were modelled and compared in the response of an aggregate as a whole in Formisano and Massimilla (2018).

In order to benefit the most from this H2020 SERA project transnational access experimental research and aiming to fulfil the gaps in knowledge, the following set of objectives was defined through numerical modelling of the test unit during its design phase (Figure 170):

- Increase the opening phenomena of the interface between Unit 1 and Unit 2;
- Have a global behaviour sensitive to the behaviour of the interface (meaning that the numerical results are sensitive to the modelling assumptions of the interface model);
- Different modal properties of the isolated units with respect to the units as a conglomerate;
- Favour shear rather than flexural failure in the piers;
- Avoid early out-of-plane behaviour;
- Respect the shaking-table limits.

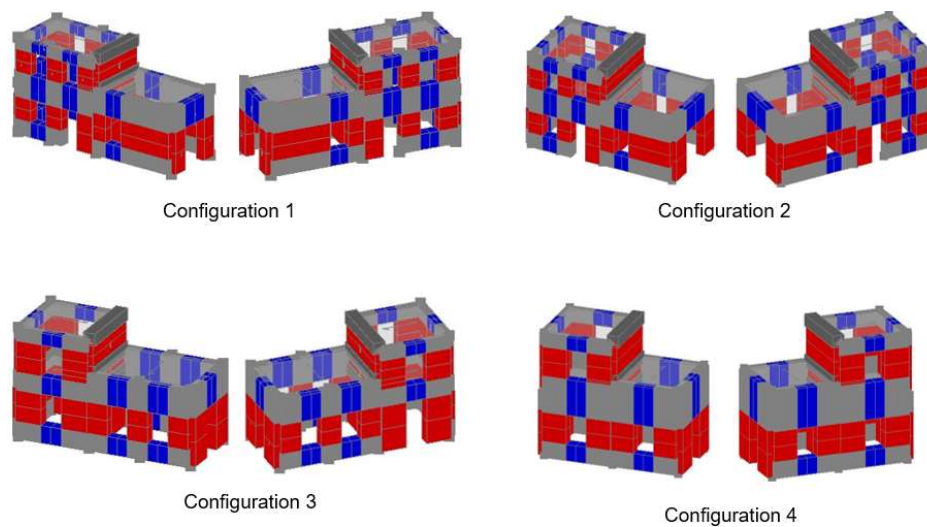


Figure 170: Evolution of specimen geometry

4.3.2 Test unit

The specimen is a half-scale stone masonry aggregate, consisting of two units with the orientation of units in relation to the strong motion direction as shown in Figure 171.

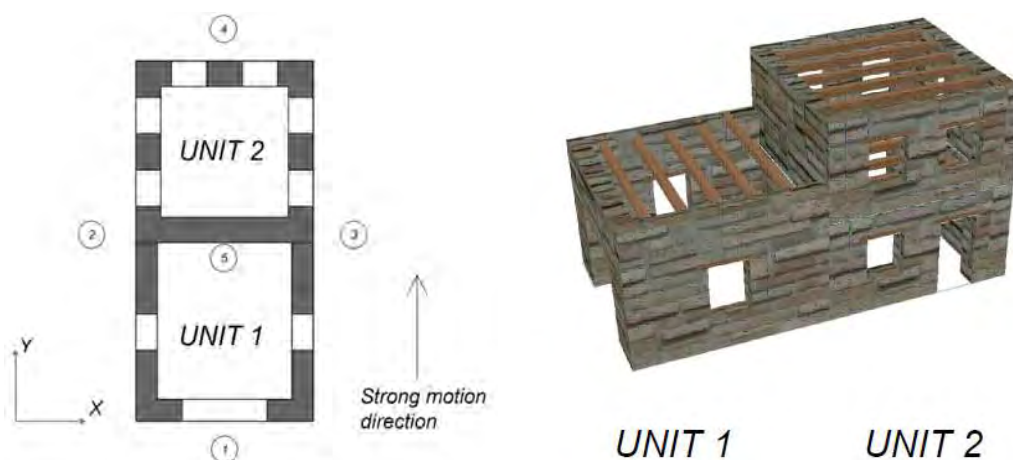


Figure 171: General unit orientation

Unit 1 has a U-shape with three walls and dimensions $2.5 \times 2.45 \text{ m}^2$. The height of Unit 1 is 2.2 m. Unit 2 has a rectangular shape with four walls and dimensions $2.5 \times 2.5 \text{ m}^2$. The first floor has a height 1.65 m and the second floor 1.5 m, resulting in the total height of 3.15 m. Their basic dimensions are shown in Figure 172. The wall thickness of Unit 1 is 30 cm, while the wall thickness of Unit 2 is 35 cm for the first floor and 25 cm for the second floor.

The most commonly used similitude relationships, such as Cauchy's or Cauchy-Froude's, were not applicable. The former would require scaling the gravitational acceleration, which is not feasible. The latter would require increasing the density of the material, which would increase the weight of the specimen, what would in turn cause the peak acceleration of the shake table to decrease. Therefore, the set of scale factors chosen are the same as the ones used in Guerrini et al. (2017, 2019) and Senaldi et al. (2019), summarized in Table 22.

The size of the stones is between 10 and 25 cm. The mortar is a commercial hydraulic lime mortar mix with added EPS spheres in 2:3 volumetric ratio of EPS spheres to mixed mortar. The EPS spheres are used to lower the strength and stiffness of the mortar in order to comply with the similitude laws shown in Table 22.

To ensure comparability of results with previous test campaigns, the construction material reproduces, as much as possible, the one used for the shaking table test at EUCENTRE (Senaldi et al., 2019). However, due to differences in the stone quarries, it was not possible to exactly replicate the stone type and shape. Therefore, the present aggregate is constructed with more irregular stones, making the whole masonry typology more irregular. Nevertheless, the research project includes a complete set of material characterization tests, including a large number of tests on mortar samples and wallettes tested in simple and diagonal compression.

The walls are constructed as double-leaf stone masonry without interlocking between the leaves, except at corners and openings, as seen in Figure 173. Irregular stone chips are placed between the leaves, accounting to about 10% of the volume.

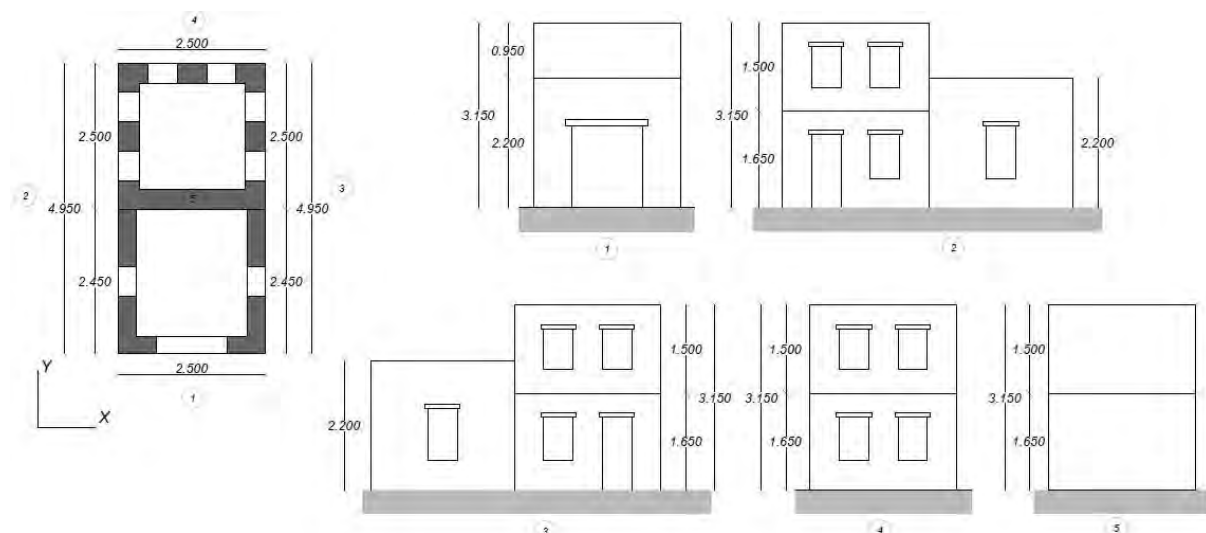


Figure 172: Elevation of the façades

Parameter		Scaling factor
Geometric parameters	Length	λ
	Area	λ^2
	Volume	λ^3
	Moment of inertia	λ^4
Dynamic parameters	Displacement	λ
	Velocity	$\lambda^{1/2}$
	Acceleration	1
	Time	$\lambda^{1/2}$
	Period	$\lambda^{1/2}$
	Frequency	$\lambda^{-1/2}$
	Mass	λ^3
	Force	λ^3
Material parameters	Density	1
	Stress	λ
	Strain	1
	Young's modulus	λ
	Poisson's coefficient	1
	Shear modulus	λ
	Strength	λ
	Cohesion	λ

Table 22: Similitude laws (Senaldi et al., 2019)



Figure 173: Masonry typology

Unit 2 was the first unit to be constructed. Before the construction of the walls of Unit 1, the contact surface between the units was made smooth with a mortar layer. This way it was ensured that there is no stone interlocking between the units, realistically representing two buildings built at different periods. This type of dry-joint, visible in Figure 174, paired with different modal properties and floor orientation were adopted to promote the out-of-phase behaviour of the two units and therefore the separation at the interface. A view of the as-built test specimen is presented in Figure 175.

The floors are composed of timber beams with cross section of 8 x 16 cm². A single layer of 2 cm thick planks was placed perpendicularly to the beams and connected by two nails at each intersection. Unit 1 beams span in the x-direction and Unit 2 beams span in the y-direction. PVC tubes were placed in the walls at the end of each beam and along each side-beam, as a strengthening precaution to be possibly

used together with steel angles and threaded rods to anchor beams into the walls in case of premature out-of-plane behaviour.



Figure 174: Interface between the units



Figure 175: As-built test specimen

The total mass of Unit 1 is 7434 kg, while the total mass of Unit 2, including additional masses, is 16272 kg. Additional masses of 1500 kg per floor were evenly distributed on the two floors of Unit 2, in the form of steel elements and mortar bags. They were placed in Unit 2 in order to further increase its modal periods and dynamically distinguish it from the stiffer Unit 1. The summary of the masses of each element in the specimen can be found in Table 23.

Specimen mass distribution	
Walls of Unit 1	7270 kg
Floors of Unit 1	164 kg
Total Unit 1	7434 kg
Walls of Unit 2	12937 kg
Floors of Unit 2	335 kg
Additional masses of Unit 2	3000 kg
Total Unit 2	16272 kg
Steel-concrete foundation	18000 kg
TOTAL	41706 kg

Table 23: Specimen masses

4.3.3 Numerical simulations

A large number of numerical simulations were performed to predict the response of the masonry building aggregate. These simulations were performed within the OpenSees framework (McKenna et al., 2000), using the newly developed macro-element by Vanin et al. (2020) – with a novel feature to model both the in-plane and the out-of-plane dynamic behaviour of masonry elements. Floors are modelled using orthotropic elastic membrane elements. The connections between the walls are modelled with one-dimensional non-linear springs, while the floor-to-wall connections are modelled using non-linear frictional interfaces. The connection between the units of the aggregate are modelled using a newly developed n-dimensional interface material model.

Due to the aleatory uncertainty of the properties of masonry as a material and of the multiple non-linear interfaces used, a set of 20 material and model uncertain parameters were identified. A Latin Hypercube Sampling (LHS) was performed to create a total of 300 sets of input parameters. For each set, Incremental Dynamic Analyses (IDAs) were performed. Based on those results, a numerical fragility curve was derived and is presented in Figure 176.

In these numerical simulations, two principal failure modes were detected. The most common failure mode is the flexural failure of the first storey piers of Unit 2. However, for sets of input parameters with weaker floor-to-wall and unit-to-unit connections, the failure mode is an out-of-plane failure of the lateral walls of Unit 1. Both failure modes are depicted in Figure 177.

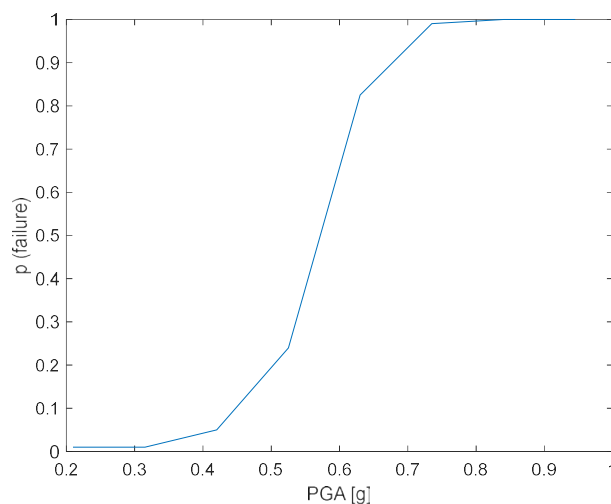


Figure 176: Numerical fragility curve

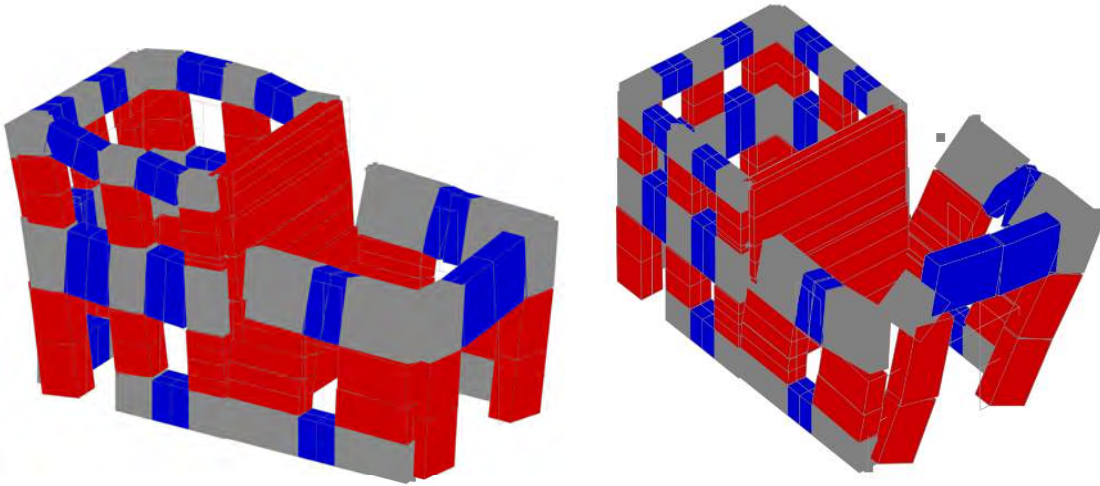


Figure 177: Examples of ultimate deformation states before the failure:
a) in-plane failure of Unit 1; b) out-of-plane failure of Unit 2

4.3.4 Test setup

The ground motion records selected for the experimental testing were the two horizontal components of the Montenegro 1979 earthquake from the Albatros station. The loading sequence consists of three testing steps and four intensity levels, as shown in Table 24. Each step consists on the excitation in the y-direction, x-direction and, finally, bidirectional excitation. The records used and their corresponding pseudo-acceleration spectra are shown in Figure 178 and Figure 179, respectively. Due to similitude laws, the time steps actually used in the shaking table test are scaled with respect to the original ones by a factor of $\lambda^{1/2}$, as defined in Table 22, while there is no similitude scaling on the acceleration values.

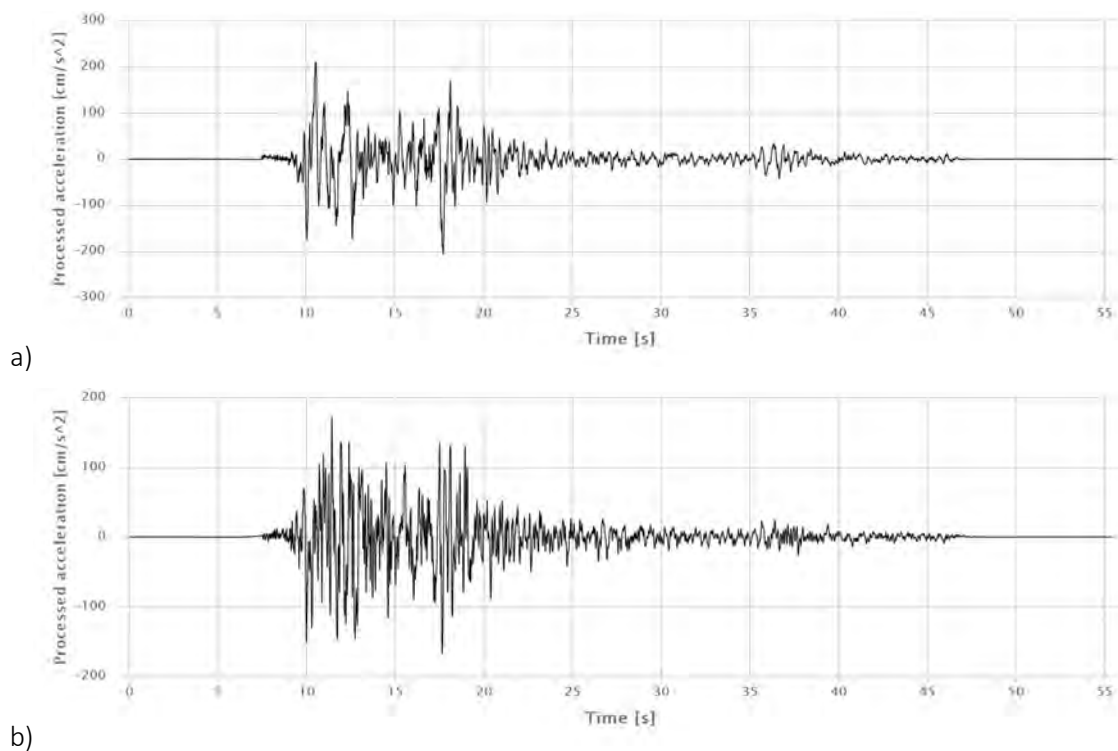


Figure 178: Processed accelerations of Montenegro 1979 earthquake records at the Albatros station:
a) East-West direction; b) North-South direction (Luzzi et al., 2016)

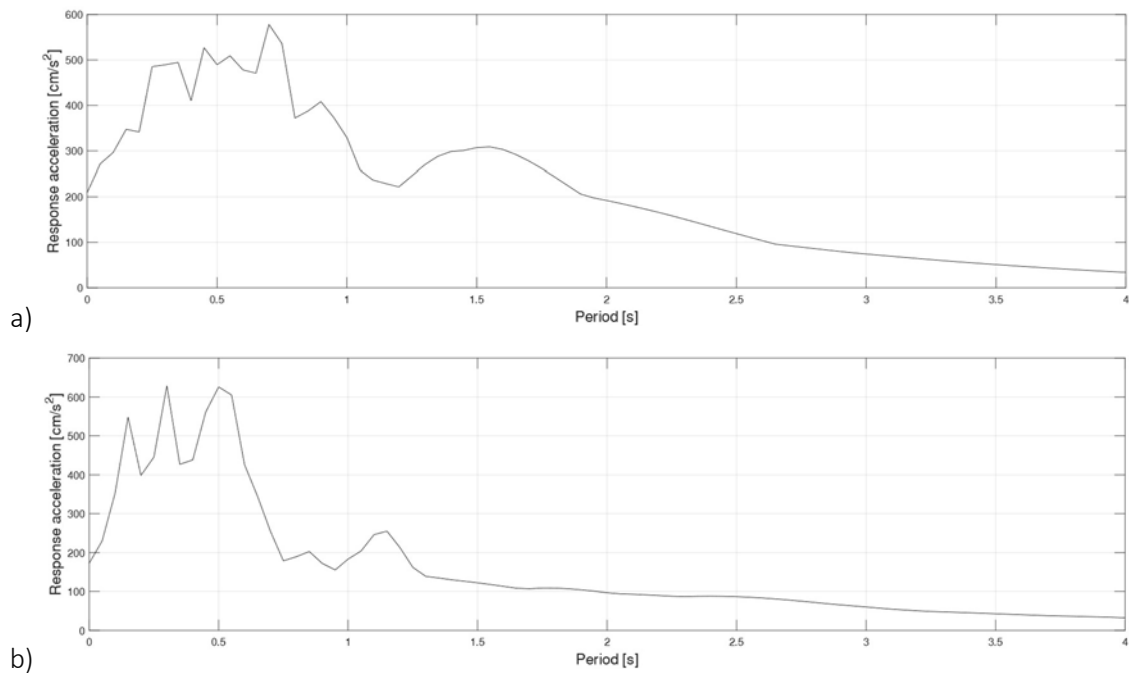


Figure 179: Response spectra of Montenegro 1979 earthquake records at the Albatros station:
a) East-West direction; b) North-South direction

Level of shaking	Substep I	Substep II	Substep III
25% shake table capacity PGA 0.219/0.156g y/x-dir	y-direction	x-direction	Both directions
50% shake table capacity PGA 0.438/0.313g y/x-dir	y-direction	x-direction	Both directions
75% shake table capacity PGA 0.656/0.469g y/x-dir	y-direction	x-direction	Both directions
100% shake table capacity PGA 0.875/0.625g y/x-dir	y-direction	x-direction	Both directions

Table 24: Loading sequence

Dynamic identification tests are performed between all intensity levels. Several types of signals are available for use in experimental modal analysis, such as random vibrations or impulsive signals. For estimating the frequency response functions (FRFs), the choice depends upon the characteristics of the system, the theory underlying the parameter estimation, and the expected use of the data. Different kinds of excitation signals have their specific characteristics, and some are more suitable for certain applications than others. For testing this specimen, a white-noise signal was adopted, characterised by a frequency content in the range of 0.1-40 Hz, with the FRFs being computed based on the input-output relationships.

This excitation was applied with a dual purpose: (i) to characterize the entire test system (i.e. shake table plus building specimen) during the adaptive tuning process for the desired target signals; (ii) to identify the dynamic response properties of the specimen. In the latter case, the FRFs are used to quantify the effect of the damage evolution on the dynamic characteristics of the specimen, i.e. to monitor the decrease in natural frequencies and to compute the increase in modal damping. For the

comparison of the analysis results, it is however essential to always use input signals of the same type and amplitude throughout the test.

The dynamic identification of the building is performed using the acceleration response-histories recorded by the sensors mounted on the structure. Accelerations of the foundations and in-plane and out-of-plane accelerations of the masonry walls are recorded using 40 accelerometers, as shown in Figure 180.

On the other hand, displacement measurements are useful for determining the response of the specimen and its damage evolution. In this case, the Optotrak LED optical measurement system and 30 other displacement transducers record absolute displacements of the chosen points and relative displacements of the beams and walls and between the units of the aggregate (opening of the interface). A schematic representation of the displacement transducers can be seen in Figure 181.

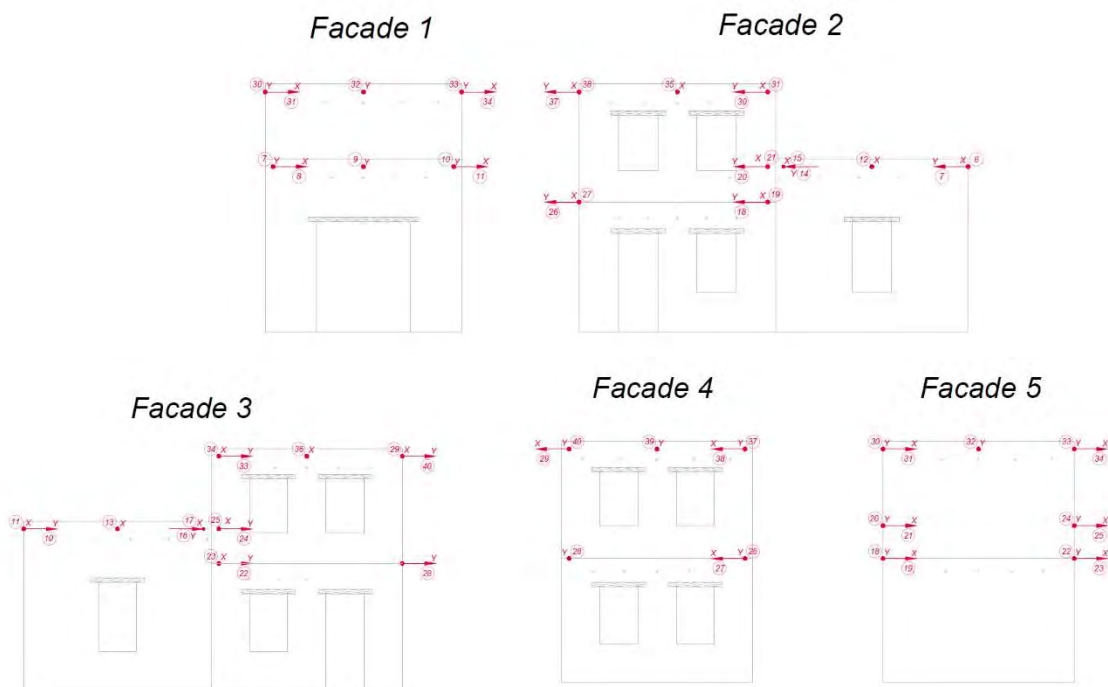


Figure 180: Layout of accelerometers~

Besides the abovementioned transducers, high-rate imaging devices are used for capturing the response of the specimen. Intensive data post-processing is required through digital image correlation methods that provide a much-detailed description of the specimen behaviour in the dynamic tests.

4.3.5 Preliminary results

Figure 182 and Figure 183 represent the target ground motions in each direction and for each intensity level corresponding to the scaled specimen, as well as the achieved shaking table motions. They are represented in terms of the pseudo-acceleration response spectra at the base of the model. The results shown herein attest the fidelity of the shake table system to comply with the desired motion.

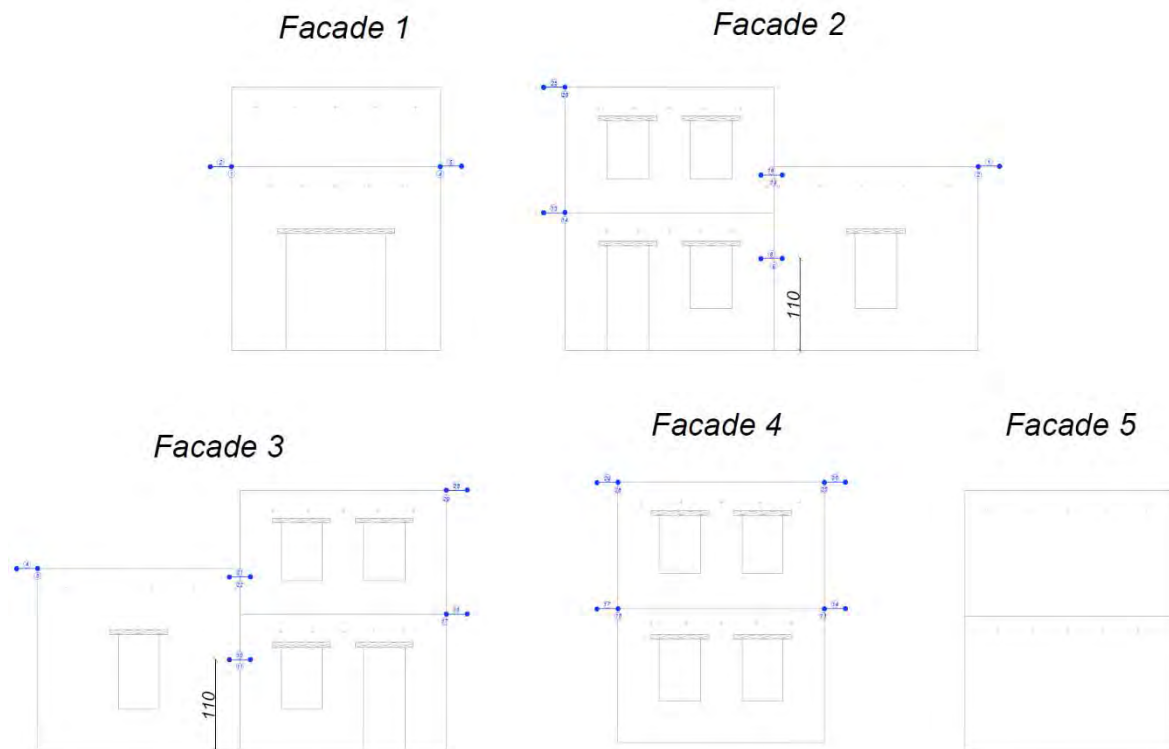


Figure 181: Layout of displacement transducers

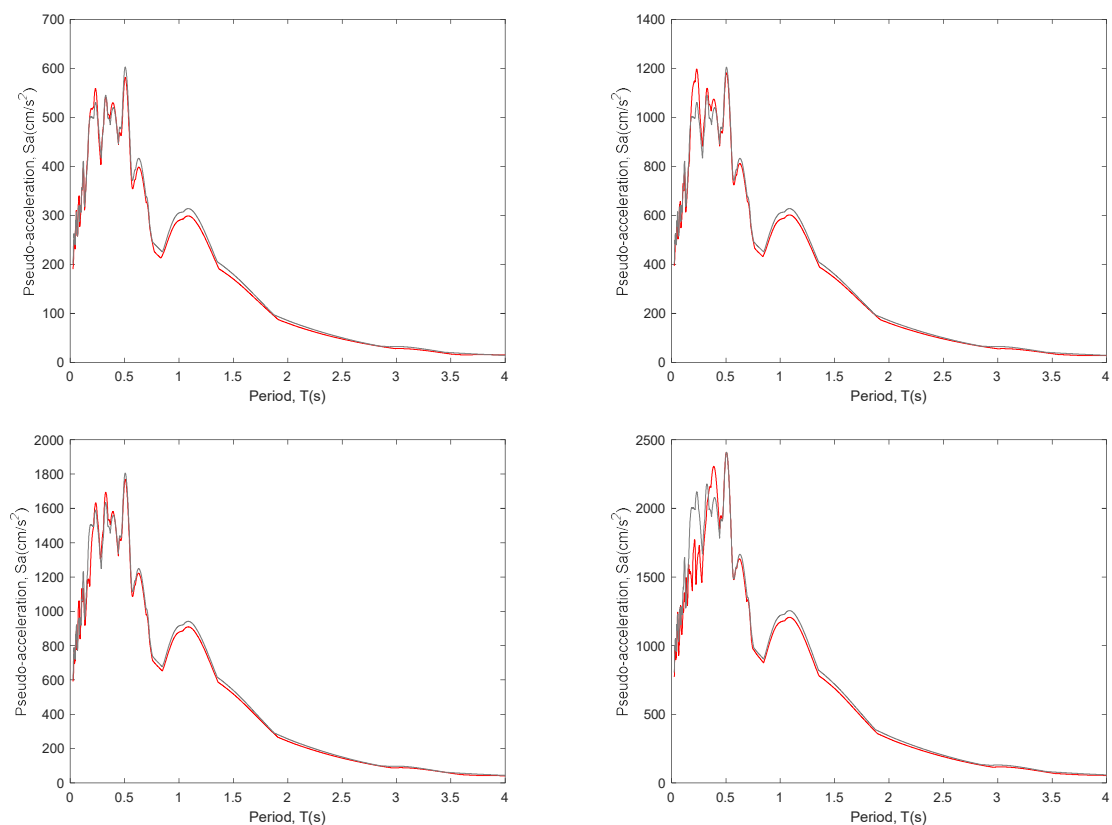


Figure 182: Target and achieved response spectra of the scaled motion for the East-West direction and for the 25%, 50%, 75% and 100% intensity levels

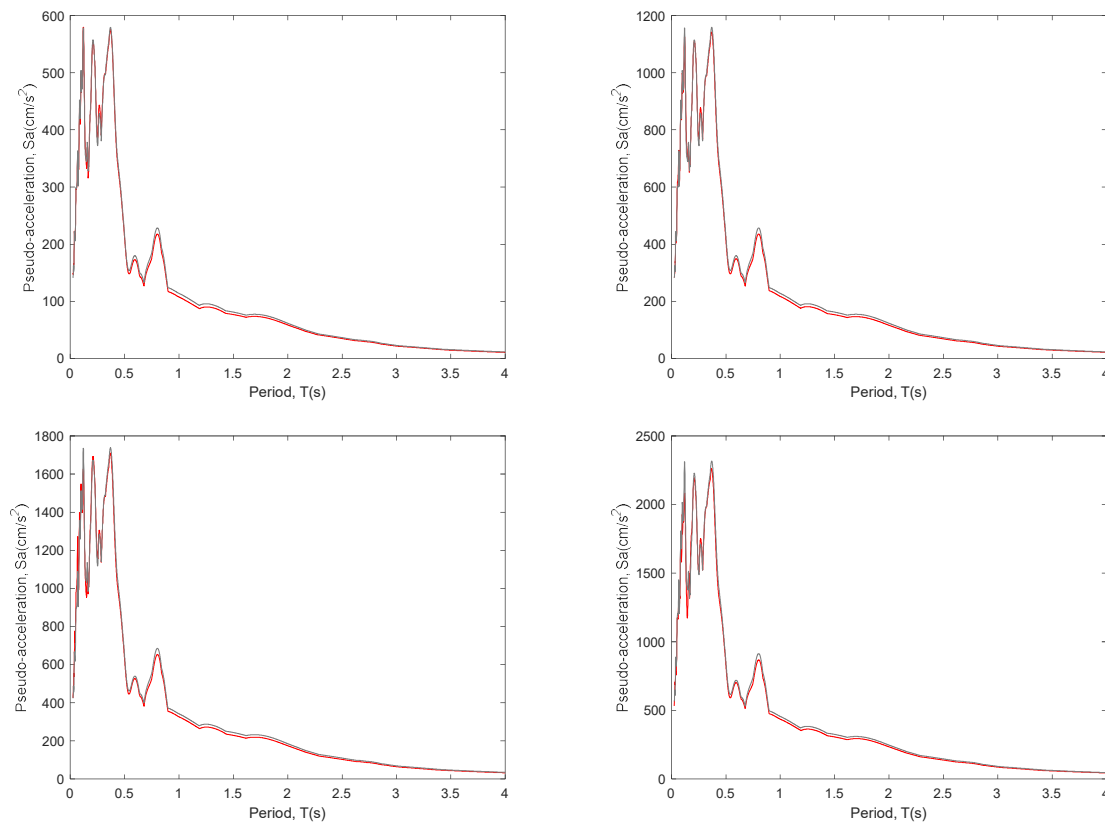


Figure 183: Target and achieved response spectra of the scaled motion for the North-South direction and for the 25%, 50%, 75% and 100% intensity levels

As a part of the experimental campaign, a blind prediction competition was organized with participants invited from both academia and industry, increasing the visibility of the research project. More than a dozen of submissions were received, yielding different results in terms of failure modes and force–displacement responses. The submitted modelling approaches comprise a wide range of methods: hand calculations, limit analyses, macro-element models, finite element models with smeared cracks and discrete element models.

The participants to the blind prediction competition have initially adopted reasonable estimates of the material properties and nominal input motions for their calculations. These may be corrected and their models calibrated on the basis of the material characterization data, the actual motions of the shaking table, and the observed damage to the building specimen.

4.3.6 Conclusions

This project deals with the seismic response of masonry building aggregates, commonly existing in European city centres. It contributes significantly to the collection and dissemination of experimental data on the interaction of building units, in order to better understand the phenomena involved in their dynamic behaviour.

This experimental data is also valuable to calibrate adequately the substantial number of complex non-linear models and modelling approaches required to capture the buildings' response. The numerous participants from academic and professional teams in the blind prediction competition organised within the project confirm the interest of the research carried out.

4.3.7 References

- Formisano A., Castaldo C., Mazzolani F.M. (2013). Non-Linear Analysis of Masonry Building Compounds: A Comparison of Numerical and Theoretical Results. *14th International Conference on Civil, Structural and Environmental Engineering*, Cagliari, Italy. DOI: 10.4203/ccp.102.66.
- Formisano A., Florio G., Landolfo R., Mazzolani F.M. (2015). Numerical calibration of an easy method for seismic behaviour assessment on large scale of masonry building aggregates. *Advances in Engineering Software*, 80:116–138. DOI: 10.1016/j.advengsoft.2014.09.013.
- Formisano A. (2017). Theoretical and Numerical Seismic Analysis of Masonry Building Aggregates: Case Studies in San Pio Delle Camere (L'Aquila, Italy). *Journal of Earthquake Engineering*, 21(2):227–245. DOI: 10.1080/13632469.2016.1172376.
- Formisano A., Massimilla A. (2018). A Novel Procedure for Simplified Nonlinear Numerical Modeling of Structural Units in Masonry Aggregates. *International Journal of Architectural Heritage*, 12(7-8):1162–1170. DOI: 10.1080/15583058.2018.1503365.
- Guerrini G., Senaldi I., Scherini S., Morganti S., Magenes G. (2017). Material Characterization for the Shaking-Table Test of the Scaled Prototype of a Stone Masonry Building Aggregate. *XVII ANIDIS Conference*, Pistoia, Italy.
- Guerrini G., Senaldi I., Graziotti F., Magenes G., Beyer K., Penna A. (2019). Shake-Table Test of a Strengthened Stone Masonry Building Aggregate with Flexible Diaphragms. *International Journal of Architectural Heritage*, 13(7):1078–1097. DOI: 10.1080/15583058.2019.1635661.
- Lagomarsino S., Penna A., Galasco A., Cattari S. (2013). TREMURI program: An equivalent frame model for the nonlinear seismic analysis of masonry buildings. *Engineering Structures*, 56:1787–1799, DOI: 10.1016/j.engstruct.2013.08.002.
- Luzzi L., Puglia R., Russo E. & ORFEUS WG5 (2016). Engineering Strong Motion Database, version 1.0. *Istituto Nazionale di Geofisica e Vulcanologia, Observatories & Research Facilities for European Seismology*. DOI: 10.13127/ESM.
- Maio R., Vicente R., Formisano A., Varum H. (2015). Seismic vulnerability of building aggregates through hybrid and indirect assessment techniques. *Bulletin of Earthquake Engineering*, 13(10):2995–3014, DOI: 10.1007/s10518-015-9747-9.
- McKenna F., Fenves G.L., Scott M.H., Jeremic B. (2000). *Open System for Earthquake Engineering Simulation (OpenSees)*. University of California, Berkeley, USA.
- Penna A., Lagomarsino S., Galasco A. (2014). A nonlinear macroelement model for the seismic analysis of masonry buildings. *Earthquake Engineering and Structural Dynamics*, 43(2):159–179. DOI: 10.1002/eqe.2335.
- Senaldi I., Magenes G., Penna A. (2010). Numerical Investigations on the Seismic Response of Masonry Building Aggregates. *Advanced Materials Research*, 133–134:715–720, DOI: 10.4028/www.scientific.net/AMR.133-134.715.
- Senaldi I., Guerrini G., Caruso M., Graziotti F., Magenes G., Beyer K., Penna A. (2019). Experimental Seismic Response of a Half-Scale Stone Masonry Building Aggregate: Effects of Retrofit Strategies. *Structural Analysis of Historical Constructions*, 1372–1381.
- Senaldi I., Guerrini G., Solenghi M., Graziotti F., Penna A., Beyer K. (2019). Numerical modelling of the seismic response of a half-scale stone masonry aggregate prototype. *XVIII ANIDIS Conference*, Ascoli Piceno, Italy.

Vanin F., Penna A., Beyer K. (2020). A three-dimensional macro-element for modelling of the in-plane and out-of-plane response of masonry walls. *Earthquake Engineering and Structural Dynamics* (submitted for publication).

5 STRULAB - University of Patras

The STRULAB facility of the Department of Civil Engineering of the University of Patras is a structural laboratory for the static and pseudodynamic testing of civil engineering structures. It employs two reaction walls (in orthogonal configuration) and a reaction floor system, accompanied by a relocatable auxiliary reaction-wall. The facility is one of the few in Europe performing tests via the Hybrid Simulation approach and along with JRC, the only ones in SERA performing pseudodynamic testing. It specializes in testing reinforced concrete structures (new or retrofitted), while also testing steel and masonry structures, base isolation systems, as well as sub-structures of industrial installations (e.g. piping systems).

The Lab attracted the interest of 6 research groups in the first call – two of the proposals were assigned to the Lab (ARISTA and ARCO) in the first Call, while a 3rd one was undertaken following the 2nd Call for Proposals.

The three projects more than completed the available access days offered by the Lab in SERA. Until M12, the first two Phases of project ARISTA were completed (i.e. design and construction of the specimen, instrumentation and free vibration testing), while the rest three ones were completed from M12 to M24. A manuscript summarizing the project goals, the experimental testing and the main conclusions was submitted for publication to the Bulletin of Earthquake Engineering (the manuscript is in the second review round). In the sequel, project ARCO started and four specimens were designed and constructed, along with the special test setup. By the end of M24, two of the ARCO specimens were tested, with the remaining specimens of ARCO been tested in the beginning of M24-M36 period. The project rationale, testing campaign and conclusions were included in a manuscript submitted for publication (ACI structural Journal) in M35. The execution of the third project, HITFRAMES developed till M36 – a 3D and a 2D specimens were constructed and tested by M36. Partial results were submitted for publication to one national and an international Conference.

5.1 Project #8 – ARISTA – Seismic Assessment of Reinforced Concrete frames with Smooth bars – Proposals for EC8-Part 3

Authors

C. Chrysostomou⁽¹⁾, N. Kyriakides⁽¹⁾, P. Kotronis⁽²⁾, S. Grammatikou⁽³⁾

S. Bousias⁽⁴⁾, X. Palios⁽⁴⁾, N. Stathas⁽⁴⁾, E. Strepelias⁽⁴⁾

⁽¹⁾ *Cyprus University of Technology, Cyprus*

⁽²⁾ *Ecole Centrale de Nantes, France*

⁽³⁾ *DENCO Structural Engineering, Greece*

⁽⁴⁾ *Structures Laboratory, University of Patras, Greece*

5.1.1 Introduction

Smooth (plain) bars are not used anymore as primary reinforcement of new concrete structures. The codes of most countries have banned them from such a use long since. Nonetheless, being common in

old structures which are assessed for retrofitting, they enjoy the renewed interest of the structural engineering community. However, still little is known about the performance of structures with smooth bars in strong earthquakes. Lack of knowledge is not only due to the rarity of such extreme events. In the heyday of smooth bars, systematic research of the modern type and scale was unknown to structural engineering. Early works (1909-1912) seem today trivial demonstrations of the effectiveness of hooked smooth bars, while later studies were motivated by the emergence of ribbed (deformed) bars as a more advanced alternative; smooth bars were studied just to show that they were inferior to ribbed bars.

The gap in knowledge is to a good extent being filled nowadays, thanks to the renewed interest in smooth bars brought about by the recent emphasis on rehabilitation and re-use of old structures. Although numerous, the tests which are of interest to earthquake engineering have, so far, essentially been limited to quasi-static cyclic loading of single members – normally columns. However, the single or double cantilever specimens or the columns fixed at top and bottom against rotation listed in these two references do not represent well the columns of real multistorey buildings, in which vertical bars are continuous through joints and typically lap-spliced at floor levels. The three-storey, two-by-two-bay, asymmetric building, pseudodynamically tested at the ELSA lab in Ispra, IT for EU-funded project SPEAR (“Seismic Performance Assessment and Rehabilitation”, 2005), was one of the very few seismic tests performed in the past on a (nearly) full-scale structure with smooth bars. However, it focused on aspects other than the type of bars: the torsional response to bi-directional earthquake, the effects of poor detailing or of column jackets consisting of Fibre-Reinforced-Polymer (FRP) or of concrete reinforced with ribbed bars, etc. Cyclic lateral load tests (2002) carried out at the University of Pavia on a three-storey, three-bay 2:3 scale plane frame without floor slabs focused on the vulnerability of exterior unreinforced beam/column joints, which failed at interstorey drifts as low as 1.6%, by diagonal compression in those joints and “push-out” action of the 180-deg hook of the beam’s compression bars. So, models developed for single members still await validation testing of near-full-scale specimens with layout and detailing representative of real-life structures with smooth bars.

A prime feature of old concrete buildings is the – typically short – lap-splicing of columns' vertical bars at floor levels, i.e., where plastic hinges form in strong earthquakes. In countries influenced in the past by British codes, lap-spliced column bars even had straight ends, without hooks; such detailing may be sufficient for gravity loads, but not for earthquake resistance. Because of these features and of the rapid loss of bond along smooth bars during cyclic loading, the structural engineering profession has doubts concerning the performance of old columns with smooth bars in earthquakes.

In order to put to test the conventional wisdom that structures with smooth bars are inherently vulnerable to earthquakes, to further our understanding of the seismic behaviour of RC frame structures with smooth bars and to support the development or validation of models, cyclic lateral load tests were conducted on a 2:3-scale three-storey one-by-two-bay RC frame structure with smooth bars in the columns. The detailing of bars, the testing program and the instrumentation focused on the behaviour of smooth bars during the test and its effect on local and global structural performance:

- the instrumentation captured the distribution of deformation along columns;
- strains in vertical bars were measured at column end sections and at the ends of lap-splices, in order to see whether they remained tensile after the cyclic decay of bond along bars;
- although most columns had their vertical bars lap-spliced at floor levels and at the connection to the foundation, for comparison, two diagonally opposite corner columns in building plan had continuous bars, from the footing to the roof;

after three half-cycles of inelastic deformation, the frame had both ends of three ground storey columns wrapped in FRP, before been subjected to larger amplitude cycles; the comparison of the FRP-

wrapped columns to the unretrofitted ones extended to the middle storey, where columns were exposed to similar deformation demands as in the ground storey.

5.1.2 Test structure

The test structure is shown in Figure 184. It was designed for gravity loads alone: beams were chosen to be stronger than the columns, not only because this is most often the case in old RC frames, but also to force inelastic action into the columns, in order to study the effect of lap-splicing of vertical bars at floor levels.

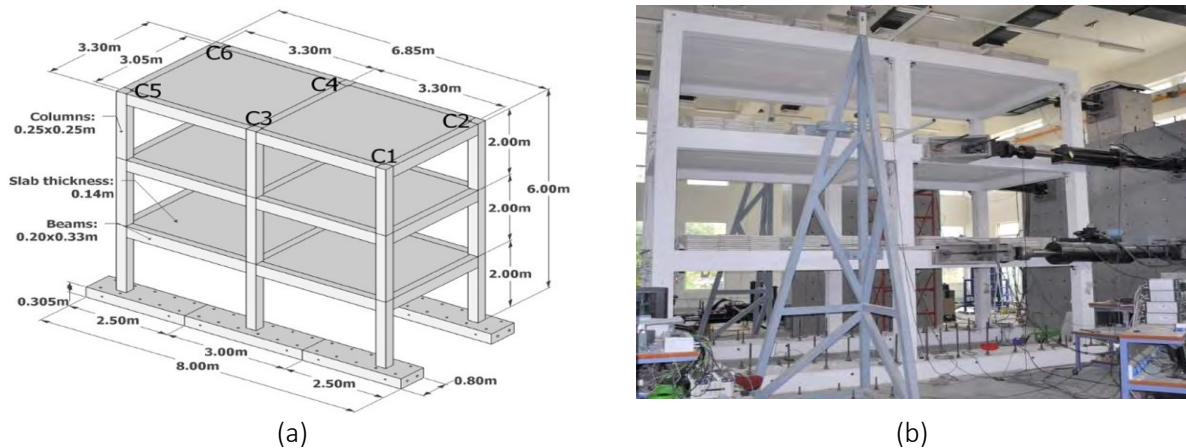


Figure 184: (a) Geometric dimensions and (b) general view of frame structure

Each one of the two 2-bay frames had a 305 mm deep by 800 mm wide strip footing – posttensioned with two longitudinal unbonded tendons and fixed to the lab's strong floor. Each column had eight 12 mm smooth vertical bars (at corners and at mid-sides) and a 6 mm perimeter tie at 150 mm centers with a 90-deg hook at a corner (Figure 185(a)). Beams had two 16 mm ribbed bars at top and bottom, continuous through interior joints and anchored at the corner ones with 90-deg bends; their ties of 8 mm ribbed bars at 100 mm centres had a 135-deg hook at one corner (Figure 185(b)). Concrete cover of ties was 10 mm in columns, 25 mm in beams. Slabs had 8 mm ribbed bars at 150 mm centres, top and bottom, in both directions. As in the past there were no design calculations of beam-column joints, the same pattern and size of ties as in columns were used in the joint (giving one 6 mm horizontal tie inside each one).

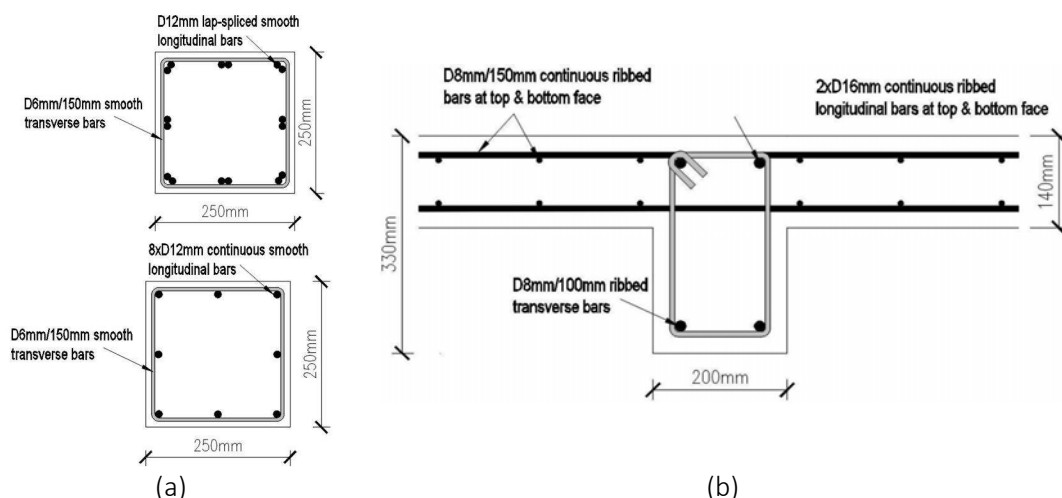


Figure 185: Layout of bars in the cross-section of (a) columns, in lap-splice region and outside; (b) beams

The vertical bars of columns C2, C3, C4 and C5 had standard 180-deg hooks and were lap spliced at each floor level, as well as to starter bars embedded in. The lappings measured 600 mm to the outside of the 180-deg hooks, or 500 mm between the hooks' starting points (Figure 186(a)). Starter bars had a 250 mm straight length embedded in the footing, ahead of a standard 180-deg hook. Columns C1 and C6, at diagonally opposite corners, had continuous vertical bars from the footing to the roof, ending with a straight embedment of 250 mm in the strip footing and in the top floor beam, followed by a standard 180-deg hook.

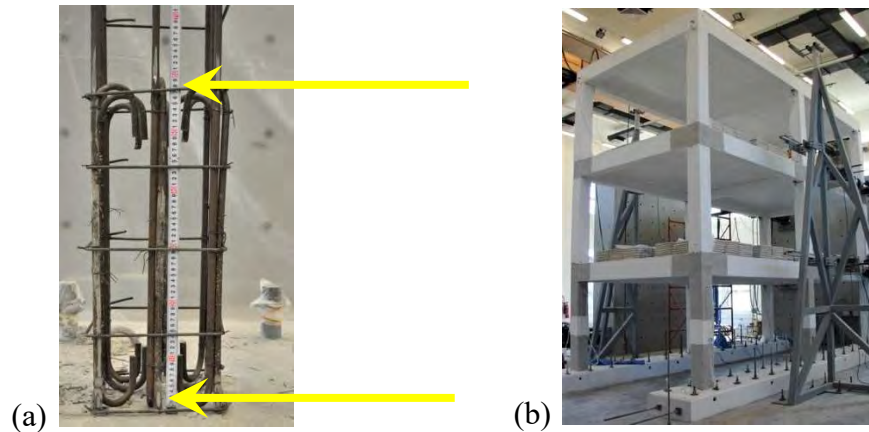


Figure 186: (a) Lap splices in column vertical bars at floor level, showing position of strain gages on lap-spliced (top arrows) and starter bars (bottom arrows); and (b) FRP overlays applied at selected points before second phase of testing

Nine test coupons of the 12 mm smooth bars gave an average 0.2% yield stress of 281 MPa (Figure 187); three coupons of the 6 mm smooth bars gave a yield stress of 206 MPa. The 8 mm and 16 mm ribbed bars in beams and slabs had average yield stress of 506 MPa or 528 MPa, respectively.

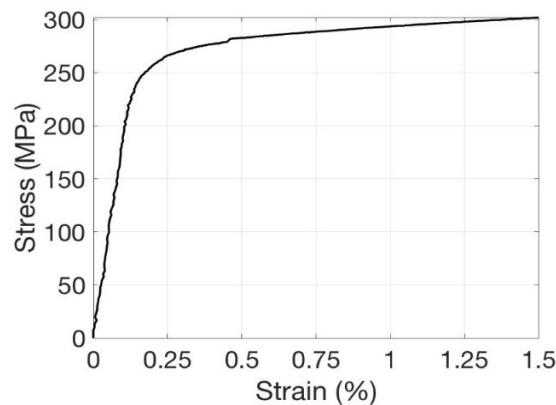


Figure 187: Stress-strain diagram of 12 mm dia. smooth bars

At the time of testing, the concrete of the ground storey had a cylinder strength of 35 MPa and a cube strength of 36.8 MPa; the corresponding values at the middle storey were 32.8 MPa and 37.4 MPa, and at the top one 34.2 MPa and 37.8 MPa, respectively. Each one of these values is an average from six 150 mm by 300 mm cylinders, or from six 150 mm cubes.

Additional weights of about 70 kN on each floor slab gave, along with the self-weight from midstorey to mid-storey a total storey weight of about 190 kN, these weights produced normalized axial forces in the outer columns, $N/A_c f_c$, of 0.01, 0.02 and 0.03 in the top, middle and bottom storey, respectively. The values of $N/A_c f_c$ in the central columns were 2.25-times those in corner ones.

5.1.3 Test setup and testing program

Lateral loads parallel to the long side of the structure were applied to the two lower floors at midpoint of each long side and to the transverse edge beam of the top floor; all loads were applied at beam mid-depth (Figure 184(b)). A prescribed history of cyclic roof displacements of increasing amplitude was applied by the actuator at the top. The actuators at the two lower floors were slaved to the top one so that an inverted triangular pattern of floor forces was applied, anchored to the force produced in the top actuator by the prescribed history of roof displacements. So, overall the test was displacement-controlled, with force control at the two lower levels.

The test structure was subjected first to a full cycle of roof displacement with 50 mm amplitude and to a half-cycle of 50 mm (Figure 188). Any damage was left unrepaired, but unidirectional Carbon FRP (with the main direction horizontal) were surface-bonded (Figure 186(b)) as follows:

- all-around the upper- and lowermost 600 mm of ground storey corner columns C5 and C6 and mid-side column C3, after chamfering the corners to a 22.5 mm mean radius;
- to the exterior surface of all beam-column joints in the two lowest storeys, up to a distance of 500 mm from the corner (providing 250 mm of anchorage to the lateral side of the beam).

The partially retrofitted frame structure was subjected to a sequence of five single cycles of top displacement, increasing in amplitude each time by 25 mm, from ± 50 mm to ± 150 mm (Figure 188); the first 50 mm half-cycle was of opposite sign with respect to the last 50 mm half-cycle applied on the frame without FRPs, serving as part of a second cycle; the subsequent 50 mm half-cycle was the third in a row with that amplitude in that half-cycle's direction.

After completing the ± 150 mm cycle to a top drift ratio of 2.5%, the top displacement was increased monotonically to 200 mm (top drift ratio 3.3%) and returned to zero.

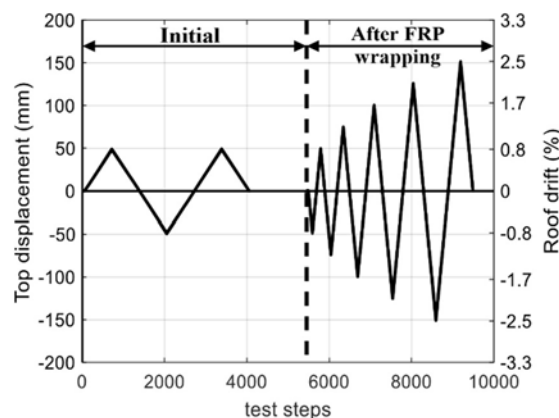


Figure 188: Time-history of applied roof displacements

Displacement transducers across all horizontal interfaces of columns and beams, and at the two sides of the column at right angles to the direction of testing, measured the opening of cracks at the top and base sections of every column in a storey, as well as the average compressive strain over a zone of 10 to 20 mm.

Strain gages measured the strains of two vertical bars on each side of the top and base sections of the ground storey in the two corner columns, C1 and C6, whose bars were continuous throughout the height of the building. In the two corner columns with lap-spliced bars, C2 and C5, bar strains were again measured only in the ground storey. Measurements at the base section of C2 and C5 were on the starter bars; they were accompanied by measurements on the bars which were lap-spliced to the

starter bars, through gages attached to these bars at the level of the hook of the starter bar (see Figure 186(a)). Bar strains were also measured at the top section of columns C2 and C5, on the bars lap-spliced at the base with the starter bars.

Inclinometers mounted on the exterior face of every first or second storey beam-column joint in the direction of testing measured the joint's rotation with respect to the horizontal (i.e., the chord rotation of the beam end(s) connected to the joint). The inclinometers were placed after the initial cycles at ± 50 mm and after strengthening the joints with an exterior CFRP overlay, right before the sequence of gradually increasing displacement amplitude in Figure 188, in order to observe the damage to the joint during the three half cycles of the ± 50 mm sequence without precipitating it.

5.1.4 Results

Global Response

Figure 189(a) shows the global response in terms of base shear vs. top displacement in the full duration of testing. Figure 189(b) to (d) show storey shear vs. interstorey drift loops of individual storeys. The first and second storey clearly yielded in the first half-cycle of loading, while overall yielding of the third storey didn't take place during the test; in fact, most components of the third storey appear to have stayed not just elastic but uncracked to the very end. The inverted-S shape of loops is typical of cyclic bond-slip behaviour and suggests that the hysteretic behaviour of all storeys in the frame was governed by bond along the column bars.

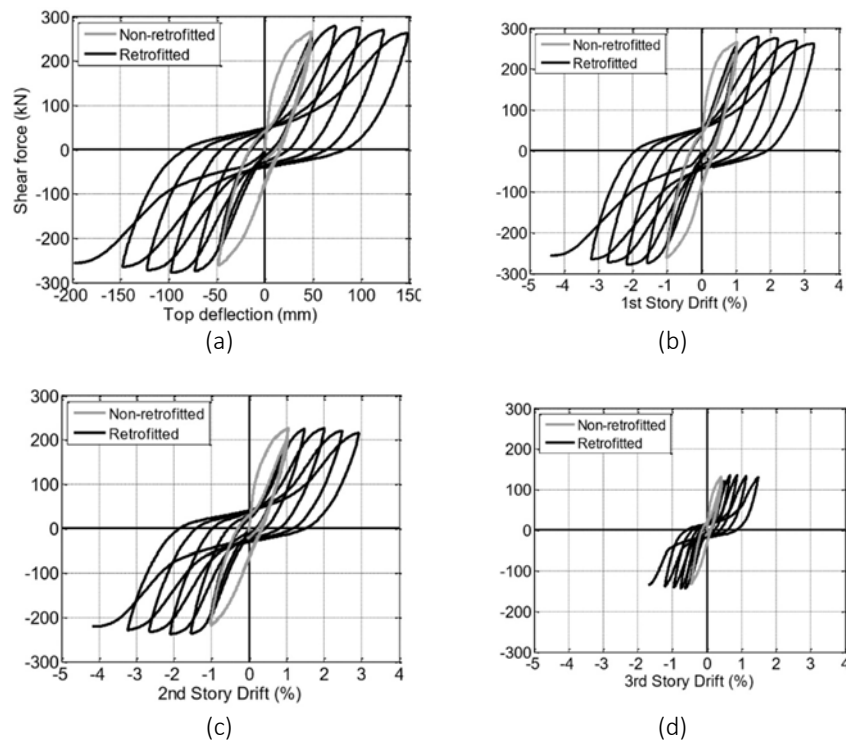


Figure 189: Shear-force vs lateral deformation loops: (a) base shear vs top displacement; (b) storey shear vs interstorey drift ratio at ground storey; (c) ibid at intermediate storey; (d) ibid at the top storey

Flexural behaviour of columns

The top and base sections of all six columns in the two lower storeys opened up from the first load cycle and kept doing so till the end of the test (see Figure 190(a), (b), which are typical of all columns in the lower two storeys).

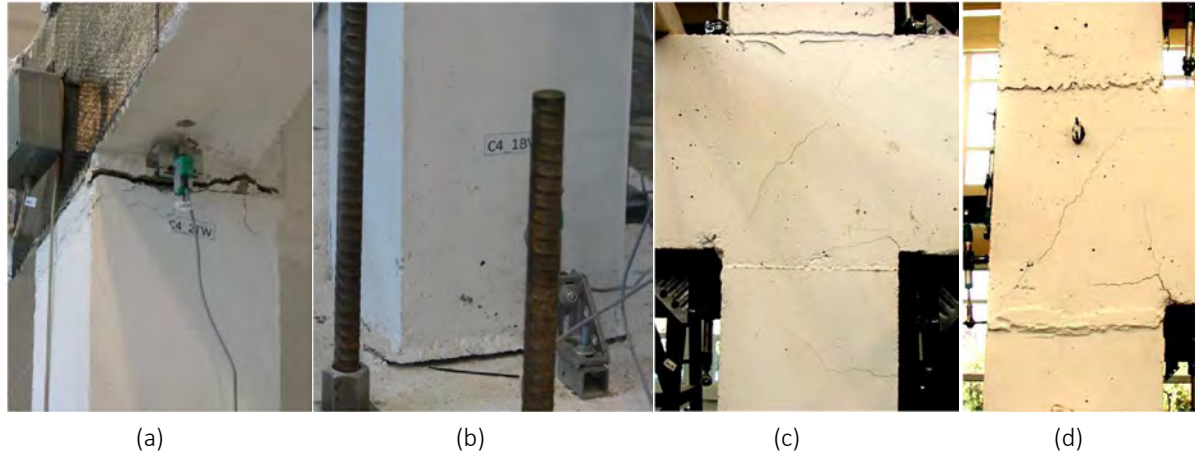


Figure 190: (a), (b) Flexural cracks typical of all top and base sections of the 1st and 2nd storey columns; (c), (d) diagonal cracks typical of all 1st and 2nd storey joints during the first phase of testing

The fixed-end rotation of those sections increased in proportion to the lateral displacement, as shown:

- in Figure 191 for corner columns C1 and C2 on the same side of the test structure;
- in Figure 192 for corner columns C5, C6 on the other side (with FRP wrapping at the ground storey);
- in Figure 193 for mid-side columns C3, C4 (C3 with, C4 without FRP wrapping at the ground storey).

There was no flexural or shear cracking between the ends of any column during the test; columns contributed to the interstorey drift the rotation of their top and bottom sections due to the opening of the cracks there. This is clear from the comparison in Figure 191 to Figure 193 of:

- the sum of the opening angle at the column's end section and the chord rotation of the beam end connected to that end of the column
- the interstorey drift during the response.

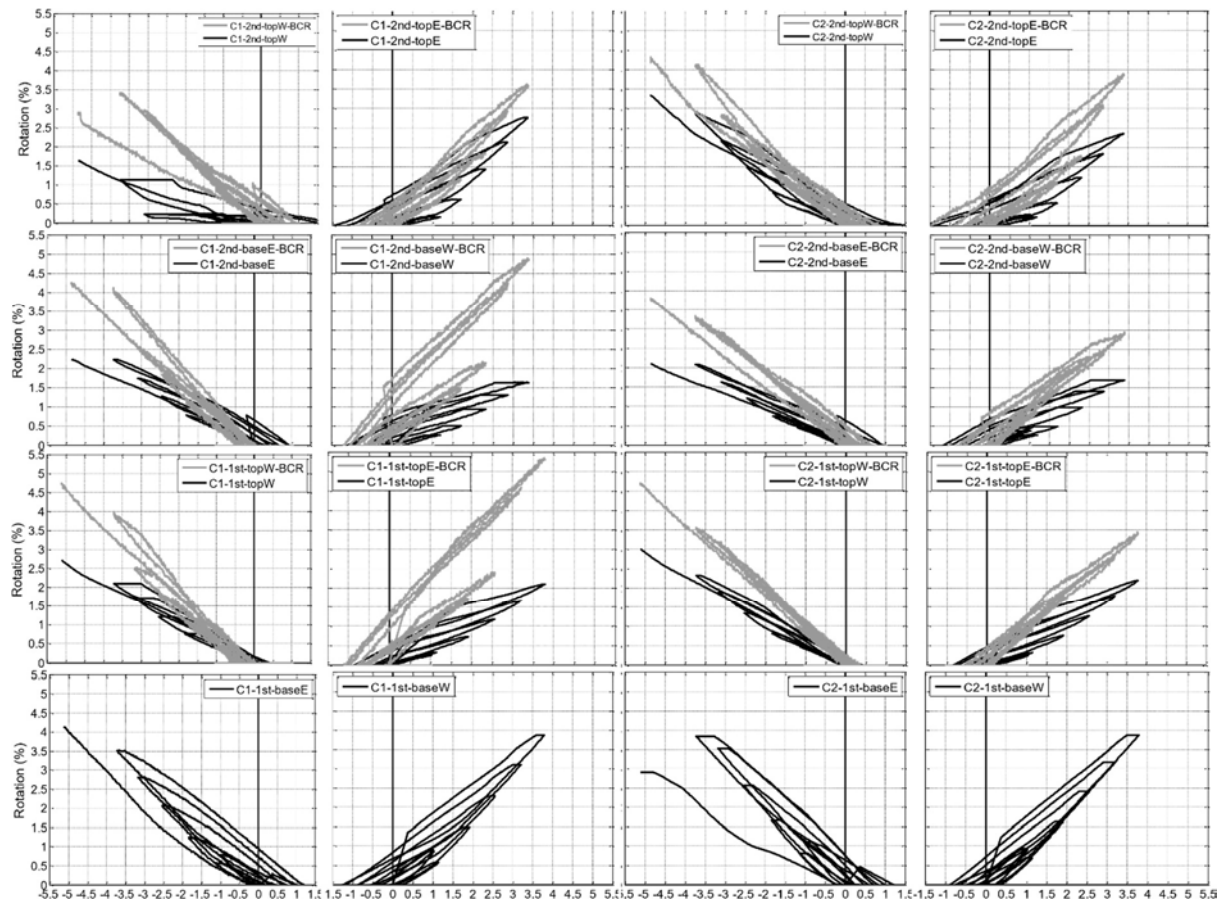


Figure 191: Interstorey drift vs rotation at column top or base section (black line) or vs that rotation plus the beam chord rotation at the same joint (grey line) in the two loading directions; (first two columns) column C1- continuous bars; (last two columns) column C2 - lap splices; (lower two rows) storey 1; (top two rows) storey 2

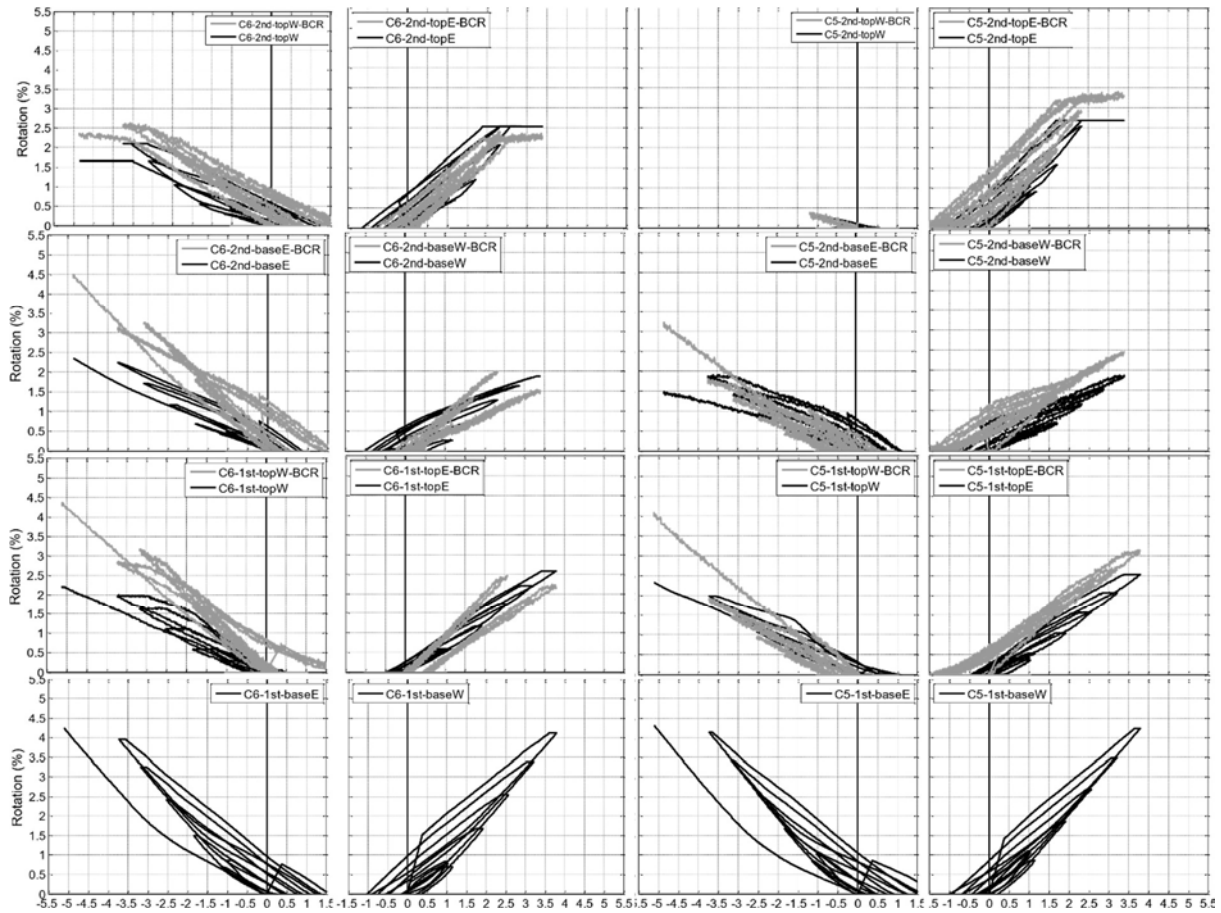


Figure 192: As in Figure 191, but for corner columns with FRP wrapping at ground storey: (first 2 columns) C6 - continuous bars; and (last two columns) C5 - lap-splices

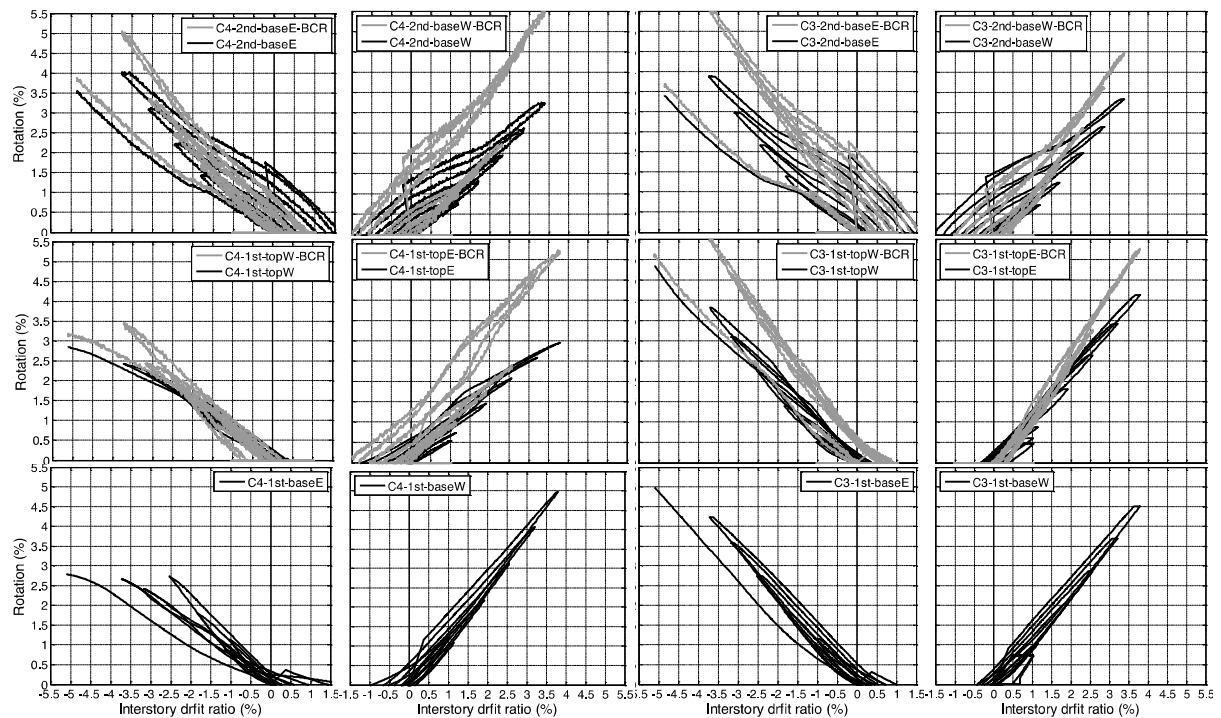


Figure 193: As in Figure 191, but for mid-side columns: (first 2 columns) C4 and (last two columns) C3 with FRP wrapping at ground storey; both columns with lap-splices

Beam/column joints

Hairline diagonal cracks at the exterior face of every beam-column joint except at the roof (see Figure 190(c), (d), which are typical of all joints in the lower two storeys) opened during the first phase of testing, i.e., before applying FRP over the joints, but were not visible afterwards.

The estimates of fixed-end-rotations shown in Figure 191 to Figure 193 were obtained from measurements by external displacement transducers, using the plane sections hypothesis to locate the neutral axis.

Recall that the interstorey drift is, at any point during the response, equal to the sum of:

- the mean chord rotation at beam ends at the upper and lower borders of the storey;
- the average chord rotation at the ends of the columns of the storey; and
- the average shear distortion of the beam-column joints.
- Figure 194 and Figure 195 compare the interstorey drift of each bay in the two lower storeys to the sum of:
 - the average chord rotation at the two beam ends above and below the bay (cf. (a) above), as derived from the joint rotations measured with inclinometers, and
 - the mean fixed-end rotation at the two ends of the two columns at the (left and right) sides of the bay, obtained by averaging the relevant fixed-end rotations in Figure 191 to Figure 193; this is the part of the mean chord rotation at these column ends (cf. (b) above) due to slippage of column bars.

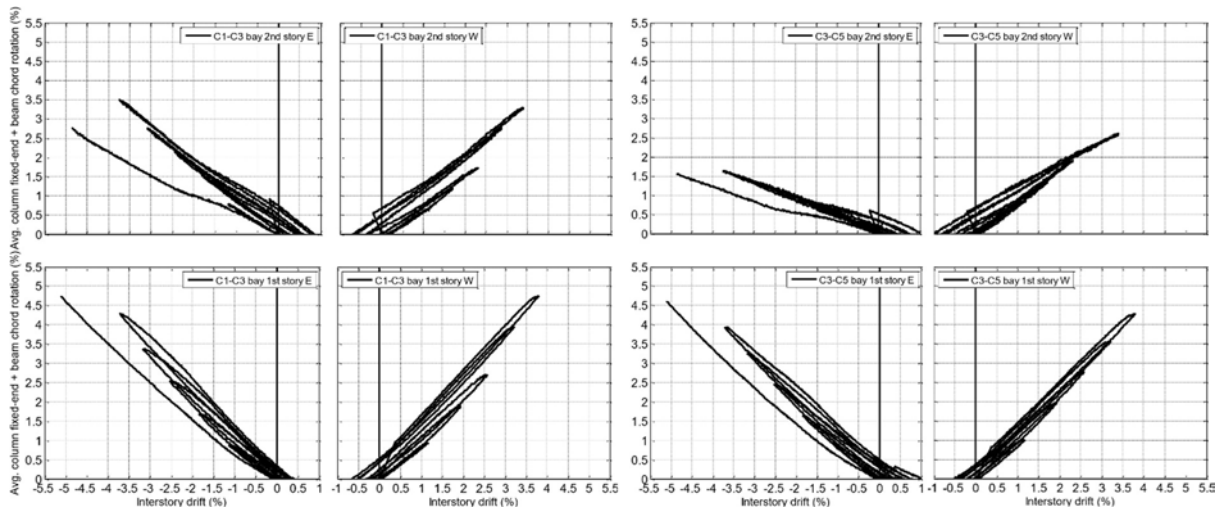


Figure 194: Interstorey drift vs total contribution to it from beam deformations and slippage of column bars in the bays of one of the two parallel frames: (top row) second storey; (bottom row) ground storey

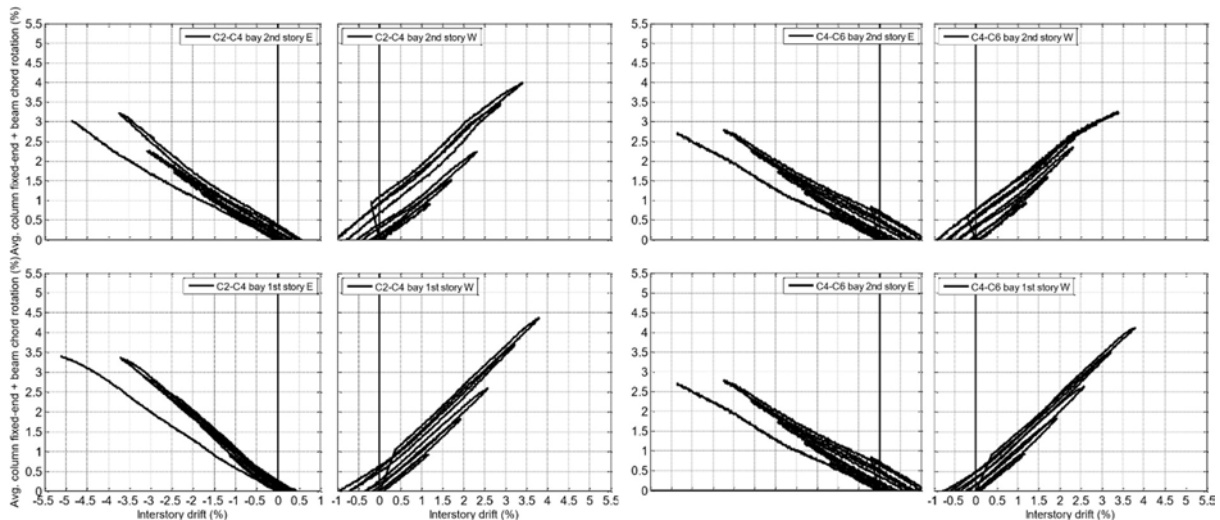


Figure 195: As in Figure 194, but for the frame on the opposite side

This comparison shows that indeed flexural and shear deformations along the columns (i.e., the balance between (b) above and what is included in the sum plotted in Figure 194 and Figure 195) and shear distortion of the joints (item (c) above) contribute little to interstorey drift in the second storey and even less in the ground storey. So, Figure 191, Figure 193, Figure 194 and Figure 195 show that:

- in this case joints behaved as though they were rigid, despite the diagonal cracking; and
- the body of columns between end sections seems to rock, uncracked and elastic, almost rigid.

Bar strains

Although Figure 189, Figure 191 to Figure 193, Figure 194 and Figure 195 suggest that slippage of smooth bars relative to the surrounding concrete is a major, almost dominant, feature of the cyclic behaviour of the frames tested, other measurements show that, thanks to bond along their straight length, these bars do go into compression. Specifically, the evolution of bar strains depicted in Figure 196 for the phase before the application of FRPs, and in Figure 197 for the phase after it, shows clearly that:

- smooth bars developed compressive stresses even after several cycles of loading, and
- the bottom end of a column bar follows more the surrounding concrete rather than the needs of the bar's top end to anchor its tension force.
- It is worth noting the lack of systematic differences between the behaviour and response of:
- columns C1 and C6, which had continuous bars without a single splice, on the one hand, and
- columns C2 and C5, whose bars were lap-spliced at three floor levels, on the other hand.

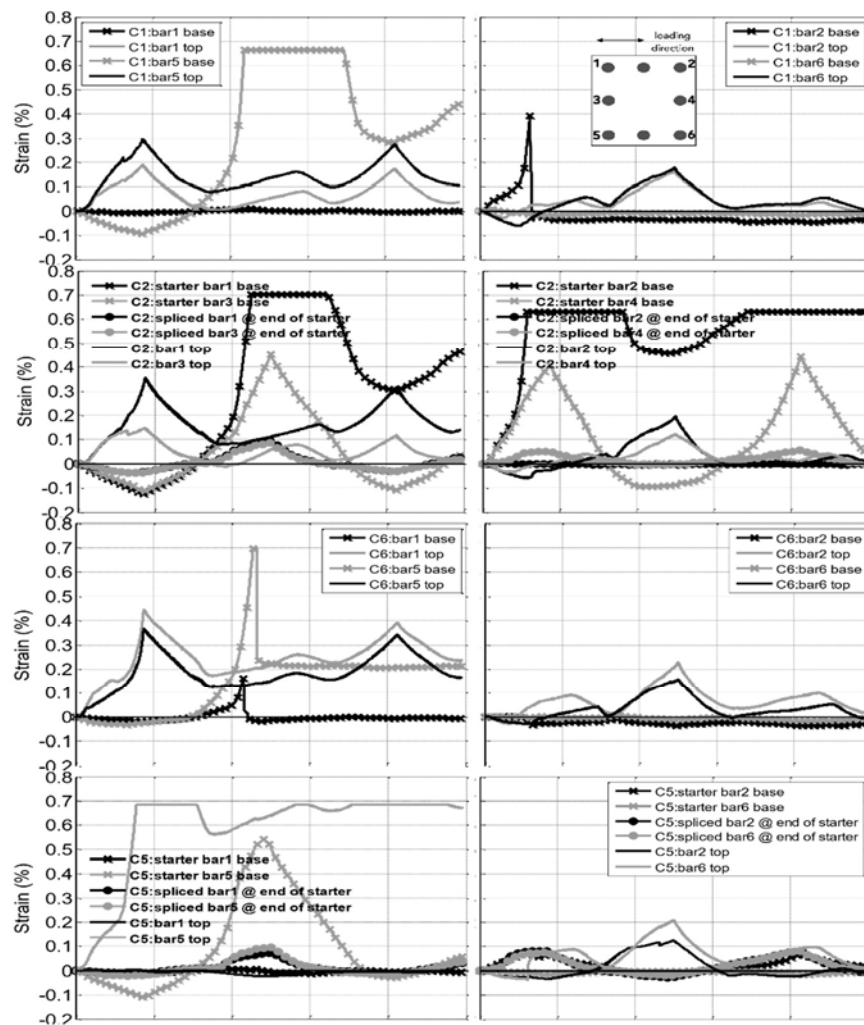


Figure 196: Bar strains on opposite sides of the ground storey columns: (top row) C1, (second row) C2

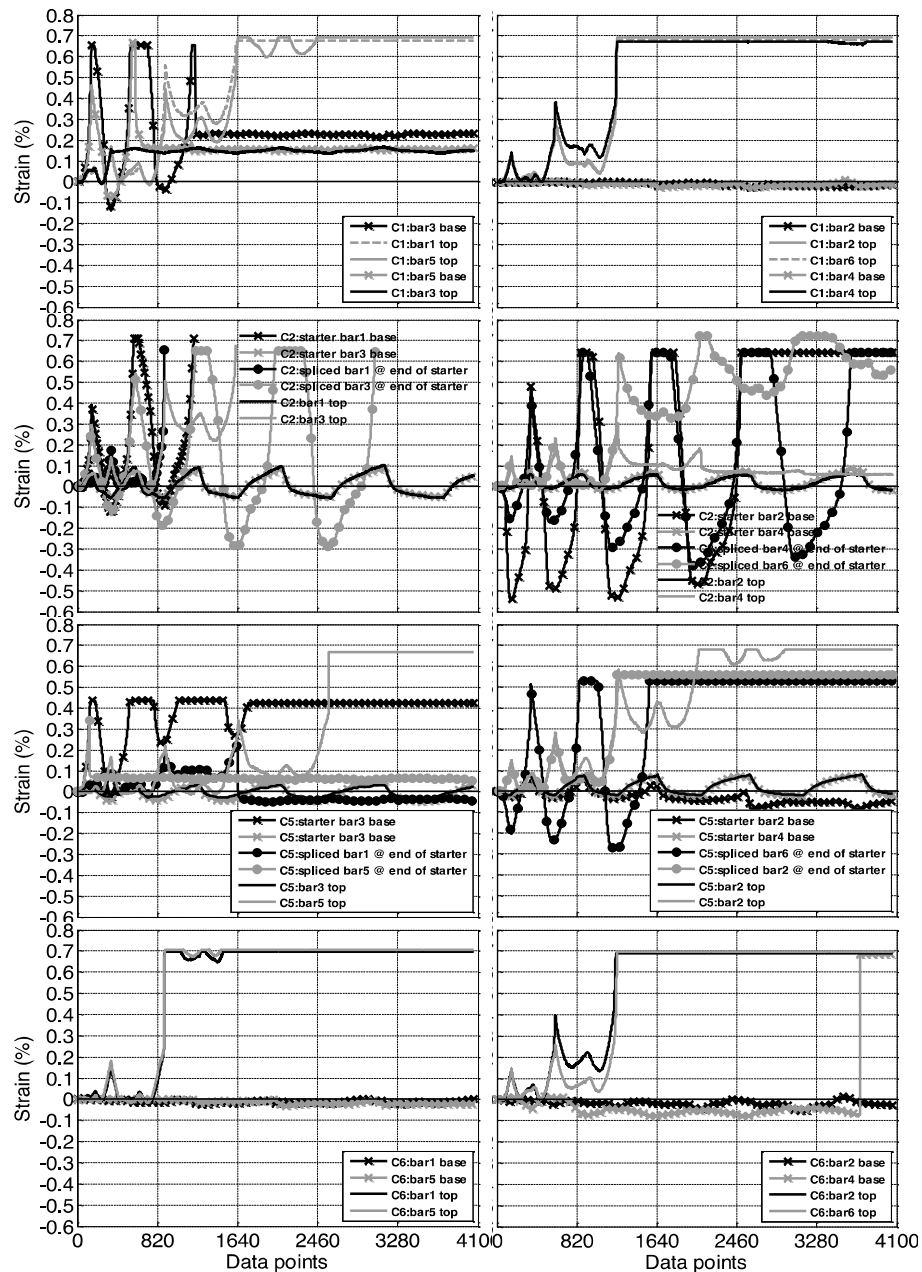


Figure 197: As in Figure 196, but in phase of testing after wrapping the ends of Columns C5 and C6 in FRP

Concrete strains

The same displacement transducers' measurements employed for fixed-end rotation estimates were used to estimate, via the position of the neutral axis, the compressive strains at the surface of concrete and at the location of bars in the compressive zone during the initial phase of the loading, i.e., until the first reversal (Figure 198). Given that these results depend weakly on the estimated location of the neutral axis, and that the concrete was not damaged at these locations in the first phase of testing, the high magnitude of these strains is worth noting. The same figures show that the so-estimated strains at the location of the "compression bars" are an order of magnitude less than those measured on the bars and often of different sign. Invalidity of the plane sections hypothesis may explain this latter discrepancy, but not the magnitude of surface strains in Figure 198. Possible explanations for the large

compressive strains sustained within a 10 to 20 mm wide end strip next to the re-entrant corner of the concrete surface include:

- confinement by the adjoining element (the top of the footing or the soffit of a beam) and
- size effects: the fitting to hundreds of ultimate curvature measurements in Grammatikou et al 2016 gives an average ultimate strain of 1% for the extreme compression fibres if the neutral axis depth is 45 mm, and even larger, for the smaller neutral axis depths of the present case.

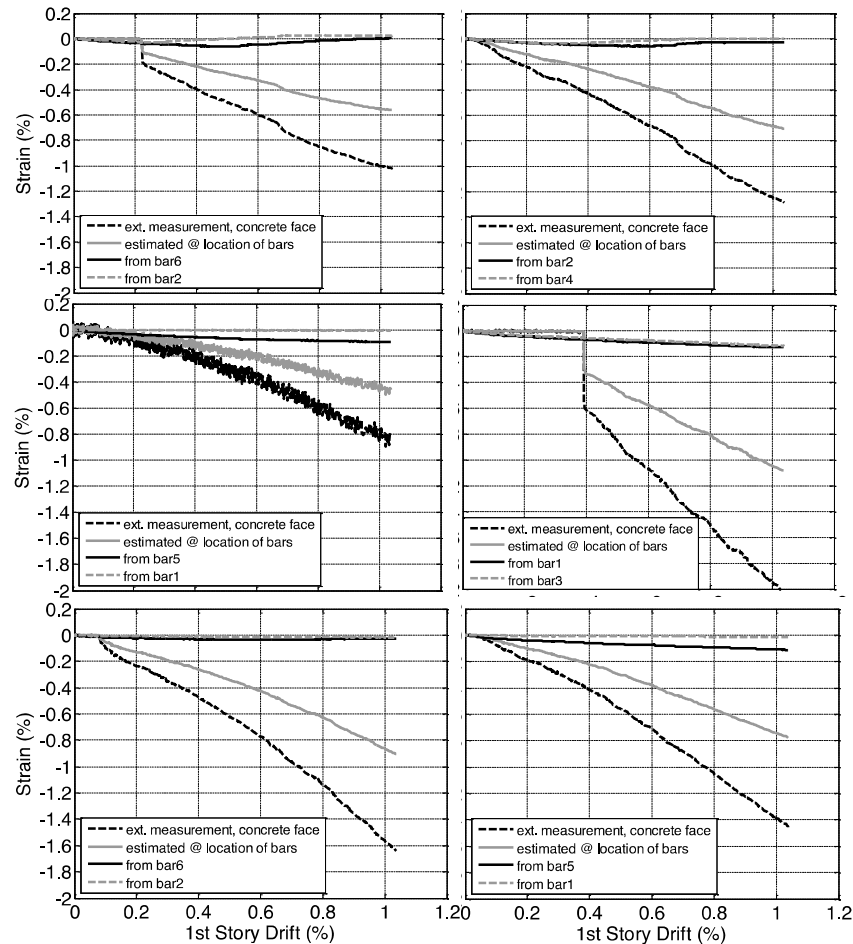


Figure 198: Concrete strains at the surface and next to the nearest vertical bar, estimated from external deformation measurements and strains in these bars from strain gages, vs interstorey drift in the first cycle of loading: (top row) top of ground storey columns C1 (continuous bars) and C2 (lap-spliced bars); (second row) base of ground storey columns C1 and C2; (bottom row) base of columns C1 and C2

Effects and behaviour of the FRP overlays at joints and around column ends

The very small impact the FRP wrapping had on the column response and behaviour came as no surprise, as FRP wrapping increases very little the yield moment and stiffness of a member, but improves drastically its flexural deformation capacity, which, however, was beyond the deformation demands on frame members, even where they reached local values of 0.055 rads. Indeed, even at top drifts of 3.3%, there was no serious damage other than debonding of the FRP overlay from joints (Figure 199), and the visible cracking of columns, beams and slabs.



Figure 199: Detachment of anchorage of FRP overlay of joints from lateral face of beam, through the concrete substrate

5.1.5 Conclusions and outlook

The behaviour observed and the results obtained during the test allow the following conclusions concerning the effects of the columns' smooth bars on local and global performance.

1. Slippage of the columns' smooth bars caused column deformations to concentrate at flexural cracks at the top and bottom sections.
2. The inverted-S shape of the storey shear-interstorey drift loops is typical of bond-slip loops, suggesting that the hysteretic behaviour of the frame was governed by bond along the column bars; nevertheless, cyclic strength decay, also typical of bond-slip loops, was not observed at any storey.
3. The damage inflicted by the cyclic loading consisted of:
 - o visible residual cracks at column end sections,
 - o diagonal cracking of the joints, early in the test and, right after global yielding;
 - o debonding of FRP overlays from the exterior face of joints that had previously suffered the diagonal cracking in (a);
 - o residual through-thickness cracks in floor slabs due to their role as effective tension flange of the frames' beams, and
 - o torsional yielding of transverse edge beams, due to transfer of the slab's eccentric in-plane forces to the frame's joints through torsion in the transverse beams (note, though, that this transfer is at the expense of shear stresses in the joint core and, hence, is beneficial concerning damage of type (b) above).

Only damage of type (a) above had to do with, or was due to, the smooth bars in the columns.

1. The large fixed-end-rotations due to slippage of column bars made possible chord rotations as high as 0.055 rads and interstorey drifts of almost 5%, without serious damage or residual deformations.
2. Strains measured on smooth bars show them to be in compression wherever the surrounding concrete is also in compression, but with compressive strains less than what strain compatibility with the surrounding concrete would imply.
3. Neither the lap splices nor the FRP wrapping of the column end regions had a systematic effect on the behaviour of columns.

Overall, the cyclic behaviour and performance of the frame may be considered satisfactory, apart from the diagonal cracking of joints, which had little to do, though, with the use of smooth bars in the columns.

5.2 Project #9 – ARCO – Effect of Axial Restraint on the Seismic Behaviour of Shear-Dominated Coupling Beams

Authors

B. Mihaylov⁽¹⁾, A. Trandafir⁽¹⁾, J. Almeida⁽²⁾, M. Ferreira⁽²⁾, L. Hagsten⁽³⁾, and J. Fisker⁽³⁾, S. Bousias⁽⁴⁾, X. Palios⁽⁴⁾, N. Stathas⁽⁴⁾, E. Strepelias⁽⁴⁾

⁽¹⁾ *University of Liege, Liege, Belgium*

⁽²⁾ *University of Lisbon, Lisbon, Portugal*

⁽³⁾ *Aarhus University, Aarhus, Denmark*

⁽⁴⁾ *Structures Laboratory, University of Patras, Greece*

5.2.1 Introduction

Reinforced concrete coupled walls are an efficient structural system for medium to tall buildings that provides large stiffness and strength against wind and seismic loads. The coupling of the individual wall units is typically provided by short and stiff coupling beams which deflect in double curvature with high shear stresses, and therefore are susceptible to brittle shear failures. At the same time, in regions of high seismicity, the coupling beams are required to possess large ductility and energy dissipation capacity. However, while a number of experimental programs have been performed to evaluate the ductility and complete cyclic response of coupling beams, the boundary conditions used in the tests deviate in an important detail regarding the boundary conditions encountered in real structures. Specifically, in coupled wall systems, the stiff walls and floor diaphragms restrain the elongation of the beams due to cracking under seismic loading, and this generates compression in the coupling members influencing their behaviour. Therefore, this type of beams is characterised by a shear-dominated response, being susceptible to brittle shear failures.

This research project intends to study the effect of axial restraint on the seismic behaviour of short coupling beams. To address the research goal, the experimental approach proposed focuses on testing to failure of four conventionally reinforced coupling beams with longitudinal reinforcement and stirrups. Such beams are common in pre-1970s coupled-wall structures and are particularly vulnerable to brittle shear failures as evidenced by past earthquakes. First, three large-scale nominally identical specimens RB1, RB2 and RB3 with variable level of axial restraint were studied under monotonic loading up to the post-peak regime. Furthermore, an unrestrained fourth beam (RB4) is tested under a large inelastic pulse in one direction followed by a push to failure in the opposite direction. This unconventional cyclic loading scenario can be associated with a near-fault pulse-type ground motion.

5.2.2 Test specimens

Geometrical properties, reinforcement layout and material properties

The geometry of the test assemblies is shown in Figure 200. All beams had a (140x800) mm rectangular section and a shear span-to-effective depth ratio $a/d=1000/737=1.37$. The reinforcement layouts of the test specimens are presented in Figure 201 and Figure 202. The shear reinforcement consisted of 8mm diameter rebars spaced at 180 mm, equivalent to stirrup ratio equal to 0.40%. The outer stirrups were positioned at 50 mm from the end sections. The flexural reinforcement consisted of symmetrical top and bottom rebars with longitudinal ratio equal to 1.22% ($4\phi 20$) for specimens RB1, RB2 and RB3, while RB4 had longitudinal reinforcement ratio equal to 0.44% ($4\phi 12$). The beams were anchored in two large concrete blocks. The reinforcement of both bottom and top foundation blocks was consisted of 18mm diameter rebars spaced at approximately 150mm at all three directions.

The concrete used had maximum aggregate size of 16 mm to ensure proper consolidation around the reinforcement. Cylindrical samples with 300 mm height and 150 mm diameter were collected from the base block, top block and coupling beam specimens. The compressive strength of the concrete was 36.4 MPa and was determined as the average value from six cylindrical samples performed shortly before the beam tests.

The properties of the coupling beams' reinforcement were obtained from tensile tests conducted on three samples for each rebar used in the tests. The stirrups (8mm diameter), had yield stress equal to 510 MPa and the yield stress of the longitudinal reinforcement (12mm and 20mm diameter) was equal to 520 MPa, as illustrated in Figure 203. It should be noted that the sudden drop in the end of the stress-strain curves does not correspond to rupture of the bar but corresponds to the phase when the displacement transducer attached on the coupons was removed shortly before the bars ruptured.

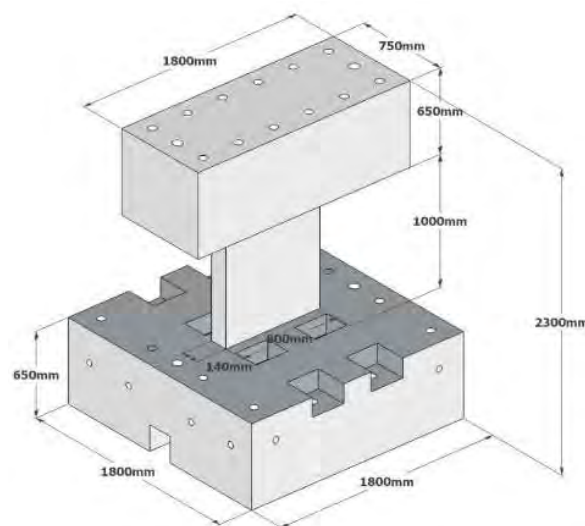


Figure 200: Geometry of test specimens

Specimens RB1, 2, 3

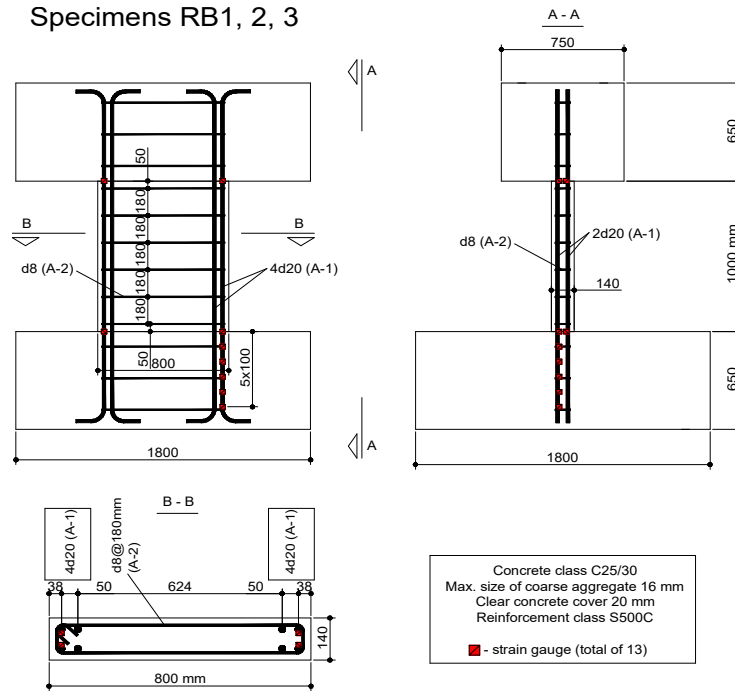


Figure 201: Reinforcement details of specimens RB1, RB2 and RB3

Specimen RB4

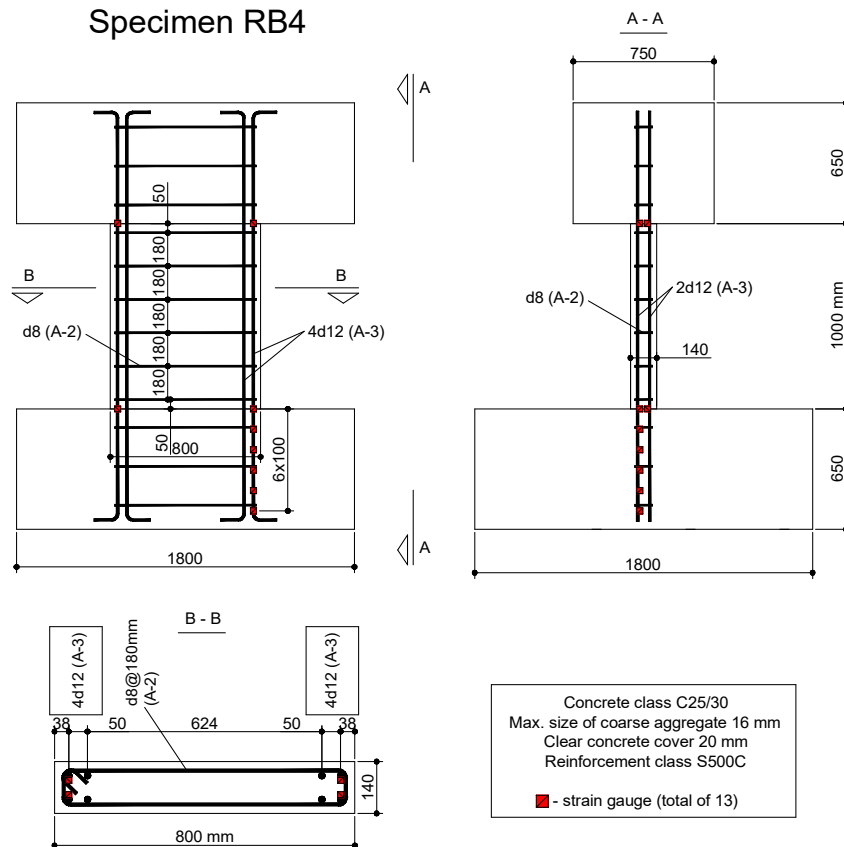


Figure 202: Reinforcement details of specimen RB4

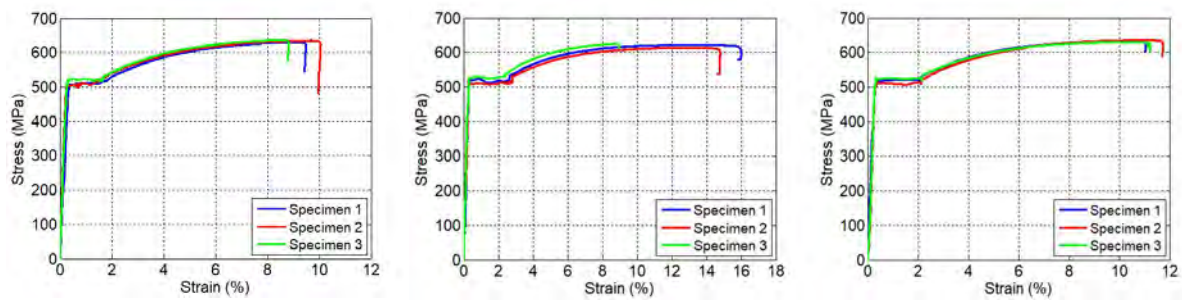


Figure 203: Stress-strain relationship for: diameter 8 mm bars (left), diameter 12 mm bars (middle), diameter 20 mm bars (right)

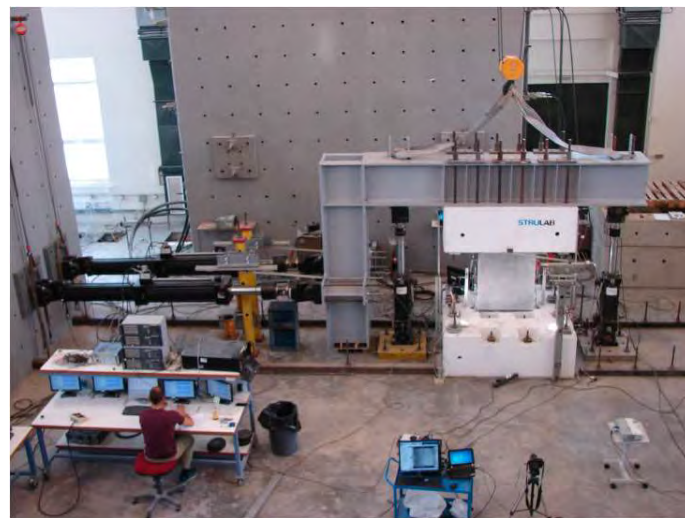


Figure 204: Global view of test setup

5.2.3 Test setup

The four tests were performed at the Structures Laboratory (STRULAB) of the University of Patras, Patras, Greece. STRULAB facility is equipped with an (18x16) m strong floor and two post-tensioned reaction walls. Figure 204 shows the global setup of the specimens at the lab.

As illustrated in Figure 204, the coupling beams were tested in a vertical position in the same way they were cast. The bottom block of the test specimen was post-tensioned to the strong floor while a L-shaped steel beam was post-tensioned to the top block. This steel member acted as a loading beam and its displacements were controlled by four servo-hydraulic actuators: two in horizontal and two in vertical position.

A detailed drawing of the test setup is shown in Figure 205 and Figure 206. The lateral load was applied by the two horizontal actuators (HA1, HA2) via an L-shaped steel beam prestressed to the top concrete block. The distance between the two horizontal actuators was 1.00m. and they applied the lateral load to the L-shaped steel beam at the level of the mid-span section of the coupling beam (i.e. 500mm above the top face of the base foundation block), leading to symmetrical double-curvature bending of the coupling beam. The vertical actuators (VA1, VA2) were used to control the rotation of the top block and to simulate axial restraint. All tests were carried out in a displacement-control manner with the horizontal actuators being slaved to impose the same displacement preventing the coupling beams from torsion.

The specimens were fixed to the strong floor by means of 16 prestressed bars. Prestressed steel rods PT1 and PT2 shown in Figure 205 and Figure 206 were used only in test RB3. Specimens RB1 and RB4 were free to axially deform during the test, therefore no axial restraint was applied on those coupling beams. Specimen RB3 was tested under full axial restraint and specimen RB2 was designed to represent an intermediate level of restraint.

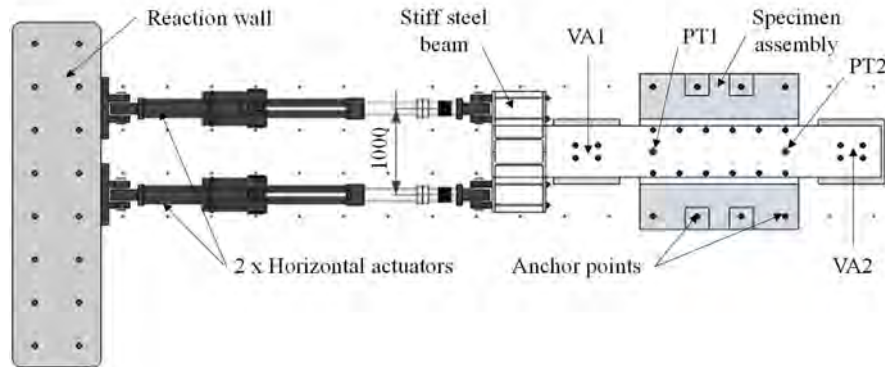


Figure 205: Plan view of test setup

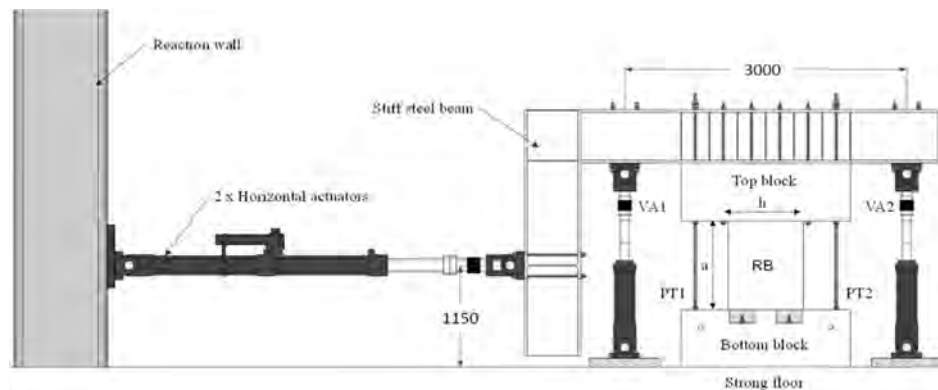


Figure 206: Side front view of test setup

The specimens were densely instrumented with strain gages (SGs) attached to their longitudinal reinforcement and displacement transducers (linear potentiometers and digital transducers) to measure various local and global deformations. Figure 207 illustrates the instrumentation scheme and the labelling of the transducers used at the tests and Figure 208 shows the position of the strain gages at the longitudinal rebars.

The transducers in the test region were attached to three of the beam sides (one long and two short), while the fourth side of specimens was prepared with a random pattern of speckles to perform digital image correlation measurements (DIC). In particular, during the tests it was measured the drift imposed on each coupling beam specimen (DT1, DT2), its axial deformation (DT3, DT4), its flexural and shear response, opening/closing of interface cracks and slippage of the beam with respect to the foundation blocks. In total, 26 displacement transducers were used in each specimen RB1, RB2 and RB3, and 28 displacement transducers in specimen RB4 along with 13 strain gages per specimen to measure the local deformation of the rebars.

In addition, manual marking of cracks and measurement of crack widths was performed at different load stages per test and a series of network cameras were used via Telepresence system to completely capture the specimens' response by synchronous measurements and images.

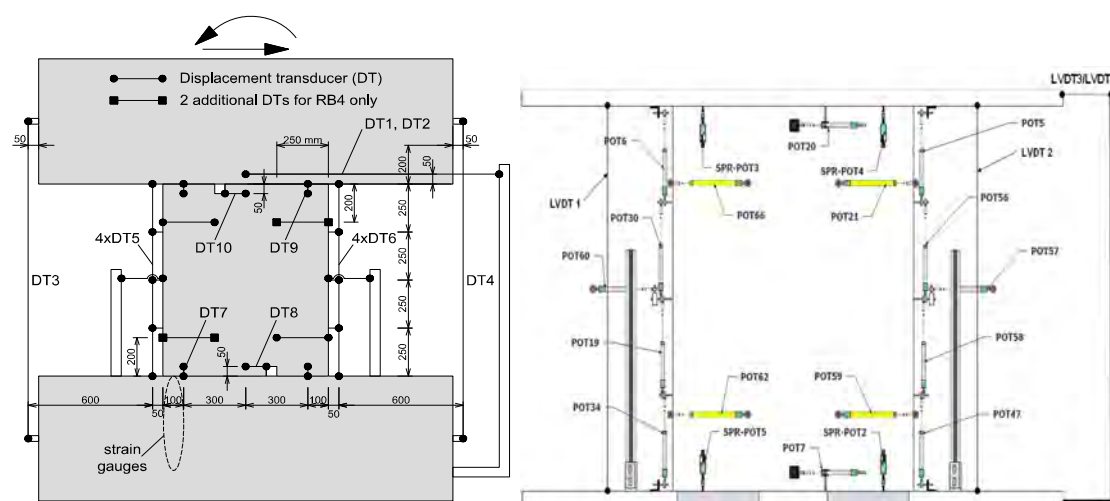


Figure 207: Instrumentation scheme and sensors' labelling

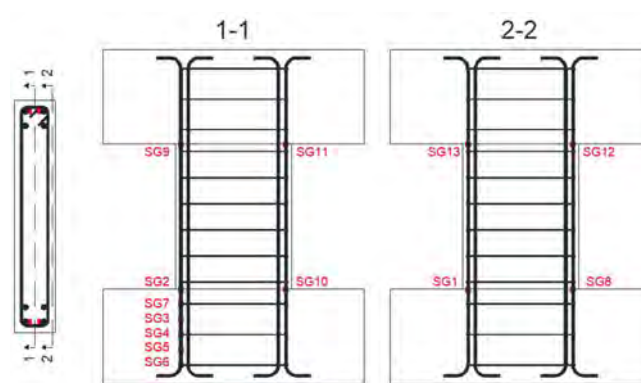


Figure 208: Position of strain gages

The front face of each specimen was free of instrumentation in order to perform digital image correlation (DIC) measurements (Figure 209). Two properly calibrated DIC systems were used simultaneously. The DIC systems allowed for tracking of the complete displacement field of the specimen on a dense grid of points.



Figure 209: DIC system and speckle pattern

Loading procedure

The test specimens RB1, RB2 and RB3 were loaded to failure under monotonic loading whereas the RB4 specimen was subjected to a cyclic loading protocol. The load was paused at various load stages in order to inspect the specimen, take photos, mark cracks, and manually measure crack widths, as mentioned before. As the weight of the test setup was eccentric with respect to the specimens (i.e. horizontal actuators and L-beam), it caused in-plane bending of the beams prior to the tests. To counteract this effect, the first step of the testing procedure was to apply equal and opposite forces of 21.3 kN with the vertical actuators VA1 and VA2. With bending being eliminated, the beams experienced an axial compression of 67 kN (1.64% of the compressive capacity of the gross concrete section) due to the weight of the top concrete block, L-beam and horizontal actuators. Following this first step, the loading procedure of each specimen continued.

Concerning the loading sequence of specimen RB1 (no axial restraint), vertical actuator VA1 was kept in force control with a force of 21.3 kN, while VA2 was under control of displacement slaved to that of VA1, such that the two actuators had the same displacements. The displacements were controlled with DT3 and DT4. In this way, the coupling beam could axially deform freely, but the end foundation blocks remained parallel to each other. Finally, the lateral load was applied monotonically by the two horizontal actuators HA1 and HA2 in displacement control.

At the loading procedure of specimen RB2 (partial axial restraint), the upward force applied by VA1 was decreased in proportion to the measured drift of the test specimen. Actuator VA2 was slaved to VA1 such that the two actuators had the same displacements. As a result, the axial compression in the coupling beam increased linearly with the drift at a rate of 50 kN/mm and the two foundation blocks remained parallel to each other. Then, the lateral load was applied monotonically by both horizontal actuators HA1 and HA2 in displacement control.

Specimen RB3 (full axial restraint) was unloaded and then reloaded by vertical actuators VA1 and VA2 in displacement control, such that to achieve the same DT3 and DT4 readings. Those displacements were kept constant for the rest of the test. In this way, the coupling beam could not elongate (full axial restraint) and the foundation blocks remained parallel to each other. Two prestressing bars were post-tensioned between the foundation blocks in an approximately symmetrical manner with forces of 271 kN (PT1) and 249 kN (PT2), as shown in Figure 206. While VA1 and VA2 were in displacement control at the same time, the tension forces in the bars generated approximately equal compressive forces in the vertical actuators, and a negligible force in the test specimen. This step was performed to reduce the tension that would build up in VA1 and VA2 during the lateral loading. The lateral load was then applied monotonically with both HA1 and HA2 in displacement control. The axial forces in PT1 and PT2 were measured continuously by strain gauges attached properly on the prestressed bars.

Specimen RB4 (no axial restraint) was subjected to multiple load reversals as shown in Figure 194. This loading protocol intended to study the response of a coupling beam under a near-fault pulse-type ground motion. Actuator VA1 was kept in force control with a force of 21.3 kN, while VA2 was slaved to VA1 such that the two actuators had the same displacements. The displacements were controlled with DT3 and DT4. In this way, the coupling beam could elongate freely but the foundation blocks remained parallel to each other. Utilising the horizontal actuators, three symmetrical load cycles were applied in force control with an amplitude of ± 70 kN, or 25% of the estimated yield load of the specimen. Three symmetrical load cycles were applied in force control with an amplitude of ± 140 kN, or 50% of the estimated yield load of the specimen. Three symmetrical load cycles were applied in force control with an amplitude of ± 210 kN, or 75% of the estimated yield load of the specimen. The specimen was unloaded and the loading was switched to displacement control, i.e. both horizontal actuators were controlled in displacements. The specimen was loaded in one direction until significant yielding of the

flexural reinforcement was observed. The load was then reversed and the beam was pushed in the opposite direction until failure (Figure 210).

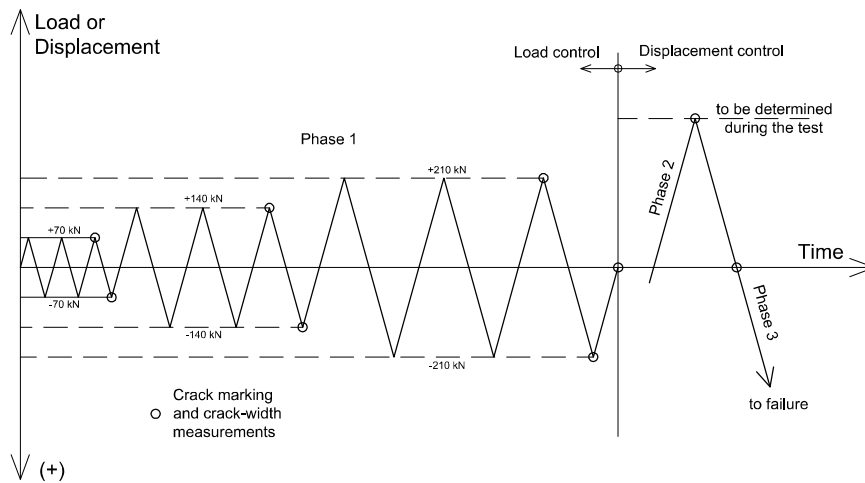


Figure 210: Lateral load history of specimen RB4

5.2.4 Test Results

Specimen RB1

Specimen RB1 had no axial restraint and was subjected to monotonic loading up to failure. The evolution of the compression force due to the actuators is shown in

Figure 211 (left) as a function of the chord rotation of the coupling beam. It can be seen that the axial compression reached a maximum value of 36.4 kN, or 0.893% of the compression capacity of the gross section. The global response of specimen RB1 in terms of shear force vs. chord rotation is shown in

Figure 211 (right). The shear strength of the beam was 456 kN and the corresponding chord rotation was 0.663%. The chord rotation corresponding to 20% loss of lateral resistance in the post-peak regime was 1.77%. The test was terminated at 30% loss of lateral resistance, which corresponded to a chord rotation of 2.41%.

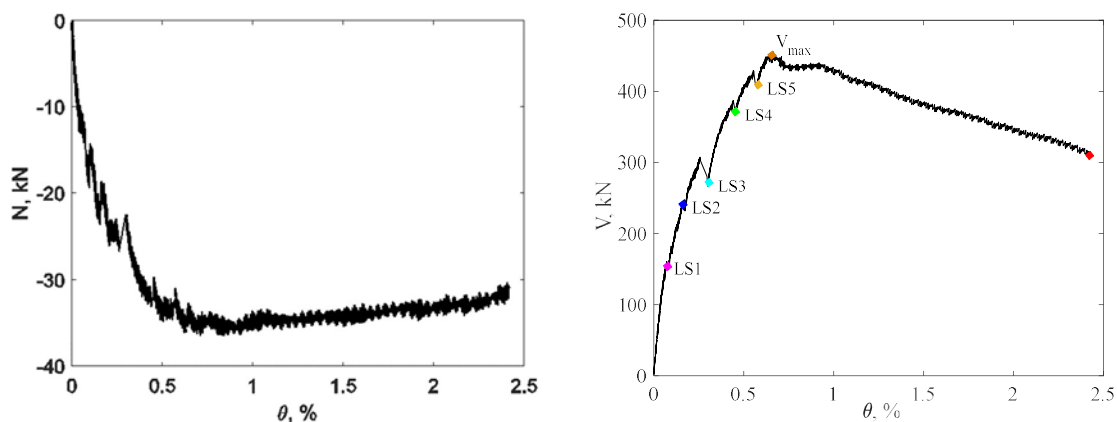


Figure 211: Axial compression force vs. chord rotation response of specimen RB1 (left), Shear force vs. chord rotation response of specimen RB1 (right)

As evident from Figure 211 (right), the beam behaved linearly up to a load of about 160 kN (LS1) when the first cracks propagated near the end sections. As the load was increased further, more flexure-shear cracks developed in the shear span (LS2). These cracks tended to propagate steeper and, eventually, were followed by the propagation of a major shear crack at 65% of the maximum load, $V \approx 300$ kN (LS3). A significant reduction of stiffness occurred upon the propagation of the diagonal crack. At LS5, this crack extended from corner to corner of the beam along the diagonal of the shear span. At a shear force of 420 kN the crack width along the diagonal measured up to 1.90 mm. The crack diagrams for peak response and prior to failure of specimen RB1 are shown in Figure 212. The beam failed in shear along the major diagonal crack without yielding of the longitudinal reinforcement. As illustrated in Figure 212, the behaviour of one compression corner was characterised by crushing and spalling of the concrete. This zone is considered to govern the shear resistance of this type of members. In addition, more steep cracks developed along the critical diagonal crack, prior to crushing of the concrete compression zone. Figure 212 shows also a photo of the beam taken at the end of the test.

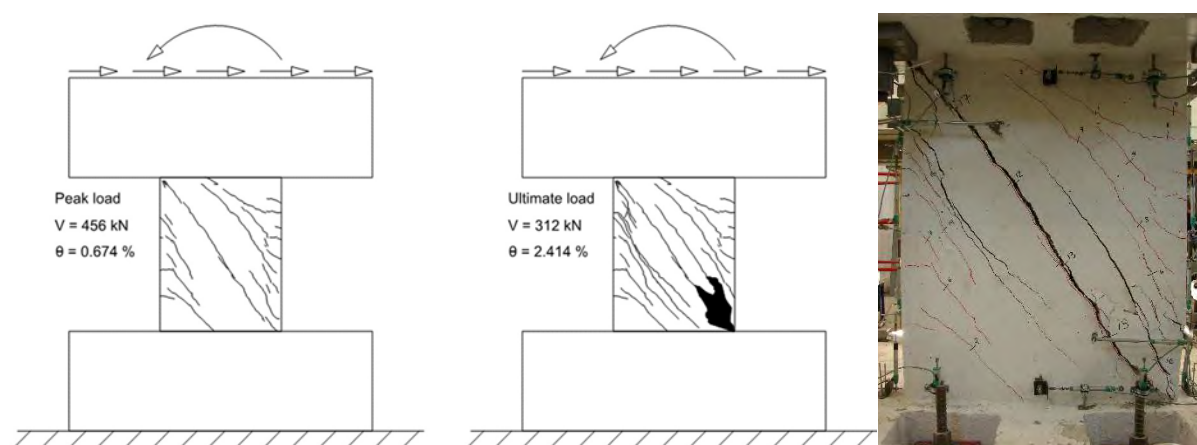


Figure 212: Crack diagrams of specimen RB1: at peak load (left) and failure (middle). RB1 specimen's post-test photo (right).

Specimen RB2

Specimen RB2 had an axially restrained boundary condition. The magnitude of the restraint compressive force was varied linearly with the beam's lateral displacement (see Figure 213). Therefore, the axial elongation of the beam was restrained gradually. The lateral load on the beam was increased monotonically until failure occurred. The global response of beam RB2 in terms of shear force vs. chord rotation is shown in Figure 213. The shear strength was 629 kN and the chord rotation corresponding to this load was 0.942%. The test was stopped at a chord rotation of 1.27% when the lateral resistance had decreased by 7%.

Up to a chord rotation of 0.1%, the specimen's response was largely linear elastic. Following the response of the uncracked beam, the first flexure-shear cracks developed in the vicinity of the end sections under the interaction between shear and flexure. This cracking pattern was influenced by the presence of shear stresses, while at this point the effect of the axial compression force is relatively small (LS2). Proceeding the loading procedure, more cracks developed. These newly propagated cracks had a steeper slope. At LS5, a major shear crack occurred in the upper part of the beam. The measured crack width was 0.2 mm, while no slip crack was observed. The propagation of this shear crack resulted in a significant reduction of stiffness at a shear force of about 300 kN. In the following load stage (LS6) a similar diagonal crack formed symmetrically with respect to the diagonal of the beam. In addition, cracking occurred at the top compression corner. Similar cracks developed at the bottom compression

corner in LS7 and the crack widths reached 1 mm. In the subsequent stages, LS8 and LS9, the major cracks continued to widen under increasing lateral displacement, while the beam's response tended to soften gradually. As the load increased further, the peak load was reached. As illustrated in Figure 214, this event corresponded also to the propagation of a major shear crack that extended along the diagonal of the beam. Moreover, more cracks were observed in the compression corners, associated with crushing of the concrete under high compressive stresses. After this event, the shear resistance of specimen RB2 degraded rapidly. Figure 214 also shows specimen RB2 at the end of the test. When compared to the response of reference specimen RB1, the effect of axial restraint increased the shear strength by 38%, while the displacement capacity was reduced by one-half.

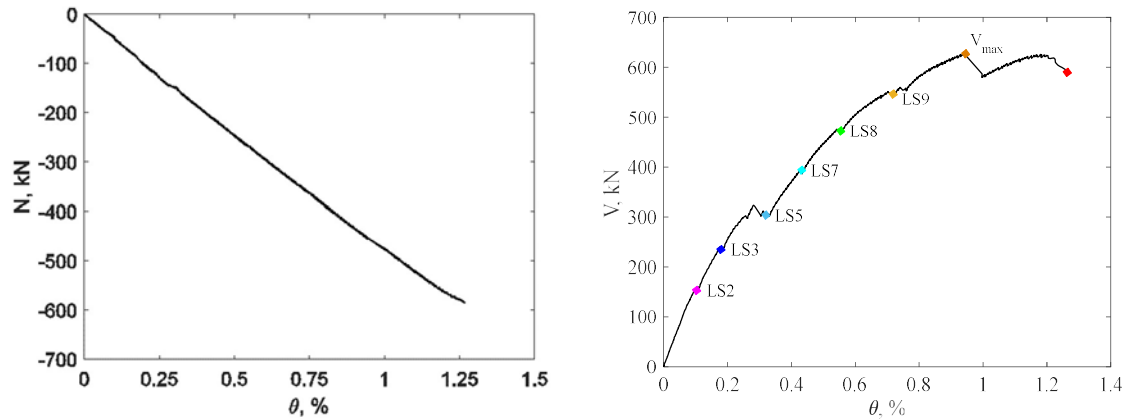


Figure 213: Specimen RB2: axial compression force vs. chord rotation (left), shear force vs. chord rotation (right)

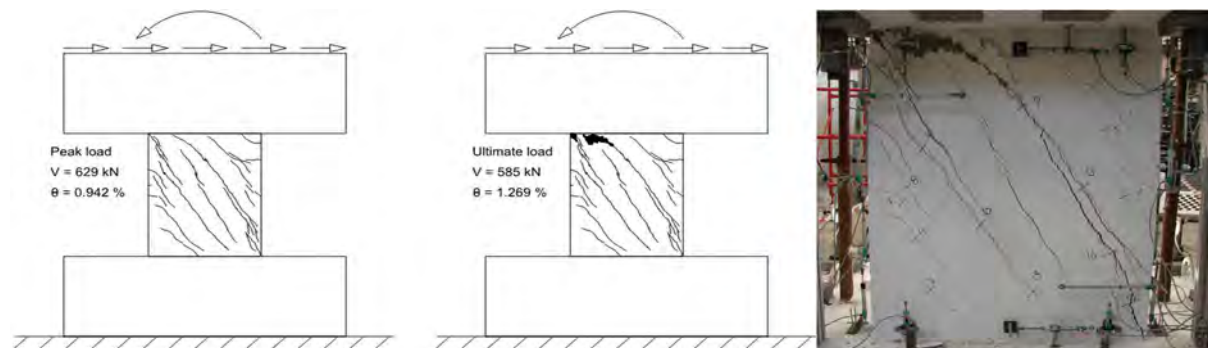


Figure 214: Crack diagrams of specimen RB2: at peak load (left) and failure (middle). RB2 specimen's post-test photo (right)

Specimen RB3

Specimen RB3 was fully axially restrained. The vertical actuators were controlled at zero displacement, and therefore any elongation of the beam due to cracking during lateral loading was prevented. As a result, the coupling beam developed a significant compression force as shown in Figure 215. The compression reached a maximum value of 359 kN or 9.69 % of the compression capacity of the gross section. This plot does not account for the compression due to the weight of the top concrete block and the steel equipment supported by the coupling beam. Specimen RB3 was loaded monotonically in shear until the failure was reached. The global response of beam RB3 in terms of shear force vs. chord rotation is presented in Figure 215. The shear strength was 379 kN and the chord rotation corresponding to this force was 0.369%. The test was terminated at a chord rotation of 1.60% when the lateral resistance has decreased by 36%.

Inclined cracks developed prior to LS1, but they did not extend from corner to corner of the beam. As the specimen was further loaded, the cracks widened (LS2). At LS3 - the lateral load reached about 300 kN - the major shear crack shifted towards the compression corner of the beam, and the stiffness gradually decreased. The pre-peak crack width measurements were completed at LS4 when the major crack reached 0.5 mm width. At this stage, a second major shear crack had formed of 0.2 mm. This crack had a more typical corner-to-corner shear pattern layout.

The peak load (failure) of the beam was reached between LS4 and LS5. Prior to LS5 several cracks had developed in both compression corners due to high compressive stresses. The maximum crack width reached 0.80 mm. It is worth mentioning that several short and densely spaced cracks were observed along the first major crack. This type of cracking can be related to aggregate interlock shear mechanism. In the subsequent load stages, crack width increased up to 2 mm, while new cracks developed at both compression corners (LS7, Figure 215). The test was terminated at a chord rotation of 1.6% when significant spalling of the concrete was observed at both corners. In addition, some isolated spalling occurred along the critical diagonal crack, particularly in the zone with high tangential stresses due to aggregate interlock. Significant slip was reported in this region, which can be associated with sliding of the top block along the crack due to the high axial stresses developed by then. Figure 216 shows specimen RB3 at the end of the test. When compared to the response of the reference specimen RB1, the effect of a fully axial restraint boundary condition decreased the shear strength of the beam by 17% and the displacement capacity by 34%.

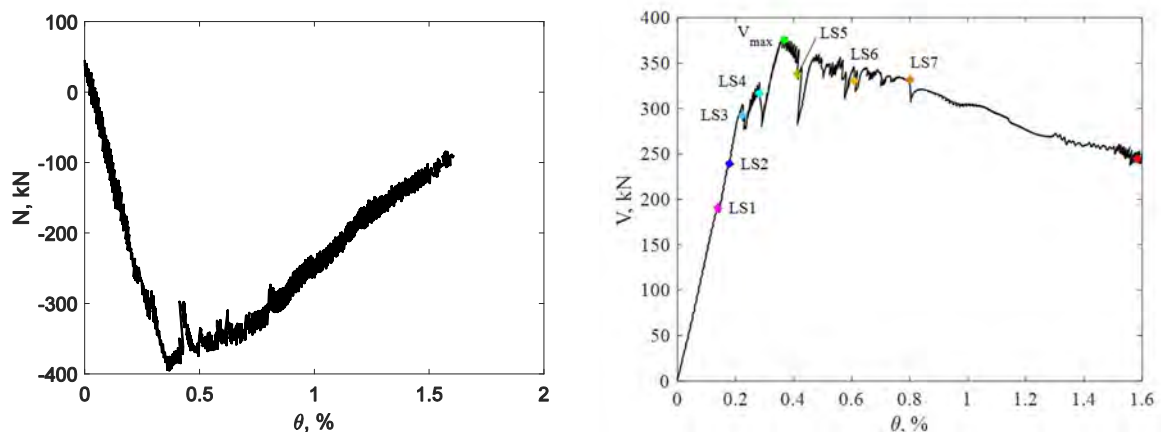


Figure 215: Specimen RB3: axial compression force vs. chord rotation (left), shear force vs. chord rotation (right)

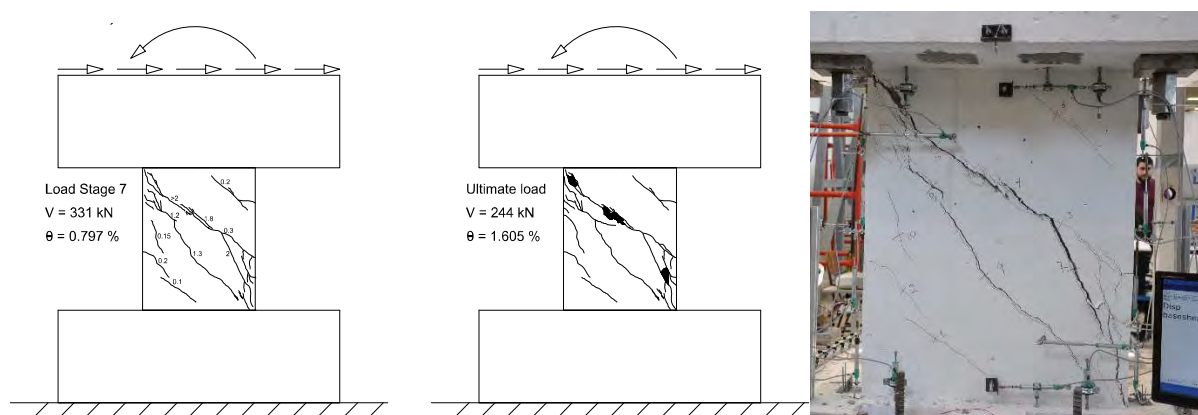


Figure 216: Crack diagrams of specimen RB3: at Load Stage 7 (left) and failure (middle). RB3 specimen's post-test photo (right)

RB4 specimen

The shear force vs. chord rotation response of RB4 specimen is shown in Figure 217. The shear strength in the negative direction was 345 kN, while in the negative cycle the peak was recorded at a value of 328 kN (5% lower). The test was terminated in the positive direction when the lateral resistance had dropped by 20% and the chord rotation had reached 3.36%.

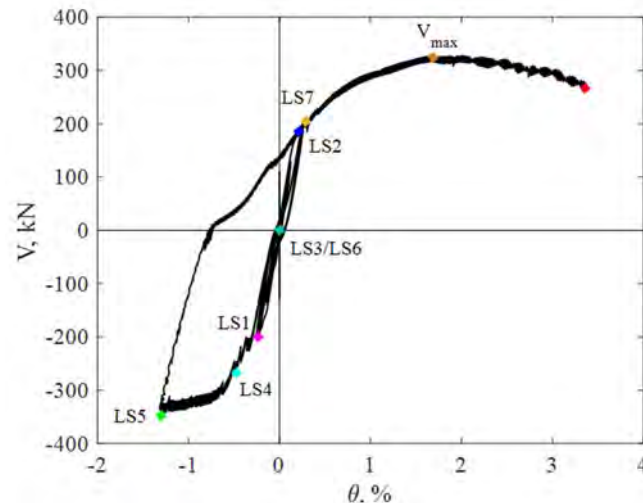


Figure 217: Shear force vs. chord rotation response of specimen RB4.

Following the initial stiff response of the uncracked beam, flexure-shear cracks developed eventually. The beam cracked progressively during the phase of force-controlled loading which reached a maximum amplitude of 75% of the expected peak resistance. At this maximum amplitude, the chord rotation reached 0.31% (LS1). Despite the fact that the specimen was subjected to relatively small lateral displacements, a maximum crack width of 0.4 mm was reported. In the following load step LS2, the specimen was loaded in the positive direction with the same amplitude of shear force. As expected, the cracking pattern showed a nearly symmetric propagation of cracks. The width of the newly formed flexure-shear cracks near the end sections of the beam was in the range of 0.2 mm to 0.3 mm. The force-controlled phase (LS3) of the test was concluded by unloading the specimen. The residual crack widths were 0.1 mm.

The second part of the test was performed in displacement-control. The beam was pushed in the negative direction up to the point in which significant yielding of the flexural reinforcement was recorded by the strain gages mounted on these bars. The initiation of yielding was detected at LS4 when the maximum measured crack width was 0.4 mm in the vicinity of the top section, and the diagonal crack had a maximum width of 0.3 mm. The chord rotation was further increased to 1.40%. At LS5, the critical diagonal crack developed from corner to corner. As a consequence, the stiffness of the beam decreased significantly. The shear crack measured 0.6 mm at specimen's mid-span and cracking was observed in the compression corners of the beam. The beam was unloaded and once again, the residual crack widths were measured. The width of the shear crack at mid-span was 0.4 mm, while the cracks near the end sections had a maximum residual width of 0.3 mm. After LS6 at zero load, the beam was loaded to failure towards the positive direction. A single load stop was performed in this final loading (LS7, Figure 217) when the shear force reached 200 kN (similar to the maximum amplitude of load that was applied in a force-controlled phase). At this load stage, a critical diagonal crack developed in the other direction. The maximum width of the diagonal shear crack measured equal to 0.7 mm.

From that point, the chord rotation was increased until the shear resistance reached its peak value and consequently decreased by 20%. Despite the beam exhibited flexural yielding, the displacement capacity of the specimen was limited by a shear failure along the critical diagonal crack. Crushing and spalling of the concrete in the bottom compression corner was also observed. A photo of specimen RB4 at the end of the testing procedure is shown in Figure 218.

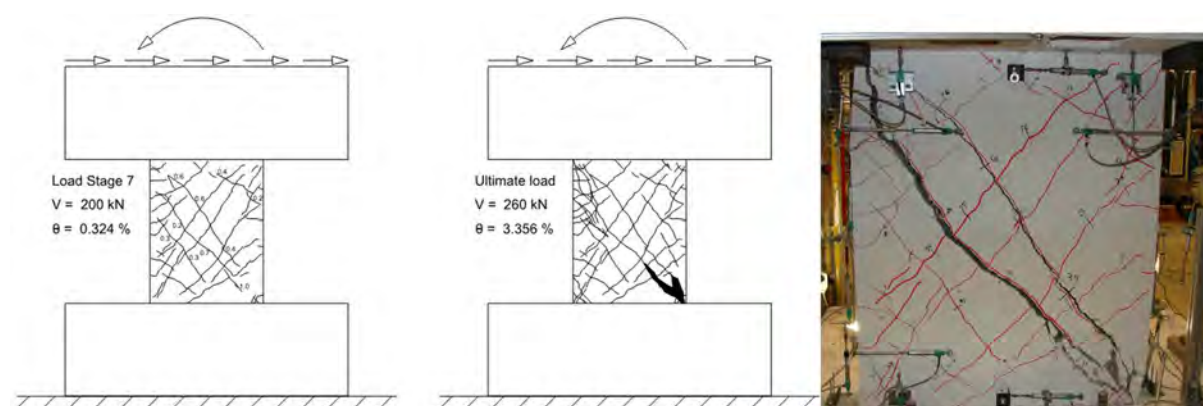


Figure 218: Crack diagrams of specimen RB4: at Load Stage 7 (left) and failure (middle). RB4 specimen's post-test photo (right)

Effect of axial restraint

The effect of axial restraint is studied by comparing the behaviour of specimens RB1 (no restraint), RB2 (partial restraint) and RB3 (full restraint). Figure 219(left) shows the shear force vs. drift response of the beams, while Figure 219(right) depicts the variation of the axial elongation with the shear load. It can be seen from the latter plot that the elongation of RB3 was controlled reasonably well at zero in the pre-peak regime and went slightly out of control after failure. As can be expected, RB1 elongated the most and, for a given shear force, the elongation of RB2 remained between those of RB1 and RB3. More surprising is the peak resistance of the beams as the partially-restrained specimen was the strongest, and the fully-restrained beam was the weakest. It can be seen from Figure 219(left) that the behaviour of the beams was very similar up to a shear force of about 300 kN when all specimens exhibited a significant drop of resistance due to major shear cracking. However, while RB2 reached a peak shear force of 629 kN, RB3 failed at only 379 kN. Thus, while RB2 was 38% stronger than the reference beam RB1, RB3 was 17% weaker.

To explain these results, it is instructive to compare the crack diagrams of the test specimens at near failure, see Figure 220(top). In addition to crack patterns and crack widths, the diagrams also show the sequence of formation of the main shear cracks indicated with circled numbers, as well as the likely location of the diagonal struts. It can be immediately seen that it is the strut action that had a very different capacity in the three cases. While RB2 had two major shear cracks with a strong wide strut in-between them, the strut in RB3 had to cross the widest crack which measured 0.5 mm at 88% of the peak shear. This crack was significantly steeper than the major cracks in RB1 and RB2, and it began to open at a very low shear of about 8 kN. A possible explanation of this early cracking could be shrinkage strains or pre-cracking of the specimens. Therefore, while the low strength of RB3 may be of concern, more tests are needed to confirm the sensitivity of the results to pre-cracking as well as to the control of the axial restraint in lab conditions. The photographs in Figure 220(bottom) show that the large strut in RB2 eventually failed due to a splitting crack along the axis of the strut, as well as crushing of the concrete at the end of the strut. Specimen RB3, in contrast, failed with large sliding displacements and spalling of concrete along the steep critical crack.

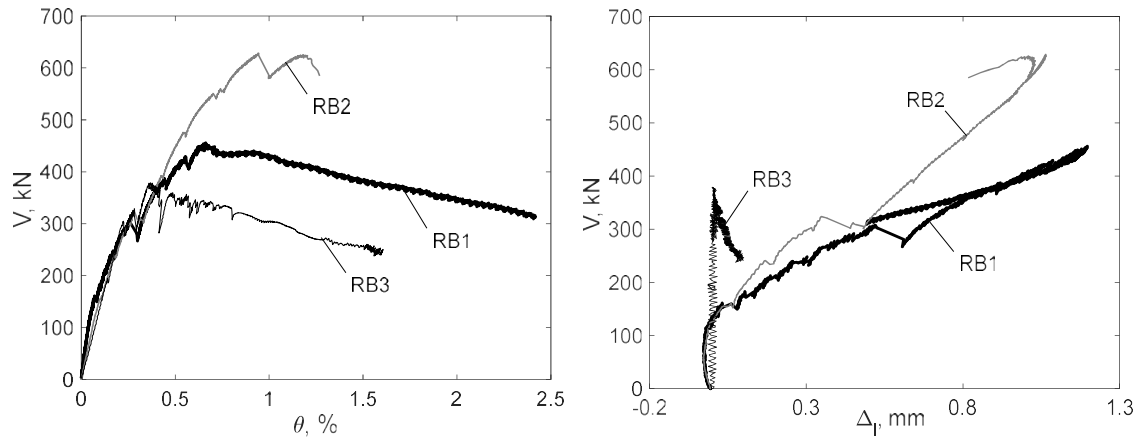


Figure 219: Effect of axial restraint – specimens RB1-3: Transverse behaviour (left) and Beam elongation (right)

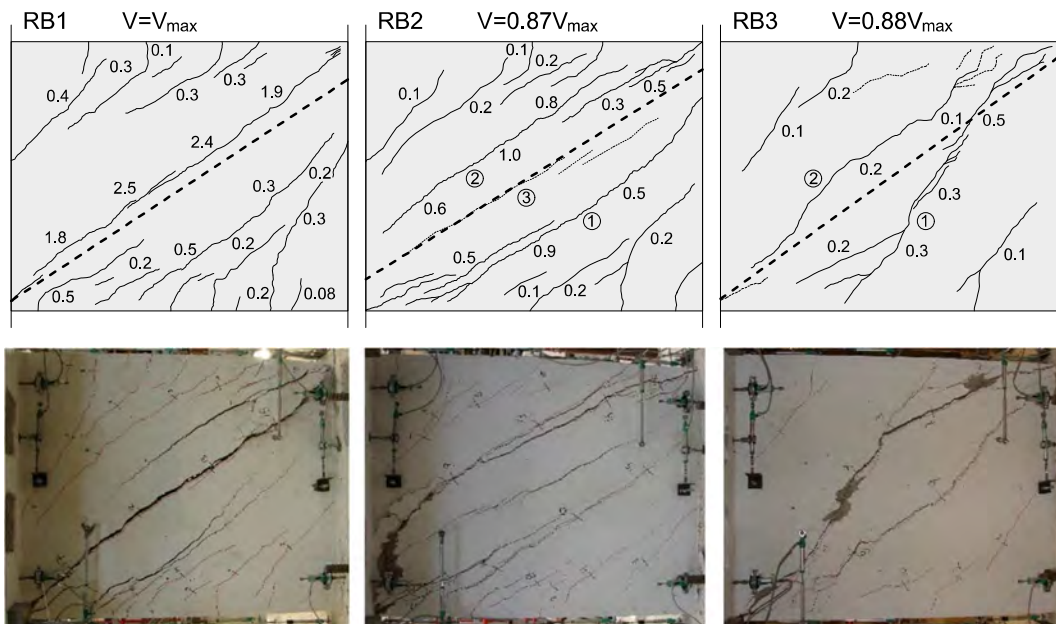


Figure 220: Crack diagrams near failure (top) and damage in the end of the test (bottom) – specimens RB1-3. (Dotted lines in the crack diagrams represent cracks that formed at failure)

The build-up of compressive restraint forces in the specimens as a function of the imposed drift, is shown in Figure 221. It can be noticed that at zero drift all three specimens experienced a certain low level of compression. In specimens RB1 and RB2 this compression was only due to the weight of the test setup and equalled 1.64% of the strength of the gross concrete section. In addition to this weight, specimen RB3 also experienced the difference between the forces in the vertical actuators (VA1 and VA2) and the post-tensioning rods (PT1 and PT2). Even though prior to the lateral loading this difference was expected to be zero, the measurements showed that the upwards push of VA1 and VA2 was slightly larger than the downwards pull of DT1 and DT2 and therefore the initial compression in RB3 was less than that in RB1 and RB2. Following this initial stage at zero drift, the compression in RB1 remained approximately constant while that in RB3 increased and reached 11.3% at failure. The compression on RB2 was controlled to increase linearly with the drift and reached a value of 12.8% at failure.

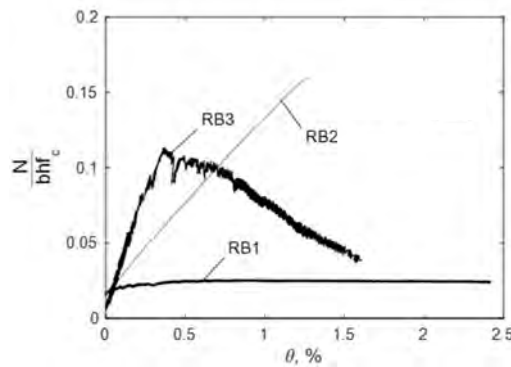


Figure 221: Build-up of axial compression forces – specimens RB1-3

Effect of longitudinal reinforcement ratio and loading history

The effect of longitudinal reinforcement ratio and loading history is evaluated by comparing specimens RB1 and RB4, both tested without axial restraint. Specimen RB4 had approximately 3 times smaller reinforcement ratio and was subjected to reversed cyclic loading. Figure 222(left) compares the complete shear force vs. drift behaviour of the two beams. After nine symmetrical load cycles with relatively small load amplitudes, RB4 was pushed to a drift of 1.3% in the negative loading direction, which resulted in significant yielding of the longitudinal reinforcement in the end sections. Owing to the yielding, the width of the cracks in these sections reached 2.9 mm and the beam exhibited a yield plateau with a peak shear force of 345 kN. When reloaded to the opposite direction, the reinforcement yielded again and the peak shear resistance reached 327 kN, 5.2% lower than in the negative direction. This shows that even though the plastic flexural deformations were significant, that did not result to a large cyclic strength degradation. However, as the drift was increased further to the positive direction, the resistance decreased and the beam failed suddenly in shear with rupture of the stirrups along a diagonal crack (Figure 222– middle, right). Significant crushing of the concrete was observed at the top right corner of the beam. Therefore, while the peak resistance was governed by flexure, the displacement capacity of beam RB4 was limited by shear. This shows that the strength of the diagonal struts decreases after flexural yielding, even though the load on the beam remains approximately constant. If the drift capacity θ_u is defined by a 20% drop of resistance in the post-peak regime, RB4 reached θ_u equal to 3.3% versus 1.8% for RB1. In contrast, RB4 was 1.4 times weaker than RB1 as a result of its smaller amount of flexural reinforcement.

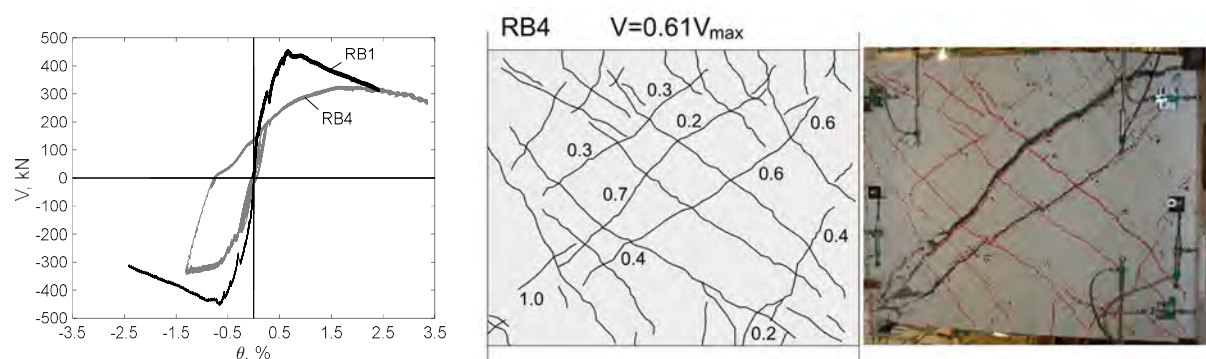


Figure 222: Effect of longitudinal reinforcement ratio and loading history of RB1, RB4 (left), Crack diagram near failure (middle) and damage in the end of the test (right) of RB4

5.2.5 Conclusions

At Table 25 the main results from the four coupling beam tests are summarized. In terms of axial compression, it is interesting to note that while the restrained beams RB2 and RB3 had very different shear strengths V_{max} , they reached very similar compression values n_{max} at failure. It can also be seen from beams RB1-3 that an increasing axial restraint resulted in a decreasing drift capacity ϑ_u , while the lower reinforcement ratio of RB4 resulted in an enhanced ϑ_u . A similar trend is also observed in the elongation of the beams $\Delta_{l,max}$ and the width of the flexural cracks $w_{flex,max}$ at peak load. In terms of contribution to ϑ_u of the slip displacements in the end sections, ϑ_{slip} is negligible for specimens RB1-3 that exhibited a brittle shear failure (max 10%) and is significant for RB4 that exhibited flexural yielding (28%).

Test	ρ_l , %	Restrain t	Load	V_{max} , kN	n_{max} , %	ϑ_{max} , %	ϑ_u , %	$\Delta_{l,max}$, mm	$w_{flex,max}$, mm	w_{sh} , mm	$\vartheta_{slip}/\vartheta_u$
RB1	1.22	No	M	456	2.53	0.66	1.80	1.20	0.29	2.5	0.06
RB2	1.22	Partial	M	629	12.8	0.94	1.27 ^b	1.06	0.30	-	0.10
RB3	1.22	Full	M	379	11.3	0.37	1.04	0	0.20	0.9	0.04
RB4	0.40	No	C	328 (345) ^a	2.31 (1.30)	1.69% (1.30%)	3.34 (-)	4.50 (4.93)	1.25 (2.87)	- (0.6)	0.28 (-)

Table 25: Summary of test results

ρ_l = longitudinal reinforcement ratio A_s/bd ; A_s = longitudinal reinforcement on one side of the section; b =140 mm= section width; d =737 mm= effective depth of section from compressive edge to center of A_s ; V_{max} = peak shear resistance (strength); $n_{max}=N_{max}/bh f_c$ = normalized axial compression force at peak resistance; ϑ_{max} = drift corresponding to V_{max} ; ϑ_u = drift capacity defined at 20% drop of resistance in the post-peak regime; f_c =36.4 MPa= compressive strength of the concrete; $\Delta_{l,max}$ = elongation of beam at peak resistance; $w_{flex,max}$ = maximum crack width at end sections at peak resistance; w_{sh} = maximum width of diagonal cracks at peak resistance; $\vartheta_{slip}/\vartheta_u$ = contribution of slip displacements in the end sections to ϑ_u .

Notes: a) values in the negative loading direction, b) value corresponding to $V_u/V_{max}=0.93$

The current project presented four large-scale tests of reinforced concrete coupling beams with detailed crack and deformation measurements. The test variables were the degree of axial restraint (no restraint, intermediate, and full restraint), the ratio of flexural reinforcement (1.22% vs. 0.44%), and the loading type (monotonic vs. cyclic). The main conclusions from the study are the following:

- As compared to no restraint, an intermediate restraint resulted in an increased shear strength and a full restraint in a decreased strength. The drift capacity was found to decrease with increasing restraint.
- The major cracks in the fully-restrained beam opened at a very low shear due to likely pre-cracking. As this caused a relatively very low shear resistance, further tests are needed to confirm the results and to study their sensitivity to pre-cracking.
- By decreasing the flexural reinforcement of the unrestrained beams from 1.22% to 0.44%, the failure mode changed from brittle shear to a more ductile shear failure following significant flexural yielding. Using strain gauge and DIC measurements, it was shown that only 3.43% of the drift capacity of the brittle specimen came from anchorage pull-out from the adjacent concrete blocks (walls).
- An unsymmetrical loading history with a large imposed drift in one direction, followed by loading to failure in the opposite direction, did not result in a significant strength degradation of the specimen with ρ_l of 0.44%. However, due to the ineffective closing of the cracks upon load reversals, large sliding displacements occurred in the end sections of the beam accounting for up to 47% of the drift at peak load.

5.3 Project #20 – hybrid Testing of an Existing Steel FRaMe with Infills under Multiple EarthquakeS (HITFRAMES)

Authors

L. di Sarno⁽¹⁾, R. Landolfo⁽²⁾, M. D’Aniello⁽²⁾, M. Dolsek⁽³⁾, F. Freddi⁽⁴⁾, O-S. Kwon⁽⁵⁾, S. Bousias⁽⁶⁾, X. Palios⁽⁶⁾, N. Stathas⁽⁶⁾, E. Strepelias⁽⁶⁾

⁽¹⁾ *University of Liverpool, UK*

⁽²⁾ *University of Naples, Federico II, Italy*

⁽³⁾ *University of Ljubljana, Slovenia*

⁽⁴⁾ *University College London, UK*

⁽⁵⁾ *University of Toronto, Canada*

⁽⁶⁾ *Structures Laboratory, University of Patras, Greece*

5.3.1 Introduction

Existing steel residential framed buildings were often designed primarily for gravity loads, as a result they exhibit low energy absorption and inadequate dissipation capacity under seismic loadings, which has been demonstrated by recent earthquakes occurred in the Mediterranean regions. Damages such as significant lateral residual drifts, buckling and failure of structural steel members, and partial collapse of masonry infills were frequently observed on existing steel framed building during post-quake investigations. A critical point in this regard is the effects of slender masonry infill walls on the seismic behaviour of existing steel frames with low lateral stiffness and strength. However, the current provisions in Europe for the seismic performance assessment of existing steel structures are scarce and they do not account for the presence of masonry infills. It is therefore necessary to provide effective methods for the seismic assessment and retrofitting of existing non-compliant steel frames. To this end, the HITFRAMES project aims at four major purposes:

- Develop reliable methods for the seismic assessment of existing steel frames, especially under earthquake sequences;
- Develop design procedures for buckling restrained braces (BRBs) considering contribution of masonry infills to the lateral load resisting system;
- Evaluate the effectiveness of BRBs as seismic retrofitting measure;
- Derive fragility curves for existing steel frames with infills and systems retrofitted with BRBs and infills, considering also the effects of earthquake sequences.

The recent 2016-2017 Central Italy earthquakes have caused widespread damage on low-to-medium rise steel buildings that do not incorporate ductile seismic detailing and highlighted the significance of an advanced assessment framework of existing steel buildings. The insufficient lateral stiffness of existing steel frames led to significant lateral drifts and buckling in the steel components, especially in the columns. Local damage (buckling) has also been observed at the beam-column connections due to the strut-action induced by the masonry infills. However, seismic performance assessment of existing steel frames still face many issues due to the complex behaviour and the interactions between beam-to-column connections, composite steel and concrete slabs and masonry infills among many others).

Additionally, the current European code for assessing existing buildings do not provide specific indications on the modelling and safety checks for steel frames with masonry infills.

Currently, most of the advanced modelling strategies of masonry infills were developed for reinforced concrete (RC) structures, among which the single-strut model is a popular approach, as it achieves a good balance between simplicity and accuracy. This model consists of a single strut in each diagonal direction to simulate the infill wall panels, which is easy to implement in finite element software and is capable of concentrating the infill wall-frame contact area to the corners. However, currently the property of such model was all calibrated based on RC frames rather than steel frames, which are usually more flexible. Therefore, the reliability of those models for estimating the performance of steel frames remains unclear and requires further justification.

Apart from the effects of masonry infills, earthquake sequence is another critical issue that needs to be addressed in the assessment of existing structures. During seismic events, the mainshocks are often accompanied by several foreshocks and aftershocks with comparable magnitude. This can lead to large cumulative seismic demand on existing structures, especially non-ductile systems. Premature fracture and local buckling may occur in plastic hinges especially of steel columns, thus leading to stiffness reduction and strength deterioration. The response of the masonry infills used for claddings of steel residential buildings is also significantly affected by the earthquake sequences. Although researchers have yet to agree on the fundamental differences in characteristics between a mainshock and major foreshocks and aftershocks, it is of great interest in assessing the effects of seismic sequences especially on the structural response of existing buildings. Extensive inelastic analyses have been recently carried out on a large ensemble of as-recorded main and aftershocks to investigate the effects of repeated earthquakes on inelastic displacement demands. Note that the above findings refer primarily to comprehensive numerical simulations carried out with advanced hysteretic models with stiffness and strength degradation.

5.3.2 Test specimen

A multi-storey steel moment-resisting frame, which was designed primarily for gravity loads with insufficient seismic detailing, was tested through pseudo-dynamic hybrid simulations at the Structures Laboratory (STRULAB) of the University of Patras in Greece. The prototype building consists of three bays and two storeys, which is believed to be a representative of existing steel frames. The building that was actually tested in the lab (the test specimen) is a two-storey one-bay substructure of the prototype building with a scaling factor of 0.75, whose plan and side views are presented in Figure 223. Three configurations of the test specimen were involved in this project, namely bare frame, infilled frame and retrofitted frame. The bare frame and infilled frame were tested as 3D frames while the retrofitted frame, which comprised of the bare frame with BRBs, was tested as a 2D frame.

The steel profiles are IPE200, IPE140 and HE180A respectively for external beams, internal beams and columns. The steel grade is S355 ($f_y = 355\text{MPa}$) for all beams and columns. All external beams are connected to columns through full penetration welding, and fully rigid beam column connections are considered in this study. It is worth noting that stiffeners were placed at all beam-column connections and column base connections. The photos in Figure 224 demonstrate the position of stiffeners. In addition, the composite slab of the test specimen consists of 250mm-thick concrete slab poured on 1.25mm-thick corrugated steel sheet (SYMDECK 73). Lastly, the designed BRB consists of a BRAD damper connecting to an elastic steel bracing in series, where the damper exhibits a nearly symmetric hysteretic behaviour in the tension and compression range with an ultimate strength of 210kN at 20mm displacement. The BRBs were installed externally to the framed structure and attached to the flange of columns with specially designed connection systems.

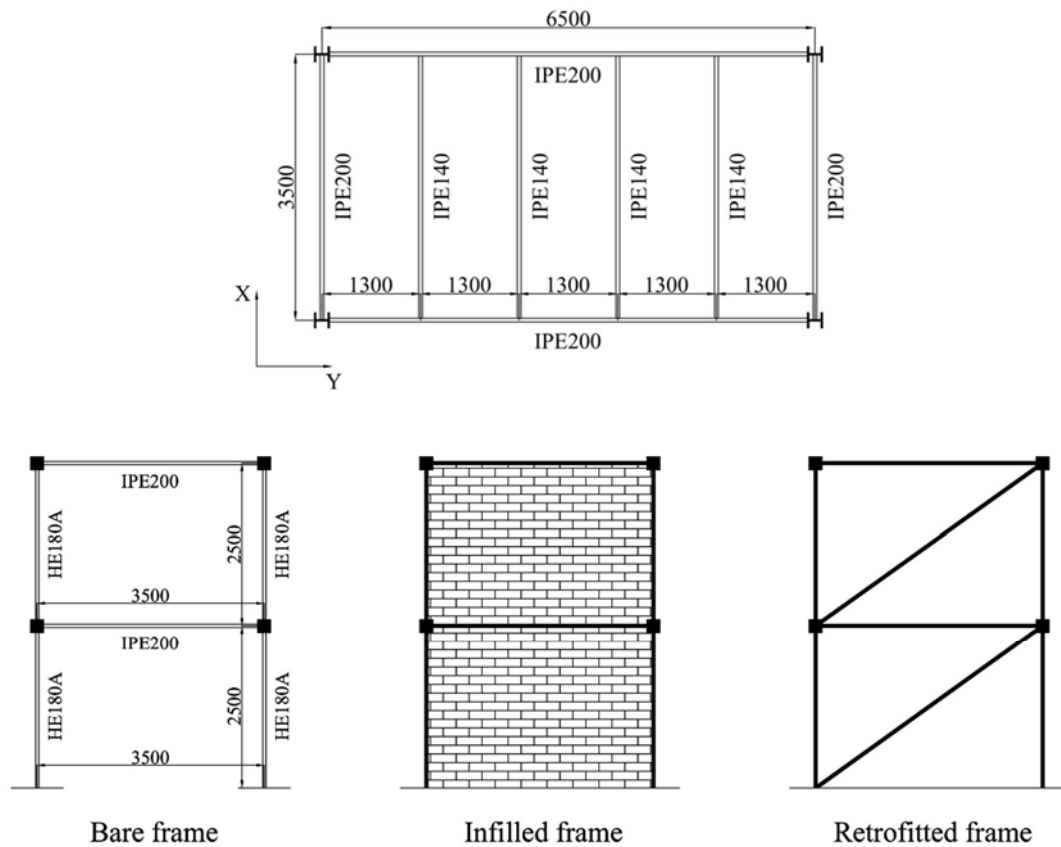


Figure 223: Plan and side views of the test specimens

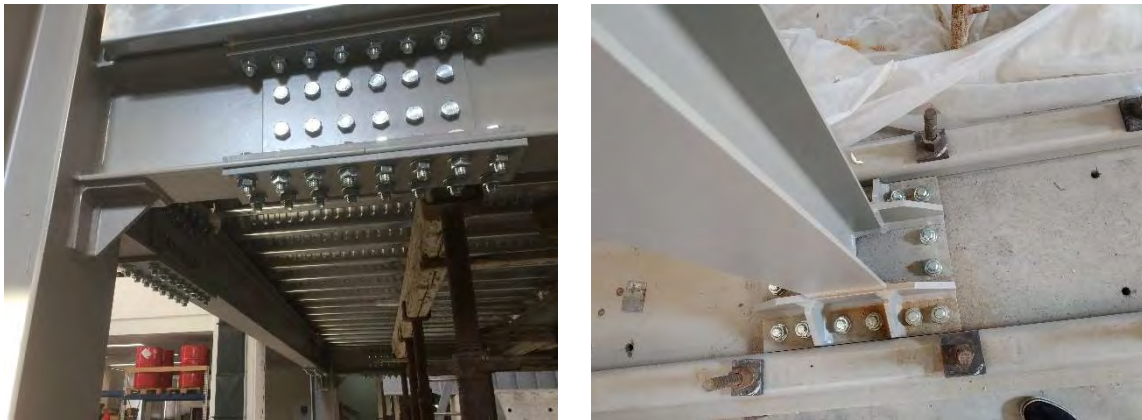


Figure 224: Positions of stiffeners at beam-column connections and at column bases

Three ground motions were selected for this study to form an earthquake sequence. The records were selected based on the requirement that they are able to reflect the moderate-to-high seismicity in some areas of the Southern Europe and to have large spectral acceleration in the region near the natural period of the test specimen. Table 26 summarised the basic information of the selected earthquakes and Figure 225 displays the time history of the earthquake sequence.

The response spectra of each individual ground motion listed in Table 26 are also shown in Figure 225, as well as the response spectrum of the earthquake sequence. It is evident that for periods ranging between 0.2 and 1.7 sec, the spectral acceleration corresponding to the mainshock is much larger than that corresponding to the foreshock or aftershock. However, for an infilled structure which usually has

an initial period of less than 0.2 sec, the mainshock does not result in a much higher spectral acceleration. Besides, it is also found that the spectrum of the whole sequence is roughly identical to the spectrum of the mainshock.

Event	Date	M_W	R_{epi} (km)	PGA (g)
foreshock	24/08/2016	6.0	15.3	0.35
mainshock	30/10/2016	6.5	4.6	0.48
aftershock	26/10/2016	5.4	9.4	0.30

Table 26: Summary of the selected ground motions

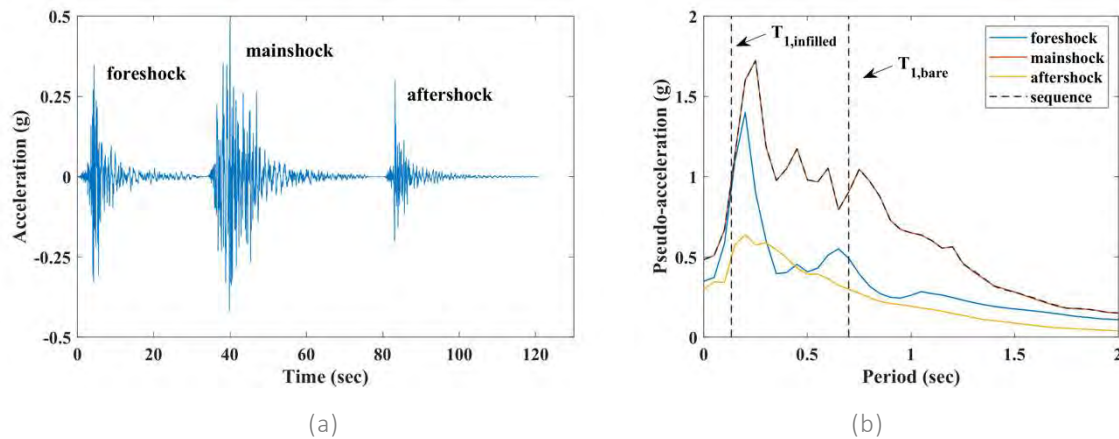


Figure 225: (a) Time history of the earthquake sequence; (b) the corresponding response spectrum

5.3.3 Numerical prediction

The three configurations of the test specimen were built in the finite element software OpenSees as three models, which were respectively labelled as BF for the bare frame, IF for the infilled frame and RF for the retrofitted frame. It should be noted that the numerical model of all three models were 3D frames, although the retrofitted frame was test as a 2D frame in the lab.

In all three models, the columns were modelled by force-based elements with ten integration points and the Steel01 uniaxial material with 2% post-yield hardening. Conversely, the beams were modelled by elastic elements with lumped plasticity. The plastic hinges were modelled by zero-length elements, whose properties were initially calibrated using the moment-rotation relationship proposed by Lignos and Krawinkler and were further modified based on Zareian and Medina. Figure 226 summarises all the materials that were defined in this study. Connections were considered as fully rigid in this study due to the stiffeners that were placed at beam-column joints. In addition, since the tests were performed in the direction along the weak axis of columns, the flexibility from the column panel zones can be neglected in this case.

In terms of the modelling of masonry infills, the single-strut model was adopted in the numerical simulation due to its simplicity and its accuracy in the reinforced concrete structures. The material property of the struts was defined based on the model by Mohammad Noh et al and Liberatore and Decanini, as also shown in Figure 226. It is worth noting that further calibration of the property of infills will be conducted based on the experimental results to achieve higher accuracy. Finally, the behaviour of the damper in the designed BRB is also presented in Figure 226d. The calibration of the BRBs was

based on the results of the experiments performed by the manufacturer and modelled by using the material model developed by Zona and Dall'Asta.

Modal analyses were performed on the three models at the beginning and the results were summarised in Table 27, which includes the periods and associated mode shapes and modal masses of the first and second mode. Figure 227 and Figure 228 present the inter-storey drift ratio (IDR) of the model IF and RF, respectively, obtained from the nonlinear dynamic analyses. To facilitate the demonstration of numerical results, the IDR limit proposed in ASCE41-06 is adapted to comply with the limit states defined in EC8-3, i.e. 0.7, 2.5 and 5% IDR for DL, SD and NC limit state, respectively.

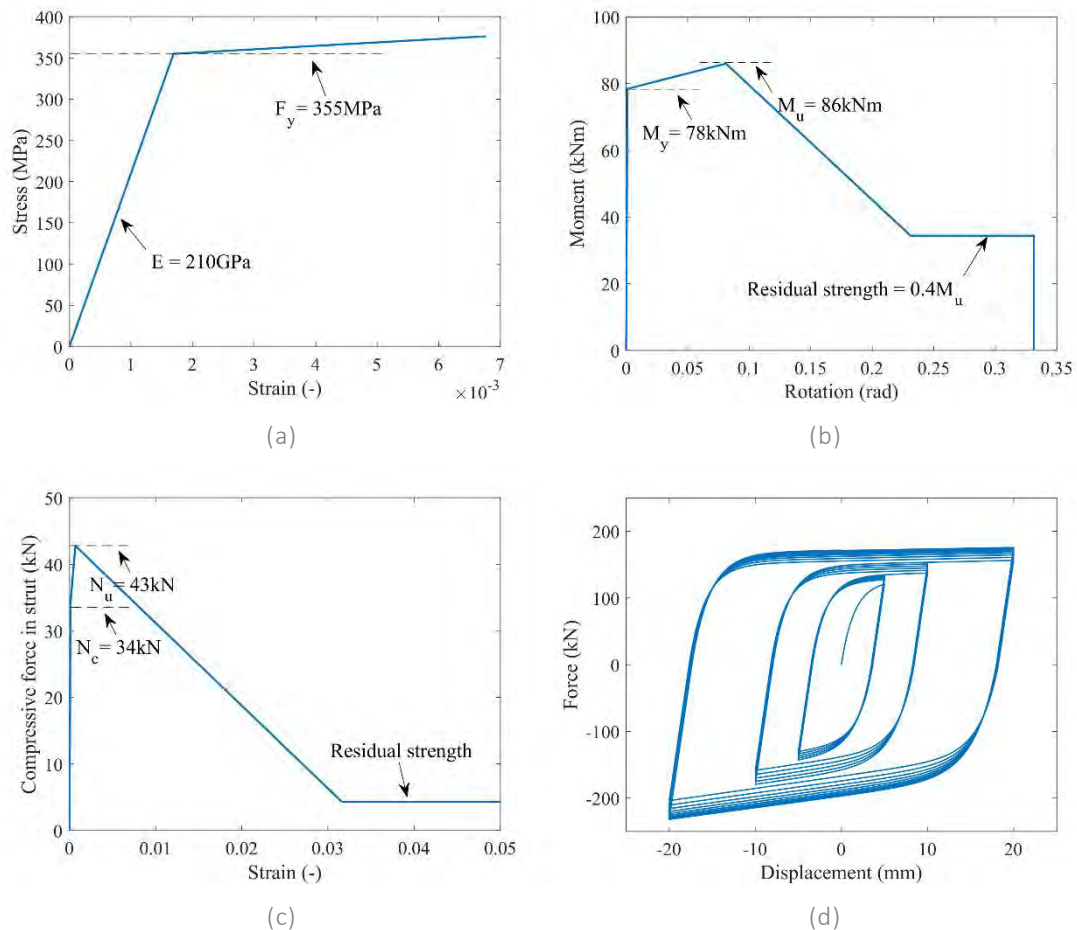


Figure 226: Material properties: (a) structural steel, (b) beam plastic hinges, (c) masonry infill struts and (d) buckling restrained braces

Model	1st mode			2nd mode		
	period (sec)	mode shape	modal mass	period (sec)	mode shape	modal mass
BF	0.71	0.4552 1.000	87.1%	0.25	-1.8674 1.0000	12.9%
IF	0.12 (-83%)	0.5644 1.000	92.5% (+6%)	0.05 (-82%)	-1.5043 1.000	7.5% (-42%)
RF	0.41 (-42%)	0.4861 1.000	88.6% (+2%)	0.16 (-36%)	-1.7487 1.000	11.4% (-12%)

Table 27: Modal properties of the test specimens

For the case of infilled frame, a scaling factor (SF) of 3.0 was applied to the input earthquake sequence record in addition to the unscaled record (SF=1.0). It is evident in Figure 227 that the first floor of the infilled frame experienced much larger lateral displacement than the top floor during the earthquake sequence, therefore, it is anticipated that damage was concentrated on the first floor. With the unscaled record, the peak transient drift was around 1.05%, which narrowly exceeded the DL limit state, and there was little residual drift of the steel frame, suggesting that the infills will not be significantly damaged and the structural elements will only slightly yield during the lab test according to the definition of the DL limit state. However, when the SF was increased to 3.0, the peak drift was increased to 6.13%, which exceeded the NC limit state, and the increasing residual drifts after each component of the earthquake sequence are clearly presented in Figure 228. This indicates that severe damage or even partial collapse of infill walls, as well as significant yielding of structural elements will occur during the lab test, with little residual strength of the steel frame.

For the case of retrofitted frame, a SF of 1.5 was applied to the input earthquake sequence record instead of 3.0 for the infilled frame, as the infills were not included in this case. Unlike the concentration of damage in the infilled frame, both floors of the retrofitted floor experienced similar lateral displacements during the simulation. With both the unscaled and scaled records, Figure 228 shows that the IDR of the retrofitted frame only slightly exceeded the DL limit state, and the increment in residual drift was not significant. Figure 229 demonstrates the response of BRBs compared to their designated behaviour in Figure 226d. It is noticed that with SF=1.0, the BRBs on neither floor were activated, as their yielding is not significant. However, when the SF was increased to 1.5, the BRB on the first floor was greatly activated, which made use of up to 90% of its displacement and load carrying capacity. This observation is desired as the purpose is to sacrifice the BRBs in order to prevent the rest of the structure from damaging.

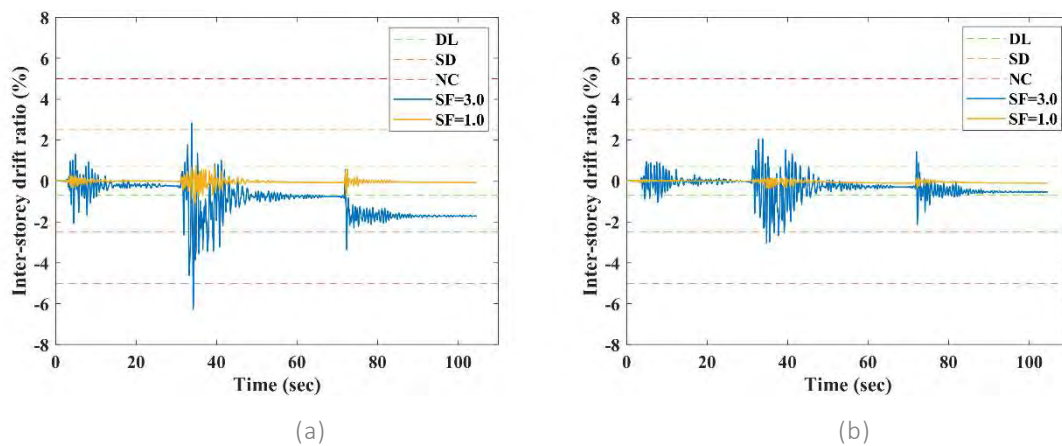


Figure 227: Inter-storey drift ratio of the infilled frame (IF): (a) first floor; (b) top floor

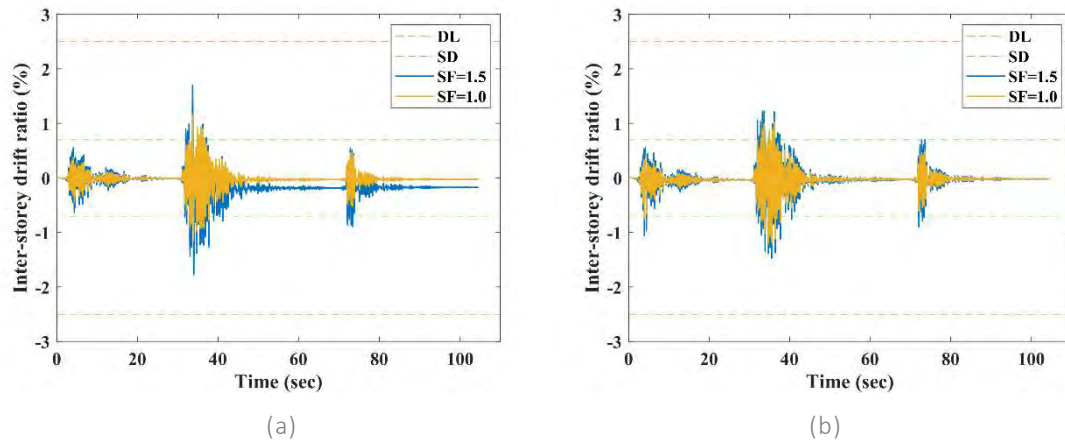


Figure 228: Inter-storey drift ratio of the retrofitted frame (RF): (a) first floor; (b) top floor

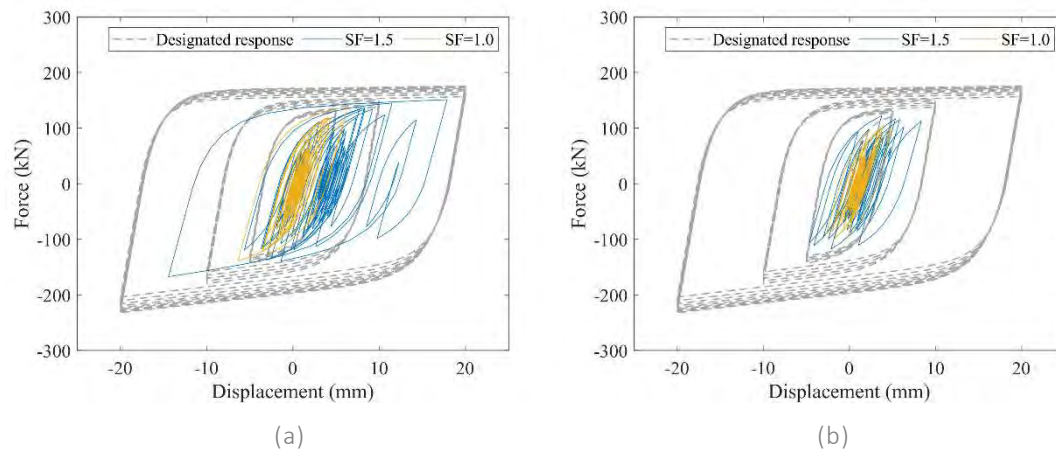


Figure 229: Response of the BRBs of the retrofitted frame (RF): (a) first floor; (b) top floor

5.3.4 Test setup

The tested structures were designed and built based on the typical construction techniques of European construction companies. Therefore, the steel frames were welded and prepared in the manufacturers workshop, brought to site and assembled directly in the lab.

Unlike real structures, the tested specimens were founded on the lab's strong floor rather than in a typical pad concrete foundation. In order to reduce the possibility of base plate sliding and to provide enough base shear capacity in the shear connectors, the frame's base plates were connected to 80 mm thick steel base plates, which distributed the lateral loads to a bigger number of floor anchors. In addition, a tubular support beam was placed on top of the thick base plates to reduce the lateral deformation and to avoid significant bending on the plate due to moment transfer from the structure. Figure 230 shows the typical base plate configuration for the experiments.



Figure 230: Typical configuration of the structures' foundation.

For the 3D structure, a steel sheet was installed on the assembled steel frame, welded by using shear connectors. The concrete slab was casted and poured on site. Two post-tensioned steel bars were located at each connection with the actuators to guarantee the correct transfer of forces in tension and compression. Two actuators were placed at each storey, connected to the largest reaction wall. Once the concrete had set, additional pre-casted concrete blocks were added on each floor to simulate the required gravity loads imposed on the structure. Finally, masonry panels were added on each frame span. These panels were built in two layers and using local construction technics. Figure 231 shows the general setup of the 3D test.



Figure 231: General setup of the 3D structure

Similarly, a concrete slab was poured on each storey of the 2D structure to simulate the stiffness of the composite beam and to transmit the forces from the actuators to the structure. In this case, the two actuators per storey were connected at both sides of the frame, to reduce any out of plane deformation. The 2D frame did not have masonry infills. After the first tests on the bare frame, the

structure was retrofitted by the inclusion of the external BRBs. The general setup of the 2D structure can be observed in Figure 232.



Figure 232: General setup of the 2D structure

The instrumentation of the 3D structure consisted in the following sensors and devices:

- Two accelerometer sensors on each storey to measure the accelerations on the free vibration test.
- An additional accelerometer sensor with higher sensitivity to validate the readings of the other 4 accelerometer sensors.
- Two optical devices per storey to externally measure the storey deformations. These sensors were placed to avoid the error in the readings from the actuators stroke due to the deformation of the strong wall, connections and actuators. These optical devices were used in all the tests.
- Four string potentiometers to measure the diagonal strain on a selected masonry panel in the bottom storey.
- Two 343mm string potentiometers to measure the diagonal strain on a selected masonry panel in the top storey.
- One 343mm string potentiometer to measure the out of plane deformation in the monitored masonry panel of the bottom storey.
- One 50mm potentiometer per storey to measure any deformations perpendicular to the main axis at the storey level.
- Two 50mm potentiometers to measure the relative deformation between the beam flanges and the colum, in order to measure the joint rotation, in a selected connection of the bottom storey.
- Two 50mm potentiometers to measure the relative deformation between the beam flanges and the colum, in order to measure the joint rotation, in a selected connection of the top storey.
- Six 25mm potentiometers to measure the relative vertical deformation, relative horizontal deformation and relative rotation of a selected column base plate.
- Four 25mm potentiometers to measure the relative vertical deformation, relative horizontal deformation and relative rotation of a selected column base plate.
- Five 25mm potentiometers along the height of the expected plastic hinge zone of a selected column to measure the column deformation.
- Three inclinometers to measure the rotations at the joints of a selected column.
- Two inclinometers to measure the rotation at the joints of a selected column.
- Twelve strain gauges to measure the strain along three sections of a selected column.

- Four strain gauges to measure the strain along two sections of a selected beam.
- Two Digital Image Correlation devices (DIC) to monitor the strain in a selected masonry panel.
- One low resolution video camera to record the experiment.
- Five network cameras to monitor the deformation in different components of the structure, including base plates, steel joints and masonry infill panels.
- All the actuators reported the force applied on the structure at all times.

Some details on the instrumentation for the 3D test can be observed in Figure 233.

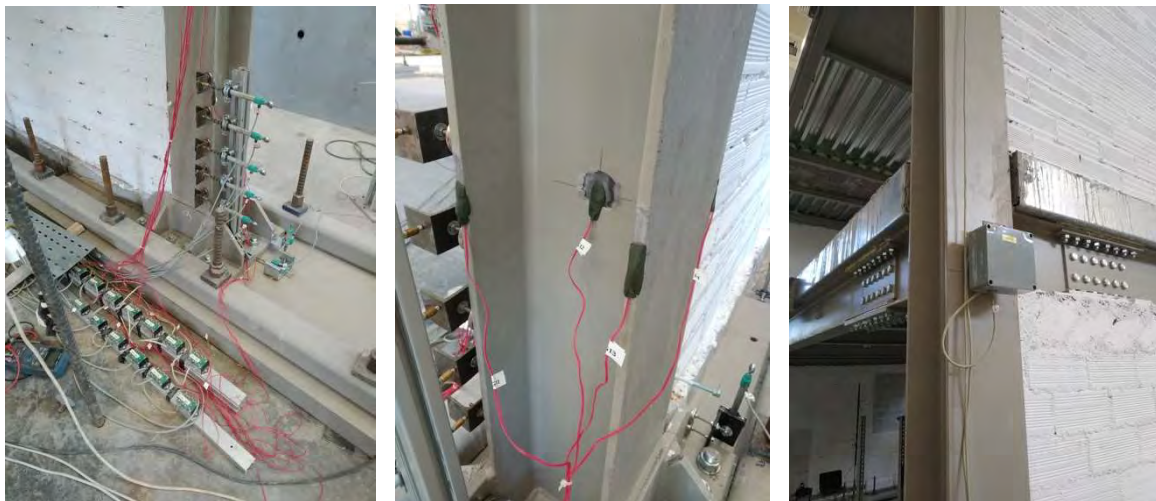


Figure 233: Some details on the instrumentation for the 3D test: Base plate and column potentiometers (left), column's strain gauges (centre) and joint inclinometer (right)

For the 2D structure testing, the monitoring devices were rearranged to monitor the single frame and the BRB retrofitting system. The instrumentation for the 2D test consisted in the following:

- Two accelerometer sensors on each storey to measure the accelerations on the free vibration test.
- Two optical device per storey to externally measure the storey deformations. These sensors were placed to avoid the error in the readings from the actuators stroke due to the deformation of the strong wall, connections and actuators. These optical devices were used in all the tests.
- One string potentiometer to measure the total diagonal deformation of the BRB and steel brace, at each storey.
- One 5mm potentiometer to measure the deformation at each BRB.
- One 25mm potentiometer to measure the deformation between each BRB and their supports due to connector sliding.
- Six 25mm potentiometers to measure the relative vertical deformation, relative horizontal deformation and relative rotation of a selected column base plate.
- Four 25mm potentiometers to measure the relative vertical deformation, relative horizontal deformation and relative rotation of a selected column base plate.
- Five 25mm potentiometers along the height of the expected plastic hinge zone of a selected column to measure the column deformation.
- Three inclinometers to measure the rotations at the joints of a selected column.
- Two inclinometers to measure the rotation at the joints of a selected column.
- Three strain gauges at each elastic brace connected to the BRBs, to measure the strain in the elastic brace and the force going through the braces.
- Eighth strain gauges to measure the strain along three sections of a selected column.
- Two strain gauges to measure the strain along two sections of a selected beam.

- One low resolution video camera to record the experiment.
- Five network cameras to monitor the deformation in different components of the structure, including base plates, steel joints and masonry infill panels.
- All the actuators reported the force applied on the structure at all times.

Some details on the instrumentation for the 2D test can be observed in Figure 234.



Figure 234: Some details on the instrumentation for the 2D test: Column potentiometers and column base inclinometer (left), elastic brace connection potentiometer to measure relative displacement (centre) BRB potentiometer to measure BRB deformation (right)

It is worth highlighting that the PsD testing of the 3D frame was performed by using the local lab system, including instrumentation, controllers and simulation, since no sub-structuring was required. On the other hand, the PsD testing of the 2D frame was performed in conjunction with a remote controller linked to the main lab instrumentation, controllers and actuators, since the physical specimen was a sub-assembly of a bigger hybrid simulation.

5.3.5 Observation during testing

Pseudo-dynamic test was firstly performed on the 3D infilled frame, where several typical damage patterns were noticed. During the first test with unscaled record, damage was mainly found on masonry infills. Cracks occurred firstly at the corners of infill panels, especially in the area that is in contact with the beam splice connections, where the bolts crushed the bricks when moving against the infill walls. Diagonal cracks were then observed, followed by horizontal cracks in the middle of infill panels due to shear sliding. There was no obvious yielding on columns and beams. However, during the second test with scaled record ($SF=3.0$), significant yielding was observed on columns, particularly at the column bases and beam-column connections. The corner of infill walls started to crush and wider cracks were observed across the infill wall panels, both diagonally and horizontally. It is worth noting that the observed response of the masonry infills, as the lateral drifts increased, is found to be rather different compared to the case of reinforced concrete framed structures, due to the different interaction between the steel beams and the masonry infills under larger lateral displacements. The type of interface between the beam-flanges and the infills, and the layout of the bolted beam joint splice also affected significantly the global response of the masonry panels at both floors of the tested frame. At the end of the test, partial collapse occurred on the outer side of the double layered infill walls at the first floor, as shown in Figure 235.

In the case of the 2D retrofitted frame, damage was found mainly at beam-column connections and the upper end of BRBs that were directly attached to column flanges. During the first test with unscaled record, no severe damage was observed on the frame and the BRBs were working smoothly. Then the structure was subjected to the scaled record (with $SF=1.5$), and the test was forced to be stopped earlier when significant torsion was observed on the 2D frame specimen and instability became a critical issue that affected the safety of test. Fracture of column web was observed due to some part of the beam flange being detached from the column web, as presented in Figure 236. An unexpected damage was noticed at the upper end of the BRBs, which were connected to the column flange through designated connection. When the frame experienced large lateral displacements, causing the BRBs to behave in compression, the outer sleeves of the BRB hit the thick plate of its connection to the column flange, which prevented the BRBs from working normally in compression. Photos of the damaged sleeves of BRB were also provided in Figure 236.



Figure 235: Damage observed on the infilled frame during the pseudo-dynamic test



Figure 236: Damage observed on the retrofitted frame during the pseudo-dynamic test

5.3.6 Preliminary results

This section provides the preliminary results of major tests performed for the HITFRAMES project. Snap-back free-vibration tests were performed on the 3D steel frame with and without masonry infills for the calibration of the numerical model. Then pseudo-dynamic tests were performed on the 3D infilled frame and 2D retrofitted frame respectively to assess their response under the earthquake sequence in Table 26.

Figure 237 shows the initial floor displacements obtained from the OpenSees model and the free-vibration tests, when a force of 26 and 62kN was applied to the top floor of the bare and infilled frame, respectively. It is clearly shown in Figure 237a that good agreement on the lateral stiffness of the bare frame has been achieved. Although the results are almost identical, the lab specimen is slightly stiffer than the numerical model, possibly due to the fact that stiffeners at the column base and beam-column connections were not accounted for in the numerical model. However, the discrepancies become larger when the masonry infills were included, as demonstrated in Figure 237b. This reflects the major limitation in the numerical modelling that the reliability of the adopted modelling method of infills remains unclear in steel frames. Table 28 shows the comparison of natural periods obtained from the lab tests and numerical models. The results are consistent with the findings in Figure 237. Despite the discrepancy in the displacements of the infilled frame, the model is still able to provide fundamental estimates of the overall response of the steel frame.

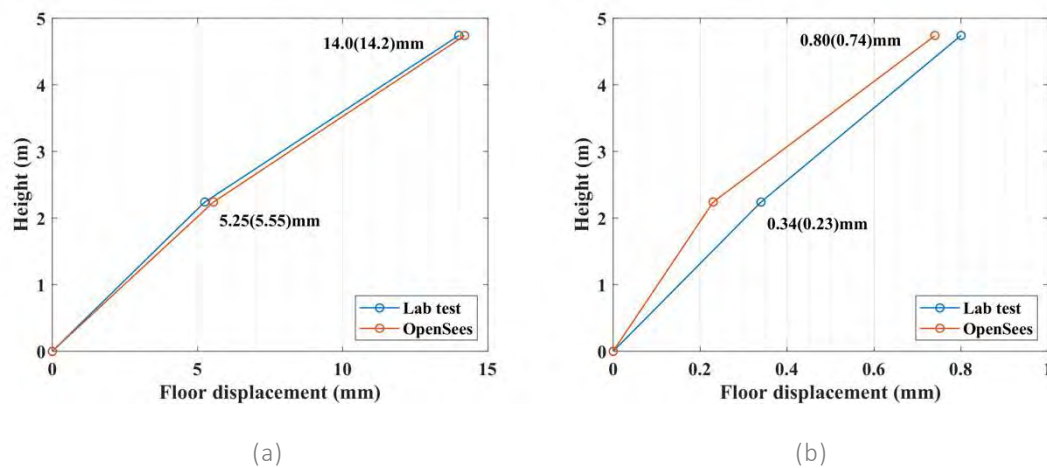


Figure 237: Initial displacements induced by actuators: (a) bare frame and (b) infilled frame

	Bare frame		Infilled frame	
	Lab	OpenSees	Lab	OpenSees
1 st Period (sec)	0.6993	0.6987	0.1333	0.1096
2 nd Period (sec)	0.2445	0.2424	N/A	N/A

Table 28: Modal properties of the test specimens

Figure 238 shows that cyclic response at both floors of the infilled frame, which exhibited significant pinching during the lab tests, which was probably due to the open and closing of cracks on the infill walls. Such response increases as the lateral drifts increase for higher values of peak ground acceleration of the earthquake input. Besides, Figure 230 also shows that the experimental specimen experienced 0.7% IDR for SF = 1.0 and 4.8% IDR for SF = 3.0, which are both smaller than the 1.1% and

6.1% IDR obtained from the numerical model, indicating that the real steel frame in the lab has a higher lateral stiffness than the numerical model.

Figure 239 presents the pseudo-dynamic tests performed on the retrofitted frame. When $SF=1.0$, the frame experienced a maximum drift that was slightly greater than 0.7% at the first floor and around 2.2% drift at the top floor. Apparently, the top floor suffered a much higher lateral drift than the first floor, which was unlike the observations on the infilled frame. The same situation was also found when the SF was raised to 1.5, where the maximum drift at the first and top floor was about 2.0 and 4.5%, respectively. It should be noted that the test with $SF=1.5$ was terminated during the foreshock in Figure 225a, so it is anticipated that the actual maximum drifts would be much higher during the mainshock.

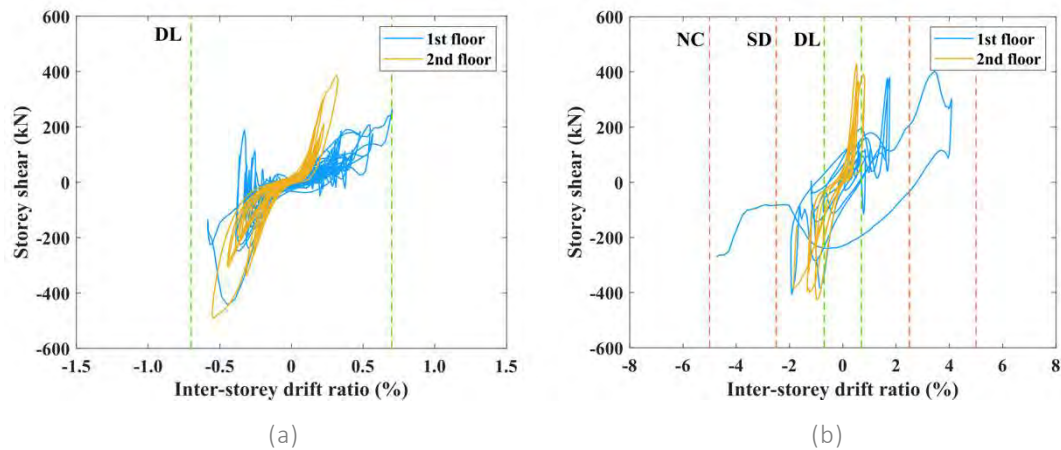


Figure 238: Storey shear-IDR response of the infilled frame: (a) $SF=1.0$; (b) $SF=3.0$

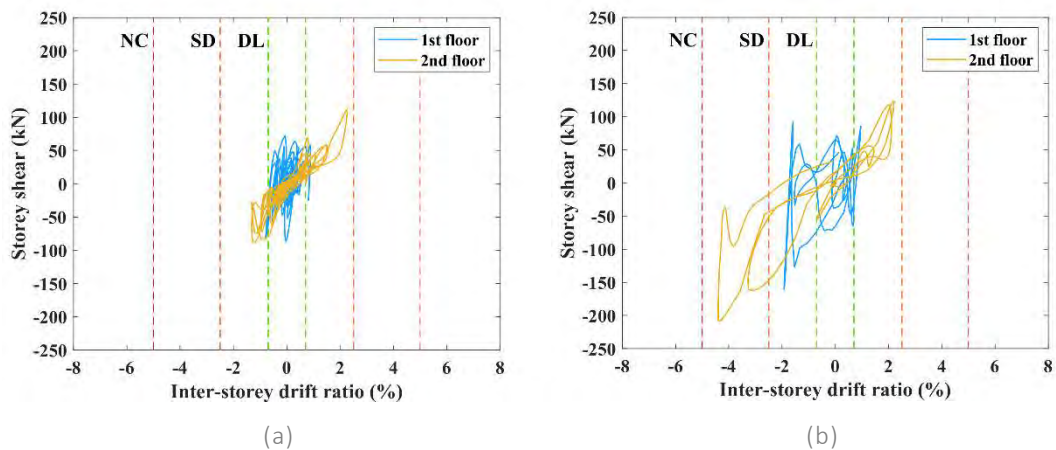


Figure 239: Storey shear-IDR response of the retrofitted frame: (a) $SF=1.0$; (b) $SF=3.0$

5.3.7 Conclusions and outlook

This report provided a brief summary of the numerical analysis and experimental tests being carried out for the HITFRAMES project. In general, the natural periods and lateral stiffness of the numerical model well matched the free-vibration test results, however, the modelling of infills introduced some discrepancies between the numerical prediction and experimental outcomes. Despite that, the results of pseudo-dynamic tests suggest that the current modelling strategy of infills is still able to capture reliably the damage state of real infills, including cracks and partial collapse. Therefore, further improvement of the modelling of infills shall be accomplished based on the data extracted from the tests, contributing to a more reliable assessment framework for infilled steel frames. The interpretation

of the data extracted from the BRBs would be a major challenge when assessing the performance of BRBs, due to the lack of useful data in the tension range, but the nearly symmetric designated behaviour of BRBs would be helpful in solving this issue.

Briefly, the following conclusions can be drawn from the test results:

- The steel infilled frame in the lab shows a lower initial lateral stiffness than the numerical model but a higher lateral stiffness during after damage occurred on the infills;
- The bolts of beam splice connections are usually also embedded in the top layer of infill walls, which tends to cause the corner of the infills to crack first and differs the response of infills in a steel frame from those in a reinforced concrete frame;
- The current modelling strategy of the infills need to be revised and adjusted to comply with the experimental results in terms of its stiffness and strength;
- The designed BRBs are believed to be effective in protecting the steel frame to some extent, however, extra attention must be paid to the strengthening of beam-column connections where the BRBs are attached;

Future assessment of BRBs based on the experimental data will also need to include the effects of infills, despite they were thought to be detached from the steel frame due to pre-existing damage, hence were not installed during the test of retrofitted frame.

6 University of Bristol

The Earthquake and Large Structures Laboratory (EQUALS) is part of the £35m Bristol Laboratories for Advanced Dynamics Engineering (BLADE) in the Faculty of Engineering at the University of Bristol, UK. It houses a 15t capacity, 6 degree-of-freedom shaking table surrounded by a strong floor and adjacent strong walls up to 15m high. The shaking table is accompanied by 40 servo-hydraulic actuators that can be configured to operate in conjunction with the table, strong floor and reaction walls, providing a highly adaptable test facility that can be used for a variety of tests. The digital control system has world leading features, including a 'hybrid test' capability in which part of the structural system of interest can be emulated by a numerical model embedded in the digital control system while only a sub-component need be tested physically. The associated control software was developed in-house. The EQUALS laboratory is a node of the UK-NEES. Data and video can also be streamed in real-time to remote users.

The shaking table consists of a stiff 3m x 3m cast aluminum platform weighing 3.8t and can carry a specimen payload of 15t. The platform has the shape of an inverted pyramid consisting of four sections having a honeycomb-like network of stiffening diaphragms giving it high strength and bending stiffness. The platform surface is an arrangement of 5 aluminum plates with a regular grid of M12 bolt holes for attaching to the platform body and for mounting of specimens. It can accelerate horizontally up to 3.7g with no payload and 1.6g with a 10t payload at an operational frequency range of 0-100Hz. Vertical accelerations are 5.6g and 1.2g, respectively. Peak velocities are 1m/s in all translational axes, with peak-to-peak displacements of 300mm. A large database of recorded earthquake records can be applied, or synthetic motions can be readily created. Extensive instrumentation is available, including up to 256 data acquisition channels.

Over the past 30 years, EQUALS has participated in several research projects involving transnational access including SERIES and SERA. The facility is equipped with two laminar, flexible, shear boxes for geotechnical testing. One of these is 6 m long, 1.5 m deep and 1 m wide; the other is 1.5 m long, 1.0 m deep and 1 m wide. EQUALS is particularly suited to testing of small to medium sized specimens. EQUALS lab has strong expertise in testing of geotechnical models.

Within the context of SERA grant, 7 projects were assigned to EQUALS Lab (SERENA, 3DRock, RE-BOND, NSFuse, SEBESMOVA3D, SHATTENFEE, SSI-STEEL). The projects were selected following 3 rounds of external reviews and covered all 115 TA days offered to SERA.

Overall, the EQUALS facility hosted fifty-six (56) users spanning twenty-eight (25) institutions and three (3) companies from eleven (11) different countries (Belgium, China, Germany, Greece, Italy, Norway, Slovenia, Spain, Switzerland, UK, USA). To support the project, UBRI allocated 7 faculty members, 4 post-docs (one full time), 1 doctoral student, 1 administrator and several lab technicians.

All 115 TA days were offered to SERA. The allocation to each project was as follows: 20 days to SERENA, 20 days to 3DRock, 20 days to RE-BOND, 15 days to NSFuse, 20 days to SEBESMOVA3D, 10 days to SHATTENFEE, and 10 days to SSI-STEEL. Following the selection of the proposals, the realization of the projects on the shaking table started in M12 and continued until M35. UBRI is currently actively engaged in uploading the collected experimental data to the Data Access Portal via Celestina software.

The final project, SSI-STEEL, was scheduled to be completed in late March 2020. However, the University closed due to the coronavirus pandemic on 24 March and the execution of the project will be completed later. At the time of the University closure, all 115 TA days had been provided by UBRI.

In terms of dissemination, four (4) conference articles and one (1) journal article have been submitted/published, while several others are in preparation.

6.1 Project #10 – SERENA – Seismic Response of Novel Integral Abutment-Bridges

Authors

G. Fiorentino⁽¹⁾, C. Cengiz⁽²⁾, F. De Luca⁽²⁾, M. Dietz⁽²⁾, L. Dihoru⁽²⁾, D. Lavorato⁽¹⁾, D. Karamitros⁽²⁾, B. Briseghella⁽³⁾, T. Isakovic⁽⁴⁾, C. Vrettos⁽⁵⁾, A. Topa Gomes⁽⁶⁾, A. Sextos⁽²⁾, G. Mylonakis^(2, 7, 8), C. Nuti^(1, 3)

⁽¹⁾ *Department of Architecture, Roma Tre University, Rome, Italy*

⁽²⁾ *Department of Civil Engineering, University of Bristol, Bristol, United Kingdom*

⁽³⁾ *College of Civil Engineering, Fuzhou University, Fuzhou, China*

⁽⁴⁾ *Faculty of Civil and Geodetic Engineering, University of Ljubljana, Ljubljana, Slovenia*

⁽⁵⁾ *Department of Civil Engineering, Technical University Kaiserslautern, Kaiserslautern, Germany*

⁽⁶⁾ *Department of Civil Engineering, University of Porto, Porto, Portugal*

⁽⁷⁾ *Department of Civil Engineering, Khalifa University, U.A.E.*

⁽⁸⁾ *University of California at Los Angeles (UCLA), U.S.A.*

6.1.1 Introduction

In the last few years the Integral Abutment Bridge (IAB) concept has generated considerable interest among bridge engineers, not only for the newly built bridges but also in the retrofit of existing ones (Briseghella and Zordan, 2006) because of the benefits associated with the elimination of expansion joints and reduced installation and maintenance costs. Although not a new concept, its formulation dating back at least to the 1930s, it has been successfully employed to address long-standing structural problems frequently occurring in conventional bridge designs (Horvath 2005). Regarding number of applications, United States has the widest experience on IABs (Burke 1993) and it is reported that more than 13,000 such bridges (Maruri and Petro 2005) were built by the mid 2000's. Nevertheless, a meaningful number of bridges within this family can be found in central Europe, mainly in Germany, Switzerland, UK, Austria, Luxembourg and France.

In view of the large number of realizations worldwide, one would expect that a consolidated design practice and guidelines would be available. On the contrary, indications are missing even in modern codes, in particular for the specific aspect of seismic design, e.g., Caltrans 1999; ATC 1996a, 1996b; Eurocode 8/2. This can be attributed, to a good extent, to the fact that from an analysis and design view point the structural continuity existing between deck, abutment wall and supporting piles makes essential a full consideration of soil–structure interaction (SSI) phenomena, an area which still requires specialized expertise. Moreover, the consideration of SSI is important also for service loads such as thermal loads. In fact, very high earth pressures can be generated on the abutment wall, which can further increase at the occurrence of the seismic action (England et al. 2000).

Regarding experimental studies, laboratory tests were performed on thermal load effects; Frosch et al. (2009) performed cyclic tests to investigate abutment-pile connections; Muttoni et al. (2013) executed push-pull tests on the transition slabs; Qian et al. (2016) studied the SSI for micropiles of a semi-integral bridge through shaking table tests. The experimental investigations of soil-structure interaction and the

role of abutments in the case of seismic excitations are rare. Recently, a comprehensive joint research of several US universities (UNR, UCSD, UCB) devoted to seismic response of bridges with seat type abutments was completed. Saiidi et al. (2013) ran shaking table tests on large scale models of two-span and four-span bridges at the University of Nevada, Reno; Wilson and Elgamal (2009) ran shaking table tests to investigate the abutment contribution in the response.

SERENA project had the aim of developing a basic understanding of IABs under seismic loads through shaking table testing on: (a) the earthquake response of such systems, and (b) ways of minimizing associated demands using pertinent design solutions such as disconnecting (i) the pile heads from the cap, and (ii) the abutments from the backfill through a compressible foam inclusion, (c) settlement due to dynamic compaction effects in the backfill. To the best of the authors' knowledge, research on the above has been very limited. Findings from the proposed research may lead to the development of more robust provisions on IABs allowing the amendments on some limitation imposed on the use of such structural system.

The objectives of SERENA were:

1. to explore earthquake response of IAB's (mainly driven by Soil-Structure Interaction (SSI) between backfill, abutment, foundation and bridge structure) on a shaking table;
2. to assess different connection schemes between: (i) abutment and piles, (ii) abutment and backfill, using a variety of materials such as foams;
3. to explore the influence of vertical motion on earthquake response.

The above experimental results will allow firstly the development of simplified analysis methods and preliminary design criteria for IAB's that could be used in engineering provisions such as the Eurocodes, secondly the validation of numerical methods and constitutive soil models for simulating such systems, and thirdly the reduction of epistemic uncertainty in IABs design leading to lower safety factors and reduction in cost.

6.1.2 Identification of prototype

The first step of the work was the review of available prototype bridges that could be used for the experimental campaign. IABs can be relatively different as they can have a simple portal configuration or multiple piers. On the other hand, the critical aspect in the design is related to the SSI between deck, abutment, foundation and backfill. Considering that the prototype needed to be properly scaled to fit with the capability of the experimental facility at the University of Bristol, first of all a simple portal shape prototype was selected to isolate the interaction between critical components avoiding to include the pier that would have resulted in a higher scaling factor of the model to fit in the soil box available. Secondly, a double pile configuration was considered as it is relatively common in seismic areas (e.g., Zordan et al. 2011) and it would allow to investigate different behaviour of the cap-foundation system, see Figure 240 as example.

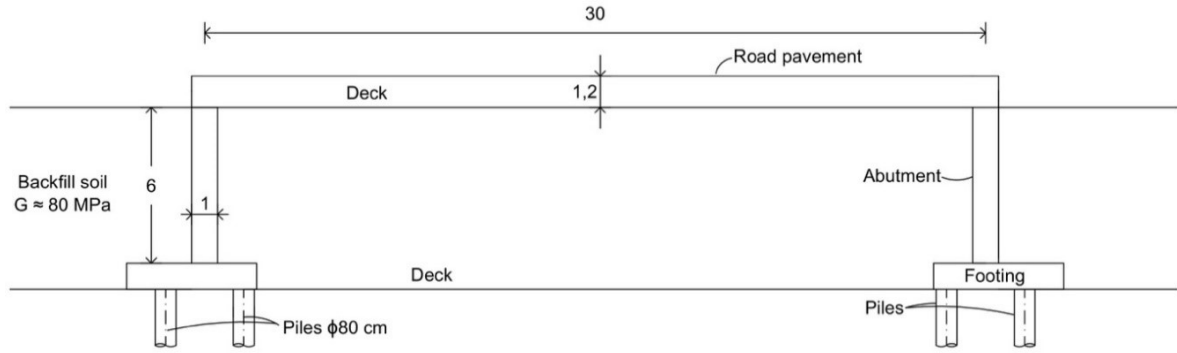


Figure 240: Example of single-span Integral Bridge (dimensions in meters)

The scaling of the prototype to define and design the model was a relatively complex procedure as, being the tested system composed of a soil-structure system, specific care was needed to maintain the stiffness proportion between these two components. Based on the above consideration, first the scaling problem between prototype and model was analysed identifying the necessity of different scaling factors for abutment-foundation and deck and then the model was designed to capture all the relevant phenomena and be representative of a realistic prototype without limiting the experiment to a specific prototype that would have increased the scaling factor frustrating the highly innovative point of having a realistic model of soil-structure-foundation at a scale that could be still defined as “large” with respect to other kind of experimental approaches.

6.1.3 Scaling Prototype to Model

The parameters influencing the response of the system are: the soil/wall system relative flexibility (Veletsos and Younan 1997), given by

$$d_w = \frac{G_s H_w^3}{D_w} \quad (1)$$

Where G_s is the shear modulus of the backfill soil, H_w is the height of the abutment wall and D_w is the wall flexural rigidity per unit of length, given by

$$D_w = \frac{E_w t_w^3}{12 (1 - \nu_w^2)} \quad (2)$$

Where E_w , t_w and ν_w are the elastic modulus, the thickness and the Poisson ratio of the abutment wall, respectively. A retaining wall can be considered as rigid if $d_w < 1$ and flexible if $d_w > 5$ (Psarropoulos et al. 2005).

By making explicit the ratio of the thickness of the wall in the model and the prototype one, and neglecting the terms containing the Poisson’s ratio (second order dependence, or incomplete plane-strain condition), one gets

$$\frac{t_{w,M}}{t_{w,P}} = \left(\frac{G_{s,M}}{G_{s,P}} \cdot \frac{H_{w,M}^3}{H_{w,P}^3} \cdot \frac{E_{w,P}}{E_{w,M}} \right)^{\frac{1}{3}} = \frac{H_{w,M}}{H_{w,P}} \left(\frac{G_{s,M}}{G_{s,P}} \cdot \frac{E_{w,P}}{E_{w,M}} \right)^{\frac{1}{3}} = \frac{1}{\lambda} \left(\frac{G_{s,M}}{G_{s,P}} \cdot \frac{E_{w,P}}{E_{w,M}} \right)^{\frac{1}{3}} = \frac{1}{\lambda} \left(\frac{\lambda_E}{\lambda_G} \right)^{\frac{1}{3}} \quad (3)$$

Where $\lambda = H_{w,P}/H_{w,M}$ is the ratio prototype/model of the wall heights (geometric scale factor), $\lambda_E = E_{w,P}/E_{w,M}$ is the scale factor for the elastic moduli of the wall and $\lambda_G = G_{s,P}/G_{s,M}$ is the scale factor of the shear moduli in the soil.

Using the symmetry of the model, the stiffness of the deck can be represented with a rotational spring. The value of the constant k_d of this spring can be obtained idealizing the deck as a beam either fixed or

pinned at one hand and fixed at the other hand, so that $k_d = 4E_d I_d / l_d$ or $k_d = 3 E_d I_d / l_d$, where E_d is the deck elastic modulus, I_d is the deck moment of inertia and $l_d = L_d / 2$, where L_d is the span length (see Figure 241).



Figure 241: Assumption made for determining the thickness of the bridge deck

By substituting the full expression of I_d , k_d for the two cases becomes:

$$k_d = \frac{4 E_d t_d^3}{6 L_d (1 - \nu_d^2)} = \frac{2 E_d t_d^3}{3 L_d (1 - \nu_d^2)} \quad (4a)$$

$$k_d = \frac{3 E_d t_d^3}{6 L_d (1 - \nu_d^2)} = \frac{E_d t_d^3}{2 L_d (1 - \nu_d^2)} \quad (4b)$$

In the same vein as in Equation 1, the relative flexibility of the rotational base constraint and retained medium d_θ can be defined, according to Veletsos and Younan (1997):

$$d_\theta = \frac{G_s H_W^2}{K_d} \quad (5)$$

All the parameters in the equation were defined above. By making explicit the ratio of the thickness of the deck in the model and the prototype one, and neglecting the terms containing the Poisson's ratio (second order dependence, or incomplete plane-strain condition), one gets:

$$\frac{t_{d,M}}{t_{d,P}} = \left(\frac{G_{s,M}}{G_{s,P}} \cdot \frac{H_{w,M}^2}{H_{w,P}^2} \cdot \frac{E_{d,P}}{E_{d,M}} \cdot \frac{L_{d,M}}{L_{d,P}} \right)^{\frac{1}{3}} = \left(\frac{\lambda_E}{\lambda_G \cdot \lambda^2 \cdot \lambda_L} \right)^{\frac{1}{3}} \quad (6)$$

Where $\lambda_L = L_{D,P} / L_{D,M}$ is the ratio prototype/model of the deck length. In the special case in which the deck and the abutment wall have the same scale factor, that is $\lambda_L = \lambda$, Equation 6 gives the same result of Equation 4:

$$\frac{t_{d,M}}{t_{d,P}} = \frac{1}{\lambda} \left(\frac{\lambda_E}{\lambda_G} \right)^{\frac{1}{3}} \quad (7)$$

The importance of the SSI on the vibrational characteristics of the structure/soil system can be described by the so-called wave parameter introduced by Veletsos and co-workers as displayed in Figure 242, given by

$$\frac{1}{\sigma} = \frac{H^* f}{V_s} \quad (8)$$

And which can be rewritten as

$$\bar{k} = \frac{\omega H}{V_s} \quad (9)$$

The wave parameter must be equal between the prototype and the model, so it is possible to write

$$\left(\frac{\omega \cdot H}{V_s} \right)_M = \left(\frac{\omega \cdot H}{V_s} \right)_P \quad (10)$$

By explicating the ratio between the cyclic frequency of the model and the prototype, one obtains:

$$\left(\frac{\omega_M}{\omega_P}\right) = \left(\frac{V_{SM}}{V_{SP}}\right) \left(\frac{H_P}{H_M}\right) = \lambda \left(\frac{V_{SM}}{V_{SP}}\right) = \frac{\lambda}{\lambda_{V_S}} \quad (11)$$

where λ (> 1) is again the geometric scale factor of the prototype to the model, and λ_{V_S} is the scale factor of shear wave velocities. Moreover, with reference to Figure 242 it is possible to write:

$$\tilde{k} = \frac{\omega d}{V_S} \quad (12)$$

Where d is the pile diameter. It is worth noting that for piles the geometric scale factor is the same for pile length and diameter:

$$\left(\frac{L_P}{d}\right)_M = \left(\frac{L_P}{d}\right)_P \quad (13)$$

The scale factor for time can be derived from Equation 11 remembering that $G \propto p^{1/2} \propto \lambda^{1/2}$, where p is the lithostatic pressure, and that the velocity of S-Waves $V_S \propto G^{1/2}$, so that $V_S \propto \lambda^{-1/4}$. In this light, one gets:

$$\left(\frac{\omega_M}{\omega_P}\right) \propto \lambda \cdot \lambda^{-\frac{1}{4}} = \lambda^{\frac{3}{4}} \quad (14)$$

From Equation 14, it is possible to derive the scaling factor for time, which is $\lambda^{3/4}$. This scaling factor can be used for the so-called “time compression” of the ground motion records, by dividing the total duration of the record for $\lambda^{3/4}$. The result of Equation 14 is confirmed by many authors (e.g. Towhata 2008).

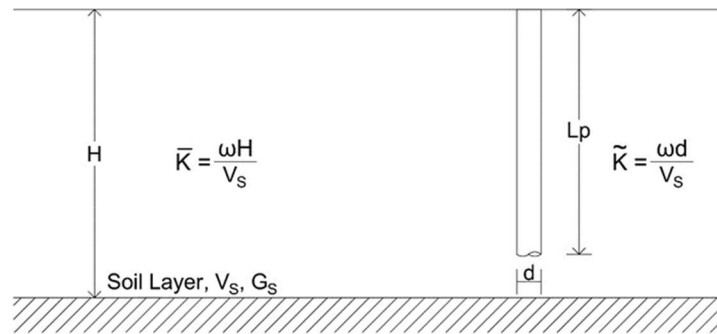


Figure 242: Time scaling laws for soil (left) and time scaling laws for piles (right)

6.1.4 Test configuration and instrumentation layout

Based on the above derivations a geometric scale factor for the bridge abutment of wall and piles of 10 was identified and a time scale factor of 5 was identified obtaining a dimensions for the model bridge shown in Figure 243.

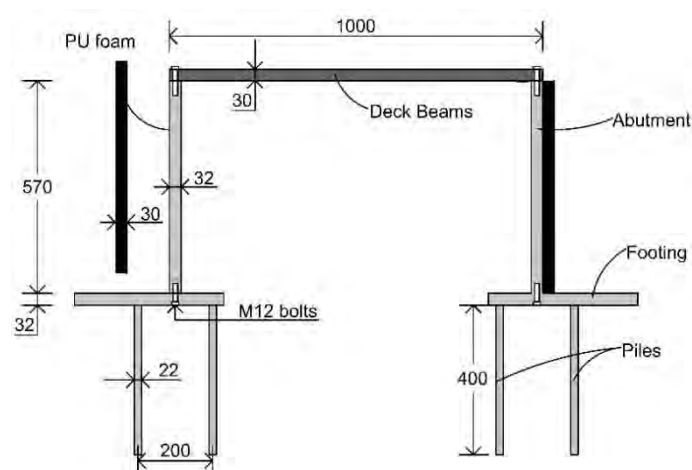


Figure 243: Dimensions of the bridge model.

A total of five test configurations are considered in which the number of EPS layers and pile head connections were varied. Tested configurations alongside with the date of experiments are tabulated in Table 29.

Test Number	Date	Designation	EPS layers	Pile Heads
1	02/07/2018	EPS2-CP	2	Fixed
2	04/07/2018	EPS1-CP	1	Fixed
3	05/07/2018	noEPS-CP	0	Fixed
4	09/07/2018	noEPS-noCP	0	Released
5	10/07/2018	EPS1-noCP	1	Released

Table 29: Performed tests and their properties

Initially, for the first test two layers of PU foam were inserted behind the abutment wall, before filling the shear stack with the backfill sand. Then, in order to remove one layer of PU foam and perform the second test, a vacuum pump was used to aspire the backfill sand, as reported in Figure 244 (it can be observed the angle created by the sand). The same process was followed to remove the last layer of PU foam.





Figure 244: Change of configuration: two layers of PU foam (top left); one layer of PU foam (top right); no compressible inclusion (bottom)

The signals used as input for the shaking table were selected among the seismic records of the Italian Accelerometric Network (RAN), which are openly accessible and can be downloaded from the website of the European Strong Motion Database (www.esm.mi.ingv.it). Only strong motion stations for which the shear wave velocity V_s is known were considered among possible candidates.

Uniform Hazard Spectra (UHS) were defined for the site of L'Aquila, in Italy, which is characterized by a medium to strong seismicity, and using three different return periods (RP), namely 50, 100 and 500/1000 years. For each RP, depending on the disaggregation of hazard, different ranges of Magnitude M and Source-to-site Distance R were used to search the database. The complete list of selected accelerograms is reported in Table 30.

The natural records (not scaled in amplitude) were compared with the Italian Seismic Code spectrum to check for a rough spectrum compatibility. In the selection of the signals, attention was paid to the frequency content. Observing the results obtained in terms of Fourier spectra in Figure 245, it is evident the time compression of the signals.

Since the selected records are reported for ground motion stations located on the ground surface, while the acceleration input applied on the shaking table has to simulate the input motion at bedrock conditions, the selected records were then deconvolved to the bedrock in order to be applied to the shaking table. To do so, the code DEEPSOIL was used, defining the shear wave profiles of the seismic stations selected from the European Strong Motion Database. The seismic stations are: AMT (Amatrice), CSC (Cascia), SELE (Sellano). The shear wave profiles were available in the Italian Accelerometric Archive.

N.	file name	RP	Station	Date	Comp.	M	R (km)
1	1_AMT_50_170118_NS	50	AMT	18/01/2017	NS	5.4	14.4
2	2_CSC_50_161026_NS	50	CSC	26/10/2016	NS	5.4	20.2
3	3_SELE_50_980321_EO	50	SELE	21/03/1998	EO	5	10
4	4_CSC_100_161030_NS	100	CSC	30/10/2016	NS	6.5	15
5	5_AMT_500-1000_160824_NS	500-1000	AMT	24/08/2016	NS	6.2	8.5
6	6_AMT_500-1000_161030_EO	500-1000	AMT	30/10/2016	EO	6.5	26.4
1 VERT	7_AMT_50_170118_VERT	50	AMT	18/01/2017	VERT	5.4	14.4
6 VERT	12_AMT_500-1000_161030_VERT	500-1000	AMT	30/10/2016	VERT	6.5	26.4

Table 30: Selected accelerograms from European Strong Motion Database

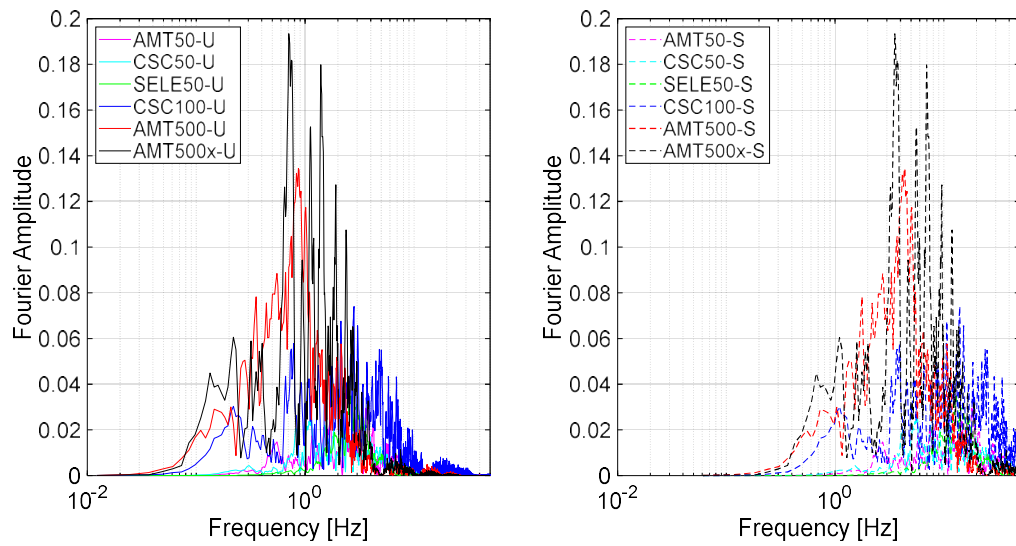


Figure 245: Fast Fourier Transform of earthquake record (a) as recorded (U) and (b) time-scaled (S).

The seismic stations are: AMT (Amatrice), CSC (Cascia), SELE (Sellano). The shear wave profiles are reported in Figure 245.

The scale of the model has an influence on the dynamic scaling of the system parameters. If a certain value of the scale factor λ is given, the following time compression scaling rules are valid for all the records. If $\lambda = 10$, $N_L = 1/10$, the duration of the accelerogram must be divided for $N_L^{3/4}$, as discussed in section 6.1.3. If the record duration on the prototype is $d_{t,p} = 20$ s, then $d_{t,M} = d_{t,p}/N_L^{3/4} = 20/5.6 = 3.56$ s. The time compression can be applied by changing the time interval dt (e.g. for a record with $dt = 0.005$ s and a $N_t = 5$ (time compression scale factor) the modified dt is $dt' = 10^{-3}$ s. So, the resulting time intervals for each N_t are:

- $N_t = 1$; $dt = 5 \times 10^{-3}$ s
- $N_t = 5$; $dt = 10^{-3}$ s

In the SERENA project the earthquake records were used only with $N_t = 1$ and $N_t = 5$ at the base of the shaking table. The effect of time scaling in time is evidence in Figure 245 where the Fourier amplitude spectra of the two waveforms are shown.

For each of the five test configurations the testing protocol shown in Table 31 was applied including horizontal and vertical hammer tests (H_i) and white noise (W_i) steps to assess the natural frequency of the system after each RP group of records.

The soil used in the shaking table tests is dry Leighton Buzzard fraction B sand. The free surface of the soil deposit was at $Z = 1000$ mm. The soil was deposited in the shear stack at two increments. Initially, a 400 mm thick layer is deposited around the model piles in the shear stack. The 400 mm thick layer was then densified with white noise induced vibrations applied through the shaking table. Following the placement of abutment walls and the bridge deck, an additional 600 mm thick sand layer was placed behind the abutment walls. Figure 248 depicts the stages for sand infill.

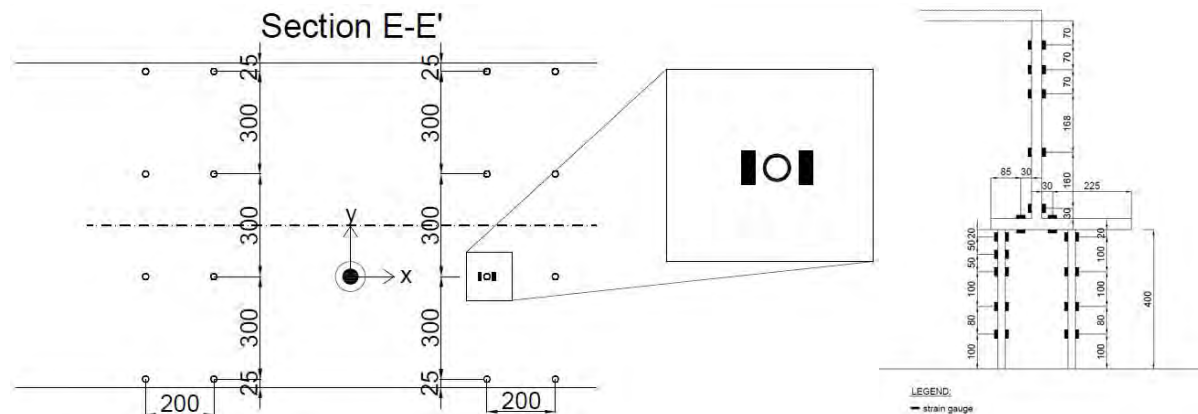


Figure 247: Piles locations under abutment footings and locations of the strain gauges on the wall and the piles

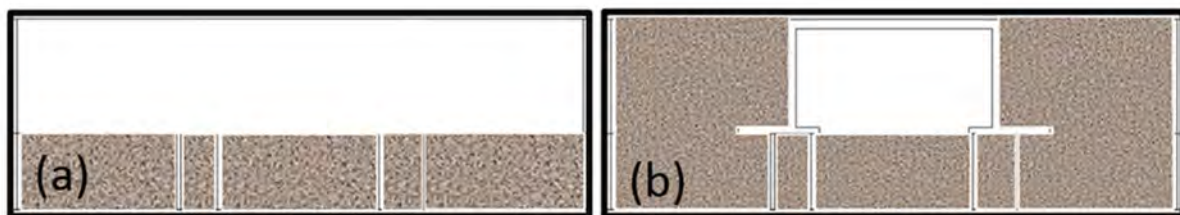


Figure 248: Shear stack filled (a) 400 mm (b) 600 mm additional fill to the level of the deck

6.1.5 Observation during testing

In the actual configuration of the test setup, the piles are slightly lifted from the bottom, because they were inserted into a plywood plug with a piece of PU foam at the base, in order to permit the relative rotation of the bridge footing during the shaking (see Figure 249a). There are two plywood layers, each one has a thickness of 15 mm, so it is possible to assume that each pile is lifted by 15 mm from the bottom of the shear stack. In the first stage of sand filling and subsequent shaking (Figure 249b), a slight settlement of the foundation layer was observed. In order to compensate for the settlement of the sand, 200 kg of sand was added, and another set of vibrations was applied to densify the deposit. At the end of this stage (Figure 249c), the foundation layer was levelled, and threaded studs were placed in the model piles.

Figure 250 illustrates photographs of the complete superstructure of the model abutment bridge, instrumented piles, and instrumented abutment wall and the footing. The abutment walls are made up of 32 mm thick aluminium sheets and the model bridge deck is composed of four steel beams with a length, width, and depth of 1000, 100, and 30 mm, respectively. A total of 16 model piles made up of

hollow aluminium tubes with a height of 400 mm and an outer diameter and vessel thickness of 22.24 and 1.3 mm, respectively. Each of the abutment wall footings was supported by eight model piles.



Figure 249: Actual set-up of the sand infill and bridge model (a) Piles in position inserted in the plywood plug and sitting on PU foam; (b) First sand infill and shaking (c) Second sand infill and shaking, studs in position

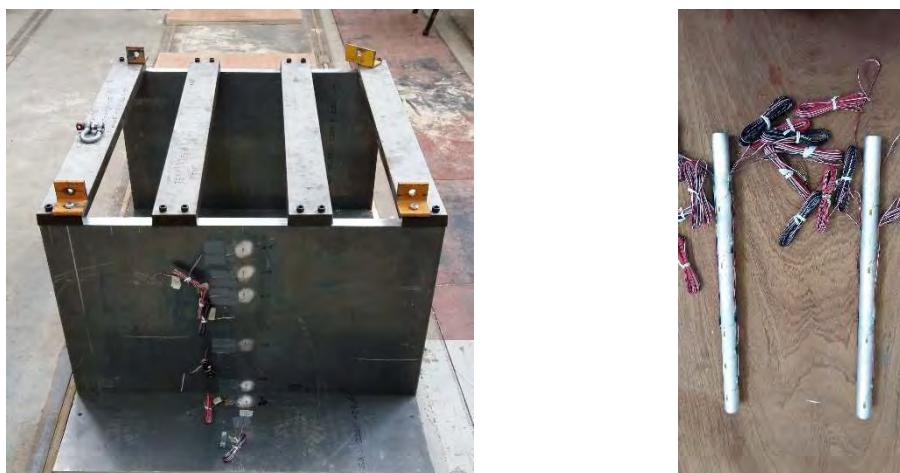
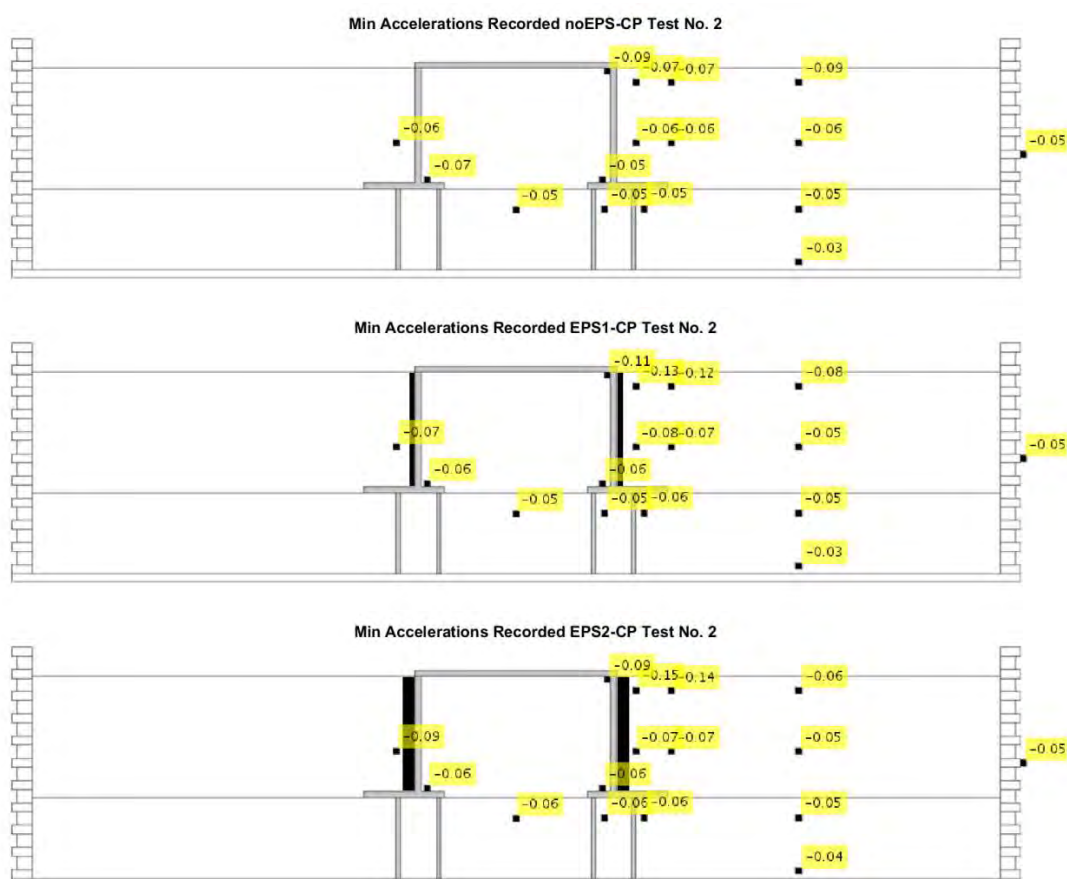


Figure 250: Model IAB and model piles

6.1.6 Preliminary results

Figure 251 and Figure 252 report the results obtained for 2 of the 9 tests. In particular, preliminary acceleration results for S2 and S8 are shown which had vertical motion applied.



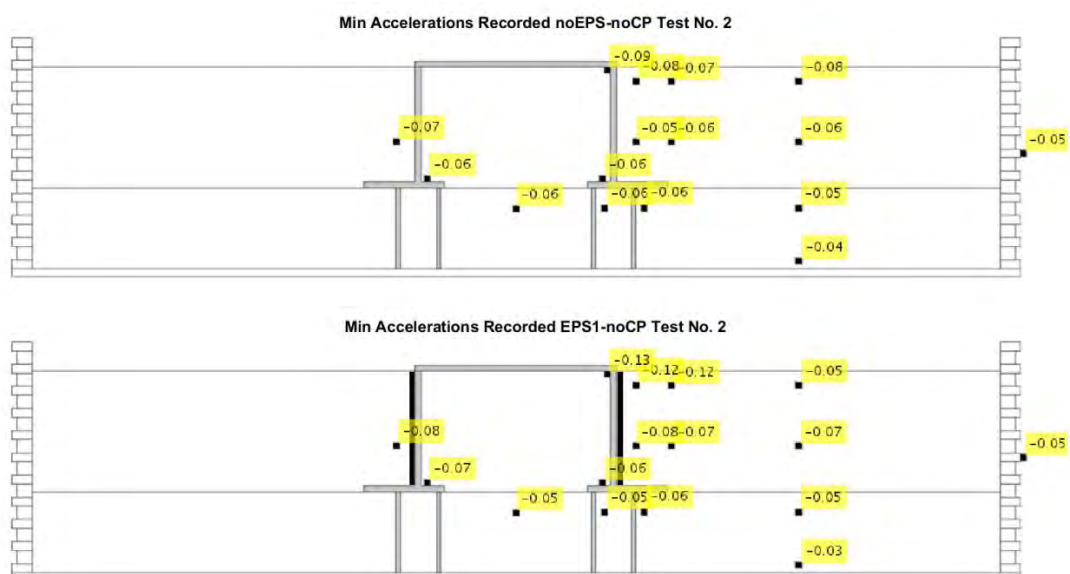
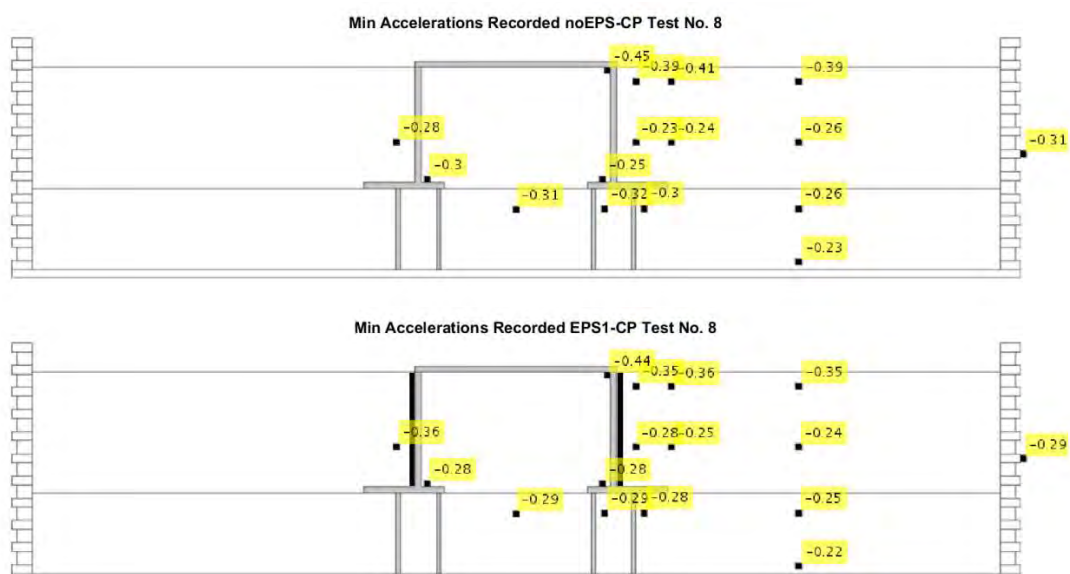


Figure 251: Example of acceleration responses for all the five configurations at the attainment of minimum acceleration– Test S2

It can be recognized the amplification of the ground motion from the bottom to the ground surface, in the “Free Field” array sensors (Channels 3, 4, 5, 6), almost for all the configurations and for minimum and maximum values. There is a good agreement between the accelerations recorded by the Free Field array and those recorded by Channel 22 located on the wall of the “shear stack”, thus confirming the good behaviour of the soil container according to its theoretical background. The accelerations in the backfill array (channels 10, 11, 12, 13) are increasing when one layer of compressible inclusion is inserted behind the abutment wall and even more when inserting two layers.



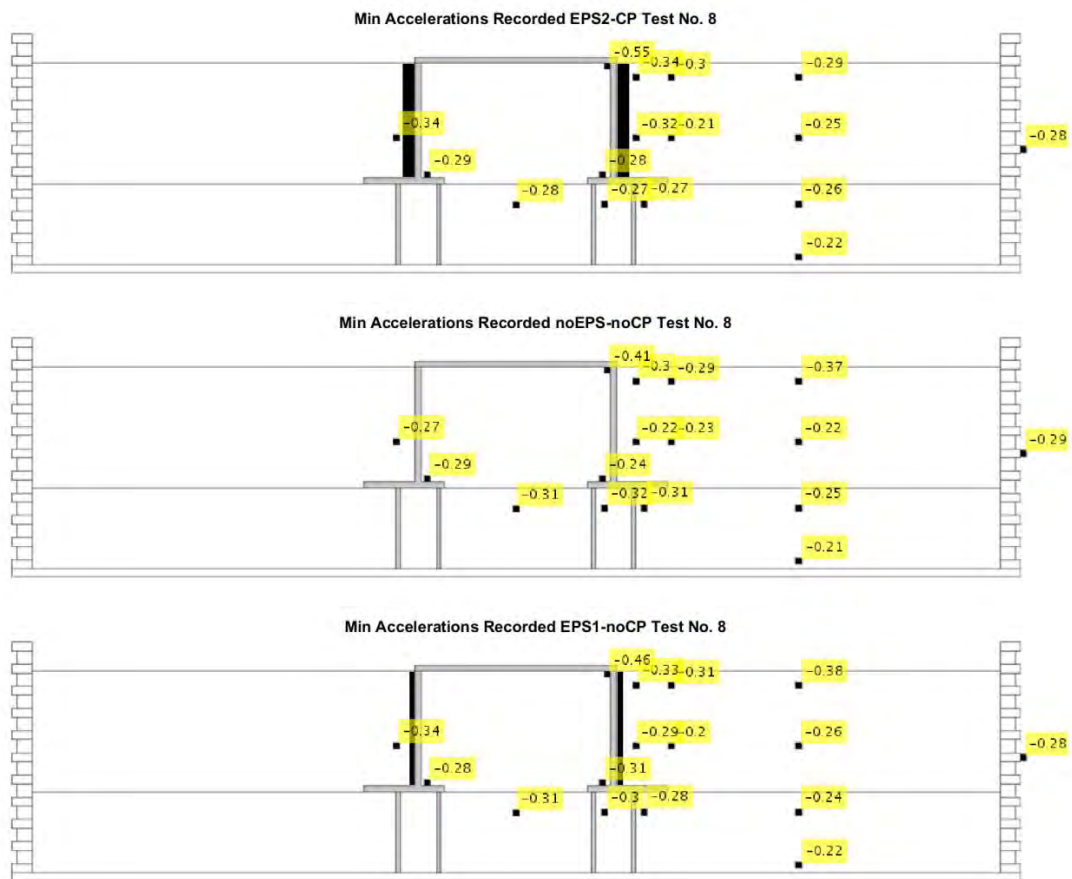


Figure 252: Example of acceleration responses for all the five configurations at the attainment of minimum acceleration – Test S8

In Figure 253 are reported the peak displacement responses recorded by LVDTs at the top, middle and bottom sections of the abutment wall, for all the configurations and for all the different tests. First of all, it can be noticed that for low ground motion intensities (tests S1 to S4) the values of peak displacements are similar for all the configurations. When the acceleration is higher (tests S5 to S8), the peak displacements are higher than the other cases in the cases with disconnected piles, and there is also a high displacement for configuration NoEPS-CP. It is possible to notice a reduction in the displacements for the configurations with connected piles and with the presence of the compressible inclusion (EPS1-CP and EPS2-CP).

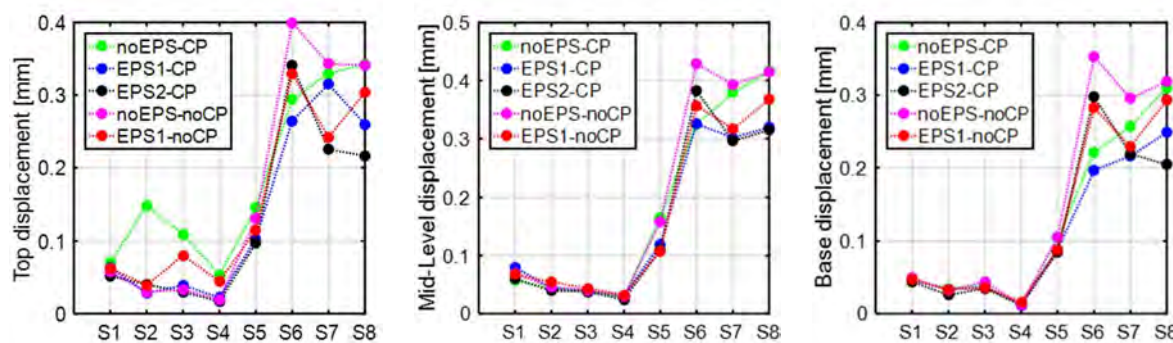


Figure 253: Displacement response recorded by the LVDTs at bottom, middle and top of the abutment

Soil settlements were monitored during the course of the experimental program for all configurations. The changes in the thickness of the surface soil layer after each shaking event was measured on the grid illustrated in Figure 254. Figure 255 shows settlement measures for shake number 2 and 6.

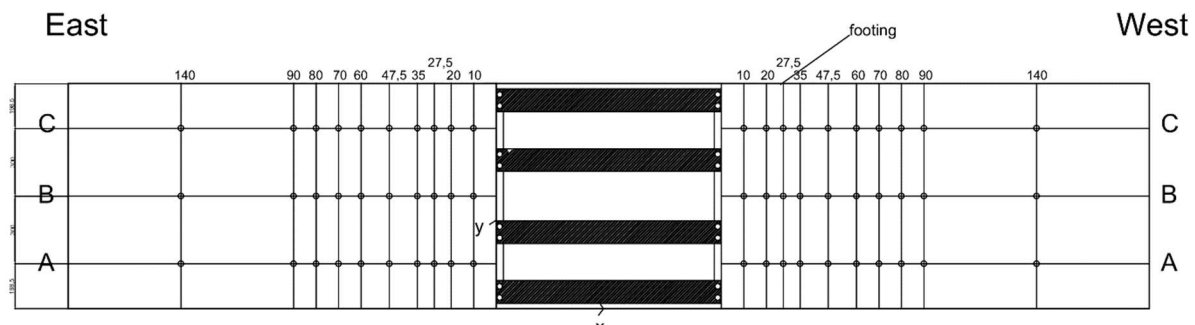


Figure 254: Soil surface measurement grid

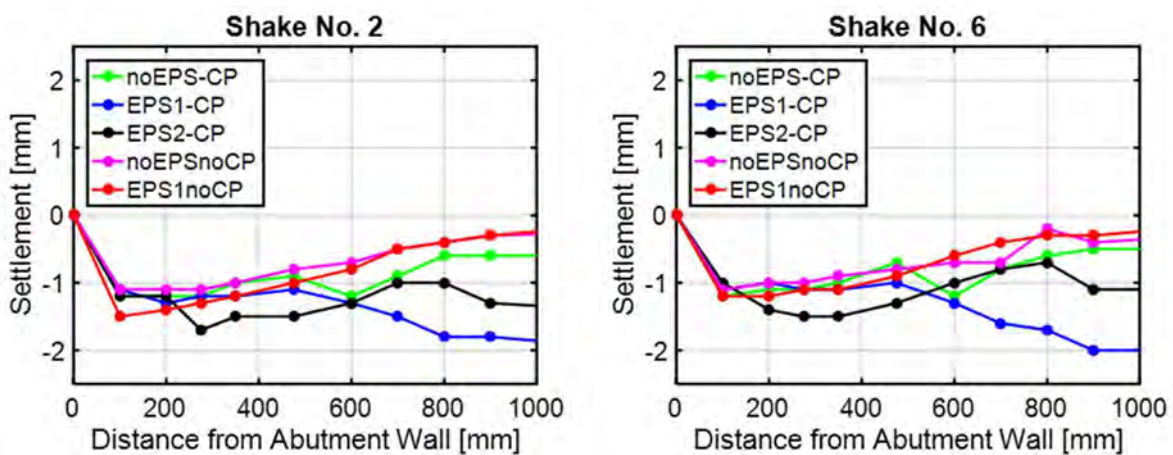


Figure 255: Settlements measured after tests S2 and S6

6.1.7 Conclusions and outlook

In this project, experimental shaking table tests were conducted on a scaled bridge model inserted into the large “shear stack” soil container of the EQUALS – BLADE Laboratory of the University of Bristol. The novelties of the project are the following: i) this is the first dynamic test on a shaking table of an Integral Abutment Bridge model including Soil-Structure Interaction; ii) the project aimed at investigating the mitigation of earth pressures on the abutment walls and, more in general, the overall effects induced by the introduction of a compressible inclusion (one or two layers of PU foam) between the soil and the abutment walls; iii) the investigation of the effects of pile disconnection and the combined effects of having both disconnected piles and compressible inclusion layers. The bridge model was scaled to a convenient dimension in order to match the dimensions of the soil container, which introduce a physical bound to the size of the model to be included inside it. In doing so, attention was paid to the development of appropriate scaling laws that will allow to extend the results obtained with the scaled model to real scale Integral Abutment Bridges. The results in terms of accelerations allow to recognize some patterns in the seismic response of the model and the soil. In the backfill, it was found that the inclusion of layers of PU foam increases the accelerations in the soil at one hand, while on the other hand in presence of the compressible inclusion the accelerations of the bridge are smaller than in the soil. Regarding the settlements measured after the tests, the measurements have highlighted larger settlements in the configurations with compressible inclusion layers behind the

abutment wall. This result indicates the necessity in real bridges of a careful design of approaching slabs.

6.1.8 References

- Applied Technology Council. (1996a). 32 Improved seismic design criteria for California bridges: Provisional recommendations. ATC-32.
- Applied Technology Council. (1996b). 40 (1996) Seismic evaluation and retrofit of concrete buildings. Applied technology council, report ATC-40. Redwood City.
- Briseghella B., Zordan T., (2006). Integral abutment bridge concept applied to the rehabilitation of a simply supported prestressed conventional concrete superstructure. *Structural Concrete* 8(1):25-33.
- Burke Jr., M.P., (1993). Integral bridges: attributes and limitations. *Transportation Research Record* 1393, 1-8.
- Burke Jr MP. Integral and semi-integral bridges. John Wiley & Sons 2009.
- California. Department of Transportation. (1999). Caltrans Seismic Design Criteria, Version 1.1. California Department of Transportation.
- England GL, Bush DI., Tsang NC. Integral bridges: a fundamental approach to the time-temperature loading problem. Thomas Telford 2000.
- Eurocode 8 - Design of structures for earthquake resistance - Part 2: Bridges.
- Frosch RJ., Kreger ME, Aaron M. Talbott AM (2009). Earthquake resistance of integral abutment bridges, Final Report, FHWA/IN/JTRP-2008/11, INDOT Office of Research & Development West Lafayette, IN 47906, USA
- Horvath, J. S. (2005). Expanding the use of expanded polystyrene (EPS) geofoam in practice. In Proc. BSCES ASCE Geo-Institute Fall 2005 Geotech. Engrg. Sem., Boston Soc. Civ. Engrs. Sec. ASCE.
- Maruri, R. F., & Petro, S. H. (2005). Integral abutments and jointless bridges (IAJB) 2004 survey summary. In *Integral Abutment and Jointless Bridges (IAJB 2005)* Federal Highway Administration West Virginia Department of Transportation.
- Muttoni, A., Dumont, A. G., Burdet, O., Savvilitidou, M., Einpaul, J., & Nguyen, M. L. (2013). Experimental verification of integral bridge abutments (No. REP_WORK). Rapport OFROU.
- Psarropoulos PN, Klonaris G, Gazetas G. Seismic earth pressures on rigid and flexible retaining walls. *Soil Dyn Earth. Eng* 2005; 25(7-10):795-809.
- Qian, H., Zhuang, Y., & Chen, Y. (2016, October). Shaking Table Experiment on Soil-Micropile Interaction of Semi-integral Abutment Bridge. In *International Symposium on Environmental Vibration and Transportation Geodynamics* (pp. 145-157). Springer, Singapore.
- Saiidi M, Vosoghi A, Nelson R. Shake Table Studies of A Four-Span Reinforced Concrete Bridge, *J Struct Eng. ASCE, Special Issue: NEES 2: Advances in Earthquake Engineering* 2013; 139(8):1352-1361.
- Towhata I. Geotechnical earthquake engineering. Springer Science & Business Media, 2008.
- Veletsos AS, Younan AH. Dynamic response of cantilever retaining walls. *J Geotech Geoenviron.* 1997; 123(2):161-172.
- Wilson P, Elgamal A. Full-scale shake table investigation of bridge abutment lateral earth pressure, *Bull N Z Natl Soc Earthquake Engng* 2009; 42(1):39-46.
- Zordan T, Briseghella B, Lan C, Analytical formulation for limit length of integral abutment bridges. *Struct Eng Int* 2011, 21(3): 304-310.

6.2 Project #11 – 3DRock - Statistical verification and validation of 3D seismic rocking motion models

Authors

M. F. Vassiliou⁽¹⁾, M. Broccardo⁽²⁾, C. Cengiz⁽³⁾, M. Dietz⁽³⁾, L. Dihoru⁽³⁾, S. Gunay⁽⁴⁾, K. Mosalam⁽⁴⁾, G. Mylonakis^(3,5,6), A. Sextos⁽³⁾, B. Stojadinovic⁽¹⁾

⁽¹⁾ *Department of Civil, Environmental, and Geomatic Engineering, ETH Zurich, Switzerland*

⁽²⁾ *University of Liverpool, United Kingdom (formerly with ETH Zurich)*

⁽³⁾ *Department of Civil Engineering, University of Bristol, Bristol, United Kingdom*

⁽⁴⁾ *University of California at Berkeley (UCB), U.S.A.*

⁽⁵⁾ *Department of Civil Engineering, Khalifa University, U.A.E.*

⁽⁶⁾ *University of California at Los Angeles (UCLA), U.S.A.*

6.2.1 Introduction

In 1963, Housner [1] published his seminal paper where he explained the remarkable properties of rocking structures: (i) the larger of two geometrically similar blocks can survive the excitation that will topple the smaller block, and (ii) out of two acceleration pulses with the same acceleration amplitude, the one with longer duration is more capable of inducing overturning.

Since then, the behavior of a simple, free-standing rigid rocking block has been systematically studied [2–14]. The dynamic behavior of assemblies or rocking bodies, such as multi-drum ancient columns [15] or rocking frames or walls [16–19], has also been studied. It was concluded that these assemblies are also remarkably stable when excited by earthquakes. Experiments show that the deterministic models of rocking motion are not easy to validate [20–23], thus necessitating a probabilistic treatment [24–26].

Rocking is treated as a 2D, in-plane, problem in most of the literature. Published research on the dynamic response of 3D rocking of rigid bodies is much more limited. In [27–29], the motion of a rigid cylinder under seismic excitation is studied. Other researchers studied the 3D response of ancient conical or cylindrical columns numerically [30, 31] or experimentally [32–34]. Makris et al. [35] experimentally tested scaled models of uplifting bridges. These studies conclude that 3D motion (so-called wobbling) is present even under in-plane initial conditions and/or under uniaxial horizontal component ground excitation. Stefanou et al. [36] proved this observation theoretically.

The 3D behavior of non-cylindrical bodies has also recently received attention. Konstantinidis and Makris [37], Zulli et al. [38], Chatzis and Smyth [39, 40] studied the motion of a 3D prism. Mathey et al. [41] studied the influence of geometric defects on the 3D response of small-sized blocks. They concluded that blocks with imperfections are less stable than the theoretically perfect ones. Pappas et al. [42] numerically explored the behavior of an ancient cylindrical column with a height of 6 m and a diameter of 0.66 m with the intention of defining proper ground motion intensity measures to characterize the rocking response of such structures.

Dynamic models used in the research discussed earlier are multi-degree-of-freedom (MDOF) models and assume unbounded 3D motion. They involve stepping or rolling rigid rocking bodies out of their initial position. This results to residual deformations. Thus, these models are suitable for equipment but not for structural components designed to uplift, because rolling out of the initial position would be prohibited for such structural components from the standpoint of seismic performance of the structures, they are a part off. Therefore, Vassiliou et al. [43] developed a simpler model in which a cylinder rocks and wobbles (rolls unsteadily) exclusively above the initial position of its base, without sliding or rolling out (i.e., a 3D inverted pendulum) (Figure 256, left). In this sense, the investigated model is a direct extension of Housner's model, which also constrains the rocking body to restore to its original position. Subsequently, the model was extended to include a slab, supported by four wobbling columns [44] (Figure 256, right).

One of the main research gaps in the study of rocking motion (from the engineering point of view) is the lack of model validation. This has led the earthquake engineering community not to trust the existing rocking models. A series of papers has been published characterizing the rocking motion as "chaotic" [45-49 among others] and employing non-linear dynamics concepts to study it. However, this work is based on idealized excitations that do not correspond to real earthquakes. Given that there is uncertainty in the ground motion itself, the engineering question is not whether the structural models can predict the response to a specific ground motion, but whether they can predict the statistics of the response to an ensemble of ground motions used for design. Based on the early work of Yim et al. [2], Bachmann et al. [50, 51] validated the Housner rocking model and concluded that it is able to predict well the response of a block rocking in-plane. They compared the numerical and experimental empirical Cumulative Distribution Functions (CDF) of the maximum rotation angle when 100 ground motion with the same statistical properties were used as excitation. They concluded that the CDFs matched well. By performing a Kolmogorov-Smirnov test, they found that the rocking motion of a rigid structure is predictable in a statistical sense, and that the 1963 Housner numerical model can be used to predict it. However, this work is limited to planar rocking motion of specimens that were engineered to concentrate the impact forces on at the impacting corner. No sliding was observed, as the specimens were relatively slender.

The research gap that this project aimed to bridge is the statistical validation of 3D rocking models. This is necessary: first, to trust and calibrate the models that are used for the study of precious equipment, and second, to use rocking as an earthquake response modification technique.

More specifically, the objectives of the 3DRock project were:

- a) To generate a dataset and to statistically validate numerical models of seismic response of unconstrained rocking objects (referred to as "Free Rocking" in this report)
- b) To generate a dataset and to statistically validate numerical models of seismic response of rocking structures comprising columns supporting a rigid plate and constrained to wobble about their original position without being able to twist and without restraining tendons (referred to as "Wobbling Frame" in this report)

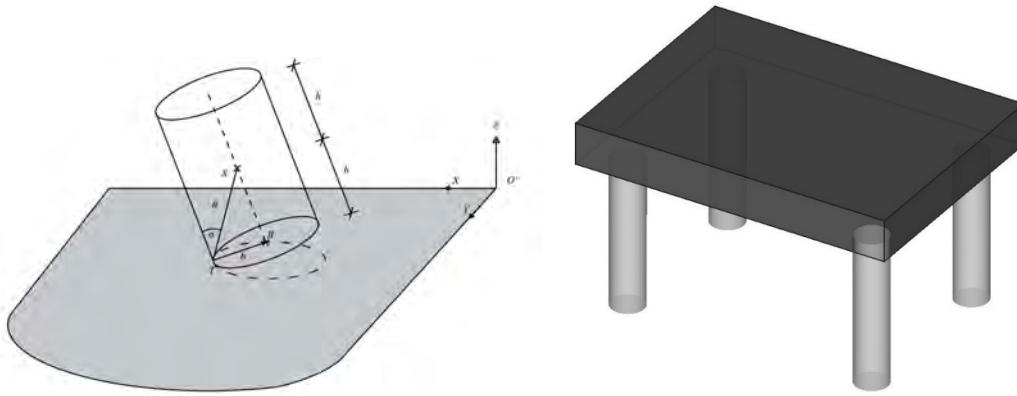


Figure 256: Left: Free rocking cylinder. Right: Wobbling frame

6.2.2 Specimens

Two different sets of specimens were tested:

Free Rocking specimens (Figure 257)

Six steel columns of three different heights and slenderness were tested simultaneously on a shaking table. A rocking column consists of a steel pipe with a steel plate on top. Three of the columns had a steel plate welded at the bottom as shown in Figure 257, so that they rock on a square surface. The other three were rolling on the perimeter of their base, i.e. a circle, machine to be flat. All the columns had a square plate welded on top so that the markers used to measure displacements could be placed there. The bottom and top plates were equal in size and material and were welded to the pipe in order to create a rigid connection. The dimensions of the tested columns are presented in Table 32.

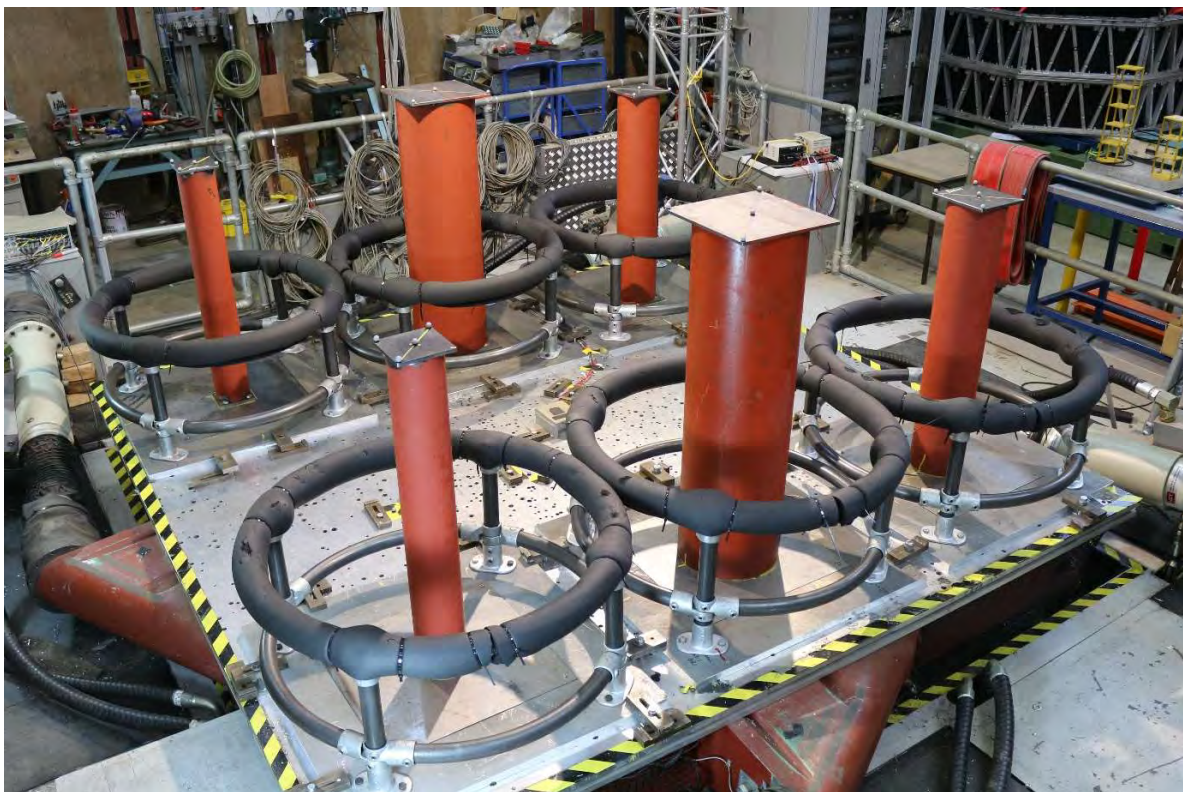


Figure 257: Free Rocking specimens

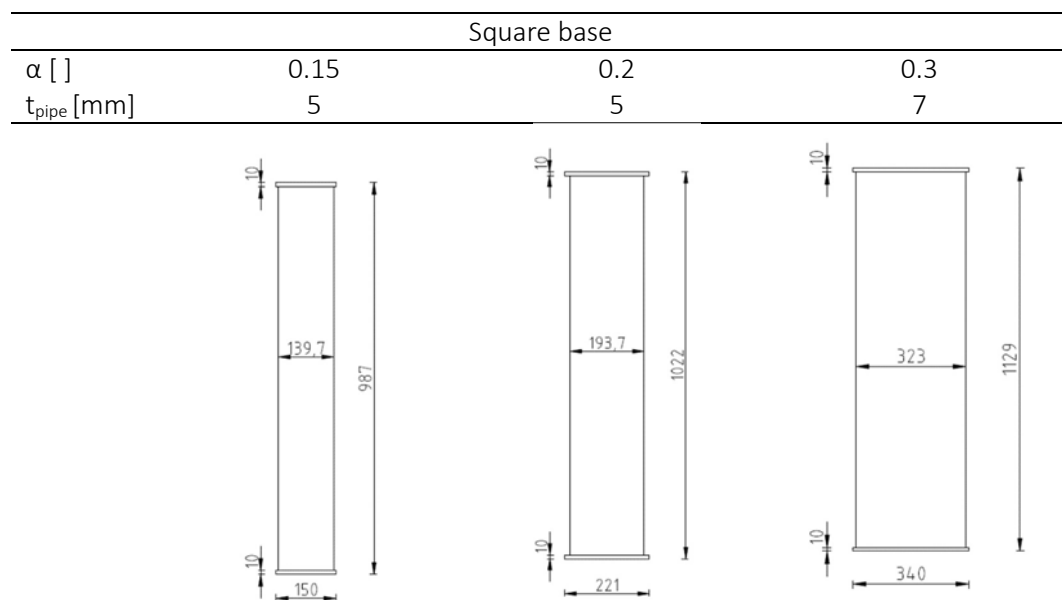
Wobbling Frame specimen (Figure 258 and Figure 259)

The wobbling specimen was designed in the ETH Zurich and comprised 4 wobbling circular steel columns supporting an aluminum slab (Figure 258). The four columns had a height, diameter and wall thickness of 1000 mm, 244.5 mm and 8 mm, respectively (Figure 259), giving a slenderness ratio of $\tan\alpha = 0.2445$. Such small size specimens are not representative of the size of a real bridge or a real podium building. As rocking response is size-dependent, the ground motions used were appropriately scaled so that in the prototype scale the model has a height similar to that of a typical bridge, as discussed in a next section. The ends of the columns were machined (lathed) to ensure the rocking surface flat and square to the column axis. Both ends of each column was placed on specially designed conical restrainers designed to stop the columns from sliding or wobbling out of their original position (Figure 260, left) but to allow for tilting of the column due to wobbling, as assumed in [44]. After the tests, scratches on the restrainers were observed, showing that the columns tried to “climb out” of the conical surfaces (Figure 261, right). The interior aluminum pegs were designed to prevent overturning and damage to the specimen and were not engaged during the tests.

6.2.3 Test setup

Excitations

To constrain the uncertainty of the ground motion excitation, the ensemble of ground motions used in the shaking table tests and the subsequent numerical model response analyses was synthesized using a spectral version of the Rezaeian and Der Kiureghian stochastic ground motion model [52-54]). The generated synthetic motions were defined as “target-spectrum-consistent”. A stochastic method to generate ground motions with similar elastic response spectra was adopted as the best-available precondition for a statistical comparison of the numerical and experimental rocking block responses, even though motions with similar elastic spectra could have very different overturning potential.



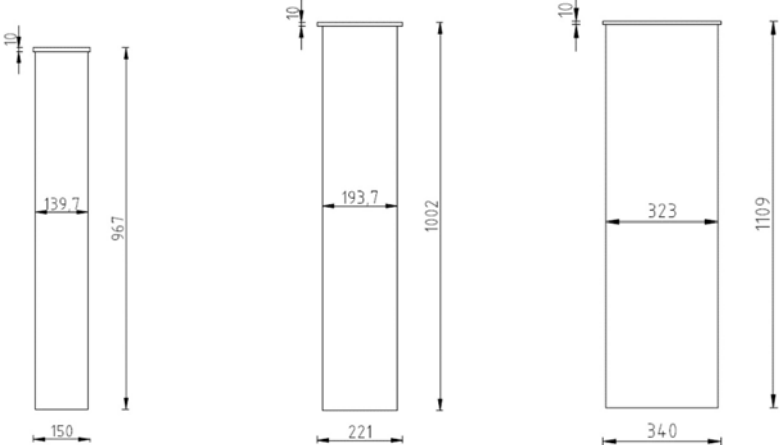
Circular base			
α [°]	0.15	0.20	0.30
t_{pipe} [mm]	5	5	7
			

Table 32: Dimensions of the six Free Rocking specimens



Figure 258: Wobbling Frame specimen on the University of Bristol Shake Table

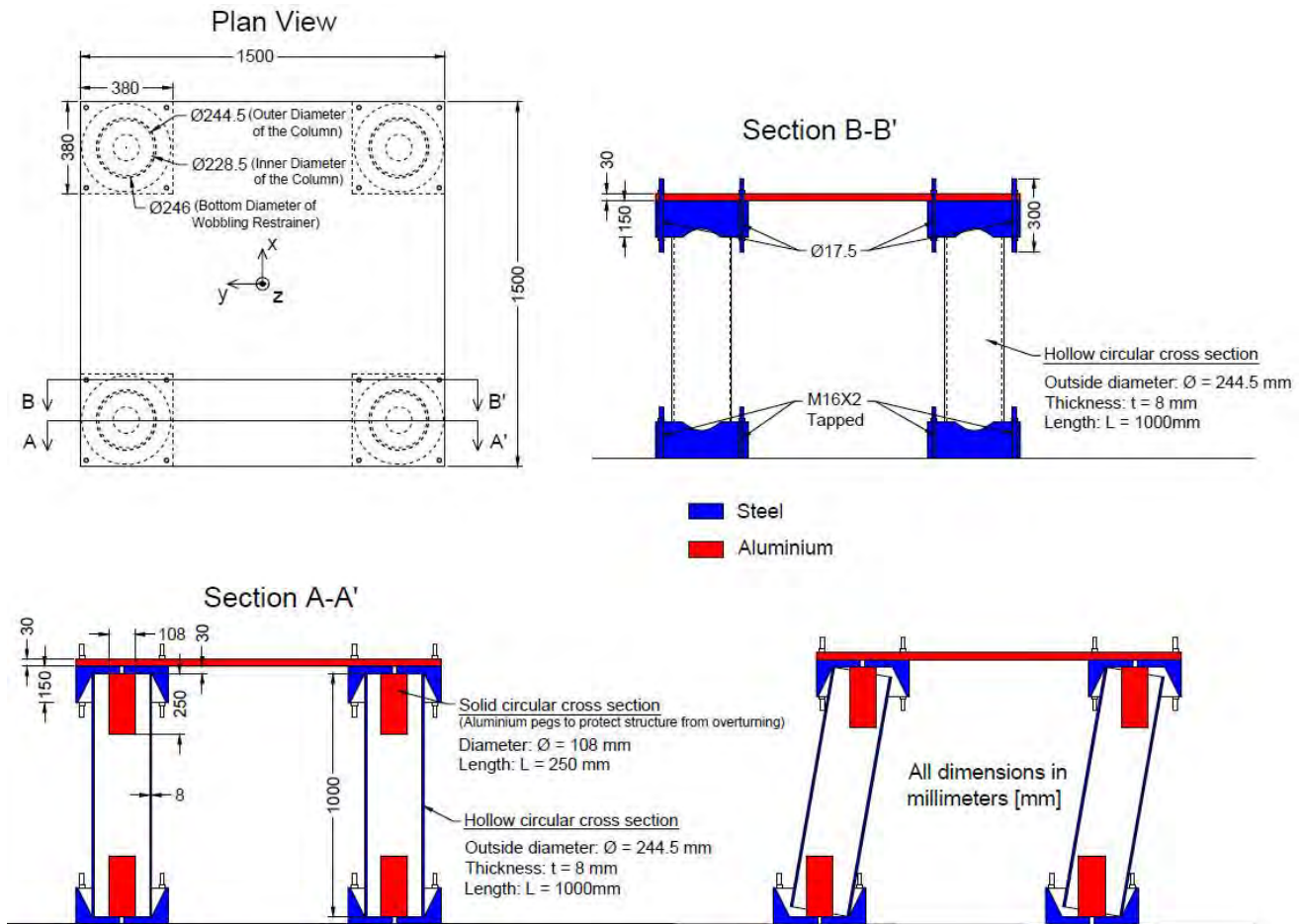


Figure 259: Top-right: Marker positions for displacement measurements on top of the aluminium slab;
Other figures: configuration of the conical restraints and pegs placed on both ends of the columns



Figure 260: Left: Conical restraint with peg designed to prevent overturn in case of excessive tilt. Right: Shavings, showing that the steel column scratched the restrainer as it was "climbing out"

Three records, the 1989 Loma Prieta UCSC Lick Observatory, the 1940 El Centro Array #9 record and the 1999 Chi Chi CHY080 record, were used as the "seed" ground motions. Three ground motion ensembles, each with 100 synthetic ground motions, were generated from the three seed ground motions. The Loma Prieta ensemble was used to excite the Free Frocking specimens, and the El Centro and Chi Chi ensembles were used to excite the Wobbling Frame specimen.

6.2.4 Scaling of the ground motion ensembles

For the Free Rocking test series (100 tests), the ground motions were used unscaled.

For the Wobbling Frame test series (two times 100 tests), the ground motions were scaled in time. Changing the size (length scale S_L) of a rigid rocking block affects its response in the same way as changing the squared frequency of the ground motion excitation (time scale S_T) in the opposite direction. To represent a (distorted) prototype structure of larger size (with a column height 9.67m), the ground motions used to excite the specimen were scaled in time by the time scale factor $S_T = (S_L)^{1/2}$, while preserving the acceleration scale. Therefore, the ground motions were time-scaled by a factor of 3.11 (i.e., the frequency of the ground motions was increased without changing the amplitude scale). The specimen is only a distorted model of a larger prototype structure because its eigen-frequency scales with S_L and because the similitude of stresses is not preserved. However, it has been shown that the deformability of large structures does not qualitatively change their rocking behavior [22, 55-61]. Moreover, an actual rocking structure would likely be designed such that the column ends are protected against local damage and that the column response remains in their elastic range. Ultimately, these tests serve for model validation and do not aim to represent a prototype structure without distortion.

Instrumentation

In all tests, the acceleration of the shake table was measured using accelerometers and the displacements of the specimens and the shake table were measured using an LED tracking system and markers. Specifically, 4 markers were placed on top of the Free Rocking specimens (shown in Figure 261 and also visible in Figure 257) and 6 markers were placed on the Wobbling Frame slab (Figure 262). The LED tracking system recorded the 3-dimensional position of these markers with an accuracy of 10^{-3} mm and a sampling rate of 100 Hz.

6.2.5 Observations during testing

- a) The plates welded to the free rocking columns were not thick enough and welding caused them to warp. Therefore 3 out of 6 specimens (i.e. the ones with the plate on the bottom, designed to rock on a square surface) were rocking on a far from perfectly flat surface, which is hard to



Figure 261: Markers on top of a free rocking column

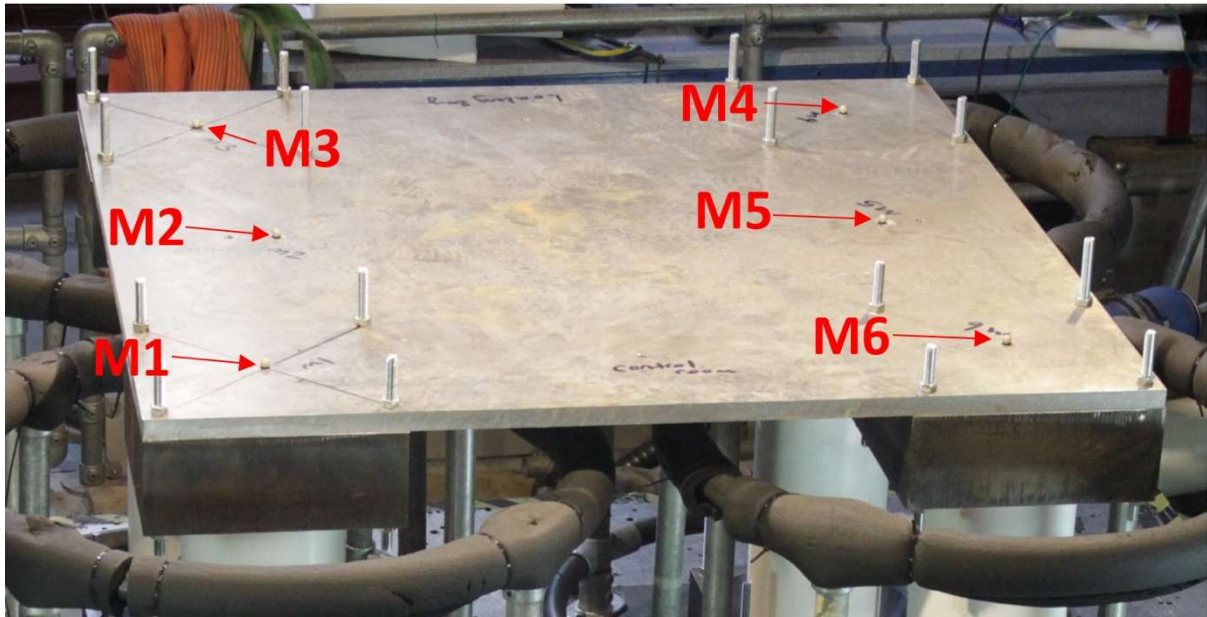


Figure 262: Marker positions for displacement measurements on top of the aluminium slab

model numerically. Therefore, they moved even for accelerations that were not supposed to uplift them, had they been perfect.

- b) The test of both the Free Rocking and the Wobbling Frame specimens were not repeatable. Some ground motions were repeated 3 times: in some repetitions, the specimens would overturn, while in others they would not.
- c) Initially the free rocking specimens were rocking on an aluminum surface, but it quickly developed scratches and dents. Therefore, the aluminum surface was replaced by a steel one.
- d) The columns of the Wobbling Frames tried to climb the restrainers and thus created scratches on the inclined surfaces of the conical restraints.
- e) Displacements of the slab were measured above the four columns. Symmetry of the system would dictate that no rotation of the slab around the vertical axis should occur. However, imperfections are always present and such a twisting rotation was observed. Based on this, the following function is defined as a measure of overall displacement:

$$d(t) = \text{abs} \left(\frac{d_1(t) + d_3(t) + d_4(t) + d_6(t)}{4} \right) \quad (1)$$

where d_i is the Euclidean norm of the relative to the shake table horizontal displacement at points M_i of Figure 262. Focusing on the displacement at the center of the slab would have not given any information on its twist.

6.2.6 Preliminary results

Free Rocking columns

A preliminary Abaqus model was built (Figure 263) and numerical simulations are currently being performed. The simulations for the 3 circular-base specimens are not as challenging as the simulations for the three square-base specimens, because of plate warping.

Wobbling Frame

The Pacific Earthquake Engineering Research center (PEER), the University of Bristol, and ETH Zurich launched a blind prediction contest in October 2019 with a deadline for submission on November 20th, 2010. The contestants were asked to predict not the response to each one of the ground motions, but the experimental CDFs of the displacement quantity specified in Equation 1, shown in Figure 264 with thick black lines, obtained from two series of about 100 tests based on the ground motions generated using the recorded El Centro and Chi-Chi motion as seeds. The contestants were ranked according to the maximum vertical distance between their predicted CDF and the experimental one. This is the Kolmogorov-Smirnov distance between the two CDFs [62-63]. The final ranking was made according to the average of the Kolmogorov Smirnov distances for the two sets of ground motions. The as built geometry and the recorded shake table accelerations were provided to the contestants, but no tests were performed to mechanically characterize the materials. The contestants were invited to submit

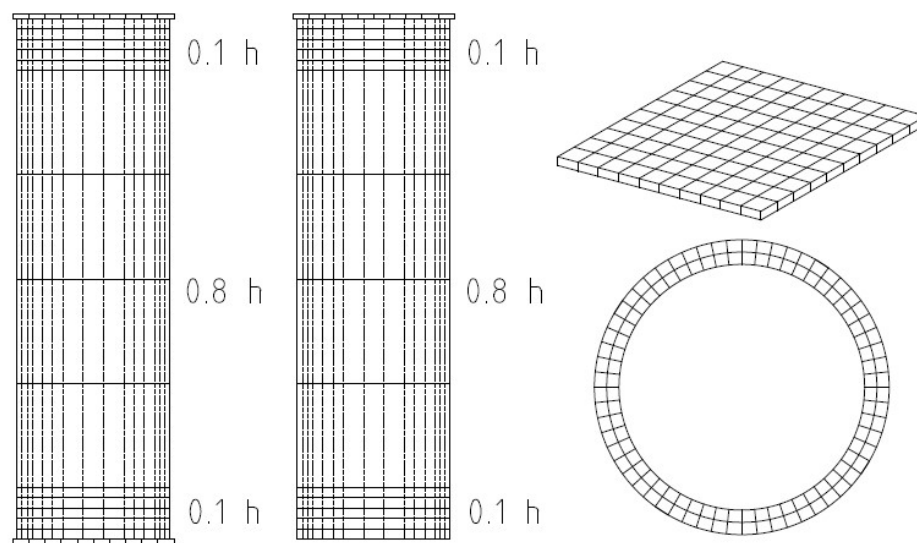


Figure 263: Meshing of the Abaqus model for the Free Rocking specimens. Front view of a column with square base (left) and circular base (middle), projection of a plate (top right), section through a pipe (bottom right)

results, even if they did not simulate the response to all 200 ground motions. The CDFs of each contestant were computed based only on the submitted results he or she submitted.

The accelerometer measurements did not start for one ground motion from the El Centro set and one ground motion from the Chi-Chi set, so there was no data on the excitation. These two ground motions (El Centro #4 and Chi-Chi #58) were excluded from the evaluation of the results.

Thirteen contestants participated in the contest. They used three modelling approaches:

- a) 8 used finite element models (FEM) and software, out of which 4 used ABAQUS, 2 used SAP2000, 1 used Midas GEN and 1 used OpenSees
- b) 4 used discrete element models (DEM) and software, out of which 3 used 3DEC and 1 Code Aster
- c) 1 used the Vassiliou [44] model (independently from the author, as he was one of the contest organizers)

Figure 264 compares the predicted CDFs with the experimental ones. Table 33 ranks the predictions based on the Kolmogorov Distances: Column 1 gives the ranking for El Centro, column 2 the ranking for

Chi-Chi and column 3 the overall ranking based on the average Kolmogorov-Smirnov distance for the two sets of ground motions.

The predictions show:

- The analytical model CDF for the Chi-Chi ensemble are better than the ones for the El Centro ensemble.
- Some teams (e.g. #9, #3 and #5) performed consistently well. They were not “just lucky”, as they ranked at the top for both sets of ground motions.
- Both FEM and DEM models can perform very well or poorly, can overestimate or underestimate the response, depending on the input parameters used.
- The specific Rigid Block model proposed by Vassiliou [44] and used by Team #11 consistently overestimates the response. Hence it is conservative; but not accurate. Apparently disregarding energy dissipation caused by scratching of the conical restrainers leads to overestimation of the response.

The two winning teams were Team #9 and Team #3.

Team #9 (Myron Chiyun Zhong and Constantin Christopoulos from University of Toronto) used FE software ABAQUS 6.13 with C3D20R quadratic brick element, with reduced integration. They assumed a coefficient of friction of 0.3 and zero inherent damping ratio [64].

Team #3 (Daniele Malomo, Anjali Mehrotra, and Matthew DeJong from UC Berkeley) used Distinct (or Discrete) element software 3DEC. The frictional mechanisms were modeled using a simplified Mohr-Coulomb criterion with friction angle $\phi=0.2$, and zero dilation (ψ), tensile strength (f_t) and cohesion (c). The rocking columns were modelled as rigid and the connection was provided by nonlinear springs with normal stiffness $k_n = 10^9 \text{ Pa/m}$ and shear stiffness $k_s = 10^9 \text{ Pa/m}$ [65]. Zero Rayleigh damping was used.

Interestingly, the two winning teams were the only ones to report using zero Rayleigh damping, thus relying only on friction for energy dissipation.

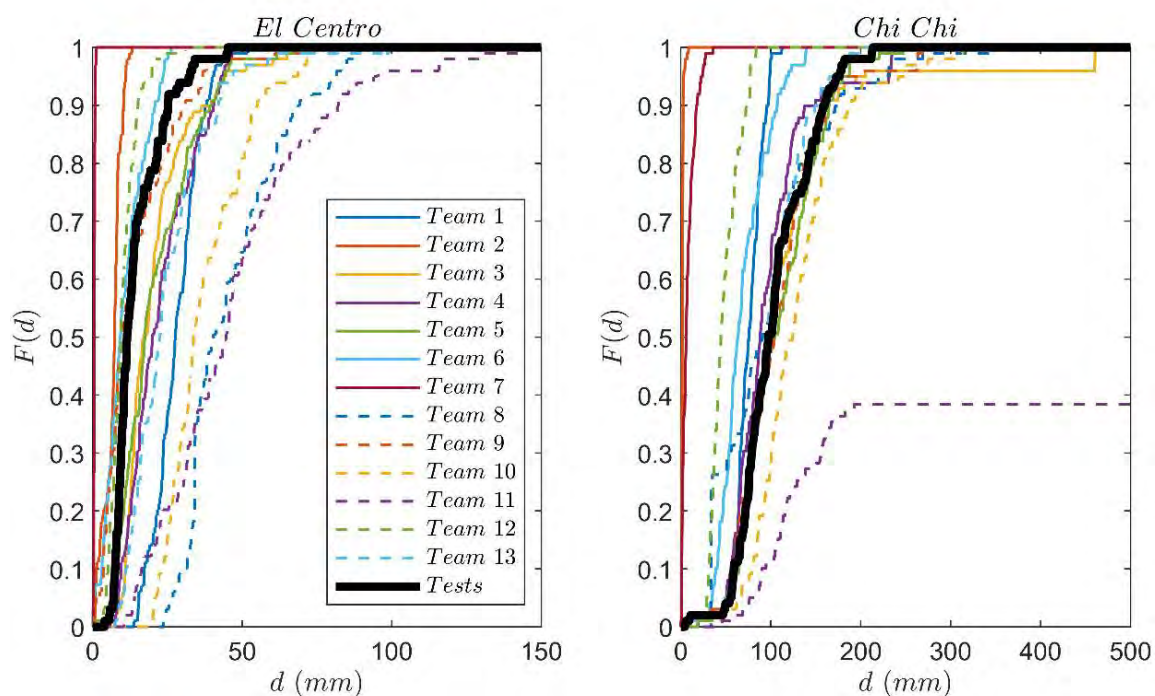


Figure 264: Cumulative distribution function of the displacement d : Tests and predictions by the 13 contestants

El Centro			Chi-Chi		Average	
	Team number (and method used)	K-S Distance	Team number (and method used)	K-S Distance	Team number (and method used)	K-S Distance
1	12 (FEM)	0.25	3 (DEM)	0.06	9 (FEM)	0.19
2	9 (FEM)	0.27	9 (FEM)	0.11	3 (DEM)	0.21
3	6 (FEM)	0.32	13 (DEM)	0.11	5 (DEM)	0.24
4	5 (DEM)	0.34	5 (DEM)	0.13	4 (FEM)	0.30
5	3 (DEM)	0.36	4 (FEM)	0.16	13 (DEM)	0.30
6	4 (FEM)	0.43	8 (DEM)	0.26	6 (FEM)	0.39
7	13 (DEM)	0.48	10 (FEM)	0.27	12 (FEM)	0.48
8	2 (FEM)	0.65	6 (FEM)	0.46	10 (FEM)	0.53
9	1 (FEM)	0.69	1 (FEM)	0.48	8 (DEM)	0.58
10	11 (RB)	0.72	11 (RB)	0.62	1 (FEM)	0.59
11	10 (FEM)	0.79	12 (FEM)	0.71	11 (RB)	0.67
12	8 (DEM)	0.89	7 (FEM)	0.98	2 (FEM)	0.82
13	7 (FEM)	1.00	2 (DEM)	0.99	7 (FEM)	0.99

Table 33: Ranking Based on Kolmogorov-Smirnov Distance

6.2.7 Conclusions and outlook

The 3D rocking oscillator model is useful both because it describes the seismic behavior of unanchored equipment and because unrestrained rocking has been suggested as a seismic response modification technique. A major critique against rocking systems has been that their responses are not only hard to predict by existing numerical models, but that the response is inherently unpredictable.

However, since the seismic response problem is inherently stochastic, as the ground motion is not known a priori, modelling uncertainties should not be a reason to deter engineers from using rocking solutions. Compare this to the case for fixed support inelastic systems, whose seismic response has a lot of uncertainty, yet these models are widely used in practice.

Therefore, in the context of earthquake engineering, the objective of this study is to answer two important questions: Is wobbling motion inherently unpredictable? If not, are existing models good enough to predict the response?

Following a methodology recently introduced by Bachmann et al. [51], this report claims that the answer to this question must be given in the statistical sense and not in the traditional deterministic sense. The quantity of interest in earthquake engineering is not the response to a given ground motion but the statistics of the response to a set of ground motions.

To this end, an experimental campaign has been designed to obtain observations of wobbling motion to be compared with those obtained from numerical simulations. Two sets of models were studied: “Free Rocking” representing unanchored equipment; and “Wobbling Frame” representing a design approach that can be used for the rocking isolation of bridges or buildings.

To constrain the uncertainty in the excitation, a stochastic model was used to generate synthetic ground motion ensembles that match the physical characteristics of recorded ground motions. Each ensemble contained 100 excitations. One ensemble was used to study the Free Rocking specimens and 2 ensembles were used to study the Wobbling Frame.

Numerical simulation of the tests on the Free Rocking specimens is being currently performed.

The response of the Wobbling Frame has been the subject of an international blind prediction contest. The contestants were invited to predict not the maximum of each response, but the Cumulative

Distribution Functions of the maxima of the responses. 13 teams using FEM, DEM and Rigid Dynamics models responded. In terms of predicting the whole CDF some contestants managed to give accurate predictions for one ensemble of excitation, but the CDF prediction of the other ensemble of excitations was poorer. This shows that there is space for improvement of the modelling assumptions used in wobbling structural models. Interestingly, both FEM and DEM can perform excellent or poorly, can overestimate or underestimate the response depending on the input parameters used. Moreover, the teams that performed the best were the ones that used zero Rayleigh damping and only relied on friction between the contact surfaces to dissipate energy, showing that damping models should be physics based. An analytical dynamics model that prevents sliding and twisting was found to consistently overestimate the response of the structure at hand, exactly because it did not model sliding. A more involved investigation on the modelling parameters that optimize the prediction of the Wobbling Frame is the subject of current research.

6.2.8 References

- [1] Housner, GW (1963): The behaviour of inverted pendulum structures during earthquakes, *Bull. Seismol. Soc. Am.* **53**, 404–417.
- [2] Yim CS, Chopra AK, and Penzien J (1980): Rocking response of rigid blocks to earthquakes, *Earthq. Eng. Struct. Dyn.*, **(8)** 565–587.
- [3] Psycharis IN and Jennings PC (1983): Rocking of slender rigid bodies allowed to uplift, *Earthq. Eng. Struct. Dyn.*, **11** (1), 57–76.
- [4] Zhang J and Makris N (2001): Rocking Response of Free-Standing Blocks under Cycloidal Pulses, *J. Eng. Mech.*, **127** (5), 473–483.
- [5] Makris N and Konstantinidis D (2003): The rocking spectrum and the limitations of practical design methodologies, *Earthq. Eng. Struct. Dyn.*, **32** (2), 265–289.
- [6] Contento A and Di Egidio A (2009): Investigations into the benefits of base isolation for non-symmetric rigid blocks, *Earthq. Eng. Struct. Dyn.*, **38** (7), 849–866.
- [7] Dimitrakopoulos EG and DeJong MJ (2012): Revisiting the rocking block: closed-form solutions and similarity laws, *Proc. R. Soc. A Math. Phys. Eng. Sci.*, **468** (2144), 2294–2318.
- [8] Dimitrakopoulos EG and DeJong MJ (2012): Overturning of Retrofitted Rocking Structures under Pulse-Type Excitations, *J. Eng. Mech.*, **138** (8), 963–972.
- [9] Vassiliou MF and Makris N (2012): Analysis of the rocking response of rigid blocks standing free on a seismically isolated base, *Earthq. Eng. Struct. Dyn.*, **41** (2), 177–196.
- [10] DeJong MJ and Dimitrakopoulos EG (2014): Dynamically equivalent rocking structures, *Earthq. Eng. Struct. Dyn.*, **43** (10), 1543–1563.
- [11] Makris N, The Role of the Rotational Inertia on the Seismic Resistance of Free-Standing Rocking Columns and Articulated Frames (2014): *Bull. Seismol. Soc. Am.*, **104** (5), 2226–2239.
- [12] Makris N, A half-century of rocking isolation (2014): *Earthquakes Struct.*, **7** (6), 1187–1221.
- [13] Makris N and Kampas G (2016): Size Versus Slenderness: Two Competing Parameters in the Seismic Stability of Free-Standing Rocking Columns, *Bull. Seismol. Soc. Am.*, **106** (1), 104–122.
- [14] Makris N and M. F. Vassiliou MF (2012): Sizing the slenderness of free-standing rocking columns to withstand earthquake shaking, *Arch. Appl. Mech.*, **82** (10–11), 1497–1511.
- [15] Konstantinidis D and Makris N (2005): Seismic response analysis of multidrum classical columns, *Earthq. Eng. Struct. Dyn.* **34** (10), 1243–1270.
- [16] Papaloizou L and Komodromos P (2009): Planar investigation of the seismic response of ancient columns and colonnades with epistyles using a custom-made software, *Soil Dyn. Earthq. Eng.*, **29** (11–12), 1437–1454.
- [17] Makris N. and Vassiliou MF (2013): Planar rocking response and stability analysis of an array of free-standing columns capped with a freely supported rigid beam,” *Earthq. Eng. Struct. Dyn.*, **42** (3) 431–449.

- [18] Makris N and Vassiliou MF (2014): Are Some Top-Heavy Structures More Stable? *J. Struct. Eng.*, **140** (5), p. 06014001.
- [19] Dimitrakopoulos EG and Giouvanidis AI (2015): Seismic Response Analysis of the Planar Rocking Frame, *J. Eng. Mech.*, **141** (7), p. 04015003.
- [20] Ma QTM, (2010): The mechanics of rocking structures subjected to ground motion (PhD Dissertation, University of Auckland, NZ.)
- [21] Peña F, Prieto F, Lourenço PB, Campos Costa A, and Lemos JV (2007): On the dynamics of rocking motion of single rigid-block structures, *Earthq. Eng. Struct. Dyn.*, **36** (15), 2383–2399.
- [22] Truniger RE, Vassiliou MF, and Stojadinović B (2015): An analytical model of a deformable cantilever structure rocking on a rigid surface: experimental validation, *Earthq. Eng. Struct. Dyn.*, **44** (13).
- [23] Bachmann JA, Blöchlinger P, Wellauer M, Vassiliou MF, and Stojadinović B (2016): Experimental investigation of the seismic response of a column rocking and rolling on a concave base ECCOMAS Congress 2016: 7th European Congress on Computational Methods in Applied Sciences and Engineering, 2016.
- [24] Psycharis, I. N., Fragiadakis, M., & Stefanou, I. (2013). Seismic reliability assessment of classical columns subjected to near-fault ground motions. *Earthquake Engineering & Structural Dynamics*, **42**(14), 2061-2079.
- [25] Dimitrakopoulos EG and Paraskeva TS (2015): Dimensionless fragility curves for rocking response to near-fault excitations, *Earthq. Eng. Struct. Dyn.*, **44** (12), 2015–2033.
- [26] Bakhtiar E and Gardoni (2016): P, Probabilistic seismic demand model and fragility estimates for rocking symmetric blocks, *Eng. Struct.*, **114**, 25–34.
- [27] Koh AS and Mustafa G (1990): Free rocking of cylindrical structures. *Journal of engineering mechanics*, **116**(1), 35-54.
- [28] Koh AS and Hsiung CM (1991): Base isolation benefits of 3-D rocking and uplift. I: Theory. *Journal of engineering mechanics*, **117**(1), 1-18.
- [29] Koh AS and Hsiung CM (1991): Base isolation benefits of 3-D rocking and uplift. II: Numerical Example. *Journal of engineering mechanics*, **117**(1), 19-31.
- [30] Ambraseys, N., & Psycharis, I. N. (2011). Earthquake stability of columns and statues. *Journal of Earthquake Engineering*, **15**(5), 685-710.
- [31] Stefanou I, Psycharis I, & Georgopoulos IO (2011). Dynamic response of reinforced masonry columns in classical monuments. *Constr. Build. Mater.*, **25**(12), 4325-4337.
- [32] Krstevska, L., Mihailov, V., Boschi, E., & Rovelli, A. (1996). Experimental dynamic testing of prototype and model of the Antonina Column in Roma. *Proceedings of the 11th world conference on earthquake engineering*. Paper (No. 546).
- [33] Mouzakis, H. P., Psycharis, I. N., Papastamatiou, D. Y., Carydis, P. G., Papantonopoulos, C., & Zambas, C. (2002). Experimental investigation of the earthquake response of a model of a marble classical column. *Earthquake engineering & structural dynamics*, **31**(9), 1681-1698.
- [34] Drosos, V., & Anastasopoulos, I. (2014). Shaking table testing of multidrum columns and portals. *Earthquake Engineering & Structural Dynamics*, **43**(11), 1703-1723.
- [35] Makris N, Alexakis H, Kampas G, Strepelias I, Kolonas C and Bousias S (2015): *Seismic protection of bridges with rocking piers which recenter with gravity*, Report EEAM, 2015-01, University of Patras Department of Civil Engineering.
- [36] Stefanou, I., Vardoulakis, I., & Mavraganis, A. (2011). Dynamic motion of a conical frustum over a rough horizontal plane. *Int. J. Nonlinear Mech.*, **46**(1), 114-124.
- [37] Konstantinidis D and Makris N (2007): The dynamics of a rocking block in three dimensions, 8th Hell. Soc. Theor. Appl. Mech. Int. Congr. Mech. Patras, Greece 9/2015.
- [38] Zulli D, Contento A, and Di Egidio A (2102): 3D model of rigid block with a rectangular base subject to pulse-type excitation, *Int. J. Non. Linear. Mech.*, **47** (6), 679–687.
- [39] Chatzis, MN, and Smyth AW (2012). Modeling of the 3D rocking problem. *International Journal of Non-Linear Mechanics*, **47**(4) 85-98.

- [40] Chatzis, M. N., & Smyth, A. W. (2012). Three-dimensional dynamics of a rigid body with wheels on a moving base. *Journal of Engineering Mechanics*, **139**(4), 496-511.
- [41] Mathey, C., Feau, C., Politopoulos, I., Clair, D., Baillet, L., & Fogli, M. (2016). Behavior of rigid blocks with geometrical defects under seismic motion: an experimental and numerical study. *Earthquake Engineering & Structural Dynamics*.
- [42] Pappas, A., Sextos, A., da Porto, F. and Modena, C. (2016) *Bull Earthquake Eng.* doi:10.1007/s10518-016-0035-0
- [43] Vassiliou, M. F., Burger, S., Egger, M., Bachmann, J. A., Broccardo, M., & Stojadinovic, B. (2017). The three-dimensional behavior of inverted pendulum cylindrical structures during earthquakes. *Earthquake Engineering & Structural Dynamics*.
- [44] Vassiliou, M. F. (2018). Seismic response of a wobbling 3D frame. *Earthquake Engineering & Structural Dynamics*, **47**(5), 1212-1228.
- [45] Yim, S. C., & Lin, H. (1991). Nonlinear impact and chaotic response of slender rocking objects. *Journal of Engineering Mechanics*, **117**(9), 2079-2100.
- [46] Lin, H., & Yim, S. C. (1996). Deterministic and stochastic analyses of chaotic and overturning responses of a slender rocking object. *Nonlinear Dynamics*, **11**(1), 83-106.
- [47] Lin, H., & Yim, S. C. S. (1996). Nonlinear rocking motions. I: chaos under noisy periodic excitations. *Journal of engineering mechanics*, **122**(8), 719-727.
- [48] Lin, H., & Yim, S. C. S. (1996). Nonlinear rocking motions. II: Overturning under random excitations. *Journal of engineering mechanics*, **122**(8), 728-735.
- [49] Jeong, M., Suzuki, K., & Yim, S. C. (2003). Chaotic rocking behavior of freestanding objects with sliding motion. *Journal of sound and vibration*, **262**(5), 1091-1112.
- [50] Bachmann, J. A., Strand, M., Vassiliou, M. F., Broccardo, M., & Stojadinović, B. (2018). Is rocking motion predictable? *Earthquake Engineering & Structural Dynamics*, **47**(2), 535-552.
- [51] Bachmann JA, Strand M, Vassiliou MF, Broccardo M, Stojadinovic B, Probabilistic validation of the Housner rocking model, *COMPADYN 2017 6th ECCOMAS Thematic Conference on Computational Methods in Structural Dynamics and Earthquake Engineering Rhodes Island, Greece*, 15-17 June, 2017.
- [52] Rezaeian S, Der Kiureghian A. (2008) A stochastic ground motion model with separable temporal and spectral nonstationarities. *Earthq Eng Struct Dyn* **37**(13):1565-1584.
- [53] Broccardo M, Dabaghi M. (2017) A spectral-based stochastic ground motion model with a non-parametric time-modulating function. In: 12th International Conference on Structural Safety and Reliability; Vienna; 2017:1-10.
- [54] Broccardo M, Der Kiureghian A. (2014) Simulation of near-fault ground motions using frequency-domain discretization. In: Proceedings of the 10th NCEE; Anchorage, Alaska; 2014:1-11.
- [55] Chopra AK, Yim SCS. Simplified earthquake analysis of structures with foundation uplift. *J Struct Eng*. 1985;111(4):906-930.
- [56] Psycharis IN. Effect of base uplift on dynamic response of SDOF structures. *J Struct Eng*. 1991;117(3):733-754.
- [57] Oliveto G, Calì I, Greco A. Large displacement behaviour of a structural model with foundation uplift under impulsive and earthquake excitations. *Earthq Eng Struct Dynam*. 2003;32(3):369-393.
- [58] Ma QTM. The mechanics of rocking structures subjected to ground motion (Doctoral dissertation, ResearchSpace@ Auckland) 2010.
- [59] Acikgoz S, DeJong MJ. The interaction of elasticity and rocking in flexible structures allowed to uplift. *Earthq Eng Struct Dynam*. 2012;41(15):2177-2194.
- [60] Vassiliou, M. F., Mackie, K. R., & Stojadinović, B. (2014). Dynamic response analysis of solitary flexible rocking bodies: modeling and behavior under pulse-like ground excitation. *Earthquake engineering & structural dynamics*, **43**(10), 1463-1481.
- [61] Vassiliou, M. F., Truniger, R., & Stojadinović, B. (2015). An analytical model of a deformable cantilever structure rocking on a rigid surface: development and verification. *Earthquake engineering & structural dynamics*, **44**(15), 2775-2794.

- [62] Andrej N Kolmogorov (1933) Sulla determinazione empirica di una legge di distribuzione. na,.
- [63] N Smirnov. (1939) Sur les _ecarts de la courbe de distribution empirique. *Matematicheskii Sbornik*, 48(1):3-26.
- [64] Zhong M.C. and Christopoulos C. (2020), Finite element analysis of the seismic response of a rocking podium structure, 2020 PEER Annual Meeting, Berkeley, USA, 16-17.01.2020 (poster presentation).
- [65] Malomo D, Mehrotra A, DeJong M.J., Discrete Element Modeling of a rocking podium structure subjected to biaxial shake-table test, 2020 PEER Annual Meeting, Berkeley, USA, 16-17.01.2020 (poster presentation).

6.3 Project #12 – REBOND – REsponse of as-Built and strengthened three-leaf masONry walls by Dynamic tests

Authors

F. Di Michele⁽¹⁾, E. Spacone⁽¹⁾, G. Camata⁽¹⁾, G. Brando⁽¹⁾, A.Sextos⁽²⁾, A. Crew⁽²⁾, G. Mylonakis^(2,6,7), M. Dietz⁽²⁾, L. Dihoru⁽²⁾, H. Varum⁽³⁾, G. Manolis⁽⁴⁾, P. Casadei⁽⁵⁾

⁽¹⁾ *Department of Engineering and Geology, University G. d’Annunzio of Chieti-Pescara, Italy*

⁽²⁾ *Department of Civil Engineering, University of Bristol, Bristol, United Kingdom*

⁽³⁾ *Faculty of Engineering, University of Porto, Portugal*

⁽⁴⁾ *Department of Civil Engineering, Aristotle University of Thessaloniki, Greece*

⁽⁵⁾ *Kerakoll Group, Sassuolo, Italy*

⁽⁶⁾ *Department of Civil Engineering, Khalifa University, U.A.E.*

⁽⁷⁾ *University of California at Los Angeles (UCLA), U.S.A.*

6.3.1 Introduction

Three-leaf masonry walls are found throughout Mediterranean seismic-prone regions, especially for the area of L’Aquila, Italy. They are made of two external relatively slender stone leaves, typically unconnected through the wall thickness, and an inner core made of loose aggregates kept together by poor quality lime mortar. Past earthquakes, and more specifically the L’Aquila earthquake of April 6 2009, have shown the intrinsic vulnerability of this masonry typology, widespread in historical centres. The problem is more evident in the presence of repeated cyclical actions over time, with unbundling of the entire wall before the mechanical resistance is achieved. Although delamination appears to be the most significant source of fragility, three-leaf walls show weak in-plane behaviour as well, depending on the weakest component material (mortar) as showed by Silva B. et al (2014). The in-plane behaviour becomes fundamental in walls strengthened by grout injections and by introducing connections between the outer leaves, as evidenced by Vintzileou et al (1995). Furthermore, the response of both as built and strengthened walls need to be fully investigated in order to understand to which extent their strength can be increased. The presence of a strong Vertical Ground Motion (VGM) could be

relevant in Near Field (NF) earthquakes, which repeatedly decompress and compress the masonry wall, reducing the shear strength of the pier, as highlighted by A. Borri in “Costruzioni storiche e qualità muraria: problematiche e possibili interventi di consolidamento”. Studies of the past on the evaluation of the masonry quality by A. Borri et al. (2010), S. Brusaporci et al. (2007), and L. Fanale et al. (2017), have shown the presence of three macrogroups of external leaf wall's types placed in the area of L'Aquila: a) stone masonry of small dimensions, mixed with natural or split pebbles and stones; b) stone masonry with lime mortar and sand mixed with stone flakes; c) block masonry made of squared stone. Figure 265 shows a typical aquilano apparatus for external leaf, using regular limestone (similar to the Poggio Picenze stone) and weak hydraulic mortar. The Filling Material (FM) is used to fill the wall between the two external leaves and is made of mortar and pebbles/waste materials. The exact composition of FM is not clear in the literature since it's always prepared randomly. The VGM could be significant in this kind of construction as FM tends to thrust with the presence of VGM.

The purpose of this project is to investigate the effects of earthquakes on three-leaf masonry walls with dynamic tests. More specifically, tests were thought to investigate: the influence of VGM on the behaviour of the as-built rectangular walls; the in-plane strength of rectangular and T-shaped as-built walls; the effectiveness of strengthening techniques.

The experimental campaign is part of Seismology and Earthquake Engineering Research Alliance (SERA) project. The project proposal is under the name REBOND (REsponse of as-Built and strengthened three-leaf masONry walls by Dynamic test).

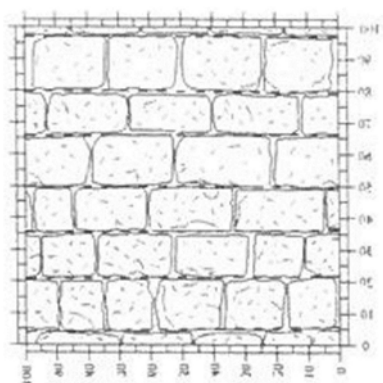


Figure 265: Aquilano apparatus for external leaves, by S. Brusaporci (2007)

6.3.2 Wall design

The wall chosen is set up considering a real case of a hypothetical pier wall on the last floor of a masonry building. The choice of the last floor wall is due to two main reasons. First of all, the pier height is lower than usual, and this leads to a greater probability of shear failure, avoiding a compression/bending failure. Also, the lower height of the tested specimens avoids logistic and safety problems in the laboratory. Secondly, a specimen from the top floor has a lower axial load N since it carried the weight of the roof only. A lower axial load is useful for two reasons: first, the total weight of the specimen plus applied load must be lower than the shake table capacity of 15 tonnes; second, a lower axial load allows to get a stronger influence of the vertical ground motion component as reported in Di Michele et al. (2019). The height of the studied piers is 180 cm. The pier is imagined to be fixed at both ends (top and bottom). The tested specimen (fixed at the base – free at the top) represents half height of the pier or around $h \approx 80/90$ cm. Another important parameter is the aspect ratio between height and length of the specimen to induce shear failure rather than a compression-bending failure. For this project a h/l ratio of 0.4 (squat wall) is assumed. To sum up the specimen geometry, $h=80$ cm, $l=200$ cm and $t=45$ cm, where h is the wall height, l its length and t its thickness. The following expressions

from the recent Italian building code are used to evaluate the pier shear strength: Shear failure due to diagonal cracking is found from the following formula (Turnšek and Čačovič, 1971):

$$V_{Rd} = l \cdot t \cdot \frac{f_{tb}}{b} \sqrt{1 + \frac{\sigma_0}{f_{tb}}} \quad (1)$$

where $\sigma_0 = N/(l \cdot t)$ is the average normal stress (with N equal to axial force applied at the wall centre, assumed positive in compression); f_{tb} is the masonry tensile strength for diagonal cracking and b is a corrective coefficient that depends on the stress distribution on the wall and on its slenderness ($1 \leq b = h/l \leq 1.5$).

Shear failure by sliding is computed from the following formula:

$$V_t = l' \cdot t \cdot (\tau_0 + 0.4\sigma_0) \quad (2)$$

where l' is the wall compression length, τ_0 is the shear strength (in terms of stress) of the masonry wall. Failure due to compression-bending is computed using the following formulation:

$$V_P = \frac{M_u}{h} \quad (3)$$

$$M_u = (l^2 t \sigma_0 / 2) (1 - \sigma_0 / (0.85 f_d)) \quad (4)$$

where f_d is the masonry compressive strength. If one approximates the three-leaf wall as a homogeneous masonry wall, it is possible to estimate the mechanical characteristics of the entire wall, using table C8A.2.1 in “Circolare n. 617” of 02/02/2009. The table shows the main mechanical features of different masonry wall types. For three-leaf masonry walls (“Muratura a conci sbozzati, con paramento di limitato spessore e nucleo interno”) the average value for compression and shear strength are $f_d = 2500 \text{ kN/m}^2$ and $\tau_0 = 43 \text{ kN/m}^2$, respectively. With the above wall geometric and mechanical properties, it is possible to estimate the failure mode expected during the shaking table tests. Figure 266 shows the graph of equations (1), (2) and (3) for different axial loads N . Considering an additional mass equal to 6 tonnes, the corresponding axial load is 66 kN. In this case, the first failure is predicted to be a shear failure with a diagonal cracking.

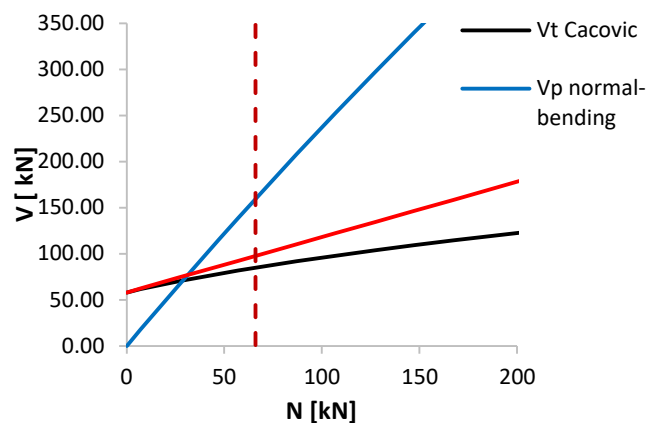


Figure 266: Normal load N vs V failure diagrams for 3 failure modes: V_t Cacovic, V_p compression-bending and V_t sliding shear

6.3.3 Seismic input

The selection of the seismic input is a key point of the tests. One of the main purposes of this project is to investigate the effects of the VGM. It is thus important to find the right earthquake. The database of 106 unscaled natural records with two horizontal and one vertical component studied by Di Michele et

al. (2019) is considered. Records are searched with large energy in the vertical direction: this is found when the seismic event is characterised by high moment magnitudes ($M_w \geq 6.5$), dip slip fault rupture and a low source-to-site distance R_{jb} (Joyner and Boore distance – 1982). Several Near Fault earthquakes are relevant in VGM effects. More specifically, one of them (Gazli 17/05/1976) was found to generate a significant increase in axial force N in a pier when the vertical component is considered in the analysis (Di Michele et al. 2019). The Gazli 17/05/1976 earthquake has $M_w=6.8$, $R_{jb}=3.92$ km, ground type C and was recorded at “Karakyr” station. A dip-slip fault failure induced a strong vertical directivity, as reflected in the amplitudes of teleseismic P and pP phases (Primary waves) as described by Hartzell (1980). Figure 267a shows the time history of the Gazli record for both components: Horizontal (labelled H) and Vertical (labelled Z). The H ground motion was obtained at each time step t as geometric mean of the two horizontal components, as recommended by Beyer and Bommer (2006). From the graph, the VGM acceleration is very intense and much larger than the horizontal acceleration. The PGA-Z is much larger than the PGA-H (PGA-H = 0.70g at $t=8.4$ s, PGA-Z=1.70g at $t=8.5$ s). Figure 267b confirms the importance of VGM. The V-spectrum is larger than the H-spectrum, particularly for high frequencies-. The peaks of the V-spectrum are around a period $T=0.05$ s and the ratio V/H is 3 ($S_a, H(T=0.05s)=2g$, $S_a, Z(T=0.05s)=6g$). This result appears to be relevant for masonry structures because they are vertically stiff (as observed in Di Michele et al., 2019) thus vertical resonance phenomena may occur as the high vertical frequencies of masonry walls may overlap with the high frequencies of the vertical seismic input.

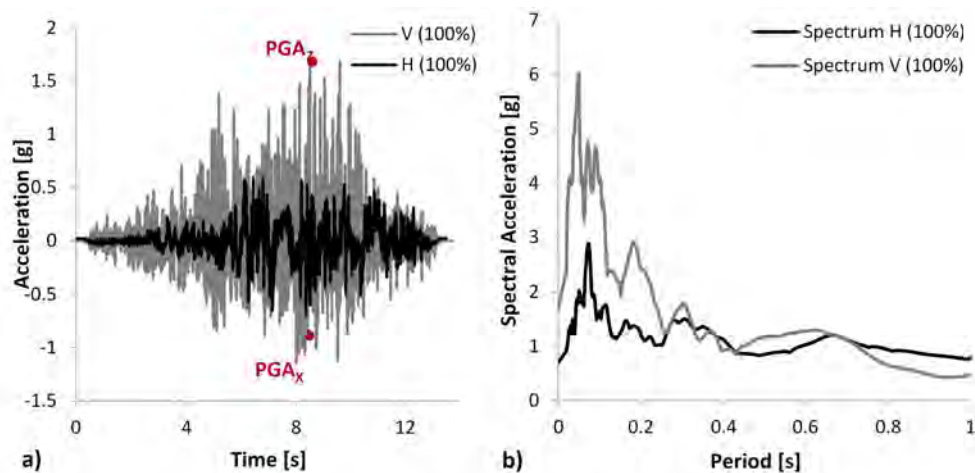


Figure 267: a) Time history for Gazli earthquake (17/05/1976) at 100% of seismic event (real event) for both Horizontal (H) and Vertical (V) directions; b) Corresponding Elastic pseudo-acceleration Spectrum for the two signals

	10%	25%	50%	75%	100%	120%	140%
PGA _H [g]	0.07	0.18	0.35	0.53	0.70	0.84	0.98
PGA _Z [g]	0.17	0.42	0.85	1.27	1.70	2.04	2.38

Table 34: Values of PGA in horizontal ground motion (PGA_X) and vertical ground motion (PGA_Z) for different intensity of the seismic event (10%, 25%, 50%, 75%, 100%, 120% and 140% of the natural earthquake of Gazli)

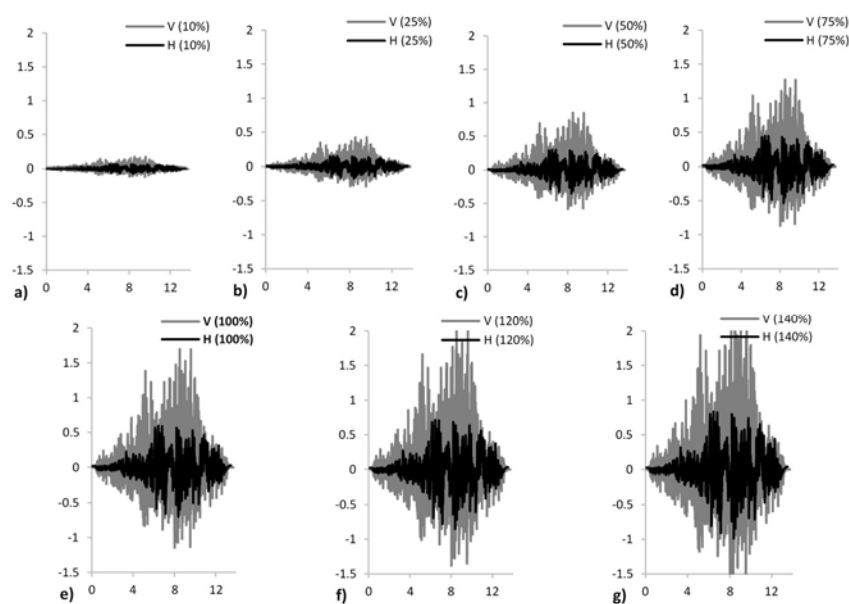


Figure 268: Time history for Gazli earthquake (17/05/1976) x axis “time” in [s] and y axis “acceleration” in [g] for both horizontal H and vertical V directions at different intensity of the seismic event: a) 10% of record; b) 25% of record; c) 50% of record; d) 75% of record; e) 100% of record; f) 120% of record; g) 140% of record

In the experimental campaign the specimens were tested scaling the above ground motion. 100% indicates the recorded ground motion. A sequence of identical but differently scaled ground motions were applied, starting at 10% and up to 140% (unless failure was recorded at lower scaling percentages). Figure 268 shows the different level of Gazli earthquake from a)10% to b)140% of the real seismic event e)100% that it will be used for the experimental test.

Table 34 summarizes the H and V PGAs for the different scaled input GMs.

Dynamic tests

The experimental campaign on three-leaf masonry walls has three main purposes:

- the influence of the VGM on the behaviour of the as-built rectangular walls;
- the in-plane strength of rectangular and T-shaped as-built walls;
- the effectiveness of strengthening techniques.

Five specimens were built. Figure 269 shows the in-plane layout in terms of geometry of the two wall types (rectangular and T-shaped). The rectangular walls consist of a single longitudinal three-leaf masonry wall with 2000mm x 455mm in-plane dimensions. The T-walls consist of a rectangular wall with the addition of a cross wall at one end (the two parts are not well connected). Table 35 reports the characteristics of the five specimens involved in the SERA-REBOND project.

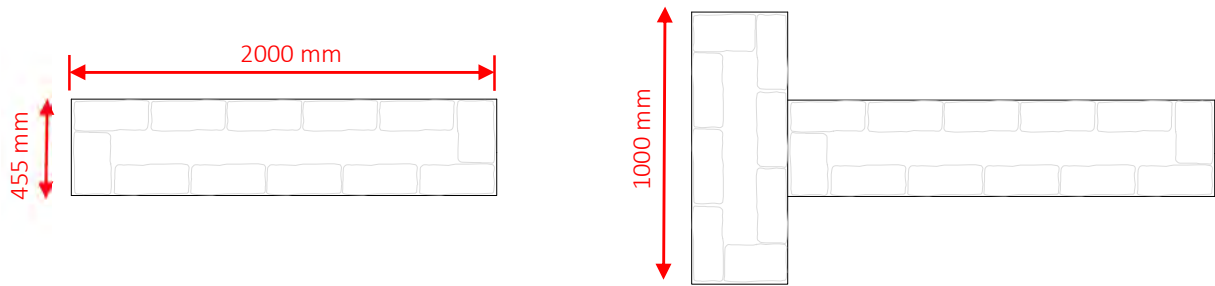


Figure 269: Plan view of the two wall-types: a) Rectangular; b) T-shape

The seismic input is discussed in the previous section. Specimen A was tested with H-component only, while all other specimens (B, C, D and E) were tested applying both H and V components. The comparison between the response of specimens A and B is important to verify the effect of VGM for rectangular walls. White noise was planned between two input GMs to record the mechanical properties of the wall and to check the damage increase. The last two specimens (D and E) were reinforced using mortar injections combined with connectors on the entire wall thickness for rectangular wall D and T-wall E and rebar connectors between the two orthogonal walls for T-wall E.

Specimen Name	Wall type	Seismic input	Reinforcement
A	Rectangular	H	No
B	Rectangular	H+V	No
C	T-wall	H+V	No
D	Rectangular	H+V	Yes
E	T-wall	H+V	Yes

Table 35: Configurations of the five tested specimens in terms of wall type (rectangular or T-wall), seismic input (horizontal seismic input H only or horizontal and vertical seismic input H+V) and reinforcement

Table 36 shows the detailed sequence of dynamic input and the GM level (percentage of recorded GM) at which failure was reported or test was interrupted to safeguard the shake table integrity. Specimens were tested two times at 100% GM intensity to give more importance at the real natural event. When possible (i.e. in cases where the shake table integrity was not an issue) a white noise test was run after failure.

Specimen A		Specimen B	
Test Name	Intensity seismic event	Test Name	Intensity seismic event
A1	White Noise	B1	White Noise
A2	White Noise	B2	10 %
A3	10 %	B3	25 %
A4	25 %	B4	50 %
A5	50 %	B5	White Noise
A6	75 %	B6	75 %
A7	1st input at 100 %	B7	White Noise
A8	2nd input at 100 %	B8	1st input at 100 %
A9	140 % - FAILURE	B9	White Noise
-	-	B10	2nd input at 100 % - FAILURE
-	-	B11	White Noise

Specimen C	
Test Name	Intensity seismic event
C1	White Noise
C2	10 %
C3	25 %
C4	50 %
C5	White Noise
C6	75 %
C7	White Noise
C8	1st input at 100 %
C9	White Noise
C10	2st input at 100 %
C11	White Noise
C12	120 % - FAILURE

Specimen D		Specimen E	
Test Name	Intensity seismic event	Test Name	Intensity seismic event
D1	White Noise	E1	White Noise
D2	10 %	E2	10 %
D3	25 %	E3	25 %
D4	50 %	E4	50 %
D5	White Noise	E5	White Noise
D6	75 %	E6	75 %
D7	White Noise	E7	White Noise
D8	1st input at 100 %	E8	1st input at 100 %
D9	White Noise	E9	White Noise
D10	2nd input at 100 %	E10	2nd input at 100 %
D11	White Noise	E11	White Noise
D12	120% - FAILURE	E12	120%
		E13	White Noise
		E14	140% - FAILURE

Table 36: Detail test runs for all five tests

6.3.4 Test configuration and instrumentation layout

Two specimens (Rectangular walls A and B) have the same geometry and were not reinforced. Specimen C (T wall) has a different geometry and was not reinforced. Specimens A and B were identical (except for expected construction deformities) were subjected to different seismic inputs: specimen A was tested in the H direction only while specimen B was tested in directions H and V. Specimen C had the same seismic input of specimen B (H+V), thus the comparison between the responses of specimens B and C should shed light on the wall behaviour differences due to the different geometric configurations. Specimen D and E are like specimens B and C, respectively, in terms of geometry and seismic input but they are reinforced. The comparison between the responses of specimens B-D and C-E should indicate the how reinforcement affects the response.

The whole specimen is made up of different parts: base (Figure 270); wall (Figure 272); timber beams; support system (Figure 274); steel frame top and additional mass (Figure 275).

Base

The base was designed to support the wall and the additional top mass during the dynamic tests. The shear and bending capacity were computed prior to testing to avoid specimen failure and collapse during construction, particularly during lifting and positioning on the shake table. Special care was paid during the lifting process using high safety factors in the verification. The location of the lifting point was chosen to coincide with the centre of mass of the whole specimen. As shown in Figure 270 the base consisted of an edge steel frame with 254x146x46 UB that was filled with a C35/45 concrete. A rebar mesh (A252) was positioned on the bottom and on the top to reinforce the concrete slab. The maximum size of the base was 2730x2670 mm in order to satisfy two needs: the limitation of the ES (3000x3000 mm) and the space needed to build the wall. The specific shape was thought to minimize the quantity of concrete and thus the base weight. Figure 271 shows the working phases of the base construction. A total of three bases were built in order to work in parallel and test multiple specimens simultaneously.

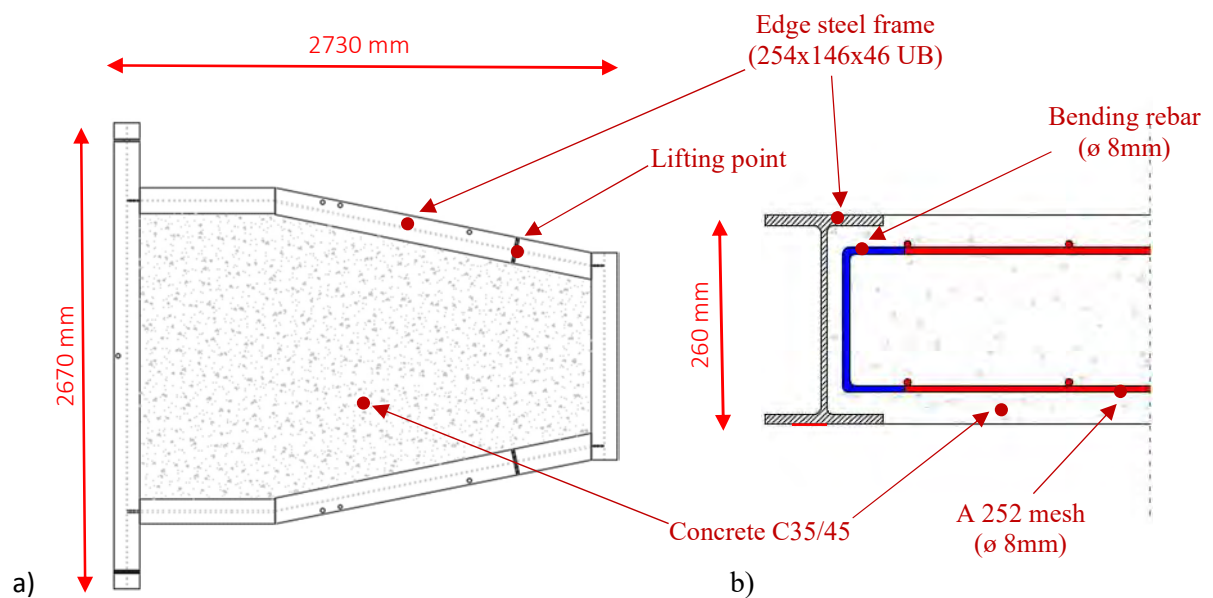


Figure 270: Base design: a) plan view and b) section close to the base edge



Figure 271: Working phases of base construction: a) addition of rebar mesh and b) concrete casting

Wall

The rectangular wall sizes (shown in Figure 272) were designed based on the considerations of §6.3.2. The stone blocks are approximately 350x140x140 mm for the blocks set parallel to the longitudinal side and 300x140x190 mm for the stones that are used along the two edges to connect the two external leaves. The mortar between the stones has a vertical thickness of about 15 mm. The FM is included between the two external leaves, made of stones and mortar, without transversal connections between them, creating a three leaves masonry wall (140 mm first external leave made of stone and mortar; 175 mm middle leave made of FM; 140 mm third external leave made of stone and mortar). The sizes were chosen based on the average values found in the literature for the L'Aquila stones, as explain in §6.3.1. Transversal C30 timber beams were placed through the wall top I with wheelbase around 800 mm to simulate a roof that rests on the wall in order to distribute the weight pointwise as in real situation. The timber beam was 1000 mm long in order to have enough space to fit the top frame. The cross section is 100x140 mm to simulate a realistic size and to satisfy shear verifications. Figure 273 shows the working phases of the wall construction. Specimen C (T-wall) had the same longitudinal wall of the rectangular walls, the difference was a transversal wall added on one side of the specimen (Figure 269b).

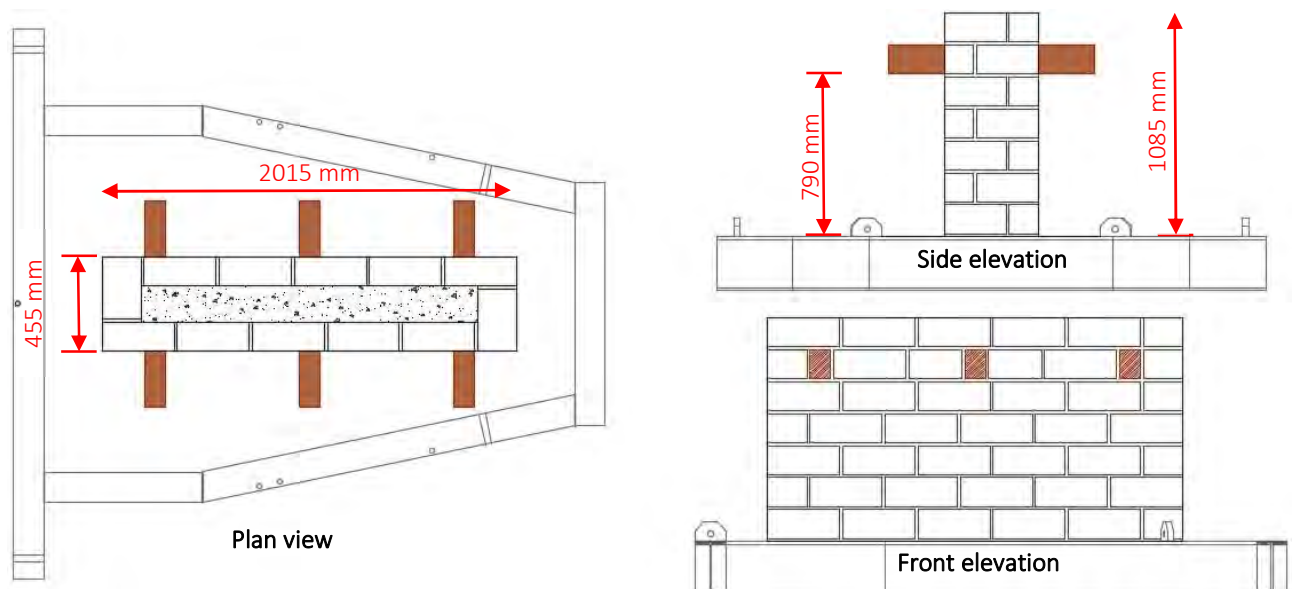


Figure 272: Rectangular wall design: plan view, side elevation and front elevation

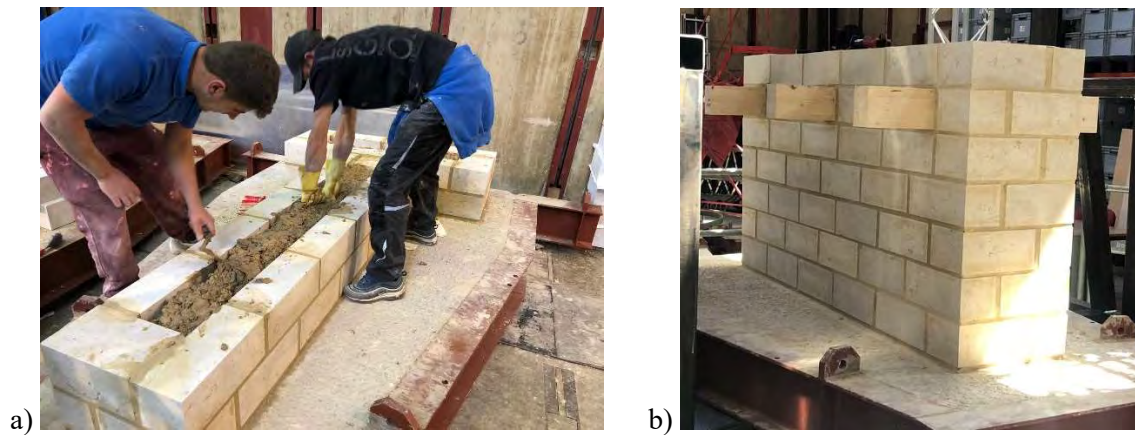


Figure 273: Working phases of wall construction: a) Addition of Filling Material between the outer leaves and b) completed rectangular wall

Support system

A support system (Figure 274) was designed and added to avoid wall rocking and collapse of the top steel frame on the shaking table. The support system did not directly touch the stone specimen and only provides a safety support. The frame was made of steel in celsius 100x100 and was assembled as a single rigid block.

Figure 275a shows the steel frame that was placed on top of the wall with a system of threaded rods that connected the top steel frame to two transversal beams with cross section 140x200 mm and length 1900 mm. The steel frame then fixed to three transversal timber beams crossing the wall (Figure 272). The steel frame top is made of four longitudinal UB 254x146x43 connected to two UPE 270 in the orthogonal direction. The plan sizes are 2640x1900 mm which account for the size of the wall and the position of the support system. Figure 275b shows a single additional steel mass with sizes 1000x1000 mm, 130 mm height and 1t weight. A total of six masses in two stacks was placed on top of the steel frame with bolts for a total top mass of around 6.5 tonnes (0.5 tonnes for the steel frame and 6 tonnes for the six additional masses), as defined in §6.1.2.

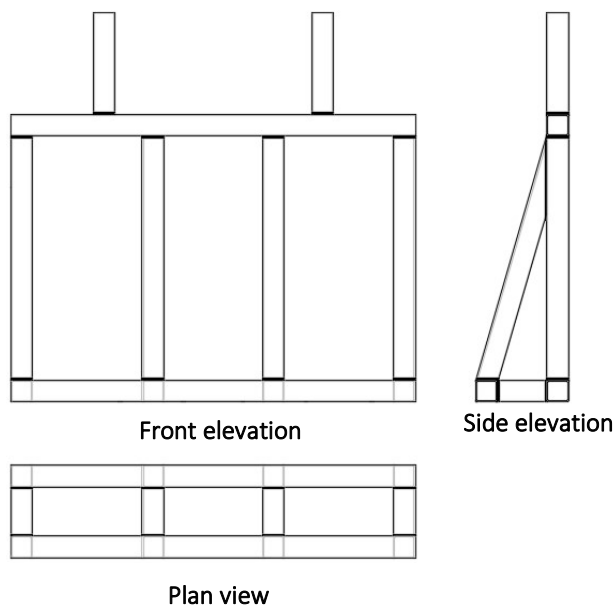


Figure 274: Support system design with celsius SHS 100x100 steel frame

Steel frame top and additional mass

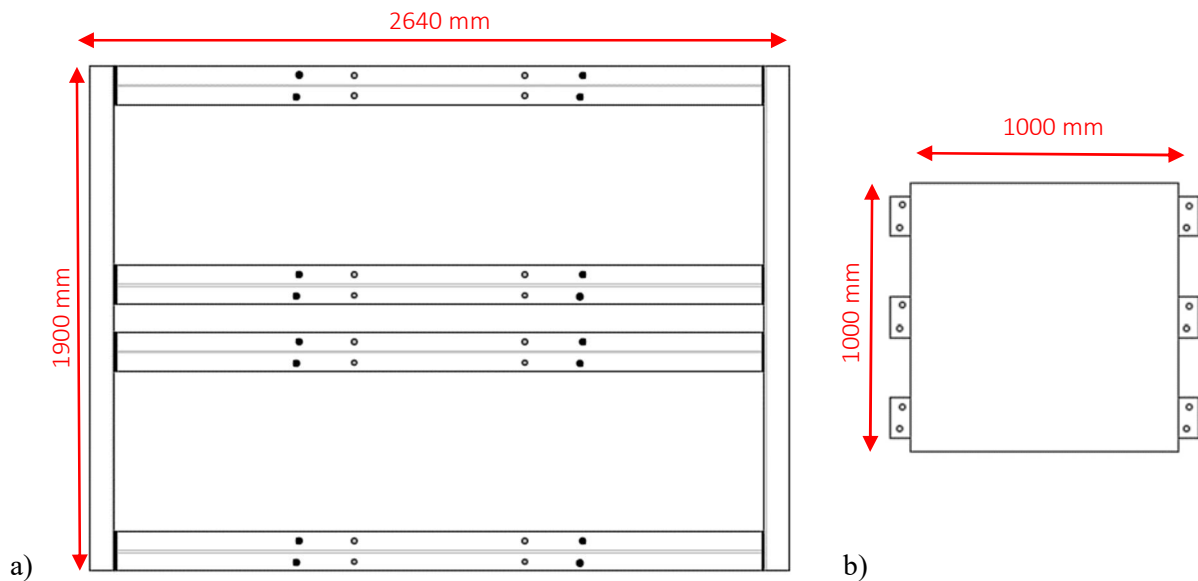


Figure 275: a) Top steel frame design with UPE 270 along transverse side and UB 254x146x43 along longitudinal side b) single 1000x1000 mm additional mass (130 mm height and 1-ton weight)

The total weight of specimens A, B and D was 13.5 tonnes each: the base weighted 3 tonnes, the wall 3.3 tonnes, the support system 0.7 tonnes, the additional mass 6.5 tonnes. The total weight of specimens C and E was 15.1 tonnes each. the base weighted 3 tonnes, the wall 4.9 tonnes, the support system 0.7 tonnes, the additional mass 6.5 tonnes.

Figure 276 and Figure 277 show the assembly process for specimens A or B. The first step was to ensure safety of the base plus wall system (1) before lifting, the second step consisted of setting the base plus wall system on the ES and to connect to the support system (2). The last step involved placing the block (3) that included the longitudinal timber beam, the top steel frame and the six additional masses. The same process was repeated for specimen C.

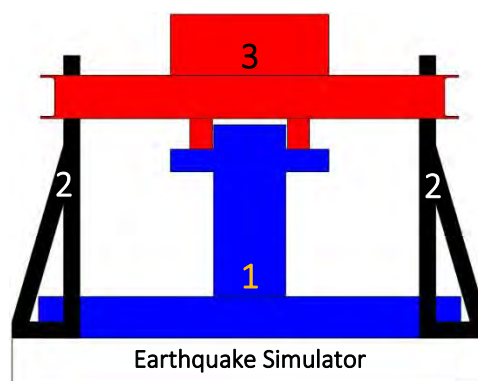


Figure 276: Specimen assembly steps: 1. Position base + wall; 2. Add support system; 3 Add additional mass

Control systems were used to check the displacements and accelerations during the dynamic tests. Displacements were recorded with infrared cameras (Figure 278b) at points marked on the wall with special reflective markers (Figure 278a). Accelerations were recorded with a total of nine

accelerometers (Figure 278d): three on the ES (one for each X, Y and Z direction) and six on the steel frame top. The six accelerometers on the frame were placed at three different points. Figure 278 shows the three locations: three accelerometers (each in one of the three X, Y and Z directions) were fixed at point 1; two accelerometers (one in the X the other in the Z direction) were fixed at point 2; one accelerometer (in the Z direction) was fixed at point 3.

Figure 279 shows the final set-up for specimens A or B and Figure 280 shows the final set-up for specimen C.

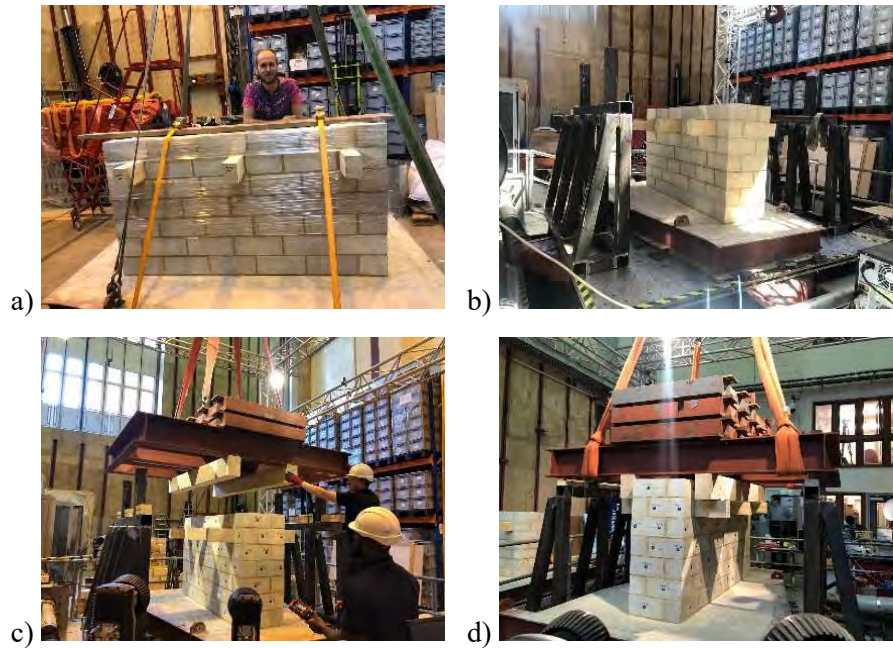


Figure 277: Assembly working phases: a) Securing the wall before lifting; b) placement of the wall + base + support system on the ES; c) lifting and placement of additional mass and frame top; d) final specimen set-up



Figure 278: Control system: a) displacement markers on the stone faces to measure the displacement of each point with b) five infrared cameras; c) accelerometers on the steel frame top in three different positions; d) accelerometer detail

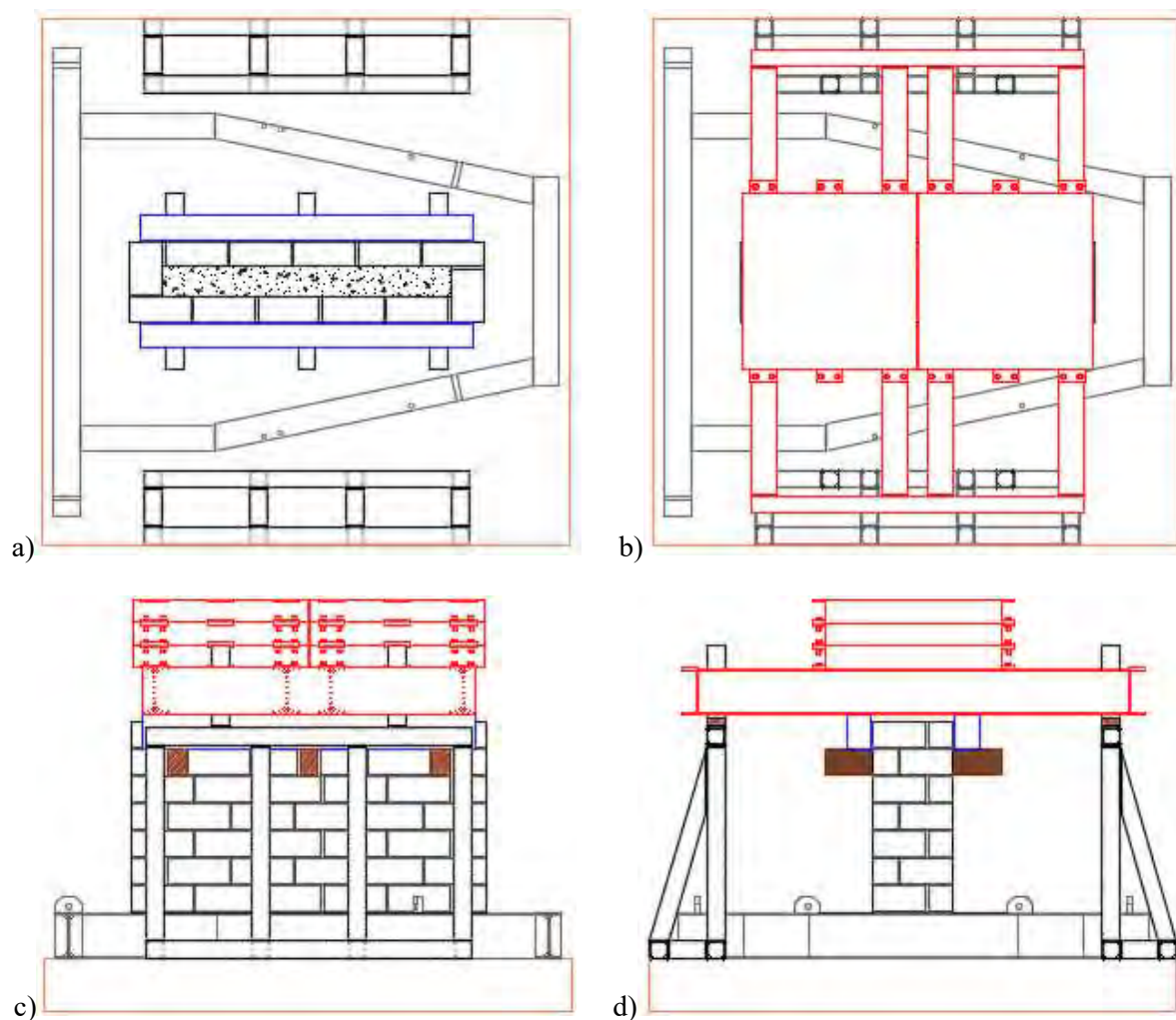
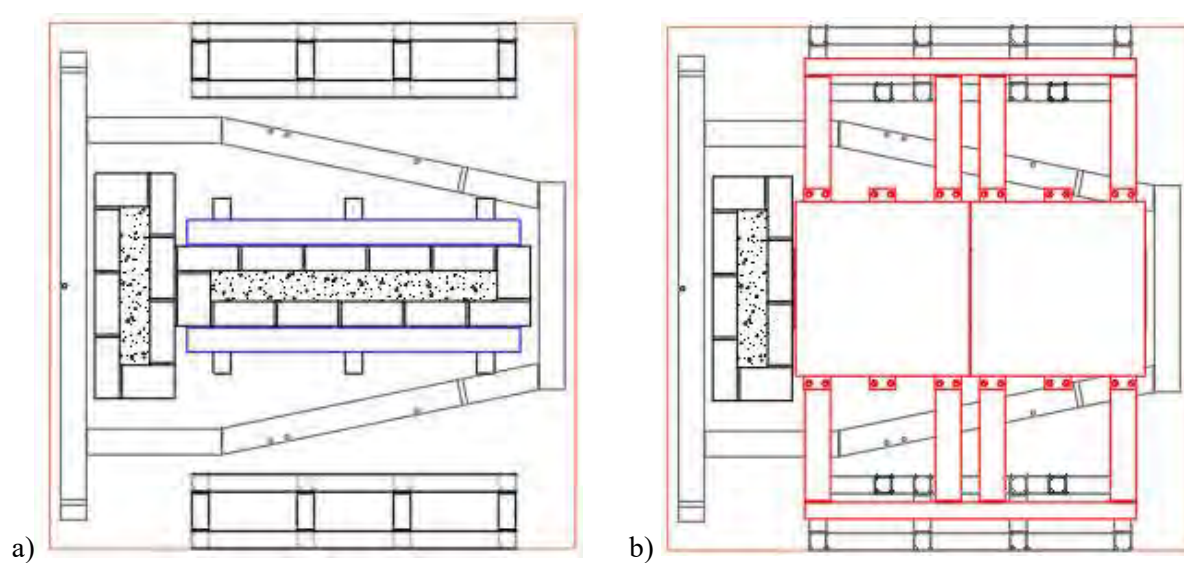


Figure 279: Rectangular wall final test set-up: a) plan view without top steel frame; b) plan view with top steel frame and additional masses; c) front elevation; d) side elevation



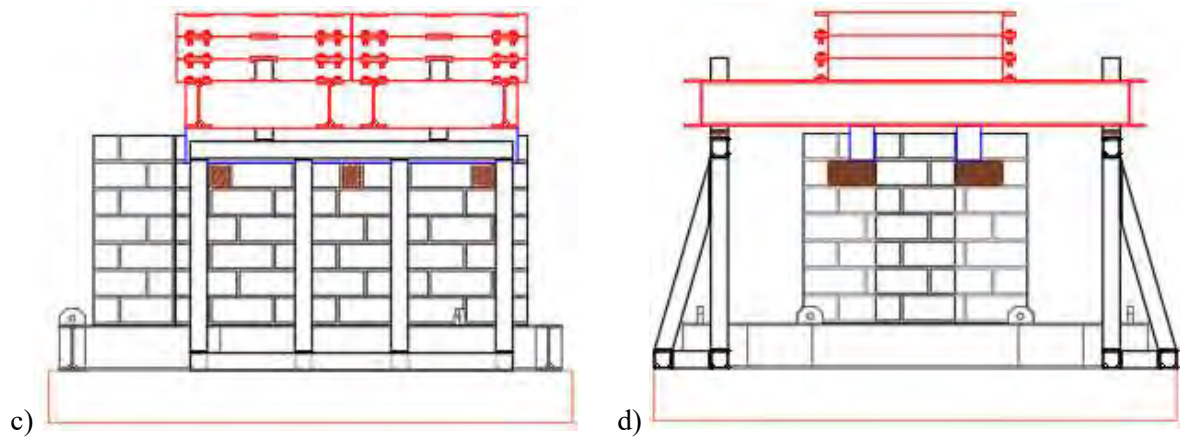


Figure 280: T-wall final set-up: a) plan view without top steel frame; b) plan view with top steel frame and additional masses; c) front elevation; d) side elevation



Figure 281: Final set-up pictures

Reinforcement by KERAKOLL group

Reinforcement of the masonry walls was applied to specimens D and E. All materials were provided by the Kerakoll group (Italy). More specifically, connectors were added made on the entire thickness of the longitudinal wall (GeoSteel) with mortar injections for specimens D and E. Diagonal steel connectors with mortar injections were added between the two orthogonal walls in specimen E (T-wall). Figure 282 shows the reinforcements for the T-wall, where both reinforcements were added. Figure 283 shows the reinforcement preparation steps.

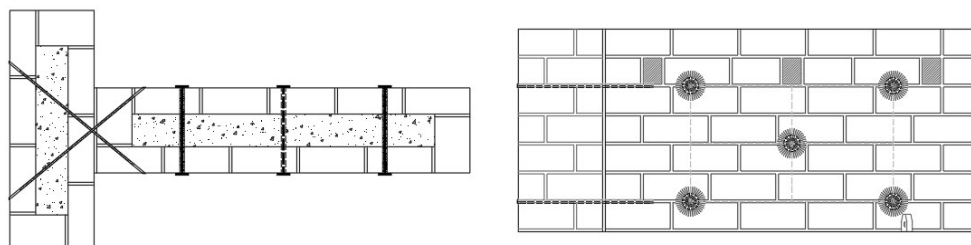


Figure 282: T-wall reinforcement: plan view (left) and front elevation (right)



Figure 283: Reinforcement preparation: a) GeoSteel insertion after drilling of the holes; b) closing of the holes; c) mortar injections

6.3.5 Preliminary results

Preliminary results can be drafted by examining the failure modes and the level of GM that induced failure. Figure 284 shows the diagonal failure for specimen A (H component only) at 140% of the recorded GM. Failure started under the middle timber beam and progressed diagonally to the base of the specimen. This failure mode was observed in all specimens, though it took place at different seismic intensities. A comparison among all specimens is made for the 100% GM. As indicated in Figure 285, specimen B shows the most significant diagonal crack.

The seismic intensity at which failure took place is reported in Table 37 for each specimen.

Specimen	Test name	Seismic intensity
A	A9	140%
B	A10	100%
C	A12	120%
D	A12	120%
E	A14	140%

Table 37: Failure of the specimens at different seismic intensity

The results show that the VGM has a significant effect on the failure of the wall. More specifically, specimen A and B have the same geometry but different seismic input. Specimen A was tested with horizontal component only and specimen B with both the horizontal and vertical components. The result shows that specimen B has a strength reduction with respect to specimen A: specimen A fails for a seismic intensity of 140% while specimen B fails for a seismic intensity of 100%. The comparison between specimens B and D (same seismic input but different geometry, specimen B rectangular and specimen C T-wall) shows the higher T-wall strength as the orthogonal wall somehow confines the longitudinal wall and fails before the longitudinal wall. Reinforcement resulted in an enhancement of the wall response: specimens B-D and C-E show an increase in seismic capacity of 20% thanks to the presence of the connectors.



Figure 284: Diagonal failure of specimen A at GM level A9 (140% - only H)

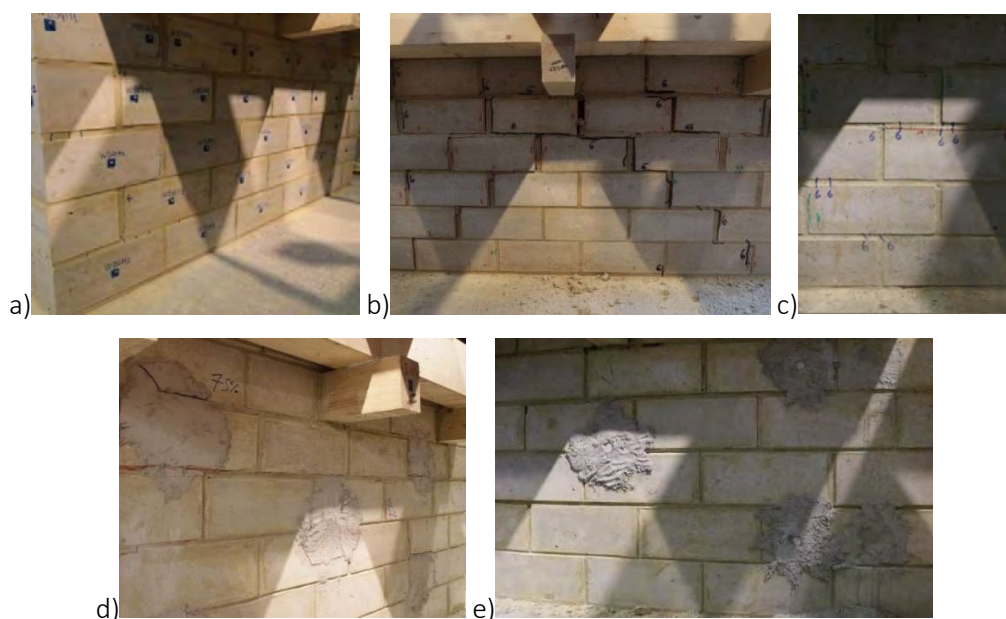


Figure 285: Failure propagation at 100% GM for: a) A8; b) B10; c) C10; d) D10; c) E10

6.3.6 Conclusions and outlook

In this project, experimental shaking table tests were carried out on three-leaf masonry walls representative of central Italy traditional masonry wall construction. The tests were run on the EQUALS Laboratory shake table of the University of Bristol. The purpose of this project was to inquire the effects of the ground motion characteristics on the behaviour of three-leaf masonry walls through shake-table dynamic tests. More specifically, the tests were designed to investigate: the influence of the VGM on the behaviour of the as-built rectangular walls; the in-plane strength of rectangular and T-shaped as-built walls; the effectiveness of strengthening/reinforcing techniques. The specimens' design and test set-up were carefully planned according to the following steps: wall design, seismic input selection, top mass, retaining steel frame design. The VGM had an important role for the failure of the specimens that showed a lower strength when the vertical component was included. The T-wall increased the strength of the longitudinal wall by confining it and dissipating some of the energy input into the specimens. The reinforced specimens showed an increase in carrying capacity by reaching a higher seismic intensity level. Numerical modelling of the tested specimens is intended to further support and confirm these preliminary results. Numerical analyses will extend the study to a whole building to investigate the effects of local and global reinforcement on the overall building behaviour.

6.3.7 References

- Borri A (2010) - Costruzioni storiche e qualità muraria: problematiche e possibili interventi di consolidamento – Sicurezza e conservazione, convegno nazionale, “Sicurezza e conservazione nel Recupero dei Beni Culturali Colpiti da Sisma”, Venezia (in Italian).
- Fanale L, Galeota D, Pietrucci A (2017) – Application of non-destructive evaluation test method for Italian masonry: Masonry Quality Index (MQI) method – 13th Canadian Masonry Symposium, Halifax, Canada.
- Brusaporci S (2007) Le murature nell’architettura del versante meridionale del Gran Sasso (secc. XI-XIV), Gangemi editore.
- <http://www.bristol.ac.uk/engineering/facilities/earthquake/>
- Lourenço P – Computational Strategy for Masonry Structures, PhD Dissertation, Delft University of Technology, 1996.
- Di Michele F, Cantagallo C, Spacone E (2019) – Effects of the vertical seismic component on seismic performance of an unreinforced masonry structures – Bulletin of Earthquake Engineering 18, 1635-1656 <https://doi.org/10.1007/s10518-019-00765-3>.
- Turnšek V, Čačovič F (1971) Some experimental results on the strength of brick masonry walls. In Proc. of the 2nd International Brick Masonry Conference, 149-156.
- Boore DM, Joyner WB, (1982) The empirical prediction of ground motion. Bulletin of the Seismological Society of America, 72(6): S43-S60.
- PEER Ground Motion Database (2015) Pacific Earthquake Engineering Research Center, University of California, California, USA, <http://peer.berkeley.edu/smcat/>
- Hartzell S (1980) – Faulting process of the May 17, 1976 Gazli, USSR earthquake – Bulletin of the Seismological Society of America, 80(5), pp. 1715-1736.
- Beyer K, Bommer JJ (2006) Relationships between median values and between aleatory variabilities for different definitions of the horizontal component of motion. Bulletin of the Seismological Society of America, 96(4A), pp.1512-1522.
- Seismosoft (2016) SeismoSignal - A computer program for post-processing of groups of earthquake records. Available from <http://www.seismosoft.com>
- Silva B, Della Benetta M, Da Porto F, Modena C (2014) – Experimental assessment of in-plane behaviour of three-leaf stone masonry walls – Constructions and Building Materials, pp. 149-161, volume 53.
- Vintzileou E, Tassios T P (1995) – Three-leaf Stone Masonry Strengthened by injecting Cement Grouts – Journal of Structural Engineering, ASCE Library, Vol. 121.

6.4 Project #21 – NSFUSE - Ductile steel fuses for the protection of critical non-structural components

Authors

A. Kazantzi⁽¹⁾, A. Elkady⁽²⁾, M. Dietz⁽³⁾, L. DiHoru⁽³⁾, R. De Risi⁽³⁾, D. Vamvatsikos⁽¹⁾, D. Lignos⁽⁴⁾, E. Miranda⁽⁵⁾, G. Mylonakis^(3, 6, 7)

⁽¹⁾ School of Civil Engineering, National Technical University of Athens, Athens, Greece

⁽²⁾ Faculty of Engineering and Physical Sciences, University of Southampton, Southampton, United Kingdom

⁽³⁾ Department of Civil Engineering, University of Bristol, Bristol, United Kingdom

⁽⁴⁾ École Polytechnique Fédérale de Lausanne, Lausanne, Switzerland

⁽⁵⁾ Department of Civil and Environmental Engineering, Faculty of Civil and Geodetic Engineering, Stanford University, Stanford, USA

⁽⁶⁾ Department of Civil Engineering, Khalifa University, U.A.E.

⁽⁷⁾ University of California at Los Angeles (UCLA), U.S.A.

6.4.1 Introduction

Recent seismic events have showcased the vulnerability of non-structural components to even low- or moderate-intensity earthquakes that occur far more frequently than design-basis ones. Thus, community-critical buildings, such as hospitals, telecommunication facilities or fire stations, often face lengthy functionality disruptions despite having suffered little structural damage during an earthquake. Notable examples of the aforementioned seismic performance are the Sylmar County Hospital in the aftermath of the 1994 Northridge earthquake (Naeim, 2004) and the Santiago and Concepcion airports during the 2010 Maule earthquake in Chile, which sustained very little structural damage but massive non-structural damage (Fierro et al. 2011; Miranda et al. 2012).

To this end, the engineering community has shifted its attention, for countries with modern seismic codes, on the development of robust methodologies for the evaluation of the acceleration demands that are imposed to the non-structural components located at any one floor level during an earthquake. A more accurate absolute acceleration demand assessment could lead to an effective design strategy of non-structural components. Relatively recent, Kazantzi et al (2020a), on the basis of an analytical study that involved floor motions that were recorded during earthquakes on instrumented buildings in the United States (US), have showcased two important attributes with reference to the performance of the non-structural components, these being:

1. The acceleration demands imposed to the non-structural components could be amplified by several orders of magnitude compared to those specified in the current seismic design code provisions (i.e. ASCE 7-16 and EN1998-1-1) if the component has its fundamental period at or close to the supporting building's predominant modal period (fundamental or any other higher mode). This is illustrated in Figure 286, adapted from Kazantzi et al. (2020a), where apparently the a_p factor, which provides a measure of how much the peak component acceleration (PCA) is amplified relatively to the peak floor acceleration (PFA), hence the ratio PCA/PFA, could reach a peak which, for the particular case of tuning with the fundamental period of the supporting

structure (i.e. $\tau_m = T_{\text{component}}/T_{\text{building}} = 1$) and a component damping ratio, β_{comp} equal to 2%, approaches a value of 8 on average.

2. Allowing for some inelasticity to occur either in the support or the bracing of the non-structural component could substantially reduce the peak component acceleration demands. Allowing for inelasticity to reduce the seismic demands is a well-known strategy in earthquake engineering that is reflected in modern seismic codes in the capacity design approach. The extension of such a strategy to the non-structural components was initially introduced by Miranda et al (2018) and further expanded in Kazantzi et al (2020a) via computing inelastic floor spectra for single-degree-of-freedom (SDOF) secondary systems assumed to have a bilinear, non-degrading hysteretic behaviour that was characterized by a post-yield stiffness of 3% of the elastic stiffness. This is shown in Figure 287, adapted from Kazantzi et al. (2020a) illustrating two inelastic floor spectra for two component ductility levels μ_p , 1.5 and 3.0. The study concluded that allowing for nonlinearity in the non-structural component has a significant effect on limiting the peak component acceleration demands. Furthermore, the component ductility utilization results in acceleration demands less conditioned to the τ_m ratio, since the computed inelastic floor spectra were substantially flatter compared to their elastic counterparts, with the latter having pure narrow-band characteristics.

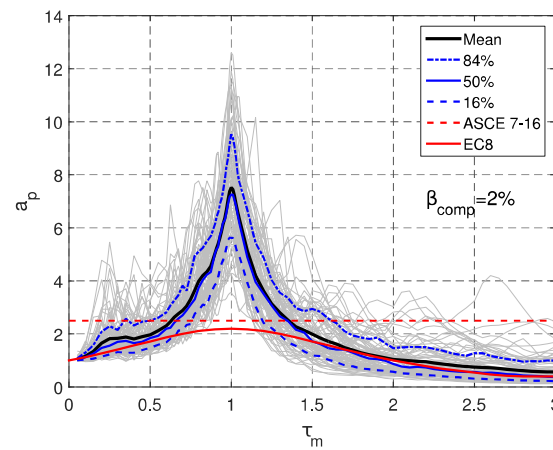


Figure 286: Mean and 16, 50, 84% percentiles for a_p as evaluated for records tuned to the fundamental period of the supporting buildings and a component damping level, $\beta_{\text{comp}} = 2\%$. Also shown are the a_p spectra of individual records (light grey), ASCE7-16 and EN1998-1-1 (adapted from Kazantzi et al., 2020a)

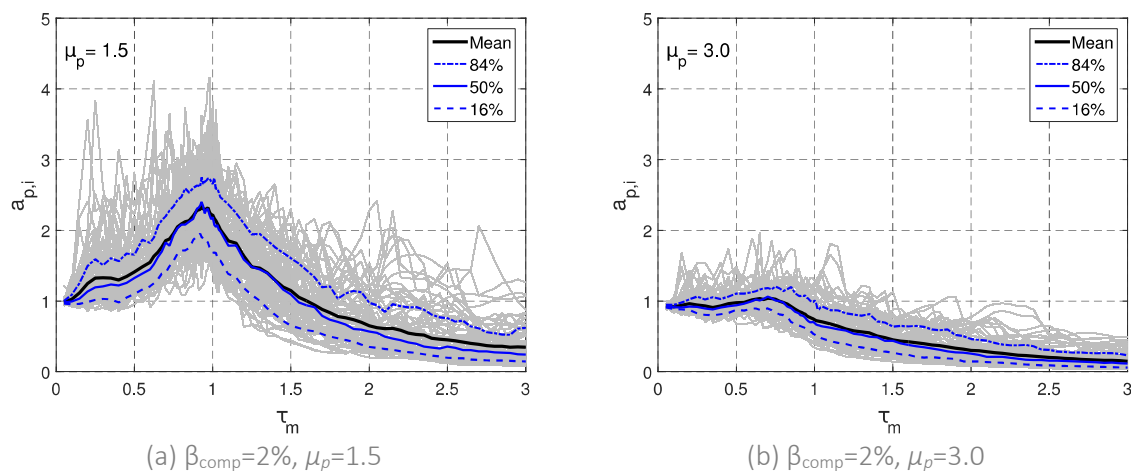


Figure 287: Inelastic floor spectra for a component damping ratio, $\beta_{\text{comp}} = 2\%$, and two component ductility levels, μ_p (adapted from Kazantzi et al, 2020a)

This report summarises the findings of the NSFUSE experimental study that was undertaken at the shake table facility of the University of Bristol during the SERA Project, to investigate the conceptual validity of using ductile steel fuses for protecting acceleration-sensitive critical non-structural components during earthquakes. The objective was to offer a reliable and inexpensive solution, via replaceable sacrificial elements, for the protection of critical non-structural elements.

6.4.2 Test specimen

The test specimen that was tested on the shake table is a carriage-like configuration, as illustrated in Figure 288. The carriage, that was supposed to simulate a non-structural component, is essentially an SDOF system. The carriage was allowed to move on two sliders (that were eventually replaced with rollers, see Comment 1 below for more information) and was attached to its one end to two “fuse” plates (initially four; see Comment 2 for more information about removing the set of fuses in one end of the carriage). The fuses essentially act as cantilevers to provide resistance to the sliding of the carriage. The lower fixed end support per each fuse was materialised via one clamp plate (15mm thick) and a rigid block, that was mounted on the shake table with two M16 bolts. At the upper end of each fuse plate, two clamp plates (15mm thick) were employed to attach them via fillet welds to a “hat” like plate assembly that is connected, by means of another plate equipped with two ball joints for nesting two $\varnothing 20$ pins per fuse, to the carriage. This configuration allows a nearly unrestrained rotation at the top end of the fuses, that again reduces the flexural stiffness of the fuses (and hence the stiffness of the overall configuration) by a factor of about 4, consequently allowing a wide range of periods to be captured with relatively low masses and low fuse plate heights.

Having set the test specimen for targeting different vibration periods, the carriage was loaded with different masses. The period of the test specimen was also adjusted by moderately modifying the fuse heights (spanning between 200mm up to 380mm), thicknesses (ranging from 5 to 10mm) and cross sections (rectangular or bog-bone). These modifications allowed us to study different component/building period ratios (tuned and slightly detuned cases) along with yield strength levels. Table 38 summarises the geometry of the different fuse typologies that were used during testing.

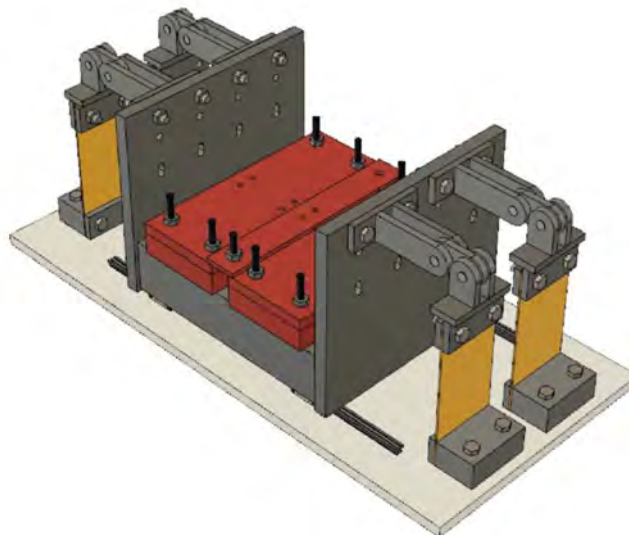


Figure 288: 3D model of the initial carriage test specimen configuration.

Comment 1: Initially the carriage was supposed to slide on two parallel high-performance polymer sliders. However, due to unanticipated high friction problems, more likely related to challenges in

perfectly aligning the sliders to allow for unresisted movement or product malfunction, the sliders were replaced with two solid steel cylindrical rods placed below the carriage, that behaved as rollers. The original sliders could restrict any uplift of the test specimens, something that the rollers could not, causing them to slide freely at the appearance of any uplift. Steel brackets were thus installed, in contact with the underside of the rails, to restrain uplift. This resolved the problem but (a) increased the friction/damping in the tests and (b) in a limited number of tests with very high accelerations the steel rods were still capable of displacing, causing the corresponding results to be discarded.

Comment 2: The initial configuration involved four fuse plates, two at each end of the carriage. However, due to limitations related to the mass that could be placed to the carriage safely, we had to remove the two of fuses from one end to bring down the stiffness and approach the intended periods with a lesser mass. A side view of the as-tested configuration of the carriage and the fuses can be seen in Figure 289 and Figure 290.

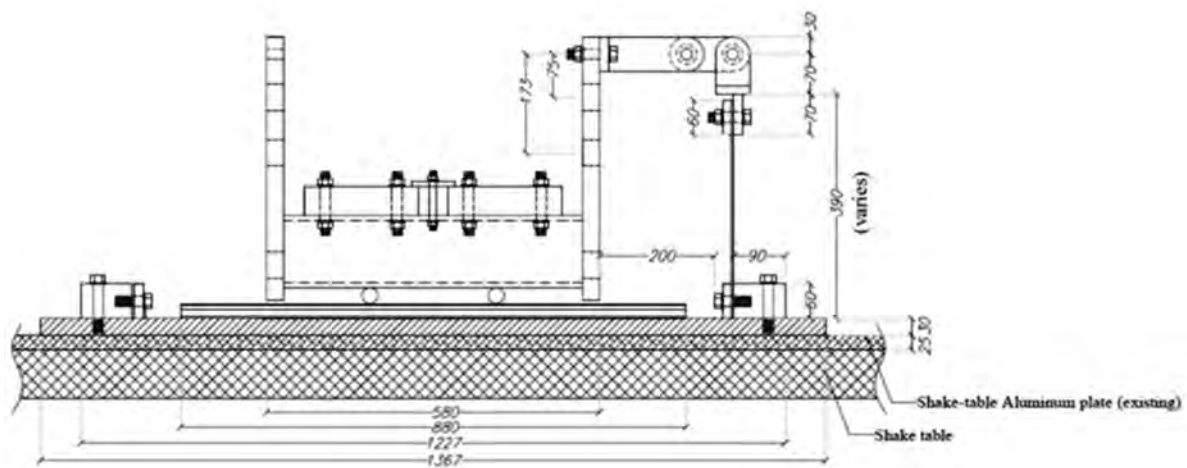


Figure 289: Side view of the actual carriage test specimen configuration (dimensions in mm)

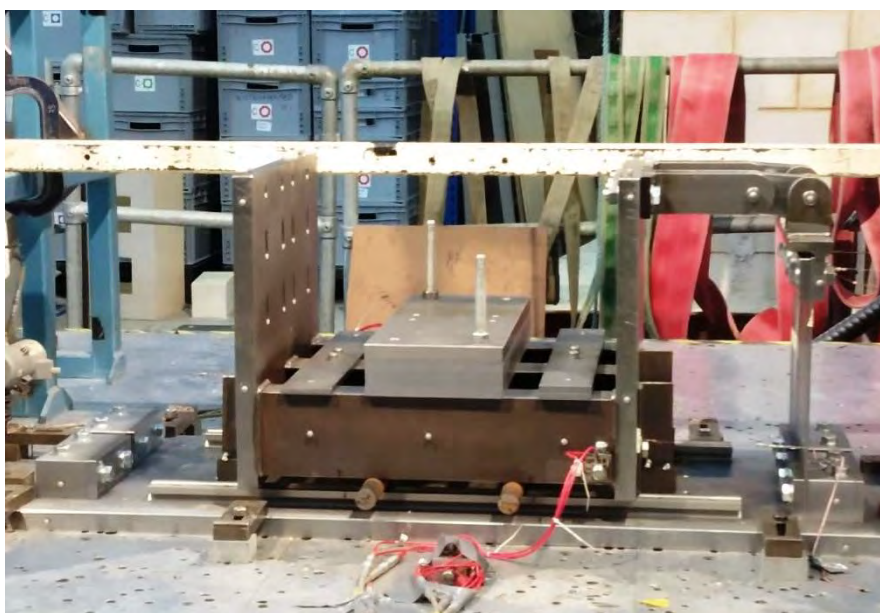


Figure 290: Side view photo of the actual carriage test specimen configuration loaded with steel plates

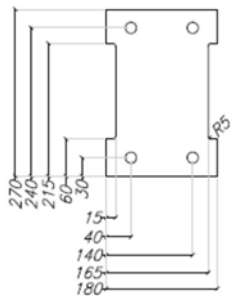
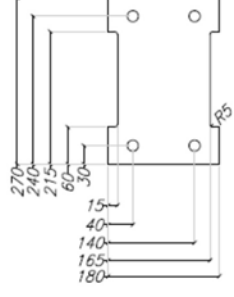
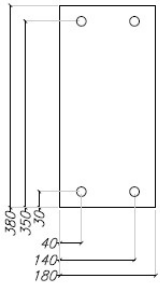
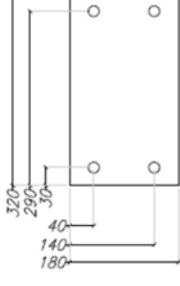
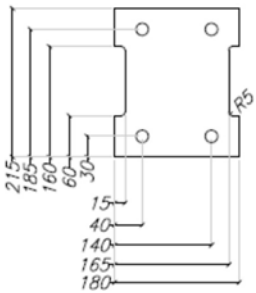
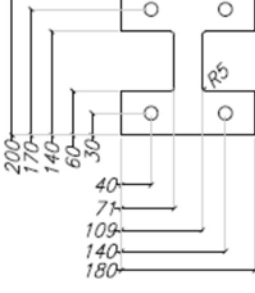
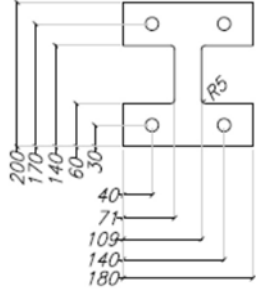
Fuse No	Thickness [mm]	Geometry	Fuse No	Thickness [mm]	Geometry
#1	8		#2	5	
#3	5		#4	6	
#5	6		#6	8	
#7	10				

Table 38: Properties of the tested fuses

6.4.3 Numerical model / prediction / simulation

A representative finite element numerical model of the sliding platform test setup was developed in the commercial software ABAQUS/CAE. The objective of this model was to provide pre-test predictions of the stiffness and strength capacity of the cantilever steel fuse plates under cyclic loading.

Figure 291 shows the layout, basic dimensions and boundary conditions of the meshed 3-dimensional model. The full model was meshed using 8-node linear hexahedral elements of type C3D8R. All the model plate parts were assigned a nonlinear material model with kinematic/isotropic cyclic hardening; representative of steel S355J2. The parameters of the material model were based on the values

recommended by (Sousa and Lignos, 2018). The bolts were assigned a similar model with parameters representative of high strength steel grade SHV 10.9. Rigid parts were assigned an elastic material model with a very large modulus of elasticity.

Referencing to Figure 291, the rigid base plates were considered fixed in all degrees-of-freedom. The in-plane displacement (δ_x) was only assumed free to allow base movement under earthquake excitation when dynamic analysis was conducted. A Reference Point (RP) was specified at the mid-length of the top rigid link. This reference point was rigidly linked to the platform's top surface (represent here as rigid bar link). The reference point was restrained from out-of-plane movements and rotations. In static analysis, δ_x at the reference point, was guided using a pre-defined lateral drift history (typically a ramped cyclic symmetric one). In dynamic analysis, the reference point was assigned a mass representative of the case being studied. In all cases, no gravity loads were applied in the model and accordingly no P-Delta forces were applied to the fuse plate. Prior to the lateral drift application, all M16 bolts were pre-tensioned at 120kN (65% of their yield force). Between all interacting surfaces, a general interaction rule was applied that enforces hard contact in compression, allows separation in tension and assumes a tangential frictional coefficient equal to 0.3.

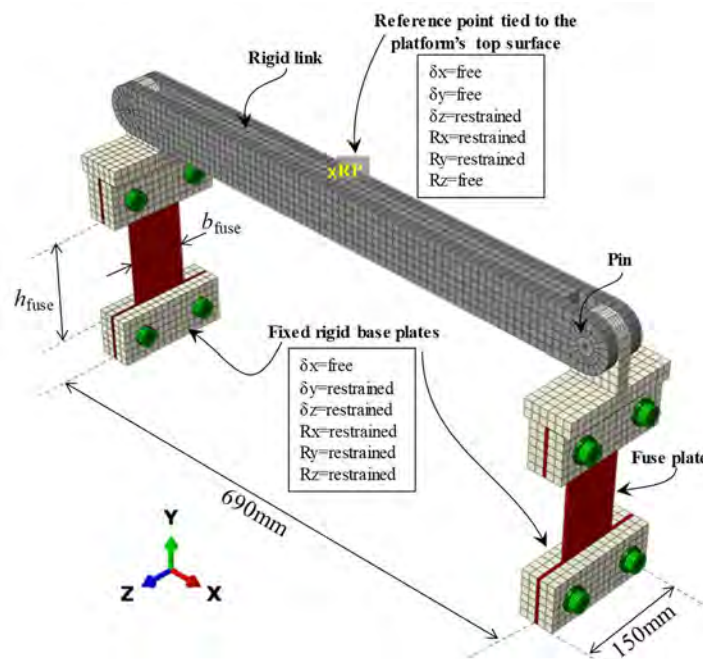


Figure 291: Overview of the finite element model.

Figure 292a shows the typical deformation profile and stress contours of a ductile fuse. Figure 292b shows the expected nonlinear response of the fuse (lateral force versus lateral displacement) when subjected to symmetric cyclic drifts. The simulated responses were then used to deduce analytical expressions for the plastic strength (F_p) and the elastic lateral stiffness (K_e), as demonstrated in Figure 292b. In particular, the following expressions were developed:

$$F_p = Z \cdot f_y / d_{\text{eff}} \quad (1)$$

$$K_e = 3E / \sum_{i=1}^4 \frac{L_i^3}{I_i} \quad (2)$$

where, Z is the plastic section-modulus of the fuse plate, d_{eff} is the effective depth of the cantilever fuse plate (taken as $h+160\text{mm}$, where h is the clear height of the fuse plate), E is the steel modulus of elasticity, I_i and L_i are the cross-section moment-of-inertia and length of region i , respectively. Note

that, as per Eqn. 2, the elastic stiffness is deduced by breaking down the deformed cantilever into four regions to compute the equivalent L^3/I term. This is demonstrated in Figure 293.

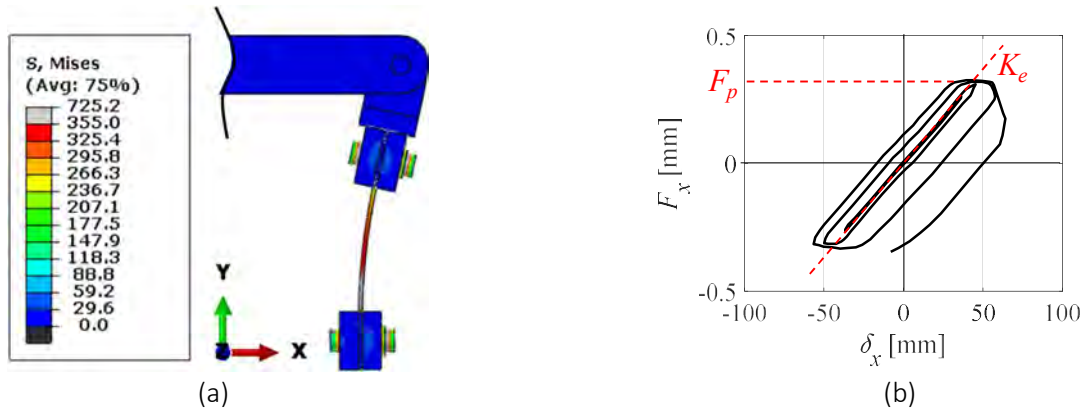


Figure 292: Simulated response of the nonlinear fuse plate based [contour stresses in MPa]

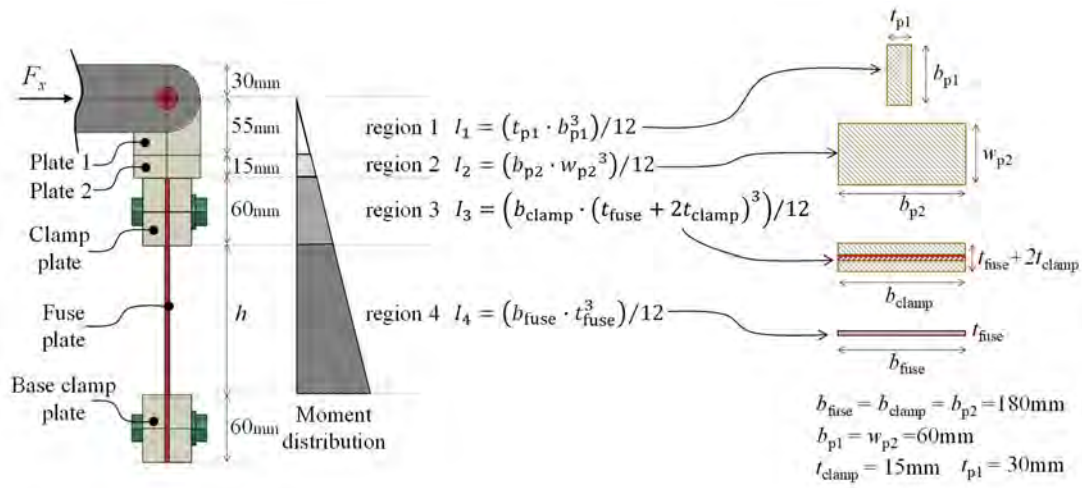


Figure 293: Idealized regions of the cantilever for elastic stiffness computation

6.4.4 Test setup

The experimental program involved a series of one-dimensional earthquake simulation tests realized on a shake table. The shake table tests were conducted using narrow-band floor acceleration input signals that were recorded in instrumented buildings through the California Strong Motion Instrumentation Program (CSMIP) during three different earthquake events.

For each test, the input signals were incrementally scaled up or down, to induce different ductility levels. The experimental campaign shed light on the seismic performance of non-structural components that are mounted on a structure and the benefits of detuning the component period from resonance with the period of the supporting structure by means of a controlled yielding element.

Displacements, accelerations and uniaxial strains were monitored during testing (see Figure 294). A comprehensive instrumentation plan was provided to the Bristol laboratory prior to testing. This plan was moderately modified since the two fuses in the West platform edge were finally removed. The displacements were recorded using three string potentiometers, two of which were attached to the carriage and one (instead of two, mainly in order to speed up the testing process when changing the

pair of fuses during testing) was attached to one of the two fuses connected to the carriage in each test, as well as a vision system with three cameras. Regarding the accelerations, three accelerometers were measuring the table accelerations in all three directions and six more accelerometers located in the SW and NE of the carriage were measuring the carriage accelerations in all three directions. Furthermore, for evaluating the strain, a strain gauge was installed in one of two fuses employed in each test, as can be seen in Figure 295 for a generic fuse geometry.



Figure 294: The modified instrumentation plan that was used during testing

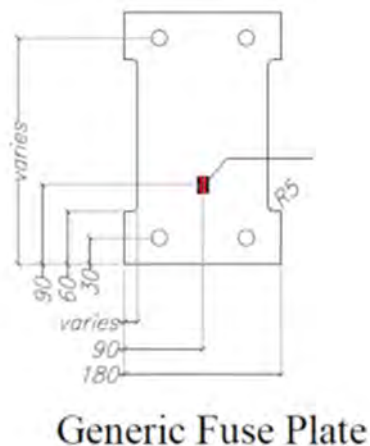


Figure 295: Location of the strain gauge in a generic fuse plate

6.4.5 Test observations

Overall, several challenges were encountered even by testing a “simple” SDOF system on a shake table. Hitting specific target periods and ductilities with low enough friction damping while maintaining masses and accelerations/velocities/displacements within what the test rig and the shake table could sustain proved to be a challenging task. The replacement of the sliders by rollers and uplift-restrainers resolved any alignment issues at the cost of higher friction damping, while the modularity of the test specimen helped adjust masses and stiffnesses as needed on the spot.

Of importance to the success of the testing campaign was the achievement of a fast turnaround time between the multiple shaking tests. For this, it was important to have a rapid assessment of the test specimen period (first) and viscous damping ratio (second) without involving the shake table. It was quickly found that the best approach to estimate the period was to perform a free vibration test,

shaking the test specimen by hand and placing a smartphone on top running a freely available app for period identification. This provided accurate enough results for the frequency (within 1Hz) to allow us to select the mass to be placed on the test specimen. After fixing the mass, damping identification became the next target. However, white noise tests would sometimes fail to sufficiently move the test specimen. Thus, free vibration testing was employed, again shaking the test specimen by hand. This is where the visual tracking system became very useful, providing displacement results within minutes that could be processed on the fly by a MATLAB script to produce accurate estimates for both the period and the damping.

Finally, placing even a single strain gauge on the fuse plates proved to be highly important in determining whether plastic deformations had taken place during testing. This allowed us to continue scaling the shaking motion until enough ductility could be observed.

6.4.6 Results / Preliminary results

The post-processing of the vast output that was produced during testing is still in progress. Preliminary findings demonstrated though, that the controlled yielding steel fuse concept to reduce the acceleration demands imposed to the non-structural components holds and the fuses at all cases were able to develop a ductile yielding mechanism.

Figure 296 to Figure 299, present results from a number of shaking table tests undertaken for “Test No1”. Test No1 refers to a series of shake table tests utilizing Fuse #3 (i.e. a rectangular plate with a thickness of 5mm and a total height of 380mm, see Table 38). The input floor motion was the GM93 floor signal, which corresponds to a floor motion that was recorded during the 1994 Northridge event in the roof of a 6-storey commercial building. It belongs to a group of records that were previously used in several analytical studies undertaken by members of this research team (e.g. Kazantzi et al, 2020a and 2000b) and it is a characteristic example of a floor motion that is tuned to a higher vibration mode. The motion was incrementally scaled via four scale factors, namely 0.75, 1.00 (unscaled case), 1.20 and 1.40 motion. Figure 296 presents the elastic floor acceleration spectra (for a component damping level equal to $\beta_{comp}=1\%$) for this particular floor motion where it can be clearly seen that the floor spectra has two peaks, the first signifying the tuning to the second mode period ($T_{comp}=0.45\text{sec}$) of the building and the second peak the tuning to its fundamental period. Apparently, for a component with a damping level equal to 1% and a vibrating period equal to 0.45sec (i.e. equal to the second mode period of the supporting structure where this floor motion was recorded) the component acceleration is close to 3g.

The total mass assigned to the carriage to get an SDOF component with a period of vibration equal to 0.45sec was 69kg. This mass, according to a free vibration test (T9), that preceded the actual testing, resulted in an actual vibration period for the carriage equal to 0.47sec (very close to the valley on the right, next to the first spectrum peak, see Figure 296) and a component damping ratio of 3.4%.

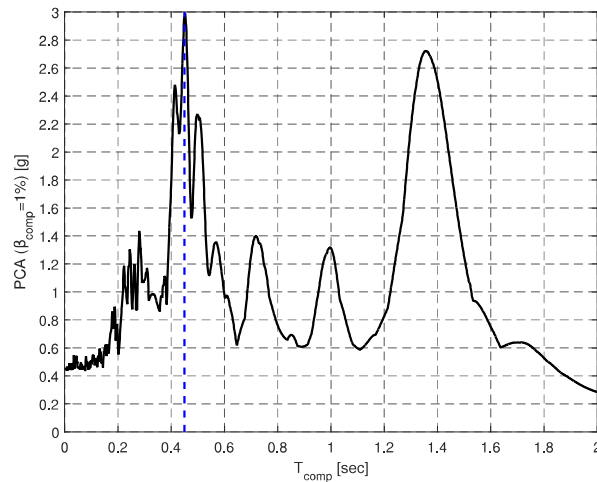


Figure 296: Elastic floor acceleration spectra for GM93 evaluated for a component damping level, $\beta_{comp} = 1\%$

For the component damping level that was observed during the free vibration test ($\beta_{comp} = 3.4\%$) and using the acceleration signal that was recorded by the Setra accelerometer located on the table (X-direction), the floor acceleration spectra illustrated in Figure 297 could be evaluated for the unscaled (Figure 297a) and the 40% scaled up (Figure 297b) input motion around the region of interest, which is the peak of the curve that occurs at the second mode period of the supporting structure.

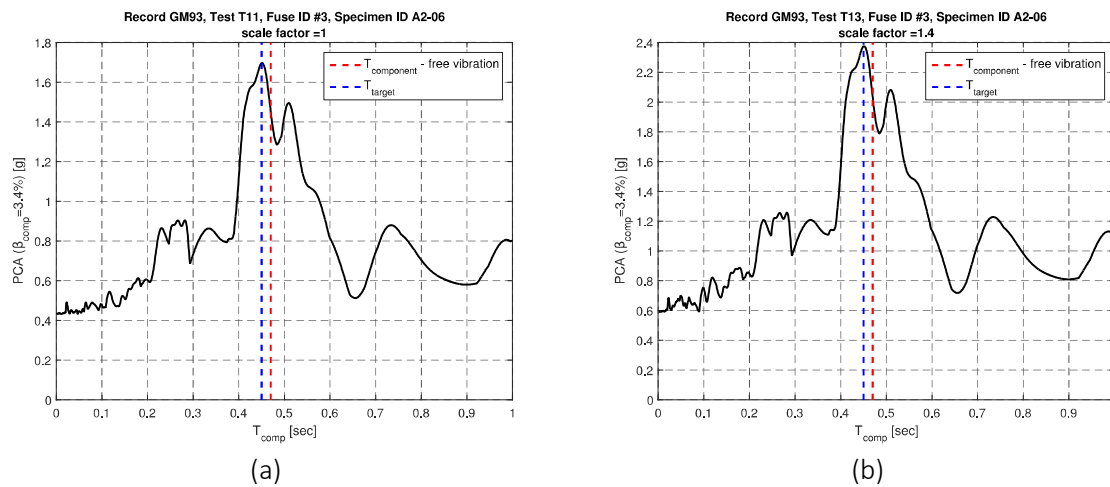


Figure 297: Elastic floor acceleration spectra for GM93 (Test No1) evaluated for a component damping level, $\beta_{comp} = 3.4\%$ using the acceleration history recorded on the table for (a) the unscaled and (b) the 40% scaled input motion. The blue dashed line depicts the second mode period of the supporting structure and the red dashed line the actual period of the carriage as evaluated from the free vibration testing

Figure 298a-d presents the component acceleration histories along with the shake table input floor acceleration histories for the four scale factors that were used to incrementally scale the initial floor acceleration motion and consequently induce different ductility levels to the steel fuses. We can broadly say that in Figure 298a the fuse response is nearly elastic whereas the response illustrated in Figure 298d is moderately inelastic, as we can also observe in Figure 299b. The peak component acceleration (PCA) for the input floor motion that was scaled down by 25% equals 1.165g whereas the a_p equals 3.5. If the system (component) was left to behave elastically, as we incrementally scaled the input motion that would have resulted in an analogous increase to the PCA. Instead, because of the

fuse yielding, for the floor motion scaled up by 40% the inelastic PCA equals 1.436g (see Figure 298d) as opposed to the elastic PCA that is approximately equal to 2.0g (see Figure 297b). In other words, the inelastic response is reduced by approximately 28% relative to the elastic one. Note that, from the elastic spectrum evaluated at the actual component damping level and for the actual period of vibration, i.e. $T_{comp}=0.47\text{sec}$, the PCA is approximately equal to 1.45g for the unscaled signal (see Figure 297a), that is only slightly higher than the recorded one, essentially implying that the response is nearly elastic for this scaling level (1.45g as opposed to 1.32g).

Even more interestingly, for the signal scaled up by 40% we find $a_{p,i}=2.43$ (note that this is the inelastic a_p), which is the lowest $a_{p,i}$ among all $a_{p,i}$ factors evaluated for this test series. That essentially means that the addition of the yielding fuses to the system (even for moderate ductility levels as could be inferred from Figure 299) resulted in the acceleration demands being reduced compared to the acceleration demands that would have been recorded if the carriage was left to behave purely elastically and this reduction is more clearly manifested as the level of the inelasticity induced to the fuses is increased.

Higher levels of induced inelasticity in the fuses have a more profound effect on peak component accelerations. “Test No7” used the same acceleration floor signal with “Test No1”. The mass added on the carriage (a total of 660kg) along with a pair of Fuse #6 plates (see Table 38) resulted in an SDOF system having a period of vibration that was equal to 0.39sec (the targeted period was 0.36sec). This is a spectrum region away from the peak. The component damping for this particular test was estimated via a free vibration test to be approximately equal to 1.70%, i.e. lower than that evaluated for Test No1, which however was less loaded and hence the damping due to friction was less (additional friction may be induced to Test No1 due to the steel rod supports not being properly lubricated). In Test No7 the input signal was again scaled to four scaling factors, these being 0.5, 0.75, 1.00 and 1.50.

For the component damping level that was evaluated again via a free vibration test ($\beta_{comp}=1.7\%$) and using the acceleration signal that was recorded by the Setra accelerometer on the table (X-direction) the floor acceleration spectra is illustrated in Figure 300 for the unscaled input motion. Apparently, the targeted region for the specific test is off the peak of the acceleration spectrum. In fact, for the actual component vibration period ($T_{comp}=0.39\text{sec}$) the elastic PCA is approximately equal to 0.96g. However, the inelastic PCA that is recorded on the carriage under the same unscaled input motion is 0.562g (see Figure 301c), which is approximately 40% less. Note that for this particular test series high levels of inelasticity develop in the fuses even for the unscaled record, whereas yielding was observed in the pair of fuses even for the lowest scaling factor as can be inferred by Figure 302.

The benefits of allowing the fuses to yield are also evident when the input motion is scaled up by 50%. In that case we found $a_{p,i}=1.65$ (see Figure 301d, note that this is the inelastic a_p) which is only marginally higher from the $a_{p,i}$ estimated for the case where the floor motion was scaled down by 50% (see Figure 301a, $a_{p,i}=1.63$).

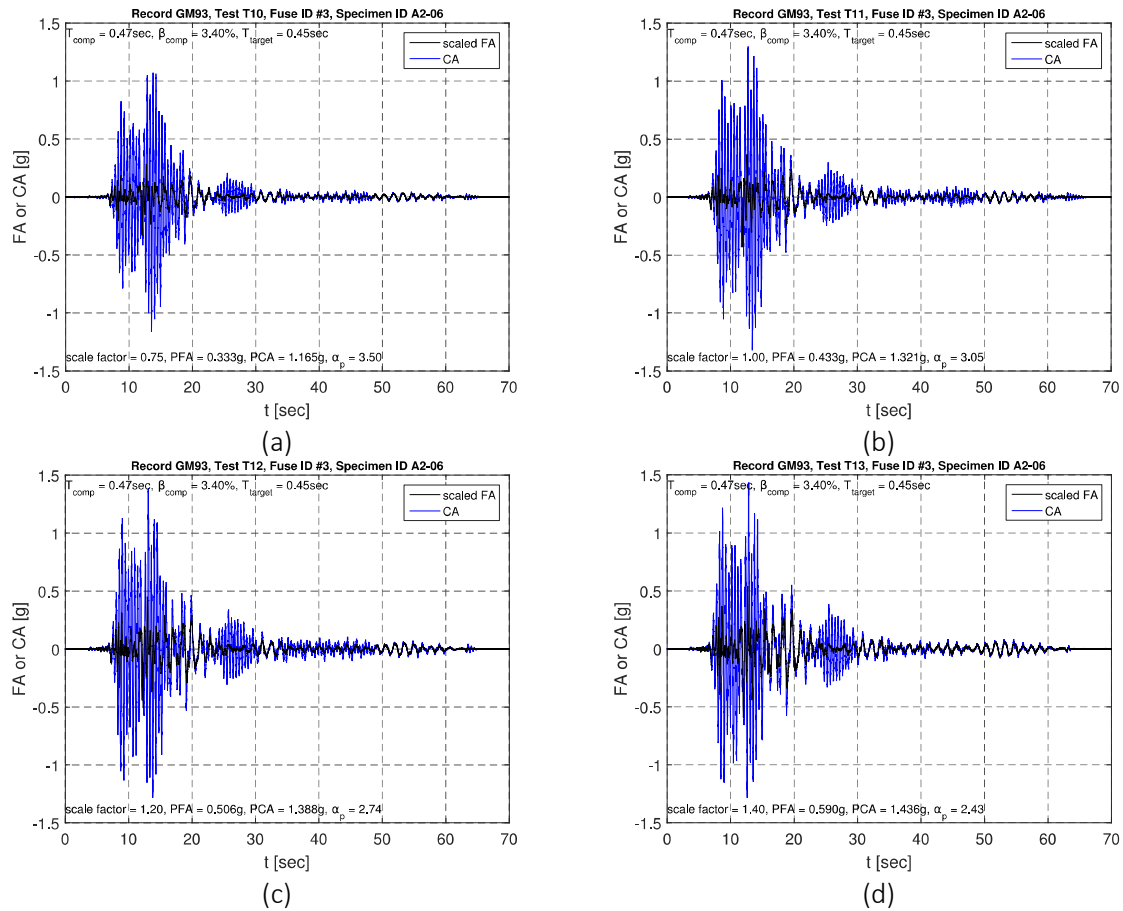


Figure 298: Floor acceleration (FA) and component acceleration (CA) histories for GM93 (Test No1) and (a) 0.75, (b) 1.00, (c) 1.20, (d) 1.40 scaling factors.

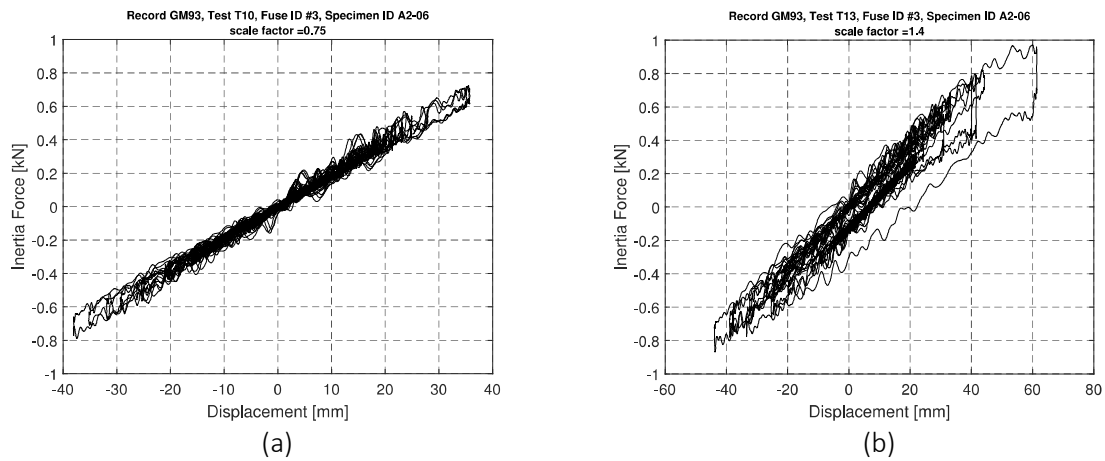


Figure 299: Inertia force vs fuse displacement for GM93 (Test No1) and (a) 0.75 (b) 1.40 scaling factors.

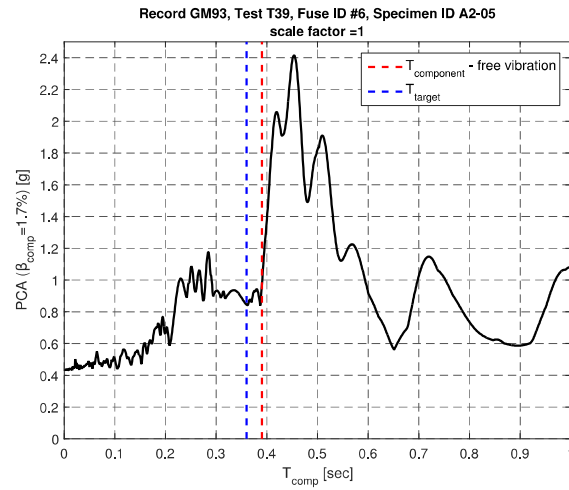


Figure 300: Elastic floor acceleration spectrum for GM93 (Test No7) evaluated for a component damping level, $\beta_{comp} = 1.7\%$ using the unscaled acceleration history recorded on the table

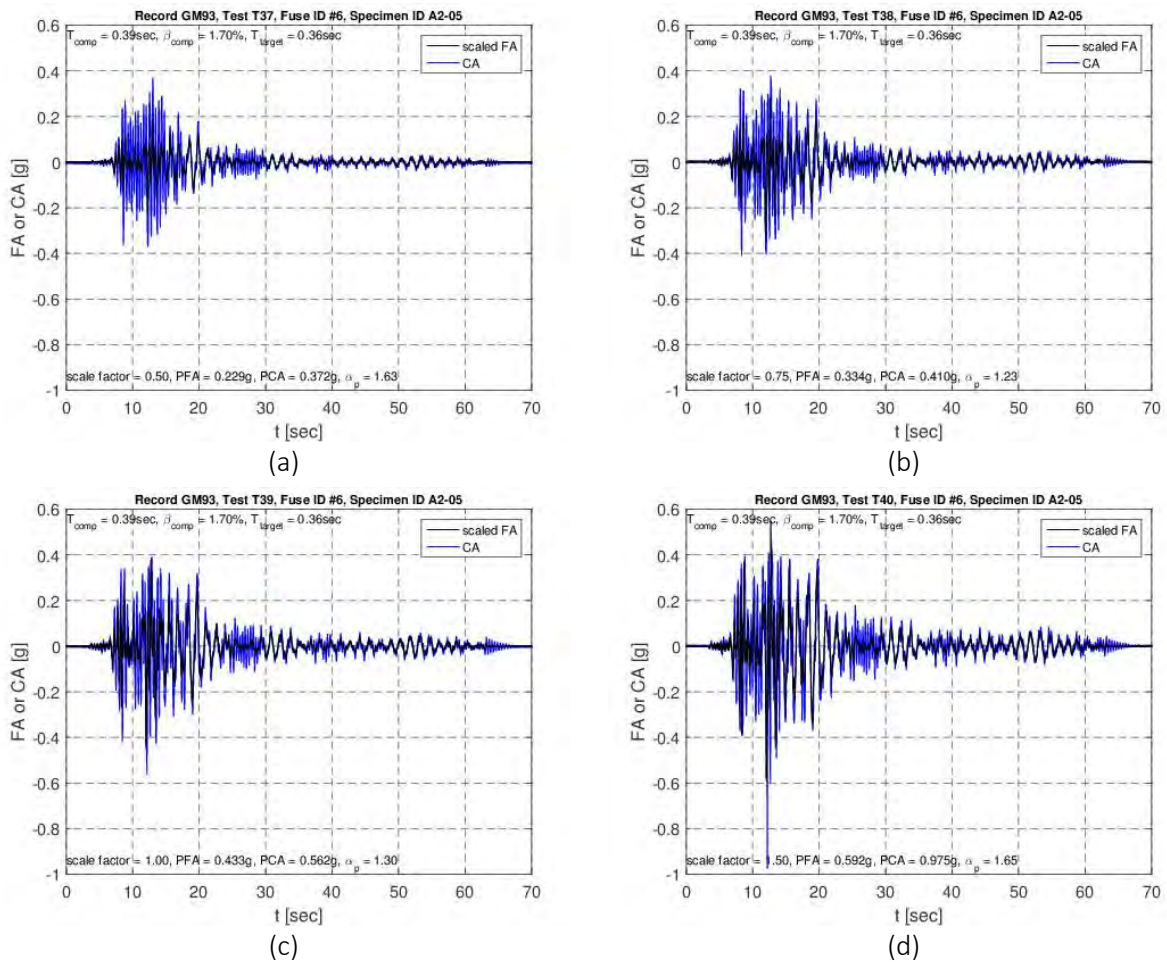


Figure 301. Floor acceleration (FA) and component acceleration (CA) histories for GM93 (Test No7) and (a) 0.50, (b) 0.75, (c) 1.00, (d) 1.50 scaling factors

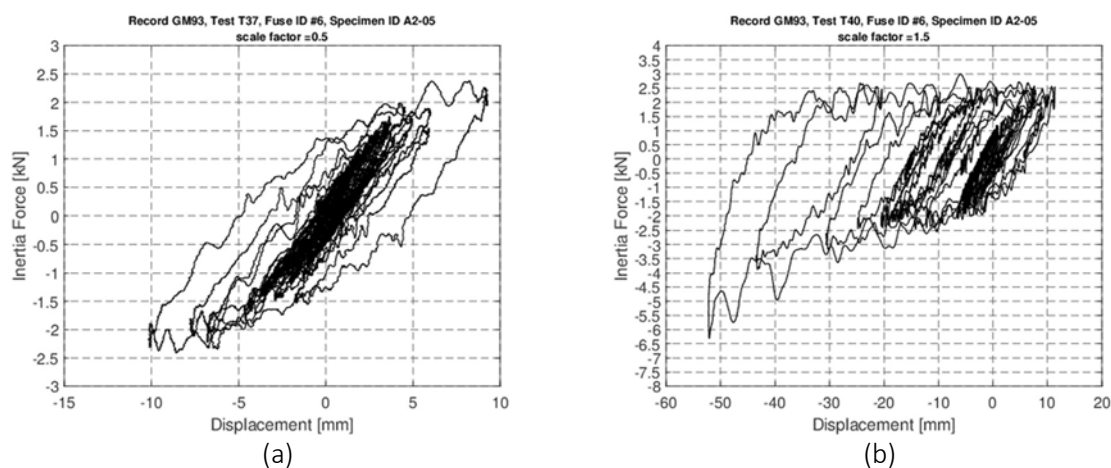


Figure 302. Inertia force vs fuse displacement for GM93 (Test No7) and (a) 0.50 (b) 1.50 scaling factors

6.4.7 Conclusions and outlook

The NSFUSE test series explored the concept of using a simple yielding connector concept to reduce acceleration amplifications for non-structural components attached to buildings. The results clearly support this idea and provide us with a valuable verification of pertinent numerical simulation models. The results open new directions of research in protective design of non-structural components and can easily find their way in prospective design codes.

6.4.8 References

- CSMIP, California Strong Motion Instrumentation Program, Department of Conservation's California Geological Survey. <https://www.conservation.ca.gov/cgs/smip>. Accessed 24 March 2020.
- Fierro EA, Miranda E, Perry CL. Behavior of nonstructural components in recent earthquakes. In AEI 2011: Building Integration Solutions, *American Society of Civil Engineers*, 369-377, 2011.
- Kazantzi AK, Vamvatsikos D, Miranda E. Evaluation of seismic acceleration demands on building nonstructural elements, *Journal of Structural Engineering*, 2020a.
- Kazantzi AK, Vamvatsikos D, Miranda E. The effect of damping on floor spectral accelerations as inferred from instrumented buildings, *Bulletin of Earthquake Engineering*, 18:2149–2164, 2020b.
- Miranda E, Kazantzi A, Vamvatsikos D. New approach to the design of acceleration sensitive non-structural elements in buildings, Proc. 16th European Conference on Earthquake Engineering, Thessaloniki, Greece, 2018.
- Miranda E, Mosqueda G, Retamales R, Pekcan G. Performance of nonstructural components during the 27 February 2010 Chile earthquake, *Earthquake Spectra*, 28(S1), S453-S471, 2012.
- Naeim F. Impact of the 1994 Northridge earthquake on the art and practice of structural engineering, *The Structural Design of Tall and Special Buildings*, 13(5): 373-389, 2004.
- Sousa AA, Lignos DG. On the inverse problem of classic nonlinear plasticity models, EPFL-REPORT-231968, Ecole Polytechnique Federale de Lausanne (EPFL), Lausanne, Switzerland, 2018.

6.5 Project #22 – SEBESMOVA3D - SEeismic BEhavior of Scaled MOdels of groin VAults made by 3D printers (SEBESMOVA3D)

Authors

D. Foti⁽¹⁾, S. Silvestri⁽²⁾, S. Ivorra⁽³⁾, D. Theodossopoulos⁽⁴⁾, S. Baraccani⁽²⁾, V. Vacca⁽¹⁾, R. White⁽⁵⁾, M. Dietz⁽⁵⁾, G. Mylonakis^(5,6,7)

⁽¹⁾ *Department of Civil Engineering Sciences and Architecture, Technical University of Bari, Bari, Italy*

⁽²⁾ *Department of Civil, Chemical, Environmental and Materials Engineering, University of Bologna, Bologna, Italy*

⁽³⁾ *Department of Civil Engineering, University of Alicante, Alicante, Spain*

⁽⁴⁾ *Edinburgh School of Architecture and Landscape Architecture, University of Edinburgh, Edinburgh, United Kingdom*

⁽⁵⁾ *Department of Civil Engineering, University of Bristol, Bristol, United Kingdom*

⁽⁶⁾ *Department of Civil Engineering, Khalifa University, U.A.E.*

⁽⁷⁾ *University of California at Los Angeles (UCLA), U.S.A.*

6.5.1 Introduction

Damages on existing masonry churches after the earthquakes occurred recently in Italy and Spain revealed that the collapse of such structures could be ascribed to the local failure of singular structural elements. Furthermore, it was shown that vaults are among the most vulnerable structural elements and it is their central portions that collapse rather than their supports, as they are embedded into the latter, while they counteract the outward thrust of the roof system (Croci 1998, Piermarini 2013, Cancino 2009).

The aim of the SEBESMOVA3D project (SEeismic BEhavior of Scaled MOdels of groin VAults made by 3D printers) is to focus the attention on the dynamic and earthquake response of the groin vault, that is one of the weakest structures found in historical constructions when not sufficiently confined. This model vault considers dry joints between the voussoirs (like many monumental structures in South Mediterranean) and was built in an innovative way to allow study of its dynamic behaviour and repetition of tests carried out until collapse.

The aim of the SEBESMOVA3D project (SEeismic BEhavior of Scaled MOdels of groin VAults made by 3D printers) is to focus the attention on the dynamic and earthquake response of the groin vault, that is one of the weakest structures found in historical constructions when not sufficiently confined. This model vault considers dry joints between the voussoirs (like many monumental structures in South Mediterranean) and was built in an innovative way to allow study of its dynamic behaviour and repetition of tests carried out until collapse.

The physical model was realised with dry-joint blocks made of a 3D-printed plastic skin filled with mortar, which provided sufficient stiffness and strength to sustain impact without damage and allow for a quick and reliable re-assembly. This technique was used in similar tests previously performed on a small barrel vault at the “Laboratorio Salvati”, Technical University of Bari, Italy (Foti et al. 2018): the

arches and vaults tested were made with modular blocks of wood and stone, respectively, and assembled with dry joints (Foti et al. 2019, Diaferio et al. 2019).

The main objectives of SEBESMOVA3D project were to evaluate the crack pattern and the collapse mechanism of groin vaults with two different support conditions:

- Configuration 1: on four fixed supports;
- Configuration 2: on two fixed springings combined with two one-directional moving supports characterized by very low lateral stiffness.

The rationale behind this choice lies in the observation that a vault under an earthquake excitation is mainly subjected to two different phenomena (Carfagnini et al. 2018):

- dynamic response of the vault itself to acceleration imposed at its springings, reproduced by Configuration 1;
- response of the vault to differential horizontal shear displacement imposed at its springings by the excitation of the underlying structures (walls and piers, characterised by different lateral stiffness), reproduced by Configuration 2.

Also, four boundary conditions along the four lateral arches (wooden panels, Plexiglass panels, Cut Plexiglass panels and no panels) were considered to account for different confinement levels.

The information to be gained from the effect of the supporting structures is fundamental to correctly plan seismic strengthening interventions in vaults and may be useful to professional engineers.

The experimental campaign was carried out in two separate sessions: August 2019 and January/February 2020.

6.5.2 Design of the vault prototype

The physical model was designed as an assembly of distinct plastic-mortar blocks. A plastic mould formed the blocks, made by a 3D printer, which was then filled up with mortar to acquire the corresponding mass for dynamic tests. The assemblage of the blocks was assisted with a polystyrene formwork, to ensure the model would be efficiently and quickly rebuilt after each collapse. In addition, to ensure a fixity condition at the base, 2-cm-thick steel plates were attached to the shaking table to prevent the four springing blocks to move in translation. The global dimensions of the vault were adjusted to fit the facilities of the EQUALS laboratory at University of Bristol, leading to a large physical model occupying a 2m x 2m area. The model was truncated at the base to encompass the effect of the base embedded in the perimeter walls and stiff springings, as observed in the vault collapses surveys briefly mentioned in the Introduction (Figure 303).

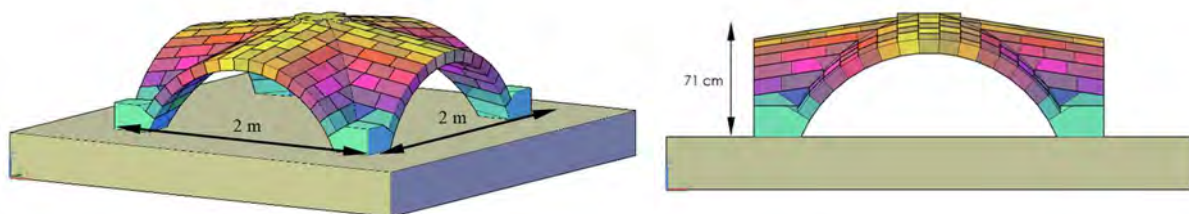


Figure 303: The vault prototype

The vault thickness is 8 cm and its height approximately 71 cm. It is composed by 172 blocks, five of them having larger dimensions than the others: the four bases on which the structure is set up (Figure

304a) and the keystone (Figure 304b), which locks all the pieces into position. The dimensions of a typical block are 12cm x 8cm x 20cm (Figure 304c).

The composite blocks of the vault are fastened to each other with a gum layer to increase frictional and dissipative properties and allow for small adjustments to be made during construction, since no fresh mortar is used between the bricks. Internal friction angle of this plastic–double gum layer–plastic interface is around 30°.

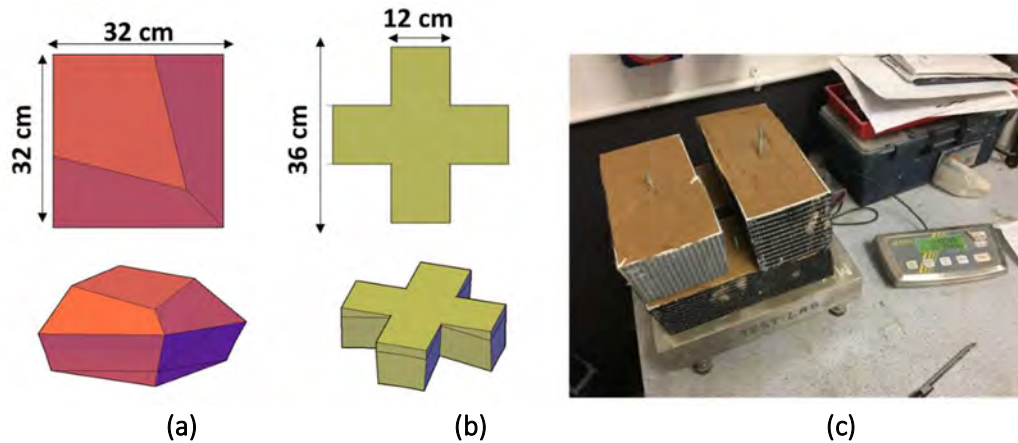


Figure 304: (a) Base block. (b) Keystone block. (c) Typical blocks

The material to fill the blocks is “Thistle bonding coat” from British Gypsum. To assess the mechanical properties of this infill mortar, a compression test of a cylindrical sample hardened in similar conditions was carried out: the elastic modulus was estimated as $E = 60 \text{ N/mm}^2$ and the compression strength was 0.25 N/mm^2 . Likewise, the mechanical properties of the mortar-skin-gum set were assessed via cyclic compression tests of a three-bricks series filled with mortar and gum-layer around (Figure 305). The initial part of the first cycle provides information about the gum layer’s elastic modulus ($E = 0.8 \div 1.0 \text{ N/mm}^2$) as this is the first element of the set that is compressed. The subsequent part of the first cycle returns an elastic modulus for the block of 40 N/mm^2 , which is mostly provided by the stiffness of the plastic skin box. For higher forces, mortar starts working.

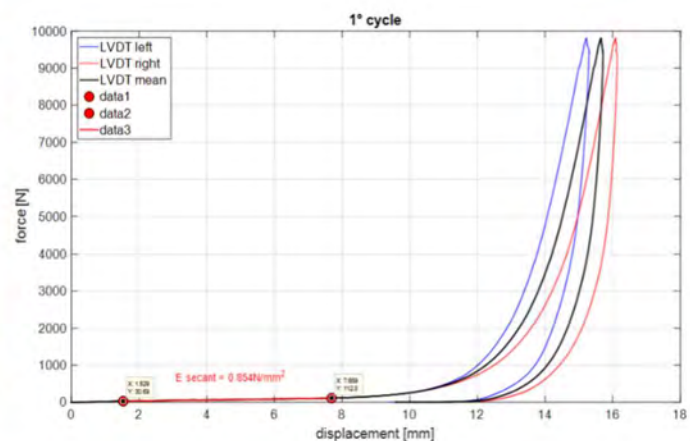


Figure 305: Force-displacement diagram for a three-bricks series filled with mortar and gum-layer around

6.5.3 Test setup (construction phases)

The plastic brick moulds were pre-assembled to verify dimensions, shapes and number of units, as shown in Figure 306. Then, the vault was dismantled to fill up the units with mortar.

For Configuration 1, the vault was placed on four steel plates that were fixed on the shaking-table (Figure 307a). For Configuration 2 the vault was placed on two fixed steel plates and on two moveable carriages running on bearings along a pair of 40mm-diameter rails enveloped by horizontal springs to give a combined stiffness of 16 N/mm (stiffness designed according a prediction of the shear displacements) (Figure 307b).

As far the assemblage process is concerned, in both cases, first, the base blocks were installed followed by the other bricks placed on the polystyrene formwork starting from the lateral arches; once the first row of blocks in every lateral arch was completed, the diagonal blocks were installed, followed by the other blocks of the webs (Figure 308).

Different lateral confinement types were provided along the lateral arches: (i) four 2 cm-thick wooden panels (Figure 309a), (ii) four 2cm-thick Plexiglass panels (Figure 309b), (iii) four 2cm-thick Plexiglass panels, with two of them (the ones along the y-direction, orthogonal to the direction of the movements allowed by the carriages) cut in the middle, and (iv) no panels (Figure 309c).



Figure 306: Pre-assembly of the plastic skin of the blocks

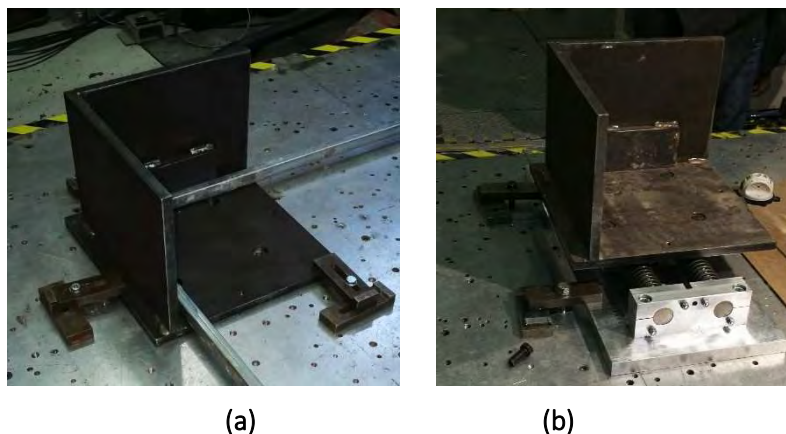


Figure 307: (a) Steel plate rigidly connected to the table to realize the fixed springing used for Configuration 1. (b) Steel plate on a moveable carriage running on bearings enveloped by horizontal springs to realize the moveable springing used for Configuration 2



Figure 308: Assembly process

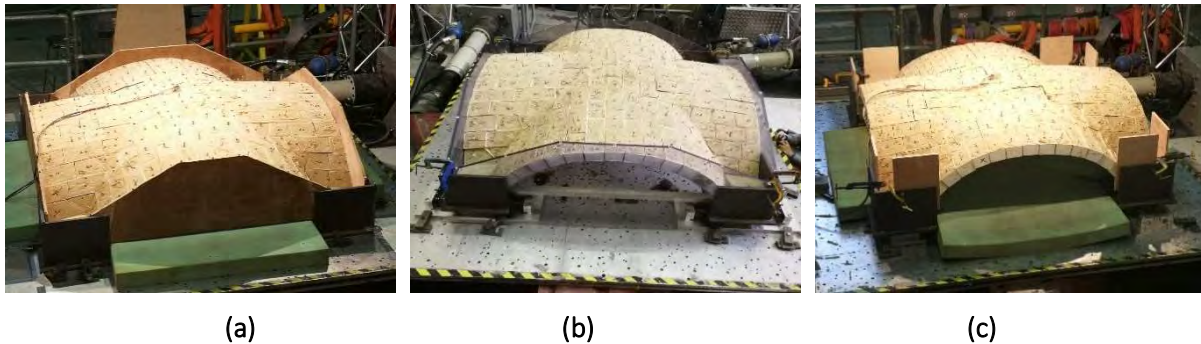


Figure 309: Different lateral confinement along the lateral arches: (a) four 2 cm-thick wooden panels, (b) four 2cm-thick Plexiglas panels and (c) no panels

6.5.4 Testing instrumentation

The testing instrumentation consists of: (a) triaxial accelerometers on the shaking table and on the keystone of the vault operating at a frequency rate of 5000 Hz (Figure 310b); (b) a vision system composed by motion capture cameras recording the positions over time of the markers placed on each brick, on the panels and on the shaking table at a frequency rate of 100 Hz (Figure 310c) and (c) a data Acquisition System that includes a 250-channel system and an advanced wireless system based on 8 high definition digital cameras.

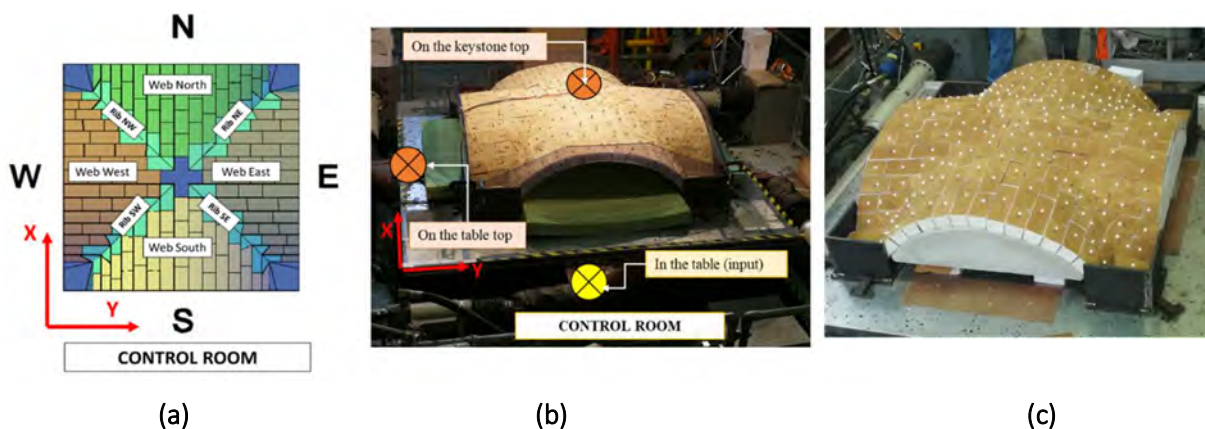


Figure 310: (a) Reference system. (b) Position of the triaxial accelerometers. (c) Position of the markers

6.5.5 Testing program

The experimental campaign was carried out in two separate sessions: August 2019 and January/February 2020.

Table 39 shows the tests performed in the first session, which were developed in three stages, each of them was a series of consecutive tests with reconstruction only after collapse, i.e. each test accumulated the damage of the preceding ones. In this session the tests were performed on the vault on four fixed supports (Configuration 1) and with four 2 cm-thick wooden panels along the lateral arches. Tests with frequencies in the range between 1 Hz and 50 Hz were explored, with special emphasis on ranges between 2 Hz and 15 Hz, in which most of the damage was observed. Additionally, six seismic tests were executed, however, no significant damage was observed since the vault seemed to be more vulnerable to harmonic motions at low frequencies. The vault collapsed three times: two at 2 Hz with PTA of 0.95g and 1.0g, and one at 5Hz with PTA of 1.4g.

In the following tables *fr* indicates the “recorded frequency” as obtained analysing the acceleration output signal of the accelerometer on the keystone of the vault.

Test n.	Description:	PTA [g]	Direction	Frequency [Hz]	Damp. Ratio [%]
1	Random test	0.05g	x direction	<i>fr</i> =19.85	11.13
2			y direction	<i>fr</i> =19.18	12.91
3			z direction	<i>fr</i> =21.63	11.93
4	Sinusoidal test-10 cycles	0.10g	x direction	1	
5				5	
6				8	
7				10	
8				15	
9	Sinusoidal test-10 cycles	0.25g	x direction	20	
10				50	
11				1	
12				5	
13				8	
14	Sinusoidal test-10 cycles	0.50g	x direction	10	
15				15	
16				20	
17				50	
18				1	
19	Sinusoidal test-10 cycles	0.75g	x direction	5	
20				8	
21				10	
22				15	
23				20	
24	Sinusoidal test-10 cycles	0.75g	x direction	50	
25				2	
26				5	
27				8	
28				10	
29	Sinusoidal test-10 cycles	0.75g	x direction	15	
30				20	
31				2	Collapse
32	Random test	0.05g	x-direction	<i>fr</i> =15.79	12.40
33	Sinusoidal test-10 cycles	0.80g	x-direction	15	
34				10	
35				8	
36				5	
37				2	
38	Sinusoidal test-10 cycles	0.85g	x-direction	15	
39				10	
40				8	
41				5	
42				2	
43	Sinusoidal test-10 cycles	0.90g	x-direction	15	
44				10	
45				8	
46-2				5	
46				5	
47	Sinusoidal test-10 cycles	0.95g	x direction	2	
48				15	
49				10	
50				8	
51				5	
52	Sinusoidal test-10 cycles	0.95g	x-direction	2	Collapse
53	Random test	0.05g	x-direction	<i>fr</i> =15.78	
54	Seismic test: Modena earthquake	0.35g	x-direction		
55	Random test	0.05g	x-direction	<i>fr</i> =15.39	
56	Seismic test: Mirandola earthquake		x-direction		
57	Seismic test: El Centro earthquake		x-direction		
58	Seismic test: El Centro earthquake	0.3g	x-direction		
59	Seismic test: El Centro earthquake	0.6g	x-direction		
60	Seismic test: El Centro earthquake	1.2g	x-direction		
61	Sinusoidal test-10 cycles	1g	x-direction	5	
62	Sinusoidal test-10 cycles	1.2g	x-direction	5	
63	Sinusoidal test-10 cycles	1.4g	x-direction	5	Part. Collapse

Table 39: List of tests performed in the first session (August 2019)

Table 40 shows the tests performed in the second session, which were developed in several stages, considering both Configurations 1 and 2 for the support conditions and all the different lateral confinement conditions (wooden panels, Plexiglass panels, cut Plexiglass panels and no panels).

Test n.	Description:	PTA [g]	Direction	Frequency [Hz]	Damp. Ratio [%]
64	Random test	0.03g	x-direction	$f_r=17$	11.18
		0.03g	y-direction	$f_r=17$	9.68
		0.05g	x-direction	$f_r=15$	13.14
		0.10g		$f_r=12.4$	18.93
		0.20g		$f_r=10.4$	17.15
		0.30g		$f_r=9.5$	22.69
		0.40g		$f_r=8.8$	28.91
		0.5g		$f_r=7.7$	27.02
		0.6g		$f_r=6.9$	50.54
73	Random test	0.03g	x-direction	$f_r=14.95$	11.09
74		0.03g	y-direction	$f_r=14.84$	11.17
75		0.05g	x-direction	$f_r=13.57$	13.65
76		0.10g		$f_r=11.58$	17.51
77		0.20g		$f_r=10.13$	20.09
78		0.03g		$f_r=14.8$	11.78
79	Sinusoidal test-10 cycles	0.25g	x-direction	50	
80				20	
81				15	
82				10	
83				8	
84				5	
85				3	
86				2	
87				1	
88	Random test	0.03g	x-direction	$f_r=14.02$	13.25
89	Sinusoidal test-10 cycles	0.50g	x-direction	50	
90				20	
91				15	
92				10	
93				8	
94				5	
95				3	
96				2	
97				1	
98	Random test	0.03g	x-direction	$f_r=14.5$	14.20
99	Sinusoidal test-10 cycles	0.75g	x-direction	50	
100				20	
101				15	
102				10	
103				8	
104				5	
105				3	
106				2	
107	Random test	0.03g	x-direction	$f_r=13.83$	14.93
108	Sinusoidal test-100 cycles	0.75g	x-direction	5	
109				3	
110	Random test	0.03g	x-direction	$f_r=15.16$	14.58
111		0.20g	x-direction	$f_r=10.5$	36.99
112	Sinusoidal test-100 cycles	0.75g	x-direction	5	
113				5	
114				5	
115				5	
116				5	
117				5	
118	Sinusoidal test-100 cycles	0.75g	x-direction	5	Collapse

Test n.	Description:	PTA [g]	Direction	Frequency [Hz]	Damp. Ratio [%]
119	Random test	0.03g	x-direction	$f_r=14.77$	11.63
120		0.03g	y-direction	$f_r=14.2$	11.25
121	Sinusoidal test-10 cycles	0.10g	x-direction	3	
122	Random test	0.03g		$f_r=14.9$	11.50
123	Sinusoidal test-10 cycles	0.20g		3	
124	Random test	0.03g		$f_r=14.85$	11.71
125	Sinusoidal test-10 cycles	0.30g		3	
126	Random test	0.03g		$f_r=14.87$	11.01
127	Sinusoidal test-10 cycles	0.40g		3	
128	Random test	0.03g		$f_r=14.62$	12.14
129	Sinusoidal test-10 cycles	0.50g		3	
130	Random test	0.03g		$f_r=14.4$	12.03
131	Sinusoidal test-10 cycles	0.60g	x-direction	3	
132	Random test	0.03g		$f_r=14.22$	12.31
133	Sinusoidal test-10 cycles	0.70g		3	
134	Random test	0.03g		$f_r=14.23$	13.29
135	Sinusoidal test-10 cycles	0.80g		3	
136	Random test	0.03g		$f_r=13.84$	13.06
137	Sinusoidal test-10 cycles	0.90g		3	
138	Random test	0.03g		$f_r=12.63$	13.71
139	Sinusoidal test-10 cycles	1.0 g	x-direction	3	Collapse
140	Random test	0.03g	x-direction	$f_r=14.37$	14.22
141		0.03g	y-direction	$f_r=13.88$	11.58
142	Sinusoidal test-10 cycles	0.90g	x-direction	3	
143	Sinusoidal test-10 cycles	1.0 g	x-direction	3	Collapse
144	Random test	0.03g	x-direction	$f_r=11.99$	16.94
145		0.03g	y-direction	$f_r=13.34$	11.33
146	Random test	0.03g	x-direction	$f_r=7.4$	19.13
147		0.03g	y-direction	$f_r=13.29$	11.34
148		0.05g	x-direction	$f_r=6.0$	19.81
149		0.10g		$f_r=5.2$	15.89
150		0.15g		$f_r=4.87$	24.76
151		0.03g		$f_r=6.88$	20.5
152	Sinusoidal test-10 cycles	0.10g	x-direction	50	
153				20	
154				15	
155				10	
156				8	
157				6	
158				5	
159				4	
160				3	
161				2	
162				1	
163	Random test	0.03g	x-direction	$f_r=6.48$	25.41
164	Sinusoidal test-10 cycles	0.25g	x-direction	50	
165				20	
166				15	
167				10	
168				8	
169				6	
170				5	
171				4	
172				3	
173	Sinusoidal test-10 cycles	0.25g	x-direction	2	Part. Collapse
174	Sinusoidal test-30 cycles	0.25g	x-direction	2	Collapse

Test n.	Description:	PTA [g]	Direction	Frequency [Hz]	Damp. Ratio [%]
175	Random test	0.03g	x-direction	$f_r = 7.07$	17.49
176		0.03g	y-direction	$f_r = 13.86$	9.44
177	Sinusoidal test-10 cycles	0.05g	x-direction	3	
178	Random test	0.03g		$f_r = 7.04$	17.15
179	Sinusoidal test-10 cycles	0.10g		3	
180	Random test	0.03g		$f_r = 6.87$	16.93
181	Sinusoidal test-10 cycles	0.15g		3	
182	Random test	0.03g		$f_r = 5.66$	20.86
183	Sinusoidal test-10 cycles	0.20g		3	
184	Random test	0.03g		$f_r = 6.42$	22.81
185	Sinusoidal test-10 cycles	0.25g		3	
186	Random test	0.03g		$f_r = 6.23$	23.25
187	Sinusoidal test-10 cycles	0.30g	3		
188		0.35g			
189		0.4g			
190		0.45g			
191	Sinusoidal test-10 cycles	0.50g	x-direction	3	Part. Collapse
192		0.60g		3	Part. Collapse
193		0.75g		3	Collapse
194	Sinusoidal test-100 cycles	1.0g	x-direction	3	Collapse
195	Random test	0.03g	x-direction	$f_r = 7.24$	15.69
196		0.20g	y-direction	$f_r = 12.69$	10.78
197	Sinusoidal test-500 cycles	0.20g	x-direction	3	
198		0.20g	x-direction	3	
199	Repaired Vault				
200	Sinusoidal test-500 cycles	0.20g	x-direction	3	
201					
202					
203					
204	Random test	0.03g	x-direction	$f_r = 6.3$	13.08
205		0.03g	y-direction	$f_r = 10.5$	10.50
206		0.05g	x-direction	$f_r = 5.4$	13.66
207		0.05g	y-direction	$f_r = 9.97$	10.48
208		0.10g	x-direction	$f_r = 4.75$	17.36
209		0.10g	y-direction	$f_r = 8.8$	13.31
210		0.15g	x-direction	$f_r = 3.9$	23.89
211		0.15g	y-direction	$f_r = 8.3$	13.86
212		0.03g	x-direction	$f_r = 6.47$	16.22
213		0.03g	y-direction	$f_r = 10.8$	10.22
214	Sinusoidal test-10 cycles	0.10g	x-direction	50	
215				20	
216				15	
217				10	
218				8	
219				6	
220				5	
221				4	
222				3	
223				2	
224	Sinusoidal test-30 cycles	0.10g	x-direction	1	
225	Random test	0.03g	x-direction	$f_r = 6.45$	20.72
226	Sinusoidal test-10 cycles	0.25g	x-direction	50	
227				20	
228				15	
229				10	
230				8	
231				6	
232				5	
233				4	
234				3	
235	Sinusoidal test-10 cycles	0.25g	x-direction	2	Part. Collapse
236	Sinusoidal test-30 cycles	0.25g	x-direction	2	Collapse
237	Random test.	0.03g	y-direction	$f_r = 9.40$	9.49
238		0.03g	x-direction	$f_r = 4.8$	48.79
239		0.05g	y-direction	$f_r = 8.7$	8.89
240		0.05g	x-direction	$f_r = 4.6$	17.06
241		0.10g	y-direction	$f_r = 7.6$	11.91
242		0.10g	x-direction	$f_r = 3.71$	15.02
243		0.15g	y-direction	$f_r = 6.65$	10.32
244		0.15g	x-direction	$f_r = 3.98$	17.93
245	Sinusoidal test-10 cycles	0.10g	y-direction	5	
246			x-direction	5	
247			y-direction	3	
248			x-direction	3	
249			y-direction	2	
250	Random test	0.03g	x-direction	2	
251			y-direction	$f_r = 10.12$	8.93
252	Sinusoidal test-10 cycles	0.05g	y-direction	$f_r = 5.27$	12.91
253			x-direction	3	
254	Random test	0.03g	y-direction	$f_r = 10.16$	8.83
255	Random test	0.03g	x-direction	$f_r = 5.4$	9.23
256	Sinusoidal test-10 cycles	0.10g	y-direction	3	
257	Sinusoidal test-10 cycles	0.10g	x-direction	3	Part. Collapse
258	Random test	0.03g	y-direction	$f_r = 9.78$	9.27
259	Random test	0.03g	x-direction	$f_r = 5.6$	
260	Sinusoidal test-10 cycles	0.15g	x-direction	3	Part. Collapse
261		0.20g		3	Part. Collapse
262		0.25g		3	Part. Collapse
263		0.30g		3	Part. Collapse
264	Sinusoidal test-10 cycles	0.40g	x-direction	3	Collapse

Table 40: List of tests performed in the second session (January/February 2020)

6.5.6 Observation during testing: dynamic properties

Random signals have been systematically carried out in order to get the dynamic properties of the vault model.

The vault was tested up to collapse many times and then rebuilt. After each reconstruction, low-amplitude (0.03g) random tests were conducted that highlighted the substantial equivalence, in terms of fundamental frequency and damping ratio, of the later construction with respect to the previous one.

The vault was also built according to different support and boundary conditions. Figure 311 displays the fundamental frequency of the vault as function of the Peak Table Acceleration (PTA) for all the

investigated configurations. In all cases, the plots indicate that the fundamental frequency decreases with increasing acceleration. Also, as expected, Configuration 2 (two moveable springs) is characterised by significantly reduced frequency values. Finally, the vaults without panels are more flexible, providing frequency values roughly equal to half of those of the corresponding confined vaults. This strong non-linear dynamic behaviour of the tested model could be explained by noting that during the motion, especially for increasing accelerations, detachments between the bricks occurred in many places, thus leading to an "equivalent/effective" Young modulus of the vault which continuously changed in time and space. On the average, calibration on the recorded frequencies carried out with linear Finite Element models shows that the effective Young's modulus of the vault, when considered as being made of an equivalent elastic material, is comparable with that of the gum layer (0.8-1.0 N/mm²).

Figure 312 illustrates the damping ratio as function of the PTA for all the investigated configurations. Firstly, in general, very high values of damping ratios were obtained (around 10% or larger), due to the considerable dissipative properties of the gum layer. Secondly, the damping ratio increases with the acceleration, due to the large movements and detachments between the bricks. Configuration 2 provides larger values with respect to Configuration 1, for which, at low acceleration levels (0.05g), the effect of the confinement panels seems to be more significant.

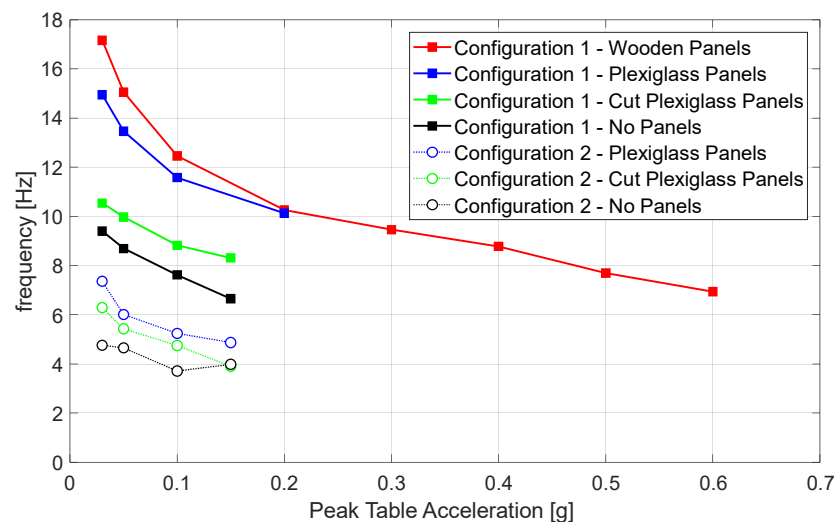


Figure 311: Frequency as a function of acceleration for Configuration 1 and Configuration 2

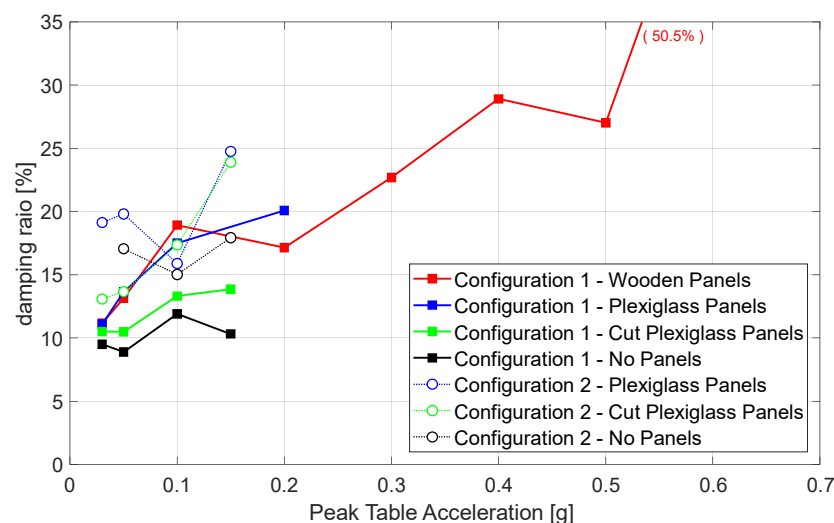


Figure 312: Damping ratio as a function of acceleration for Configuration 1 and Configuration 2

6.5.7 Preliminary results: collapse behaviour and numerical modelling

Firstly, simple inspection of Table 39 and Table 40 allows the following observations to be made.

All other conditions being kept the same (i.e. same lateral confinement given by the Plexiglass panels), Configuration 2 (differential horizontal shear displacements at the supports through two moveable springs) reached the collapse condition, for low-frequency excitation, for a lower acceleration (around 0.4g, as a sound average between total collapse at 0.25g for 2 Hz input and partial collapse at 0.6g for 3 Hz input) than that of Configuration 1 (around 1.0g for 2Hz input). This underlines that the pseudo-static response of the vault induced by imposed shear displacements at its springings often represents the predominant cause of damage/failure, overshadowing the dynamic response of the vault itself.

The analyses on the cumulative displacements within the different series of tests and the collapse accelerations obtained in test n. 139 (collapse after cumulative damage due to several sinusoidal input) and test n. 143 (imposing directly the previously collapse acceleration) show that the vault made of plastic mortar bricks with gum-layer interfaces is not particularly susceptible to cumulative damage.

The vault seemed to be more vulnerable to low-frequency harmonic input than to seismic input. As a matter of fact, tests n. 56 to 60 (applying the acceleration recorded during the earthquakes of: Mirandola and Modena 2012 and El Centro 1940) did not produce any visible damage on the model.

Then, the time-history of the displacements obtained by the Vision data system for each marker were analysed for specific portions of the vaults (such as the lateral arches) or specific elements (such as the keystone), in order to: (i) obtain the maximum displacement recorded during every test, (ii) evaluate the cumulative displacements before collapse within the different test sequences, and (iii) calibrate the Discrete Element Models (DEM) and Finite Element Models (FEM).

With regards to the first session of tests, the physical model was vulnerable to low frequencies, especially near 2Hz, whose maximum induced displacements far exceed the displacements produced by inputs of higher frequencies and same accelerations (Figure 313). Keystone maximum relative displacements (with respect to the table) to frequency inputs such as 50Hz, 20Hz or 15Hz exhibit an almost horizontal asymptotic behaviour as the acceleration increases and can be considered small. Inputs with frequencies between 5Hz and 10Hz produced maximum displacements that increase “linearly” with acceleration. Inputs of 2Hz induced large movements (unexpected amplification), which could indicate that the “natural frequency” of the physical model is around that value, at least for large acceleration values (>0.8g).

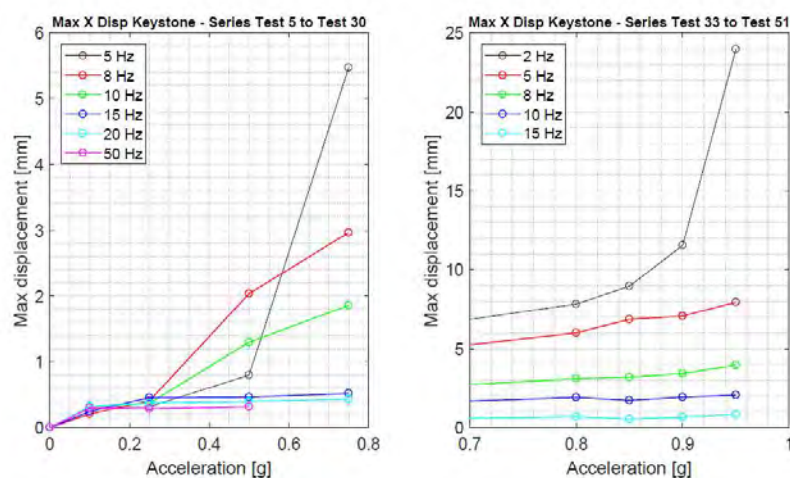


Figure 313: Maximum displacement of the keystone as function of the PTA for sinusoidal input characterized by different frequencies (two series of tests)

Since no reassembly of blocks was done prior to collapse, each test naturally starts from a displaced condition that can be interpreted as a “cumulative damage” state. Figure 314 and Figure 315 show the cumulative displacement of the keystone for the tests sequences before collapse at PTA of 0.75g and 0.95g, respectively. In the horizontal direction (X, the one of the applied input), the cumulative displacement before the last test of the first sequence is around 1.5 mm, while in the vertical direction (Z) it is 13.5 mm. For the second sequence, displacements seem to be higher than in the first one (i.e., 2.8 mm in the horizontal and 57 mm in the vertical direction, respectively).

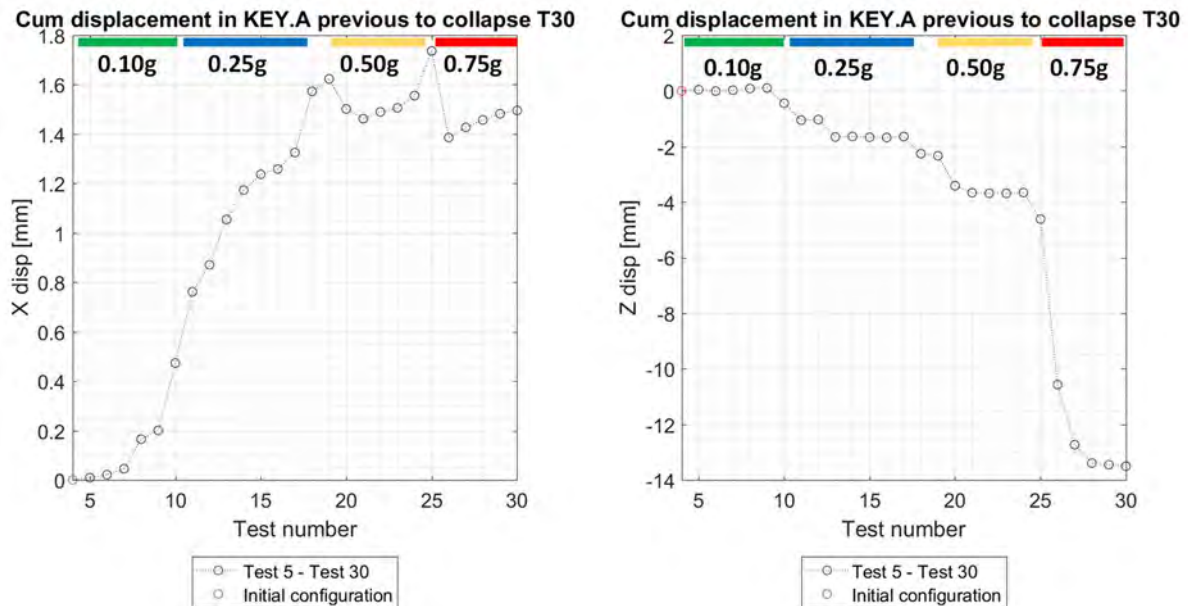


Figure 314: Cumulative displacement series T4 – T30 in X and Z directions

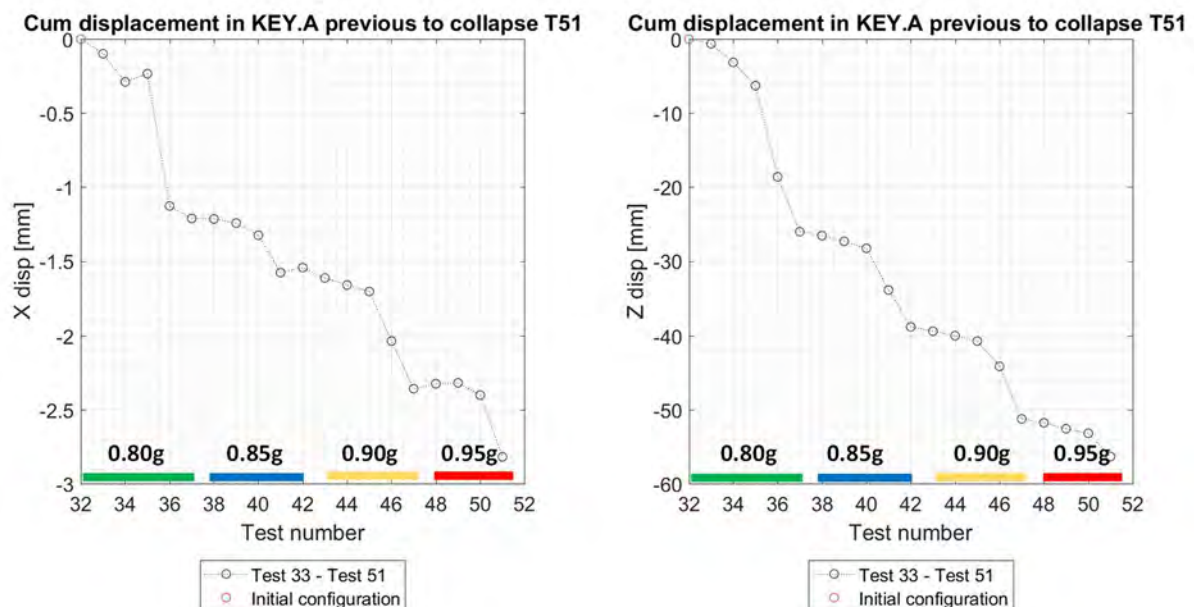


Figure 315: Cumulative displacement series T33-T51 in X and Z directions

The seismic response of the physical model, in terms of cracks opening, collapse behavior and displacements of the blocks, was investigated through Discrete Element (DE) modelling by means of the software Three-Dimensional Universal Distinct Element Code (3DEC) (Itasca, 2004).

The vault is modelled as an assemblage of rigid blocks with elasticity concentrated in the joints (Figure 316a). No tensile strength is considered.

Considering an "equivalent/effective" elastic modulus of the vault, result of the mortar-skin-gum interaction, of $E_b = 3.7 \text{ N/mm}^2$, Figure 316c and Figure 317 display the failure mechanisms and the displacements of the keystone as obtained from the DEM model and the vision data system for the harmonic excitation of frequency 2Hz with a PTA equal to 0.95g, respectively. It can be noticed that the DEM model is able to well numerically reproduce the experimentally detected global response, in terms of cracking pattern before collapse.

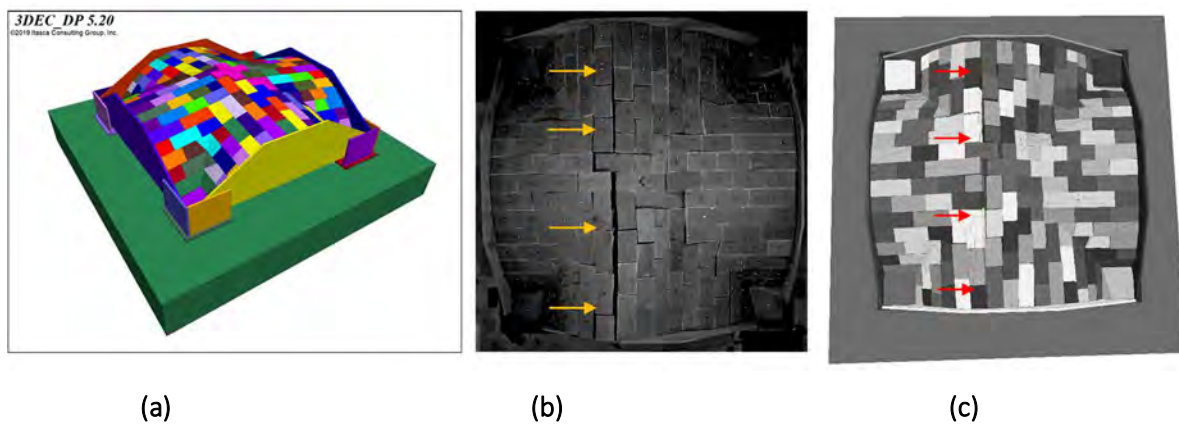


Figure 316: (a) DEM model of the tested vault. (b) Failure mechanism (hinges before collapse occurred in Test n. 52) as observed on the physical model. (c) Failure mechanism as reproduced by DEM model

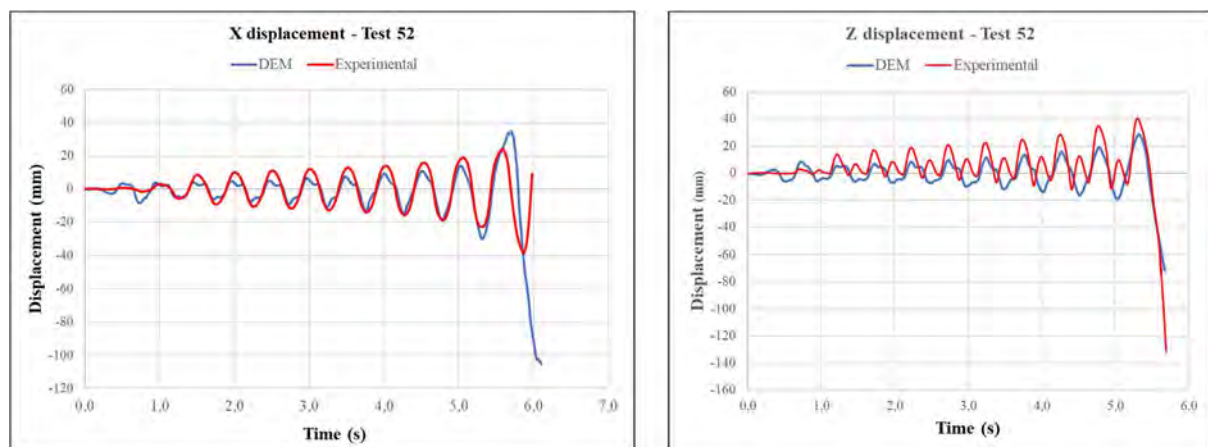


Figure 317: Displacement comparison DEM and experimental: Test 52

The data recorded during the experimental campaigns were also compared with the results of calibrated Finite Element models developed by SAP2000 software. The FE models were built on the continuum-based approach, where structures are conceived as continuous bodies having homogeneous mechanical characteristics such as elasticity and density.

For sake of brevity, and with reference to the second session of tests, only some results obtained from the FE model of the groin vault with springs at the base and no panels are here presented (Figure 318). An iterative procedure has been used to calibrate the elastic modulus of the equivalent material the vault is made of on the basis of the experimental frequencies recorded during the random tests (tests n. 237 to 244, see black dotted line in Figure 311). The equivalent elastic modulus to get the expected frequencies turned out to be around $E_b = 6.6 \text{ N/mm}^2$.

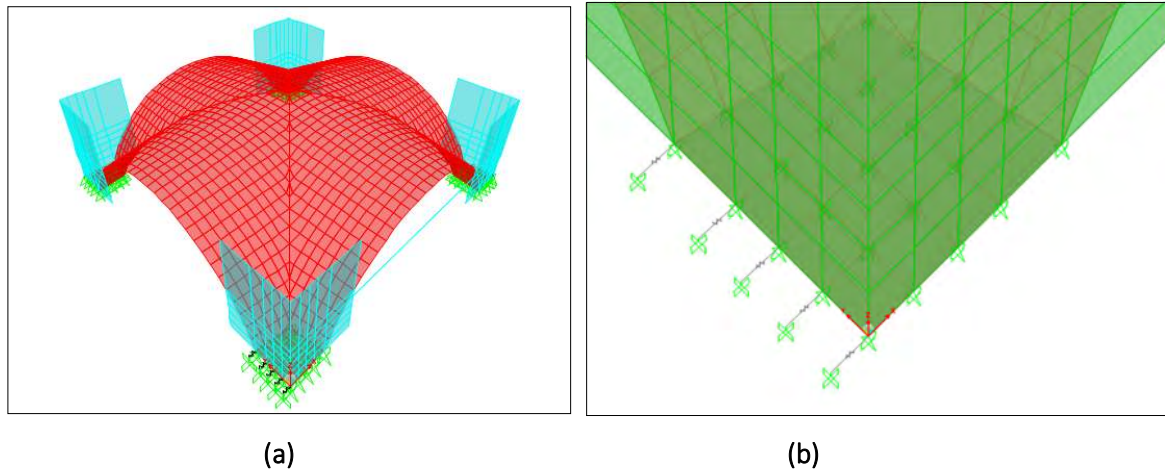


Figure 318: (a) FEM model with two springs at the base and no panels. (b) Details of the springs

Figure 319 displays the x-accelerations and the x-displacements of the keystone as obtained from the FEM model and the vision data system for the harmonic excitation of frequency 3Hz with a PTA equal to 0.10g. Calibrating the model in the movable configuration on the basis of the input acceleration-frequency relationship leads to a good agreement between the experimental and numerical results. The experimental displacement response was characterized by a decreasing trend due to damage accumulation in the real structure. Thus, in order to carry out a sound comparison with the SAP2000 output, as obtained of course with reference to an undamaged model, the experimental signal has been detrended.

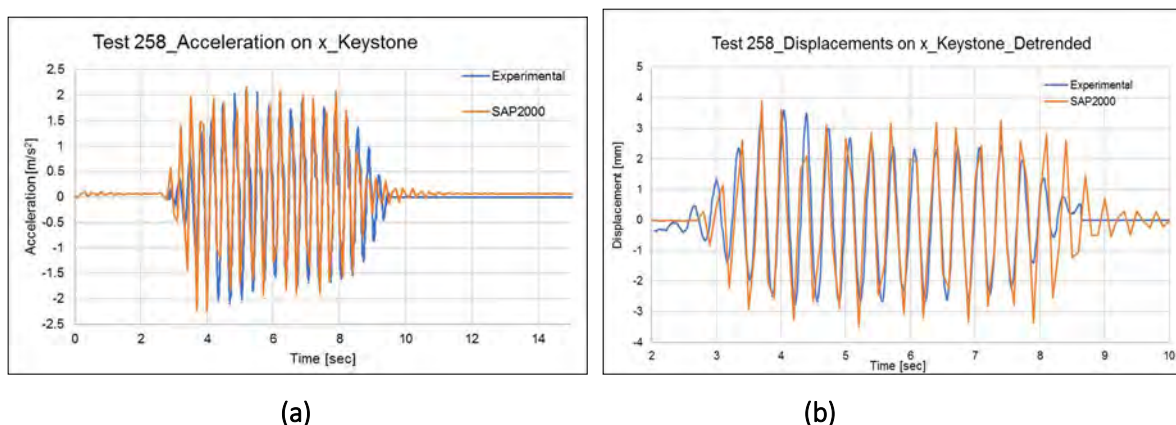


Figure 319: Comparison FEM and experimental data for Test 258: (a) X-acceleration of the keystone and (b) x-displacement of the keystone

6.5.8 Conclusions and outlook

A huge number of shaking table tests was performed on a scaled groin vault model made of plastic 3D printed blocks filled with mortar. The advantages of using 3D printers to manufacture the blocks relate to the workability and the repeatability of the tests: the plastic-mortar blocks can be immediately reused after each test as they are fixed with a gum layer, not fresh mortar.

The vault was built according to two support conditions (on four fixed supports and on two fixed supports and two one-way moveable carriages equipped with lateral springs) and different boundary conditions along the four lateral arches (wooden panels, Plexiglass panels, cut Plexiglass panels and no panels) to account for different confinement levels.

Random signals were systematically carried out in order to get the dynamic properties of the vault model. Harmonic inputs with different frequencies ranging between 1Hz and 50Hz were imposed in one horizontal direction with increasing amplitude, up to collapse. After each construction, low-amplitude (0.03g) random tests were conducted that highlighted the substantial equivalence, in terms of fundamental frequency and damping ratio, of the subsequent construction with respect to the previous one. For sake of completeness, few seismic tests were also performed.

The presence of the gum layer, essential for the rapid reconstruction of the models, has a strong influence on the global behaviour and seems to govern the dynamic response of the structure, especially for high-acceleration and low frequency harmonic inputs. The results of the experimental campaign revealed a tendency to activate different stiffness for each PTA level and each frequency, which indicates a strongly non-linear behaviour.

The most important results that may provide insight to the general dynamic behaviour of vault structures can be summarised as follows:

1. The fundamental frequency of the vault model decreases with increasing acceleration.
2. All other conditions being equal, Configuration 2 (differential horizontal shear displacements at the supports through two moveable springs) reaches the collapse condition for a lower acceleration than that of Configuration 1. This underlines that the pseudo-static response of the vault induced by imposed shear displacements at its springings often represents the predominant cause of damage/failure, overshadowing the dynamic response of the vault itself, justifying the need for this series of tests, which are often not considered in similar seismic tests.
3. The analysis of the cumulative displacements and the collapse acceleration values show that the vault made of plastic mortar bricks with gum-layer interfaces is not particularly susceptible to cumulative damage.
4. The vault with these specific geometry and support conditions seems to be more vulnerable to low-frequency (resonance) harmonic input as compared to seismic input.
5. The construction phases, as well as the fact that the seismic response of the vault with no panels along the lateral arches is similar to that of the vault weakly confined through the Plexiglass panels, indicate that the corner areas close to the springings are the critical ones, upon which attention should be paid to get static stability and higher seismic performances. This response is well known since ancient times, when past repairs showed that these portions were constantly strengthened in order to be better embedded in the surrounding vertical masonry structures.

6.5.9 References

- Croci, G. (1998). The Collapses Occurred in the Basilica of St Francis of Assisi and in the Cathedral of Noto. Structural Analysis of Historical Constructions II. Barcelona: CIMNE.
- Piermarini, E. (2013). The Dynamic Behavior of the Basilica of San Francesco of Assisi. Master Thesis. Massachusetts Institute of Technology.
- Cancino, C. (2009). Estudio de daños a edificaciones históricas de tierra después del terremoto del 15 de agosto del 2007 en Pisco, Perú. The Getty Conservation Institute, Los Angeles: J. Paul Getty Trust 2011.
- Acland JH (1972). Medieval structure: the Gothic vault. Toronto: University of Toronto Press.
- Fitchen J (1961). Construction of Gothic cathedrals: a study of medieval vault erection. Oxford: At the Clarendon Press.
- Foti, D., Vacca, V., Facchini, I. (2018). DEM modelling and experimental analysis of the static behavior of a dry-joints masonry cross vaults, Construction and Building Materials, 170, 111-120.
- Foti, D., Lerna, M., Sabbà, M.F., Vacca, V. (2019). On the collapse behavior of a wood arch made with modular hollow blocks. WSEAS Transactions on Environment and Development 15, Article number 31, 279-287.
- Diaferio, M., Dassisti, M., Foti, D., Vacca, V. (2019). Analysis of a Mock-Up of a New Sustainable Easy-Assembling Modular Arch. Structures, 19, 309-321.
- Carfagnini, C., Baraccani, S., Silvestri, S., Theodossopoulos, D. (2018). The effects of in-plane shear displacements at the springings of Gothic cross vaults. Construction and Building Materials, 186, 219–232.
- Itasca C.G. (2016). Distinct Element Modeling of Jointed and Blocky Material in 3D. Code Version 5.2. 3DEC Manual.

6.6 Project #35 – SHATTENFEE - SHAKing Table Testing for Near Fault Effect Evaluation (SHATTENFEE)

Authors

A.L. Simonelli⁽¹⁾, M. Fragiadakis⁽²⁾, A. Gajo⁽³⁾, A.M. Kaynia⁽⁴⁾, J. de Novais Bastos⁽⁵⁾, G. Anoyatis⁽⁶⁾, L. Di Sarno^(1,7), A. Penna⁽¹⁾, D. Aliperti⁽¹⁾, I. Taflampas⁽²⁾, S. Diamantopoulos⁽²⁾, FG. Esfahani⁽³⁾, P. Kowalczyk⁽³⁾, M. Dall'Acqua⁽¹⁾, F. Fossi⁽¹⁾, E. Marotti⁽¹⁾, F. Zotti⁽¹⁾, R. De Risi⁽⁸⁾, D. Karamitros⁽⁸⁾, M. Dietz⁽⁸⁾, C. Taylor⁽⁸⁾, G. Mylonakis^(8, 9, 10)

⁽¹⁾ University of Sannio, Benevento, Italy.

⁽²⁾ National Technical University of Athens, Athens, Greece

⁽³⁾ DICAM University of Trento, Trento, Italy

⁽⁴⁾ Norwegian Geotechnical Institute, Oslo, Norway

⁽⁵⁾ Faculty of Architecture, University of Lisbon, Lisbon, Portugal

⁽⁶⁾ KU Leuven, Bruges, Belgium

⁽⁷⁾ *University of Liverpool, Liverpool, UK.*

⁽⁸⁾ *Department of Civil Engineering, University of Bristol, Bristol, United Kingdom*

⁽⁹⁾ *Department of Civil Engineering, Khalifa University, U.A.E.*

⁽¹⁰⁾ *University of California at Los Angeles (UCLA), U.S.A.*

6.6.1 Introduction

Recent surveys conducted after destructive earthquakes demonstrated that, in near-fault conditions, combined vertical and horizontal motions caused unusual damage to geotechnical and structural systems. The investigation of vertical ground motion, mono-dimensional propagation, and the ensuing soil-structure interaction is still scarce; therefore, this project aimed at investigating the soil response for near-fault response. To do so, the vertical dynamic behaviour of a typical soil deposit, with and without the presence of a foundation pile, has been explored experimentally on the 6-Degree-of-Freedom shaking table at the University of Bristol. A newly designed soil container has been utilized to analyse experimentally the vertical wave propagation.

The SHATTENFEE project was carried out to investigate experimentally the following learning outcomes (LOs):

1. Vertical response analysis of a typical soil column, e.g., estimation of natural frequency and amplification, vertical frequency variation due to densification induced by prolonged shaking;
2. Validation of numerical and theoretical models based on a reliable experimental database;
3. Potential nonlinear effects due to increased amplitude of input;
4. Assessment of the effects of the response of a piled foundation – SSI response.

The main objective of the above LOs includes the vertical dynamic identification/response of the soil model. Hence the experimental investigation mainly focused on the vertical dynamic behaviour in free-field conditions considering the following fundamental response quantities:

- fundamental vertical period of vibration (T_v);
- compression wave velocity (V_p);
- verification of the theoretical formulations correlating T_v , V_p and soil height H ;
- vertical amplification amount (A_v).

Particular attention is paid to the definition of the test phases (as described in Section 6.6.7). Focal points have been the input signal type (i.e. white noise, harmonic input, and natural earthquake records), the input characteristics (i.e. duration, frequency and intensity), the identification of the dynamic response of the model, taking into account the soil-container interaction. Additionally, tests were also carried out on the empty cylindrical container.

The characterization of the vertical dynamic response was developed both experimentally and numerically. An extensive preliminary analytical study was carried out; the results are illustrated in Section 6.6.8. The observations obtained from the testing phases are described in Section 6.6.7. The advanced experimental activity, the large dataset collected during the numerous shake table tests, and the analysis results provide insights for the understanding of the soil response. Such results can guide further research to improve the study of the seismic near-fault effects and may lead to guidelines and pre-code documents.

6.6.2 Identification of prototype and preliminary analysis

The first step of the present experimental work was the identification of the prototype. It consists of a 30 m thick homogeneous subsoil (Figure 320). This prototype was subsequently scaled to fit the capabilities of the experimental facility at the University of Bristol. To do so, several parametric analyses were conducted.

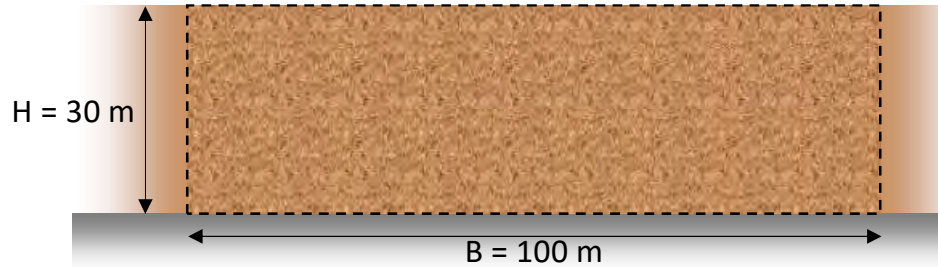


Figure 320: indefinite homogeneous subsoil prototype on horizontal bedrock

The preliminary numerical analyses were conducted on a cylindrical container (i.e. the model); this selection allows to reproduce reliably the free-field conditions of the prototype during the experimental tests. A parametric analysis was conducted to investigate the response of the cylindrical container by varying the size (e.g., diameter) and the boundary conditions (e.g. interaction between soil and container).

The soil was modelled as an elastic medium since the aim of the analyses was to investigate the soil response at low deformations. Mechanical properties were defined according to the elasticity theory, starting from desired values of shear wave velocities V_s , considering a Poisson ratio (ν) of 0.3 and a constant density ρ . In particular, the mechanical parameters are as follows:

- Homogeneous soil: Leighton Buzzard Sand-B (Penna et al., 2016);
- Equivalent Viscous Damping Coefficient $\xi=5\%$;
- Shear wave velocity $V_s = 100$ m/s;
- Soil density $\rho = 2$ t/m³;
- Shear modulus $G = 20$ MPa;
- Young Modulus $E = 52$ MPa;
- Bulk modulus $K = 43.30$ MPa;
- Compressional wave velocity $V_p = 187$ m/s

The relationships used to derive the mechanical properties of the soil are as follows:

$$V_s = \sqrt{G/\rho} \quad E = G \cdot \rho \cdot (1 + \nu) \quad K = E/[3 \cdot (1 - 2 \cdot \nu)] \quad (1)$$

Figure 321(a) shows the geometry of the analysed system; two monitored points, denoted as P0 (input) and P1 (output), are also included in the figure. It is a polar axis symmetry configuration where $H=3$ m and $D=1$ m. The case-study system includes only half of the cylinder; on the left-hand side of the model, a boundary condition modelling the axial symmetry is applied. On the right-hand side of the model boundary, conditions blocking the horizontal displacements (i.e., along x) are assigned. Support boundaries are defined, and the external input is applied at the base of the structural system. The input at P0 point (Figure 321(a)) is a velocity time history (Figure 321(b), up) that excites all frequencies in a specified range, and can be defined by the following expression:

$$f(t) = \sin[2\pi(f_0 + \alpha \cdot t) \cdot t] \quad (2)$$

where f_0 is the initial frequency of the selected frequency range, α is frequency increasing rate, and t is time. The duration of the signal defines the last value of the frequency range. Such a signal, in the frequency domain, gives a constant function between the minimum and maximum values of frequencies (see Figure 321(b), down).

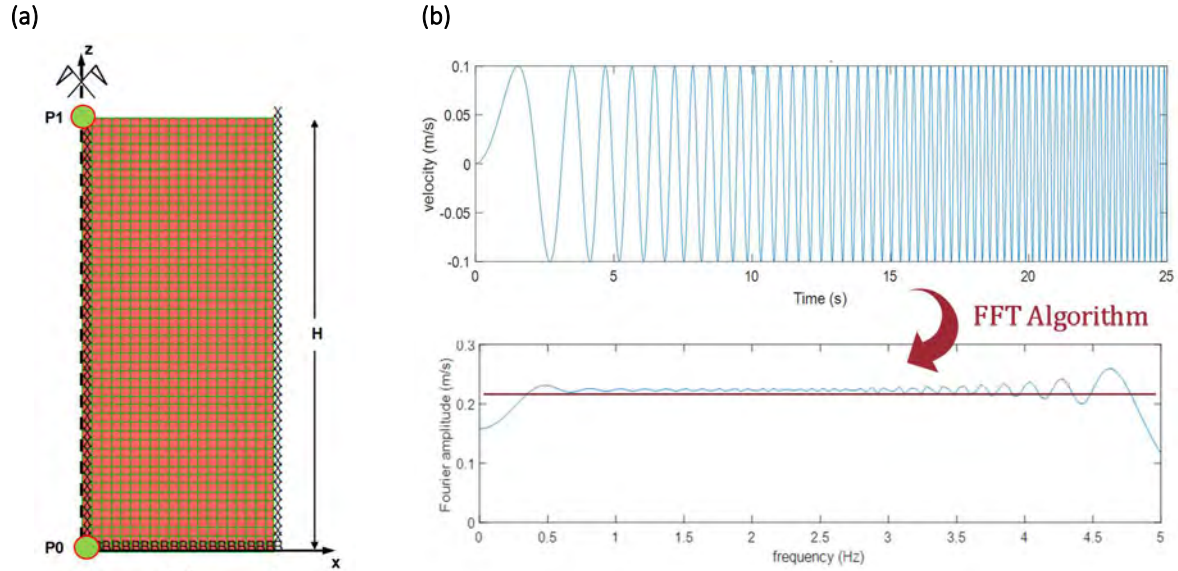


Figure 321: (a) Geometry of the analysed system; (b) Input signal in the time and frequency domain

By recording the response at the point $P1$ in Figure 321 (a) it is possible to calculate the response function (Figure 322).

The maximum amplification is obtained for the first vibration period that is within the working range of the shaking table at the University of Bristol (i.e., 0-100 Hz). Both frequency and maximum amplification are very similar to the values derived with theoretical formulations:

$$f = \frac{V_p}{4 \cdot H} = \frac{187}{4 \cdot 3} = 15,58 \text{ Hz} \quad A_{Max} = \frac{2}{\pi \cdot \xi} = \frac{2}{\pi \cdot 0.05} = 12,73 \quad (3)$$

The above calculations do not account for the effects of friction between soil and external container. The external container is made of PERSPEX[®]. In the literature, the friction angle (f) between sand and plexiglass is given as 15° (O'Rourke et al., 1990). Figure 323 shows the results in terms of the response function for different values of friction angle (f). It is observed that the first frequency is still in the range of values that can be applied by the shaking table at the University of Bristol (i.e., 0-100 Hz).

Based on the combination of the previous parametric analyses and cost-benefit analysis (e.g. economic and technical assessments) the model shown in Figure 324 was selected for the test set-up.

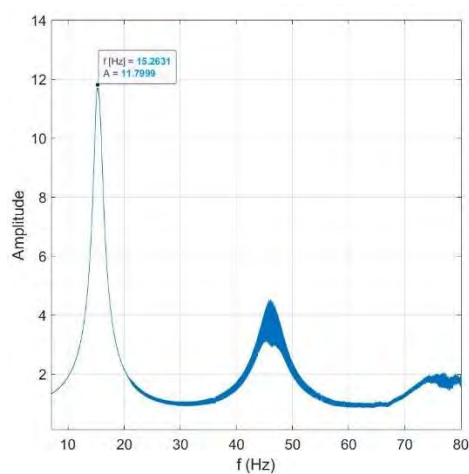


Figure 322: Response function of the case study system

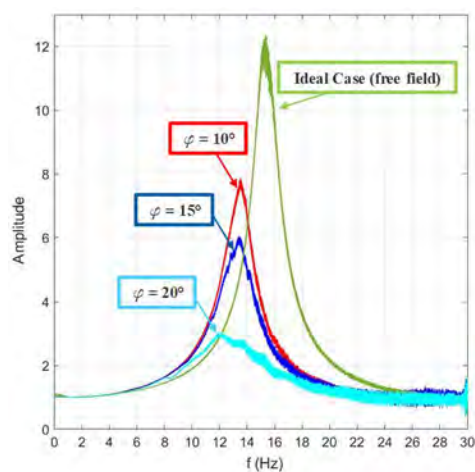


Figure 323: Response functions for different values of the friction angle

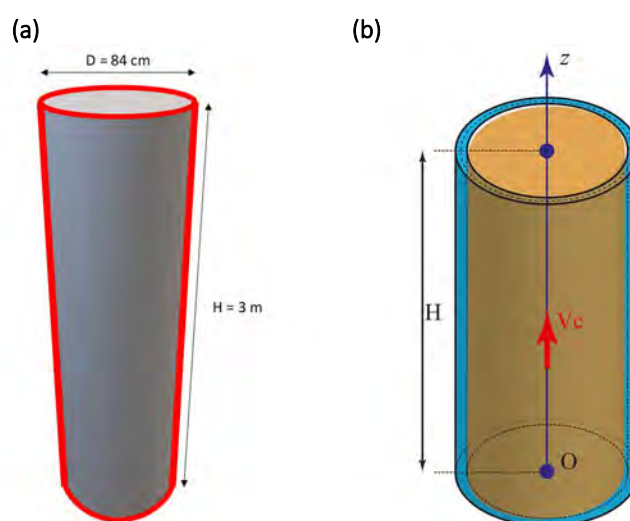


Figure 324: (a) Final model geometry. (b) Reference system

6.6.3 From the Prototype to the Model

Scaling factors - geometry

The prototype shown in Figure 320 is an indefinite soil layer of height $H = 30\text{m}$. The tested models have the geometry schematically represented in Figure 324. Therefore, the resulting geometrical scaling factor for the tested model is 0.1 (scale 1:10).

Scaling factors – Time

For scaling the time, the frequency similitude between the prototype and the model has been accounted for. The dimensionless wave number is:

$$e^{i\left(\frac{\omega H}{V_c}\right)\left(\frac{z}{H}\right)} \quad (4)$$

To keep the similitude between the prototype (the real case study) and the model (the specimen) it is necessary that:

$$\frac{\omega_M H_M}{V_{c,M}} = \frac{\omega_P H_P}{V_{c,P}} \quad (5)$$

where the subscripts M and P indicate the characteristics of the Model and the Prototype, respectively. From equation (5), it is possible to derive:

$$\frac{\omega_M}{\omega_P} = \frac{H_P}{H_M} \frac{V_{c,M}}{V_{c,P}} \quad (6)$$

Therefore, if the scope is to replicate the propagation of the vertical excitation across a column of the soil of 30 m, from equation 5 it follows:

$$\frac{\omega_M}{\omega_P} = \frac{30}{3} \frac{V_{c,M}}{V_{c,P}} = 10 \frac{V_{c,M}}{V_{c,P}} \quad (7)$$

The compression wave velocity can be assumed equal to $V_c = 2V_s$. Therefore:

$$\frac{\omega_M}{\omega_P} = 10 \frac{V_{s,M}}{V_{s,P}} \quad (8)$$

Two cases can be assumed for the scaling: (a) Soft or (b) Stiff soil. For the first case, a V_s of 150 m/s can be assumed. For the second case, a V_s of 300 m/s can be assumed. Therefore, assuming a shear wave velocity for the model of 100 m/s:

$$\frac{\omega_M}{\omega_P} = 10 \frac{100}{150} = 6.7 \quad \text{for soft soil} \quad (9)$$

$$\frac{\omega_M}{\omega_P} = 10 \frac{100}{300} = 3.3 \quad \text{for stiff soil} \quad (10)$$

Based on the above calculations, it was selected 7 and 3 for the soft and stiff soil, respectively. Therefore, it is now possible to calculate the time scale factor as:

$$\frac{t_M}{t_P} = \frac{\omega_P}{\omega_M} = \frac{1}{7} = 0.14 \quad \text{for soft soil} \quad (11)$$

$$\frac{t_M}{t_P} = \frac{\omega_P}{\omega_M} = \frac{1}{3} = 0.33 \quad \text{for stiff soil} \quad (12)$$

6.6.4 Test configuration

Three test configurations, as shown in Figure 325a, b and c, have been tested: (1) cylinder (container) filled with soil, (2) cylinder filled with soil with a 700mm long aluminium pile, (3) empty cylinder. The tests were carried out also on the empty cylinder, to verify that the dynamic response of the whole system is driven by the soil column, and not by the cylindrical container.

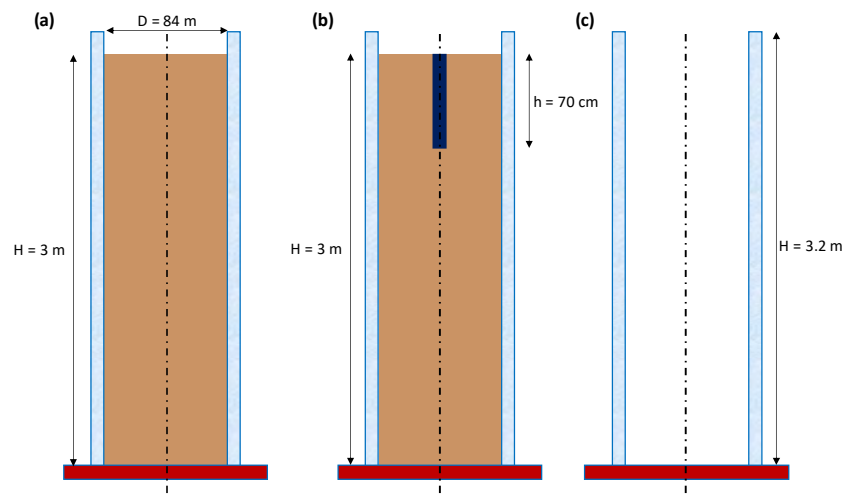


Figure 325: Cylinder (a) filled with homogeneous soil (b) with an aluminium 0.7 m long pile (c) empty

6.6.5 Test rig

The test rig is composed of a PERSPEX® cylinder containing the soil, and a group of metal and rubber components (*e.g.* the bottom plate and the support frame). A cylindrical shape was chosen for the container, to take advantage of the polar symmetry of the system and avoid potential stress concentrations due to other geometric shapes. PERSPEX® material was chosen because it allows observing the soil behaviour during the tests. The PERSPEX® cylinder has an external diameter of 0.9 m and an internal diameter of 0.84 m, being the wall thickness of 3 cm; the wall thickness was designed to ensure the required stiffness and strength, both laterally and axially. The whole container is formed by four cylindrical segments 80 cm long, as shown in Figure 326; hence the real container height is 3.2 m. The metal components are the base plate, consisting of a 1300 mm × 1300 mm aluminium plate. Neoprene rubber gaskets were used to avoid direct contact between the cylinder segments and between the cylinder and the base plate. The cylindrical elements have been provided with flanges at the two ends to allow effective and secure connections. Flanges are 25 mm thick, have a width of 100 mm; 16 M12 holes are realised along the circumference of the flange with an inter-distance of about 195 mm. The M12 stainless steel bolts and nuts have been tightened using additional neoprene washers. The weight of each cylinder element was around 100 kg.

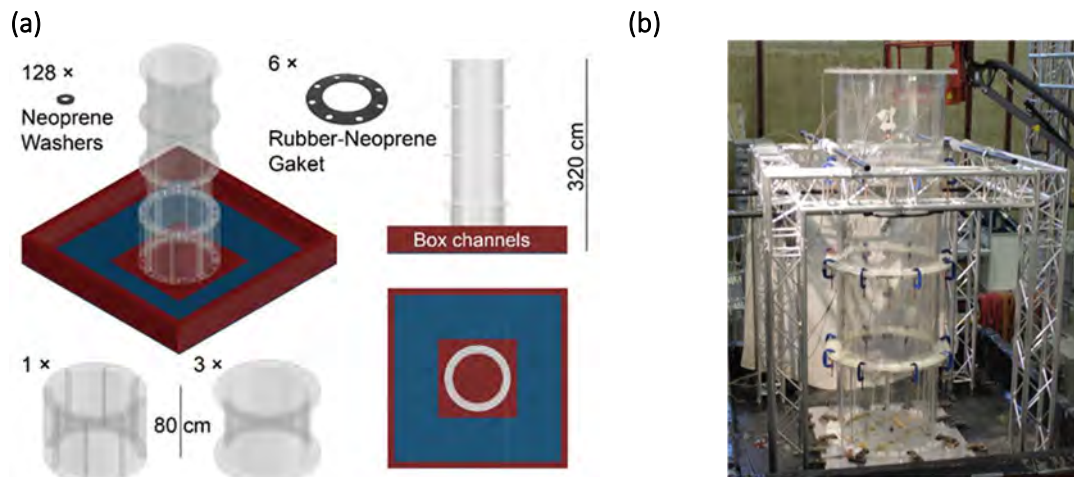


Figure 326: Sketch of the container elements and photo of the whole container located on the table.

6.6.6 Instrumentation layout

The system behaviour was monitored by means of uniaxial and triaxial accelerometers, displacement transducers and flat pressure sensors. The position of the installed sensors is shown in Figure 327.

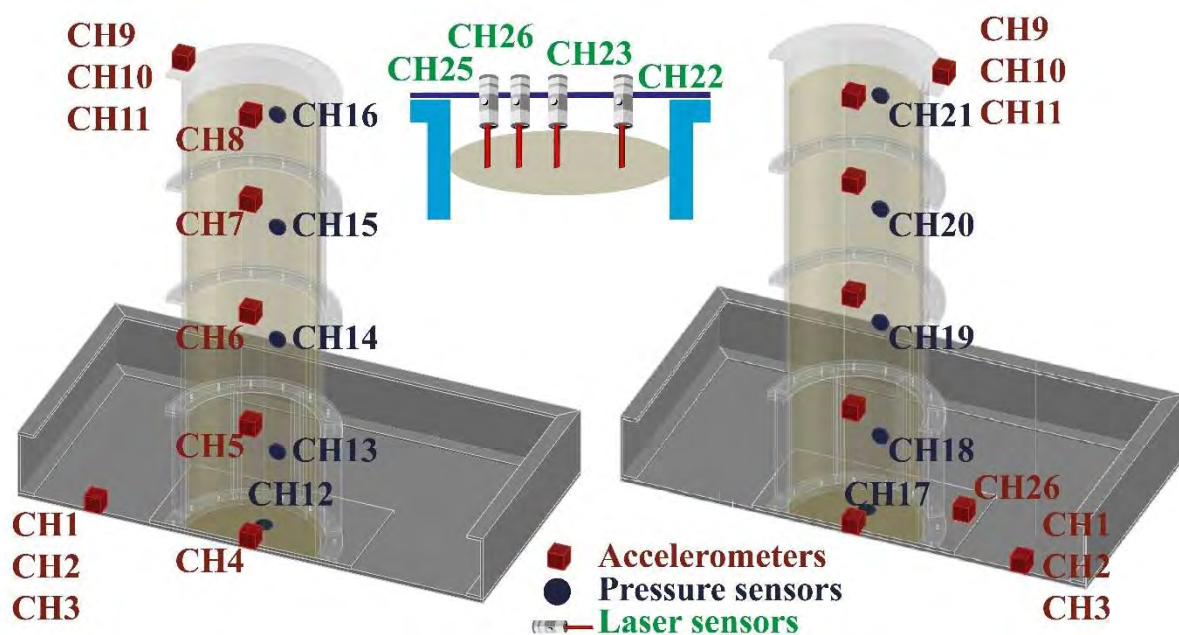


Figure 327: Location of sensors (see Table 42)

One triaxial accelerometer was positioned directly on the table; it is used to record the base input motion for the cylindrical specimen. Five uniaxial vertical accelerometers were located along the vertical axis in the centre of the cylinder: they served to record the vertical response of the soil. Pressure sensors were used to measure the soil pressure against the container surface. Two typologies of sensors were utilised: one has a diameter of 15 mm and can record up to a maximum load of 45N, the other has a diameter of 8 mm and can record up to a maximum of 10N. The first two sensors (CH12-CH17) were applied on the bottom plate, for measuring the vertical pressure of the soil at the column base. Other ten sensors were applied on the wall of the container, 5 along each of two vertical alignments on opposite sides of the wall.

No-contact displacement transducers were located over the top of the soil column, fixed on a support beam, as shown in Figure 328, to monitor the displacement of the soil free surface. The operation range of the transducers is $\pm 100\text{mm}$.

The detailed overview of the measurement channels is reported in the Table 41.



Figure 328: Non-contact displacement transducers (INDIKON type)

Type	Location	Channel Number
ACC	Table, x,y,z	CH1,CH2,CH3
ACC	Sand 1 st section base Z, top z	CH4,CH5
ACC	Sand 2 nd , 3 rd , 4 th section top Z	CH6, CH7, CH8
ACC	Cylinder top, X, y, z	CH9, CH10, CH11
DISPLACEMENT	Z Settlement, -X quarter point, centre	CH22, CH23
DISPLACEMENT	Z Settlement, +X quarter point	CH24
DISPLACEMENT	Z Settlement, +X Boundary	CH25
ACC	Base plate, Z	CH26
ACC	Pile, Z	CH27
Strain	Pile 1 top, middle, bottom	CH28, CH29, CH30
ACC	Cylinder section 2, X, y, z	CH31, CH32, CH33
Pressure		From CH12 to CH21

Table 41: Typology and position of measurement channels

6.6.7 Test phases

A total of 209 tests were carried out during the experimental activity in different phases. A first series of tests were performed in the first phase of the activity, during the construction of the test rig. Four different configurations were tested: only the 1st cylinder segment ($H_{\text{tot}}=0,80\text{m}$, $H_{\text{soil}}=0,75\text{m}$); the first two segments ($H_{\text{tot}}=1,60\text{m}$, $H_{\text{soil}}=1,50\text{m}$); the first three segments ($H_{\text{tot}}=2,40\text{m}$, $H_{\text{soil}}=2,25\text{m}$); the whole cylinder (4 elements, $H_{\text{tot}}=3,20\text{m}$, $H_{\text{soil}}=3,00\text{m}$).

The second series of tests were performed on the final configurations of the soil-container column ($H_{\text{tot}}=3,20\text{m}$, $H_{\text{soil}}=3,00\text{m}$). The third and final series of tests were carried out at the end on the soil-container configuration with an aluminium pile, and the empty cylinder.

Different types of functions and seismic records were adopted as input motion at the base of the cylindrical model. To perform the dynamic identification of the system, vertical noise functions and sweep functions (sinusoidal waveforms) were adopted. The noise functions were applied with very low amplitude (0,01g, 0,03g, 0,05g, 0,1g, 0,015g) and duration of 120 seconds. Even the sweep functions had low amplitude values (0,03g and 0,05g), and were applied at different frequency ranges (60Hz-30Hz, 52Hz-26Hz, 48Hz-35Hz, 35Hz-48Hz, 38Hz-48Hz, 44Hz-50Hz and 35Hz-70Hz). Furthermore, pulse functions with frequencies of 40Hz, 46Hz, 42Hz, 44Hz, 48Hz and 50Hz, amplitude from 1mm to 5mm, and duration 3seconds were applied at the end of the main tests.

To assess the seismic response of the system, natural earthquake ground motions were applied. Three vertical accelerograms were selected from the Italian Strong Motion Network (RAN database); they comprised recent near-fault earthquakes: L'Aquila 2009 (AQK station), Mirandola 2012 (MRN station) and Centro Italia 2016 (AMT station, near Amatrice). The selected accelerograms were recorded at stations located on the ground surface. Hence, they are affected by local soil amplification effects. Therefore, the selected accelerograms were deconvoluted to the bedrock level for each recording site, by means of DEEPSOIL code (Hashash et al., 2016). Some main accelerogram characteristics are summarised in Table 42.

All accelerometric data have been recorded in the time domain; they were then processed both in time and frequency domain.

N.	Event	PGA (m/sec ²)	Station code	Date	Comp.	R_{epi} (km)
1	L'Aquila	3.56	AQK	6/04/2009	VERT.	1.8
2	Mirandola	2.97	MRN	20/05/2012	VERT.	16.1
3	Amatrice	8.50	AMT	08/24/2016	VERT.	8.5

Table 42: Selected accelerograms from Italian Strong Motion Database, where R_{epi} is the epicentral distance

Time scaling factors have been applied according to Section 6.6.3. Figure 329 shows the scaled and un-scaled AQK records and the corresponding Fourier spectra.

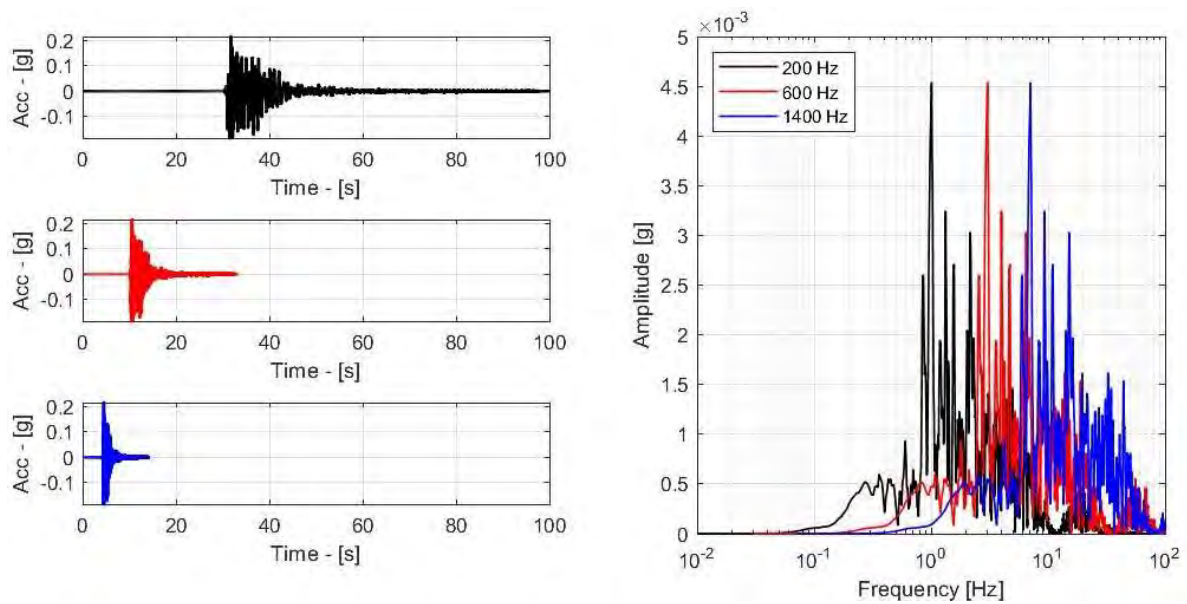


Figure 329: (a) AQR, (b) MRN, and (c) AMT for the employed time scaling factors of 3: 1 (unscaled), 3 and 7, respectively

6.6.8 Preliminary results

Some preliminary results are illustrated hereafter. Such results correspond to the main objectives listed in Section 6.6.1: (i) identification of the fundamental vertical period of vibration (T_v); (ii) measurement of compression wave velocity V_p (for the verification of the theoretical formulas correlating T_v , V_p and soil height H); (iii) evaluation of vertical amplification amount (A_v). To achieve such objectives, only vertical acceleration was utilised as input at the base of the soil-container.

Vertical dynamic identification

Initially, to perform the dynamic identification of the soil column, input motions of very low intensity were applied. Subsequently, dynamic excitations with increasing intensity were applied. The dynamic response is studied by analysing and comparing the acceleration time-histories recorded at different levels of the soil column. Specifically, to identify the natural vertical frequency of the soil model, the ratio between the accelerogram Fourier spectra at the top and at the base of the soil model, i.e. the amplification function, is computed. The main vibration frequency of the soil model is characterised by the maximum amplification of the motion (i.e. the first peak of the amplification diagram). Additional peaks, present in the same diagram, would indicate superior modes of vibration.

An example of vertical dynamic identification is shown in Figure 330, where the results obtained by test number T25 are illustrated. The input motion is a vertical noise function with an amplitude of 0.05g and duration of 120 seconds. In the figure, from left to right, the soil motion at the base (CH4) and at the top (CH8) of the soil model are plotted together (a); then the Fourier spectra of the two motion (b); finally the Amplification function (c). The last diagram clearly shows that the fundamental frequency of the soil column is 46,5 Hz.

This value is practically confirmed by the results of almost all the other test. Figure 331 shows the case where the input is a sweep function with an amplitude of 0.05g, frequency ranging from 33 to 66Hz, duration 220 sec. The amplification function (Figure 331, c) clearly indicates the main frequency equal to 45.3 Hz.

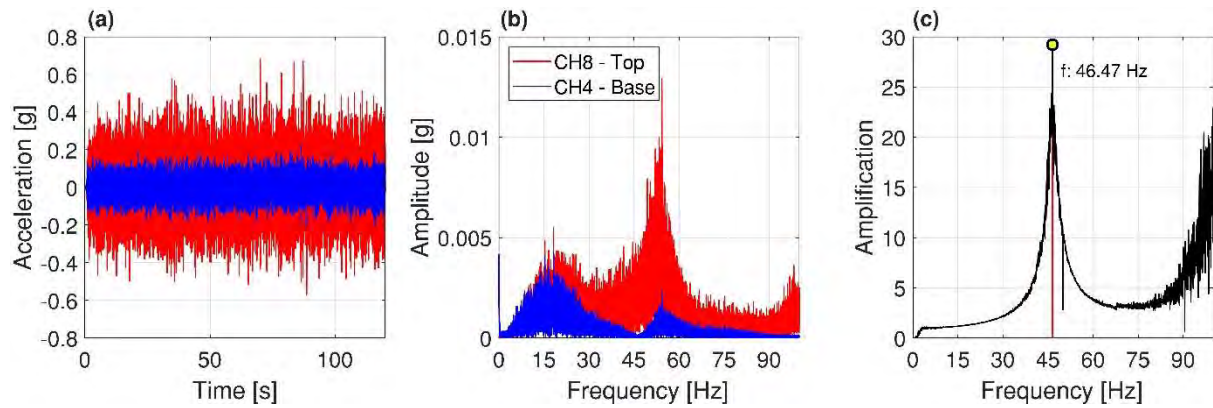


Figure 330: Example of fundamental vertical frequency determination - TEST 25: noise input motion, amplitude 0.05 g, duration 120 sec - (a) Acceleration time-histories at the base (CH4) and top (CH8) of the soil model; (b) Fourier spectra of the two signals; (c) Amplification function and determination of the main frequency f

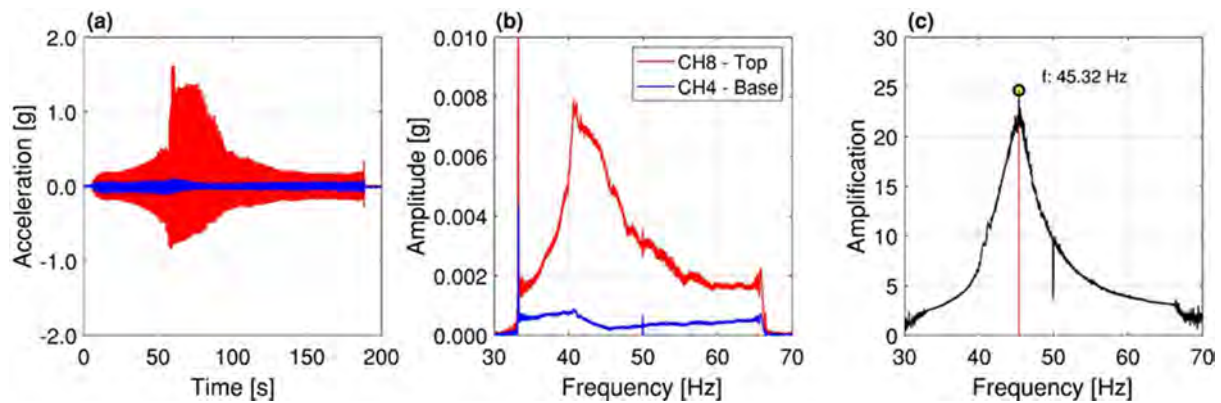


Figure 331: Example of fundamental vertical frequency determination - TEST 30: sweep function, amplitude 0.05 g, frequency range 33-66 Hz; duration 200 sec - (a) Acceleration time-histories at the base (CH4) and top (CH8) of the soil model; (b) Fourier spectra of the two signals; (c) Amplification function and determination of the main frequency f

Compression wave velocity V_p

The compression wave velocities were computed, for deriving the variation in stiffness of the soil during the tests. Starting from the value of V_p , the natural frequency of the soil column was determined by the theoretical formula ($f=V_p/4H$). The latter frequency was then compared with the experimental value with the aim of validating the theoretical approach.

The wave velocity V_p is calculated by measuring the travel time of the accelerometric signal between two points at a given distance. For an accurate determination of the travel time, the cross-correlation has been calculated between two signals.

An example of determination of P wave travel time is given in Figure 332, where the results of the test T19 are illustrated. The input motion is a pulse function with amplitude 1 mm and frequency 45Hz. In the figure, from left to right, the soil motion at the base (CH4) and at the top (CH8) of the soil model are plotted together (a); then the Cross-Correlation function between the two pulse signals is plotted, (b); finally, the two signals are plotted again, with a base shift equal to the time delay, for enhancing the best waveform fitting (c). The time delay is the interarrival that provides the maximum cross-correlation (yellow point in Figure 332b).

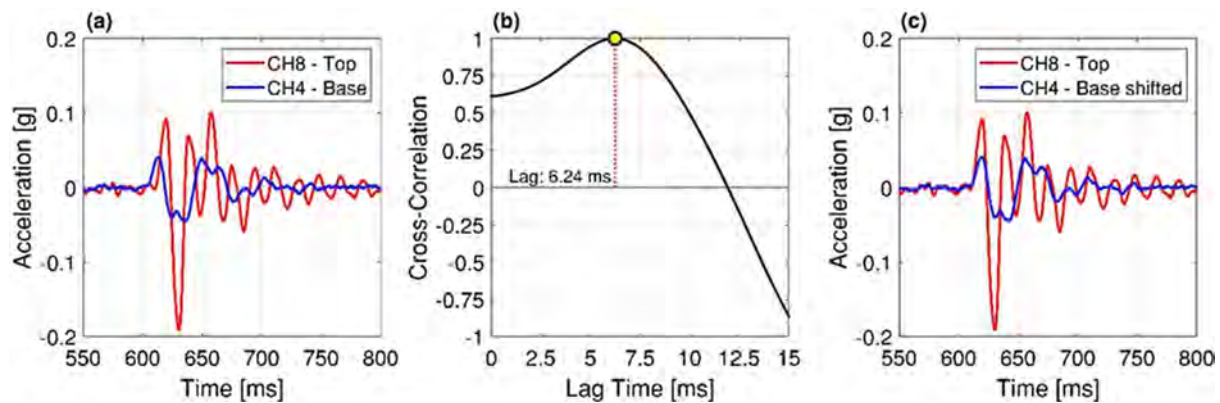


Figure 332: Example of compression wave velocity (V_p) measurement – TEST 30: pulse function, amplitude 1 mm; duration 100 sec - (a) Acceleration time-histories at the base (CH4) and top (CH8) of the soil model; (b) Cross-Correlation function and determination of the time delay (travel time); (c) Representation of the shifted acceleration time histories base shifted

Response in terms of amplification

The vertical amplification effect was evaluated analysing the response of the soil column under seismic input motion, both in the time domain as “amplification coefficient” (the ratio between the peak acceleration on the ground surface and peak acceleration of the input at the base) and in the frequency domain. (the amplification function between the two accelerograms at the top and the base of the soil column was utilized).

An example of vertical amplification evaluation is given in Figure 333, where the results obtained by test T45 are illustrated. The input motion is a scaled accelerogram (total duration 20 seconds) obtained by L’Aquila 2009 earthquake (AQK station). In the figure, from left to right, the soil motion at the base (CH4) and the top (CH8) of the soil model are plotted together (a). Then the Fourier spectra of the two accelerograms are plotted (b). The Amplification function in (c) shows a maximum amplification of about 12.6 in correspondence of 49 Hz, which represents the main frequency of the soil column. Hence, even if the input motion has a frequency content that is quite far from the main frequency of the soil, the amplification effect is significant, both in terms of “amplification coefficient” and “amplification function”.

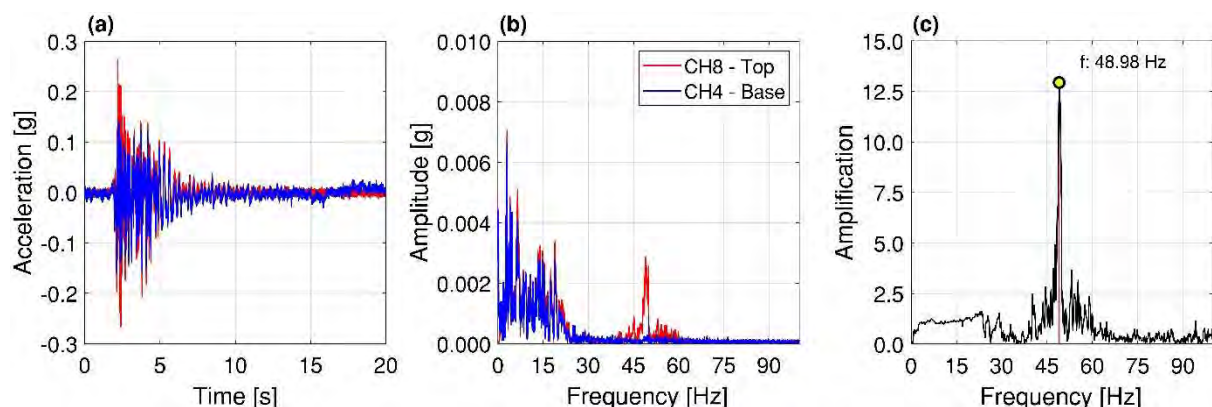


Figure 333: Example of vertical acceleration amplification - TEST 45: L’Aquila 2009 earthquake (AQK station, UP component): input accelerogram scaled to a total duration of 20 sec - (a) Acceleration time-histories at the base (CH4) and top (CH 8) of the soil model: the amplification factor between the two signals is about 1.7; (b) Fourier spectra of the two signals; (c) Amplification function, with a maximum amplification of 12.6 for the main frequency component at 49.0 Hz (the main frequency of the system is clearly indicated by the amplification function)

The amplification of the vertical motion is even more evident by a different representation of test T45 results. In Figure 334 the acceleration time-histories recorded along the soil height are plotted all together, in a window of only ten seconds for better distinguish the different waveform: the motion at the base (CH4), at three intermediate levels (CH5, CH6 and CH7) and on the top of the soil model (CH8). The acceleration values of the time histories increase towards the top surface. In particular, the peak value of each signal is plotted against the column height in (b). The acceleration diagram starts from about 0.152g at the base and reaches the value of 0.268g, exhibiting an increasing gradient towards the surface.

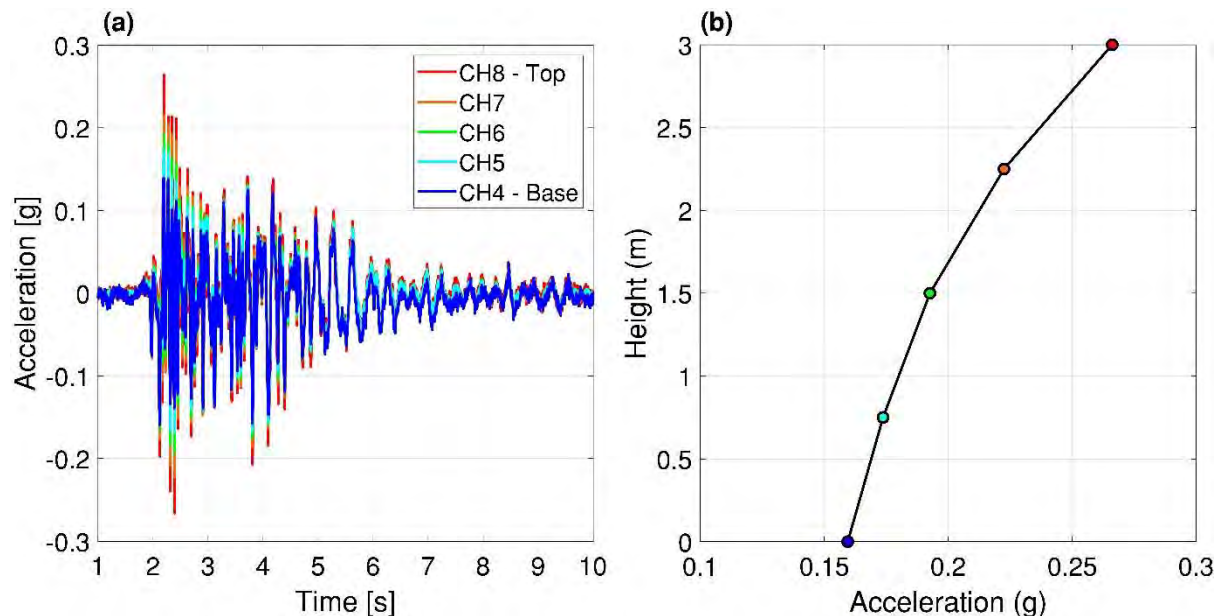


Figure 334: Example of vertical acceleration amplification - TEST 45: L'Aquila 2009 earthquake (AQK station, UP component): input accelerogram scaled to a total duration of 20 sec (here only the first 10 sec window is represented)- (a) Acceleration time-histories along the soil height: at the base (CH 4), at intermediate levels (CH. 5, 6 and 7) and on the top of the soil model (CH 8); (b) Maximum acceleration values recorded at each level, from the base to the top

6.6.9 Conclusions and outlook

The aim of the experimental research was the evaluation of the seismic response of a soil deposit in the so-called near-fault conditions, where the site is subjected to significant vertical accelerations, comparable to the horizontal ones both for the amplitude values and the frequency content. In such conditions, the potential amplification effects of vertical motion can play a crucial role. Therefore, it is mandatory to investigate on the vertical response of soil deposits, which is traditionally assumed to be negligible.

The SHATTENFEE project investigated the response of a soil model representing an infinite homogeneous soil deposit, in free field condition, excited by vertical dynamic and seismic input motions, by means of the 3D shaking table at EQUALS – BLADE Laboratory of the University of Bristol. Preliminary analyses were conducted for defining the material and the optimal dimensions of the soil container to match the soil prototype characteristics. A first novelty was the construction of a specific 3.2 m tall container, realized in PERSPEX material, made of four cylindrical segments.

The first part of the tests was devoted to the dynamic identification of the soil-container model: the main vertical frequency of the soil was determined with various approaches; the scarce influence of the container on the soil response has been verified.

Compression wave propagation was investigated: accurate measurements of V_p were performed during the experimental phases, allowing the evaluation of the soil stiffness and frequency variation with the level of excitation (soil non-linearity in compression). The measurement of the V_p allowed the validation of the theoretical formula for the vertical period T_v ($T_v = 4H/V_p$).

Particular attention was devoted to the amplification amount of the vertical input motion. The accelerometric data recorded at the base, along the soil columns, and at the soil surface, analysed both in the time and in the frequency domain, revealed that the vertical amplification is significant, confirming the results previously obtained numerically.

The research results confirm the importance of the near-fault effects and provide useful tools for studying the soil response under vertical actions. The success of this experimental project stimulates further investigations on more complex soil-foundation configurations.

6.6.10 References

- Porat Boaz 2008. Digital processing of random signals: theory and methods. Courier Dover Publications.
- Hashash, Y.M.A., Musgrove, M.I., Harmon, J.A., Groholski, D.R., Phillips, C.A., and Park, D. (2016). "DEEPSOIL 6.1, User Manual". Urbana, IL, Board of Trustees of University of Illinois at Urbana-Champaign.
- Itasca (2011). FLAC, Fast Lagrangian Analysis of Continua, Version 7.0 User's Guide, Itasca Consulting Group. Inc., Minneapolis, Minnesota, USA.
- Naik, N. K., & Perla, Y. (2008). Mechanical behaviour of acrylic under high strain rate tensile loading. *Polymer Testing*, 27(4), 504-512.
- O'Rourke, T. D., Druschel, S. J., & Netravali, A. N. (1990). Shear strength characteristics of sand-polymer interfaces. *Journal of geotechnical engineering*, 116(3), 451-469.
- Sica, S., Simonelli, A.L., 2015. Seismic propagation in near-source conditions: effects on large embankments. *Proc. of the XVI ECSMGE Geotechnical Engineering for Infrastructure and Development*. P. 2117-2122, Ice Institution of Civil Engineering, Isbn: 978-0-7277-6067-8, Edimburgh (UK).
- Penna, A., Sorrentino, G., d'Onofrio, A., Silvestri, F., & Simonelli, A. (2016). Dynamic behaviour of the Leighton Buzzard Sand-B under very low confining stresses. *1th International Conference on Earthquake Geotechnical Engineering, (ICEGE 2019)*, June 17-20, 2019, Rome, Italy.
- Siviour, C. R., & Jordan, J. L. (2016). High strain rate mechanics of polymers: a review. *Journal of Dynamic Behavior of Materials*, 2(1), 15.
- Simonelli A.L., Fredella M.I., Sorrentino G., Aliperti D. & Penna A. (2019) Site seismic response in near-fault conditions: role of vertical input motion. *7th International Conference on Earthquake Geotechnical Engineering, (ICEGE 2019)*, June 17-20, 2019, Rome, Italy.

6.7 Project #36 – SSI-STEEL Soil-Structures Interaction effects for STEEL structures

Authors

T. L. Karavasilis⁽¹⁾, G. Brando⁽²⁾, A. Pagliaroli⁽²⁾, S. Bhattacharya⁽³⁾, A. Benavent-Climent⁽⁴⁾, P. Kloukinas⁽⁵⁾, G. Camata^(2,6), M. Mariotti⁽⁷⁾, M. Dietz⁽⁸⁾, D. Karamitros⁽⁸⁾, G. Mylonakis^(8, 9, 10)

⁽¹⁾ *Department of Civil Engineering, University of Patras, Patras, Greece.*

⁽¹⁾ *Department of Engineering and Geology, University “G. d’Annunzio” of Chieti-Pescara, Pescara, Italy.*

⁽³⁾ *Department of Civil and Environmental Engineering, University of Surrey, Guildford, United Kingdom*

⁽⁴⁾ *Technical University of Madrid, Madrid, Spain.*

⁽⁵⁾ *Department of Civil Engineering and Science, University of Greenwich, Chatham, United Kingdom.*

⁽⁶⁾ *ASDEA Software Start Up Innovativa s.r.l., Pescara, Italy.*

⁽⁷⁾ *SARA electronic instruments s.r.l., Perugia, Italy.*

⁽⁸⁾ *Department of Civil Engineering, University of Bristol, Bristol, United Kingdom*

⁽⁹⁾ *Department of Civil Engineering, Khalifa University, U.A.E.*

⁽¹⁰⁾ *University of California at Los Angeles (UCLA), U.S.A.*

6.7.1 Introduction

Although modern Codes and Provisions concerning steel structures have been refined more and more in the last decades, however, several issues have not been solved yet. Among these, the one related to the fact that, in the current design practice, steel structures are modelled rigidly restrained at the base, neglecting the Soil-Structure Interaction (SSI) effects, is of paramount interest.

The dynamic response of structures founded on soft deposits may be different with respect to the one of the same structures on a rigid subsoil. In general, higher the structure-to-soil relative stiffness, higher the SSI effects (Veletsos and Meek, 1974). This relative stiffness, thus the SSI effects can be quantified by the so-called "Wave Parameter" ($1/\sigma$), defined according to eq. (1) (NEHRP Consultants Joint Venture, 2012):

$$\frac{1}{\sigma} = \frac{h}{V_s \cdot T} \quad (1)$$

Where, referred to an equivalent SDOF system, V_s is the shear velocity of the soil deposit, T is the main structural period of the structure in the fixed-base condition, h is the height of the mass.

On the one hand, the period elongation, due to the additional deformability, and the added damping, due to the dissipation of a part of the vibrational energy through the ground, could lead to reduced seismic actions/effects on the structural system. Thus, SSI is commonly neglected, since it is assumed that its omission leads to conservative seismic response results.

On the other hand, tests and analyses demonstrate that, for some period ranges, SSI could provoke an undesired detriment of the structural response, in terms of unexpected demands of strength and ductility.

Several numerical studies proved that the inclusion of SSI in practical seismic analyses can be performed approximately by employing spring-dashpot-mass discrete linear models, as those developed by (Mulliken and Karabalis, 1998) and (Wolf, 1994). Nevertheless, these models cannot capture non-linear phenomena near the soil-structure region, e.g. the foundation uplift/sliding and the plasticity of the soil, which, conversely, can be taken into account only by using macro-elements (Millen *et al.*, 2018), beam-on-non-linear-Winkler foundations (Harden and Hutchinson, 2009) or other contact models (Gajan and Kutter, 2009).

In literature, so far, few researchers have studied SSI effects on the seismic response of steel structures. Among these, the numerical works of (Raychowdhury, 2011), (Farhadi, Saffari and Torkzadeh, 2018), (Minasidis, Hatzigeorgiou and Beskos, 2014) are surely worth of being mentioned. Also, some efforts have been undertaken in order to investigate the SSI effects on structures with dampers: (Flogeras and Papagiannopoulos, 2017) carried out some analyses on buckling restrained braces, whereas (Zhou, Guo and Yong, 2012) investigated structures with velocity-dependent dampers, proving that SSI significantly modifies frequencies, damping and mode shapes. Nevertheless, several issues remain unexplored, such as the influence of SSI on structures with dampers that use materials with significant strain-rate dependency (e.g. shape memory alloys).

As far as the experimental studies are concerned, one of the most interesting campaign concerning SSI effects was carried out at the BLADE laboratory of the University of Bristol as part of the European project SERIES (Durante *et al.*, 2015), (Durante *et al.*, 2016). Shake table tests were carried out on a group of five piles crossing two different layers of soil. The superstructure was a simple oscillator formed by an aluminium or steel column with an added mass on the top that was varied in order to get different dynamic responses. The obtained results allowed to appraise the influence of SSI in terms of change of natural frequencies due to the SSI, also depending on the piles head conditions. Furthermore, experimental tests in order to study the response of two physical models characterized by a partially embedded shallow foundation were carried out at the same laboratory (Massimino and Maugeri, 2013). All the results of these tests were used to calibrate SSI nonlinear models.

In this frame of research, the SSI-STEEL project (Soil-Structures Interaction effects for STEEL structures) deals with an experimental campaign, through shake-table tests, to be carried out on different steel structural systems in order to achieve a better knowledge on the SSI effects on their dynamic linear and non-linear responses. In particular, three structural types are investigated, those are: *i)* a Concentrically Braced Frame (CBF), *ii)* a Moment Resisting Frame (MRF) -also considering the presence of a beam reduced end sections- and *iii)* dual steel frame (DSF) with a new brace-type damper made of a shape memory alloy material.

Few similar experimental researches concerning SSI effects on steel frames are currently present in literature. They are often focused on SDOF systems made of a column with a mass atop -as the study of Durante *et al.* (2015)- or, when more complex structures are considered, just investigate specific aspects influencing the structural response of steel structures. For example (Tabatabaiefar, Fatahi and Samali, 2014) performed shake table tests on a 15-story properly scaled steel frames under four different earthquakes: the experimental and numerical outcomes obtained by validated numerical models allowed to evidence the detrimental effects due to the SSI in terms of elastic displacements.

On the other hand, there are not experimental studies that compares the SSI influence on the responses of different structural types designed according the same criteria, as well as that consider also nonlinear

phenomena such as buckling and yielding. These are the aspects that the project aims to investigate. The goal is to lead the current knowledge to a larger extent and to propose modification factors, to be expressed as a function of the soil-to-structure relative stiffness, to be included in the current design formulations that are of interest for technicians. Therefore, the proposed research represents a significant breakthrough in the field of structural / geotechnical engineering, with evident returns in terms of Code/Provisions updates and meaningful design tools that will be used by engineers in the future.

The whole research activity is articulated into five steps:

- Step 1.** Design of the frames to be tested
- Step 2.** Set up of preliminary numerical models
- Step 3.** Shake Table Tests
- Step 4.** Validation of the Numerical Simulation Procedure
- Step 5.** Execution of Numerical Parametric Analyses.

Steps 1-2-3 are the core of the project presented in the current report. Steps 4-5 are activities that will be carried out after the project, according to a refinement/validation of the model developed in Step 2 based on the tests developed in Step 3.

It must be pointed out that, so far, the shaking table tests, which have been designed and for which all the specimens been manufactured, have not been carried out yet. In fact they were scheduled for the second decade of March (starting from the 16th), but, because of the national/international restrictions due to the SARS-CoV-2 all the involved researchers have had limitations to mobility, this making impossible to do the tests, which, anyway, will be carried out in a later phase, immediately after the end of the ongoing Coronavirus pandemic.

6.7.2 Identification of prototypes: Design of the frames to be tested

The basic assumptions for conceiving the prototypes to be tested have concerned the following design constraints:

- **Global Geometry/Mass of the prototypes**

Given the bearing capacity of the shaking table in the EQUALS laboratory of Bristol (about 10/15 tons for table accelerations ranging from $1g$ to $1.5g$) and considered that, for investigating the SSI effects, the frames have to be mounted on a box with a height of 1.2 m and dimensions in plan of 1.0x5.5 (m) that, filled with a soil of about 1.5 ton/m^3 , has a total weight (including the box weight) of 10.5 tons, it was decided to design the superstructures in order to do not exceed 2 tons, inclusive of the weight of the mass to be put atop to be mobilized during the seismic test.

It has been also decided that the superstructure have to be realized according to a scale factor as close as possible to 1:1, so to have frames behaviors, in terms of element buckling and plastic hinges development, close to the ones that are usually considered in the common practice according to the Standards and Codes.

This led to select 1:2 scaled spatial frames characterized by a height of 1.5 m, with plan dimensions of 2.5 m in the longitudinal direction -along which the seismic acceleration of the shake table is applied- and 1.0 m in the transversal direction.

- **Selection of the foundation system**

As it is commonly done in the practice, a slab shallow foundation has been considered for the *MRF* system. The same foundation has been adopted for the *CBF* and the *DSF* prototypes, but, in these cases,

tubular steel piles have been installed below. The slab has been obtained by a rigid reticulated steel structure coated with a steel sheeting, as it will be shown forward.

- **Target fundamental period of the structure**

Once that the geometry of the system has been defined, the entity of the mass to put on the frames has been selected so to have a wave parameter $1/\sigma$ lower than 0.3. In fact, also based on studies carried out in the past and recently (Fiorentino *et al.*, 2019), it has been assumed that this is a lower bound value of the wave parameter to emphasize SSI effects.

Considering that the soil selected for the tests is formed, as described in (Durante *et al.*, 2016), by two-layers made of by Leighton Buzzard sand (LB) fraction *E*, for the top layer, and by a mix of LB fractions *B* and *E* (85% and 15%, respectively), for the bottom layer, the shear velocity of the soil V_s is of about 100 m/s. As a consequence, a fundamental period of 0.045 sec has been selected for obtaining a wave parameter $1/\sigma$ of 0.3, according to the calculation reported in eq. (2).

$$\frac{1}{\sigma} = \frac{h}{V_s \cdot T} = \frac{1.5}{100 \cdot 0.045} = 0.3 \quad (2)$$

- **Section/Elements Design -CBF**

In order to design the CBF members, a S275 steel has been considered for beams and columns, whereas a S235 steel has been assumed for the braces. Moreover, a fixed base condition has been imposed.

The calculation scheme is shown in Figure 335a, where one of the two 2D braced frames that form the whole structure, represented in plan in Figure 335b, is depicted. All the members are considered mutually hinged, because of the types of adopted connections.

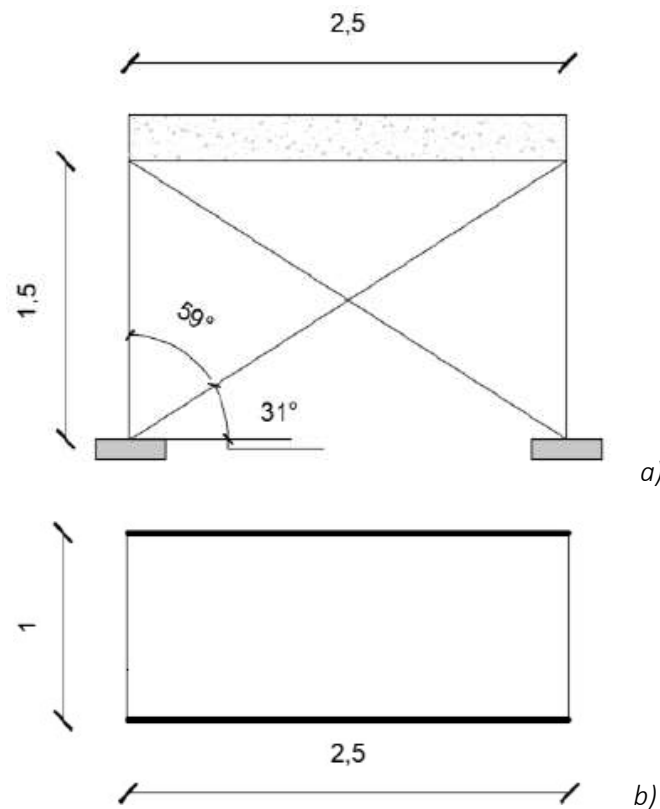


Figure 335: Structural scheme of the tested CBF. (a) Longitudinal view of the elevation and (b) plan (dimensions in meters)

As a first attempt, a mass of 1.6 ton has been imposed at the top of the frame. In order to get a structure with a fundamental period of 0.045 sec, a total lateral stiffness of 23400 kN/m should be provided, according to eq. (3), where a SDOF has been considered for describing the dynamic behavior of the frame. This means that each of the two 2D braced frames must be characterized by a lateral stiffness of 11680 kN/m. Thus, a minimum area of 189000 mm² must be assumed for each brace, according to eq. (4).

A “class 1” hollow circular cross section 48.3x1.2, with a sectional area of 178 mm² has been adopted. This area is slightly lower than the one obtained in eq. (4), but it has been assumed anyway. It gives a lateral stiffness of the whole frame of 22000 KN/m and a period of 0.053. In order to get a wave parameter $1/\sigma$ equal to 0.3, then, the mass has been reduced to 1.1 tons.

$$K = 4 \cdot \pi^2 \frac{M}{T^2} = 4 \cdot \pi^2 \frac{1600}{0.045^2} = 23370903 \text{ N/m} \quad (3)$$

$$A = \frac{K \cdot L}{2 \cdot E \cdot \cos \alpha} = \frac{23370,903 \cdot 2915}{2 \cdot 210000 \cdot \cos 31^\circ} = 189 \text{ mm}^2 \quad (4)$$

The proposed cross section corresponds to a normalized slenderness of $\bar{\lambda}=2$ which complies with the upper bound imposed by prEN1998 ((CEN), 2009) in order to guarantee a suitable behavior under cyclic loads. However, the yield strength of the brace, equal to is $F_y=178 \cdot 235=41830$ N, would be triggered for a value a ground acceleration a_y of 2.96g -see eq. (5) , which, considering a conventional amplification factor of $F_0=2.2$ for the structure.

$$a_y = \frac{2 \cdot F_y \cdot \cos 31^\circ}{F_0 \cdot M} = \frac{2 \cdot 41830 \cdot \cos 31^\circ}{2.2 \cdot 1100} = 29.6 \frac{\text{m}}{\text{s}^2} = 2,96 \text{ g} \quad (5)$$

The obtained acceleration is not compatible with the shake table capacity. For this reason, braces have been re-designed with two end portions having a length of 86,5 mm and that are characterized by a reduced hollow circular section 14x0.5. It is steel a “class 1” section with a transversal area of 21 mm², which gives a yielding force $F_{y,r}=21 \cdot 235=4935$ N, that would be triggered for a value a ground acceleration $a_{y,r}$ of 0.35g -see eq. (6) .

$$a_{y,r} = \frac{2 \cdot F_{y,r} \cdot \cos 31^\circ}{F_0 \cdot M} = \frac{2 \cdot 4935 \cdot \cos 31^\circ}{2.2 \cdot 1100} = 3.50 \frac{\text{m}}{\text{s}^2} = 0.35 \text{ g} \quad (6)$$

Then in order to leave unchanged both the axial and the flexural stiffness of the brace, the section of the central portion has been enlarged to a value of 48.3x2.9.

The final configuration of the brace is shown in Figure 336, whereas, in Figure 337 the exploded representation of the whole structure is shown.

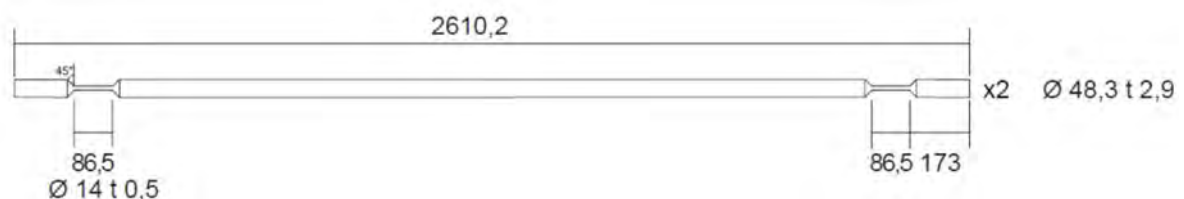


Figure 336: The designed brace with reduced end hollow circular sections

Apart from the designed braces, HEB100 and IPE80 cross sections have been adopted for columns and beams, respectively. Indeed, these sections are oversized for resisting to the forces transmitted by the braces, but they have been selected anyway for reasons that will be explained during the description of the design process of the MRF. However, they do not contribute significantly to the lateral stiffness of the frame, as they are -purely- hinged each other.

In order to stabilise the scheme, the structure is completed through braces put in the transversal direction and on the top floor.

Finally, a sandwich panel is arranged on the top in order to support the mass.

- **Section/Elements Design -MRF**

The MRF has been simply obtained by removing the braces in the CBF described above and by reinforcing the beam-to-column joints and the column bases so to convert those from pinned joints to full strength/rigid joints. This has been possible as the frame members are characterized by low Demand/Capacity ratio with respect to the gravity loads.

The final exploded representation of the whole structure is shown in Figure 338, whereas, in Figure 339 a detail of the steel elements to be added, through welds and bolts, is provided.

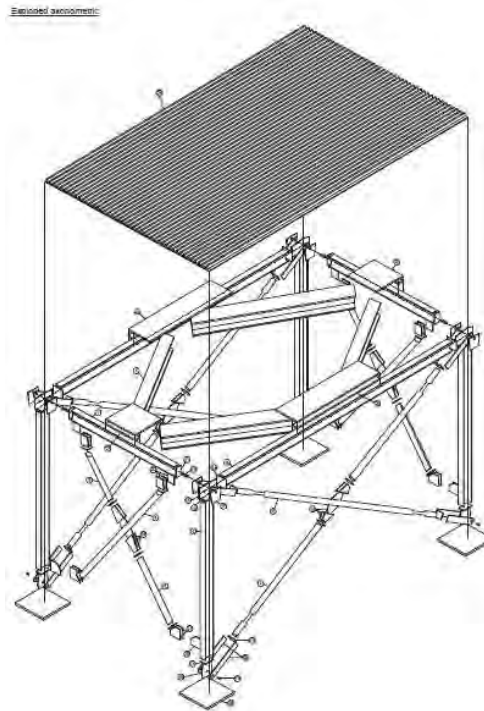


Figure 337: The exploded representation of the CBF frame to be tested

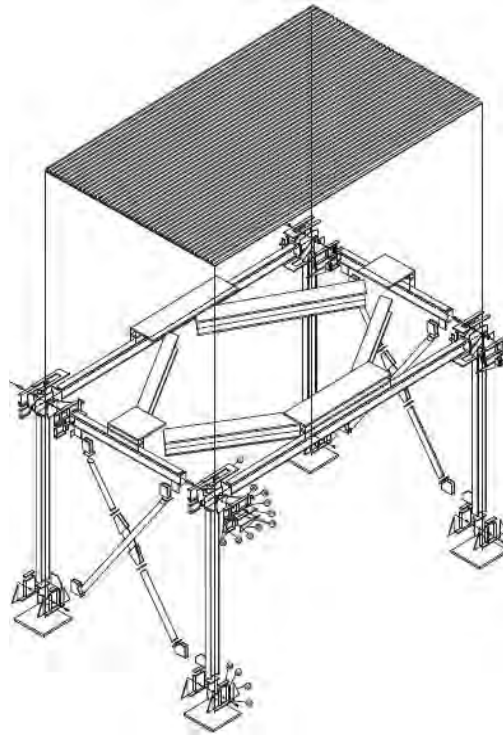


Figure 338: The exploded representation of the MRF frame to be tested

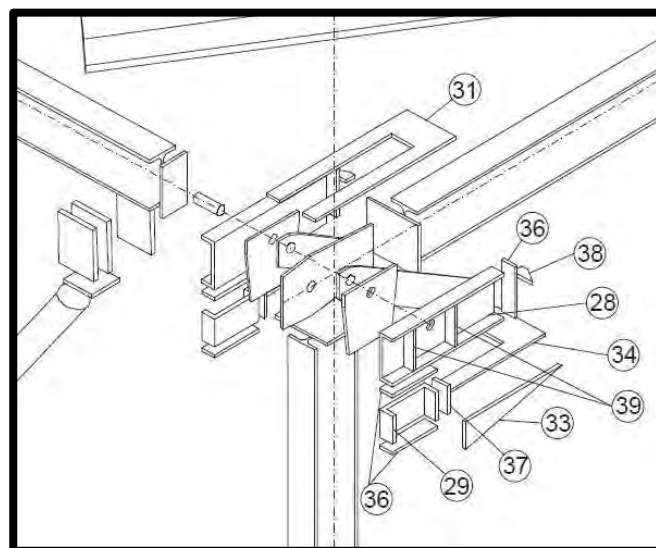


Figure 339: A detail of the elements to be added in order to transform the CBF in a MRF, once that the braces have been removed

The proposed MRF configuration requires very high ground accelerations for triggering the first plastic hinges on the beams. For this reason, after a first test, the beam will be replaced by beams having the same geometry, but a reduced section at the two ends, which have been sized in order to yield for ground accelerations of 0.4g.

- **Section/Elements Design -DSF with Damper**

The purpose of the tests to be carried out on the DSF with damper is to investigate the influence of SSI on structures with displacement-dependent dampers that use materials with significant strain-rate dependency such as the shape memory alloys.

The MRF discussed previously is equipped with a damper that is installed, at the mid span of the transverse beams, as a conventional diagonal member. Figure 340 shows a general view. The damper consists on a tube-in-tube (telescopic) assemblage of two commonly available hollow structural sections (exterior and interior tube) with a central bar made of Shape Memory Alloys (SMA) material (NiTi), as shown in Figure 340a. The NiTi bar is connected to the hollow tubes in such a way that when the inner and exterior tubes experience a relative displacement along their axes, one half of the NiTi bar is subjected to tension while the other half remains unstressed. The hollow structural sections with the central NiTi bar are connected to the frame through auxiliary steel elements.

For designing the DSF with damper, a mass of 1500 kg has been considered on the top of the frame. A single damper is installed in the frame in order to not increase too much the lateral strength of the structure. The damper connects the base level of the frame with the mid-point of the upper (short) IPE 80 member of the frame.

Based on estimated values of the mechanical properties of the materials, the fundamental period of the structure with dampers assuming all joints of the frame as rigid is about 0.1s, and the $1/\sigma$ factor is equal to 0.14 (assuming a soil with $V_s=100$ m/s). The absolute response acceleration required on the mass located at the top of the frame to induce the yielding of the NiTi bar is about 2.2g.

If the base of the columns of the frame are pinned, then the fundamental period would enlarge to about 0.16s and the $1/\sigma$ factor would be about to 0.1. In this case, the absolute response acceleration required on the mass located at the top of the frame to induce the yielding of the NiTi bar is about 1.1g.

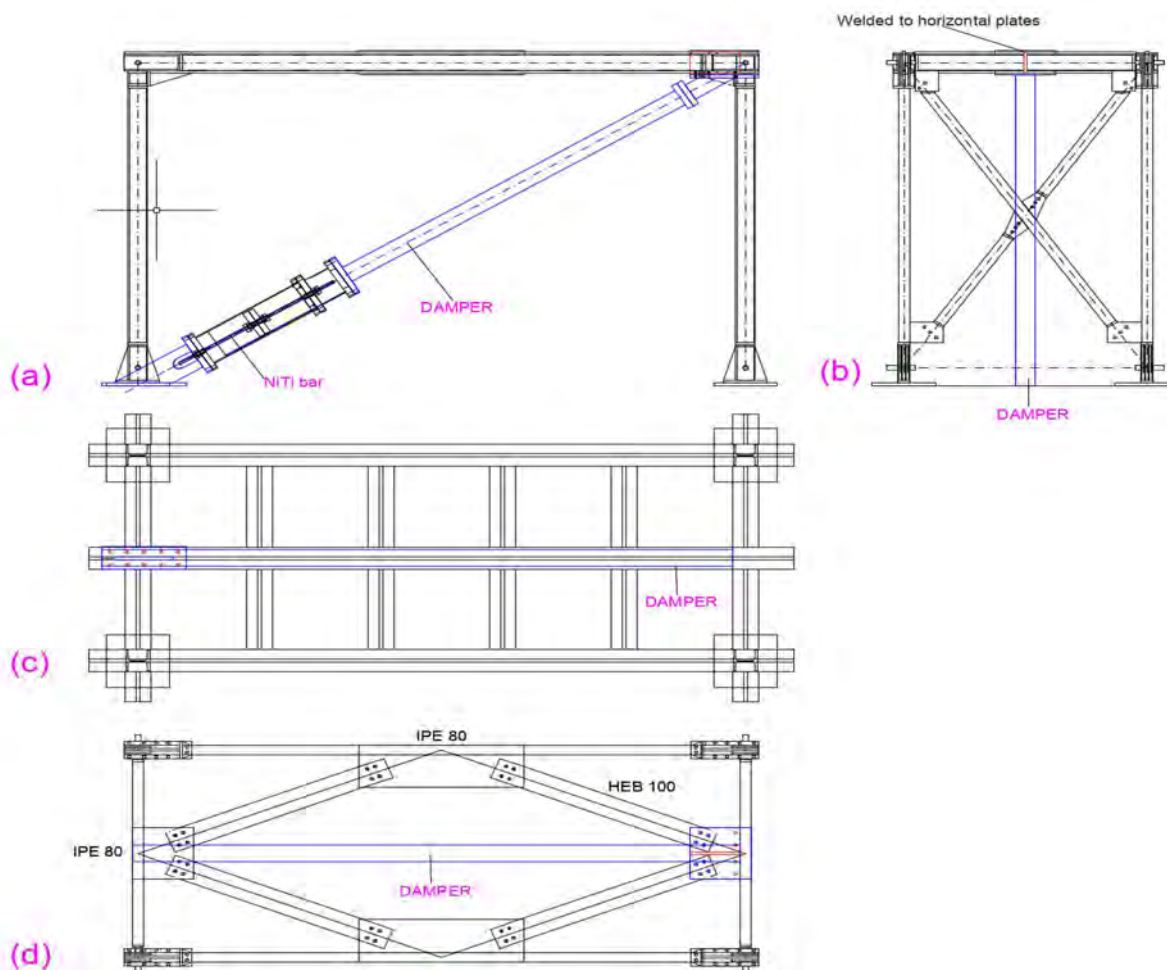


Figure 340: Test specimen. (a) elevation (front view); (b) elevation (lateral view); (c) column bases in plan; (d) top view in plan

6.7.3 Scaling Prototype to Model

As said before, a 1:2 scale factor has been considered for the frames. This scaling factor has been considered for modelling the input records, which are dealt with in the next Section. For all input motions the original time step of the recordings is 0.005s. Considering a geometric scale factor of 2 for the prototype to be tested, the scaling rules proposed by (Wood, Crewe and Taylor, 2002) suggest a scaling factor of 1.7 for dynamic time leading to a scaled time step of 0.0029 s.

6.7.4 Test configuration and instrumentation layout

- **The input records**

The input motion to be applied in the shaking table tests has been defined in terms natural accelerograms. The signals were extracted from the Italian Accelerometric Archive ITACA (Luzi, Pacor and Puglia, 2019) containing recordings from the Italian Accelerometric Network (RAN) and openly accessible at http://itaca.mi.ingv.it/ItacaNet_30/.

The following ranges for seismological parameters were considered for the selection: Magnitude 5.5-6-9 and Epicentral distance 0-25 km. Flat outcropping rock conditions at recording site were considered, i.e. subsoil class A according Eurocode 8. Some restrictions were also applied to PGA of the signals ($PGA > 0.1g$) in order to avoid too large scaling factors during the tests (Pagliaroli and Lanzo, 2008).

The available ITACA recordings extracted according to the following constrains are reported in Table 43. A total of 14 pairs of signals were obtained while the corresponding 5% damped acceleration response spectra are reported in Figure 341. Note that the response spectra have been computed using the scaled time step to be employed in the shaking table test. Signals were processed by using the software In-Spector developed by (Acunzo, Pagliaroli and G., 2014).

In order to select the accelerograms to be used for the tests from the initial set of Table 43, recordings characterized by predominant period in the range of fundamental vibration periods of models were considered. In particular, a period range of 0.03-0.06 s (15-30 Hz) has been assumed for CBF steel structure model while 0.2-1 s (1-5 Hz) pertains to MRF model. Both ranges roughly consider the elongation of the fixed-base model vibration period due to soil-structure interaction effects.

The accelerograms selected for CBF testing are reported in Table 44 and Figure 342a (acceleration time histories and response spectra). In Figure 342a the accelerograms are unscaled in amplitude while the time step is the scaled one (0.0029 s) to be used in the shaking table tests. Note that the vertical component has been also included.

Event id	Date	Stat. Code	M _w	M _L	Repi [km]	Corr. PGA [cm/s ²]
EMSC-20161030_0000029	2016-10-30 06:40:18	IV.T1213	6.5	6.1	11.98	868.89
EMSC-20161030_0000029	2016-10-30 06:40:18	IT.CLO	6.5	6.1	7.80	782.02
IT-2009-0102	2009-04-07 17:47:37	4A.MI05	5.5	5.4	3.60	651.51
EMSC-20161030_0000029	2016-10-30 06:40:18	IT.ACC	6.5	6.1	18.56	546.90
EMSC-20161030_0000029	2016-10-30 06:40:18	IV.T1212	6.5	6.1	10.46	274.43
EMSC-20161026_0000095	2016-10-26 19:18:06	IT.CLO	5.9	5.9	10.84	215.13
EMSC-20161030_0000029	2016-10-30 06:40:18	IT.MMO	6.5	6.1	19.17	185.32
IT-1997-0137	1997-10-14 15:23:09	IT.CESM	5.6	5.5	8.70	175.51
EMSC-20161026_0000095	2016-10-26 19:18:06	IT.MMO	5.9	5.9	16.20	16936
IT-1998-0103	1998-09-09 11:28:00	IT.LRS	5.6	5.5	18.00	161.93
IT-2009-0102	2016-04-07 17:47:37	IV.RM13	5.5	5.4	15.60	130.95
EMSC-20161026_0000095	2016-10-26 19:18:06	IT.MNF	5.9	5.9	17.38	118.54
IT-1984-0004	1984-05-07 17:49:43	IT.ATN	5.9	5.9	10.10	109.60
IT-2009-0102	2009-04-07 17:47:37	IV.RM03	5.5	5.4	3.40	102.32

Table 43: Preliminary list of accelerograms extracted from ITACA database with relevant information. All the records corresponds to a normal faulting mechanism, have been measured on a soil type A (EC8 classification) and have been manually processed

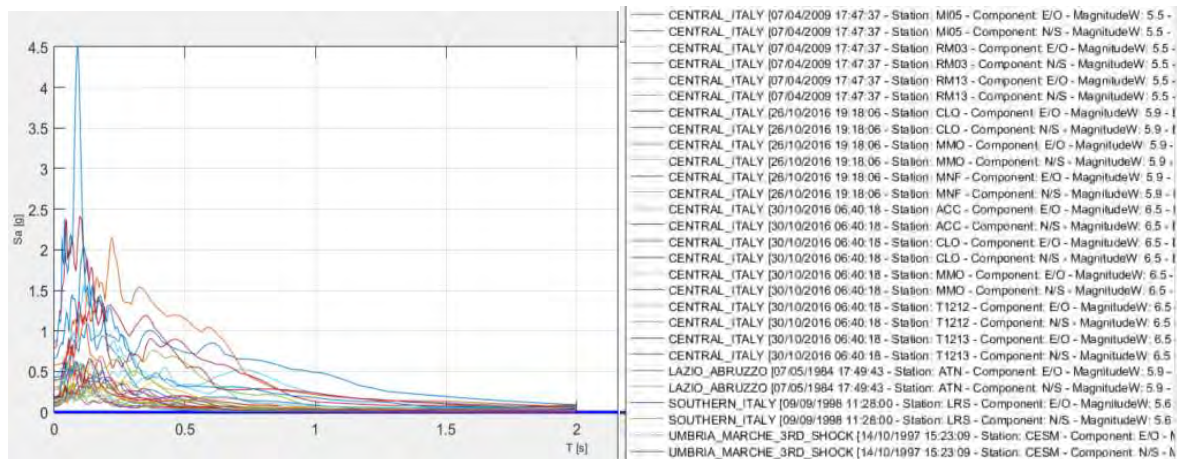


Figure 341: Preliminary accelerogram selection from ITACA database: acceleration response spectra

ID	Date (DD/MM/YY)	Station	Site class	M _w	R* [km]	Comp.	PGA [g]
1	26/10/2016	MMO	A*	5.9	16.2	NS	0.165
						UP	0.087

Table 44: Accelerograms selected for CBF testing (*epicentral distance)

The accelerograms selected for MRF and DSF with Damper are reported in Table 45 and Figure 342bFigure 343 (horizontal and vertical acceleration time histories and response spectra). In Figure 337 the accelerograms are unscaled in amplitude while the time step is the scaled one (0.0029 s) to be used in the shaking table tests. Note that the vertical component has been also included.

ID	Date (DD/MM/YY)	Station	Site class	M _w	R* [km]	Comp.	PGA [g]
2	30/10/2016	CLO	A*	6.5	7.8	NS	0.571
						UP	0.782

Table 45: Accelerograms selected for MRF testing (*epicentral distance)

• Testing protocol

For the experimental campaign on the prototypes described previously, the phases described in Table 46 have been established. White Noise (WN) vibrational analyses and Incremental Dynamic Analyses (IDAs) have been considered for testing:

As for the incremental dynamic analyses, for CBF, during the tests the horizontal input motion will be scaled to the following values of PGA = 0.02g, 0.05g, 0.1g, 0.15g, 0.2g, 0.25g, 0.3g, 0.4g, 0.5g, 0.6g, by applying the following scaling factors which are lower than 4 and therefore acceptable (Pagliaroli and Lanzo, 2008):

PGA(g)	0.02	0.05	0.1	0.15	0.2	0.25	0.3	0.4	0.5	0.6
SF	0.121	0.303	0.606	0.909	1.212	1.515	1.818	2.424	3.030	3.636

The vertical components will be scaled using the same SF applied on the corresponding horizontal component. For MRF and DSF with Damper, the horizontal input motion will be scaled to the following values of PGA = 0.05g, 0.1g, 0.2g, 0.3g, 0.4g, 0.5g, 0.8g, 1g, 1.2g, 1.5g during the tests, by applying the following scaling factors (for both horizontal and vertical components):

PGA (g)	0.05	0.1	0.2	0.3	0.4	0.5	0.8	1	1.2	1.5
SF	0.088	0.175	0.350	0.525	0.701	0.876	1.401	1.751	2.102	2.627

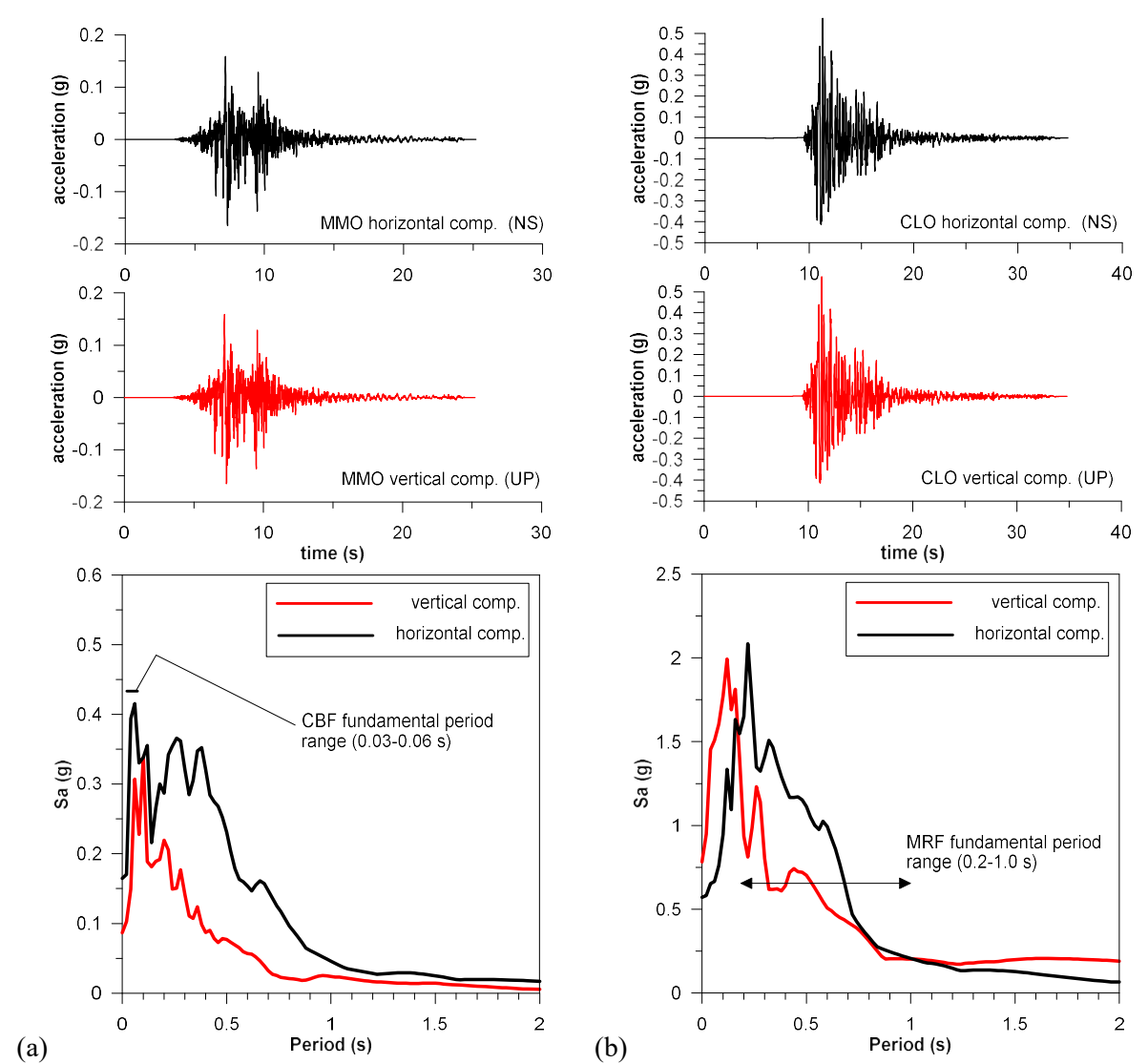
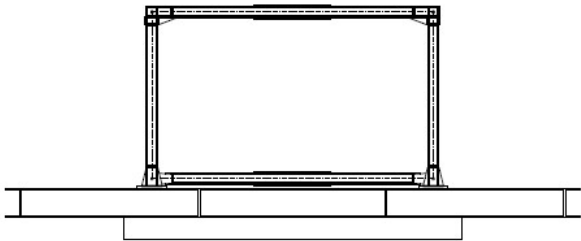
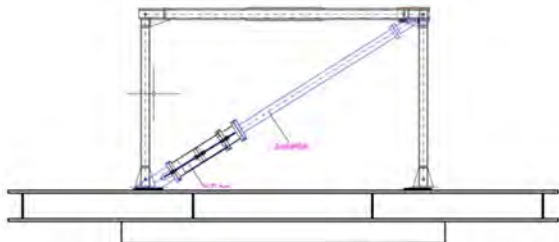
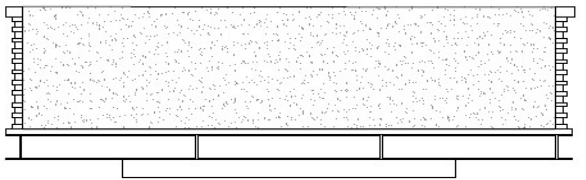
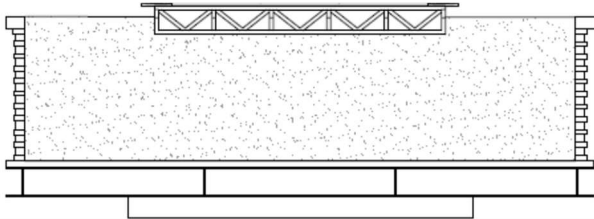
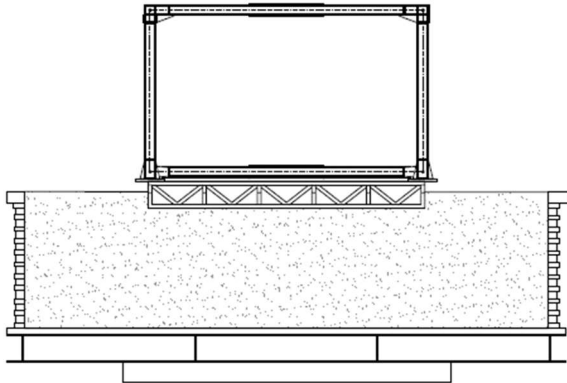
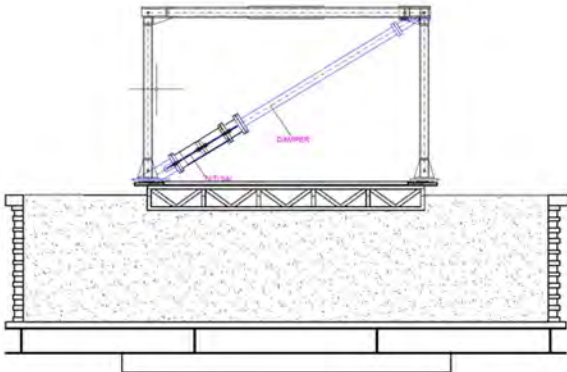


Figure 342: (a) Input motion for CBF testing, acceleration time histories and response spectra for vertical and horizontal components; (b) Input motion for MRF testing, acceleration time histories and response spectra for vertical and horizontal components

Test	Description	Type	Representation
1	Fixed-Base CBF	WN+IDA	

2	Fixed-Base MRF	WN+IDA	
3	Fixed-Base DSF+Damper	WN+IDA	
4	Box+Soil	WN	
5	Box+Soil+Shallow Foundation	WN	
6	Box+Soil+Shallow Foundation+MRF	WN+IDA	
7	Box+Soil+Shallow Foundation+DSF with Damper	WN+IDA	

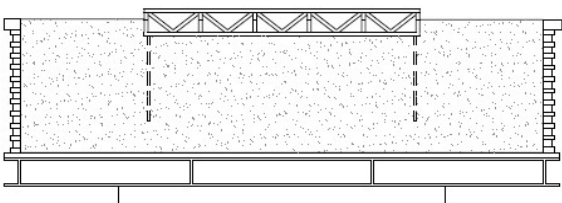
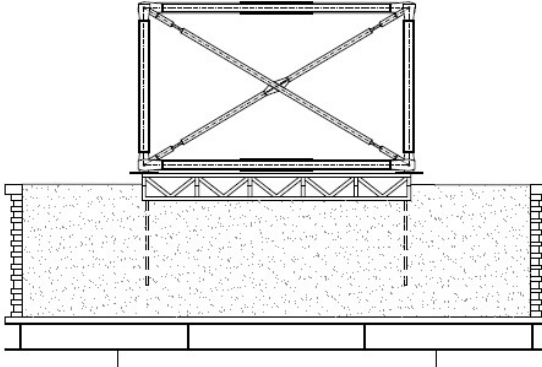
8	Box+Soil+foundation on piles	WN	
9	Box+Soil+ Foundation on piles+CBF	WN+IDA	

Table 46: Description of the whole experimental campaign

- **The measurement equipment**

The measurement equipment to be used during the tests are described in Figure 343a, Figure 343b and Figure 343c for the CBF, the MRF and the DSF with Damper, respectively.

6.7.5 Preliminary results

As already mentioned, the scheduled tests have not been carried out yet because of the national/international restrictions due to the SARS-CoV-2 that led to the closure of the lab (despite the 10 TA days provided by UBRI). For this reason, no results are available yet.

6.7.6 Conclusions and outlook

In this report, we presented an experimental campaign to be realized within the SERA project SSI-STEEL (Soil-Structures Interaction effects for STEEL structures). Shaking table tests on different steel structural types have been scheduled in order to investigate the influence of SSI effects on the linear and nonlinear response. The considered structural types are: *i*) a Concentrically Braced Frame (CBF) on pile foundation, *ii*) a Moment Resisting Frame (MRF) on shallow foundation -also considering the presence of beam reduced end sections- and *iii*) dual steel frame (DSF) with a new brace-type damper made of a shape memory alloy material, on shallow foundation again.

In a first part, the prototypes to be tested have been presented and the conditions imposed for their design have been discussed. Then the test campaign has been shown, by discussing the selected accelerograms and the sequence of tests to be carried out.

Although all the specimens been manufactured (Figure 344), so far, the shaking table tests, scheduled to be completed in late March 2020 have not performed, because of the national/international restrictions due to the SARS-CoV-2. For this reason, it is not possible to provide any conclusions yet.

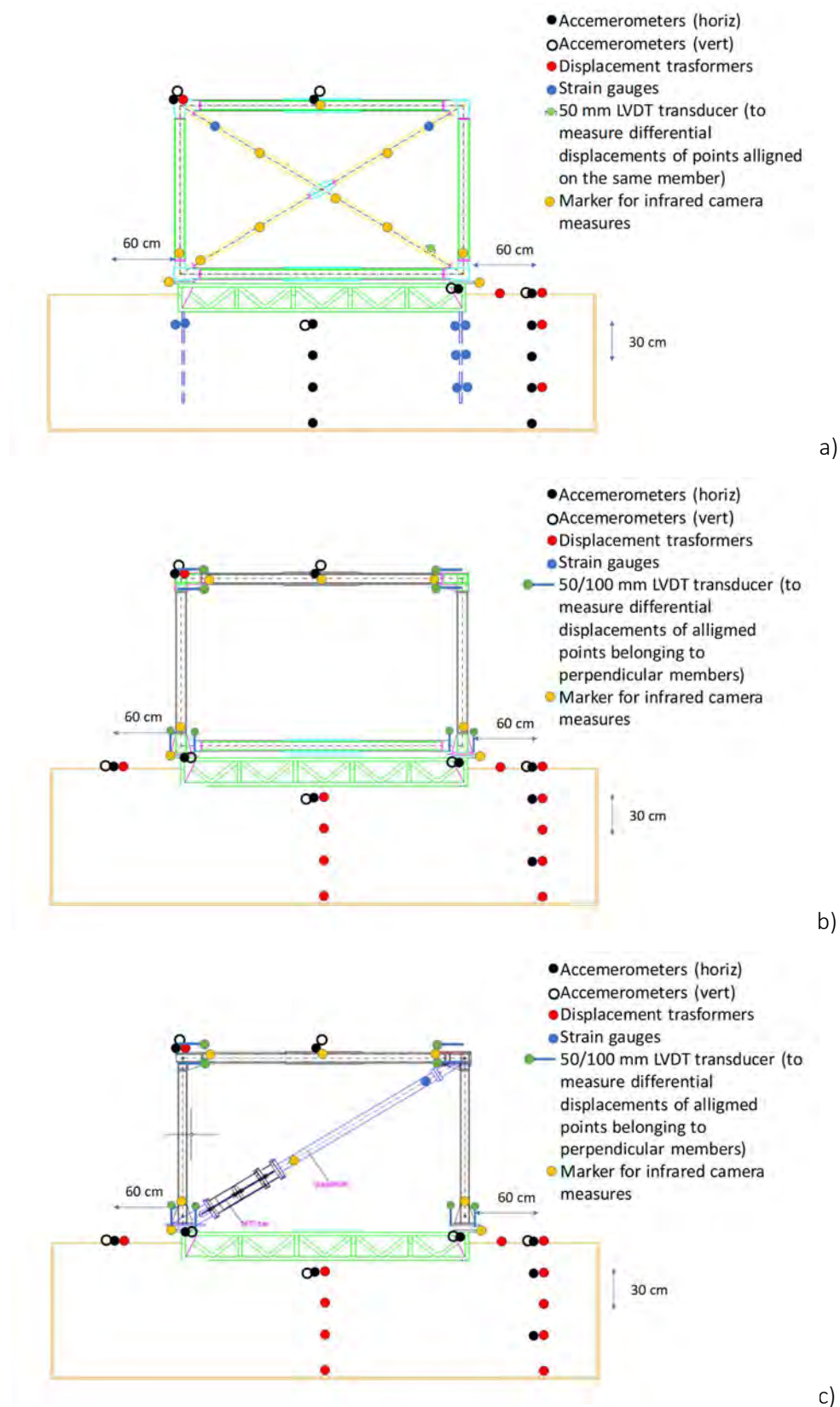


Figure 343: Test equipment for (a) CBF, (b) MRF and (c) DSF with Dampers



Figure 344: The manufactured and assembled CBF to be tested

6.7.7 References

- (CEN), E. C. for S. (2009) 'PrEN1998, Eurocode 8-Design of structures for earthquake resistance, Part 1: General rules, seismic actions and rules for buildings'. Brussels.
- Acunzo, G., Pagliaroli, A. and G., S. (2014) 'In-Spector: un software di supporto alla selezione di accelerogrammi naturali spettrocompatibili per analisi geotecniche e strutturali.', in *33° Convegno Nazionale GNGTS*. Bologna, pp. 107–1014.
- Durante, M. G. *et al.* (2015) 'Soil-pile-structure-interaction: Experimental results and numerical simulations', in *COMPDYN 2015 - 5th ECCOMAS Thematic Conference on Computational Methods in Structural Dynamics and Earthquake Engineering*, pp. 4339–4349. doi: 10.7712/120115.3699.2830.
- Durante, M. G. *et al.* (2016) 'Soil-pile-structure interaction: Experimental outcomes from shaking table tests', *Earthquake Engineering and Structural Dynamic*, 45(7), pp. 11041–1061. Available at: <https://onlinelibrary.wiley.com/doi/epdf/10.1002/eqe.2694>.
- Farhadi, N., Saffari, H. and Torkzadeh, P. (2018) 'Estimation of maximum and residual inter-storey drift in steel MRF considering soil-structure interaction from fixed-base analyses', *Soil Dynamics and Earthquake Engineering*, 114(October 2017), pp. 85–96. doi: 10.1016/j.soildyn.2018.06.034.
- Fiorentino, G. *et al.* (2019) 'Seismic reassessment of the leaning tower of Pisa: Dynamic monitoring, site response, and SSI', *Earthquake Spectra*, 35(2), pp. 703–736. doi: 10.1193/021518EQS037M.
- Flogeras, A. K. and Papagiannopoulos, G. A. (2017) 'On the seismic response of steel buckling-restrained braced structures including soil-structure interaction', *Earthquake and Structures*, 12(4), pp. 469–478. doi: 10.12989/eas.2017.12.4.469.
- Gajan, S. and Kutter, B. L. (2009) 'Contact interface model for shallow foundations subjected to combined cyclic loading', *Journal of Geotechnical and Geoenvironmental Engineering*, 135(3), pp. 407–419. doi: 10.1061/(ASCE)1090-0241(2009)135:3(407).
- Harden, C. W. and Hutchinson, T. C. (2009) 'Beam-on-nonlinear-winkler-foundation modeling of shallow, rocking-dominated footings', *Earthquake Spectra*, 25(2), pp. 277–300. doi: 10.1193/1.3110482.
- Luzi, L., Pacor, F. and Puglia, R. (2019) 'Italian Accelerometric Archive v3.0'. Istituto Nazionale di Geofisica e Vulcanologia, Dipartimento della Protezione Civile Nazionale. doi: 10.13127/itaca.3.0.
- Massimino, M. R. and Maugeri, M. (2013) 'Physical modelling of shaking table tests on dynamic soil-foundation interaction and numerical and analytical simulation', *Soil Dynamics and Earthquake Engineering*. Elsevier, 49, pp. 1–18. doi: 10.1016/j.soildyn.2013.01.023.
- Millen, M. D. L. *et al.* (2018) 'A macro-element for the modelling of shallow foundation deformations

- under seismic load', *Soil Dynamics and Earthquake Engineering*. Elsevier Ltd, 106(May 2017), pp. 101–112. doi: 10.1016/j.soildyn.2017.12.001.
- Minasidis, G., Hatzigeorgiou, G. D. and Beskos, D. E. (2014) 'SSI in steel frames subjected to near-fault earthquakes', *Soil Dynamics and Earthquake Engineering*. Elsevier, 66, pp. 56–68. doi: 10.1016/j.soildyn.2014.06.030.
- Mulliken, J. S. and Karabalis, D. L. (1998) 'Discrete model for dynamic through-the-soil coupling of 3-D foundations and structures', *Earthquake Engineering and Structural Dynamics*, 27(7), pp. 687–710. doi: 10.1002/(SICI)1096-9845(199807)27:7<687::AID-EQE752>3.0.CO;2-O.
- NEHRP Consultants Joint Venture (2012) 'Soil-Structure Interaction for Building Structures', *Nist Gcr*, 12, pp. 917–21. doi: 12-917-21.
- Pagliaroli, A. and Lanzo, G. (2008) 'Selection of real accelerograms for the seismic response analysis of the historical town of Nicastro (Southern Italy) during the March 1638 Calabria earthquake', *Engineering Structures*, 30(8), pp. 2211–2222. doi: 10.1016/j.engstruct.2007.06.002.
- Raychowdhury, P. (2011) 'Seismic response of low-rise steel moment-resisting frame (SMRF) buildings incorporating nonlinear soil-structure interaction (SSI)', *Engineering Structures*. Elsevier Ltd, 33(3), pp. 958–967. doi: 10.1016/j.engstruct.2010.12.017.
- Tabatabaiefar, S., Fatahi, B. and Samali, B. (2014) 'Numerical and experimental investigations on seismic response of building frames under influence of soil-structure interaction', *Advances in Structural Engineering*, 17(1), pp. 109–130. doi: 10.1260/1369-4332.17.1.109.
- Veletsos, A. S. . and Meek, J. W. (1974) 'DYNAMIC BEHAVIOUR OF BUILDING-FOUNDATION SYSTEMS', *Engineering, Earthquake Dynamics, Structural*, 3(January), pp. 121–138.
- Wolf, J. P. (1994) *Foundation Vibration Analysis Using Simple Physical Models*. 1994th edn. Englewood Cliffs, New Jersey: Prentice Hill. Available at: <http://books.google.com/books?id=fjF-dMkSs18C&pgis=1>.
- Wood, D. ., Crewe, A. and Taylor, C. (2002) 'Shaking table testing of geotechnical models.', *International Journal of Physical Modelling in Geotechnics*, (1), pp. 1–13.
- Zhou, Y., Guo, Y. and Yong, Z. (2012) 'Influence of soil-structure interaction effects on the performance of viscous energy dissipation systems', in *15th World Conference on Earthquake Engineering (15WCEE)*.

7 IZIIS DYNLAB - University in Skopje

The Dynamic Testing Laboratory (DYNLAB) is part of the Institute of Earthquake Engineering and Engineering Seismology (IZIIS), ss Cyril and Methodius University in Skopje, Republic of North Macedonia. Established in 1965, the Institute represents one of the oldest research facilities of this type in the world, continuously operating more than five decades.

The Institute has a long tradition in experimental in situ forced and ambient vibration testing and experimental laboratory quasi-static and shake table testing. The first shake table tests were carried out at IZIIS in the seventies of the last century. The shake table that has been offered to the users in this project represents a five degrees-of-freedom MTS shake table. It is presently one of the most advanced shake tables since it possesses a new state-of-the-art digital control system produced by MTS, known as the most renowned producer of these simulators. The main characteristics of the shake table are:

- Size of table: 5.0 x 5.0 m;
- Weight of table: 30 t;
- Payload: 40 t;
- 5 DOF, two lateral and four vertical actuators;
- Type of excitation: random, harmonic or computer generated;
- Frequency range: 0.1-80Hz;
- Maximum stroke: horizontal ± 125 mm, vertical ± 50 mm;
- Maximum acceleration (bare table): horizontal 3.0 g, vertical 1.5g;
- Maximum velocity: horizontal 1.0 m/s, vertical 0.5 m/s.

The overall objective of SERA (Seismology and Earthquake Engineering Research Infrastructure Alliance for Europe) is to give a significant contribution, to improve the access to data, services and research infrastructures and deliver solutions based on innovative R&D in seismology and earthquake engineering, aiming at reducing the exposure of our society to the risk posed by natural and anthropogenic earthquakes. SERA proposes an integrated set of activities responding to the priorities identified in the H2020 call INFRAIA-01-2016-2017 Research Infrastructure for Earthquake Hazard in support of earthquake risk mitigation. After the completion of the first, second and third call, three projects were selected for realization at DYNLAB-IZIIS:

- Project 13 – Influence of the floor-to-wall interaction on the seismic response of coupled wall systems. TA User group leader: University of Ljubljana, Faculty of Civil and Geodetic Engineering, Slovenia. Total of 5 users;
- Project 23 – Investigation of Seismic Deformation Demand, Capacity and Control in a Novel Self-Centring Steel Braced Frame (SC-CBF). TA User group leader: School of Engineering, Trinity College, Dublin, Ireland. Total of 9 users;
- Project 37 – Infills and Masonry structures protected by deformable Polyurethanes in seismic areas (INMASPOL). TA User group leader: Democritus University of Thrace, Greece. Total of 11 users.

7.1 Project #13 - Influence of the floor to piers interaction on the seismic response of coupled wall systems

Authors

Z. Rakicevic⁽¹⁾, A. Bogdanovic⁽¹⁾, L. Krstevska⁽¹⁾, R. Apostolska⁽¹⁾, G. Jekic⁽¹⁾, T. Isakovic⁽²⁾, M. Fishinger⁽²⁾,
M. Gams⁽²⁾, J. Wallace⁽³⁾, K. Kolozvari⁽⁴⁾

⁽¹⁾ *IZIIS-Institute of earthquake engineering and engineering seismology, R. N. Macedonia*

⁽²⁾ *University of Ljubljana, Faculty of Civil and Geodetic Engineering*

⁽³⁾ *University of California, Los Angeles, Department of Civil Engineering*

7.1.1 Introduction

Buildings with RC walls have been one of the most frequently and successfully used structural systems to resist seismic action. Nevertheless, in several cases (in particular during the recent earthquakes in Christchurch and Chile) some walls were heavily damaged, requiring high cost of repair or even demolition.

In many such structures the damage was due to poor understanding of the complex interaction between the floor system and wall piers. This problem was therefore recognized as one of the priority research goals within the Virtual International Institute for Performance Assessment of Wall Systems (NSF SAVI Wall Institute) joining together most of the leading researchers in the field from all over the world.

However, the experimental studies of RC coupled walls, which could significantly contribute to the clarification of these response mechanisms, are very rare. Due to the specific geometry and high resistance of walls, experiments have required large and costly experimental facilities. This problem becomes particularly relevant when floor to walls system interaction is studied.

The shape and the reinforcement of the piers provided a realistic representation of the floor-pier interaction as well as realistic boundary conditions for the floor system.

Two 1:2 scale 3-story coupled walls were tested within the project. The first test was performed on 13th -14th February 2019, and the second one on 23rd -24th August 2019. Description of the tests with brief results will be provided in this report.

The improved numerical models and the findings of the experiments will be used to propose adequate design procedure, which might be included into the future versions of seismic codes, in particular, Eurocodes. The proposed research is compatible with the work of the project partner UCLA, particularly in the frame of NSF SAVI Wall Institute, which has been established with the main goal to improve the design practice for RC walls and wall systems, and to develop the appropriate tools to achieve this goal. Through the partners of the Institute, the results of the project will be efficiently disseminated.

7.1.2 Test unit_MODEL01

The main objective of the whole project was to experimentally study the interaction between piers and floors in RC coupled walls. The influence of slabs to this interaction and redistribution of demand between components at different seismic intensities, as well as numerical models, which can more reliably simulate the response have been studied.

A laboratory specimen-model01 consisting of piers coupled only by the slabs was tested in this project.

The geometry of the specimen is illustrated in Figure 345. More details can be found in the construction and detailing plans of the specimen. The dimensions of the specimen have been defined considering a wall configuration and pertinent floor area of typical residential RC wall building in Europe. The dimensions of the floor are 3.0 m x 3.0 m. The typical story height of the model is 1.5 m.

The specimen consists of two coupled walls, consisting of two rectangular piers each. The thickness of the walls in the model is 10 cm. The length of the single pier is 75 cm. The clear distance between piers is 50 cm. This corresponds to the typical door openings in walls (1.0 m in the prototype). The total height of the piers is 4.5 m. The height of the specimen and the number of stories has been selected considering the appropriate height-to-length ratio of piers, which is in the coupling direction larger than 4 ($4.5 / 0.75 = 6.3$). This will ensure the predominately flexural response of piers and reasonably realistic distribution of the bending moments. The coupling of piers will be provided only by 8 cm thick slab.

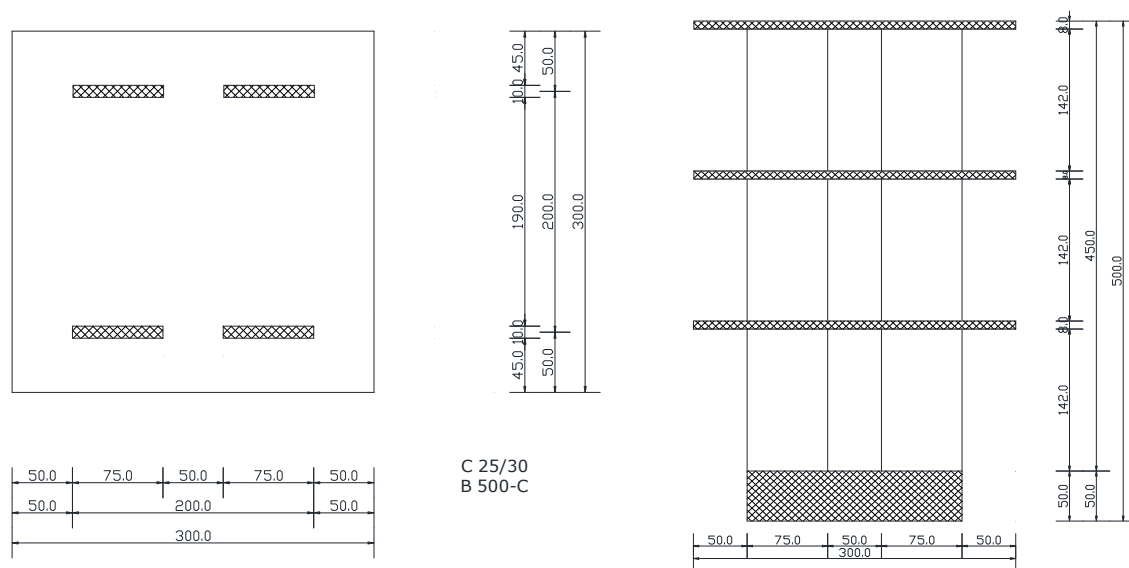


Figure 345: Geometry of the specimen with coupling beams - Typical floor plan (left), Typical cross-section (right)

Standard concrete C25/30 has been used for all structural components. The selected scale allows the use of the standard reinforcement B500-C. The concrete walls have been reinforced by 6Φ6 on each face of the walls and for the slabs Q-131 meshes were mounted as top and bottom reinforcement.



Figure 346: Mounted reinforcement in the bearing walls (left) and slab concreting (right)



Figure 347: Laboratory specimen after construction (left) and mounted on the shaking table (right)

7.1.3 Test setup

The laboratory specimen has been instrumented with linear variable differential transformers (LVDT), Linear potentiometers (LP), Accelerometers. The positions of the instrumentation scheme for accelerometers, linear potentiometers, linear variable displacement transducers and strain gages are given in the Figure 348 to Figure 353.

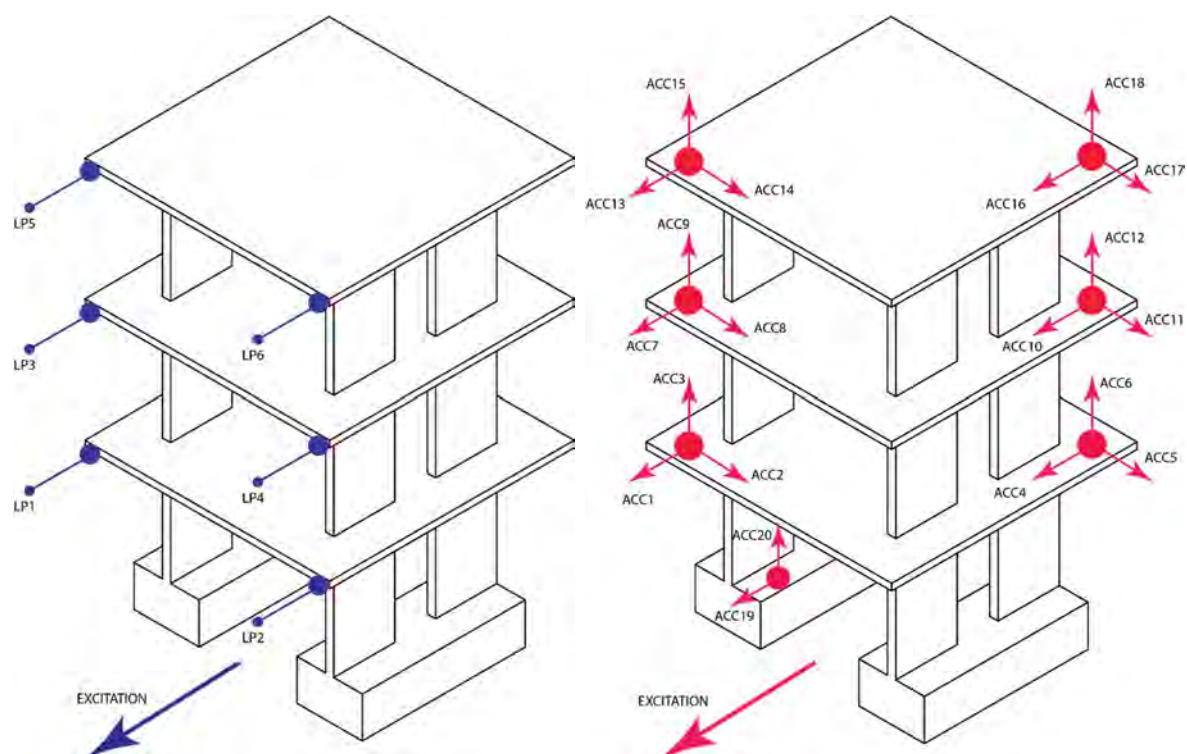


Figure 348: Position of the linear potentiometers (left) in the model and accelerometers (right)

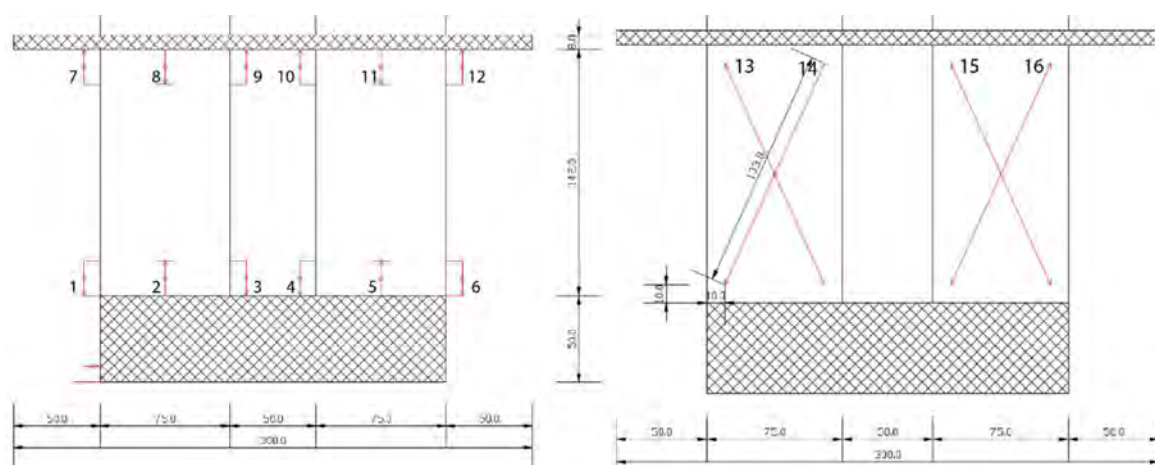


Figure 349: LVDTs 1st floor (1/2) (left) and LVDTs 1st floor (2/2) (right)

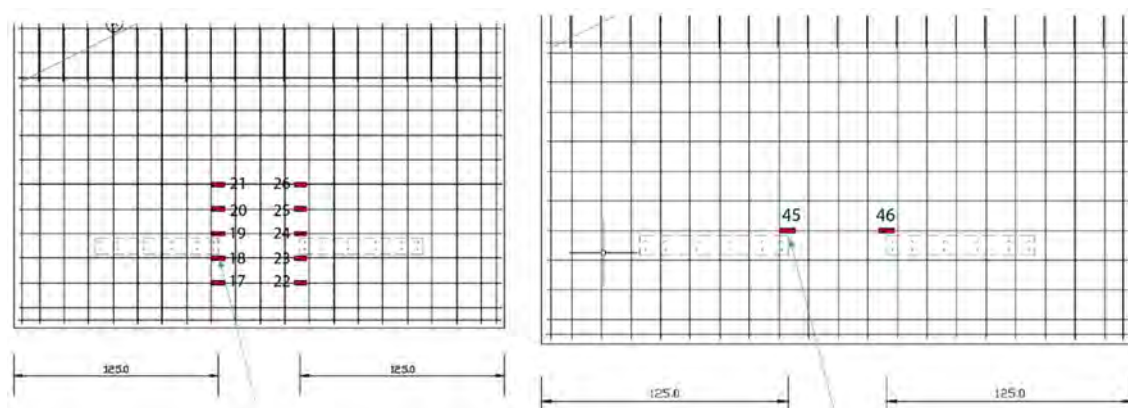


Figure 350: Strain gauges – 1st slab, bottom mesh (let) and 2nd slab, bottom mesh (right)

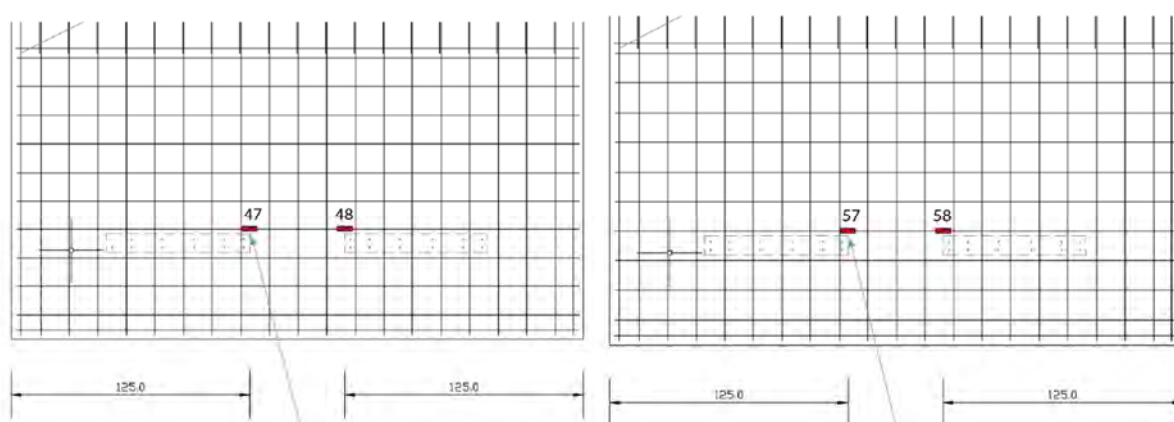


Figure 351: Strain gauges – 2nd slab, top mesh (left) and 3rd slab, bottom mesh (right)

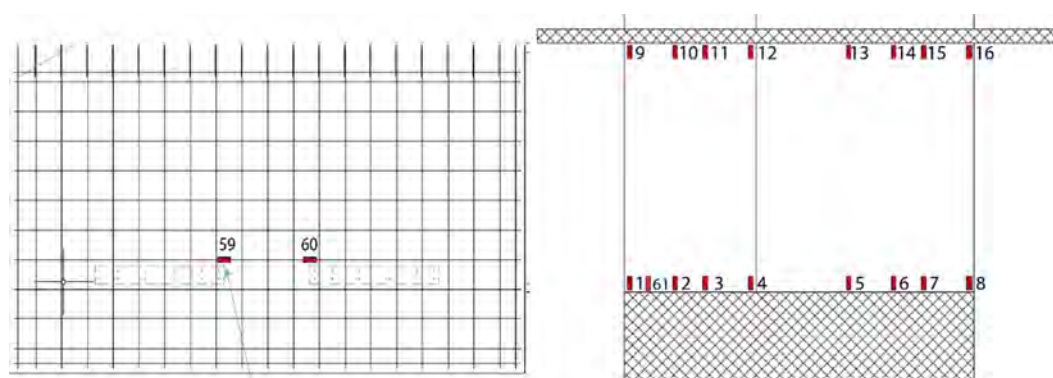


Figure 352: Strain gauges – 3rd slab, top mesh (left) and 1st floor walls (on longitudinal bars) (right)

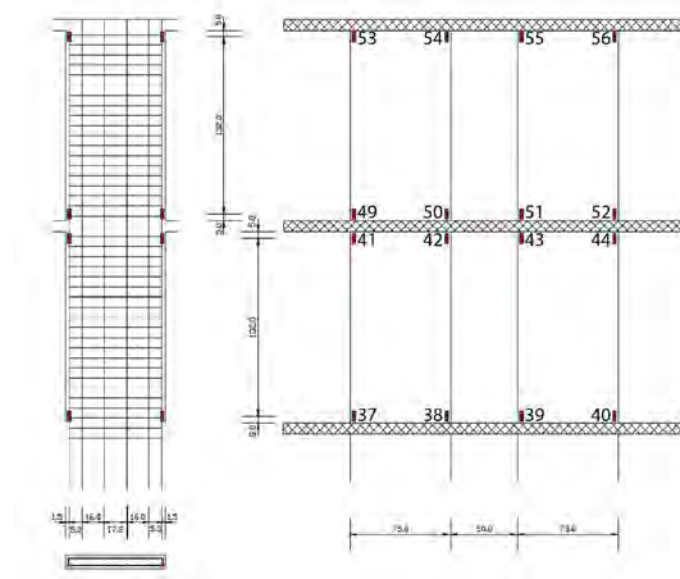


Figure 353: Strain gauges – 2nd and 3rd floor walls (on longitudinal bars)

7.1.4 Testing protocol

The test method consisted of the following activities:

- Resonant frequency search tests – Random and Sine Sweep tests
- Time history shake table uniaxial tests with gradually increase of the input excitation.

The input excitation was an artificially generated accelerogram given by the users from University of Ljubljana (Figure 354). The target spectrum of the generated accelerogram was in correlation with EC8-1, Type 1, soil type A and 2 % damping.

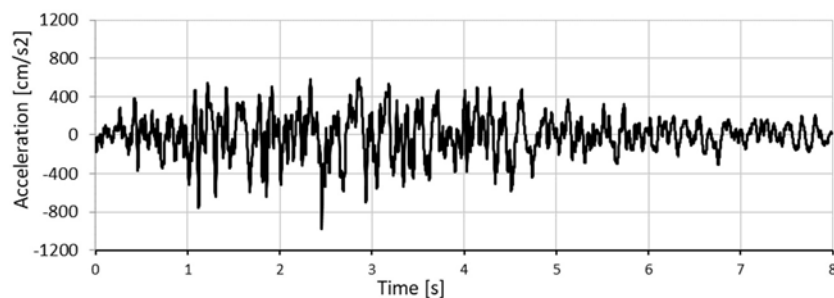


Figure 354: The artificially generated accelerogram scaled to 1.0 g. (prepared by University of Ljubljana)

The spectrum of the accelerogram is shown on Figure 355 and shows a good match with the target spectrum.

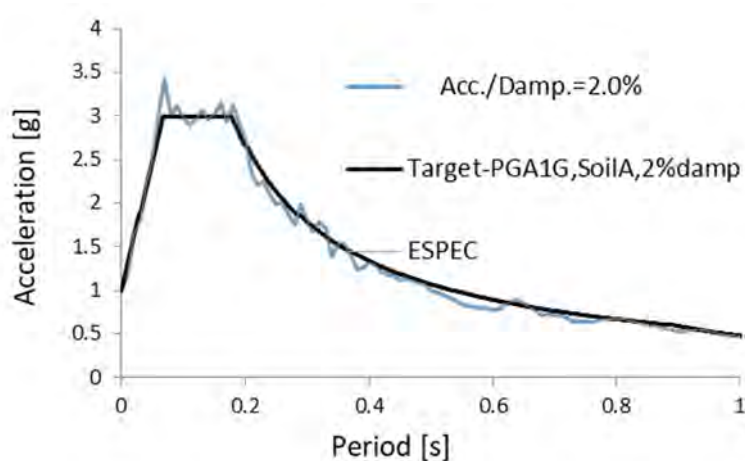


Figure 355: Spectrum of the generated accelerogram (prepared by University of Ljubljana)

In Table 47 a complete list with description of all performed tests is shown.

Test ID	Test type	Axis	Test parameters
Test 7	Random	Y	f: 1÷35 Hz, a=0.02 g
Test 8	Sine sweep test	Y	f: 1÷35Hz, a=0.02 g sweep rate: 1 oct/min
Test 9	Time History Seismic test 10	Y	Ref. peak acc.: 0.091 g (Y)
Test 10	Time History Seismic test 30	Y	Ref. peak acc.: 0.183 g (Y)
Test 11	Sine sweep test	Y	f: 1÷35Hz, a=0.02 g sweep rate: 1 oct/min
Test 12	Random	Y	f: 1÷35 Hz, a=0.02 g
Test 13	Time History Seismic test 50	Y	Ref. peak acc.: 0.304 g (Y)
Test 14	Sine sweep test	Y	f: 1÷35Hz, a=0.02 g sweep rate: 1 oct/min
Test 15	Random	Y	f: 1÷35 Hz, a=0.02 g
Test 16	Time History Seismic test 70	Y	Ref. peak acc.: 0.473 g (Y)
Test 17	Sine sweep test	Y	f: 1÷35Hz, a=0.02 g sweep rate: 1 oct/min
Test 18	Random	Y	f: 1÷35 Hz, a=0.02 g
Test 19	Time History Seismic test 100	Y	Ref. peak acc.: 0.620 g (Y)
Test 20	Sine sweep test	Y	f: 1÷35Hz, a=0.02 g sweep rate: 1 oct/min
Test 21	Random	Y	f: 1÷35 Hz, a=0.02 g
Test 22	Time History Seismic test 130	Y	Ref. peak acc.: 0.779 g (Y)
Test 23	Sine sweep test	Y	f: 1÷35Hz, a=0.02 g sweep rate: 1 oct/min

Test 24	Random	Y	f: 1÷35 Hz, a=0.02 g
Test 25	Time History Seismic test 160	Y	Ref. peak acc.: 0.961 g (Y)
Test 26	Sine sweep test	Y	f: 1÷35Hz, a=0.02 g sweep rate: 1 oct/min
Test 27	Random	Y	f: 1÷35 Hz, a=0.02 g
Test 28	Time History Seismic test 200	Y	Ref. peak acc.: 1.114 g (Y)
Test 29	Sine sweep test	Y	f: 1÷35Hz, a=0.02 g sweep rate: 1 oct/min
Test 30	Random	Y	f: 1÷35 Hz, a=0.02 g
Test 31	Time History Seismic test 250	Y	Ref. peak acc.: 1.473 g (Y)
Test 32	Sine sweep test	Y	f: 1÷35Hz, a=0.02 g sweep rate: 1 oct/min
Test 33	Random	Y	f: 1÷35 Hz, a=0.02 g

Table 47: Sequential order of performed tests – Test SET-UP

7.1.5 Observation during testing

Shake table tests were carried out for various earthquake load levels as explicitly shown in Table 47. In the same time the white noise tests gave insight of the progressive change of the dynamic characteristics of the system. The visual observations during testing as well as direct control of the drifts and change in eigen frequencies, then indirectly the stiffness, led to several conclusions during testing.

Slabs were considerably cracked over the entire width between two rows of piers. The response of the wall piers was considerably different from that typical for the cantilever walls. The considerable rocking was observed in the piers subjected to relatively large tension. In the piers subjected to the compression, the buckling of the longitudinal bars was occurred due to the relatively large compressive stresses also induced by the frame action of the slab. (Figure 356)



Figure 356: Cracks in second slab(left) and pier foundation contact (right)

7.1.6 Results

In Table 50, characteristic changes of measured frequencies before and after seismic tests are presented. Graphical presentations of frequency response function for the first, middle and the last random tests are given on the Figure 357 where it can be clearly seen the decreasing of the frequency as a result of global change of the stiffness of the model. Operational modal analysis was performed using ARTeMIS Modal software and the natural frequencies and mode shapes of vibrations were determined using the Peak Picking technique and the Frequency Domain Decomposition technique. The results were obtained for the first and last random test. Graphical presentation of the obtained results is presented on Figure 358.

Test No.	Name of the test	Frequency [Hz]
7	Random	7.35
12	Random	7.30
15	Random	7.23
18	Random	6.81
21	Random	6.35
24	Random	5.55
27	Random	5.17
30	Random	4.47
33	Random	2.86

Table 48: Frequencies after each earthquake test

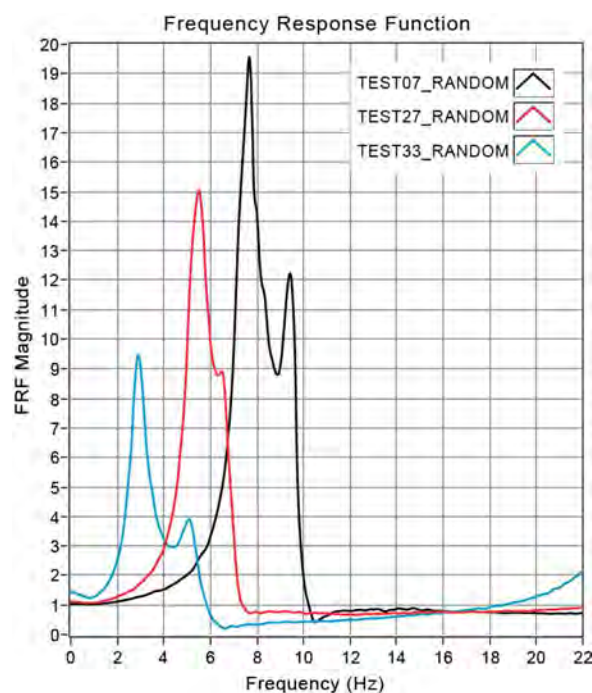


Figure 357: Frequency response function for picked Random Tests

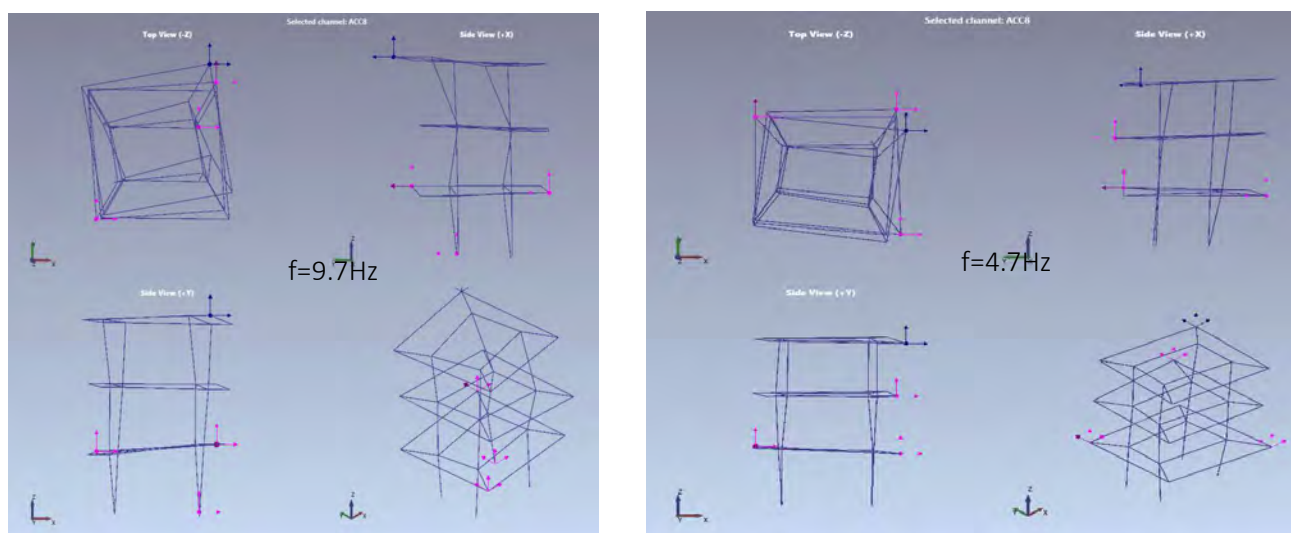


Figure 358: First natural frequency (mode shape) MODEL01 in Y direction-ambient vibration test at the beginning of testing (left) and at the end of testing (right)

In Table 49 to Table 51 are presented the values of the response parameters measured during the most intensive seismic tests. Selected response time histories are given on Figure 359.

Sensor	Test 28	Test 31
ACC1	2.39	3.39
ACC2	0.8	2.32
ACC3	1.01	3.70
ACC4	1.71	1.50
ACC5	0.79	1.83
ACC6	0.61	0.68
ACC7	3.20	3.37
ACC8	1.21	1.02
ACC9	1.36	3.67
ACC10	1.99	1.96
ACC11	1.36	1.26
ACC12	0.78	0.83
ACC13	7.68	5.27
ACC14	1.75	1.60
ACC15	1.60	4.48
ACC16	2.63	3.05
ACC17	1.50	1.73
ACC18	0.94	1.12
ACC19	1.10	/
ACC20	0.65	/

Table 49: Maximum accelerations (g) for test28 & test31

Sensor	Test 28	Test 31
LP1	51	58
LP2	44	55
LP3	30	37
LP4	54	63
LP5	79	88
LP6	64	75
LVDT1	1.19	1.74
LVDT2	0.38	0.56
LVDT3	0.32	0.42
LVDT4	1.20	1.77
LVDT5	0.13	0.18
LVDT6	1.13	5.2
LVDT7	0.24	0.45
LVDT8	0.09	0.23
LVDT9	0.41	0.53
LVDT10	0.36	0.46
LVDT11	0.05	0.11
LVDT12	1.34	1.36
LVDT13	0.56	0.69
LVDT14	0.34	0.39
LVDT15	0.16	0.31
LVDT16	0.24	0.46

Table 50: Maximum displacement (mm) for test 28 & test 31

Sensor	Test 9	Test 22	Test 31
SG1	183	1718	3694
SG 4	118	1963	4851
SG 5	58	797	2465
SG 8	174	2387	4283
SG 18	53	989	2820
SG 21	32	996	2853
SG 37	85	1224	2343
SG 39	51	745	1738
SG 45	39	1120	4109
SG 53	78	529	959
SG 56	6	25	150
SG 57	35	633	1755

Table 51: Maximum strain (μ Strain) for selected strain gauges

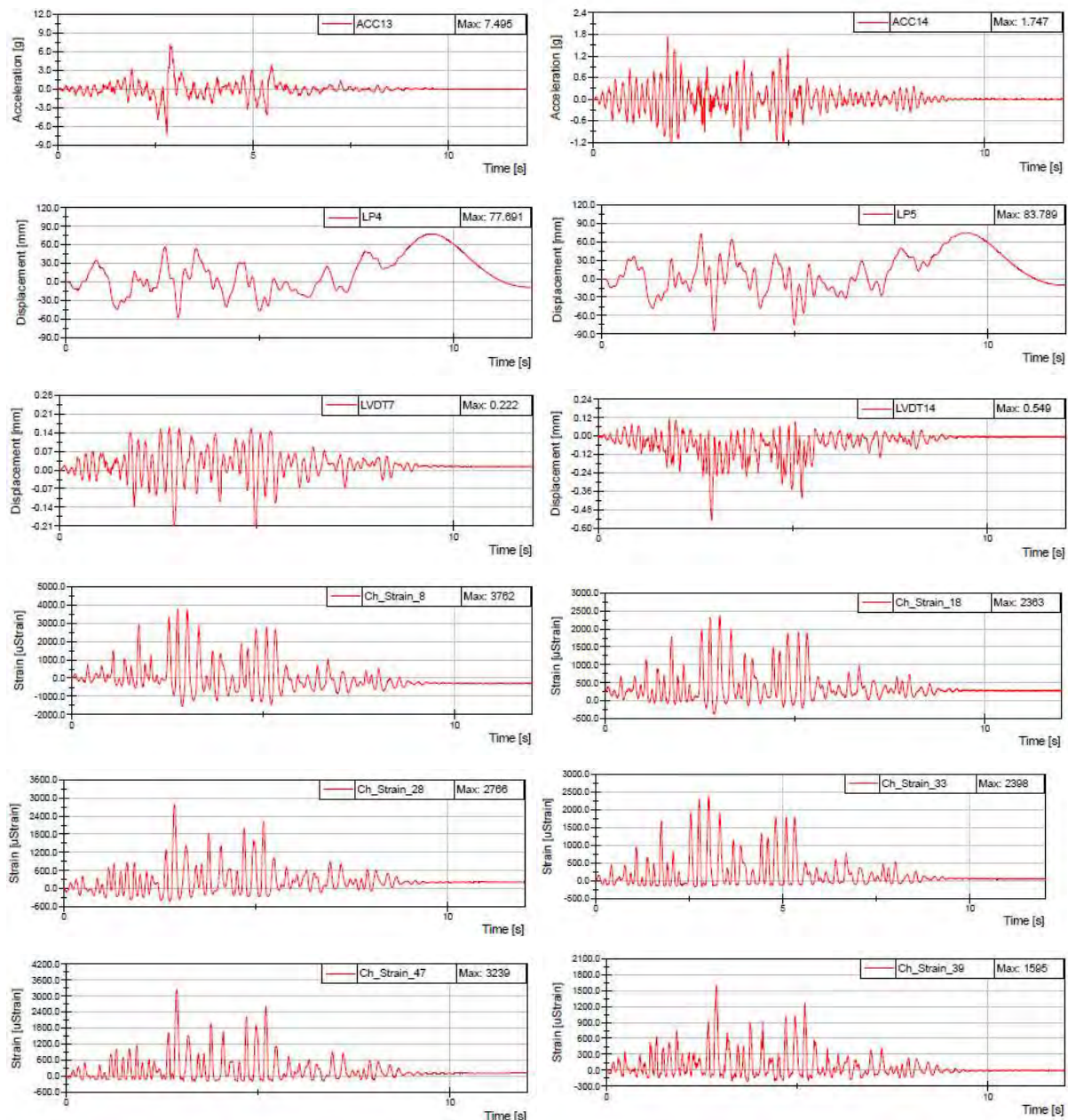


Figure 359: Response time histories for acceleration, displacements and strains for selected test

All data from the tests including response histories of accelerations, displacements, and dilatations, as well as videos from each test will be available on the SERA Data Access Portal and on DVDs as a part of this short technical report.

7.1.7 Test unit_MODEL02

The main objective of the whole project was to experimentally study the interaction between piers and floors in RC coupled walls. The influence of slabs to this interaction and redistribution of demand between components at different seismic intensities, as well as numerical models, which can more reliably simulate the response have been studied.

A laboratory specimen-model01 consisting of piers coupled only by the slabs was tested in this project.

The geometry of the specimen is illustrated in Figure 360. More details can be found in the construction and detailing plans of the specimen. The dimensions of the specimen have been defined considering a wall configuration and pertinent floor area of typical residential RC wall building in Europe. The dimensions of the floor are 3.0 m x 3.0 m. The typical story height of the model is 1.5 m.

The specimen consists of two coupled walls, consisting of two rectangular piers each. The thickness of the walls in the model is 10 cm. The length of the single pier is 75 cm. The clear distance between piers is 50 cm. This corresponds to the typical door openings in walls (1.0 m in the prototype). The total height of the piers is 4.5 m. The height of the specimen and the number of stories has been selected considering the appropriate height-to-length ratio of piers, which is in the coupling direction larger than 4 ($4.5 / 0.75 = 6.3$). This will ensure the predominately flexural response of piers and reasonably realistic distribution of the bending moments. The coupling of piers will be provided only by 8 cm thick slab.

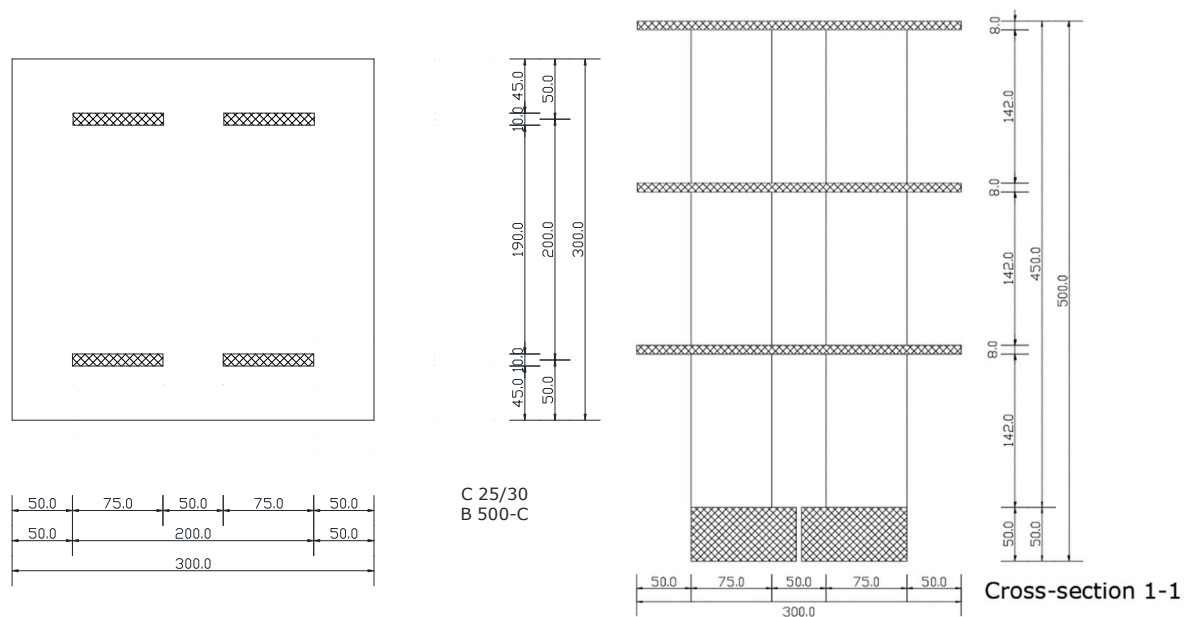


Figure 360: Geometry of the specimen with coupling beams - Typical floor plan (left), Typical cross-section (right)

Standard concrete C25/30 has been used for all structural components. The selected scale allows the use of the standard reinforcement B500-C. The concrete walls have been reinforced by 6Φ8 on each face of the walls and for the slabs Q-131 meshes were mounted as top and bottom reinforcement.



Figure 361: Mounted reinforcement in the bearing walls (left) and slab concreting (right)

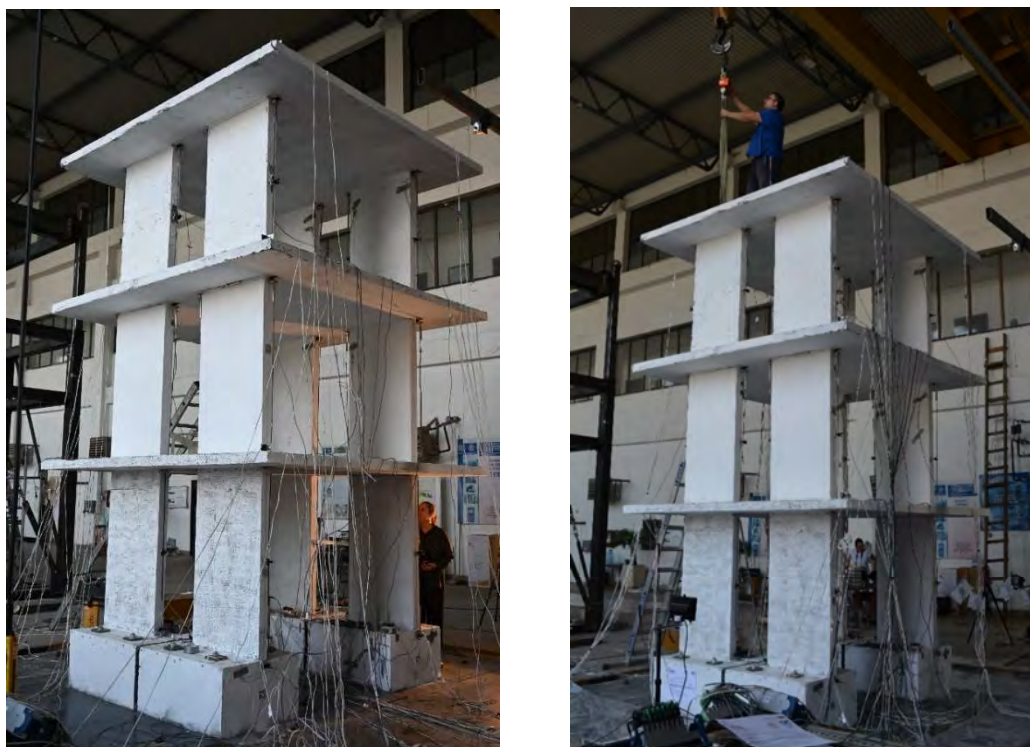


Figure 362: Laboratory specimen after construction (left) and mounted on the shaking table (right)

7.1.8 Test setup

The laboratory specimen has been instrumented with linear variable differential transformers (LVDT), and accelerometers. The positions of the instrumentation scheme for accelerometers, linear variable displacement transducers and strain gages are given in the Figure 363 to Figure 368.

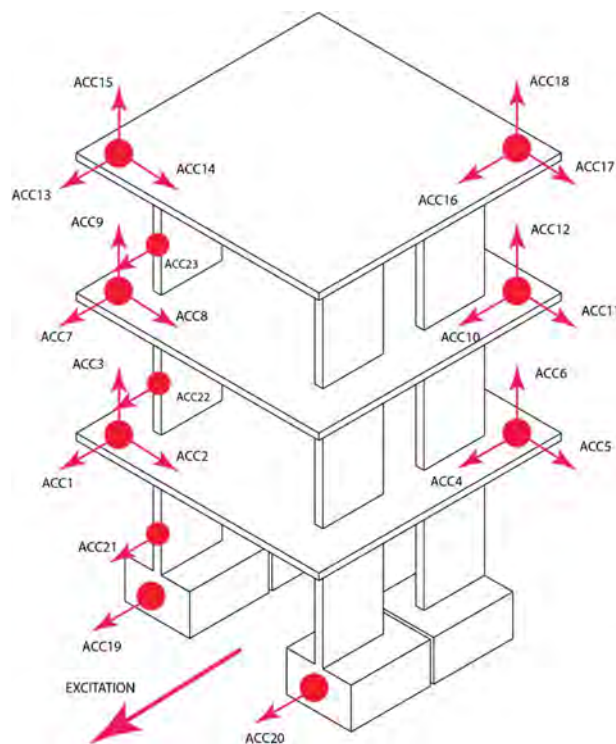


Figure 363: Position of the linear potentiometers (left) in the model and accelerometers (right)

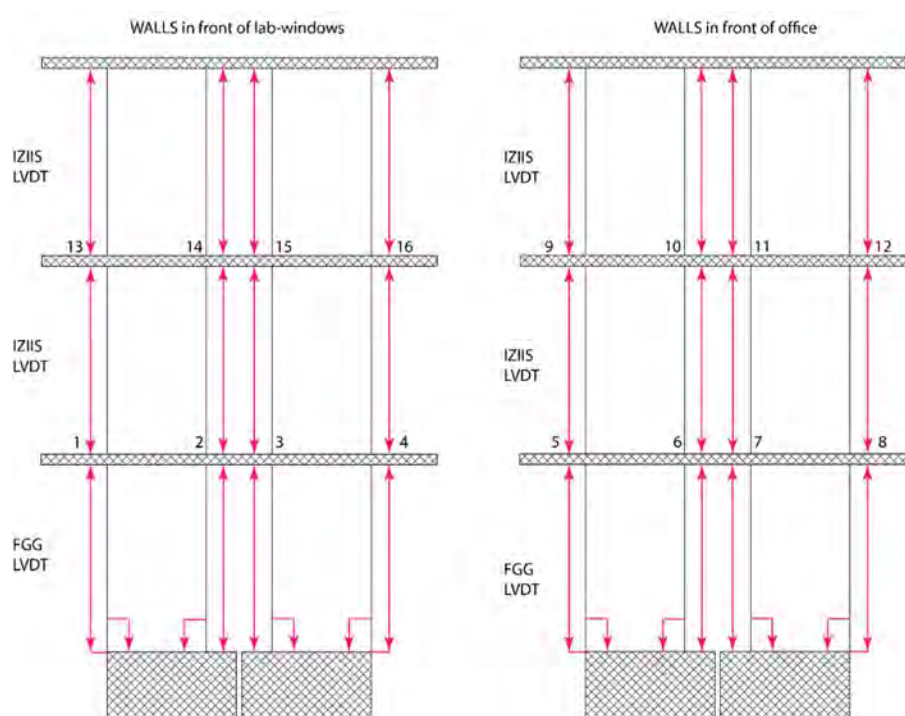


Figure 364: Positions of LVDTs in the model

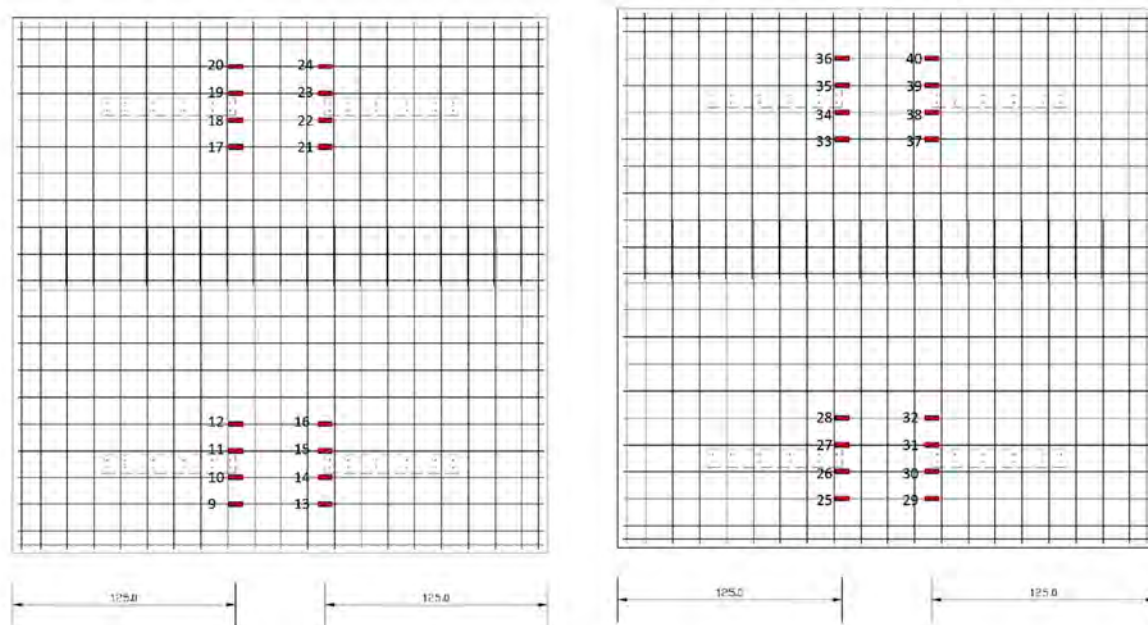


Figure 365: Strain gauges – 1st slab, bottom mesh (let) and top mesh (right)

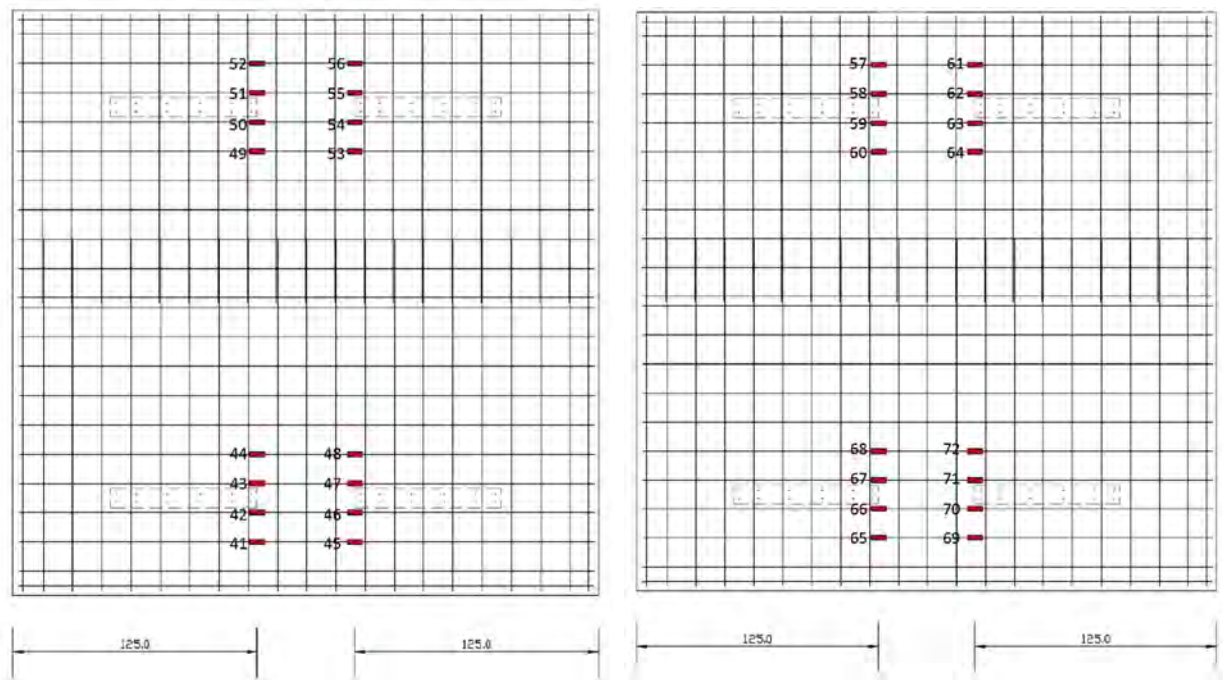


Figure 366: Strain gauges – 2nd slab, bottom mesh (left) and top mesh (right)

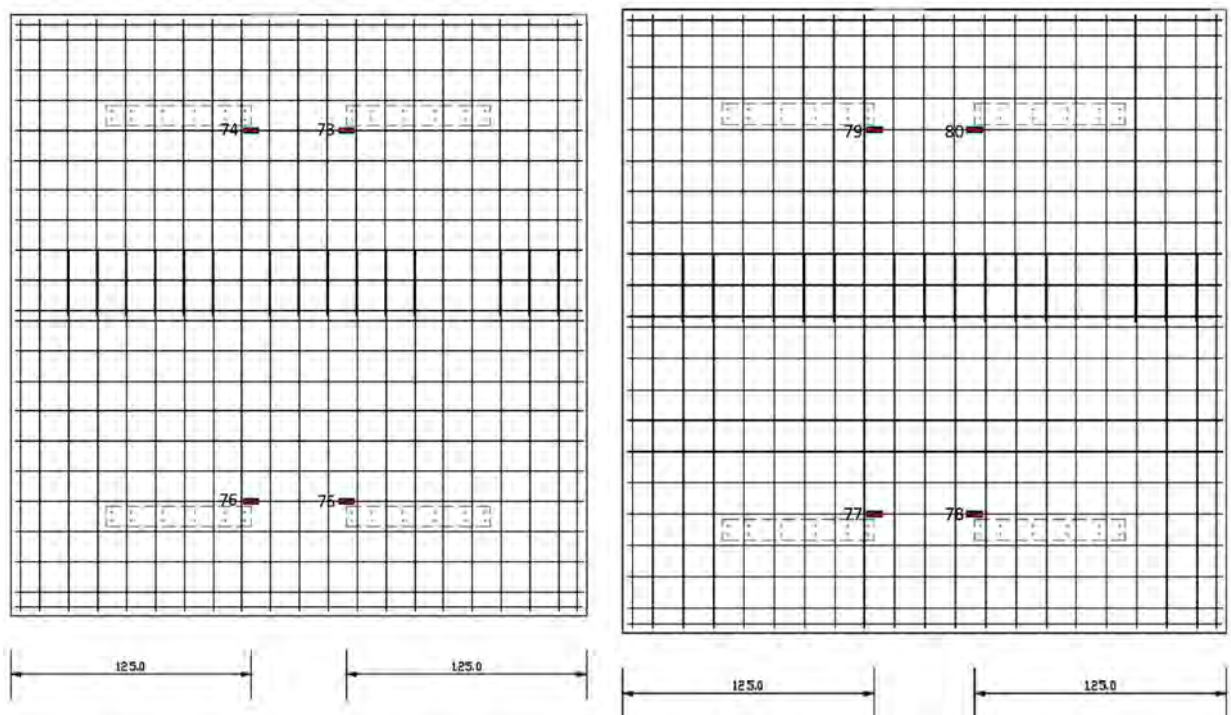


Figure 367: Strain gauges – 3rd slab, bottom mesh (left) and top mesh (right)

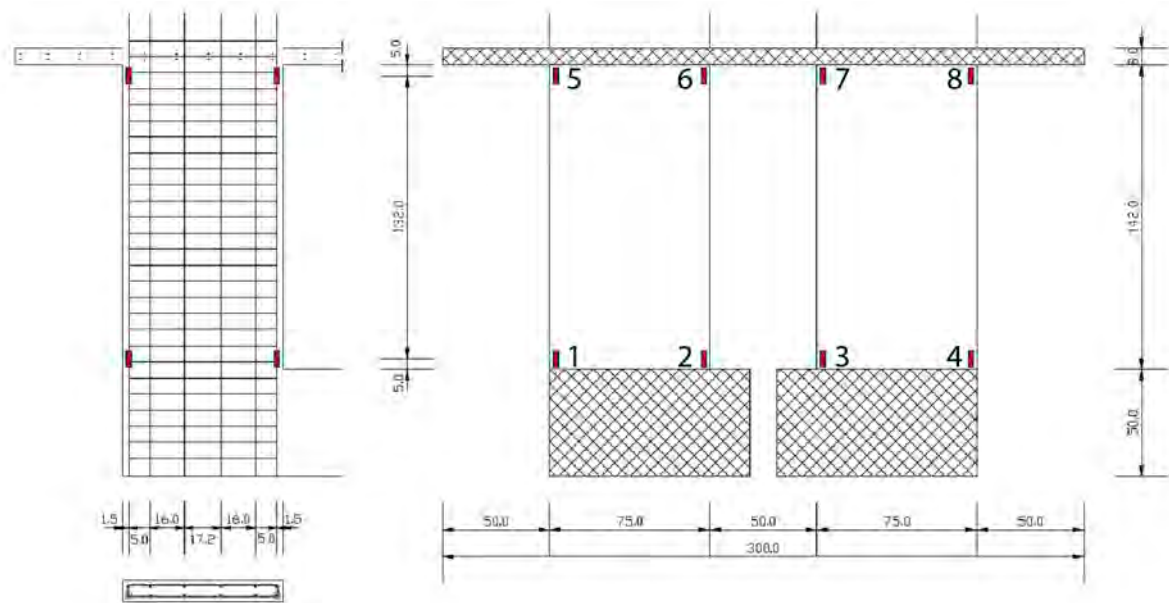


Figure 368: Strain gauges – 1st floor walls (on longitudinal bars)

7.1.9 Testing protocol

The test method consisted of the following activities:

- Resonant frequency search tests – Random and Sine Sweep tests
- Time history shake table uniaxial tests with gradually increase of the input excitation.

The input excitation was an artificially generated accelerogram given by the users from University of Ljubljana (Figure 369). The target spectrum of the generated accelerogram was in correlation with EC8-1, Type 1, soil type A and 2 % damping.

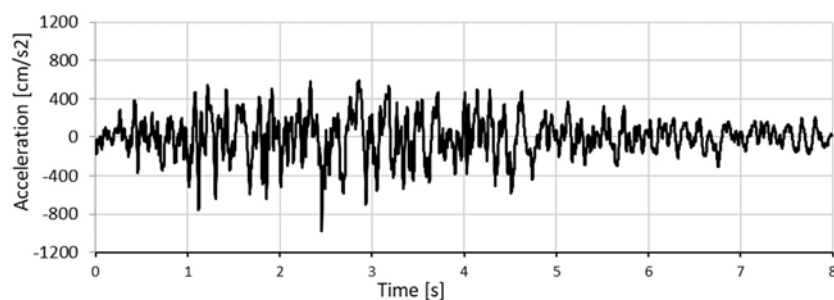


Figure 369: The artificially generated accelerogram scaled to 1.0 g. (prepared by University of Ljubljana)

The spectrum of the accelerogram is shown on Figure 370 and shows a good match with the target spectrum.

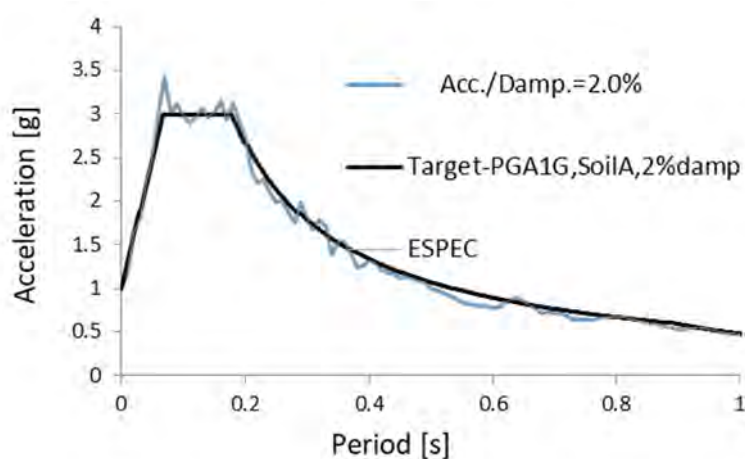


Figure 370: Spectrum of the generated accelerogram (prepared by University of Ljubljana)

In Table 52 a complete list with description of all performed tests is shown.

Test ID	Test type	Axis	Test parameters
Test 3	Random	Y	f: 1÷35 Hz, a=0.02 g
Test 4	Time History Seismic test 10	Y	Ref. peak acc.: 0.071 g (Y)
Test 5	Time History Seismic test 30	Y	Ref. peak acc.: 0.179 g (Y)
Test 6	Time History Seismic test 50	Y	Ref. peak acc.: 0.307 g (Y)
Test 7	Time History Seismic test 70	Y	Ref. peak acc.: 0.465 g (Y)
Test 8	Time History Seismic test 100	Y	Ref. peak acc.: 0.601 g (Y)
Test 9	Time History Seismic test 100	Y	Ref. peak acc.: 0.567 g (Y)
Test 10	Random	Y	f: 1÷35 Hz, a=0.02 g
Test 11	Random	Y	f: 1÷35 Hz, a=0.02 g
Test 12	Time History Seismic test 130	Y	Ref. peak acc.: 0.764 g (Y)
Test 13	Time History Seismic test 160	Y	Ref. peak acc.: 0.922 g (Y)
Test 14	Time History Seismic test 200	Y	Ref. peak acc.: 1.186 g (Y)
Test 15	Time History Seismic test 250	Y	Ref. peak acc.: 1.512 g (Y)
Test 16	Random	Y	f: 1÷35 Hz, a=0.02 g
Test 17	Time History Seismic test 250	Y	Ref. peak acc.: 1.537 g (Y)
Test 18	Random	Y	f: 1÷35 Hz, a=0.02 g

Table 52: Sequential order of performed tests – Test SET-UP

7.1.10 Observation during testing

Shake table tests were carried out for various earthquake load levels as explicitly shown in Table 52. In the same time the white noise tests gave insight of the progressive change of the dynamic characteristics of the system. The visual observations during testing as well as direct control of the drifts and change in eigen frequencies, then indirectly the stiffness, led to several conclusions during testing.

Slabs were considerably cracked over the entire width between two rows of piers. The response of the wall piers was considerably different from that typical for the cantilever walls. The considerable rocking was observed in the piers subjected to relatively large tension. In the piers subjected to the compression, the buckling of the longitudinal bars was occurred due to the relatively large compressive stresses also induced by the frame action of the slab. (Figure 371)



Figure 371: Cracks in walls (left) and slabs (right)

7.1.11 Results

In Table 53, characteristic changes of measured frequencies before and after seismic tests are presented. Graphical presentations of frequency response function for the first, middle and the last random tests are given on the Figure 372 where it can be clearly seen the decreasing of the frequency as a result of global change of the stiffness of the model. Operational modal analysis was performed using ARTeMIS Modal software and the natural frequencies and mode shapes of vibrations were determined using the Peak Picking technique and the Frequency Domain Decomposition technique. The results were obtained for the first and last random test. Graphical presentation of the obtained results is presented on Figure 372a.

Test No.	Name of the test	Frequency [Hz]
3	Random	8.24
10	Random	5.86
11	Random	6.1
16	Random	3.3
18	Random	3.1

Table 53: Frequencies after each earthquake test

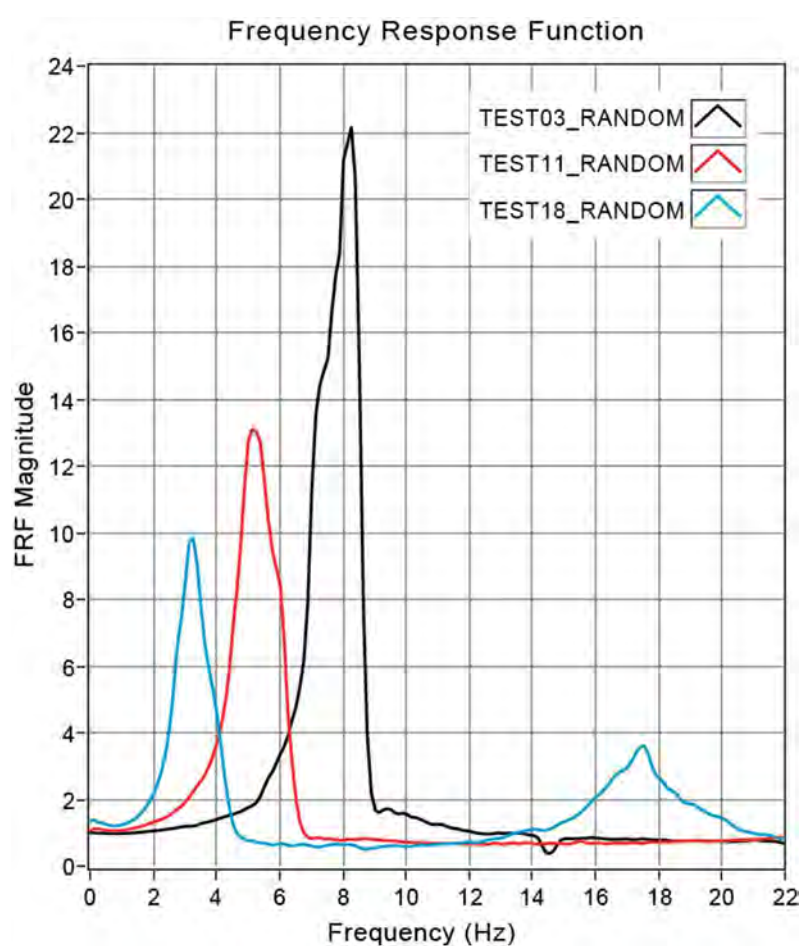


Figure 372: Frequency response function for picked Random Tests

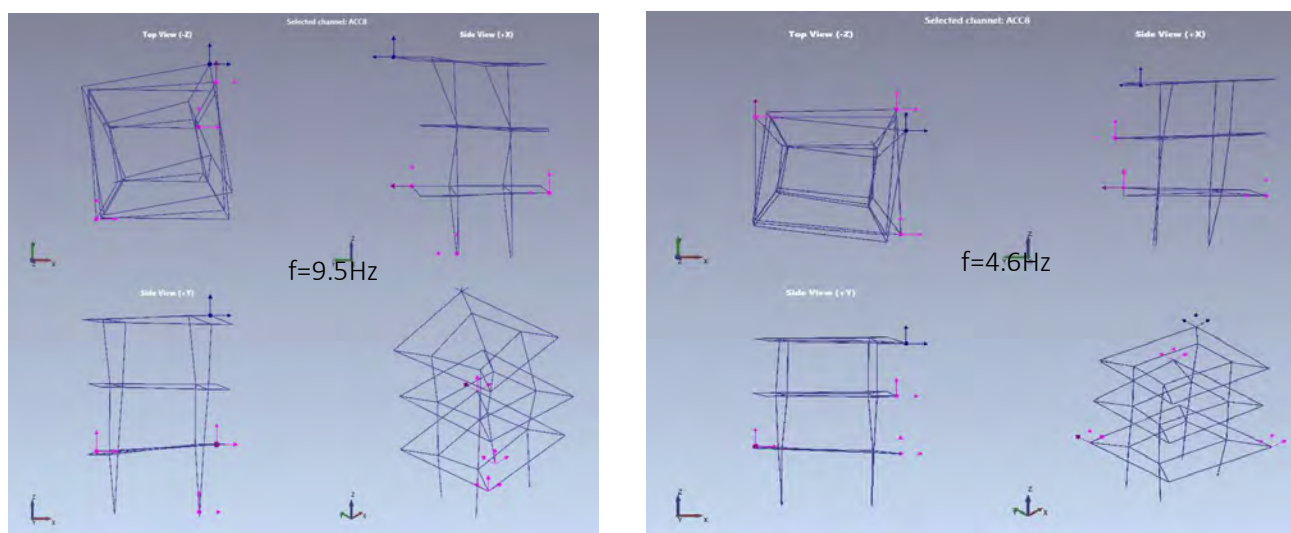


Figure 373: First natural frequency (mode shape) MODEL02 in Y direction-ambient vibration test at the beginning of testing (left) and at the end of testing (right)

In the Table 54 to Table 56 are presented the values of the response parameters measured during the most intensive seismic tests. Selected response time histories are given on Figure 374.

Sensor	Test 14	Test 17
ACC1	1.928	2.125
ACC2	0.71	1.457
ACC3	0.85	0.96
ACC4	1.42	1.84
ACC5	0.62	0.98
ACC6	0.66	0.83
ACC7	2.86	2.78
ACC8	0.86	1.02
ACC9	0.87	0.85
ACC10	1.94	2.1
ACC11	0.92	1.03
ACC12	0.88	0.93
ACC13	3.86	4.12
ACC14	1.25	1.69
ACC15	1.11	1.32
ACC16	3.15	3.30
ACC17	1.28	1.61
ACC18	0.93	1.19
ACC19	/	/
ACC20	1.14	1.56
ACC21	/	/
ACC22	2.41	2.18
ACC23	3.03	3.11

Table 54: Maximum accelerations (g) for test14 & test17

Sensor	Test 14	Test 17
LVDT1	0.041	0.042
LVDT2	0.17	0.26
LVDT3	0.37	0.44
LVDT4	0.4	0.37
LVDT5	0.86	1.42
LVDT6	1.1	1.02
LVDT7	23	13
LVDT8	/	/
LVDT9	0.025	0.031
LVDT10	0.164	0.303
LVDT11	0.056	0.114
LVDT12	0.028	0.042
LVDT13	0.091	0.139
LVDT14	12.42	3.4
LVDT15	2.01	2.38
LVDT16	0.06	0.25

Table 55: Maximum displacement (mm) for test 14 & test 17

Sensor	Test 4	Test 14	Test 17
SG1	118	630	194
SG 4	50	804	256
SG 5	558	/	/
SG 8	662	/	/
SG 18	299	3409	4378
SG 21	664	2294	2289
SG 37	57	4124	4332
SG 39	118	2351	/
SG 45	29	2046	2663
SG 53	145	2862	8723
SG 56	159	2779	/
SG 57	78	2745	8455

Table 56: Maximum strain (μ Strain) for selected strain gauges

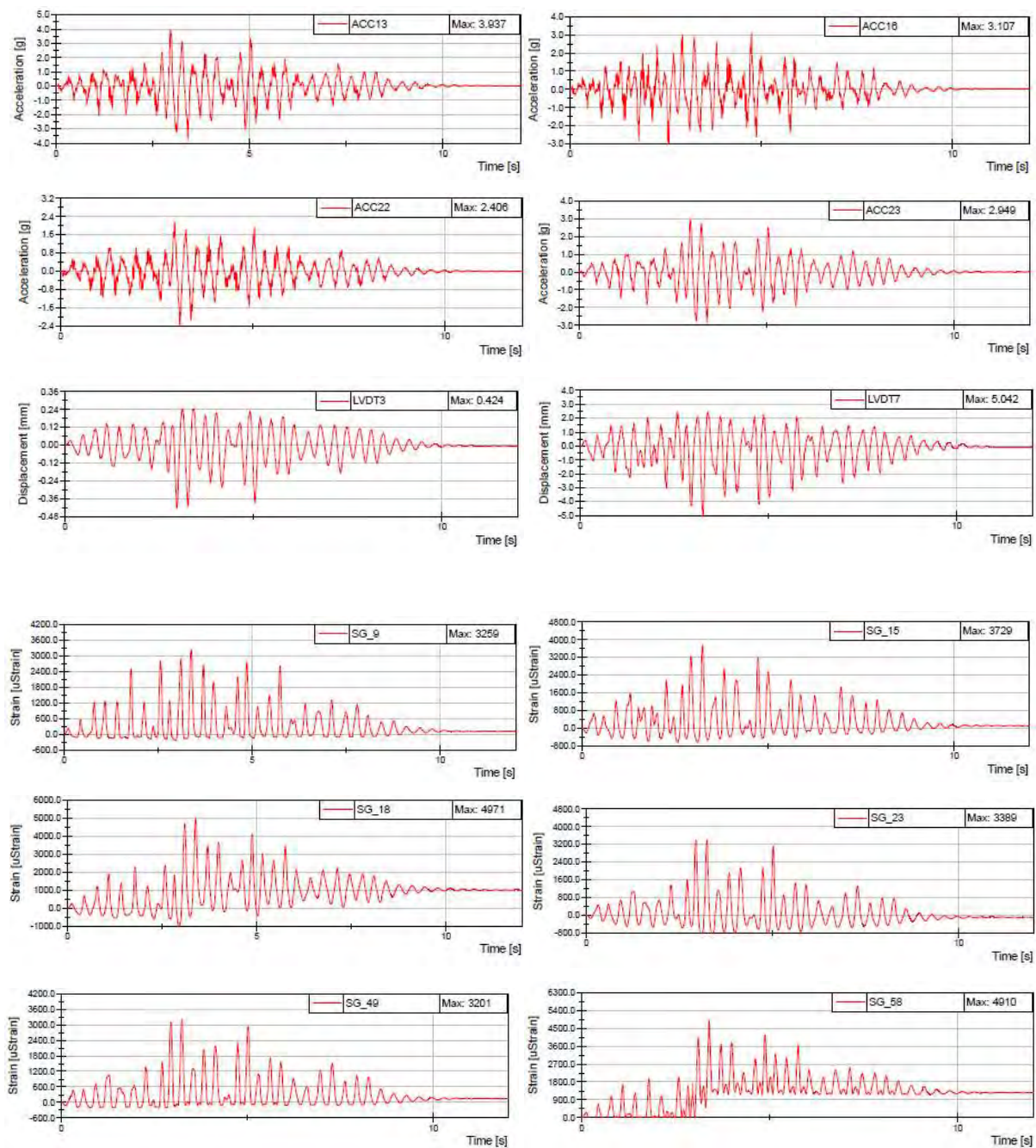


Figure 374: Response time histories for acceleration, displacements and strains for selected test

All data from the tests including response histories of accelerations, displacements, and dilatations, as well as videos from each test will be available on the SERA Data Access Portal and on DVDs as a part of this short technical report.

7.1.12 Conclusions and outlook

In the project, two 1:2 scale three-floor RC models were tested on the shaking table to study the effect of coupling in coupled shear walls. In this report, the results of the second test are shown and analyzed.

The tests have shown that coupling has a considerable effect on the response of the structure, as the coupling ratio (CR), defined as the moment provided by axial forces divided by the total overturning moment resistance, amounted to about 50 %.

All slabs were fully activated. They were considerably cracked over the entire width between two rows of piers. The response of the wall piers was considerably different from that typical for the cantilever walls. The considerable rocking was observed in the piers subjected to relatively large tension, which was induced by the frame effect. In the piers subjected to the compression, the buckling of the longitudinal bars was occurred due to the relatively large compressive stresses also induced by the frame action of the slab.

The failure occurred with actual PGA intensity 1.54 g that corresponds to 0.62 g in real scale.

The presented experiment confirmed the indications of some other experiments that can be found in the literature, that for certain building configurations only the slabs without beams can provide considerable coupling of wall piers. In such cases, the common design, based on the assumptions that the walls respond as cantilever walls, can lead to significant underestimation of the demand in piers. This can further lead either to brittle shear failure of walls or to their failure caused by the buckling of the longitudinal bars induced by large compression stresses, which were underestimated in the design.

7.2 Project #23 – Investigation of Seismic Deformation Demand, Capacity and Control in a Novel Self-Centring Steel Braced Frame (SC-CBF)

Authors

Z. Rakicevic⁽¹⁾, A. Bogdanovic⁽¹⁾, I. Gjorgjiev⁽¹⁾, B. Petreski⁽¹⁾, A. Poposka⁽¹⁾, B. Broderick⁽²⁾, J. Goggins⁽³⁾, Y. Jiang⁽³⁾, S. Salawdeh⁽⁴⁾, A. Elghazouli⁽⁵⁾

⁽¹⁾ *University of Ss. Cyril and Methodius, Institute of Earthquake Engineering and Engineering Seismology, Skopje, North Macedonia*

⁽²⁾ *Trinity College Dublin, Dept of Civil, Structural and Environmental Engineering, Dublin, Ireland*

⁽³⁾ *National University of Ireland, Galway, Ireland*

⁽⁴⁾ *Galway Mayo Institute of Technology, Galway, Ireland*

⁽⁵⁾ *Imperial College London, Department of Civil and Environmental Engineering, London, UK*

7.2.1 Introduction

Diagonal bracing members in CBFs are critical elements and during strong seismic loading experience repeated cycles involving yielding in tension and member buckling in compression. The performance of these members depends on various factors, including global slenderness, local slenderness, material strengths and end restraint/connections [1]. Due to the difficulty of accurately modelling this complex response, experimental studies have been employed to study the cyclic inelastic behaviour of bracing members. Early studies examined the load-displacement hysteretic response which was shown to be most strongly influenced by global slenderness [2]. Slender members lost compressive resistance more rapidly than stocky members, resulting in fewer inelastic response cycles and less energy dissipation. Later research examined the factors influencing the fracture life of bracing members. Through

experimental testing, both global and local slenderness were found to influence fracture life [3]. The structural efficiency of thin-walled hollow section members has led to their widespread use as bracing members in CBFs. However, in the post-buckling phase, local buckling occurs in the plastic hinges which form at mid-length of these members. The high strain demands in these local buckles cause crack initiation, leading to complete fracture in subsequent load cycles, with a number of empirical expressions for fracture life and ductility capacity being proposed [4].

Gusset-plate connections employed in CBFs in which out-of-plane brace buckling is envisaged must be designed to accommodate the large end-rotations experienced by buckled compression braces at large storey drifts. This requires the formation of a stable ductile plastic hinge within the gusset plate, while the connection design details must also prevent gusset plate buckling in compression or yielding in tension [5]. Current design guidance and practice on these issues can lead to the use of over-sized plates which can reduce the seismic performance of the brace members themselves. More recently, improved gusset plate detailing rules have been recommended that result in more efficient connection designs, while improving the seismic performance of the CBF overall [6].

To support the development and validation of design rules for CBFs in Eurocode 8, members of the user team completed shake table tests to investigate the influence of brace slenderness and overstrength on hysteretic behaviour [7]. Further tests examined the response of brace members with realistic brace connection details subjected to low, medium and high levels of seismic excitation, including ultimate response and fracture (Figure 375) [8,9].

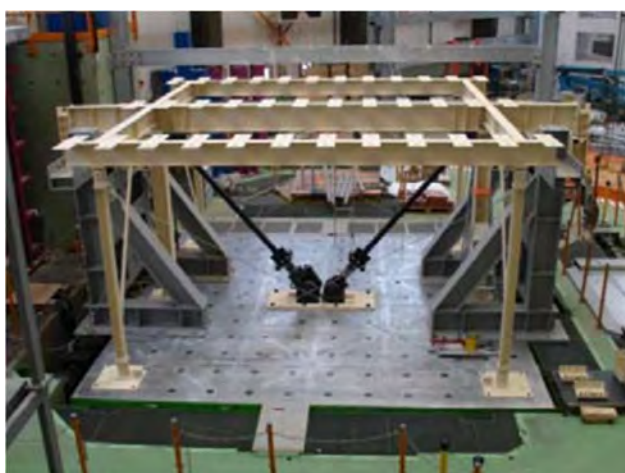


Figure 375: Test frame on Azalee shake table (CEA Saclay) without added masses showing pair of brace-gusset plate specimens [9]

These shake table experiments were supported by complementary cyclic testing of brace members with a wide range of member slenderness and connection details at Trinity College Dublin and NUI Galway [10,11]. Additional testing at Imperial College London characterised cyclic material behaviour in hot-rolled and cold-formed tubular members through cyclic axial and cyclic bending tests on coupon specimens [4], providing a strain-based damage criterion for modelling low cycle fatigue failure, validated through quasi-static cyclic axial loading tests on tubular bracing members with a wide range of member and cross-section slendernesses [4]. Complementary 3D continuum model analysis using ABAQUS was employed in sensitivity and parametric investigations at NUI Galway [11], and in an extensive numerical study on the cyclic behaviour of concentric bracings with different cross-sections (angles, U, RHS) at the University of Ljubljana. Optimum procedures for accurately modelling the global

response of CBFs in OpenSees have also been developed and validated through comparison with experimental results [12].

The CBFs in the above shake table tests suffered large residual drifts after high level seismic excitations that were associated with asymmetric hysteretic brace response and deteriorations in strength and stiffness. Peak and residual drifts were observed to be greater when the brace gusset plates were connected to a beam only (which is common practice in European construction) rather than both a beam and a column (which is typical practice in other regions including the USA). For a more resilient CBF with minimum residual drifts, several innovative damage control procedures have been suggested such as buckling-restrained braces (BRB) [13,14,15] and self-centring systems [16,17,18]. In self-centring systems, post-tensioning arrangements are used to return the structure to its original position following inelastic deformation demands. A novel self-centring CBF system has been developed at NUI Galway and validated through push-over physical laboratory tests and nonlinear time-history analysis of numerical models [19]. Hence, these shake table tests are required to fully validate this novel system under representative dynamic response conditions.

Generally, the necessity of the shake table tests for this project can be summarized through the following objectives:

- Experimentally investigate the variation of seismic deformation demands in CBFs with ground motion characteristics and CBF design parameters;
- Advance the development of a novel self-centring method for damage control in CBFs (SC-CBF);
- Obtain experimental data for the validation of numerical models.

A unique set of data is obtained on the seismic deformation demand and capacity of SC-CBFs with realistic brace members and connections subjected to a variety of ground motions. The processed results include residual frame and brace deformations, brace ductility demand and capacity; the influence of connection detailing on maximum and residual deformations; and measurements of effective stiffness and equivalent viscous damping in SC-CBFs.

7.2.2 Test specimen

The specimen is single-storey structure, consisting of one middle frame and two external frames. The middle frame is a two-bay SC-CBF (Figure 376). The braces varied and four different configurations were tested. The testing was carried out with uniaxial excitation following a defined testing methodology, definition of the dynamic characteristics of the specimens and definition of the dynamic behaviour of the specimens under earthquake/dynamic excitation. The results of the tests are provided in digital format as well as selected representative results, time histories and fast Fourier transformation (FFT) plots in the framework of this report.



Figure 376: Testing model assembled on IZIS shake table

The novel self-centring system employed in the model SC-CBF is designed to eliminate residual deformations in CBF structures. This system employs additional horizontal post-tensioning elements at floor level that ensure that the structure self-centres following an earthquake. The current stage in the development of this novel technology is the use of full-scale shake table testing to prove the self-centring capability of the system to eliminate residual drifts after major seismic loading. The shake table tests should validate the performance of this system under dynamic earthquake loading at different intensities.

The test set-up is similar to that successfully employed by the User Group at CEA Saclay in the ‘BRACED’ SERIES TA Project. The test model comprises a single storey steel frame with a central SC-CBF containing the brace specimens and self-centring system (Fig 32), and two external non-braced gravity frames with very low lateral resistance. These three frames support a test mass of approximately 20 tons at a height of 2.5m above the shake table. The beam and column members used in the middle frame were selected from European H and IPE sections database and remain the same during the testing, whereas the brace elements and the gusset plate varied, providing four different configurations. Bolted connections between the brace and beam members facilitate the easy exchange of the brace specimens between tests. The brace members are fabricated from cold formed tubular steel sections (S235/275). Cross-section dimensions are selected to obtain normalised brace slenderness in the practical range. The test specimens collectively capture the most important brace parameters known to affect seismic performance, brace section sizes and gusset plate design. The frame middle column was connected to the storey mass and shake table via two pinned connections, whilst the external columns were connected using slot connections. These connections could fix the roller vertical displacement, but allow a relative horizontal movement of ± 30 mm. This combination of two connection types ensured that the inertial force from the mass block is only transferred to the SC-CBF through the centre pin during an earthquake excitation. As indicated in Fig. 32, the beams were connected to the columns via rocking connections. The beam end could rock against the face of the column flange via two slotted connections. Measures to prevent frame collapse after brace fracture were required.

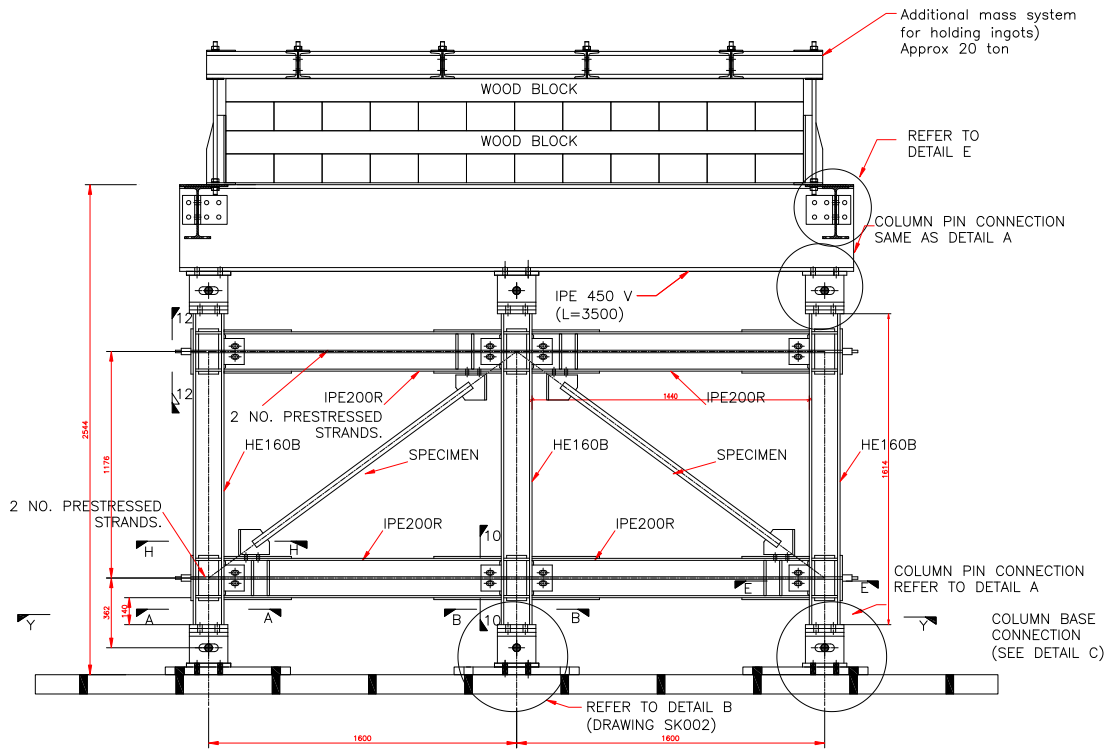


Figure 377: Technical drawing of the tested system (middle frame elevation view)

7.2.3 Test setup

Total number of 76 instruments were used, of which 4 load cells (LC), 9 accelerometers (ACC), 12 linear variable differential transformer (LVDT), 2 linear potentiometer (LP) and 52 strain gauges (SG). They are described below in Table 57, categorised according to the type of measurement recorded.

Instrument		Measured quantity (units)	CH No.
LC1	Load cell	Force (kN)	1
LC2	Load cell	Force (kN)	2
LC3	Load cell	Force (kN)	3
LC4	Load cell	Force (kN)	4
ACC 1	Accelerometer	Acceleration (g)	5
ACC 2	Accelerometer	Acceleration (g)	6
ACC 3	Accelerometer	Acceleration (g)	7
ACC 4	Accelerometer	Acceleration (g)	8
ACC 5	Accelerometer	Acceleration (g)	9
ACC 6	Accelerometer	Acceleration (g)	10
ACC 7	Accelerometer	Acceleration (g)	11
ACC 8	Accelerometer	Acceleration (g)	12
ACC 9	Accelerometer	Acceleration (g)	13
LVDT 1	Linear variable differential transformer	Relative disp. (mm)	14
LVDT 2	Linear variable differential transformer	Relative disp. (mm)	15
LVDT 3	Linear variable differential transformer	Relative disp. (mm)	16
LVDT 4	Linear variable differential transformer	Relative disp. (mm)	17
LVDT 5	Linear variable differential transformer	Relative disp. (mm)	18
LVDT 6	Linear variable differential transformer	Relative disp. (mm)	19
LVDT 7	Linear variable differential transformer	Relative disp. (mm)	20
LVDT 8	Linear variable differential transformer	Relative disp. (mm)	21
LVDT 9	Linear variable differential transformer	Relative disp. (mm)	22
LVDT 10	Linear variable differential transformer	Relative disp. (mm)	23
LP1	Linear potentiometer	Absolute disp. (mm)	24
LP2	Linear potentiometer	Absolute disp. (mm)	25
LVDT11	Linear variable differential transformer	Relative disp. (mm)	26
LVDT12	Linear variable differential transformer	Relative disp. (mm)	27
SG1-SG52	Strain Gauges	Strain (μ str)	1-52

Table 57: Complete model instrumentation description

It should be noted that the instrumentation scheme is the same for all configurations of the model specimen. Their exact position on every tested setup is clearly shown in the technical drawings below, (Figure 378-Figure 385).

Strain Gauges

For the purposes of this project the strain gauges are categorised into two sets, permanent strain gauges fixed to the frame (SGF) and short-term use gauges fixed to each specimen (SG). The primary functions of the SGF gauges are to provide strain information to (i) estimate forces in frame members and (ii) check for undesirable behaviour in the test frame. Four SGF gauges were located in each column of the middle frame (Fig. 33) to allow column axial loads to be estimated. The gauges were placed on the outer edges of the column flanges in pair. Two gauges pairs were positioned on each beam of the middle frame to check the bending moment in this member and facilitate checks for inelasticity in the beam and column flanges. Total of 28 strain gauges were placed on the frame structure.

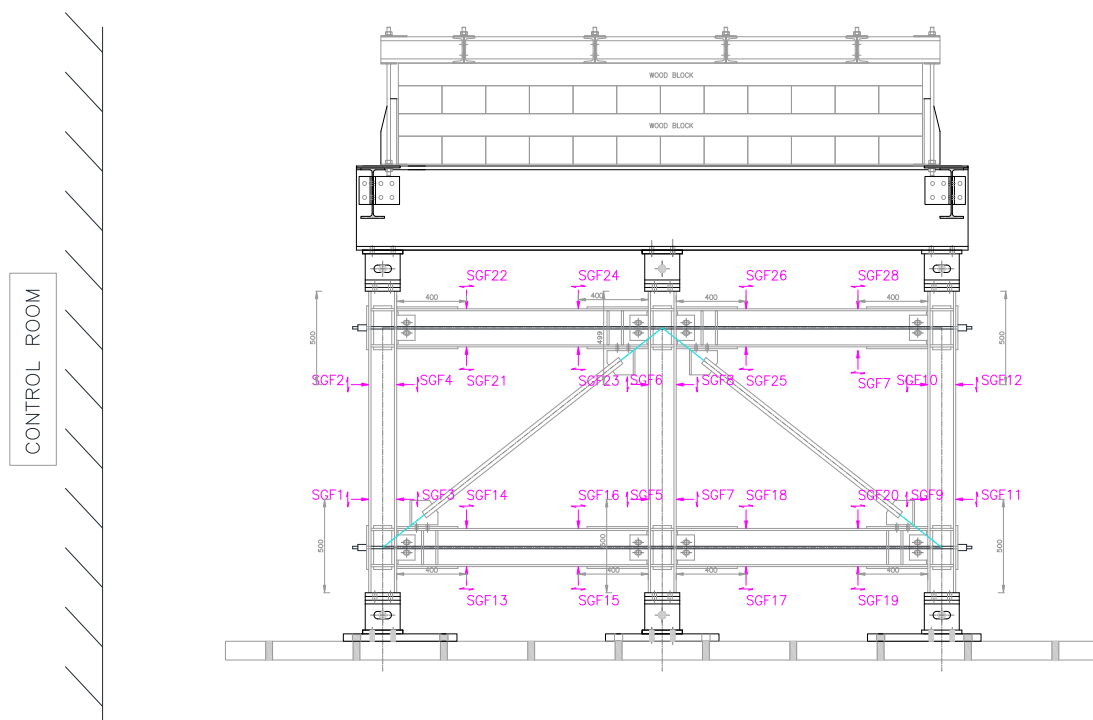


Figure 378: Permanent strain gauge 'SGF' location

The SG gauges were positioned on the brace and gusset specimens (Figure 379 and Figure 380). Eight gauges were located at the brace mid-length and near the brace ends to estimate axial and bending forces in the brace and the degree of plastic hinge development in the brace. Six SG gauges were located within and outside of the plastic hinge zones of the gusset plate, while other six are positioned to monitor the compression and tension induced in the gusset plate during frame rotation. Additional 4 strain gauges were placed on the other brace. Total of 20 strain gauges for each configuration were used.

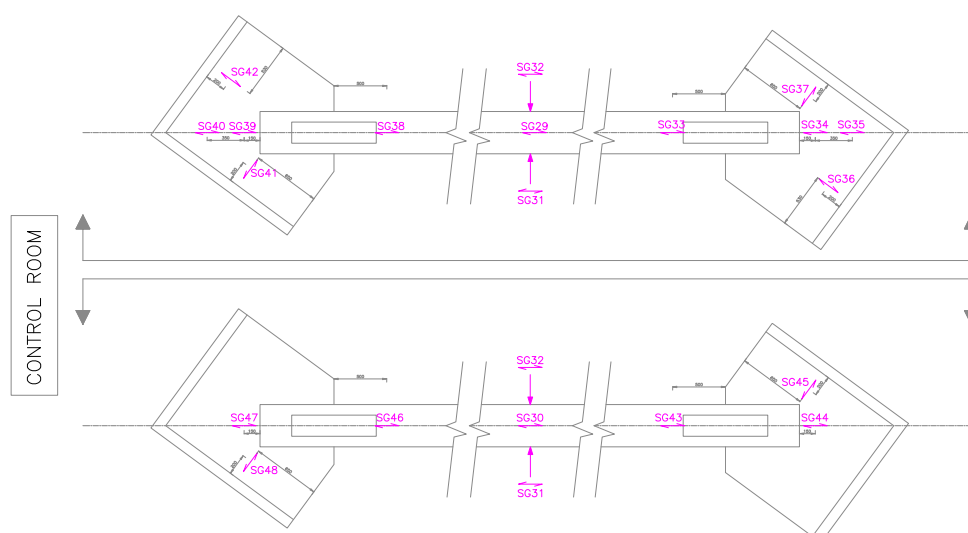


Figure 379: Temporary strain gauge 'SG' location for the main instrumented brace

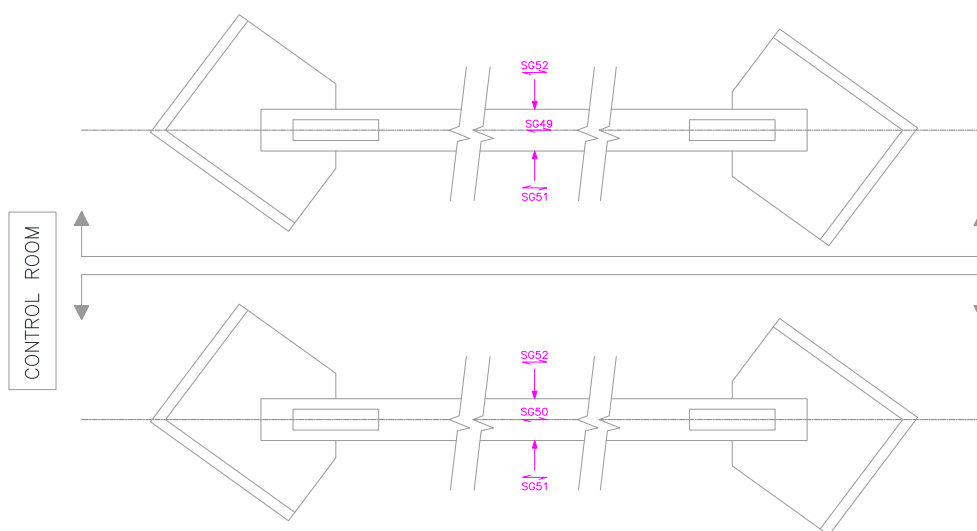


Figure 380: Temporary strain gauge 'SG' location for the other brace

Accelerometers

The main accelerometers 'A1-A4' are positioned on the main frame and they were used to capture the amplification in the acceleration from the bottom of the structure to the top (Figure 381).

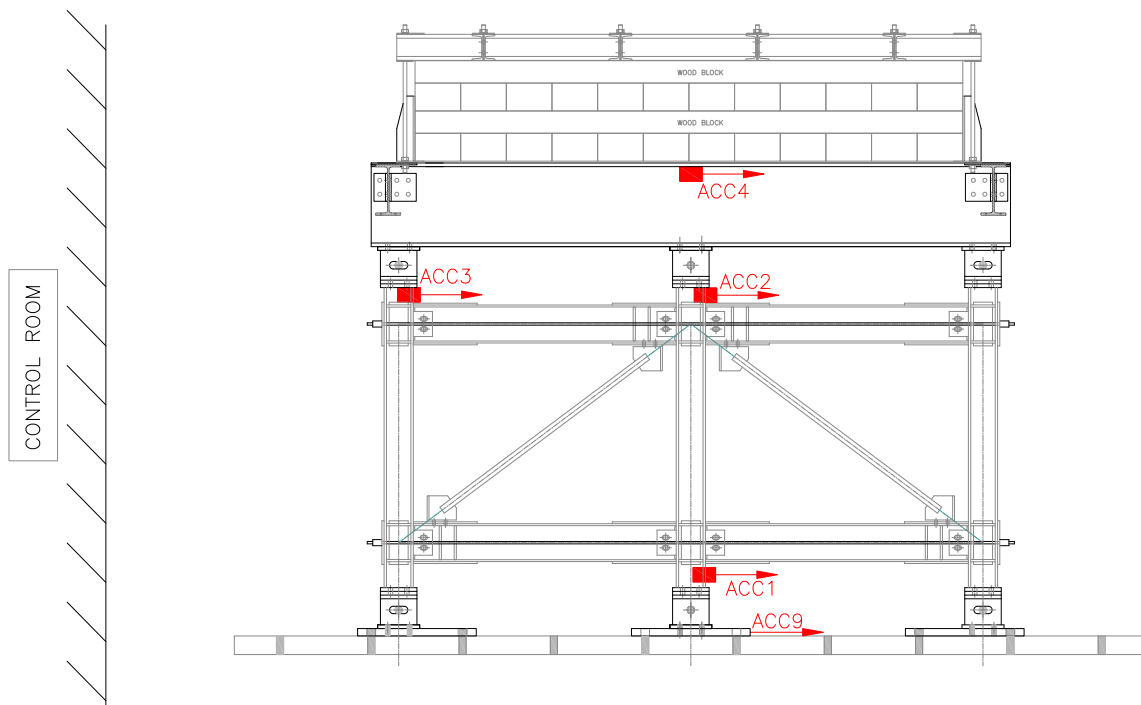


Figure 381: Location of the accelerometers (middle frame elevation view)

Additionally, four primary accelerometers should be used for recording acceleration at the roof level (Figure 382). The four accelerometers located at the frame top are indicated as 'A5', 'A6', 'A7' and 'A8', while one accelerometer, 'A9', is mounted in the middle of the shake table, as shown in Figure 381 in order to capture the input motion as produced by the shaking table. In addition, the accelerometer instrumentation set of the proprietary MTS system located within the shake table should also be recorded to check for any undesirable table-structure interaction.

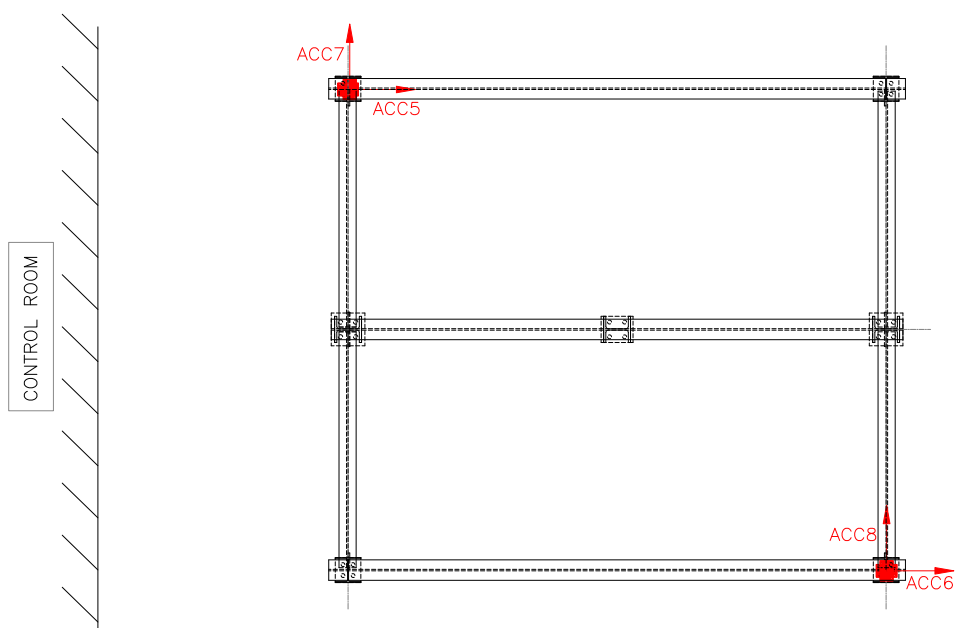


Figure 382: Location of the accelerometers (roof plan view)

Displacement Transducers and Linear Potentiometers

Twelve linear displacement transducers were located in the middle frame structural elements in order to depict the relative displacements between crucial points at the connections. Four displacement transducers (D1, 2, 3 & 4) were placed at the two roller connections relative to the shake table and two roller connections to the additional mass system (Figure 383) to monitor the roller sliding distance during testing. Two pairs of the displacement cable sensors were located at the bottom (D5/D6) and top (D7/D8) beams of the middle frame. Each displacement cable sensor measures the relative displacement of the beam flange and the central column. The beam-column connection rotation and inter-storey drift could also be calculated from the measurements.

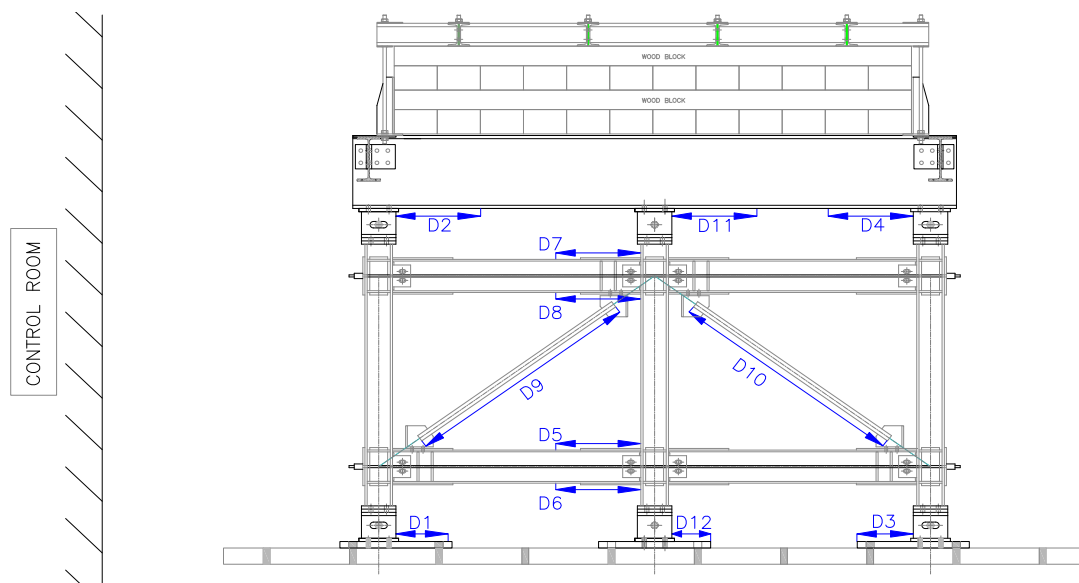


Figure 383: Location of the LVDTs at the middle frame

Furthermore, two displacement cable sensors were positioned between the brace ends. These cable sensors are designated 'D9' and 'D10' and measure brace elongation across the total brace length. The LVDTs D11 and D12 were positioned at the connections between the additional mass system and the upper fixed connection of the middle column and also the base plate of the middle column and the pin. Their function was to establish whether the connection is working properly and there is no movement in the fixed joint. After the movement was eliminated, these LVDTs were removed from the instrumentation scheme.

The displacement cable sensors LP1 and LP2 for these measurements were attached to a fixed reference points as shown in Figure 384.

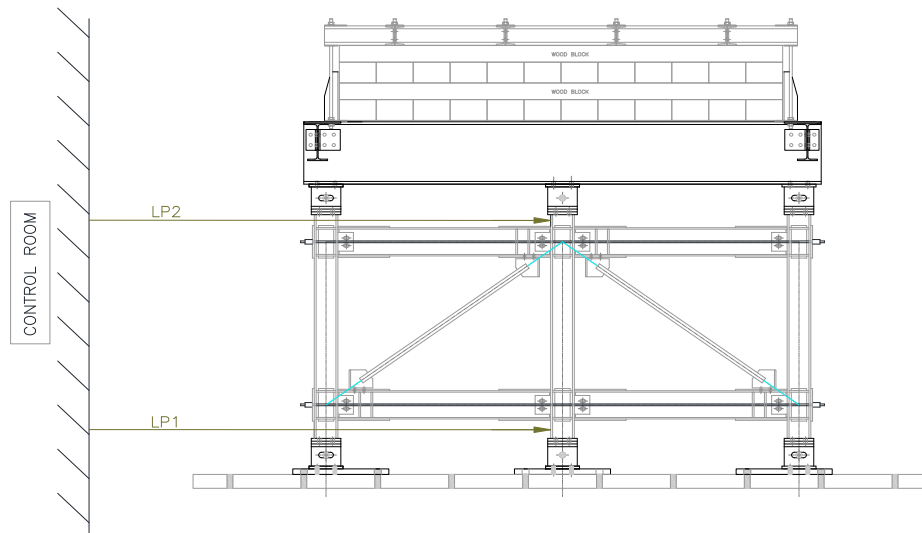


Figure 384: Schematic for the position of linear potentiometers

Load Cells

Four High-Performance Fatigue Rated Cylindrical Load Cells (250kN capacity) were used to measure the forces in the four post-tensioning (PT) strands. They were located at the ends of the PT strands (one load cell per PT strand), and are designated 'LC1', 'LC2', 'LC3' and 'LC4' (Figure 385), respectively.

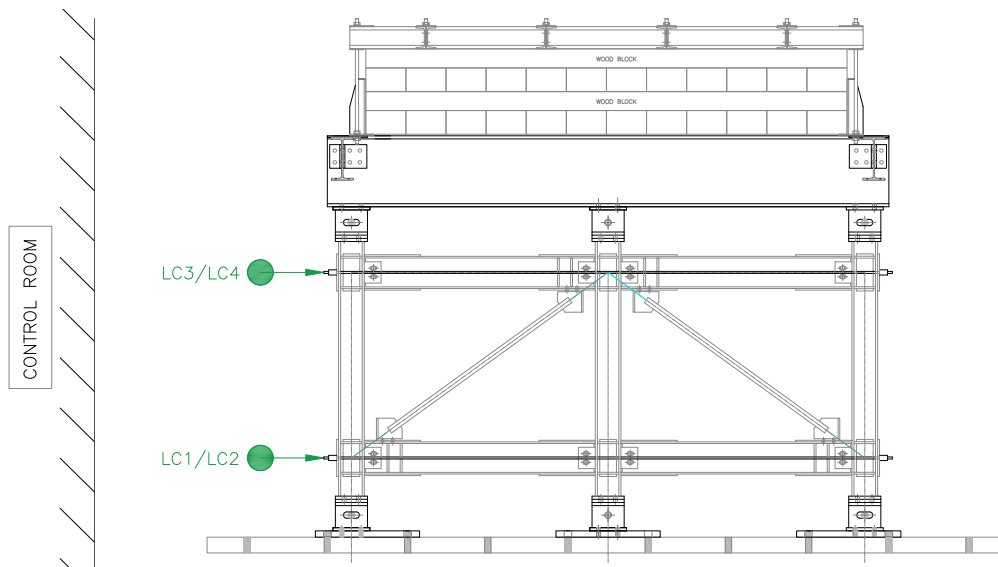


Figure 385: Location of the load cells

Testing Methodology

Five series of experiments were completed, with a different pair of brace specimens inserted into the central SC-CBF for each test. Same testing methodology was used for testing of all configurations. More in detail, different types of excitations were carried out:

- Resonant frequency search tests – white noise;
- Uni-axial time history shake table testing.

For resonant frequency search tests uniaxial random excitations have been applied in Y direction. Resonant frequency search tests were performed at the beginning of the testing of each configuration (initial state) and after the final excitation of each configuration (final state), with the following characteristics:

- Frequency range: from 1.0 to 40.0Hz;
- Peak excitation level of 0.03g.

In this shake table experiment, the brace specimens were tested using several excitations, scaled to induce (i) elastic response, (ii) brace buckling or initial yield and (iii) brace fracture. Two different ground motion records were used for the testing, with gradually increasing their intensity. The input excitation parameters for each test are given in Figure 386. It should be noted that the high-frequency and low-frequency components of the two selected ground motions were filtered according to the shake table technical specifications in respect to the original records.

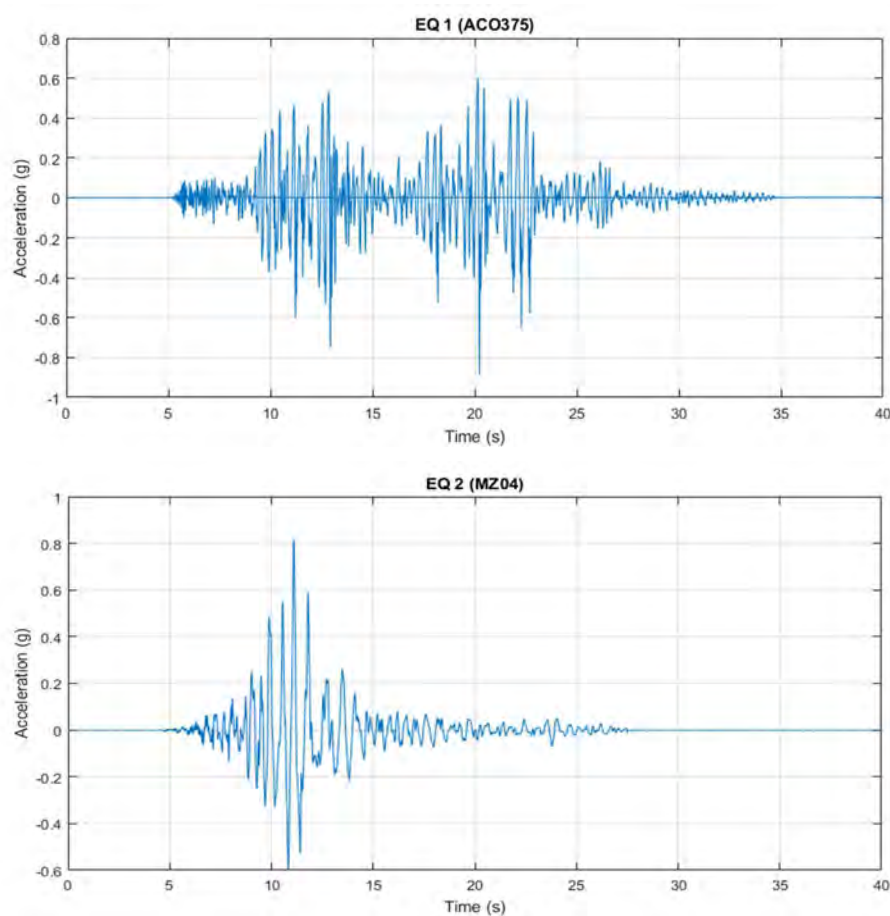


Figure 386: Acceleration time-histories of the selected ground motions

Complete list of all performed tests is presented in Table 58. It should be noted that Table 49 starts with test number 39 instead of 1 in order to comply with the experimental data acquisition procedure numeration. The tests from 1-38 were part of the first phase of the testing where the model manufacturing deficiencies needed to be tackled. In the first phase of the experimental procedure, techniques such as: replacement of joints, welding of structural elements, adding additional stiffening elements and replacement of bolts were undertaken, in order to activate proper behaviour of the self-centring system and to guide the energy dissipation in the brace members only.

Test No.	Type of excitation	Characteristics	Input acc. [g]	Comment
SC-CBF 4 – 20.20.2.5 – 04.11.2019				
39	Random	f=1-40.0Hz; t=300s	0.03	/
40	EQ 1 (ACO375)	10%	0.10	/
41	EQ 1 (ACO375)	20%	0.21	/
42	Random	f=1-40.0Hz; t=300s	0.03	/
43	EQ 1 (ACO375)	55%	0.45	/
44	Random	f=1-40.0Hz; t=300s	0.03	/
45	EQ 1 (ACO375)	55%	0.41	It is repeated because of the welding of the middle column
46	Random	f=1-40.0Hz; t=300s	0.03	/
SC-CBF 3.1 – 25.25.2.5 - 05.11.2019				
47	Random	f=1-40.0Hz; t=300s	0.03	/
48	EQ 1 (ACO375)	10%	0.10	/
49	Random	f=1-40.0Hz; t=300s	0.03	/
50	EQ 1 (ACO375)	25%	0.25	/
51	Random	f=1-40.0Hz; t=300s	0.03	/
52	EQ 1 (ACO375)	65%	0.48	/
53	Random	f=1-40.0Hz; t=300s	0.03	/
SC-CBF 3.2 – 25.25.2.5 - 05.11.2019				
54	Random	f=1-40.0Hz; t=300s	0.03	/
55	EQ 2 (MZ04)	10%	0.09	/
56	EQ 2 (MZ04)	25%	0.22	/
57	Random	f=1-40.0Hz; t=300s	0.03	/
58	EQ 2 (MZ04)	40%	0.43	/
59	EQ 2 (MZ04)	80%	0.84	/
60	Random	f=1-40.0Hz; t=300s	0.03	/
SC-CBF 2.1 – 30.30.2.5 - 06.11.2019				
61	Random	f=1-40.0Hz; t=300s	0.03	/
62	EQ 1 (ACO375)	10%	0.09	/
63	EQ 1 (ACO375)	25%	0.25	/
64	Random	f=1-40.0Hz; t=300s	0.03	/
65	EQ 1 (ACO375)	65%	0.50	/
66	Random	f=1-40.0Hz; t=300s	0.03	/
67	EQ 1 (ACO375)	50%	0.44	/
68	Random	f=1-40.0Hz; t=300s	0.03	/
SC-CBF 2.2 – 30.30.2.5 - 06.11.2019				
69	Random	f=1-40.0Hz; t=300s	0.03	/
70	EQ 2 (MZ04)	10%	0.09	/

71	EQ 2 (MZ04)	25%	0.24	/
72	Random	f=1-40.0Hz; t=300s	0.03	/
73	EQ 2 (MZ04)	60%	0.62	/
74	Random	f=1-40.0Hz; t=300s	0.03	/
75	EQ 2 (MZ04)	70%	0.68	/
76	Random	f=1-40.0Hz; t=300s	0.03	/
Testing of the Bare Frame				
77	Random	f=1-40.0Hz; t=300s	0.03	/
78	EQ 1 (ACO375)	10%	0.10	/

Table 58: Testing programme and comments

7.2.4 Observation during testing

During the experimental testing procedure, varying observations were indicated related to the structural brace configuration and the ground motion applied. However, some general observations were derived for all tests and they are portrayed as following:

- Negligible residual drifts were observed, even though there were big maximum drifts at higher intensity level tests;
- Excellent functioning of the PT strands, as shown by the increase of force during tests and returning to initial force at the end of the excitation;
- Energy dissipation through the braces, as displayed through buckling and strain measurement;
- No damage in other structural members besides the braces;

As stated before, the main advantage of this self-centring system is the elimination of the residual drifts following strong earthquake excitations. Figure 387 shows the displacement time-history of the frame following test number 59. The structure was subjected to the pulse-like ground motion (EQ 2 - MZ04) with a maximum PGA of 0.84g and exhibited large inter-story drifts of around 3%. Nevertheless, the residual drifts following this ground motion were determined as almost negligible.

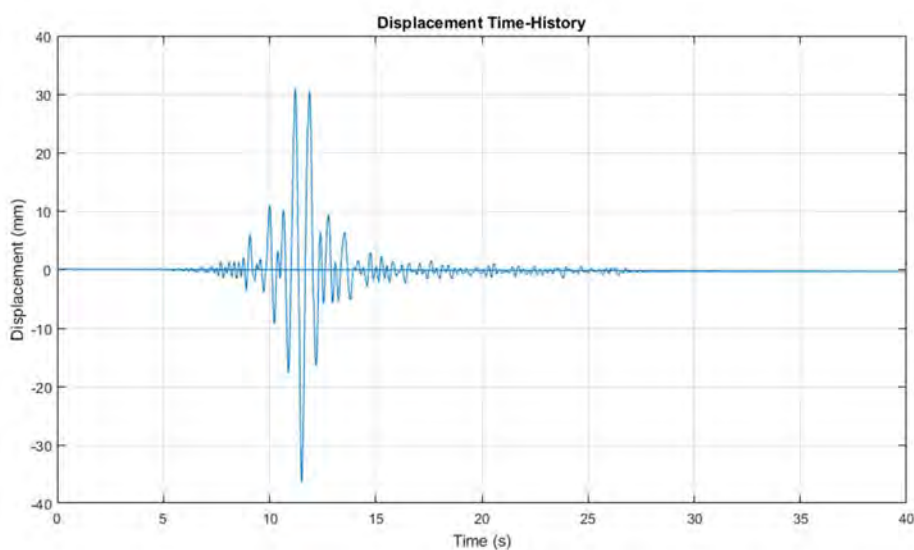


Figure 387: Displacement time-history for test 59

The testing of the SC-CBF on the IZIS shake table provided improved understanding for the behaviour of the braces in this novel system under ground motion earthquake loading. Consequently, following the higher intensity earthquakes, the braces reached their yielding strengths and significant buckling was observed. That is a proof of the energy dissipation in these structural elements and a display of the proper design of the system. Figure 388 shows the characteristic post-experimental deformations of the braces and other elements of the self-centring concentrically braced following the testing procedure.



Figure 388: Characteristic damage observed after tests

7.2.5 Results

The frequency response function for the initial and the final state for the configurations with largest damage - 3.2 and 2.1, recorded in ACC4, are presented in Figure 389 and Figure 390, respectively. It is noticed that there is a decrease in the frequency after the last test of each configuration, suggesting structural damage due to the earthquake loading.

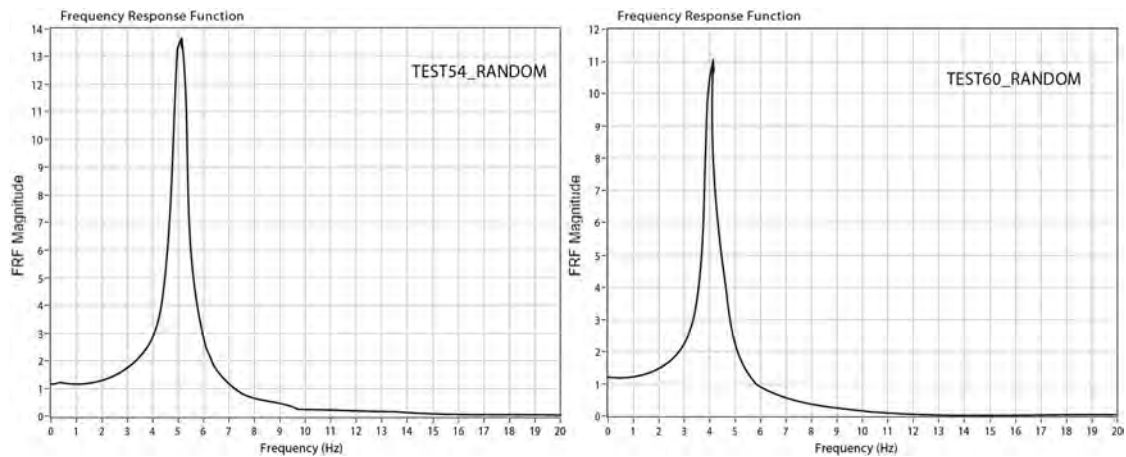


Figure 389: Frequency Response Function for the response in ACC4 for initial test 54, $f = 5.1\text{Hz}$ (left) and final test 60, $f = 4.1\text{Hz}$ (right) of configuration 3.2

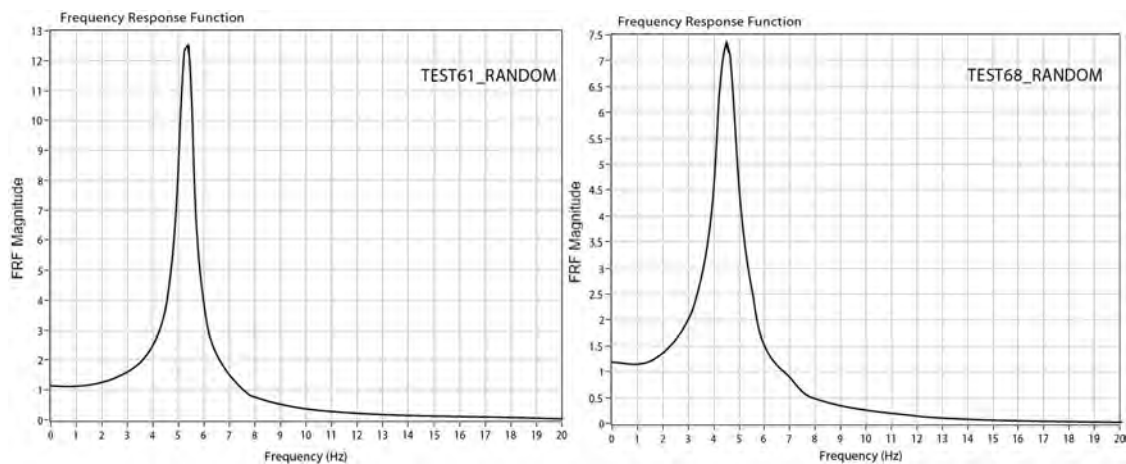


Figure 390: Frequency Response Function for the response in ACC4 for initial test 61, $f = 5.3\text{Hz}$ (left) and final test 68, $f = 4.6\text{Hz}$ (right) of configuration 2.1

The results of the testing under seismic load are presented in form of time history records of accelerations, displacements and strains. The time history records measured in the accelerometers are processed with band-pass filter, within the range of 0.5-35Hz, whereas the signals in the LVDTs and LPs are filtered with low pass filter of 35.0Hz. Below, several results from the test 59, characterised with the highest PGA earthquake loading and greatest force increase in PT strands are presented (Figure 391 - Figure 393).

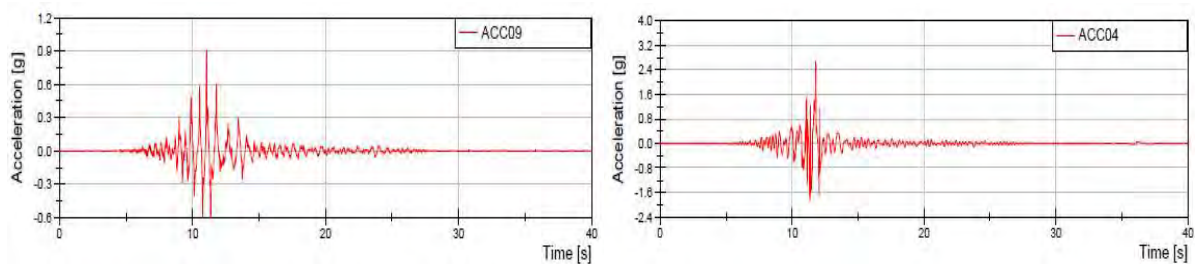


Figure 391: Time history record of the response in ACC9 (left) and ACC4 (right) for test 59

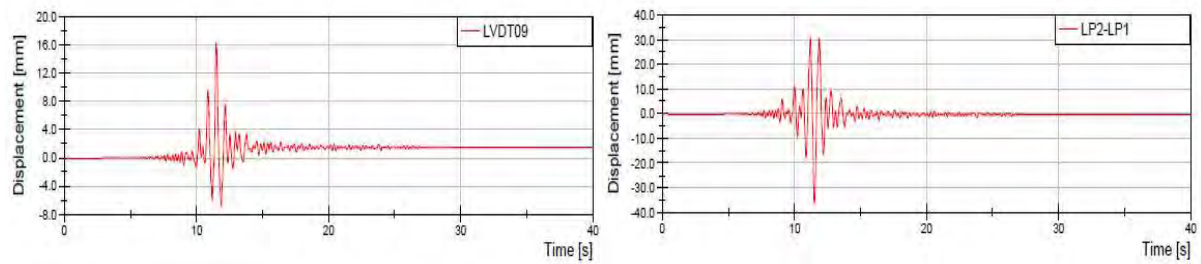


Figure 392: Time history record of the response in LVDT9 (left) and drift (right) for test 59

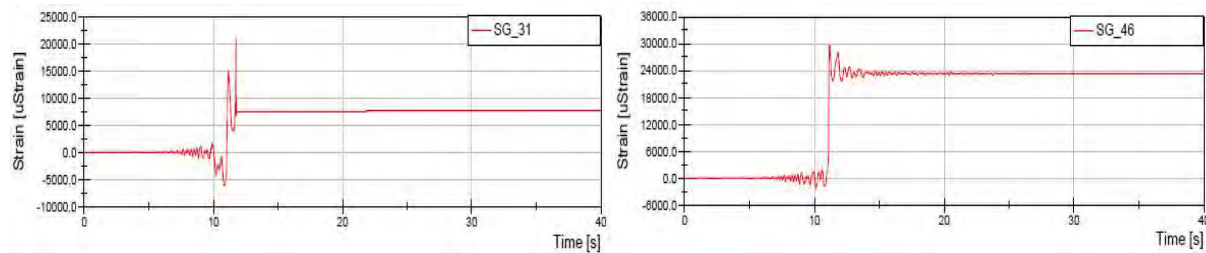


Figure 393: Time history record of the response in SG31 (left) and SG46 (right) for test 59

Another important parameter for discussion, following the SC-CBF testing procedure is the force in the PT strands and their behaviour during the seismic loading of the frame. The load cells installed at the connection between the frame and the strands were used to capture the increase of the PT force needed for returning of the system to initial positions after the significant displacements caused by the excitation.

The largest force undertaken by the cables was measured in the same test as the largest maximum drift, described above. That is consistent with the hypothesis that the excessive seismic force after the failure of the braces is transferred to the system of PT strands and these elements prevent the structure from collapse. Thus, Figure 394 demonstrates the change in the force of one of the PT strands during the excitation of test 59. It can be observed that the initial post-tensioning force of 80kN is increased during the experiment up to 134kN, in order to assist the lateral bearing system of the frame and then it returns to the initial position with a negligible loss (around 6kN) after the earthquake ends.

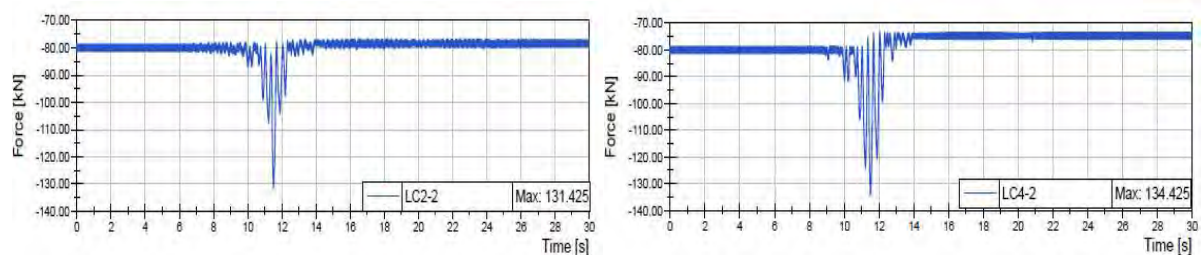


Figure 394: Time-history the change in the force in LC2 (left) and LC4 (right) for test 59

7.2.6 Conclusions and outlook

Within this research project, an extensive experimental testing procedure was performed in order to certify the behaviour of a novel self-centring system for concentrically braced frames. Several configurations of the test specimen were examined, subjected to two different earthquake ground motions with different time-history and frequency characteristics. Wide-ranging instrumentation was installed on the testing model in order to capture the essential parameters of the structural behaviour

of the novel system. Following the testing and the observations from the procedure, several conclusions were drawn.

The main conclusion is that the combined action of the post-tensioned strands and rocking connections between beams and columns provided the system with excellent self-centring behaviour under earthquake excitation. Additionally, due to the above-mentioned rocking behaviour, the beams and the columns were prevented from yielding and greater damage, meaning that the braces dissipated all the imposed energy. On the other hand, the buckled bracing members were replaced easily from the system, meaning that residual damage of the frame was not observed. This behaviour proves the main requirement of the self-centring system, thus reducing the time and cost for repair of concentrically braced frames following large inelastic deformations.

7.2.7 References

- [1] Elghazouli AY. "Seismic design procedures for concentrically braced frames". *Structs and Builds* (2003) 156: 381-94.
- [2] Popov EP, Black RG. "Steel struts under severe cyclic loadings". *J Struct Div, ASCE* (1981)107(7):1857-81.
- [3] Tremblay R. "Inelastic seismic response of steel bracing members". *J Construct Steel Res* (2002) 58(5-8):665-701.
- [4] Nip, K. H., Gardner, L., and Elghazouli, A. Y. "Cyclic testing and numerical modelling of carbon steel and stainless steel tubular bracing members", *Engineering Structures*, (2009), in press, available on-line.
- [5] AISC Seismic Provisions for Structural Steel Buildings, AISC/ANSI Standard 341-05, American Institute of Steel Construction, Chicago, IL. (2005).
- [6] Yoo, J.H., Roeder, C.W. and Lehman, D.E. "Analytical performance simulation of special concentrically braced frames". *Journal of Structural Engineering* (2008) 134:6, 881-889.
- [7] Elghazouli, A.Y., Broderick, B.M., Goggins, J.M., Carydis, P.G., Moussopoulous, H., Plumier, A. Bouwkamp J.G. "Shake table testing of steel frames with tubular bracing members", *Proc. Instn. Civil Engrs, Structures and Buildings*. 158 (2005) 229-241.
- [8] Salawdeh, S., English, J. Goggins, J., Elghazouli, A. Y., Hunt, A., Broderick, B. M., "Shake Table Assessment of Gusset Plate Connection Behaviour in Concentrically Braced Frames", *J Construct Steel Res*, 138 (2017) 432–448.
- [9] Goggins, J., B. Broderick, A. Elghazouli, S. Salawdeh, A. Hunt, P. Mongabure and J. English. "Shake table testing of concentrically braced steel structures with realistic connection details subjected to earthquakes." *Structures*, 13 (2018), 102 - 118.
- [10] Goggins, J.M., Broderick, B.M. and Elghazouli, A.Y. "Experimental cyclic response of cold-formed hollow steel bracing members", *Engineering Structures*, 27 (2005) 977-989.
- [11] Hassan, M. S., S. Salawdeh and J. Goggins. "Determination of geometrical imperfection models in finite element analysis of structural steel hollow sections under cyclic axial loading." *Journal of Constructional Steel Research* 141(2018): 189-203.
- [12] Ryan, T., Broderick, B.M., Hunt, A., Goggins, J. and Salawdeh, S. "Recommendations for numerical modelling of concentrically braced steel frames with gusset plate connections subjected to earthquake ground motion", *J of Structural Integrity and Maintenance* 2(3), (2017) 168–180.

- [13] Watanabe, A., Hitomi Y., E. Saeki, A. Wada and M. Fujimoto. "Properties of Brace Encased in Buckling-Restraining Concrete and Steel Tube". 9th World Conference on Earthquake Engineering, Tokyo-Kyoto, Japan (1988).
- [14] Tremblay, R., L. Poncet, P. Bolduc, R. Neville and R. DeVall. "Testing and Design of Buckling Restrained Braces for Canadian Application". 13th World Conference on Earthquake Engineering, Vancouver, B.C., Canada. (2004).
- [15] Fahnestock, L. A., J. M. Ricles and R. Sause. "Experimental Evaluation of a Large-Scale Buckling-Restrained Braced Frame". Journal of Structural Engineering 133(9), (2007) 1205-1214.
- [16] Christopoulos, C., A. Filiatrault, and B. Folz, "Seismic response of self-centring hysteretic SDOF systems". Earthquake Engineering & Structural Dynamics, 2002. 31(5): p. 1131-1150.
- [17] Ricles, J. M., R. Sause, M. M. Garlock and C. Zhao. "Posttensioned Seismic-Resistant Connections for Steel Frames", Journal of Structural Engineering 127(2), (2001) 113-121.
- [18] O'Reilly, GJ; Goggins, J, "Comparing the seismic performance of concentrically braced frames with and without self-centering behaviour", 2nd International Conference on Structures and Architecture (ICSA2013) Guimaraes, Portugal (2013).
- [19] Reilly G.J., Goggins J., Mahin S.A., "Behaviour and Design of a Self-Centering Concentrically Braced Steel Frame System". 15th World Conference on Earthquake Engineering (15WCEE), 24 - 28 September 2012. Lisbon, Portugal.

7.3 Project #37 – INfills and MASonry structures protected by deformable POLyurethanes in seismic areas (INMASPOL)

Authors

Z. Rakicevic⁽¹⁾, A. Bogdanovic⁽¹⁾, F. Manojlovski⁽¹⁾, A. Shoklarovski⁽¹⁾, T. Rousakis⁽²⁾, A. Ilki⁽³⁾, A. Kwiecień⁽⁴⁾, A. Viskovic⁽⁵⁾, M. Kramar⁽⁶⁾, B. Ghiassi⁽⁷⁾, A. Benedetti⁽⁸⁾, M. Karpala⁽⁹⁾, K. Agis⁽¹⁰⁾, B. Zając⁽¹¹⁾, M. Gams⁽¹²⁾

⁽¹⁾ Institute of earthquake engineering and engineering seismology, Ss. Cyril and Methodius University, Skopje, Republic of North Macedonia

⁽²⁾ Democritus University of Thrace, Greece

⁽³⁾ Istanbul Technical University, Turkey

⁽⁴⁾ Cracow University of Technology (CUT), Poland

⁽⁵⁾ G. D'Annunzio University of Chieti – Pescara, Italy

⁽⁶⁾ Slovenian National Building and Civil Engineering Institute, Ljubljana, Slovenia

⁽⁷⁾ University of Nottingham, UK, University Park Nottingham, UK

⁽⁸⁾ Alma Mater Studiorum-Universita' di Bologna, Italy

⁽⁹⁾ SIKa Poland Sp. z o.o., Cracow, Poland

⁽¹⁰⁾ *KEBE SA, Head Offices-Factory Nea Santa, Kilkis, Greece*

⁽¹¹⁾ *FlexAndRobust Systems Ltd, Cracow, Poland*

⁽¹²⁾ *University of Ljubljana (UL), Slovenia*

7.3.1 Introduction

The behaviour of RC frames with masonry wall infills is influenced a lot by the stiffness and yield displacement difference between the frame and the infill. The flexible frame is unable to carry high loads at low displacements and this can cause the infill to damage already at moderate seismic intensity. In case of aftershocks, the damaged infills can fail out-of-plane. On the other hand, if the stiff infill is too strong relative to the column, it may cause undesirable behaviour of the frame or even shear failure in the column. The response of structural system can be improved by using a flexible interface between the frame and the infill. This project consisted of testing RC frames with a flexible joint made of polyurethane (PUFJ) with the masonry wall infills. The application of around 2 cm thick PUFJ reduces the stress concentrations at the contact and thereby reduces damage to infills and RC frames and improves the displacement capacity of the structural system. Furthermore, it offers additional amount of damping. Despite the flexibility of the polyurethane (PU), the bond between the PU and the other materials can transfer significant loads during in-plane and out-of-plane excitations. The PUFJ is versatile because different types of PU with very different stiffness, damping and strength characteristics can be used to manipulate the system dynamic behaviour. In case of premature out-of-plane flexural or in-plane diagonal tension infill failure, PUs can be used for bonding of various composite fibres to the weak masonry substrate to form Fiber Reinforced PU (FRPU) as well as for repair of damaged RC frames. The PU can cover emergency situations as it cures within hours and is easy to apply. The proposed project assessed the efficiency of the method through testing of full-scale infilled RC building on shake table. The seismic tests validated in-plane and out-of-plane infill performance when modified, repaired or strengthened with PUFJ and FRPU systems.

7.3.2 Test specimen

The test specimen was fully symmetrical 3D frame RC structure (shown in the Figure 395 and Figure 396) with 4 identical columns with dimensions $a/b=20/20$ cm, reinforced with 8 longitudinal rebars $\varnothing 10$ and double perpendicular stirrups $\varnothing 8/5$ cm. The beams $b/d=20/20$ were incorporated in the slab and comprised also of 8 longitudinal rebars $\varnothing 10$ with single perpendicular stirrups $\varnothing 8/5$ cm. Protective layer of 4.2cm was made, hence the distance from the edge of the element (beam and column) to the centerline of the longitudinal rebars was 5.5cm. The foundation beams intended to fix the model to the shake table were $b/d=40/40$ cm with 10 longitudinal rebars $\varnothing 18$ with stirrups $\varnothing 8/15$ cm. The slab $d=20$ cm was reinforced with steel rebar nets type Q503. The materials used to construct the bearing elements were concrete C30/37 and rebars B500C.

Infills as non-load bearing masonries were constructed of KEBE Ortho Block K100 system with half bricks at both ends of every second layer using Mounting Mortar M10.

The walls were divided in two types:

- the first parallel pair, type B, built with 2cm gap between the bricks and RC columns and slab. After completion of brick laying procedure, the RC interface was covered with Sika ZP Primer and the gaps were covered with thin longitudinal Sika PS sheets. After the curing process finished then the final step consisting of injection with Sika PUFJ Injection was performed.

- The second parallel walls, type C was built on already glued PUFJ Sika PM laminates on all 4 sides connecting with RC elements (columns, slab and foundation) with cross section $b/d=2/10\text{cm}$.



Figure 395: Completely instrumented and loaded test specimen placed on shake table

7.3.3 Test setup

In general, the experimental investigations were divided in 4 phases:

- phase A, where the walls type B were tested in plane, in direction of the excitation and walls type C were tested out of plane, perpendicular to the direction of excitation.
- Phase A', where only the walls type B were strengthened using GFRPU SikaWrap 350G Grid and SikaPS adhesive.
- Phase B, the specimen was rotated 90 degrees and now, the walls type C were tested in plane and walls type B out of plane.
- Phase B', the walls C were strengthened using the same technique but with tighter sheets.



Figure 396: Final phase of tests with strengthening on all walls

The testing methodology consisted of shake table tests for determination of dynamic characteristics of the system by means of white noise and sine sweep low amplitude time histories of acceleration. The focus was on the seismic tests and seismic response of the structure of real earthquake – Chavriata 2014 (Greece) E-W direction with varying intensity, from low amplitude to high amplitude. On the following Figure 397, a time history plot of the maximum tested level of intensity input acceleration is shown. The direction of the excitation in the laboratory is also east – west, as noted by the two-end arrow in the Figure 397 and Figure 398.

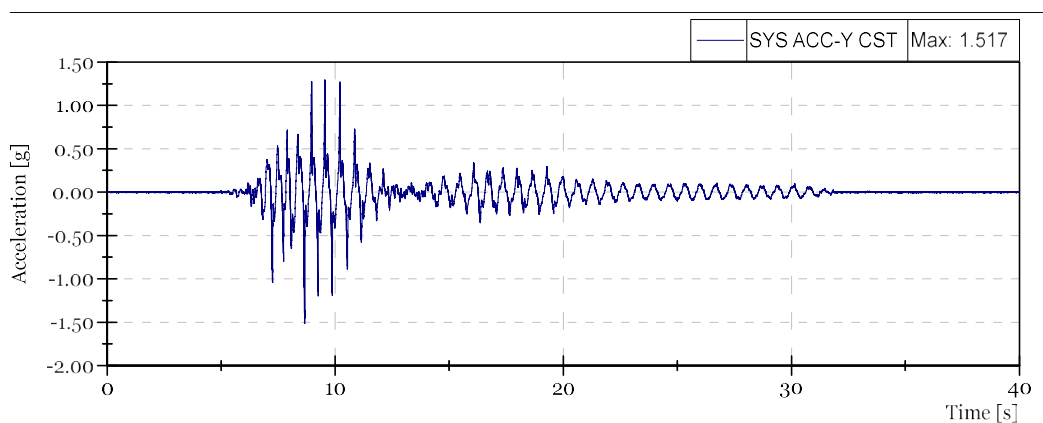


Figure 397: Input acceleration time history for the maximum tested level of intensity

The instrumentation of the tested model comprised of accelerometers (ACC), linear potentiometers (LP) and linear variable differential transformers (LVDT) measuring acceleration, total and relative displacements respectively. Their exact position on every tested setup is clearly shown on the Figure 398 and Figure 399 as well as in the following text.

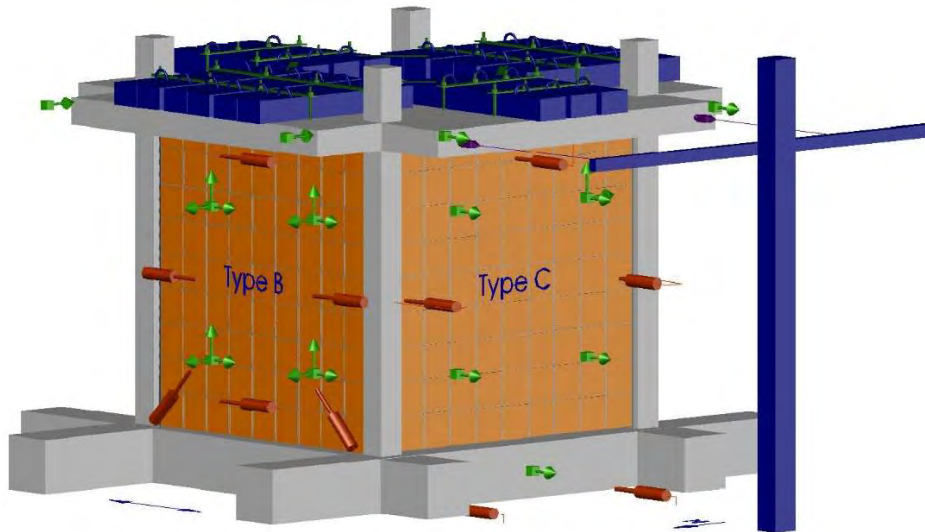


Figure 398: Instrumentation – phase A and A'

The exact location of the transducers in the testing phase A and A' was as follows (note that the only difference is that in phase A' the accelerometers ACC 12, ACC 19 and ACC 20 were detached):

- Ch 1 ACC 1 on the foundation, horizontal dir. (y); Ch 2 ACC 2 on the slab, on the left corner, horizontal dir. (y); Ch 3 ACC 3 on the slab, on the right corner, horizontal dir. (y); Ch 4 ACC 4 on the slab, on the right corner, horizontal dir. (x); Ch 5 ACC 5 on the slab, on the left corner, horizontal dir. (x); Ch 6 ACC 6 on the infill type C, on the lower left side, horizontal dir. (y); Ch 7 ACC 7 on the infill type C, on the lower right side, horizontal dir. (y); Ch 8 ACC 8 on the infill type C, on the upper left side, horizontal dir. (y); Ch 9 ACC 9 on the infill type C, on the upper right side, horizontal dir. (y); Ch 10 ACC 10 on the infill type C, on the upper right side, horizontal dir. (x); Ch 11 ACC 11 on the infill type B, on the lower left side, horizontal dir. (x); Ch 12 ACC 12 on the infill type B, on the lower right side, horizontal dir. (x); Ch 13 ACC 13 on the infill type B, on the upper left side, horizontal dir. (x); Ch 14 ACC 14 on the infill type B, on the upper right side, horizontal dir. (x); Ch 15 ACC 15 on the infill type B, on the upper right side, horizontal dir. (y); Ch 16 ACC 16 on the infill type C, on the upper right side, vertical dir. (z); Ch 17 ACC 17 on the infill type B, on the lower left side, horizontal dir. (y); Ch 18 ACC 18 on the infill type B, on the lower left side, vertical dir. (z); Ch 19 ACC 19 on the infill type B, on the lower right side, horizontal dir. (y); Ch 20 ACC 20 on the infill type B, on the lower right side, vertical dir. (z); Ch 21 ACC 21 on the infill type B, on the upper left side, horizontal dir. (y); Ch 22 ACC 22 on the infill type B, on the upper left side, vertical dir. (z); Ch 23 ACC 23 on the infill type B, on the upper right side, vertical dir. (z); Ch 24 LVDT 1 diagonal, tie slab-foundation, in the direction of excitation; Ch 25 LVDT 2 diagonal, slab-foundation, in the direction of excitation; Ch 26 LVDT 3 foundation-Infill type B, horizontal dir. (y); Ch 27 LVDT 4 RC column-left side of Infill type B, horizontal dir. (y); Ch 28 LVDT 5 RC column-right side of Infill type B, horizontal dir. (y); Ch 29 LVDT 6 RC column-left side of Infill type C, horizontal dir. (y); Ch 30 LVDT 7 slab-Infill type C, horizontal dir. (y); Ch 31 LVDT 8 RC column-right side of Infill type C, horizontal dir. (y); Ch 32 LVDT 9 on the left side of foundation-Shake table, horizontal dir. (y); Ch 33 LVDT 10 on the right side of foundation-Shake table, horizontal dir. (y); Ch 34 LP1 on the slab, on the left corner, horizontal dir. (y); Ch 35 LP2 on the slab, on the right corner, horizontal dir. (y).

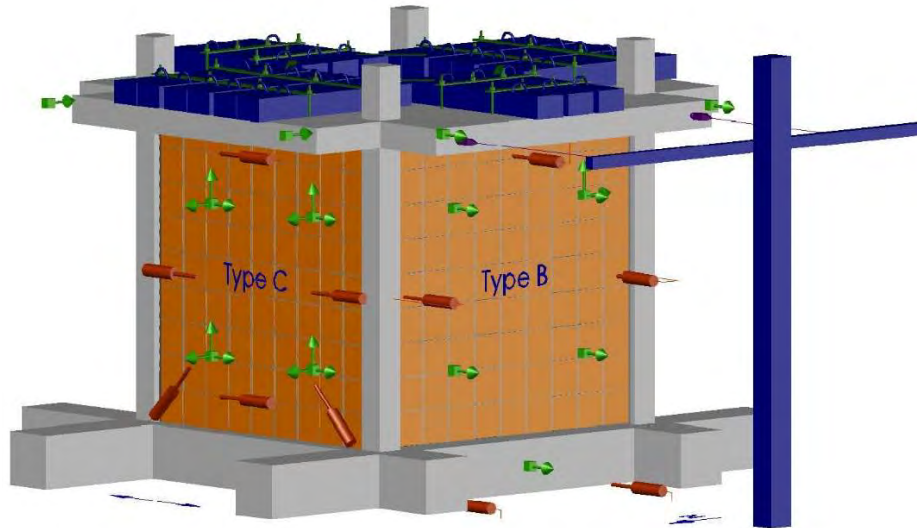


Figure 399: Instrumentation – phase B and B'

The exact location of the transducers in the testing phase B and B' was as follows:

- Ch 1 ACC 1 on the foundation, horizontal dir. (y); Ch 2 ACC 2 on the slab, on the left corner, horizontal dir. (y); Ch 3 ACC 3 on the slab, on the right corner, horizontal dir. (y); Ch 4 ACC 4 on the slab, on the right corner, horizontal dir. (x); Ch 5 ACC 5 on the slab, on the left corner, horizontal dir. (x); Ch 6 ACC 6 on the infill type B, on the lower left side, horizontal dir. (y); Ch 7 ACC 7 on the infill type B, on the lower right side, horizontal dir. (y); Ch 8 ACC 8 on the infill type B, on the upper left side, horizontal dir. (y); Ch 9 ACC 9 on the infill type B, on the upper right side, horizontal dir. (y); Ch 10 ACC 10 on the infill type B, on the upper right side, horizontal dir. (x); Ch 11 ACC 11 on the infill type C, on the lower left side, horizontal dir. (x); Ch 12 ACC 12 on the infill type C, on the lower right side, horizontal dir. (x); Ch 13 ACC 13 on the infill type C, on the upper left side, horizontal dir. (x); Ch 14 ACC 14 on the infill type C, on the upper right side, horizontal dir. (x); Ch 15 ACC 15 on the infill type C, on the upper right side, horizontal dir. (y); Ch 16 ACC 16 on the infill type B, on the upper right side, vertical dir. (z); Ch 17 ACC 17 on the infill type C, on the lower left side, horizontal dir. (y); Ch 18 ACC 18 on the infill type C, on the lower left side, vertical dir. (z); Ch 19 ACC 19 on the infill type C, on the lower right side, horizontal dir. (y); Ch 20 ACC 20 on the infill type C, on the lower right side, vertical dir. (z); Ch 21 ACC 21 on the infill type C, on the upper left side, horizontal dir. (y); Ch 22 ACC 22 on the infill type C, on the upper left side, vertical dir. (z); Ch 23 ACC 23 on the infill type C, on the upper right side, vertical dir. (z); Ch 24 LVDT 1 diagonal, tie slab-foundation, in the direction of excitation; Ch 25 LVDT 2 diagonal, slab-foundation, in the direction of excitation; Ch 26 LVDT 3 foundation-Infill type C, horizontal dir. (y); Ch 27 LVDT 4 RC column-left side of Infill type C, horizontal dir. (y); Ch 28 LVDT 5 RC column-right side of Infill type C, horizontal dir. (y); Ch 29 LVDT 6 RC column-left side of Infill type B, horizontal dir. (y); Ch 30 LVDT 7 slab-Infill type B, horizontal dir. (y); Ch 31 LVDT 8 RC column-right side of Infill type B, horizontal dir. (y); Ch 32 LVDT 9 on the left side of foundation-Shake table, horizontal dir. (y); Ch 33 LVDT 10 on the right side of foundation-Shake table, horizontal dir. (y); Ch 34 LP1 on the slab, on the left corner, horizontal dir. (y); Ch 35 LP2 on the slab, on the right corner, horizontal dir. (y)

On the following Table 59, a complete list of performed dynamic and seismic tests is shown for all 4 phases of testing. Note that the test number follows the internal laboratory numeration of all performed tests.

Performed tests							
Test No.	Name	Type of excitation	Intensity	Test No.	Name	Type of excitation	Intensity
PHASE A				PHASE B			
18	Test 2	White noise	0.01g	127	Test 28	White noise	0.01g
20	Test 4	Earthquake	5%	128	Test 29	Earthquake	10%
21	Test 5	Earthquake	10%	129	Test 30	White noise	0.01g
22	Test 6	Earthquake	20%	130	Test 31	Earthquake	20%
23	Test 7	White noise	0.01g	131	Test 32	White noise	0.01g
33	Test 8	Earthquake	40%	148	Test 33	Earthquake	30%
34	Test 9	Earthquake	60%	149	Test 34	White noise	0.01g
35	Test 10	White noise	0.01g	PHASE B'			
36	Test 11	Earthquake	80%	182	Test 35	White noise	0.01g
37	Test 12	White noise	0.01g	183	Test 36	Earthquake	10%
38	Test 13	Earthquake	90%	184	Test 37	White noise	0.01g
39	Test 14	White noise	0.01g	185	Test 38	Earthquake	20%
56	Test 15	Earthquake	90%	186	Test 39	White noise	0.01g
57	Test 16	White noise	0.01g	187	Test 40	Earthquake	30%
58	Test 17	Earthquake	80%	188	Test 41	White noise	0.01g
59	Test 18	White noise	0.01g	189	Test 42	Earthquake	40%
60	Test 19	Earthquake	90%	190	Test 43	White noise	0.01g
PHASE A'				191	Test 44	Earthquake	50%
87	Test 20	White noise	0.01g	192	Test 45	White noise	0.01g
91	Test 24	Earthquake	10%	209	Test 46	Earthquake	60%
92	Test 25	Earthquake	20%	210	Test 47	White noise	0.01g
93	Test 26	Earthquake	30%	211	Test 48	Earthquake	70%
94	Test 27	White noise	0.01g	212	Test 49	White noise	0.01g

Table 59: List of performed shake table tests

7.3.4 Observation during testing

Shake table tests were carried out for various earthquake load levels as explicitly shown in Table 59. In the same time the white noise tests gave insight of the progressive change of the dynamic characteristics of the system. The visual observations during testing as well as direct control of the drifts and change in eigen frequencies, then indirectly the stiffness, led to several major conclusions during testing.

- There was no sliding between the specimen foundations and shake table;
- During the first phase of testing (Phase A) the maximum reached acceleration was 1.64g and there was considerable amount of damages on the walls infill B, while the walls infill C did not experience any out of plane damage;
- The strengthened Phase A' was tested up to only 0.39g due to considerable accumulated damage in the bottom and top joints on the column while the walls were protected by the GFRPU net;
- The rotated specimen on the Phase B was also tested up to 0.35g and then stopped due to the damage on the wall infill C which was later on protected in similar manner as the wall infill type B with GFRPU net;

- Phase B', consisting of all repaired walls was tested up to 0.95g due to fact that the walls were able to withstand horizontal and vertical loads considerably larger than initial setup despite the fact that the RC columns lost a part of its bearing capacity

7.3.5 Results

Shake table tests were carried out for various earthquakes load levels, described in Table 59. Analysis of results were carried out first for horizontal relative displacements of the slab related to the building foundation, measured by two linear potentiometers attached to the support and the shake table displacement (Figure 398 and Figure 399). The relevant drifts of the in-plane tested infills (presented in %) were calculated, assuming their height of 230 cm. Next, changes in eigen-frequencies were analysed.

Setup with wall infills type B tested in-plane (Phase A and A')

In the Phase A, the infills B were tested in-plane in an initial phase up to 90% intensity, where damages of the infills B were hardly observed. During repeated loading by earthquake runs of 90% intensity, the capacity limit state was reached and additional damages in the building occurred due to sudden stop of the shake table, but without visible degradation of the specimen. After checking and correction in the shake table system, the infills B were tested further in the damage phase with 80% and 90% intensity. Formation of significant damages (Figure 404 and Figure 405) were observed during the last one excitation.

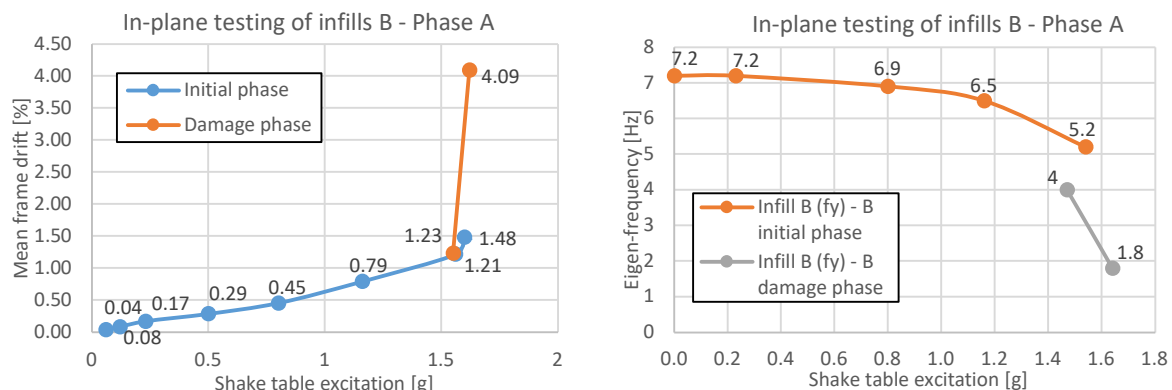


Figure 400: (a) Changes of the drift of the slab (ph. A) (b) Changes of eigen frequency of the str. (ph. A)

Changes in measured maximum horizontal relative displacement of the slab (Y-direction) were used to calculate the RC frame drift using the height of the columns up to the centre of the joint with the beams 240cm (Figure 400a). Observation related to the drift changes are confirmed by the reduction of the main eigen-frequency of the building in the Y-direction from 7.2 Hz to 1.8 Hz, obtained from the random tests (Figure 400b). Significant damages to infills B, appeared in the damage phase with 90% intensity. They correspond to reduction of the eigen-frequency below 4 Hz and interfering in resonance with the dominant excitation frequency of the earthquake signal (2.5 - 4.0 Hz).

Almost linear behaviour of the structure was observed up to 60% intensity (1.28 g). The structure started with softening due to the development of plastic hinges in the top and the bottom of columns and cracks pattern in head and bed mortar joints. Degradation process started with 80% intensity (1.70 g) and was developing when excitation was continuing up to 90% intensity (1.91 g) with meantime repetition of levels 90% and 80%. Drop of main eigen-frequency to 1.8Hz (Figure 400b) and significant damages to the infills B (Figure 404) occurred within 90% intensity excitation, but the structure did not collapse, and no collapse deflection was observed. Moreover, the blocks were kept by the PUFJs on the position with only single blocks rushing out.

The infills B (in such condition) were able to be repaired and strengthened using GFRPU system (Figure 396). After strengthening the infills B, the structure revealed increased eigen-frequency in the Y direction up to 3.6 Hz. After in-plane testing of the strengthened infills B up to 30% (0.64 g) in Phase A', no additional damages were observed, but the eigen-frequency dropped to 2.6 Hz (Figure 401b). Maximum drift obtained during 30% intensity was 1.69% (Figure 401a).

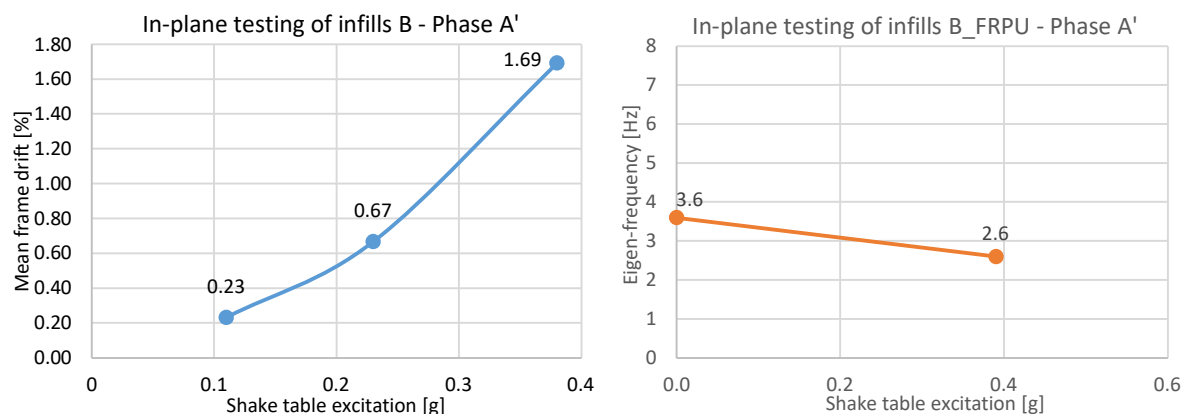


Figure 401: (a) Changes of the drift of the slab (ph. A') (b) Changes of eigen frequency of the str. (ph. A')

The strengthened infills B withstood all out-of-plane earthquake excitations applied to the structure after rotation of the building by 90 degree. The presented results related to the infills B indicate that PUFJ and GFRPU systems effectively protect RC frames and infill walls during strong earthquakes.

Setup with wall infills type C tested in-plane (Phase B and B')

In the Phase A (the infills B tested in-plane), the infills C were tested out-of-plane in the initial phase up to 90% intensity and then in the damage phase with 80% and 90% intensity. Practically no serious damages to the infills C were observed at this stage (only fissures in mortar), as well as after the harmonic resonance test with 16 Hz and 32 Hz frequencies (resonance frequencies of the infills C – out-of-plane moving on PUFJs and bending, respectively). After rotation of the building, the infills C presented slightly non-linear behaviour during in-plane tests. Changes in maximum relative horizontal displacement of the slab and the calculated drift are presented in Figure 402a for the increasing excitation intensity up to 30%. Observation related to the drift changes are confirmed by small reduction of the eigen-frequency – Figure 402b in the Y-direction: from 3.5 Hz to 2.9 Hz, even if the structure worked in the resonance frequency range of the KEF earthquake excitation (2.5-4.0 Hz).

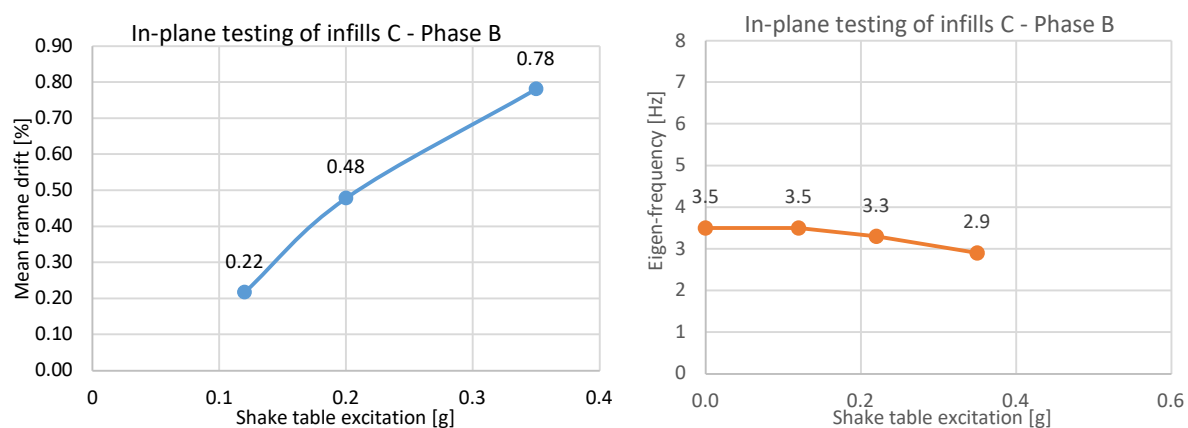


Figure 402: (a) Changes of the drift of the slab (ph. B) (b) Changes of eigen frequency of the str. (ph. B)

In the last phase B', the type C walls were repaired and strengthened using GFRPU system (Figure 396). After strengthening the infills C, the structure revealed increased eigen-frequency in the Y direction up to 5.6 Hz. Strengthened infills C were tested up to 70% (0.95 g) intensity, where the eigen-frequency dropped to 4.6 Hz (Figure 403a). Maximum drift obtained during 70% was 0.99% (Figure 403b).

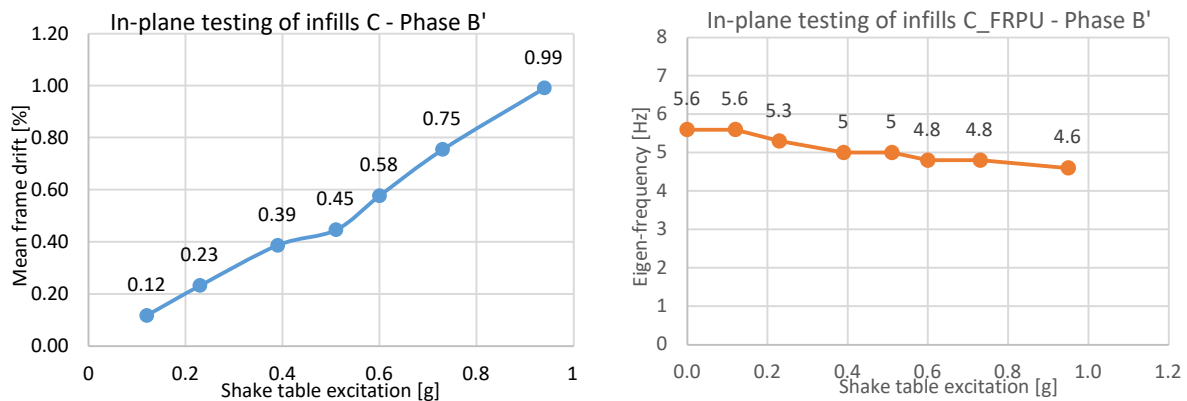


Figure 403: (a) Changes of the drift of the slab (ph. B') (b) Changes of eigen freq. of the str. (ph. B')



Figure 404: Final state of damage – Phase A



Figure 405: Spalled concrete cover of the column in the bottom

7.3.6 Conclusions and outlook

The tests of full-scale structure on a shake table have shown that infills significantly influence the seismic response of the structure. The effects of strong earthquakes on the stiffness and the eigen-frequencies of the structure – both denoting damage accumulation are better controlled in case the ortho block infill-RC frame boundaries are protected with PUFJ joints.

It was observed that due to the flexibility of the 2cm polymer joint, the interaction between the special (KEBE K100) ortho block infill and the RC frame can be manipulated so as to achieve the delay of serious infill damages at very high RC frame inter-storey drifts. The present tests suggest that first brick disintegration (that may cause injuries) occurs at levels far higher than 12% drift while avoiding undesirable effects on the RC columns, caused by the infills. Further, it is validated that the PUFJ protection enables the infill to be strengthened even after very high inter-storey drift of the structure up to 3.8%. Such a level is higher than the one corresponding to repairable damages for RC frames. Therefore, the PUFJ protected ortho block infill can be effectively transformed to a mechanism remarkably increasing the initial stiffness of the bare RC structure. Secondly, the infill maintains its integrity and bears part of horizontal but most important of vertical loads at high drift levels.

Finally, the applied GFRPU system efficiently protects damaged infills against collapse under out-of-plane excitation while they restore large part of their in-plane stiffness that is countable at RC structure level.

The tests offer direct comparison between joint on three sides (left, top, and right) and joint on all four sides for low excitation levels because of the poor condition of the RC frame after numerous sequential excitations. As expected, a RC structure with ortho block infills protected with polymer joints on all four sides is more flexible in-plane. Both PUFJ systems protect efficiently the ortho block brick in-fills against out of plane failure for very high inter-storey drifts and accelerations. Both PUFJ systems protect the structure with damaged columns against collapse, being able to bear part of the horizontal and vertical load.

8 University of Cambridge

The Turner Beam Centrifuge facility is housed in the Schofield Centre at Cambridge University, UK. It provides facilities for the testing of Geotechnical models at elevated gravity in order to achieve stress similitude between models and full-size prototypes. This is vital for the testing of geotechnical systems owing to the highly non-linear behaviour of soils. The principles of centrifuge modelling and operations of the facilities in Cambridge are summarised by Schofield (1980). Over the decades the centrifuge facilities have been vastly improved and are still considered as world leading in this area. More details of the centrifuge modelling at Cambridge were described by Madabhushi (2014).

The Turner Beam Centrifuge is a 10m diameter balanced beam machine, capable of subjecting models weighing up to 1 tonne to up to 125g of centripetal acceleration. The facility can thus modelling a prototype system of approximately 100 m in lateral extent and a soil depth of up to 50 m.

For the purposes of the dynamic tests carried out as part of the SERA project, the centrifuge is equipped with a servo-hydraulic earthquake actuator shaker whose capabilities are summarised by Madabhushi et al (2012). This earthquake actuator which enables models to be subjected to pre-defined acceleration time histories such as the Kobe, Imperial Valley, Chichi motions etc., subjecting the models to strong earthquake motions at the bedrock level. In addition to the servo-hydraulic earthquake actuator, the Schofield centre has also developed specialist model containers that mimic the semi-infinite extent of the soil strata. Several different concepts exist in which either the dynamic soil stiffness is matched by the end walls of the model container (the so-called Equivalent Shear Beam concept) or the end walls are tied together using laminae running on cylindrical bearings. During the SERA project the participating research teams chose the model containers that are most appropriate for their projects. For example, soil-structure interaction is best modelled using the ESB model containers, while liquefaction problems utilise the laminar model container. High speed imaging facilities with a 1000 frames per second capability @ 1Mpix resolution are also available. Images from this facility are subsequently used to carry out Particle Image Velocimetry (PIV) to determine the soil deformations (and hence the strains) and in identifying the predominant failure mechanisms. Miniature instrumentation was also made available to all of the SERA projects including use of miniature Piezo-electric accelerometers, MEMS accelerometers, LVDTs, Pore Pressure Transducers and strain gauging of structures specific to the projects, where required. Fast data acquisition systems were used to log the data from these instruments during and after the earthquake motion using in-flight computer systems.

During the SERA project, the facility hosted four projects, with a total of 49 access days being provided as forecast within the SERA proposal. All available access days were allocated within the first two calls with several further projects not being selected owing to a lack of available resources within the project. All testing was carried out as forecast and completed by summer 2019.

Schofield, A.N. (1980) Cambridge Geotechnical Centrifuge operations, *Geotechnique* **30**(3) 227-268.

Madabhushi, S.P.G., Haigh, S.K., Houghton, N.E. & Gould, E. (2012) Development of a servo-hydraulic earthquake actuator for the Cambridge Turner beam centrifuge. *International Journal of Physical Modelling in Geotechnics* **12**(2) 77-88

8.1 Project #14 – Seismic behaviour of anchored Steel Sheet-Piling (SSP) retaining walls: experimental investigation, theoretical interpretation and guidelines for design

Authors

R. Conti⁽¹⁾, C. Prum⁽²⁾, G. Caputo⁽¹⁾, A. Fusco⁽³⁾, P. El Boueiz⁽²⁾, S.P.G. Madabhushi⁽³⁾, G. Viggiani⁽³⁾

⁽¹⁾ *University of Rome Niccolò Cusano, Italy*

⁽²⁾ *Arcelor Mittal, Luxembourg*

⁽³⁾ *Cambridge University, U.K.*

8.1.1 Summary of the project

Steel Sheet-Piling (SSP) walls are frequently adopted as retaining structures in quays and wharves, as they may be more economical with respect to concrete caissons or other types of retaining structures.

In current design practice, SSP retaining walls are usually designed using simple calculation tools, based on Sub Grade Reaction Models (SGRM) or Limit Equilibrium Methods (LEM). If the seismic action is introduced following a pseudo-static approach, then the same methods can be used, at least in principle, for the seismic design of SSP walls. However, depending on wall flexibility, contact properties at the soil-wall interface, strength properties of the system, and assumptions on both the seismic action (amplification/phase shift of accelerations within the soil) and the stress distribution into the soil, these methods can lead to highly over-conservative or un-conservative predictions. Numerical Finite Difference (FD) and Finite Element (FE) methods often provide more economical solutions than SGRM or LEM methods. However, numerical modelling of geotechnical systems under dynamic conditions is quite complex, requiring careful consideration of many factors (e.g.: the definition of the input motion and of suitable boundary conditions and, most of all, the choice of an adequate constitutive model for the soil), and not always readily accessible for the practicing engineer.

Following the Performance-Based Design methodology, in recent years a new design concept has started to be explored for the seismic design of retaining structures. This is based on the idea that the structure can experience permanent displacements during the design earthquake, provided that the related damage does not exceed some allowable threshold, defined on the basis of a given required performance level. Within this context, the attention has progressively moved from the computation of the maximum internal forces in the retaining structure under an equivalent system of pseudostatic forces, to the prediction of the permanent displacements experienced by the structure under a given acceleration time history (earthquake). To this end, the Newmark's sliding block procedure has been successfully applied to the evaluation of permanent displacements of both gravity and cantilevered walls, and the critical acceleration has been proved to control both the maximum internal forces in the structural members and the final permanent displacement.

A possible extension of these procedures to the seismic design of anchored SSP walls requires a better understanding of the dynamic behaviour of these systems to identify the main factors affecting their response under seismic actions. In this respect, centrifuge tests carried out on reduced-scale physical

models provide a powerful tool to investigate the seismic response of geotechnical systems in idealised situations, in which the initial state of the soil, the hydraulic and kinematic boundary conditions and the dynamic input motion are controlled and well defined.

This project aimed to provide a better insight into the seismic behaviour of anchored SSP walls, focusing on the main physical mechanisms affecting the distribution of earth pressures on the wall during the earthquake, the possible increase of internal forces in the structural members and the progressive accumulation of permanent displacements. To this end, four centrifuge tests were carried out at the University of Cambridge, considering different layouts and input earthquakes. The experimental results allowed to understand how the critical acceleration of the soil-wall system governs the behaviour of SSP walls, both in terms of maximum internal forces and permanent displacements, and how the activation of different plastic mechanisms can affect the overall observed behaviour. Moreover, based on the experimental outcome, new theoretical methods have been explored for the seismic design of anchored SSP walls.

8.1.2 Main research objectives and expected contribution to the seismology and earthquake engineering community

The main objective of this project is to provide a better understanding of the seismic behaviour of anchored SSP walls, focusing on the main physical mechanisms affecting the possible increase of internal forces in the structural members and the progressive accumulation of permanent displacements during the earthquake. Accordingly, the research project has three objectives:

- Identify the possible plastic mechanisms actually occurring in the soil-wall-anchor system, depending on the geometrical layout of the problem, and the critical acceleration associated to each mechanism.
- Understand if the maximum internal forces and displacements experienced by the wall during the earthquake are effectively controlled by the critical acceleration, as it is the case for gravity and cantilever walls. In other words, verify that the internal forces remain essentially constant when the critical acceleration of the system is attained and that permanent displacements are only accumulated when the soil acceleration exceeds the critical value.
- Validate the theoretical limit equilibrium method recently proposed by Caputo et al. (2018) for computing the critical acceleration of the wall, which takes into account all the possible global and local failure mechanisms (failure of the anchor system or full mobilization of the soil passive resistance in front of the wall).

The experimental results and theoretical findings coming from this project will have not only a clear scientific value, as a close combination of experimental and theoretical tools to the interpretation of the dynamic behaviour of anchored SSP walls has not been attempted so far in the scientific literature, but also a direct technical impact. As a matter of fact, based on these results, simple methods for the seismic design of SSP walls will be eventually developed, capable of extending also to these structures a more rational Performance-Based Design methodology.

8.1.3 Project status

Four dynamic centrifuge tests were carried out in the 10 m diameter Turner beam centrifuge of the University of Cambridge. Figure 406 shows the layout of the wall-anchor system in the four tests (dimensions at prototype scale). The main parameters that were varied are the position of the anchor rod with respect to the anchor plate (b_a/H_a), the normalized embedment depth of the wall (D/h) and the normalised anchor length (L/h). As a matter of fact, very recent theoretical developments have

shown that these three dimensionless parameters control the nature of the plastic mechanism effectively taking place during shaking, to be either local anchor failure or global failure of the whole system, and thus eventually affecting the expected value of the critical acceleration.

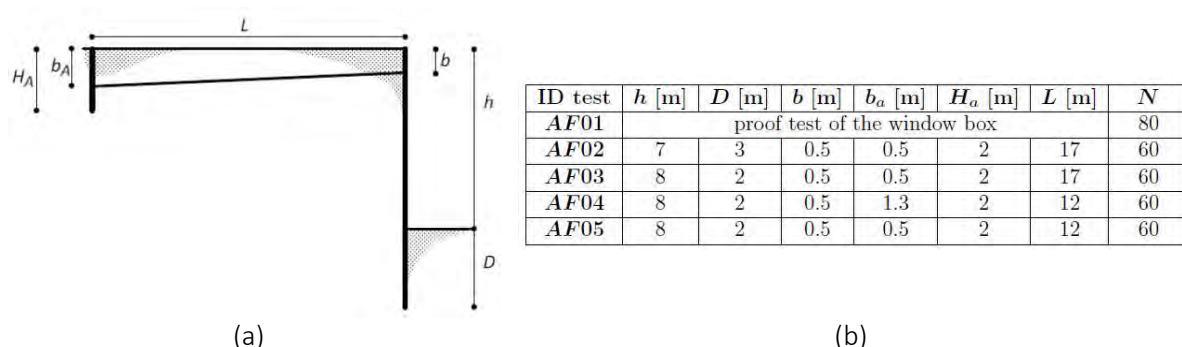


Figure 406: (a) Layout of the wall-anchor system in the centrifuge tests and (b) main geometrical quantities (at prototype scale)

The tests were carried out in plane strain conditions, at a centrifugal acceleration of 60g, preparing the models within a homogeneous dry medium-dense layer ($DR = 50\%$) of fine-grained siliceous Hostun sand. Both the retaining wall and the anchor plate were modelled using aluminium alloy plates with a bending stiffness at prototype scale similar to that of an AZ28 steel sheet pile profile, while the tiebacks were modelled using four steel cables hinged to both ends.

The models were prepared within a rigid container with a Perspex viewing window, allowing soil deformations and wall displacements to be measured during the tests with a Particle Image Velocimetry (PIV) technique. A layer of DUXSEAL was included between the rigid end walls and the soil in order to prevent generation of P-waves and multiple wave reflection during shaking.

As far as the instrumentation is concerned (Figure 407), accelerations at different locations in the model were measured using miniaturized piezoelectric accelerometers, while accelerations of the wall were recorded using MEMS accelerometers; displacements were measured using LVDTs transducers; the axial load in the anchors was measured using miniature load cells, while strain gauges were used to measure the bending moments of the wall; finally, a fast digital camera was used for the PIV analysis.

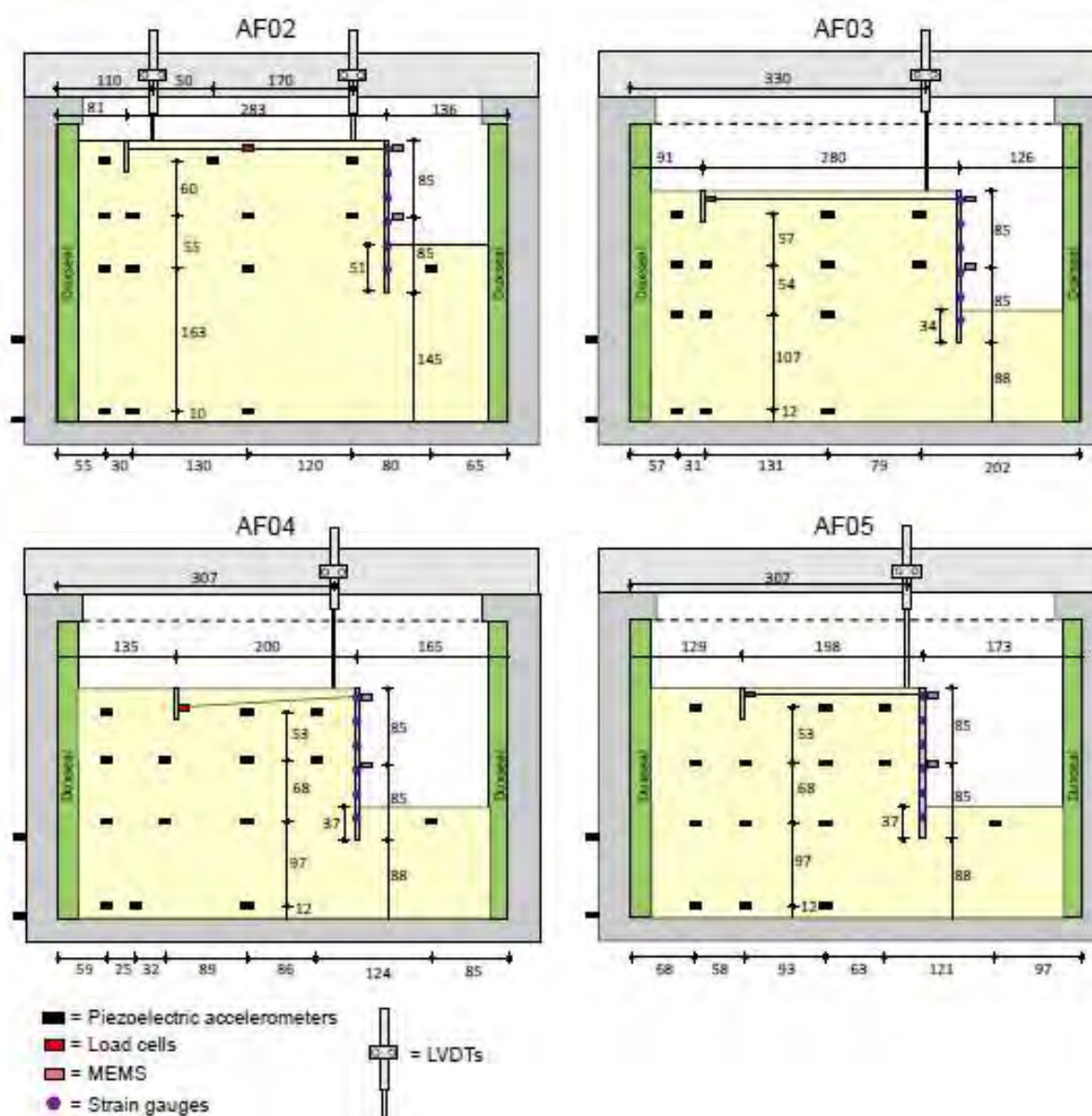


Figure 407: Position of the instrumentation used in each test

The dynamic input was provided by a Servo-Hydraulic earthquake actuator, capable of applying both trains of approximately sinusoidal waves and more realistic earthquake motions. Some details of the adopted instrumentation is shown in Figure 408.

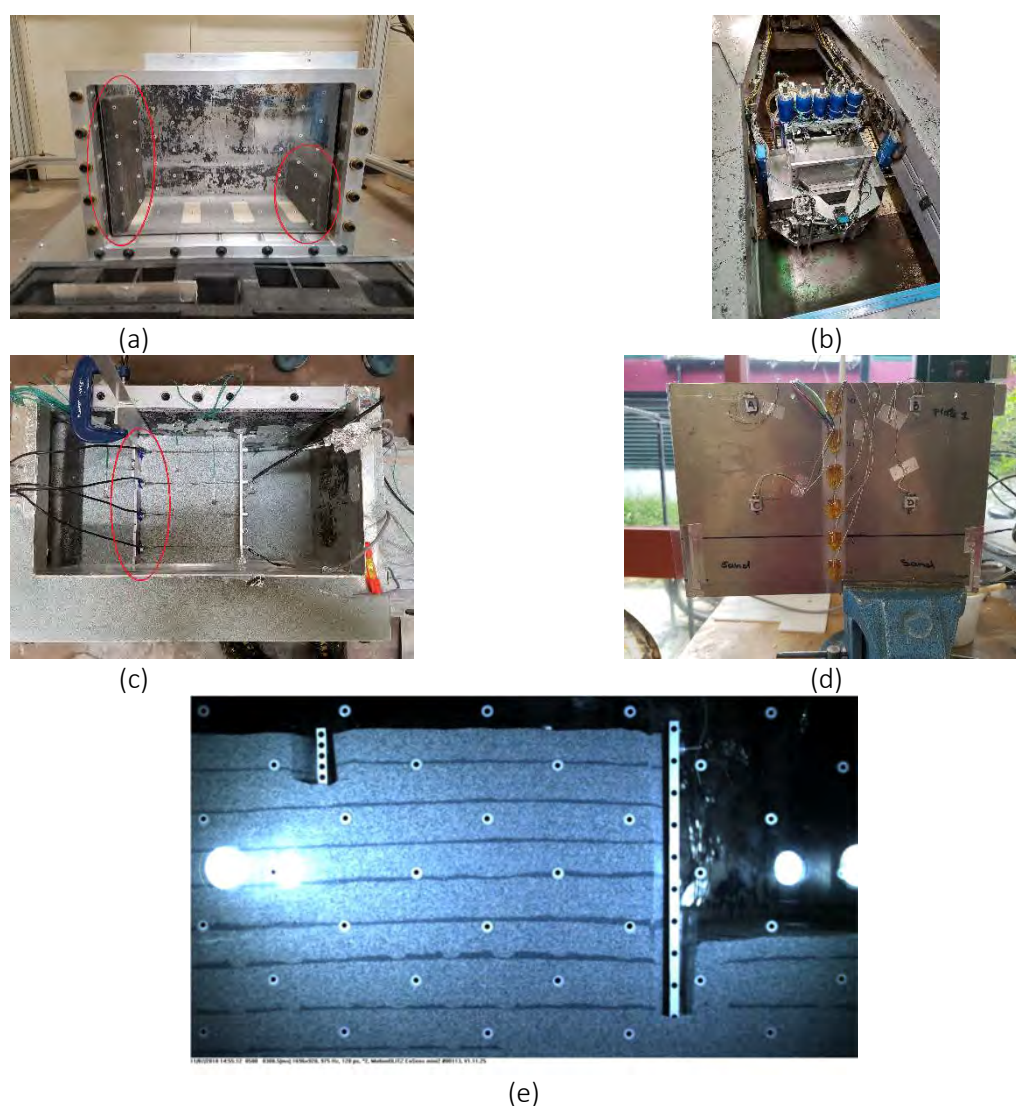


Figure 408: (a) rigid container with a Perspex viewing window and Duxseal layers at the sides; (b) servo-shaker mounted on the centrifuge; (c) load cells in the tie-backs in the test AF04; (d) small-scale model of the retaining wall, with details of the instrumentation placed on it; (e) side view of the model in test AF04

Table 60 reports, for each test, the critical acceleration and the expected failure mechanism according to the theoretical model proposed by Conti & Caputo (2018), adopting two values for the soil peak friction angle, estimated using the empirical formula proposed by Bolton (1986). In the first two tests (AF02 and AF03) a local failure of the anchor system was expected, while a global failure mechanism was predicted for the last two tests (AF04 and AF05).

ID test	a_c [g] ($\varphi = 38^\circ$)	a_c [g] ($\varphi = 39^\circ$)	expected failure mechanism
AF02	0.21	0.24	anchor failure
AF03	0.12	0.16	anchor failure
AF04	0.145	0.165	global failure
AF05	0.095	0.11	global failure

Table 60: Estimated critical acceleration and expected failure mechanism for each test

From the analysis of the experimental data, it was possible to compute the evolution, during the applied earthquakes, of the internal forces in the structural members (axial force in the tieback and bending moment distribution in the wall) and of the displacements of the anchor plate and the main wall. Moreover, from a preliminary analysis of the experimental results, it was possible to highlight the role played by the critical acceleration on the maximum internal forces and the maximum displacements experienced by the system during the applied earthquake.

For the sake of brevity, only the experimental results obtained from the PIV analysis are presented in the following. Specifically, in order to identify the plastic mechanism effectively activated during the centrifuge tests, the shear strains developed into the soil between the anchor plate and the retaining wall were estimated from the displacements computed by the PIV analysis. As an example, Figure 409 shows the contours of shear strains computed during the strongest earthquake applied in test AF02 (earthquake EQ4) and AF05 (earthquake EQ3). In the first case (Figure 409a), shear strains are mostly clustered in a wedge behind the retaining structure and above dredge level, consistently with the development of a local anchor failure and the rotation of the retaining wall around the toe. In the second case (Figure 409b), instead, the shear strains mainly develop along a failure surface going from the bottom of the anchor wall to the toe of the retaining wall, suggesting a global failure mechanism of the whole anchor-soil-wall system. As shown in Figure 410, this observation is fully consistent with the theoretical log-spiral failure surface proposed by Conti & Caputo (2018).

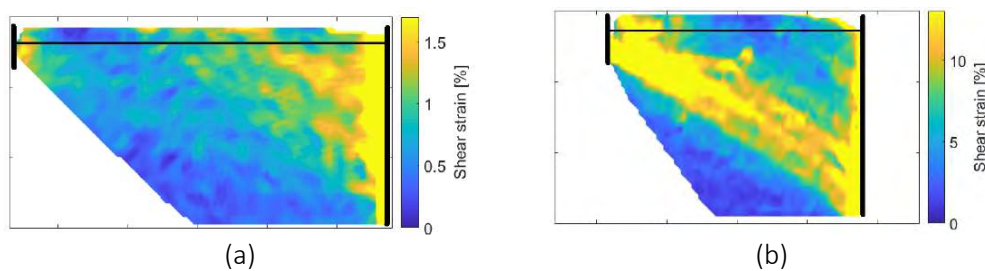


Figure 409: Soil shear strains obtained from PIV analyses: (a) test AF02 and (b) test AF05

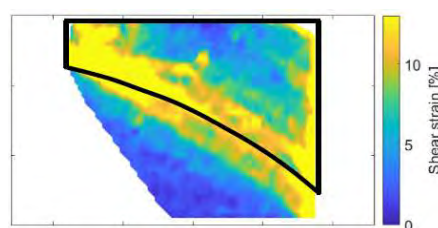


Figure 410: Test AF05 (Earthquake EQ3): comparison between soil shear strains obtained from PIV analyses and theoretical prediction of the global failure mechanism (black lines)

8.1.4 Conclusions

The Project formally ended on December 2018, we are still working on the interpretation of the huge amount of experimental data coming from the four centrifuge tests carried out within the Project. The preliminary results have demonstrated that anchored sheet pile walls in liquefiable soils can suffer very large permanent deformations due to anchor pullout if the anchor is an insufficient distance behind the wall. Global failure mechanisms which can be used to assess the appropriate geometry for the anchor position fit well with those proposed from the modelling of Conti & Caputo (2018).

References

Bolton M.D. (1986) The strength and dilatancy of sands, *Geotechnique*, **36**(1), 65-78.

Conti, R. & Caputo, G. (2018) A numerical and theoretical study on the seismic behaviour of yielding cantilever walls. *Geotechnique*, **69**(5) 377-390.

8.2 Project #15 – STILUS – Structure-Tunnel Interaction in Liquefiable Sand

Authors

E. Bilotta⁽¹⁾, V. Nappa⁽¹⁾, G. Miranda⁽¹⁾, S.K. Haigh⁽²⁾, S.P.G. Madabhushi⁽²⁾

⁽¹⁾ *University of Napoli, Federico II, Italy*

⁽²⁾ *Cambridge University, U.K.*

8.2.1 Summary of the project

Relatively shallow and light underground structures, such as urban tunnels, may cross liquefiable sand deposits and liquefaction has induced floatation and large uplift to sewer pipes or open-cut tunnels in some recent strong earthquakes. It is worth noticing that in urban area shallow tunnels are likely close to the foundations of buildings and easily interact with them during earthquakes (i.e. Soil-Structure-Underground Structure-Interaction, SSUSI). Nevertheless, the reciprocal influence of a tunnel and an adjacent building in presence of soil liquefaction has not been investigated in the literature yet. This problem appears rather important considering the rapid extension of the built environment, both above- and underground, to areas that may be subjected to seismic-induced soil liquefaction.

The research investigates the problem of the dynamic interaction of an underground structure and a building founded in liquefiable sand. To this aim a series of centrifuge tests are carried out on a reduced scale model of a rectangular tunnel embedded in a liquefiable layer of sand, with and without a model building founded in proximity, as a typical case of a cut-and-cover tunnel in urban environment. Furthermore, tests will be carried out on models where the liquefiable ground is improved by adding nanomaterials (laponite) to increase locally the fine content. The position of the improved ground is varied in the models: either a layer of sand beneath the tunnel or a layer of sand beneath the building is improved.

The mechanism of the uplift behaviour of underground structures, focusing on the influence of the degree of liquefaction, the external forces acting on the underground structure and the deformation of the liquefied ground, has been investigated in past studies with reference to free ground surface conditions. Recent centrifuge testing on the behaviour of buildings founded in liquefiable ground layers have, however, shown that smaller net excess pore pressures are generated within the liquefiable layer under a structure by increasing the contact pressure and height/width ratio of the building. Other studies have shown the reciprocal influence of adjacent buildings, affecting non-uniform settlement during liquefaction.

How the uplift mechanism of an adjacent underground facility is influenced by the presence of the building and how the development of a mechanism beside the building due to the floating of the underground structure can affect the tilt and settlement of the building are both aspects that have not been investigated in the literature.

This problem appears rather important for the earthquake engineering community considering the rapid extension of the built environment, both above- and underground, to areas that may be subjected to risk of liquefaction. Hence the study intends to contribute to the wider topic of the resilience of urban environment to natural hazards.

The models are created at reduced scale and tested accordingly at N-times increased g-level in the Turner Beam Centrifuge at the Schofield Centre of the University of Cambridge.

The ground layer consists of homogenous Hostun sand at a relative density of about 45%-50%. This is dry pluviated in thin layers through an automatic hopper system. During the model preparation, arrays of miniature pore pressure transducers (PPTs), piezoelectric and MEMS accelerometers are deployed at the desired locations. Displacement transducers (LVDTs) are used to measure the settlements at different locations.

During model preparation a model tunnel is embedded in the sand layer (see the list of tests later on). The rectangular model tunnel is made using an extruded section of aluminium alloy. Rough dimensions are provided in the sketches of Figure 411. The rectangular tunnel represents a section of a metro station tunnel that can accommodate two separate platforms. The soil cover above the tunnel corresponds to an embedment ratio $C/HT = 1$.

A linear-elastic sway frame (SDOF) made of aluminium is founded in the sand layer in most tests (see the list of tests later on). Rough dimensions are provided in the sketch in Figure 411. The figure shows the centrifuge models including the sway frame (i.e. the building), that is located beside the tunnel. The sway frame is fitted with accelerometers to capture its horizontal sway as well as rocking behaviour. Two vertical accelerometers are positioned on the base of the structure to enable measurement of rocking angles. A displacement transducer is located at the base of the frame to measure vertical settlement.

The sand layer needs to be saturated before testing. To avoid the incompatibility between the dynamic and diffusion time scaling laws, a high viscosity aqueous solution of hydroxypropyl methylcellulose (HPMC) is used to saturate the sand layer, with a viscosity N times larger than water.

Considering the need to study the displacement field around the tunnel, high speed photogrammetry is used in the tests. Hence stems the choice to use a transparent side container. A rigid container with a Perspex window is used. It is known that this type of model container may cause boundary effects affecting the response, particularly when liquefaction is reached. Therefore, a soft material called Duxseal® is used on the walls, to minimize the boundary effects: it has been showed that it can reduce the stress wave reflections by about two-thirds.

In total 4 centrifuge models were tested (Figure 411), according to the following sequence:

1. Tunnel only, in window box;
2. Tunnel and adjacent building;
3. Tunnel and adjacent building, ground treatment below the tunnel floor;
4. Tunnel and adjacent building, ground treatment below the building.

A servo-hydraulic earthquake actuator is used to apply near-sinusoidal earthquake motions to the centrifuge model. The amplitude of the signal will be increased during the test, until soil liquefaction is achieved.

Time histories of acceleration and pore pressure in the ground are recorded during shaking, along vertical and horizontal arrays. Similarly, displacement time histories at a few points at ground surface (settlement) and on the sway frame (settlement, horizontal displacement and tilt) are monitored.

PIV Photogrammetry enables a deep insight on the triggering of uplift and the evolution of the mechanism. This is very useful for the calibration of a numerical model to simulate the centrifuge tests and to reliably extend later the study to different geometrical conditions.

Comparing the time histories measured in model #1 and #2 will enable to highlight the influence of tunnel-building interaction on the displacements field induced by soil liquefaction.

In model #3 a volume of sand below the tunnel is improved by pouring the sand in a laponite/water suspension during model making. An amount of laponite corresponding to 1% of the dry weight of sand is mixed to water in concentration equal to 5%.

In model #4 a similar improved volume is located beneath the foundation level of the sway frame. A comparison among results of tests #2, #3 and #4 enables to discuss the effectiveness of laponite injection in the ground to reduce the effects of sand liquefaction on both the underground structure and the building.

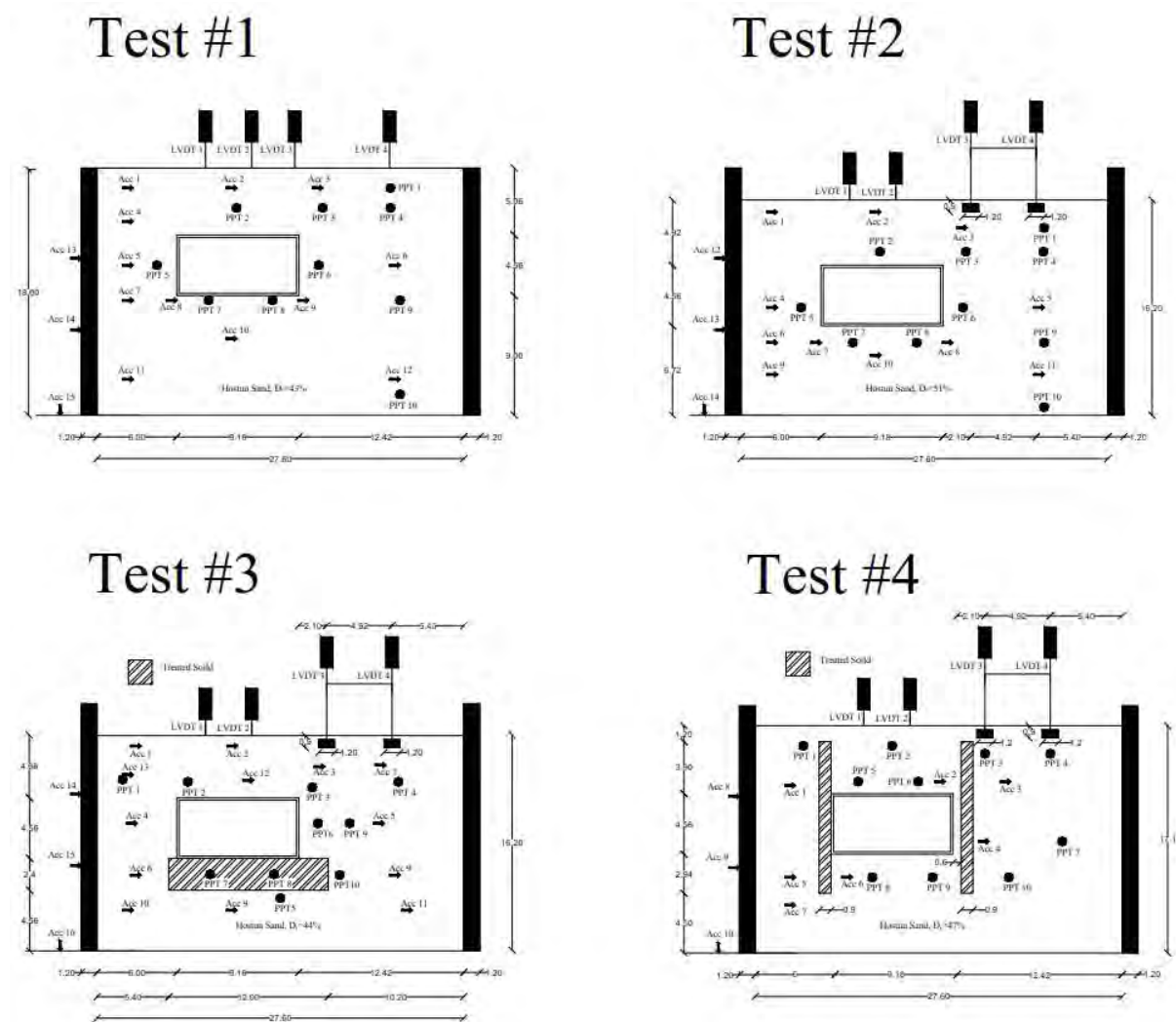


Figure 411: Schematic drawings of the four centrifuge models

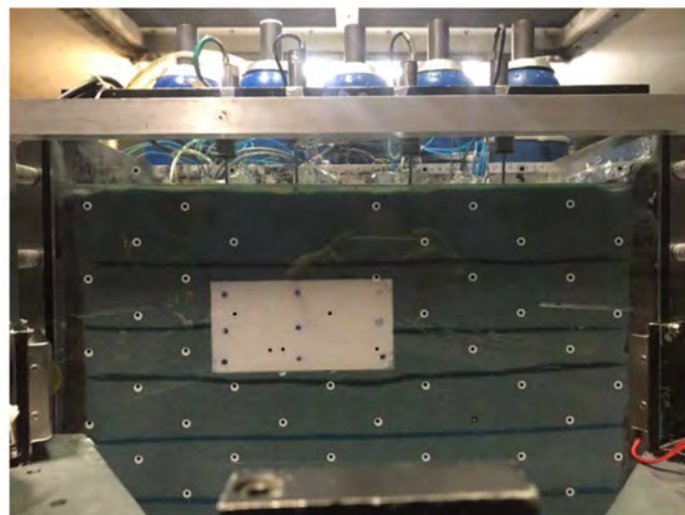
8.2.2 Model Layouts

The influence of soil liquefaction on the tunnel-building interaction was investigated in the project STILUS. Four models were created at reduced scale and tested accordingly at 60-times increased g-level in the Turner Beam Centrifuge at the Schofield Centre of the University of Cambridge. The layout of the four tests are shown in Figure 411.

In the first model a tunnel was embedded in the sand layer, in the second model a simplified structure was added in order to study the interaction between the tunnel and the building during the liquefaction phenomenon. The objective of the last two tests was to assess the effectiveness of a mitigation technique to reduce tunnel and building displacements induced by soil liquefaction. In these tests a high-plasticity nanoparticle synthetic clay, laponite, was mixed to sand to verify its ability to mitigate the effect of liquefaction on the tunnel. The distribution of excess pore pressure induced around the tunnel and the building basement in the first two tests was useful to identify where the mitigation technique to reduce pore pressure build-up would have been most effective against the effects of soil liquefaction, hence defining where it should be implemented in the last two tests. Two different geometrical configurations were adopted, in the first one a horizontal layer of sand- laponite mixture was placed below the tunnel, while in the second one two vertical layers of the same mixture were created at the sides of the rectangular tunnel.

The ground layer consisted of homogenous Hostun sand at a relative density of about 45%-50%. The instrumentations adopted in the tests was constituted by pore pressure transducers (PPTs), piezoelectric and MEMS accelerometers. Displacement transducers (LVDTs) were used to measure the settlements at different locations. Considering the need to study the displacement field around the tunnel, high speed photogrammetry is used in the tests (PIV). A rigid container with a Perspex window is used. It is known that this type of model container may cause boundary effects affecting the response, particularly when liquefaction is reached. Therefore, Duxseal® is used on the walls, to minimize the boundary effects. For each test, four sinusoidal signals, characterized by different amplitude, and one real signal were used.

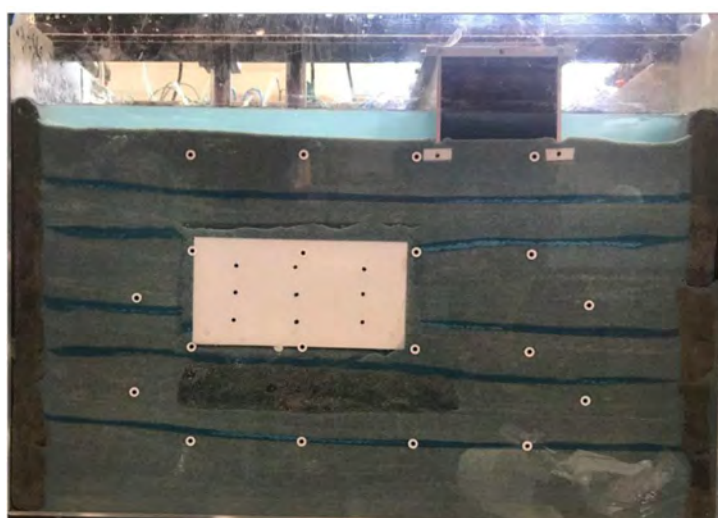
Figure 412 shows pictures of the models before testing.



a) model #1



b) model #2



c) model #3

Figure 412: Model cross-sectional photos

The main characteristics of the shaking applied to the models 1 to 3 are shown in Table 61. The first shaking of each model is generally very weak and it was applied to improve the homogeneity of the model prior to the following shakings. Shaking no.2 is generally able to provide information on the dynamic behaviour of the model without inducing liquefaction. From shaking 3 onwards, significant liquefaction is expected to occur in the model. Most of the shakings were induced by pseudo-harmonic input signals, although on models 1 and 3 a final shaking was excited, that corresponds to the natural record of Kobe.

earthquake	frequency (Hz)	cycles	PGA (g)
model 1			
1	1	10	0.058
2	1	10	0.100
3	1	10	0.310
4	1	15	0.339
Kobe	-	-	0.167
model 2			
1	1	10	0.067
2	1	10	0.105
3	1	10	0.369
4	-	15	0.416
model 3			
1	1	10	0.054
2	1	10	0.097
3	1	10	0.390
4	1	15	0.390
5	1	15	0.440
Kobe	-	-	0.142

Table 61: Input motions used in the tests

8.2.3 Experimental Results

Figure 413 shows the contours of vertical displacements at the end of earthquake 3 and 4 in all the models tested until date. They were measured by using PIV. As a general comment, it should be noted that larger displacements occurred during earthquake 3 than during earthquake 4, although in the latter higher accelerations were applied. This indicates possible densification of the sand layer as a consequence of liquefaction occurring during earthquake 3.

Figure 414 to Figure 416 show the time histories of vertical displacement of selected target in the tunnel and on the structure (or in corresponding points in the free-field model) as they were obtained from PIV.

A comparison between “model 2 - earthquake 3” and “model 1 - earthquake 3” shows that lower upheaval of the tunnel is observed in model 2, due to the higher initial relative density (51% vs. 43%), despite the input PGA in model 2 is slightly higher than in model 1.

When comparing “model 3 - earthquake 3” and “model 1 - earthquake 3”, the upwards displacements of the soil around the tunnel (above it in particular) are similar in terms of magnitude, despite the PAG of earthquake 3 in model 3 is about 30% higher than the corresponding value in model 1, and the two models have comparable relative density (44% vs. 43%). This indicates that the layer of sand improved with laponite that has been created in model 3 beneath the tunnel is able to reduce the tunnel uplift.

Figure 417 shows a comparison of time histories of excess pore pressure. Excess pore pressure within the layer treated with laponite (7 and 8) are lower than outside the layer (5), indicating the effectiveness of laponite suspension to reduce excess pore pressure that produces the tunnel uplift.

Concerning the structure, a reciprocal influence between the tunnel and the structure movements can be detected by looking at the displacement patterns in Figure 413. Measurements seem to indicate that the improvement of sand with laponite beneath the tunnel has a limited effect on the structure. Numerical analyses are needed to verify this conclusion.

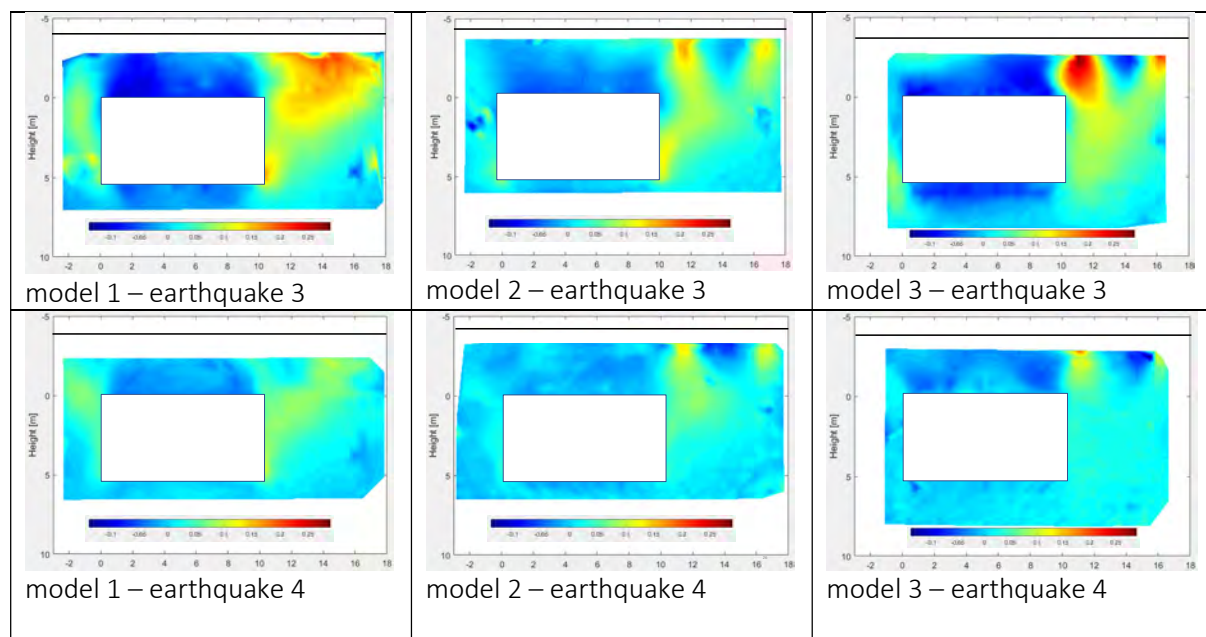


Figure 413: contours of vertical displacement from PIV at the end of earthquake 3 and 4 in models 1,2 & 3

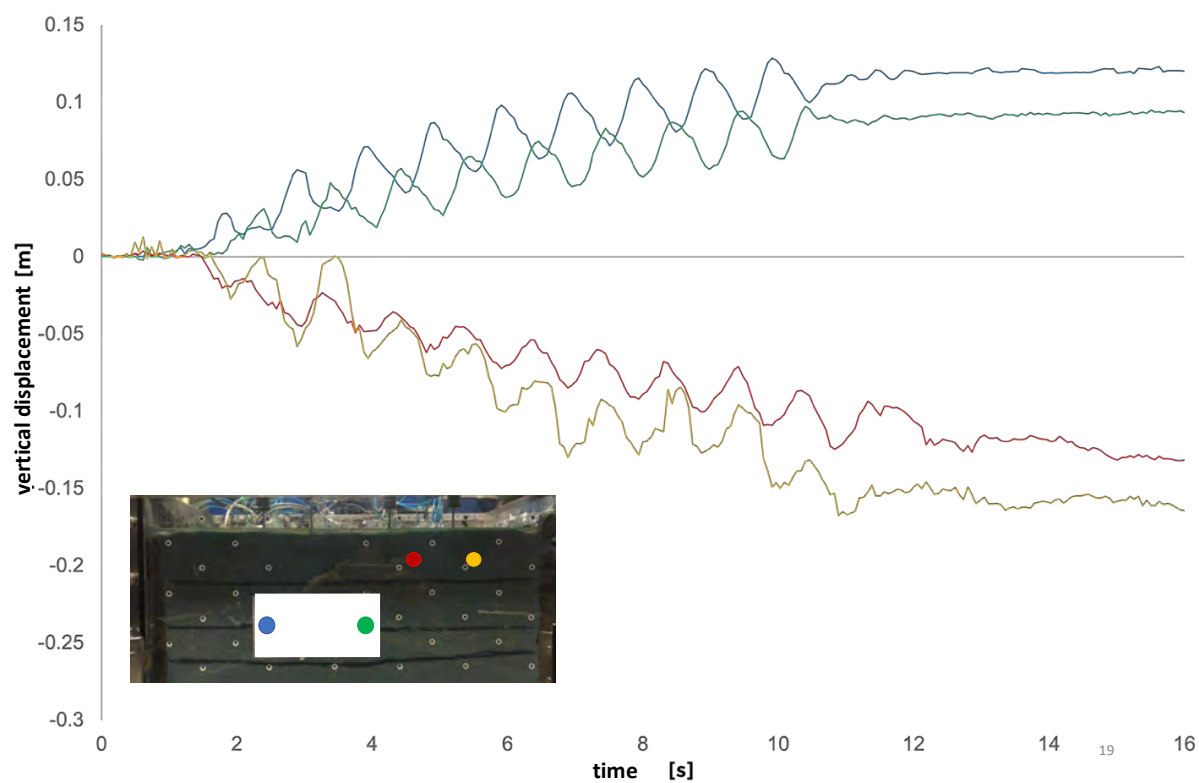


Figure 414: time history of vertical displacement from PIV: tunnel and free-field, model 1, earthquake 3

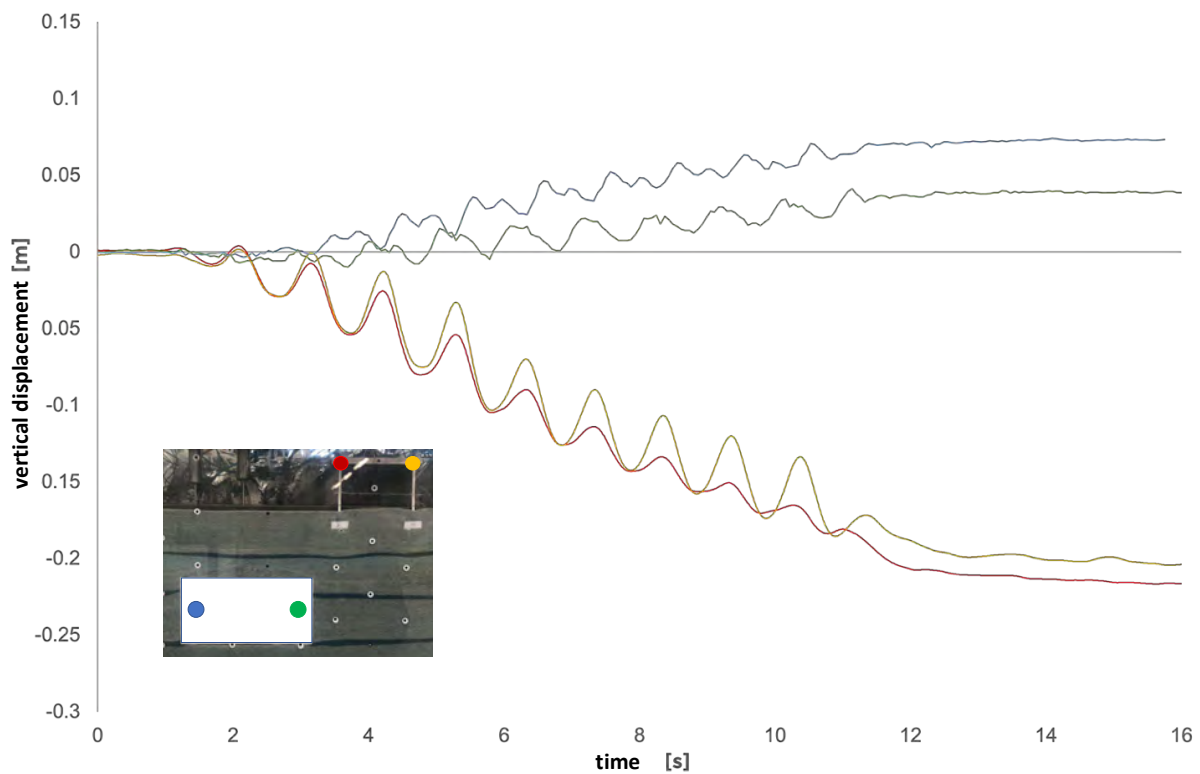


Figure 415: time history of vertical displacement from PIV: tunnel and building, model 2, earthquake 3

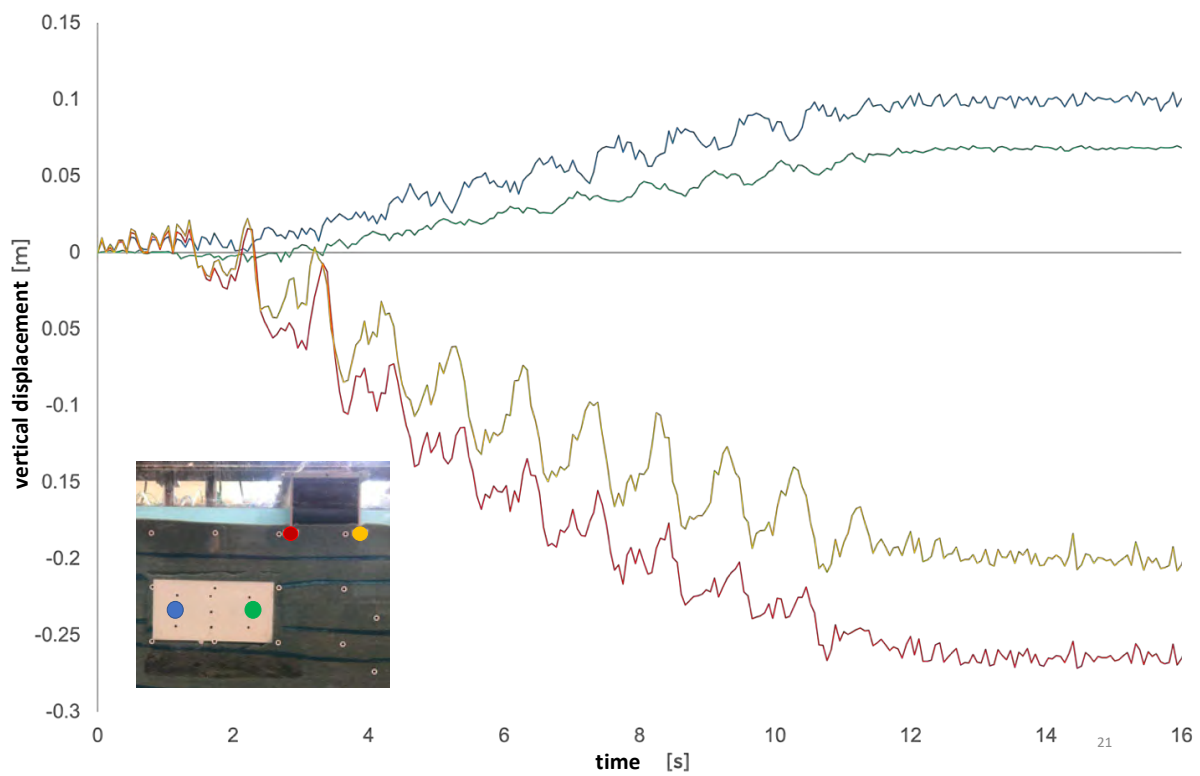


Figure 416: time history of vertical displacement from PIV: tunnel and building, model 3, earthquake 3

Interaction between the tunnel and the building

The third sinusoidal signal characterized by an amplitude equal to 0.3 g triggered liquefaction, as showed in Figure 417, in terms of pore pressure ratio recorded by the transducers placed at the top of the model.

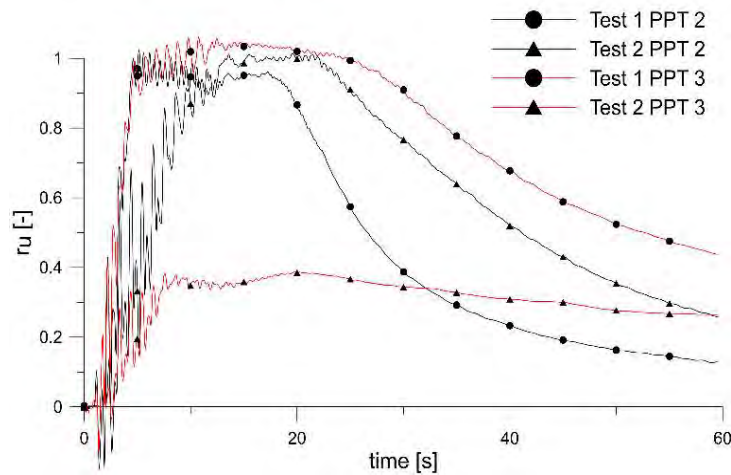


Figure 417: Pore pressure ratio calculated for the tests 1 and 2

The results clearly show how the distribution of excess pore pressure induced by shaking is affected by the presence of the tunnel and of the building.

Effect of laponite-sand mixture as a mitigation technique

The effect of the laponite was investigated in terms of accelerations, pore pressure build-up and displacements. In Figure 418 the pore pressures recorded in the model 3 (with laponite below the tunnel) are shown. It is evident the effect of the laponite in reduction of the pore pressures (green and blue line).

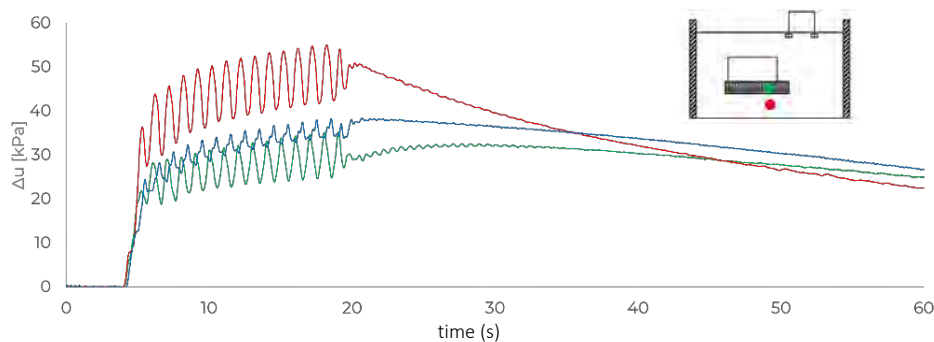


Figure 418: Pore pressure calculated for the test 3

Figure 419 shows some results in terms of displacements obtained for the input signal 3 for all the models. The PIV results showed that the third input signal induced liquefaction of the soil, causing settlements of the structure and uplift of the tunnel. The results indicate that some beneficial effects on the vertical displacements of the building are produced by the creation of two “barriers” of sand mixed to laponite at the sides of the tunnel.

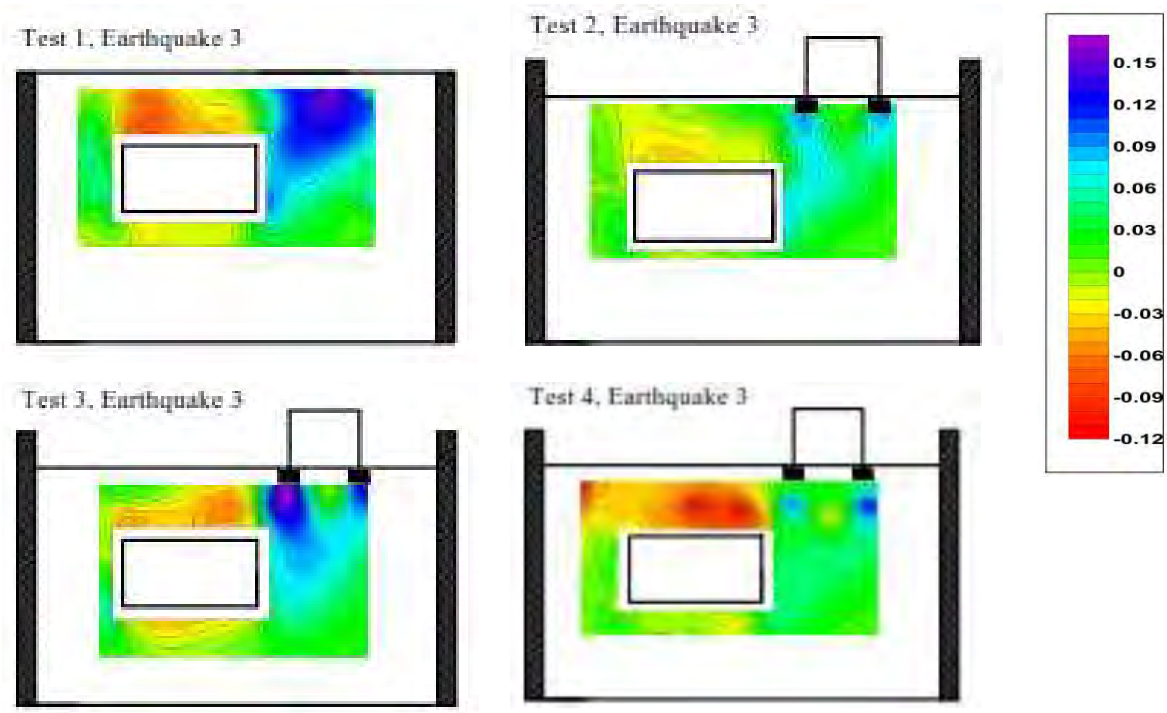


Figure 419: Vertical displacements fields at the end of shaking (EQ3).

8.2.4 Conclusions

The final results of the tests are still being analysed and compared to other analytical and numerical solutions, but some initial conclusions can be made from the preliminary analyses completed to date.

The behaviour of buildings next to tunnels cannot merely be considered as a direct superposition of the tunnel and building in free-field conditions, as the stress fields caused by each affect the behaviour of the other. It has been shown that the concentrated stresses existing beneath the foundations of the building reduce the liquefaction potential of the soil in this region. This can counter-intuitively result in structural settlements being less than the free-field settlement that might be predicted in this region due to tunnel uplift. The reduction in liquefaction potential of this heavily loaded soil may also restrict tunnel flotation movements close to existing structures.

Laponite has also been shown to have interesting effects on reducing the flotation of tunnels, acting as a non-liquefiable material in critical regions close to the tunnel. The optimisation of its placement to reduce tunnel flotation is still an active area of research.

8.3 Project #24 – Seismic Behaviour of Rigid Pile Inclusions

Authors

B. Teymür⁽¹⁾, U. Çilingir⁽²⁾, B.B. Ayraçma⁽¹⁾, E. Bayram⁽¹⁾, S. Öztoprak⁽³⁾, Z.A. Arama⁽³⁾, S.K. Haigh⁽⁴⁾

⁽¹⁾ *Istanbul Technical University, Istanbul, Turkey*

⁽²⁾ *Arup, London, UK*

⁽³⁾ *Istanbul University, Istanbul, Turkey*

⁽⁴⁾ *Cambridge University, U.K.*

8.3.1 Introduction

Vertical rigid pile inclusions are frequently used as supports for the foundations built on soft soils. They act as load transferring elements onto more resistant and less compressible soils. Although the rigid pile inclusions are envisaged as a form of ground improvement method in current design practice, their performance in transferring loads on the structure under dynamic conditions are not well studied. Some of the recent examples, where rigid pile inclusions not connected to the structure are used as foundation support, include the New Mexico City Airport (NAICM), Rion – Antirion and Izmit Bay Bridges.

There is increasing interest in assessing whether such foundation systems offer an advantage in terms of seismic demand on the structures over traditional pile foundations where the piles are connected to the structure through a raft or pile cap. Moreover, the performance criteria set out for such foundation systems may also require some measure of pile structural assessment. Apart from detailed numerical Dynamic Soil-Structure Interaction (DSSI) models, there is no widely-accepted method for the assessment of this type of foundation systems. In this context, centrifuge testing can provide useful insight in terms of the underlying physical mechanisms for the load transfer.

The main objective of this research is to study the seismic behaviour of rigid pile inclusion systems. The focus of the study will be the dynamic soil-structure interaction mechanisms involved in these systems. Three small-scale dynamic centrifuge experiments using the beam centrifuge at the University of Cambridge are proposed that will supply information about the inertial and kinematic interaction between the rigid pile inclusions and the structure. Numerical models calibrated based on the experimental results will also complement the study. The study will be used as a basis for further study through the dissemination of the research outcome.

8.3.2 Test specimen

In order to investigate the behaviour of groups of disconnected piles and to compare them to the behaviour of a conventional pile group, a centrifuge model was constructed consisting of a group of 37 aluminium piles each with a prototype diameter of 0.6 m at 1.3 m spacings supporting a 9m diameter circular foundation.

The soil consisted of a soft normally consolidated kaolin clay layer prepared at 1g using downward hydraulic gradient consolidation. This involves subjecting the base of the model to negative pore-pressure by attaching a vacuum pump via a catch-tank. Applying a negative pore-pressure at the base

while the total stress remains low results in a high effective stress and hence consolidation of the soil. The kaolin clay was initially mixed at twice the liquid limit, giving a water content of 125% before being consolidated to give a final clay layer with a height of 270mm overlying a sand drain, as shown in Figure 420.

The pile cap was connected to the piles and installed as a single unit with the piles bearing on the lower sand layer using a hydraulic press to provide the necessary vertical force whilst keeping the group vertical. Gantries were installed on top of the model carrying LVDTs in order to measure the vertical settlement and rotation of the pile cap and an air hammer was placed on the clay surface in order to measure the shear wave velocity in the clay through wave arrival times. A T-bar penetrometer was also used to measure the soil strength profile. The fully assembled package is shown in Figure 421.

In the first test carried out on the model the pile cap bore directly onto the clay and was connected to the piles. After loading onto the centrifuge, the model was then subjected 60 g centrifugal acceleration and allowed to reconsolidate for 60 minutes to dissipate any excess pore pressures that were generated during the loading process. The model was then subjected to 6 earthquakes of increasing amplitude, imposed using the servo-hydraulic earthquake shaker.

The piles were connected to the pile cap via a stud passing through a sleeve which formed the upper 0.6 m of the pile length. This arrangement allowed the uppermost section of the pile to be removed between centrifuge flights allowing two separate models to be tested with the same soil bed. In the second flight on each model the pile cap was removed along with the upper sleeved section of the piles and a recess was excavated in the clay surface as shown in Figure 420. This recess was filled with coarse sand to form a gravel mat filling the 0.6 m gap between the top of the piles and the base of the pile cap. The test was then repeated in this new configuration.

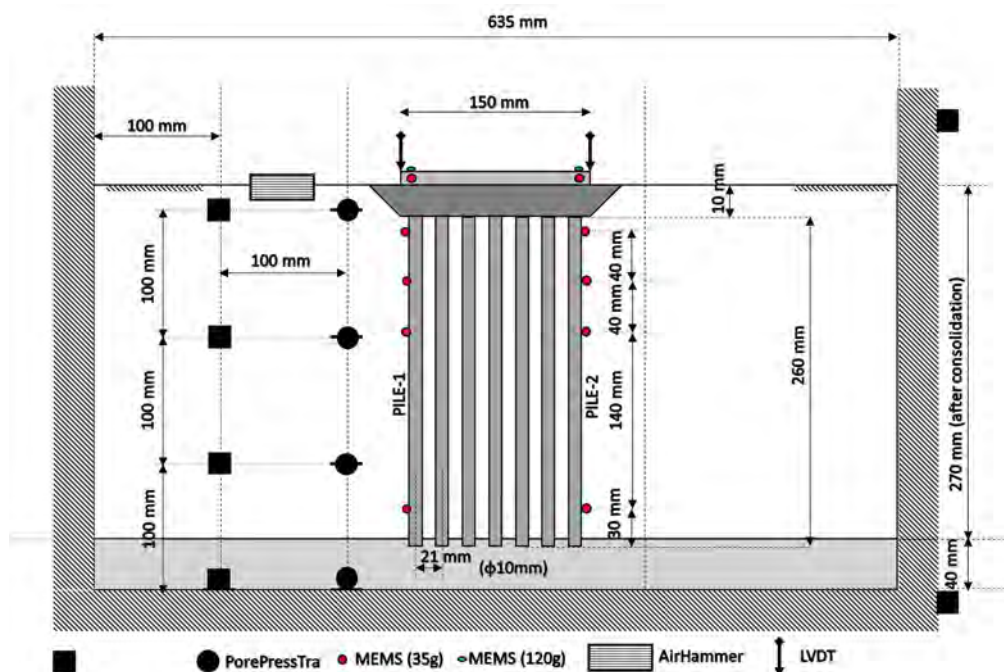


Figure 420: Cross section of the centrifuge model

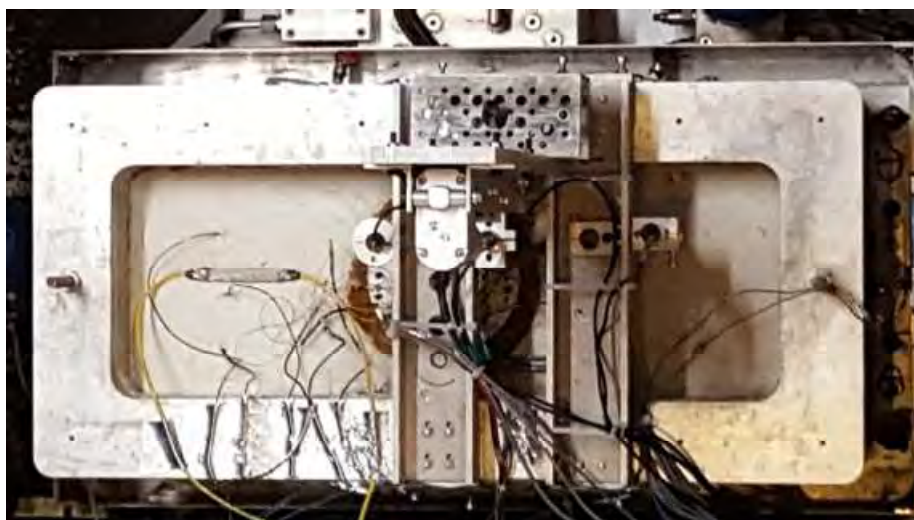


Figure 421: Centrifuge model plan view

8.3.3 Test setup

The model was contained within an equivalent shear beam model container to minimise reflection of stress waves from the lateral boundaries during model earthquakes. The design of these containers is discussed in detail by Teymur & Madabhushi (2003). The container was initially designed to be compatible with the stiffness of a sand layer and so will be stiffer than the soft clay layer used in this model. Some stress wave reflection will hence occur from the model boundaries, but this should not be significant for the model tested here.

The soil model was instrumented with piezoelectric accelerometers and miniature pore-pressure transducers as shown in Figure 420. MEMS accelerometers were attached to the pile cap to enable monitoring of the pile cap motion in 3D together with LVDTs measuring the average settlement and rotation of the pile cap. These LVDTs were mounted on overhead gantries spanning the model container as shown in Figure 421.

The model was subjected to a sequence of 6 earthquakes in each flight; three sinusoidal motions of increasing amplitude, a sine-sweep to identify system natural frequencies and two real earthquake records from Kobe, Japan (1995) and Imperial Valley, USA (1979). The properties of these earthquakes are summarised in Table 60.

Earthquake No	Description	PGA		
		Test 1	Test 2	Test 3
EQ_1	60 Hz, 10 cycles-0.8V	0.03g	0.08g	0.075g
EQ_2	60 Hz, 10 cycles-1.2V	0.12g	0.13g	0.12g
EQ_3	0-60 Hz Sine sweep-1V	0.05g	0.06g	0.05g
EQ_4	Kobe Earthquake-0.35V	0.24g	0.23g	0.20g
EQ_5	Imperial Valley Eq.-4V	0.11g	0.11g	0.12g
EQ_6	60 Hz, 10 cycles-3V	0.33g	0.33g	0.38g

Table 62: Input motions used in experiments

8.3.4 Results

The seismic behavior of disconnected pile foundation systems was investigated, a topic on which little previous work exists. To shed light upon such a foundation system's dynamic behavior the horizontal displacements, settlements and accelerations of the foundation plate were recorded and analyzed under various seismic loads. A set of 6 ground motions (PGA 0.03 ~ 0.33g) were used in centrifuge tests at 60g as detailed in Table 62. Response spectrums plotted for the top of the foundation plate for both connected and disconnected support systems are shown in Figure 422. It can be seen that for the sinusoidal earthquakes (EQ1, EQ2, EQ6) the peak spectral acceleration values at a the fundamental 1 second period are very similar between connected and disconnected scenarios, however the third harmonic at a period of 0.3s is substantially reduced for the large EQ6 when the piles are disconnected. This is to be expected as slip in the gravel mat will allow peak accelerations to be attenuated once the frictional resistance of the soil is overcome. Truncating the acceleration records will remove the spikes associated with the third harmonics from the peaks of the recorded acceleration trace, resulting in a more sinusoidal motion.

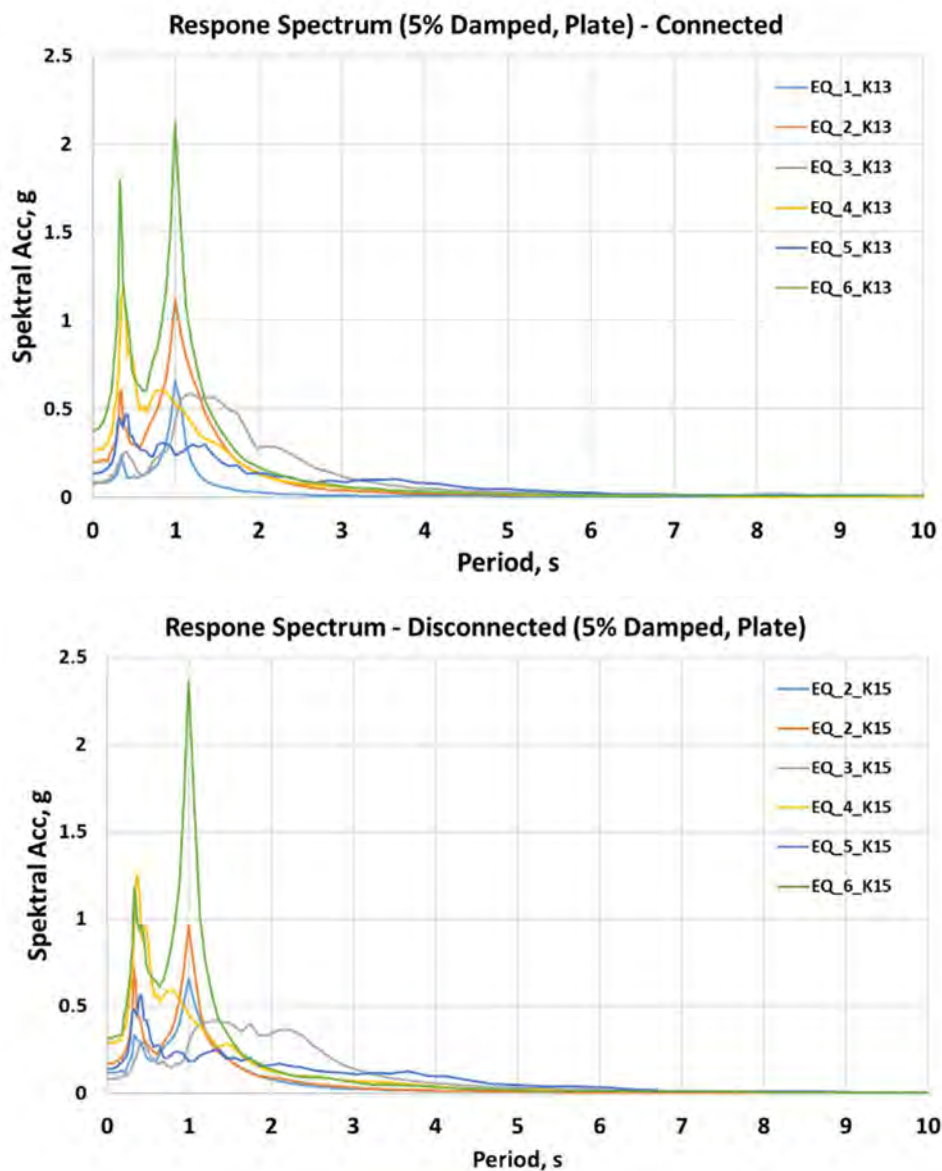
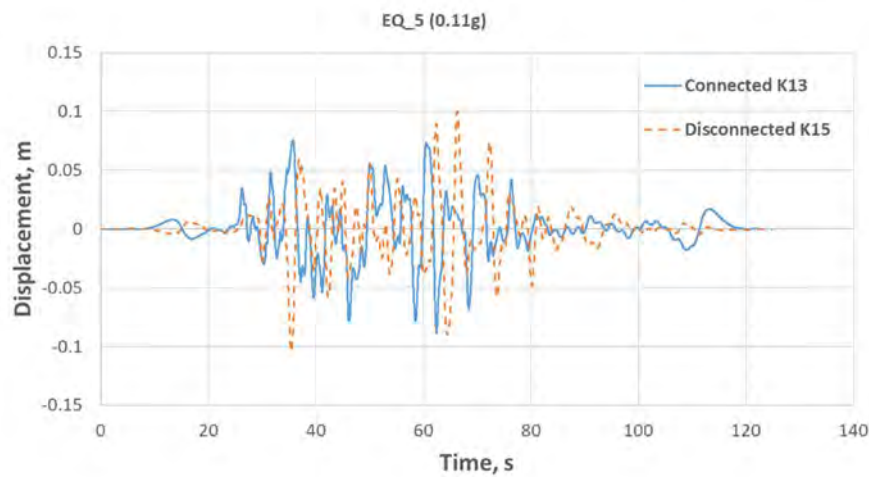
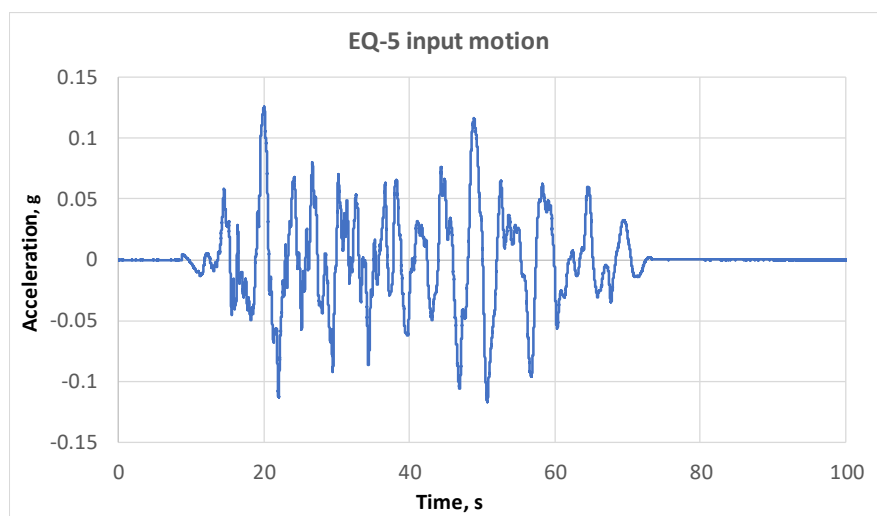


Figure 422: Response spectrum on top of the foundation plate: (a) Connected. (b) Disconnected

The slip within the gravel mat associated with truncation of the acceleration traces could plausibly give an excessive horizontal displacement of the foundation system. Figure 423 shows the horizontal displacements of pile cap under the action of the 0.1g Imperial Valley earthquake which could be considered the design basis earthquake. It can be seen that while the displacements in the connected and disconnected cases differ, with the disconnected case having much higher frequency behavior, the residual displacements measured are close to zero and the dynamic peak displacements are both small and comparable between the two cases.



a)



b)

Figure 423: a) Lateral displacements of the plate during EQ_5 and b) input motion

Analyses of the settlement of the foundation yields different results, as shown in Figure 424. As expected, the system supported with structurally connected piles suffers from low vertical settlements, the piles being founded on the strong sand layer underlying the soft clay. The disconnected foundation plate that sits on top of a 0.6 m dense gravel cushion layer undergoes unrecoverable, permanent vertical deformations about 3 ~ 12cm, whereas this value is relatively small or negligible for the more traditional foundation design. While the gravel cushion is relatively stiff, the deformations of the surrounding soft clay substantially reduce the vertical foundation stiffness. For most of the

earthquakes, the settlement values of the disconnected system are still small, especially in comparison to a shallow type foundation on the soft clay soil, and take place within the allowable range.

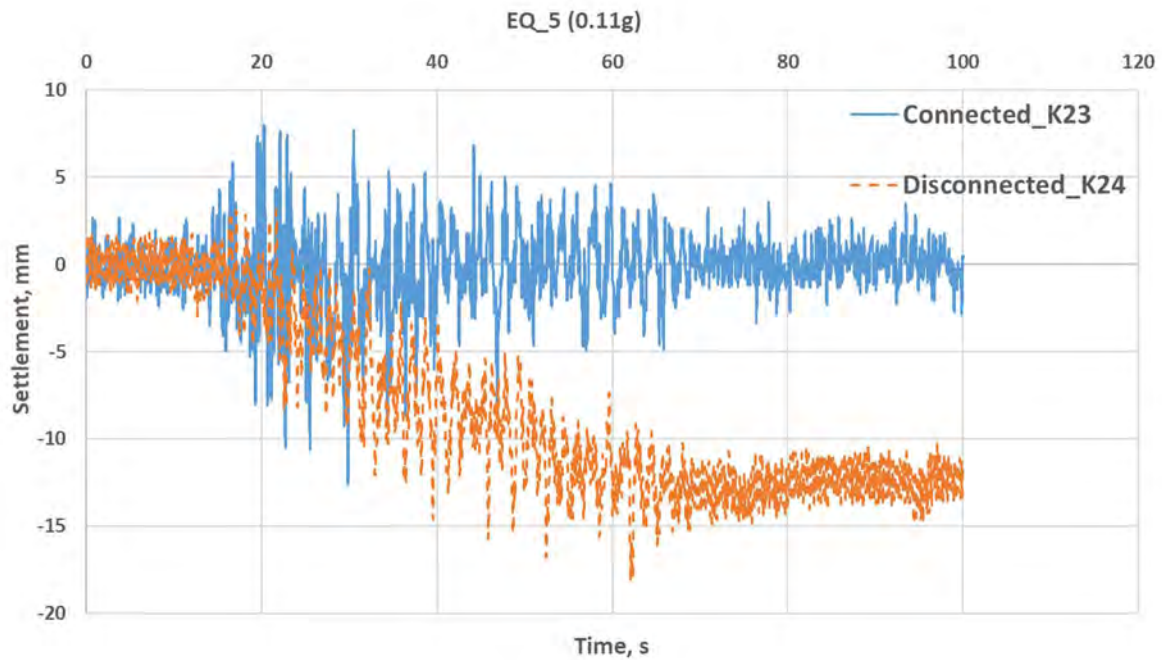


Figure 424: Settlements of the plate during EQ_5

Another effect of having irrecoverable settlements is rocking of the foundation plate over the load transfer platform (cushion layer.) A distinct rocking motion is seen in the disconnected system as shown in Figure 425. Up to 0.0035 radians of rotation are observed during the inflicted earthquake motions. However, recent studies suggest that allowing a certain rocking mode to a degree could be helpful to reduce internal stresses developed within the foundation plate and subsequent structural elements. However, considering such a design should be thoroughly investigated as excessive rocking undoubtedly could pose damage to structures. The overall results of the study suggest that geotechnical engineering could benefit from the use of disconnected rigid inclusions in foundation systems. While no considerable lateral displacements in the plate are seen against the strong ground motions used, settlements –differential and total– should be broadly investigated as they seem to be the governing concern between the two different foundation design.

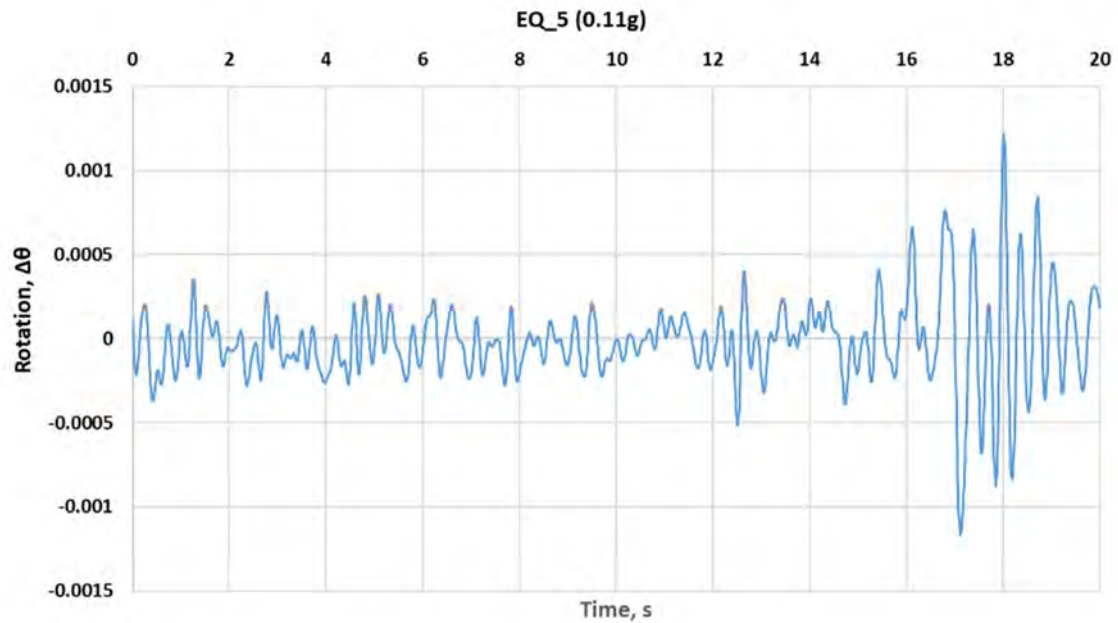


Figure 425: Rotation of the disconnected plate during EQ_5: (a) Unitless, $\Delta h/L$

8.3.5 Conclusions

The centrifuge tests have demonstrated that disconnected pile foundations have adequate performance in limiting the settlement and rotation of structures in both small and large earthquakes for foundations in soft clay. The tests have further revealed that disconnected foundations may have advantages in very large earthquakes as the introduction of a deformable element between the stiff piles and the superstructure can concentrate deformations in an area not susceptible to damage and limit the transfer of peak accelerations to the superstructure through both rocking and sliding deformations. Further ongoing analysis of this behaviour will allow geometries to be optimised and the effect of these deformations on structures to be assessed.

References

Teymur, B. & Madabhushi, S.P.G. (2003) Experimental study of boundary effects in dynamic centrifuge modelling. *Géotechnique* **53**(7):655-663.

8.4 Project #25 – COSMO: Change Of Seismic MOtion due to pile-soil kinematic interaction

Authors

L. De Danctis⁽¹⁾, R. Cairo⁽²⁾, E. Conte⁽²⁾, R. Di Laora⁽³⁾, L. Di Sarno⁽⁴⁾, M. Iovino⁽¹⁾, E. Rovithis⁽⁵⁾, S.K. Haigh⁽⁶⁾, T. Garala⁽⁶⁾

⁽¹⁾ *University of Napoli Parthenope, Italy*

⁽²⁾ *University of Calabria, Italy*

⁽³⁾ *University of Campania Vanvitelli, Italy*

⁽⁴⁾ *University of Liverpool, UK*

⁽⁵⁾ *Earthquake Planning and Protection Organization EPPO-Research Unit ITSAK, Greece*

⁽⁶⁾ *Cambridge University, U.K.*

8.4.1 Introduction

Seismic analysis of structures supported on piles is conventionally performed by considering the free-field motion as the base excitation. In this regard, possible piles-induced modification of the seismic motion due to the interplay between soil and piles, which is referred to as ‘kinematic soil-pile interaction’, is neglected. However, piles, depending on their stiffness, are not always able to follow motions with short wavelengths induced by the surrounding soil. As a result, piles may filter the high-frequency components of the free-field motion and, thus, modify the input motion of a pile-supported structure. The above physical phenomenon which is referred to as ‘filtering effect’ may be particularly relevant for soft soils, where piles represent the most common design option. Experimental evidence on this filtering action of piles is still limited to some instrumented pile-supported buildings in Japan. These experimental data clearly indicate that piles filter out the high frequency component of the free-field motion. However, the above acceleration recordings at the foundation of these buildings include inherently the effect of the superstructure oscillation. Thus, there is a lack of experimental evidence on the alteration of seismic motion that can be attributed exclusively to piles.

COSMO research project aims to advance the present state-of-the-art on the above critical issue of piles-induced filtering effect. For this reason, a series of centrifuge tests are proposed on models of aluminium piles embedded in soft soils. The proposed model tests include both single piles and groups of three piles rigidly connected by a cap under harmonic excitations. The influence of diameter, soil-cap contact and cap-embedment on the alteration of seismic motion will be also investigated.

Objectives

The main objective of this experimental program is to provide well-documented experimental evidence on the critical issue of the change of seismic motion induced by pile-soil kinematic interaction. Moreover, the testing campaign within COSMO project will be complementary to a relevant series of centrifuge test already performed at the Schofield Centre of the University of Cambridge on models of aluminium piles rigidly connected by a cap (clear to the soil) and embedded in kaolin with variable pile spacing (under Reluis 2017 research project granted by the Italian Emergency Management Agency). The additional tests planned within COSMO project will investigate for the first time a set of critical

parameters that are involved in the kinematic response of a piled foundation such as the cap-soil contact and the cap embedment. The proposed model tests will be also examined numerically by the use of a hysteretic non-linear model based on Ramberg-Osgood formulation, so as to reproduce in a realistic manner the degradation of the shear stiffness of soil, the increase of soil damping ratio generated by the passage of seismic waves and the occurrence of earthquake induced excess pore pressures. The experimental evidence supplied by the above projects will serve as a benchmark to assess the validity of the simplified methods of analysis aimed at the evaluation of the base excitation for pile-supported structures. The experimental assessment of the transfer functions for both pile groups and the isolated piles, will have a remarkable scientific, technical and economic impact. First, the results of this testing campaign will have a direct positive impact on the understanding of the physical problem under examination. Second, the experimental evidence supplied by this work will enhance the ability to predict the seismic input motion of pile-supported structures, thus allowing for a more rational allocation of resources in seismic risk mitigation strategies. Third, the investigation of the basic aspects of the mechanism governing the change of seismic motion by pile-soil kinematic interaction will provide guidance for the selection of physical model of pile groups to be tested in the future.

The originality and innovation of the proposed project lie within the following research advancements:

Development of a new well-documented database of recordings for piles filtering effect

As outlined before, the available experimental evidence on the filtering effect exerted by piles is limited to published works that go back to the early 70s (Kawamura et al. 1977) and 80s (Otha et al. 1980, Gazetas 1984). The experimental data that will be acquired from the COSMO project will advance the database which is already available from project ReLUIS 2017, to provide a well-documented database on the alteration of seismic motion due to pile-soil kinematic interaction.

Validation of theoretical/numerical models and analysis tools: The Users Team of COSMO proposal has established a strong theoretical background on the issue of the filtering action of piles by means of pertinent analysis methods, as reflected in several publications of the research group. Part of the above research has resulted in simple analytical expressions of pile-to-soil kinematic response ratios in the frequency domain. The above analytical expressions were obtained under the assumption of raft clear to the soil. Within COSMO project, predictions of the above models will be compared with the centrifuge tests results in order to check the applicability of the published formulae under circumstances where the raft is in contact with the soil or embedded and, eventually, develop ad hoc design oriented formulae for quantifying the filtering effect in the presence of a piled raft.

Contribution towards seismic design practice of piles.

Di Laora & de Sanctis (2013) observed that, in case of large diameter pile in soft soils, the filtering action may result in a reduction of the seismic demand up to 50% - 70% (for low-period structures). The reduction of spectral accelerations between pile-head and free-field may be even higher when piles are embedded in inhomogeneous soil (Rovithis et al. 2015, 2017). The above considerations will be validated accordingly by means of the experimental dataset produced by the COSMO project and may have a direct impact in future revisions of seismic codes with reference to the design of structures on piles. Under this perspective, piles in the future may be also viewed as 'seismic demand reducers' in the design of a structure.

In view of the fact that European researchers, practitioners and companies will be the beneficiaries of the outcome of this research, the following benefits are expected:

- Improvement of the accuracy of existing methods for seismic vulnerability assessment of buildings and infrastructures;
- Improvement of public safety, as current design practice will surely benefit from the results obtained;
- Improvement of European competitiveness, as the experimental evidence supplied by this research can be used by European companies and exported abroad to support innovative solutions for seismic risk mitigation strategies.

8.4.2 Test specimens

In the first centrifuge experiment, PSKI-A, we examined the response of models of aluminium single piles and pile groups embedded in soft kaolin clay and excited by both sinusoidal excitations and earthquakes. The centrifuge experiment was performed at 50-g in the Equivalent Shear Beam (ESB) container (Brennan & Madabhushi, 2002) and included two flights. In the first flight (F1), the pile cap was made of Perspex, so as to minimize the effect of inertial interaction (in any case, the overall response of both the pile groups and the isolated piles unavoidably include the small inertial effect due to Perspex cap which is needed to install the measurement devices). In the second flight (F2), we added an elevated aluminium cap to each foundation model, in order to investigate essentially the response to inertial actions. For a given diameter, the influence of the cap-embedment on the alteration of seismic motion was investigated.

In the second centrifuge experiment, PSKI-B, we examined the response of models of aluminium single piles and pile groups embedded in soft kaolin clay and both excited by earthquakes. The centrifuge experiment was performed at 50-g in the Equivalent Shear Beam (ESB) container (Brennan & Madabhushi, 2002) and included two flights. In the first flight (F1), the pile cap was made of Perspex and therefore considered as negligible, so as to minimize the effect of inertial interaction; in any case, the overall response of both the pile groups and the isolated piles unavoidably include the small inertial effect due to Perspex cap which is needed to install the measurement devices. In the second flight (F2), we added an elevated aluminium cap to each foundation model, in order to investigate essentially the response to inertial actions. For soil-cap contact, the influence of pile diameter on the alteration of seismic motion was investigated.

MODEL CONTAINER

The model was prepared inside an Equivalent Shear Box (ESB) (Schofield and Zeng 1992), in order to simulate field conditions accurately. It is a 645×230×400 mm rectangular box having alternate layers of rubber and aluminium rings (of width 75 mm), in order to reproduce the K_0 conditions (zero lateral strains) and to match the shear deformation of the soil layer for a given earthquake in a step-wise fashion.

MODEL PILE FOUNDATION AND SUPERSTRUCTURE

TEST PSKI-A

Aluminium tubular model piles of lengths $L_1 = 200$ mm and $L_2 = 190$ mm, $d = 15$ mm in diameter and thickness $t = 1$ mm were used to simulate the behaviour of single piles and pile groups at prototype scale. The flexural stiffness of the prototype piles is equivalent to a 0.75 m diameter and high-strength concrete piles. The pile lengths of 10 and 9 meters at the prototype scale are large enough to consider the pile as 'long' from a mechanical viewpoint and therefore its response to dynamic loading represents also the response of any other longer pile. Pile spacing is constant and equal to $s = 64$ mm. All single and grouped piles were covered by hollow Perspex caps of different heights, $D_1 = 20$ mm (mass = 90 g)

and $D_2 = 40$ mm (mass = 170 g), representing two different foundation embedments. Figure 426 shows single and grouped piles along with their pile caps used in the first flight (dimensions are in model scale).

Single degree of freedom systems were made by the mean of steel structures with a fundamental period of 0.2 s. This value was confirmed by tests on these (fixed base) structures subjected to an impulse, by measuring the acceleration through MEMS. Figure 427 shows single and grouped piles along with their pile caps and superstructures used in the second flight.

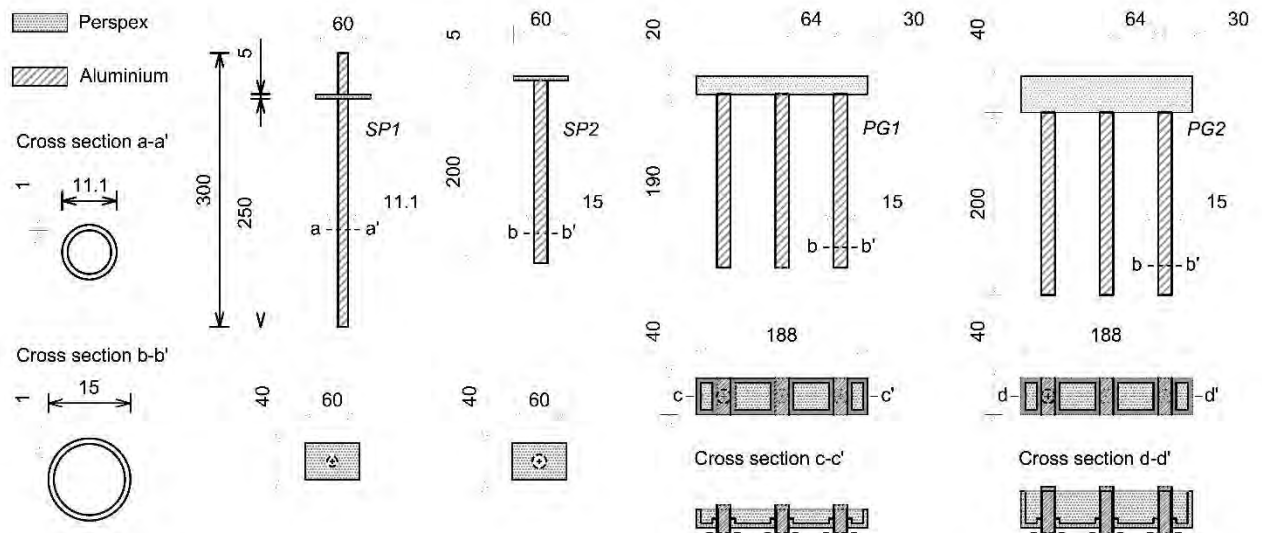


Figure 426: Model pile foundations used for the experiment PSKI-A in flight 1 (dimensions at model scale)

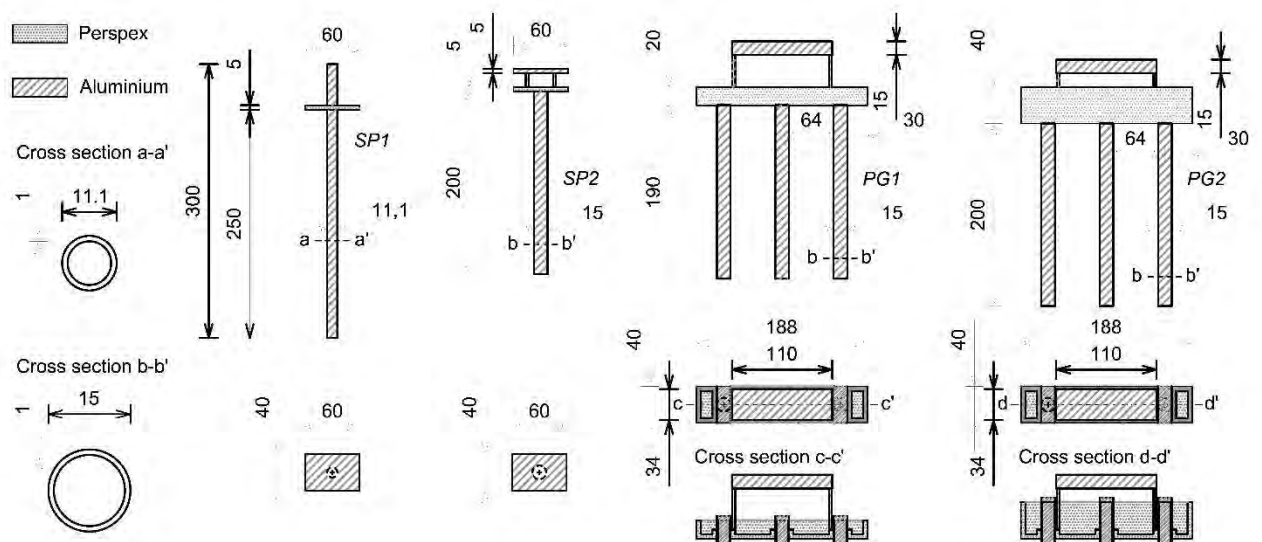


Figure 427: Model superstructures used for the experiment PSKI-A in flight 2 (dimensions at model scale)

PSKI-B

Aluminium tubular model piles of lengths $L_1 = 240$ mm and $L_2 = 200$ mm, $d_1 = 24$ mm and $d_2 = 15$ mm in diameter and thickness $t_1 = 1.6$ mm and $t_2 = 1$ mm were used to simulate the behaviour of single piles

and pile groups at prototype scale. The flexural stiffness of the prototype piles is equivalent to a 1.2 m diameter and a 0.75 m diameter and high-strength concrete piles, respectively. The pile lengths of 12 and 10 meters at the prototype scale are large enough to consider the piles as 'long' from a mechanical viewpoint and therefore its response to dynamic loading represents also the response of any other longer pile. Pile spacing is constant and equal to $s = 64$ mm. The grouped piles were covered by hollow Perspex caps of height $D = 20$ mm (mass = 90 g). Figure 426 shows single and grouped piles along with their pile caps used in the first flight (dimensions are in model scale).

Single degree of freedom systems were made by the mean of steel structures with a fundamental period of 0.2 s. This value was confirmed by tests on these (fixed base) structures subjected to an impulse, by measuring the acceleration through MEMS. Figure 428 and Figure 429 show single and grouped piles along with their pile caps and superstructures used in the second flight.

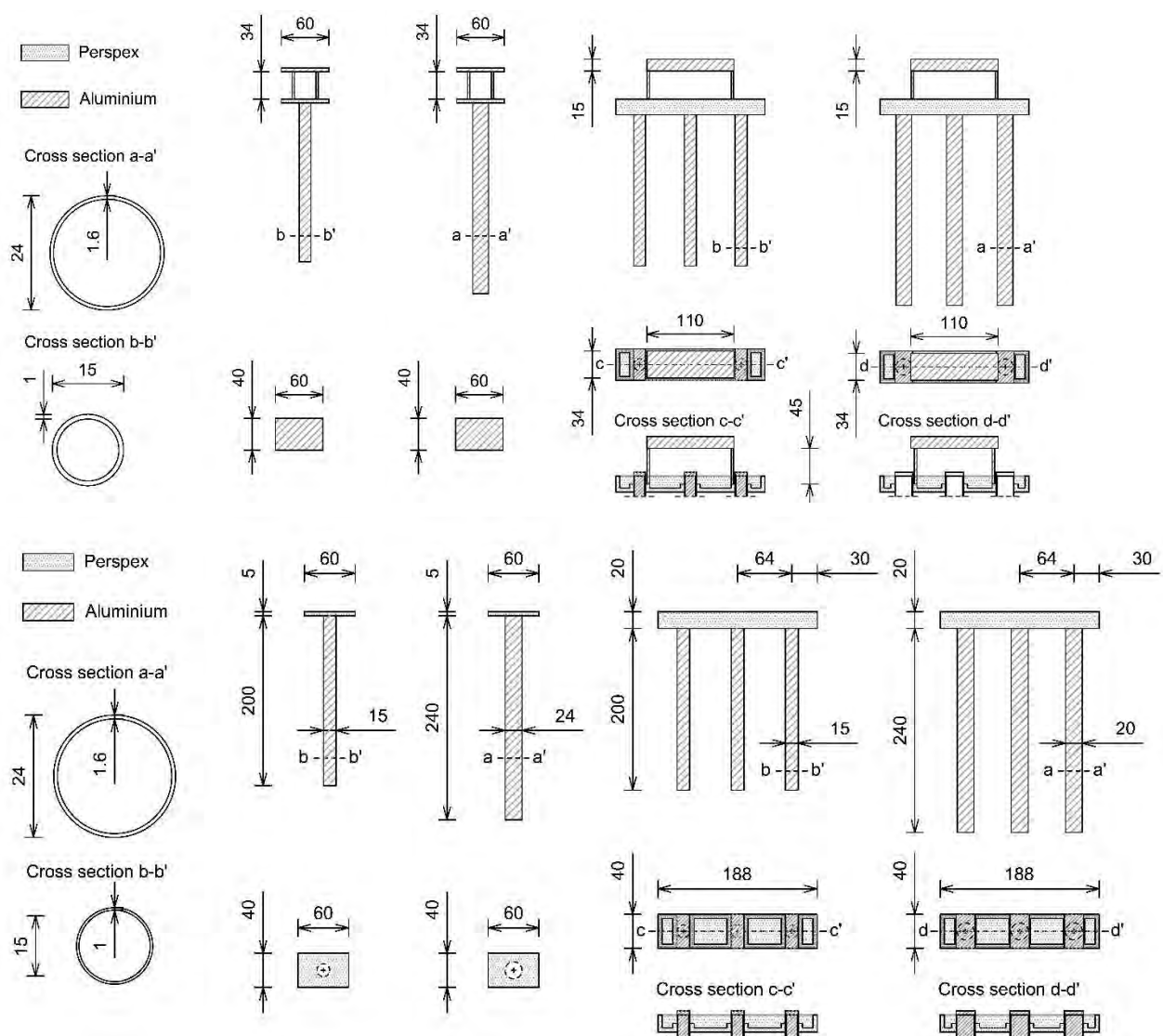


Figure 428: Model pile foundations used for the experiment PSKI-A in flight 1 (dimensions at model scale)

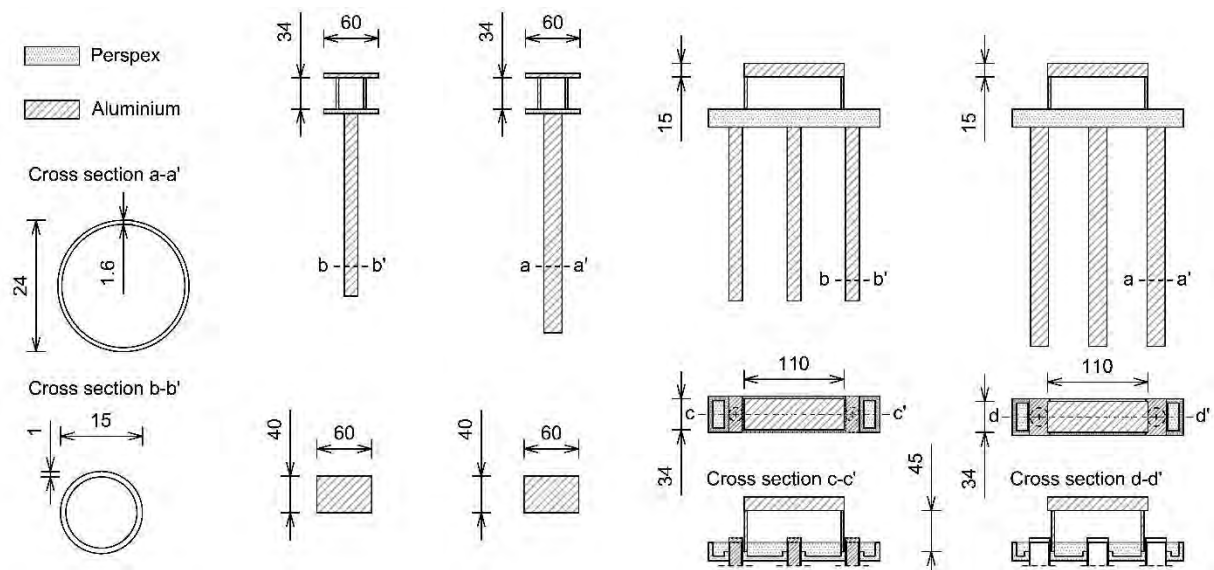


Figure 429: Model superstructures used for the experiment PSKI-A in flight 2 (dimensions at model scale)

CLAY

Laboratory grade speswhite kaolin, whose mechanical behaviour has been extensively studied (Take 2003, Lam 2010 and Lau 2015) was used in the tests. This artificial clay has been widely used in many experimental campaigns in Cambridge (Lau 2015), helping to keep the clay mineralogy constant between the tests and thus eases the repeatability of tests.

INSTRUMENTS

In order to capture the response of consolidated clay and pile foundations during the test, different types of instruments were used in the test PSKI-A [PSKI-B], as listed below:

- 11 Piezo-electric Accelerometers (PA): to record the seismic accelerations developed in the clay.
- Before installing PA in clay sample, their surfaces were sealed with wax to avoid direct contact with water.
- 20 [24] Micro-Electro-Mechanical System accelerometers (MEMS): to measure both horizontal and vertical accelerations of pile foundations.
- 4 Pore Pressure Transducers (PPT): to measure the pore pressure within the soil model.
- This is done by applying known water pressures and measuring the voltage output from the PPT.
- 6 [1] Linearly Variable Differential Transformer (LVDT): to monitor the settlement of clay, single piles and pile groups at different phases of testing.
- Calibration factors were determined before and after the tests

T-BAR PENETROMETER

The strength of the consolidated clay was determined using a T-bar test (Lau 2015). It measures the resistance to penetration of a cylinder attached perpendicularly to the shaft, as it advances through the soft clay layer at constant speed. The T-bar used in the test is of 8 mm diameter and 40 mm length rod. A driving actuator of stroke length 100 mm was used to push the T-bar in to the clay and the depth of penetration was measured using the LVDT fixed next to the actuator, while the resistance offered by the soil was measured by a load cell at the end of the bar. Assuming that the soil flows around the cylinder without forming a gap, the penetration resistance, q , was converted into the undrained soil

shear strength, c_u , using a T-bar bearing factor, $NT = q/c_u$. According to Randolph and Houlsby (1984), Stewart and Randolph (1991) and Martin and Randolph (2006) analytical value of NT is dependent on the surface roughness of the cylinder and its value lies in the range of 9.14 (for lower values of adhesion factor or smooth bar) and 11.94 (for higher values of adhesion factor or fully rough bar). An average value of 10.5 was used in this study.

AIR HAMMER DEVICE

The stiffness of clay was evaluated using a miniature Air Hammer Device (Ghosh and Madabhushi 2002). It consists in a small brass tube containing a metal pellet within it, that is made to accelerate by applying high-pressure air on alternative ends. Its striking the end of the tube induces a share wave at the base of the model which propagate upward towards the soil surface. Accelerometers placed at different but known locations record the arrival times, hence shear wave velocity, V_s between adjacent accelerometers can be computed ($V_s = \Delta z / \Delta t$, where Δz is the distance between the instruments and Δt is the lime lag between the signals), as well as the small strain shear modulus G_0 ($= \rho_s V_s^2$, where ρ_s is the density of the soil).

8.4.3 Test setup

The speswhite kaolin clay powder was first mixed with de-aired water in 1:1.25 ratio under vacuum for two-three hours using the clay-mixer available in Schofield Centre. The bottom of ESB box was then covered with a thin layer of filter material and its inner surface was coated with silicone grease to minimize friction against the clay. In order to fix the location of instrument inside the box, five horizontal aluminium wires were settled in it.

The prepared clay slurry was then transferred into the ESB box to the required depth. The top surface of clay was covered with a filter material and top loading plate was placed over it. The clay slurry was allowed to consolidate on its self-weight for 24 hours. To obtain a soft clay profile with a given strength at the surface and then increasing strength with depth, a combination of consolidation under vertical stress and hydraulic consolidation by suction-induced seepage (HCSS) were used to consolidate the clay slurry. The working principle of the procedure along with a discussion on its validity is reported in Robinson et al. (2003). The ESB box with clay slurry was placed under a computer-controlled hydraulic press (Fig. 3.2) to consolidate under a vertical stress of 8 kPa [10 kPa]. Once the clay consolidated for the applied vertical stress, the sample was subjected to suction induced seepage consolidation by applying a suction pressure of -80 kPa [-90 kPa] at the bottom of ESB box in increments of -10 kPa. A vertical stress of 5 kPa [10 kPa] on top of clay was added and constantly maintained even during this suction induced seepage consolidation. Once the clay was consolidated, sample was unloaded and taken out from the consolidation chamber. Then, the clay top was slightly trimmed to obtain levelled surface. Piles were installed by gentle push into the clay sample, with intermittent stops to check for the verticality of the piles. The depth, H , and density, ρ_s , of the clay after consolidation and trimming for the levelled surface were 290 mm [270 mm] and 1623 kg/m³, respectively.

MEMS accelerometers were directly glued on to the pile caps of both single pile and pile groups.

Figure 430 shows the schematic view of plan and sections of the model and the instrument locations, in which model (and prototype) dimensions are in *mm* (and *m*). This is shown for PSKI-A but is representative of that in all tests. Though the single pile and the pile group positioned on the same vertical plane in the direction of shaking, the clear gap between them minimised any dynamic interaction between the two. Also, the response from piezo accelerometers in the clay model can be

considered as free-field clay response as the accelerometers were located reasonably far from the pile foundations.

The model was then swung up to 50 g by applying increments of 10 g with a closed bottom drain in the centrifuge. It is worthy to mention that the consolidated clay sample would be under suction after unloading from the hydraulic press. When the clay sample is in the centrifuge, these suction pressures reduce due to an increase in the body forces and hence to the occurrence of large effective stresses. No water was allowed to flow into the model after unloading the soil sample from the hydraulic press, even in the centrifuge. This procedure was adopted to obtain a relatively soft clay profile with depth. Once the clay model attained equilibrium, nine earthquakes (Table 63) were fired one after the other using the Servo-hydraulic earthquake actuator. The strength and stiffness of clay are evaluated using T-bar and an Air Hammer Device, respectively. T-bar tests were performed at 1 g before centrifuge, at 50 g and at 1 g after centrifuge. Air Hammer tests were performed at 1g before centrifuge, at 50 g, between each earthquake and the next and at 1 g after centrifuge. The data from all the instruments were monitored using Dasy Lab. The data were logged at 1000 Hz sampling frequency during swing up and swing down, and at 6000 Hz during the earthquakes. Air hammer tests were sampled at a frequency of 20 kHz. After this, the model was swung down and elevated aluminium caps were added to each foundation model, in order to investigate the response to inertial actions in flight 2.

Clay samples were collected at different depths to know the moisture content after the test.

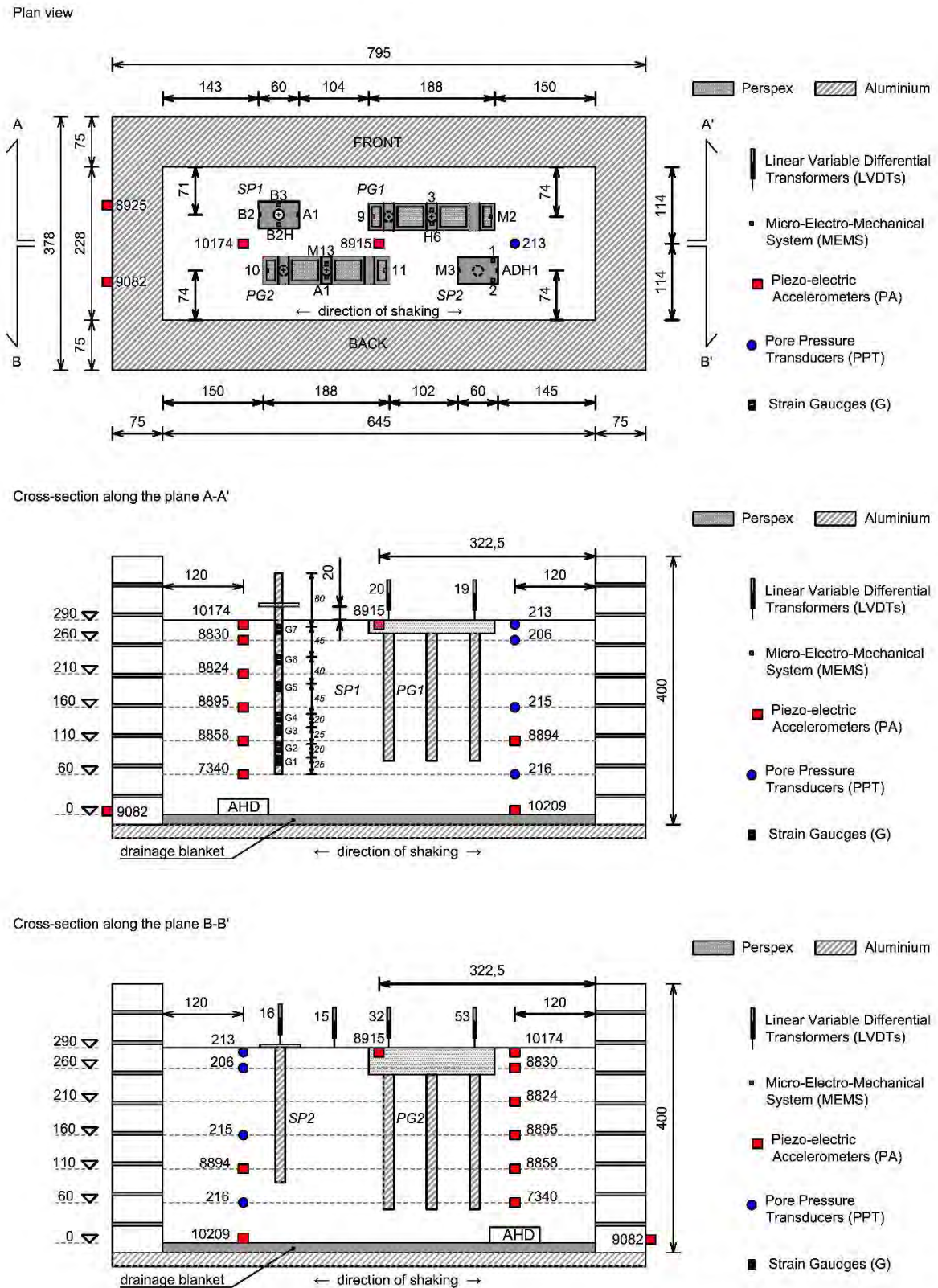


Figure 430: Plan view and cross-sections of the model used for the experiment PSKI-A in flight 1

n.	type	name	frequency [Hz]	cycles	peak base acceleration [g]
1	sinusoidal		30	12	0.07
2	sinusoidal		40	16	0.09
3	sinusoidal		60	24	0.18
4	sinusoidal		50	20	0.24
5	real earthquake	Kobe (mult. 0.25)			0.15
6	real earthquake	Imperial Valley (mult. 4)			0.13
7	sine sweep		30 up to 150		0.08
8	real earthquake	Kobe (mult. 4)			0.42
9	sinusoidal (CF=7g/V)			12	0.08

Table 63: Excitations considered in the study (at prototype scale)

8.4.4 Results

The research work builds up on previous experimental activity on filtering action exerted by piles carried out under research project Reluis 2017, granted by Department for Civil Protection in Italy. A detailed strategy for data analysis and interpretation has been preliminary defined starting from the last test on filtering action exerted by piles carried out under ReLuis project. The test is very similar to PSKI-B, and differ from it in that the raft is not in contact with the soil. As per experiments carried out under the current project, the foundation models consist of an isolated pile and two groups of piles embedded in speswhite kaolin clay, subjected to a centrifugal acceleration of 50 g and shaken by 4 quasi-sinusoidal waves having different amplitude and frequency content. No real earthquakes were applied. Also, in this case, the inertial interaction phase is missing. A sketch of the foundation models examined in the above test is depicted in Figure 431.

Aluminium tubular model piles of length, L , 210 mm, diameter, d , 15 mm and thickness, t , 1 mm were used to fabricate a single pile and two 3×1 row pile group configurations with different pile spacing, s (2.67 d and 5.33 d). The flexural stiffness of the prototype piles is equivalent to a 0.75 m diameter and high-strength concrete piles. The pile lengths of 10.5 m at the prototype scale is large enough to consider the pile as “long” from a mechanical viewpoint and therefore its response to dynamic loading represents also the response of any other longer pile. Figure 431 shows the single pile (SP), the closely spaced pile group (PG1) and widely spaced pile group (PG2) models along with their pile caps used in the study. The dimensions are in model scale and the values within the parenthesis represents the dimensions in prototype scale. Both pile groups carry the same mass per pile from the pile cap, irrespective of pile spacing, and slightly less than the mass carried by the single pile. In terms of force, single pile and pile groups carry a vertical load of 41.5 N and 87.5 N respectively at model scale (103.75 kN and 218.75 kN respectively at prototype scale). The overall response of both the pile groups and the isolated pile unavoidably include the small inertial effect due to these caps, which are needed to install the measurement devices.

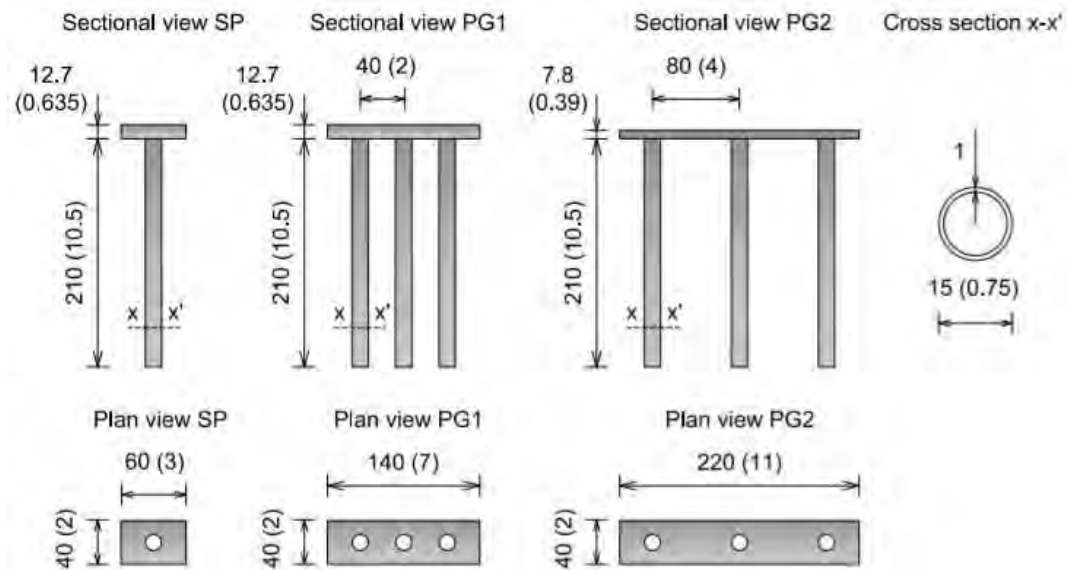


Figure 431: Pile foundations used in the study. Model and prototype dimensions are in mm and m, respectively

In order to capture the response of consolidated clay and pile foundations during the test, different types of instruments were used in the test, as listed below: (a) 12 Piezo-electric Accelerometers (PA), to record the seismic accelerations developed in the clay; (b) 12 Micro-Electro-Mechanical System accelerometers (MEMS), to measure both horizontal and vertical accelerations of pile foundations; (c) 6 Linearly Variable Differential Transformers (LVDTs), to monitor the settlement of clay, single piles and pile groups at different phases of testing; (d) 4 Pore Pressure Transducers (PPTs), to measure the pore pressure within the soil model; (e) T-bar penetrometer, to determine the undrained shear strength of clay along the depth; (f) Air hammer device, to determine soil stiffness.

The model was then swung up to 50 g by applying increments of 10 g with a closed bottom drain in the centrifuge. Once the clay model attained equilibrium, four signals were fired one after the other using the SAM actuator. T-bar tests were performed at 1g before centrifuge and after centrifuge. Air Hammer tests were performed at 1g before centrifuge, at 50g, between each earthquake and the next one and at 1g after centrifuge. The results of the tests are back-analysed for the purpose of the SERA project through a two-step procedure. First, one-dimensional ground response analysis is performed. In these regards, the small shear strain modulus, G_0 , is evaluated using data from air hammer tests, whereas, a literature model (Darendeli 2001) is used to take into account the variation of normalized modulus and material damping with the shear strain. Second, the soil stiffness and damping mobilized under free field are introduced into a finite-element (FE) model to examine the problem of pile-soil interaction. The overall response of both the pile groups and the isolated pile (unfortunately) include the small inertial effect due to caps needed to install the measurement devices. The numerical model developed to back-figure the response of the foundations tested in the centrifuge was also adopted to evaluate the change of seismic motion that the same foundation models would have induced without the cap (purely kinematic interaction). All data shown in the following have been processed for the purposes of the SERA project.

STRENGTH AND STIFFNESS OF MODEL CLAY

To obtain a soft clay profile with an undrained shear strength equal to a pre-defined value at surface and then increasing with depth, a combination of consolidation under vertical stress of 40 kPa at the top and hydraulic consolidation by suction-induced seepage of -50 kPa at the bottom was used. Figure

432 (continuous line) shows the undrained shear strength of clay, s_u , determined from the T-bar tests (Lau 2015) at 1 g, before and after the centrifuge that, however, was found to be unreasonable. The mobilised maximum shear stress (τ) profile during each signal, obtained as the integration of density times acceleration through higher levels, are shown in Figure 432 (symbols). It can be noted that the mobilised shear stresses at lower depths are greater than those obtained by the T-bar test, which proves the higher strength of the soil. Thus, the well-known expression by Ladd et al. (1977) was used, as detailed below.

Skempton (1954, 1957) showed data of s_u/σ'_v , (σ'_v is the vertical effective stress) for a number of soils that were supposed normally consolidated (NC) and deduced the relationship

$$\left(\frac{s_u}{\sigma'_v} \right)_{NC} = 0.11 + 0.37 I_p (\%) \quad (1)$$

which links the ratio s_u/σ'_v with plasticity I_p . The overconsolidation ratio, OCR, was found to have a significant effect on undrained shear strength. Based on critical state theory, Ladd et al. (1977) showed that:

$$\frac{\left(\frac{s_u}{\sigma'_v} \right)_{NC}}{\left(\frac{s_u}{\sigma'_v} \right)_{NC}} = OCR^\Lambda \quad (2)$$

where Λ is an empirical exponent, which may decrease with increasing OCR from 0.85 to 0.75. Schofield and Wroth (1968) and Muir Wood (1990) showed that Λ is given by

$$\Lambda = \frac{\lambda - \kappa}{\lambda} \quad (3)$$

Based on data collected by Mayne (1980) and presented by Muir Wood (1990), Λ varies between 0.2 and 1.0 with a mean value of 0.63 and a standard deviation of 0.18. This range is significantly wider than the interval coming from Eq. (2). Using the properties of the speswhite kaolin (Lau 2015) leads to $\Lambda = 0.8$. Figure 432a shows (at prototype scale) the obtained undrained shear strength profile coming from this last assumption.

The stiffness of the model clay was evaluated using shear wave perturbations generated by the air hammer embedded in the clay sample. The propagation of the shear waves was examined by a vertical array consisting of six piezo-electric accelerometers above the device. The average shear wave velocity in a soil layer can be calculated by measuring the elapsed time for shear wave to travel between two adjacent accelerometers. Peak to peak and cross correlation methods are commonly used to determine wave travel time. The peak to peak method uses the time difference between the first two peak as the travel time, whereas, the cross-correlation method works by performing a pointwise multiplication to determine where two signals are best aligned. The time shift between two correlated signals is obtained at the maximum (or minimum if the signals are negatively correlated) of the cross correlation function. This method avoids complications with picking characteristic points (i.e. first peak) from discrete signals, and was used here to calculate the elapsed time for shear wave to travel between two adjacent accelerometers. Figure 432b shows the maximum shear wave velocity profiles measured at any stage in the test. Note that those recorded after earthquakes are lower than the one measured after the swing up stage at 50 g. This is because the tests were carried out immediately after the end of the signals and, therefore, the induced excess pore pressures had no time to dissipate. Thus, the initial shear wave velocity profile was deduced from the first set of results (swing up).

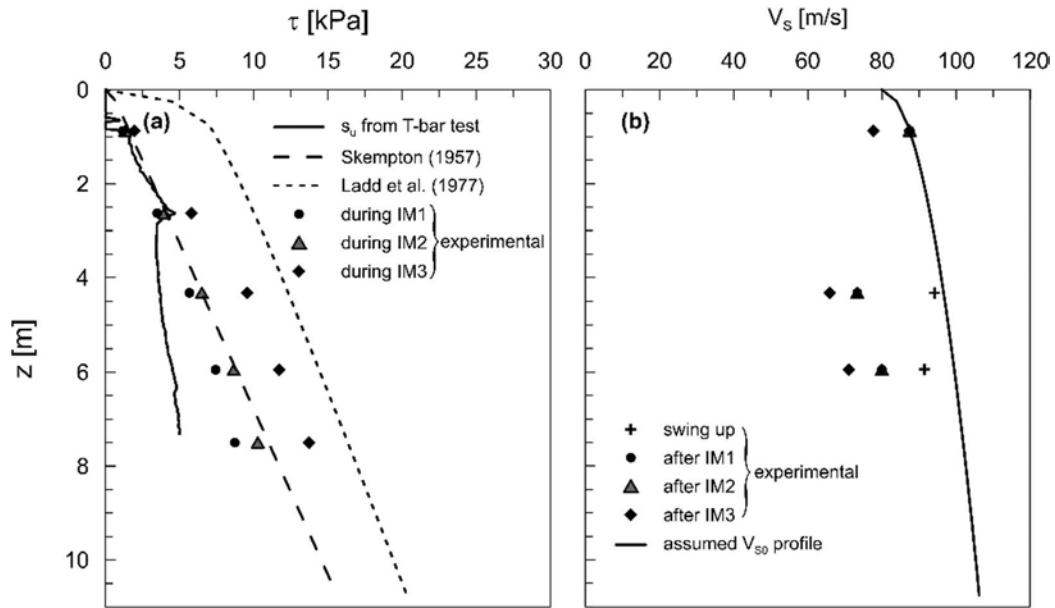


Figure 432 (a) s_u profile from T-bar test and literature expressions vs. maxima shear stresses mobilised during earthquakes; (b) shear wave velocity from air hammer tests and initial profile assumed in this study

A four-parameter model was used to characterize normalized modulus reduction and material damping curves, as proposed by Darendeli (2001), who modified the basic hyperbolic relationship between stress and strain developed by Hardin and Drnevich (1972) so as to accommodate a better fit to the modulus reduction curves measured in the laboratory. The normalized modulus reduction curve based on Darendeli's model utilizes two parameters and can be expressed as:

$$\frac{G}{G_0} = \frac{1}{1 + \left(\frac{\gamma}{\gamma_r} \right)^\alpha} \quad (4)$$

where the reference strain γ_r corresponds to the strain amplitude when shear modulus reduces to one half of G_0 and the coefficient α has an impact on the curvature of the curve. The damping ratio curve is expressed by the equation:

$$D = b \left(\frac{G}{G_0} \right)^p D_{\text{Masing}} + D_{\text{min}} \quad (5)$$

where (b, p) are model parameter and D_{min} the initial damping ratio. This four-parameter (γ_r, α, b and D_{min}) model was used to characterize the normalized modulus reduction and material damping curves of the clay in this study. However, due to the lack of available dynamic tests investigating the variation of shear modulus and damping with shear strain amplitude, the parameters were selected so as to identify the pair of curves that better reproduced the centrifuge data in terms of acceleration time histories, Fourier spectra and amplification functions simultaneously. The resulting values of the model parameters are listed in Table 64. Figure 433 shows the computed normalised shear modulus and damping, along with typical modulus reduction and damping curves available in the literature for $I_p = 33\%$.

Parameter	Value
γ_r [%]	0.07
a	0.9
D_{min} [%]	2
β	1.2

Table 64: Values of the parameters used in the Darendeli's model to characterize normalized modulus reduction and material damping curves of the clay

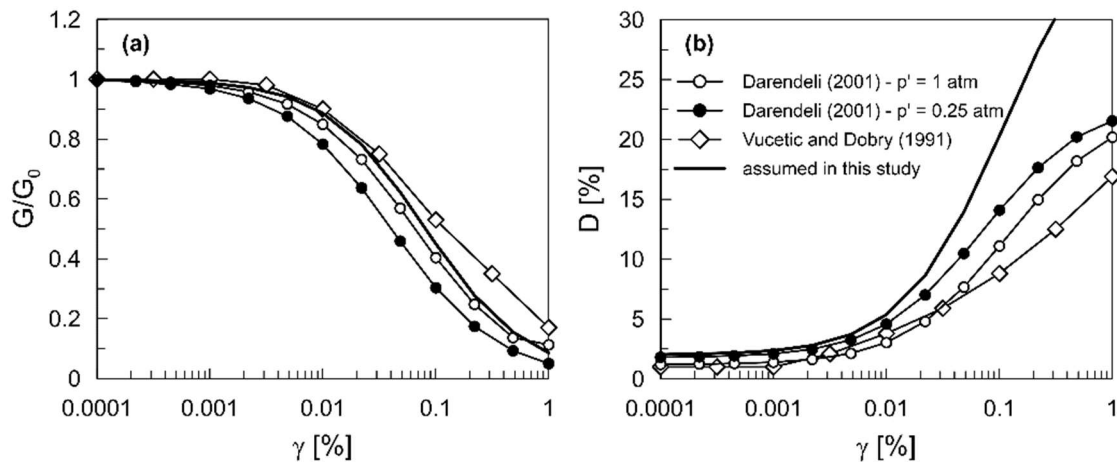


Figure 433:(a) Normalised shear modulus and (b) damping curves used in this study

GROUND RESPONSE ANALYSIS

DEEPSOIL code (Hashash et al. 2017) was employed to perform equivalent-linear analysis of the free-field soil response. Bedrock was modelled at the level of -11 m as rigid and the acceleration recorded by the deepest accelerometer in the clay profile during the centrifuge test was used as the base excitation for the analysis. The degradation of shear modulus and the increase of hysteretic damping of the soil with increasing shear strain was modelled by implementing the curves from Figure 433, while the effective shear strain ratio was set at 0.65. The low-strain shear modulus was defined from the V_{S0} profile and a frequency independent expression (i.e. $G^* = G(1+2iD)$) was adopted for its complex formulation.

The results of the analysis in terms of amplification functions from bedrock to each layer are shown in Figure 434. All the figures also show the experimental data for comparison. Figure 435 shows the results of the analysis, along with experimental data, in terms of maximum shear stress, mobilised shear wave velocity and damping ratio. Noticeably, the mobilized shear stress is well below the limiting value s_u , ensuring the suitability of the EQL approach.

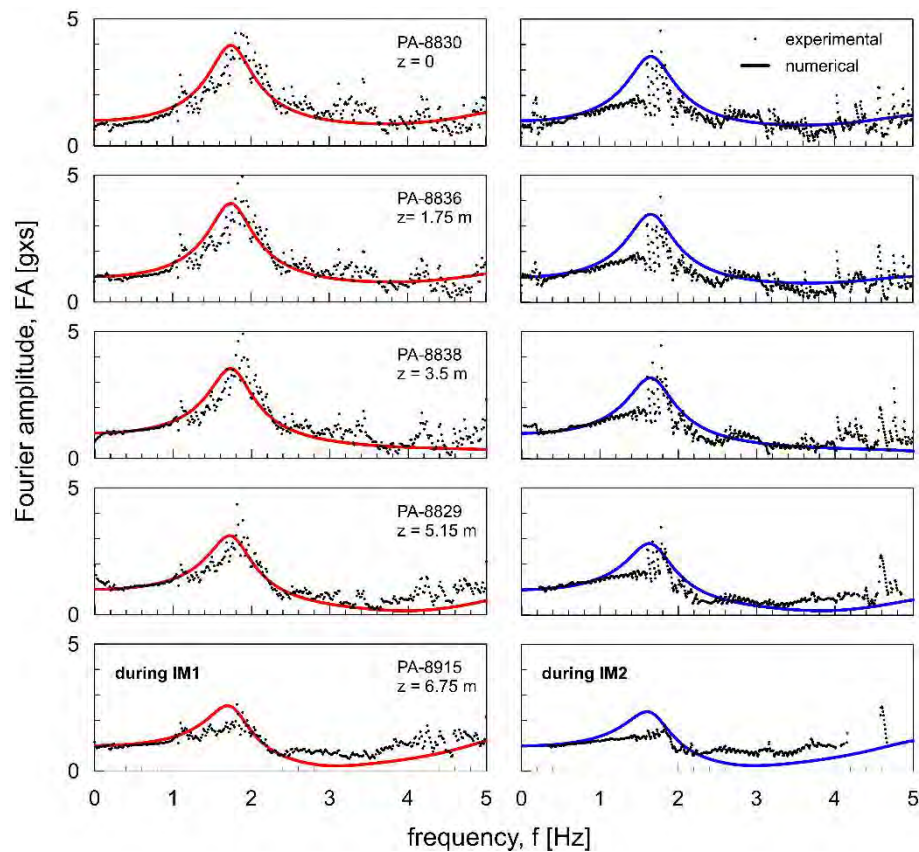


Figure 434: Free field response: comparison between amplification functions bedrock to layer from recorded centrifuge data and DEEPSOIL analysis

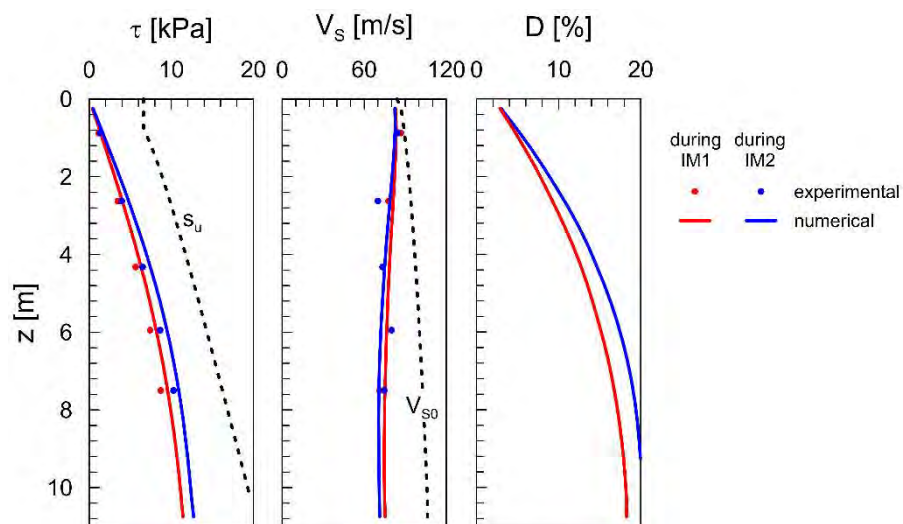


Figure 435: Free field response: mobilised shear stress, shear wave velocity and damping profiles

DYNAMIC SOIL-FOUNDATION-STRUCTURE INTERACTION

The strain compatible stiffness and damping ratio of the free field soil obtained from EQL analyses were introduced into a FE model of the soil-pile system to investigate the kinematic-induced filtering action

of the piles. In the following, only the response of model single pile SP and pile group PG2 is discussed, as a block failure was observed in PG1 while increasing the centrifugal acceleration from 40 to 50 g.

The numerical analyses were carried out using the FE code ANSYS. For the pile group, a more computationally expensive 3D model with 8-noded brick elements was adopted (Figure 436). One fourth of the soil-foundation system was modelled, taking advantage of the double geometrical symmetry.

All materials were modelled using a complex elastic modulus, so as to simulate a constant hysteretic (frequency-independent) damping ratio, variable with depth for soil elements according to the average mobilized values obtained from 1D site response analysis. The load, consisting of a horizontal acceleration, was applied in the form of a body force imposed to the elements.

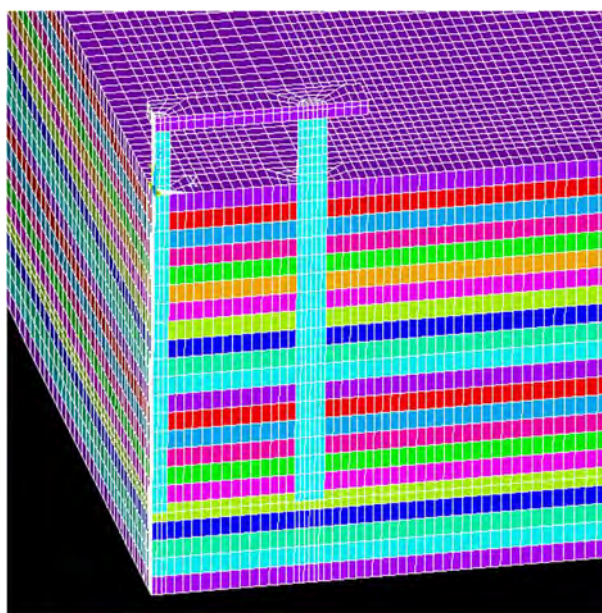


Figure 436: Finite Element Analyses: three-dimensional model for pile foundation PG2

The response of pile foundations in terms of acceleration time histories and Fourier amplitude spectra is shown in Figure 437, referring to signals IM1. In the same figures, the response of clay surface is also reported, highlighting the higher accelerations at foundations' cap. The elaboration of the experimental data in terms of the ratio between the maximum acceleration at the pile head and that at the soil surface clearly showed a remarkable peak in this amplification functions, at about 5 Hz for SP (Figure 438) and between 3 and 4 Hz for PG2 (Figure 439) foundations. This can be attributed to the fact that the overall response of both the pile groups and the isolated pile include the inertial effect due to the caps needed to install the measurement devices. The experimental peaks occur at a frequency which is lower than the one obtained numerically employing the mobilised stiffness derived from the free-field response, as evident in Figs 5.11 (curves 'numerical (1)'). This can be attributed to the separation of pile and soil due to installation procedure.

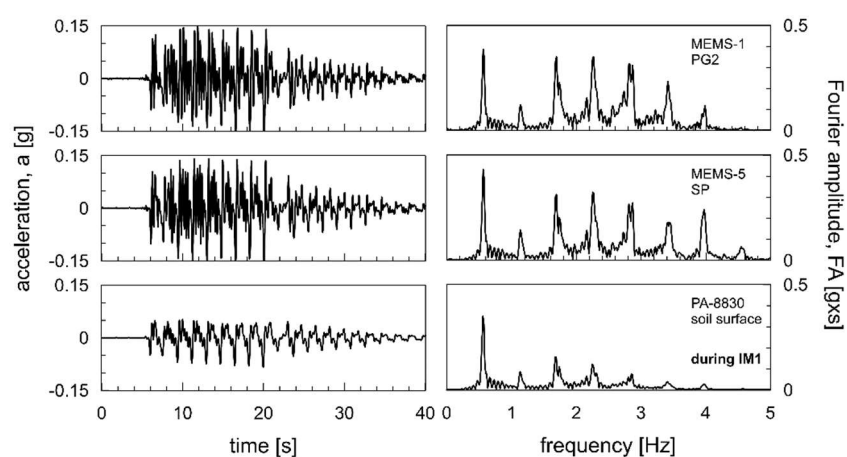


Figure 437: Response of pile foundations during input motion IM1

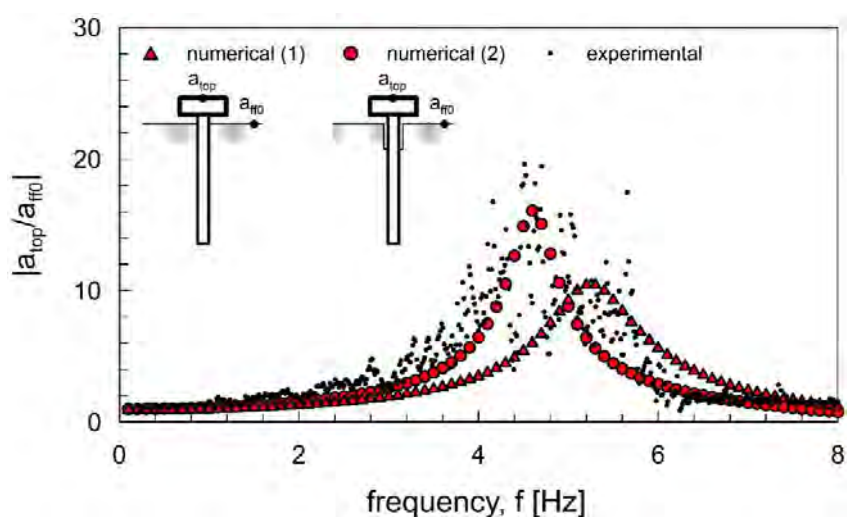


Figure 438: Acceleration transfer function of single pile for IM1 signal: experimental data vs numerical analyses

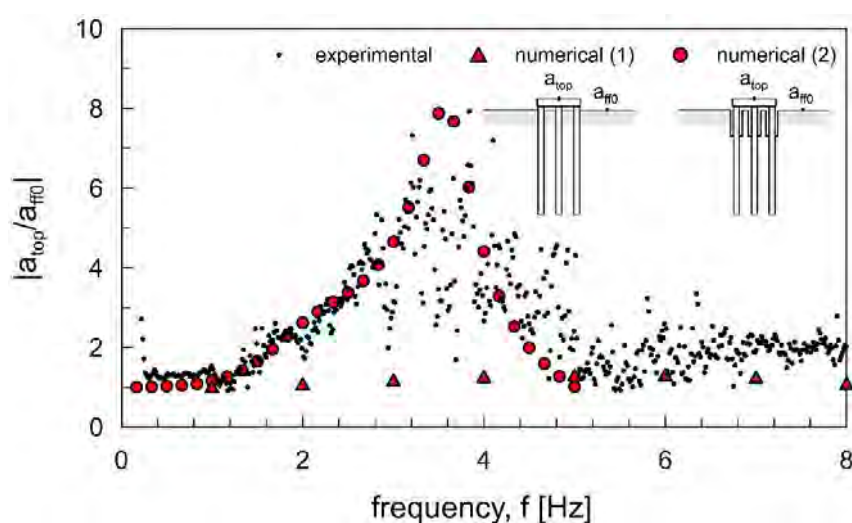


Figure 439: Acceleration transfer function of pile group PG2 for IM1 signal: experimental data vs numerical Analyses

The good agreement between experimental and numerical data allowed to extrapolate the kinematic interaction factor, I_u , defined as the ratio between the maximum acceleration at the head of the fixed head pile and that at the soil surface, in the absence of structural mass and without any separation between pile and soil (no gap assumption). As expected, the group response is similar to that of the single pile (Figure 440). Moreover, the expression proposed by Iovino et al. (2019) was found to be in very good agreement with the numerical results. The simplified assumption of homogeneous soil, with stiffness equal to the mobilised one at half pile active length, allows use of the simpler expression by Anoyatis et al. (2013). This formula also performs in a satisfactory manner, as shown in Figure 440 as the mobilised stiffness profile coming from the free-field response analysis is quasi-constant for the problem under examination.

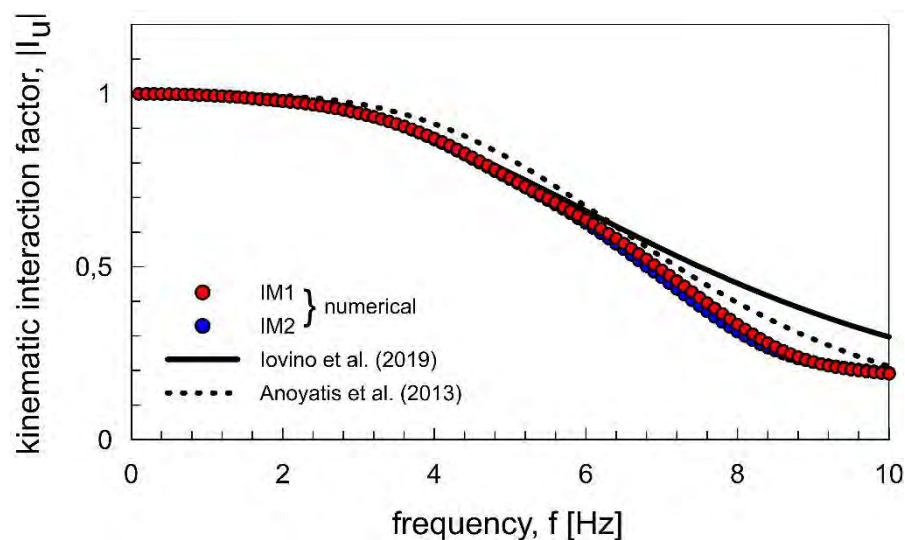


Figure 440: Extrapolated the kinematic interaction factor, I_u , for single pile and comparison with simplified expressions

8.4.5 Conclusions

Summing up, the numerical analyses well reproduce the experimental outcome if the gap formed during the installation procedure is properly taken into account. This assumption allows a satisfactory match of acceleration transfer function, in terms of both resonant frequency and peak amplification, for both IM1 and IM2 signals. The ‘two-stage’ procedure for data processing and interpretation suggested in this summary report has therefore proven to be fully satisfactory and will be extended also to data collected for tests carried out under SERA. Due to the Equivalent Linear assumption, only IM1 and IM2 signals were considered, given that the IM3 signal, of higher amplitude, was not creating conditions for which the EQL assumption can be deemed to be reliable. For higher amplitude signals and real earthquakes, a non-linear soil response analysis is probably mandatory. The numerical results confirm the well-known concept that piles in soft soils can exert an important filtering on the Foundation Input Motion which excites the superstructure, thereby having a beneficial effect on its seismic response. The application of this procedure to tests of the SERA project will definitely allow to assess whether the amount of filtering action is modified by the raft-soil contact.

References

- Anoyatis G, Di Laora R, Mandolini A, Mylonakis G (2013) Kinematic response of single piles for different boundary conditions: analytical solutions and normalization schemes. *Soil Dyn Earthq Eng* 44 183–195.
- Brennan, AJ and Madabhushi, SPG (2002) Design and performance of a new deep model container for dynamic centrifuge testing. In: *The International Conference on Physical Modelling in Geotechnics*, 183-188.
- Darendeli, M.B. (2001) Development of a new family of normalized modulus reduction and material damping curves. PhD thesis, University of Texas at Austin.
- Di Laora R, de Sanctis L (2013) Pile-induced filtering effect on the foundation input motion. *Soil Dyn Earthq Eng* 46:52–63.
- Gazetas G (1984) Seismic response of end-bearing single piles. *Int J Soil Dyn Earthq Eng* 3(2):82–93.
- Ghosh, B and Madabhushi, SPG (2002) An efficient tool for measuring shear wave velocity in the centrifuge. In: *The International Conference on Physical Modelling in Geotechnics*, 119-124.
- Hardin, BO and Drnevich, VP (1972) Shear Modulus and damping in soils: Design equations and curves. *ASCE Journal of Soil Mechanics and Foundations Div.* 98(SM7) 667-692.
- Hashash YMA, Musgrove MI, Harmon JA, Okan I, Groholski DR, Phillips CA, Park D (2017) DEEPSOIL 7.0, user manual. University of Illinois at Urbana-Champaign.
- Iovino, M, di Laora, R., Rovithis, E. & di Sanctis, L. (2019) The beneficial role of piles on the seismic loading of structures. *Earthquake Spectra* 35(3) 1141-1162.
- Kawamura S, Umemura H, Osawa Y (1977) Earthquake motion measurement of a pile-supported building on reclaimed ground. *Proceedings of 6th WCEE, India*.
- Ladd, CC, Foot, R, Ishihara, K., Schlosser, F. and Poulos, H.G. (1977) Stress-deformation and strength characteristics. 9th ISMFE Volume 2, 421-494.
- Lam, S. (2010), Ground movements due to excavation in clay: physical and analytical models , PhD thesis, Cambridge University.
- Lau, B.H. (2015), Cyclic behaviour of monopile foundations for offshore wind turbines in clay , PhD thesis, Cambridge University.
- Martin, C.M. and Randolph, M.F. (2006) "Upper bound analysis of lateral pile capacity in cohesive soil." *Géotechnique* 56 2:141-145.
- Muir Wood (1990) *Soil Behaviour and Critical State Soil Mechanics*. Cambridge University Press, UK.
- Ohta, T, Uchiyama, S., Niwa, M and Ueno, K. (1980) Earthquake response characteristics of structure with pile foundation on soft subsoil layer and its simulation analysis. In *proceedings of the 7th World Conference on Earthquake Engineering*, Vol. 3. Istanbul, Turkey.
- Randolph, MF and Houlsby GT (1984), The limiting pressure on a circular pile loaded laterally in cohesive soil, *Geotechnique*, 34(4) 613-623.
- Robinson RG, Tan TS, Lee FH (2003) A comparative study of suction-induced seepage consolidation versus centrifuge consolidation. *Geotech Test J* 26(1):92–101.
- Rovithis, E, di Laora, R and de Sanctis, L. (2015) Foundation motion filtered by piles: effect of soil inhomogeneity. *Geotechnical Engineering for Infrastructure and Development. Proceedings of the XVI ECSMGE*.
- Rovithis, E, di Laora, R, Iovino, M. and di Sanctis, L. (2017) Reduction of seismic loading on structures induced by piles in inhomogeneous soil. *Proc. Compdyn* 2017.

Schofield, AN. and Wroth CP (1968) Critical State Soil Mechanics, McGraw Hill, London.

Zeng X. and Schofield A.N. 1992 Design and performance of an equivalent-shear-beam container for earthquake centrifuge modelling. *Geotechnique* 46(1) 83-102.

Skempton, A.W. 1954. Discussion: Sensitivity of clays and the c/p ratio in normally consolidated clays. *Proceedings of the American Society of Civil Engineers, Separate 478*: 19–22.

Skempton, A.W. 1957. Discussion: Further data on the c/p ratio in normally consolidated clays. *Proceedings of the Institution of Civil Engineers, 7*: 305–307.

Stewart, DP and Randolph MF (1991) T-bar penetration testing in soft clay. *Journal of Geotechnical Engineering* 120(12).

Take, W.A. (2003), The influence of seasonal moisture cycles on clay slopes, PhD thesis, Cambridge University.

9 EUROSEISTEST and EUROPROTEAS

EUROSEISTEST is a multidisciplinary European experimental site for integrated studies in earthquake engineering, engineering seismology and soil dynamics. Established in 1993, it is the longest running valley-instrumentation project worldwide and it is located in the Mygdonian valley (epicentral area of the 1978 M6.4 earthquake), approximately 30km to the NE of the city of Thessaloniki in northern Greece. It consists of a 3D strong motion array and an SDOF structure (EUROPROTEAS). EUROSEISTEST and EUROPROTEAS facility is operating under the responsibility of the Research Unit of Soil Dynamics and Geotechnical Earthquake Engineering (SDGEE) of the Civil Engineering Department of the Aristotle University of Thessaloniki.

The permanent accelerometric network includes 21 broadband high resolution triaxial accelerographs, 15 of which are located at the ground surface and 6 in down-hole arrays at the center and at the northern edge of the instrumented area. More than 200 events of local magnitude $1.5 \leq M_L \leq 6.6$, at epicentral distances in the range 1–500km have been recorded by the network. All strong motion records and accompanying earthquake and stations metadata (V_s profiles, borehole data, dynamic properties of the soil etc.) have been stored in a database which is updated each time a new event is recorded (<http://euroseisdb.civil.auth.gr/>).

EUROPROTEAS large-scale prototype soil-foundation-structure system has been built in EUROSEISTEST. Its name is symbolic derived from two Greek words “Euro” and “Proteas” for the first large-scale model structure in Europe dedicated to study soil-foundation-structure interaction phenomena. The concept that led the design of EUROPROTEAS was to have a reconfigurable simplified structure able to demonstrate clearly the salient effects of soil-foundation-structure interaction on the superstructure and soil response.

During SERA, EUROSEISTEST and EUROPROTEAS facility hosted in total 9 User Groups and 9 Projects.

1. IMPEC - On the broadband synthetic signals enhancement for 3D Physic based numerical analysis, the EUROSEISTEST Case study
2. Dynamic Soil Structure Interaction: Three-dimensional Time-domain Analysis of Field Model Scale Experiments
3. “SISIFO” - Seismic Impedance for Soil-structure Interaction From On-site tests
4. Ambient and forced vibration techniques for improving design and performance assessment of structures with consideration of soil-structure interaction
5. Seismic site effects in sedimentary basins from 3D physics-based numerical modeling (SITE3D)
6. Comparison of rocking on rigid and compliant base using the EUROPROTEAS real-scale facility
7. Resonant metamaterial-based earthquake risk mitigation of large-scale structures and infrastructure systems: assessment of an innovative proof-of-concept via medium-size scale testing
8. “DYMOBRIS” - DYnamic identification and MONitoring of scoured BRIdgeS under earthquake hazard
9. Soil Frame-Interaction Analysis through large-scale tests and advanced numerical finite element modeling (Acronym: SOFIA)

9.1 Project # 16 – IMPEC – On the broadband synthetic signals enhancement for 3D Physic based numerical analysis, the EUROSEISTEST Case study

Authors

F. Lopes-Caballero⁽¹⁾, F. Gatti⁽¹⁾, S. Touhami⁽¹⁾, A. Vratsikidis⁽²⁾, M. Manakou⁽²⁾, D. Pitilakis⁽²⁾

⁽¹⁾ *Laboratoire Mécanique des Sols, Structures et Matériaux (MSSMat) UMR CNRS 8579 CentraleSupélec, France*

⁽²⁾ *Aristotle University of Thessaloniki, Thessaloniki, Greece*

9.1.1 Introduction

In the past two decades, the seismic hazard analysis and vulnerability assessment took progressively advantage of the ever-increasing computational power available (Paolucci et al., 2014). This outstanding technological and numerical progress seemingly broke through the evergreen and most stringent bottleneck in computational seismology: the impossibility to solve the complete source-to-site seismic wave propagation problem in a single-step analysis. All the ingredients (i.e. source, path and site effects) can nowadays naturally be convolved in one-step all-embracing analysis, capable of predicting a realistic seismic wave-field and to explain the observed time-histories in sedimentary deposits (local scale, i.e. approximatively 1-10 km of characteristic length) and/or at the continental scale (i.e. 100 km or greater, De Martin, 2011). Once shattered these computational barriers, a new holistic philosophy took place, driven by the deterministic modelling of the physics underlying each aspect of the earthquake phenomenon, for more accurate sensitivity analyses and uncertainty quantification of models and related parameters. In spite of the inherent complexity and the huge dimensions of those computational models, their power is essentially embodied by the higher broadband accuracy they provide (i.e. up to 4-5 Hz, De Martin, 2011), gradually bridging the gap between low-frequency source models obtained via wave-form inversion techniques and the structural modal frequencies (i.e. up to 20 Hz). This achievement is paving the way to fully couple the large-scale seismological models for the region of interest, with local engineering models for geotechnical, site-effect and structural analyses, in the next few years.

A major challenge related to the high-fidelity earthquake numerical simulation is represented by the accuracy of the predicted wave-motion at the frequency of interest. Unfortunately, due to the well-known spatial aliasing of the computational grid, major computational efforts are required to enlarge the wave-field frequency bandwidth propagated with accuracy, since finer meshes are required. Moreover, the simulation of realistic ground shaking scenarios in a broad-band frequency range (BB2S2S) requires a reliable estimation of several different parameters, related to the source mechanism, to the geological configuration and to the mechanical property of the soil layers and crustal rocks. The great impedance contrast between soft sedimentary layers and crustal bedrock entail the need for smaller time steps, i.e. increasing the overall CPU-time required to simulate realistic time-histories (e.g. of approximately 30 s), containing the P- and S-wave strong phases, as long as the coda-waves. Finally, due to the enormous extension of those regional scale scenarios, the degree of uncertainty associated to the whole earthquake process (from fault to site) is extremely high. At this

point, it appears necessary to build up a multi-tool HPC-platform (High Performance Computing) capable to tackle the following issues:

1. to mesh the domain of interest, its geological conformation (bedrock to sediment geological surfaces), the surface topography and the bathymetry (if present)
2. to represent the material rheology (i.e., elastic, viscous-elastic, non-linear hysteretic)
3. to describe the natural heterogeneity of the Earth's crust and soil properties, at different scales (i.e., regional geology, local basin-type structures and heterogeneity of granular materials)

9.1.2 EUROSEISTEST Array

The Mygdonian basin is located 30 km east-northeast of Thessaloniki, northeastern Greece (see Figure 441a), at the center of the sedimentary basin between the Volvi and Lagada lakes, in the epicentral area of the magnitude 6.5 event that occurred in 1978 and damaged the city of Thessaloniki. The Mygdonian basin represents an experimental site of several different investigation campaigns since a decade ago (Pitilakis et al., 2009; Pitilakis et al., 2013, among others). Therefore, it has been instrumented with surface and borehole accelerometers, and the 3-D elevation and geological models are available (see Figure 441b and Figure 441c, Manakou et al., 2010). Maufroy et al. (2015) performed verification/validation tests at the Mygdonian basin by running 3-D earthquake simulations between 0.7-4 Hz, addressing the description of the material heterogeneities, of the attenuation model, the approximation of the free surface, and of the absorbing boundaries.

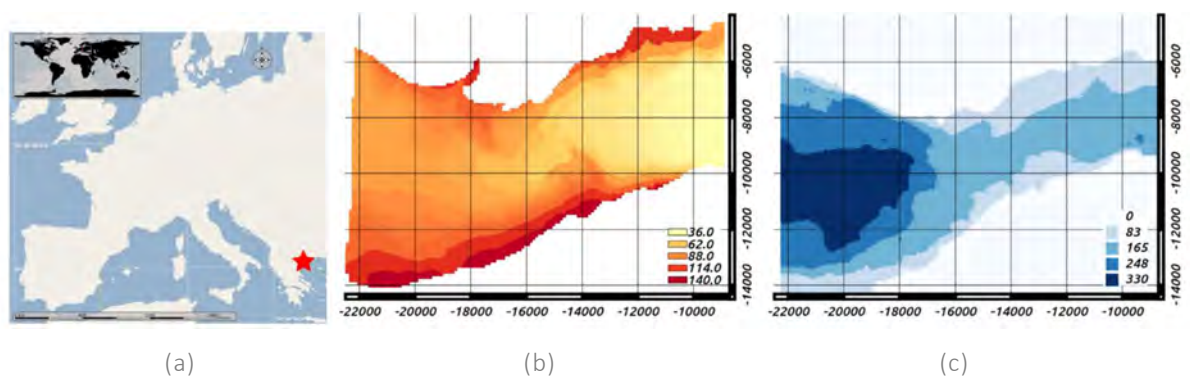


Figure 441: (a) Georeferenced map of Europe with Mygdonian basin location. (b) Georeferenced elevation tour of the Mygdonian basin (Hatt Projection, Bessel ellipsoid). (c) Georeferenced depth contour of the sedimentary basin (all the layers) in Hatt coordinates

The predictions well reproduce some, but not all, features of the actual site effect, due to the uncertainty on the source parameters (location, hypocentral depth, and focal mechanism), on the description of the geological medium (damping, internal sediment layering structure, and shape of the sediment-basement interface). Based upon the works of Chaljub et al. (2015) and Maufroy et al. (2015) (EUROSEISTEST Verification and Validation Project, E2VP), in this paper, the Mygdonian basin (Greece) is chosen as a suitable case study to test the performances of the mentioned BBS2S HPC-platform, constructing a numerical model of the earthquake scenario (valid in the 0.15-7 Hz frequency bandwidth) and focusing on the influence of the 3-D geology and of the soil heterogeneity on the earthquake ground motion spatial variability. Manakou et al. (2010) provided a detailed description of the geometry and of the dynamic properties of the soil layers within the Mygdonian basin, obtained by inverting data from microtremor array measurements, seismic refraction profiles, boreholes, and geotechnical investigations. S-wave velocity profiles were inverted from the phase-velocity dispersion curves obtained at 27 different sites placed in the whole valley. The proposed 3-D model describes the

geometry and shear-wave velocities of the Mygdonian and pre-Mygdonian sedimentary systems, and the top bedrock surface. In this paper, the pre-Mygdonian system was solely considered as first approach, surrounded by the outcropping bedrock with an average shear-wave velocity of 650 m/s.

9.1.3 Numerical model

The main numerical tool is represented by SEM3D, a numerical code tailored to solve the 3-D wave propagation problem in large solid/fluid computational domains. SEM3D is based on the Spectral Element Method (SEM, based on the pioneering works in fluid dynamics performed by Patera, 1984; Korczak and Patera, 1986; Maday et al., 1987; Mayday et al., 1989) and it has been developed upon the code RegSEM (Cupillard et al., 2012; Festa and Vilotte, 2005), thanks to the synergistic effort of three research teams, at CentraleSupélec, Institut de Physique du Globe de Paris (IPGP) and the Commissariat d’Energie Atomique (CEA), respectively. Among the advantages of SEM3D, two main aspects must be stressed, namely (1) its efficient and cost-effective massively parallel implementation (by Message Passing Interface, MPI) on large super-computers and (2) its ability to accurately take into account 3-D discontinuities such as the sediment-rock interface. Moreover, the code makes use of a library called HexMesh, that implements an efficient linear 27-tree finite element mesh generation scheme and it is capable to generate large computational grids (i.e. ≈ 100 km) by extruding the Digital Elevation Model (DEM) provided and progressively top-down coarsen it, so to obtain a non-structured grid. The SEM is well known for the high number of integration points in each element, compared to the FEM. This feature renders the SEM naturally prone to model the heterogeneity of soil material, which is among the main issues responsible of wave dispersion and scattering. e computed in the SEM semi-discretized equations. To generate random samples, an open-source library ScaRL was developed linked to SEM3D (Paludo et al., 2015). In this paper, the fluctuation of the soil properties within the sedimentary basins, observed in-situ, is reproduced numerically. ScaRL is employed, coupled with SEM3D, so to obtain a spatially variable field for the elastic shear modulus $\mu(x)$ for the first 500 m depth. As portrayed in Figure 442, the elastic shear modulus $\mu(x)$ is represented by a non-stationary random field all over the uppermost part of the Earth’s crust. $\mu(x)$ was generated by ScaRL, characterized by an anisotropic Von Karman Correlation structure ($l_x = l_y = 90$ m, $l_z = 40$ m), over a domain of ≈ 13 km \times 11 km \times 0.4 km. Its standard coefficient of variation CV is equal to 10%, with a first order marginal that is assumed to follow a log-normal pdf-distribution (see Gatti et al., 2018 for more details).

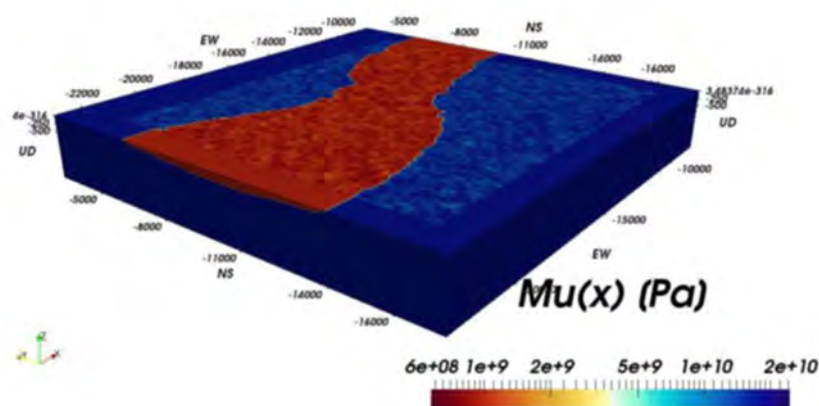


Figure 442: Example of the heterogeneous shear modulus field $\mu(\underline{x}) = \sqrt{\mu(\underline{x}) / \rho(\underline{x})}$

The numerical grid employed in this analysis was designed with a structure texture, featured by average element sizes of approximately $90 \text{ m} \times 90 \text{ m} \times 40 \text{ m}$ (resulting into $5.5 \cdot 10^{+07}$ hexahedral elements and $5.8 \cdot 10^{+07}$ GLL), to grant the propagation of a seismic wave at 7 Hz (with 7 GLL points per minimum wavelength). The model was enclosed by non-reflecting Perfectly Matched Layers (PML) and no surface topography was introduced. This mesh was used to perform an extensive comparison between three geological models of the Mygdonian basin area is presented, namely (1) horizontally bi-layered half-space (LAY), (i.e. classical Green's function model), (2) homogeneous (HOM) 3-D basin embedded into outcropping bedrock (see Figure 443a) and (3) heterogeneous (HET) 3-D basin embedded into outcropping bedrock (see Figure 442). To integrate the complex 3-D geology into the computational grid, a not-honouring approach was employed, i.e. the geological interface was not directly meshed, but the heterogeneous mechanical properties were interpolated over the structured computational grid. No viscous dissipation was introduced at this stage. A point-wise double-couple seismic source ($\phi_s = 22.5^\circ$, $\lambda = 0^\circ$, $\delta = 90^\circ$) was employed at this stage, located southwards, at 5 km depth (in the bedrock stratum), to discount the effect of the extended fault rupture from the wave-field at surface (Chaljub et al., 2015). The computations were performed on the super-computer cluster Fusion, held by the Université Paris Saclay. The LAY model took approximately 310 h CPU-time to run 30 seconds of simulation on 216 MPI cores. HOM and HET took instead approximately 1487 h CPU-time. For more details, refer to Gatti et al. (2018).

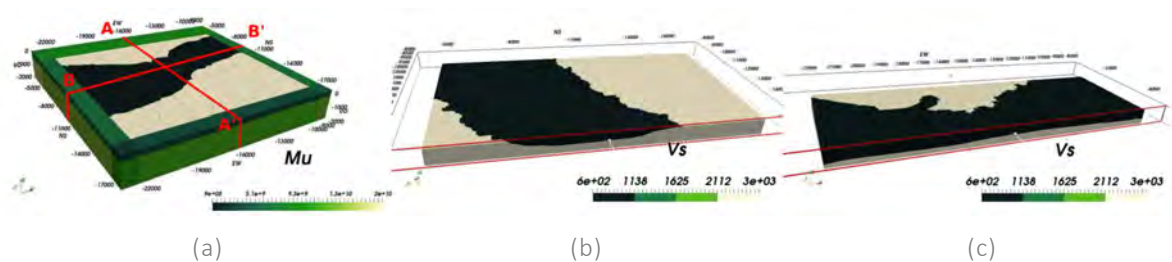


Figure 443: (a) Layout of the SEM3D model of the Mygdonian basin. Two representative cross-sections depicted: (b) A-A' and (c) B-B'

9.1.4 Test setup

The “IMPEC - On the broadband synthetic signals enhancement for 3D Physic based numerical analysis, the EUROSEISTEST Case study” didn't include performance of any experiment. Remote access on the EUROSEISTEST database containing seismological geotechnical and geological data was granted.

9.1.5 Observation during testing

The “IMPEC - On the broadband synthetic signals enhancement for 3D Physic based numerical analysis, the EUROSEISTEST Case study” didn't include performance of any experiment. Remote access on the EUROSEISTEST database containing seismological geotechnical and geological data was granted.

9.1.6 Results

The effects of complex 3-D basin-like geological structures have been vastly observed and studied in the past (see Faccioli and Vanini, 2003 and Smerzini et al., 2017, for instance). The present case study confirms the complexity introduced by the complex interaction between the incident seismic wave-motion and the 3-D interfaces, when the former impinges the latter while travelling towards the surface.

Figure 444 shows the comparison between synthetic velocigrams obtained for three different geological models. The strong phase arrivals are delayed in the LAY case (black traces), as expected. Moreover, both in the HOM (blue traces) and HET (red traces) cases, late waveforms appear (some sort of coda-waves), due to the wave-motion interaction with the basin structure. Smaller differences are encountered between the two latest cases, highlighting the moderate contribution of the soil unit mass heterogeneity in this case dominated by the 3-D basin effect. However, the corresponding acceleration Fourier's spectra are plotted: those spectra better show the actual different response obtained by either considering the heterogeneity or not. It is worth to mention that the vertical components have amplitudes comparable to the horizontal ones, suggesting that some surface waves have been generated, due to both the presence of the basin and the added soil heterogeneity.

Figure 445 portrays the interferograms obtained for section A-A' (polarization EW) and B-B' (polarization NS). From the interferogram, it is noticeable that a complex wave-motion is generated by the multi-pathing effect taking place within the basin's borders due to the high impedance contrast with respect to the surrounding outcrop. Long coda-waves can be noticed within the softer sedimentary area, that seem trapped within it.

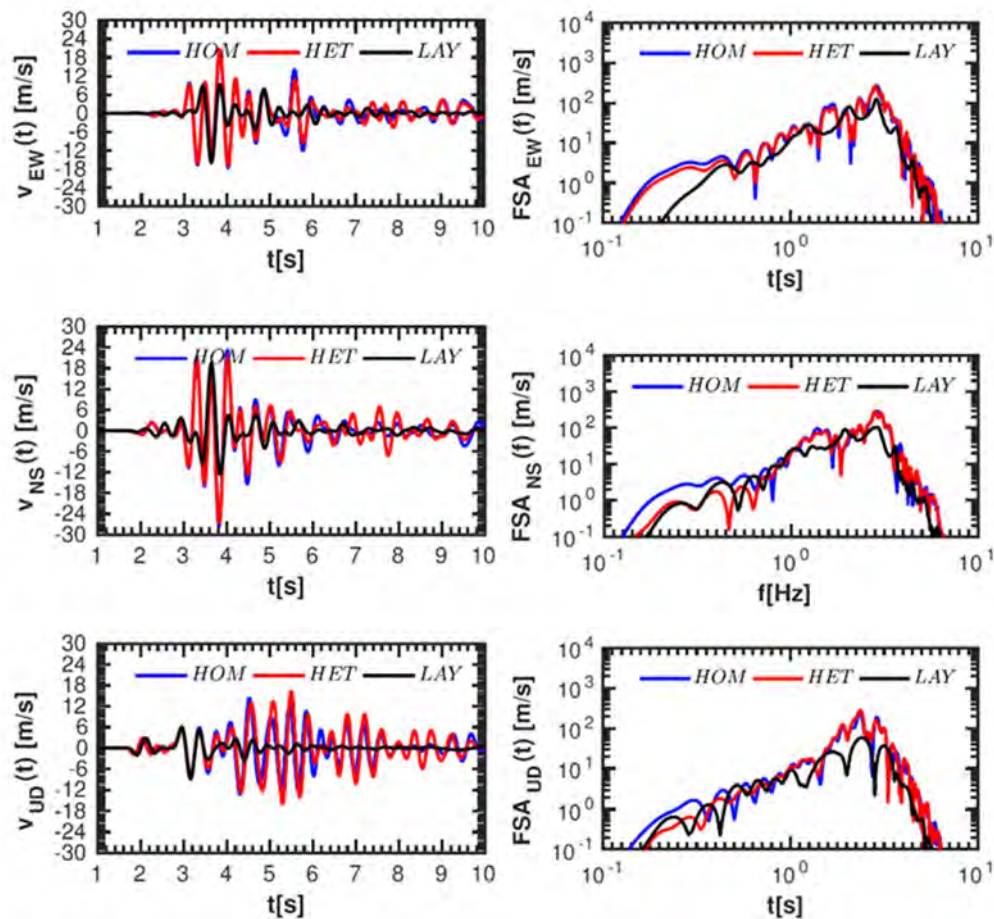


Figure 444: On the left: Velocigrams obtained for HOM (blue), HET (red) and LAY (black) respectively at the intersection between sections A-A' and B-B' (EW=-16100, NS=-10400, see Figure 443a). On the right: the corresponding Fourier's spectra. The time-histories and Fourier's spectra (referring to synthetics filtered at 7Hz) correspond to EW direction (upper row), NS direction (middle row) and UD direction (bottom row) respectively

The latter remark is even more evident when one looks at the velocity contours showed in Figure 446, where wavelets seem trapped within the basin's boundaries. Finally, the wave motion coherency of the synthetic wave motion was analysed. For the sake of brevity, just the HET case is considered herein.

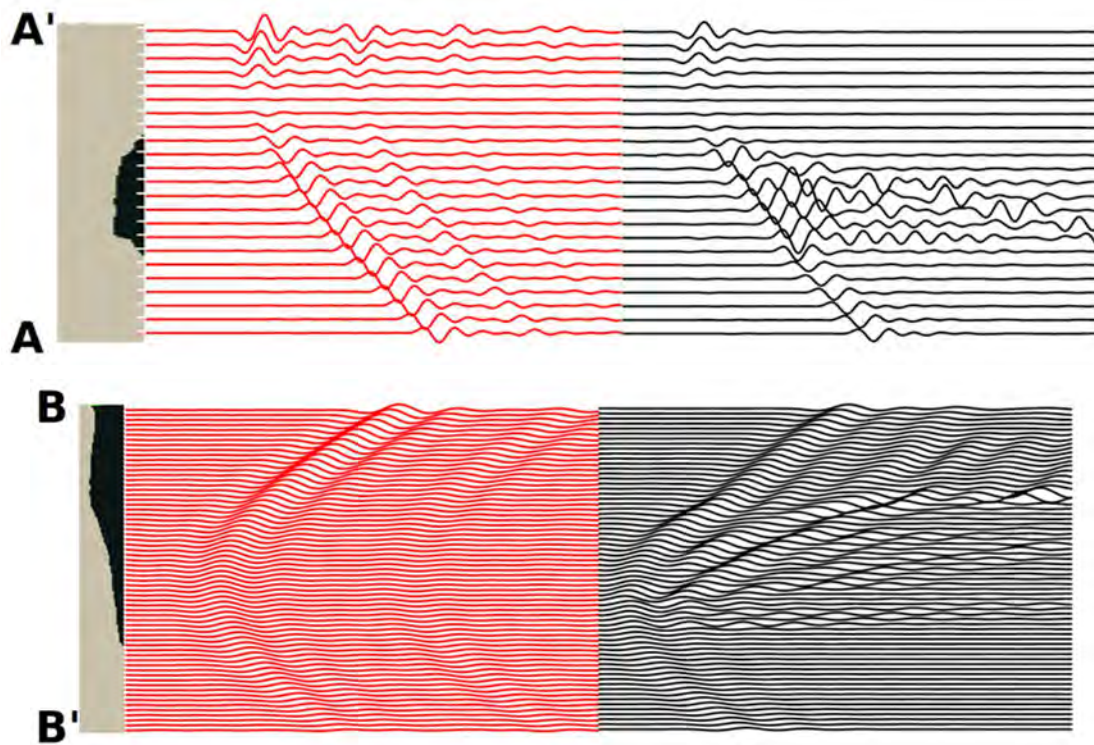


Figure 445: Interferograms for sections A-A' and B-B'. Red velocigrams refer to the layered test case; black velocigrams refer to the homogeneous basin case

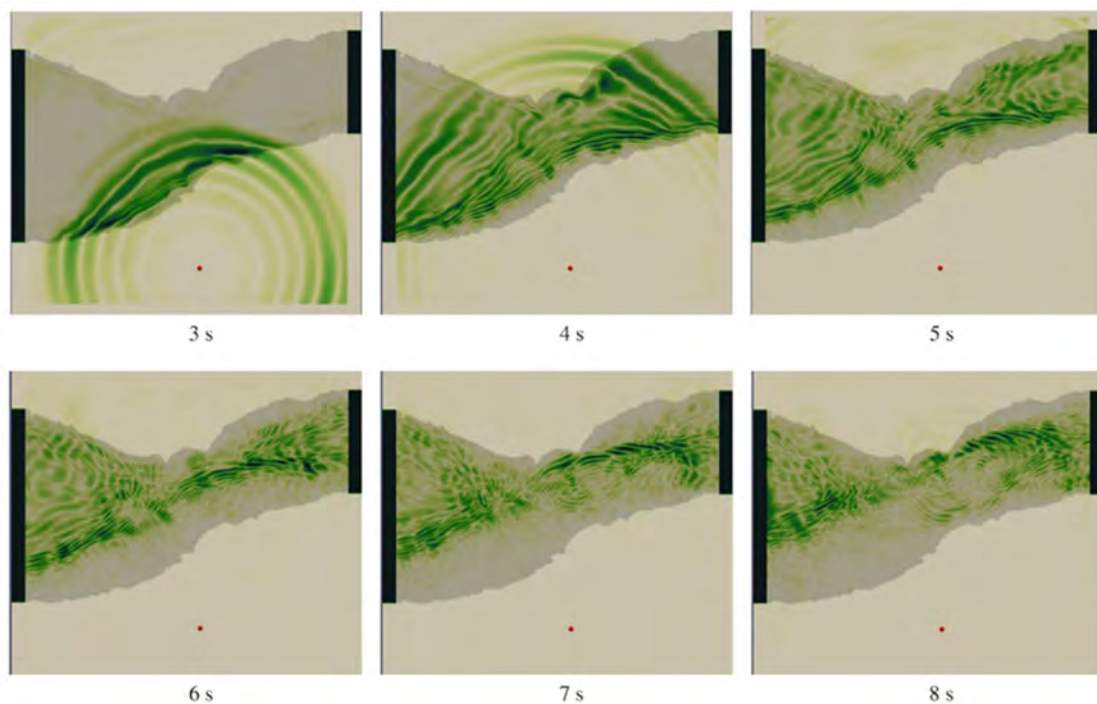


Figure 446: Velocity contours of the SEM3D simulation of the wave propagation throughout the Mygdonian basin

Figure 447a shows some plane wave coherency curves γ_{PW} calculated along the section A-A' (at surface) at a lag-distance of 200 m and 400 m. The wave passage effect was removed.

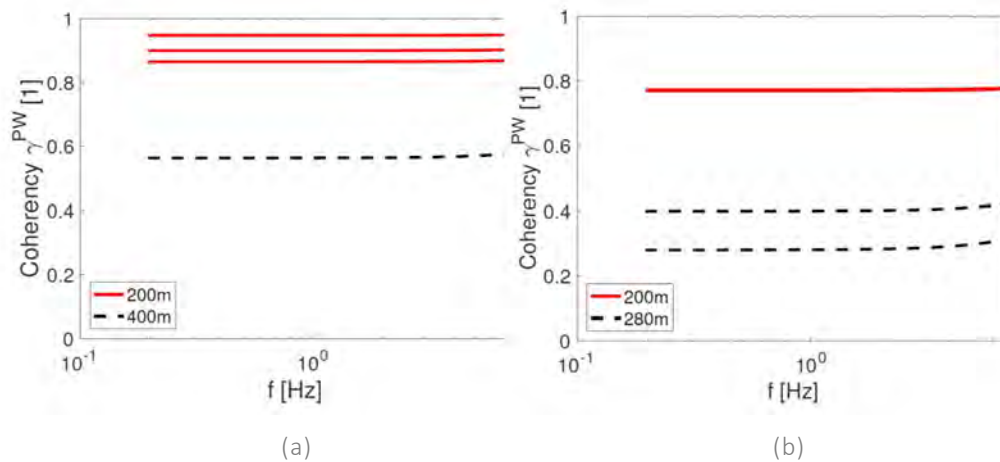


Figure 447: Plane-wave coherency curves obtained for the HET case at the three stations (a) aligned along the A-A' section and (b) aligned along the 45° diagonal

A coherency drop can be clearly observed, although the coherency curves appear to be rather flat, most probably due to the short duration of the coda-waves and to the limited frequency range. It is interesting to notice that the same coherency drop can be observed even at closer lag-distances, for instance when considering a EW-NS diagonal line across A-A' and B-B', as depicted in Figure 447b. The coherency drop appears at 280 m, indicating the fact that the basin and the soil heterogeneity effectively scatter the incident wave motion propagate by the source.

9.1.7 Conclusions and outlook

In this report, a 3-D source-to-site earthquake scenario is presented. The selected case study is the well documented Mygdonian basin, in Greece. A 3-D numerical model (of approximately 10 km of characteristic size) of the shallow sedimentary basin is constructed, by means of a SEM model. The heterogeneous model of the Earth's crust at the regional scale (the soft soil deposit within the basin valley) is integrated by heterogeneous soil properties at the mesoscopic scale, obtained by generating a random field representing one spatial realization of the unit mass distribution. The 3-D analyses are accurate up to 7 Hz. The effect of the basin is studied in terms of time histories recorded at the surface and in terms of wave motion coherency. The basin scatters the wave motion propagated from the point-wise source, trapping the radiated energy due to the great basin-crust great impedance contrast. The soil heterogeneity, on the other hand, acts at a smaller scale, inducing local scattering which however is poorly visible in this frequency range. Both the basin configuration and soil heterogeneity, however, cause a coherency drop in the wave motion at surface. As future developments, the softer basin layers will be included in the analysis, along with an increased frequency range to be able to follow the coherency drop broad-band and specify the role of the soil heterogeneity at higher frequencies.

9.1.8 References

Chaljub, E., Maufroy, E., Moczo, P., Kristek, J., Hollender, F., Bard, P.-Y., Priolo, E., Klin, P., de Martin, F., Zhang, Z., Zhang, W. & Chen X. (2015). 3-D numerical simulations of earthquake ground motion in sedimentary basins: testing accuracy through stringent models. *Geophysical Journal International* 201 (1), 90–111.

Cupillard, P., Delavaud, E., Burgos, G., Festa, G., Vilotte, J.-P., Capdeville, Y. & Montagner, J.-P. (2012). RegSEM: a versatile code based on the spectral element method to compute seismic wave propagation at the regional scale. *Geophysical Journal International* 188 (3), 1203–1220.

De Martin, F. (2011). Verification of a Spectral Element Method Code for the Southern California Earthquake Center LOH.3 Viscoelastic Case. *Bulletin of the Seismological Society of America* 101 (6), 2855–2865.

Faccioli, E., Maggio, F., Paolucci, R. & Quarteroni A. (1997). 2D and 3D elastic wave propagation by a pseudo-spectral domain decomposition method. *Journal of Seismology* 1 (3), 237–251.

Faccioli, E. & Vanini, M. (2003). Complex seismic site effects in sediment-filled valleys and implications on design spectra. *Progress in Structural Engineering and Materials* 5 (4), 223–238.

Festa, G. & Vilotte, J.-P. (2005). The Newmark scheme as velocity-stress time-staggering: an efficient PML implementation for spectral element simulations of elastodynamics. *Geophysical Journal International* 161 (3), 789–812.

Gatti, F., Touhami, S., Lopez-Caballero, F. & Pitilakis, D. 3-D source-to-site numerical investigation on the earthquake ground motion coherency in heterogeneous soil deposits. *9th European Conference on Numerical Methods in Geotechnical Engineering*, 25-27 June 2018, Porto (Portugal), 2018

Göddeke, D., Komatitsch, D. & Möller, M. (2014). Finite and Spectral Element Methods on Unstructured Grids for Flow and Wave Propagation Methods, Chapter 9, pp. 183–206, Springer.

Graves, R. W. (1996). Simulating seismic wave propagation in 3D elastic media using staggered-grid finite differences. *Bulletin of the Seismological Society of America* 86 (4), 1091–1106.

Komatitsch, D. & Tromp, J. (1999). Introduction to the spectral element method for three-dimensional seismic wave propagation. *Geophysical journal international* 139 (3), 806–822.

Komatitsch, D. & Vilotte, J.-P. (1998). The Spectral Element Method: An Efficient Tool to Simulate the Seismic Response of 2D and 3D Geological Structures. *Bulletin of the Seismological Society of America* 88 (2), 368–392.

Korczak, K. Z. & Patera, A. T. (1986). An isoparametric spectral element method for solution of the Navier-Stokes equations in complex geometry. *Journal of Computational Physics* 62 (2), 361 – 382.

Maday, Y., Patera, A. T. & Ronquist, E. M. (1987). A well-posed optimal spectral element approximation for the Stokes problem.

Manakou, M., Raptakis, D., Chavez-Garcia, F., Apostolidis, P. & Pitilakis K. (2010). 3D soil structure of the Mygdonian basin for site response analysis. *Soil Dynamics and Earthquake Engineering* 30 (11), 1198 – 1211.

Maufroy, E., Chaljub, E., Hollender, F., Kristek, J., Moczo, P., Klin, P., Priolo, E., A. Iwaki, T. Iwata, V. Etienne, F. De Martin, N. P. Theodoulidis, M. Manakou, C. Guyonnet-Benaize, K. Pitilakis, & P.-Y. Bard (2015). Earthquake Ground Motion in the Mygdonian Basin, Greece: The E2VP Verification and Validation of 3D Numerical Simulation up to 4 Hz. *Bulletin of the Seismological Society of America* 105(3), 1398–1418.

Mayday, Y., Patera, A. & Rønquist E. (1989). Optimal Legendre spectral element methods for the multi-dimensional Stokes problem. *SIAM J. Num. Anal.*

Paludo, L., Bouvier, V., Cottureau, R. & Clouteau D. (2015). Efficient Parallel Generation of Random Field of Mechanical Properties for Geophysical Application. In *6th International Conference on Earthquake Geotechnical Engineering*.

Paolucci, R., I. Mazziere, C. Smerzini, & M. Stupazzini (2014). Physics -Based Earthquake Ground Shaking Scenarios in Large Urban Areas. In A. Ansal (Ed.), *Perspectives on European Earthquake Engineering and*

Seismology, Volume 34 of Geotechnical, Geological and Earthquake Engineering, pp. 331–359. Springer.

Patera, A. (1984). A spectral element method for fluid dynamics: Laminar flow in a channel expansion. *Journal of Computational Physics* 54(3), 468 – 488.

Pitilakis, K., G. Manos, D. Raptakis, A. Anastasiadis, K. Makra, & M. Manakou (2009). The EUROSEISTEST experimental test site in Greece. In *EGU General Assembly Conference Abstracts*, Volume 11, pp. 13729.

Pitilakis, K., Z. Roumelioti, D. Raptakis, M. Manakou, K. Liakakis, A. Anastasiadis, & D. Pitilakis (2013). The EURO-SEISTEST Strong-Motion Database and Web Portal. *Seismological Research Letters* 84(5), 796–804. Rosenblatt, M. (1952). Remarks on a multivariate transformation. *The annals of mathematical statistics* 23(3), 470–472.

Seriani, G. (1998). 3-D large-scale wave propagation modeling by spectral element method on Cray T3E multiprocessor. *Computer Methods in Applied Mechanics and Engineering* 164(1), 235–247.

Shinozuka, M. & G. Deodatis (1991). Simulation of stochastic processes by spectral representation. *Applied Mechanics Reviews* 44(4), 191–204.

Simo, J., N. Tarnow, & K. Wong (1992). Exact energy- momentum conserving algorithms and symplectic schemes for nonlinear dynamics. *Computer Methods in Applied Mechanics and Engineering* 100(1), 63–116.

Smerzini, C., K. Pitilakis, & K. Hashemi (2017, Mar). Evaluation of earthquake ground motion and site effects in the Thessaloniki urban area by 3D finite-fault numerical simulations. *Bulletin of Earthquake Engineering* 15(3), 787–812.

Taborda, R. & J. Bielak (2011). Large-scale earthquake simulation: computational seismology and complex engineering systems. *Computing in Science & Engineering* 13(4), 14–27.

9.2 Project # 26 – Dynamic Soil Structure Interaction: Three-dimensional Time-domain Analysis of Field Model Scale Experiments

Authors

M. Koronides⁽¹⁾, S. Kontoe⁽¹⁾, L. Zdravkovic⁽¹⁾, A. Vratisikidis⁽²⁾, A. Anastasiadis⁽²⁾, D. Pitilakis⁽²⁾

⁽¹⁾ *Imperial College London, United Kingdom*

⁽²⁾ *Aristotle University of Thessaloniki, Thessaloniki, Greece*

9.2.1 Introduction

Dynamic soil-structure interaction (SSI) is a complex phenomenon that takes place as a result of seismic loading or other types of dynamic excitation. Dynamic SSI phenomena are typically distinguished in inertial and kinematic interaction effects. The kinematic interaction, which is more important for embedded structures, stems from the inability of a structure to comply with the free-field deformation pattern induced by a particular ground-motion. This can be the case for foundations of structures which

are much stiffer than the surrounding soil and therefore cannot follow free-field deformations. The inertial interaction results from the development of inertial forces in the vibrating structure associated with the compliance of the foundation, which would not occur in a fixed-base structure. If the surrounding soil is compliant, the imposed inertial stresses can cause the foundation to displace and rotate.

Many studies have shown that structural response affects the foundation soil and vice versa. When a structure is founded in soft soil, SSI effects play a significant role due to founding soil compliance. It is known that SSI effects increase the natural period and damping of a soil-structure system and can decrease the seismic intensity at the foundation level. Due to these facts, it is conventionally believed that SSI effects are beneficial. Therefore, these effects are neglected conservatively in practice or they are considered by using simplified approaches that take into account their beneficial effects only. However, Mylonakis and Gazetas (2000) have shown that under certain circumstances, such as in soft soil sites, SSI effects could be detrimental. These circumstances are not captured by design provisions. It is clear that more research is needed to explain better SSI effects.

In engineering practise, there are two methods that are used to account for SSI effects; the substructure and the direct methods. The substructure method involves two independent analyses that consider kinematic and inertial interaction effects separately. This method facilitates the physical interpretation of SSI effects and can be easily employed with existing numerical tools. Kinematic interaction is considered by reducing the free-field motion at the foundation levels by employing analytical solutions (e.g. Veletsos and Prasad 1989, FEMA 2015). As far as inertial interaction effects are considered, the simplest application of the substructure method is the use of SDOF fixed-base models that have an increased structural natural period and damping of the first mode of oscillation. Another way to apply the substructure method is to employ flexible-based structures where the soil compliance is modelled using frequency dependent springs and dashpots at the foundation positions (e.g. Gazetas 1983; 1991). The spring and dashpots properties were derived based on a number of assumptions, using analytical, semi-analytical formulations and finite element models. The analytical formulations assume that frictional shear tractions cannot develop during vertical and rocking vibrations, while for horizontal vibrations the normal tractions at the interface are assumed to be zero. The analytical, semi-analytical formulations and finite element models that are employed for the calculation of the dynamic stiffness and dashpot properties are typically based on the assumptions of massless, rigid foundations that are subjected to machine-type loading. Foundations rest on a homogeneous half-space, or on a soil stratum underlying bedrock or a half-space. These assumptions limit the reliability of the substructure method as they are unrealistic for most engineering structures. Additional limitation of models that consist of SDOF structures that are either fixed or flexible at their base, is that they are applicable only for structures whose response is dominated mainly by the first mode. Few substructure approaches involve frequency domain analyses. For example, in modal analysis the response is estimated as the superposition of uncoupled vibration modes that are computed independently. An important limitation of this method is its inability to reproduce wave propagation and therefore soil material and radiation damping. An equivalent-linear substructure approximation method in the frequency domain was developed to overcome the latter limitation and approach soil nonlinearity. It employs Fourier transforms to approximate loading time series and it calculates the total response by adding the solution of each harmonic. However, neither modal analyses nor equivalent linear analyses are applicable for non-linear systems, as they use superposition and they do not account for soil nonlinearity that is resulted from structural response.

The most rigorous approach for SSI systems is the direct method. This method simulates soil-structure interaction in a single step in the time domain and overcomes the limitations of the frequency domain

methods. Limitations of this method are the large number of degrees of freedom and the computational time needed for analyses to run. Thus, sophisticated 3D analyses are very scarce in the literature. More importantly literature lacks 3D finite element methodologies that are validated against field real-scale SSI experiments and account for nonlinear soil behaviour realistically. This is one of the motivations for this research programme.

The first objective of the research programme run by Imperial College London is to investigate key parameters of SSI by using data from the real-scale experiments conducted in collaboration with Aristotle University of Thessaloniki (AUTH). The advantage of these experiments over other similar studies which can be found in the literature (e.g. Barros and Luco 1995; Tileyliloglu 2008), is the large number of instruments (e.g. seismometers, accelerometers) that were installed on both the structure and soil. These instruments allow the detailed examination of the structural response, as well as the thorough investigation of the soil response. Appreciating the complexity of SSI effects, sets of real-scale experiments were carefully designed to identify and characterise the main factors that affect SSI phenomena. The experiments involve forced and free vibrations, involving inertial interaction effects of structures founded on shallow foundations. In comparison with other experiments, which involve both inertial and kinematic effects, for example structures subjected to seismic excitations, the present set of experiments allows to focus on inertial effects. The structural design of the current research programme allows the reconfiguration of the structure's dynamic properties, stiffness and mass. The examined structure was exposed to free and forced vibration tests, and during the latter tests, sinusoidal forces of different frequencies and magnitudes were applied. Therefore, the design of the experiments allows the separate investigation of factors that, as generally accepted, influence the severity of SSI effects. These factors are structural mass, structural stiffness, motion frequency content and motion intensity.

The second aspect of this research programme is related to the numerical modelling of dynamic soil-structure interaction effects. The objective is to simulate the carefully designed set of real-scale experiments, with a rigorous modelling of both the soil behaviour and structural aspects. The developed numerical model is validated against the SSI experimental data, while the model calibration will be based on previous site investigation campaigns (Pitilakis et al. 1999, Raptakis et al. 2000, Pitilakis et al. 2014). The numerical analyses are carried out by using the bespoke software, Imperial College Finite Element Program (ICFEP) (Potts and Zdravković 1999) which includes state-of-the-art features for the modelling of geotechnical problems. In order to capture the soil-structure interaction effects, a 3D numerical model will be developed, consisting both the structure and the soil and accounting for soil nonlinearity. Such simulations involve many challenges such as the exact spatial discretization of both the structure and the soil, the use of boundary conditions which will ensure a realistic wave propagation over a wide range of frequencies. Another challenging aspect is the investigation of the effect of soil nonlinearity on the response of the SSI system. Finally, comparisons will be made between results of 2D and 3D models and between numerical analyses, analytical and simplified approaches that are used in practice. The comparisons will allow the examination of the extent to which the use of those approaches which are currently used in engineering practice is acceptable.

In summary, the aim of the project is to provide results supported by both experiments and numerical analyses to enrich the current knowledge in the field of Soil-Structure-Interaction. The main ambition of this research is to establish newly validated advanced 3D FE modelling procedures that will guide numerical studies of SSI problems. The validation procedure will also provide guidance on the performance of different constitutive models and the use of boundary conditions for direct SSI simulations. In addition, the project will improve the general understanding of the inertial interaction mechanism and give an insight on the impact of structural rocking. Finally, it will provide guidance on

the adequacy of 2D plane strain approximation and the range of applicability of simplified approaches used in practice to study dynamic SSI problems.

9.2.2 EUROPROTEAS

Structure

EuroProteas prototype structure was particularly designed to mobilize strong interaction with its foundation soil as it is a stiff structure with a large superstructure mass founded on soft foundation soil. EuroProteas is a perfectly symmetric and reconfigurable structure. It is founded on a square reinforced concrete slab (C20/25) with dimensions 3.0m x 3.0m x 0.4m which rests on the ground surface. The superstructure mass consists of two identical to the foundation reinforced concrete slabs that are supported by four square hollow steel columns (QHS 150 x 150 x 10mm) which are clamped on the foundation. L-shaped (100 x 100 x 10mm) X-braces are connecting the steel columns in all the sides of the structure ensuring its total symmetry. Assuming a uniform unit weight of 25kN/m³ for the concrete, the total mass of each slab is estimated at 9.16Mg, while the total mass of the structure is calculated approximately at 28.5Mg. Its outer dimensions are 3.0m x 3.0m x 5.0m (Figure 448).

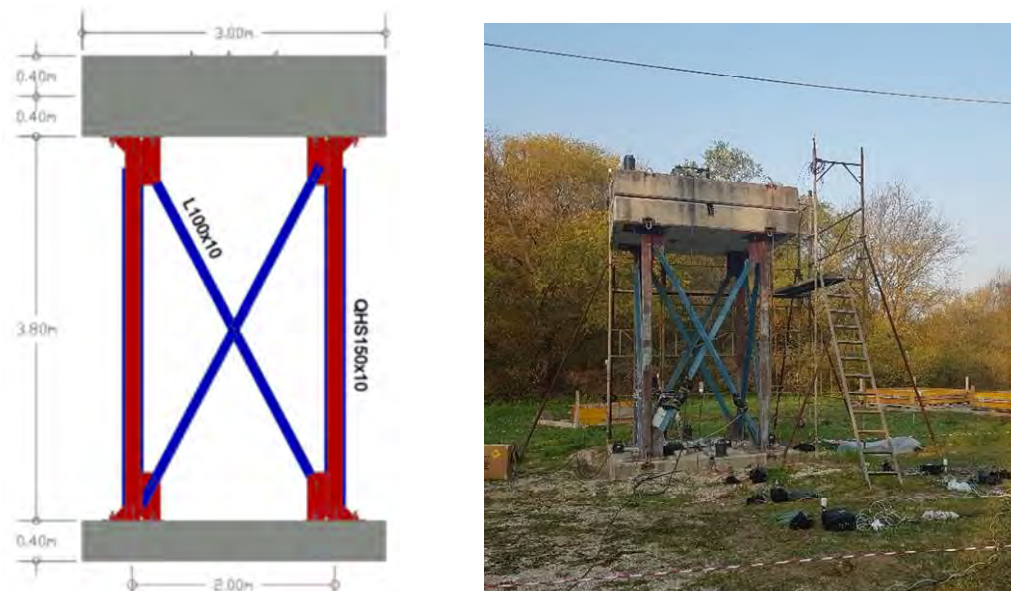


Figure 448: A 2D sketch and a view of EUROPROTEAS prototype structure

The bracing system and the upper roof slab of the structure are removable allowing the modification of the mass and/or the stiffness. Depending on the number of the roof slabs and the arrangement of the X-bracing system the fixed-base frequency of EuroProteas covers a range between 1.78Hz and 13.06Hz as calculated numerically (Pitilakis et al. 2018).

Foundation Soil

The foundation soil is well investigated and reported in earlier studies. Specifically, between 1993 and 2004, an extensive program of seismic prospecting and geotechnical testing was undertaken (Pitilakis et al. 1999). It comprised of in-situ (sampling boreholes, Standard and Cone Penetration Test measurements) and laboratory (conventional classification tests, strength tests, consolidation tests and resonant column and cyclic triaxial tests) geotechnical surveys. The elaboration of all geophysical and

geotechnical data, led to the classification of the main soil formations, validation of soil properties stemming from different methodologies and design of representative 1D, 2D and 3D soil models.

Additional field investigation of the test site was undertaken prior to the construction of the structure in the framework of the European project "Seismic Engineering Research Infrastructures for European Synergies, SERIES" including Standard Penetration Test measurements, downhole tests, sampling according to EC7 regulations, resonant column and cyclic triaxial tests. The small stiffness of the top soil layer is pronounced by the low recorded NSPT values down to a depth equal to two times the foundation width. Close to the soil surface the shear wave velocity is estimated approximately at 100m/s (Figure 449). A detailed report on the geotechnical and geophysical data derived from this investigation is presented in Pitilakis et al. (2018).

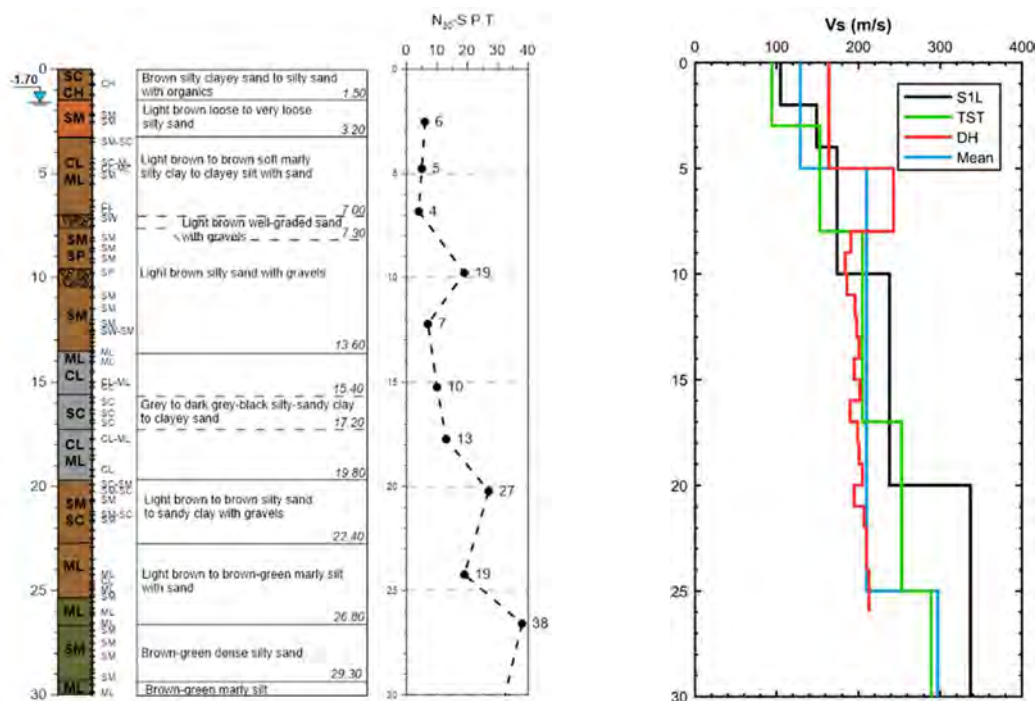


Figure 449: Soil stratigraphy of the 30m deep borehole at the geometrical center of the foundation, the N_{SPT} blow counts and the Vs profile as derived from down-hole (DH) tests prior to the construction of EuroProteas (Pitilakis et al. 2018) compared with the Vs profile at S1L site approximately 50m south of EuroProteas (Raptakis et al. 1998), a reference mean Vs model of the valley cross-section (Raptakis et al. 2000) and the proposed Vs profile by Pitilakis et al. (1999)

9.2.3 Numerical model

Due to the complexity of a full 3D numerical model of SSI, a set of preliminary 2D sensitivity analyses are undertaken to explore several aspects of the SSI response before developing the 3D model. The experiment that is chosen to be simulated first by the 2D model is the one that gives the smallest structural motion in the direction perpendicular to the loading direction. This experiment is the one where the structure was partly-braced, the loading was applied along the structure's weak axis and the load frequency was up to 3Hz.

Figure 450 shows the 2D mesh along with the model dimensions and the boundary conditions for the dynamic analysis. The superstructure of the system consists of a concrete top slab of mass 18Mgr and dimensions 3.00m x 0.80m. The top slab is supported by beam element columns of 3.8m length which

are connected to the concrete foundation slab that has 9Mgr mass and dimensions 3.00m x 0.40m. The concrete slabs are discretized with 8-noded quadrilateral solid elements, while 3-noded beam elements are employed for the structural columns. All the structural members are assumed to behave elastically, the incorporated elastic structural properties are selected based on the design provisions (EN 1992, 1993), while a target damping ratio of 2% is assumed for the beam elements adopting a Rayleigh damping formulation. As Figure 450 shows, a unidirectional sinusoidal force is applied at the centre node of the top slab in the tangential direction. The magnitude of the vibrator's force is calculated as described in Pitilakis et al. (2013).

The simulated soil domain has dimensions 23m x 10m, is fixed at the lower corners of the mesh and viscous dashpots are applied along the horizontal and vertical directions of the boundaries. The selection of the dimensions of the soil domain and the imposition of the dashpots aim to model the geometric spreading of energy from the structural response. The extent of the vertical boundaries was decided based on the interpretation of the experimental data. The data recorded by the instruments that were located on the soil surface has shown that most of the motion in the soil surface is dissipated at a distance of 6m from the edge of the base slab. Unlike vertical boundaries, the depth of the horizontal boundary cannot be decided based on the experimental data. The experimental data has shown that the soil motion amplitude recorded underneath the centre of the foundation at a depth of 1.50m was dissipated by approximately 30% in comparison with the motion at 0.80m depth. However, the experimental data cannot provide the extent of the stress bulbs underneath the foundation, therefore, the depth of the horizontal boundary was decided based on past studies. A numerical analysis study conducted by Heidarzadeh, Mylonakis and Stewart (2015) for a similar experimental configuration showed that the computed motion can be significant within the soil domain up to 10m depth from the foundation due to constructive and destructive wave interference.

As Figure 450 shows, the soil domain consists of three soil layers. The free-field soil profile and properties are calibrated based on geotechnical and geophysical surveys conducted in the past (Pitilakis et al. 1999, Raptakis et al. 2000, Pitilakis et al. 2014), as well as based on site response analyses. The soil properties were based on site response analyses which simulated recorded strong motion data. These sets of data were recorded over the last 25 years by a downhole array of accelerometers that is permanently installed in the field near the structure. The soil domain is discretized with 8-noded quadrilateral solid elements. The dimensions of the solid elements are decided according to Kuhlemeyer and Lysmer (1973), so that the frequencies in the range of interest can be captured by the numerical model. The numerical model aims to reproduce the recorded experimental data of both the soil and structure, however, at the first stages of model calibration, more attention is paid on the structural response. Therefore, for the preliminary analyses, the soil is assumed to behave elastically while inelastic constitutive models will be incorporated in the model in a subsequent stage.

One of the most challenging parts of SSI numerical models is the simulation of the interface between foundations and soil, that allow horizontal displacements and rocking of foundations. For this purpose, interface elements (Day and Potts 1994) are employed at the soil-foundation interface. The interface elements are coupled with Mohr-Coulomb plasticity model in which zero cohesion is incorporated. This configuration prohibits any tensile stresses to develop at the interface between the soil and the foundation and allows the uplift of the foundation. Parametric analysis conducted so far has investigated the impact of the interface elements' properties which are the shear and normal stiffness. Preliminary results of these analyses highlight the significant impact of these parameters on the structural and soil response.

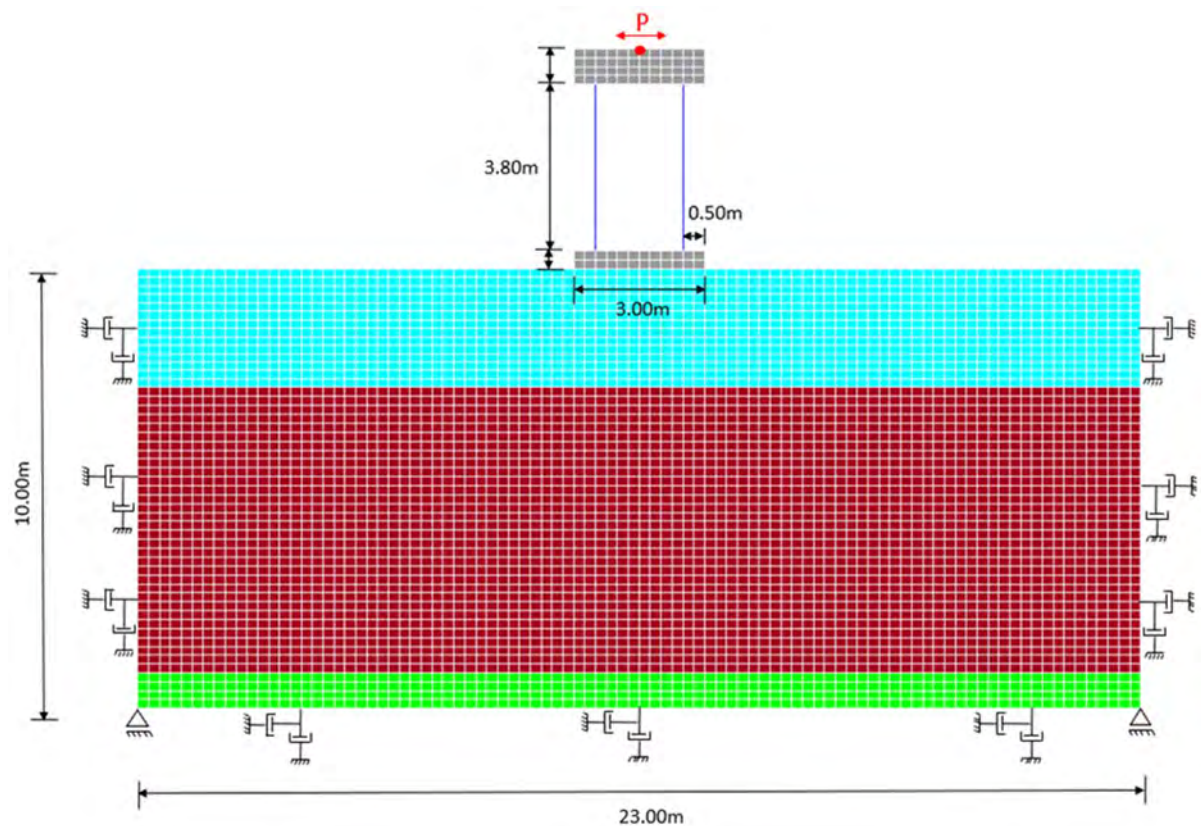


Figure 450: Mesh of the preliminary 2D model

9.2.4 Test setup

Instrumentation

The general instrumentation scheme was designed particularly to capture the response of the structure and the foundation in both in-plane and out-of-plane direction as well as the soil surface response in the same directions and also below the foundation. The instruments used are:

- 5 triaxial accelerometers GMG-5T (Guralp)
- 4 triaxial accelerometers CMG-5TCDE (Guralp)
- 1 borehole triaxial accelerometer CMG-5TB (Guralp)
- 6 digital broadband seismometers CMG-40T (Guralp)
- 6 digital broadband seismometers CMG-6TD (Guralp)
- 1 3m long shape acceleration array (SAAR) (Measurand)

The instrumentation layout of the structure is presented in Figure 451. Three different instrumentation configurations of the soil were implemented in the experiments as shown in Figure 452. Instrumentation configuration (a) aimed to record the motion near the corners of the foundation slab where large strains were anticipated to be induced. Configuration (b) aimed to examine the validity of plane strain approximation and to evaluate the potential applicability of the axis of symmetry in a future numerical model. Finally, configuration (c) aimed to assess the energy dissipation and damping (decay) with distance along both in and out of plane directions. All the instruments were configured at a sampling frequency of 200 Hz and were connected to external global positioning system (GPS) antennas.

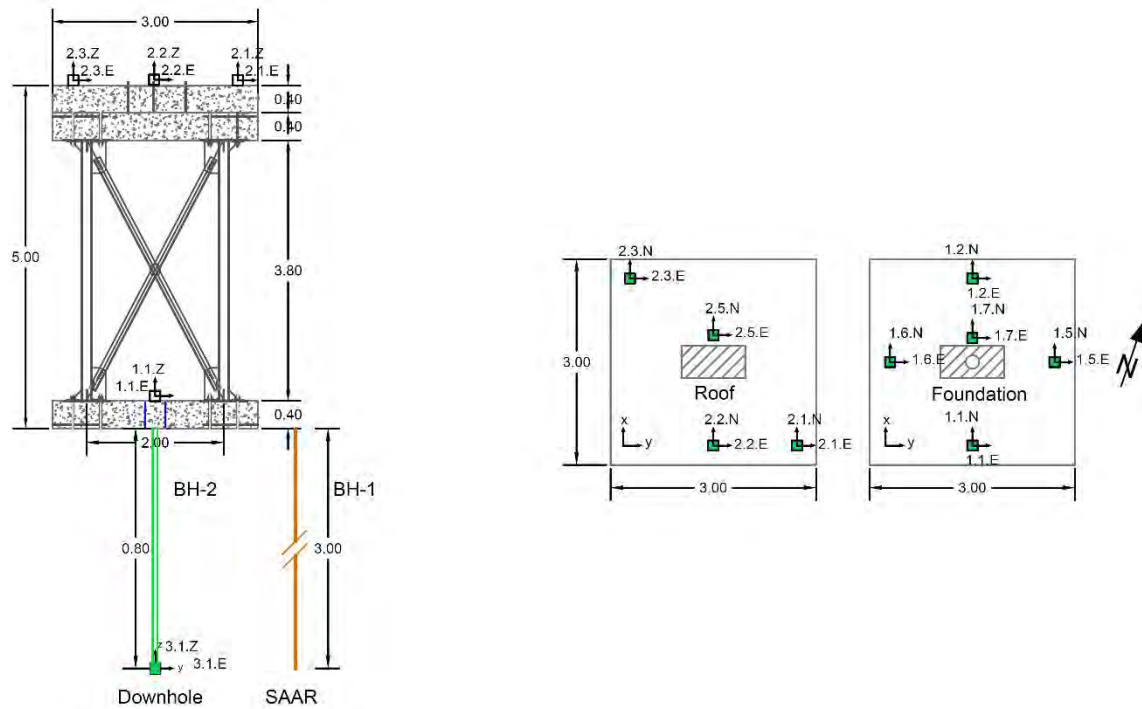


Figure 451: A cross-section and a plan view of the instrumentation layout of EUROPROTEAS structure

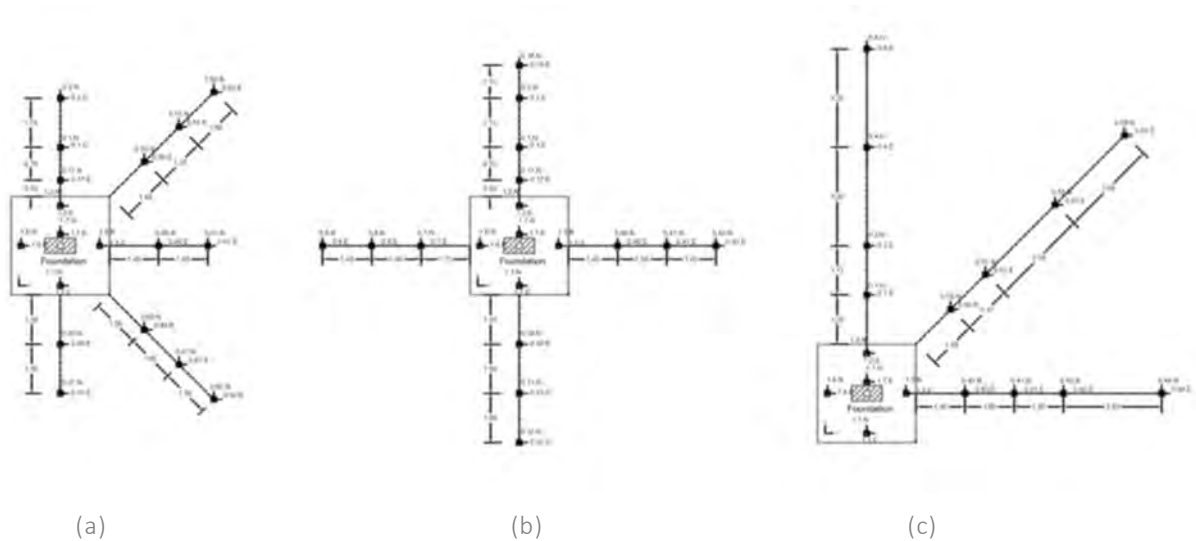


Figure 452: Plan view of the three different instrumentation layouts (a), (b) and (c) of the soil surface around EUROPROTEAS structure

Forced-Vibration tests

The eccentric mass shaker MK-500U owned by the Institute of Engineering Seismology and Earthquake Engineering (ITSAK) was implemented as a source of harmonic excitation. It is a portable uniaxial dual counter-rotating shaker that can produce a maximum force amplitude of 5 tons in a frequency range between 0.1-20Hz. Eight mass plates in four different sizes (A, B, C and D) can be used in pairs to adjust the eccentricity of the shaker and hence the output force. The amplitude of the output force of the shaker is given by Eq. (1)

$$F = E(2\pi f)^2 \quad (1)$$

where F is the shaker output force in Newtons, E is the total eccentricity of the shaker in kg-m and f is the rotational speed of the shaker in Hz.

The eccentric mass shaker was placed at the geometrical centre of the top roof slab of the structure and it was orientated to produce a force having a direction that formed an angle of 30 degrees with the magnetic North.

Free-Vibration tests

Pull-out forces were applied on the roof of the structure by a wire rope. A load cell, with which the applied tension force was measured, was attached to the roof slab and to the one end of the rope. The other end of the wire rope was attached to a wire rope pulling hoist having a working load limit of 32kN. The pulling hoist was clumped to a buried counterweight of 3 tons. The total length of the wire rope was 27m.

9.2.5 Observation during testing

Forced Vibration tests

Some of the SSI effects were clearly observed. The most prominent indication of the interaction between the structure and the soil due to soil compliance was that foundation rocking could be easily observed during most of the experiments. The most noticeable impact of soil compliance on the structural response is the lengthening of the predominant period of the soil-structure system. When the structure was braced at all four directions (configuration A) the first natural frequency of the system is approximately 3Hz, while for the corresponding fixed-base structure the fundamental resonance is at 9Hz (Pitilakis et al. 2014, 2018). A similar resonance frequency value of 3Hz was observed during the experiments where the structure was braced at two sides only and the force was applied along the braced plane (configuration B). In contrast, the lengthening of the predominant period of the structure with the same configuration loaded at its weak axis (configuration C) was much smaller. The first natural frequency of this structure was observed to be around 1.33Hz, while the corresponding fixed base structure would have a natural frequency of around 2Hz (based on a simplified SDOF model). Therefore, the first resonance of this structure is less affected by the SSI effects than the fully-braced structure. This observation is in agreement with the generally accepted theory that stiffer structures are affected more by SSI phenomena. It should be noted that during the experiments, higher modes of oscillation were also observed as explained in the next paragraphs. A consistent feature for all the experiments was that for the same structural configuration, the natural frequency of the system was smaller when the vibrator was rotating with larger eccentricity, which produces larger applied forces. These larger applied forces can produce larger nonlinearity at the foundation base. The nonlinearity refers to the detachment of the foundation from the soil, which makes the overall system more flexible.

The first mode of oscillation for the fully braced structure consisted of structural motions in both directions parallel and perpendicular to the loading direction. This can be probably attributed to SSI system's imperfections, and the high stiffness of the braces that resist the structural oscillation along the planes where they are placed, which makes the diagonal axis the most flexible. On the contrary, the structural oscillation was observed to be different when the structure had an obvious weak axis. When the partly braced structure was loaded along either its weak axis (NS) or strong axis (EW), the first mode of the structure was a translational oscillation along the loading direction only.

As mentioned above, higher modes of oscillation were also observed on site. These could be identified by an abrupt increase or change in the structural motion. A higher mode of oscillation, for the fully-braced structure, was observed around 7Hz where torsion became apparent. For the partly-braced structure loaded along its weak axis, it was observed that at a frequency around 5Hz, an out of plane motion was initiated, implying that a higher mode of resonance was achieved. Finally, for the same structural configuration loaded along the strong axis of the structure, a higher mode of oscillation appeared at 5-6Hz. It is worth to mention that for this frequency range, the motion perpendicular to the loading direction was observed to be more pronounced than the motion parallel to the loading direction.

On site observations during the experiments verified the general accepted idea that stiffer structures interact more with the soil. The foundation rocking and translation was much weaker during the experiments with configuration C than during the experiments with configurations A and B. Therefore, it is evident that both structural stiffness and loading direction affect the decision whether SSI effects are important or not. This claim is further invigorated in the next section.

Free Vibration tests

Conclusions based on visual inspection during free vibration tests were achieved by comparing the structural response between experiments. The most important observation has to do with the damping of the soil-structure system. When the structure was fully braced, for the same pull-out force, the initial displacement and the duration of the motion of the structure were much smaller than the ones of the partly-braced structure. This is ascribed to the fact that more flexible structures interact less with soil and therefore, soil compliance contributes less to the increase of the system's damping. The increase of damping of a soil-structure system comes from the radiation damping. This type of damping is the most important damping mechanism for most of the cases where SSI effects are significant. Apart from the excess radiation damping of the stiffer system, the difference in the structural response of the flexible and stiff systems is attributed to the existence of braces which limit the initial displacement and increases further the damping of the system. Therefore, the system's damping for the braced structure is larger and the motion is damped quicker than for the case of the partly braced structure.

9.2.6 Results

System identification was the main aim of the data post-processing that is conducted so far. More specifically, the resonance frequencies of the different structural configurations and loading directions were investigated quantitatively, while damping was investigated qualitatively. The results presented herein refer to experiments where the structure's top mass consists of two slabs. The data from the tests on the structure with one top slab have not been processed yet.

Forced Vibration tests

In order to identify the natural frequencies of the soil-structure system, this study uses the acceleration time histories recorded during the forced vibration tests and Fourier spectra of the structural motion recorded during free vibration tests. This system identification procedure is simple, comprehensive and exploits the advantages of forced vibration tests over earthquake records or ambient noise tests. These advantages are that the recorded structural motions are periodical and do not contain high frequency peaks.

Natural frequencies can be identified through acceleration time histories at the frequency where there is an abrupt increase in the acceleration values. This is illustrated as an example in Figure 453 which presents acceleration time history recorded by an instrument located at the edge of the top slab of the fully-braced structure during a forced vibration test. During forced vibration tests, the applied frequencies were kept constant for a certain time period and then they were increased by a prescribed value. Each step shown in the Figure 453 corresponds to a different applied frequency. During free vibration tests, structures oscillate at their natural frequencies. Therefore, natural frequencies can be identified from the ordinates that correspond to peaks of Fourier spectra of the structural motion (Figure 454). It should be noted though that in order to identify all the system's natural frequencies that were triggered during the experiments, different records from different positions of both top and base slab should be investigated. In most cases, all records of all the North-South, East-West and vertical motion directions should be exploited. Natural frequencies can be even identified from soil records, although time histories recorded in the soil contain high frequency motion that may make the conclusions uncertain (Figure 455). It should be noted that the accuracy of this method is dependent on the frequency step taken during experiments. In the conducted experiments, this step was sufficiently small to allow accurate identification of the fundamental frequencies for the purpose of the project.

Table 65 compares the natural frequencies identified by employing the described system identification procedure that exploits the data recorded during the experiments of different configurations (A, B and C). It shows the natural frequencies observed from acceleration time histories recorded by instruments at different locations during forced-vibration tests, as well as from Fourier spectra of the structural motion recorded during free-vibration tests. During the experiments, different structural modes of oscillation were observed. Each mode corresponds to a certain frequency which is indicated in the table by different colour. It can be seen that the same colours are repeated for the different experimental configurations, meaning that a structure may retain some of its natural frequencies even when its stiffness or the loading direction change. It is found that the frequency of the first mode of oscillation of configuration A is similar to the one of the first mode of configuration B as well as to the frequency of the second mode of configuration C. The similarity is ascribed to the fact that during these frequencies the structural oscillations of the three cases were similar. Comparing the experiments where the only difference was the loading direction, during the first mode of configuration B and the second mode of configuration C, the structure was oscillating parallel to the braced plane. Therefore, in both cases, these modes triggered the stiffness of the braces. The first mode of oscillation of the fully braced structure was similar to the above two modes as well. Although, for the first mode of this configuration the structural motion existed in both directions parallel and perpendicular to the loading one, the motion along the former direction was much stronger than the other one. Thus, for all three cases, the structural oscillations triggered similar structural stiffness, which was the reason that the three examined resonance frequencies were similar. The observation that the same modes of oscillation were observed at the same frequency during the three experiments implies that modes of oscillation control the stiffness involved in structural response and therefore the natural frequencies of the certain modes.

It can be observed from Table 65 that some natural frequencies cannot be identified by processing records of the motion parallel to the loading direction (in-plane), but they can be identified by the transversal (out of plane) or the vertical one. Also, for the unbraced structure loaded along its strong axis, some natural frequencies may be associated more to the base slab motion than to the top slab. Finally, Table 65 shows that Fourier spectra of the free vibration tests data give a relatively wide range of natural frequencies. During these tests various magnitudes of pull-out forces were applied on the top slab, which gave different initial vertical and horizontal displacement of the top and base slabs. For

larger pull-out forces the detachment of the base slab from the foundation soil is larger and more rocking takes place, which makes the SSI system more flexible.

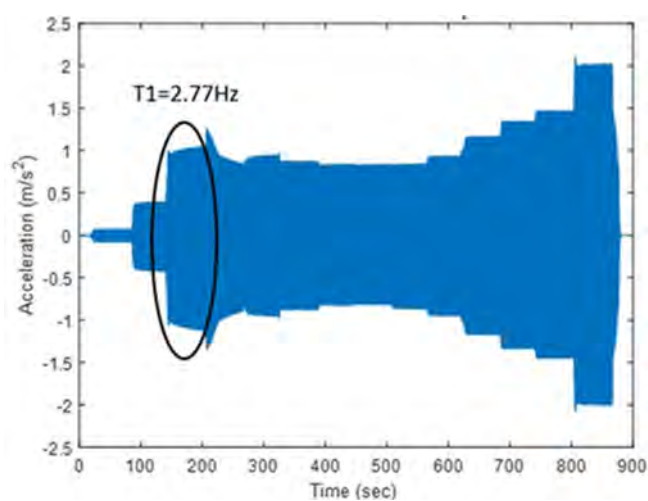


Figure 453: Acceleration time history recorded by an instrument located at the edge of the top slab of the fully-braced structure during a forced vibration test. The first frequency of the resonance is indicated

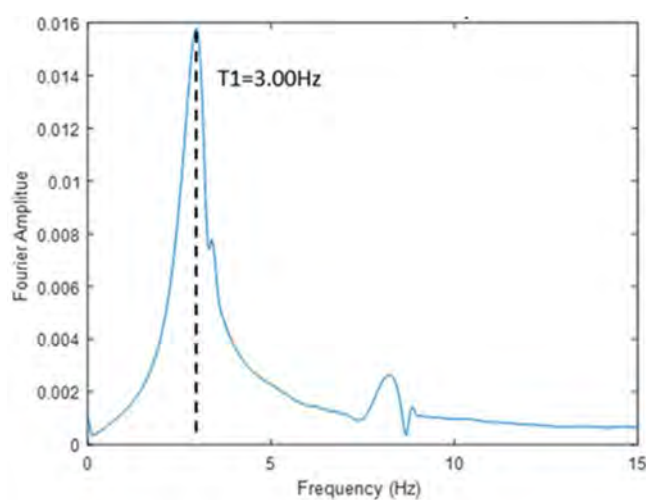


Figure 454: Fourier spectra of data recorded by an instrument mounted at the edge of the top slab of the fully-braced structure during a free-vibration test. The frequency of the first resonance is indicated

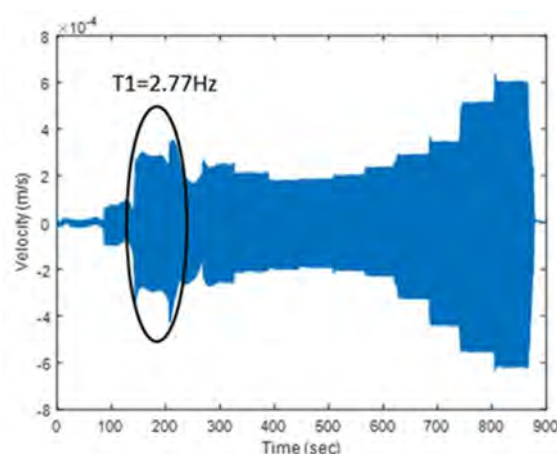


Figure 455: Velocity time history recorded by a soil instrument located near the foundation of the fully-braced structure during a forced vibration test. The frequency of the first resonance is indicated

9.2.7 Conclusions and outlook

The envisaged experiments were successfully conducted and provide meaningful results. Some of the experiments were repeated more than once. By comparing the results of those experiments to each other, it is verified that the results are reliable, while most of the instruments worked properly during the experiments. The carefully designed locations of the instruments have facilitated the system identification and the post processing of the data which has been completed to a large extent. This research programme is a promising opportunity to provide useful insights of inertial SSI effects and a fully validated procedure for the numerical modelling of such problems.

The experiments have verified that the frequency, magnitude and direction of the input motion, as well as the structural stiffness play a significant role on the response of SSI systems. For the purpose of the experiments a wide range of frequencies were applied on the structure that triggered different modes of oscillation. It was shown that the soil-structure system becomes more flexible for larger load magnitudes due to larger foundation nonlinearity. From the free vibration tests, it was observed that the stiffer structure interacted more with the soil, than the flexible one, and this higher interaction produced higher damping for the system. Interestingly though, forced vibration tests have shown that the structural stiffness is not the only factor that determines the amount of interaction of structures with soil, but it should be combined with the mode of oscillation. The interaction is dependent on the structural stiffness that is triggered during a certain mode of oscillation. The damping of the system has not been quantified yet, but it will be assessed harvesting the data from the free vibration tests.

This study exploits the experimental data to develop a rigorous 3D finite element model for SSI problems which will be fully validated against the field experiments. A first preliminary numerical 2D model is currently developed which enables to do sensitivity analyses on a number of important numerical aspects (e.g. properties of interface elements, model dimensions and boundary conditions, optimisation of structural elements). Once this preliminary phase is completed the next milestone is the setup of the 3D model.

	Configuration A: Fully-braced structure		Configuration B: Partly-braced structure loaded at its strong axis			Configuration C: Partly-braced structure loaded at its weak axis			
	F1 (Hz)	F2 (Hz)	F1 (Hz)	F2 (Hz)	F3 (Hz)	F1 (Hz)	F2 (Hz)	F3 (Hz)	F4 (Hz)
Top slab acceleration time histories. In-plane motion direction	2.77	-	3-3.23	5.03	-	1.33	-	-	-
Top slab acceleration time histories. Out of plane motion direction	2.97	8	3-3.23	5.03	-	1.33 (not clear)	3.5	-	6
Top slab acceleration time histories. Vertical motion direction	2.77	7.00	3.23	5.03	-	1.33 (not clear)	3.5	-	7
Base slab acceleration time histories. In-plane motion direction	2.77	8	3.03 (not clear)	5.03	-	1.33 (not clear)	3.5	-	7.5
Base slab acceleration time histories. Out of plane motion direction	2.77	8	3.03	5.03	7	1.33 (not clear)	3.5	-	7.5
Base slab acceleration time histories. Vertical motion direction	2.77	-	2.77	5.03 (not clear)	7 (not clear)	-	3.5	-	8
Fourier amplitude spectra of Free vibration tests	3-3.4	8.6-9.2				1-1.14	3.15-3.4	5.2-5.8	7.3-7.5

Table 65: Natural frequencies as observed from acceleration time histories recorded during forced vibration tests and Fourier spectra from data recorded during free vibration tests. Results are presented as obtained from recorded motions in the directions parallel (in-plane) and transversal (out of plane) to the loading one; and in the vertical direction

9.2.8 References

- Barros F.C.P. De and Luco J.E. (1995). Hualien containment model, *Soil Dynamics and Earthquake Engineering*, 14(94): 229–248.
- British Standards Institution (2004) *BS EN 1992-1-1:2004. Eurocode 2. Design of concrete structures. General rules and rules for buildings.*
- British Standards Institution (2005) *BS EN 1993-1-1:2005, Eurocode 3. Design of steel structures. General rules and rules for buildings.*
- Day, R. A. and Potts, D. M. (1994) ‘Zero thickness interface elements—numerical stability and application’, *International Journal for Numerical and Analytical Methods in Geomechanics*, 18(10), pp. 689–708. doi: 10.1002/nag.1610181003.
- EUROSEISTEST (EV5V-CT.93-0281). Volvi – Thessaloniki: a European test-site for engineering seismology, earthquake engineering and seismology. Funded by the European Commission, Directorate General XII for Science, Research and Development, (Environment and Climate Programme: Climate and Natural Hazards Unit), 1993-1995.
- FEMA P-1050 (2015) ‘NEHRP Recommended seismic provisions for new buildings and other structures’, *Building Seismic Safety Council*, II, p. 388. doi: 10.1017/CBO9781107415324.004.
- Gazetas, B. G. (1991) ‘FORMULAS AND CHARTS FOR IMPEDANCES OF SURFACE AND EMBEDDED FOUNDATIONS’, *Journal of Geotechnical Engineering*, 117(9), pp. 1363–1381.
- Gazetas, G. (1983) ‘Analysis of machine foundation vibrations: State of the art’, *International Journal of Soil Dynamics and Earthquake Engineering*, 2(1), pp. 2–42. doi: 10.1016/0261-7277(83)90025-6.
- Heidarzadeh, B., Mylonakis, G. and Stewart, J. P. (2015) ‘Stresses Beneath Dynamically Applied Vertical Point Loads’, in *6th International Conference on Earthquake Geotechnical Engineering*.
- Kuhlemeyer, R. L. and Lysmer, J. (1973) ‘FINITE ELEMENT METHOD ACCURACY FOR WAVE PROPAGATION PROBLEMS’, *Soil Mechanics & Foundations Div*, 99(sm5), pp. 421–7.
- Mylonakis, G. and Gazetas, G. (2000) ‘Seismic soil-structure interaction: Beneficial or detrimental?’, *Journal of Earthquake Engineering*, 4(3), pp. 277–301. doi: 10.1080/13632460009350372.
- Pitilakis, D. *et al.* (2014) ‘System identification of soil-foundation structure systems by means of ambient noise records: the case of Europroteas model structure in Euroseistest’, *Proceedings of the Second European Conference on Earthquake Engineering and Seismology (2ECEES)*, (August), pp. 1–11.
- Pitilakis, D. *et al.* (2018) ‘Field evidence of SSI from full-scale structure testing’, *Soil Dynamics and Earthquake Engineering*. Elsevier Ltd, 112(March), pp. 89–106. doi: 10.1016/j.soildyn.2018.04.024.
- Pitilakis, K. *et al.* (1999) ‘Geotechnical and geophysical description of euro-seistest, using field, laboratory tests and moderate strong motion recordings’, *Journal of Earthquake Engineering*, 3(3), pp. 381–409. doi: 10.1080/13632469909350352.
- Pitilakis, K. *et al.* (2013) ‘Full-Scale Testing of a Model Structure in Euroseistest To Study Soil-Foundation-Structure Interaction’, (January), pp. 1175–1188. doi: 10.7712/120113.4585.c1546.
- Potts, D. M. and Zdravković, L. (1999) *Finite element analysis in geotechnical engineering: theory*. Thomas Telford, London.
- Raptakis D., Anastasiadis A. & Pitilakis K. (1998). Preliminary instrumental and theoretical approach of site effects in Thessaloniki. In *Proceedings of the 11th European Conference on Earthquake Engineering*.



Raptakis, D., Chávez-García, F., Makra, K., Pitilakis, K. (2000). Site effects at EuroSeistest-I. Determination of the valley structure and confrontation of observations with 1D analysis. *Soil Dynamics and Earthquake Engineering*, 19, 1, 1–22.

Tileylioglu (2008) *Evaluation of Soil-Structure Interaction Effects from Field Performance Data*.

Veletsos, A. S. and Prasad, A. M. (1989) ‘Seismic interaction of structures and soils: stochastic approach’, *Journal of Structural Engineering*, 115(4), pp. 935–956.

9.3 Project # 27 – SISIFO – Seismic Impedance for Soil-structure Interaction From On-site tests

Authors

C. Amendola^(1, 2), F. de Silva⁽²⁾, F. Silvestri⁽²⁾, A. Vratsikidis⁽¹⁾, A. Anastasiadis⁽¹⁾, D. Pitilakis⁽¹⁾

⁽¹⁾ Aristotle University of Thessaloniki, Thessaloniki, Greece

⁽²⁾ Università di Napoli Federico II, Napoli, Italy

9.3.1 Introduction

It is well known since several decades that the seismic response of structures is affected by the dynamic interaction with the underlying soil (Gazetas 1983, Mylonakis and Gazetas 2000, Kausel 2010). If the foundation depth is significant, the ‘kinematic interaction’ due to the relative soil-foundation stiffness may introduce a ‘filtering effect’ on the seismic motion transmitted to the superstructure with respect to the free-field condition (Elsabee and Morray 1977). For structures founded on shallow foundations, the filtering effect is often negligible, and the soil-foundation-structure (SFS) interaction reduces to the so called ‘inertial interaction’, determined by the compliance of the soil to the structural motion. As a result, with respect to a fixed-base structure, the fundamental period of the system increases and additional energy is dissipated by downward wave radiation and soil hysteresis (Richart et al. 1970).

Simplified approaches based on the uncoupled ‘substructure method’, as well as refined complete SFS models, have been proposed in the literature to catch the effects of the inertial interaction. Finite elements or finite difference complete models are generally justified only for high-value buildings (e.g., Pitilakis and Karatzetzou 2015, de Silva et al. 2017, de Silva et al. 2018) due to the computational effort required for the analysis. In the most widespread simplified approach, also suggested by some international guidelines (e.g. BSSC 2004), the structural model is placed on translational and rotational springs and dashpots (Veletsos and Meek 1974). The stiffness of springs and the dashpot coefficients are computed on the basis of the real and imaginary parts of the frequency-dependent ‘impedance functions’, usually with reference to the fundamental frequency of the SFS system.

Numerous analytical formulations of impedance functions are available in literature for rigid shallow foundations resting on the surface of a homogeneous half-space or finite thickness layer, with linear visco-elastic behaviour. Modifications of the classical solutions were proposed by Gazetas (1991), Pitilakis and Karatzetzou (2015) and Iguchi and Luco (1982) to take into account the embedment and the deformability of the foundation, respectively. The main issue related to the use of such analytical

formulations remains the choice of equivalent values for the stiffness and the damping coefficient of the linear homogeneous soil, since the actual foundation is generally embedded in a layered subsoil with non-linear behaviour, in which the above properties vary with depth and strain level. Some authors (Gazetas 1991, Mylonakis et al. 2006, Stewart et al. 2003) suggested assuming an equivalent stiffness as the mean shear wave velocity, V_s , throughout the depth of the soil volume involved in the foundation motion, which is typically related to the foundation width. With respect to the value measured in free-field geophysical tests, the mean V_s should be in principle corrected to account for the overburden pressure induced by the structural weight and for soil non-linearity.

In the analysis of existing buildings, the introduction of equivalent properties often represents a difficult issue, since the geometry of the foundation is usually unknown and the properties of the underlying soil are, on the average, not fully documented.

Laboratory-scale investigations on the SFS interaction are usually performed by shaking table and centrifuge tests (Richart and Whitman 1967, Dobry et al. 1986, Knappett et al. 2015). These model tests provide precious insights on the effects of the non-linear soil behavior, but they show limits in the reproduction of the radiation damping, due to the small size of the test container.

Full-scale field tests on instrumented facilities were performed to evaluate the impedance associated to horizontal translation (swaying) and rotation (rocking) in the vertical plane. The on-site investigations available in the literature provide results over a limited range of frequency (Lin and Jennings 1984, Luco et al. 1988, Wong et al. 1988) or for specific structures, such as an accelerograph station Crouse et al. 1984) and a nuclear reactor (de Barros and Luco 1995). In all cases 1) the limited resolution of the data acquisition system introduced significant noise, leading to spurious results; 2) the shear wave velocity profile was measured in free-field conditions, neglecting the stress increment exerted by the structural weight.

More recently, forced-vibration tests were executed on a steel frame prototype in California (Tileylioglu et al. 2011). The tests were executed monitoring the structural response only, without any instrument recording the soil motion. Since a very low amplitude excitation was applied, the structural motion was disturbed by the noise; the experimental data were successfully compared to analytical impedance functions in a frequency range limited to 5-15Hz.

Summarizing, the available inventory of both model and prototype tests is still limited to validate the analytical solutions on impedance functions in the range of frequency of interest for earthquake engineering. Moreover, the few and heterogeneous past experiences do not allow for individuating the most appropriate experimental layout to facilitate the computation of the impedance functions from the recorded data.

9.3.2 EUROPROTEAS

The prototype structure of EUROPROTEAS, located in the EUROSEISTEST site, was specifically designed for full-scale tests for the assessment of SFSI models. Established in the Mygdonian Valley in Northern Greece, EUROPROTEAS structural pattern was particularly addressed to mobilize strong soil-foundation-structure interaction phenomena, as it is a stiff structure founded on a soft silty sand subsoil. It consists of a simple steel frame with reconfigurable X-bracings, supported by a shallow foundation constituted by a reinforced concrete mat and overtopped by two similar portable RC slabs, resulting in outer dimensions of 3x3x5m. The perfect symmetry ensures the same bending stiffness in both vertical plane directions. The removable parts (X-bracings and upper RC slab) permit four different configurations of structural mass and stiffness, covering a wide range of natural frequencies, between 3Hz and 11Hz. The soil profile immediately below EUROPROTEAS structure was investigated by drilling

a 30m borehole at the center of the foundation slab and a 12m borehole at a distance of 0.5m from the east edge of the structure. The subsoil properties measured by on-purpose in-situ and laboratory tests are detailed in Pitilakis et al. (1999) and Raptakis et al. (2000). Summarizing, the soil profile is composed of a first layer of silty clay with sand about 7 m thick, a layer of clayey or silty sand with local contents of gravel between 7m and 22m, and a last layer of marly silt and silty sand down to a depth of 30 m. The shear wave velocity of the uppermost 5 m resulted equal to 150 m/s from a DH test and to 100 m/s from the interpretation of geophysical tests (Pitilakis et al. 1999). All the performed tests led to about the same $V_s=300\text{m/s}$ from a depth of 5 to 25 m.

The tests executed in the frame of the SISIFO project were performed on the structure with the X-bracing and both the upper reinforced concrete slabs, to maximize the available stiffness and mass. In fact, the effects of soil-structure interaction are emphasized by increasing the structure-soil relative stiffness, but numerical studies (de Silva 2020, Piro et al. 2020) highlight that a very stiff structure on soft soil behaves as a rigid block, showing negligible bending displacement. The increase of the roof mass moves the gravity center of the system closer to the roof making the structural configuration more similar to that of a single-degree-of-freedom system instead of a rigid block. Finally, the soil around the foundation was intentionally removed to reduce to zero the embedment, in order to test on a perfectly shallow footing.

9.3.3 Background

The impedance is a complex and frequency-dependent function conceived by Lamb (1904) and extended by Reissner (1936) to quantify the soil displacement under an oscillating rigid foundation. In its more classic formulation, it is composed of a real part representing the stiffness and an imaginary part accounting for the radiation damping, i.e. the energy dissipated by the waves scattering from the foundation through the soil. When the degrees of freedom of the foundation motion are more than one, the impedances are organized in a matrix, the components of which are expressed through:

$$\bar{K}_{ij} = k_{ij}(a_0)K_{ij} + i\omega c_{ij}(a_0)C_{ij} \quad (2)$$

In Eq. (2): the subscripts i,j indicate that \bar{K}_{ij} links the component i of the vector of the loads transmitted by the foundation into the soil to the component j of the displacement vector; the low-frequency stiffness, K_{ij} , and the dashpot coefficient, C_{ij} , depend on the soil shear modulus, G , and Poisson ratio, ν , as well as on a characteristic dimension of the foundation, r (for instance the radius if the geometry is circular or the half-width for a rectangular shape); the dynamic coefficients, $k_{ij}(a_0)$ and $c_{ij}(a_0)$, depend on the vibration frequency, ω , the characteristic dimension of the foundation, r , and the soil shear wave velocity, V_s , through the frequency factor, $a_0=\omega r/V_s$.

When the response of a compliant-base system is studied through the aforementioned uncoupled approach, the real part is assigned as stiffness to the base spring, while the ratio, $\xi_{ij}(a_0)$, between the imaginary and the real part leads to a damping ratio equivalent to the energy dissipated by the wave radiation:

$$\xi_{ij} = \frac{i\omega c_{ij}(a_0)C_{ij}}{2k_{ij}(a_0)K_{ij}} \quad (3)$$

Either a viscous, ξ_{vis} , or a hysteretic, ξ_{hys} , damping ratio of the soil can be added to the contribution of the radiation damping. To directly introduce the hysteretic damping through an equivalent viscosity in

the analytical impedance, Veletsos and Verbic (1973) or Liou et al (1991) replaced the elastic and real G with the complex soil shear modulus:

$$\tilde{G} = G \left[1 + i\omega \frac{\eta}{G} \right] \quad (4)$$

In Eq. (4) η is the viscous damping coefficient and $2\pi\omega \frac{\eta}{G}$ is the ratio between the energy dissipated by the viscoelastic material in each loading-unloading cycle and the energy stored by a perfectly elastic material which experiences the same load pattern. Being η constant, such ratio is frequency-dependent. Actually, laboratory tests on soils indicate that such ratio is almost independent of the frequency of the applied load, so that the product $\omega \frac{\eta}{G}$ in Eq. (4) can be substituted by $2\xi_{hys}$, which is constant with frequency but increases with the mobilized shear strain.

When a harmonic response is considered, the damping coefficient η is conveniently expressed through the critical damping ratio, ξ_{vis} , which turns to be correlated to ξ_{hys} through the frequency factor as follows:

$$\xi_{vis} = \frac{1}{a_0} \xi_{hys} \quad (5)$$

Analytical expressions for the real and complex impedance components available in the literature mostly refer to regular or irregular rigid massless foundations, more or less embedded in the soil. The latter is generally assumed to be an elastic homogeneous half-space (Pais and Kausel 1988, Gazetas 1991); nevertheless, some authors provided formulas for an elastic stratum placed on a half-space (e.g. Gazetas 1983) or a layered soil profile, even including a reduction of the shear modulus of the layer below the foundation soil deposit (e.g. Liou 1993). As usual in soil dynamics, the variation of the impedance under moderate to strong motions due to the reduction of the shear modulus can be taken into account through the equivalent-linear approach (Pitilakis et al. 2013).

Some analytical formulations accounting for different hypothesis on the soil behaviour are listed in Table 66. They were applied to the shallow square foundation of the tested prototype. The shear wave velocity was assumed equal to 100 m/s, in accordance with the in-situ value measured along the shallowest 3m layer, expected to be affected by the foundation motion. A value of $G=18350$ kPa was calculated from the assumed V_s for a soil density $\rho=1.84$ g/cm³ and a Poisson ratio $\nu=0.3$ inferred from the ratio between the volume and the shear wave velocity of the uppermost soil layer.

Figure 456 compares the variation with the frequency ratio of the real and the imaginary parts of the analytical impedance formulations associated to the swaying and the rocking modes of the foundation motion, normalized with respect to the shear modulus and the foundation half-width, B .

All the predicted analytical impedances will be compared to the experimental data.

Authors	Soil profile	Foundation type
Veletsos and Verbic, 1973	Viscoelastic – hysterethic halfspace	massless rigid disk
Pais and Kausel, 1988	Homogeneous elastic halfspace	rigid square
Gazetas, 1991	Homogeneous elastic halfspace – elastic layer	rigid with arbitrary shape
Liou, 1993	Viscoelastic layer on a layered medium	rigid square
Pitilakis et al., 2013	Equivalent-linear halfspace	rigid circular

Table 66: Soil and foundation types assumed in the analytical formulation of the impedance functions

The real part is almost flat and slightly affected by the hypothesis on the soil behaviour, if the soil is homogeneous. When there is an inversion in the shear modulus profile, the real K_x increases with frequency proportionally to the ratio between the shear moduli of the deeper softer layer and that of the foundation deposit (G_2/G_1 in Figure 456). Conversely, the real rocking impedance K_θ is more significantly influenced by the soil model and decreases systematically with frequency, except for the extreme case of an upper layer ten times stiffer than the lower, i.e. $G_2/G_1=0.1$. The imaginary parts for both the motions are proportional to the frequency factor; they are higher when the contribution of soil hysteresis or viscosity and the inversion in the G -profile is considered.

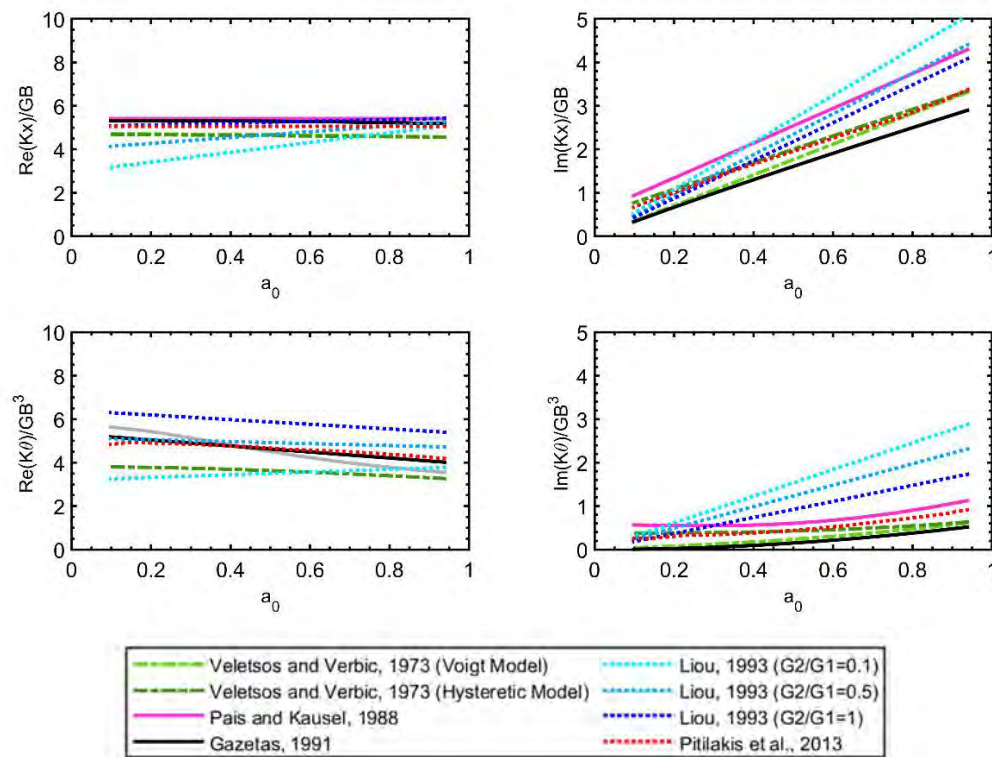


Figure 456: Real and imaginary parts of the analytical impedance functions for foundation swaying and rocking

9.3.4 Test setup

A dense 3D instrumentation network was arranged to record the structure, foundation and soil responses. Five triaxial accelerometers were mounted on the roof and four on the foundation slabs. One triaxial accelerometer was clamped inside the borehole below the foundation slab. Seven seismometers were placed on the ground surface, five along the loading direction, up to a distance of three times the foundation, whereas two were placed along the out-of-plane axis. Long-shape

acceleration arrays were deployed inside the borehole next to the foundation slab and on the free soil surface, along the loading direction. Figure 457 shows the layout of the instruments recording the response of structure and soil during the performed tests.

The dynamic response of the instrumented facility was investigated under:

1. random noise test, in which the structural response was recorded with no external excitation;
2. snap-back tests, in which the roof is slightly displaced and released to induce the free vibration of the prototype;
3. harmonic forced vibration tests, in which the frequency of the shaker force was held constant until the system achieved the steady state.

The snap-back tests were performed by a suitable pull-out equipment. In particular, the structure was displaced along approximately the NS direction, using a wire rope connected from one side to the roof and anchored from the other side on a counterweight embedded on the soil. Once the pull-out force was applied, the cable was cut at a properly dedicated section of lower thickness, and the structure underwent free vibration. The test was repeated five times (see Table 67) by increasing the force applied to displace the roof, in order to investigate on the mobilization of soil-nonlinearity.

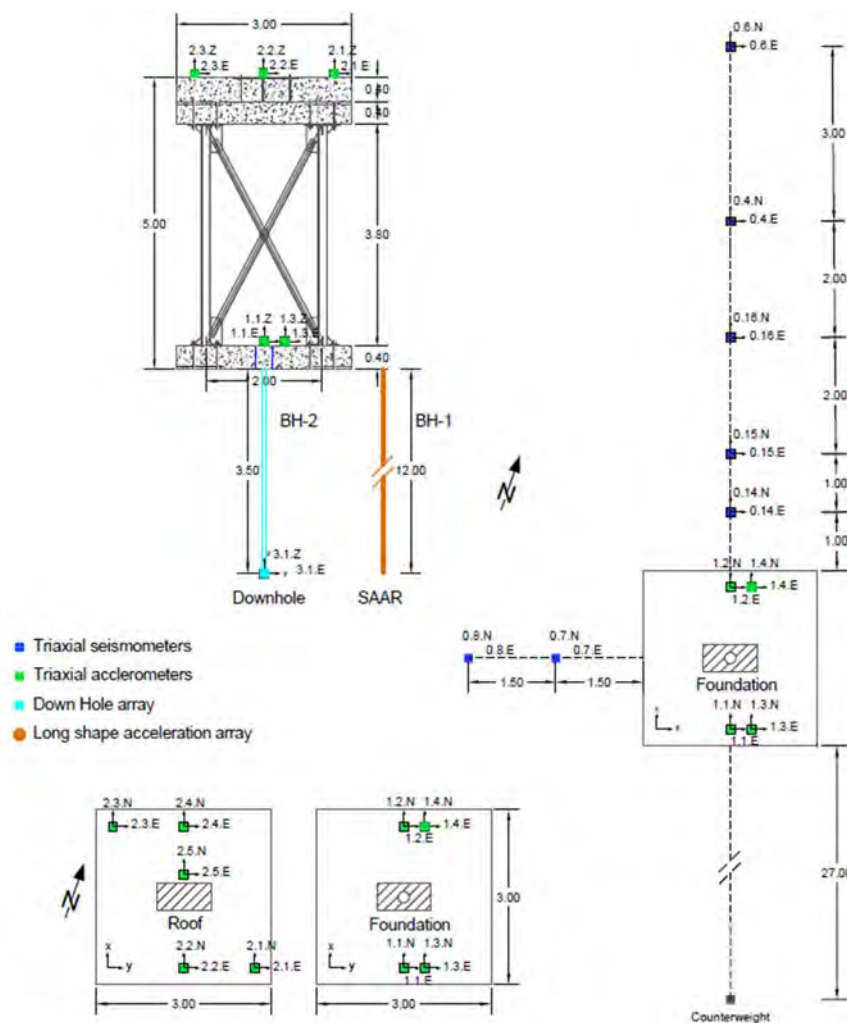


Figure 457: Layout of the instruments recording the structure and the soil response during the tests

Snap back test	A	B	C	D	E
Force (kN)	1.18	2.14	2.65	3.25	4.77

Table 67: Force amplitude applied during the snap-back tests

During the forced vibration tests, a MK-500U (ANCO Engineers Inc) eccentric mass shaker was placed in the center of the roof and of the foundation. It is a portable, unidirectional dual counter-rotating shaker, powered by an electric drive motor controlled by an adjustable speed drive. The generated harmonic load is expressed by the following equation:

$$F_s = E(2\pi f)^2 \sin(2\pi ft) \quad (6)$$

where E is the mass eccentricity, t is the time and $f=\omega/2\pi$ the frequency value. The test was repeated by changing the frequency of the excitation and the rotating mass of the shaker, as reported in Table 68. Each applied frequency was locked for 60 s and then incremented by 1 Hz steps in the range 1 Hz – 10 Hz. The frequency step was reduced to 0.5 Hz close to the first vibration mode previously identified from the noise and snap-back tests, to catch the resonance response. Eq. (6) highlights that the force amplitude grows proportionally to the square of the excitation frequency, even when the mass eccentricity is kept constant. Thus, the frequency range was intentionally stopped to 8 Hz during the experiments tagged as Forced-C and Forced-D, to avoid too high force amplitudes and a consequent excessive non-linear response. Nevertheless, the values reached by the dynamic loading force at the highest applied frequencies (see red solid lines plotted in Figure 458) significantly exceeded the static forces applied during the free-vibration tests (horizontal red dotted lines in the same figure). Evidences of non-linear effects due to the different amplitude of the applied forces will be pointed out by the comparison among the impedances back-figured from the different tests (see §9.3.6).

Experiment	Eccentricity E (-)	Frequency range $f=\omega/2\pi$ (Hz)	Force range (min-max) $E\omega^2$ (kN)
Forced-A	1.85	1-2-3-3.5-4-4.5-5-6-7-8-9-10	0.07-7.30
Forced-B	3.93	1-2-2.5-3-3.5-4-5-6-7-8-9-10	0.15-15.51
Forced-C	6.93	1-2-2.5-3-3.5-4-5-6-7-8	0.27-17.51
Forced-D	11.31	1-2-2.5-3-3.5-4-5-6-7-8	0.45-28.58

Table 68: Loading conditions during the forced-vibration tests

9.3.5 Observations during testing

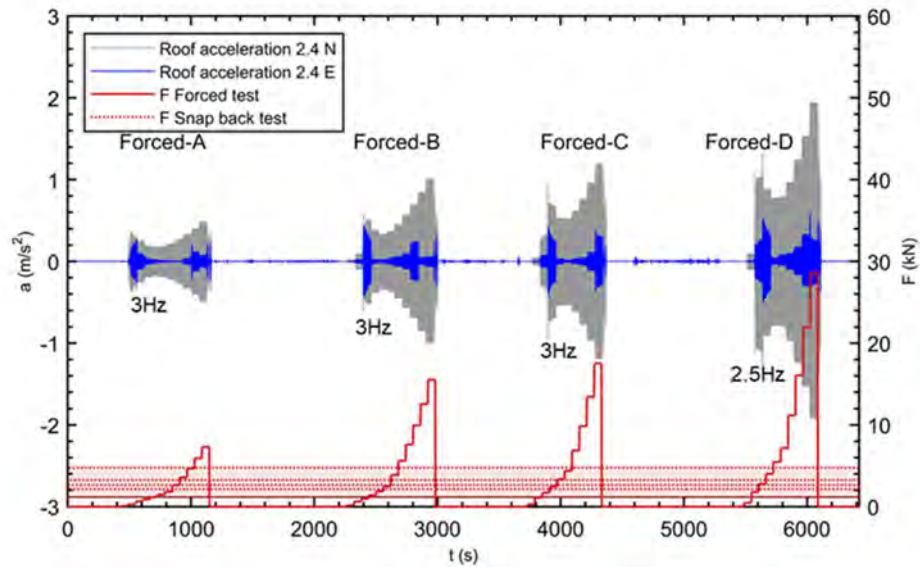


Figure 458: Time histories of the in-plane and out-of-plane roof accelerations (left axis) and loading amplitude (right axis) during the forced vibration tests (the dotted lines indicate the static forces applied during snap-back tests)

As an example, Figure 458 shows the evolution with time of the acceleration recorded by the sensor 2.4 along (2.4N) and orthogonally (2.4E) to the loading direction during the four forced vibration tests. The measured acceleration shows a sharp amplification until resonance, i.e. around 2.5 Hz and 3 Hz, after which a slight decrease and a subsequent increase are observed, in accordance with the frequency-dependent loads. The peak of the acceleration time histories at resonance occurs at slightly lower values of frequency moving from Forced-A to Forced-D, i.e. with increasing applied load: such variation highlights evidences of mobilized non-linearity. Note that the out-of-plane motion (sensor 2.4E) is significantly lower than the in-plane component (2.4N), except for frequencies close to resonance, so that an in-plane interpretation model can be assumed as reasonable to examine the response in the loading direction.

A time window lasting 20 s of the signal recorded by accelerometers 2.4 N, 1.4 N, 1.3 Z and 1.4 Z was framed after the steady-state condition had been recognized in each frequency step. Each selected time window was filtered through a 4th order band-pass Butterworth filter in the range of the corresponding exciting frequency ± 1 Hz. The filter was necessary in order to avoid unrealistic drift in the displacement time histories, which were computed by double-integrating the filtered accelerations. Thereafter, the three components of the vector of motion, U , were derived as follows:

- the foundation rocking, θ_f , resulted from the difference between the vertical records 1.3 Z and 1.4 Z divided by their distance;
- the foundation swaying, u_f , was coincident with the displacement obtained from the record of sensor 1.4N minus the displacement induced by the foundation rocking, i.e. θ_f , multiplied by the thickness of the foundation slab;

the bending displacement, u_s , was calculated as the roof displacement from sensor 2.4N minus the foundation swaying and the rigid displacement induced by rocking in the roof. The latter was again computed by multiplying the rotation for the total structural height, under the assumption that the centre of rotation lays at the foundation level.

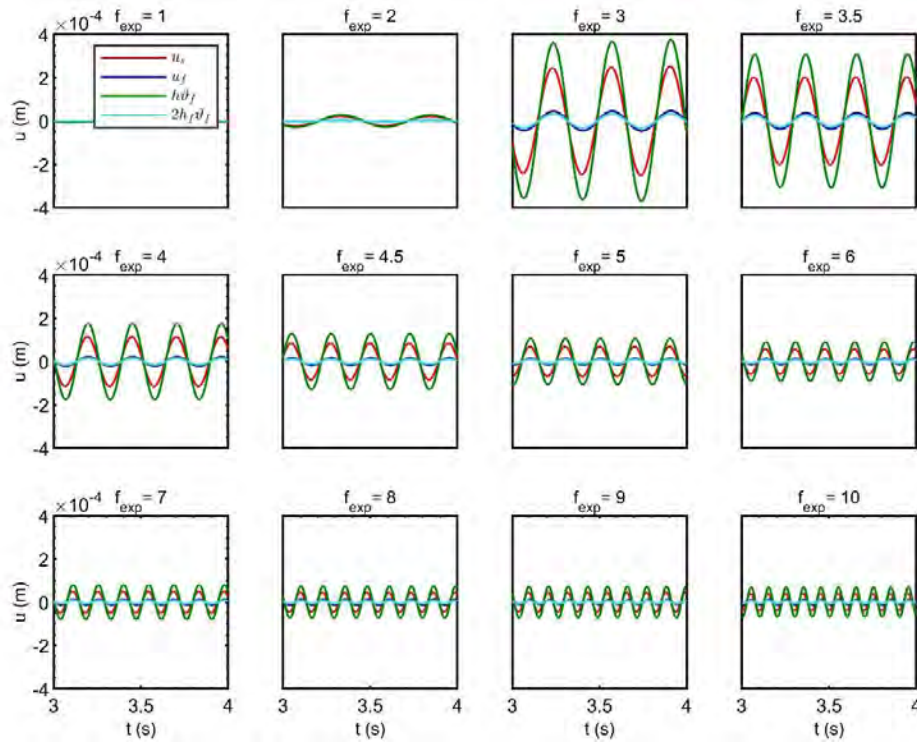


Figure 459: Components of the recorded displacements during the forced vibration test ‘Forced-A’

Figure 459 shows the components of the horizontal displacement of the roof and foundation slab during the ‘Forced-A’ test under the different exciting frequencies. The comparison clearly highlights that rocking ($h\theta_f$, green colour) is the predominant motion, even exceeding the bending displacement (u_s , red). If the roof is assumed as control point to quantify the structural behaviour, foundation swaying (u_f , dark blue) appears negligible, being one order of magnitude lower than the bending and the rocking contributions.

9.3.6 Results

Interpretation model for the experimental data

Except for likely irregularities in the foundation soil, the symmetric geometry allows for assuming that the dynamic behaviour of the structure is uncoupled along the axes of symmetry and that torsional motions are absent in the range of the exciting frequencies. Under these hypotheses, the dynamic response of the prototype along the direction of the applied force is theoretically determined by three degrees of freedom (see Figure 460), i.e. the roof horizontal bending displacement, u_s , and the swaying, u_f , and rocking, θ_f , motions of the rigid foundation slab:

$$U = [u_f, \theta_f, u_s]^T \quad (7)$$

The activation of each degree of freedom depends on the location and direction of the force, F_s , generated by the eccentric mass shaker. Being the shaker located at the centre of the roof slab, during the forced vibration tests the vector of the loading forces is given by:

$$F = [F_s, F_s h, F_s]^T \quad (8)$$

The amplitude of the mobilized displacement is controlled by the magnitude of F_s as well as by the mass, the stiffness and the damping of the structure, the foundation and the involved soil. Assuming that the low-to-moderate values of F_s do not mobilize soil or structural plastic straining, so that the behaviour of the system is nearly linear, the consequent equation of motion in the frequency domain is expressed by Crouse et al. 1984:

$$M\ddot{U} + KU = F \quad (9)$$

In Eq. (9), M is the real and symmetric mass matrix:

$$M = \begin{bmatrix} M_x & M_{x\theta} & M_{xs} \\ M_{\theta x} & M_\theta & M_{\theta s} \\ M_{sx} & M_{s\theta} & M_s \end{bmatrix} = \begin{bmatrix} m_f + m_s & m_f h_f + m_s h_s & m_s \\ m_f h_f + m_s h_s & I_f + m_f h_f^2 + m_s h_s^2 & m_s h_s \\ m_s & m_s h_s & m_s \end{bmatrix} \quad (10)$$

while K is the complex symmetric and frequency-dependent stiffness matrix:

$$K = \begin{bmatrix} K_x & K_{x\theta} & 0 \\ K_{\theta x} & K_\theta & 0 \\ 0 & 0 & K_s \end{bmatrix} \quad (11)$$

Symbols m_s , m_f , and I_f are, respectively, the structural mass, the foundation mass and moment of inertia, while h and h_f are the height of the prototype and the thickness of the foundation slab; the above inertial and geometrical parameters are defined in Figure 460 and reported in Table 69.

The complex components K_x , $K_{x\theta} = K_{\theta x}$ and K_θ of the stiffness matrix are the unknown soil-foundation impedance functions, while K_s combines the bending lateral stiffness (k_s in Figure 460) and the damping ratio, ξ_s , of the superstructure. Since the determination of K_s is out of the scope of this paper, the third equation of motion “included” in the matrix equation (9) is neglected in this paper, while the others were used to determine the impedance functions:

$$K_x u_f + K_{x\theta} \theta_f = F_s + \omega^2 (M_x u_f + M_{x\theta} \theta_f + M_{xs} u_s) \quad (12)$$

$$K_{x\theta} u_f + K_\theta \theta_f = F_s h + \omega^2 (M_{\theta x} u_f + M_\theta \theta_f + M_{\theta s} u_s) \quad (13)$$

For each value of the angular frequency, ω , of the applied harmonic force, Eqs. (12) and (13) are simultaneously satisfied by infinite sets of values of K_x , $K_{x\theta} = K_{\theta x}$ and K_θ ; thus, the identification of a unique meaningful solution requires tests under other loading conditions (Crouse et al. 1984) or additional assumptions (Tileylioglu et al. 2011). In this work, the experimental data were interpreted basing on two different hypotheses:

- A) the off-diagonal terms $K_{x\theta} = K_{\theta x}$ were neglected, implying that the foundation swaying is only activated by F_s , as well as the rotation is mobilized by the moment $F_s h$. This is a widespread assumption of the spring-based approach to simulate the dynamic response of building on shallow footings (Gazetas 1991), confirmed by comparisons with more refined simulations (Piro et al. 2020).
- B) the foundation swaying in the global response of the soil-foundation-structure system was assumed as negligible, if compared to the rocking-induced displacement of the superstructure. This is a typical assumption when the behavior of slender structural systems founded on shallow slabs are studied (de Silva et al. 2018). In fact, i) tall structures transmits higher bending moments to their basement, as readily demonstrated by the dependence on h of the second

term of the load vector (Eq. (8)); ii) rocking stiffness is proportional to the foundation embedment, consequently shallow slabs on soft soil are rocking-prone footings.

Both the hypotheses are consistent with the actual geometry of the prototype, characterized by a slenderness ratio $h/2B = 1.67$ and founded on a 0.4m thick slab with null embedment, since the covering soil was intentionally removed.

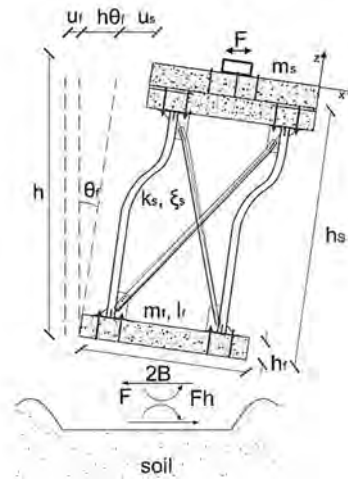


Figure 460: In-plane motion model adopted for the interpretation of experimental data to compute the impedance functions

m_s (kg)	m_f (kg)	I_f (kgm ²)	h_s (m)	h_f (m)	h (m)
18000	9000	6870	4.6	0.4	5

Table 69: Mass and inertia of the prototype

Experimental impedance functions

The above-described procedure was applied for the interpretation of the forced-vibration tests. In lack of a specific record of the applied harmonic force, the phase angle, φ , between the applied force and the prototype response was assumed equal to that characterizing the force-displacement time shift of a simple oscillator with an overall damping ratio, ξ , and a natural frequency, f_n , calculated from the interpretation of noise and free-vibration tests:

$$\varphi = \arctan \left(\frac{2\xi \frac{f}{f_n}}{1 - \frac{f^2}{f_n^2}} \right) \quad (14)$$

Since the outcomes of the free vibration tests demonstrated a certain variability of f_n and ξ in the range 3 Hz – 3.5 Hz and 2% - 6%, respectively, the sensitivity of the phase angle was checked to such dynamic properties. The comparison among the resulting curves illustrated that, as expected, the phase angle is poorly affected by the variability of damping ratio, while it is more sensitive to the natural frequency. Such influence was considered by selecting the curve associated to a constant value of $\xi=5\%$ and $f_n=$

3.4 Hz, 3.35 Hz, 3.3 Hz and 3 Hz in the computation of the impedance from the forced vibration test A, B, C and D, respectively, in accordance with the observed reduction of f_n with increasing loads. So, the phase angle predicted by Eq. (14) for each value of the loading frequency f was added to the sinewave argument in Eq. (6), to compute the load vector F in Eq. (8).

The Fast Fourier transform of the abovementioned resulting component of the motions, U , and those of the load vector, F , were computed and introduced in Eqs. (12) and (13) to back-figure the impedance functions.

Figure 461 shows the real part and the imaginary part divided by the applied angular frequency of the impedance functions derived by either considering (a) or neglecting (b) the foundation swaying for computing the rocking impedance, i.e. hypotheses A vs. B. A single value was obtained for each exciting frequency and the dashed line connecting the light to dark blue data points was plotted to individuate the trend of the results. The real part of the only impedance associated to the swaying motion, K_x , linearly increases with frequency, showing a drop at the highest applied frequency during the Forced-B and Forced-C tests. The real part of the rocking impedance, K_θ , derived under the hypothesis A) decreases from 1 Hz to 3 Hz and then increases more than linearly. The trend is inverted around the frequency associated to the first vibration mode of the prototype identified under noise and free vibration tests. The same reduction and even similar values of real K_θ are obtained under the hypothesis B) in the range 1 Hz - 3 Hz, while the trend is almost flat after the resonance.

The imaginary part exhibits a reduction and a subsequent increase with an apparent trough around the fundamental frequency of the prototype. The increase seems to be an effect of the amplitude of the exciting force, as the aforementioned changes of the real part of K_x and K_θ at high frequencies. Certainly, a clearer evidence of the influence of soil non-linearity is recognized in the reduction of the real part with the applied force, i.e. moving from Forced-A to Forced-D experiments. As the force applied by the shaker increases, higher strain levels are mobilized with the consequent decrease of shear stiffness in the soil volume affected by the foundation motion, which turns into a reduction of the real K_x and K_θ . The observed reduction is more pronounced in the rocking than in the swaying impedance, since rocking-induced strains are higher and concentrated in a thinner volume below the foundation level with respect to the swaying-induced deformations.

The dependence of the zone of influence on the foundation motion is corroborated by the literature, where its depth is defined as a function of the radius of a circle with the same area for the swaying, r_{eq_x} , or moment of inertia for the rocking, $r_{eq_ \theta}$, of the actual foundation. Being the analysed footing a square slab, $r_{eq_x} \approx r_{eq_ \theta} = r_{eq} \approx 1.7\text{m}$, the typical depths of $0.75 r_{eq_x}$ and $0.75 r_{eq_ \theta}$ proposed by Stewart et al. (2003) led to the same depth of influence. In a previous work, Gazetas (1983) suggested that the shear stress induced in the soil by a horizontal load becomes negligible (i.e. less than 10%) at a depth greater than $2r_{eq}$, while the increment of vertical tension derived by a loading moment extinguishes below $1.25r_{eq}$.

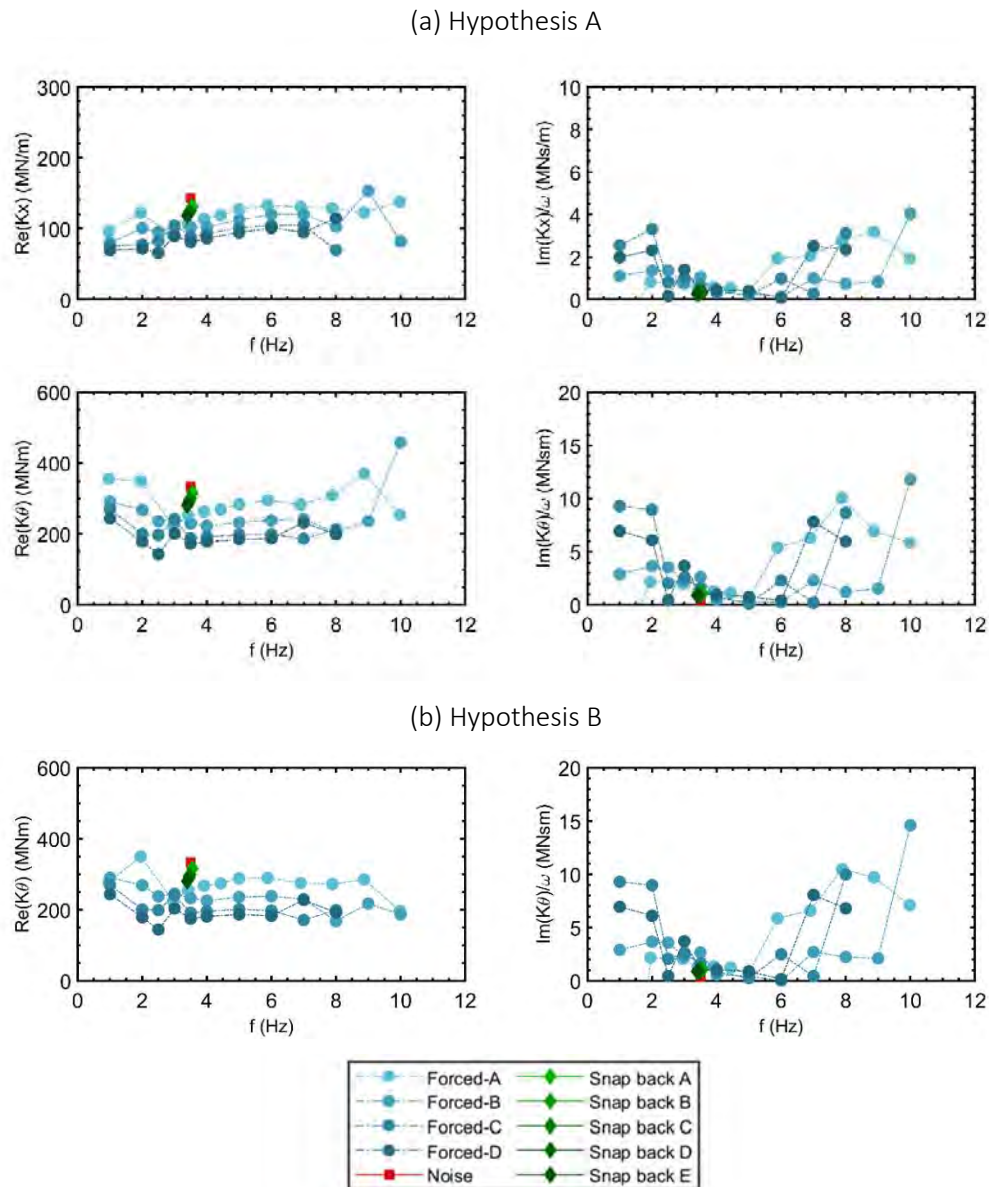


Figure 461: Real and imaginary parts of the foundation impedances derived by either (a) considering or (b) neglecting the foundation swaying, i.e. hypotheses A vs. B

Finally, the higher strains mobilized by the rocking of slender structures have been experimentally observed (e.g. Gajan and Kutter 2008, Shirato et al. 2008) and numerically simulated (e.g. de Silva 2020, Gelagoti et al. 2012, Gazetas 2015) so that current research on soil-foundation-structure interaction is paying great attention to quantify its contribution to dissipate seismic energy through soil hysteresis. Obviously, the applied load amplitudes are far from inducing permanent strains in the soil, but the higher non-linearity mobilized by rocking is evident from the more significant reduction of the real part, as well as from the higher values of imaginary part compared to those associated to the swaying.

When the vector F of applied load in Eqs. (12) and (13) tends to zero, the response of the system tends to its predominant vibration mode. Under this assumption, the calculation of the impedances was repeated by introducing in Eqs. (12) and (13) a null force vector, F , together with the displacement vector, U , derived from the acceleration recorded during the noise and the free-vibration tests. The resulting impedances are plotted in Figure 461 with red and green colours, respectively. The real part turned to be close to the values resulted from the forced vibration test when the lowest load-amplitude

is applied, while the imaginary part is always the lowest. Moreover, the real part always shows its maximum value under the noise recording, while it tends to reduce with the applied force in the free-vibration tests, again confirming the effect of non-linearity.

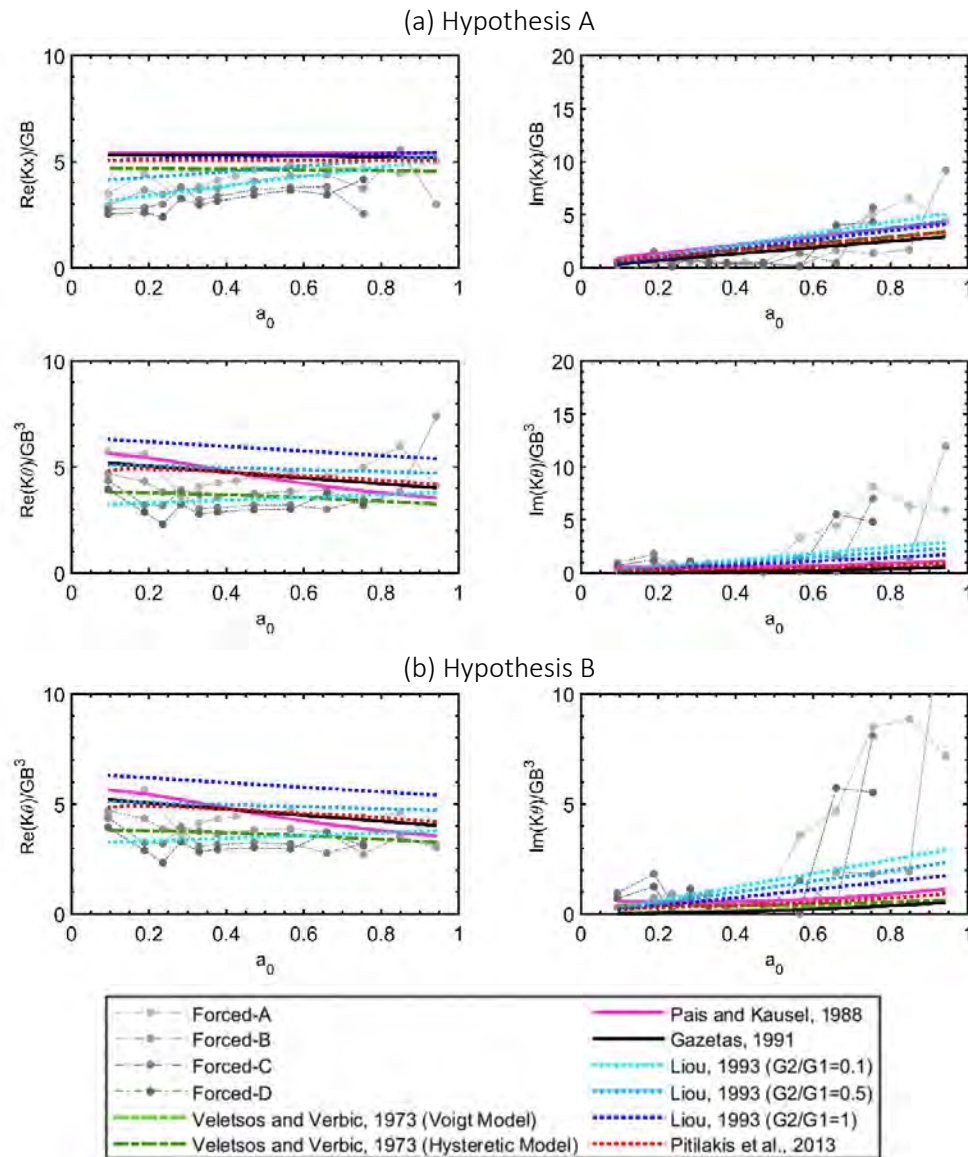


Figure 462: Comparison between experimental and analytical real and imaginary parts of the foundation swaying and rocking derived by either (a) considering or (b) neglecting the foundation swaying, i.e. hypotheses A vs. B

Figure 462 compares the real and the imaginary parts of the analytical and experimental impedances normalized with respect to the shear modulus G of the soil and the foundation half-width B . Both the real and the imaginary parts of the swaying impedance computed from the on-site records are successfully reproduced by the analytical solutions. It is worth noting that the best agreement is found for the forced vibration test A, in which the lowest loading amplitude is applied and the soil behaviour is likely linear, as implied by the analytical formulas. On the other hand, the real part of the experimental rocking impedance obtained under the hypothesis A increases with frequency, while an opposite trend is shown by the analytical predictions. A significant better accordance is recognized between the experimental and analytical real part of the rocking

impedance when the hypothesis B) on the interpretation model is followed. Independently from the assumed hypotheses, the imaginary part associated to the rocking is very low at low frequencies for both analytical and experimental results. Increasing the frequency of the applied load, the experimental $Im(K_\theta)$ is much higher than the value predicted analytically, probably because of the contribution of the hysteretic damping mobilized by the aforementioned frequency-proportional load amplitude.

9.3.7 Conclusions and outlook

A fundamental outcome of the performed tests was the individuation of the experimental layout most appropriate to facilitate the experimental characterization of the impedance functions on similar prototypes and, more generally, on true buildings. Pros and cons of the experimental set-up can be assessed with reference to: 1) the most suitable excitation, 2) the best position of the shaker during the forced vibration tests, 3) the minimum number of instruments required and their most appropriate arrangement.

1) About the excitation. The impedance functions back-figured from the interpretation of the acceleration recorded on the prototype during the different tests resulted consistent, demonstrating the effectiveness of the selected experimental procedures. In fact, the real and imaginary parts computed from the noise and free vibration tests turned to be close to the values resulting from the forced vibration test driven at the lowest load amplitude. Moreover, they resulted poorly affected by the hypothesis on the interpretation model, highlighting that a direct measurement of the impedance from the interpretation of on-site weak motion records can be reliable and more accurate than any analytical procedure, since no simplified assumptions are necessary. Forced vibration potentially represents the most powerful test, since a wide range of frequency can be investigated, including and not limited to the fundamental value. On the other hand, the frequency-dependent amplitude of the applied force induces significant non-linear effects, spoiling the interpretation of the results. The latter are likely due to the inelastic soil behaviour even at the lowest strain levels, but additional effects due to material and/or geometrical non-linearity relevant to the structure are hard to distinguish and cannot be excluded.

2) About the shaker position. Records of the forced vibration test in which the shaker was placed at the foundation level resulted very noisy with respect to the clear harmonic waveforms obtained when the roof was excited. Additional tests under eccentric loads may be useful i) to compute the cross-coupling terms of the impedances matrix, which are traditionally assumed as negligible in the response of slender structures on shallow footings, ii) to evaluate the possible effects of the load vector on the impedance values.

3) About number and arrangement of instruments. The dynamic response of such a simple structure, in which the first vibration mode is expected to be predominant, seemed to be effectively monitored through one accelerometer on the roof slab and two placed in opposite corners of the foundation. A redundancy of the instrumental network is surely useful to prevent the loss of data due to broken or ill-installed sensors, as well as to catch the behaviour of more complex structures. If only one-directional sensors are available, it should be avoided missing the vertical motion of the foundation of slender structures rather than taking care of the horizontal component, since the foundation swaying confirmed to be negligible. In the tests executed, base rocking has been certainly emphasized by the removal of the surrounding soil; the effect of the foundation swaying and rocking on the global response is expected to be more equally distributed if the experiments are repeated on the same prototype with a slight foundation embedment. Finally, results show an influence of the interpretation model especially at high frequency, where the observed trend of a given impedance component is increasing or decreasing, depending on the

assumption on the relevance of the foundation swaying. Fortunately, the different hypotheses led to similar values around resonance, where the real and the imaginary parts are traditionally calibrated in practice to compute the stiffness and the damping ratio of base springs and dashpots.

9.3.8 References

- BSSC (2004). NEHRP recommended provisions for seismic regulations for new buildings and other structures (FEMA450).
- Crouse C.B., Liang G.C., Martin G.R. (1984). Experimental study of soil-structure interaction at an accelerograph station. *Bull. Seismol. Soc. Am*, 74, 5, 1995-2013.
- de Barros C.P., Luco J.E. (1995). Identification of foundation impedance functions and soil properties from vibration tests of the Hualien containment model. *Soil Dynamics and Earthquake Engineering*, 14, 4, 229-248.
- de Silva F. (2020). Influence of soil-structure interaction on the site-specific seismic demand of masonry towers. *Soil Dynamics and Earthquake Engineering*, 131, 106023.
- de Silva F., Ceroni F., Sica S., Silvestri F., 2018. Non-linear dynamic analysis of the Carmine bell tower accounting for the soil-foundation-structure interaction, *Bulletin of Earthquake Engineering*.
- de Silva F., Silvestri F., Ceroni F., Sica S. (2017). Carmine bell tower in Napoli: simulating soil-structure interaction under seismic actions. Technical Committee for the Preservation of Historic Sites, ISSMGE (ed.) Historic Towers and Geotechnics.
- Dobry R., Gazetas G., Stokoe K.H.II (1986). Dynamic response of arbitrarily shaped foundations: experimental verifications. *J. Geotech. Eng.* 112,2,136-154.
- Elsabee F., Morray J. P. (1977). Dynamic behavior of embedded foundations. Research Report R77-33, MIT, Cambridge, Massachusetts.
- Gajan S., Kutter B.L. (2008). Capacity, settlement, and energy dissipation of shallow footing subjected to rocking. *Journal of Geotechnical and Geoenvironmental Engineering*, 134(8):1129-1141.
- Gazetas G. (1983). Analysis of machine foundation vibrations: state of the art. *Soil Dynamics and Earthquake Engineering*, 2(1), 1-41.
- Gazetas G. (1991), Formulas and charts for impedances of surface and embedded foundations. *Journal of Geotechnical Engineering*, 117, 1363-1381.
- Gazetas G. (2015). 4th Ishihara lecture: Soil–foundation–structure systems beyond conventional seismic failure thresholds. *Soil Dynamics and Earthquake Engineering* 68 23–39.
- Gelagoti F., Kourkoulis R., Anastasopoulos I., Gazetas G. (2012). Rocking isolation of low-rise frame structures founded on isolated footings. *Earthq Eng Struct Dyn* 41:1177–97.
- Iguchi M., Luco J.E. (1982). Vibration of flexible plate on visco-elastic medium. *J. Eng. Mech.* 186,6,1103-1120.
- Kausel E. (2010). Early history of soil-structure interaction. *Soil Dyn and Earthq Eng*, 30, pp 822-832.
- Knappett J. A., Madden P., Caucis K. (2015). Seismic structure–soil–structure interaction between pairs of adjacent building structures. *Geotechnique* 65:5, 429–441.
- Lamb H. (1904). On the propagation of Tremors over the Surface of an Elastic Solid. *Philosophical Transactions of the Royal Society, London*, 203, 1-42.
- Lin A. N., Jennings P.C. (1984). Effect of embedment on foundation-soil impedance. *J. Eng. Mech.* 110,7,1060-1075.

- Liou G.S. (1993). Impedance for rigid square foundation on layered medium. *Structural engineering and earthquake engineering* 10,2,83-93.
- Liou G.S., Lee G.C., Ketter R.L. (1991). Analytical solutions for dynamic loading on half-space medium. *Journal of engineering mechanics* 117,7, 1485-1494.
- Luco J., Trifunac M.D., Wong H.L. (1988). Isolation of soil structure interaction effects by full scale forced vibration tests. *Earthquake Eng. Strct. Dyn.* 16,1, 1-21.
- Mylonakis G., Gazetas G. (2000). Seismic soil-structure interaction: beneficial or detrimental. *Earthq Eng*, 4, pp 277-301.
- Mylonakis G., Nikolaou S., Gazetas G. (2006). Footings under seismic loading: Analysis and design issues with emphasis on bridge foundations. *Soil dynamics and earthquake engineering*, 2006; 824-853.
- Pais A., Kausel E. (1988). Approximate formulas for dynamic stiffnesses of rigid foundations. *Soil Dynamics and Earthquake Engineering*, 7, 4, 213-227.
- Piro A., de Silva F., Parisi F., Scotto di Santolo A., Silvestri F. (2020). Soil-structure interaction effects on equivalent damping ratio and fundamental frequency of historical masonry building sub-structures. *Bulletin of Earthquake Engineering*, 18,1187–1212.
- Pitilakis D., Karatzetzou A. (2015). Dynamic stiffness of monumental flexible masonry foundations. *Bulletin of Earthquake Engineering* (13), 67-82.
- Pitilakis D., Modaressi-Farahmand-Razavi A., Clouteau D. (2013). Equivalent-linear dynamic impedance functions of surface foundations. *Journal of Geotechnical and Geoenvironmental Engineering*, 139, 7, 1130-1139.
- Pitilakis K., Raptakis D., Lontzetidis K., Tika-Vasillikou T., Jongmans D. (1999). Geotechnical and geophysical description of EUROSEISTEST, using field, laboratory tests and moderate strong motion records. *Journal of Earthquake Engineering*, 3, 3, 381-409.
- Raptakis D., Anastasiadis A. & Pitilakis K. (1998). Preliminary instrumental and theoretical approach of site effects in Thessaloniki. In *Proceedings of the 11th European Conference on Earthquake Engineering*.
- Raptakis, D., Chávez-García, F., Makra, K., Pitilakis, K. (2000). Site effects at EuroSeistest-I. Determination of the valley structure and confrontation of observations with 1D analysis. *Soil Dynamics and Earthquake Engineering*, 19, 1, 1–22
- Reissner E. (1936). Stationäre, axialsymmetrische durch eine schüttelnde Masse erregte Schwingungen eines homogenen elastischen Halbraumes. *Ingenieur Archivieren* 7, 381-396.
- Richart F. E., Hall J. R., Woods R. D. (1970). Vibrations of soils and foundations. Prentice-Hall.
- Richart F.E., Whitman E.V. (1967). Comparison of footing vibration tests with theory. *J. Soil Mech and Found.Div.* 93,6, 143-168.
- Shirato M., Kuono T., Asai R., Fukui J., Paolucci R. (2008). Large scale experiments on nonlinear behavior of shallow foundations subjected to strong earthquakes. *Soils Found* 48:673–92.
- Stewart J., Kim S., Bielak J., Dobry R., Power M. (2003). Revisions to soil structure interaction procedures in NEHRP design provisions. *Earthquake spectra*, 19 (3), 677-696.
- Tileyiloglu S., Stewart J.P., Nigbor R. (2011). Dynamic stiffness and damping of a shallow foundation from forced vibration of a field test structure. *Journal of Geotechnical and Geoenvironmental Engineering ASCE*, 137, 4, 344-353.
- Veletsos A., Meek J.W. (1974). Dynamic behavior of building-foundation systems. *J Earthq. Eng. and Structural Dynamics*, 3, 121-138.

Veletsos A.S., Verbic B. (1973). Vibration of viscoelastic foundations. *Earthquake Engineering and Structural Dynamics*, 2, 87-102.

Wong H.L., Trifunac M.D., Luco J. (1988). A comparison of soil-structure interaction calculations with results of full-scale forced vibration tests. *Soil Dynamics and Earthquake Engineering*, 7, 1, 22-31.

9.4 Project # 28 – Ambient and forced vibration techniques for improving design and performance assessment of structures with consideration of soil-structure interaction

Authors

M. Kosič⁽¹⁾, M. Dolšek⁽¹⁾, A. Vratsikidis⁽²⁾, A. Anastasiadis⁽²⁾, D. Pitilakis⁽²⁾

⁽¹⁾ *University of Ljubljana, Faculty of Civil and Geodetic Engineering, Ljubljana, Slovenia*

⁽²⁾ *Aristotle University of Thessaloniki, Thessaloniki, Greece*

9.4.1 Introduction

Excessively simplified design of new buildings or performance assessment of existing buildings, without eliminating major sources of epistemic uncertainties, can lead to incorrect decision-making. Ongoing research is thus focused on the improvement of design and assessment procedures of structures without increasing their complexity. The objective of the proposed project is to support such research by investigating the usability of detailed measurement of soil-structure interaction (SSI) based on ambient and forced vibrations of a simple structure. Two series of experiments were performed at EuroProteas site:

- a) Ambient-vibration measurements;
- b) Free- and forced-vibration measurements.

The results of the first series of experiments can be used to validate different methods for system identification, and to study how these results can be used to reduce epistemic uncertainties involved in seismic assessment of existing buildings. The results of the second series of experiments can supplement the results of the first series of experiments and can be used to validate nonlinear models which can then be used in parametric studies in order to develop a simplified method for definition of design spectrum with consideration of soil-structure interaction.

The proposed experimental campaign at EuroProteas is in line with ongoing research at University of Ljubljana, which addresses the development of design response spectrum with approximate consideration of soil-structure interaction and the usability of the non-destructive dynamic system identification techniques for the risk assessment of existing structures. The interest of the user group is also to acquire the knowledge to design and perform such experiments.

9.4.2 EUROPROTEAS

Structure

EuroProteas prototype structure was particularly designed to mobilize strong interaction with the foundation soil as it is a stiff structure with a large superstructure mass founded on soft soil.

EuroProteas is a perfectly symmetric and reconfigurable structure. It is founded on a square reinforced concrete slab (C20/25) with dimensions 3.0m x 3.0m x 0.4m which rests on the ground surface. The superstructure mass consists of two identical to the foundation reinforced concrete slabs that are supported by four square hollow steel columns (QHS 150 x 150 x 10mm) which are clamped on the foundation. L-shaped (100 x100 x 10mm) X-braces are connecting the steel columns in all the sides of the structure ensuring its total symmetry. Assuming a uniform unit weight of 25kN/m³ for the concrete, the total mass of each slab is estimated at 9.16Mg, while the total mass of the structure is calculated approximately at 28.5Mg. Its outer dimensions are 3.0m x 3.0m x 5.0m (Figure 463).

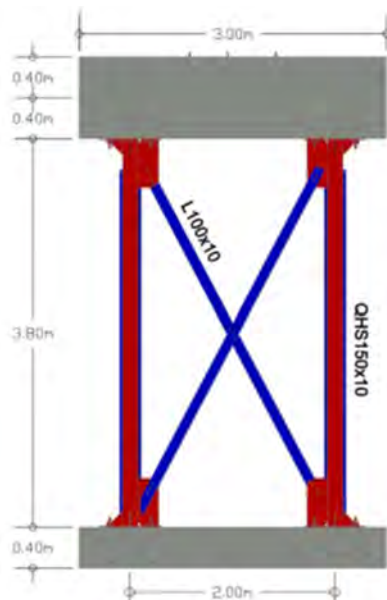


Figure 463: A 2D sketch and a view of EUROPROTEAS prototype structure

The bracing system and the upper roof slab of the structure are removable allowing the modification of the mass and/or the stiffness. Depending on the number of the roof slabs and the arrangement of the X-bracing system the fixed-base frequency of EuroProteas covers a range between 1.78Hz and 13.06Hz as calculated numerically (Pitilakis et al. 2018).

Foundation Soil

The foundation soil is well investigated and reported in earlier studies. Specifically, between 1993 and 2004, an extensive program of seismic prospecting and geotechnical testing was undertaken (Pitilakis et al. 1999). It comprised of in-situ (sampling boreholes, Standard and Cone Penetration Test measurements) and laboratory (conventional classification tests, strength tests, consolidation tests and resonant column and cyclic triaxial tests) geotechnical surveys. The elaboration of all geophysical and geotechnical data, led to the classification of the main soil formations, validation of soil properties stemming from different methodologies and design of representative 1D, 2D and 3D soil models.

translational, rocking and out-of-plane response. One accelerometer (3.1) was clamped inside the borehole BH-2 located at the geometrical center of the foundation at the depth of 3m.

Five seismometers (0.14 to 0.16, 0.4 and 0.6) were placed on the soil surface along the direction of loading. This parallel to the loading direction array, which is denser close to the foundation, was able to record the soil response and wave emanation due to the oscillation of the structure. Additionally, two seismometers (0.7 and 0.8) were placed on the soil surface in the out-of-plane direction. Finally, one shape acceleration array was installed in the borehole BH-1 adjacent to the foundation.

All the instruments were configured at a sampling frequency of 200 Hz and were connected to external global positioning system (GPS) antennas.

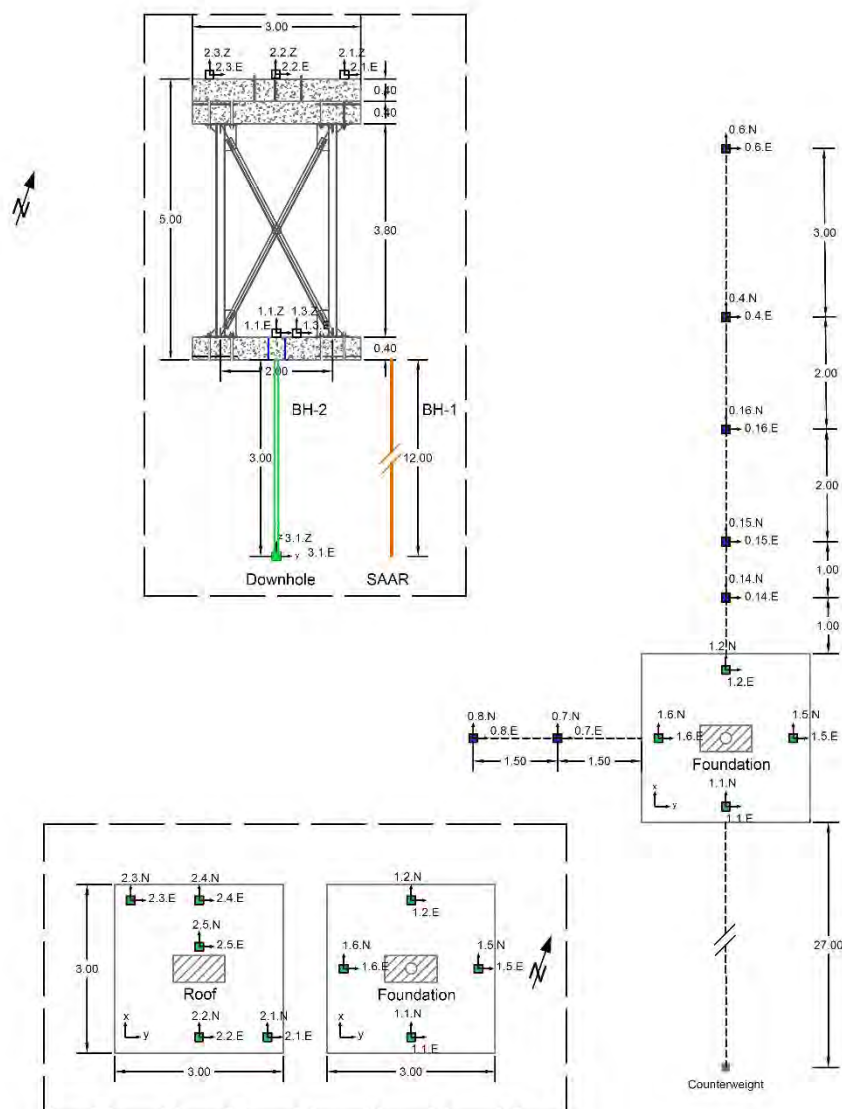


Figure 465: A cross-section and a plan view of the instrumentation layout of EUROPROTEAS structure and foundation soil

Forced-Vibration tests

The eccentric mass shaker MK-500U owned by the Institute of Engineering Seismology and Earthquake Engineering (ITSAK) was implemented as a source of harmonic excitation. It is a portable uniaxial dual counter-rotating shaker that can produce a maximum force amplitude of 5 tons in a frequency range

between 0.1-20Hz. Eight mass plates in four different sizes (A, B, C and D) can be used in pairs to adjust the eccentricity of the shaker and hence the output force. The amplitude of the output force of the shaker is given by the equation:

$$F = E(2\pi f)^2 \quad (15)$$

where F is the shaker output force in Newtons, E is the total eccentricity of the shaker in kg-m and f is the rotational speed of the shaker in Hz.

The eccentric mass shaker was placed at the geometrical centre of the top roof slab of the structure and it was orientated to produce a force having a direction that formed an angle of 30 degrees with the magnetic North. In Table 70 the forced-vibration tests performed are summarized.

Experiment No.	Mass / Plates	Shaker Frequency (Hz)	Force Amplitude (kN)
A	A	1 – 10	0.07 – 7.30
B	A + B	1 – 10	0.15 – 15.51
C	A + B + C	1 – 10	0.27 – 17.51
D	A + B + C + D	1 – 10	0.45 – 28.58

Table 70: Summary of the forced-vibration experiments

Free-Vibration tests

Pull-out forces were applied on the roof of the structure by a wire rope. A load cell, with which the applied tension force was measured, was attached to the roof slab and to the one end of the rope. The other end of the wire rope was attached to a wire rope pulling hoist having a working load limit of 32kN. The pulling hoist was clumped to a buried counterweight of 3 tons. The total length of the wire rope was 27m. In Table 71 the free-vibration tests performed are summarized.

Experiment No.	Force (kN)
A	6.83
B	4.32
C	10.58
D	16.14

Table 71: Summary of the free-vibration experiments

9.4.4 Observation during testing

During the performed test, several sensors failed to record the response or suffered from synchronization problems. This means that not all instrumentation could be used for examination of the performed tests. In the case of the instrumentation of the structure, the following notes can be made:

- The instrument placed at location 2.3 did not record the response in East-West direction. Additionally, the recordings in North-South and vertical direction were not synchronized according to the GPS absolute time;
- The instruments placed at locations 2.2 and 2.5 did not record the response in the vertical direction.

- The recordings from instrument placed at location 1.5 were not synchronized according to the GPS absolute time;
- The instrument placed at the location 1.6 didn't record the response of the foundation for forced vibration experiment B;
- The instrument placed at the location 1.1 didn't record the response of the foundation for free vibration experiment A.

In the case of the instrumentation of the soil, the following notes can be made:

- The instrument placed at location 0.8 did not record the response in East-West and vertical direction. The recordings obtained for North-South direction are unreliable;
- The instrument placed at location 0.7 did not record the response in East-West direction.

The measured initial perturbation force in case of free vibration test B, i.e. $F=4.32$ kN, is inaccurate. The actual applied force in test B was likely larger than the value applied in test A ($F=6.83$ kN), which is suggested based on larger response of the system. The inaccurate measurement was likely result of non-instantaneous cut of the wire rope used for load application.

9.4.5 Results

Free-Vibration tests

Selected results of free vibration test C are presented in Figure 466 to Figure 468. Figure 466 presents the distribution of soil velocities at different measuring points, whereas Figure 467 and Figure 468 present the measured foundation and roof accelerations of the structure. As can be seen the peak response in the soil and the structure is reached at the time of the first impact of the structure to the ground. The response of soil and the structure then attenuates as the free vibration of the structure dissipates.

Based on results of Figure 466 and Table 72, it can be seen that the soil velocities decrease with increasing distance from the structure. In addition to this, the time at which the peak value of soil velocity is reached is slightly shifted due to the travelling time need by the vibration to reach the sensor.

Location	0.14	0.15	0.16	0.6
Distance (m)	1	2	4	9
Peak vel. (m/s)	1,32E-04	1,02E-04	1,00E-04	7,99E-05
Time (s)	6,48	6,67	6,69	6,73

Table 72: Peak soil velocity and corresponding time at different distances from the structure for free vibration test C

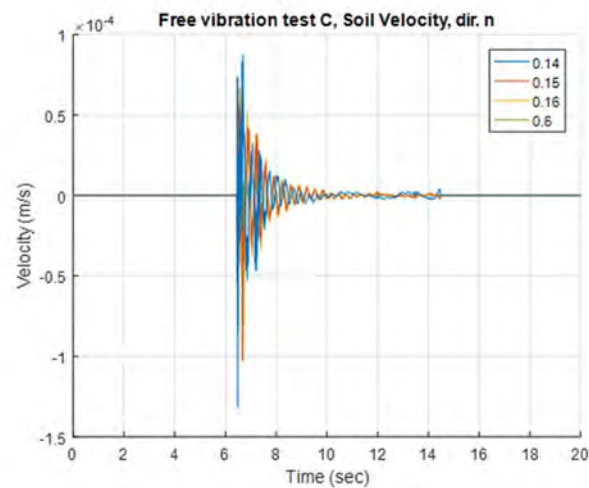


Figure 466: Soil velocity in direction North-South (direction n) for free vibration test C

Based on Figure 467 and Figure 468 it can be observed that the free vibration gradually attenuates in about 5 seconds after the perturbation is applied. The attenuation of free vibration is a result of loss of energy which is the field of structural dynamics modelled by viscous damping.

As can be seen from Figure 467, the foundation accelerations have similar distribution among all sensors. On the other hand, in the case of the roof accelerations, the sensor located at the corner of the building (location 2.1) measured larger accelerations than the sensors located in the axis of the building (locations 2.2, 2.4, 2.5) (see Figure 468). This result indicates that the response of the roof was slightly torsional, which can be a consequence of slight imperfections of the structure or non-ideal application of initial perturbation.

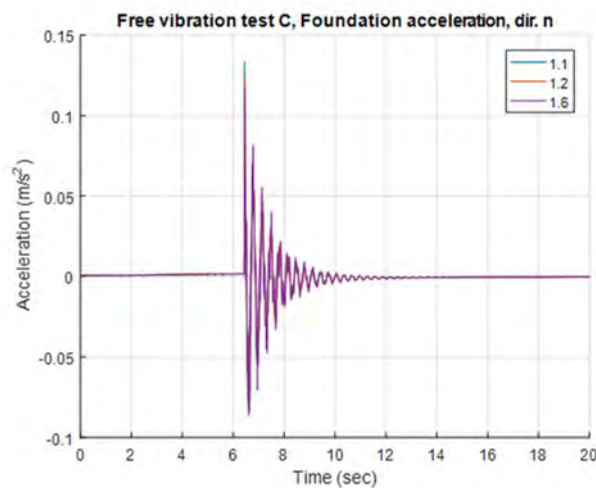


Figure 467: Foundation accelerations in direction North-South (direction n) for free vibration test C

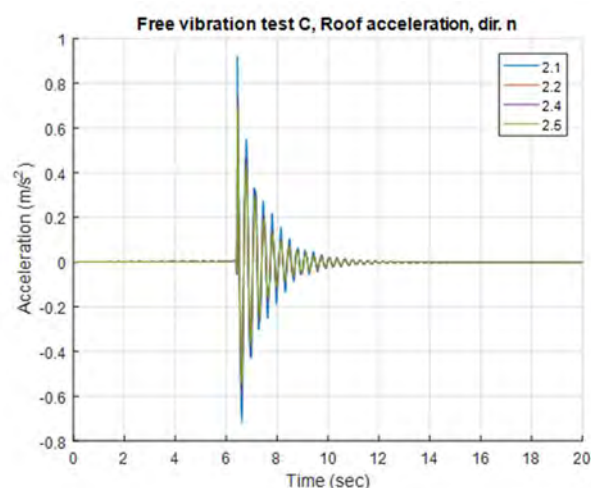


Figure 468: Roof accelerations in direction North-South (direction n) for free vibration test C

The comparison of roof accelerations from free vibration tests A to D is presented in Figure 469. Based on results of Table 73, it can be observed that the peak roof accelerations increase with increasing force of initial perturbation. The only exception is the results obtained for test B, for which the initial force was inaccurate due to a measurement error.

	Test A	Test B	Test C	Test D
Force (kN)	6.83	4.32*	10.58	16.14
Peak accel. (m/s²)	0.31	0.38	0.71	0.98

Table 73: Peak roof acceleration for free vibration tests A to D.

* Force obtained in test B is inaccurate due to a measurement error.

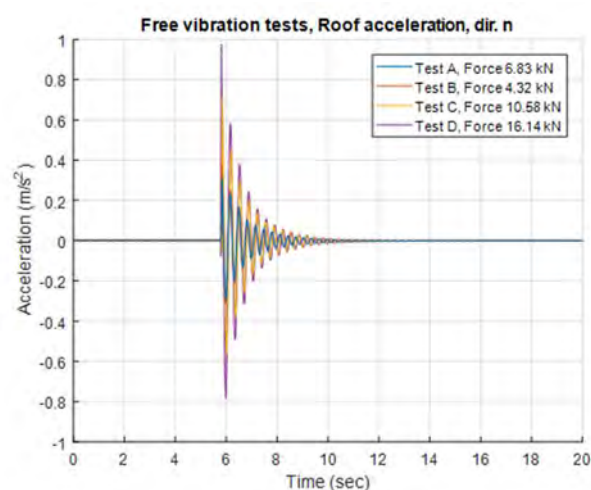


Figure 469: Comparison of roof accelerations from free vibration tests A to D

The roof accelerations were used to obtain the Fourier spectra and acceleration response spectra for all performed tests, which are presented in Figure 470 and Figure 471. A summary of the peak amplitude and the corresponding frequency of Fourier spectra is presented in Table 74. The results can be used to identify the prevailing frequency of the roof response in the direction of loading. This value

represents the first translational frequency of the soil-structure system. If the vibration frequencies from Table 74 are compared to the vibration frequency of the fixed-base system 9.13 Hz, estimated by Pitilakis and Vratsikidis (2017), it can be concluded that the effects of SSI produced a significant decrease in the vibration frequency of the system. The results of Table 74 also shows that the translational frequency of the system decreases with increasing intensity of free vibration test.

	Test A	Test B	Test C	Test D
Peak amp.	2.75E-03	2.84E-03	5.06E-03	6.49E-03
Freq. (Hz)	3.09	3.08	2.99	2.88

Table 74: Peak amplitude and corresponding frequency of Fourier spectra for free vibration tests A to D

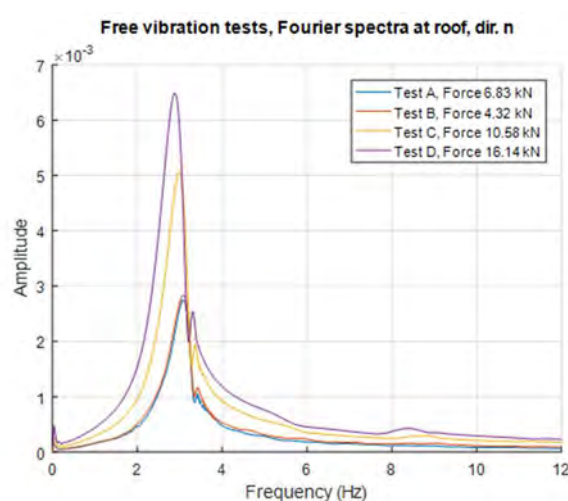


Figure 470: Comparison of Fourier spectra from free vibration tests A to D

	Test A	Test B	Test C	Test D
Peak S_a (m/s^2)	1.18	1.26	2.21	2.89
Period (s)	0.33	0.33	0.34	0.35

Table 75: Peak amplitude and corresponding period of acceleration response spectra (5% damping)

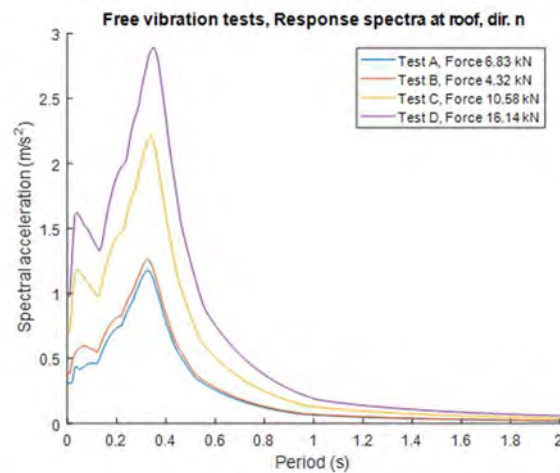


Figure 471: Comparison of acceleration response spectra (5 % damping) from free vibration tests A to D

A similar conclusion can be made based on comparison of acceleration response spectra. Based on Figure 471 and Table 75, it can be seen that the peak in the acceleration response spectrum shifts to the right with increasing intensity of free vibration test. This indicates an increase in the first translation period of the system. Because the structure remained in the linear-elastic range during all tests, it is reasonable to assume that the observed phenomenon is the consequence of nonlinear response of the soil. This conclusion is supported by the results of Figure 472 and Table 76, which demonstrate that the response of the soil (the soil velocity) near the structure increased, implying a larger contribution of the soil to the total response of the system. In addition to the increase in the period of the system, SSI can also increase the damping of the soil-structure system. The results of free vibration tests provide a valuable basis for estimation of the damping ratios of the soil-structure system.

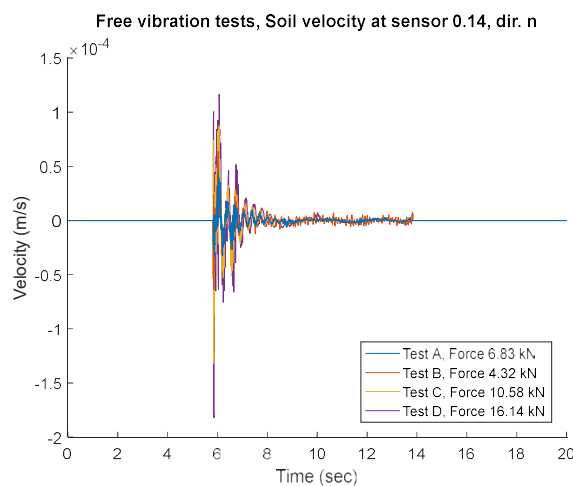


Figure 472: Comparison of soil velocities at sensor 0.14 from free vibration tests A to D

	Test A	Test B	Test C	Test D
Peak vel. (m/s)	-3.38E-05	-6.36E-05	-1.32E-04	-1.82E-04

Table 76: Peak soil velocity at sensor 0.14 for free vibration tests A to D

Figure 473 and Table 78 present an example of the estimation of the damping ratio based on logarithmic decrement of acceleration time-history. According to Pitilakis and Vratsikidis (2017), for lightly damped systems like the EuroProteas, the damping ratio over j cycles after the i th cycle is obtained as:

$$\zeta = \frac{1}{2\pi j} \ln \frac{a_i}{a_{i+j}} \quad (16)$$

As can be observed from Table 78, the damping ratio was estimated separately for positive and negative peaks over 3 cycles starting from the three most severe amplitudes in each direction. The obtained damping ratios are summarized in Table 77. Depending on the intensity of free vibration tests, the estimated damping ratios of the soil-structure system varied between 6% and 7%. The obtained values are significantly greater than the damping ratio of the steel structure alone, which is judged to be in a range of 2%. Thus, it can be concluded that SSI increased significantly the total damping of the system. In addition to this, it can be seen that the damping ratio tends to increase with the intensity of free vibration test. This result is again the consequence of the nonlinearity of soil response.

Peak i	Peak i+j	j	a_i	a_{i+j}	ζ
Positive peaks					
1 (1)	4 (7)	3	0.58	0.20	0.06
2 (3)	5 (9)	3	0.45	0.14	0.06
3 (5)	6 (11)	3	0.30	0.10	0.06
Negative peaks					
1 (2)	4 (8)	3	-0.56	-0.17	0.06
2 (4)	5 (10)	3	-0.38	-0.12	0.06
3 (6)	6 (12)	3	-0.26	-0.09	0.06

Table 77: Estimated damping ratios for free vibration tests A to D

	Test A	Test B	Test C	Test D
ζ	0.060	0.066	0.066	0.070

Table 78: Estimated damping ratios for free vibration test C. The notations of peaks in accordance with notations used in Figure 473 is provided in brackets

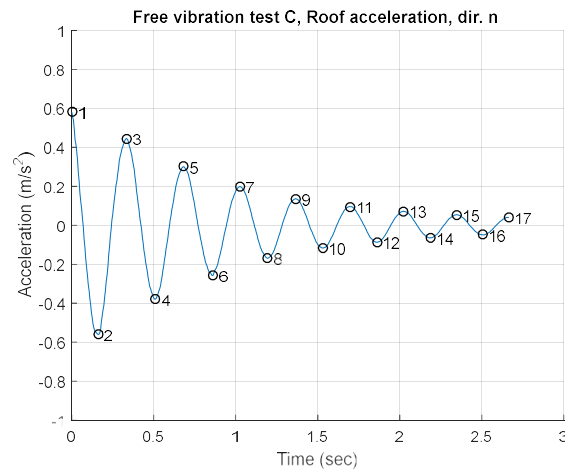


Figure 473: Estimation of peaks for the roof acceleration of the structure in free vibration test C

Forced-Vibration tests

Selected results of forced vibration tests A and C are shown in Figure 474 to Figure 479. Figure 474 and Figure 475 show the distribution of soil velocities at different measuring points, whereas Figure 476 to Figure 479 present the measured foundation and roof accelerations of the structure. It can be observed that the response of the soil and the structure increases during forced vibration tests because the applied harmonic force also increases with increasing frequency of input excitation. Important parameters which influence the response are the frequency of input excitation and the frequency of the soil-structure system. The response of the system can increase significantly if the frequency of the excitation is in resonance with the vibration frequency of the system. For example, during test A, a significant increase in response was observed when the frequency of input excitation was increased from 3 Hz to 3.5 Hz (steps 4 & 5 in Figure 474, Figure 476 Figure 478). This indicates that one of the vibration frequencies of the system is in between the listed frequencies. In fact, as it will be shown later, the first translational frequency of the system roughly equals to 3.1 Hz for low level of applied excitation. On the other hand, in case of test C, the significant increase in response was observed when the frequency of input excitation was increased from 2.5 Hz to 3.0 Hz (steps 3 & 4 in Figure 475, Figure 477 and Figure 479). This implies that the first translational frequency of the system decreased. Later, it will be shown that the first translational frequency of the system roughly equals to 2.9 Hz for a larger level of applied excitation. The decrease of the translational frequency of the system is related to the nonlinear response of the soil.

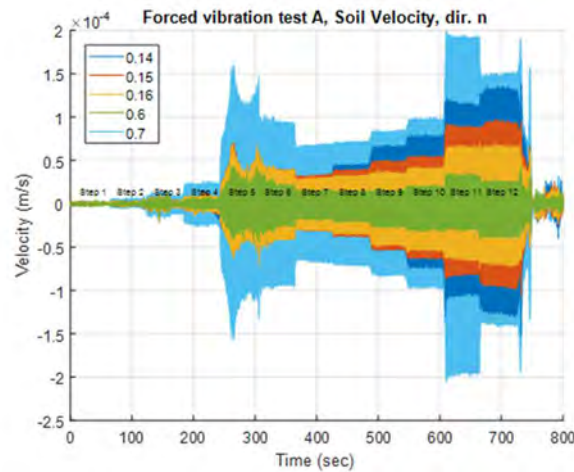


Figure 474: Soil velocity in direction North-South (direction n) for forced vibration test A

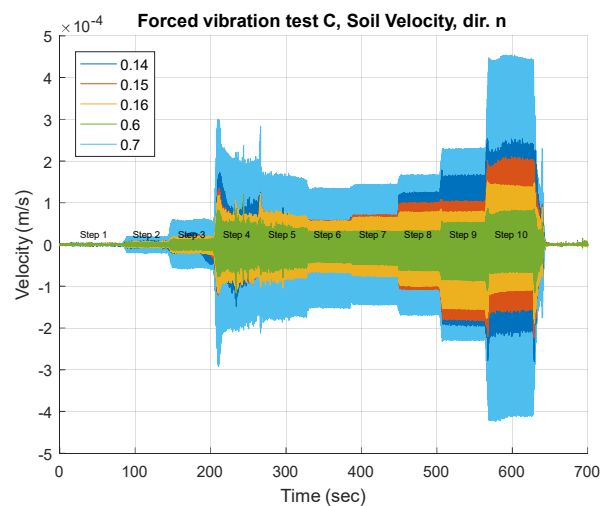


Figure 475: Soil velocity in direction North-South (direction n) for forced vibration test C

A similar increase in the response was also observed between step 11 and 12 in case of forced vibration test A (Figure 478). However, in this case, the increase in the response was observed only for the sensor located at the corner of the roof of the structure (sensor 2.1). This result indicates a large torsional response of the system and implies that the torsional frequency of the building is between 9 Hz and 10 Hz. In fact, results of system identification technics based on ambient vibrations results presented by Pitilakis and Vratsikidis (2017) indicate that the torsional frequency of the system roughly equals to 9.6 Hz. A similar trend was also observed at the foundation level (Figure 476). However, it seems that largest torsional response is attained at a slightly lower frequency (between 8 and 9 Hz, steps 10 & 11 in Figure 476).

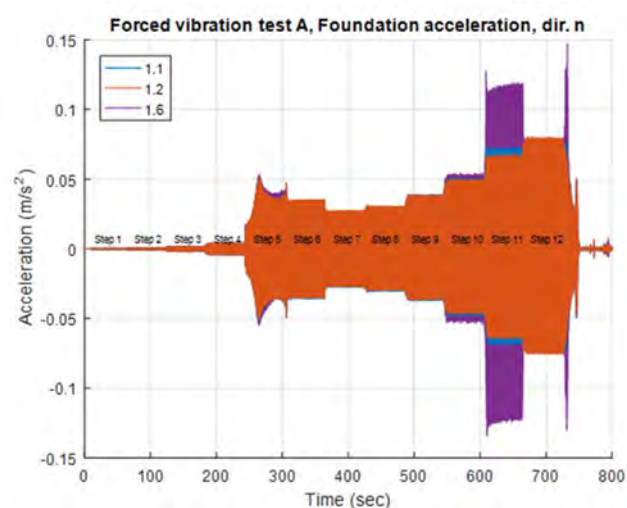


Figure 476: Foundation acceleration in direction North-South (direction n) for forced vibration test A

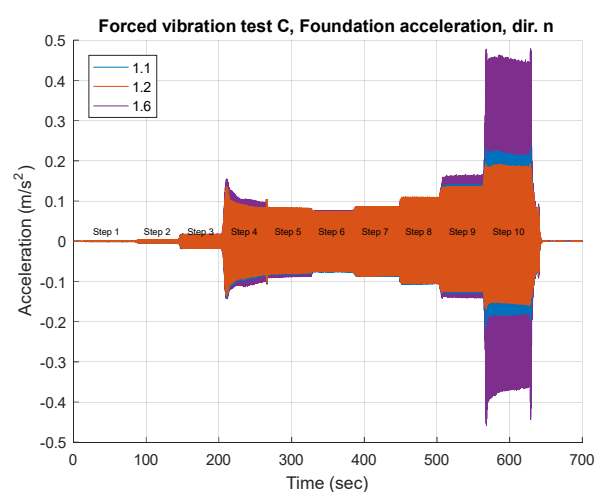


Figure 477: Foundation acceleration in direction North-South (direction n) for forced vibration test C

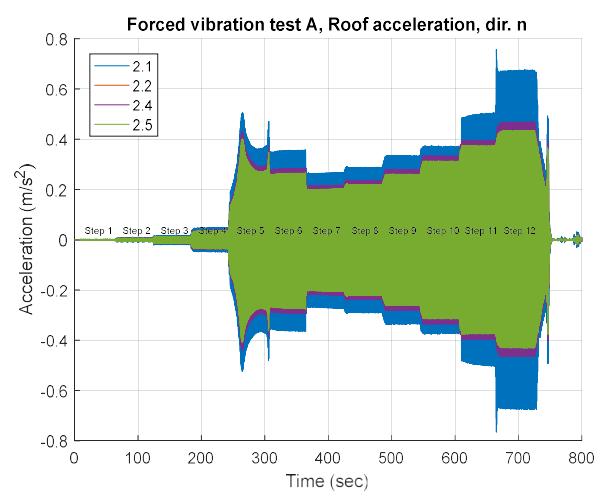


Figure 478: Roof acceleration in direction North-South (direction n) for forced vibration test A

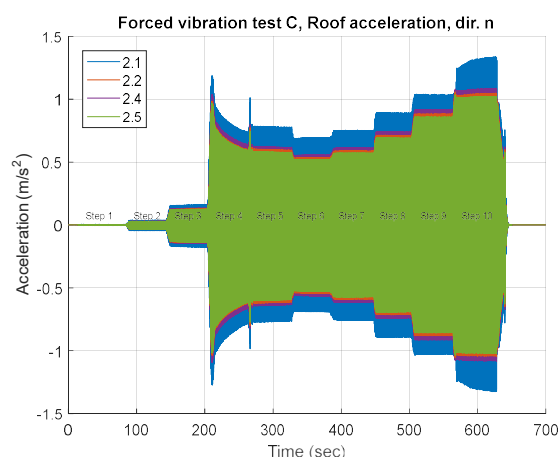


Figure 479: Roof acceleration in direction North-South (direction n) for forced vibration test C

The comparison of roof accelerations from forced vibration tests A to D is presented in Figure 480. It can be seen that the roof accelerations increase during the duration of forced vibration test due to increasing frequency of input excitation, which also implies larger force of harmonic excitation. Additionally, the mass of the shaker was increased between different tests, which resulted in an increased response of the system. The most interesting aspect of forced vibration test is the examination of frequencies of input excitation, which produce significant amplification of system response. These frequencies correspond to the predominant frequencies of the soil-structure system. In the following, the focus is placed in the examination of the first translation frequency of the system in the direction of the test.

From Figure 480, it can be observed that during forced vibration tests A and B, the largest increase in response was obtained between steps 4 and 5 (between frequencies 3 Hz and 3.5 Hz). This implies that the first translational frequency of the system is in between these frequencies. Such an observation is confirmed by results of free vibration test A and B, which indicate that the vibration frequency of the system roughly equals to 3.1 Hz for the low level of applied free vibration excitation. On the other hand, in case of forced vibration tests C and D, the largest increase in response was obtained between steps 3 and 4 (between frequencies 2.5 Hz and 3.0 Hz). This implies that the first translational frequency of the system decreased. This observation is consistent with the results of free vibration test C and D, which indicate that the translational vibration frequency of the system roughly equals to 2.9 Hz. Again, it can be concluded that the decrease in the translational frequency of the system is related to the nonlinear response of the soil.

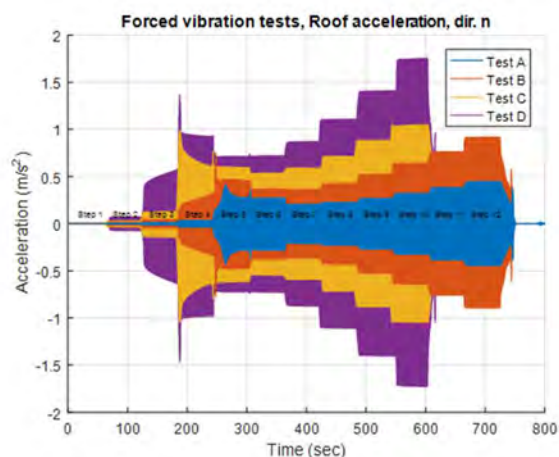


Figure 480: Comparison of roof accelerations from forced vibration tests A to D

A similar observation can be made based on the examination of the acceleration response spectra from forced vibration tests, which are presented in Figure 481. Examining the shape of the response spectra, it can be seen that all spectra feature two evident peaks. The first (largest) peak is a result of the forced vibration test at larger frequencies, which are performed for greater force of harmonic excitation. The second and most interesting peak is related to the response of the system in the predominant vibration mode (in this case first translational mode). It should be noted, however, that in the case of forced vibration tests, the peak or the response spectra represent the predominant period of the response of the system, and as such can be different than the natural period of the system (it depends on force vibration excitation). Nevertheless, based on Figure 481, it can be seen that the location of the second peak is shifted to the right when the intensity of the forced vibration test is increased. This implies that the predominant period of response increases with the severity of input excitation, demonstrating again the influence of nonlinear response of the soil.

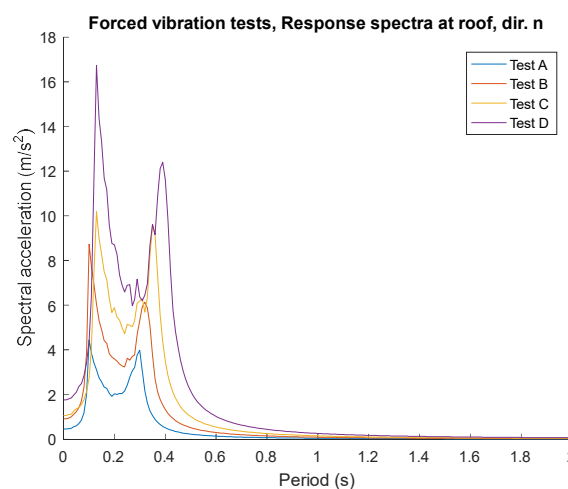


Figure 481: Comparison of acceleration response spectra (5 % damping) from forced vibration tests A to D

9.4.6 Conclusions and outlook

The performed full-scale experimental campaign provided insight into the basic effects of soil-structure interaction (SSI). SSI increases the flexibility of the system due to additional compliance of the foundation, which increases the vibration period of the system. In the case of the EuroProteas, the vibration period of the fixed-base system increased from 0.11 s to about 0.35 s due to consideration of SSI effects. The effects of SSI caused additional energy-losses which increased with the severity of excitation. This is reflected in the effective damping of the system. For example, the estimated effective damping of the EuroProteas was estimated to about 6% to 7%, which is significantly greater than the damping ratio of the steel structure alone (about 2%). The variation of the effective damping from 6% to 7% is the consequence of increasing the intensity of applied loading, which caused the nonlinearity in the response of the soil.

The implications of SSI effect on the seismic design of buildings is examined in Figure 482 considering the example of the EuroProteas structure. In the example, it is assumed that the EuroProteas structure is designed for earthquake resistance according to Eurocode 8 (CEN, 2004). For simplicity, the Eurocode 8 elastic spectrum for soil type C is assumed instead of the Eurocode 8 design spectrum. The peak ground acceleration on soil type C ($a_g \cdot S$) was assumed to amount to 0.3 g. The design of the building is performed considering two assumptions regarding the characteristics of the system. In the first case,

the system is designed considering the typically used fixed-base assumption, which neglects the influence of SSI. In this case, the period and the damping ratio of the fixed-base system were estimated to amount 0.11 s and to 2%, respectively. In the second case, the actual characteristics of the EuroProteas soil-structure system are used (period 0.35 s and damping ratio 7% based on Section 9.4.5). The comparison of the obtained seismic demand for the two design assumptions is presented in Figure 482. The figure highlights two basic effects of SSI on the earthquake-resistant design of buildings. The first effect is the reduction of the response spectrum amplitudes due to increased damping of the system. This effect is considered beneficial. The second effect is the increase in period of vibration of the system, which can have, both, beneficial or detrimental effect on the seismic demand depending on the region of response spectra. For the presented example, the consideration of the effect of SSI causes an increase in seismic demand (spectral acceleration 0.69 g instead of 0.60 g), which means that designing the structure considering a fixed-base assumption would yield to non-conservative design of the building. This result demonstrates the importance of the consideration of SSI effects in the design of stiff structures located on soft soils.

Despite well-known effects of SSI on structural response, explicit modelling of SSI is still rarely used in practical applications. As reported in (NIST, 2012), the reason may lay in a poor understanding of SSI principles, complicated procedures for the estimation of properties of soil springs and dashpots, and limited coverage of this topic in regulatory documents. Current seismic design practices can thus be improved by the development of novel yet simplified methods which will allow the consideration of the SSI effects without increasing the complexity of the design state-of-practice.

The results of the experimental campaign at EuroProteas provided valuable data for validation of existing design procedures and for the development of new procedures. The obtained results will be used for supporting ongoing research at the University of Ljubljana, which addresses the development of design response spectrum with approximate consideration of soil-structure interaction and the usability of the dynamic system identification using ambient/forced-vibration measurements for the risk assessment of existing structures.

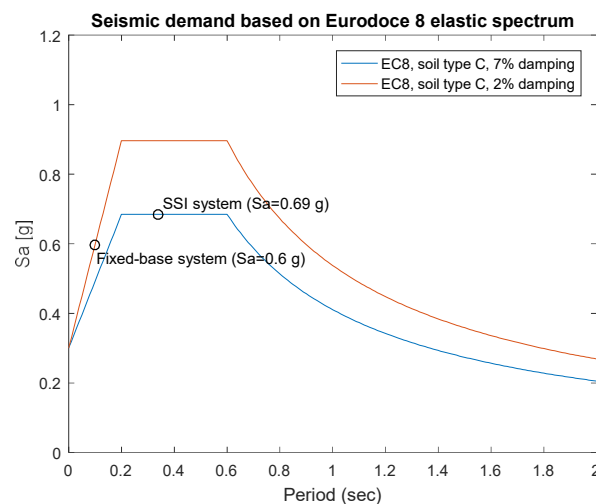


Figure 482: Comparison of acceleration spectra based on Eurocode 8 elastic spectrum (soil type C, $a_g \cdot S = 0.3$ g) for the fixed-base and SSI system of the EuroProteas

9.4.7 References

ASCE. “ASCE/SEI 41-17. Seismic Evaluation and Retrofit of Existing Buildings (41-17)”, American Society of Civil Engineers, 2017.

ASCE. “ASCE/SEI 7-16 standard. Minimum Design Loads and Associated Criteria for Buildings and Other Structures (7-16)”, American Society of Civil Engineers, 2016.

CEN. “European standard EN 1998. Eurocode 8: Design of structures for earthquake resistance”, European Committee for Standardization, Brussels, December 2004.

Raptakis D., Anastasiadis A. & Pitilakis K. (1998). Preliminary instrumental and theoretical approach of site effects in Thessaloniki. In *Proceedings of the 11th European Conference on Earthquake Engineering*.

Pitilakis D. *et al.* (2018). Field evidence of SSI from full-scale structure testing, *Soil Dynamics and Earthquake Engineering*. Elsevier Ltd, 112(March), pp. 89–106.

Pitilakis D. and Vratsikidis A. (2017). Dynamic system properties from real-scale free-vibration soil-structure interaction experiments, *Proceedings of the 7th International Conference On Advances in Experimental Structural Engineering*, EUCENTRE Foundation, Pavia, 6-8 September 2017.

Pitilakis K. *et al.* (1999) Geotechnical and geophysical description of euro-seistest, using field, laboratory tests and moderate strong motion recordings, *Journal of Earthquake Engineering*, 3 (3), 381–409.

9.5 Project # 29 – Seismic SITE effects in sedimentary basins from 3D physics-based numerical modeling (SITE3D)

Authors

C. Smerzini⁽¹⁾, X. Chen⁽²⁾, A.G. Ozcebe⁽³⁾, M. Infantino⁽¹⁾, A. Vratsikidis⁽⁴⁾, M. Manakou⁽⁴⁾, D. Pitilakis⁽⁴⁾

⁽¹⁾ *Department of Civil and Environmental Engineering, Politecnico di Milano, Italy*

⁽²⁾ *Visiting PhD student – China Scholarship Council, Department of Civil and Environmental Engineering, Politecnico di Milano, Italy*

⁽³⁾ *EUCENTRE, European Centre for Training and Research in Earthquake Engineering, Pavia, Italy*

⁽⁴⁾ *Aristotle University of Thessaloniki, Thessaloniki, Greece*

9.5.1 Introduction

It is widely recognized that local geologic irregularities may affect significantly strong ground motion, modifying its amplitude, duration and frequency content characteristics. Therefore, an accurate evaluation of local site effects is crucial for the definition of site-specific ground motions for the earthquake-resistant design of structures.

EUROSEISTEST is one of the best-documented sites worldwide from both an instrumental and geological-geophysical-geotechnical point of view, making it an excellent case study for testing and validating numerical methods for earthquake ground motion prediction in complex geological configurations. The main purpose of the SITE3D project is to evaluate seismic site effects in the

Mygdonian basin (EUROSEISTEST site), located about 30 km northeast of the city of Thessaloniki (Northern Greece), based on 3D physics-based numerical simulations of seismic wave propagation from the seismic fault rupture up to the site. Specifically, the main objectives of the project are: (1) set-up of a 3D numerical model of the Mygdonian basin area, including both the 3D basin structure and the active faults located in proximity of the investigated area; (2) physics-based numerical simulation of different earthquake scenarios; (3) evaluation of 3D site amplification effects within the Mygdonian basin.

In the framework of this project, the 3D numerical modelling of the Mygdonian basin is carried out through the high-performance open-source spectral element code SPEED - Spectral Elements in Elastodynamics with Discontinuous Galerkin, see <http://speed.mox.polimi.it/> (Mazzieri et al. 2013). The SPEED code is the result of a ten-year research activity involving the Department of Civil and Environmental Engineering and the Department of Mathematics at Politecnico di Milano, and its development has been supported by several international research projects funded by both public and private institutions.

After the set-up of a large-scale “source-to-site” 3D spectral element model of the broader EUROSEISTEST area, 3D physics-based numerical simulations of ground motion in the Mygdonian basin by SPEED are prompted to account for a representative set of earthquake scenarios along the seismogenic fault sources. Then results are processed to get ground motion time histories at selected soft sites, maps of different ground motion intensity measures, and to estimate 3D site amplification functions with respect to ideal outcropping bedrock.

9.5.2 EUROSEISTEST Array

EUROSEISTEST is a multidisciplinary European experimental site for integrated studies in earthquake engineering, engineering seismology, seismology, geotechnical engineering and soil dynamics. Established in 1993, it is the longest running basin-instrumentation project worldwide. It is located in the tectonically active Mygdonia basin (epicentral area of the June 20th, 1978, M6.4 earthquake), about 30km to the NNE of the city of Thessaloniki, which is the largest urban area in northern Greece. The basin is part of the Servomacedonian Massif zone that presents high seismicity (1904 Kresna M7.4 and 1932 Ierissos M7.2 earthquakes).

The basin is about 5.5 km wide in the NNW–SSE direction and has a maximum depth of 200 m. The subsoil structure is investigated in detail and defined using geological, geophysical and geotechnical state-of-practice tools in earlier studies (Pitilakis et al. 1999, Raptakis et al. 2000, Manakou et al. 2010). Shear wave velocity, V_s , values evaluated by inverting data from microtremor array measurements, seismic refraction profiles and properly correlated were used, along with other parameters, to construct detailed and accurate 1D, 2D & 3D profiles for seismic ground response analysis (Figure 483).

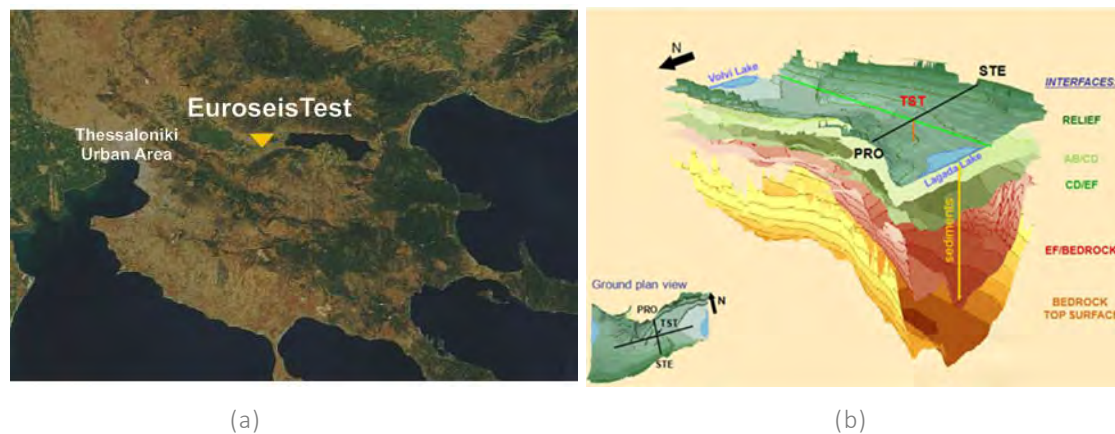


Figure 483: (a) Location of the EUROSEISTEST and (b) the benchmark 3D model of the Mygdonia basin geological structure (Manakou et al. 2010)

EUROSEISTEST array consists of a permanent accelerometric network includes 21 strong motion broadband three-components accelerographs, 15 of which are located at the ground surface and 6 in down-hole arrays at the center and at the northern edge of the instrumented area.

Acceleration time series and accompanying earthquake and stations metadata have been stored in a database (<http://euroseisdb.civil.auth.gr/>).

9.5.3 Numerical model

Based on the available data regarding both the characterization of the seismic sources and geological, geotechnical and geophysical aspects, two 3D numerical models were constructed to study seismic site effects in the EUROSEISTEST area. The extended numerical encompasses the broader Mygdonian graben while the reduced model includes the portion of the basin belonging to the EUROSEISTEST area.

The extended numerical model

The 3D spectral element mesh of the extended numerical model is displayed in Figure 484, which includes the following features:

1. Ground topography as retrieved from 90 m SRTM Digital Elevation Model (<http://srtm.csi.cgiar.org/>), covering the broader Mygdonian Basin area (see Figure 485).
2. Three seismogenic sources posing a hazard to the Mygdonian basin (see Figure 484a) , i.e., Gerakarou Fault (GRIS101, the fault responsible of the M6.5 1978 Volvi earthquake), Langadhas Fault (GRIS102) and Apollonia Fault (GRIS103), as retrieved from the GreDaSS database (<http://gredass.unife.it/>). The three faults are segments of a larger fault zone (Mygdonia CS GRCS100) that bounds the southern margins of the Mygdonia Basin.
3. Horizontally layered crustal model for deep rock materials in Table 79 (from Smerzini et al. 2017).
4. 3D velocity model of the Mygdonian basin (see below for further details).

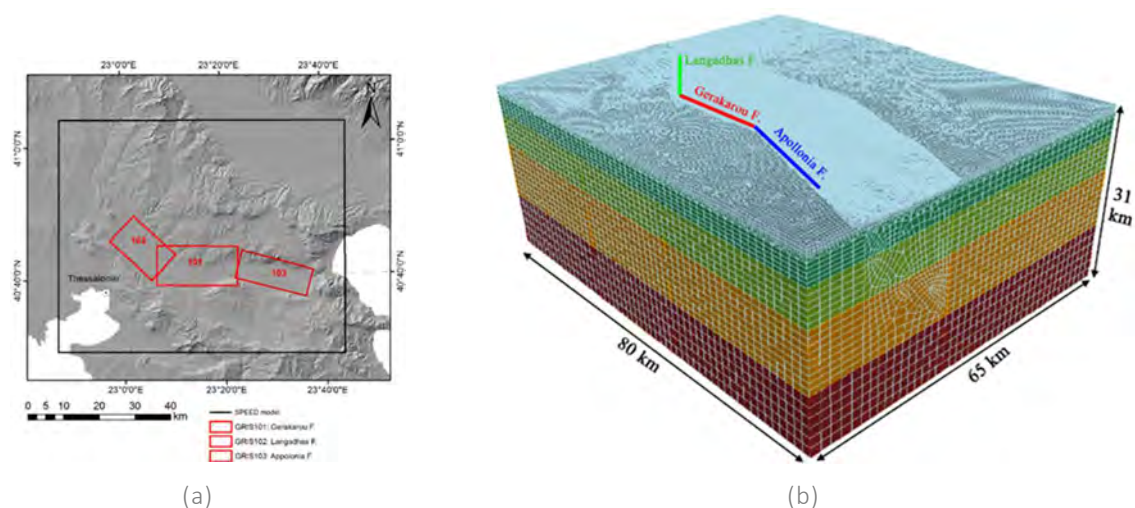


Figure 484: (a) Map of the main seismogenic sources taken into account in the numerical modelling of the broader Mygdonian area. Faults are from GreDASS database: 101-Gerakarou, 102-Langadhas and 103-Apollonia Faults. The boundaries of the extended SPEED model are also shown (black lines) and (b) 3D spectral element mesh (448'276 hexahedral elements)

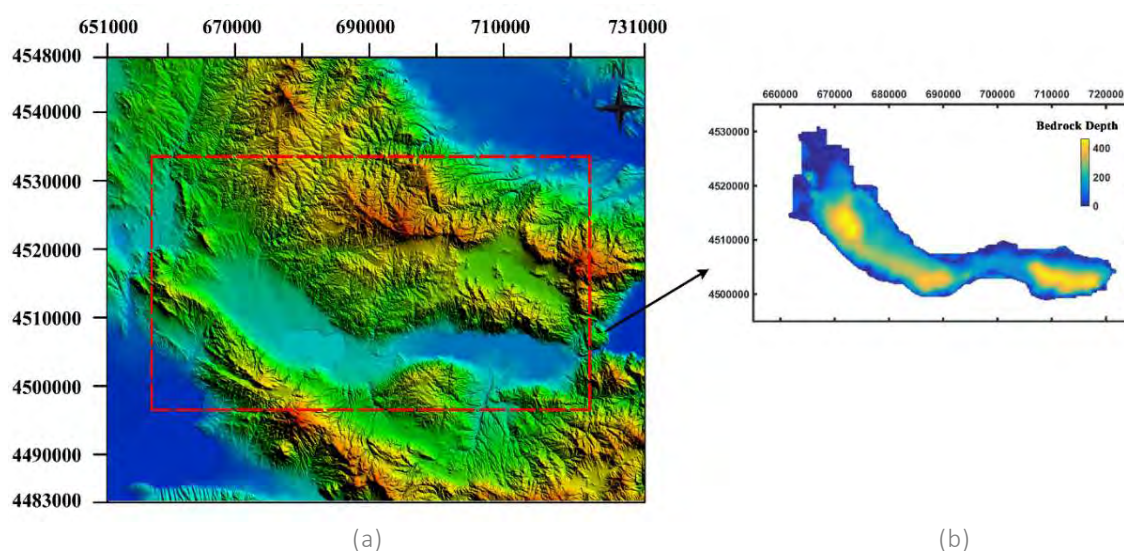


Figure 485: (a) Digital Elevation Model (DEM) of the broader Mygdonian area and (b) depth of the alluvial-bedrock interface

Depth (km)	ρ (kg/m ³)	V_P (m/s)	V_S (m/s)	Q_S (-)	Q_P (-)
0 – 1	2400	4500	2000	200	400
1 – 5	2700	6060	3440	300	600
5 – 11	2800	6070	3460	300	600
11 – 21	2900	6370	3640	300	600
21 – 31	3000	6960	3980	400	600

Table 79: The crustal model for deep rock materials of the Mygdonian area (from Smerzini et al. 2017)

The mesh extends over a volume of about $80 \times 65 \times 31 \text{ km}^3$ and is discretized using an unstructured hexahedral conforming mesh with characteristic element size ranging from a minimum of about 100 m at ground surface inside the basin to about 2000 m at the bottom of the model. The model consists of 448'276 spectral elements, leading to 12'519'562 nodes with a third-order polynomial approximation degree. Considering a rule of thumb of 5 grid points per minimum wavelength for non-dispersive wave propagation in heterogeneous media by the SE approach, this model can propagate frequencies up to about 1.5 Hz. Numerical simulations were performed exploiting the parallel computing capabilities of SPEED. For this project, they were carried out on the Marconi A2 Cluster at CINECA, the largest high-performance computing center in Italy (www.cineca.it).

As regards the extended Mygdonian basin model, the 3D shape of the alluvial-bedrock interface is taken from Maufroy et al. (2016). The mechanical properties of soft soil deposits between ground surface and the bedrock interface are characterized by a linear gradient from a minimum shear wave velocity of 150 m/s, as follows:

- for S (shear) wave velocity, $V_S(z) = 150 + 1.63 \cdot z$ (V_S is in m/s, z is in m)
- for P (shear) wave velocity, $V_P(z) = 1500 + 3.0 \cdot z$ (V_P is in m/s, z is in m)
- for soil density, $\rho(z) = 2075 + 0.44 \cdot z$ (ρ is in kg/m^3 , z in m).

Besides, a frequency-proportional quality factor $Q_s = Q_0 \cdot f/f_0$ is assumed, with $f_0 = 1 \text{ Hz}$ and $Q_0 = V_S/10$. Note that $Q = V_S/10$ is a rule-of-thumb for estimating Q based on the V_S profile often used in the literature (see e.g. Laurendeau et al. 2018). Note that in SPEED geologic discontinuities, such as alluvial basins, are defined by a not-honoring technique, where material properties are given node by node.

The reduced numerical model

The 3D spectral element mesh of the reduced numerical model is illustrated in Figure 486. The reduced model shares the same crustal model with the extended model (see Table 79), while it contains only one seismogenic fault source, i.e., Gerakarou Fault, and the depth of the alluvial-bedrock interface, as provided by Manakou et al. (2010), see Figure 486.

Being designed for the same maximum frequency of 1.5 Hz, the reduced model extends over a volume of about $25 \times 25 \times 31 \text{ km}^3$ and consists of 375'513 spectral elements. Rupture scenarios along the Gerakarou fault can be simulated also by this reduced model, even though the maximum magnitude of the simulated scenario is limited to an upper bound of around 5.5, to limit the effects of spurious reflections from the absorbing boundaries.

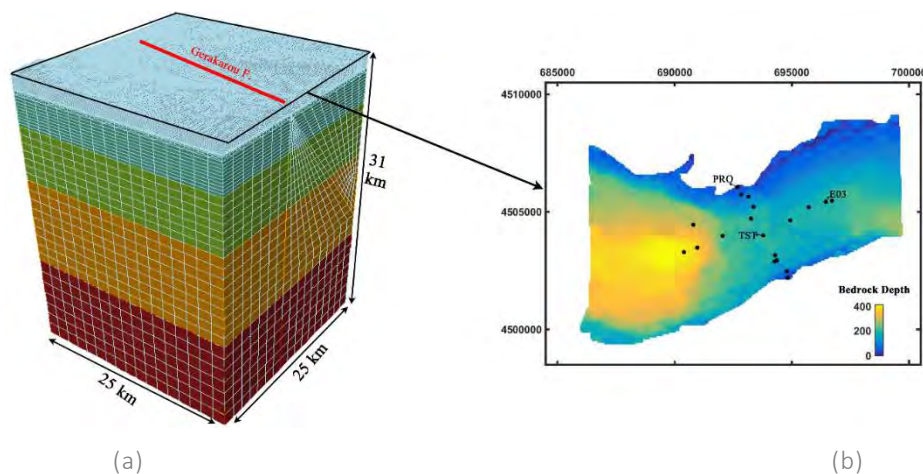


Figure 486: (a) 3D spectral element mesh for the reduced area of the Mygdonian basin and (b) depth of the alluvial-bedrock interface. The locations of the EUROSEISTEST stations are also indicated

9.5.4 Test setup

The “Seismic site effects in sedimentary basins from 3D physics-based numerical modeling (SITE3D)” didn’t include any physical experiments. Remote access on the EUROSEISTEST database containing seismological geotechnical and geological data was granted.

9.5.5 Observation during testing

The “Seismic site effects in sedimentary basins from 3D physics-based numerical modeling (SITE3D)” didn’t include any physical experiments. Remote access on the EUROSEISTEST database containing seismological geotechnical and geological data was granted.

9.5.6 Preliminary results

The extended numerical model was adopted to perform the simulations of:

- Scenario S1: M_w 4.4 Sept 12 2005 earthquake, recorded in the field and, hence, used as target event to validate the numerical model. Due to the small target magnitude, this event is modelled in SPEED as a double couple point-source with focal mechanism as listed in Table 80;
- Scenario S2: Finite-fault rupture scenario for a hypothetical M_w 6.0 earthquake originating from the Gerakarou fault. The fault parameters along with the co-seismic slip distribution are shown in Table 81.

For all simulations, a linear visco-elastic model for soil response was adopted and results are provided in the frequency range correctly propagated by the numerical model (1.5 Hz). Issues like impact of non-linear soil effects and generation of broadband signals will be investigated in further studies.

Hypocenter (°N, °E)	Depth (km)	Mw (-)	Strike (°)	Dip (°)	Rake (°)
(40.7255, 23.3408)	10	4.40	281	52	-98

Table 80: Focal mechanism of the M_w 4.4 Sept 12 2005 earthquake (S1), from Maufroy et al. (2016)

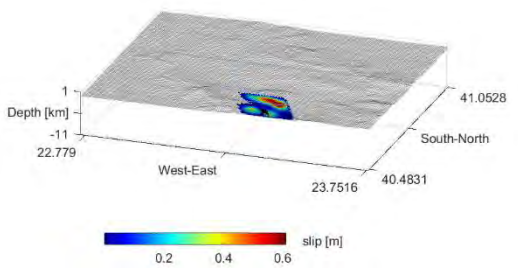
Scenario S2		Co-seismic slip distribution	
Moment Magnitude M_w	6.0		
Top depth [km]	1.8		
Length L [km]	15		
Width W [km]	12		
Hypocenter (Lon°E, Lat°N)	(23.285, 40.706)		
Focal Depth [km]	8.1		
Strike [°]	272		
Rake [°]	270		
Dip [°]	50		
		Slip distribution according to Herrero and Bernard (1994)	

Table 81: Finite-fault rupture scenario for M_w 6.0 earthquake scenario (scenario S2)

Validation results

As a first step of this study, the numerical model was validated by comparing the results of S1 simulations with the recordings available for the 2005 event (data available at <http://euroseisdb.civil.auth.gr/>). Figure 487 shows the comparison between SPEED synthetics and recordings at E03 station (see location in Figure 486) in terms of three-component (EW, NS and UP) velocity time histories (top panel) and corresponding Fourier Amplitude Spectra (FAS, bottom panel). A low-pass filter with cut-off frequency of 1.5 Hz has been applied to both synthetics and recordings. At this station, an excellent agreement of first arrivals, phases, amplitudes and frequency content is found. Furthermore, in Figure 488 the simulated values of Peak Ground Velocity (PGV: EW, NS, UP) at the entire set of surface stations are compared with the corresponding recorded values as a function of epicentral distance (R_{epi}). These results point out a good agreement between simulations and observations, apart from the trend of SPEED results to overestimate recordings, especially on the NS component.

Evaluation of 3D Spectral Amplification Ratios

To evaluate the 3D amplification ratios with respect to “ideal” outcropping bedrock conditions, for each of the two scenarios S1 and S2, two twin simulations were performed: (1) a simulation with the numerical model including the basin structure (as described previously); (2) another simulation where the basin is fictitiously removed and replaced by the top layer of the crustal model (see Table 79).

Figure 489 shows the ground shaking maps obtained for scenarios S1 and S2, in terms of different ground motion intensity measures, namely: PGV, elastic pseudo-Spectral Acceleration (SA) at $T=1$ s and SA at $T=3$ s, for the horizontal geometric mean component.

The availability, for each scenario earthquake, of a couple of simulations, with and without the basin, allows one to compute the ideal 3D amplification function and its spatial variability within the basin. The spectral amplification ratios, SAR, are computed as follows:

$$SAR(T) = \frac{SA_{basin}(T)}{SA_{rock}(T)} \quad (17)$$

where $SA_{basin}(T)$ and $SA_{rock}(T)$ are the 5% damped elastic spectral acceleration ordinates from simulations obtained with and without the presence of the basin, respectively.

Figure 490 reports the maps of the SAR (horizontal geometric mean) computed for both scenarios, S1 (left) and S2 (right), for the periods $T=2$ s and $T=3$ s, in the EUROSEISTEST area. It is interesting to note that, although the hypocenter-to-site configurations are rather similar, there is a significant dependence of site amplification with respect to the considered earthquake scenario, owing to the coupling of source properties (radiation pattern for point source, plus rupture propagation features for extended fault) with focalization phenomena associated with the geometry of the bedrock interface and generation of surface waves at basin edges. This is further clarified by Figure 491, where SARs are shown for three stations, E03, PRO and TST (see Figure 486 for the corresponding location), for both scenarios. We note that the amplification is larger in proximity of the source slip, which is concentrated in point source model and distributed in the finite fault model. At stations E03 and PRO, S1 provides larger SAR than S2 over the entire period range, while the opposite is found at TST (basin center), most likely due to the influence of the up-dip asperity in the extended rupture scenario. A detailed study of the dependence of the amplification function on the earthquake scenario will be object of future research.

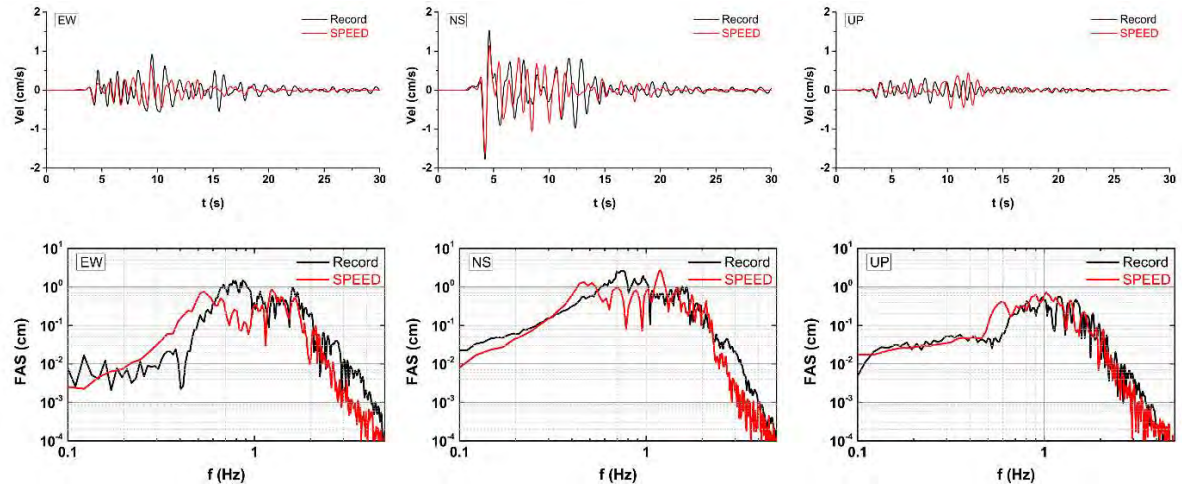


Figure 487: Comparison between synthetics and observations at E03 station in terms of three component (EW, left; NS, center; UP, right) velocity time histories (top panel) and corresponding Fourier Amplitude Spectra (FAS, bottom panel), for the Mw4.4 Sept 12 2005 earthquake (S1)

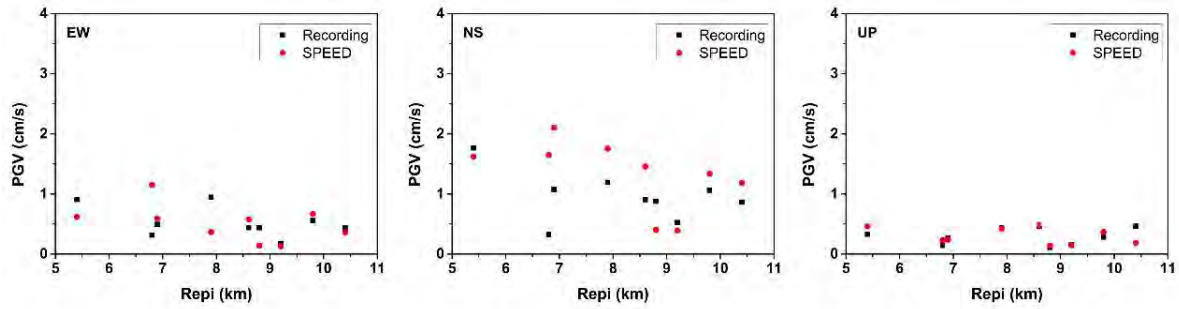


Figure 488: Comparison of PGV (EW, left; NS, center; UP, right) vs epicentral distance (R_{epi}) for surface receivers obtained from SPEED simulations (S1) and recordings

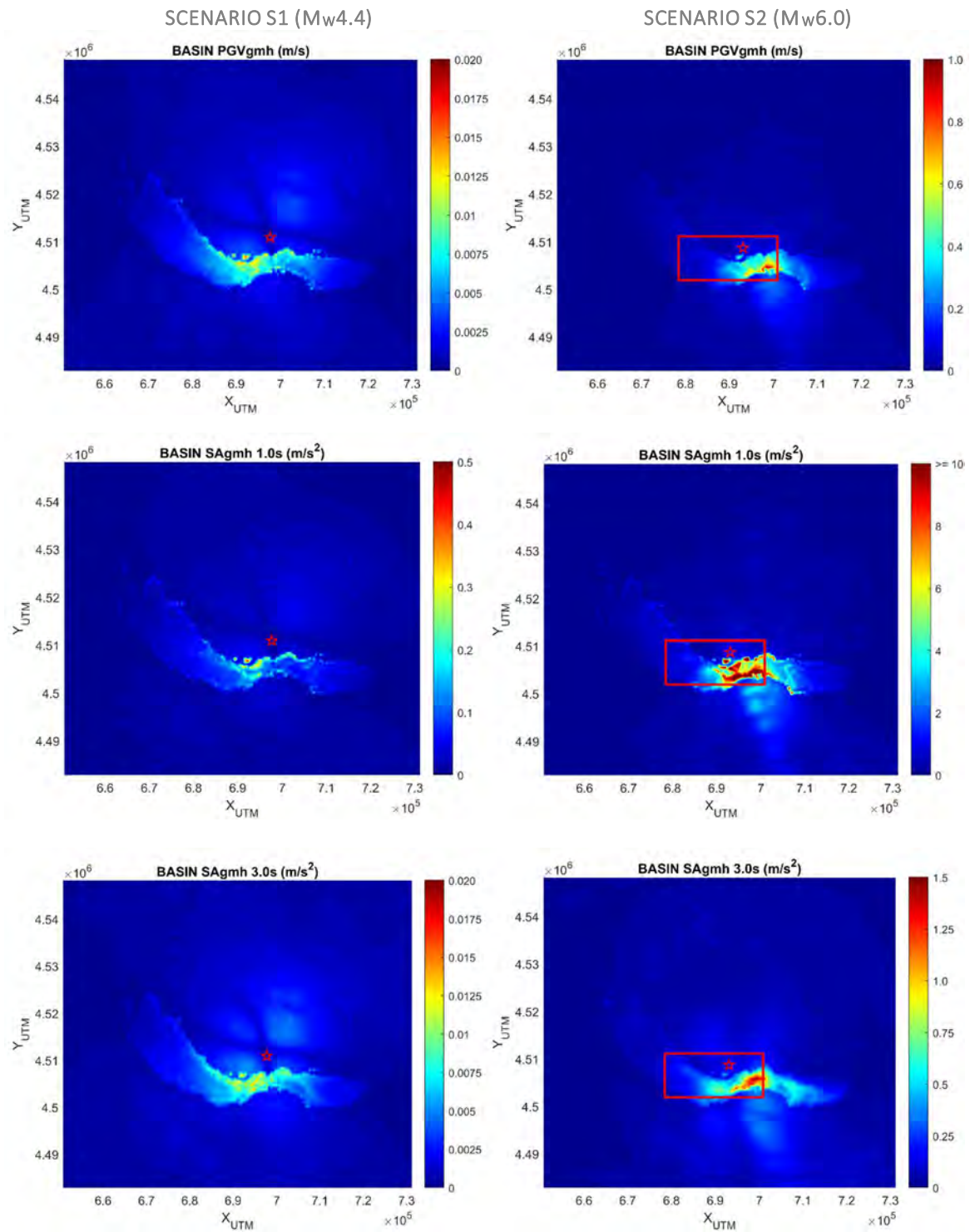


Figure 489: Ground shaking maps (geometric mean of horizontal components: gmh) in terms of PGV, Spectral Acceleration (SA) at $T=1$ s, and SA at $T=3$ s, for scenario S1 (left) and S2 (right)

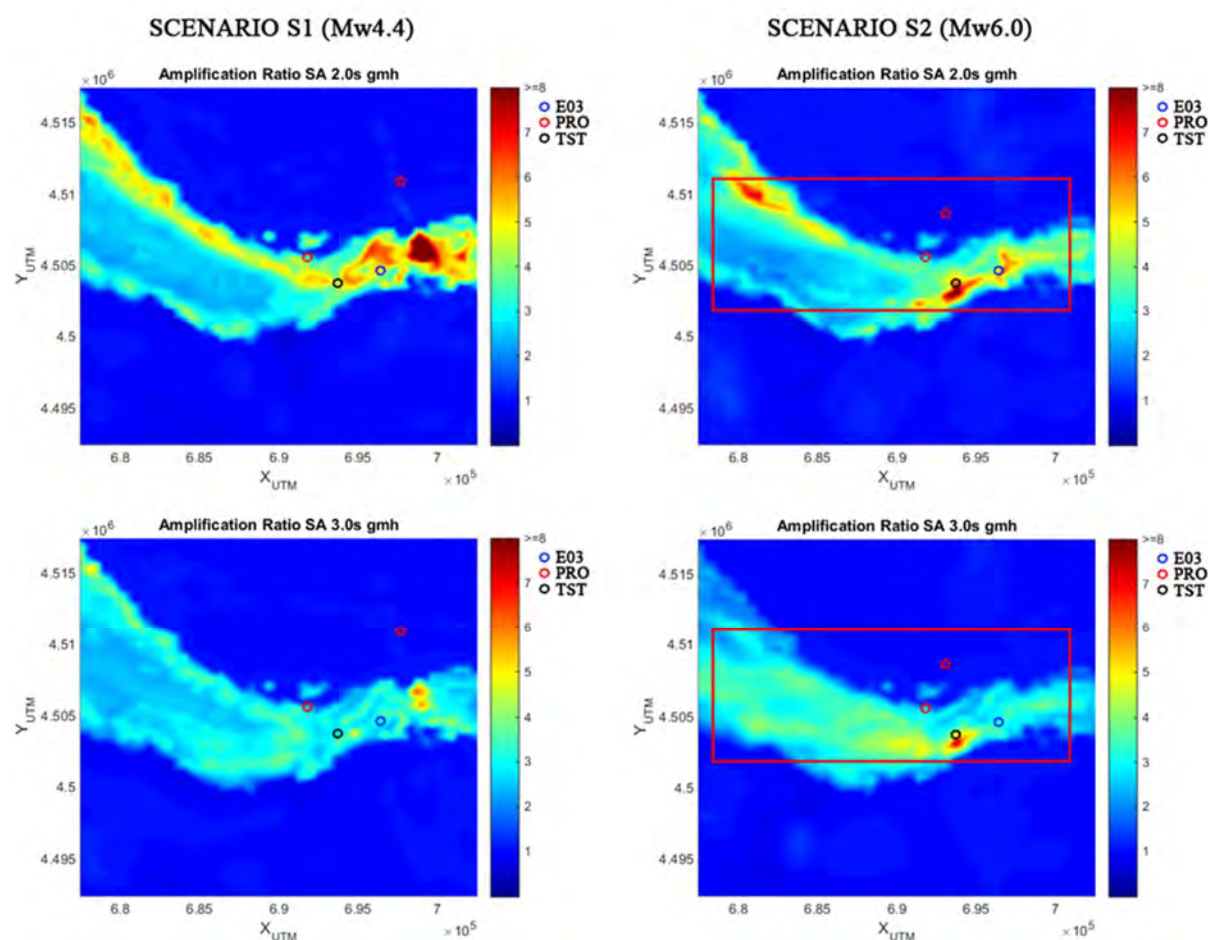


Figure 490: Maps of Spectral Amplification Ratios (SAR) for SA(2s) and SA(3s), gmh, for scenario S1 (left) and S2 (right) in the EUROSEISTEST area

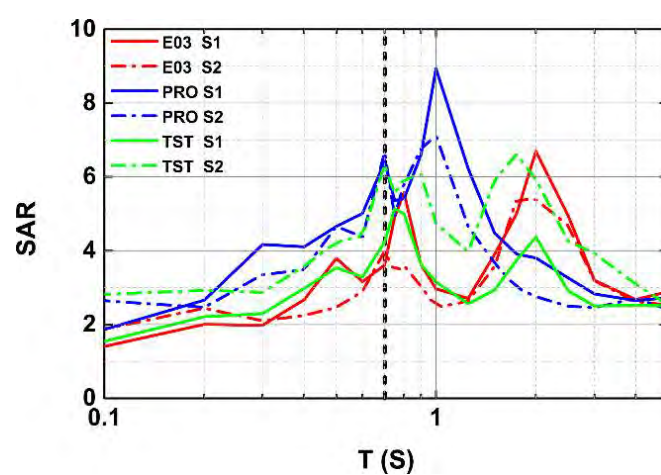


Figure 491: SAR (gmh) for three stations, namely, E03, PRO and TST (see location in Figure 486), and for the two scenarios S1 and S2. The dashed line indicates the minimum period of the numerical model

9.5.7 Conclusions and outlook

In the framework of the SITE3D project, the geological, geophysical and seismological data regarding the EUROSEISTEST site have been used to generate 3D numerical models, with different spatial extents, including both the 3D structure of the Mygdonian basin and the seismic sources located in the proximity of the site. The extended numerical model encompasses the major active faults surrounding the Mygdonian basin (Gerakarou, Langadhas and Apollonia), including the one responsible of the destructive M6.5 1978 earthquake. Therefore, the model can be used to simulate arbitrary finite-fault rupture scenarios and to estimate the resulting near-fault earthquake ground motion in the broader Mygdonian area.

Physics-based numerical simulations of seismic wave propagation for two earthquakes, namely, the M4.4 Sept 12 2005 earthquake (scenario S1, point source) and a hypothetical Mw6.0 event (scenario S2, extended source), were carried out using the open-source spectral element code SPEED. Consideration of the real M4.4 event allows us to successfully validate the numerical model by comparison of SPEED results with available recordings in the frequency range up to 1.5 Hz. Preliminary results for these scenarios allowed us to produce maps of different ground motion intensity measures, such as PGV and SA at different periods. Furthermore, as main outcome of this study, 3D site effects were estimated by computing the ratio of response spectral ordinates at the surface of the basin sediments with respect to the one simulated on ideal outcropping bedrock conditions. Results suggest that site amplification response may be significantly affected by the considered earthquake rupture scenario.

Further studies may involve: (a) comparison of the numerical 3D site amplification functions with the ones from available recordings, for a larger set of earthquakes; (b) generation of a wider suite of finite-fault rupture scenarios, with varying slip distribution, magnitude and hypocenter location; (c) generation of broadband ground motions using techniques based on Artificial Neural Networks (Paolucci et al. 2018); (d) parametric analysis and quantification of the source-related variability of the 3D spectral amplification ratios.

9.5.8 References

- Herrero A., Bernard P. (1994). A kinematic self-similar rupture process for earthquakes, *Bulletin of Seismological Society of America*, 84: 1216-1229.
- Laurendeau A., Bard P.Y., Hollender F., Perron V., Foundotos L., Ktenidou O.J., Hernandez B. (2018). Derivation of consistent hard rock ($1000 < V_S < 3000$ m/s) GMPEs from surface and down-hole recordings: analysis of KiK-net data. *Bulletin of Earthquake Engineering*, 16(6): 2253-2284.
- Manakou M. V., Raptakis D. G., Chávez-García F. J., Apostolidis P.I., Pitilakis K.D. (2010). 3D soil structure of the Mygdonian basin for site response analysis, *Soil Dynamics and Earthquake Engineering*, 30(11): 1198-1211.
- Maufroy E., Chaljub E., Hollender F., Bard P.Y., Kristek J., Moczo P., De Martin F., Theodoulidis N., Manakou M., Guyonnet-Benaize C., Hollard N., Pitilakis K. (2016). 3D numerical simulation and ground motion prediction: Verification, validation and beyond—Lessons from the E2VP project, *Soil Dynamics and Earthquake Engineering* 91: 53–71.
- Mazzieri I., Stupazzini M., Guidotti R., Smerzini C. (2013). SPEED: SPectral Elements in Elastodynamics with Discontinuous Galerkin: a non-conforming approach for 3D multi-scale problems, *International Journal for Numerical Methods in Engineering*, 95(12): 991–1010.

Paolucci R., Gatti F., Infantino M., Smerzini C., Özcebe A.G., Stupazzini M. (2018). Broadband Ground Motions from 3D Physics-Based Numerical Simulations Using Artificial Neural Networks. *Bulletin of Seismological Society of America*, 108: 1272-1286.

Pitilakis K., Raptakis D., Lontzetidis K., Tika-Vasillikou T., Jongmans D. (1999). Geotechnical and geophysical description of EUROSEISTEST, using field, laboratory tests and moderate strong motion records, *Journal of Earthquake Engineering*, 3(3): 381-409.

Raptakis D., Chávez-García F., Makra K., Pitilakis K. (2000). Site effects at EuroSeistest-I. Determination of the valley structure and confrontation of observations with 1D analysis, *Soil Dynamics and Earthquake Engineering*, 19(1): 1–22.

Smerzini C., Pitilakis K., Hashemi K. (2017) Evaluation of earthquake ground motion and site effects in the Thessaloniki urban area by 3D finite-fault numerical simulations. *Bulletin of earthquake engineering*, 15(3): 787-812.

9.6 Project # 30 – Comparison of rocking on rigid and compliant base using the EUROPROTEAS real-scale facility

Authors

I. Anastasopoulos⁽¹⁾, O. Adamidis⁽¹⁾, K. Kassas⁽¹⁾, A. Vratsikidis⁽²⁾, A. Anastasiadis⁽²⁾, D. Pitilakis⁽²⁾

⁽¹⁾ ETH, Zurich, Switzerland

⁽²⁾ Aristotle University of Thessaloniki, Thessaloniki, Greece

9.6.1 Introduction

Inspired by the remarkable behavior of tall and slender structures such as water tanks and tombstones during the 1960 Chilean Earthquake, Housner (1963) published his seminal paper where he explained the dynamic stability of rocking structures. During the same earthquake, other seemingly more stable structures, such as buildings and bridges, collapsed. Since then, the rocking motion has been extensively studied using conceptual models (e.g. Yim et al., 1980; Psycharis and Jennings, 1983; Zhang and Makris, 2001; Dimitrakopoulos and DeJong, 2012) to conclude that large slender structures present remarkable stability against earthquakes.

A salient conclusion of such models is that the stability of rocking objects is controlled by both the frequency of the excitation and the size of the rocking structure: ground motions whose spectra are dominated by high frequency content have less overturning potential, while out of two rectangular rigid blocks with the same aspect ratio, the largest one is more stable. The latter can be easily understood through displacement-based design concepts: a larger block has a larger “displacement capacity” up until it reaches the point of unstable equilibrium. This superior performance of rocking structures has led researchers to propose rocking as an earthquake hazard mitigation technique, using the term “rocking isolation” (e.g. Meek 1975; Huckelbridge and Clough, 1978; Mergos and Kawashima, 2005; Chen et al., 2006; Anastasopoulos et al., 2010).

According to the concept of rocking isolation, instead of fixing the structure firmly to the ground, uplifting and rocking is allowed. Uplifting acts as a mechanical fuse, limiting the forces transmitted to the structure. Rocking isolation aims to increase the safety of a structure against collapse, while simultaneously decreasing its residual displacements. Thus, it can be used for the design of resilient structures while it also often emerges as a cost-effective approach for seismic upgrading.

Two main rocking isolation concepts are of interest for this project. The first refers to rocking of a structure onto a rigid base while the second promotes rocking of the structure along with its foundation on the underlying soil.

The first concept has been studied, with the use of a restraining tendon (Mander and Cheng, 1997; Palermo et al., 2004; Chen et al., 2006; Cheng, 2008; Makris and Vassiliou, 2014; Vassiliou and Makris, 2015), or without. Most studies use rigid body models (e.g. Housner, 1963; Hogan, 1989; Makris and Roussos, 2000; Zhang and Makris, 2001). However, research has also been conducted taking into account the flexibility of the structure (Acikgoz and DeJong, 2012; Vassiliou et al., 2014, 2015, 2017). Despite the wealth of work on this topic, real-scale experimental results are scarce, despite the great significant such results could have for the validation of analytical or numerical tools.

The second concept introduces the deliberate under-sizing of the foundation to promote full mobilization of its moment capacity during strong seismic shaking. This way, the soil experiences inelastic behavior and the footing is allowed to uplift (e.g. Mergos and Kawashima, 2005; Gajan and Kutter, 2008; Anastasopoulos et al., 2010; Gelagoti et al., 2012; Antonellis et al., 2015). Depending on the safety factor against static (vertical) loading, the mode of intentional foundation failure is either uplifting (for large FS_v) or soil yielding (for small FS_v) (Anastasopoulos et al., 2012). Despite its proven beneficial seismic performance, such reversal of capacity design (from the superstructure to the soil) is still not allowed by current seismic codes, which only allow limited uplifting of the foundation, prohibiting full mobilization of soil bearing capacity. However, there are a few exceptions of structures that have been designed and constructed employing the concept of rocking footings, such as the Rio-Antirrio bridge in Greece and the Vasco de Gama bridge in Portugal (Pecker, 2003). The comparative advantage of such a design concept lies in its simplicity and compatibility with the current state of practice. There is no need for special connections, and methods compatible to elastic design spectra have been developed (Gelagoti et al., 2012). Once again, real-scale experimental results are particularly limited (e.g. Antonellis et al., 2015) despite the great potential for validation of numerical predictions.

Conventional foundation capacity design aims to guide failure to structural members (i.e., the base of a column or pier) by “over-designing” the foundation. The collapse of the Hanshin Expressway Fukae bridge during the 1995 Kobe earthquake dramatically demonstrated that such design principles do not guarantee avoidance of collapse. Rocking isolation is an alternative design concept, which aims to limit the inertia loading of a structure by allowing foundation uplifting and full mobilization of its bearing capacity, at the expense of increased settlement and rotation.

Overall, rocking isolation concepts have been shown to be beneficial in the event of an earthquake, protecting a structure against collapse, limiting structural failure and potentially limiting residual displacements. As part of this project, both rocking concepts discussed above were examined by experimenting on the real-scale structure of EUROPROTEAS in order to assess their performance, compare their effectiveness and produce data for the validation of analytical and numerical tools.

9.6.2 EUROPROTEAS

Structure

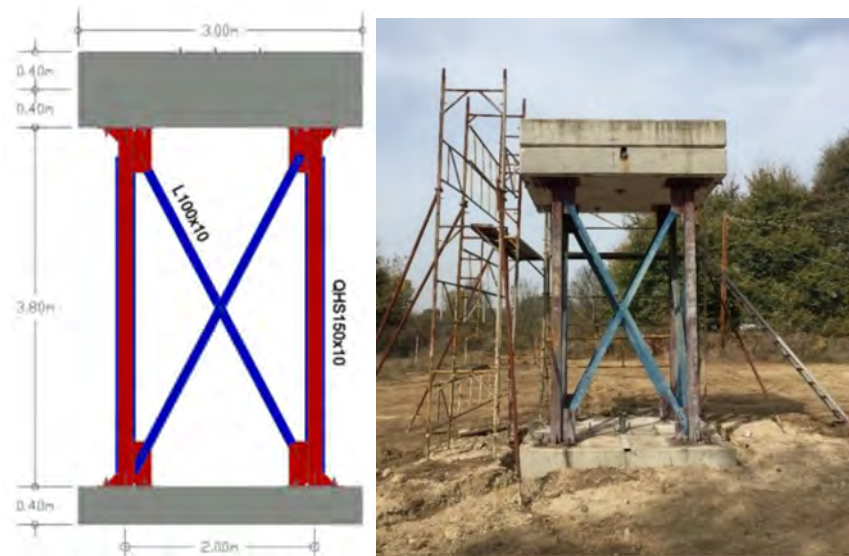


Figure 492: A 2D sketch and a view of EUROPROTEAS prototype structure

EuroProteas prototype structure was particularly designed to mobilize strong interaction with its foundation soil as it is a stiff structure with a large superstructure mass founded on soft foundation soil. It is a perfectly symmetric and reconfigurable structure. It is founded on a square RC slab (C20/25) with dimensions 3.0m x 3.0m x 0.4m which rests on the ground surface. The superstructure mass consists of two identical to the foundation RC slabs that are supported by four square hollow steel columns (QHS 150 x 150 x 10mm) which are clamped on the foundation. L-shaped (100 x 100 x 10mm) X-braces are connecting the steel columns in all the sides of the structure ensuring its total symmetry. Assuming a uniform unit weight of 25kN/m^3 for the concrete, the total mass of each slab is estimated at 9.16Mg, while the total mass of the structure is calculated approximately at 28.5Mg. Its outer dimensions are 3.0m x 3.0m x 5.0m (Figure 492). The bracing system and the upper roof slab of the structure are removable allowing the modification of the mass and/or the stiffness. Depending on the number of the roof slabs and the arrangement of the X-bracing system the fixed-base frequency of EuroProteas covers a range between 1.78Hz and 13.06Hz as calculated numerically (Pitilakis et al. 2018).

Foundation Soil

The foundation soil is well investigated and reported in earlier studies. Specifically, between 1993 and 2004, an extensive program of seismic prospecting and geotechnical testing was undertaken (Pitilakis et al. 1999). It comprised of in-situ (sampling boreholes, Standard and Cone Penetration Test measurements) and laboratory (conventional classification tests, strength tests, consolidation tests and resonant column and cyclic triaxial tests) geotechnical surveys. The elaboration of all geophysical and geotechnical data, led to the classification of the main soil formations, validation of soil properties stemming from different methodologies and design of representative 1D, 2D and 3D soil models.

Additional field investigation of the test site was undertaken prior to the construction of the structure including SPT measurements, downhole tests, sampling according to EC7 regulations, resonant column and cyclic triaxial tests. The small stiffness of the top soil layer is pronounced by the low recorded NSPT values down to a depth equal to two times the foundation width. Close to the soil surface the shear

wave velocity is estimated approximately at 100m/s (Figure 493). A detailed report on the geotechnical and geophysical data derived from this investigation is presented in Pitilakis et al. (2018).

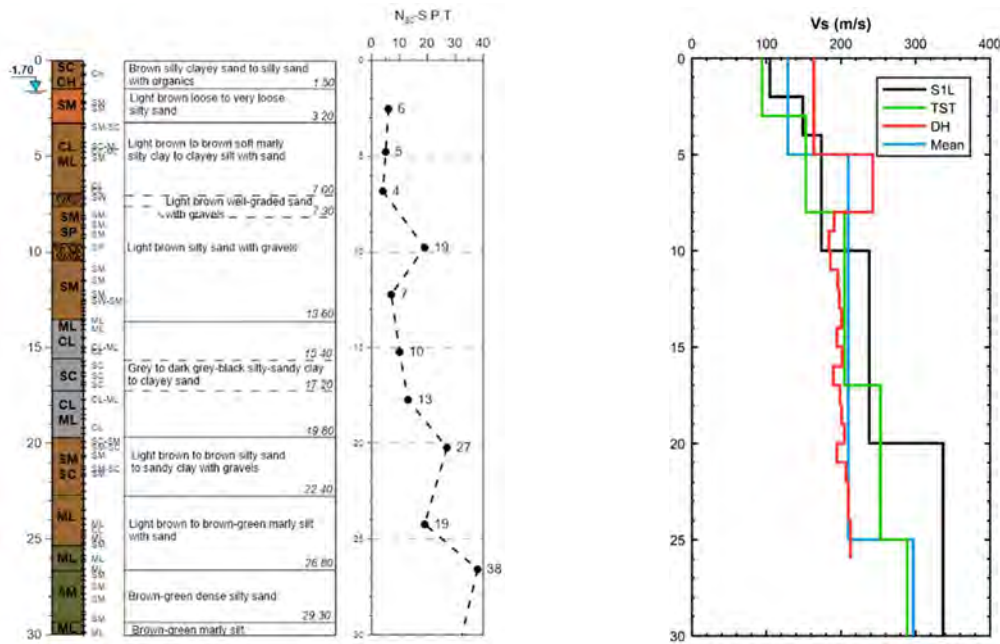


Figure 493: Soil stratigraphy of the 30m deep borehole at the geometrical center of the foundation, the N_{SPT} blow counts and the Vs profile as derived from down-hole (DH) tests prior to the construction of EuroProteas (Pitilakis et al. 2018) compared with the Vs profile at S1L site approximately 50m south of EuroProteas (Raptakis et al. 1998), a reference mean Vs model of the valley cross-section (Raptakis et al. 2000) and the proposed Vs profile by Pitilakis et al. (1999)

9.6.3 Numerical model / prediction / simulation

In order to investigate the structure's response the first and second natural frequencies $f_{n,1}$, $f_{n,2}$ of both systems were extracted through finite element analyses in the commercially available finite element code ABAQUS. The superstructure was modelled in detail while the soil stratum was modelled as linear elastic and the interface between the foundation and the soil was neglected. The elasticity modulus of soil is $E_{soil} = 66$ MPa based on the SPT tests which have been conducted in the EUROPROTEAS site.

Figure 494 illustrates the calculated natural modes of the rocking system (left) and the conventional foundation system (right). The first natural mode of the rocking system results in motion in the direction of loading, where the foundation stiffness is lower too, while the second natural mode promotes the shaking in the out of plane direction of the loading. Is important to point out that the second natural mode of the conventional system, consists of pure torsion around the center of the foundation.

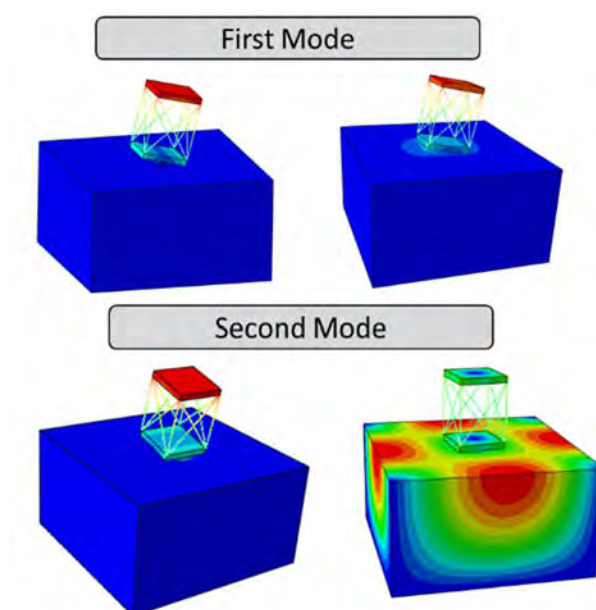


Figure 494: First and second natural modes of the two tested set-ups

Table 82 and Table 83 presents the first and second eigenfrequencies of the two systems assuming a uniform elasticity modulus for the soil stratum equal to $E_{soil} = 66 \text{ MPa}$. We observe that the first natural frequency of the rocking base system is 1.9 Hz while the natural frequency of the second system equals 4.19 Hz. It is important to point out that apart from the relative small uncertainty regarding the soil stiffness, the numerical analysis also neglects nonlinearities stemming from soil plastification, soil – foundation interface and geometric nonlinearities such as uplifting, all of which can significantly affect the response, particularly for the case of the rocking foundation system.

$E_{soil} = 66 \text{ MPa}$		
#	$F_{n,1} \text{ (Hz)}$	$F_{n,2} \text{ (Hz)}$
Rocking Base	2.01	4.37
Conventional Foundation	6.53	8.27

Table 82: Calculated natural frequencies for the rocking base structure and the conventional system resting on the soil layer

Fixed Base	
#	$F_{n,1} \text{ (Hz)}$
Rocking Base	11
Conventional Foundation	15.1

Table 83: Calculated natural frequencies for the rocking base structure and the conventional system for fixed base foundation

9.6.4 Test setup

Foundation types

Two different set-ups were tested regarding structure's foundation. For the first type a new concrete foundation having dimensions 0.8m x 3m was placed below the foundation of the structure. In the second set of experiments the foundation of the original structure was used having dimensions 3 x 3m. The first set-up reflects the alternative design concept of the rocking isolation. The second corresponds to the conventional foundation capacity design.

Instrumentation

The general instrumentation scheme was designed particularly to capture the response of the structure and the foundation in both in-plane and out-of-plane direction as well as the soil surface response in the same directions. The instruments used are:

- 5 triaxial accelerometers GMG-5T (Guralp)
- 4 triaxial accelerometers CMG-5TCDE (Guralp)
- 6 digital broadband seismometers CMG-40T (Guralp)
- 6 digital broadband seismometers CMG-6TD (Guralp)
- 4 laser sensors (Waycon)

The instrumentation layout of the structure and the soil surface is presented in Figure 495. All the instruments were configured at a sampling frequency of 200 Hz and were connected to external global positioning system (GPS) antennas.

Forced-vibration experiments

Table 84 and Table 85 contain the eccentricities (E) of the mass shaker for each test of the two different experimental set-ups (Rocking base and Conventional foundation) and the corresponding rotational loading frequencies (f). For the first set-up four different tests were conducted (A, B, C and D) with mass shaker eccentricities equal to 1.85, 3.93, 6.93 and 11.31 kg·m. With respect to the second set-up (conventional foundation), seven different tests were conducted (D, C, D1, B, C1 and C2).

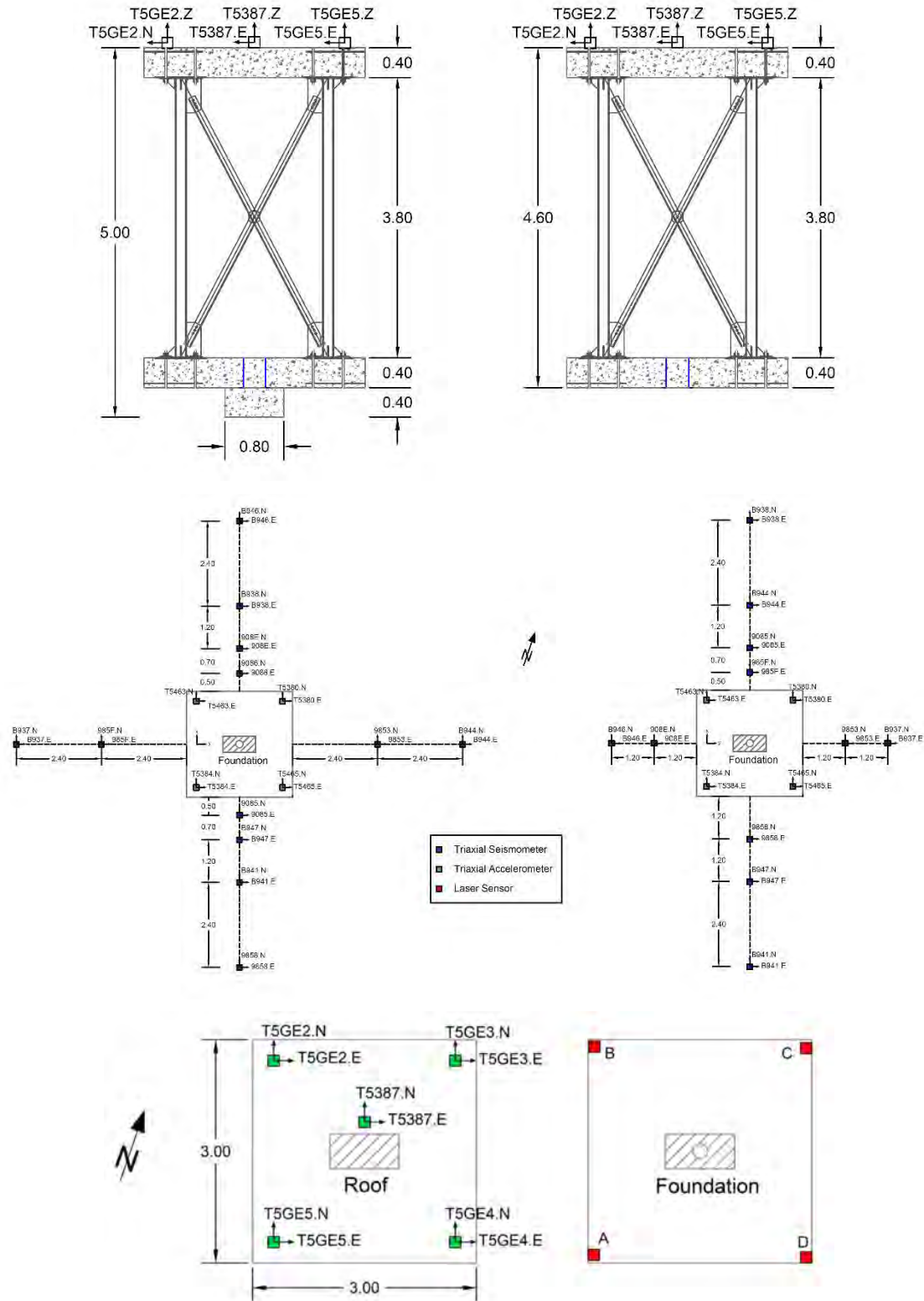


Figure 495: Cross section of the instrumentation layout of the structure with the new concrete foundation (upper left) and the conventional foundation (upper right), plan view of the instrumentation layout of the foundation and the soil surface with the new concrete foundation (middle left) and the conventional foundation (middle right) and plan view of the instrumentation layout of the roof (bottom left) and the position of the laser sensors at the foundation (bottom right) in both experimental series

Experiment	Experiment A	Experiment B	Experiment C	Experiment D
Eccentricity	Shaker Frequency (Hz)	Shaker Frequency (Hz)	Shaker Frequency (Hz)	Shaker Frequency (Hz)
Frequency (Hz)	0.33	0.33	0.96	1.03
	1.03	1	1.53	1.3
	2	1.5	1.7	1.5
	3	2	2.034	1.73
	4	2.5	2.5	1.96
	5	3	3	2.23
	6	4	5	2.5
	6.96	5	3	2.7
	8	6	2	5
	1.9	7	1.7	6
		1.9	1.4	7
		1.6	1	2
				1.73
				1.46
				1.36
				1.23
				1

Table 84: Eccentricities and rotational loading frequencies for each of the conducted tests for the rocking foundation

Experiment	Experiment D	Experiment C	Experiment D 1	Experiment B	Experiment C 1	Experiment D 2
Eccentricity	Shaker Frequency (Hz)	Shaker Frequency (Hz)	Shaker Frequency (Hz)	Shaker Frequency (Hz)	Shaker Frequency (Hz)	Shaker Frequency (Hz)
Frequency (Hz)	1	1	1	1	1.034	1
	2	2	2	2	2.034	1.967
	3	3	3	2.5	3	3
	4	3.5	3.5	3	3.534	3.5
	5	4	4	3.5	4	3.967
	6	4.5	4.5	4	5	4.967
	7	5	5	5.034	6	6
	8	6	6	6	7	
	4	7	7	7.034	8	
	3.467	8	8	8		
	2.967			9.034		
				9.967		

Table 85: Eccentricities and rotational loading frequencies for each of the conducted tests for the conventional foundation

The amplitude of the shaker output force can be calculated as a function of the total eccentricity and the rotational frequency from Eq. (18). Figure 496 and Figure 497, illustrate the calculated force amplitude for the conducted experiments.

$$F = E(2\pi f)^2 \quad (18)$$

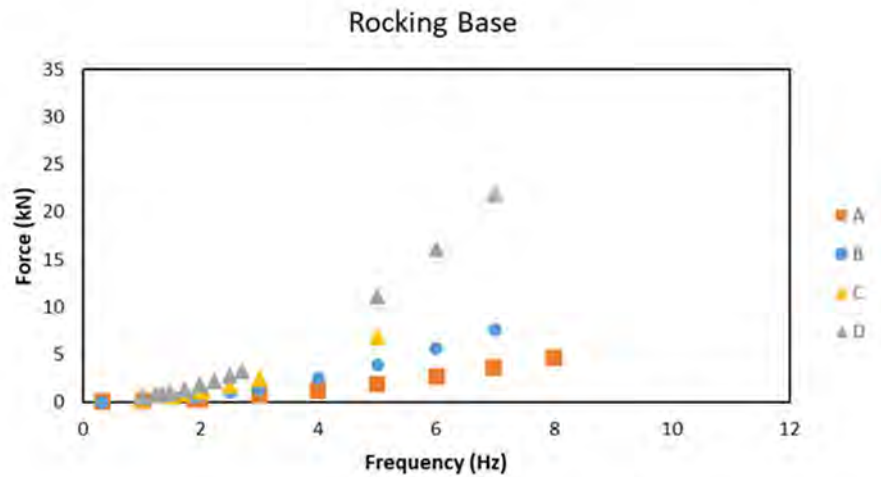


Figure 496: Eccentric mass vibrator amplitude force as a function of the loading frequency for each of the conducted test for the rocking foundation (see Table 84)

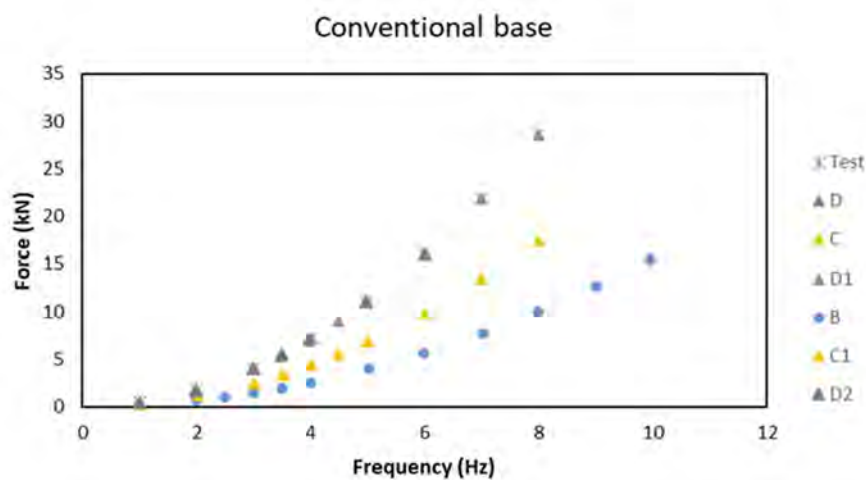


Figure 497: Eccentric mass vibrator amplitude force as a function of the loading frequency for each of the conducted test for the conventional foundation (see Table 85)

9.6.5 Observation during testing

Figure 498 and Figure 499 illustrate the recorded acceleration at the center of the top slab for all the tests with the rocking and the conventional foundation in the direction of loading and in the out of plane direction. It can be observed that for the case of the rocking foundation no significant acceleration in the out of plane direction was recorded and the structure is shaking mainly in the direction of loading. On the contrary, the out of plane excitation for the case of the conventional foundation was significant for all the experiments. Particularly, in some cases (EXP D, D1, and D2) the structure experienced stronger shaking in the out of plane direction than that of the loading.

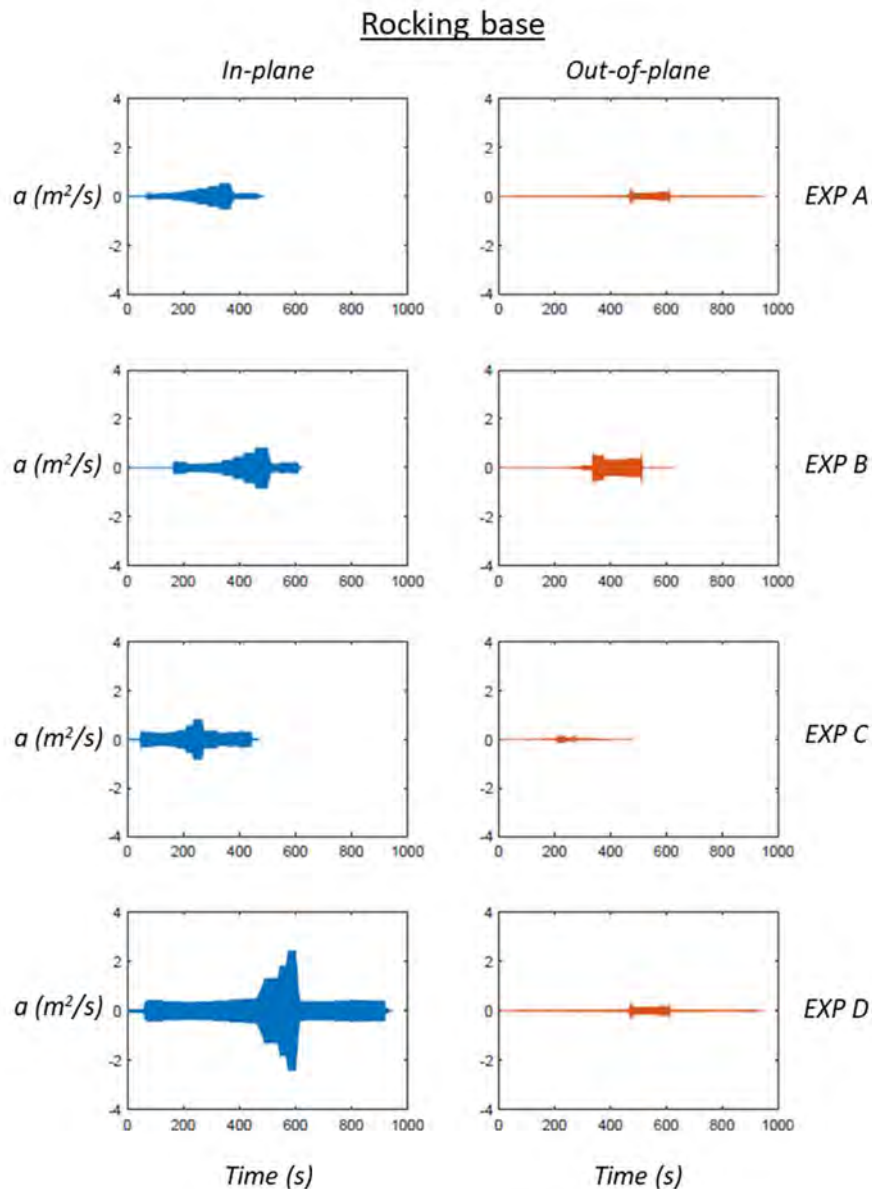


Figure 498: Recorded accelerations at the center of the top slab for the four conducted experiments with the rocking base foundation

Multiple factors could have led to this behaviour. Firstly, it is possible that the structure leveling prior testing was not perfect. An initial rotation towards the out of plane direction could have led to this result. Furthermore, it is possible that the set-up of the rotating masses of the eccentric mass shaker was inaccurate leading to an out-of-plane shaking too. Additionally, the stiffness symmetry of the structure with the conventional foundation introduces also torsion modes, which promote the out of plane motion. This effect is much more insignificant for the case of the rocking foundation, which is much more prone to in plane shaking due to the lower foundation stiffness in the direction of loading. In any case, the significant out of plane shaking recorded at the Experiment B of the rocking foundation indicates that stiffness symmetry itself could not justify the out of plane shaking. Moreover, if the initial rotation prior shaking was the reason for the out of plane shaking, significant out of plane shaking should have been recorded during all tests of the rocking foundation set-up. Probably more than one factor played cumulatively a role.

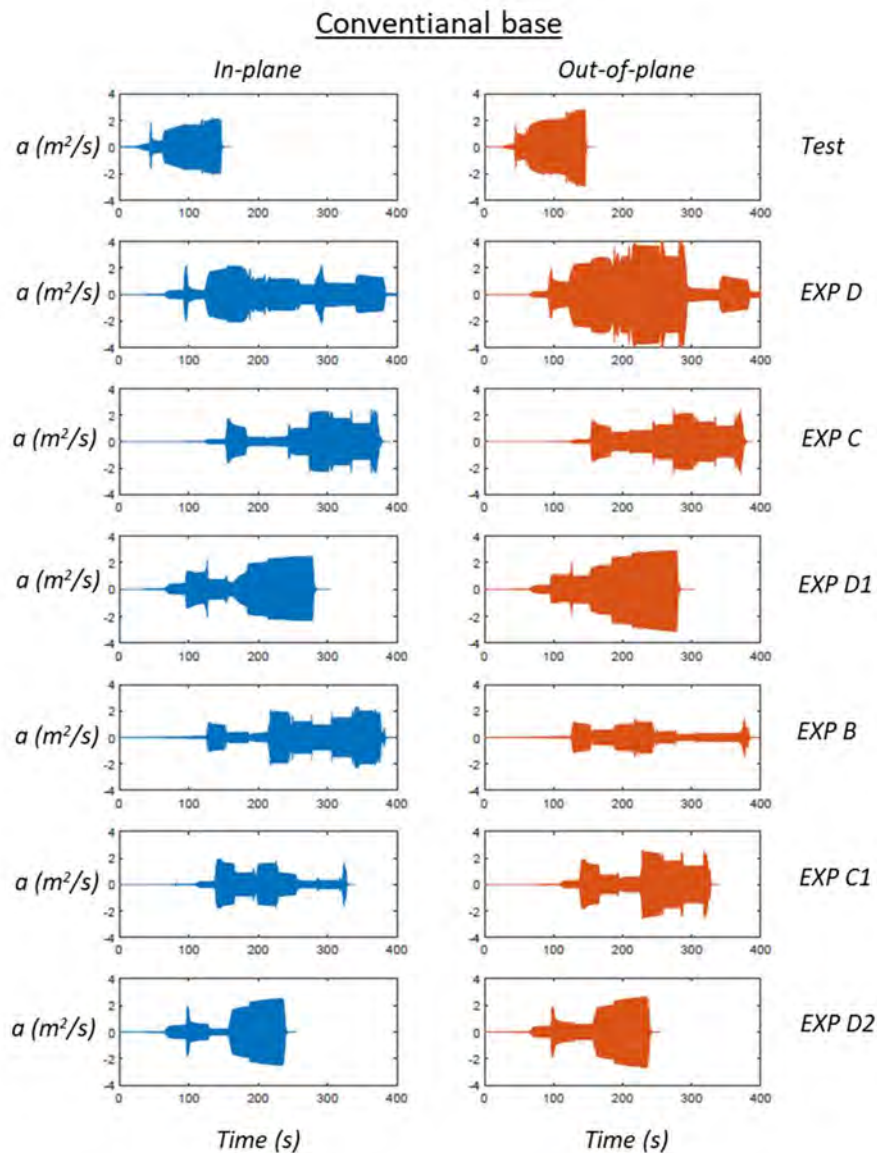


Figure 499: Recorded accelerations at the center of the top slab for the seven conducted experiments with the conventional foundation

9.6.6 Results

Figure 500 focuses in the comparison between the experiment D (rocking foundation) and experiment D1 (conventional foundation). The recorded acceleration at the center of the top slab is plotted for both the in plane and out-of-plane direction of loading. Each consecutive loading frequency has been plotted with a different color, aiming to illustrate the different loading frequency bands. As mentioned before, significant out of plane shaking is recorded for the conventional structure but not for the rocking structure. It is noteworthy that the out of plane shaking for the rocking structure takes place in the interval of loading frequencies of 5-7 Hz that coincides with the second natural frequency of the system and is related to the out of plane motion. This effect was not observed in the second set-up where out-of-plane movement was significant for all the loading frequencies. However, for this case there is an amplification of the recorded acceleration between the loading frequencies of 3.5 and 4 Hz. This band coincides with the calculated natural frequency of the system from finite element analysis.

In order to gain more insight into the response of the two systems the Fourier components of the recorded acceleration at the top slab for each structure and frequency have been calculated and are plotted in Figure 501. The rocking structure follows its loading frequency in all the cases. Frequencies related to its natural frequencies are not excited. On the other hand, the conventional foundation is always responding with its natural frequency. The effect is more pronounced as the loading frequency is increasing (6, 7 and 8 Hz), where the frequency of 4.2 Hz – the first natural frequency – is always excited.

Figure 502 presents the calculated rotations from the recorded data of lasers for both set-ups resulting from the in-plane and the out-of-plane motion. It is observed that the amplitude of rotation is increasing significantly for both structures at frequencies close to the first natural frequencies of the systems.

The experiments were also modelled numerically in finite element code Abaqus. Non-linear (inelastic) soil behavior is modeled with a thoroughly validated kinematic hardening model, with a Von Mises failure criterion and associated flow rule ([Anastasopoulos et al., 2011](#)). The constitutive law of the model consists of a non-linear kinematic hardening component, which describes the translation of the yield surface in the stress space, and an isotropic hardening component, which defines the size of the yield surface as a function of plastic deformation ([Gerolymos and Gazetas, 2005](#)). Calibration of the model parameters requires knowledge of: (a) undrained shear strength S_u ; (b) the small-strain stiffness (expressed through G_0 or V_s); and (c) the stiffness degradation ($G-\gamma$ and $\xi-\gamma$ curves). Figure 503 presents the finite element model and the evolution of undrained shear strength and modulus of elasticity with the depth. Tensionless interfaces with an appropriate friction coefficient $\mu = 0.5$ are introduced between the subsoil and the footings to model uplifting and sliding.

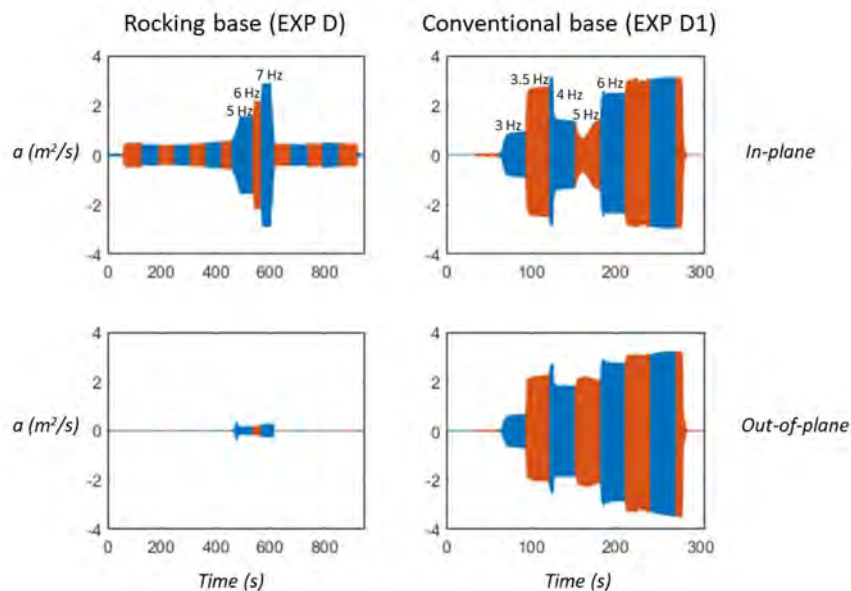


Figure 500: Recorded accelerations at the center of the top slab for experiments D (left) and D1 (right) at the direction of loading (top) and at the out-of-plane direction (bottom)

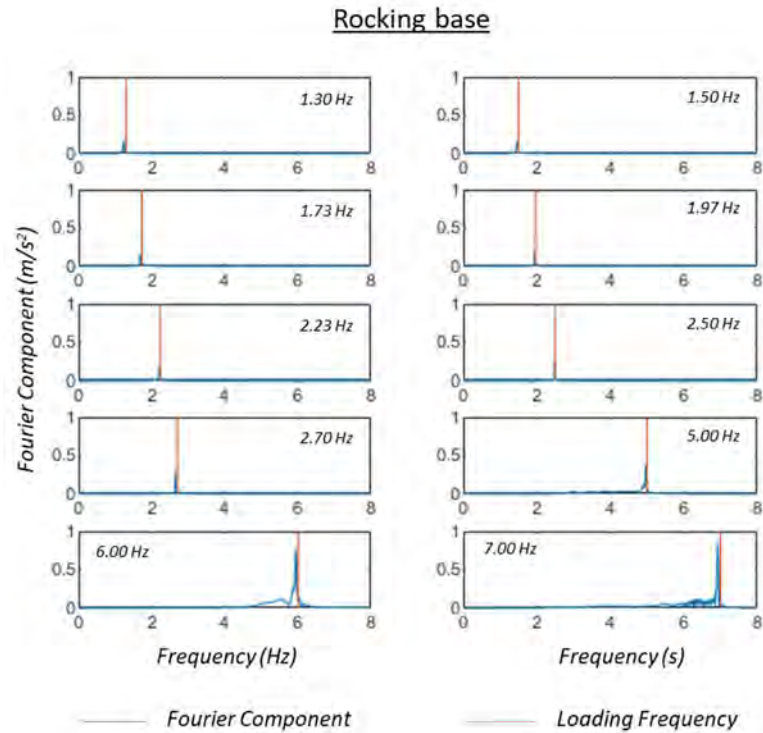


Figure 501: Fourier components of the recorded acceleration in the direction of shaking at the center of the top slab for the rocking base experiment D (top) and the conventional base experiment D1 (bottom)

Figure 504 plots the computed accelerations at the center of the top slab. Both set-ups were modelled and three different sinusoidal loads of 20 loading cycles were applied with frequencies 1.5, 3 and 7 Hz respectively. The maximum amplitude of each load was calculated from Eq. (18). It is observed that the rocking base structure experiences higher acceleration than the conventional base structure for the lower loading frequencies (1.5 and 3 Hz). This phenomenon is not only attributed to its lower

foundation stiffness but mainly to the fact that the aforementioned frequencies are closer to the first natural frequency of the rocking base structure (Figure 505, Table 83). This behaviour is also consistent for the case of the loading frequency of 7 Hz, where the structure with the conventional foundation experiences higher acceleration than the structure with the rocking type foundation. Again, we observe in Figure 505 that the loading frequency of 7 Hz is very close to the calculated first natural frequency of the structure with the conventional foundation.

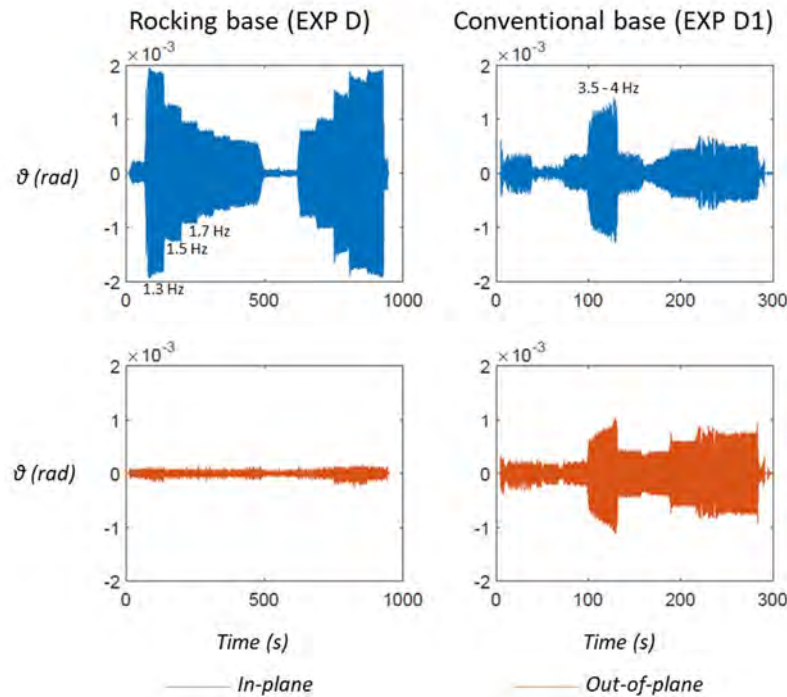


Figure 502: Rotations extracted from the lasers for the rocking base foundation experiment (D) and the conventional foundation experiment (D1)

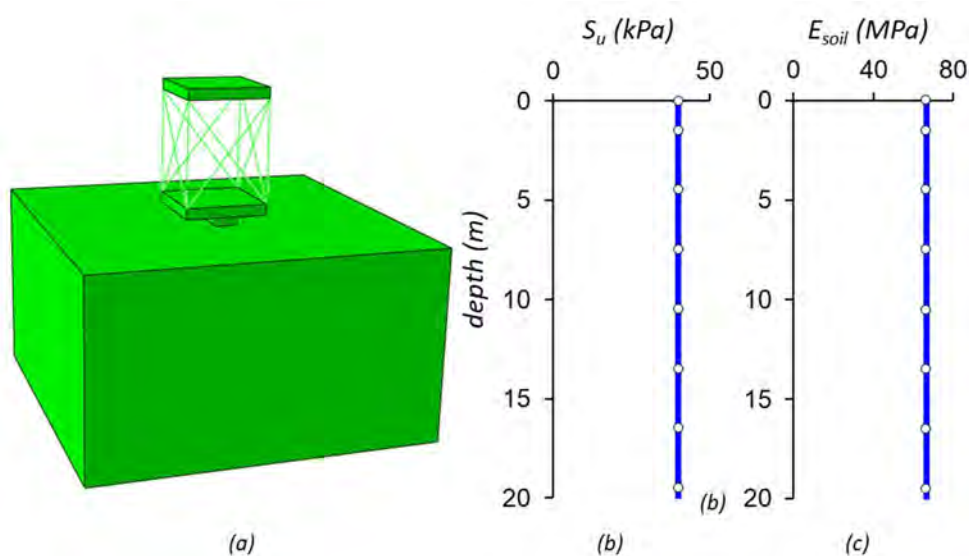


Figure 503: (a) Finite element model for the rocking base structure; (b) soil's undrained shear resistance (S_u) as a function of depth and (c) soil's elasticity modulus E_{soil} as a function of depth

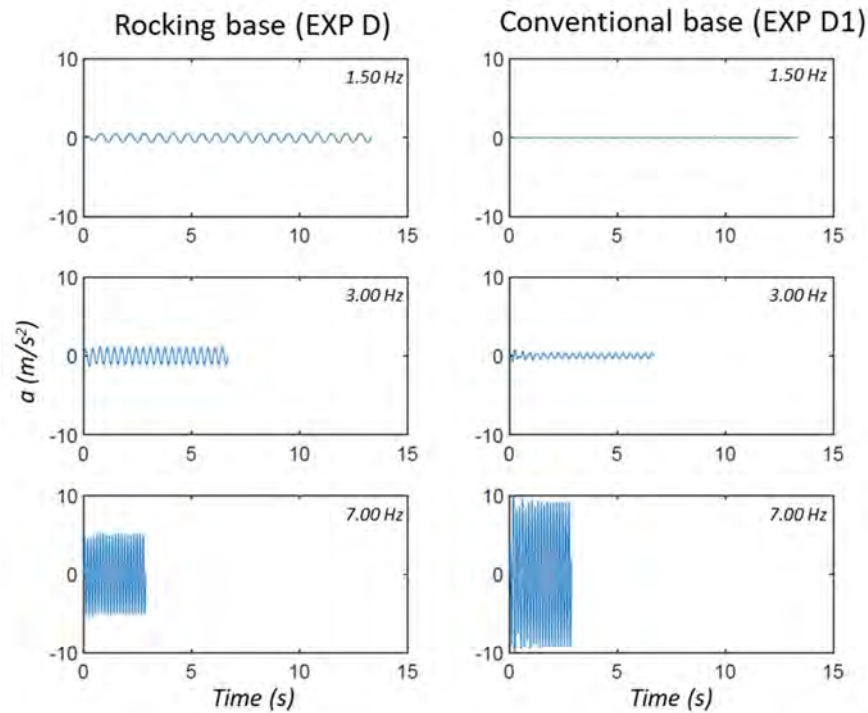


Figure 504: Computed acceleration at the center of the top slab for experiments D (left) and D1 (right) at the direction of loading

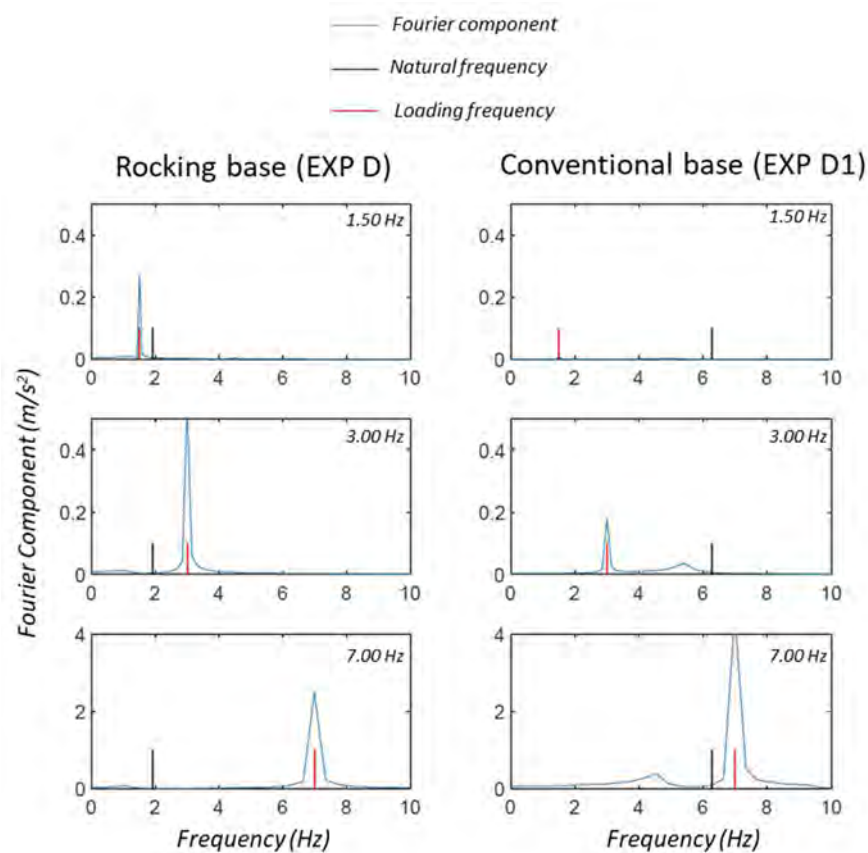


Figure 505: Fourier components of the calculated acceleration in the direction of shaking at the center of the top slab for the rocking base experiment D (left) and the conventional base experiment D1 (right)

Figure 506 plots the calculated rotation for both set-ups and the three applied sinusoidal loadings. It can be observed that for all the cases the structure with the rocking foundation exhibits lower amplitude of rotation due to its lower foundation stiffness. Furthermore, each structure experiences higher rotation, when the corresponding loading frequency is closer to the first natural frequency of the system (EXP D at 1.5 Hz, EXP D1 at 7 Hz) even if the amplitude of the loading force is lower (1 kN at 1.5 Hz and 23.58 kN at 7 Hz).

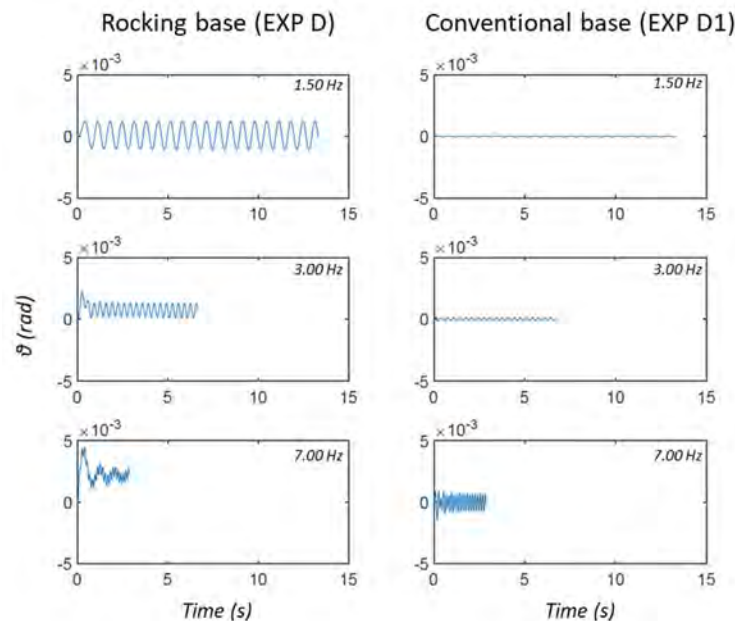


Figure 506: Calculated rotation for the rocking base foundation experiment (D) and the conventional foundation experiment (D1)

It is interesting that both in the numerical analysis and the experiment D the loading frequency that lead to the higher acceleration at the top slab (7 Hz), lead to the lowest foundation rotation too (Figure 500 and Figure 502). This is due to the fact that this frequency is closer to the first natural frequency of the fixed base structure (11 Hz) and far from the first natural frequency of the structure-foundation system.

Figure 507 illustrates the comparison between the maximum recorded and computed rotation of the bottom slab and acceleration at the top slab for both experimental set-ups. All the values have been normalized with the maximum amplitude of the eccentric mass vibrator force for each loading frequency. The numerical analysis offers a good prediction especially for the case of the rocking base structure. In the case of the conventional foundation, the analysis also captures the peak at 4 Hz. This frequency band is far from the calculated first natural frequency (6.53 Hz). The reason for the resonance can be nonlinearities in the soil, which lead to period elongation. Furthermore, it is possible that the soil in the specific region is softer than the one considered in the numerical analysis.

Figure 508 illustrates the recorded vertical velocities at the soil around the two set-ups in an array of points both in the direction of loading and in the out-of-plane direction. For both experiments the vibration level at the surrounding soil is higher for larger loading frequencies. Secondly, for the case of the rocking foundation, the recorded vertical velocities in the out-of-plane direction are unsurprisingly lower than in the direction of loading. This response is explained by the much larger out-of-plane shaking that has been recorded in the structure with the conventional foundation. Finally, despite the fact that the levels of structural acceleration and rotation are similar between the two set-ups, the

vibrations in the surrounding soil for the case of the rocking base structure are lower by a factor of 10. This can be attributed to the plastification of the soil below the smaller rocking foundation, which damped the transmitted waves.

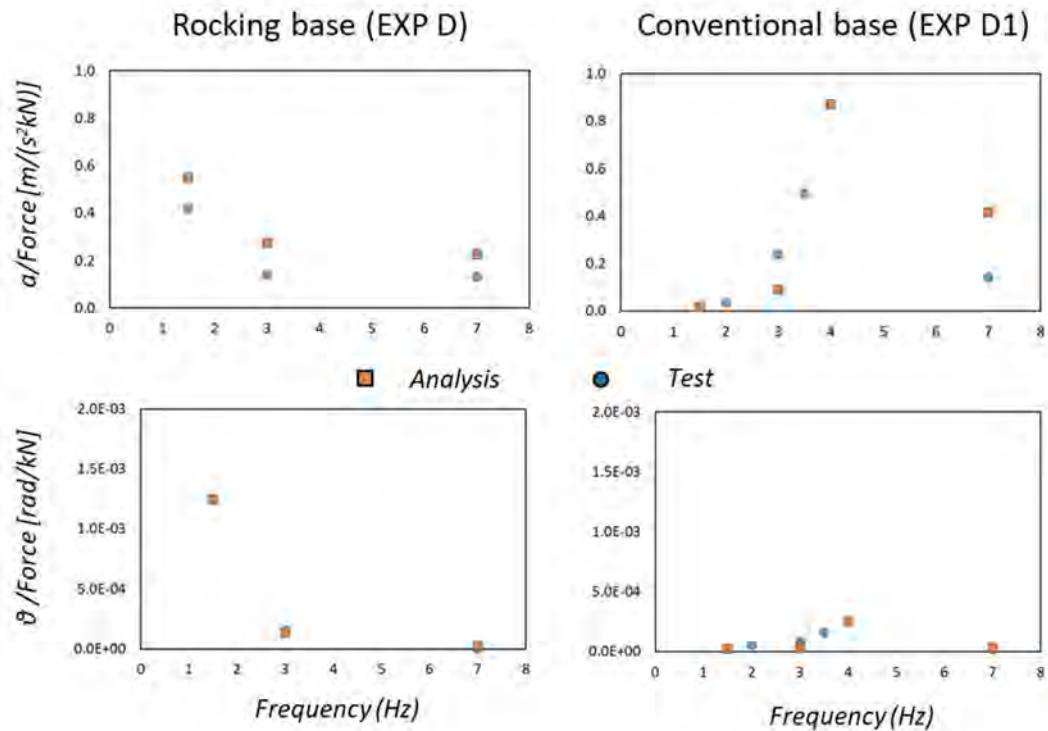


Figure 507: Comparison between maximum computed and recorded rotation of the bottom slab (bottom) and maximum acceleration at the center of the top slab (top) normalized with the maximum amplitude of the eccentric mass shaker for each frequency for both experimental set-ups

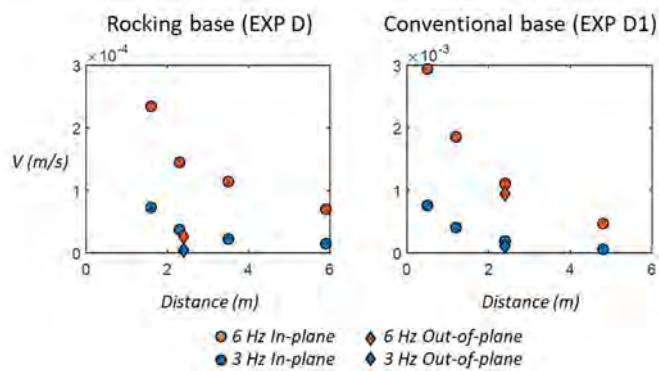


Figure 508: Vertical velocities recorded from the seismometers in the surrounding soil, for the rocking base foundation (EXP D) and the conventional foundation (EXP D)

9.6.7 Conclusions and outlook

EuroProteas has outer dimensions 3 m-by-3 -by- 5m and rests on the free surface of soft soil. Two different foundation concepts were tested in the Euroseistest site in the North of Thessaloniki, Greece, to study SSL and wave propagation in the soil. An extensive experimental campaign was performed, including ambient noise measurements, free- and forced-vibration tests, covering a wide range of different loading amplitudes and frequencies. Forced-vibration loading was exerted by an eccentric

mass shaker, mounted at the top or at the foundation reinforced concrete slab. The response was recorded by a dense array of seismometers and accelerometers, on the structure and in the soil around the structure. The experiments were also modelled numerically in finite element code Abaqus. The finite element analysis managed to capture the key features of the recorded response and provide useful insight.

9.6.8 References

- Acikgoz, S., and DeJong, M. J. (2012). The interaction of elasticity and rock- ing in flexible structures allowed to uplift. *Earthq. Eng. Struct. Dyn.* 41, 2177–2194. doi:10.1002/eqe.2181.
- Anastasopoulos, I., Gazetas, G., Loli, M., Apostolou, M., and Gerolymos, N. (2010). Soil failure can be used for seismic protection of structures. *Bull. Earthq. Eng.* 8, 309–326.
- Anastasopoulos, I., Kourkoulis, R., Gelagoti, F., and Papadopoulos, E. (2012). Rocking response of SDOF systems on shallow improved sand: an experimental study. *Soil Dyn. Earthq. Eng.* 40, 15–33.
- Antonellis, G., Gavras, A. G., Panagiotou, M., Kutter, B. L., Guerrini, G., Sander, A. C., et al. (2015). Shake table test of large-scale bridge columns supported on rocking shallow foundations. *J. Geotech. Geoenviron. Eng.* 141, 04015009. doi:10.1061/(ASCE)GT.1943-5606.0001284.
- Chen, Y. H., Liao, W. H., Lee, C. L., and Wang, Y. P. (2006). Seismic isolation of viaduct piers by means of a rocking mechanism. *Earthq. Eng. Struct. Dyn.* 35, 713–736. doi:10.1002/eqe.555.
- Cheng, C. T. (2008). Shaking table tests of a self-centering designed bridge sub- structure. *Eng. Struct.* 30, 3426–3433. doi: 10.1016/j.engstruct.2008.05.017.
- Dimitrakopoulos, E. G., and DeJong, M. J. (2012). Revisiting the rocking block: closed-form solutions and similarity laws. *Proc. R. Soc. A, Vol. 468 (The Royal Society)*, 2294–2318.
- Gajan, S., and Kutter, B. L. (2008). Capacity, settlement, and energy dissipation of shallow footings subjected to rocking. *J. Geotech. Geoenviron. Eng.* 134, 1129–1141.
- Gelagoti, F., Kourkoulis, R., Anastasopoulos, I., and Gazetas, G. (2012). Rocking- isolated frame structures: margins of safety against toppling collapse and simplified design approach. *Soil Dyn. Earthq. Eng.* 32, 87–102. doi:10.1016/j. soildyn.2011.08.008.
- Hogan, S. J. (1989). On the dynamics of rigid-block motion under harmonic forcing. *Proc., Royal Soc., London*, A425, 441–476.
- Housner, G. W. (1963). The behavior of the inverted pendulum structures during earthquakes. *Bull. Seismol. Soc. Am.* 53, 403–417.
- Huckelbridge A. A., and Clough R. W. (1978). Seismic response of uplifting building frame. *J Struct Div* 104(8):1211–1229.
- Makris, N., and Roussos, Y. (2000). Rocking response of rigid blocks under near-source ground motions. *Geotechnique, London*, 50(3), 243–262.
- Makris, N., and Vassiliou, M. F. (2014). Dynamics of the rocking frame with vertical restrainers. *J. Struct. Eng.* 141, 04014245. doi:10.1061/(ASCE) ST.1943-541X.0001231.
- Mander, J. B., and Cheng, C. T. (1997). “Seismic resistance of bridge piers based on damage avoidance design,” in *Technical Rep. NCEER, 97* (Buffalo, NY: National Center for Earthquake Engineering Research, State Univ. of New York at Buffalo).
- Meek J.W. (1975). Effects of foundation tipping on dynamic response. *J Struct Div* 101(7):1297–1311.
- Mergos, P. E., and Kawashima, K. (2005). Rocking isolation of a typical bridge pier on spread foundation. *J. Earthq. Eng.* 9, 395–414. doi:10.1142/S1363246905002456.

Palermo, A., Pampanin, S., and Calvi, G. M. (2004). The Use of Controlled Rocking in the Seismic Design of Bridges. Doctorate thesis, Technical Institute of Milan, Milan.

Pecker, A., (2003). Aseismic foundation design process, lessons learned from two major projects: the Vasco de Gama and the Rion Antirion bridges, *ACI International Conference on Seismic Bridge Design and Retrofit*, La Jolla, 2003.

Psycharis, I. N., and Jennings, P. C. (1983). Rocking of slender rigid bodies allowed to uplift. *Earthq. Eng. Struct. Dyn.* 11, 57–76. doi:10.1002/eqe.4290110106.

Raptakis D., Anastasiadis A. & Pitilakis K. (1998). Preliminary instrumental and theoretical approach of site effects in Thessaloniki. In *Proceedings of the 11th European Conference on Earthquake Engineering*.

Vassiliou, M. F., Mackie, K. R., and Stojadinović, B. (2017). A finite element model for seismic response analysis of deformable rocking frames. *Earthq. Eng. Struct. Dyn.* 46, 447–466. doi:10.1002/eqe.2799.

Vassiliou, M. F., Mackie, K. R., and Stojadinović, B. (2014). Dynamic response analysis of solitary flexible rocking bodies: modeling and behavior under pulse- like ground excitation. *Earthq. Eng. Struct. Dyn.* 43, 1463–1481. doi:10.1002/eqe.2406.

Vassiliou, M. F., and Makris, N. (2015). Dynamics of the vertically restrained rocking column. *J. Eng. Mech.* 141, 04015049. doi:10.1061/(ASCE)EM.1943-7889.0000953.

Vassiliou, M. F., Truniger, R., and Stojadinović, B. (2015). An analytical model of a deformable cantilever structure rocking on a rigid surface: development and verification. *Earthq. Eng. Struct. Dyn.* 44, 2775–2794. doi:10.1002/eqe.2608.

Yim, C. S., Chopra, A. K., and Penzien, J. (1980). Rocking response of rigid blocks to earthquakes. *Earthq. Eng. Struct. Dyn.* 8, 565–587. doi:10.1002/eqe.4290080606.

Zhang, J., and Makris, N. (2001). Rocking response of free-standing blocks under cycloidal pulses. *J. Eng. Mech.* 127, 473–483. doi:10.1061/(ASCE)0733-9399(2001)127:5(473).

9.7 Project # 38 – Resonant metamaterial-based earthquake risk mitigation of large-scale structures and infrastructure systems: assessment of an innovative proof-of-concept via medium-size scale testing

Authors

A. Marzani⁽¹⁾, A. Palermo⁽¹⁾, F. Zeighami⁽¹⁾, A. Vratsikidis⁽²⁾, A. Anastasiadis⁽²⁾, D. Pitilakis⁽²⁾

⁽¹⁾ University of Bologna, Bologna, Italy

⁽²⁾ Aristotle University of Thessaloniki, Thessaloniki, Greece

9.7.1 Introduction

Periodic and resonant foundations and buried anti-vibration barriers designed to attenuate the propagation of seismic waves can represent a breakthrough for the safety and the preservation of historical and strategic infrastructures, including hospitals and power plants (Bao et al, 2011; Basone et al., 2019; Krodel et al., 2015; Miniaci et al., 2016; Palermo et al., 2016; Shi et al., 2014; Smith and Smith, 2015; Sun et al., 2019; Yan et al., 2014). These isolation systems commonly referred to as “seismic metamaterials” (Brule et al., 2014; Colombi et al., 2016), base their capabilities on physical concepts recently developed in material science and solid-state physics, where novel materials dubbed “phononic crystals” and “resonant metamaterials” have been introduced to control the propagation of elastic waves (Deymier, 2013).

Phononic crystals are periodic materials that can exhibit large band gaps, i.e., frequency regions where the propagation of waves with wavelengths in the order of material periodicity is hindered. For seismic scale applications, meter size phononic crystals made of cylindrical holes in sedimentary soil have proved the possibility of reflecting seismic elastic energy, achieving attenuation of ground accelerations at a frequency range around 50 Hz (Brule et al., 2014). Although revolutionary in their conception, implementation of these systems at the low frequencies characteristic of seismic events (<30 Hz) requires very large structures, since the wavelengths of typical seismic waves can be of several decameters.

Unlike phononic crystals, resonant metamaterials exploit an array of sub-wavelength units to attenuate the propagating waves without relying on material periodicity. Therefore, for seismic waves characterized by long wavelengths, resonant metamaterials allow for the construction of more viable devices, i.e., of smaller and feasible dimensions. Based on this paradigm, meter-size buried structures, in the form of resonant metafoundations (Cheng and Shi, 2013) or resonant metabarriers (Palermo et al., 2016), have been proposed in recent years to isolate buildings and infrastructures from incoming seismic longitudinal and shear waves or to shield them from surface Rayleigh waves, respectively. The idea of a resonant metabarrier is motivated by the fact that far from the epicenter surface waves can carry a significant portion of the earthquake energy (Graff, 1975) and that existing structures may be hard to be retrofitted with innovative foundation systems.

The resonant metabarrier exploits purposely designed resonant units able to interact with surface waves in the low-frequency regime (<10 Hz). The resonant units are passive devices (mass-stiffness resonators), placed atop of the soil or buried below the surface, and excited by the vertical component of the Rayleigh wave motion. Once activated, their dynamic interaction with the soil redirects part of the surface elastic Rayleigh wave energy into the soil deposit as vertically polarized shear waves. The dynamics of these resonant systems has been predicted analytically and verified numerically at different wave scales, or in other words, at different frequencies. Conversely, experimental proofs of their working mechanism and attenuation capabilities are up to now limited to few table-top experimental tests (Palermo et al., 2016). Nonetheless, measurements at the geophysical scale have shown a reduction of the surface motion due to the resonance of forest trees (Colombi et al., 2016), encouraging the realization of an experimental proof of a metabarrier working in the Hz range. Indeed, full-scale realizations and tests of a resonant barrier are still missing, probably due to its cost of realization as well as due to the significant resonating mass needed to activate the wave conversion.

Therefore, the REWARD project has been designed to make a further step towards the realization of this isolation system for seismic waves by testing the effectiveness of a resonant metabarrier at a medium-size scale, within a 50–100 Hz frequency range, taking into account the variability in stiffness and strength of the soil profile. Here we report the results of the experimental campaign, developed at

the Euroseistest TA facility (Pitilakis et al., 2008), where a metabarrier has been designed according to the in-situ soil properties and the available operative frequency range of the measuring equipment and tested.

9.7.2 Test object

The metabarrier

The tested metabarrier consists of an array of resonators arranged in a regular square grid of 5×10 m, spaced apart of 0.5 m (see Figure 509a). The fundamental element of the metabarrier is the resonator (see Figure 509b). Resonators have been realized using simple construction materials (steel and plastic). Our prototype resonator consists of a PVC barrel (diameter 40 cm and height approximately 50 cm) filled with dry sand. The mass of the resonator can be thus varied up to 100 kg by pouring different amounts of dry sand within the barrel. The barrel is placed on a bed of 4 to 8 vertical steel springs kept between two 10 mm thick steel plates of planar dimensions 40×40 cm. By varying the number of springs, the overall stiffness of the resonator can be changed. The scaled-prototype resonator is designed to provide a surface wave attenuation between 50 to 55 Hz, well above the frequency range of the seismic action, but limiting the overall experimental cost. For a mass of 50 kg and a resonant frequency $f_r = 50$ Hz, the overall required stiffness is $K_{tot} = 50 \times (2\pi f_r)^2 = 4935$ KN/m.

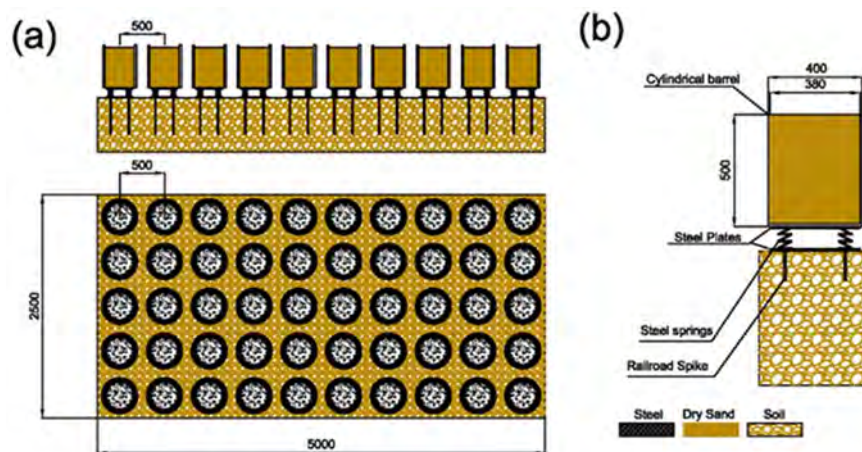


Figure 509: (a) Side view and top view of the 5×10 m array of resonators composing the metabarrier. (b) Schematic of a single resonator

The modular and tunable design of the resonator allows realizing metabarriers with different resonant frequencies (even once the resonators are in place). Adjustments of the resonator frequency are achievable by varying the compaction of the soil below the resonator base or varying the number/stiffness of some/all springs. Moreover, this flexible design approach of the resonator allows building metabarriers characterized by lines of resonators with different resonant frequencies. This design strategy, known as the rainbow trapping concept in the metamaterial community, can widen the attenuation frequency range of the barrier.

Description of the EUROSEISTEST site

Previous analytical and numerical studies (Palermo et al., 2016; 2018a; 2018b) indicate that the metabarrier isolation performance, both in terms of frequency width and wave amplitude decay, highly depends on the soil mechanical properties (e.g., mass density, longitudinal and shear bulk speeds).

Hence, detailed knowledge of the soil stratigraphy is of paramount importance for a proper design of the barrier. The EUROSEISTEST site is the longest-running valley instrumentation project worldwide. The site is located in the centre of the Mygdonian basin, Thessaloniki (Greece), in a high seismicity region, where the epicentral area of the destructive Magnitude 6.5 Volvi earthquake (1978) is included. The soil stratigraphy of the site is already well-documented from previous extended geotechnical and geophysical surveys (Pitilakis et al., 1999; Pitilakis et al., 2008; 2018; Raptakis et al., 2000). In Figure 510, the longitudinal (a) and shear (b) bulk waves speed of the site versus the soil depth are given. The density of the soil is assumed to be $\rho = 1500 \text{ kg/m}^3$. The depth-dependent speed profile is used to compute the surface wave dispersion curves supported by the soil. To such purpose, a 2D soil column (e.g., the model unit cell) of dimensions $d \times h = 0.5 \times 70 \text{ m}$ is modeled via the Finite Element (FE) method in Comsol Multiphysics as shown in Figure 511a. As expected, due to the heterogeneous soil stratigraphy, multiple and dispersive surface modes are found (see Figure 511b and Figure 511c).

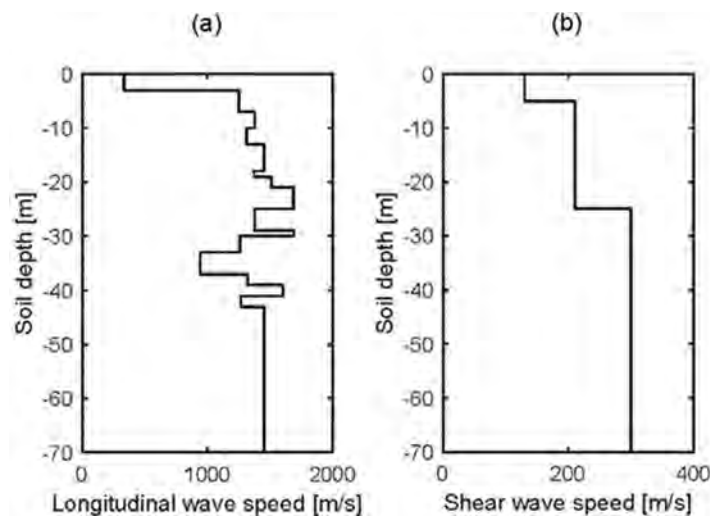


Figure 510: Longitudinal (a) and shear (b) bulk waves speed of the EUROSEISTEST site soil profile

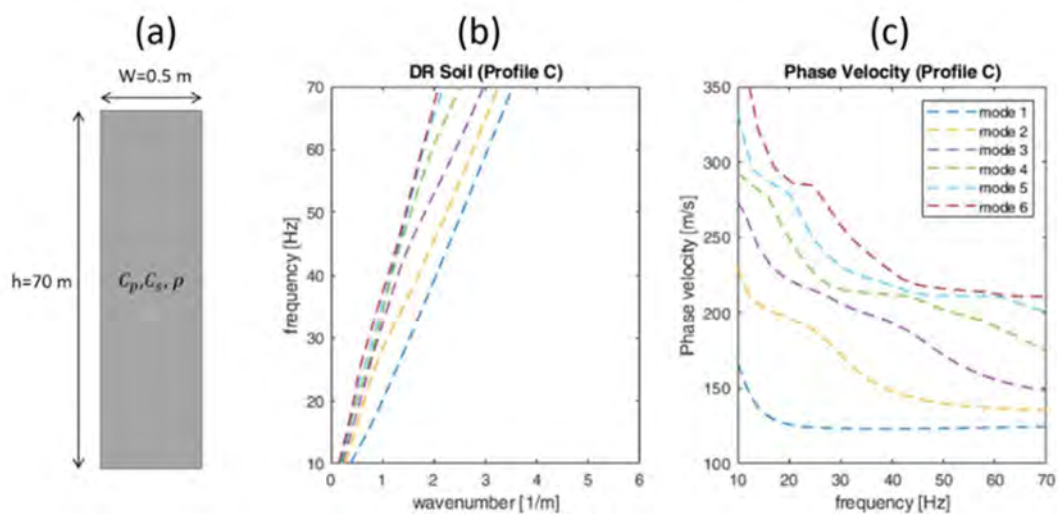


Figure 511: (a) Schematic of the reference soil model (RSM); (b) Dispersion curves for the RSM and (c) Phase velocity vs. frequency

9.7.3 Numerical simulations

Metabarrier design via numerical simulations

The analysis of the resonant metabarrier is performed numerically by extracting the barrier dispersion curve via FEM. In the 2D soil model of Figure 511, we introduce the numerical model of a resonator, e.g., the mass-spring system depicted in Figure 512a. The resonator introduces a flat dispersive branch around 47 Hz, generated by the coupling between the lowest order surface wave and the vertical motion of the resonator over the soil (Palermo et al., 2016; 2018a; 2018b). This significant change in the surface waves dispersion curve introduces substantial wave attenuation around the resonator resonance due to the impedance mismatch between surface waves in soil and waves traveling within the barrier.

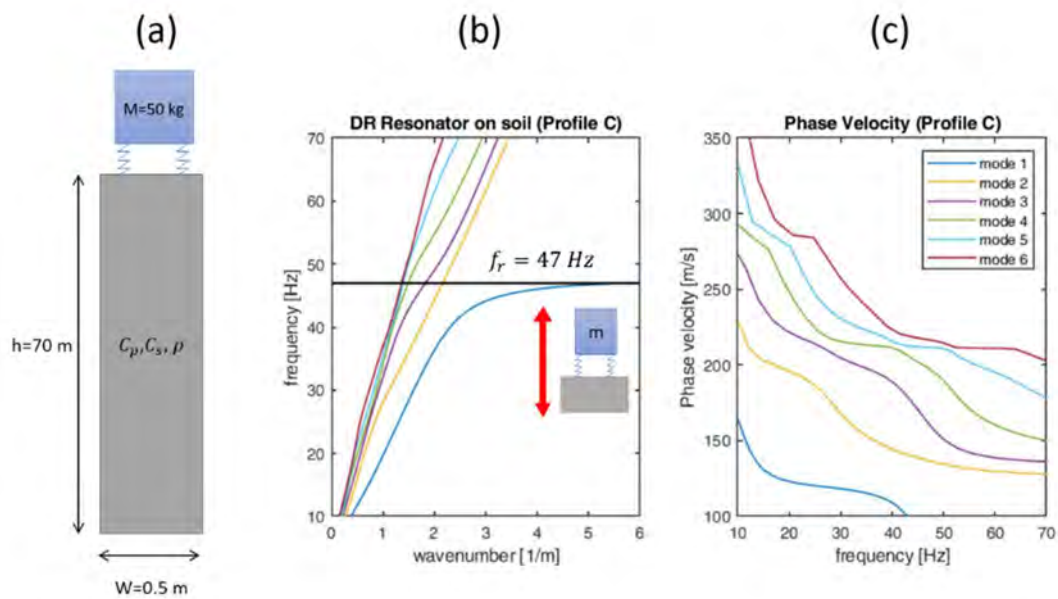


Figure 512: (a) Schematic of the metabarrier. (b) Dispersion curves and (c) the longitudinal velocity vs. frequency of the metabarrier

Time transient analysis is performed employing FE simulations to confirm these observations. The signal of choice is a Ricker Wavelet centered at 50 Hz, able to excite the whole frequency range of interest. As in the experimental setup, the barrier counts ten lines of resonators with dimensions and spacing defined according to the schematic in Figure 509. The output wavefield is evaluated as the averaged vertical displacement extracted over a grid of 11 points (i.e., equivalent to an array of physical sensors in the real scenarios) distributed over 10 m after the barrier (Figure 513a). The output displacement of the pristine soil is used as a reference case, e.g., the reference soil model (RSM). Fourier spectra of the averaged displacements for different test configurations are used to evaluate the attenuation performance of the barrier in terms of amplitude and frequency range. Two different scenarios are compared, a case with an array of masses placed over the soil without elastic connection (dead mass configuration) and the metabarrier case.

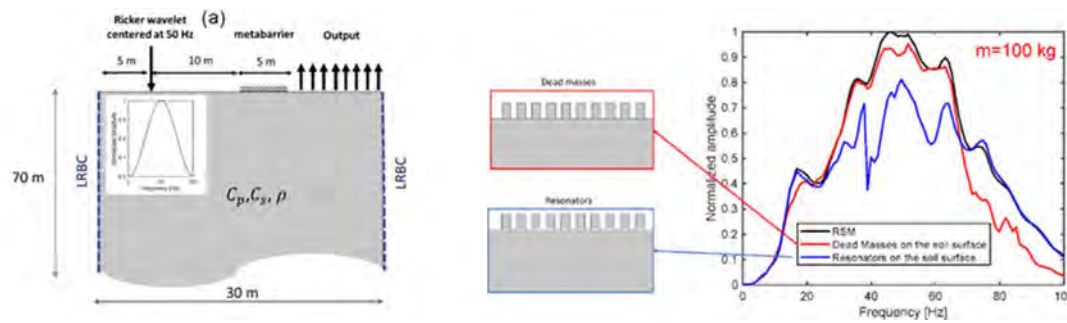


Figure 513: (a) Schematic of the full 2D FE model used in numerical simulations. Frequency spectra of the reference soil model (RSM, black line), barrier of dead masses (red line) placed over the soil surface and barrier of resonator (blue line)

The presence of the masses does not introduce an observable reduction in the surface wave spectrum. Conversely, the addition of the resonators introduces a marked reduction in the spectrum amplitude around the resonance frequency of resonators. This marked peak in frequency could be further widened by using resonators of different nominal resonant frequency and exploiting the so-called rainbow trapping concept (Krodel et al., 2015).

9.7.4 Test setup

The experimental tests were planned to be carried out in two different phases (P1) and (P2) for an overall set of 5 different experimental tests (T0-T4). The first phase was executed on 05/06/2019 in the EUROSEISTES facility and comprised two sets of tests (see Figure 514):

1. T₀: Ambient noise, Impact load (Sledgehammer loading) and vibration testing (pneumatic vibrator) on the soil in pristine conditions. This preliminary set of tests aimed at defining a baseline of records with different vibrating sources, defining the operational frequency range of the sources, the amplitude of the records within the test field and the dispersive features of the records.
2. T₁: Ambient noise, Impact load and vibration testing on the soil equipped with an array of 5X10 (2.5 m X 5 m) masses, placed directly over the soil surface, e.g., “dead mass configuration”.
- 3.

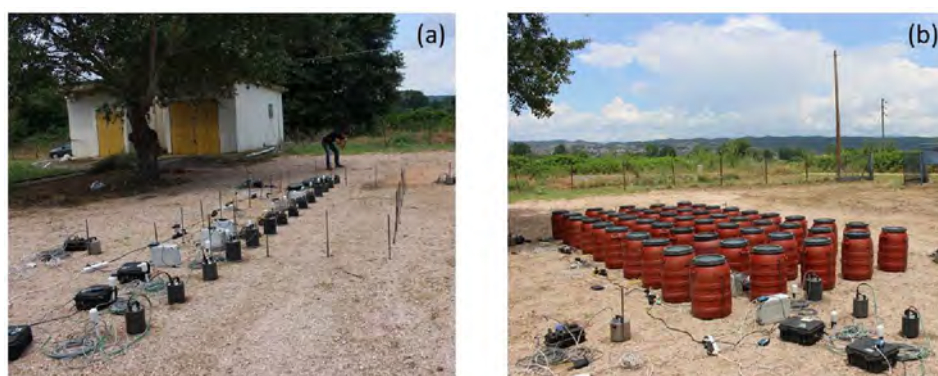


Figure 514: (a) On-field line measurement setup across barrier length on soil pristine (T0 setting).
(b) Dead mass configuration atop soil surface (T1 settings)

The second phase of tests, originally planned for the first week of March 2020, currently delayed due to travel restrictions related to COVID-19, will comprise three sets of tests:

1. T_0 : Multichannel Analysis of Surface Waves (MASW) recorded via 24 geophones, distributed within the test field, on soil in pristine conditions generated with impact loading sources and harmonic sources placed at different location within the field.
2. T_1 : MASW across the 5X10 grid (2.5 m X 5 m) of “dead-mass” configuration.
3. T_2 : MASWs across the metabarrier (5x10 resonators, T_1 settings) for different resonators arrangements and varying the mass of resonators (rainbow trapping configuration).

In what follows a detailed description of the experimental setup and the related results for phase P1 is given.

Source and Instrumentation description.

Three types of loading sources (Linear Pneumatic Vibrator NTP-25, Rotary Pneumatic Vibrator VT-24, and Hammer impact) are used for the generation of seismic surface waves.

NTP-25 vibrator can produce a maximum force of approximately 0.85kN having a frequency of 12400 rounds/minute or 140Hz approximately. VT-24 vibrator can produce a maximum force of approximately 6.2kN having a frequency of 8780 rounds/minute or 200Hz approximately. The pneumatic vibrators were clamped on heavy weights (concrete slabs) in order to maximize their efficiency. Their air supply was achieved by connecting them to an air compressor having maximum pressure of 6bars.

For the hammer loading, 10-15 strikes per each recording session were used.

Figure 515 depicts the layout of the placement of the sensors. Fourteen synchronized sensors, including six seismometers (CMG-6T) and eight accelerometers (CMG-5TD and CMG-5TCDE), were aligned across the barrier area for line measurement purposes. Four seismometers (CMG-40) were placed at one meter of distance from the corners of the barrier.

Resonators arrangement and source location

Fifty plastic barrels with a volume of 60 litres each, (40 cm diameter) filled with dry sand were used to realize the masses prototype (see Figure 514b). Different source locations were considered for surface wave excitation, as depicted in Figure 515. Locations 1,2,3 and 4 are aligned with the measurement instruments, while the rest of them are placed at the sides of the barrier. A concrete slab was installed in location 1, to accommodate the Pneumatic Vibrator.

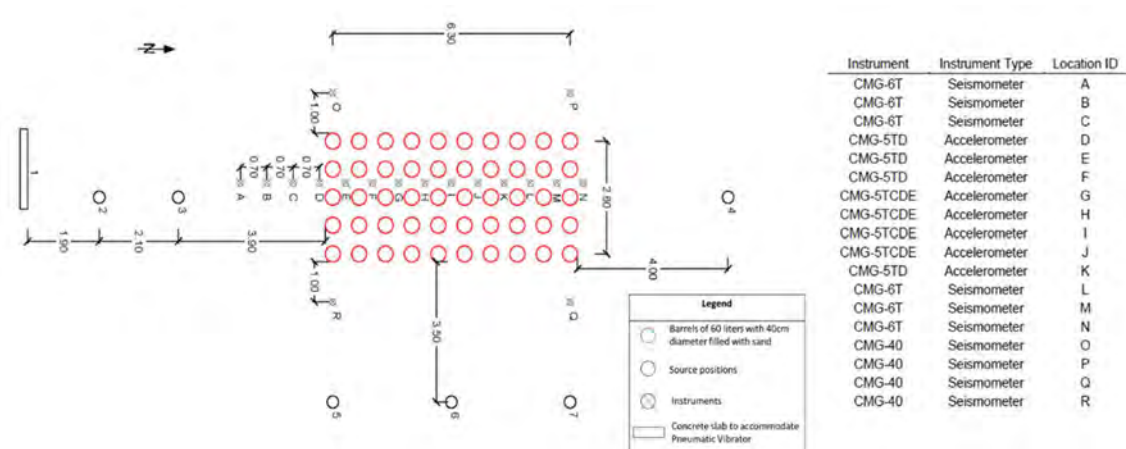


Figure 515: Source locations

Test sequence description

The sequence, source position, duration, and synchronized time of all the tests conducted during phase 1 are reported in Table 86 and Table 87 for T_0 and T_1 configurations, respectively.

1. **T_0 setting:** Soil pristine (RSM)

Experiment Type	Source	Source Position	Duration ¹ (sec)	No. of strikes	Start Time ^{1,2}
Ambient Noise	-	-	120	-	09:00:00.000
Pneumatic Vibrator	Linear NTP-25 (5 bars)	1	120	-	09:03:00.000
Pneumatic Vibrator	Rotary VT-24	1	120	-	09:06:00.000
Hammer loading	Hammer	3	-	10	09:08:00.000
Pneumatic Vibrator	Linear NTP-25*	1	120	-	09:10:00.000
Hammer loading	Hammer	2	-	12	09:12:00.000
Hammer loading	Hammer	4	-	15	09:20:00.000
Pneumatic Vibrator	Linear NTP-25	3	120	-	09:25:00.000
Pneumatic Vibrator	Rotary VT-24 (4 bars)	3	120	-	09:28:00.000
Pneumatic Vibrator	Rotary VT-24 (6 bars)	3	120	-	09:33:00.000

Table 86: Experiment type, source and duration for T_0 setting (soil pristine)

2. T₁ setting: Across dx10 grid of weights (Dead Mass)

Experiment Type	Source	Source Position	Duration ¹ (sec)	No. of strikes	Start Time ^{1,2}
Ambient Noise	-	-	100	-	09:56:00.000
Pneumatic Vibrator	Linear NTP-25	3	120	-	09:57:00.000
Pneumatic Vibrator	Rotary VT-24	3	120	-	10:00:00.000
Hammer loading	Hammer	2	-	15	10:03:00.000
Hammer loading	Hammer	7	-	10	10:08:00.000
Hammer loading	Hammer	6	-	10	10:10:00.000
Hammer loading	Hammer	5	-	10	10:12:00.000
Hammer loading	Hammer	3	-	10	10:12:30.000
Pneumatic Vibrator	Linear NTP-25	1	120	-	10:13:10.000
Pneumatic Vibrator	Rotary VT-24	1	120	-	10:17:00.000
Hammer loading	Hammer	4	-	10	10:22:00.000

Table 87. Experiment type, source and duration for T₁ setting (Dead Mass)

1: Approximately

2: GPS Time

*: loosen bolts – not entirely fixed

9.7.5 Observation during tests

Due to weak GPS signal related to weather conditions, the seismometers at location B and F stopped working during experiments; the seismometer at location N did not record hammer strikes from sources 2 and 4. In addition, O, P, Q, and R were not synchronized, e.g., did not record the real-time data. The maximum operational frequency for the sensors in O, P, Q, and R is 50Hz, limiting their practical contributions to the designed experiments.

9.7.6 Preliminary Results

In this section, we summarize the results obtained from the first experimental campaign (P1). These results are currently used to update the experimental setup, revise the excitation source type and measurement equipment for the planned second phase of experiments.

Data processing of the first experimental campaign

We analyzed the data obtained from the experiments by examining the source type, considering the limitations of the sensor nodes discussed above and comparing the results for the soil pristine (T_0) versus dead mass case (T_1).

- Source characterization

For the 3 sources utilized during phase 1 (P1), e.g., Linear pneumatic vibrator NTP-25, rotary pneumatic vibrator VT-24, and hammer impact, we performed Fast Fourier Transform (FFT) of the records at different locations to obtain the frequency spectra of the source. Here, we report the results obtained from the pristine soil data set (T_0)

For the Linear Pneumatic vibrator NTP-25, we considered the excitation from source number 1 (7.9 m from the barrier front) and used sensor H (accelerometer) for data acquisition, as shown in the schematic of Figure 516a. Two cases are considered: a pneumatic vibrator tightly fixed on the concrete plate and a vibrator with loosen connection. The spectra calculated from the time domain records are shown in Figure 516b and Figure 516c, respectively. In the fixed case, two peaks are observed, one narrow pick around 47 Hz and the other around 75 Hz. The same narrow pick is also observed in the loose bolt case, while the rest of the frequency content is spread between 60 to 90 Hz.

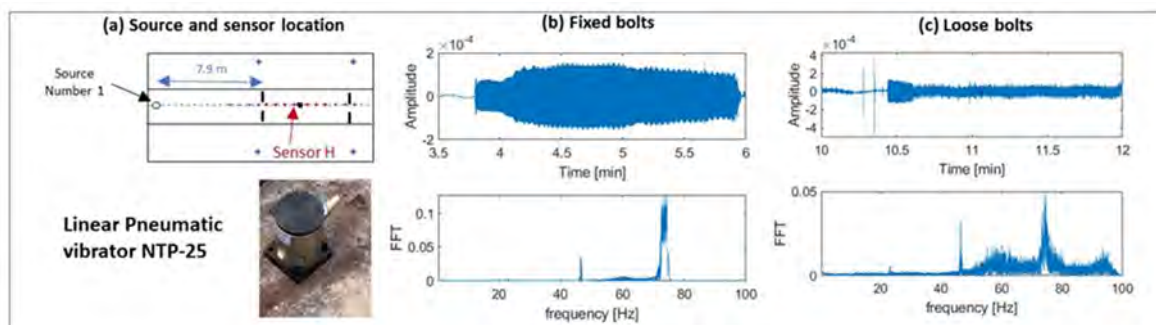


Figure 516: Linear Pneumatic Vibrator NTP-25 source. (a) source location in position 1 used for the excitation and sensor H (accelerometer) measures the response; (b) time trace and FFT for the fixed bolts and (c) loose bolts conditions

The same procedure is applied for the Rotary Pneumatic Vibrator VT-24 source. The location of the source is changed to number 3 (with 3.9 m distance from the edge of barrier zone), and sensor H is selected to extract the data again. Two excitation signals are considered, respectively generated by 4 and 6 bars of input pressure (Figure 517b and Figure 517c, respectively). The frequency content of both the input falls within two frequency windows, 35 to 55 Hz and 75 to 100 Hz, therefore the use of such pneumatic vibrator is not adequate for the assessment of the resonator dynamics, which is expected within the frequency range from 50 to 70 Hz.

For the hammer impact loading, we characterize the frequency spectra by windowing the received signal time trace for each impact. We then calculated the FFT of the time traces for each strike and calculate the mean spectrum as depicted. A schematic of the procedure and some relevant time and frequency domain records are provided in Figure 518 for soil in pristine conditions (T_0). The same approach has been used to analyze the records for the “dead-mass” configuration (T_1). The frequency content of the hammer impact obtained from a single strike covers a wide frequency range from 0 to

100 Hz, with maxima around 30 and 60 Hz, suitable to investigate the signal attenuation introduced by the resonators.

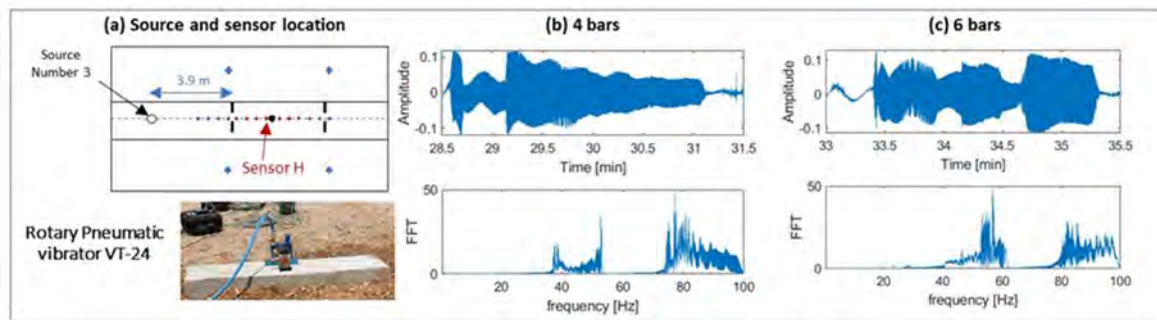


Figure 517: Rotary Pneumatic Vibrator VT-24 source. (a) source located in position three used for the excitation and sensor H (accelerometer) measures the response; (b) time trace and FFT for 4 bar and (c) 6 bar of input pressure

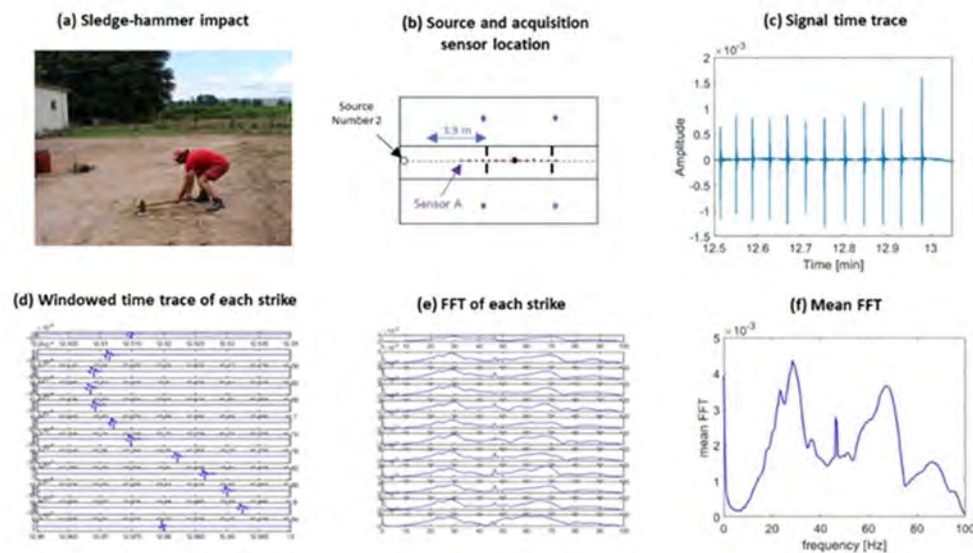


Figure 518: T_0 Data processing example for (a) Hammer loading input; (b) Source location at point 2 and receiving sensor A are selected; (c) Signal time trace for 12 hammer strikes; (d) windowing the time trace for each strike; (e) Spectral content of each strike; (F) Mean spectral content

- Soil vs. Dead Mass on the soil surface

We compare the response of the soil in the presence and absence of the “dead masses” by selecting the hammer impact as input source. Figure 519 compares the mean spectra for T_0 and T_1 configurations considering different signal acquisition locations. The addition of masses on the soil surface (T_1), generally results in a minimal reduction of the surface response, in accordance to what predicted by the numerical model. We also observe that the mean frequency spectra are highly influenced by the type of sensor (seismometer (which records velocities) or accelerometer) used to record the signal due to the different frequency content between velocities and acceleration records. For instance, the T_1 response is lower than T_0 for the whole record acquired at location H (e.g., accelerometer in the middle of the barrier), while for the record in M (the seismometer at the far end of the barrier), the T_1 response exceeds the response of the pristine soil T_0 in the high-frequency range.

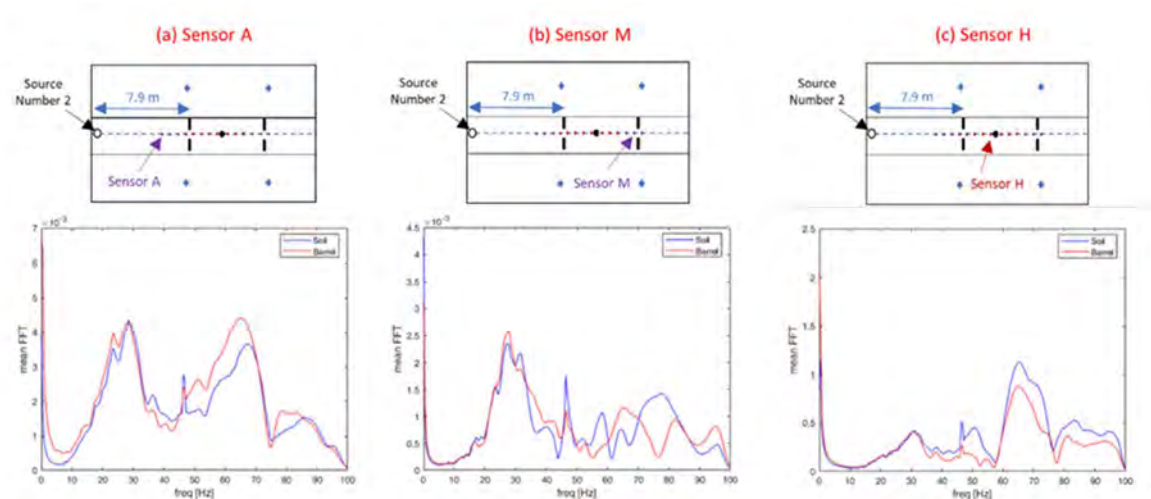


Figure 519: Comparison of Mean FFTs for soil and dead Mass. (a) Result obtaining from sensor A (placed at the wavefront of the barrier), sensor M (at the end of the barrier), and sensor H (in the middle of barrier zone)

Limitations of the adopted measurements /source setup

- **Type of source:** The adopted harmonic sources (Pneumatic Vibrators) have an output frequency out of the range of interest. The impossibility of tuning the signal at the desired frequency range makes this source of limited use for the test of the metabarrier dynamics. In phase (P2) the Pneumatic Vibrators will be equipped with an appropriate frequency control system to variate its output frequency
- **Measurement instruments:** In phase P1, the combined use of seismometers and accelerometers, and their synchronization problem, added complexity in the data interpretation. In the second phase P2, a MASW instrumentation (equipped with 24 geophones) will be used to ensure synchronization and uniformity of the data set across the different recording nodes.

9.7.7 Conclusions and outlook

In this project, we conducted an experimental campaign to test a medium-scale resonant barrier designed to attenuate the propagation of surface waves within a 50–100 Hz frequency range. This report presents the preliminary results of the first phase (P1) of the experimental campaign consisting in:

1. T_0 : Ambient noise, Impact load (Sledgehammer loading) and vibration testing (pneumatic vibrator) on the soil in pristine conditions.
2. T_1 : Ambient noise, Impact load and vibration testing on the soil equipped with an array of 5X10 (2.5 m X 5 m) masses, placed directly over the soil surface, e.g., “dead mass configuration”.

The tests were supported by FE numerical simulations to predict the behaviour of surface waves in the pristine soil and analyse the influence of the added mass on the dynamics of such surface waves. The data recorded during the first phase showed a negligible attenuation induced by the added mass on the propagating surface waves, qualitatively in accordance with the numerical simulations. Nonetheless, a quantitative interpretation of the data was hindered by the technical limitations induced by the adopted sources and measurement instruments. In particular, the first stage of measurements evidenced:

- The need for an appropriate frequency control system to variate the output frequency of the pneumatic vibrators
- The combined use of seismometers and accelerometers, and their synchronization problem, added complexity in the data interpretation.

To this reason, in the second phase (P2) of the experimental campaign, the generation and record of surface waves in the reference soil, “dead mass” configuration and metabarrier will be evaluated experimentally through a standard MASW technique and compared to numerical simulations. We expect to confirm an attenuation of the ground motion in the presence of the metabarrier.

9.7.8 References

Bao, J., Shi, Z., and Xiang, H. Dynamic responses of a structure with periodic foundations. *Journal of Engineering Mechanics* 138, 7 (2011), 761–769.

Basone, F., Wenzel, M., Bursi, O. S., and Fossetti, M. Finite locally resonant metafoundations for the seismic protection of fuel storage tanks. *Earthquake Engineering & Structural Dynamics* 48, 2 (2019), 232–252.

Krodel, S., Thome, N., and Daraio, C. Wide band-gap seismic metastructures. *Extreme Mechanics Letters* 4 (2015), 111 – 117.

Miniaci, M., Krushynska, A., Bosia, F., and Pugno, N. M. Large scale mechanical metamaterials as seismic shields. *New Journal of Physics* 18, 8 (2016), 083041.

Palermo, A., Krodel, S., Marzani, A., and Daraio, C. “ Engineered metabarrier as shield from seismic surface waves. *Scientific Reports* 6 (Dec 2016), 39356 EP –. Article.

Shi, Z., Cheng, Z., and Xiang, H. Seismic isolation foundations with effective attenuation zones. *Soil Dynamics and Earthquake Engineering* 57 (2014), 143–151.

Smith, A., and Smith, C. Book Title Book Title Book Title Book Title Book Title. Publisher of the Book, City, 2015.

Sun, F., Xiao, L., and Bursi, O. S. Optimal design and novel configuration of a locally resonant periodic foundation (lrpf) for seismic protection of fuel storage tanks. *Engineering Structures* 189 (2019), 147 – 156.

Yan, Y., Laskar, A., Cheng, Z., Menq, F., Tang, Y., Mo, Y., and Shi, Z. Seismic isolation of two dimensional periodic foundations. *Journal of Applied Physics* 116, 4 (2014), 044908.

Brule, S., Javelaud, E. H., Enoch, S., and Guenneau, S. ‘ Experiments on seismic metamaterials: Molding surface waves. *Phys. Rev. Lett.* 112 (Mar 2014), 133901.

Colombi, A., Roux, P., Guenneau, S., Gueguen, P., and Craster, R. V. Forests as a natural seismic metamaterial: Rayleigh wave bandgaps induced by local resonances. *Scientific Reports* 6 (Jan 2016), 19238 EP –. Article.

Deymier, P. A. *Acoustic Metamaterials and Phononic Crystals*. Springer, 2013.

Cheng, Z., and Shi, Z. Novel composite periodic structures with attenuation zones. *Engineering Structures* 56 (2013), 1271 – 1282.

K.F. Graff. *Wave motion in elastic solids*. Dover, 1975.

Pitilakis, D., Dietz, M., Wood, D. M., Clouteau, D., and Modaressi, A. Numerical simulation of dynamic soilstructure interaction in shaking table testing. *Soil Dynamics and Earthquake Engineering* 28, 6 (2008), 453 – 467.

Palermo, A., Krodel, S., Matlack, K. H., Zaccherini, R., Dertimanis, V. K., Chatzi, E. N., Marzani, A., and Daraio, C. Hybridization of guided surface acoustic modes in unconsolidated granular media by a resonant metasurface. *Phys. Rev. Applied* 9 (May 2018), 054026.

Palermo, A., Vitali, M., and Marzani, A. Metabarriers with multi-mass locally resonating units for broad band rayleigh waves attenuation. *Soil Dynamics and Earthquake Engineering* 113 (2018), 265 – 277.

Pitilakis, D., Rovithis, E., Anastasiadis, A., Vratsikidis, A., and Manakou, M. Field evidence of ssi from full-scale structure testing. *Soil Dynamics and Earthquake Engineering* 112 (2018), 89 – 106.

Pitilakis, K., Raptakis, D., Lontzetidis, K., Tika-Vassilikou, T., and Jongmans, D. Geotechnical and geophysical description of euro-seistest, using field, laboratory tests and moderate strong motion recordings. *Journal of Earthquake Engineering* 3, 3 (1999), 381–409.

Raptakis, D., Chvez-Garca, F., Makra, K., and Pitilakis, K. Site effects at euroseistesti. determination of the valley structure and confrontation of observations with 1d analysis. *Soil Dynamics and Earthquake Engineering* 19, 1 (2000), 1 – 22.

9.8 Project # 39 – “DYMOBRIS” Dynamic identification and Monitoring of scoured BRIdgeS under earthquake hazard

Authors

E. Tubaldi⁽¹⁾, C. Antonopoulos⁽¹⁾, S. Mitoulis⁽²⁾, S. Argyroudis^{(2),(5)}, F. Gara⁽³⁾, L. Ragni⁽³⁾, S. Carbonari⁽³⁾, F. Dezi⁽⁴⁾, A. Vratsikidis⁽⁵⁾, A. Anastasiadis⁽⁵⁾, D. Pitilakis⁽⁵⁾

⁽¹⁾ *University of Strathclyde, Glasgow, United Kingdom*

⁽²⁾ *University of Surrey, Guilford, United Kingdom*

⁽³⁾ *Polytechnic University of Marche, Ancona, Italy*

⁽⁴⁾ *University of San Marino, Republic of San Marino*

⁽⁵⁾ *Aristotle University of Thessaloniki, Thessaloniki, Greece*

9.8.1 Introduction

Bridge scour, the removal of sediments surrounding underwater foundations due to water flow and turbulence (Melville and Coleman, 2000; Pizarro et al., 2020) is the leading cause of bridge failure worldwide. Exacerbated by climate change effects (Imam, 2019; Fioklou and Alipour, 2017), this phenomenon induces considerable fatalities, traffic disruption, and significant economic and societal losses. Notable examples of recent failures in Europe are the Margarola bridge in Spain (two casualties) and the Hintze Ribeiro bridge in Portugal, that collapsed in 2001 due to general degradation of the riverbed, causing 60 casualties (Innovation & Research Focus Issue 93, 2013).

Foundation scour has two main effects on bridges: loss of foundation carrying capacity, and increased flexibility of the soil-foundation-structure (SFS) system. Many types of bridges, such as masonry-arch or multi-span bridges, have shallow foundations and are very vulnerable to scour (Tubaldi et al, 2018),

which often worsens with time due to accumulation of the effects, i.e. scour, under multiple floods (Tubaldi et al., 2017). New bridges usually have deep foundations, making them less vulnerable to scour. However, even for these bridges, the scouring of their foundations may result in changing of the boundary conditions, which may modify and eventually decrease their capability to withstand loadings.

It is well known that the overall response of bridges to dynamic loads such as those induced by earthquakes is dependent on SFS interaction effects (Gazetas, 1991). Thus, scour has also a significant potential to alter this response, by affecting both the kinematic and inertial soil-structure interaction (Guo, 2014) and increasing modal periods. Since many bridges spanning waterways are located in seismically active regions, the occurrence of earthquakes in the presence of flood-induced scour is a very likely, and hence critical design scenario (Yilmaz et al., 2016). Thus, understanding the complex interaction between the continuously evolving scour process and the dynamic behaviour of the affected bridges is of paramount importance for quantifying the risk and resilience of our infrastructure under multiple hazards (Argyroudis et al., 2020). This also calls for the development and deployment of innovative sensors and monitoring strategies for assessing scour and its effects on bridges (Prendergast and Gavin, 2014), without having to resort to potentially costly and inaccurate visual underwater inspections. In this context, monitoring the change of dynamic features of bridge superstructure, without recourse to underwater instrumentation, appears to be a very promising technique to detect scour (Foti and Sabia, 2011). For example, Briaud et al. (2011) focused on the use of accelerometers and tiltmeters to monitor scour, and for this purpose, they carried out two large scale laboratory models of a column and a column on piles. Subsequently, two individual monitoring systems were designed and installed on two real bridges. The results of the experimental campaigns showed that the instruments could be successfully employed to provide warnings of potential bridge failure. However, there were shortcomings with regard to the accelerometers, which are related to lack of sufficient excitation from traffic and the high-power consumption required for the transmission of accelerometer data, for which typical solar panel and battery are not sufficient. Another study (Prendergast et al., 2013) focused on single cantilever piles with the bottom part embedded in the soil, excited by a top impulse force, and on the development of a finite element model for capturing the effects of scour. The study showed that the effect of water on the measured natural frequencies of the cantilevers is negligible. Bao et al. (2017) conducted similar experiments for vibration-based monitoring of scour and also investigated the effect of the scour hole shape. This is usually assumed as symmetric in experiments, whereas in reality it has a non-symmetric shape (Tubaldi et al., 2018). Unsymmetrical scour hole scenarios were tested, shedding light on the importance of this factor for vibration-based scour detection.

Even though many studies have investigated experimentally and numerically the dynamic behaviour of bridges with deep foundations subjected to scour (Zhang et al., 2017), it is surprising that researches on bridges with shallow foundations are quite scarce. To our best knowledge, only the works of Guo (2014) and Yuan et al. (2019) have investigated numerically the impact of scour on bridges with shallow foundations. Guo (2014) analysed the changes of foundation impedances due to foundation scour, highlighting the reduction of foundation stiffness and radiation damping, and evaluating the effects on the seismic performance. Based on the study results, it was found that scour may be beneficial for mitigating seismic force demands, though it may induce excessive displacement demands in case of severe foundation scour profiles. Yuan et al. (2019) investigated the effect of scour on the seismic vulnerability of a two-dimensional bridge model, showing how the various bridge components may be differently affected by scour. Thus, further research on shallow foundations is urgently needed, given the importance of the problem, the high number of bridges with shallow foundations, and the higher impact of scour on this type of foundations compared to deep ones.

The DYMOBRIS project was conceived with the objective of contributing to fill this knowledge gap. For this purpose, full-scale tests, from ambient vibrations to forced-vibrations, were carried out on the EuroProteas SFS system at Euroseistest to evaluate the effects of foundation scour on the dynamic properties, i.e. frequency and damping, of a Soil- Foundation-Structure (SFS) system. The experimental tests were complemented by numerical analyses, aimed to identify the extent of the scour hole to be excavated in the tests, and to evaluate the suitability of various modelling strategies for simulating the effects of scour.

9.8.2 EUROPROTEAS

Structure

EuroProteas prototype structure was particularly designed to mobilize strong interaction with its foundation soil as it is a stiff structure with a large superstructure mass founded on soft foundation soil.

EuroProteas is a perfectly symmetric and reconfigurable structure. It is founded on a square reinforced concrete slab (C20/25) with dimensions 3.0m x 3.0m x 0.4m which rests on the ground surface. The superstructure mass consists of two identical to the foundation reinforced concrete slabs that are supported by four square hollow steel columns (QHS 150 x 150 x 10mm) which are clamped on the foundation. L-shaped (100 x100 x 10mm) X-braces are connecting the steel columns in all the sides of the structure ensuring its total symmetry. Assuming a uniform unit weight of 25kN/m³ for the concrete, the total mass of each slab is estimated at 9.16Mg, while the total mass of the structure is calculated approximately at 28.5Mg. Its outer dimensions are 3.0m x 3.0m x 5.0m (Figure 520).

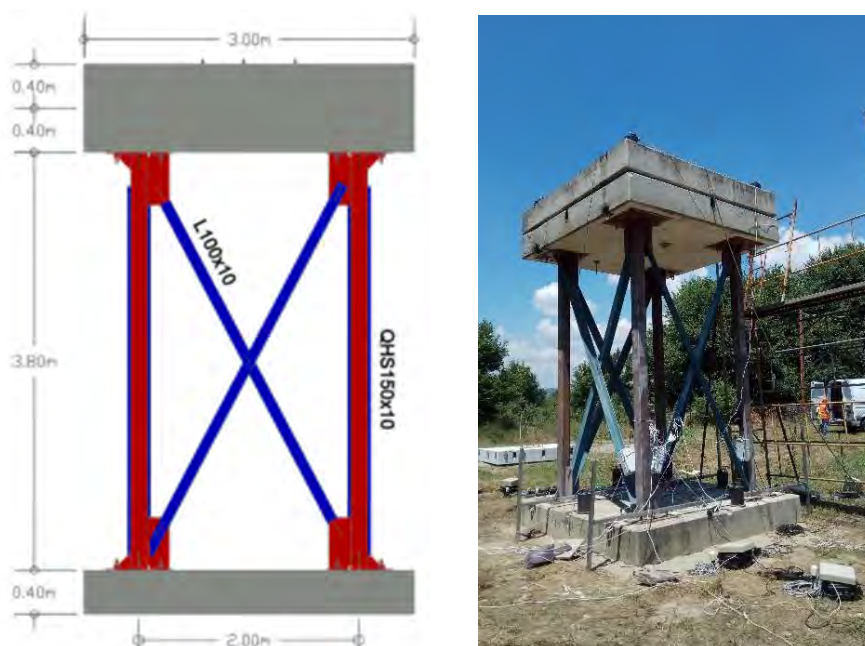


Figure 520: A 2D sketch and a view of EUROPROTEAS prototype structure

Foundation Soil

The foundation soil is well investigated and reported in earlier studies. Specifically, between 1993 and 2004, an extensive program of seismic prospecting and geotechnical testing was undertaken (Pitilakis et al., 1999). It comprised of in-situ (sampling boreholes, Standard and Cone Penetration Test

measurements) and laboratory (conventional classification tests, strength tests, consolidation tests and resonant column and cyclic triaxial tests) geotechnical surveys. The elaboration of all geophysical and geotechnical data, led to the classification of the main soil formations, validation of soil properties stemming from different methodologies and design of representative 1D, 2D and 3D soil models.

Scour Holes

Two different scour stages were preliminary designed in order to investigate the scour effects on structures. The soil beneath the north-west side of the foundation was excavated to simulate the scour of an actual foundation. The first excavated scour hole covered an area of 0.3m x 3m, whereas the second one covered an area of 0.7m x 3m and the corresponding ratio of the length of scour hole to the foundation width was 0.1 and 0.23.

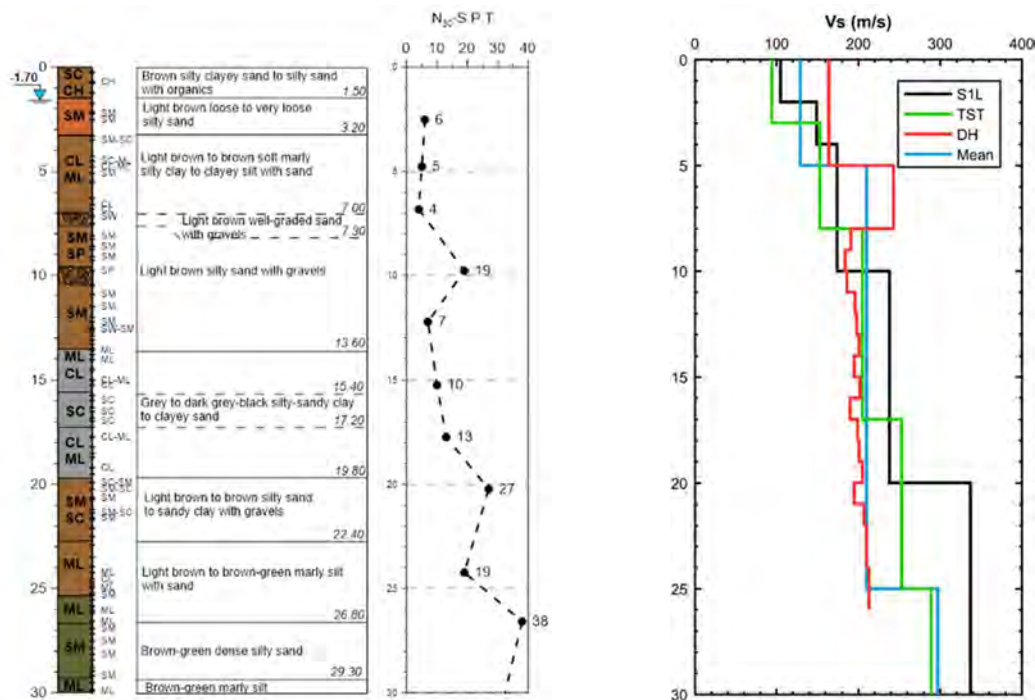


Figure 521: Soil stratigraphy of the 30m deep borehole at the geometrical center of the foundation, the N_{SPT} blow counts and the V_s profile as derived from down-hole (DH) tests prior to the construction of EuroProteas (Pitilakis et al. 2018) compared with the V_s profile at S1L site approximately 50m south of EuroProteas (Raptakis et al. 1998), a reference mean V_s model of the valley cross-section (Raptakis et al. 2000) and the proposed V_s profile by Pitilakis et al. (1999)

9.8.3 Numerical model and predictions

This subsection illustrates the preliminary numerical analyses carried out to design the experimental full-scale tests to predict effects of scour on the foundation response and the variations of the SFS dynamic properties. For this purpose, a three-dimensional finite element model of the EuroProteas SFS system (Manakou et al., 2010) has been developed in the Finite Element code Abaqus (Dassault Systemes, 2014). In particular, various models are built, namely the Fixed Base (FB) structure, the structure with the soil-foundation system modelled using linear springs and dashpots, which simulate impedance functions, and the structure with a continuous soil domain.

The three models share the same description of the superstructure (Figure 522), with two-node linear beam elements used to model the columns and the braces, and 20-node quadratic brick elements

(C3D20) used to model the slabs. The columns are connected to the slabs using multi-point tie constraints, whereas the X-braces are connected to the column ends via a hinge connector. The connections between the two X-braces are based on joint connectors.

The steel Young's modulus and Poisson's ratio are $E_s=210,000$ MPa and $\nu_s=0.2$ respectively, whereas the concrete mechanical properties are $E_c=29,962$ MPa and $\nu_c=0.2$. A 1% damping factor is assigned to both materials by using the following Rayleigh model. The Rayleigh damping coefficients are calibrated to achieve the target damping factor in correspondence of the first and the third modes of vibration of the system, characterized by the highest participation of the superstructure masses along the x direction.

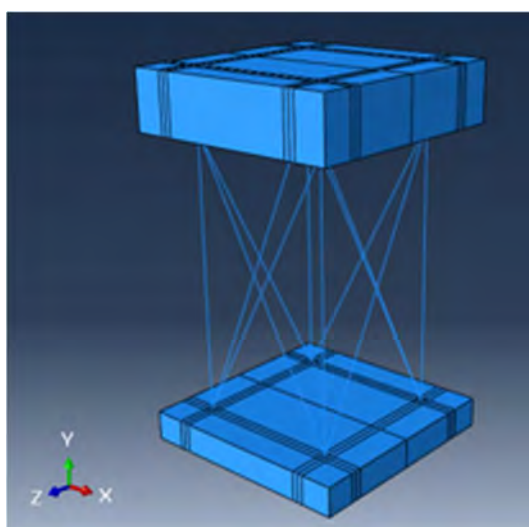


Figure 522: Superstructure used in fixed-base model

Fixed-base model (FB)

The FB model is obtained by restraining the displacements at the base of the foundation slab. This model, characterised by a fundamental vibration frequency of 9.26 Hz (Table 88), is used to estimate the effects of SSI on the vibration properties by comparison with the other two models, namely the one with linear springs and dashpots and the one with the soil considered as a continuum. In the next subsection, these two SFS models are described in detail and denoted as SFS_1 and SFS_2, respectively.

Structural configuration	Resonant frequency [Hz]	
	Abaqus	Experimental
FB model	9.26	-
SFS_1 model	4.48	4.1
SFS_2 model	4.22	4.1

Table 88: Resonant frequencies for different structural configurations (case without scour)

Structure with soil modelled using a simplified impedance function model (SFS 1)

In this model, the semi-infinite soil-domain is replaced by a set of distributed springs and dampers with the aim of obtaining a simplified description of the SSI problem. This approach is similar to the one followed in Tubaldi et al. (2018) and Ragni et al. (2019), with zero-thickness cohesive interface elements resisting only compression stresses at the bottom of the foundation describing the soil reaction. The cohesive interface elements have a visco-elastic behaviour, with properties based on the work of Gazetas (1991).

The springs constants (stresses per unit displacements) have been evaluated as follows:

$$k'_{s,x} = \frac{k_{s,x}}{A_x}, k'_{s,y} = \frac{k_{s,y}}{A_y}, k'_{s,z} = \frac{k_{s,z}}{A_z} \quad (19)$$

where $k_{s,x}$, $k_{s,y}$ and $k_{s,z}$ are given by Gazetas (1991) as a function of the shear modulus, $G_s = V_s \cdot \rho^2 = 31.47 \text{ N/mm}^2$, the Poisson's ratio, $\nu = 0.4$, and of the foundation geometry, whereas A is the foundation area in contact with the soil.

The dashpots are in parallel with the springs and represent the soil radiation damping according to the following expression (Gazetas, 1991):

$$c'_x = (\rho V_s) \cdot \tilde{c}_x, c'_z = (\rho V_s) \cdot \tilde{c}_z, c'_y = (\rho V_{La}) \cdot \tilde{c}_y \quad (20)$$

Where ρ is soil material density, V_{La} is Lysmer's shear wave velocity, related to V_s , and \tilde{c}_x , \tilde{c}_y and \tilde{c}_z are function of the foundation geometry and mechanical soil properties. A 5% damping factor is considered to reflect the soil hysteretic damping. In this work, it is assumed that the damping does not change with frequency, and the values of \tilde{c}_x , \tilde{c}_y and \tilde{c}_z are those corresponding to the system natural frequency. The values of the subgrade reactions are $k'_{s,x} = 0.0295 \text{ N/mm}^3$, $k'_{s,z} = 0.0295 \text{ N/mm}^3$, and $k'_{s,y} = 0.0397 \text{ N/mm}^3$. The values of the damping coefficients (including the hysteretic component) are $c'_x = 3062.4 \text{ N}\cdot\text{s/mm}$, $c'_z = 3062.4 \text{ N}\cdot\text{s/mm}$, and $c'_y = 4932.2 \text{ N}\cdot\text{s/mm}$.

To simulate scour in Abaqus, the “model change” capability is employed, allowing to progressively eliminate the cohesive interface elements at the foundation-soil interface that represent the portion of eroded soil.

Structure with soil modelled as a continuum with absorbing boundaries (SFS 2)

This sub-section describes the three-dimensional model including the semi-infinite soil-domain. This domain is modelled with solid elements with elasto-plastic behaviour. The elastic soil behaviour is described by assigning $G_s = 31.47 \text{ N/mm}^2$ and $\nu = 0.4$. The plastic behaviour is defined by the Mohr-Coulomb model, with a friction angle $\Phi' = 32.6^\circ$, dilatation angle $\varphi = 2.6^\circ$, and cohesion $c' = 0.003 \text{ MPa}$. The soil material damping is described through the Rayleigh formula, with a damping ratio of 5%.

The interaction between the foundation and the soil is modelled using the “surface to surface” contact approach. The interface has a very high stiffness in compression to avoid penetration, can resist only compressive forces, and has a friction coefficient of $\mu = 0.6$ along the tangential direction.

The soil is represented by a finite domain with local Absorbing Boundary Conditions (ABCs) to avoid reflection of outgoing waves (Figure 523). The length of the solid domain from the foundation slab

outwards is 18m; the absorbing elements are infinite brick elements, and their length is equal to that of the soil domain.

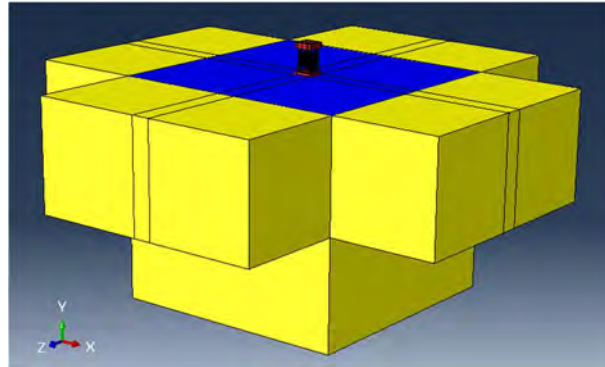


Figure 523: Model of SFS system with soil domain (in blue) and ABCs (in yellow)

In order to accurately model wave propagation, the mesh size satisfies the following relation (Kuhlemeyer and Lysmer, 1973):

$$l_{max} \leq \left(\frac{1}{8} \sim \frac{1}{5}\right) \lambda_{min} \leq \frac{V_{s,min}}{8f_{max}} \quad (21)$$

where l_{max} is the maximum element size, λ is shear wavelength, equal to 13 m, $V_{s,min}$ is the shear-wave velocity, equal to 130 m/s², and $f_{max} = 10$ Hz is the maximum frequency of interest.

Simulation of forced-vibration tests

This section illustrates the results of the simulation of the response of the structure under several load and scour conditions. For each model and scour condition considered, a static analysis is firstly carried out under the dead loads of the system. Then, a steady-state analysis is performed to simulate the effects of forced-vibrations imposed by the forces applied through a shaker placed on the roof slab. Finally, the Frequency Response Function (FRF), expressing the relationship between the input force and the output displacement at the top slab, is evaluated. This is used to estimate the resonant frequency of the system, f_R , corresponding to the peak of the FRF, and the damping ratio, which is obtained through the half-power bandwidth method.

The amplitude F of the harmonic force applied through the shaker for each excitation frequency is governed by the following equation:

$$F = E(2\pi f)^2 \quad (22)$$

where F is in N, E is the total eccentricity of the shaker (in kg·m) and f is the rotational speed of the shaker (in Hz) (Pitilakis et al., 2018).

It is noteworthy that some experiments were already carried out on the EuroProteas system considering an intact foundation (no scour) (Pitilakis et al., 2018). The results of these tests, carried out for a shaker eccentricity $E = 1.85$ kg·m, are used in this study to validate the proposed numerical models, by comparing the estimates of the resonant frequency with the experimental ones.

Figure 524 shows the variation with the excitation frequency of the FRF obtained by simulating the forced-vibration test in the model implementing the impedance functions to describe the SSI. The frequency value corresponding to the peak of the corresponding FRF, reported in Table 88, is equal to 4.48 Hz. This value is significantly lower than the one of the fixed base structure (9.26 Hz), demonstrating the high influence of SSI effects on the system response. Moreover, it is slightly higher than the one calculated experimentally (4.1 Hz) by Pitilakis et al. (2018). The difference between the experimental and numerical estimates may be due to the simplifications inherent to the impedance model, and the fact that the impedance function has been spread uniformly in plane along the foundation base. The numerical estimate of the damping ratio is equal to $\xi=4.55\%$.

In order to evaluate the influence of scour on the SFS dynamic properties, the cohesive interface elements located below a portion of the foundation of width 575 mm along the x direction, from the right extreme of the slab towards the center, are progressively removed during the time history analysis, before performing the steady-state forced-vibration analysis. It can be observed in Figure 524 that scour results in a shift of the FRF peak towards lower frequencies, and in an increase of the peak value, due to the reduced stiffness of the system. In particular, in presence of scour the resonant frequency is equal to 3.67 Hz, and the damping ratio increases from the value of 4.55% in the case of no scour to 7.50%.

Figure 524 also shows the variation with the frequency of the input of the FRF obtained for the model including the continuous soil domain. The steady-state response is very close to the one evaluated experimentally, with a similar value of the resonant frequency (4.22 Hz instead of 4.1 Hz) and a damping ratio is equal to 4.76%.

When scour is present, the resonant frequency is equal to 3.27 Hz, and the damping ratio is equal to 6.25%. Thus, the trend of the variation of these parameters due to scour is similar to the one observed for the previous simplified model with impedance functions. However, the frequency shift and amplitude increase are much higher in the case of the model with continuous soil domain.

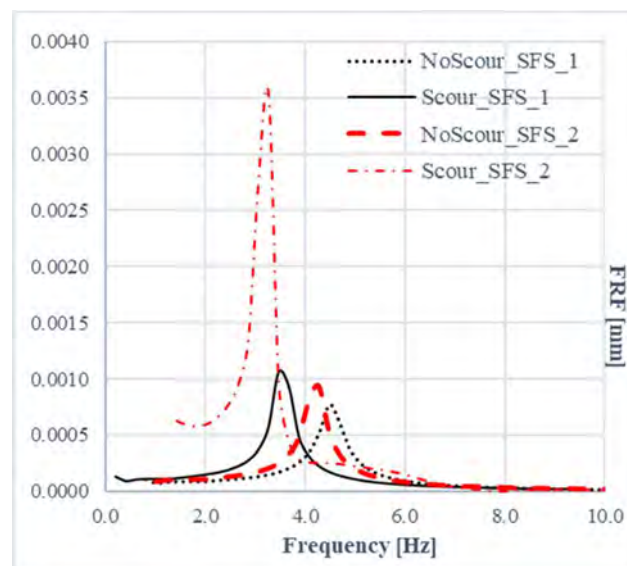


Figure 524: FRF for model with impedance function (SFS_1) and with continuous soil domain (SFS_2)

9.8.4 Test setup

Scour Holes

Three experimental series were performed in total, each with a different scour stage. In particular, the first set of experiments was conducted while EUROPROTEAS was founded on natural soil, whereas the next two series were performed for two different progressive scour stages excavated between the tests, as shown in Table 89. The first excavated scour hole had a length of $S = 0.3\text{m}$, whereas the length of the second was $S = 0.7\text{m}$ and the corresponding ratio of the length of scour hole to the foundation width was 0.1 and 0.23 respectively. The scour holes are presented in Figure 525.

Scour ID	S (m)	S / B
Natural Soil	-	-
A	0.3	0.1
B	0.7	0.23

Table 89: Experimental series and scour stages excavated

Instrumentation

The general instrumentation scheme was designed particularly to capture the response of the structure and the foundation in both in-plane and out-of-plane direction as well as the soil surface response in the same directions and also below the foundation. The instruments used are:

- 5 triaxial accelerometers GMG-5T (Guralp)
- 4 triaxial accelerometers CMG-5TCDE (Guralp)
- 6 digital broadband seismometers CMG-40T (Guralp)
- 5 digital broadband seismometers CMG-6TD (Guralp)
- 4 laser sensors (Waycon)

The instrumentation layout of the structure is presented in Figure 525. All the instruments were configured at a sampling frequency of 200 Hz and were connected to external global positioning system (GPS) antennas.

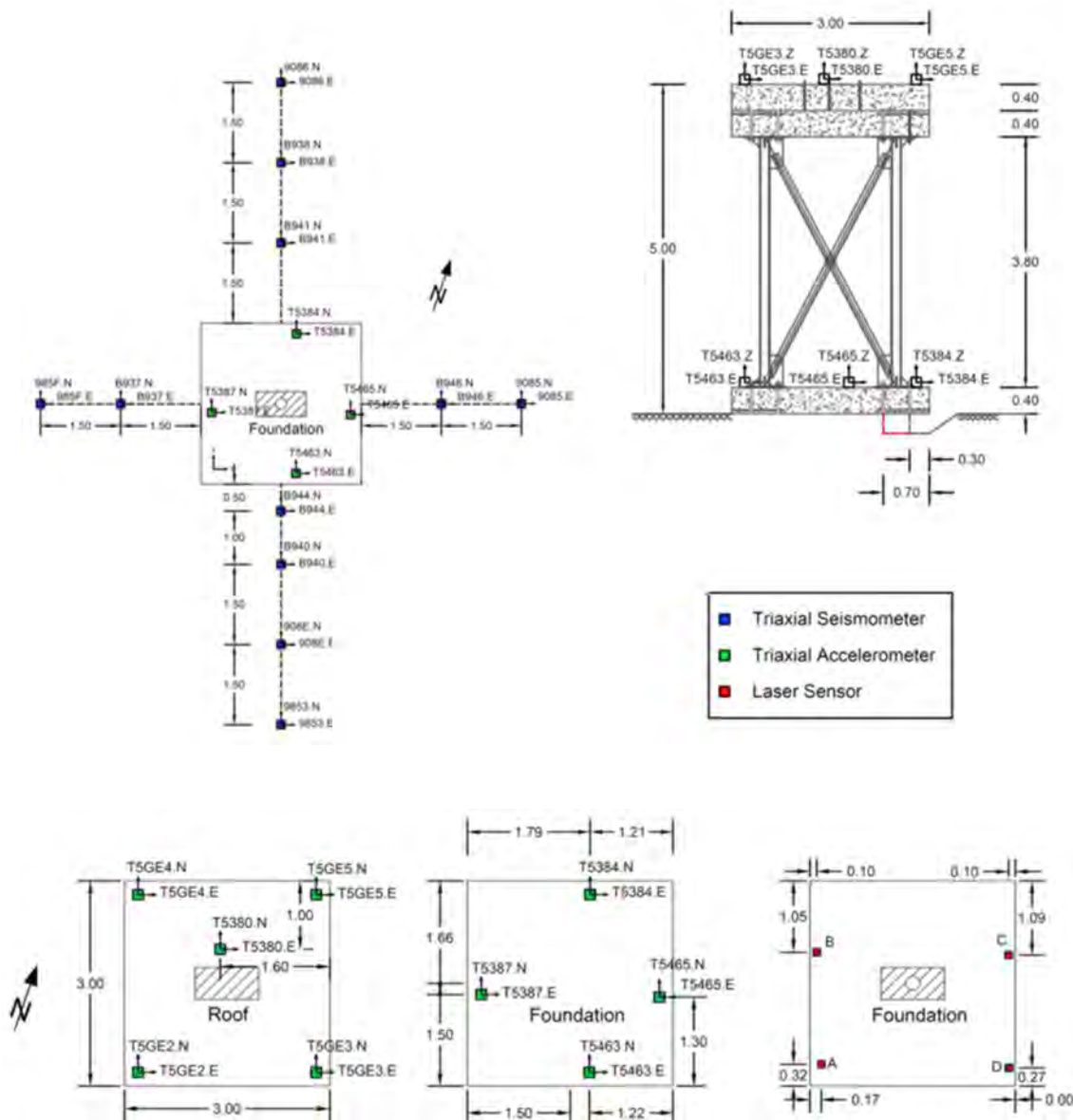


Figure 525: Plan view of the instrumentation layout of the foundation and the soil surface (upper left), of the roof and foundation slab (bottom) and a cross-section of the layout with the scour holes of $s = 0.3\text{m}$ (black line) and $s = 0.7\text{m}$ (red line)

Forced-Vibration tests

The eccentric mass shaker MK-500U owned by the Institute of Engineering Seismology and Earthquake Engineering (ITSAK) was implemented as a source of harmonic excitation. It is a portable uniaxial dual counter-rotating shaker that can produce a maximum force amplitude of 5 tons in a frequency range between 0.1-20Hz. Eight mass plates in four different sizes (A, B, C and D) can be used in pairs to adjust the eccentricity of the shaker and hence the output force. The amplitude of the output force of the shaker is given by Eq. (22).

The eccentric mass shaker was placed at the geometrical centre of the top roof slab of the structure and it was orientated to produce a force having a direction that formed an angle of 30 degrees with the magnetic North.

9.8.5 Observation during testing

During the performed test, a few instruments failed to record the response or suffered from synchronization problems. As a result, not all instrumentation could be used for examination of the performed test. In the case of the instrumentation of the structure, the following notes can be made:

- All the recordings of the instrument T5380 are not synchronized according to the GPS absolute time.
- The instrument T5GE4 recorded only the last experiments

In the case of the instrumentation of the structure, the following notes can be made:

- The instrument B941 didn't record the Vertical component of the last part of the last experiment with scour $S = 0.7\text{m}$
- The instrument B941 didn't record the North-South and East-West components of the soil response in the first experimental series
- The instrument B940 didn't record the East-West component of the soil response
- The instrument B944 didn't record the North-South component of the soil response

9.8.6 Preliminary results

Output-only modal identification is performed using the ambient vibrations signals recorded by the accelerometers before inducing scour and for two different stages of scour ($s=0.3\text{m}$ and $s=0.7\text{m}$). The identification of the modal parameters is carried out using the Frequency Domain Decomposition (FFD) method proposed by Brincker et al. (2001).

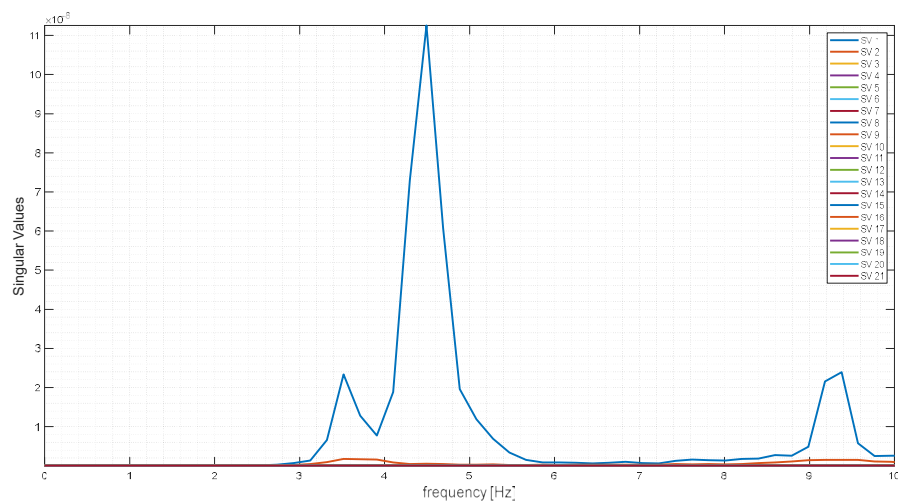


Figure 526: Singular values (SVs) of the PSD matrix of the response to ambient vibration in the case of no scour

Figure 526 illustrates the singular value of the power spectral density matrix of the response of the SSI system to the ambient vibration before inducing scour. It can be observed that the system response at the various frequencies is dominated by the first singular value, and that three peaks are visible. These corresponds to three vibration modes, which are illustrated in Figure 527 together with the corresponding modal vibration frequencies.

The first two vibration modes correspond to the vibration of the system along to orthogonal directions that are rotated with respect to the principal axes of the superstructure. The third mode is associated with the torsion of the superstructure about the vertical axis. Based on the plot of the first two vibration

modes, it is possible to infer that the base of the structure is not perfectly in contact with the soil, thus generating some asymmetries in the dynamic response of the system. Nevertheless, the frequencies of the first two modes of vibration (respectively 3.51 Hz and 4.5 Hz) are quite close to that of the first mode of vibration of the FE models, i.e., 4.1 Hz for both Model 1 and 2.

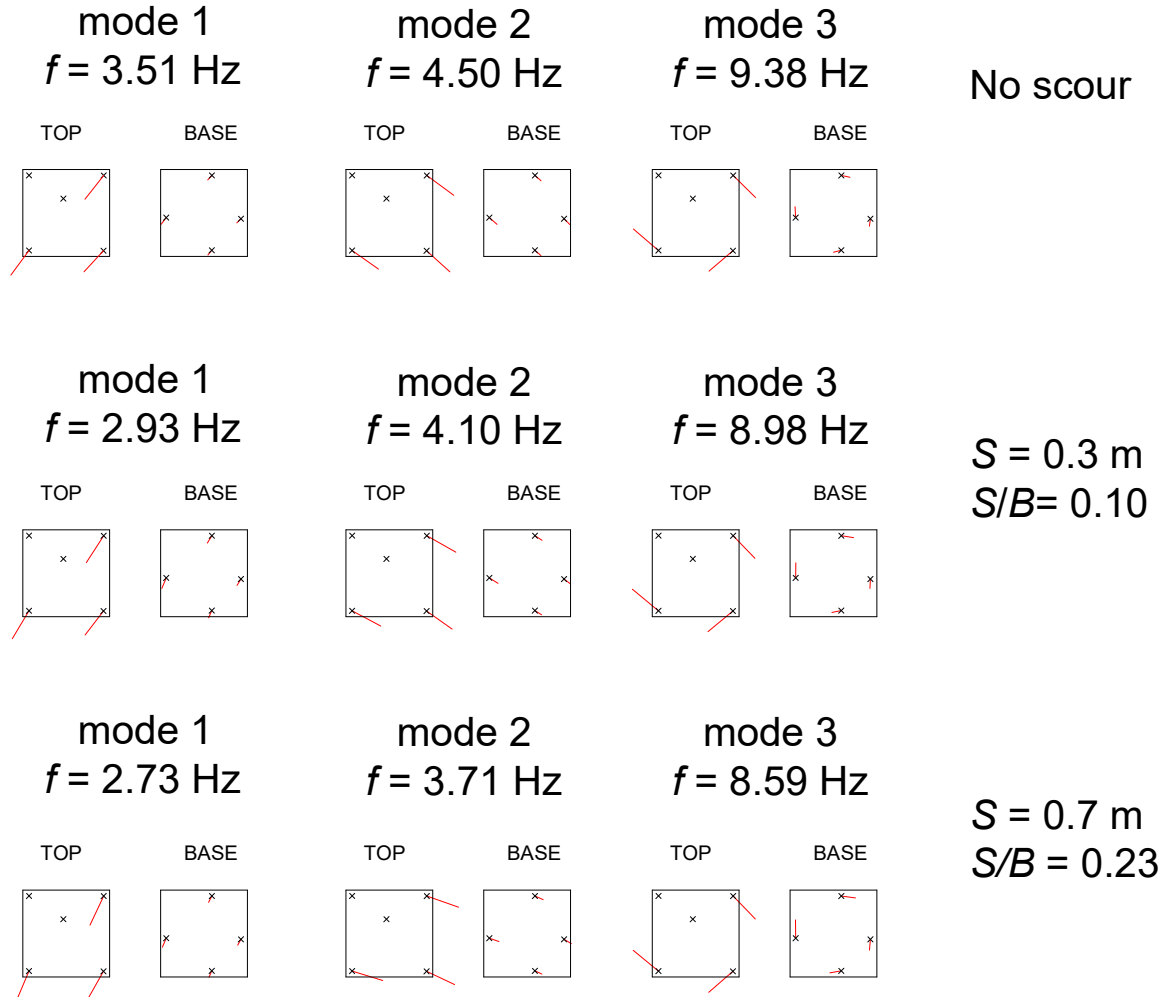


Figure 527: Experimental modal shapes for system with no scour, and scour widths $s=0.3$ m and $s=0.7$ m. Plan view of top and base horizontal displacements (scale factor of 2 for base displacements)

The FFD method is applied again by considering the ambient vibration recordings obtained after excavating the soil and inducing a scour width beneath the foundation of respectively $S=0.3$ m and $S=0.7$ m. The corresponding experimental modal shapes and vibration frequencies are illustrated in Figure 527. As expected, the vibration frequencies of the monitored modes reduce by increasing the scour width.

Figure 528 plots the variation of these frequencies vs. the scour width normalized by the foundation width (S/B). It can be observed that the variation of the frequencies with S/B has a linear trend for all the monitored vibration modes. Plotted in the same figure are the vibration frequencies of the fundamental mode of vibration of the numerical models. The results from the numerical models are in quite good agreement with those from the experimental test, despite the numerical model is characterized by two identical translation modes in the two directions while in the experiments the

translational modes are coupled due to possible asymmetries in the foundation support or in the connections between the braces and the frame.

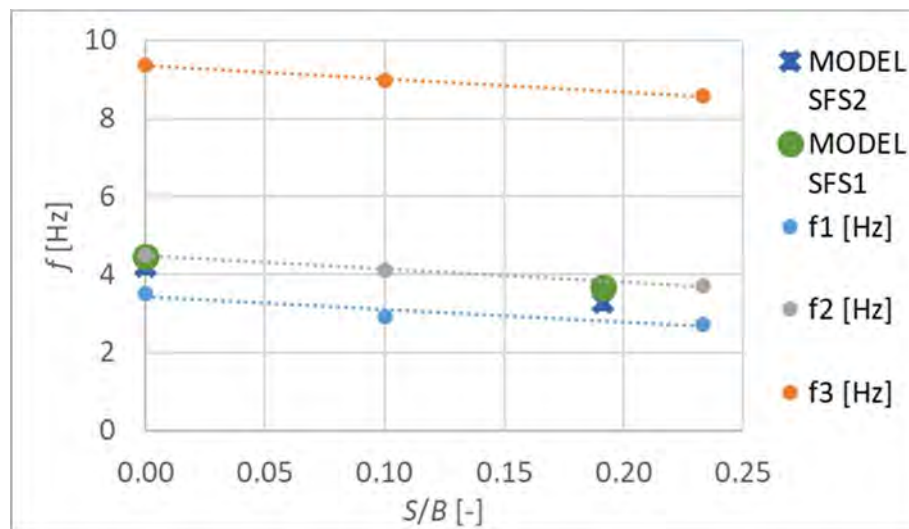


Figure 528: Variation of the vibration frequencies of the monitored modes with the normalized scour width S/B . Conclusions and outlook

This report has presented the results of an experimental and numerical campaign aimed at evaluating the influence of scour on the dynamic behaviour of a system with shallow foundation.

The experimental tests were performed on the EuroProteas system at Euroseistest and consisted of both free-vibration and force-vibration tests, carried out for the case of no scour and for different levels of scour. Regarding the instruments, a few of them failed to record the response or suffered from synchronization problems. Based on the recording of the accelerometers, seismometers and laser displacementmeters, it can be observed that scour results in a decrease of the frequency of vibration, an increase of the peak response, and a reduction of the damping ratio of the system. These effects are the effect of the increased flexibility of the system and the reduced capabilities of the system to dissipate energy through radiation in the soil.

With regard to the numerical study, two different modelling strategies have been calibrated and validated against the experimental ambient-vibration data obtained from tests carried out on the EuroProteas. One strategy simulates the interaction with the soil by means of a series of distributed springs and dampers, whereas the second one by including the soil domain in the FE model and using absorbing elements at the boundaries. In both these models the effects of scour are simulated by removing the elements representing the soil that is eroded. The comparison between the experimental and numerical vibration frequencies proves that both the approaches can provide accurate estimates of the effects of scour on the dynamic behaviour of the system. However, the causes in the asymmetry of the behaviour of the system, resulting in coupled modes in the two horizontal directions, remains to be investigated, even though it may be attributed to a non-uniform contact between the foundation and the soil.

An extended article is currently under preparation and will be submitted to a journal in the field (e.g. Soil Dynamics and Earthquake Engineering, Earthquake Engineering and Structural Dynamics, Bulletin of Earthquake Engineering) in order to disseminate the results of this report to a larger academic audience. Future studies will investigate the influence of scour on the kinematic and inertial interaction of bridges with scoured shallow foundations under seismic input, by considering more realistic soil

profile scenarios and bridge configurations. These results will be used to inform the design and assessment of bridges subjected to scour and earthquake hazards.

9.8.7 References

Abaqus V. 6.14 Documentation. Dassault Systemes Simulia Corporation; 2014.

Argyroudis SA, Mitoulis SA, Hofer L, Zanini MA, Tubaldi E, Frangopol DM (2020). Resilience assessment framework for critical infrastructure in a multi-hazard environment. *Science of the Total Environment*, 714, 136854.

Assessing scour risk on bridges. *Innovation & Research Focus Issue* 93, 2013.

Bao T., Swartz A.R., Vitton S., Sun Y., Zhang C., Liu Z. Critical insights for advanced bridge scour detection using the natural frequency. *Journal of Sound and Vibration* 2017; 386: 116-133.

Briaud, Jean-Louis, Stefan Hurlbaeus, Kuang-An Chang, Congpu Yao, Hrishikesh Sharma, Ok-Youn Yu, Colin Darby, Beatrice E. Hunt, and Gerald R. Price. "Realtime monitoring of bridge scour using remote monitoring technology." Report FHWA/TX-11/0-6060-1.

Brincker, R., Zhang, L., & Andersen, P. (2001). Modal identification of output-only systems using frequency domain decomposition. *Smart materials and structures*, 10(3), 441.

Capatti M.C., Tropeano G., Morici M., Carbonari S., Dezi F., Leoni G., Silvestri F. Implications of non-synchronous excitation induced by nonlinear site amplification and soil-structure interaction on the seismic response of multi-span bridges founded on piles. *Bulletin of Earthquake Engineering*, 2017; 15(11): 4963-4995.

Carbonari S., Dezi F., Leoni G. Seismic soil-structure interaction in multi-span bridges: Application to a railway bridge. *Earthquake Engineering and Structural Dynamics*, 2011; 40(11), 1219-1239.

Carbonari S., Morici M., Dezi F., Gara F., Leoni G. Soil-structure interaction effects in single bridge piers founded on inclined pile groups. *Soil Dynamics and Earthquake Engineering*, 2017; 92: 52-67.

Denton S., Tsionis G. The evolution of Eurocodes for bridge design. JRC Scientific and Technical Research Report, 2012.

Dezi F., Carbonari S., Tombari A., Leoni G. Soil-structure interaction in the seismic response of an isolated three span motorway overcrossing founded on piles. *Soil Dynamics and Earthquake Engineering*, 2012; 41;151-163.

European Committee for Standardization (ECS). Eurocode 8 – Design of structures for earthquake resistance; EN1998, Brussels; 2005.

Fioklou A., Alipour A. *Climate Change Impact on Highway Bridges: Flood-Induced Bridge Scour*. 17 (2017); 04559.

Foti S., Sabia D. Influence of foundation scour on the dynamic response of an existing bridge. *Journal of Bridge Engineering*, 2011; 16(2):295–304.

Gavin K., Prendergast L.J. Reliable performance indicators for bridge scour assessments. TU1406 COST Action Workshop Meeting, Barcelona, Spain. Available from https://www.researchgate.net/publication/327917282_Reliable_performance_indicators_for_bridge_scour_assessments

Gazetas G. Formulas and charts for impedances of surface and embedded foundations. *Journal of Geotechnical Engineering*, 117(9), 1991.

Guo, X. Seismic vulnerability analysis of scoured bridge systems. PhD Thesis, 2014, University of Missouri-Kansas City.

Imam, B. (2019). Climate Change Impact for Bridges Subjected to Scour and Corrosion. In *Climate Adaptation Engineering* (pp. 165-206). Butterworth-Heinemann.

Kuhlemeyer R.L., Lysmer J., Finite element method accuracy for wave propagation problems. *Journal of the Soil Dynamics Division*, 1973;99: 421-427.

Liang F., Zhang H., Huang M. Influence of flood-induced scour on dynamic impedances of pile groups considering the stress history of undrained soft clay. *Soil Dynamics and Earthquake Engineering*, 2017; 96, 76-88.

Manakou M.V., Raptakis D.G., Chavez-Garcia F.J., Apostolidis P.I., Pitilakis K.D. 3D soil structure of the Mygdonian basin for site response analysis. *Soil Dynamics and Earthquake Engineering*, 2010; 30: 1198-1211.

Maroni A., Tubaldi E., Zonta D., et al. Using Bayesian Networks for the assessment of underwater scour for road and railway bridges. *Proceedings of Structural Faults and Repair & 17th European Bridge Conference 2018*, 15th-17th of May. Edinburgh, UK: Engineering Technics Press.

Melville B.W., Coleman S.E. *Bridge scour*, Water Resources Publications, Highlands ranch, Colorado, USA; 2000, 550 pp.

Michalis P., Tarantino A., Tachtatzis C., Judd, M.D. Wireless monitoring of scour and re-deposited sediment evolution at bridge foundations based on soil electromagnetic properties. *Smart Materials and Structures*, 2015; 24(12).

Mylonakis G., Nikolaou S., Gazetas G. Footings under seismic loading: Analysis and design issues with emphasis on bridge foundations. *Soil Dynamics and Earthquake Engineering*, 2006; 824-853.

Pitilakis D., Lamprou D., Manakou M., Rovithis E., Anastasiadis A. System identification of soil-foundation-structure system by means of ambient noise records: the case of Europroteas model structure in Euroseistest. *Second European Conference on Earthquake Engineering and Seismology*, Istanbul, August 25-29 2014.

Pitilakis D., Rovithis E., Anastasiadis A., Vratsikidis A., Manakou M. Field evidence of SSI from full-scale structure testing. *Soil Dynamics and Earthquake Engineering*, 2018;112: 89-106.

Pitilakis D., Rovithis E., Massimino M.R., Gatto M.P.A. Numerical simulation of large scale soil-foundation-structure interaction experiments in the EuroProteas Facility, 6th International Conference on Earthquake Geotechnical Engineering, 1-4 November 2015, Christchurch, New Zealand.

Pitilakis K., Raptakis D., Lontzetidis K., Tika-Vasillikou T., Jongmans D. Geotechnical and geophysical description of EUROSEISTEST, using field, laboratory tests and moderate strong motion records. *Journal of Earthquake Engineering*, 1999; 3(3): 381-409.

Pizarro A., Manfreda S., Tubaldi E. The science behind scour at bridge foundations: a review." *Water* 2020; 12(20): 374.

Prendergast, L. J., & Gavin, K. (2014). A review of bridge scour monitoring techniques. *Journal of Rock Mechanics and Geotechnical Engineering*, 2014; 6(2): 138-149.

Prendergast, Luke J., David Hester, Kenneth Gavin, and J. J. O'Sullivan. "An investigation of the changes in the natural frequency of a pile affected by scour." *Journal of Sound and Vibration*, 2013; 332,25: 6685-6702.

Ragni L., Scozzese F., Tubaldi E., Gara F. Dynamic properties of a masonry arch bridge subjected to local scour. *2nd International Conference on Natural Hazards & Infrastructure ICONHIC 2019*, June 23 – 26 2019, Chania, Greece.

Raptakis D., Anastasiadis A. & Pitilakis K. (1998). Preliminary instrumental and theoretical approach of site effects in Thessaloniki. In *Proceedings of the 11th European Conference on Earthquake Engineering*.

Raptakis D., Chávez-García F., Makra K., Pitilakis K. Site effects at EuroSeistest-I. Determination of the valley structure and confrontation of observations with 1D analysis. *Soil Dynamics and Earthquake Engineering*, 2000;19(1): 1-22.

Tileylioglu S., Stewart J.P., Nigbor R.L. Dynamic stiffness and damping of a shallow foundation from forced vibration of a field test structure. *Journal of Geotechnical and Geoenvironmental Engineering*, 2010; 137(4), 344-353.

Tubaldi E., Macorini L., Izzuddin B.A. Three-dimensional mesoscale modelling of multi-span masonry arch bridges subjected to scour. *Engineering Structures* 165 (2018): 486-500.

Tubaldi E., Macorini L., Izzuddin B.A., Manes C., Laio F. A framework for probabilistic assessment of clear-water scour around bridge piers. *Structural safety* 69 (2017): 11-22.

Yilmaz, T., Banerjee, S., & Johnson, P. A. Performance of two real-life California bridges under regional natural hazards. *Journal of Bridge Engineering*, 2016; 21(3).

Yuan V., Argyroudis S., Tubaldi E., Pregolato M., Mitoulis S. Fragility of bridges exposed to multiple hazards and impact on transport network resilience. SECED2019 Earthquake risk and engineering towards a resilient world, Greenwich– September 9-10, 2019.

Zhang H., Chen S., Liang F. Effects of scour-hole dimensions and soil stress history on the behavior of laterally loaded piles in soft clay under scour conditions. *Computers and Geotechnics*, 2017; 84; 198-209.

9.9 Project # 40 – SOil Frame-Interaction Analysis through large-scale tests and advanced numerical finite element modeling (Acronym: SOFIA)

Authors

M.R. Massimino⁽¹⁾, S. Grasso⁽¹⁾, G. Abate⁽¹⁾, S. Corsico⁽¹⁾, A. Vratsikidis⁽²⁾, A. Anastasiadis⁽²⁾, D. Pitilakis⁽²⁾

⁽¹⁾ *University of Catania, Catania, Italy*

⁽²⁾ *Aristotle University of Thessaloniki, Thessaloniki, Greece*

9.9.1 Introduction

The Project SOFIA was devoted to studying full-coupled large-scale soil-structure systems including new isolating materials (GRM mixtures), investigated by full-scale experimental tests on the existing EUROPROTEAS structure in the EUROSEISTEST site, to be subsequently modelled by advanced numerical FEM codes. The main goals have been: investigating the material and radiation damping of the wavefield emanating from the foundation; studying the wave propagation away from the structure; investigating the influence of rubberized foundation soil on the response of the structure; validating advanced FEM modelling of DSSI (dynamic soil-structure interaction).

As for field and laboratory studies, DSSI phenomena are commonly studied in small-scale by 1-g or N-g shaking-table tests (Pitilakis et al., 2010; Abate et al., 2010; Abate & Massimino, 2016; Massimino et al.,

2019a). Laboratory studies are particularly precious for the known initial and boundary conditions, and a large number of applied instrumentations. However, very often they show some disadvantages, such as certain limitations in reproducing actual field conditions (unbounded subsoil medium, radiation condition to infinity and realistic stress fields in the soil). On the other hand, large-scale field experiments account for realistic boundary conditions and fulfil the radiation condition to infinity; but up to now, very few large-scale experiments have been performed, such as that at EUROSEISTEST [Pitilakis et al., 1999; 2013; 2014; Abate et al., 2017].

Among numerical approaches, finite element (FE) modelling is nowadays widely performed. FE modelling allows a realistic evaluation of coupled soil-foundation-superstructure system, in terms of initial and boundary conditions, soil profile, geometry, nonlinearity of soil and/or soil-foundation interface, even if, nowadays, fully-coupled analyses are still very rare, above all concerning the interface modelling (De Barros & Luco, 1995; Massimino et al, 2018; Massimino et al., 2019b).

However, FEM modelling, combined with field and laboratory tests, is the most useful tools for investigating the complexity of DSSI (Combescuré & Chaudat, 2000; Paolucci et al., 2000; Massimino & Maugeri, 2013; Biondi et al., 2003; 2015; Ueng et al., 2006; Abate et al., 2007; 2008a, 2008b; 2017; Ugalde et al., 2007; Anastasopoulos et al., 2013; Pitilakis et al., 2015).

The pressing environmental need for recycling waste automobile tires led to reuse these materials. In the last two decades, many geotechnical projects have been devoted to recycling rubber poor or mixed with granular soils (SRM = sand-rubber mixtures; GRM = gravel-rubber mixtures) in an innovative manner. The mixtures of granular soils with granulated rubber display satisfactory natural and mechanical properties (low specific weight, high strength, high flexibility and high level of permeability). Primary geotechnical field applications include backfilling in embankments, road constructions and retaining walls structures (Zhang et al., 2018; Khatami et al., 2020). Feasibility studies on the capability of rubberized soils for vibration isolation against earthquake have also been carried out (Tsang et al., 2009; Senetakis et al., 2015; Argyroudis et al., 2016). Vibration is isolated mainly by the high damping ratio and energy-absorbing attributes of the rubber inclusions. For these reasons, these mixtures can represent a very useful isolation systems for buildings.

So, the impact of the results of the SOFIA Project, dealing with new large-scale tests on fully-coupled systems with different GRM, can be remarkable both on current and future research and on practice.

9.9.2 EUROPROTEAS

Structure

EuroProteas prototype structure was particularly designed to mobilize strong interaction with its foundation soil as it is a stiff structure with a large superstructure mass founded on soft foundation soil.

EuroProteas is a perfectly symmetric and reconfigurable structure. It is founded on a square reinforced concrete slab (C20/25) with dimensions 3.0m x 3.0m x 0.4m which rests on the ground surface. The superstructure mass consists of two identical to the foundation reinforced concrete slabs that are supported by four square hollow steel columns (QHS 150 x 150 x 10mm) which are clamped on the foundation. L-shaped (100 x100 x 10mm) X-braces are connecting the steel columns in all the sides of the structure ensuring its total symmetry. Assuming a uniform unit weight of 25kN/m³ for the concrete, the total mass of each slab is estimated at 9.16Mg, while the total mass of the structure is calculated approximately at 28.5Mg. Its outer dimensions are 3.0m x 3.0m x 5.0m (Figure 529).

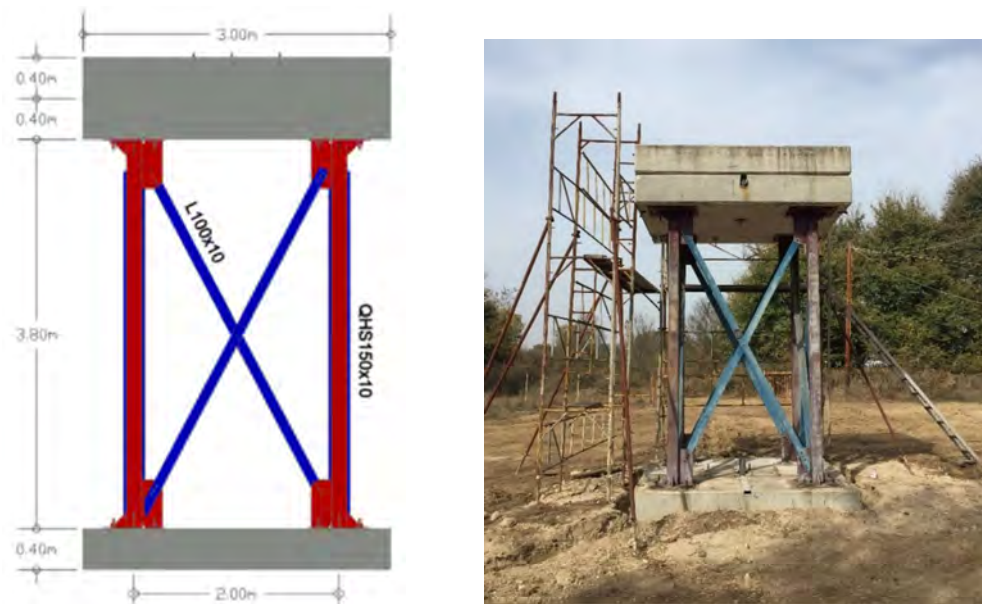


Figure 529: A 2D sketch and a view of EUROPROTEAS prototype structure

The bracing system and the upper roof slab of the structure are removable allowing the modification of the mass and/or the stiffness. Depending on the number of the roof slabs and the arrangement of the X-bracing system the fixed-base frequency of EuroProteas covers a range between 1.78Hz and 13.06Hz as calculated numerically (Pitilakis et al. 2018).

Foundation Soil

The foundation soil is well investigated and reported in earlier studies. Specifically, between 1993 and 2004, an extensive program of seismic prospecting and geotechnical testing was undertaken (Pitilakis et al. 1999). It comprised of in-situ (sampling boreholes, Standard and Cone Penetration Test measurements) and laboratory (conventional classification tests, strength tests, consolidation tests and resonant column and cyclic triaxial tests) geotechnical surveys. The elaboration of all geophysical and geotechnical data, led to the classification of the main soil formations, validation of soil properties stemming from different methodologies and design of representative 1D, 2D and 3D soil models.

Additional field investigation of the test site was undertaken prior to the construction of the structure in the framework of the European project "Seismic Engineering Research Infrastructures for European Synergies, SERIES" including Standard Penetration Test measurements, downhole tests, sampling according to EC7 regulations, resonant column and cyclic triaxial tests. The small stiffness of the top soil layer is pronounced by the low recorded NSPT values down to a depth equal to two times the foundation width. Close to the soil surface the shear wave velocity is estimated approximately at 100m/s (Figure 530). A detailed report on the geotechnical and geophysical data derived from this investigation is presented in Pitilakis et al. (2018).

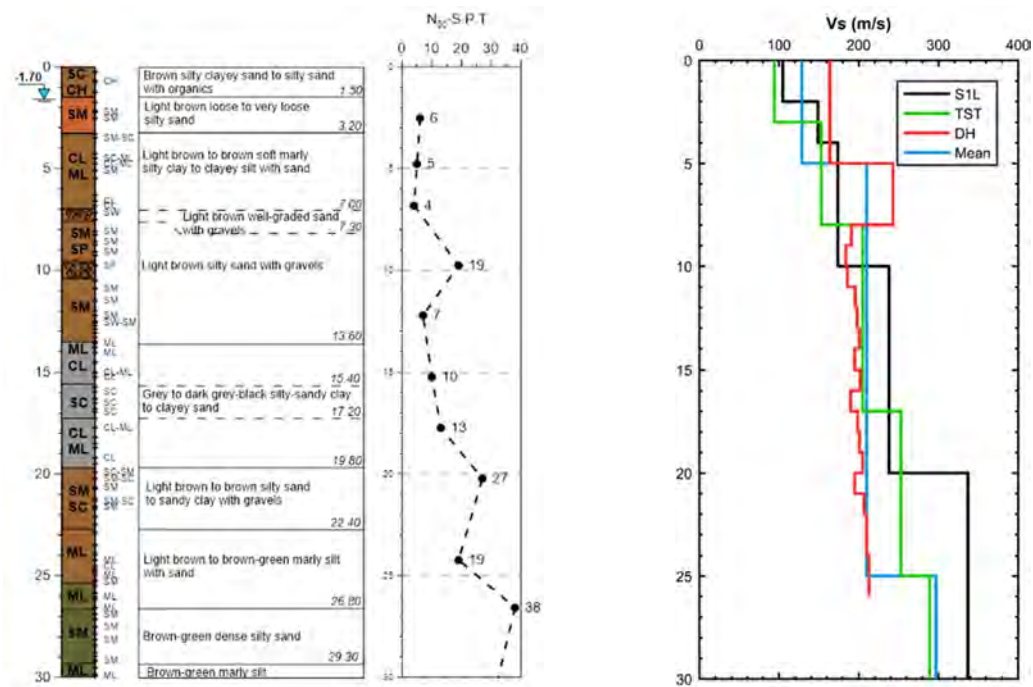


Figure 530: Soil stratigraphy of the 30m deep borehole at the geometrical center of the foundation, the N_{SPT} blow counts and the Vs profile as derived from down-hole (DH) tests prior to the construction of EuroProteas (Pitilakis et al. 2018) compared with the Vs profile at S1L site approximately 50m south of EuroProteas (Raptakis et al. 1998), a reference mean Vs model of the valley cross-section (Raptakis et al. 2000) and the proposed Vs profile by Pitilakis et al. (1999)

Gravel-Rubber Mixtures (GRM)

The foundation soil was replaced with three different rubber-gravel mixtures (RGM) backfills in order to investigate the response of the soil-structure system under the effects of different rubber content per mixture weight and to determine the optimum rubber content.

A preliminary study was conducted for the definition of the major properties of the RGM mixtures used as foundation soil improvement. We tested 3 configurations of RGM having rubber content 0%, 10% and 30% by mixture weight, as shown in Table 90.

Foundation ID	Rubber by mixture weight (%)	$D_{50,r}/D_{50,s}$	γ_d (kN/m ³)
G/R 100/0	0	-	16.2
G/R 90/10	10	0.18	15.2
G/R 70/30	30		11.8

Table 90: Foundation soil types used in the experiments

Three soil pits having dimensions 3.2 x 3.2 x 0.5m were excavated. The first soil pit was filled only with gravel having mean grain size $D_{50}=17.187$ mm to serve as a benchmark foundation type. The other two pits were filled with RGM of different rubber content by mixture weight.

9.9.3 Numerical model

The performed forced-vibration tests were simulated by 2D finite element models through the ADINA code. In particular, different FEM models were developed, considering the different configurations of the soil foundation: the first model (Figure 531) concerned the configuration of the system tested in April, that consisted in the structure resting on the effective in-situ soil; the second model simulated the configuration of the system tested on October in which the foundation soil was replaced just by gravel (G/R 100/0) for a volume equal to $3.20 \times 3.20 \times 0.50$ m; the third and the fourth model simulated the configurations of the system tested in the next days, in which the foundation soil was replaced for the same volume previously considered by the two adopted GRMs G/R 90/10 and G/R 70/10, characterized by different percentages per unit weight of gravel and rubber, 90% gravel and 10% rubber and 70% gravel and 30% rubber respectively.

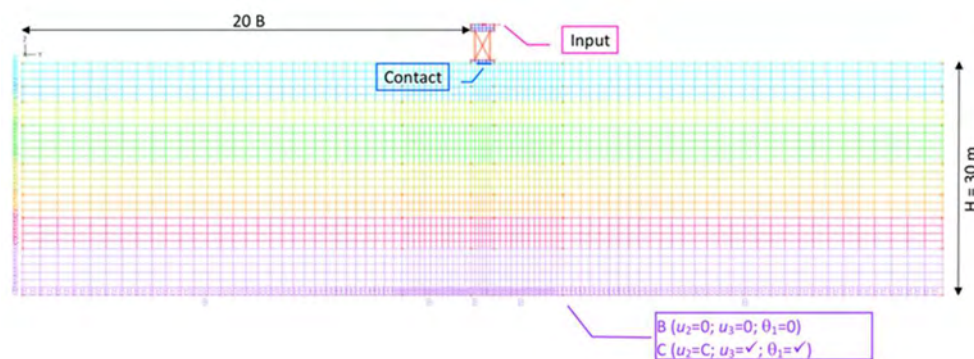


Figure 531: First FEM model, showing geometry, loading and boundary conditions

The horizontal bottom boundary was fixed 30.00 m down from the structure and the two lateral boundaries were chosen considering a distance equal to $20B$ from the structure, where $B = 3$ m is the dimension of the foundation slab, to minimize as much as possible boundary effects.

Two loading conditions were applied: i) a “mass proportional” load was applied to the whole system, to take into account the unit weight of the soil, the concrete and the steel elements; ii) the acceleration time-history recorded by the 102650N accelerometer has been applied in the loading direction at the roof to simulate the applied excitation.

The soil, the foundation slab and the roof slabs were modelled using 9-node 2D solid elements, the steel columns and the X-braces were modelled using 2-node Hermitian beam elements. As for the first FEM model, the soil was modelled using the data by in-situ tests and RCT tests previously performed (Abate et al., 2017). As for the other FEM models, the GRMs were modelled according to the recent laboratory tests (see Table 90).

The structure was modelled using a linear visco-elastic constitutive model. In order to take into account the soil non-linearity, an equivalent linear visco-elastic constitutive model was adopted, updating the shear modulus G and the damping ratio D . Finally, in line with the Rayleigh damping approach, the damping matrix was assumed proportional to the mass and stiffness matrices.

The response of the above-described system has been analysed in the time and frequency domains to detect the main aspects of SSI, considering the following quantities: maxima accelerations as well as acceleration time-histories concerning the structure and the soil; Fourier spectra and amplification functions in the structure and the soil surface; acceleration amplification ratios from the top to the base of the structure, through the soil-foundation interface and along the ground surface.

9.9.4 Test setup

Instrumentation

Two instrumentation schemes were designed, the first concerning the experiments performed in April 2019, in which EUROPROTEAS was founded on the natural soil, and the second for the experiments performed in October 2019 when the foundation soil was replaced by the GRM described in Table 90. The instrumentation schemes were designed particularly to capture the response of the structure and the foundation in both in-plane and out-of-plane direction as well as the soil surface response in the same directions and below the foundation. The instruments used in both the experimental series are:

- 6 triaxial accelerometers ETNA2 (Kinematics)
- 4 triaxial accelerometers CMG-5TCD (Guralp)
- 5 triaxial accelerometers CMG-5TD (Guralp)
- 10 digital broadband seismometers CMG-40T (Guralp)
- 5 digital broadband seismometers CMG-6TD (Guralp)
- 1 3m long shape acceleration array (SAAR) (Measurand)

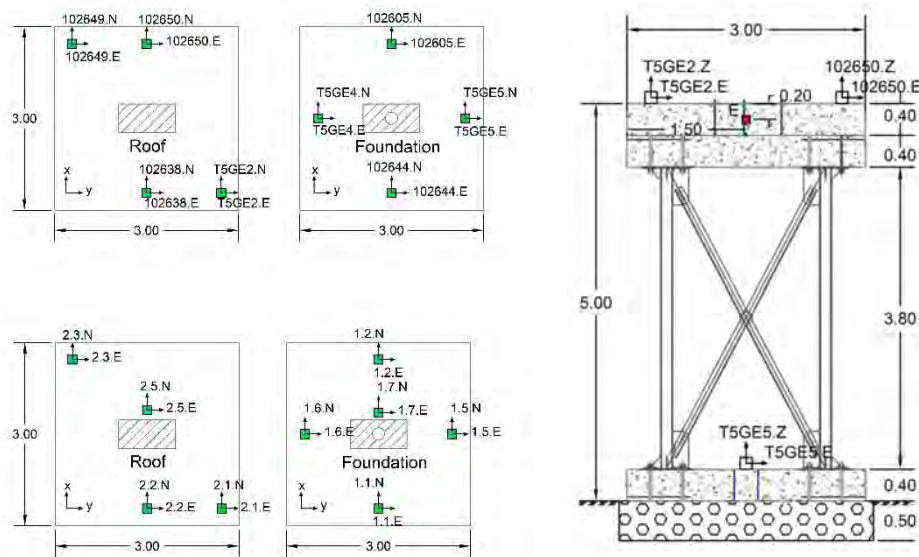


Figure 532: Plan view of the instrumentation layout of the roof and the foundation during the experiments performed on the natural soil (bottom left) and after replacing it with GRM (upper left) and cross-section of the structure and the GRM foundation

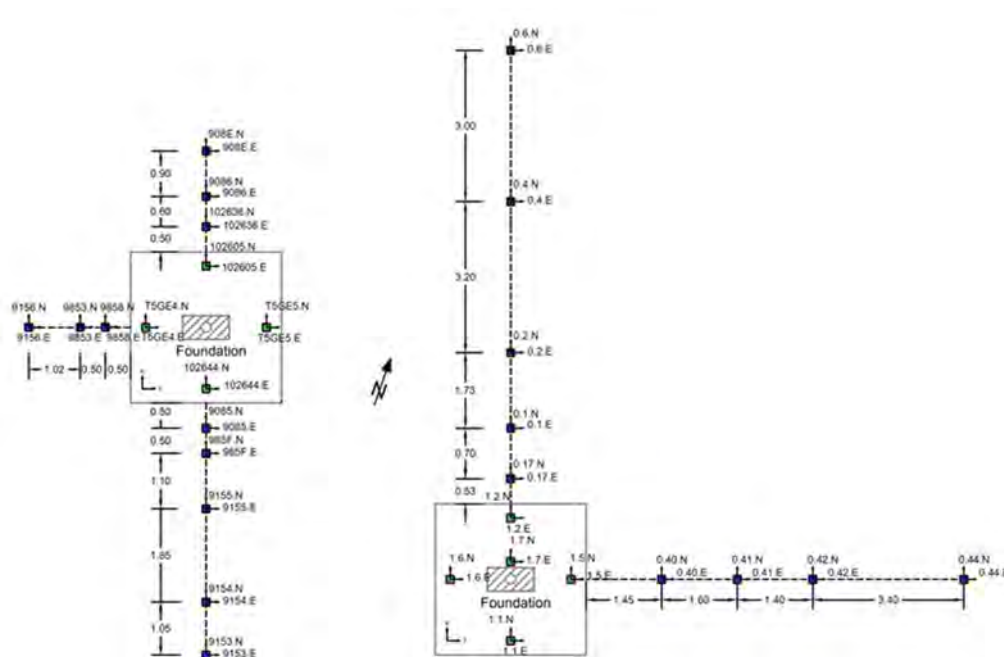


Figure 533: Plan view of the instrumentation layout of the foundation and the soil surface during the experiments performed on the natural soil (right) and after replacing it with GRM (left)

Forced-Vibration tests

The eccentric mass shaker MK-500U owned by the Institute of Engineering Seismology and Earthquake Engineering (ITSAK) was implemented as a source of harmonic excitation. It is a portable uniaxial dual counter-rotating shaker that can produce a maximum force amplitude of 5 tons in a frequency range between 0.1-20Hz. Eight mass plates in four different sizes (A, B, C and D) can be used in pairs to adjust the eccentricity of the shaker and hence the output force. The amplitude of the output force of the shaker is given by the equation

$$F = E(2\pi f)^2 \quad (23)$$

where F is the shaker output force in Newtons, E is the total eccentricity of the shaker in kg-m and f is the rotational speed of the shaker in Hz.

The eccentric mass shaker was placed at the geometrical centre of the top roof slab of the structure and it was orientated to produce a force having a direction that formed an angle of 30 degrees with the magnetic North.

Free-Vibration tests

Pull-out forces were applied on the roof of the structure by a wire rope. A load cell, with which the applied tension force was measured, was attached to the roof slab and to the one end of the rope. The other end of the wire rope was attached to a wire rope pulling hoist having a working load limit of 32kN, clumped to a buried counterweight of 3 tons. The total length of the wire rope was 21m.

9.9.5 Observation during testing

The forced-vibration tests were characterized by different values of eccentricities and corresponding different frequency ranges, but just the tests performed by eccentricity equal to 6.93 kg-m, considering three masses, were focused in this report.

Figure 534a shows the placement of the instruments during testing in April, Figure 534b and Figure 534c show, respectively, the placement of the GRM mixture and of the frame during testing in October.

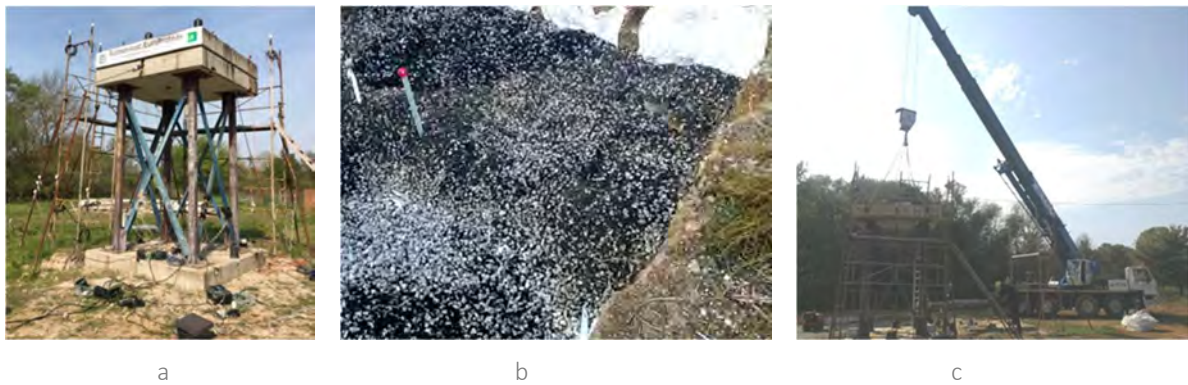
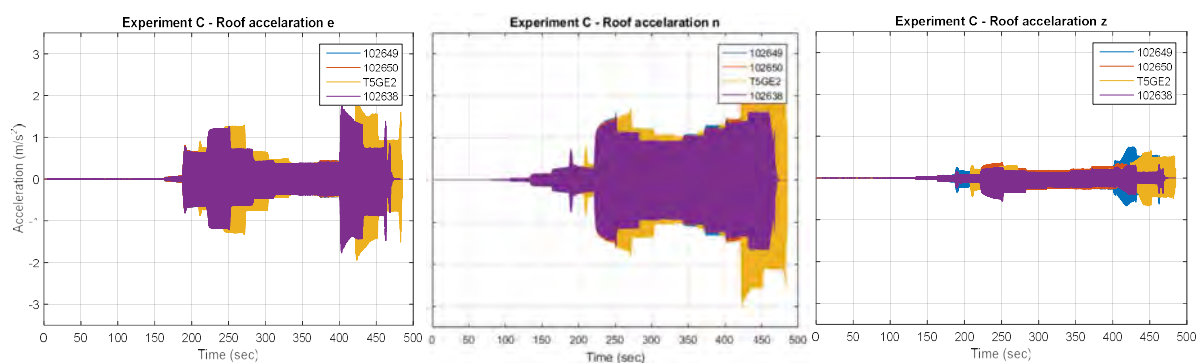


Figure 534: (a) Placement of the instruments during testing in April 2019; (b) GRM mixture and (c) placement of the frame during testing in October 2019

During the three groups of performed tests, acceleration time-histories concerning the response of the structure as well as velocity time-histories concerning the response of the soil, were recorded; they allowed us to evaluate the wave propagation along the structure – from the roof to the foundation, and along the soil surface, considering the three spatial directions, “E” and “N” horizontal directions and “Z” vertical directions. In particular, Figure 535, Figure 537 and Figure 539 show the comparison among the accelerations recorded on the structure; Figure 536, Figure 538 and Figure 540 show the comparison among the velocities recorded on the soil surface. These figures show the response of the system for the entire duration of the tests, in the frequency range 1-10 Hz.



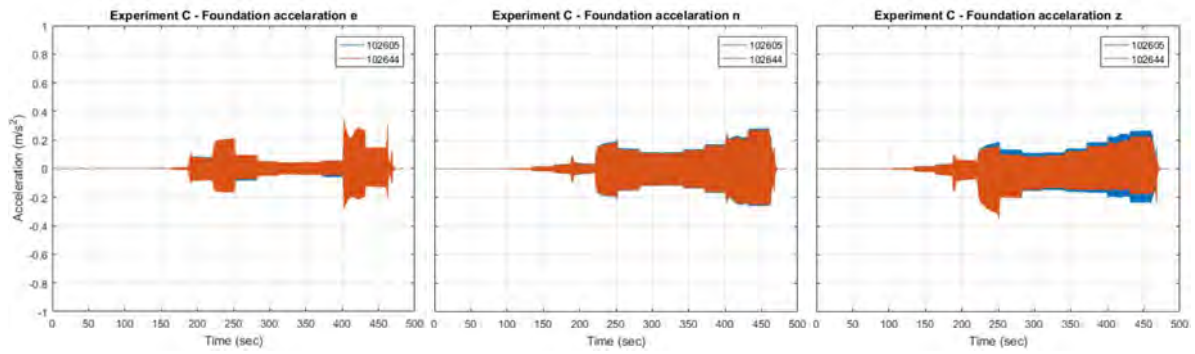


Figure 535: Comparison among acceleration recorded on the roof (upper row) and on the foundation (lower row) for Experiment C for the entire frequency range, in which the soil foundation was replaced by gravel (G/R 100/0)

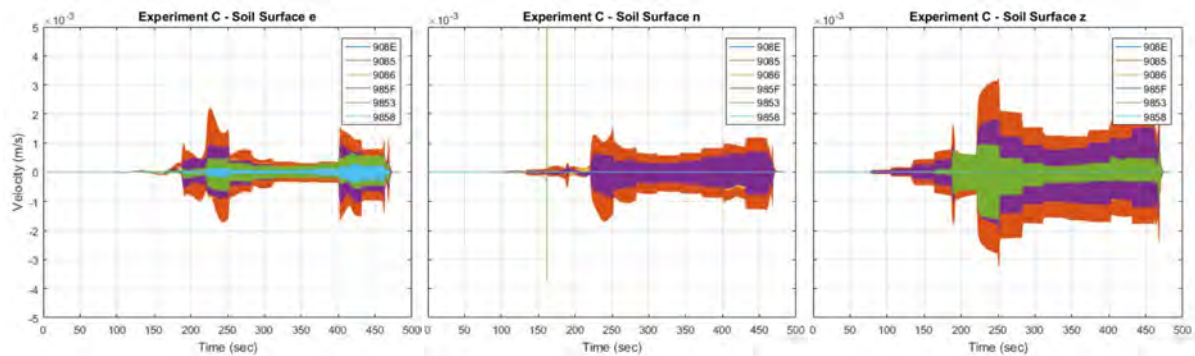


Figure 536: Comparison among velocities recorded on soil surface along for Experiment C for the entire frequency range, in which the soil foundation was replaced by gravel (G/R 100/0)

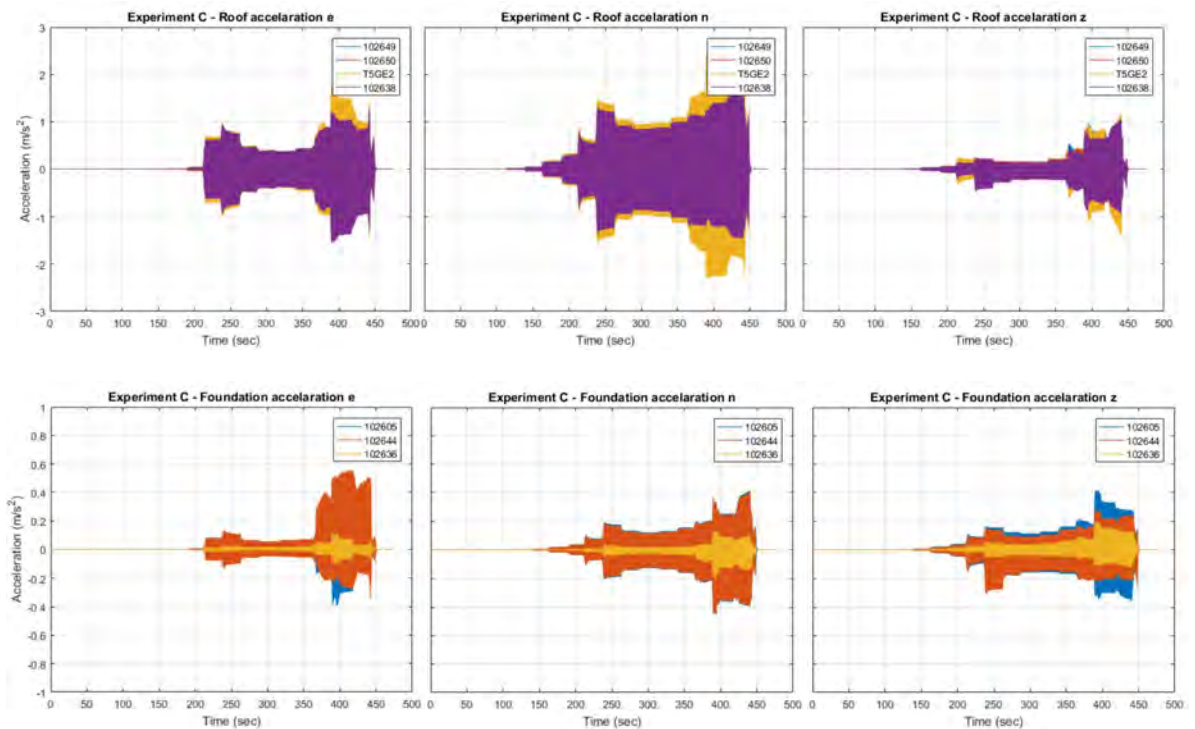


Figure 537: Comparison among acceleration recorded on the roof (upper row) and on the foundation (lower row) for Experiment C for the entire frequency range, in which the soil foundation was replaced by GRM G/R 90/10

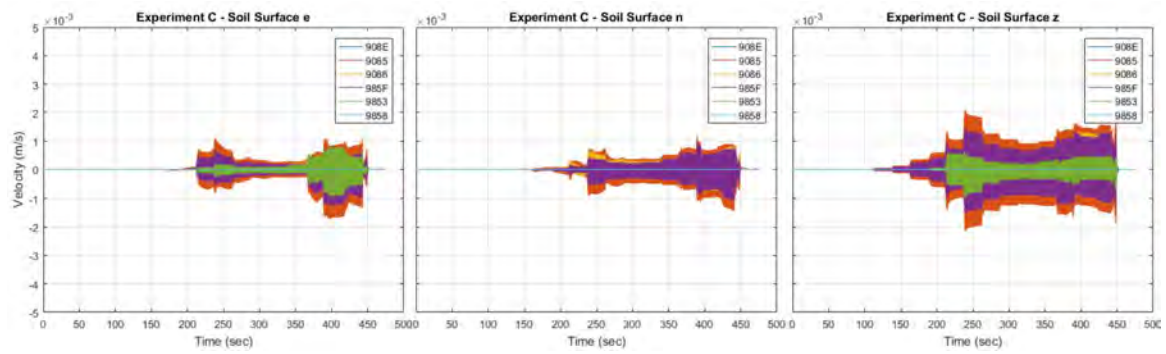


Figure 538: Comparison among velocities recorded on soil surface along for Experiment C for the entire frequency range, in which the soil foundation was replaced by GRM G/R 90/10

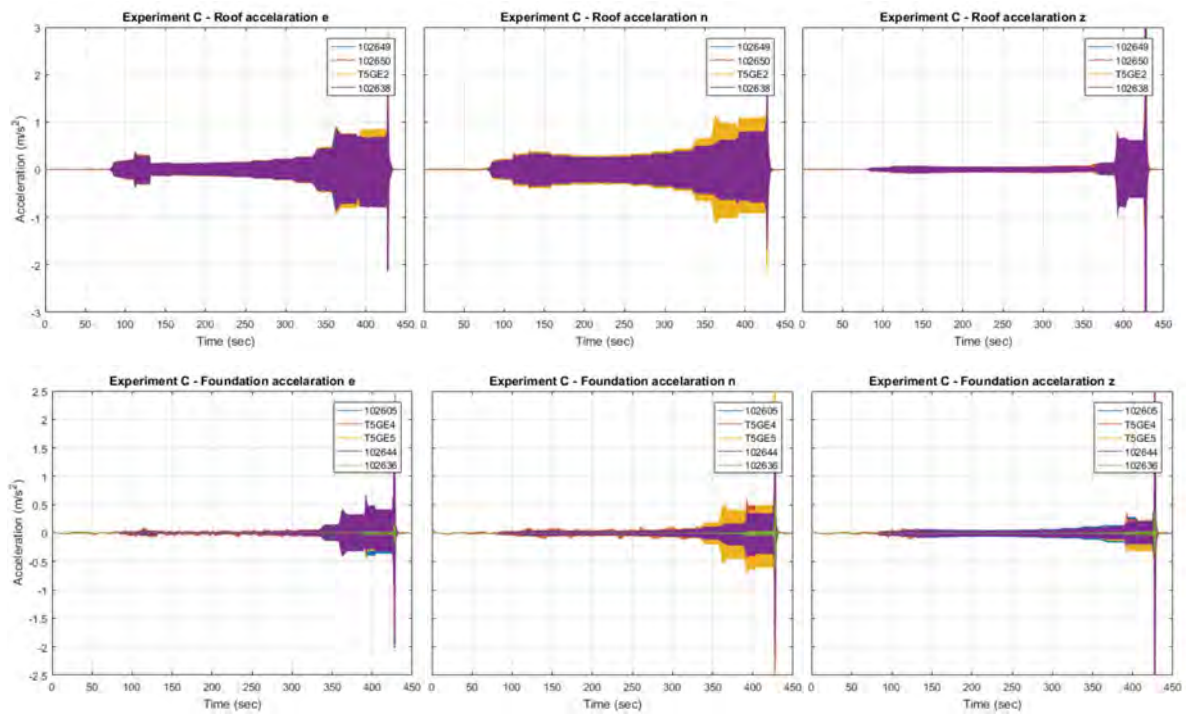


Figure 539: Comparison among acceleration recorded on the roof (upper row) and on the foundation (lower row) for Experiment C for the entire frequency range, in which the soil foundation was replaced by GRM G/R 70/30

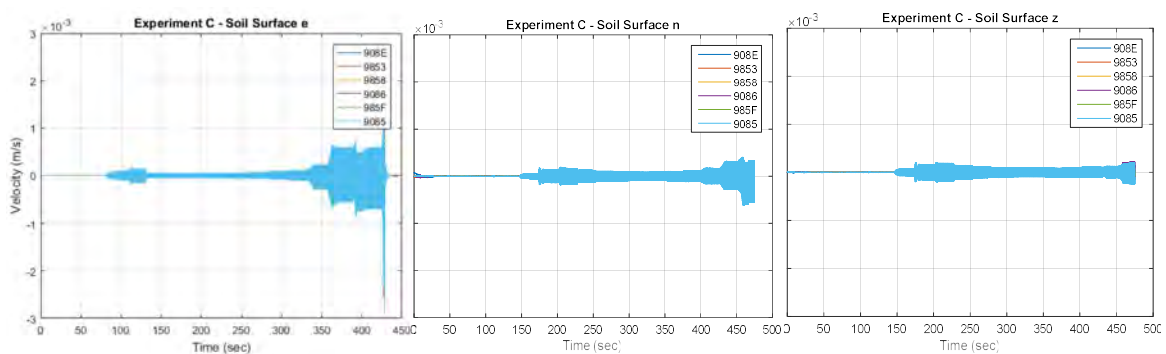


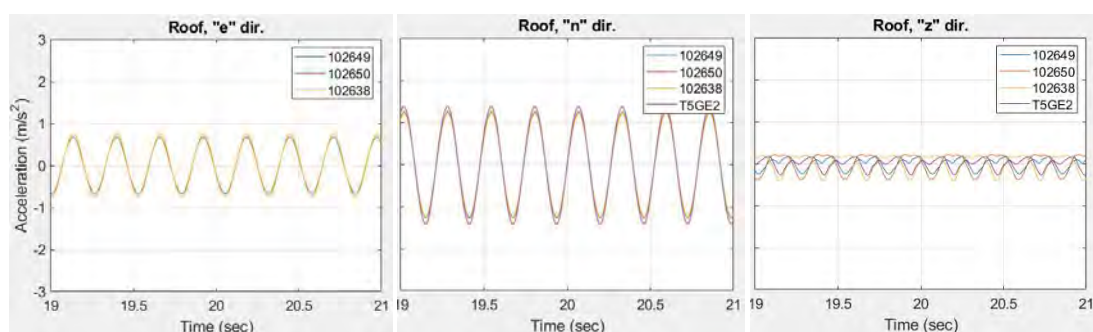
Figure 540: Comparison among velocities recorded on soil surface along for Experiment C for the entire frequency range, in which the soil foundation was replaced by GRM G/R 70/30

In these figures it is possible to observe a significant increase of the amplitude of the recorded quantities approaching the input characterized by the frequency close to the natural frequency of the system. This phenomenon was observed for the structure resting on the gravel at the time ranges equal to about 230-260 s and 400-430 s, to which the input frequencies equal to about 4.5 Hz and 9 Hz correspond. For the G/R 90/10 similar considerations can be made. For the G/R 70/30 it was observed that the critical input frequencies were equal to about 2.5 and 5 Hz. When the input frequency approached the first natural frequency of the system, the oscillation of the structure was visible to naked eye.

9.9.6 Results

On the basis of the observations on the recordings, the attention was devoted to the frequency $f = 4.5$ Hz, that is close to the system frequency, in a significant time window $\Delta t = 2$ s, between 19 s and 21 s for the single recording corresponding to the range 257-259 s for the entire recording.

Figure 541 and Figure 542 refer to the tests performed on the system resting on the G/R 90/10. In particular, they show the response of structure (Figure 541) and of the soil surface (Figure 542) in terms of accelerations. The velocities recorded by the seismometers located on the soil surface were appropriately derived in order to facilitate the comparisons. Considering the response of the roof, Figure 541 shows that the largest amplitudes of the accelerations are found in the N-direction, that is the direction of the application of the input, instead the accelerations recorded in Z-direction are the lowest. The Z-accelerations recorded in the two diametrically opposite positions (102650 and 102638, red line and yellow one respectively) differ in phase, due to a torsion occurred during the tests. This behaviour may be observed also in foundation, in fact also the Z-accelerations recorded in the two diametrically opposite positions (102605 and 102644, blue line and red one respectively) differ in phase. Considering the response of the foundation, Figure 541 shows that the amplitudes of the accelerations are lower than the accelerations recorded at the roof, so we can affirm that the signal suffers a deamplification of one order of magnitude, from values of about 1.0 m/s^2 to values of about 0.1 m/s^2 . As for the response of the soil surface (Figure 542), the signal suffers a further significant deamplification moving away from the foundation, as it can be observed from the seismometer 102636 (at a distance of 0.50 m from the foundation) to the seismometer 908E (at a distance of 2.00 m from the foundation) in S-N direction (violet line and blue one, respectively), as well as from the seismometer 9085 (at a distance of 0.50 m from the foundation) to the seismometer 985F (at a distance of 1.00 m from the foundation) in N-S direction (red line and yellow one, respectively). The difference in phase is visible also at the soil surface between the Z-accelerations recorded by 9085 and 985F at the South side (red line and yellow one, respectively), and the accelerations recorded by 102636 and 908E at the North side (violet line and blue one, respectively).



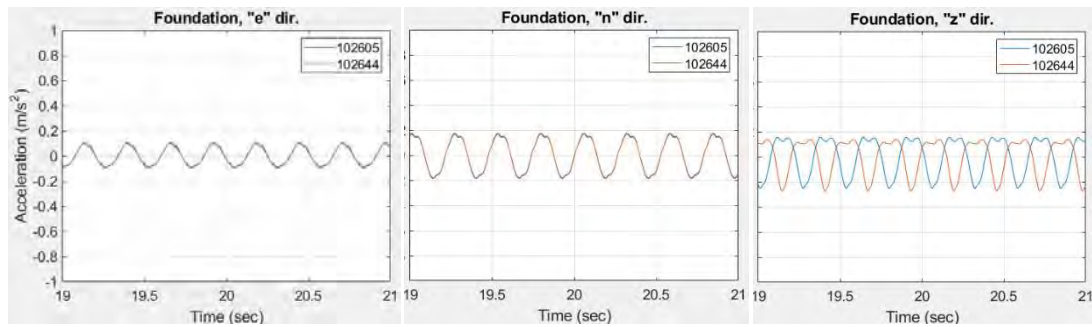


Figure 541: Comparison among acceleration recorded on the roof (upper row) and on the foundation (lower row) for Experiment C for $f = 4.5$ Hz, in which the soil foundation was replaced by GRM G/R 90/10

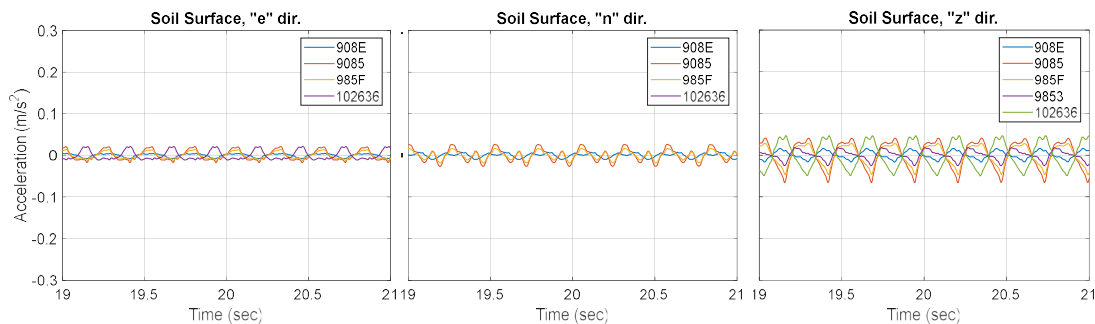


Figure 542: Comparison among accelerations recorded on soil surface along for Experiment C for $f = 4.5$ Hz, in which the soil foundation was replaced by GRM G/R 90/10

A further comparison regards the wave propagation from the roof of the structure to the foundation and from it to the soil surface considering the two S-N and N-S directions (Figure 543), referring to the same previous tests. So, Figure 544 shows the acceleration time-histories recorded by the accelerometer 102650 on the roof, by the accelerometer 102605 on the foundation and finally by the seismometers 102636 and 908E located on the soil surface at a distance from the structure equal to 0.50 m and 2.0 m respectively (these instruments are placed in S-N direction, see Figure 543). Similarly, Figure 545 shows the acceleration time-histories recorded by the accelerometer 102638 on the roof, by the accelerometer 102644 on the foundation and finally by the seismometers 9085 and 985F located on the soil surface at a distance from the structure equal to 0.50 m and 1.0 m respectively (these instruments are placed in N-S direction, see Figure 543).

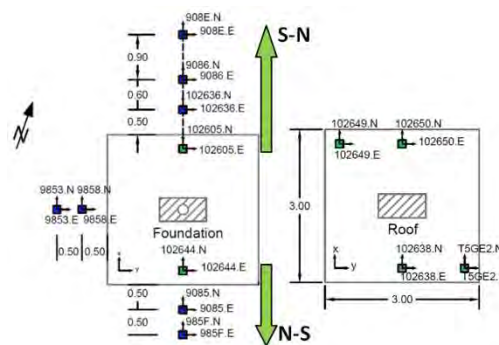


Figure 543: : Instrumentation layout: analysis of the wave propagation from the roof to the foundation and from it to the soil surface in S-N (12650-102605-102636,908E) and N-S (102638-102644-9085,985F) directions

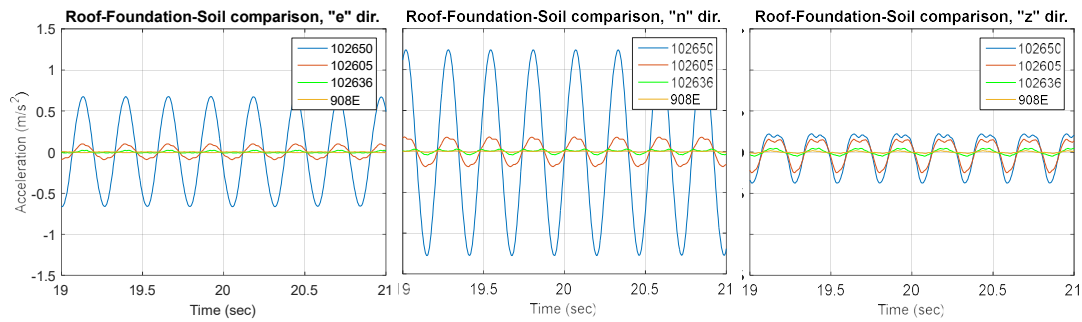


Figure 544: Comparison among acceleration recorded on the roof, on the foundation and on the soil surface, in S-N direction, for Experiment C for $f = 4.5$ Hz, in which the soil foundation was replaced by GRM G/R 90/10

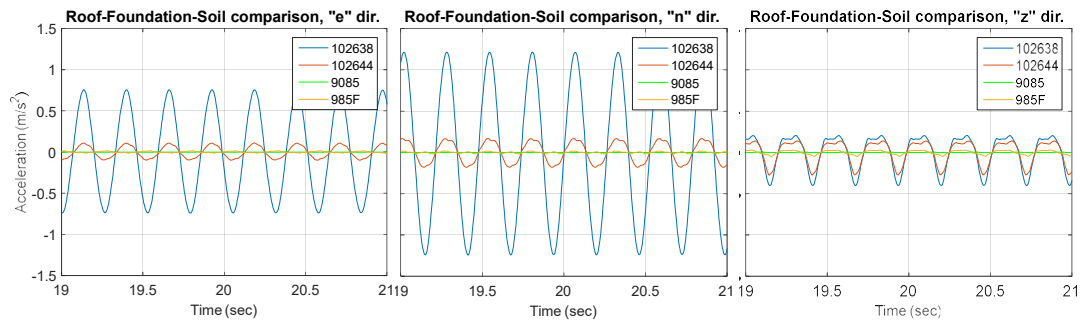


Figure 545: Comparison among acceleration recorded on the roof, on the foundation and on the soil surface, in N-S direction, for Experiment C for $f = 4.5$ Hz, in which the soil foundation was replaced by GRM G/R 90/10

Both the figures show more clearly the important deamplification of the signal from the roof to the soil surface. The amplitudes of the acceleration decrease from a peak of about 1.2 m/s^2 recorded, in n-direction, by the accelerometers 102650 and 102638 located at the roof, to a peak of 0.2 m/s^2 recorded by the accelerometers 102605 and 102644 located at the foundation (blue lines and red lines, respectively). Then, the accelerations recorded at the soil surface by the seismometers 102636 and 908E in S-N directions and by the seismometers 9085 and 985F in N-S directions (green lines and yellow ones, respectively) are much lower than the accelerations recorded at the foundations. No difference can be observed between Figure 544 and Figure 545.

Finally, the effects of the foundation soil are detected, comparing the response of the system with only gravel, G/R 90/10 and G/R 70/30. Figure 546 and Figure 547 show the comparisons concerning the acceleration time histories recorded by two instruments placed on the foundation (102644 accelerometer) and on the soil surface (9085 seismometer), respectively, for the three different soil foundation: gravel, G/R 90/10 and G/R 70/30.

It is possible to observe a reduction of the transmission of the signal by the changing of the soil foundation from gravel to G/R 90/10 and then to G/R 70/30. The effect of isolating is visible with the placement of the G/R 90/10 underneath the foundation and it is more evident with the placement of the G/R 70/30. The peaks of the foundation accelerations are about: 0.2 m/s^2 using the gravel; 0.12 m/s^2 using the G/R 90/10; 0.04 m/s^2 using the G/R 70/30.

Similarly, on the soil surface a deamplification occurs moving from gravel to G/R 90/10 and in turn from G/R 90/10 to G/R 70/30.

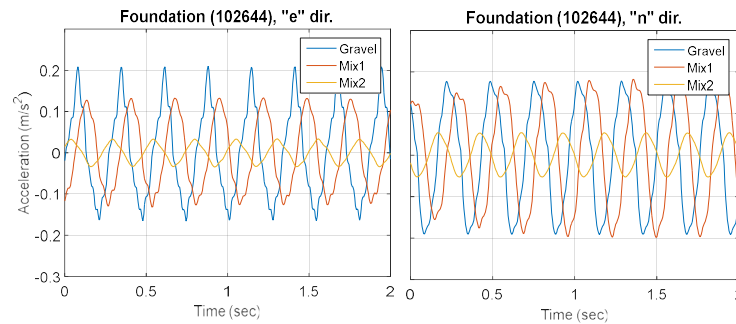


Figure 546: Comparison among accelerations recorded on the foundation for the Experiment C for $f = 4.5$ Hz, for all the three tests performed on soil foundation replaced by gravel, GRM G/R 90/10 and GRM G/R 70/30

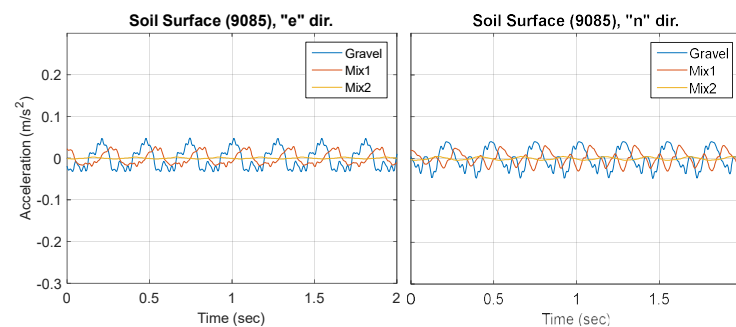


Figure 547: Comparison among accelerations recorded on the soil surface for the Experiment C for $f = 4.5$ Hz, for all the three tests performed on soil foundation replaced by gravel, GRM G/R 90/10 and GRM G/R 70/30

9.9.7 Conclusions and outlook

Investigating the response of the above-described system in the time and frequency domains (maxima accelerations; Fourier spectra and amplification functions; acceleration amplification ratios from the top to the base of the structure, through the soil-foundation interface and along the ground surface) has a fundamental scientific and technical value and interest because concern a fully-coupled large-scale soil-structure system, rarely investigated.

The important deamplification of the signal from the foundation to the soil surface, observed during all the tests, confirms once more the effect of soil-structure interaction and particularly the role played by the soil-foundation interface.

As regards the influence of the material immediately underneath the foundation on the response of the structure, the effect of isolating is visible with the placement of the G/R 90/10 underneath the foundation and it is more evident with the placement of the G/R 70/30. Similarly, on the soil surface a deamplification occurs moving from gravel to G/R 90/10 and in turn from G/R 90/10 to G/R 70/30.

The particular attention devoted to the effects of the new advanced way of isolating structures using GRM mixtures offers interesting ideas for less expensive seismic designs.

9.9.8 References

Abate G., Massimino M., Maugeri M., 3-D finite element modelling of a shaking table test for DSSI analysis. In: *Geotechnical Aspects of EC8. XIV Eur. Conf. on Soil Mech. and Geotech. Eng (ISSMGE), Special Session of ERTC-12*. Madrid, Spain. September 25, 2007. Pàtron Editore (Italy), 2007.

Abate G., Massimino M.R., Maugeri M., Simulation of shaking table tests to study soil-structure interaction by means of two different constitutive models. *Proc. of 6th Int. Conf. on Case Histories in Geotech. Eng.* Arlington, VA, USA, August 11-16, 2008-a.

Abate G., Massimino M., Maugeri M., Finite element modelling of a shaking table test to evaluate the dynamic behaviour of a soil-foundation system. 2008 Seismic Engineering International Conference Commemorating the 1908 Messina and Reggio Calabria Earthquake, MERCEA 2008; Reggio Calabria; Italy; July 8-11, 2008. Volume 1020, Issue PART 1, pp. 569-576. AIP Conference Proceedings, 2008-b.

Abate G., Massimino M.R., Maugeri M., Muir Wood D., Numerical modelling of a shaking table test for soil-foundation-superstructure interaction by means of a soil constitutive model implemented in a FEM code. *GEOT GEOL ENG*, 28, 37-59, 2010.

Abate G., Massimino M.R., Dynamic soil-structure interaction analysis by experimental and numerical modelling. *Rivista Italiana di Geotecnica*. 50(2), 44-70, 2016.

Abate G., Gatto M., Massimino M.R., Pitilakis D., Large scale soil-foundation-structure model in Greece: dynamic tests vs FEM simulation. *Proc. 6th ECCOMAS Thematic Conference on Computational Methods in Structural Dynamics and Earthquake Engineering. COMPDYN 2017*. M. Papadrakakis, M. Fragiadakis (Eds.). Rhodes Island, Greece, 15–17 June 2017.

Anastasopoulos M., Loli T., Georgarakos V., Drosos, Shaking Table Testing of Rocking–Isolated Bridge Pier on Sand. *J EARTHQ ENG*; 17, 1–32, 2013.

Argyroudis S., Palaiochorinou A., Mitoulis S., Pitilakis D. Use of rubberised backfills for improving the seismic response of integral abutment bridges. *Bulletin of Earthquake Engineering*, 14: 3573-3590. 2016.

Biondi G., Massimino M.R., Maugeri M., Taylor C., Influence of the input motion characteristics on the dynamic soil-structure interaction by shaking table tests. *Advances in Earthquake Engineering. 4th International Conference on Earthquake Resistant Engineering Structures, ERES IV*; Ancona; Italy; September 22-24; Editors: Latini G., Brebbia C.A. Vol. 13, pp. 225-234, 2003.

Biondi G., Massimino M.R., Maugeri M., Experimental study in the shaking table of the input motion characteristics in the dynamic SSI of a SDOF model. *Bulletin of Earthquake Engineering*. Vol. 13, Issue 6, 1 June 2015, pp. 1835-1869, 2015.

Combescure D., Chaudat T., Icons European program seismic tests on R/C walls with uplift; CAMUS IV specimen. ICONS Project, CEA/DRN/DMT Report, SEMT/EMSI/RT/00-27/4. 2000.

De Barros F.C.P., Luco J.E., Identification of foundation impedance functions and soil properties from vibration tests of the Hualien containment model. *Soil Dynamics and Earthquake Engineering*; 14, 229–248, 1995.

EC8-Part 5 (2003). Design of structures for earthquake resistance – Part 5: Foundations, retaining structures and geotechnical aspects. ENV 1998, Europ. Com. For Standard, Brussels.

Gazetas G., Analysis of machine foundation vibrations: State of the art. *Soil Dynamics and Earthquake Engineering*; 2(1), 2–42, 1983.

Gourvenec S., Randolph M.F., Effect of strength non-homogeneity on the shape and failure envelopes for combined loading of strip and circular foundations on clay. *Geotechnique*; 53(6), 527–33, 2003.

Khatami H., Deng An, Jaksa M. B. The arching effect in rubber–sand mixtures. *Geosynthetics International*. DOI: 10.1680/jgein.20.00007. 2020.

Massimino M.R., Abate G., Corsico S., Grasso S., Motta E. Dynamic behaviour of coupled soil-structure systems by means of FEM analysis for the seismic risk mitigation of INGV building in Catania (Italy). Special Issue, *Annals of Geophysics*. 61, 2, SE216, 2018; DOI: 10.4401/ag-7739, 2018.

Massimino M.R., Abate G., Grasso S., Pitilakis D. Some aspects of DSSI in the dynamic response of fully-coupled soil-structure systems. *Rivista Italiana di Geotecnica*. Volume 1/2019, Pages: 44-70. ISSN: 0557-1405. DOI:10.19199/2019.1.0557-1405.044. 2019a.

Massimino M.R., Abate G., Corsico S., Louarn R. Comparison between two approaches for non-linear fem modelling of the seismic behaviour of a coupled soil-structure system. *Geotech Geol Eng*. Volume: 37. Issue: 3, pp:1957-1975. DOI: 10.1007/s10706-018-0737-y. 2019b.

Massimino M.R., Maugeri M., Physical modelling of shaking table tests on dynamic soil-foundation interaction and numerical and analytical simulation. *Soil Dynamics and Earthquake Engineering*; 49, 1-18, DOI: 10.1016/j.soildyn.2013.01.023. 2013.

Paolucci R., Shirato M., Yilmaz M.T., Seismic behaviour of shallow foundations: shaking table experiments vs numerical modelling. *Earthquake Engineering and Structural Dynamics*, 37(4), 577–95, 2000.

Pecker R., Enhanced seismic design of shallow foundations: example of the Rion Antirion bridge. *Proc. of 4th Athenian Lecture on Geotech Eng*, Athens, Greece, 2006.

Pitilakis, D., Raptakis D, Lontzetidis K., Tika-Vassilikou T., Jongmans D., Geotechnical & Geophysical description of EURO-SEISTEST, using field, laboratory tests and moderate strong-motion recordings. *Journal of Earthquake Engineering*, 3(3), 381-409, 1999.

Pitilakis D., Clouteau D., Equivalent linear substructure approximation of soil–foundation–structure interaction: model presentation and validation. *Bulletin of Earthquake Engineering*, 8(2), 257–282, 2010.

Pitilakis D., Dietz M., Muir Wood D., Clouteau D., Modaressi-Farahmand-Razavi A., Numerical simulation of dynamic soil–structure interaction in shaking table testing. *Soil Dynamics and Earthquake Engineering*, 28(6), 453–467, 2008.

Pitilakis K., Anastasiadis A., Pitilakis D., Rovithis E., Full-scale testing of a model structure in EUROSEISTEST to study soil-foundation-structure interaction. *COMPDYN 2013, 4th ECCOMAS Thematic Conference on Computational Methods in Structural Dynamics and Earthquake Engineering*, M. Papadrakakis, V. Papadopoulos, V. Plevris (eds.). Kos Island, Greece, 12–14 June 2013.

Pitilakis D., Lamprou D., Manakou M., Rovithis E., System identification of soil-foundation structure systems by means of ambient noise records: the case of Europroteas model structure in Euroseistest. *Proc. of the 2nd European Conf. on Earthquake Engineering and Seismology*. Istanbul, Turkey, 2014.

Pitilakis D., Rovithis E., Massimino M.R., Gatto M.P.A., Numerical Simulation of Large-Scale Soil-Foundation-Structure Interaction Experiments in the EuroProteas Facility, *6th International Conference on Earthquake Geotechnical Engineering*, 1-4 November 2015. Christchurch, New Zealand, 2015.

Raptakis D., Anastasiadis A. & Pitilakis K. (1998). Preliminary instrumental and theoretical approach of site effects in Thessaloniki. In *Proceedings of the 11th European Conference on Earthquake Engineering*.

Raptakis, D., Chavez-Garcia, F., Makra, K., and Pitilakis, K. Site effects at euroseistesti. determination of the valley structure and confrontation of observations with 1d analysis. *Soil Dynamics and Earthquake Engineering* 19, 1 (2000), 1 – 22

Senetakis K., Anastasiadis A., Pitilakis K. A comparison of material damping measurements in resonant column using the steady-state and free-vibration decay methods. *Soil Dynamic and Earthquake Engineering*, 74 (2015): 10-13, 2015.

Tsang H. H., Lam J. Y. K., Yaghmaei-Sabegh S., Sheikh M. N., Ziong W., Shang S. Protecting low-to-medium-rise buildings by scrap tyre-soil mixtures. *Proc. Australian Earthquake Engineering Society Conference*, Newcastle, Australia, 1-8, 2009.

Ueng T.S., Wang M.H., Chen M.H., Chen C.H., Peng L.H., A large biaxial shear box for shaking table test on saturated sand. *GEOTECH TEST J*; 29(1), 1-8, 2006.

Ugalde J.A., Kutter B.L., Jeremic B., Gajan S., Centrifuge modelling of rocking behaviour of bridges on shallow foundations. *Proc. of 4th Int. Conf. Earthq. Geotech. Eng.* Thessaloniki, Greece, June 25–28, 2007 (Paper No. 1484).

Veletsos A.S., Meek J.W., Dynamic behaviour of building-foundation systems. *EARTHQ ENG STRUCT D*; 3, 121-38, 1974.

Zhang T., Cai G., Duan W. Strength and microstructure characteristics of the recycled rubber tire-sand mixtures as lightweight backfill. *Environmental Sciences and Pollution Research*, 25: 3872-3883. 2018

10 NORSAR

DD Stiftelsen NORSAR or shortly NORSAR is a not-for-profit research foundation located at Kjeller near Oslo (Norway). As TA10, NORSAR offered Transnational Access to its infrastructure, which consists primarily of a data centre and field installations on Norwegian territory in Northern Europe, the Arctic and Antarctica. It comprises five seismic and three infrasound arrays (with apertures ranging from 0.5 to 60 km) and four single 3C broadband stations. Going back to 1971, the permanently growing unique data base stores seismic data from NORSAR's arrays and 3C stations as well as from many other (mostly European) arrays and 3C stations, which are all open for research. In addition, NORSAR's staff contributes with its expertise on 1) array seismology, 2) automatic on-line data processing, 3) near real-time seismic monitoring in various scales, from regional seismicity, aftershock sequences and induced seismicity to microearthquakes associated with natural or anthropogenic ground instabilities, and 4) seismic hazard and risk assessment as well as earthquake engineering.

All eight planned TA projects at NORSAR have been finalized. Nine of the users visiting NORSAR for these projects are early career scientists either working on their Master (2) or PhD (3) thesis or have recently finalized their PhDs (4). The projects focused on different aspects of array-data analysis. Four research visitors came with their own data, observed with different arrays in different environments:

- infrasound array data from the Romanian infrasound station, to be used as classifier to distinguish between earthquakes and explosions (quarries, mines).
- short period data from a temporary small aperture array in Russia, to detect and locate low magnitude seismicity in the Lena trough region, Siberia.
- strong motion accelerometer near field observations from the first array in Iceland, to investigate the characteristics of the mainshock of a M 6.3 earthquake and its aftershock sequence in the South Iceland Seismic Zone.
- broadband data from small aperture array-like installations on the Peloponnese and in the Gulf of Corinth region, Greece, to search for seismic tremor signals caused by slow motion earthquakes in the Ionian subduction zone.
- the three other array related projects were about:
- the investigation of Moho depth and structure of the mantle transition zone (receiver function method) below southern Fennoscandia, with data observed by the large NORSAR array, the NORES array and other permanent and temporary seismic stations in southern Norway.
- testing a theoretically developed blind beamforming algorithm, with data from NORSAR's small aperture array ARCES in northern Norway.
- investigating location and optimized geometry for a new seismic array planned to be installed in southwest Portugal.

During the about one month long stays at NORSAR, the TA users became familiar with different aspects of array-data processing: the influence of array geometry and instrumentation, the resolution of array specific measurements (backazimuth and slowness), different beamforming techniques, the influence of frequency contents on signal processing results, the separation between signals and noise with array techniques, and the importance of including the entire wavefield (vertical and horizontal components) in the analysis.

The last project was related to NORSAR's seismic engineering expertise:

- A user group from the University of Chieti-Pescara, Pescara, Italy including two master students visited NORSAR to carry-out seismic risk assessment (earthquake ground shaking, induced-liquefaction and losses) for two Italian historical towns: Offida (Ap) in Marche Region and Cavezzo (Mo) in Emilia Romagna Region. The activity involving the use of NORSAR's seismic risk software tool, recently developed in the framework of H2020 LIQUEFACT project, the development and

compilation of exposure database, generating potential earthquake risk scenarios that could represent an important tool for decision support and development of regional risk reduction programmes.

Until now (status March 2020) the results from the different projects have contributed to eight conference papers (talks/posters) and one PhD-thesis.

10.1 Project # 17 – Blind beamforming in array processing

Authors

E.-V. Picoulis⁽¹⁾, J. Schweitzer⁽²⁾

⁽¹⁾ *University of Patras, Rio Patras, Greece*

⁽²⁾ *NORSAR, Kjeller, Norway*

10.1.1 Project Summary

Contrary to the conventional model-based beamforming, blind beamforming operates directly on the available signals, without making any assumptions regarding the mechanism(s) that generated them. In other words, blind beamforming stands for data-driven instead of model-driven beamforming apart from its superior enhancement capabilities, the direct estimation of the time delays enables a more natural formulation of the signal detection and parameter estimation problems that truly captures the advantage of seismic arrays over conventional networks.

10.1.2 Main Research Objectives

The visit had two main objectives. The first one was to offer the visiting researcher the opportunity to familiarize himself with state-of-the-art array processing techniques as well as gain insight on modern array applications, through the collaboration with the experienced researchers at the hosting institute. The second objective of the visit was the realization of a preliminary investigation concerning the use of blind beamforming techniques, based on Semi-Definite Programming (SDP-BB), for the solution of the signal detection and parameter estimation problems in seismic arrays. Regarding signal detection, the main idea was to formulate the detection problem as a hypothesis testing problem, discriminating between the hypotheses of structured vs random time delays. With this goal in mind, one of the objectives of the visit was the examination of time-delay sets from real array data, with the purpose of determining the statistical properties of the obtained delays under the scenarios of “pure noise” and “signal”. On the other hand, regarding the parameter estimation problem, the goal was to formulate an inverse problem based on the obtained delay-estimates, for the estimation of the back-azimuth and apparent velocity parameters of the incoming wave. For this purpose, the objective was to analyse several cases of seismic phases with known wave parameters, recorded at the hosting institute.

10.1.3 Main Research Outcomes and Outlook

From the user's point of view the one-month long research visit can be characterized as a very successful endeavour, leading to very fruitful collaborations and exchange of ideas between the visiting researcher and the staff at the hosting institute. The objectives of the visit were fulfilled to a very satisfactory level. More specifically, with the guidance of NORSAR researchers, the user was able to establish a deeper understanding regarding the particularities of seismic array signals and array processing techniques. On the other hand, through numerous discussions as well as a formal presentation, the visitor was able to convey and refine his ideas regarding the incorporation of blind beamforming in seismic array methodology. The most graspable result of the visit was the formulation and initial evaluation of a new, delay-based technique for the joint detection and estimation of plane waves in seismic arrays. The preliminary results of the technique, using real array data, were very promising. The technique is still under development and both a conference presentation and subsequently a full paper submission are planned for the near future. Ideas for other interesting collaborative projects were also established during the visit. In conclusion, the outcome of the visit has provided the visiting researcher with a significant first step towards his goal of developing new array processing methodologies based on the use of blind beamforming.

Some project results were presented at the ESC General Assembly in Malta in 2018 (8) and a publication of the results is in preparation.

10.2 Project #31 – Seismic tremor detection in Greece using small aperture arrays

Authors

V. Kapetanidis⁽¹⁾, J. Schweitzer⁽²⁾

⁽¹⁾ *National and Kapodistrian University of Athens, Athens, Greece*

⁽²⁾ *NORSAR, Kjeller, Norway*

10.2.1 Project Summary

The main objective of this research proposal is to detect tremors of tectonic origin in Greece using seismic arrays and array data processing techniques. This type of signal is usually associated with slow-slip events, which have been mostly observed in several subduction zones worldwide. In Greece no such tremor recordings have ever been documented. There are, however, two candidate zones where they could possibly occur: the Hellenic Arc subduction zone, where the observed strain is mostly aseismically accommodated, and the western Corinth Rift. In the latter case, a strain transient associated with a slow-slip event was observed in December 2002, while there is evidence of creeping that occurs on a developing detachment within the brittle-ductile transition zone.

In the proposed research, an array that consists of 7 broadband seismometers, installed near the town of Magoula, at the western margin of the Corinth Rift, will be employed to detect tremors that may

have occurred in the region using beamforming techniques. Candidate signals will be evaluated using a conventional method, such as envelope cross-correlation, at the stations of the local Corinth Rift Laboratory (CRL) network. The developed methodology will be also applied to another seismic array, composed of 9 stations, that is installed in Pylos, South Peloponnese, in collaboration with the National Observatory of Athens. This could target the SW portion of the Hellenic Arc, where tectonic tremors are more likely to be observed, but may be more difficult to evaluate due to the sparse distribution of stations of the regional Hellenic Unified Seismological Network (HUSN). The detection of tectonic tremors in Greece could reveal sites where slow-slip occurs, explaining part of the aseismically accommodated strain and could have implications on the seismic hazard assessment.

10.2.2 Main Research Objectives

The main objective of the SERA-TA visit was the development of array processing tools for the detection and location of tectonic tremors in the region of Greece. Prior to the visit at NORSAR, data had been collected from two arrays in Greece; one located in Pylos, S. Peloponnese, close to the interface between overriding and subducting plates of the Hellenic Arc, which is considered as a possible zone where tectonic tremors might occur; the other array is located in Magoula, in the W. Corinth Gulf, a region characterized by intense microseismic activity, where at least one slow slip event has been recorded as a strain transient signal by a dilatometer in December 2002. A data-sample of about one month was to be processed during the TA-visit at NORSAR. A “training dataset” of recorded tremors in Cascadia was also available to test the various array-processing techniques for their tremor-detecting capability. The latter appear as emergent, noise-like, coherent signals, mainly within the 2-8 Hz band, which may persist for several minutes to hours, days or even weeks. Their source is expected to be sustained for a long time in the same fault patch or gradually migrate over time. The source location can be determined using back-projection techniques, preferably using observations from multiple arrays, or other constraints such as a fixed depth. The detection and location of such events may provide information on aseismic slip that could possibly accelerate the occurrence of significant earthquakes in the area of study.

10.2.3 Main Research Outcomes and Outlook

During the one-month long research visit, several methods were examined for their capability to detect tectonic tremors on a “training dataset” from the SOOKE array in Cascadia. Scripts (macros) were written in the environment of the NORSAR proprietary software “EP”. The implemented techniques included the following: Classic FK analysis on each available component; Average correlation coefficient between traces aligned at the maximum FK-power time-delays; Time-domain delay-and-sum beamforming; Cross-correlation beamforming. Other methods, e.g., FK analysis on envelopes or STA/LTA triggering using the “DP” software, did not yield usable results. The most efficient method was classical FK, averaging measurements from all components with a correlation threshold of about 0.7, as it provided results close to those expected for the “training dataset”. Tests showed that a window length of 60 s achieves balance between adequate temporal resolution and low scattering of observations during tremors. Almost 2-years of recordings from Greece were processed on various bands using the preferred recipe, largely exceeding the original plan of a 1-month-long sample to be processed during the visit at NORSAR. The results were post-processed and candidate signals were visualized for evaluation. Many of the observations were associated with earthquakes, possible microseisms, noise of anthropogenic origin or even conventional seismics (e.g., repeated airgun shots) in the W. Corinth Gulf. So far, no observations were associated with tremor on either site. However, the

developed tools are now available for the processing of the rest of the data from the arrays and will be used for further monitoring of tremors in Greece.

Some project results will be presented at the ESC General Assembly in Corfu, Greece, in 2020 (6) and a publication of the results is in preparation.

10.3 Project #32 – A new velocity model up to 300 km deep based on receiver function data from the NORES array (Baltic Shield)

Authors

A. Goev⁽¹⁾, J. Schweitzer⁽²⁾

⁽¹⁾ *Russian Academy of Sciences, Moscow, Russian Federation*

⁽²⁾ *NORSAR, Kjeller, Norway*

10.3.1 Project Summary

The main goal of the proposed research is to construct a P- and S-wave seismic velocity of the crust and uppermost mantle of the southern part of Norway (Fennoscandian shield) by combining P-wave receiver-function data and S-wave receiver-function data of the NORSAR/NORES seismic arrays. For this purpose, we are going to use well known method of the receiver-function analysis, developed by the Institute of Physics of the Earth of Russian Academy of Sciences, along with classical array techniques. The model will include:

- a) P-wave velocity model;
- b) S-wave velocity model;
- c) position of the major seismic interfaces in the crust and upper mantle.

In particular, we will investigate the basic mantle boundaries such as Lithosphere-Asthenosphere-Boundary (LAB) and Lehmann discontinuity along with the mantle transition zone in 410 – 660 km depth. The model will be combined with the P- and S-wave velocity models of the crust and upper mantle obtained by the NORSAR local event studies.

10.3.2 Main Research Objectives

To investigate the velocity structure of the crust and uppermost mantle of the southern part of Norway using NORSAR data along with all the broadband seismic data for the region that could be obtained. Another goal of our attempts is to look for the mantle transition zone in 410 – 660 km to see whether any topography of this boundaries exists in southern Fennoscandia. The final goal is to get an accurate velocity model of the investigated area. To successfully obtain these goals the receiver function method has been chosen.

10.3.3 Main Research Outcomes and Outlook

During the one-month long research visit, we created three seismic event catalogues for each seismic broadband station, one for each phase of interest (P, S, SKS) to calculate the receiver function. The catalogues contain events since 1971 based on Harvard and ISC bulletins. Then, individual P-to-S receiver functions (PRF) were processed for each appropriate event observed with the NORSAR seismic broadband station, the MAGNUS project stations (11) and several close-by located seismic station like KONO and HFS. The total amount of PRFs is more than 5000. The observed onset times in the PRFs from the 410-km and 660-km discontinuities are slightly shorter than expected according to standard models and the onset time difference between these two phases is also smaller. Both observations agree with the model of a weak rift in the investigated area that affects at least 410-km discontinuity. Another result is that the 410-km discontinuity seems to be less sharp and more like a gradient zone than the 660-km discontinuity. After the data processing intense work during the TA visit, all these observations have to be proved, compared with theoretical models then combined in a topographic of 410-km and 660-km discontinuities. Finally, the velocity structure up to 300 km deep using P, S and SKS phases has to be modelled.

Some of the project results were already presented during a conference in Petropavlovsk-Kamchatsky, Russian Federation (4) and were used for the PhD thesis (3). Another two publications are in preparation.

10.4 Project #33 – Joint processing of seismo-acoustic array data as tool to discriminate between man-made explosions and earthquakes

Authors

R. Dinescu⁽¹⁾, J. Schweitzer⁽²⁾

⁽¹⁾ *National Institute of Earth Physics, Magurele, Romania*

⁽²⁾ *NORSAR, Kjeller, Norway*

10.4.1 Project Summary

Recently, a constant increasing of interest in analysing the infrasound data to include them in interdisciplinary domains as physics and geoscience have been observed at the global scale. The worldwide infrasound monitoring stations have proven capable to detect and locate atmospheric explosions as well as other natural phenomena generating infrasound signals. The proposed research is aimed to monitoring geophysical man-made hazard, i.e., controlled explosions, by jointly using data well-recorded with the Romanian seismic and infrasonic arrays, focusing on the Plostina seismo-acoustic site (PLOR and IPLOR stations).

During the project, infrasound and seismic array data recorded by Romanian stations will be processed and analysed in order to discriminate between tectonic sources (earthquakes) and artificial events (quarry blasts and mine explosions). The examination of the infrasound propagation changes over time

and distance is essential to understand the differences between real propagation through atmospheric layers and a hypothetical propagation along the earth's surface. The capability of the Romanian dense seismic network to detect and locate small events led to an undesirable side-effect as including of many man-made blasts and explosions in the Romanian earthquake catalogue ROMPLUS (7).

10.4.2 Main Research Objectives

To monitor man-made hazards by jointly using data well-recorded with the Romanian seismic and infrasonic arrays, focusing on the Plostina seismo-acoustic site (PLOR and IPLOR stations) by building an efficient tool to discriminate between man-made explosions and earthquakes, followed by seismic catalogue decontamination

Activities to follow:

- selection of natural and artificial reference events for the seismo-acoustic analysis and the stations (seismic and infrasound) where they were detected
- analysis of the infrasound data using standard processing methods to extract the waveform characteristics (direction of arrival - backazimuth, phase apparent velocity, frequency, amplitude, SNR)
- analysis of IPLOR infrasound station detection capacity to observe the diurnal and seasonal variations and identification of the causes which produce these variations
- analysis of seismic data from reference events in order to extract the characteristics of their seismic signature, such as waveform, frequency, amplitude, particle motion for determining the direction of arrival of the energy at the measuring sensor
- association of the infrasound detections obtained (backazimuth and arrival time measured with the IPLOR array) with the seismic events in the analysed set (theoretical backazimuth and arrival time), considering the effect of the dynamics of atmospheric propagation
- inspection of the recorded seismic waveforms for events identified as acoustic sources based on their association with infrasonic detections (aspect, frequency content, radiated energy) for their validation as quarry bursts
- creation of templates of seismo-acoustic signals generated by man-made explosions in order to compare them with the other recorded waveforms.

10.4.3 Main Research Outcomes and Outlook

During the one-month long research visit the following activities were done in order to accomplish the user-objectives:

- selection of the promising events recorded on PLOR and BURAR from the earthquake catalogue in order to analyse the recorded data at seismic and infrasound stations
- analysis of the infrasound recordings at IPLOR and BURARI stations using NORSAR processing software ep in order to extract the waveform characteristics (direction of arrival - backazimuth, phase apparent velocity, frequency, amplitude, SNR)
- analysis of the seismic recordings at PLOR and BURAR stations with NORSAR processing software ep in order to extract the characteristics of the seismic signatures
- association of the infrasound data with the seismic data obtained after the processing, considering the effect of atmospheric propagation
- scripts creation for seismo-acoustic signals in order to process and check the infrasound recordings at IPLOR and BURARI stations.

Some results of the research visit were presented in three conference contributions (1; 2; 5) and will be part of the planned PhD thesis.

10.5 Project #41 – Earthquake Spectral Provisions and Urban Fragility Evaluation - EPUFE

Authors

S. Biondi⁽¹⁾, A. Meslem⁽²⁾, J. Schweitzer⁽²⁾

⁽¹⁾ *University of Chieti-Pescara, Pescara, Italy*

⁽²⁾ *NORSAR, Kjeller, Norway*

10.5.1 Project Summary

Seismic prevention and mitigation of historical towns/centers have gained a central position within earthquake engineering topics, particularly in such areas having a high seismic risk. They have been modelled in terms of structural safety with a comprehensive strategy for seismic prevention and mitigation. In this project, two complex cases of Italian historical town have been selected for development of risk reduction programmes. The carried-out approach was based on two main parts:

- the first was urban risk assessment
- the second was a prioritization of retrofitting interventions to optimally increase urban safety.

Seismic input has been assumed as a function of the earthquake intensity expressed in terms of Mercalli-Cancani-Sieberg (MCS) intensity scale and fragility functions was defined in order to evaluate the probability of failure of each class of buildings or infrastructures. The MCS intensity scale is linked to the detected damage (post-earthquake damage). The detected damage is depending both on damage evaluation procedure and on social “pressure” on infrastructure under evaluation.

10.5.2 Main Research Objectives

Due to the uncertainties involved in the analysis, a probabilistic approach had to be applied. Generally, the proposed methodology involves the following steps:

- (i) identification of the Urban Minimum System (UMS);
- (ii) selection of the target safety level, which is dependent on the component type;
- (iii) definition for each component of the fragility curve, which gives the probability of a structure to exceed a certain limit state;
- (iv) evaluation of the fragility behaviour of the whole system by applying structural reliability methods;
- (v) identification of an optimal retrofitting strategy.

With respect to performance levels Significant Damage (SD) and Damage Limitation (DL) have been considered. The obtained fragility functions define the probability of failure of each class of buildings as a function of the earthquake intensity expressed in terms of Mercalli-Cancani-Sieberg (MCS) intensity scale.

The implemented procedure concerns exclusively the urban configuration and it shows a weak aspect in the earthquake intensity definition in terms of Mercalli-Cancani-Sieberg (MCS) intensity scale. The logical steps within the improved project are the followings:

- (i) definition of a site catalogue of historical seismicity at different sites involved in recent earthquakes;
- (ii) seismic hazard definition by means of deterministic or probabilistic approach including site effects (using NORSAR's Liquefact Software and collected pre-earthquake data);
- (iii) earthquake input definition for the UMS probabilistic approach (i.e., PGA maps, MCS maps, ...) to the selected urban area;
- (iv) fragility curves fitting to this selected earthquake input (using NORSAR's Liquefact Software and proposed new fragility curves calibrated on post-earthquake data).

10.5.3 Main Research Outcomes and Outlook

Following the approach of the LIQUEFACT Software for assessment and mitigation the impact (damage, economic and insurance losses) of earthquake ground shaking and liquefaction potential across Europe (the software uses a holistic approach to protect structures/infrastructures and to improve resilience to Earthquake-induced ground shaking and liquefaction disasters) the proposed methodology has been carried out considering two different sites in Italy: Offida (Ap) in Marche Region and Cavezzo (Mo) in Emilia Romagna Region in order to take into account both ground shaking and liquefaction phenomena induced by Earthquake.

- The first site Offida (Ap) (ground shaking phenomena) is a small town in the Central Italy. It suffered from the 2016 Central Italy earthquake with distance of 43 km to the epicentre. The area has also suffered from the 30th October 2016 earthquake (M 6.4) that was the most important event for this region.
- The second site Cavezzo (Mo) (liquefaction phenomena) is a small town in the Central Italy, suffered the 2012 Emilia Romagna Earthquake induced liquefaction.

Further research and project activities will be discussed during a common workshop between the research group and NORSAR planned for summer 2020.

10.6 Project #42 – Beamforming of aftershock strong-motion time-histories recorded on the ICEARRAY for earthquake source studies

Authors

T. Sonneman⁽¹⁾, J. Schweitzer⁽²⁾

⁽¹⁾ *University of Iceland, Reykjavik, Iceland*

⁽²⁾ *NORSAR, Kjeller, Norway*

10.6.1 Project Summary

Using a unique dataset of over 1700 ml 0.4-4.8 aftershocks of the Mw 6.3 Ölfus earthquake in the South Iceland Seismic Zone on 29 May 2008, recorded at hypocentral distances between 3 to 18 km by the ICEARRAY accelerometric array of 11 stations with inter station distances between 54 and 1900 m, we have applied conventional array data analysis at first and intend to apply a beamforming algorithm to produce clear waveforms that allow a detailed earthquake source analysis using a suite of theoretical crack rupture source models. A relocation of the aftershocks based on the array data will be done to decide whether a specific array response calibration can yield higher array-derived direction of arrival accuracy. Additionally, the near-source array data may allow tracking of the mainshock's rupture front propagation across its two faults, which can be a valuable addition to training datasets of array-based Earthquake Early Warning applications. Created code will be made available to increase the capabilities of the community.

10.6.2 Main Research Objectives

Phase detection and identification using frequency wavenumber analysis and cross-correlations are to be carried out, improved location of all recorded aftershocks using a circular wavefront assumption due to proximity, and determination of magnitude are to be done as well. Since many strong and shallow earthquakes have been recorded, attempts at analysing larger events through full waveform simulations will be made to study near-source effects. The earthquake spectra will be analysed to derive physical source parameters through Bayesian inference. These studies will give indications as to how well earthquake parameters can be resolved with a near-source array and physical modelling. The rupture propagation of the main shock (2008-05-29 M6.3) shall be illuminated using the array data. Besides posters, presentations and papers about the findings to be published, created computer code (mostly Python) useful to the community will be published online. The gained insight, training and new code will be useful in routine and advanced analysis of real-time data from the new array HEKSISZ of the Icelandic Meteorological Office, which will monitor the seismicity under the volcano Hekla and in the surrounding active region.

10.6.3 Main Research Outcomes and Outlook

Conventional frequency wavenumber analysis has been carried out on all aftershocks and derived azimuths have been compared to available network locations. Analysis has been focused on first phase

onsets as corresponding picks were available. Python code to incorporate near real-time data and further analyse secondary phases is in development. Project discussions with scientists at NORSAR and IMO have guided further steps to include more advanced analysis methods and take known issues into account, such as cross-correlation and waveform simulations to improve results in the face of strong subsurface heterogeneities and very near source distances.

Some results of the research visit are ready to be presented at the EGU2020 conference (10) and a publication is in preparation.

10.7 Project #43 – Investigation of (micro-)seismicity of the Laptev Sea using a small-aperture array

Authors

A. Plötz⁽¹⁾, J. Schweitzer⁽²⁾

⁽¹⁾ *Alfred-Wegener-Institute, Bremerhaven, Germany*

⁽²⁾ *NORSAR, Kjeller, Norway*

10.7.1 Project Summary

So far, the local (micro-)seismicity of the Laptev Sea region is poorly described, due to a lack of local seismological stations and data sets. To investigate the regional seismicity of the Laptev Sea, 13 stations were temporarily installed as a seismological small-aperture array of 2 km width close to Tiksi. Over a period of nine months, these instruments continuously recorded seismic data under the extremely harsh environmental conditions. The data of the Tiksi-Array shows a large number of small events and the array azimuth determination points to the nearby coastline of the Buor Khaya Bay. The results from array-processing will help to investigate the geodynamic processes of the Laptev Sea Rift and to better describe this amagmatic rifting and its consequences in an Arctic and global context.

10.7.2 Main Research Objectives

The project is aimed to investigate the seismicity of the continental Laptev Sea Rift using new data from a small-aperture array. Located north to the Laptev Sea, the ultraslow spreading Gakkel Ridge is propagating into a continental rift system – the Laptev Sea Rift. This rift system separates the North American plate from the Eurasian plate and presents a rare opportunity to investigate mechanisms of recent continental breakups. In general, divergent plate boundaries are accompanied by magmatic and earthquake activities. The earthquake activity at the Gakkel Ridge shows a sharp image of seismicity, confined to the rift valley that extends to the continental shelf of the Laptev Sea. In contrast, the Laptev Sea region indicates less and more diffuse seismicity and an absence of magmatic activity. However, new data from a local array close to Tiksi show a large number of small events. With array processing techniques the main objective will be to detect these events and analyse their spatio-temporal distribution.

10.7.3 Main Research Outcomes and Outlook

The project started with the transnational access at NORSAR from 29. April to 28. May 2019. During the one month at NORSAR, we implemented a semi-automatic processing for recordings of the Tiksi-array. For this a representative month (November 2016) from the nine months long recording period was chosen. The main task was to adjust the parameters for the earthquake detection processing to identify all onsets of the more distant as well as the very local earthquakes. For that purpose, we integrated 13 different bandpass filters, which are sensitive for the expected different frequency contents of these signals. These bandpass filters were then applied on array beams (delay-and-sum) calculated for different apparent velocity and backazimuth parameters. Incoherent energy (noise) will be suppressed by this processing and coherent energy (signals) will be emphasized. Then, a classical STA/LTA detector was running over these filtered beams to find possible earthquake onsets and their signal attributes were measured. These processing steps had to be tested and eventually adjusted for the complete dataset.

Some results of the research visit are already presented at a conference (9) and a publication is in preparation. The results will then also be part of the planned PhD thesis.

10.8 Project 44 – Design, location and processing of a regional array in SW Portugal - Europe

Authors

J. Fontiela⁽¹⁾, J. Schweitzer⁽²⁾

⁽¹⁾ *University of Évora, Évora, Portugal*

⁽²⁾ *NORSAR, Kjeller, Norway*

10.8.1 Project Summary

A permanent seismic array will be installed in Portugal to study its seismicity and that of adjacent zones, and to support the national Earthquake Early Warning System (EEWS). Nevertheless, Portugal does not have own experience in this field of seismic research. To install a seismic array, several subjects must be addressed before the installation such as location, seismic instrumentation, and aperture and geometry of the array.

Visiting NORSAR is paramount to acquire skills in the seismic array design and processing. Concerning data processing, there are several processing methods available like beamforming, f-k analysis, VESPA process, slant stacks. The access to NORSAR is advantageous to gather knowledge and experience from a leading institution in seismic arrays.

With the research visit, we will define the design and siting of the seismic array that fulfil the following goals: monitoring in detail the seismicity, refine velocity models, detection of small-scale heterogeneities, forensic seismology.

10.8.2 Main Research Objectives

The main goals proposed were attained with the design of the seismic array and data processing.

The implementation of a seismic array in Portugal will allow to study in detail the micro-seismicity and seismicity on the offshore of SW Iberia and the Iberia itself. The array is a paramount infrastructure on the study of the seismogenic sources of the 1755 Lisbon earthquake (M 8.5-9.0) and the one of 1969 (Mw 8.0).

Improving the knowledge of the seismogenic sources on the offshore is essential to assess and review the seismic hazard models and develop scenarios.

10.8.3 Main Research Outcomes and Outlook

The SERA - Transnational Access is concluded with the one month long stay at NORSAR. During the project a future temporary small aperture array for southwest Portugal was designed and its theoretical performance tested. Concerning future array data processing, several processing methods like Beam Forming, f-k analysis, VESPA process and Slant Stack techniques were studied and investigated.

Foreseen activities are the installation of a temporary set of seismic stations at different distances to analyse the noise conditions at the selected array site chosen during the research visit at NORSAR. In this experiment we will deploy five broadband stations for seven days; then we move four stations to new sites at different distances. Based on the analysis of the noise level recorded at these sites the final configuration of the seismic array will be decided.

10.9 References

1. Dinescu, R., D. Ghica, J. Schweitzer, S.P. Näsholm, M. Popa & C. Ionescu (2019). Monitoring man-made hazards using data recorded with the Romanian seismic and infrasonic arrays. 16th EGU General Assembly, Vienna, Austria, April 2019.
2. Dinescu, R., D. Ghica, F. Borleanu, M. Popa, M. Rogozea & A. Chircea (2019). Monitoring regional explosions with Romanian seismo-acoustic arrays. Case study: 09th of October 2018, Ukraine. Balkan Geophysical Society (BGS), Albena, Bulgaria September 2019.
3. Goev, A.G. (2019). PhD thesis 'Velocity structure of the earth crust and upper mantle of the collision zone of East-European craton', Russian Academy of Sciences, defended 24 December 2019.
4. Goev, A.G., G.L. Kosarev, I.A. Sanina, O.Y. Riznichenko (2019). On the stability of modelling a velocity discontinuity with the receiver function method, Proceedings of the 7th Scientific and Technical Conference "Problems of the complex geophysical monitoring of the Far East of Russia", Petropavlovsk-Kamchatsky, Russian Federation, 29 Sep – 5 Oct 2019.
5. Grecu, B., D. Ghica, F. Borleanu, C. Neagoe & R. Dinescu (2019). On the Use of Seismo-Acoustic Arrays for Environmental Monitoring in Romania. 27th IUGG General Assembly, Montreal, July 2019.
6. Kapetanidis, V., J. Schweitzer, N. Voulgaris & V. Karastathis (2020). Seismic tremor monitoring using small-aperture arrays: application in Greece. Submitted to 37th ESC General Assembly, Corfu, Greece, September 2020.
7. Oncescu M.C., Marza V.I., Rizescu M., Popa M., 1999. The Romanian earthquake catalogue between 984-1997. In: F. Wenzel and D. Lungu (eds), Contributions from the First International Workshop on Vrancea Earthquakes, Bucharest, Romania, November 1-4, 1997, Kluwer Academic Publishers, 43-48. https://doi.org/10.1007/978-94-011-4748-4_4.

8. Pikoulis, E.-V., E. Psarakis & J. Schweitzer (2018). Joint signal detection and parameter estimation in seismic arrays. 36th ESC General Assembly, Valletta, Malta, September 2018.
9. Plötz, A. (2019). Local seismicity in the SW Laptev Sea Rift. AGU Chapman Conference on "Large-scale Volcanism in the Arctic: The Role of the Mantle and Tectonics", Selfoss, Iceland, October 2019.
10. Sonneman, T., K. Vogfjörð, C. Bean, B. Halldórsson & J. Schweitzer (2020). Implementation of array analysis on seismic signals from volcanoes in Iceland recorded on the small-aperture HEKSISZ array. EGU2020-20877, doi: 10.5194/egusphere-egu2020-20877.
11. Weidle, C., V. Maupin, J. Ritter, T. Kværna, J. Schweitzer, N. Balling, H. Thybo, J. I. Faleide, F. Wenzel (2010). MAGNUS – a seismological broadband experiment to resolve crustal and upper mantle structure beneath the Southern Scandes mountains in Norway. *Seism. Res. Lett.*, 81, (1), 76-84, 2010, doi:10.1785/gssrl.81.1.76.

Contact

Project lead	ETH Zürich
Project coordinator	Prof. Dr. Domenico Giardini
Project manager	Dr. Kauzar Saleh
Project office	ETH Department of Earth Sciences
Sonneggstrasse 5, NO H-floor, CH-8092 Zürich	
sera_office@erdw.ethz.ch	
+41 44 632 9690	
Project website	www.sera-eu.org

Liability claim

The European Commission is not responsible for any use that may be made of the information contained in this document. Also, responsibility for the information and views expressed in this document lies entirely with the author(s).